Petrogenesis of granitic rocks: a source-based perspective

Tony I. S. Kemp

B.Sc (Hons), La Trobe, Melbourne

A thesis submitted for the degree of Doctor of Philosophy

The Australian National University

Canberra

August 2001

To Karen,

for your love, strength and patience

DECLARATION

All of the results, and interpretations derived therefrom, reported in this thesis are my own, except where due reference is made in the text. The people who provided scientific input essential for formulating ideas, and those involved in the production of the thesis, are listed in the acknowledgements.

I certify that this thesis contains no material that has been submitted for any degree or qualification in any other tertiary institution.

Tony I.S. Kemp August 2001

ACKNOWLEDGEMENTS

I am indebted to my supervisor, Professor David Ellis, who provided immense support, guidance and friendship throughout my time at the A.N.U., especially during some trying times. His inspiration and insight was the catalyst for the evolution of many ideas in the thesis, and I greatly appreciate his patience in explaining (and re-explaining) concepts that I found difficult to grasp.

This study also owes much to the wisdom and foresight of Dr Chris Gray, discussions with whom were instrumental in my decision to further pursue the granites and migmatites of the GRC. I am particularly grateful for the invaluable advice and assistance during geochemical sampling, which was crucial to obtaining the data that underpins the conclusions of this thesis, and for the thorough evaluation of chapter drafts. James Anderson is also thanked for his interest and for field assistance, where his typically astute observations clarified some confusing outcrops.

Steve Eggins provided a lifeline out of the 'vortex of confusion' on more than one occasion and kindly obtained the ICP-MS data, which provided considerable insight into the enigmas of the GRC. I am grateful his keen interest and enthusiasm throughout this study, assistance during sampling, and for sharing with me his knowledge of igneous geochemistry and tectonics.

I also greatly appreciate the continued encouragement of Professor Richard Arculus during the course of this study, his willingness to discuss esoteric ideas, and the much-needed doses of scientific sanity at various times.

I would also like to acknowledge useful discussions about granitic rocks with John Sheraton, Phil Blevin and Charlotte Allen, which clarified my thoughts somewhat. The familiar faces of Andy, Helen, Moose, Ulli, and Watcharaporn provided some comfort during those times of frustration. Likewise, the friendship of Georgie Burch, Dan & Kim Isaacs, Dave Ryan and Cameron Mitchell was important for maintaining high spirits, and helping keep sight of the important things in life.

The assistance of the Geology Department technical staff is gratefully acknowledged, especially John Vickers, Norm Fraser, Tony Phimphisane, Brian Harold, Dr Ulrich Senff and Geoff Olley. Special thanks go to Maree Coldrick, who was helpful far beyond the call of duty, and whose constant cheerfulness alleviated many a gloomy moment.

The arduous task of completing this thesis was lightened considerably by the generous personal, moral and financial support of my Canberra parents, Gabby and Pepe Alarcon, who went to great lengths and personal inconvenience for my benefit, especially towards the end. Sunday night dinners were something to look forward to, and essential to preserving health, sanity and an undistorted perspective. Michelle Alarcon and Levi Foster also provided much moral support and some welcome distractions. The continued encouragement of my mother and father, Josephine and Ivan Kemp is also appreciated, especially during long fieldwork stints.

Mr Mikey and Miss Lucy performed the important task of lap warming during writing and map preparation, and are partly responsible for some of the more sinuous creek traces.

Lastly, the very existence of this thesis is testament to the unwavering support and dedication of my wonderful wife Karen. In addition to a multitude of other things, she invested immense effort into preparation of diagrams, maps, formatting, photography, and tolerated my bizarre midnight ramblings about migmatites and geochemical data. Karen's professionalism, perseverance and extraordinary courage were a constant source of admiration and motivation throughout the course of this study. I can only hope that it may reflect a small glimmer of her brilliance.

Abstract

The origin of granitic magmas is a first order geological problem, and bears directly and fundamentally upon the growth and differentiation of the continental crust. Unlike the traditional approach, which relies upon deductions from upper crustal batholiths, this study constrains models of these processes by conducting a detailed field and geochemical examination of phenomena in the *source region* of granitic plutons. A new paradigm for granitic petrogenesis is presented, which involves deep crustal mixing between efficiently-segregated 'minimum melts', derived from fluid-rich anatexis of metasedimentary protoliths, and a range of coeval, subduction-related mafic magmas. This challenges the notion that migmatites are 'failed granites' and reconciles inconsistencies inherent within previous models, in particular eliminating the requirement for high temperatures and mafic protoliths for the formation of metaluminous granites.

The Cambro-Ordovician Glenelg River Complex (GRC) (southeastern Australia) exposes a diverse range of granitic and more mafic igneous lithologies in a deep-seated metamorphic environment associated with migmatites. The latter include stromatic varieties and diatexites, both generated by water-fluxed, muscovite-involved partial melting of quartzofeldspathic protoliths, during which biotite was refractory. Three groups of primary muscovite-bearing granitic rocks are resolved, felsic adamellites-granodiorites (which are predominant), leucotonalites and biotite-rich granodiorites, all derived exclusively from metasedimentary precursors. Plutons of the first group are enveloped by stromatic migmatites and formed by coalescence of leucosome partial melts, transported from source migmatites by sheet-like magma conduits. Striking K_2O, Sr and Ba variation within individual bodies mirrors that of *in situ* leucosomes, and reflects pluton assembly by successive amalgamation of chemically distinct, but poorly blended magma 'batches', extracted from a range of metasedimentary protoliths. Depleted TiO_2, (Fe_2O_3t+MgO) and Rb manifest the remarkably effective segregation of constituent partial melts from the residual biotite-rich melanosome. Similarly, very low Zr, P and rare earth element concentrations result from the low solubility and minor entrapment of accessory minerals, and the occlusion of these by refractory biotite during anatexis. Leucotonalites have a similar petrogenesis, but were tapped from alkali feldspar-poor leucosomes. Felsic adamellite-granodiorites and leucotonalites therefore demonstrate the extraction and accumulation of granitic magma from crustal protoliths at low melt fraction *without* significant entrainment of residual material, culminating in production of restite-poor plutons *near the source region.*

In contrast, biotite-rich granodiorites are residue-replete and formed by wholesale mobilisation of melt-rich diatexite horizons, to which they are transitional. With progressive separation of the entrained residuum component, these plutons evolve towards the field of felsic plutons. However, biotite-rich granodiorites and felsic adamellites-granodiorites are not end-members of a single magmatic lineage, but result from fundamentally contrasting melt generation and segregation processes.

Mafic to intermediate igneous rocks have subduction geochemical signatures and range temporally from back-arc basalts and high-Al gabbros to boninitic diorites and late syn-compressional shoshonites. In addition, chemically distinct granodiorites are resolved that are the plutonic equivalent of adakites, generated by fusion of subducted oceanic crust. The occurrence of these arc-derived intrusives invalidates previous tectonic models and indicates development of the GRC in a supra-subduction zone setting, shedding new light on the tectonic evolution of the Gondwana continental margin in the Cambrian.

Weakly peraluminous to metaluminous granitic plutons were emplaced synchronous with *in situ* anatexis and are subdivided into seven magma 'types'. Direct field observation, confirmed by geochemistry, demonstrates that these were produced by mixing between cleanly-segregated leucosome partial melts at source and various mafic arc magmas; the compositional spectrum was extended in some cases by fractional crystallisation. The systematic petrographic and compositional differences between each successive granitic type largely reflect variation in the mafic end-member in the mixing system, itself related to the changing geodynamic environment during orogenesis. No chemical variation results from restite unmixing. Hence, the compositional features of GRC granitic rocks do not 'image' their sources, but reflect an interplay between the different mantle-derived components of their parentage and the processes involved in generating the felsic end-member from metasedimentary rock.

This study therefore highlights the significance of source-based magma generation processes, and exposes the folly of using upper crustal granitic rocks to infer the chemical character of the protolith or the thermal regime of the deep crust. As a result, petrogenetic models for high level granitic batholiths, and their implications for crustal evolution, require re-evaluation. Specifically, the efficacy of melt-residue separation at source questions the extent to which a residual component is incorporated into granitic magmas in general during formation, and casts doubt upon the applicability of restite separation for generating compositional diversity within upper crustal batholiths. The potentially pivotal role of segregated leucosome partial melts in the petrogenesis of both peraluminous and metaluminous granitic plutons, via interaction with mafic magmas, can no longer be dismissed.

Contents

Chapter 1: Introduction

1.1 Introduction

From a geochemical and isotopic perspective, the development of the Earth's continental crust, of bulk andesitic composition and unique in our solar system, has had enormous ramifications for the evolution of the entire planet. Despite this, the way in which felsic crustal materials have been extracted from the peridotitic mantle during Earth's history is not well understood. Particularly contentious are the processes responsible for intra-crustal differentiation, which have resulted in a mafic, broadly basaltic lower crust depleted in granitic components and a complementary quartzofeldspathic upper crust of 'granodioritic' composition. That granitic[1] magmatism has played the paramount role in this stratification is inescapable, and most strikingly evidenced by the fact that granitic plutons (and metamorphic and sedimentary rocks of overall granitic composition) are the most abundant constituents of the upper continental crust (Wedepohl 1991).

However, the petrogenesis of granitic rocks, specifically the nature of their sources and the causes of their wide mineralogical, geochemical and isotopic diversity, remains one of the longest standing, and consistently acrimonious, controversies in earth science (see review in Pitcher 1997). The 'granite problem' therefore bears directly and fundamentally on the origin and evolution of the crust-mantle system. For example, in the broadest sense, granitic magmas may result from two end-member processes, (1) partial melting of pre-existing crustal rocks, and (2) fractional crystallisation from mantle-derived magmas. Although these would seem intrinsically opposed, the incipient stages of (1) and the end-point of (2) necessarily produce granitic liquids of the Tuttle & Bowen (1958) 'minimum melt' composition. The implications of the disparate processes for crustal growth and differentiation are however, drastically different; the first constitutes intra-crustal recycling, with no net production of new crust, whereas the second results in considerable addition of juvenile crustal material. Hence, in considering the evolution and coupling between the mantle and the continental crust through time, ascertaining the origin and protolith of granitic plutons, particularly the proportions of crustal and mantle components, is of first order importance.

Most uncertainty concerning the 'granite problem' is sustained by the realisation that the composition of granitic magmas is shaped by many different petrogenetic processes subsequent to generation. Several of these may operate in concert at various stages during ascent of a granitic magma from its source region to final emplacement site, continuing into the sub-solidus stage (see below). Inevitably, by emplacement in the upper crust, the final mineralogy and geochemistry of the pluton therefore reflects a complex summation of multifarious petrogenetic

[1] Throughout this thesis, 'granitic' and 'granite' are used in a general sense for plutonic rocks with > 20% quartz, encompassing the alkali feldspar granite through to tonalite categories of Le Maitre (1989).

phenomena, which contrive to disguise the nature of the protolith. The composition of granitic magmas is also strongly influenced by the tectonic environment at the time of magma genesis, or during the formation of the source rocks (Barbarin 1996, 1999). Since granitic intrusives are concentrated in the upper crust, the formidable challenge confronting petrologists is to deduce the origin of granitic magmas and the nature of their sources by examining the *end product* of the various modifying processes. Unravelling these is assisted if it is known that a particular process has a specific chemical or isotopic 'fingerprint'. However, the intrinsic subjectivity associated with interpretation of indirect petrological evidence has provoked enduring debate, with the result that no consensus has yet been reached on the origin of the vast granitic batholiths in many of the worlds orogenic belts.

The alternative approach, adopted by this study, is to examine petrogenetic phenomena in the *generative regions* of granitic magmas, ideally in such areas where there is a spatial and demonstrable genetic link between partial melting and the production of granitic bodies. This enables direct comparison of the pluton with its source rocks, facilitating evaluation of the relative importance of various genetic processes in generating granitic magmas. The most commonly represented scenario in this regard is a gradual, more or less *in situ* field transition from unmelted protolith, to partially melted (i.e. 'migmatitic') rocks and ultimately a structurally concordant granitic body, as sometimes encountered in regional metamorphic terranes. Excellent examples of this are the Cooma Complex, southeastern Australia (Joplin 1942; Pidgeon & Compston 1965; White *et al.* 1974; Flood & Vernon 1978; Munksgaard 1988; Ellis & Obata 1992), the Anatectic Complex of Toledo, Spain (Barbero & Villaseca 1992; Barbero *et al.* 1995), the St. Malo Migmatite Belt, France (Brown 1979; Brown & D'Lemos 1991; D'Lemos *et al.* 1992) and the Trois Seigneurs Massif, France (Wickham 1987). In all of these cases, the central granitic body (or bodies) is considered to have derived exclusively by anatexis of the enclosing country rocks (references as cited above).

Yet even this approach is not without its shortcomings. For example, such auspicious geological situations are exceptionally rare, typically very complex, and commonly overprinted by later deformational events or retrograde metamorphism, which blur the 'primary' processes under investigation. Furthermore, in many instances, there is no similarity between the central granitic body and the volumetrically more important granitic plutons of upper crustal batholiths. This is particularly the case for low temperature, water-saturated partial melting, where the resulting granitic rocks are unusually felsic, typically muscovite-rich and have strongly fractionated geochemistry relative to the upper continental crust (e.g. Le Fort *et al.* 1987; Wickham 1987). In other cases the relationship between the migmatites and the granitic body they envelope is enigmatic; the migmatites may in fact be the *result of* rather than the underlying *cause of* granitic magmatism (e.g. White *et al.* 1967). Consequently, the connection between outcrop-scale partial melting and the formation of high level granitic batholiths is obscure, and a genetic relationship has been seriously questioned (e.g. White & Chappell 1990; Clemens 1990). The irony of this is that the conspicuously granitic-looking leucosome portion of migmatites persuaded early workers that granitic liquids could be generated from crustal rocks (e.g. Holmquist 1921, cited in Sederholm 1967), yet now the migmatite-granite nexus is regarded as tenuous at best.

However, the Cambro-Ordovician Glenelg River Complex (GRC) in southeastern Australia presents a rare opportunity to re-evaluate the migmatite-granite link. Here, a diverse range of granitic rocks, including hornblende-bearing varieties similar to those of upper crustal batholiths, are exposed in a deep-seated environment, closely associated with both migmatites and mantle-derived igneous rocks. This area therefore potentially offers a unique, source-oriented insight into- (1) the formation of various granitic bodies, (2) the processes responsible for imparting petrochemical variation between and within plutons, and (3) the interplay between crustal melting and mantle-derived magmatism during orogenesis.

1.2 Aim and organisation of the thesis

In view of the above discussion, the primary aim of this thesis is to evaluate the petrogenesis and magmatic evolution of the migmatites and igneous rocks of the GRC by an integrated field, petrographic and geochemical approach. Pursuant to this, two interrelated topics to be investigated are- (1) consideration of the mechanisms of partial melting and magma segregation and migration in the continental crust, and (2) the relationship between coeval mafic magmatism, *in situ* anatexis and granitic plutonism. The ultimate aim is to elucidate some problematic aspects concerning the origin of granitic bodies in general, with implications for crustal growth/evolution.

To achieve these aims, the thesis is organised into three parts. Part I places the GRC into a regional geological and tectonic framework (Chapter 2), provides an overview of GRC geology (Chapter 3) and outlines the approach and definitions used throughout the thesis (Chapter 4). Part II is concerned with the formation of migmatites and muscovite-bearing granitic rocks, whereas Part III deals with the petrogenesis of more mafic granitic plutons and intermediate-mafic-ultramafic rocks, discussing the implications of these for the tectonic setting of the GRC. Specific details on the internal structure of Parts II and III, together with the justification of the subdivision, is provided by section 4.2.

The remainder of this chapter reviews magmatic differentiation processes that are commonly invoked to account for the compositional diversity of granitic rocks, as a background to petrogenetic discussions in this thesis.

1.3 Petrogenesis and evolution of granitic magmas

The remarkable compositional diversity of granitic rocks, and ensuing complexity of classification schemes, is testament to the large variation in their origins, potential mantle and crustal sources, conditions of magma formation, evolutionary processes and their emplacement at differing crustal levels, in a variety of tectonic environments (Barbarin 1999). Assuming a common source, specific factors proposed to account for variation within and between granitic plutons are, in sequence from generation to emplacement-

(a) different degrees of partial melting
(b) magma mixing
(c) progressive separation of residual source material ('restite')

(d) fractional crystallisation

(e) assimilation of country rocks

None of these are mutually exclusive, and they may overlap at different stages of the evolution of any granitic magma, or occur sequentially. However, the striking linear geochemical variation that characterises many granitic batholiths is commonly ascribed to a *single* dominant differentiation process, such as magma mixing, restite unmixing or fractional crystallisation. These mechanisms are discussed below. Magma mixing is the most controversial, and the most directly relevant to this thesis, and is therefore outlined in the greatest detail.

1.3.1 Magma mixing

The term 'magma mixing' is typically used in a blanket sense for the mutual interpenetration of two coexisting magmas, generally a mafic magma and more felsic magma of different origins (e.g. Wiebe 1980). In detail, however, as different types of interactions between juxtaposed mafic and felsic magmas are possible, distinction has been made between *magma mingling*, mechanical interaction in which the participating magmas largely retain their separate identity, and magma mixing, whereby mingling is accompanied by extensive chemical exchange, blurring the identity of the original magmas (e.g. Barbarin & Didier 1992). Mixing therefore involves the thorough blending of two components, resulting in a homogeneous 'hybrid' magma in which any pre-existing crystals are rendered stable or armoured by stable minerals (Vernon 1983). Conversely, the outcome of 'magma mingling' is the physical dispersal of one magma into another as enclaves (kilometre to millimetre scale), though mechanical exchange may also occur on the scale of individual crystals. An example of this is the transfer of phenocrysts, such as quartz (Vernon 1990; Hibbard 1991; Platevoet & Bonin 1991), alkali feldspar (Reid *et al.* 1983; Vernon 1990; Bussy 1991; Elburg & Nicholls 1995), plagioclase (Reid *et al.* 1983; Barbarin 1990; Waight *et al.* 2000), hornblende (Tate *et al.* 1997), pyroxenes (Bateman *et al.* 1992) or even zircon (Elburg 1996) from one magma to another, where they become xenocrysts. The general process where a particular magma is chemically modified by interaction with a contrasting magma is termed *'hybridisation'*. Thus magma mingling induces limited hybridisation, whereas the development of a uniform intermediate rock represents the end-point of hybridisation resulting from magma mixing.

Mingling between coeval mafic and felsic magmas is a widespread and spectacular feature of many different plutonic terranes, such as the Palaeoproterozoic Lemland intrusion of southwestern Finland (Lindberg & Eklund 1988), Proterozoic Nain Anorthositic Complex, Canada (Wiebe 1980), Siluro-Devonian Lachlan Fold Belt, southeastern Australia (Vernon *et al.* 1988; Keay *et al.* 1997), the Carboniferous Sardinia-Corsica batholith, Italy (Zorpi *et al.* 1991; Poli *et al.* 1996; Poli & Tommasini 1999) and Iberian Massif, Spain (Menendez & Ortega 1999), the alkaline Permian anorogenic province of Corsica (Platevoet & Bonin 1991), Late Mesozoic Pingtan Complex, SE China (Xu *et al.* 1999) and the subduction-related Mesozoic Sierra Nevada (Reid *et al.* 1983; Frost & Mahood 1987; Barbarin 1991) and Idaho-Bitterroot (Foster & Hyndman 1990) batholiths of the western U.S.A. These examples demonstrate that physical

interaction between contrasted magmas has occurred throughout Earth's history, in diverse geodynamic environments, and involving a plethora of igneous compositions. Infusions of mafic magmas into granitic magmas, with attendant hybridisation, may occur at various stages of the pluton's crystallisation, and anywhere from the source region to the final emplacement site (Barbarin & Didier 1992). The compelling outcrop relationships are the cornerstone for petrogenetic models involving production of the granitic rocks by mixing between mafic and felsic magmas (references as cited above). In other instances, a more mafic, mantle-derived component in granitic plutons is inferred by indirect means, typically by large variation in initial Nd and Sr isotopic ratios between samples (e.g. DePaolo 1981; Gray 1984, 1990; Moreno-Ventas *et al.* 1995; Di Vincenzo *et al.* 1996; Azevedo & Nolan 1998), or by changes in Hf isotopic composition recorded by magmatically-zoned zircon crystals (Griffin *et al.* 2000). The almost ubiquitous igneous-textured mafic 'microgranular' enclaves in granitic rocks are also cited in support of magma mixing, as these are interpreted as hybridised globules of a coeval mafic magma that have quenched in the felsic granitic host (Vernon 1983, 1984, 1990; Vernon *et al.* 1988; Barbarin & Didier 1992). This interpretation is particularly robust where the enclaves form trains that are continuous with syn-plutonic mafic dykes, as described from the Coastal Batholith of Peru (Pitcher & Bussell 1985; Pitcher 1991) and the Sierra Nevada Batholith, U.S.A. (Reid *et al.* 1983). In this interpretation, the hybridisation processes that produced the microgranular enclave are, on a macroscopic scale, also considered responsible for formation of the enclosing granitic batholith (Poli & Tommasini 1991).

However, the significance of magma mingling in generating large-scale variation in granitic rocks is subject to vigorous debate, perhaps best encapsulated in the Lachlan Fold Belt of southeastern Australia. Here, combined field, geochemical and isotopic evidence leads to the postulation that granitic batholiths result from mixing crustally-derived magmas with basalt, the proportion of which increases from the cordierite-bearing to the mafic hornblende-bearing plutons (Gray 1984, 1990; Collins 1996; Keay *et al.* 1997). Some of the strongest evidence for this is that, although thought to derive from different sources (see below), the mineralogically diverse granitic rocks define a single, overlapping ε_{Nd}-initial $^{87}Sr/^{86}Sr$ isotopic array, bracketed between values for the depleted mantle and host metasedimentary rocks (e.g. Keay *et al.* 1997). Yet other workers reject magma mixing scenarios on specific chemical grounds (e.g. Chappell 1994, 1996a, 1996b; Chappell *et al.* 1987,1999, 2000), though do not provide alternative explanations for the isotopic array.

A more general objection to the applicability of magma mixing for the formation of granitic rocks is the intrinsic physical difficulty of blending hot, fluid basaltic magma with cool, highly viscous felsic magma. As summarised by Barbarin & Didier (1992), interactions between coexisting felsic and mafic magmas are constrained by their relative rheology, in turn dependent on their initial temperatures, compositions, H_2O content, degree of crystallinity and viscosity. Initially juxtaposed basaltic and felsic magmas remain discrete entities until thermal equilibration is attained, during which freezing of the basic magma and superheating of the felsic magma along the interface may occur (Sparks & Marshall 1986; Frost & Mahood 1987). Subsequent crystal exchange or mixing is only permitted if the equilibrium temperature of the mingled system is

above the solidus of the mafic component (Frost & Mahood 1987) and both magmas have low absolute viscosities and minimal viscosity contrast (Huppert *et al.* 1984; Campbell & Turner 1986). Mixing at this stage is further enhanced by convection (Campbell & Turner 1985). Rheological modelling also suggests that the relative volumes of juxtaposed mafic and felsic magmas are critical in determining the nature of their interaction (Furman & Spera 1985; Sparks & Marshall 1986). A large proportion of mafic magma (>50%) allows attainment of thermal equilibration before complete crystallisation, promoting mixing, whereas mingling occurs if the felsic component is volumetrically predominant (Sparks & Marshall 1986). In the latter case, the injected mafic magma is quenched by rapid heat loss to the felsic system, inhibiting chemical exchange and hybridisation.

These aspects are vividly exemplified by the field relations around the Lamarck Granodiorite, Sierra Nevada (Frost & Mahood 1987). Here, local hybridisation with syn-plutonic high-Al basalt becomes more pronounced where the proportion of the latter is greatest and the compositional contrast between the two magmas is the smallest (Frost & Mahood 1987). Modelling such interaction, Frost & Mahood (1987) conclude that homogenisation between juxtaposed magmas is only likely if the compositional difference is less than 10% SiO_2, or if the proportion of mafic magma exceeds 50%; even in the most favourable thermal circumstances, basalt-granite mixing cannot generate hybrids with greater than 63% SiO_2. As noted by Chappell (1996b), most granitic rocks are more silicic than this, implying the operation of other differentiation processes. However, the calculations of Frost & Mahood (1987) pertain to upper crustal pressures only and do not account for evolution of the mafic magma by fractional crystallisation or assimilation (e.g. Poli & Tommasini 1991), or double-diffusive chemical exchange between the felsic and mafic magmas (Oldenburg *et al.* 1989), which diminish temperature and compositional contrasts. Furthermore, mixing will be more effective for more fluid-rich basaltic melts than those modelled by Frost & Mahood (1987), since these have markedly lower liquidus temperatures (Sisson & Grove 1993). Such low temperature (<1000°C) 'wet' (4-6% H_2O) high-Al hornblende gabbros outcrop elsewhere in the Sierra Nevada, and are compositionally appropriate to generate the granitic rocks of the batholith at ~25% proportion in the mixture (Sisson *et al.* 1996).

Notwithstanding rheological obstacles, fluid dynamic analogue experiments have simulated a number of geological situations where extensive hybridisation between (initially) contrasting magmas is favoured. These include- (1) intrusion of basaltic sills into the continental crust, whereby buoyant partial melts generated in the underlying wallrocks rise and mix in with the overlying convective basalt (Huppert & Sparks 1988), (2) injection of mafic magma into a felsic magma chamber as a fountain (Huppert *et al.* 1984; Blake & Campbell 1986; Campbell & Turner 1986, 1989), (3) turbulent stirring in magma ascent conduits following magma chamber evacuation (Koyaguchi 1985, 1987), and (4) magma mixing in a rising magma batch (Koyaguchi 1987; Koyaguchi & Blake 1989).

Furthermore, rather than a single static event, Barbarin & Didier (1992) emphasise that magma interaction is likely to be a progressive, dynamic process, involving multiple mingling events

and producing several generations of hybrids, which become further ingredients in the mixing system. During thermal equilibration, dispersion of the intruding mafic magma as quenched globules in a felsic magma chamber increases the interface area between the magmas, enhancing diffusional exchange, and reducing the physiochemical contrast between the components (Barbarin & Didier 1992). Alkali and H_2O diffusion into the mafic liquid is expected (Johnston & Wyllie 1988), reducing its liquidus temperature. The basic magma is also continuously evolving, by fractional crystallisation of mafic phases (releasing latent heat of crystallisation to be absorbed by the felsic magma; Frost & Mahood 1987), assimilation of felsic melt or mechanical crystal exchange, all of which further reduce rheological contrasts (Poli & Tommasini 1991; Poli *et al.* 1996). Replenishment of the mafic magma may also occur, in some instances enhancing its compositional evolution (e.g. Wiebe 1996), maintaining partially molten conditions, and triggering further turbulent mingling between the juxtaposed magmas. Continued mingling during differentiation of the mafic magma produces a range of variably evolved mafic enclaves in the felsic magma, itself becoming progressively more mafic, hotter and crystal-poor, as earlier-formed phenocrysts are resorbed (Frost & Mahood 1987). As the temperatures and viscosities of the juxtaposed mafic and felsic magmas converge, successive hybrids become more homogeneous, and ultimately a single mixed magma is produced. The process is more effective in a deep crusted environment, where slow cooling rates allow more time for mechanical and diffusive liquid-liquid homogenisation (Frost & Mahood 1987). For this reason, mafic-granitic magma interactions in *deep-seated terrains* such as the GRC should be the most petrogenetically informative.

1.3.2 Restite unmixing

The restite model of White & Chappell (1977) and Chappell *et al.* (1987), developed through geochemical inferences from high level batholiths, contends that granitic plutons are mixtures of felsic melt and suspended, magmatically-equilibrated residual source material ('restite'), which becomes mobilised en masse following 30-40% partial melting of a crustal source (see also White & Chappell 1990). Subsequent differential separation of these melt and restite components during pluton ascent is invoked to engender the compositional diversity within granitic 'suites' (i.e. group of samples sharing a common source; Chappell & White 1992). In this closed-system scenario, the composition of the source, melt and restite are constrained to lie along the linear granitic chemical variation trends (White & Chappell 1977; Chappell *et al.* 1987) (Figure 1.1). This has two implications- (1) the distinctive mineralogical, geochemical and isotopic features which characterise a particular granitic suite are entirely inherited from the source rocks, and (2) the composition of the most mafic (i.e. restite-dominated) granitic sample of a suite approaches that of the protolith (Figure 1.1). Chappell (1979, 1984, 1996) and Chappell *et al.* (1987) emphasise that in this way granitic rocks 'image their sources' and therefore may be utilised as probes into the deep, inaccessible parts of the crust (Chappell *et al.* 1988).

It follows from this that the nature of the restite contained by a granitic magma depends on its inferred protolith. For granitic rocks of Lachlan Fold Belt two fundamentally contrasting sources are postulated, (meta)igneous or infracrustal rocks that have not undergone a weathering cycle,

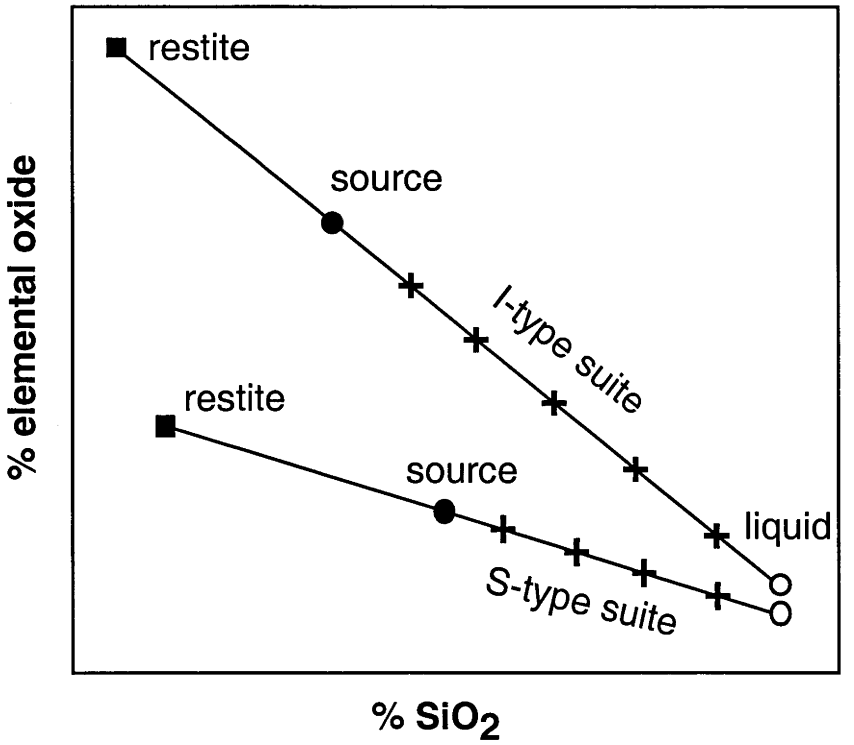

Figure 1.1. Production of a hypothetical I- and S-type granitic suite by partitioning of the source composition into restite and melt components. Granitic rocks (crosses) comprise variable proportions of these components. Note that the linear granitic variation could also result from simple mixing between two end-member magmas.

such as an accreted mafic underplate, and (meta)sedimentary or supracrustal rocks that have experienced weathering at the surface. A contemporaneous mantle-derived magma is not involved, and thus granitic generation amounts to large scale reworking of older crust. Granitic rocks derived from meta-igneous protoliths ('I-types') are metaluminous to weakly peraluminous, typically containing hornblende, clinopyroxene (both of which are diagnostic), titanite, allanite and Al-poor biotite, and are usually strongly oxidised or magnetite-bearing (White & Chappell 1977; Chappell & White 1992). Restite in I-types consists of hornblende-rich microgranular enclaves, clots of mafic minerals, especially pyroxene mantled by hornblende and/or biotite, and corroded, calcic plagioclase cores (White & Chappell 1977; Chappell *et al.* 1987).

Granitic rocks derived from metasedimentary protoliths ('S-types') are strongly peraluminous and contain dark red-brown aluminous biotite, accompanied by cordierite, aluminosilicate, garnet or muscovite. The inferred restite component includes high grade metasedimentary enclaves, orthopyroxene-bearing microgranular enclaves, biotite aggregates pseudomorphing orthopyroxene, garnet and cordierite with sillimanite inclusions, corroded plagioclase cores and cores of zircon crystals with U-Pb ages older than emplacement ages (White & Chappell 1977; Chappell *et al.* 1987). Notably, the latter also occur in the Lachlan I-types (Williams *et al.* 1992), indicating that these also incorporate a recycled or sedimentary-derived component, at variance with the 'I'-type status.

However, much of the petrographic evidence for restite in the Lachlan Fold Belt granites is ambiguous and has been repeatedly challenged (e.g. Vernon 1983, 1990; Wall *et al.* 1987). In some cases, the hornblende-bearing enclaves in I-types are clearly derived by syn-magmatic mingling with coeval basaltic intrusions and are not restite (Vernon *et al.* 1988; Keay *et al.* 1997). In addition, microgranular enclaves in S-types have distinctive igneous textures that are compatible with the undercooling and hybridisation of an intermingled basaltic globule, rather than entrainment as solid, refractory restite (Vernon 1983, 1990; Elburg & Nicholls 1995; Collins 1999).

Many uncertainties concerning the restite model therefore persist. For example, how much restitic debris is actually entrained by granitic magmas upon migration from the source, and can this impart the observed geochemical variation in granitic suites? What is the nature of this material, and what factors control its incorporation, or otherwise? Although these remain open questions, they are most likely to be resolved by examination of deep crustal anatectic terranes, rather than by studies of upper crustal plutons that have ascended kilometres from their generative region.

A final point is that restite separation cannot account for large isotopic variation within a particular granitic suite. That such isotopic variations occur is the basis for magma mixing models (see above). A corollary of this is that the mineralogy, geochemistry or isotopic composition of a granitic pluton with a mantle-derived component does not necessarily reflect that of the source, invalidating the I-S dichotomy. The latter is also meaningless for granitic rocks that have mixed crustal sources or have experienced other open-system behaviour, such as crustal assimilation or melt loss during consolidation. For these reasons, the genetic I-S notation is not used in this thesis. GRC granitic rocks are alternatively classified entirely by mineralogical and geochemical means that convey no implication for putative protoliths (section 4.1.3).

1.3.3 Fractional crystallisation

The potential importance of fractional crystallisation in generating compositional diversity in granitic rocks was first advocated by Bowen (1928). Although the physiochemical aspects are complicated (see Chapter 4 of Wilson 1989), the process fundamentally involves the continuous removal of precipitated crystals from a crystallising granitic liquid, the composition of which is progressively modified as a result. Granitic rocks may therefore comprise accumulations of the precipitated minerals, or represent one or more of the residual liquid compositions, in the simplest case defining a 'liquid line of descent' (Bowen 1928). For granitic magmas, at the extreme the latter must tend towards the Tuttle and Bowen (1958) 'minimum melt composition', the lowest temperature that hydrous melt can be in equilibrium with quartz and feldspar. This commonly results in linear chemical variation for the major elements against differentiation indices (e.g. Wyborn *et al.* 1987), though inflections may occur for certain elements with the appearance of a new phase in the fractionating assemblage (e.g. Figure 4.7 in Wilson 1989). Incompatible trace element abundances or incompatible/compatible element ratios (e.g. Rb/Ba, La/Yb) characteristically exhibit curved or inflected trends, reflecting the exponential functions describing melt-solid partitioning and variation of partition coefficients during crystallisation (e.g. Rb and Ba concentrations in the Koetong suite of the Lachlan Fold Belt, Chappell 1996b).

Changes in certain elemental ratios with differentiation of granitic liquids can provide insight into the identity of the fractionating phase. For example, markedly increasing Rb/Sr is the signature of plagioclase fractionation, since this excludes Rb and accommodates Sr in silicic liquids (Rollinson 1993).

In contrast, the composition of cumulate rocks is generally more variable, as these are affected not only by the chemistry of the accumulating minerals but also by the amount of trapped interstitial liquid. An example of granitic rocks thought to form by progressive crystal accumulation from a high temperature parental liquid is the Boggy Plain 'Supersuite' of the eastern Lachlan Fold Belt (Wyborn *et al.* 1987).

A likely outcome of fractional crystallisation is the production of vertically stratified and concentrically zoned plutons. These may either be cumulates complementary to fractionating liquids, form virtually *in situ* by sidewall crystallisation, (e.g. Loch Doon Pluton, Scotland, Tindle & Pearce 1981; Boggy Plain Supersuite, Wyborn 1998), or originate by the successive emplacement of fractionated liquid pulses tapped from an underlying evolving magma chamber (e.g. Mahood & Cornejo 1992).

PART I

Geological and tectonic framework of the Glenelg River Complex

(includes Chapters 2 to 4)

Chapter 2: Regional geology of the Glenelg River Complex

2.1 Tectonic overview

Southeastern Australian geology is dominated by two major tectonic entities, the Neoproterozoic to Late Cambrian Delamerian Orogenic Belt and the Palaeozoic Lachlan Fold Belt (Figure 2.1). The Delamerian Orogenic Belt is equated with the Tyennan Orogen in Tasmania and the trans-Antarctic Ross Orogen, and has most prominent exposure in the Mount Lofty Ranges of South Australia. Developed along the eastern palaeo-Pacific margin of Gondwana, it records intermittent periods of rift-related sedimentation commencing in the Neoproterozoic (Preiss 1990), eventually terminated by the convergent deformation and crustal thickening of the Cambro-Ordovician Delamerian Orogeny. The underlying cause of this massive tectonic upheaval, which involved a transition from extension to intense east-west shortening, remains problematic.

The Lachlan Fold Belt extends from northeastern NSW to western Victoria, and is dominated by quartz-rich Late Cambrian to Ordovician deep marine turbidites, deposited following the Delamerian Orogeny. Rocks have been subjected to several deformational and metamorphic episodes, coupled with voluminous igneous intrusion, from the Late Ordovician to Middle Devonian, collectively referred to as the Lachlan Orogeny (Gray & Foster 1997).

In Victoria, rocks of the Lachlan Fold Belt have been placed into a number of tectonic zones (e.g. Gray *et al.* 1988) (Figure 2.1), distinguished by subtle differences in structural grain, timing of deformation and tectonic vergence (Gray & Foster 1997). However, several studies, summarised by VandenBerg *et al.* (2000), have established that the westernmost of these, the Glenelg and Grampians-Stavely Zones, actually constitute the eastern extension of the Delamerian Orogen. The main component of the Glenelg Zone is the enigmatic Glenelg River Complex (GRC), comprising ~1750 km^2 of diverse igneous and metamorphic lithologies that are unique in Victoria. The Grampians-Stavely Zone further east incorporates low grade metasedimentary and largely buried metavolcanic sequences, some of the latter being subduction-related, and lies at the interface with the Lachlan Fold Belt.

Unlike in South Australia, the Delamerian Orogen segments in western Victoria are poorly documented, in part reflecting deep weathering and limited exposure. This applies especially to the GRC, which has been historically neglected in reviews of Victorian geology (e.g. Douglas & Ferguson 1988). As such, the significance of the GRC, and its relationship with other elements of the Delamerian Orogenic Belt, has remained poorly understood. The terrane has consequently endured as a major stumbling block in tectonic reconstructions of southeastern Australia.

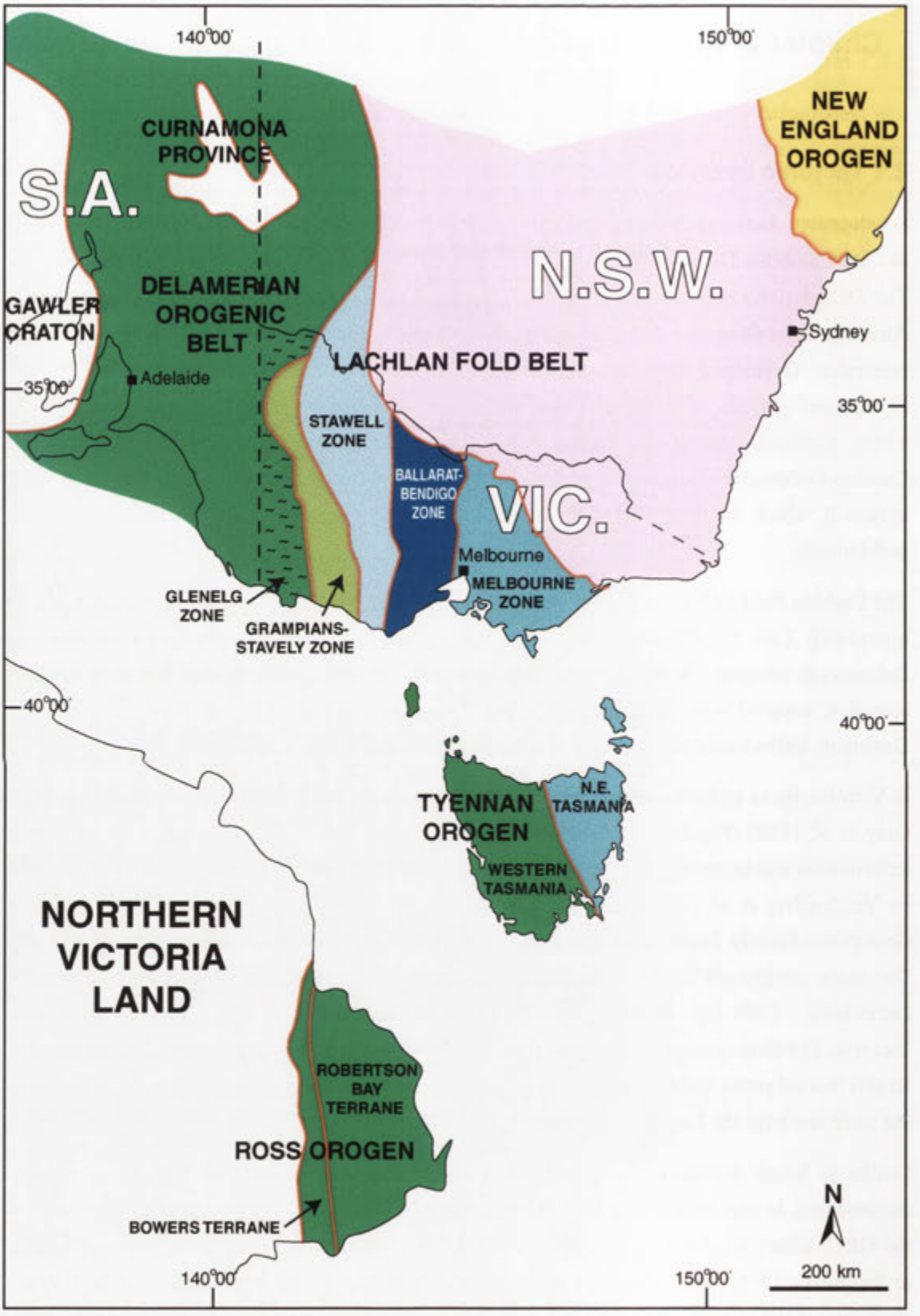

Figure 2.1. Tectonic map of southeastern Australia and Northern Victoria Land (Antarctica), showing the main orogenic entities and structural zones of central and western Victoria (modified from VandenBerg *et al.* 2000, with the Antarctica-Australia reconstruction from Royer & Rollet 1997). The Lachlan Fold Belt zones of eastern Victoria and New South Wales are not shown.

2.2 Delamerian Orogenic Belt in South Australia

2.2.1 Major geological elements

The Delamerian Orogenic Belt comprises a 750 km, N-S trending segment of a 5000 km long orogenic structure developed along the eastern Gondwana margin in the Neoproterozoic. It borders the Archaean to Mesoproterozoic Gawler Craton to the west, and the Palaeoproterozoic-Mesoproterozoic Mount Painter and Willyama Inliers of the Curnamona Province to the north and east (Haines & Flottman 1998) (Figure 2.1). Fault-bounded slices of Palaeoproterozoic-Mesoproterozoic basement also occur on the Fleurieu Peninsula (Sandiford & Flottman 1999) (Figure 2.2). To the east, the Delamerian Orogen is transitional to the slightly younger Lachlan Fold Belt.

The Delamerian Orogenic Belt is characterised by repeated and protracted episodes of rift- and sag-related sedimentation in intra-cratonic basins, spanning the Late Proterozoic to Early Ordovician (Preiss 1993). Initial subsidence commenced ~850 Ma (Belperio *et al.* 1998) with deposition of siliciclastic and carbonate rocks, followed by voluminous extrusion of tholeiitic basalt (Crawford & Hilyard 1990). The termination of volcanism is marked by a tuffaceous unit dated at 802±10 Ma (Fanning *et al.* 1986), whereupon further rifting induced deposition of the platformal Callana, Burra, Umberatana and Wilpena Groups (Hilyard 1990; Sandiford & Flottman 1999). These rocks exhibit sigmoidal structural trends and extend from the Flinders Ranges south to the Fleurieu Peninsula.

In the southern Delamerian Orogen, reactivation of subsidence in the Early Cambrian produced two major sedimentological packages, the Normanville and Kanmantoo Groups (Gravestock & Gatehouse 1995). The oldest is the fossiliferous Normanville Group, prograding from basal sandstone to platformal carbonates and phosphatic shale (Daily *et al.* 1976). Submarine alkaline lavas and pyroclastics of the Truro Volcanics are intercalated within the latter, from which a U-Pb (zircon) age of 526±4 Ma has been obtained (Cooper *et al.* 1992). The Normanville Group is disconformably overlain by the turbiditic Kanmantoo Group (Haines *et al.* 2001), deposited rapidly during further crustal attenuation in the Early Cambrian (Preiss 1993). The type Kanmantoo Group sequence occurs along the Fleurieu Peninsula, where thickly-bedded metagreywackes are predominant, variously interspersed with metasiltstone, phyllite, minor calcareous members and pyritic black slate (Sprigg & Campana 1953; Daily & Milnes 1971, 1973; Flottman *et al.* 1998). The entire sequence is ~7-8 km thick (Haines *et al.* 2001) though structural repetition of some units may exist (Sandiford & Flottman 1999). Deposition commenced shortly after eruption of the Truro Volcanics and continued to the onset of the Delamerian Orogeny at ~520-515 Ma (see below).

With the Normanville Group, the Kanmantoo Group outcrops in an arcuate belt traced from the Mount Lofty Ranges southwest to the Fleurieu Peninsula and Kangaroo Island (Figure 2.2). Although overlain by Murray Basin sediments further east, a bifurcation of this belt is geophysically traced southeastwards towards the GRC in western Victoria (Brown *et al.* 1988; see below).

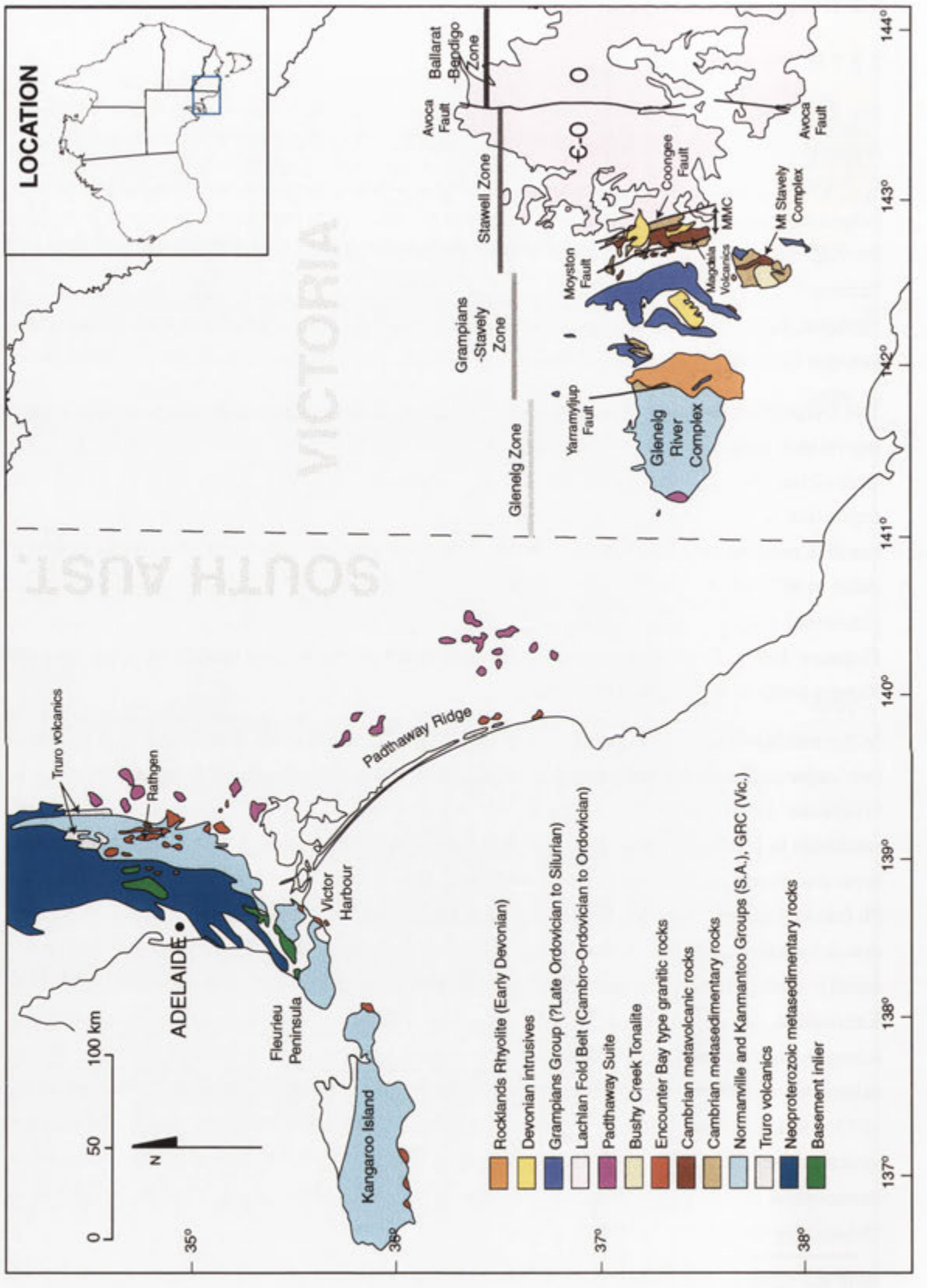

Figure 2.2. Geological map of the southern Delamerian Orogenic Belt and western Lachlan Fold Belt, highlighting specific localities and rock units referred to in the text; sedimentary cover rocks are omitted for clarity (MMC = Moornambool Metamorphic Complex). South Australian geology is from Foden *et al.* (1999) and Victorian geology is modified from VandenBerg *et al.* (2000).

2.2.2 Delamerian Orogeny

The Neoproterozoic and Cambrian sedimentary sequences were subsequently deformed and metamorphosed during the Cambro-Ordovician Delamerian Orogeny, involving west- and southwest-directed convergence towards the Gawler Craton (Thomson 1969; Drexel & Preiss 1995; Haines & Flottman 1998). Deformation and metamorphism was most intense in the southeast, with thrust-accommodated and basement-involved shortening of up to 50% (Flottman *et al.* 1998) and local attainment of migmatite grade. The onset of orogenic activity is thought to be signalled by the emplacement of a pre- to syn-D_1 igneous body, the Rathjen Gneiss, at 514±5 Ma (Foden *et al.* 1999; see below). Alternatively, Haines & Flottman (1998) consider that uplift associated with incipient Delamerian compression commenced slightly earlier at 523±2 Ma. Termination of convergent orogenesis is constrained by the intrusion of undeformed bimodal igneous rocks, which have inferred crystallisation ages of ~480-490 Ma (Turner *et al.* 1996).

Regional metamorphism in the southern Delamerian Orogen was of high temperature, low pressure type and imposed chlorite to migmatite metamorphic zones, rocks of which record the imprint of three deformational episodes (Offler & Fleming 1968; Mancktelow 1990). Although the metamorphic zone configuration is complicated by large-scale folding and faulting, grade progressively increases from northwest to southeast across the orogen, with the highest grades confined to the Kanmantoo Group sequence of the southeastern Mount Lofty Ranges. Here, biotite zone rocks prograde through successive andalusite-staurolite, fibrolite and prismatic sillimanite zones, ultimately reaching migmatite grade around a cluster of syn-tectonic felsic intrusives (Offler & Fleming 1968; Mancktelow 1990). Peak metamorphic temperatures are estimated at 640-650°C in the migmatite zone (Mancktelow 1990), where Fleming & White (1984) argue that partial melting preceded penetrative deformation and persisted throughout the structural history. An early thermal perturbation is also implied by the pre-deformational injection of basaltic dykes, concentrated in the highest grade zones of the Kanmantoo Group (Liu & Fleming 1990).

2.2.3 Granitic rocks of the southern Delamerian Orogenic Belt

Most granitic plutons of the Delamerian Orogen are confined to the highest grade parts of the Kanmantoo Group (Foden *et al.* 1990), where intrusion spanned 30 million years (Sandiford *et al.* 1992). Following Gray (1990) two distinct associations are recognised, Encounter Bay type plutons and Murray Bridge type plutons.

(a) Encounter Bay type

Major plutons of this association include those at Palmer, Reedy Creek and Monarto in the migmatite zone, and the 'Encounter Bay Granites' around Victor Harbour and the southern coast of Kangaroo Island (Milnes *et al.* 1977; Foden *et al.* 1990; Milnes 1990) (Figure 2.2). They range from tonalite to granite (*sensu stricto*) and are typically metaluminous, with biotite sometimes accompanied by hornblende, magnetite and titanite (Foden *et al.* 1990). All exhibit contacts against Kanmantoo Group metasedimentary rocks and were emplaced throughout the

deformational history, with variable development of tectonic fabrics. Radiometric dating (Rb-Sr) by Milnes *et al.* (1977) brackets crystallisation of the 'Encounter Bay Granites' between 506-515 Ma, although a 523±6 Ma age (Rb-Sr) has been obtained for the foliated Vivonne Bay Granite on Kangaroo Island (Drexel & Preiss 1995). More recent U-Pb (zircon) dating reveals an emplacement interval for syn-tectonic igneous bodies from ~514±5 Ma for the sheet-like Rathjen Gneiss (Foden *et al.* 1999) through to 486±6 Ma for the Summerfield Granodiorite (Drexel & Preiss 1995).

Chemically, Encounter Bay type plutons at the lower silica range are rather sodic but otherwise similar to average Lachlan Fold Belt 'I-types' (Foden *et al.* 1990). Isotopic compositions are mostly primitive, with the Reedy Creek Granodiorite having low initial $^{87}Sr/^{86}Sr$ (0.706) and moderately high initial ε_{Nd} (-2.5) (Sandiford *et al.* 1992). These vary continuously through to more felsic compositions, like the Monarto, Palmer and 'Encounter Bay Granites', some of which also have more evolved isotopic compositions approaching those of the host Kanmantoo Group sequence (e.g. Vivonne Bay Granite, initial $^{87}Sr/^{86}Sr = 0.719$, $\varepsilon_{Nd} = -13.6$) (Sandiford & Flottman 1999).

(b) Murray Bridge type

Isolated granitic outcrops of Murray Bridge type protrude from Tertiary sediments east of the Mount Lofty Ranges (Figure 2.2). Exposures are scattered along a geophysically-imaged basement high, the Padthaway Ridge, that trends southwest under the Murray basin towards the Victorian border. Plutons lack deformational fabrics and were therefore emplaced after the compressional phase of the Delamerian Orogeny (Turner *et al.* 1996). Granitic rocks are associated with gabbros and comagmatic rhyolite (Foden *et al.* 1990), with all grouped as the 'Padthaway Suite' (Turner *et al.* 1992). Local mingling and hybridisation between mafic and felsic lithologies confirms that basaltic and granitic magmas were contemporaneous (Turner & Foden 1996).

Although contacts are concealed, drilling and aeromagnetic data reveal that Murray Bridge type plutons intrude high grade metasedimentary rocks analogous to those of the Kanmantoo Group (Parker 1986; Brown *et al.* 1988). Aeromagnetic trends indicate that both metasedimentary and granitic lithologies have sub-surface continuation southeastward to the vicinity of the GRC (Brown *et al.* 1988). Importantly, granitic outcrops of the western GRC closely resemble the distinctive intrusives of the Padthaway Ridge (section 3.5.1), suggesting that the two terranes are contiguous (Foden *et al.* 1990; Turner *et al.* 1993a; Anderson & Gray 1994). The link is reinforced by similarity between the Kanmantoo Group and metasedimentary rocks of the GRC (Foden *et al.* 1990; Turner *et al.* 1993a; Anderson & Gray 1994).

Murray Bridge type plutons exhibit profound petrographic, isotopic and geochemical differences from the slightly older, deformed Encounter Bay type intrusions. All are homogeneous, coarse grained and siliceous pink to green rocks with abundant alkali feldspar phenocrysts, commonly with albitic overgrowths (Foden *et al.* 1990; Turner *et al.* 1992). They are further distinguished by large smoky quartz grains, granophyric textures and sporadic

fluorite (Turner *et al.* 1992). Hornblende and biotite are minor mafic phases, rarely accompanied by titanite, pigeonite or relict fayalite (Turner *et al.* 1992). Geothermometry establishes that minerals crystallised from high temperature, water-poor magmas that were emplaced at shallow crustal levels (~1000°C at <100 Mpa; Turner *et al.* 1992), corroborated by the association with volcanics (Turner & Foden 1996).

Compared to Encounter Bay types, Murray Bridge type plutons are silica- and K_2O-rich, with much lower TiO_2, MgO and CaO (Foden *et al.* 1990). Depletions in Sr, Eu and Ba, with enrichment in Rb, Ga, Nb, light rare earth elements and Zr, indicate a highly fractionated 'A-type' affinity (Foden *et al.* 1990; Turner & Foden 1996). The isotopic composition of Murray Bridge type plutons is uniformly primitive (initial $^{87}Sr/^{86}Sr$ <0.707; Gray 1990) and resembles that of coeval gabbros (Sandiford *et al.* 1992; Turner & Foden 1996). Accordingly, Turner *et al.* (1992) infer derivation by prolonged fractionation from parental tholeiitic basalt.

2.3 The Lachlan Fold Belt in western Victoria

From east to west, the Lachlan Fold Belt in central and western Victoria comprises the thrust-bounded Melbourne, Ballarat-Bendigo and Stawell Tectonic Zones (Gray & Foster 1997) (Figures 2.1, 2.2). Rocks of the latter are extensive in western Victoria (Gray *et al.* 1988; Wilson *et al.* 1992) and adjoin the Grampians-Stavely Zone further west (Gray *et al.* 1988; VandenBerg 1999). Accordingly, the Stawell Zone – Grampians-Stavely Zone boundary is a major crustal discontinuity that separates the Lachlan Fold Belt from the slightly older Delamerian Orogen.

2.3.1 Stawell Zone of the Lachlan Fold Belt

The Palaeozoic geology of the Stawell Zone is concealed to the north by Cainozoic Murray Basin sediments and to the south by Tertiary volcanics, but is otherwise dominated by turbidites of the Cambro-Ordovician St Arnaud Group (Wilson *et al.* 1992; Cayley & Taylor 1999). These overlie a Cambrian metabasaltic substrate of oceanic affinity, slivers of which are exposed in major fault zones (Anderson *et al.* 1998; Cayley & Taylor 1998). The turbidites experienced deformation and intermediate pressure metamorphism (Offler *et al.* 1998) during the Late Ordovician to Early Silurian (~450-420 Ma; Cayley & Taylor 1999), plus emplacement of Early to Middle Devonian granitic intrusives (~380-410 Ma; Richards & Singleton 1981). These rocks are separated from the younger Ordovician turbidites of the Ballarat-Bendigo Zone further east by the Avoca Fault (Gray *et al.* 1988) (Figure 2.2).

To the west, across the Coongee Fault, the St Arnaud Group turbidites are supplanted by higher grade, complexly deformed metasedimentary and metabasitic rocks of the Moornambool Metamorphic Complex (MMC) (Cayley & Taylor 1999) (Figure 2.2). Metabasites of this assemblage, collectively termed the Magdala Volcanics, were derived from tholeiitic basalt to ultramafic boninitic precursors, and define an aeromagnetically-prominent belt at the eastern fringe of the Grampians Ranges (VandenBerg *et al.* 2000) (Figure 2.3). Although the geochronological characteristics of MMC rocks are yet to be ascertained, they are interpreted as upthrust, mid-crustal representatives of the LFB (Cayley & Taylor 1998, 1999). The 15 km wide

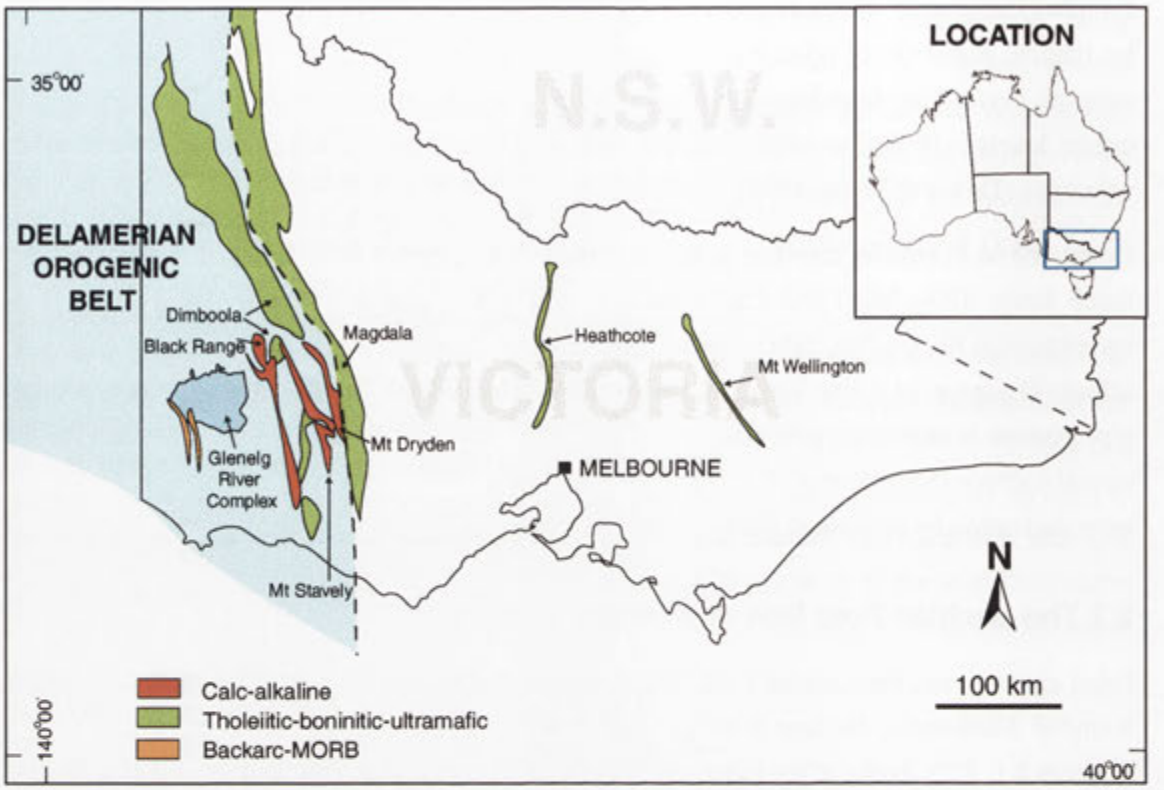

Figure 2.3. Distribution of Cambrian (or older) metavolcanic rocks in Victoria, as constrained by outcrop, drillhole and geophysical evidence (modified from VandenBerg *et al.* 2000). Only the major occurrences are indicated.

MMC sequence is dissected by west-dipping faults and extends west to a major east-dipping thrust, the Moyston Fault (Cayley & Taylor 1999) (Figure 2.2). Towards this structure the MMC progrades from lower greenschist facies, adjacent the Coongee Fault, to middle amphibolite facies in the immediate hangingwall of the Moyston Fault, with concomitant intensification of shear strain and development of mylonitic foliations (Cayley & Taylor 1999). Here, structurally interleaved amphibolite and metapelitic schist form broad zones of tectonic melange (VandenBerg *et al.* 2000).

2.3.2 Western boundary of the Lachlan Fold Belt

Due to limited exposure and paucity of age constraints, the nature and placement of the western boundary of the Stawell Zone with the Delamerian Orogen is contentious, and has been variously located by different authors (see discussion in Gibson & Nihill 1992 and Anderson & Gray 1994). However, the recent consensus is that the contact between the zones is demarcated by the Moyston Fault (Foster *et al.* 1998; Cayley & Taylor 1999), where highly strained MMC rocks are thrust over weakly deformed sandstone (Cayley & Taylor 1999). The latter is correlated with the Glenthompson Sandstone, which is part of the Delamerian Orogen (see below). Based on these relationships, Cayley & Taylor (1999) propose that the Moyston Fault separates mid-crustal Lachlan Fold Belt lithologies from older, less deformed Delamerian

Orogenic Belt crust, and thus defines the interface between the two major orogenic structures of southeastern Australia. However, the geological affinity of the MMC remains uncertain, and thus proper evaluation of this suggestion awaits more detailed study.

2.4 Delamerian Orogen in western Victoria

Encompassing basement rocks overprinted by the Delamerian Orogeny, the Glenelg and Grampians-Stavely Zones constitute the eastern extension of the Delamerian Orogenic Belt into Victoria. Glenelg Zone exposures are covered by Murray Basin sediments west of the Glenelg River, but, as outlined above, the geology is contiguous with that of the Mount Lofty Ranges. The eastern boundary with the Stawell Zone of the Lachlan Fold Belt is tentatively assigned to the Moyston Fault.

2.4.1 Grampians-Stavely Zone

This zone, which includes the younger sedimentary and plutonic rocks of the Grampians Ranges (below), extends west from the Moyston Fault to the Yarramyljup Fault (Figure 2.2). In the east, Cambro-Ordovician geology is dominated by two sub-parallel, northwesterly-trending belts of volcanic, pyroclastic and epiclastic rocks, the Mount Dryden Greenstone Belt and the Mount Stavely Volcanic Complex (Buckland 1986) (Figures 2.2, 2.3). Both of these are flanked by, and faulted against, the quartz-rich Glenthompson Sandstone, of Cambrian age (Buckland 1986). All lithologies are mildly deformed and overprinted by prehnite-pumpellyite facies metamorphism (Buckland 1986).

At the eastern fringe of the Grampians mountains, the 5 km wide Mount Dryden Greenstone Belt comprises a conformable sequence of pillowed mafic andesite-dacite lavas and agglomerates, overlain by volcanogenic sediments (Crawford 1988). Like rocks at Mount Stavely, primary igneous mineral assemblages and textures are widely preserved (Crawford 1988).

Further west, the Mount Stavely Volcanic Complex outcrops over a strike length of ~18 km, though aeromagnetic trends indicate continuation northwest beneath the Grampians Ranges and Murray basin (Gray *et al.* 2001). It encompasses three main volcano-sedimentary units, and a thin serpentinite lens (Buckland 1986). Andesitic lavas, breccias and volcanogenic sandstones are predominant, with lesser dacite, basalt and minor rhyolite; thin bands of pyritic shale, siltstone and chert are intercalated (Buckland 1986). The sequence is intruded by several small bodies of the hornblende- and plagioclase-phyric Lalkaldarno Tonalite (Buckland 1986). Delamerian ages of 500±2 Ma obtained from the tonalite (Ar-Ar, hornblende; Foster *et al.* 1998) and 495±5 Ma for a metadacite (U-Pb, zircon; Stuart-Smith & Black 1994) provide minimum age constraints on formation of the volcano-sedimentary rocks. Chemically, Mount Stavely lavas have medium-K calc-alkaline affinity, consistent with either eruption in a mature island arc setting (Crawford 1988) or a post-collisional continental rift-related origin (Stuart-Smith & Black 1994; Crawford *et al.* 1996). In contrast, mafic andesites at Mount Dryden have distinctly low TiO_2 and high MgO contents (Crawford 1988), features diagnostic of the boninite magma series, erupted exclusively above subduction zones.

Several granitic bodies occur west of the Mount Stavely Volcanic Complex, which crosscut and contact metamorphose the Glenthompson Sandstone. The largest of these, the hornblende-bearing Bushy Creek Tonalite, is Ar-Ar dated (biotite) at 500±2 Ma and 499±2 Ma (Foster *et al.* 1998) and manifests the easternmost extent of Delamerian plutonism.

Immediately west of Mount Stavely, a striking linear magnetic body, which extends ~360 km northwest to the South Australian border, outlines the Dimboola Igneous Complex (VandenBerg *et al.* 2000) (Figure 2.3). This is largely buried, dismembered by numerous faults, and structurally intercalated with the Mount Stavely Volcanic Complex in the subsurface. Drilling at several localities has identified a complex assemblage of mafic to ultramafic, tholeiitic to boninitic volcanic and plutonic rocks that are variably altered to greenschist facies assemblages (VandenBerg *et al.* 2000). Based on comparison with similar rocks in western Tasmania, the Dimboola Igneous Complex has been interpreted as a Cambrian arc-forearc complex accreted to the Gondwana margin during the Delamerian Orogeny (Taylor *et al.* 2000; VandenBerg *et al.* 2000), and is crucial in tectonic reconstructions of southeastern Australia (see below).

Delamerian Orogenic Belt rocks are obscured further north and west by the ?Late Ordovician to Silurian Grampians Group, which constitutes the Grampians-Black Ranges and several western outliers (Figure 2.2). The sedimentary succession is dominated by quartz sandstone, with lesser siltstone and mudstone, and is thought to have been deposited in a passive marine basin along the Delamerian Orogen margin (Cayley & Taylor 1999). In the Grampians Ranges, the stratigraphy is duplexed by bedding-parallel thrusts (Cayley & Taylor 1999) and intruded by ~400 Ma granitic bodies (Gray 1990). Emplacement of these plutons post-dates thrusting (Cayley & Taylor 1999), confirming that deformation and igneous intrusion was broadly coeval with that of the Stawell Zone, and that the Grampians Group is an outlier of the Lachlan Fold Belt. The Early Devonian Rocklands Rhyolite, co-magmatic with granitic rocks in the Grampians Ranges (C.M. Gray, *unpubl. data*), is extensive to the west of the Black Ranges, overlying erosional Grampians Group remnants and basement rocks of the Glenelg Zone (Figure 2.2).

West of the Grampians Ranges, Cambro-Ordovician basement rocks are blanketed by Tertiary basalt, laterite and recent alluvium. However, in the Black Ranges, lenses of altered Cambrian volcanic rock, overlain by weakly metamorphosed chert, slate and siltstone, are faulted against Grampians sandstone (Spencer-Jones 1965). Volcanic lithologies are dominantly basalt and andesite, though dacite and rhyolite also occur (VandenBerg *et al.* 2000). Aeromagnetic trends imply that these rocks form branching belts in the subsurface (Cayley & Taylor 1997) (Figure 2.3).

The Grampians-Stavely Zone is separated from the Glenelg Zone further west by the Yarramyljup Fault, which juxtaposes amphibolite facies GRC schists with low grade slates (Gibson & Nihill 1992) (Figure 2.4). The affinity of the slates is uncertain but they are unconformably overlain by Grampians Group rocks (Gibson & Nihill 1992) and therefore possibly equivalent to the Cambrian slates in the Black Ranges.

2.4.2 Glenelg Zone

Located in far western Victoria, the Glenelg Zone encapsulates the geology of the Glenelg River Complex (Chapter 3). Rocks of the GRC underlie the Dundas Tablelands, a dissected Tertiary laterite peneplain developed on a deep weathering profile, and occupy a triangular ~1750 km^2 area approximately between the towns of Balmoral, Dergholm and Coleraine (Figure 2.4). Exposures commence immediately west of the Yarramyljup Fault, and are demarcated from the recent Murray Basin sediments to the northwest by the Glenelg River. To the southwest, GRC geology is overlain by Early Cretaceous sedimentary rocks.

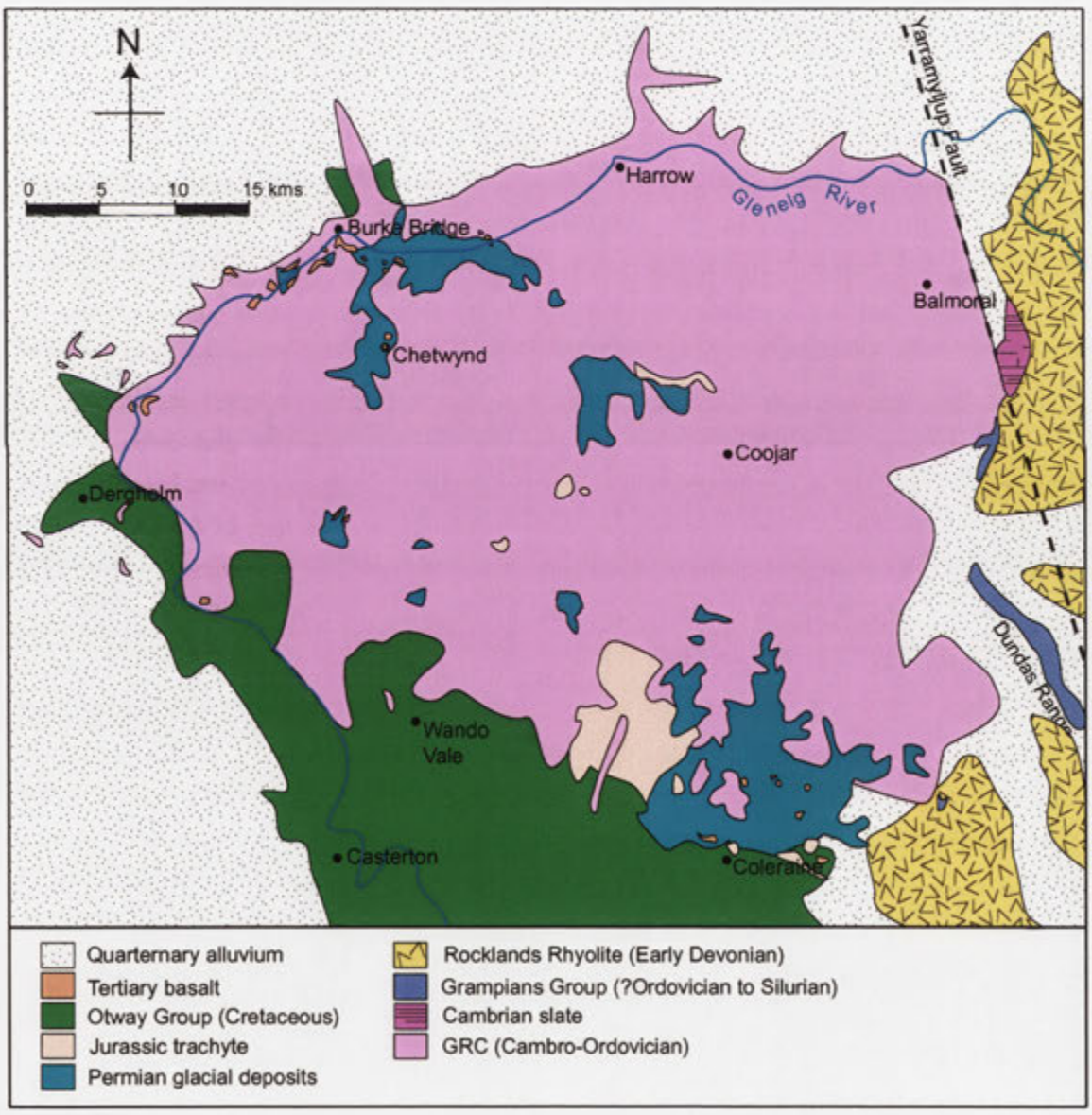

Figure 2.4. Simplified geology of the Glenelg Zone (excluding Tertiary laterite), depicting the distribution of rocks of the various lithological components (adapted from Douglas & Spencer-Jones 1971).

Beneath the lateritic capping, the GRC is also variably obscured by unconsolidated Tertiary sediments, Permian fluvioglacial deposits, prominent around the Coleraine and Chetwynd districts, and extensive flows and domes of Jurassic trachyte between Coleraine and Wando Vale (Figure 2.4). Eocene 'Older Volcanics', alkaline basaltic lava flows, dykes and plugs, occur sporadically across the GRC, most notably along the Glenelg River southwest of Burke Bridge.

Accordingly, GRC lithologies are poorly exposed and only manifest along the valleys of incised watercourses, where outcrop is commonly intensely weathered. Nevertheless, semi-continuous exposure is present along many larger drainages such as the Glenelg and Wando Rivers, and reasonably fresh material is obtainable from water-washed outcrops in stream beds.

2.5 Tectonic models

Tectonic reconstructions for the eastern Delamerian Orogen have been plagued by geological uncertainties associated with the GRC and Grampians-Stavely Zones. The most recent models are those of Scheibner & Veevers (1999) and Taylor *et al.* (2000), both of which advocate formation of the GRC (and Delamerian Orogen) by collision between an active island arc and the rifted Gondwana continental margin. This expands on a similar concept proposed by Gray & Webb (1995). Scheibner & Veevers (1999) invoke the Mount Stavely Volcanic Complex as the colliding outboard arc, whereas Taylor *et al.* (2000) consider that the latter is represented by the Dimboola Igneous Complex (Figure 2.5). In both models, the putative arc lies above an east-dipping subduction zone and consumes the marginal basin oceanic crust upon which the Kanmantoo Group/GRC turbidites are deposited. Deformation and thickening of the turbidite sequence, accompanied by igneous intrusion, transpired during convergence between the colliding arc and continental landmass. The Mount Stavely Volcanic Complex formed during subsequent post-collision magmatism, according to Taylor *et al.* (2000). This scenario closely resembles that proposed for the coeval Tyennan Orogeny in Tasmania, though here collision is succeeded by west-directed subduction (Crawford & Berry 1992).

As will be demonstrated, the Scheibner & Veevers (1999) and Taylor *et al.* (2000) models have insurmountable defects. Neither can satisfactorily explain the generation of the high grade metamorphic rocks or the diverse igneous components of the GRC, particularly regarding the striking secular changes in igneous geochemistry. Further, both models are inconsistent with the occurrence of subduction-related rocks in the GRC, which are documented for the first time in this thesis. These rocks clearly hold the key to unravelling the geotectonic evolution of the Delamerian Orogenic Belt.

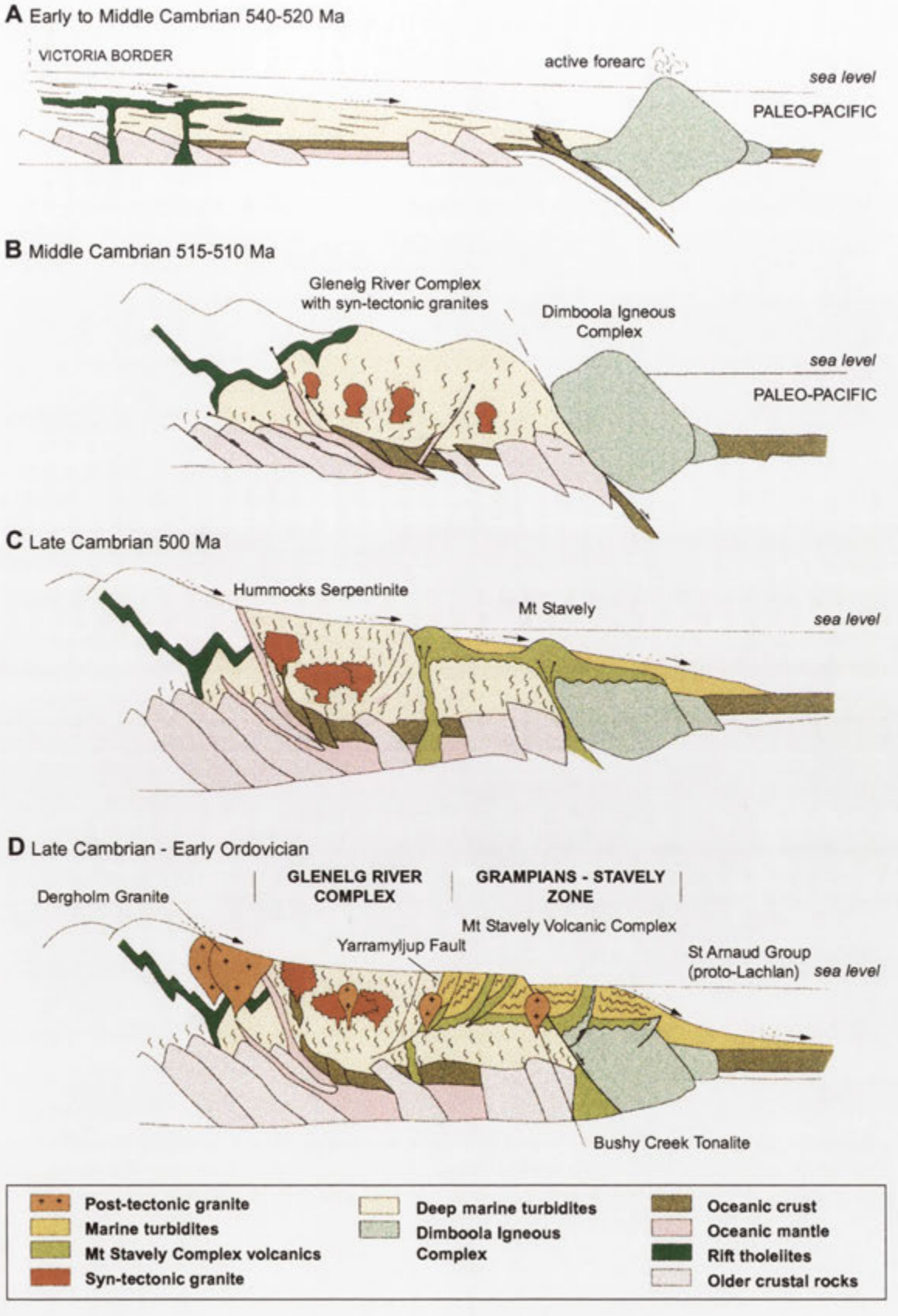

Figure 2.5. Model for the Cambrian tectonic evolution of the eastern Delamerian Orogenic Belt proposed by VandenBerg *et al.* (2000), advocating collision between an outboard island arc (the Dimboola Igneous Complex) and the rifted Gondwana margin. Note the inferred older continental substrate, and post-collisional eruption of the Mount Stavely Volcanic Complex. Modified from VandenBerg *et al.* (2000).

Chapter 3: Geological and geochronological framework of the Glenelg River Complex

3.1 Previous work

Prior study has established that the GRC encompasses a polydeformed, turbiditic metasedimentary sequence intruded by various igneous phases (Anderson & Gray 1994). The name 'Glenelg River Complex' was originally proposed by Wells (1956), who recognised the progressive metamorphic zonation and first expounded the similarity between the GRC metasedimentary sequence and the Early Cambrian Kanmantoo Group of southeastern South Australia.

Regional mapping of GRC exposures was initially undertaken by the Geological Survey of Victoria, as part of the 1:250 000 Hamilton sheet (Douglas & Spencer-Jones 1971). Subsequently, granitic outcrops near Coleraine, Dergholm, Harrow and Wando Vale were K-Ar dated by Richards & Singleton (1981), who note the age correspondence of these rocks with intrusives in southeastern South Australia. Gray (1990) presents Sr isotope data for rocks of the latter two localities, and groups these with the Encounter Bay type plutons.

As part of a wider consideration of Delamerian magmatism, Foden *et al.* (1990) also correlate various GRC granitic phases with Cambro-Ordovician intrusives of the Mount Lofty Ranges, and emphasise the similarity of the magmatic cycle in both areas. Turner & Foden (1990) allude to the chemical resemblance of metagabbroic intrusives of the GRC with metamorphosed mafic dykes of the northern Delamerian Orogen. More extensive geochemical and isotopic exposition (Sm-Nd) by Turner *et al.* (1993a) on granitic and mafic rocks, combined with a K-Ar cooling history reconstruction, yield results consistent with this conclusion. Gibson & Nihill (1992) investigate lithological associations of metasedimentary rocks, compare inferred deformational and metamorphic histories of these with those established for the Kanmantoo Group, and highlight the disparity of structural style between the GRC and the Lachlan Fold Belt to the east.

All available geological criteria are reappraised by Anderson & Gray (1994), who also present detailed information on the structure and geochemistry of the Wando Vale district, in an attempt to elucidate the tectonic affinity of the GRC. Kemp & Gray (1999a) discuss the geology of the Harrow district in detail, with emphasis on the field relations and petrology of muscovite-bearing granitic rocks. A summary of the structural and anatectic history of migmatitic rocks with associated tectonic implications is provided by Kemp & Gray (1999b).

Recent La Trobe University Honours theses completed in the GRC include Anderson (1990; Wando Vale), Ferguson (1993; Dergholm-Burke Bridge), Kemp (1995; Harrow district), Bushell (1996; Coleraine district), O'Hara (1996; Balmoral-Coojar) and Fitzherbert (1998; Balmoral district). Sourced largely from these, and augmented by aeromagnetic data of Slater (1995), a synthesis of stratiform GRC geology is compiled by Gray *et al.* (2001), accompanied by an overview of the tectonometamorphic evolution of the terrane.

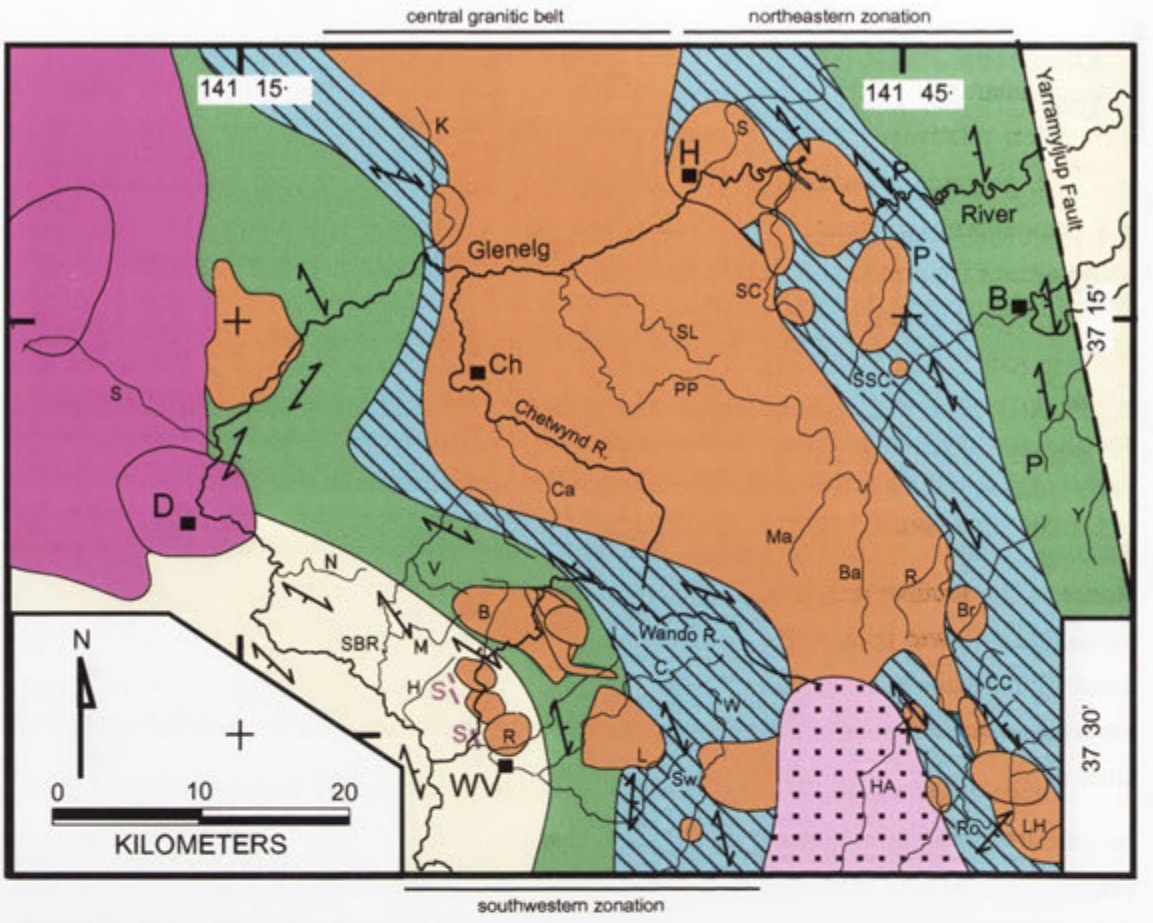

METAMORPHIC ROCKS (Cambro-Ordovician)

Greenschist facies	Southwest: metagreywacke, metasiltstone, slate and phyllite. Quartzofeldspathic schist, semi-pelitic schist and calc-silicate at higher grade Northeast: metasandstone, metasiltstone and slate
Amphibolite facies	Quartzofeldspathic schist, minor metapelitic schist. Diopsidic calc-silicate, metaquartzite and amphibolite in southwest.
Migmatite zone	Stromatic migmatite, quartzofeldspathic schist, quartzofeldspathic gneiss. Minor metapelitic rocks. Metaquartzite in southwest, diatexite in northeast.

IGNEOUS ROCKS

- Hassall Creek Granodiorite
- Dergholm type granitic rock
- Undifferentiated GRC plutonic rock

- P — Peak of pegmatite development
- S — Serpentinite outcrop
- Orientation of S_2 foliation and differentiated layering
- Inferred fault
- Lithological boundary
- Drainage

Figure 3.1. Metamorphic zonation, structural trends and general occurrence of granitic rocks in the GRC; all younger lithologies are removed for clarity (adapted from Gray *et al.* 2001). Note that the Hummocks Serpentinite corresponds to the southernmost serpentinite outcrop trace indicated near Wando Vale. Towns and major watercourses referred to throughout this study are labelled.

Towns: B = Balmoral; **Ch** = Chetwynd; **D** = Dergholm; **H** = Harrow; **WV** = Wando Vale.

Creeks: B = Boundary Ck; **Ba** = Basin Ck; **Br** = Bryan Ck; **C** = Corea Ck; **Ca** = Cairns Ck; **H** = Harvester Ck; **Ha** = Hassall Ck; **K** = Kadnook Ck; **L** = Loftus Ck; **LH** = Log Hut Ck; **M** = Majors Ck; **Ma** = Mather Creek; **N** = Nolans Creek; **PP** = Pigeon Ponds Creek; **R** = Robertson Ck; **Ro** = Robson Ck; **S** = Salt Ck; **SBR** = Steep Bank Rivulet; **SL** = Sugarloaf Ck; **SC** = Schofield Ck; **SSC** = Scabbing Station Ck; **Sw** = Sawyer Ck; **V** = Vines Ck; **W** = Wennicott Ck; **Y** = Yarramyljup Ck.

3.2 Metamorphic zonation in metasedimentary rocks

Metasedimentary rocks of the GRC exhibit a coherent regional metamorphic zonation, whereupon relatively low grade rocks, outcropping in the southwest and northeast of the complex, prograde inwards towards a high grade core dominated by migmatitic lithologies, in turn enveloping a granitic batholith (Figure 3.1). Quartzofeldspathic metasedimentary compositions are prevalent at all metamorphic grades across the GRC, but minor differences in the lithological package, and significant disparity of deformational and metamorphic histories, between rocks of the southwest and northeast GRC are recognised (Kemp & Gray 1999a; Gray *et al.* 2001). Accordingly, it is necessary to consider the metamorphic succession either side of the central batholith separately.

3.2.1 Southwestern metamorphic zonation

Rocks of the southwestern metamorphic zonation exhibit a systematic grade increase from the biotite zone (lower greenschist facies) in the southwest through to the migmatite zone (upper amphibolite facies) in the northeast. Detailed petrographical accounts are provided by Wells (1956), Anderson & Gray (1994) and Gray *et al.* (2001), with an abbreviated description below.

Biotite zone rocks comprise metagreywackes, with lesser metasiltstones, slates and calcareous slates (Gray *et al.* 2001), that are exposed in the southwest corner of the GRC between Steep Bank Rivulet and Nolan Creek. Most units are pervasively recrystallised to the lower greenschist facies assemblage biotite-muscovite-chlorite-albite (Wells 1956) and support a metamorphic mica foliation; sedimentary structures are largely obliterated. The thickly bedded metagreywacke horizons of Steep Bank Rivulet and Harvester Creek are an exception, preserving load casts, flame structures, graded bedding and ripple cross-lamination. The immaturity of these rocks is indicated by matrix-supported detrital grains of alkali feldspar, plagioclase, biotite and muscovite. As such, metagreywackes are considered to represent metamorphosed proximal turbidites (Gibson & Nihill 1992; Gray *et al.* 2001). This is supported by a measured stratigraphic column in Harvester Creek, in which repetitive alternating metagreywacke and metasiltstone horizons are interpreted as A and E units of the Bouma turbidite sequence (Gray *et al.* 2001).

Further east, along the Wando River, these lithologies are replaced with increasing grade by fine grained biotite-chlorite schists (Wells 1956; Anderson 1990) and ultimately quartzofeldspathic and semi-pelitic schists of the amphibolite facies, in which narrow garnet-andalusite and sillimanite metamorphic zones are recognised (Gray *et al.* 2001). The amphibolite facies commences east of the staurolite isograd of Wells (1956) with the first appearance of hornblende in a metabasite (Anderson 1990). This coincides with an andalusite-staurolite-almandine assemblage within adjacent metapelites (Anderson & Gray 1994), and progradation of interstratified calcareous units from actinolite-calcite-quartz schists to diopside-hornblende calc-silicates (Anderson & Gray 1994). Throughout the amphibolite facies, quartzofeldspathic schists remain essentially quartz-plagioclase-biotite, with sporadic alkali feldspar. Semi-pelitic interlayers have primary muscovite, garnet, and rarely andalusite porphyroblasts, with

sillimanite appearing at higher grades. Subequal in abundance, and intergradational with quartzofeldspathic schists, are thick horizons of internally layered calc-silicates with modal variations upon a quartz-plagioclase-alkali feldspar-diopside-hornblende ± scapolite ± titanite mineralogy (Anderson 1990).

The onset of the upper amphibolite facies in northeastern Wando Vale is signalled by the assemblage sillimanite-alkali feldspar ± garnet in semi-pelitic schists, coupled with incipient development of anatectic leucosomes within quartzofeldspathic metasedimentary rocks.

Ferguson (1993) has identified an analogous grade sequence within metasedimentary rocks from Dergholm northwestwards along the Glenelg River valley to Burke Bridge, although here the progression is interrupted by several thin retrograde muscovite-chlorite schist zones. Nevertheless, this has allowed considerable northwestwards extrapolation of the Wando Vale metamorphic zonation. That individual marker metasedimentary units cannot be similarly traced indicates a lack of lateral stratigraphic continuity, attributed to large scale isoclinal folding, transposition (see later) and outcrop limitations (Gray *et al.* 2001).

Eastwards, along the Wando River quartzofeldspathic, psammitic and calcareous metasedimentary rocks undergo a gradual transition into the migmatite zone, defined as the first appearance of metasedimentary rocks with >10% anatectic leucosome (Gray *et al.* 2001). Lithologies of the southwestern migmatite zone are most comprehensively described within Loftus, Sawyer and Wennicott Creeks further east by Bushell (1996) and Gray *et al.* (2001). A migmatitic succession with a higher proportion of leucosome and intimately interleaved muscovite granite occurs further north along strike within Kadnook Creek (C.M. Gray pers. comm. 1998).

As evident in Figure 3.1, large areas of the southwestern zonation attained metamorphic grade commensurate with crystallisation of high temperature mineral assemblages and partial melting. Gibson & Nihill (1992) infer that the medium to high grade metamorphism in the Wando Vale district results from heat advection from nearby granitic intrusives. However, this is refuted by Anderson & Gray (1994), who demonstrate that plutons are either thermally discordant, truncating metamorphic isograds and imposing contact aureoles on host schists, or have themselves been overprinted by amphibolite facies metamorphism. Further, the isograd configuration at Wando Vale is part of a larger metamorphic regime that reaches highest grades (i.e. migmatite zone) remote from exposed granitic intrusives (see Figure 3.1).

Similar arguments preclude local gabbroic dykes providing the thermal energy for metamorphism. These rocks are restricted to the low grade sequence, where their high temperature igneous mineralogy is retrograded to greenschist facies metamorphic assemblages. The metamorphic attributes of the southwestern zonation are clearly independent of the distribution of exposed intrusives and require a profound, regional-scale heat source.

3.2.2 Northeastern metamorphic zonation

Metasedimentary rocks of the northeastern GRC are entirely within the upper amphibolite facies, prograding from the sillimanite zone to the migmatite zone from northeast to southwest. Quartzofeldspathic compositions are predominant and lithological variation is minor.

Sillimanite zone quartzofeldspathic schists have prominent outcrop immediately east of the Yarramyljup Fault and, unlike those of the southwestern zonation, contain abundant prograde muscovite, in addition to sporadic alkali feldspar and occasional leucosomes (Gray *et al.* 2001). Thin horizons of biotite schist are interlayered, rarely with fibrolite, and a 120 m wide metapelitic band containing garnet and sillimanite occurs in the Glenelg River (Fitzherbert 1998). Layer-parallel, boudinaged, pegmatite sheets, with sheared margins and internal muscovite foliations, become progressively more numerous southwestwards, until, near the sillimanite-migmatite zone transition, they comprise a 1-2 km wide band accounting for >90% of exposure (Gray *et al.* 2001; see Figure 3.1). Fine to medium grained muscovite ± garnet granitic rock is intimately associated and partly gradational with pegmatite (Gray *et al.* 2001).

The appearance of thin stromatic migmatite horizons within quartzofeldspathic schist immediately west of the pegmatite band signals the commencement of the migmatite zone. Rocks of the migmatite zone are well exposed along the Glenelg River valley and tributaries for another 15 km west towards Harrow, where described by Kemp (1995). Major lithologies include quartzofeldspathic schist, quartzofeldspathic gneiss, and various migmatitic rocks that are complexly interleaved with felsic, muscovite-bearing granitic bodies.

Since the geology of the northeastern migmatite zone is a major focus of this study, full documentation of these rocks is deferred to later chapters. Nevertheless, it is worth noting that in Schofield Creek (a major tributary of the Glenelg River) interleaved muscovite granite and metasedimentary rock undergoes a transition to a fundamentally different rock type, the Tuloona Granodiorite (Kemp 1995). This 'contact' is traced ~3.5 km west to the Glenelg River valley and defines the northeastern boundary of the central granitic batholith, which separates the northwestern metamorphic zonation from the southwestern zonation.

3.3 Metabasites

Metabasites with mafic igneous protoliths are restricted to the southwestern metamorphic zonation. They are most prominent in the Wando Vale-Steep Bank Rivulet vicinity as concordant sheets with varying degrees of metamorphic recrystallisation.

Metabasites of the lower grade (biotite zone) sequence are fine to medium grained and consist of variable proportions of plagioclase, biotite and interstitial carbonate, usually with a relict doleritic texture (Gray *et al.* 2001); intensely deformed variants have albitic plagioclase augen enveloped by an anastomosing fabric of biotite and chlorite (Wells 1956; Gray *et al.* 2001).

Within the amphibolite facies of Wando Vale Gray *et al.* (2001) distinguish three metabasite types, all of which have geochemical affinities with mid-ocean ridge basalt (MORB). The first

is a curved, stratiform body of finely layered hornblende-plagioclase schist that extends from Robertson Creek, where it is ~150 m thick, to the Wando River, where it forms a series of 2.5 m wide bands (Anderson 1990). Although recognised in Major and Vines Creek further west, it is apparently absent from Boundary Creek, suggesting lenticular or podiform geometry. Based on textural evidence, Gray *et al.* (2001) postulate that the hornblende schist represents a recrystallised gabbroic intrusive that predated deformation. A thick amphibolite body exposed in the Glenelg River valley north of Dergholm is similar to hornblende schist at Wando Vale and may be an equivalent horizon (Gray *et al.* 2001).

The second metabasite type is massive metagabbro in Majors Creek and Steep Bank Rivulet, with lath-shaped plagioclase and actinolite pseudomorphs after clinopyroxene (Gray *et al.* 2001). Rocks are unfoliated and deformation features are relatively minor; relict ophitic igneous textures are widely preserved (Gray *et al.* 2001).

Texturally distinctive high-alumina metagabbroic sheets (to 15 m wide) interlayered with metasedimentary rocks at Wando Vale (Anderson & Gray 1994) form the third metabasite variety of Gray *et al.* (2001). Bodies have massive cores, where subhedral actinolite (after pyroxene phenocrysts) occurs in a matrix of finer plagioclase and actinolite, that grade into strongly foliated margins where cummingtonite porphyroblasts are wrapped by aligned mats of fibrous actinolite and albite prisms. Chemically, metagabbros of this type have more incompatible element-rich compositions, and some exhibit clear arc signatures (Kemp & Eggins *unpubl. data*). Gray *et al.* (2001) postulate a late-D_2, post-metamorphic peak emplacement to reconcile the occurrence of actinolite, seemingly out of grade context with the amphibolite facies mineralogy of host schists.

3.4 Metamorphosed ultramafic rocks

Metamorphosed ultramafic rocks outcrop in the biotite zone of the southwestern GRC (Figure 3.1) and are associated with parallel belts of higher magnetic intensity; a full account of their petrology and occurrence is discussed by Gray *et al.* (2001). The most conspicuous body is the Hummocks Serpentinite near Wando Vale (Wells 1956), which constitutes a NNW-trending series of elongate hills immediately west of the Edenhope road. Enveloped by sheared talc-magnesite schist (Gray *et al.* 2001), the serpentinite comprises dark blue-green antigorite transected by chrysotile-lined slip surfaces (Turner *et al.* 1993a). Pseudomorphed olivine, orthopyroxene and chromite outline a relict coarse grained cumulate texture (Turner *et al.* 1993a). This, together with low CaO and Al_2O_3 and depleted incompatible element geochemistry, identify the precursor as a refractory harzburgite from which basaltic magma has been extracted (Turner *et al.* 1993a). It is further postulated by Turner *et al.* (1993a) that the Hummocks Serpentinite is an obducted fragment of an ophiolite sequence.

A series of conformable serpentinite sheets in Steep Bank Rivulet have foliated, talc-dominated margins and more massive cores, where relict peridotite textures are preserved (Gray *et al.* 2001). Wells (1956) describes similarly altered peridotites in nearby Major Creek.

3.5 Plutonic Rocks

The metamorphic substrate of the GRC is intruded by numerous plutonic phases that are the subject of very few detailed studies, despite comprising over sixty percent of the exposed geology of the complex. Early workers distinguished the Wando Granodiorite in the southwestern GRC (Wells 1956), and the Harrow Granodiorite in the northeast (Douglas & Spencer-Jones 1971; Foden *et al.* 1990). Foden *et al.* (1990) recognised that the former has a gneissic tonalite phase, more precisely defined by Anderson (1990) who further subdivides the 'Wando Granodiorite' into the Deep Creek, Torah, Meissen and Sawpit Gully Granodiorites. Kemp (1995) resolved the 'Harrow Granodiorite' into numerous phases, most notably Marn Mering, Carrigeen and Tuloona Granodiorites, and the Schofield Adamellite. Bushell (1996) identified the foliated Wennicott and Warradale Tonalites in Wennicott Creek east of Wando Vale, whereas quartz diorite, gabbronorite and pyroxenite are recognised north of Dergholm (Ferguson 1993; Turner *et al.* 1993a). Nevertheless, prior to this study large areas of undifferentiated granitic rock in the central and eastern parts of the GRC, as shown on the 1:250 000 Hamilton Sheet (Douglas & Spencer-Jones 1971), remain unexplored, preventing any meaningful synthesis of GRC magmatism.

3.5.1 Granitic rocks of the Dergholm district

Distinct from other granitic phases of the GRC are the coarse grained, pink to green adamellites that outcrop over a wide area near the western edge of the complex around Dergholm, and thought to be even more extensive in the subsurface (Kemp *et al.* 2001; Figure 3.1). These exposures were originally mapped as 'Dergholm Granite' by Wells (1956), and have been more recently studied by Foden *et al.* (1990), Turner *et al.* (1993a) and Ferguson (1993), who consider their emplacement to post-date compressive deformation. Careful examination has resolved four main plutons (Kemp *et al.* 2001), each with slightly different petrographic characteristics and magnetic signatures, which are grouped as 'Dergholm type' granitic rocks (Kemp *et al.* 2001). All have smoky quartz, pinkish microcline with patch perthite, green to buff sodic plagioclase and annitic biotite; titanite and fluorite are common accessories (Kemp *et al.* 2001). Plutons were emplaced at high crustal levels, and weakly metamorphose host slates south of Dergholm (Wells 1956; Ferguson 1993). Geochemically, Dergholm type phases have an 'A-type' affinity, with strongly depleted Sr, Ba, P and Ti and enriched incompatible element concentrations (Zr, Nb, Y, Ga), both features reflecting prolonged fractionation (Foden *et al.* 1990; Turner *et al.* 1993a). Exposures in Salt Creek north of Dergholm have the most primitive isotopic ratios of any measured GRC granitic rock, with initial $^{87}Sr/^{86}Sr = 0.7031$ (calculated at 487 Ma; Turner *et al.* 1993a).

As noted by Foden *et al.* (1990), Turner *et al.* (1993a) and Anderson & Gray (1994), Dergholm type phases are petrographically and chemically analogous to Murray Bridge type granitic rocks of southeastern South Australia, and outcrop along the same basement high, the Padthaway Ridge (see section 2.2.3b). Accordingly, it is likely that Dergholm type plutons constitute the southeastern extremity of the large post-compressional A-type granitic batholith that extends southeastwards under the Murray basin from the eastern Mount Lofty Ranges, and thus link the GRC with the Delamerian Orogen in South Australia (Anderson & Gray 1994). The petrogenesis

of these rocks in South Australia is evaluated by Turner *et al.* (1992), who conclude that they represent the end-product of extreme basalt fractionation (section 2.2.3b). This origin is also apposite for Dergholm types and consistent with their mantle-like isotopic composition (Turner *et al.* 1993a).

3.6 Structural History

Although a coherent structural entity (Kemp & Gray 1999a), minor deformational differences between the northeastern and southwestern metamorphic zonations are recognised (Kemp & Gray 1999b). The structural history of the southwestern zonation is outlined by Gibson & Nihill (1992), Turner *et al.* (1993a) and most comprehensively by Anderson & Gray (1994). That for the northeastern zonation is described in detail by Kemp (1995) and Kemp & Gray (1999a, 1999b). The results for both metamorphic zonations are briefly synthesised below.

3.6.1 First Deformation, D_1

Due to intense later deformation, F_1 folds are very rare and have only been unambiguously identified in the low grade rocks of the Wando River (Anderson 1990). Elsewhere, D_1 features are preserved primarily as a remnant S_1 foliation in S_2 microlithon or a fine layering being rotated by F_2 closures. The latter situation is consistently observed in the coarser grained migmatitic rocks of both northeastern and southwestern zonations, where anatectic leucosomes are isoclinally folded by D_2. Here, the S_1 fabric, defined by muscovite and biotite in melanosomes bordering the leucosome, is folded around the outside of the isoclinal closure, but does not endure in the fold cusp, where micas are recrystallised parallel to the axial surface of the fold (Kemp & Gray 1999b).

3.6.2 Second Deformation, D_2

D_2 imposed the pre-eminent structural imprint of the GRC, with S_2 being the penetrative northwesterly trending regional fabric recorded by all metasedimentary rocks. Isoclinal F_2 folds, with thickened apices and attenuated limbs, are ubiquitous, plunge NW or SE, with a pervasive axial planar foliation (S_2) being diagnostic. This fabric is a crenulation cleavage in metapelitic rocks, derived by recrystallisation of S_1. In areas of higher flattening strain, F_2 closures are rootless or intrafolial, and contained within strongly transposed layering; this is commonly observed in quartzofeldspathic gneiss of the northeastern zonation, but also conspicuous in lower grade rocks in the southwest. Elsewhere, intense non-coaxial strains are indicated. Markedly asymmetric boudins within stretched pegmatite sheets in Yarramyljup Creek are attributed to layer-parallel shearing during D_2 (Gibson & Nihill 1992). Shear sense indicators imply that these structures developed by west-vergent thrusting during progressive regional simple shear (Gibson & Nihill 1992) or transpression (Turner *et al.* 1993a). Similarly, Gray *et al.* (2001) conclude that ultramafic rocks were emplaced by thrusting during D_2 crustal thickening.

3.6.3 Third Deformation, D_3

Third generation folds coaxially rotating S_2 are widely developed across the GRC, but most

numerous in amphibolite facies rocks. F_3 generally forms tight, upright to inclined similar folds with slightly thickened hinges and V-shaped profiles. F_3 in quartzofeldspathic schist or thick pegmatite dykes are close to open parallel folds. The S_3 fabric is poorly developed and essentially localised to metapelites or micaceous melanosomes in fold cores. An incipient S_3 crenulation cleavage is occasionally visible.

3.6.4 Fourth Deformation, D_4

Structures of this mild deformation have not been clearly defined in the southwestern GRC and are apparently localised to migmatitic rocks of the northeastern zonation. Here, F_4 occurs as close to open crenulations in S_2 or S_3, with planar limbs and angular hinge zones (Kemp 1995). They are coaxial to F_2 and F_3, and thus difficult to distinguish, but are never as tight as F_3 and produce no axial fabric. This deformation is broadly synchronous with extensive anatexis in the northeastern metasedimentary zonation.

3.6.5 Fifth Deformation, D_5

D_5 structures are pervasive in all GRC metasedimentary rocks as open parallel folds that warp S_2 without production of an axial foliation. F_5 is geometrically distinct, plunging steeply NE-SW, perpendicular to earlier coaxial generations. Granitic rocks in the northeastern zonation are also conspicuously deformed by D_5, with rotation of micaceous schlieren into broad asymmetrical warps coplanar with F_5 in schists (Kemp 1995). Pegmatite and leucogranitic dykes of Schofield Creek support open dextral folds, which are related to extensive jointing and fracturing. Intense fracturing and minor faulting within some homogeneous plutons of the northeastern zonation is also attributed to D_5 (Kemp 1995; Kemp & Gray 1999b).

Significantly, macroscopic D_5 folds occur across the GRC. At Wando Vale, an F_5 antiform is responsible for the arcuate geometry of metamorphic isograds and broad curvature of the lithological layering (see Figure 3.1) (Anderson & Gray 1994). This implies that the macrostructural and metamorphic attributes of the GRC are governed by F_5 folding, and that D_5 was a fundamental event within the tectonic evolution of the eastern Delamerian Orogen.

3.7 Relationship between metamorphic crystallisation, anatexis & deformation

The timing of metamorphic mineral growth as a function of deformation for the Wando Vale district of the southwestern zonation is outlined by Anderson (1990) and Gibson & Nihill (1992), and summarised by Figure 3.2. The highest metamorphic grades were attained syn-D_2 (Anderson 1990), concomitant with intrusion of most local granitic phases, followed by a decline to biotite grade by D_3. Isoclinally folded leucosomes at the southern margin of the Wando Tonalite (Turner *et al.* 1993a) and in sillimanite schists at Burke Bridge also indicate incipient partial melting pre- to syn-D_2. At Wando Vale, peak temperatures of 650°C (at 300-400 Mpa; Gibson & Nihill 1992) and 590-660°C (at 400-500 Mpa; Turner *et al.* 1993a) are estimated by garnet-biotite geothermometry, with an average pressure of ~570 Mpa calculated thermodynamically by Turner *et al.* (1993a). Although the highest grade rocks of this area have attained hypersolidus

conditions, the persistence of primary muscovite with alkali feldspar and sillimanite indicates that the stability of muscovite with quartz has not been exceeded (Gibson & Nihill 1992). Temperatures may have been higher in the southwestern migmatite zone, where isoclinally folded leucosomes constitute up to 30 percent of some exposures (Gray *et al.* 2001).

Conversely, in the northeastern metamorphic zonation metasedimentary rocks experienced a more protracted high-grade metamorphic history (Figure 3.2). In the migmatite zone of the Harrow district, crystallisation of sillimanite and widespread partial melting also occurred pre- to syn-D_2 (first anatectic episode, M_1; Kemp 1995). However, anatectic conditions were re-established after D_2 and persisted through to post-D_4, resulting in the generation of extensive leucosome-dominated migmatitic rocks (Kemp 1995; Kemp & Gray 1999a). This period coincided with the emplacement of granitic plutons near Harrow, and proceeded whilst metamorphic conditions had waned to sub-biotite grade at Wando Vale and nearby Burke Bridge (Ferguson 1993). The P-T environment of this anatectic culmination (M_2) has not been properly quantified, though survival of prograde muscovite, lack of kyanite, and constraints imposed by water-saturated solidi lead Kemp (1995) to postulate temperatures of 680-700°C at 550-800 Mpa. The crystallisation of primary muscovite by migmatitic rocks further suggests that M_2 anatexis transpired under fluid-rich conditions (Kemp & Gray 1999a).

3.8 Geochronological constraints

Radiometric dating of metamorphic and igneous rocks of the GRC has been undertaken by several workers, though coverage is far from comprehensive.

Of the high grade rocks in the southwestern zonation, a sillimanite schist at Burke Bridge is dated at 512±12 Ma (VandenBerg & Wilkinson 1982) and 491±6 Ma (K-Ar, Turner *et al.* 1993a).

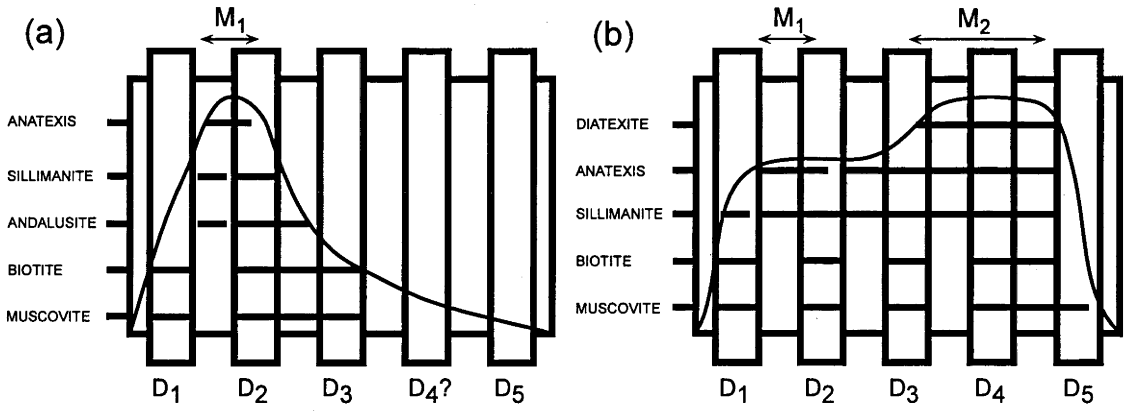

Figure 3.2. Summary of metamorphic mineral crystallisation and anatexis as a function of deformation for (a) the Wando Vale district of the southwestern zonation (modified Anderson & Gray 1994), and (b) the Harrow district of the northeastern zonation (from Kemp & Gray 1999a).

These ages are compatible with K-Ar (biotite) cooling ages of 490±6 Ma from amphibolite facies schist at Wando Vale (Turner *et al.* 1993a) and confirm that metamorphism is contemporaneous with the Delamerian Orogeny.

The available chronological data for GRC granitic rocks is presented in Table 3.1; ages for selected intrusives of the Delamerian Orogen in South Australia and the western Lachlan Fold Belt are provided for comparison.

Lithology	*Reference*	*Method*	*Age (Ma)*
Wando Tonalite	Morand *et al.* (2001)	U-Pb (zircon)	493±8
Carrigeen Granodiorite	Richards & Singleton (1981)	K-Ar (biotite)	466±6
	Richards & Singleton (1981)	K-Ar (muscovite)	487±6
Deep Creek Granodiorite	Richards & Singleton (1981)	K-Ar (biotite)	476±6
	Turner *et al.* (1993a)	Sm-Nd (whole rock)	516±90
Loftus Ck Granodiorite	Morand *et al.* (2001)	U-Pb (zircon)	491±8
	VandenBerg *et al.* (2000)	U-Pb (zircon)	484±7
Dergholm Granite	Richards & Singleton (1981)	K-Ar (biotite)	453±6
	Richards & Singleton (1981)	K-Ar (plagioclase)	443±7
	Turner *et al.* (1993a)	K-Ar (biotite)	485±5
Hassall Creek Granodiorite	Richards & Singleton (1981)	K-Ar (biotite)	401±5
Vivonne Bay Granite*^{E}	Drexel & Preiss (1995)	Rb-Sr	523±6
Palmer Granite*^{E}	Drexel & Preiss (1995)	Rb-Sr	506±6
Encounter Bay Granite*^{E}	Milnes *et al.* (1977)	Rb-Sr (whole rock)	508±14
Marcollat Granite*^{M}	Turner *et al.* (1996)	U-Pb	490±10
Reedy Creek Diorite*^{M}	Sandiford *et al.* (1992)	U-Pb	487±2
Mannum Granite*^{M}	Drexel & Preiss (1995)	Rb-Sr	481±9
Zumsteins Granodiorite$^{\#}$	Richards & Singleton (1981)	Rb-Sr (whole rock)	400±3
Stawell Granodiorite$^{\#}$	Richards & Singleton (1981)	K-Ar (biotite)	396±5

Table 3.1. Radiometric ages for plutonic phases of the GRC, Delamerian Orogenic Belt (*^{E} = Encounter Bay type; *^{M} = Murray Bridge type) and Lachlan Fold Belt (#).

Three important points emerge from this. Firstly, granitic lithologies of the GRC are comparable in age with South Australian intrusives, given that K-Ar mineral dates are cooling ages and likely to reflect minimum ages of emplacement. Maher *et al.* (1997) report a 524±7 Ma U-Pb (zircon) age for a gabbro obtained from a drillhole under Murray Basin cover, indistinguishable from the Vivonne Bay Granite on Kangaroo Island (section 2.4.4). This confirms that the GRC and western Delamerian Orogen have a shared magmatic history that extended back this far at least.

Secondly, U-Pb (zircon) ages of the intensely deformed Wando Tonalite (pre- to syn-D_2 emplacement) and the undeformed Loftus Creek Granodiorite (post-D_4 emplacement) are virtually identical. This indicates that Delamerian granitic magmatism in the GRC was shortlived, and that deformational episodes were closely spaced in time.

Finally, the age of the Hassall Creek Granodiorite, an undeformed pluton intruding migmatites of the southeastern GRC (Figure 3.1), is indistinguishable from that of the Zumsteins Granodiorite (Grampians-Stavely Zone) and Stawell Granodiorite (Stawell Zone) of the western Lachlan Fold Belt. The Hassall Creek Granodiorite is therefore assumed to be the westernmost manifestation of the extensive Early Devonian magmatic episode in Victoria, and hence part of the Lachlan Fold Belt (Richards & Singleton 1981). However, the geological affinity of the pluton is uncertain and requires further evaluation.

Chapter 4: Overview and approach of this study

4.1 Geological outline of the GRC

From the perspective of this thesis, the GRC may be considered in terms of four geological entities- (1) metasedimentary rocks, (2) leucocratic and muscovite-bearing granitic plutons containing metasedimentary enclaves, (3) lower silica, weakly peraluminous to metaluminous granitic plutons hosting mafic igneous-textured enclaves, and (4) ultramafic, mafic and intermediate igneous rocks intimately associated with more felsic granitic bodies. The distribution of each is illustrated by Figure 4.1. 'Dergholm type' rocks have been investigated by previous studies (section 3.5.1) and are not addressed here.

4.1.1 Metasedimentary lithologies

These range from lower greenschist facies to upper amphibolite facies, the latter having undergone varying degrees of partial melting. The succession is resolved into two separate regional metamorphic zonations, which occur either side of, and prograde towards, a central granitic batholith (Figure 3.1). Rocks of the southwestern metamorphic zonation exhibit a continuous grade increase from the biotite zone in the southwest through to a migmatite zone adjacent the central batholith (section 3.2.1). Here, quartzofeldspathic and semi-pelitic protoliths experienced migmatite formation pre- to syn-D_2 (i.e. 'M_1'; section 3.7).

The northeastern metamorphic zonation has sillimanite grade quartzofeldspathic to semi-pelitic schists that undergo a transition southwestwards into gneissic and migmatitic rocks of the broad migmatite zone, flanking the central granitic batholith. In contrast to their southwestern counterparts, northeastern migmatite zone rocks have experienced a more complicated anatectic history, with partial melting during M_1 and more extensively pre-D_3 to post-D_4 ('M_2', section 3.7). Both stromatic (layered) migmatites and diatexites (see below) are represented, the former characterised by complexly interconnected leucosome arrays, which are commonly linked to metre-scale bodies of leucocratic muscovite granite.

4.1.2 Felsic muscovite-bearing granitic rocks

Muscovite-bearing leucogranitic rocks (adamellite to granodiorite with minor tonalite) are virtually localised to the northeastern migmatite zone, where enveloped by migmatites. Although encountered in the Wando River area, and the southeastern corner of the GRC near Coleraine, they are particularly clustered in the Harrow district further north (Figure 4.1). Accordingly, these plutons are hereafter referred to as 'Harrow type' granitic rocks. All are strongly peraluminous with alumina saturation index (A.S.I.[1]) greater than 1.1. Unmodified magmatic textures, together with rotated enclaves of complexly-deformed metasedimentary rock, indicate emplacement late

[1] A.S.I. = molar $Al_2O_3/(CaO + Na_2O + K_2O)$ after Zen (1986)

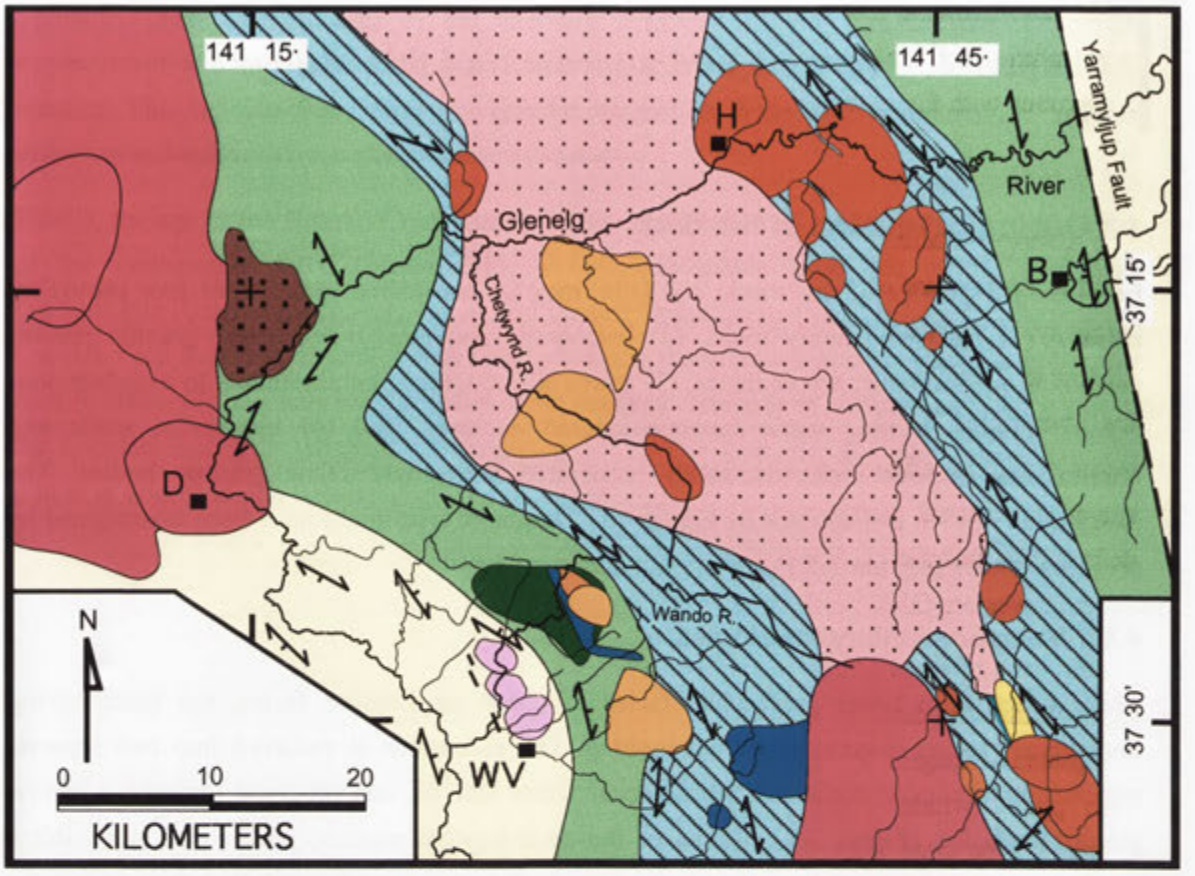

Figure 4.1. Simplified geological map of the GRC showing the distribution of rocks of each magma type and other plutonic bodies. Lithological details are outlined in the text and Table 4.1. Townships and major watercourses are labelled, with symbols as indicated in Figure 3.1.

in the deformational history, synchronous with M_2 partial melting. Many Harrow type plutons have intimately interleaved and gradational boundaries with surrounding migmatites and are contiguous with the interconnected leucosome networks of these rocks.

4.1.3 Metaluminous to weakly peraluminous granitic plutons

The diverse metaluminous (A.S.I.<1.0) to weakly peraluminous (A.S.I. between 1.0 and 1.1) granitic rocks were emplaced during two stages of the deformational history, pre- to syn-D_2 (early syn-compressional) or post-D_2, pre-D_5 (late syn-compressional), coinciding with the two distinct anatectic peaks in the host metasedimentary sequence. Early syn-compressional plutons are overprinted by D_2, and thus support variably recrystallised microfabrics and pervasive tectonic mineral alignments that are correlated with D_2 structures in metamorphic rocks. Late syn-compressional phases are predominant and post-date D_2, but exhibit relatively minor deformation features imposed by D_3, D_4 or D_5. Early syn-compressional plutons are restricted to the southwestern GRC, whereas late syn-compressional phases outcrop throughout the complex.

Within each of these structural subdivisions, smaller groups of granitic rocks are resolved that share similar and distinctive mineralogical, textural and geochemical features. These groups are designated as magma 'types' rather than 'suites' to avoid the associated genetic implication that each pluton within a group derives from the same source rocks, where the distinctive characteristics were inherited (e.g. Chappell & White 1992). Under this scheme, early syn-compressional plutons are grouped into the Wando, Wennicott and Deep Creek magma types and late syn-compressional phases comprise the Tuloona, Loftus Creek and Kassingbrook type. Note that the muscovite-bearing Harrow type granitic rocks are also included in the late syn-compressional association.

The critical petrographical and geochemical criteria used to justify grouping of granitic rocks into the above magma types is summarised by Table 4.1, with the location of plutons of each magma type illustrated by Figure 4.1. The Wando and Wennicott magma types of the southwestern GRC comprise variably deformed mafic hornblende tonalites to minor granodiorites with abundant mafic igneous-textured enclaves, and are primarily distinguished by different geochemical evolutionary trends. Deep Creek type rocks include the Deep Creek and Torah Granodiorites of Anderson (1990) and are also geochemically distinctive, with unusually high Al_2O_3 and Na_2O. Of the late syn-compressional groups, weakly deformed rocks of the Tuloona magma type are predominant, and comprise the large central batholith of the GRC. These range from tonalite through to more felsic granodiorite and adamellite which contain minor primary muscovite. Mafic igneous enclaves are ubiquitous, but less prominent in more felsic plutons, where they are accompanied by metasedimentary enclaves. Significantly, rocks of the central granitic batholith are transitional to the interleaved muscovite leucogranite and migmatitic sequences of the flanking northeastern migmatite zone. All above plutons are post-dated by discrete bodies of texturally-distinctive hornblende granodiorite of the Loftus Creek magma type, of which a high-K signature and elevated Sr contents are diagnostic.

Magma type	*Emplacement timing*	*Silica range (wt%)*	*A.S.I. range*	*Mafic mineral assemblage*	*Unifying features*	*Distinctive chemical features*
Wando	Early syn-comp.	56.0 - 65.9	0.83 - 1.09	hbl, bio, mag, epi	Abundant hornblende, strong S_2 foliation. MME common.	Evolves to high K_2O
Wennicott	Early syn-comp.	57.9 - 70.9	0.88- 1.08	bio ± hbl ± ilm	Afs rare to absent MME common	Evolves to low K_2O
Deep Creek	Early syn-comp.	68.2 - 68.9	1.01 - 1.09	bio, mag ± hbl	Poikilitic microcline MME very rare.	High Al_2O_3, Na_2O, moderately high Sr, low TiO_2, K_2O, P, Y
Tuloona	Late syn-comp.	66.9 - 73.5	1.03 - 1.10	bio, mag	Clots of biotite and magnetite, strongly zoned plagioclase. MME common.	Steeply increasing K_2O with silica
Loftus Creek	Late syn-comp.	66.2 - 72.9	0.96 - 1.09	hbl, bio, tit, mag	Euhedral biotite phenocrysts, poikilitic microcline, large titanite crystals. MME very rare.	High K_2O, Na_2O, Sr, Zr
Kassingbrook	Late syn-comp.	64.0 - 74.7	0.93 - 1.13	bio ± hbl	Afs phenocrysts, association with mafic-ultramafic rocks. MME ubiquitous and locally clustered.	High but extremely variable K_2O, moderately high Sr
Harrow	Late syn-comp.	71.7 - 76.7	1.10 - 1.33	bio ± garnet	Magmatic muscovite, red-brown biotite, no opaque phase. MME absent.	High but extremely variable K_2O, low Fe_2O_3t, TiO_2, CaO, Zr, REE

Table 4.1. Summary of the distinctive field, petrographic and geochemical attributes of the various granitic magma types of the GRC. Chemical data is presented separately for each magma type in Appendix C and D, and discussed fully in later chapters.

Abbreviations are: Afs = alkali feldspar; bio = biotite; epi = epidote; hbl = hornblende; ilm = ilmenite; mag = magnetite; tit = titanite.

4.1.4 Closely associated mafic to ultramafic, intermediate and granitic rocks

Interspersed mafic (and minor ultramafic), intermediate and more felsic granitic lithologies have exposure near both the northwestern and southeastern peripheries of the GRC. In the northwest, a composite plutonic body, referred to as the Caupaul Igneous Complex, is dominated by mafic hornblende tonalite but also has several bodies of hornblende gabbronorite to pyroxenite enveloped by pyroxene-bearing diorite (Figure 4.1). Diverse gabbroic lithologies are also represented. In the southeast, small pods and dykes of hornblende-rich gabbro-diorite[2], diorite and mafic hornblende tonalite are enclosed by late syn-compressional, muscovite-bearing granitic rocks of Kassingbrook type (Figure 4.1). At several localities mafic rocks are intimately mingled and intergradational with their granitic host, which has imparted considerable lithological and textural complexity at outcrop scale.

Other mafic rocks of the GRC include the texturally-diverse metagabbros of the Wando Vale-Steep Bank Rivulet district, some of which have MORB-like geochemical signatures (section 3.3). These bodies are intercalated within the metasedimentary sequence, being overprinted by greenschist to low amphibolite facies metamorphism, and are not spatially associated with more felsic igneous lithologies; their relationship to the mafic rocks outlined above is explored in later chapters.

4.2 Approach of this research

Although outlined separately above, field relationships compellingly suggest that the four lithological entities are linked, and that the GRC comprises a continuous geological spectrum from schist, migmatite and felsic muscovite granite, through to lower silica peraluminous and metaluminous granite, intermediate hornblende- and pyroxene-bearing lithologies, and finally gabbroic to ultramafic rocks. As the major aim of this study is to evaluate the petrogenesis of migmatites and plutonic igneous rocks of the GRC (Chapter 1), the nature of the relationship between these rock types is fundamentally important.

To investigate this, it is expedient to resolve the geological progression into two separate but interrelated segments, which are explored in Part II and Part III of this thesis. Part II, encompassing Chapters 5 to 9, is concerned with the field relations, petrology and petrogenesis of northeastern migmatite zone metasedimentary rocks and closely associated Harrow type granitic plutons. The intimate outcrop relationships between these units necessitate description as a single lithological assemblage rather than as separate rock types. This integrated approach is adopted in Chapter 5, for intercalated metasedimentary and Harrow type granitic rocks of the Coleraine district, and Chapter 6, which examines the similar style of geology in the Harrow district further north. As these rocks are the subject of few detailed studies, and given the petrogenetic significance of the complex outcrop relationships, the field and petrographic aspects are outlined in detail. Metasedimentary rocks of the southwestern metamorphic zonation have been documented by previous workers (see section 3.2.1) and are not considered further.

[2] Throughout this thesis, 'gabbro-diorite' is used for melanocratic igneous rocks that have >52% SiO_2 and are modally classified as diorites according to the IUGS recommendations of Le Maitre (1989), but which have >65% mafic minerals. Diorite is applied to similar rocks with <65% mafic mineralogy.

Part III (Chapters 10 to 18) examines the petrology and petrogenesis of weakly peraluminous to metaluminous granitic and mafic igneous rocks (geological entities 3 and 4), culminating in the first full synthesis of the magmatic and tectonic evolution of the GRC and eastern Delamerian Orogen (Chapter 17). Chapters 10 and 11 deal with the occurrence and petrology of early syn-compressional and late syn-compressional granitic rocks respectively, whereas Chapters 12 and 13 outline the petrography and field relations of interspersed granitic, mafic to ultramafic and intermediate igneous rocks. Although in most cases being documented for the first time, for practical reasons only those aspects of the various igneous rock bodies essential for geochemical and petrogenetic interpretation are conveyed in the main text; formal pluton definitions and complete petrographic descriptions of type specimens and important variants are provided in Appendix E. A more detailed approach is justified for Chapter 12, where outcrop-scale interactions between felsic and mafic igneous rocks have profound implications for the genesis of the granitic plutons outlined in Chapters 10 and 11.

Petrogenetic discussions in Part II (Chapters 8 and 9) and Part III (Chapters 14 and 16) are underpinned by the detailed field relations, petrography and physical characteristics of the various rock types, together with mineral chemistry and whole rock geochemistry, including consideration of the rare earth elements (REE). To augment this, a reconnaissance Sr and Nd isotopic study of metasedimentary and igneous rocks has also been carried out, though a full exposition of the isotopic character of GRC rock units is beyond the scope of this study. The magmatic and tectonic synthesis in Chapter 17 integrates all geological information presented in earlier chapters.

The final chapter (Chapter 18) explores the broader implications of this thesis for granitic petrogenesis and the growth and differentiation of the continental crust, in view of the problems with these issues outlined in Chapter 1.

Two significant points are worth emphasising at this stage. Firstly, the main theme of this thesis is the description and interpretation of a complete spectrum of geology. Although the approach outlined above necessarily introduces artificial subdivisions, it should be kept in mind that rocks of each of the lithological entities are thought to be part of a single, continuous geological lineage. Secondly, the field and petrographic descriptions in Part II and III are directed towards petrogenetic interpretation. Hence, geochemical samples are alluded to specifically in descriptive chapters (sample numbers in bold type) to establish their geological context.

4.3 Definitions of terms used throughout the thesis

Before progressing, it is necessary to define and review the background behind specialist terms and introduce classification schemes that will be used throughout the following chapters.

4.3.1 Terminology of migmatites

A 'migmatite' is here considered to be a mesoscopically composite rock comprising portions of broadly metamorphic and igneous appearance. Following Ashworth (1985), the latter are

referred to as 'leucosomes', and the metamorphic part of the rock is termed 'mesosome'. In many migmatites, leucosomes and mesosomes are separated by material that is enriched in mafic minerals, or 'melanosomes'. Note that throughout this study rocks that exhibit development of a leucosome component may be referred to as 'migmatitic' but 'migmatite' is reserved only for rocks that comprise at least 10% leucosome, or exhibit diatexitic character (see below).

Although migmatites have many possible modes of formation (e.g. Johannes 1983), an anatectic origin is most commonly advocated. Here, leucosomes are generated by *in situ* partial melting, the residue of which is represented by the melanosome (but see below). Melting may have proceeded along more compositionally favourable horizons in the protolith (e.g. Johannes 1985; Brown *et al.* 1995), in which case the mesosome is more refractory or 'infertile' material that resisted anatexis. Alternatively, the mesosome may itself have differentiated upon melting into leucosomes and melanosomes, whereupon some workers substitute the term 'palaeosome' (e.g. Olsen 1985). In other models, mesosomes comprise the residues of anatexis following melt extraction (Kriegsman 2001).

Throughout this study, the term leucosome is applied to any discrete, millimetre- to centimetre-scale quartzofeldspathic body which is thought to have formerly contained a partially melted fraction. Mesosomes are considered to be those parts of the original rock that were largely unmodified by anatexis, whereas melanosomes include material that is demonstrably depleted in a feldspathic component, or enriched in mafic phases. The difficulties with recognising the former presence of melt within leucosomes due to obscuration of magmatic textures by slow cooling and/or later recrystallisation are discussed at length by Ashworth & McLellan (1985). With these in mind, the textural and field criteria that are considered to be characteristic of melt-derived or 'anatectic' leucosomes are outlined in Table 4.2. Note that although any combination of these features is used by this study to infer the former presence of partial melt within leucosomes, the occurrence of euhedral plagioclase and alkali feldspar is considered to be virtually diagnostic.

Criteria	*Leucosome features*
a. Textural	Euhedral grains or crystal faces of plagioclase or alkali feldspar (Vernon & Collins 1988) Euhedral zone boundaries in plagioclase (Ashworth & McLellan 1985) Carlsbad twinning in plagioclase (Shelley 1993)
b. Field	Occurrence in dilatant sites such as boudin necks or small shear zones (e.g. Brown 1994) Discordance with respect to major planar fabric Formation of complex and incoherent fold structures, i.e. 'viscous' or flow folds (McLellan 1984) Content of rotated fragments of foliated melanosome Contiguity with larger, obviously magmatic bodies

Table 4.2. Textural and field criteria used by this study for the recognition of former partial melt within leucosomes.

4.3.2 Origin and significance of melanosomes

It is commonly regarded that melanosomes of anatectic migmatites represent the direct residues of partial melting, concentrated by the efficient segregation or extraction of melt increments during leucosome formation (e.g. Johannes & Gupta 1982; Brown *et al.* 1995; Collins & Sawyer 1996; Sawyer 1999; Mengel *et al.* 2001). As such, they are complementary to leucosomes and comprise either minerals that are in excess amounts required for the melt reaction, the solid byproducts of peritectic melting reactions or refractory phases that did not participate in anatexis. Under this scenario, the mineralogy of melanosomes provides significant clues as to the nature of the partial melting reaction.

Alternatively, some melanosomes might also form by retrograde reaction between residual minerals and *in situ* crystallising melt (i.e. the 'rehydration crystallisation' of Ashworth 1985 and Brown 1994), or the reversal of the prograde melting reaction during cooling of the leucosome. For example, a vapour-absent incongruent or peritectic melting reaction of the general form–

$$\text{hydrous mineral} = \text{anhydrous mineral} + \text{MELT}$$

will reverse during crystallisation such that the anhydrous reaction products react with the cooling, fluid-rich melt to partly re-establish the original hydrous mineralogy of the protolith, i.e.–

$$\text{MELT} + \text{anhydrous mineral} = \text{hydrous mineral}$$

This mechanism is proposed to account for the occurrence of thick biotite-rich selvedges around migmatite leucosomes elsewhere, thought to be the 'back reacted' product of a biotite-involved melting reaction (Le Breton & Thompson 1988; Spear *et al.* 1999; Kriegsman 2001). Note that effective retrogression of anhydrous mineral assemblages requires closed-system cooling and minimal migration of melt or fluid during leucosome consolidation (see Ellis & Obata 1992). Importantly, the melt fraction generated by a peritectic reaction is necessarily modified during reaction with solid mineral phases, and hence the final leucosome composition may differ substantially from that of the original partial melt (Ellis & Obata 1992; Fourcade *et al.* 1992; Kriegsman 2001).

Which of these scenarios is apposite for the origin of melanosomes within a migmatite may be elucidated by textural studies (e.g. Ashworth & McLellan 1985). Nevertheless, in either case, the presence of melanosomes supports the *in situ* development of leucosomes within the rock (e.g. Sawyer 1996; Collins & Sawyer 1996; Oliver & Barr 1997; Sawyer 1999). The origin of melanosomes within GRC migmatites, with associated petrogenetic implications, is explored throughout the course of this study.

4.3.3 Classification of migmatites

Migmatitic rocks may be classified on the basis of morphology, (e.g. Mehnert 1968), of which two types are relevant, 'stromatic' migmatites and diatexites. Stromatic migmatites are those in

which the lithological components exhibit a repetitious, grossly layered structure, which may be planar or complexly folded. Leucosomes are sharply defined elongate bodies that are sometimes discontinuous but are generally concordant with pre-existing anisotropies, such as metamorphic fabrics or compositional layering. In contrast, diatexites have a vague granitic appearance and are characterised by a wispy layering, defined by elongate schlieren and diffuse bands slightly enriched in mafic minerals. Discrete leucosomes and mesosomes are difficult to resolve in these rocks, which is attributed to the development of a pervasive melt fraction and limited segregation of partial melt from solid residuum (Brown 1983; Sawyer 1996). Melanosomes are generally represented by elongate lenticular bodies of concentrated mafic minerals, referred to here as 'micaceous enclaves'. Many diatexites also contain tapering enclaves of more refractory rock where pre-migmatisation structures are preserved (e.g. Sawyer 1996).

4.3.4 Interpretation of complex field relations involving migmatitic rocks

Extreme complexity at outcrop scale is a recurrent theme in migmatite terranes worldwide, imparted by an interplay between tectonically-driven deformation on one hand and melt generation, segregation and migration phenomena on the other (e.g. Brown 1994). This level of complexity is also encountered in the northeastern migmatite zone of the GRC. Migmatitic exposures commonly contain geometrically diverse arrays of anatectic leucosomes, many of which are interconnected and apparently contiguous with irregularly-shaped, discordant granitic bodies and thick granitic sheets and dykes. The latter are in turn possibly linked to pluton-scale bodies of muscovite granite, though polyphase folding provides additional complication.

To effectively describe and to convey the significance of these relationships, a certain level of genetic interpretation is unavoidable. This is particularly true with regard to whether the granitic melt is generated and segregated *in situ*, thereafter migrating from the outcrop via progressively larger conduits, or is externally derived and complexly intruding a metasedimentary horizon, which may also contain an *in situ* partial melt fraction. Obviously in the first case, the petrogenesis of the larger magmatic bodies is intricately linked to the formation and segregation of *in situ* partial melts, though the significance of the latter is greatly diminished in the second interpretation.

As an integral part of this research is to evaluate the connection between migmatite and larger granitic bodies, the interpretation of such field relationships is crucial, and potentially the foundation for petrogenetic discussions in later chapters. Accordingly, within Chapters 5 and 6 it is proposed to firstly describe the migmatitic phenomena from various 'type' localities, where relationships are clearest, and to follow the description by a separate section in italics outlining the interpretation of key features within the outcrop. This device has the advantage of clearly distinguishing between observation and interpretation, but also of cementing important field based conclusions early and avoiding reiteration in later sections. It is acknowledged that interpretations of complicated exposures necessitates unravelling several competing geological processes and thus may be subjective to a certain extent, which partly accounts for the enduring controversies surrounding the origin of migmatitic rocks (e.g. Ashworth 1985, p.6). The outcrop interpretations throughout the descriptive parts of this thesis will therefore be justified as far as possible, with this achieved by forward reference to geochemistry in some cases.

4.3.5 Classification and terminology of enclaves

Following Didier (1973) and Didier & Barbarin (1991) lithological fragments enclosed by magmatic rock bodies are referred to as 'enclaves'. Enclaves are common in granitic rocks of the GRC, with two fundamentally different types recognised, metasedimentary enclaves and mafic microgranular enclaves (Didier & Barbarin 1991).

Metasedimentary enclaves represent incorporated regionally metamorphosed sedimentary rocks, or rocks of originally sedimentary parentage subsequently modified by anatectic processes. As such, the definition includes generally lenticular, melanosome-like objects dominated by aligned micaceous minerals, herein termed 'micaceous enclaves'.

Objects with pervasive igneous textures that are darker coloured and finer grained than the granitic host are referred to as **mafic microgranular enclaves**. Although 'microgranular' implies a grainsize of ~1 mm or less, enclaves of this type may be medium grained (e.g. Barbarin 1988) or have strongly bimodal grainsize, with large individual crystals (Chen *et al.* 1991). Mafic microgranular enclaves are 'composite' if they enclose smaller microgranular or metasedimentary enclaves.

Didier & Barbarin (1991) also define 'schlieren' as elongate objects with gradational margins, formed primarily by disruption of pre-existing enclaves. However, throughout this research, 'schlieren' is a general morphological term applied to very elongate bodies with higher concentrations of mafic minerals than the magmatic host, and may have either discrete or diffuse contacts; no specific mode of formation is implicit.

PART II

Field relations, petrology and petrogenesis of migmatites and muscovite-bearing 'Harrow type' granitic rocks of the northeastern Glenelg River Complex

(includes Chapters 5 to 9)

Chapter 5: Metasedimentary rocks and muscovite-bearing granitic bodies of the northeastern migmatite zone

(A) Coleraine District

5.1 Introduction

Metasedimentary rocks of the northeastern migmatite zone include large tracts of quartzofeldspathic schist and quartzofeldspathic gneiss, interlayered with, and transitional to, a diverse assemblage of migmatitic rocks, exposed along major watercourses such as the Glenelg River and Bryan Creek. Semi-pelitic horizons are minor. Anatexis proceeded during two episodes of the structural history, initially pre- to syn-D_2 (M_1), but most extensively during the interval pre-D_3 to post-D_4 (M_2), when the largest proportion of granitic melt was generated (section 3.7).

Leucocratic granitic rocks of 'Harrow type' are also a major component of the northeastern migmatite zone (section 4.1.2), occurring as dykes, plutons and structurally concordant sill-like bodies enveloped by migmatites. These granitic phases generally have pristine igneous textures and contain abundant muscovite, accompanied by garnet in more felsic lithologies or sillimanite in biotite-rich varieties. Most muscovite forms coarse euhedral plates, commonly intergrown with magmatic-looking biotite, and is therefore melt-precipitated (Miller *et al.* 1981c; Zen 1988). In contrast, ragged spindly flakes enclosed by feldspar or overgrowing fibrolite that occur in some samples are probably of subsolidus origin. Biotite is typically subordinate to muscovite and deep reddish-brown in thin section, whereas opaque minerals are absent, consistent with the iron deficient nature of most phases. Alkali feldspar exhibits patchy development of microcline twinning, most conspicuous around plagioclase and quartz inclusions. Metasedimentary enclaves and megacrysts of graphic alkali feldspar are characteristic, and, apart from the Nangkita Adamellite (below), mafic microgranular enclaves are absent. Importantly, metasedimentary enclaves commonly support F_3 and/or F_4 structures (see Figure 6.5). This confirms that emplacement of Harrow type granitic rocks postdated the development of the regional S_2 foliation and was broadly synchronous with M_2, consistent with the unrecrystallised igneous microfabric.

Harrow type granitic bodies of the Harrow and Coleraine districts are additionally classified as either structurally concordant or structurally discordant, based upon their field relationships with the surrounding metasedimentary rocks. The former group are texturally and compositionally heterogeneous, exhibit intimate and complex field relationships with host migmatites, and have a directional fabric that parallels S_2. The fabric, defined principally by micaceous schlieren, is non-imposed and relates to magmatic flow (Kemp & Gray 1999a). In contrast, structurally concordant bodies are relatively homogeneous, with weak annular foliations, and have sharply intrusive contacts.

This chapter focuses upon the field relations and petrography of metasedimentary and Harrow type granitic rocks outcropping in watercourses near Coleraine, with those of the Harrow district discussed in the following companion chapter. Of the Coleraine region, the most important Harrow type plutons are the Nangkita Adamellite, exposed in Robson and Log Hut Creeks, and the Bryan

Creek Granodiorite of Bryan Creek. Both are structurally concordant and intricately enmeshed with migmatitic and other metasedimentary lithologies; neither has been previously described.

5.2 Geology of Robson Creek

The most continuous and well exposed transect through the migmatitic sequence of the northeastern metamorphic zonation occurs along the convoluted channel of Robson Creek, which flows northwestwards into Bryan Creek. Metasedimentary outcrop commences with prominent exposure of quartzofeldspathic gneiss in the western section of the watercourse, and progresses through a lithologically variable sequence of interlayered quartzofeldspathic schist, semi-pelitic schist, stromatic migmatite (which hosts high proportions of M_1 and M_2 leucosomes) and diatexite, eventually adjoining the Nangkita Adamellite 2.4 km to the east (Figure 5.1). Dykes and interlayered sheets of muscovite leucogranite are numerous, commonly connected to networks of *in situ* leucosomes, and become increasingly abundant as the Nangkita Adamellite is approached.

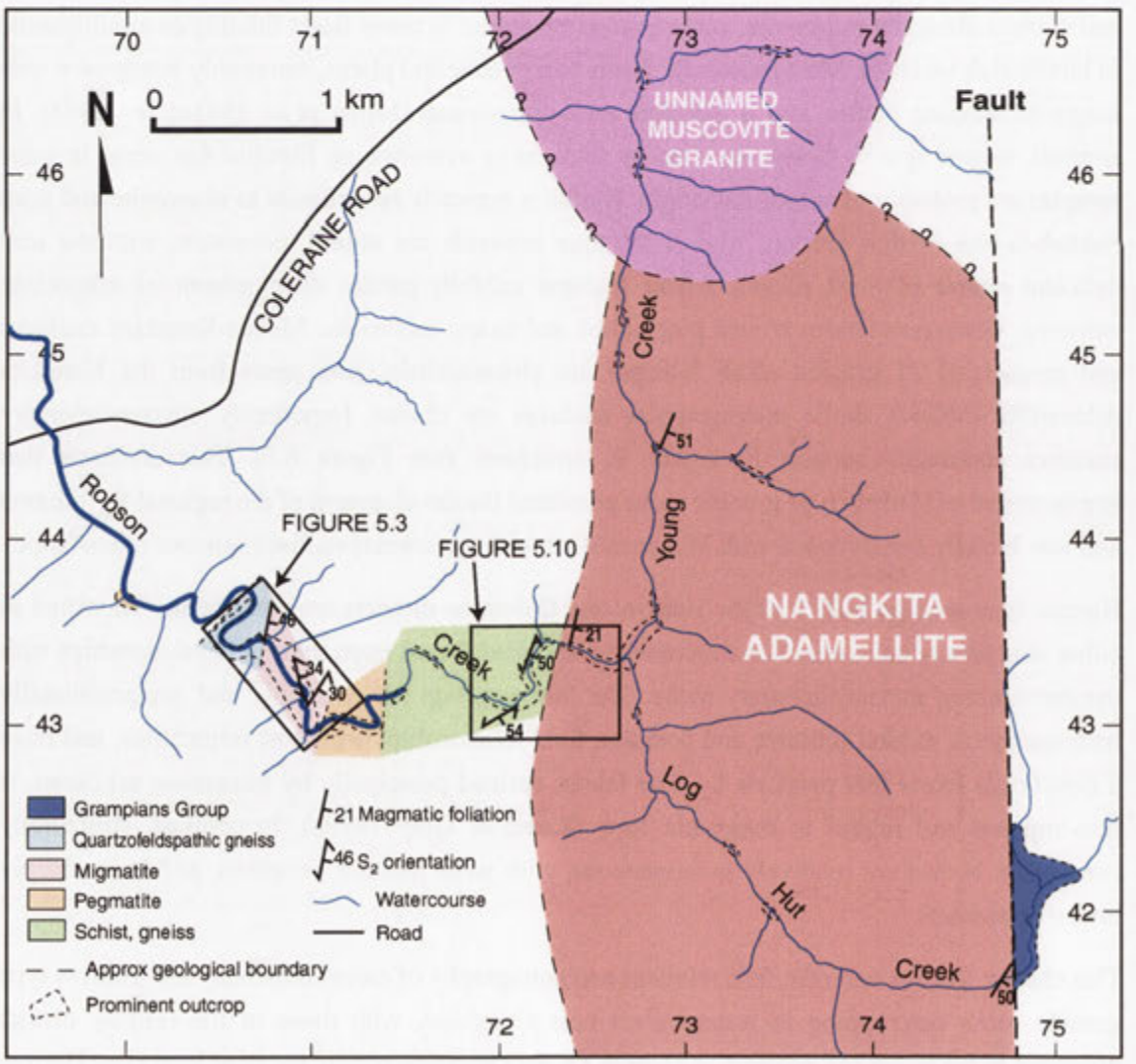

Figure 5.1. Simplified geological map of Robson Creek and tributaries.

Due to the significance of these relationships, the geology of Robson Creek is described in detail, sequentially from quartzofeldspathic gneiss in the western part of the watercourse through to the adamellite pluton in the east. Prominent outcrop is noted in two distinct segments of the watercourse, the first being a ~600 m tract of the steeply incised gorge section of the creek, and the second occurring immediately adjacent the junction with the Nangkita Adamellite further east. These segments are treated separately.

5.3 Robson Creek Gorge

5.3.1 Geological overview

The three main components of the Robson Creek gorge metasedimentary sequence are- (1) relatively unmigmatitic quartzofeldspathic gneiss and schist, (2) M_1 stromatic migmatite, and (3) M_2 stromatic migmatite and diatexite. The criteria used to discriminate between leucosomes of different generations are summarised by Table 5.1 and Figure 5.2. M_2 anatectic phenomena are localised into four main horizons, interspersed with bands of gneissic rocks and M_1 stromatic migmatites. For simplicity, this sequence is treated as eight individual units, labelled from 'A' to 'H' from west to east along Robson Creek gorge (Figure 5.3, Table 5.2). Decimetre- to metre-sized bodies of muscovite-bearing leucogranitic rock are another important ingredient. Representative examples of these lithologies and their field relations are described below; the mineral assemblages of migmatite samples from different horizons are summarised by Table 5.3 (M_1 samples) and Table 5.4 (M_2 samples). The modal mineralogy of granitic dykes/sheets is presented in Table 5.5. Layer parallel pegmatites (up to 5 m wide) also occur in all units, many being isoclinally folded, boudinaged and tightly refolded by D_3 and D_4 structures.

Timing	*Leucosome geometry*	*Leucosome texture/mineralogy*
M_1 (pre/syn-D_2)	• outlines hinge-thickened isoclinal folds	• either coarse grained and quartz-rich or fine grained and sugary-textured
	• may be boudinaged or transposed	• Pfs dominant, Afs usually minor
	• always concordant with S_2 in the mesosome	• strongly foliated, deformation and recrystallisation features obvious in thin section, e.g. kinked Pfs twins, subgrains
M2 (pre-D_3 to post-D_4)	• mostly concordant with S_2 but transgressive varieties common, especially oriented parallel to S_3	• medium or coarse grained, commonly heterogeneous-textured • 'granitic-looking', magmatic texture • poikilitic Afs phenocrysts
	• may be rotated by F_3	• disseminated micas non-aligned • may have fragments of F_3-crenulated melanosome

Table 5.1 Features used to discriminate between M_1 and M_2 leucosomes in migmatitic rocks. The criteria used to ascertain an anatectic origin for leucosomes are listed in Table 4.2 (Afs = alkali feldspar, Pfs = plagioclase feldspar).

Figure 5.2. Migmatitic gneiss in Robson Creek exhibiting evidence for two episodes of partial melting. The first generation leucosomes (M_1) are parallel to the foliation/layering (S_2, parallel to long edge of the photo), and rotated by F_3 (centre left). These are overprinted by second generation leucosomes (M_2) (top) which truncate the S_2 fabric. The preferred orientation of M_2 leucosomes, vaguely parallel to S_3, suggests structural control and syn-tectonic melt generation.

Unit	*Timing of anatexis*	*Lithological assemblage*	*Remarks*
A	Mostly M_1	• qf gneiss, lesser semi-pelitic schist & stromatic migmatite	• boundary with unit B is sharp and conformable
B	M_2	• diatexite	• some retrograde D_5 shearing at contact with unit C
C	Mostly M_1	• qf gneiss, lesser semi-pelitic schist & stromatic migmatite	
D	Mostly M_2	• stromatic migmatite, diatexite, qf gneiss	• commences with bluff-like outcrop
E	Mostly M_1	• qf schist, laminated schist, qf gneiss	• separated from unit D by a 2 m thick qf schist horizon
F	M_2	• stromatic migmatite, qf gneiss, laminated schist	• relatively recessive outcrop
G	Mostly M_1	• stromatic migmatite, semi-pelitic schist, qf schist, qf gneiss	• commences with bluff-like outcrop and a large waterfall
H	Mostly M_2	• stromatic migmatite, qf schist, qf gneiss, diatexite	• demarcated from unit H by a thin diatexite band.

Table 5.2. Summary of the main anatectic and lithological characteristics of the geological units A-H of Robson Creek gorge. Rock types in each unit are listed in order of relative abundance in the sequence (qf = quartzofeldspathic).

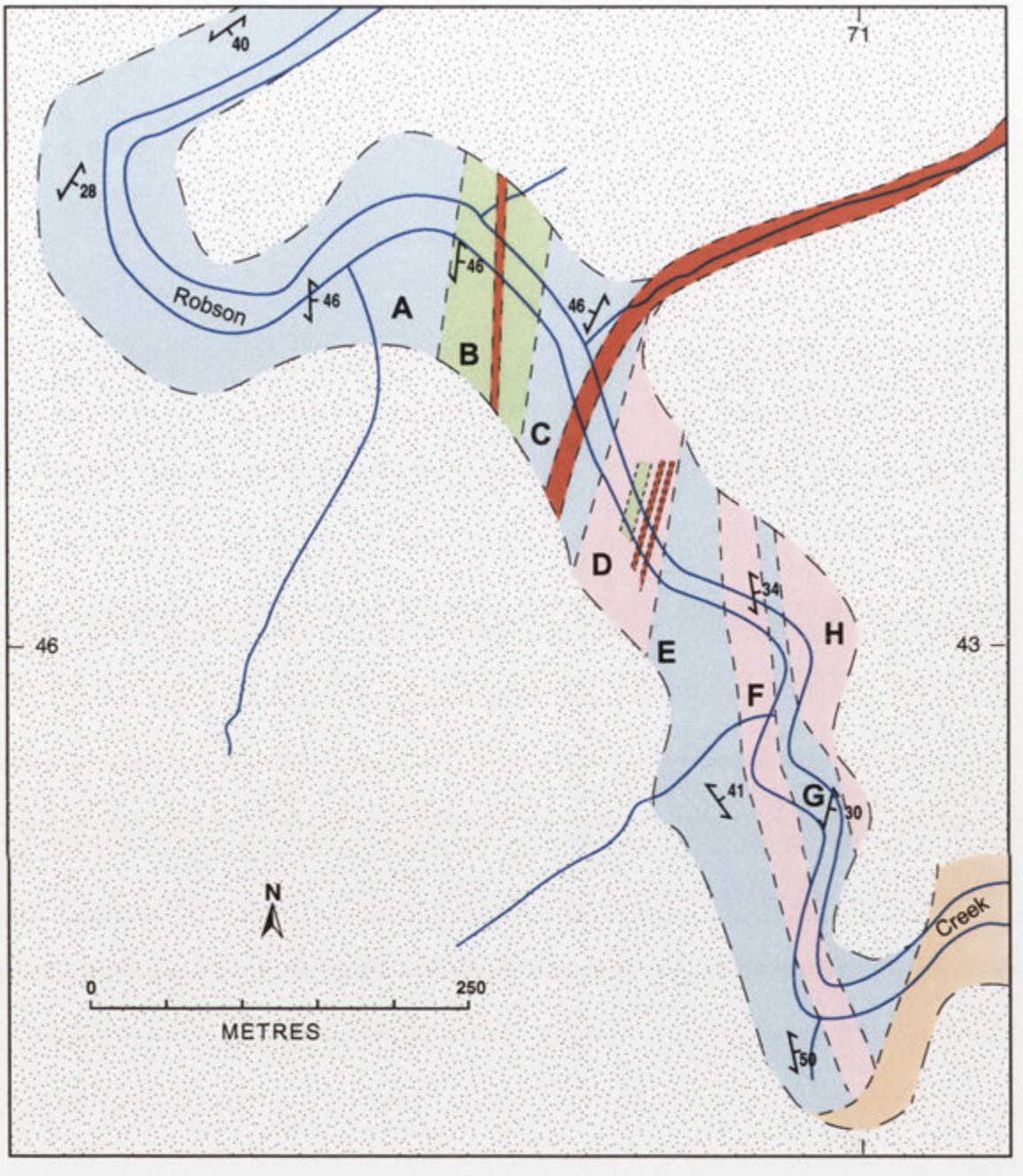

Figure 5.3. Map of Robson Creek gorge showing geological units A to H. The location is shown in Figure 5.1.

Sample	*Locality*		*Modal Percent*							
M_1			Qtz	Pfs	Afs	Biotite	Musc	Sill	Musc*	Acc.
99-5	Robson Ck	leuco.	35	24	35	1	1	2	1	-
(Sp)	(unit G)	meso.	27	20	10	30	10	1	2	ap
		melano.	25	10	-	45	5	5	10	-
97-R1	Robson Ck	leuco.	35	42	20	2	1	-	-	ap
(Qf)	(valley)	meso.	35	25	12	20	5	-	3	ap
		melano.	30	10	-	57	1	-	2	ap, z
98-RG3	Robson Ck	leuco.	40	57	-	2	1	-	-	ap
(Sp)	(valley)	meso.	-	-	-	-	-	-	-	-
		melano.	-	15	-	45	40	-	-	ap, z
99-15	Robson Ck	leuco.	60	40	-	<1	<1	-	-	ap
(Qf)	(valley)	meso.	35	35	-	20	5	-	1	ap
		melano.	-	-	-	80	1	-	1	ap, z
97-R2C*	Robson Ck	leuco.	35	64	<1	<1	1	-	-	ap
(Qf)	(valley)	meso.	45	37	-	15	3	-	-	ap
		melano.	25	5	-	65	-	-	5	ap
98-WF2A*	Schofield Ck	leuco.	42	50	-	3	5	-	-	ap
(Sp)		meso.	15	15	-	30	40	-	-	-
		melano.	15	5	-	40	40	-	-	-
98-25M1	Schofield Ck	leuco.	58	50	-	3	5	-	-	ap
(Sp)		meso.	15	10	-	35	40	-	-	ap, z
		melano.	10	5	-	70	20	-	<1	ap, z
97-315	Chin Chap Ck	leuco.	55	43	-	1	1	-	-	ap
(Sp)		meso.	35	30	-	30	5	-	<1	ap
		melano.	10	5	-	50	35	-	-	-

Table 5.3. Mineralogy of M_1 stromatic migmatites of the GRC. Modes are estimated from one thin section (25 x 75 mm) and approximate only. Musc* denotes muscovite of inferred secondary or retrograde origin. The bulk composition of each sample is indicated as either semi-pelitic (Sp) or quartzofeldspathic (Qf). No mesosome thin section is available for sample 98-RG3.

Abbreviations are: Qtz = quartz; Pfs = plagioclase feldspar; Afs = alkali feldspar; Bio = biotite; Musc = muscovite; sill = sillimanite; ap = apatite; z = zircon.

5.3.2 Gneissic and schistose rocks

Although quartzofeldspathic gneiss and thinly interspersed horizons of semi-pelitic and quartzofeldspathic schist are predominant in units A and C, these rocks occur in all lithological units of Robson Creek gorge and have minor modal variations (Table 5.6).

Quartzofeldspathic gneiss has a repetitive, planar compositional layering, where quartzofeldspathic bands (2.5-5 mm thick) bordered by thin biotite concentrations alternate with finely laminated, more biotite-rich layers. In some gneissic rocks felsic bands have a lenticular geometry and outline rootless isoclinal closures, suggesting that the discontinuous banding is S_2 transposition layering. Quartzofeldspathic layers comprise essentially polygonal quartz and anhedral plagioclase, though the latter rarely exhibits Carlsbad twins and crystal faces against

quartz; in places, lath-like grains also have an interlocking geometry. These are relict igneous features and imply that felsic bands were partially molten subsequent to recrystallisation. The finer grained, more biotite-rich layers have a foliation defined by biotite and variable amounts of interleaved muscovite, and sometimes contain poikiloblastic alkali feldspar, erratically distributed along the bands. The S_2-aligned muscovite is well shaped and penetrates biotite, which throughout this thesis is taken to indicate crystallisation during prograde metamorphism. M_1 leucosomes are typically sporadic, but where these become concentrated the gneiss grades into stromatic migmatite.

Sample	*Locality*		*Modal Percent*							
M_2			Qtz	Pfs.	Afs	Bio	Musc	Sill	Musc*	Acc.
98-RM1	Robson Ck	leuco.	32	44	22	<1	2	-	<1	a
(Qf)	(unit D)	meso.	38	32	4	21	5	-	<1	
		melano.	34	-	-	60	5	-	1	a, z
98-R2A	Robson Ck	leuco.	30	45	21	3	<1	-	1	a, g
(Qf)	(unit D)	meso.	40	30	7	16	7	-	<1	a, z
		melano.	15	-	-	80	3	-	2	a, z
98-RG3	Robson Ck	leuco.	34	39	25	1	1	-	<1	
(Qf)	(unit D)	meso.	21	26	20	25	5	-	3	a
		melano.	5	5	-	80	2	-	8	a, z
98-R5B	Robson Ck	leuco.	32	39	29	<1	<1	<1	-	a
(Qf)	(unit F)	meso.	45	28	7	18	2	-	<1	a
		melano.	58	-	-	36	-	<1	5	a, z
99-7	Robson Ck	leuco.	28	31	32	3	1	3	2	
(Sp)	(unit H)	meso.	25	20	15	27	2	3	8	a
		melano.	38	-	-	55	-	1	6	a, z
97-244	Robson Ck	leuco.	33	36	24	2	5	-	<1	
(Qf)	valley	meso.	46	22	-	26	5	-	1	a
		melano.	28	3	-	63	8	-	1	a ,z
98-WF1A	SC (nth)	leuco.	35	44	15	<1	6	-	<1	a
(Qf)		meso.								
		melano.	5	-	-	55	40	-	-	a, z
98-25M2	Schofield Ck	leuco.	35	47	13	<1	5	-	-	a
(Sp)		meso.	18	13	-	37	32	-	-	a
		melano.	6	-	-	80	6	-	8	
98-65A	Schofield Ck	leuco.	31	37	26	3	1	<1	2	
(Qf)		meso.	36	29	15	16	2	-	2	a
		melano.	25	-	-	70	-	-	5	a, z
98-65B	Schofield Ck	leuco.	36	32	31	<1	1	-	-	
(Qf)		meso.	36	29	15	16	2	-	2	a
		melano.	30	-	-	65	-	-	5	a
97-349	Bryan Ck	leuco.	39	47	5	6	2	-	1	a
		meso.	40	31	9	17	2	-	1	a
		melano.	50	10	-	35	-	-	5	a, z
98-102	Chin Chap Ck	leuco.	34	49	10	4	3	-	-	a
(Qf)		meso.	36	30	6	25	2	-	1	a
		melano.								

Table 5.4. Mineralogy of M_2 stromatic migmatites of the GRC. Modes are estimated from one thin section and approximate only. Note that Musc* denotes muscovite of inferred secondary or retrograde origin. The bulk composition of each sample is indicated as either semi-pelitic (Sp) or quartzofeldspathic (Qf). Mineral abbreviations are as in Table 5.3, with g = garnet.

Sample	*Geometry*	*Grid Ref.*	*Modal Percent*						*Comment*
		(WD)	**Qtz**	**Plag.**	**K-felds.**	**Musc.**	**Bio.**	**Acc.**	
Robson gorge									
98-R5A	Sheet	710432	36.8	21.1	28.5	13.1	0.1	a, g	Linked to *in situ* leucosomes and dyke **98-R7**
98-R6	Dyke	710432	32.9	38.4	24.0	2.7	1.5	a	Possibly linked to granitic dyke **98-R7**
98-R7	Dyke	709431	32.1	21.0	35.8	7.5	2.5	a (0.8%)	Irregularly-shaped dyke joined to *in situ* leucosomes and larger segregations
98-R8	Sheet	710431	26.5	31.5	36.5	4.1	1.3	c	Connected to the discordant segregation in Figure 5.8a
Robson valley									
97-R2D	Sheet	720431	24.1	31.7	41.4	2.5	0.1	c	Intrudes quartzofeldspathic schist
97-R2E	Sheet	720431	35.3	39.8	23.0	1.1	0.6		Contained by quartzofeldspathic schist, has bifurcating geometry
97-R2F	Sheet	721431	27.6	27.8	35.6	6.8	1.5	c	5m thick body concordantly interlayered with migmatite. Contains micaceous schlieren.
97-XCL	Dyke	721431	41.0	32.0	18.6	8.0	0.1	a, c	Crosscutting dyke-like body joined to layer-parallel leucosomes
97-R3	Dyke	721431	33.0	31.6	24.5	7.6	3.0	a	Thick, internally-heterogeneous sheet
97-R3-2A	Dyke	721431	45.3	31.6	19.5	1.3	2.1		Quartz-rich domain within **97-R3**
Bryan Creek									
97-396	Sheet	684506	38.9	29.6	14.7	5.6	10.7	a, sill	1 m wide body intimately interlayered with migmatite
97-396B	Sheet	684506	36.1	31.6	25.5	2.1	4.5		Interlayered with more biotite-rich granite
Schofield Creek									
98-WF1B	Sheet	591863	28.6	41.1	26.6	2.6	0.6	a	Linked to *in situ* leucosome **98-WF1A**
98-SC	Pool	588851	37.5	40.6	19.6	2.1	0		Linked to *in situ* leucosomes in Fig. 6.12

Table 5.5 Modal mineralogy of small granitic bodies of the eastern GRC, determined by thin section point count (1500 points). Note that alkali feldspar exhibits patchy microcline twinning. The geochemistry of all samples is listed in Appendix C. Grid references quoted in this Table and throughout the thesis correspond to Australian Geodetic Datum 1966, Map Grid Zone designation 54H WD. Abbreviations are: a = apatite; c = chlorite; ga = garnet; sill = sillimanite.

Quartzofeldspathic schist samples are homogeneous, fine grained bluish-grey rocks with continuous weak biotite foliations, sometimes augmented by minor primary muscovite; micas may also be concentrated into fine laminae. Plagioclase is abundant, and poikiloblastic alkali feldspar occurs in many samples, but is unevenly distributed throughout the rock.

Semi-pelitic schist contains higher proportions of interleaved biotite and muscovite, with minor quartz and plagioclase; alkali feldspar is absent or minor. Rarely, non-aligned, ragged muscovite plates (to 4 mm) enclose interwoven mats of fibrolite. Sample 99-SP5, interlayered with M_1 migmatites, has prograde muscovite and S_2-aligned fibrolite aggregates coexisting with poikiloblastic microcline. However, this assemblage is most uncommon. Note that tiny accessory zircon and monazite crystals (identified by electron microscopy) occur in most metasedimentary rocks and are almost invariably enclosed by micas. In contrast, apatite, which forms coarser, equant granules (up to 0.8 mm in gneissic samples), exhibits greater tendency to occur at grain boundaries.

Sample	*Lithology*	*Grid Ref.*	*Modal Percentage*					
		(WD)	Qtz	Plag.	K-felds.	Biotite	Musc.	Acc.
Robson Ck gorge								
96-R1	Qf gneiss	708434	42.0	30.1	4.6	21.3	1.8	a
98-R2B	Qf gneiss	708433	39.2	28.7	6.2	17.2	8.2	
98-R4	Diatexite	709433	34.5	40.7	9.4	11.7	2.0*	sill (1.4%)
99-R5	Diatexite	710432	32.4	36.5	14.8	14.0	2.0	a, sill
98-R3	Diatexite	708433	34.0	34.8	20.5	9.2	1.2*	a
99-5	Diatexite	709432	21.7	14.3	6.4	33.7	16.9*	a, sill (6.7%)
Robson Ck valley								
98-R1	Qf schist	721431	38.0	27.8	10.6	21.2	2.4*	a
Chin Chap Creek								
97-316	Qf gneiss	707508	38.6	29.6	4.8	24.5	2.3*	
97-317A	Mica schist	707507	15.8	4.1	0	37.6	42.3*	a, sill
Schofield Creek								
T2-CC20	Qf schist	591863	44.8	32.2	0.2	22.1	0.4*	a
98-13B	Qf schist	580848	41.1	27.6	5.8	18.0	7.1	a
98-14B	Qf schist	580848	42.0	37.4	0	20.1	0.5*	a
T2-302B	Qf gneiss	577809	37.8	27.9	12.9	20.2	0.9*	a
98-WF2A	Sp schist	591863	34.1	14.8	1.1	30.8	19.0	
Glenelg River								
T2-146MG	Qf gneiss	646840	40.6	29.0	6.8	21.1	6.1*	a
T2-2B	Qf gneiss	641839	38.9	34.3	0	23.2	3.6*	a
T2-35	Sp schist	570867	27.7	18.5	15.4	22.8	15.6	
T2-64	Sp gneiss	643839	40.1	26.1	0	27.4	6.1	a
98-69	Sp gneiss	553866	36.0	28.5	0	34.0	1.5	a
98-75	Qf gneiss	533868	38.0	19.8	15.5	24.5	2.1*	a
Scabbing Station Ck								
97-429	Sp schist	652835	36.0	12.2	3.4	37.4	10.6	a

Table 5.6. Modal mineralogy of representative metasedimentary rocks and diatexites of the GRC, determined by thin section point count (2000 points) (Qf = quartzofeldspathic; Sp = semi-pelitic). * denotes muscovite of dominantly secondary origin.

5.3.3 M_1 migmatites

Stromatic migmatites developed during M_1 are prominent in units E and G of the metasedimentary sequence, but most clearly exposed in large, water-washed pavements at a small waterfall in unit G. This locality is therefore taken as the type occurrence for M_1 stromatic migmatites in Robson Creek gorge.

Here, M_1 stromatic migmatite horizons (10 cm to 1 m thick) are interspersed with, and transitional to, migmatitic quartzofeldspathic gneiss, quartzofeldspathic schist and semi-pelitic schist (5-50 cm thick layers). Migmatites are intensely deformed, and exhibit interference structures between F_2, F_3 and F_5 folds, with F_2 structures prevalent (Figure 5.4a). Leucosomes are thus morphologically complex, occurring as irregular elongate patches, translated hinge-thickened isoclinal closures, or discontinuous, contorted veins with pinch-and-swell geometries, sometimes being boudinaged into lenticular segments. Note that the latter indicates leucosomes were more competent (i.e. mechanically stronger) than the surrounding melanosome/mesosome during deformation, only possible if they were largely or wholly solidified at this time. This relationship, consistently observed in migmatites across the GRC, implies that M_1 partial melting had largely ceased by the end of the second deformation.

Leucosomes are also very heterogeneous within a single horizon, varying in grainsize, proportion of quartz to feldspar and biotite content. The commonest varieties are coarse grained and quartz-rich, where clots of fibrolite (up to several millimetres thick) are embedded within clear quartz grains. More feldspathic, granitic-looking leucosomes with conspicuous biotite are also prominent, and are typically sugary textured due to D_2 recrystallisation. Elongate sillimanite strands sometimes occur in these leucosomes (e.g. 99-5 in Table 5.3), particularly when hosted by sillimanite-bearing semi-pelitic mesosomes. Although deformation features are obvious in thin section, such that plagioclase has undulose extinction, distorted twin planes and cuspate boundaries against recrystallised quartz aggregates, crystal faces (against alkali feldspar) and almost perfectly euhedral plagioclase laths are surprisingly common and testify to the anatectic origin. Alkali feldspar is consistently interstitial to quartz and plagioclase, or poikilitically encloses these minerals, and clearly crystallised last. Importantly, some leucosomes vary from coarse grained and quartz-rich to finer grained and more feldspathic along their length, with concomitant change in the nature of the melanosome (below). Intensely deformed pegmatitic leucosomes, with alkali feldspar augen, also rarely occur.

Most leucosomes are bordered by thick melanosomes that are also variable in composition, but whose mineralogy correlates with that of the respective leucosome. The coarser grained quartz-rich leucosomes are mostly bordered by discontinuous selvedges of coarse biotite (up to 1 cm thick) or biotite and quartz (to 5 cm thick), with overprinting secondary muscovite only (Figure 5.4b). Tufts of fibrolite are also common, enclosed by polycrystalline quartz masses. Sillimanite-bearing feldspathic leucosomes (e.g. 99-5) have fibrolite aggregates (enclosed by ragged muscovite) in melanosomes, accompanied by primary muscovite. However, many melanosomes rimming feldspathic or pegmatitic leucosomes contain foliated euhedral muscovite (up to 30%) to the exclusion of sillimanite. This muscovite is intimately interleaved

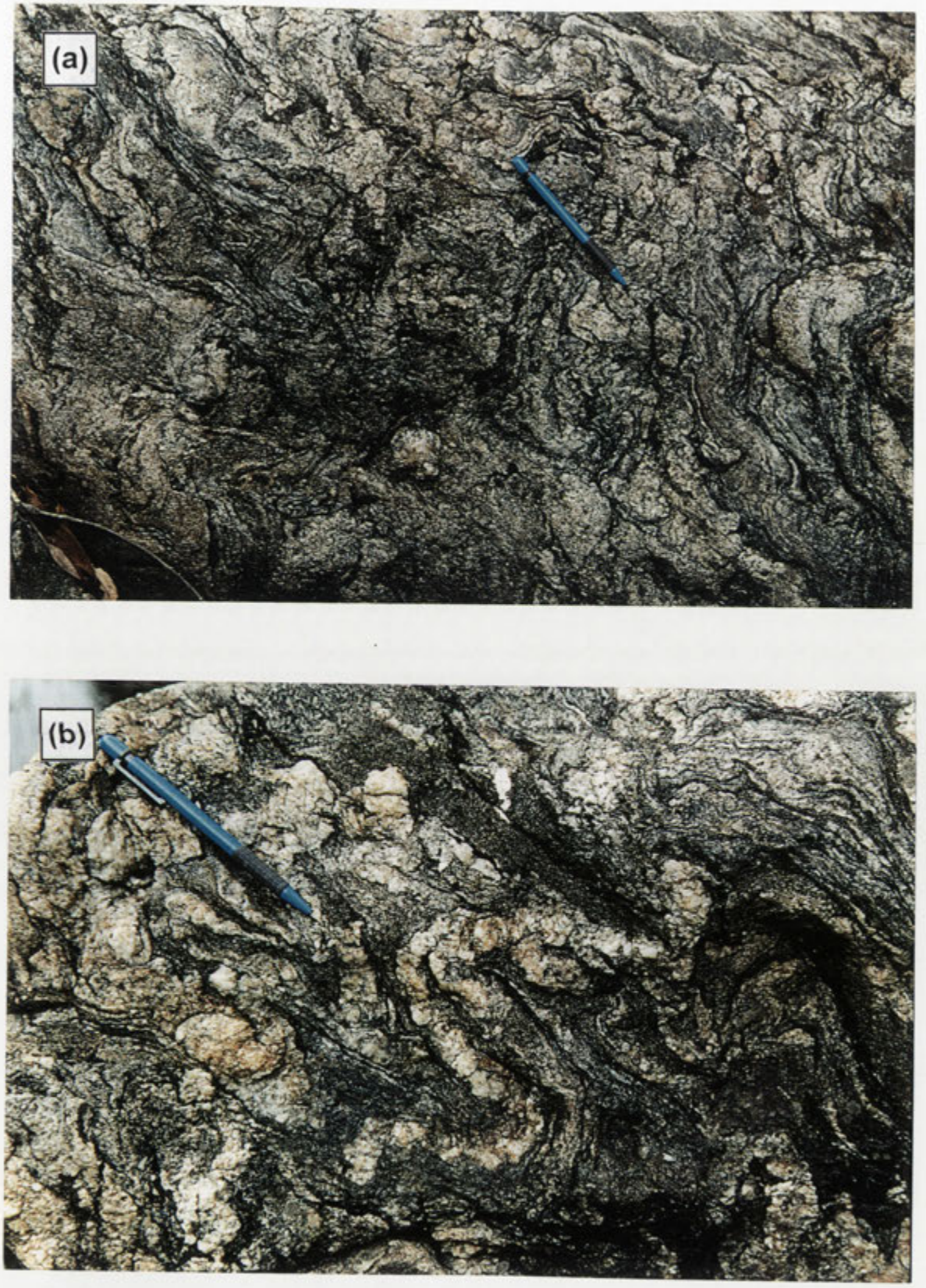

Figure 5.4. M_1 stromatic migmatites. (a) Structurally-complex exposure, where isoclinally-folded, commonly transposed leucosomes (e.g. centre right) are rotated by D_3 and D_4 folds. (b) Closer view of a leucosome with biotite-rich melanosomes deformed by F_3. Ragged secondary muscovite flakes are conspicuous (e.g. reflective grains near pencil tip and at top centre) (WD700431).

with biotite and texturally identical to muscovite in adjacent mesosomes and unmelted gneisses. Rarely, small lenticular pockets of polygonal plagioclase grains also occur in the thickest melanosome segments.

Mesosomes of M_1 stromatic migmatites within unit G are either semi-pelitic schist, laminated schist or quartzofeldspathic gneiss, with all being more biotite-rich than similar non-migmatitic rocks. Rarely, semi-pelitic mesosomes contain coexisting primary muscovite, sillimanite, and alkali feldspar.

5.3.4 M_2 diatexites

The second anatectic episode (M_2) resulted in the formation of stromatic migmatites and diatexites throughout the metasedimentary sequence of Robson Creek gorge, these lithologies being most prominent in units B, D, F and H (Table 5.2).

The 50 m thick diatexite horizon comprising Unit B has a strikingly regular layering of sinuous micaceous schlieren and diffuse biotite-rich streaks, alternating with medium to coarse grained granitic bands that have conspicuous non-aligned biotite (Figure 5.5). The layered aspect is accentuated by lenticular pockets and sheets of coarser grained leucogranite (to ~15 cm thick), that have diffuse margins and resemble leucosomes of stromatic migmatites. Parallel asymmetric micaceous enclaves (1-8 cm long) and tapering 'boudin-like' quartzofeldspathic schist enclaves (up to 50 cm long) deflect the schlieric banding, along with anhedral alkali feldspar megacrysts and occasional quartz chunks. Megacrysts are commonly wrapped by micaceous schlieren, such that an asymmetric 'augen-like' appearance results, suggestive of rotation. The schlieric fabric is otherwise concordant with S_2 in adjacent gneisses. Fibrolite is occasionally interwoven with biotite and muscovite in schlieren, but more commonly forms strands or elongate bundles (to 30 mm long, 2 mm wide) enclosed by ragged secondary muscovite and aligned with the schlieric layering.

The diatexite horizon is internally variable with respect to the proportion of these lithological constituents. All gradations exist between enclave- and schlieren-rich varieties that are essentially evolved stromatic migmatites (e.g. Figure 5.5b), and more leucosome-rich rocks approaching schlieric granite; nevertheless the 'granitic' component is of higher proportion than that of most stromatic migmatites. In all varieties micaceous enclaves are primarily coarse, S_2-aligned biotite, though euhedral muscovite is a constituent of some. Micaceous and quartzofeldspathic schist enclaves support D_3 crenulations, consistent with development of the diatexite syn- to post-D_3, during M_2.

Despite the heterogeneous aspect, in thin section the diatexite has a broadly igneous texture, such that alkali feldspar forms large poikilitic masses (to 5 mm) enclosing euhedral, apparently melt-precipitated plagioclase, muscovite, biotite and quartz grains (Figure 5.6), and may itself have crystal faces against quartz. Elsewhere alkali feldspar is interstitial to rounded quartz grains. These features imply formation of alkali feldspar late in the crystallisation history. Small elongate muscovite flakes are interleaved with biotite, though larger, plate-like crystals occur in felsic domains and appear to be magmatically precipitated. Disseminated biotite grains are also well shaped, with euhedral terminations. An igneous microfabric also occurs within the more

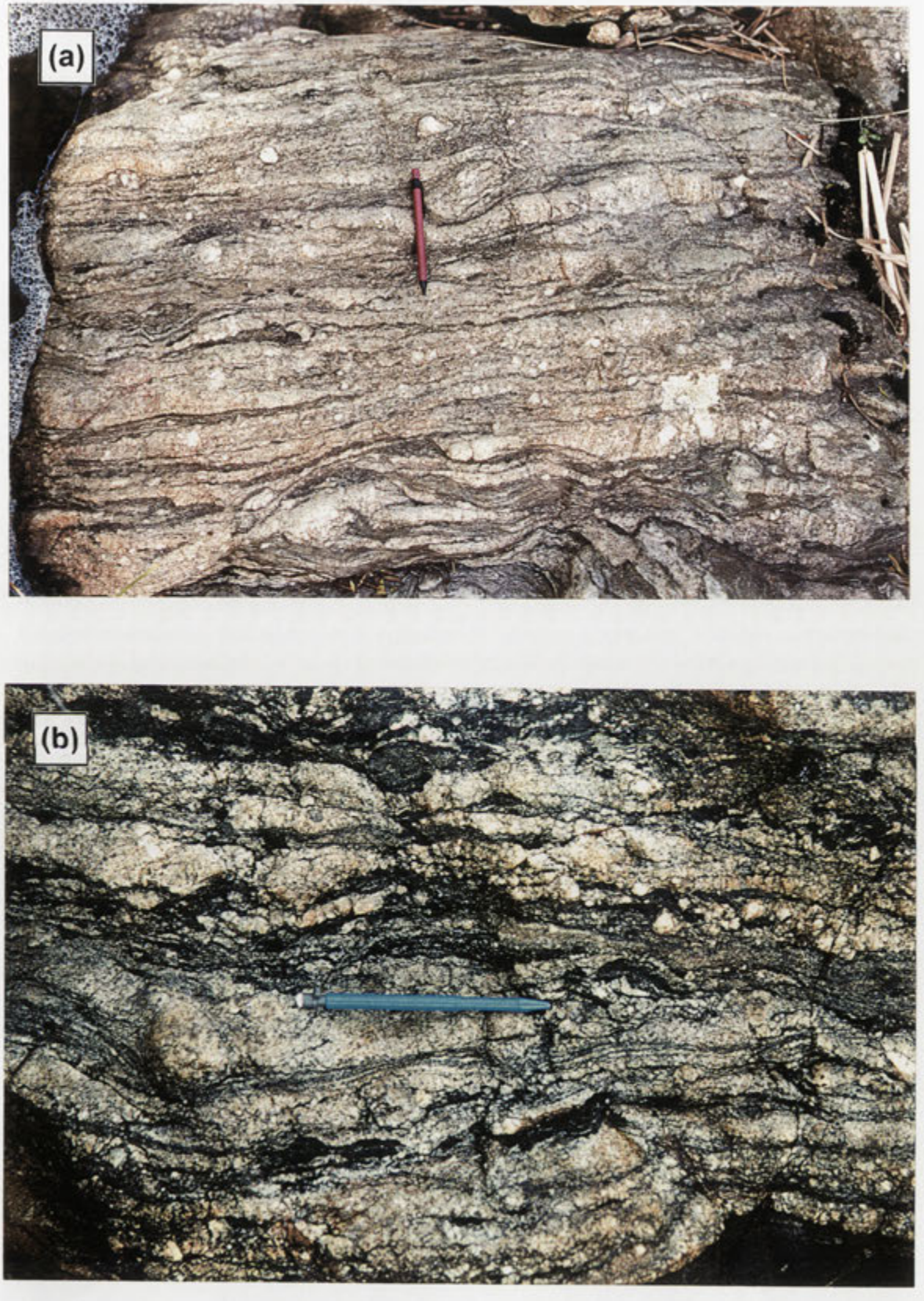

Figure 5.5. (a) Unit B diatexite, with dispersed alkali feldspar megacrysts and quartz chunks, some of which have an augen-like appearance. (b) More melanosome-rich portion of the diatexite, exhibiting biotite-sillimanite enclaves, some of which are asymmetric. Leucogranitic segregations are also more conspicuous (WD707436).

schlieric, biotite-rich portions of diatexite samples, implying that a partial melt fraction occurred throughout the diatexite horizon.

The thin diatexite horizons of unit D (2 m wide; **98-R4**) and unit H (0.5 m wide; **99-R5**, 99-5) are lithologically similar, though the latter is semi-pelitic, with an overall higher proportion of biotite and sillimanite (Table 5.6). Sample **99-R5** also has centimetre-scale felsic domains that comprise amoeboid quartz masses (~5 mm), the grain boundaries of which are lined by small polygonal plagioclase grains. Sillimanite clumps (1-2 cm) are common in these quartz-rich areas.

5.3.5 M_2 stromatic migmatites

Compared to their M_1 counterparts, M_2 stromatic migmatites of lithological units D, F and H contain higher proportions of leucosome, these being thicker (mostly 1-6 cm), more feldspathic and coarser grained, with a distinct 'granitic' appearance. However, the mineralogy and texture of leucosomes, melanosomes and mesosomes of M_2 stromatic migmatites also exhibits considerable outcrop-scale variability. Further, water-washed pavements reveal that M_2 leucosomes are morphologically diverse, and form complex networks that are intricately linked to small pond-like bodies and interlayered horizons of muscovite leucogranite.

Numerous excellent examples of this occur in units D, F and H, but due to the scale of petrographic variation and morphological complexity it is impractical to comprehensively document all. Instead, an outcrop from unit D, believed to be representative of the overall spectrum of migmatitic phenomena, is described below in detail. This is followed by a section

Figure 5.6. Diatexite in thin section, showing poikilitic alkali feldspar enclosing euhedral plagioclase (with fine sericite alteration), biotite, quartz and muscovite (M) inclusions (crossed polars, 2.5 mm across).

in italics outlining the interpretation of the critical aspects of the exposure (see section 4.3.4). For completeness, stromatic migmatite outcrops in unit F and H exhibiting slightly different characteristics are also briefly described.

(a) Stromatic migmatites of unit D

Stromatic migmatites of unit D are dominated by M_2 leucosomes, and, as these typically have complex geometries, many outcrops have a chaotic or 'sloppy' appearance (Figure 5.7). Leucosomes form vein-like bodies that are rarely planar (0.5-3 cm thick) but mostly have irregular thickness (0.5-5 cm thick), with bulbous and tapering geometries. The most common variety (e.g. **98-R2A**) is uniformly medium to coarse grained, whereas others have slightly larger alkali feldspar and quartz masses (to 6 mm). Anhedral megacrysts of graphic alkali feldspar (2.5-3 cm) occur in some leucosomes. Subhedral plagioclase is generally predominant, in thin section having oscillatory or complex mottled zoning. Alkali feldspar forms irregularly-shaped poikilitic masses or rectangular grains with patchy microcline twinning. Euhedral muscovite plates are abundant and disseminated biotite is usually minor, but varies slightly between leucosomes. Occasionally, biotite appears to be entrained from the melanosome as individual ragged flakes, small foliated clots, or, more rarely, interwoven muscovite-biotite schlieren (see Figure 5.7). Small apatite grains (0.5 mm) also occur. Melanosomes (1-12 mm thick) are conspicuous, but impersistent and vary in thickness along their length. They comprise variable proportions of interleaved muscovite and biotite, both of which enclose numerous monazite, zircon and (to a lesser extent) apatite grains. Leucosomes are hosted by quartzofeldspathic gneiss mesosomes that contain abundant alkali feldspar and small amounts of prograde muscovite (e.g. **98-R2B**). Thin M_1 leucosomes are also present in the mesosome. Notably, the gneissic layering within mesosomes is clearly rotated by D_3 folds, which appear to have also influenced the geometry of small M_2 leucosomes. Parts of the outcrop also contain a weak fracture cleavage parallel to S_3 (parallel to short edge of Figure 5.7a).

A key feature of the outcrop is that M_2 leucosomes on all scales are consistently interconnected. This commonly occurs by merging of sub-parallel leucosomes, such that the interface is partially lined by thin melanosome screens. This is obvious in the top of Figure 5.7a, where a series of layer-parallel leucosomes have merged, and, although mostly separated by melanosome, in places the leucosomes are directly contiguous.

Just below this, several thicker leucosomes are joined in a similar manner with a thicker leucosome body (near pen). In this case pronounced textural differences occur between the connecting leucosomes, those on the right being mostly medium, even-grained, and those on the left being coarser grained with larger alkali feldspar crystals (to 12 mm). The central leucosome body is texturally heterogeneous, and a sharp textural contrast occurs with the connecting leucosome on the lower left-hand side. However, a subtle transition occurs between the leucosome on the upper right-hand side with the larger central body, such that no textural discordance occurs at the junction.

Linking of the layer-parallel leucosome network is also achieved by discordant leucosomes, two of which are prominent in Figure 5.7a, both being oriented nearly orthogonal to the gneissic

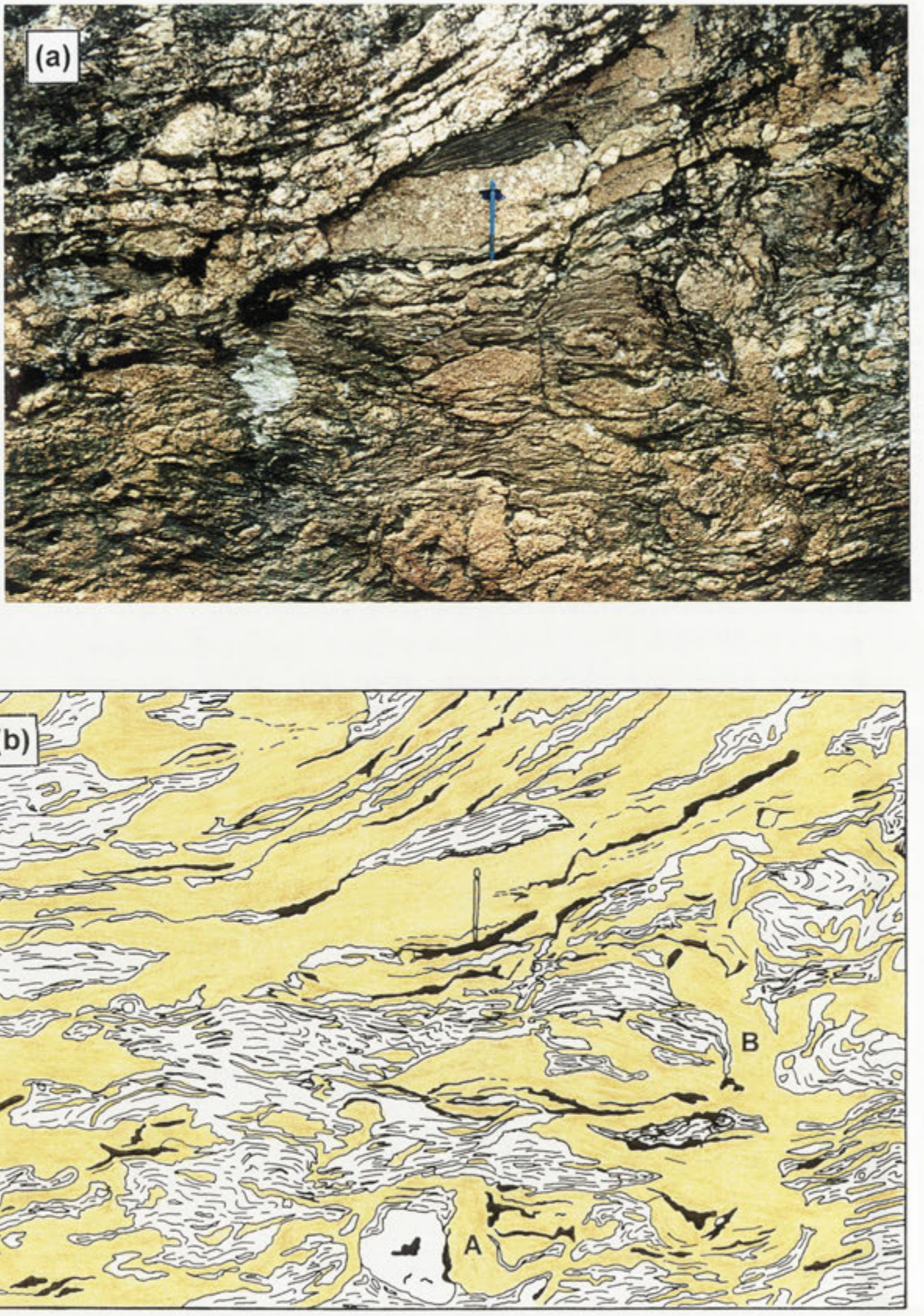

Figure 5.7. Unit D stromatic migmatite. (a) Outcrop face described in the text. (b) Line drawing of (a), highlighting the pertinent segregation features (labelled A and B). Drawing was traced from the actual outcrop and several detailed photographs.

Figure 5.7 contd. Unit D stromatic migmatite. (c) Wider view of the outcrop face. The bulbous granitic body is visible at centre left. (d) Large detached block showing the reverse features of (c). The bulbous granitic body (above coin) is clearly attached to several different layer-parallel leucosomes. F_3 structures are prominent in the gneissic mesosome (WD708434).

foliation, but parallel to the axial surface of F_3. The smaller (13 cm long, "A" in Figure 5.7b) is connected to layer-parallel leucosomes at the top and bottom, and two pod-like leucosome segments along its right margin. The discordant body abuts a chunk of pegmatite to the left, which deflects the leucosome network. The larger discordant leucosome ("B" in Figure 5.7b) has a more irregular, bulbous geometry, is connected to layer-parallel leucosomes on either side, and enlarges into a pool-like body towards the bottom that is joined to the smaller discordant leucosome. In both cases the granitic material comprising the discordant leucosome bodies is homogeneous and resembles that in the thinner, connected leucosome network.

Larger granitic bodies (0.5 m across) with irregular, meandering geometries also occur within the outcrop but are also linked to the layer-parallel leucosome system. In one example, an initially planar leucosome with thick melanosomes progressively widens into a bulbous, but broadly concordant granitic sheet ~50 cm across (Figure 5.7c and d). Larger examples occur in unit F (see below). The thinner part of the leucosome is uniformly medium grained but the wider section of the body is texturally heterogeneous on the scale of a few centimetres, containing irregular domains of medium grained muscovite leucogranite interspersed with coarser areas having alkali feldspar phenocrysts and slightly more biotite. Quartz chunks and alkali feldspar megacrysts are erratically distributed throughout. The latter have angular outlines, enclose pinhead-sized garnets and have graphic textures, thereby resembling the alkali feldspar porphyroclasts of deformed pegmatite dykes. The thick bulbous part of the granitic sheet is also contiguous with several other layer-parallel leucosomes (see Figure 5.7b), which have slightly different textures, one containing numerous alkali feldspar megacrysts. The lithological heterogeneity with the granitic sheet therefore mirrors the overall textural variation of thinner leucosomes within the outcrop.

A critical aspect of this outcrop is that the layer-parallel M_2 leucosomes have well developed melanosomes. This suggests that the large leucosome fraction within the exposure was generated by in situ partial melting and was not externally derived, with the protolith possibly represented by the gneissic mesosome. Although it is difficult to establish how much of the leucosome component was partially liquid at the same time, the consistent interconnection between leucosomes implies that most were simultaneously molten. It is envisaged that segregated partial melts impinged upon each other as the leucosome fraction in the rock increased, possibly by 'anatectic erosion' of the mesosome, and ultimately coalesced into thicker bodies, whereupon bordering melanosomes become isolated as schlieren. Although in some cases the merging leucosomes have different textures, the junction involves a textural gradation from one leucosome to the other, as would be expected if both were partially melted; sharp textural contrasts are rare. The irregularly-shaped discordant leucosomes and sheet-like body in the centre of Figure 5.7a are interpreted to result from migration of these segregated partial melts laterally along leucosomes, and are therefore considered to be sites of magma ponding or storage. The formation of such structures further supports the notion of a high contemporaneous melt fraction within the outcrop. As the three-dimensional geometry of these bodies is unknown, it is also possible that the partial melts within these structures are migrating out of the plane of the outcrop.

The bulbous granitic sheet in Figure 5.7c is connected to several layer-parallel leucosomes with melanosomes and tapers into the in situ leucosome network. Importantly, the contiguous leucosomes differ from each other in terms of grainsize and texture. These features are inconsistent with the granitic sheet being 'injected' into the migmatite, but alternatively imply channelling of locally-derived leucosome partial melts into the larger magma body. Alkali feldspar megacrysts of probable pegmatitic derivation were also introduced into the larger granitic segregation by coalescence of 'feeder' leucosomes. Megacrystic leucosomes may represent partially remelted pegmatite dykes, or have inherited the pegmatitic debris by disruption of deformed pegmatite veins during extensive anatexis and migration of partial melt. In any case, it is clear that the marked textural heterogeneity within the granitic sheet reflects an imperfect blending of the diverse granitic aliquots introduced from different 'feeder' leucosomes. Under this scenario the granitic sheet represents a conduit by which segregated granitic magma is transported from its site of generation; efficient draining of magma from the highly melted migmatite by this pathway is greatly expedited by the interconnected nature of the leucosome network.

Two other important points are worth emphasis. Firstly, the entrainment of melanosome is very minor in leucosomes of all scales, which implies efficient segregation of the partial melt from the mafic residue during anatexis. As the larger granitic sheets are interpreted to form by coalescence of in situ partial melts, the biotite-poor character of these bodies is an artefact of this source-based process. Schlieren of melanosome are most commonly incorporated where layer-parallel leucosomes coalesce, and smaller melanosome fragments are also occasionally entrained at the junction of in situ leucosomes with larger leucosomal accumulations. A lenticular 'enclave' of mesosome gneiss also appears to have been detached and engulfed where thick layer-parallel leucosomes merge at the top of Figure 5.7a. Elsewhere, single flakes and small foliated clots of biotite may have been entrained during migration of partial melts into leucosomes across the melanosome-leucosome interface, or by 'erosion' of melanosomes during flow of melt along leucosomes.

Secondly, in the light of the inferred high proportion of partial melt in the outcrop, it is unclear whether the contorted or 'intestinal' aspect of stromatic migmatites within unit D is imparted by movement of magma or tectonic deformation. With respect to the latter, the migmatite outcrop has clearly been overprinted by D_3, but spalled melanosome fragments and gneiss enclaves within larger leucosome bodies support F_3 crenulations. These features are only reconciled by partial melting within the outcrop being contemporaneous with D_3 deformation.

(b) Stromatic migmatites of unit F and H

Stromatic migmatites within units F and H include semi-pelitic compositions (e.g. **99-7**) and contain a lower proportion of leucosome than those in unit D. Melanosomes are also more variable, comprising either coarse biotite with minor S_2-aligned muscovite (~1 cm thick) or diffuse, slightly more biotite- and quartz-enriched areas up to 4 cm thick around leucosomes. Although some appears to be primary, most muscovite in these melanosomes occurs as spindly, randomly oriented grains or large (2-5 mm) distorted plates enclosing fibrolite aggregates. Melanosomes of semi-pelitic migmatites enclose millimetre-sized leucogranitic domains with subhedral feldspars that

represent trapped partial melt pockets, indicating that melt segregation is less efficient in these horizons. Melanosomes grade into finer mesosomes that mostly contain abundant alkali-feldspar, which coexists with sillimanite in sample **99-7**. As with M_1 migmatites, elongate sillimanite tufts occur in leucosomes that are complementary to sillimanite-bearing melanosomes.

The key migmatitic phenomena outlined from unit D are also prominent in stromatic migmatites of units F and H, though structural control on the geometry of larger scale granitic segregations is more obvious. A critical outcrop in unit F contains a granitic body with an irregular, bulbous geometry hosted by migmatitic quartzofeldspathic schist (Figure 5.8). Although discordant to S_2, the granitic structure is elongate parallel to S_3. The body is quite narrow towards the top of the outcrop (12-15 cm thick) but widens towards the bottom (to ~35 cm thick) and ultimately merges into a larger, sheet-like magmatic structure (~1.5 m across, obscured by lichen in the left of Figure 5.8a). The constituent granitic material is also variable, mostly uniformly medium to coarse grained and dominated by subhedral alkali feldspar (**98-R8**), though portions with alkali

Figure 5.8. (a) Irregularly-shaped, S_3-aligned leucogranitic body joined to *in situ* leucosomes and a larger granitic sheet (obscured by lichen at bottom left).

feldspar megacrysts are observed. The discordant body is connected to a number of smaller leucosomes at various points, many of which also have complex, contorted geometries that may be transgressive to S_2 in the host rock. Although these lack melanosomes, they taper into thinner, layer-parallel M_2 leucosomes that have conspicuous biotite-rich selvedges and are therefore *in situ* (Figure 5.8a, bottom left and 5.8b). Note that on the bottom right-hand side of the discordant granitic structure several thick connecting leucosomes are partially merged, though their original outline is preserved by melanosome screens (see Figure 5.8a).

The striking contiguity between granitic bodies of all scales within this outcrop suggests it is another example of where partial melts have migrated from layer-parallel leucosomes into progressively larger magmatic structures. The efficacy of the segregation mechanism is borne out by the paucity of residual biotite within granitic bodies. Melanosome fragments are only entrained into the discordant granitic structure by coalescence of 'feeder' leucosomes as they widen towards the junction with the thicker body; enclaves of unmelted mesosome are apparently incorporated by the same process. The localisation of the discordant granitic body parallel to S_3 is highly significant, implying that the segregation and migration of partial melts was related to, and potentially stimulated by, D_3 deformation. Plausibly, the discordant structure originated in a transient syn-D_3 dilational site or shear zone, where locally-derived partial melts preferentially collected during compressional deformation. Smaller scale examples of this occur

Figure 5.8. (b) Closer perspective of the top left of (a), illustrating the complexity of the connection between leucosomes of various scales and the presence of melanosomes around layer-parallel bodies (WD710431).

along Robson Creek valley (section 5.4.2). This exemplifies an extremely efficient mechanism for draining in situ partial melts from stromatic migmatites, and accounts for the effective melt-residue separation. Linkage with the thick granitic sheet at the bottom of Figure 5.8a confirms that these are conduits by which partial melt aliquots are ultimately transported from the source metasedimentary horizons. The petrographic and chemical similarity between this granitic sheet and the thick leucogranitic dykes of Robson creek valley suggest the same petrogenesis for the latter (see below and section 8.7).

5.3.6 Interlayered granitic sheets and dykes

Besides the geometrically-complex examples described above, muscovite leucogranite also occurs as more regular, sheet-like bodies (to 2 m thick) throughout the metasedimentary sequence of Robson Creek gorge. Although many of these are structurally concordant, some are transgressive and truncate the S_2 foliation and gneissic layering of the host rocks. Nevertheless, in places these bodies are still contiguous with *in situ* M_2 leucosomes. For example, quartzofeldspathic schist in relatively unmigmatitic unit E contains a leucogranitic dyke (15-60 cm thick) that is connected to both discordant leucosomes (5-10 cm wide; Figure 5.9a) and sparse, layer-parallel M_2 leucosomes with thin melanosomes (Figure 5.9b). The merging leucosomes are lithologically variable, some being medium, even-grained whereas others are coarse grained with alkali feldspar phenocrysts; content of biotite varies between leucosomes. The granitic sheet is also texturally non-uniform, with alkali feldspar megacrysts and large quartz chunks (Figure 5.9b).

Lithological similarity and geochemical evidence (section 7.6.2) suggests that the leucogranitic dyke in Figure 5.9 is the lateral equivalent of the bulbous granitic body in Figures 5.7c and 5.8, and formed by coalescence of migmatite-derived partial melts; it is therefore similarly 'rooted' in an in situ M_2 leucosome network. However, the dyke also incorporates partial melt contributions from heterogeneous in situ M_2 leucosomes in the wallrocks (which have melanosomes and were therefore locally generated), imparting the small-scale textural heterogeneity evident in Figure 5.9b. The discordant 'feeder' leucosomes in Figure 5.9a possibly originate from the adjacent melt-dominated M_2 migmatitic horizons, where segregations of comparable scale are numerous. Thus, the leucogranitic dyke actually comprises a collection of disparate partial melt batches derived from various metasedimentary horizons. As with others in Robson Creek gorge, the felsic character of the granitic dyke reflects the almost complete disengagement of partial melt from mafic residue at the generative site.

5.4 Robson Creek valley

5.4.1 Outcrop relationships

The Robson Creek gorge sequence is replaced further east by pegmatite rubble, upstream of which subdued outcrop of migmatitic quartzofeldspathic gneiss, interlayered with leucogranitic sheets (1-5 m wide), recommences along the valley segment of the watercourse (Figure 5.1). These rocks have sporadic exposure for about 500 m eastwards along Robson Creek valley, until

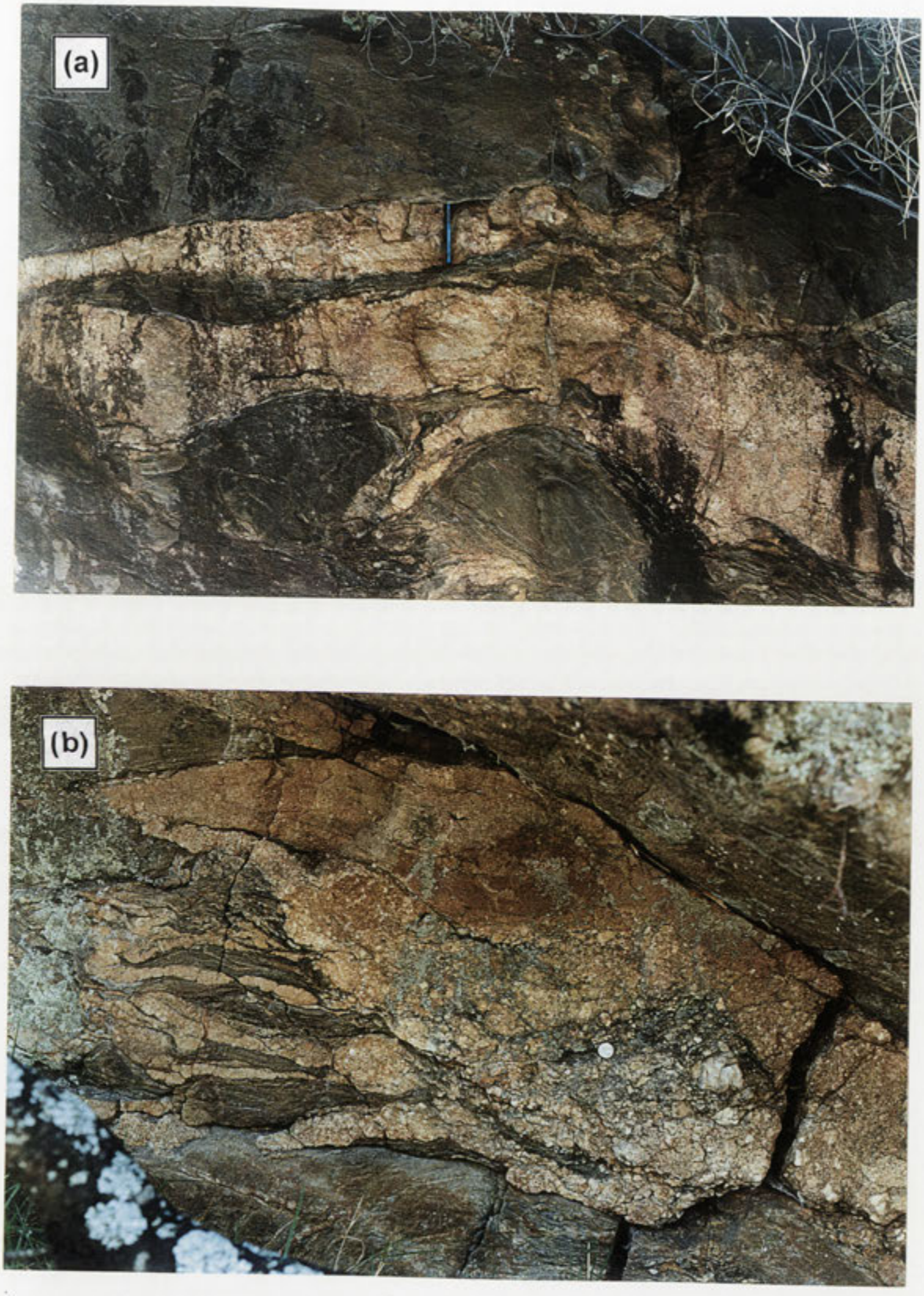

Figure 5.9. (a) Leucogranitic sheet, hosted by quartzofeldspathic schist, that is joined to several discordant granitic bodies; note the apparent incorporation of a schist enclave near the junction with a merging granitic 'feeder' (lower centre). (b) Thinner portion of the same body several metres to the north, contiguous with heterogeneous layer-parallel leucosomes (coin 16 mm across). The boudinaged and isoclinally folded leucosome (centre left) is an M_1 feature (WD709432).

supplanted by a tract of predominantly quartzofeldspathic schist. This lithology provides much more prominent outcrop over a strike width of ~400 m, and adjoins the western periphery of the Nangkita Adamellite (Figure 5.10). The western edge of the outcrop area is homogeneous to laminated quartzofeldspathic schist, which has thin, plagioclase-dominated M_1 leucosomes (e.g. **97-R2C**, Table 5.3), though interlayers of semi-pelitic schist, migmatitic gneiss and M_1 stromatic migmatite (~10 cm to 50 cm thick) become prominent further east. Migmatites include both semi-pelitic and quartzofeldspathic compositions. Semi-pelitic migmatites have boudinaged veins (0.5-1.5 cm thick) or irregular patches of leucosome enveloped by extensive muscovite-biotite selvedges (1-10 mm thick). Leucosomes are coarse grained and mostly tonalitic, comprising consertal quartz, anhedral plagioclase (~3-5 mm) and magmatic muscovite plates, all of which vary in proportion between and within leucosomes (e.g. samples 98-RG3 and 99-15 in Table 5.3). Some leucosomes also contain alkali feldspar, with these being complementary to alkali feldspar-bearing mesosomes.

Thicker stromatic migmatite horizons (to 2 m) are of quartzofeldspathic composition, with mesosomes of quartzofeldspathic gneiss or laminated schist. Here, M_1 leucosomes are quartz-rich, but feldspathic varieties with abundant alkali feldspar also occur (sample **97-R1** in Table 5.3). All have muscovite-biotite melanosomes.

5.4.2 M_2 leucosomes

Alkali feldspar-rich M_2 leucosomes (1-6 cm wide) also occur sparsely within quartzofeldspathic migmatites of Robson Creek valley (sample 97-244 in Table 5.4). In one key exposure, migmatitic laminated schist contains thin, layer-parallel M_2 leucosomes which have disproportionately thick melanosomes (1-1.5 cm) dominated by prograde, S_2-oriented muscovite. These are connected to a larger discordant leucosome that is localised along a small dextral (D_3) shear zone, and linked in turn to a larger granitic pool (Figure 5.11). The discordant segregation also contains distinct muscovite-rich melanosomes, however, micas are aligned parallel to the shear zone (i.e. S_3) and oblique to S_2 in the host schist.

It is proposed that incipient M_2 melting within the schist during D_3 caused mechanical weakening, such that a small dilatant shear zone was initiated. Subsequent anatexis preferentially proceeded along this shear zone, causing formation of a marginal melanosome, where residual micas were recrystallised parallel to the shear zone as shearing continued. Partial melts in the adjacent layer-parallel leucosomes were continuously pumped into the dilatant shear, concentrating the residue and accounting for the disproportionately thick melanosomes. Ultimately, it is envisaged that as shearing continued rotation of the shear zone into a compressive orientation facilitated channelling of magma into the small pond. As with segregation features observed in Robson Creek gorge, removal of magma from the site of generation was very efficient, with minimal melanosome entrainment.

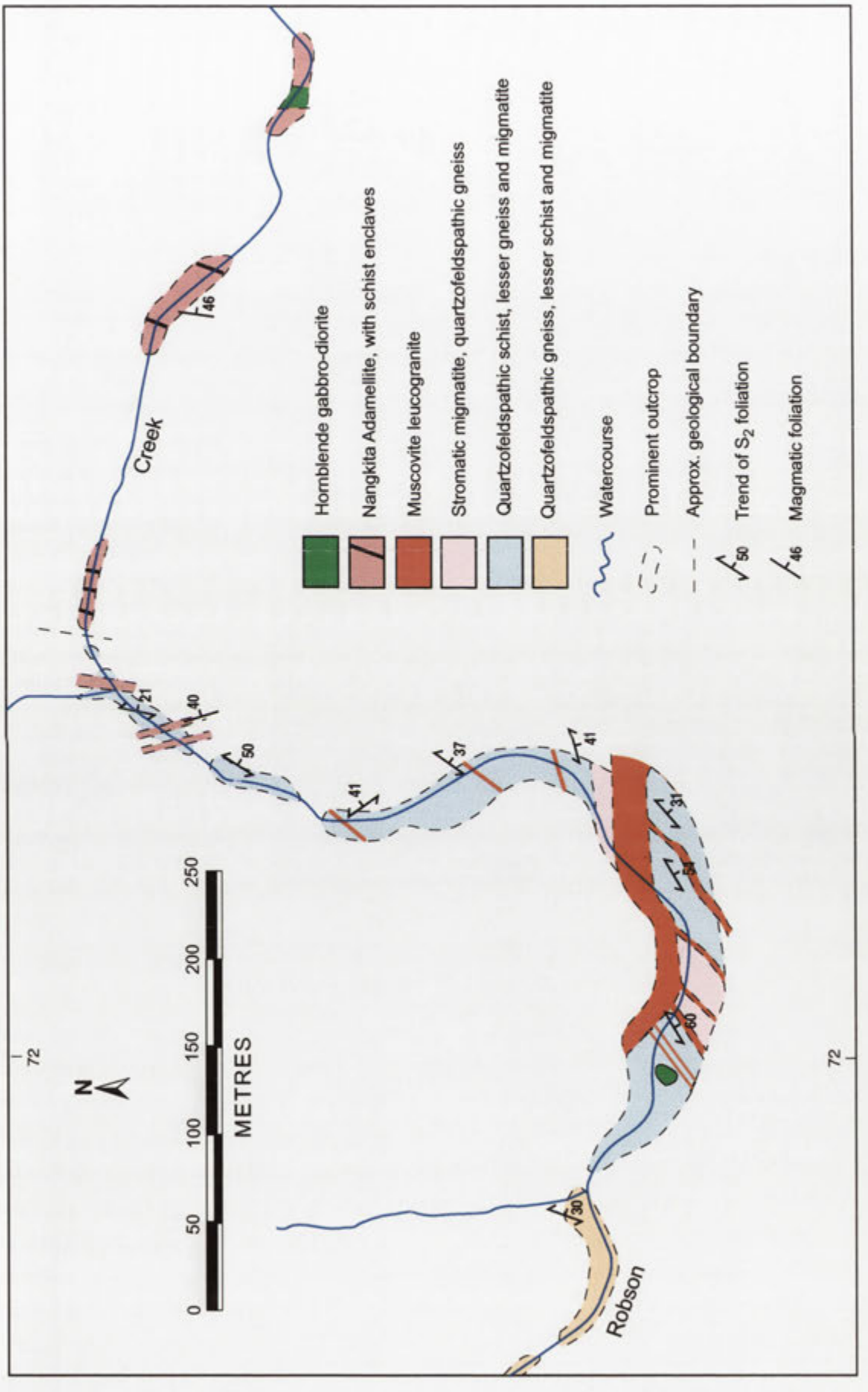

Figure 5.10. Geological relationships of Robson Creek valley. The location is indicated in Figure 5.1.

Figure 5.11. Discordant leucogranitic segregation localised in an S_3 shear zone in migmatitic schist. The segregation is joined to *in situ* leucosomes (rotated by F_3 near the pen) and a larger granitic structure at the bottom of the photograph. Note the development of melanosome along the discordant segregation (right of pen) and the thick melanosomes bordering layer-parallel leucosomes (WD722432).

5.4.3 Leucogranitic sheets and dykes of Robson Creek valley

Foliation-parallel sheets and transgressive dykes of muscovite leucogranite are also present in the metasedimentary succession of Robson Creek valley. These become thicker (to 5 m) and increasingly abundant as the western periphery of Nangkita Adamellite is approached. Most resemble the leucogranitic bodies of Robson Creek gorge, being emplaced syn- to post-D_3 and characterised by paucity of biotite and unmodified igneous microfabrics. However, mineral proportions (especially plagioclase to alkali feldspar) and textures vary significantly between (and within) individual bodies (Table 5.5). This is most apparent in a 2 m thick dyke at WD721431, which contains elongate lenticular areas (several centimetres long) that differ in proportions of biotite and alkali feldspar phenocrysts (**97-R3**). Several adjacent metre-sized granitic sheets merge with this body, but are also internally heterogeneous. These mostly comprise medium grained and alkali feldspar-rich leucogranitic rock (e.g. **97-R3-2A**), but coarser lenticular domains with more biotite and plagioclase (**97-R3-2B**) are intimately

intermixed. The nature and scale of these heterogeneities is therefore identical to that of leucogranitic granitic bodies in Robson Creek gorge, which reflect different melt batches introduced by different 'feeder' leucosomes (see above). Some leucogranitic sheets in Robson Creek valley also contain micaceous clots and schist enclaves at the margins, apparently stripped from the enclosing migmatites.

5.4.4 Transition to Nangkita Adamellite

Further east along Robson Creek valley, the interleaved migmatitic schist and leucogranite described above also encloses tracts (1-25 m across) of coarser grained granitic material, which is taken as Nangkita Adamellite (Figure 5.10). The proportion of adamellite rapidly increases eastwards until it comprises >50% of exposure, whereupon the western periphery of the pluton is delineated; the transition from schist to adamellite pluton occurs over ~75 m.

Immediately east of this arbitrary boundary, the Nangkita Adamellite is choked with metasedimentary enclaves (Figure 5.12), primarily quartzofeldspathic schist rafts (1-10 m across), or tapering slabs of migmatitic gneiss, many of which retain the pre-existing S_2 orientation. These are parallelled by biotite schlieren and elongate micaceous enclaves with F_3 crenulations. Many smaller enclaves, especially migmatitic varieties, are partially disaggregated.

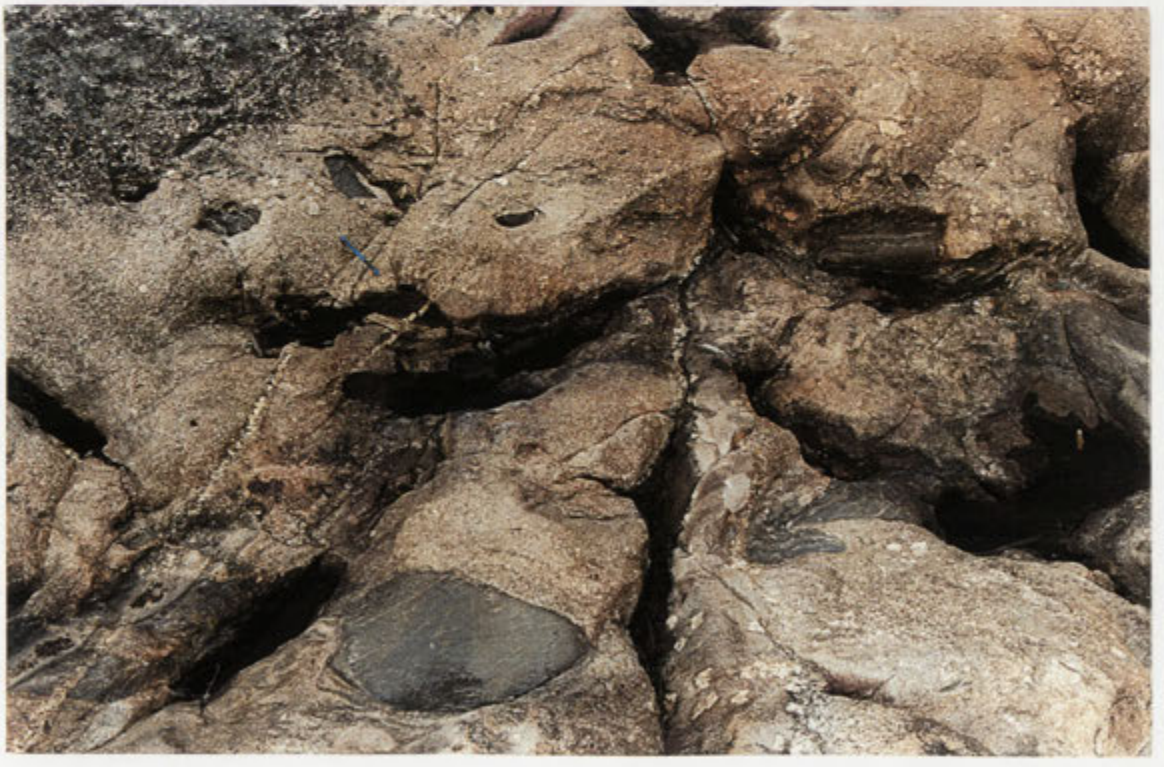

Figure 5.12. Peripheral Nangkita Adamellite outcrop hosting various metasedimentary enclaves. Marked textural heterogeneity, particularly regarding distribution of alkali feldspar megacrysts, is evident across the exposure. Micaceous schlieren are stripped from the schist enclave at bottom centre (WD727434).

Specimens of Nangkita Adamellite from here (**97-233**; Table 6.1) are white, unfoliated, and medium to coarse grained, with anhedral alkali feldspar megacrysts (0.5-5 cm) and occasional tiny garnets. Euhedral muscovite plates are plentiful (~2-3 mm, to 10 mm), whereas small biotite grains are relatively minor. In thin section, alkali feldspar is strikingly poikilitic, enclosing numerous tiny plagioclase crystals that are concentrically aligned parallel to former growth surfaces. Many plagioclase inclusions exhibit strong continuous zoning outwards from euhedral calcic cores, which is also evident in the larger plagioclase laths (section 9.2.1). Coarse primary muscovite plates project into plagioclase and alkali feldspar, and commonly have thin biotite slivers parallel to cleavages.

Mafic microgranular enclaves are also present in heterogeneous, peripheral Nangkita Adamellite exposures, including biotite-rich types and texturally diverse hornblendic varieties. These have affinity with mafic rocks of Chin Chap Creek further north and are discussed in Chapter 12.

Metasedimentary enclaves decline rapidly in Nangkita Adamellite east along Robson Creek, becoming rare about 500 m from the boundary. Conversely, enclave-laden Nangkita Adamellite outcrops continue for about 3.2 km southeast along Log Hut Creek (see Figure 5.1).

5.5 Discussion of field relations in Robson Creek

Synthesising the rock descriptions, field relations and outcrop interpretations presented above permits resolution of the complex geology of Robson Creek into three fundamental aspects, namely the *generation*, *segregation* and *migration* of granitic magma.

Magma generation occurred throughout the entire metasedimentary succession of Robson Creek during M_1, with the development of thin anatectic leucosomes in quartzofeldspathic schist and gneiss. However, more profound anatexis proceeded during M_2, with the generation of leucosome-dominated stromatic migmatites and diatexites, these lithologies virtually localised to discrete horizons along Robson Creek gorge. A consistent feature of M_2 stromatic migmatites is the remarkably efficient *segregation* of the newly formed partial melt phase from the solid, biotite-rich residue, resulting in the formation of biotite-deficient leucosomes with minimal entrainment of melanosome. This contrasts with diatexite horizons where relatively limited segregation of the partial melt occurred, resulting in the typical interpenetrating leucosome-melanosome structure.

Another conspicuous attribute of M_2 stromatic migmatites is that leucosomes are intricately interconnected, and form contiguous arrays throughout the outcrop. This is thought to result from the high *in situ* melt fraction, and be ultimately responsible for the *migration* of segregated partial melt batches from leucosomes into larger magmatic bodies, observed in all M_2 stromatic migmatite horizons. In Robson Creek gorge, it is proposed that discordant pond-like magma accumulations have formed via migration of *in situ* partial melts along networks of layer-parallel leucosomes. A similar process is envisaged in Robson Creek valley, apparently stimulated by syn-anatectic shearing.

Magma migration is also evident on a larger scale. In M_2 stromatic migmatites of Robson Creek gorge, coalesced partial melt increments are apparently channelled from discordant leucosomes into decimetre- to metre-sized granitic sheets and dykes, which are ultimately transporting magma from the generative region. Similar features are encountered in M_1 horizons, where layer-parallel and discordant M_2 leucosomes amalgamate with larger magmatic conduits. In Robson Creek valley, schists are interleaved with dykes and sheets of muscovite leucogranite that appear to merge into larger granitic bodies. Significantly, these rocks are texturally heterogeneous, and possibly represent an imperfect blending of different batches of granitic material, sourced from various metasedimentary protoliths. On the basis of petrographic similarity, they are plausibly the lateral equivalents of those in Robson Creek gorge, thought to form by collection of *in situ* partial melts.

Hence, to summarise, it is envisaged that the Robson Creek gorge sequence represents a zone where partial melts were generated during M_2, efficiently separated from residuum and ultimately channelled into magma escape conduits, whereas Robson Creek valley is predominantly a region through which these partial melts were transferred *en route* to emplacement. Of potential significance is that the interspersed granitic/metasedimentary rocks of the latter are adjoined to the east by the leucocratic Nangkita Adamellite, whose emplacement coincided with M_2. The adamellite itself is intimately interleaved with migmatitic schist at its western periphery, but owing to outcrop limitations the relationship between the adamellite pluton and thick granitic sheets/dykes is not explicit. Nevertheless, petrographic similarity, combined with the marked increase in the size and number of granitic sheets as the Nangkita Adamellite is approached, strongly imply a genetic link. Following this reasoning, a possible scenario is that the Nangkita Adamellite represents a pluton-scale accumulation of cleanly-segregated partial melts derived from the Robson Creek migmatitic sequence, and transported from the generative region to the emplacement site via a series of dykes and sheets; a 'source to sink' magmatic plumbing system is implicit. Obviously this field-based proposition can be tested geochemically and has implications for the origin of other Harrow type plutons. These aspects are pursued in later chapters.

5.6 Chin Chap Creek

Similar metasedimentary and interleaved leucogranitic rocks to those of Robson Creek occur further north along strike in Chin Chap Creek, an eastern tributary of Bryan Creek (see Figure 12.1). The main outcrop area in the northern part of the watercourse is predominantly quartzofeldspathic gneiss, with lesser quartzofeldspathic and muscovite-biotite schist (Table 5.6). Quartzofeldspathic gneiss hosts M_1 leucosomes (0.5-2 cm thick) and grades into stromatic migmatite (10-50 cm thick horizons). As at Robson Creek valley, semi-pelitic M_1 stromatic migmatites have quartz-plagioclase leucosomes bordered by muscovite-rich melanosomes without sillimanite (sample 97-315, Table 5.3). M_2 leucosomes are minor. Further south, similar lithologies form a 15-20 m wide raft within a felsic pluton (the Kassingbrook Granodiorite), though here M_2 leucosomes are more common (e.g. **98-102**, Table 5.4; see section 12.3.2).

5.7 Bryan Creek and tributaries

5.7.1 Geological overview

A varied migmatitic metasedimentary sequence outcrops for ~3.6 km along the Bryan Creek valley (Figure 5.13), from the junction with Chin Chap Creek northwards to the southern margin of a mafic granitic body, the Patawilya Tonalite (section 11.2.6). The metasedimentary succession is complexly interspersed with diverse muscovite-bearing granitic sheets (comprising up to 50% of exposure), the most distinctive variety of which is biotite-rich and characterised by numerous small micaceous enclaves. Several metre-sized sheets of such rock are encountered in the main watercourse and minor tributaries, but in the southern part of Bryan Creek tors of this material form a 150-200 m thick sill-like body, referred to as Bryan Creek Granodiorite (Figure 5.13). Another sheet (~75 m wide) of similar rock occurs further north along the watercourse.

Due to lower calibre exposure, detailed mapping and documentation of the full spectrum of granitic and metasedimentary rocks exposed along Bryan Creek has not been attempted. Nevertheless, as differences with the Robson Creek metasedimentary package are apparent, and to provide context for the Bryan Creek Granodiorite, the main geological elements are summarised.

5.7.2 Metasedimentary rocks

The Bryan Creek metasedimentary sequence comprises massive to laminated quartzofeldspathic schist, metapelitic schist and quartzofeldspathic to semi-pelitic gneiss, interspersed with horizons of M_2 stromatic migmatite and diatexite. Quartzofeldspathic schist and gneiss is lithologically similar to that of Robson Creek and contains sparse M_1 leucosomes. Metapelitic schist (10-50 cm interlayers) is dominated by biotite, with lesser primary muscovite, and abundant millimetre-sized fibrolite tufts.

Stromatic (M_2) migmatite (20 cm to 2 m wide bands) is mostly of quartzofeldspathic composition and contains numerous elongate, but irregularly-shaped, granitic leucosomes (4 mm-4 cm) with diffuse boundaries. Although these rocks are grossly layered, the melt fraction is more pervasive, resulting in a 'nebulitic' appearance (Figure 5.14a). Larger, medium to coarse grained leucogranitic segregations also occur, these being texturally heterogeneous and containing conspicuous, non-aligned biotite (Figure 5.14b). Many leucosomes also incorporate biotite schlieren, which represent entrained melanosome fragments. *In situ* melanosomes are dominated by biotite and quartz (e.g. 97-349, Table 5.4), with fibrolite in semi-pelitic samples. Melanosomes mostly form diffuse areas around leucosomes and larger segregations (up to 3 cm), and are only resolved from mesosomes by a slightly coarser grainsize and higher concentration of biotite and quartz. Mesosomes are mostly quartzofeldspathic gneiss or laminated schist with small amounts of primary muscovite; most muscovite overprints the foliation and is secondary. Alkali feldspar is abundant, but erratically distributed and absent from within several centimetres of leucosomes. Many mesosomes also contain isolated lenticular clots of interleaved biotite (5-20 mm), which may be residual from the segregation and extraction of partial melt. The highly disrupted (almost randomised) S_2 fabric and localised feldspar depletion in these mesosomes is consistent with this.

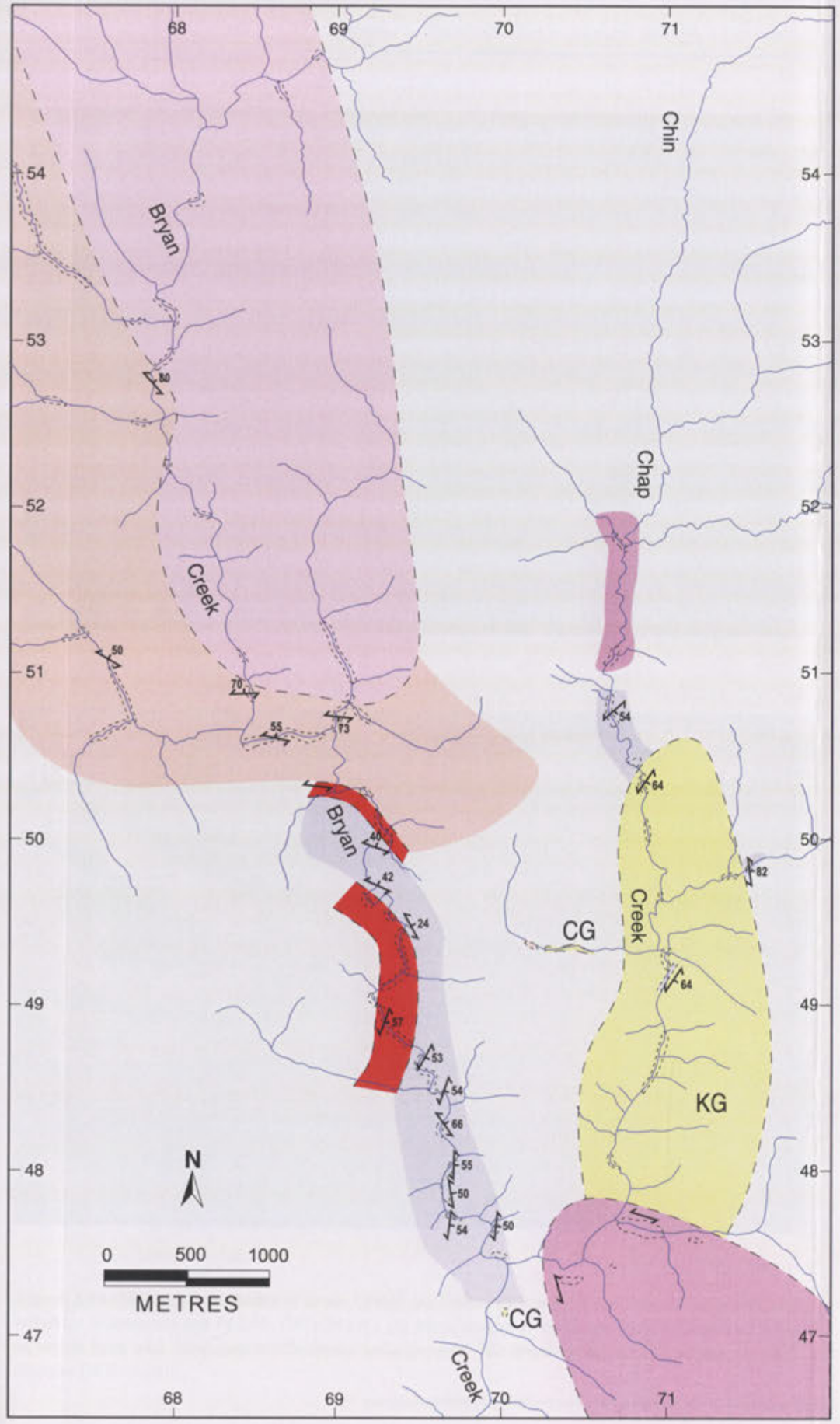

Unnamed muscovite granite

Patawilya Tonalite (Tuloona type)

Kassingbrook Granodiorite (KG), Coolami Granodiorite (CG)

Bryan Creek Granodiorite

Muscovite granite with interleaved schist, gneiss and migmatite

Quartzofeldspathic gneiss, schist, migmatite, interleaved muscovite granite

Watercourse

Prominent outcrop

Approx. geological boundary

Trend of S_2 foliation

Trend of magmatic foliation

LOCATION

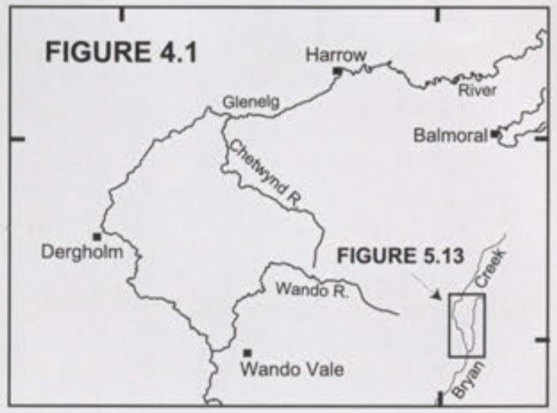

Figure 5.13. Geological map of Bryan Creek and tributaries. Chin Chap Creek geology is shown in more detail by Figure 12.1.

Figure 5.14. Stromatic migmatites in Bryan Creek. (a) Typical diffusely-layered migmatitic gneiss with indistinct leucosomes and F_3 folds (WD684509). (b) More conspicuous leucogranitic segregations, some of which have well developed biotite-quartz melanosomes. The larger grains in leucosomes are alkali feldspar (WD696485).

With increasing melt fraction, stromatic migmatites are transitional to biotite-rich diatexites. The thickness of these horizons is difficult to estimate due to poor exposure, but they are most prominent in the northern part of Bryan Creek as bands up to 10 m wide. Diatexites resemble those of Robson Creek, except that in places the layering is highly contorted, with rotation of micaceous enclaves and localised randomisation of the schlieric banding. These features occur in the most melt-enriched parts of the diatexite horizon and suggest mobilisation of the granitic melt component. Diatexites are interlayered with, and gradational to, sheets of heterogeneous granitic rock that are choked with partially disaggregated metasedimentary enclaves (10 cm to 50 m across). These have a diffuse schlieric banding, parallelled by numerous biotite-rich clots and quartzofeldspathic schist enclaves. The granitic matrix is even-grained and contains abundant biotite, with lesser muscovite and fibrolite (**97-396**) (Table 5.5).

Although most prominent in the northern part of the watercourse, horizons of this heterogeneous granitic material occur throughout the metasedimentary sequence of Bryan Creek. Schists and gneisses are also interleaved with sheets (20 cm to 2 m wide) of coarser grained, muscovite-rich leucogranite (e.g. **97-396B**) (Table 5.5), which resemble segregations in stromatic migmatites.

5.7.3 Bryan Creek Granodiorite

Bryan Creek Granodiorite is distinguished from the enclave-rich granitic horizons described above in being texturally homogeneous and lacking a regular schlieric layering, but is interlayered with this material at its northern margin. To the south, Bryan Creek Granodiorite concordantly borders migmatitic gneiss and pelitic schist. The curved outcrop shape of this body (Figure 5.13) reflects D_5 folding.

Typical samples (**97-349**; Table 6.1) are medium grey and porphyritic, with blocky plagioclase phenocrysts (up to 7 mm, most 4-5 mm) and masses of polycrystalline quartz sparsely dispersed through a fine to medium grained, biotite-rich matrix (Figure 5.15). Muscovite flakes are prominent, whereas alkali feldspar megacrysts (2-4 cm) are rarer. A regular and pervasive foliation of groundmass biotite and muscovite is coplanar with S_2 in the enclosing metasedimentary rocks.

In thin section, plagioclase phenocrysts have large, oscillatory zoned, euhedral cores overgrown by a thick sodic rim. Groundmass plagioclase (~1 mm) has strong continuous zoning and forms a mosaic with abundant quartz (~1 mm). Small, irregularly shaped alkali feldspar grains are interstitial, though larger pools (~1 mm) also occur. Tufts of fibrolite occupy the cores of some quartz grains. Biotite flakes (~0.5 mm) are mostly interleaved with spindly muscovite and occasionally form thin foliated trains (~3-7 mm long). Larger, more ragged biotite flakes (~2-3 mm) partially enclose groundmass plagioclase. Tiny apatite needles are abundant and clustered inside plagioclase and alkali feldspar, commonly with concentric arrangement.

The most striking aspect of the Bryan Creek Granodiorite is the abundance of small, foliated biotite-rich clots (~5 mm) or micaceous enclaves (to 6 cm), very conspicuous on weathered surfaces (Figure 5.15). Micaceous enclaves are spherical or ovoid, but lenticular or sheet-like in profile, and generally contain fine plagioclase-quartz laminae; minor wispy muscovite is

replacing sillimanite. These enclaves are thus identical to the distinctive lenticular melanosome segments in stromatic migmatites. Less common are large matted clumps of unaltered fibrolite (1-6 cm across), associated with clear quartz masses, and quartzofeldspathic schist enclaves (10-15 cm long).

Schist and micaceous enclaves are mostly aligned with the planar fabric of the enclosing granodiorite, though many are also rotated, such that the internal S_2 foliation is oblique to that of the host. Importantly, the fabric in some micaceous clots is rotated by tight crenulations that are either F_3 or F_4. Sillimanite clots are more intensely folded, and exhibit complex structures typical of superimposition of F_4 on F_3. These features confirm that emplacement of the Bryan Creek Granodiorite post-dated D_2, supported by the essentially unmodified igneous texture. In view of this, the directional fabric within the body cannot have been tectonically imposed and probably results from magmatic flow, consistent with deflection of schlieren around schist enclaves, and the variable rotation of entrained micaceous clots (see Figure 5.15).

Figure 5.15. Slab of the biotite-rich Bryan Creek Granodiorite, exhibiting plagioclase (light brownish) and quartz phenocrysts and characteristic biotite-rich clots (WD693491).

5.8 Discussion

5.8.1 Interpretation of outcrop features in diatexites

Structures in diatexite outcrops of Robson and Bryan Creeks, such as asymmetric metasedimentary enclaves, 'augen-like' feldspar megacrysts and anastomosing schlieric banding, imply intense solid-state shearing. However, this is inconsistent with the unstrained and clearly magmatic textures of these rocks. Alternatively, following Sawyer (1998), these features are interpreted to result from shear-driven bulk flow while a melt fraction was pervasive throughout the diatexite horizon. This situation is most easily envisaged for the unit B diatexite in Robson Creek gorge, which is contained within thick, competent quartzofeldspathic gneiss horizons, and therefore might be expected to preferentially accommodate shear strain. As micaceous enclaves support F_3 crenulations, shearing of the partially-melted diatexite layer is possibly associated with D_3 deformation, responsible for small syn-anatectic shear zones elsewhere in Robson Creek (e.g. Figure 5.11).

Importantly, bulk magmatic flow can stimulate localised separation of the partial melt and solid residuum components of the diatexite (Sawyer 1996). This arises due to the heterogeneity within the diatexite magma and perturbations in the flow regime, and can cause formation of small 'clean' granitic domains around enclaves, aggregates of residual phases, oriented trains or schlieren of mafic minerals, banding-parallel leucogranitic sheets with diffuse margins, and subtle variations in the proportion of residue versus melt fraction across the exposure (Sawyer 1996). As these features are conspicuous in GRC diatexites, 'flow assisted melt segregation' is evidently important here too. In particular, the process explains the centimetre-scale leucogranitic domains in Robson Creek diatexites, interpreted as pockets of segregated partial melt. The striking metre-scale variation in the proportion of residual material to the 'granitic' fraction in Robson Creek diatexites also implies internal redistribution of the melt phase, as described by Sawyer (1998). Unfortunately, the magnitude of these variations laterally along the diatexite horizon, or their relationship to large fold structures (e.g. Sawyer 1994), is indeterminable due to outcrop limitations. Disruption of the schlieric banding in the most melt-enriched parts of Bryan Creek diatexites indicates more pronounced mobilisation of the magmatic component, consistent with the gradation to biotite-rich granitic sheets.

5.8.2 Comparison of Bryan Creek with Robson Creek

Although both watercourses are occupied by interleaved metasedimentary and muscovite-bearing granitic rock, in many respects the geology of Bryan Creek contrasts with that of Robson Creek. Firstly, stromatic migmatites of Bryan Creek are characterised by a pervasive melt fraction, such that leucosomes are diffuse and enveloped by indistinct melanosomes that are difficult to resolve from mesosomes. However, leucosomes in Robson Creek migmatites are well-defined and bordered by discrete melanosomes that are easily distinguished from mesosomes. They are also generally much poorer in biotite and contain less entrained melanosome fragments than their Bryan Creek counterparts.

Secondly, leucosomes of stromatic migmatites in Bryan Creek are mostly not interconnected, and linking with larger granitic bodies is only occasionally evident, unlike Robson Creek where these features are almost ubiquitous. Thirdly, interlayered granitic rock is much more variable in Bryan Creek and includes heterogeneous, metasedimentary enclave-rich lithologies that are transitional to diatexites with disrupted layering. Biotite-rich granitic horizons with abundant metasedimentary enclaves are not represented in Robson Creek where granitic dykes and sheets are uniformly leucocratic. Further, Robson Creek diatexites are regularly layered and exhibit no evidence for the agitation characteristic of some Bryan Creek diatexites. Finally, and following from the previous point, the Bryan Creek Granodiorite, with abundant biotite, sillimanite, and micaceous enclaves, is markedly different from the Nangkita Adamellite of Robson Creek, which is felsic, lacks sillimanite and contains metasedimentary enclaves at the peripheries only.

These contrasting features may be reconciled in part by the operation of fundamentally different segregation processes during anatexis. In Robson Creek, segregation of partial melt from residue is efficient, resulting in the formation of discrete leucosomes that lack entrained melanosome. As larger granitic bodies, including the Nangkita Adamellite, are thought to derive from migration and amalgamation of these leucosome partial melts, they are similarly felsic and residue-free. In contrast, melt segregation is clearly much less effective in Bryan Creek, such that differentiation of partial melt and residue into discrete leucosome and melanosome components is poorer, and pervasively-melted diatexitic rocks are more common. The occurrence of heterogeneous granitic rocks with abundant entrained residuum appears to reflect this, supported by the intimate association of these rocks with diatexites. In this light, a link between the residue-rich Bryan Creek Granodiorite and diatexites is also implied.

Chapter 6: Metasedimentary rocks and muscovite-bearing granitic bodies of the northeastern migmatite zone

(B) Harrow District

6.1 Introduction

The best exposure of Harrow type granitic rock occurs in the Harrow district ~50 km north of Coleraine, with prominent and almost continuous outcrop along the Glenelg River valley and a major tributary, Schofield Creek. The distribution of major plutons in this area is illustrated by Figure 6.1. Structurally concordant bodies include the Kout Norien Granodiorite, exposed around Harrow township, and the elongate Scrubby Junction Granodiorite, Schofield Adamellite, and Carrigeen Granodiorite of Schofield Creek further east. These rocks are heterogeneous and complexly interleaved with migmatitic metasedimentary horizons, but crosscut by the intrusive Harrow Granodiorite (west) and Marn Mering Granodiorite (east) plutons, which are uniform-textured and free of metasedimentary enclaves by contrast. Significantly, east of the latter another structurally concordant pluton, the Dunmore Leucotonalite, outcrops along the Glenelg River and tributaries of Scabbing Station Creek. This body is ensconced within stromatic migmatites and differs from other Harrow types in being alkali feldspar-poor. Another large muscovite-bearing leucotonalitic pluton surrounded by migmatites occurs further east (the Glendene Tonalite, Fitzherbert 1998) but has not been examined by this study. Lithologies of the Harrow district are also intruded by sheets and small plutons of garnet-bearing leucoadamellite, and zoned pegmatitic dykes (5-20 cm thick) post-date all granitic phases.

Migmatitic metasedimentary rocks are subordinate to granitic rocks and are exposed along Schofield Creek but most extensively along the Glenelg River valley and Scabbing Station Creek immediately west of the Dunmore Leucotonalite (Figure 6.1). Importantly, stromatic leucosomes and diatexites of the latter areas are exclusively of alkali feldspar-poor or 'tonalitic' composition. In contrast, most leucosomes and diatexites of Schofield Creek have abundant alkali feldspar, though tonalitic varieties are locally developed.

The occurrence and petrology of these metasedimentary and Harrow type granitic rocks are addressed by this chapter, with emphasis on structurally concordant plutons and their migmatitic envelopes. The modal mineralogy of representative Harrow type samples from the northeastern migmatite zone is summarised by Table 6.1 and Figure 6.2.

6.2 Dunmore Leucotonalite and associated metasedimentary rocks

6.2.1 Metasedimentary rocks of the western Glenelg River valley

Metasedimentary rocks occupy ~8 km of the Glenelg River valley between the Horsham-Balmoral Road and the Dunmore Leucotonalite, itself 11.5 km east of Harrow. The eastern part of the metasedimentary tract is dominated by amphibolite facies quartzofeldspathic schists, with

interleaved metapelitic horizons and deformed pegmatitic sheets. These rocks are described by Fitzherbert (1998) and Gray *et al.* (2001), and briefly reiterated in section 3.2.2. Metamorphic grade gradually increases westward along the Glenelg River towards Harrow, and 3 km from the Dunmore Leucotonalite, a transition to the migmatite zone is manifested by the appearance of stromatic migmatite horizons.

Metasedimentary rocks of the migmatite zone in this area are described by Kemp (1995), and resemble those of Robson Creek (section 5.3.2) (Table 5.6). Near the confluence of Scabbing Station Creek with the Glenelg River, massive to laminated quartzofeldspathic schist is predominant, interspersed with thin metapelitic layers (5-50 cm thick) where primary foliated muscovite is abundant. Eastwards, these rocks are interlayered with quartzofeldspathic gneiss, which abruptly becomes predominant ~2 km west of the onset of the migmatite zone (Kemp 1995). Near the schist-gneiss transition in Scabbing Station Creek, a ~1m thick semi-pelitic schist horizon (sample **97-429**) has abundant prograde muscovite and contains alkali feldspar (~1 mm) (Table 5.6).

The metasedimentary sequence is also abundantly intercalated with isoclinally-folded and boudinaged sheets of pegmatite (2 cm to 50 m thick), most of which was emplaced pre- to syn-D_2. The thinner sheets are highly strained, composed of smeared alkali feldspar augen in a matrix of splintery muscovite, alkali feldspar, quartz and garnet that contains the S_2 foliation. However, the larger pegmatite bodies are more heterogeneous, such that concentrations of alkali feldspar megacrysts are interspersed with garnetiferous leucogranite (**97-11**).

6.2.2 Tonalitic migmatites

Quartzofeldspathic schist and layered gneiss of the Glenelg River valley, Scabbing Station Creek and Dunmore Creek (a tributary of the latter) commonly contain leucosomes, and are intercalated with (and partly gradational to) horizons of stromatic migmatite (10 cm to 2 m thick). As described by Kemp (1995) migmatites are tonalitic, with plagioclase-quartz leucosomes hosted by alkali feldspar-deficient mesosomes; textural evidence and the presence of melanosomes indicates development by *in situ* partial melting (Kemp & Gray 1999a). Many leucosomes are isoclinally folded and variably recrystallised, consistent with generation pre- to syn-D_2 (i.e. M_1). However undeformed M_2 leucosomes (up to 10 cm thick) are also prominent. The latter may be transgressive but are mostly concordant with S_2. Leucosome microfabrics are predominantly igneous, with interlocking subhedral plagioclase laths (Figure 6.3); disseminated micas are non-aligned. Muscovite forms coarse plates that are occasionally euhedral against plagioclase, indicating early crystallisation (Figure 6.3). Some leucosomes also contain large apatite prisms (to 1.5mm). Significantly, plagioclase is of strongly varying abundance in both M_1 and M_2 leucosomes (from 10% to 80%), and the plagioclase to quartz ratio changes visibly along the length of many leucosomes. The proportion of melanosome in migmatitic rocks increases as leucosomes become more quartz-rich. Thin bands (10-30 cm) comprising essentially lenticular 'leucosomes' of polycrystalline quartz and coarse micaceous selvedge in Dunmore Creek are an extreme development.

FIGURE 6.1

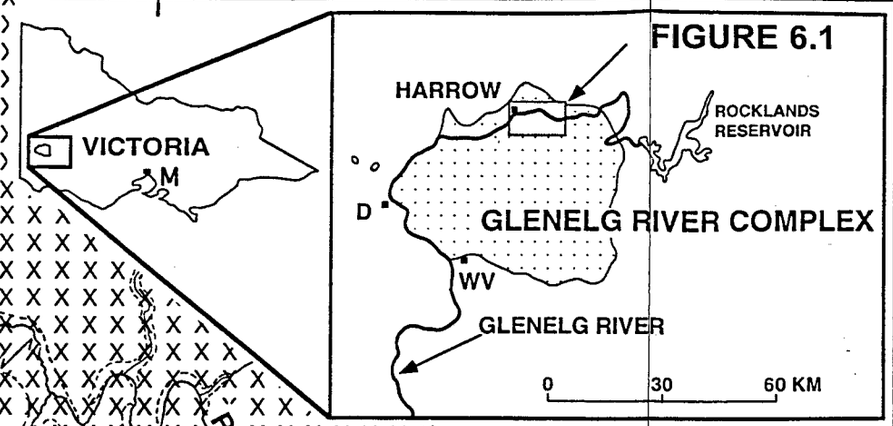

CAMBRO-ORDOVICIAN
- HARROW GRANODIORITE
- MUSCOVITE ADAMELLITE
- GARNET ADAMELLITE
- MARN MERING GRANODIORITE
- TULOONA GRANODIORITE
- KOUT NORIEN GRANODIORITE
- SCHOFIELD ADAMELLITE
- CARRIGEEN GRANODIORITE
- SCRUBBY JUNCTION GRANODIORITE
- DUNMORE LEUCOTONALITE

? MIDDLE CAMBRIAN
- QUARTZOFELDSPATHIC SCHIST
- NEBULITIC MIGMATITE, HETEROGENEOUS GRANITE
- TONALITIC MIGMATITE, QUARTZOFELDSPATHIC GNEISS

TN

1 km

- Road
- Watercourse
- Prominent exposure
- Approx. geological boundary
- Inferred geological boundary
- S_2 Foliation (strike & dip)
- Schlieric foliation (strike & dip)
- Schlieren trend
- F_3^2 (strike & plunge)
- F_4^2 (strike & plunge)
- F_5^2 (strike & plunge)
- Mineral lineation (L_2) ML
- Metasedimentary raft (strike & dip)

Figure 6.1. Geology of the Glenelg River Complex in the Harrow district (modified after Kemp 1995), with overlying Tertiary laterite omitted for clarity. Inset shows locality of the mapped area in the Glenelg River Complex. M, Melbourne; D, Dergholm; WV, Wando Vale.

Lithology	*Sample*	*Locality*	*Grid ref. (WD)*	*Modal Percentage*					*Accessory Minerals*
				Quartz	**Plagioclase**	**Alkali Felds.**	**Muscovite**	**Biotite**	
Kout Norien Granodiorite	**98-76**	Glenelg R.	529866	37.5	24.2	21.6	6.4	9.8	a, sill
Scrubby Junction Gd	**98-38(2)**	Schofield Ck	592865	42.2	31.0	11.5	8.7	6.4	a
Schofield Adamellite	**T2-CC9D**	Schofield Ck	579846	36.8	50.6	7.6	1.8	2.9	c
	98-13	Schofield Ck	581847	36.0	31.9	21.6	9.4	0.6	a, c, z
	98-14A	Schofield Ck	583849	35.2	31.1	22.4	3.1	7.6	a, c
	CC11	Schofield Ck	583849	29.1	31.5	34.0	3.2	1.8	a, sill
	98-23	Schofield Ck	587855	36.3	40.5	17.8	3.1	1.6	a, c
	98-25	Schofield Ck	587858	35.3	33.1	21.2	8.4	1.7	a
	98-26	Schofield Ck	588858	36.3	25.9	25.4	9.8	1.8	a
	T2-39	Glenelg R.	582868	35.3	31.6	17.3	10.3	5.2	a
Carrigeen Granodiorite	**CC2**	Schofield Ck	578837	40.9	36.7	9.1	5.5	8.3	a, c
	T2-3	Schofield Ck	578833	36.2	39.7	10.2	9.1	4.4	a, c
	T2-69	Schofield Ck	576835	33.4	31.4	26.4	5.4	2.4	a, ga (0.9%)
Dunmore Leucotonalite	**98-105**	Glenelg R.	639842	34.6	58.3	2.9	2.2	1.5	c
Bryan Creek Granodiorite	**97-349**	Bryan Ck	693491	34.7	33.3	11.28	5.0	15.4	a, sill
Nangkita Adamellite	**97-233**	Robson Ck	728435	30.1	37.7	27.5	2.3	1.5	a, c
Harrow Granodiorite	**98-86**	Glenelg R.	556861	37.1	32.4	17.6	4.7	7.2	c, sill
Marn Mering Granodiorite	**T2-1**	Glenelg R.	620850	37.3	37.5	11.3	8.8	4.8	a, c
	98-58	Glenelg R.	604863	29.6	41.7	21.5	5.3	1.3	a, c
Roseate Adamellite	**CC13**	Schofield Ck	587855	35.0	28.3	27.7	6.1	2.5	a
Garnet Adamellite	**98-19**	Schofield Ck	585852	33.6	30.4	26.8	8.0	1.1	a, c, ga
Garnet Adamellite	**T2-258**	Schofield Ck	583849	26.6	27.2	37.7	5.9	0.8	ga (1.7%)
Glengoyne Adamellite	**97-98**	Chetwynd R.	488657	32.9	37.0	20.0	8.9	0.8	a, ga
Blair Atholl Adamellite	**97-201**	Wando R.	418580	22.8	44.0	28.1	1.9	2.3	a, c, ga (0.5%)

Table 6.1 Mineralogy of Harrow type granitic rocks of the Glenelg River Complex, determined by point count from thin sections (2500pts). In all cases, alkali feldspar has patchy microcline twinning, mostly developed along cleavages and around inclusions. Sample numbers in bold type have been analysed (see Appendix C).

Abbreviations are: a = apatite; c = chlorite; ga = garnet; sill = sillimanite; z = zircon.

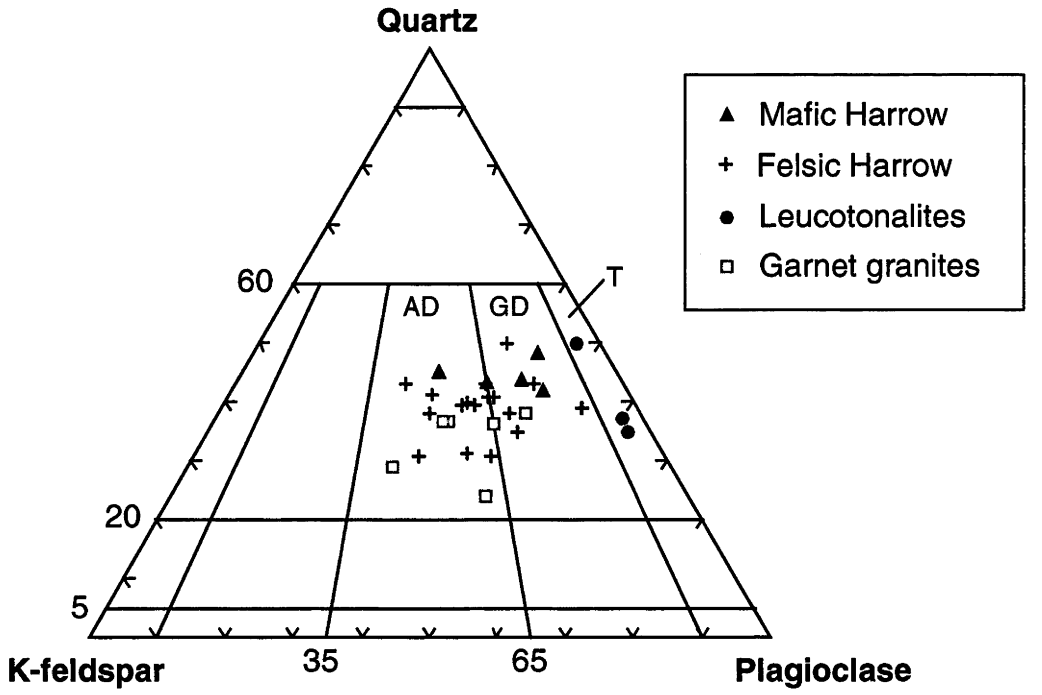

Figure 6.2. Modified Streckeisen (1976) diagram depicting the felsic modal mineralogy of Harrow type granitic rocks. The four-fold subdivision is based upon physical and geochemical characteristics (see section 9.3.1). 'Mafic Harrow' encompasses the relatively biotite-rich Bryan Creek Granodiorite, Kout Norien Granodiorite, Carrigeen Granodiorite and Harrow Granodiorite. 'Felsic Harrow' includes all other plutons, apart from leucotonalites and garnet-bearing samples, which are plotted separately. Lithological fields are adamellite (AD), granodiorite (GD) and tonalite (T).

Melanosomes of tonalitic migmatites comprise differing proportions of interleaved biotite and S_2-aligned muscovite, which contain abundant apatite, monazite and zircon inclusions. The more extensive melanosomes associated with quartz-rich leucosomes or leucosome-dominated M_2 migmatites are mostly biotite. Here, muscovite occurs as elongate, ragged grains with a vague fibrous appearance that are pseudomorphing sillimanite. Retrogressed sillimanite of this nature is observed in both M_1 and M_2 melanosomes, but most prominent in the more evolved M_2 migmatites.

6.2.3 The transition to Dunmore Leucotonalite

Interlayered with gneiss and migmatite are sheets of heterogeneous tonalite (up to 5 m across, most ~30-50 cm thick), containing variable amounts of muscovite-rich micaceous enclaves, schlieren and small, rotated stromatic migmatite enclaves (10-20 cm). Although mostly concordant with S_2, tonalitic sheets commonly have thinner offshoots that crosscut the foliation and migmatitic layering of host gneisses. However, at several localities in Dunmore Creek, tonalitic sheets are complexly linked to *in situ* tonalitic leucosomes in adjacent M_2 stromatic migmatites. Elsewhere, migmatite leucosomes merge into small pool-like tonalitic segregations (5-20 cm), generally surrounded by thick melanosomes.

Figure 6.3. Thin section view of a tonalitic leucosome, showing crystal outlines and euhedral zoning in plagioclase and primary muscovite flakes. Biotite-muscovite melanosome is visible at bottom left (cross polars, field of view ~8.1 mm).

Figure 6.4. Pronounced diatexite-like layering in a Dunmore Leucotonalite exposure, defined by diffuse schlieren and elongate muscovite-biotite enclaves. Note the grainsize variation within the leucotonalitic portion of the outcrop (Glenelg River, WD624842).

Westwards along Dunmore Creek, the proportion of stromatic migmatite and interlayered heterogeneous tonalite increases within the metasedimentary sequence. M_2 leucosomes become predominant within migmatitic horizons, many of which are enriched in melanosome, enclosing numerous elongate 'slugs' of quartz. Some thick tonalitic bands (to 10 m wide) have a regularly layered schlieric fabric, augmented by aligned biotite flakes and large micaceous enclaves (to 30 cm long), that is concordant with S_2 in adjacent migmatitic gneisses. Micaceous enclaves comprise either interleaved biotite and primary muscovite, or biotite with subordinate retrogressed sillimanite, mirroring the variation exhibited by migmatite melanosomes.

Diatexite outcrop commences at WD640833 (incorporating aligned, metre-sized rafts of gneiss and stromatic migmatite), that is directly transitional (after 50 m) to the eastern margin of the Dunmore Leucotonalite pluton. The location of the boundary is somewhat arbitrary, and is placed where the schlieric diatexite fabric becomes randomised and micaceous enclaves and metasedimentary rafts are rotated.

Hence, the westwards gradation from tonalitic migmatite to Dunmore Leucotonalite in Dunmore Creek, taken from the first appearance of heterogeneous tonalite sheets and where M_2 tonalitic migmatites become prominent, occurs over about 700 m. A similar transition is evident along the Glenelg River valley further north, though exposure is poorer and relationships consequently less clear-cut. However, tonalitic diatexite also occurs near the eastern periphery of the leucotonalite pluton, along strike from that in Dunmore Creek.

Further south in Dunmore Creek, the southwestern boundary of the Dunmore Leucotonalite with migmatitic gneiss is also concordant with the regional trend of S_2 (Kemp & Gray 1999a). Significantly, immediately south of the boundary a 120 m thick horizon of unusual coarse muscovite-biotite schist occurs, irregularly interlayered with lenticular tonalitic sheets (1 cm to 1 m thick). The schist generally exhibits a layering, whereby laminae and veins of clear quartz are liberally interspersed. However, elsewhere it is almost purely mica, being up to ~50% biotite and ~30% muscovite, and resembles a large scale melanosome.

6.2.4 Petrology of the Dunmore Leucotonalite

Typical Dunmore Leucotonalite specimens (e.g. **98-105**) are white to pale green and dominated by coarse interlocking oligoclase laths and quartz, with minor interstitial alkali feldspar (Table 6.1). Muscovite plates are abundant and commonly exhibit crystal faces against plagioclase, as observed in tonalitic leucosomes. Biotite is rare and invariably replaced by chlorite. Diffuse schlieren and abundant micaceous enclaves (up to 40 cm long, 5 cm thick) define a pronounced directional fabric. This is generally contorted but also more regular in places, imparting a layered 'diatexitic' aspect (Figure 6.4). Micaceous enclaves are particularly concentrated at the peripheries of the leucotonalite pluton and are distinctively enriched in coarse, S_2-aligned muscovite plates, which comprise up to 70% of the enclave. Many also contain veins and 'slugs' of bluish polycrystalline quartz, and thus closely resemble the thick melanosomes of adjacent stromatic migmatites. These objects are variously disintegrated, such that coarse mica flakes and quartz chunks draped by thick micaceous selvedge (3-10 cm) are strewn throughout the host.

Figure 6.5. Migmatitic schist enclave hosted by the Schofield Adamellite, showing isoclinally folded leucosomes (F_2) being overprinted by F_3 structures (arrowed).

Semi-pelitic gneiss and stromatic migmatite enclaves are also numerous. In Dunmore Creek, migmatitic enclaves form slabs up to 2 m^2, where thick M_2 leucosomes are complexly folded and melanosomes are in the process of entrainment by the host tonalite. Coarse biotite-muscovite schist also forms large enclaves (up to 3 m long), many of which are intensely folded by F_3 and F_4 structures (e.g. samples **98-MEL**, **98-151**, **98-152**). Thin, impersistent laminae (0.5-2 mm thick) in these rocks comprise foliated muscovite and biotite, and alternate with more quartzose layers where mica flakes are poorly aligned and enclosed by large quartz masses (~5 mm). Samples **98-MEL** and **98-151** also contain numerous quartz-rich laminae (1-10 mm) and lenticular veins of clear quartz (5-20 mm thick). Unusually, plagioclase is very minor in these schist enclaves and in thin section forms small, corroded grains embayed by quartz, or tiny pools surrounded by biotite flakes; it commonly has a pitted 'sponge-like' appearance. This, combined with considerable disruption of the S_2 fabric, is consistent with enclaves being residual from extraction of a melt phase (section 8.6.4). Similar feldspar-poor micaceous schists outcrop *in situ* near the southwestern margin of the leucotonalite in Dunmore Creek (see above).

6.2.5 Summary of Dunmore Leucotonalite field relations

Like the Nangkita Adamellite of Robson Creek (section 5.5), field relationships imply a genetic link between the Dunmore Leucotonalite and partial melting phenomena in the adjacent migmatitic envelope. In both examples, migmatitic rocks contain *in situ* leucosomes connected

in turn to small bodies and sheets of granitic rock that become increasingly abundant throughout the sequence as the pluton margin is approached. In Robson Creek, these features are considered to represent migration of locally-generated partial melts into progressively larger magmatic conduits, ultimately with ponding to produce the Nangkita Adamellite pluton. Owing to outcrop similarities, this interpretation is also appropriate for the Dunmore Leucotonalite. In this case, the postulated link with enclosing migmatites is strengthened by the shared alkali feldspar-poor character of *in situ* leucosomes, contiguous granitic sheets, and the pluton itself.

6.3 Interleaved granitic and migmatitic rocks of Schofield Creek

A diverse assemblage of complexly intercalated metasedimentary and granitic rocks is prominently exposed for 9 km along the flanks of Schofield Creek (Figure 6.6). The southernmost reaches of the watercourse are occupied by the Tuloona Granodiorite of the Tuloona magma type, and thus the geology of Schofield Creek records the fundamental transition from rocks of the northeastern metamorphic zonation to the quite distinct granitic lithologies of the central batholith.

North of the Tuloona Granodiorite to the junction with the Glenelg River, three main geological components are distinguished in Schofield Creek, migmatitic metasedimentary rocks, strikingly heterogeneous, structurally concordant granitic rocks and intrusive leucogranitic bodies (Kemp 1995). Structurally concordant granitic lithologies with schlieric flow fabrics and complexly deformed migmatite enclaves (Figure 6.5) are predominant, and are resolved into four bodies, from north to south, the Scrubby Junction Granodiorite, Schofield Adamellite, Carrigeen Granodiorite and Awaiti Adamellite (felsic Tuloona Granodiorite of Kemp & Gray 1999a). These elongate plutons are aligned with the regional S_2 orientation and are traced northwest to the Glenelg River and tributaries. All are internally layered, have very intimate (generally transitional) field relationships with migmatitic horizons, and are interspersed with thick pegmatitic sheets, such that the geology of Schofield Creek has a strongly layered or sequential aspect. For convenience, this lithological package is documented below in two separate parts, from Greens Lane north (downstream) to the Glenelg River (northern segment, ~4 km) and from Greens Lane south to the Harrow-Balmoral road (southern segment ~5 km).

6.4 Northern segment of Schofield Creek

6.4.1 Carrigeen Granodiorite

An elliptical pluton, Carrigeen Granodiorite has a homogeneous core that outcrops as large tors on the eastern slopes of Schofield Creek near Greens Lane. However, it becomes progressively more variable towards the periphery and ultimately grades into diatexites to the north and south along the watercourse.

(a) Homogeneous core

Carrigeen Granodiorite samples from here (e.g. **T2-3**) are bluish-white, medium grained and approximately equigranular, though rare plagioclase phenocrysts occur (5-7 mm).

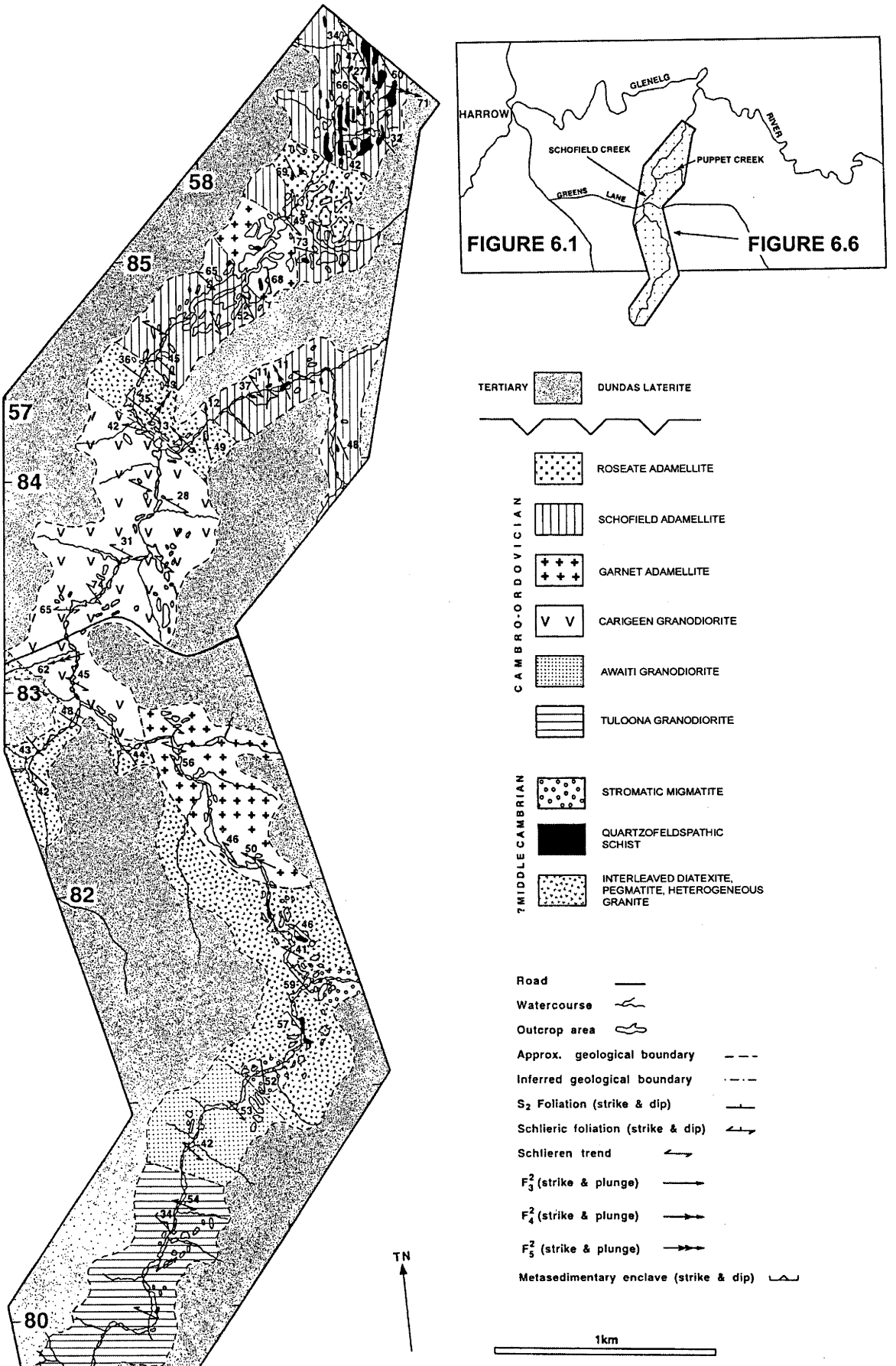

Figure 6.6. Outcrop map of Schofield Creek. The inset depicts the locality in Figure 6.1. Modified from Kemp (1995).

Coarse muscovite plates (1-2 mm) are prominent, with euhedral grains characteristically enclosed by blocky, oscillatory-zoned plagioclase laths. Disseminated biotite (~1 mm grains) is conspicuous, with flakes being non-aligned and interleaved with muscovite. Except for the occasional foliated micaceous clot (1-3 cm), metasedimentary enclaves are absent.

Exposures in Schofield Creek are slightly more felsic (e.g. **98-2**) and may contain tiny euhedral garnets. Some outcrops here also have a conspicuous schlieric fabric, the broad warping of which is testament to D_5 folding (Kemp & Gray 1999a).

(b) Tonalite gneiss enclaves

Large enclaves of coarse grained gneissic tonalite (slabs up to 1.5x3 m) occur sporadically along a 300 m stretch of Schofield Creek near the centre of the Carrigeen Granodiorite. These objects are variably rotated, such that the internal foliation is oblique to the weak schlieric fabric of the host granodiorite, which encircles the enclaves (Figure 6.7). Tonalitic material is medium grey, even-grained and comprises recrystallised quartz and plagioclase masses flattened parallel to intensely aligned flakes of coarse biotite (**98-3**). This lithology is clearly distinct from Harrow type rocks and has affinity with the deformed granitic bodies of the southwestern GRC (section 10.4).

(c) Transition to diatexite

Towards the northern boundary, remote from homogeneous central outcrops, a weak alignment of disseminated biotite first becomes apparent in Carrigeen Granodiorite, augmented by occasional schlieren and elongate micaceous enclaves. A vague lithological layering also occurs parallel to this fabric, where lenticular domains of slightly more felsic and coarser grained material are interspersed. Near the junction of Puppet and Schofield Creeks, the granodiorite is relatively biotite-rich (**98-1**) and strongly heterogeneous, with abundant alkali feldspar megacrysts, quartzofeldspathic schist slabs (10 cm to 1 m long) and biotite-dominated micaceous enclaves. Besides flesh coloured phenocrysts and megacrysts, alkali feldspar is of diminished abundance in the granitic host, which is tonalitic. Large quartz masses are also evident (to ~10 mm). Biotite schlieren, occasionally interwoven with fibrolite and muscovite, define a conspicuous gneissosity, parallelled by diffuse biotite-rich streaks. Many of these appear to be stripped from large migmatitic enclaves (30-50 cm), which are partially digested by the host. The planar fabric is augmented by aligned flakes and elongate clots of coarse biotite and muscovite.

Exposures become even more heterogeneous further north, choked with clusters of micaceous enclaves (to 10 cm across), commonly with random dispositions, and contorted migmatitic schist slabs (Figure 6.8). Many granodiorite samples (e.g. **98-64A**) exhibit an irregular and discontinuous banding, defined by alternating biotite-rich and relatively felsic granodioritic domains, and parallelled by micaceous schlieren. Graphic alkali feldspar megacrysts (to 8 cm) are scattered throughout and commonly embedded in lenticular patches of coarse grained alkali feldspar-rich leucogranite, elongated parallel to the layering/schlieric fabric.

The planar fabric in peripheral Carrigeen Granodiorite exposures becomes increasingly intense and regular, and biotite becomes more abundant, until the rock merges into diatexite. The distinction between granodiorite and diatexite is wholly arbitrary, but the boundary is placed

Figure 6.7. Blocky enclave of gneissic tonalite hosted by the Carrigeen Granodiorite. The strong foliation of the tonalite (parallel to the pen) is oblique to a weak schlieren-defined fabric in the host (Schofield Creek, WD576835).

Figure 6.8. Strikingly heterogeneous peripheral Carrigeen Granodiorite exposure, with clusters of rotated micaceous enclaves, alkali feldspar megacrysts and an enclave of quartzofeldspathic schist (left). (Schofield Creek, WD577843). Note the irregular outlines of feldspar megacrysts (arrowed).

where the rock becomes strongly layered and gneissic, exhibiting the slabby outcrop character typical of metasedimentary rocks. This results from micaceous enclaves, quartzofeldspathic schist slabs and especially disseminated biotite flakes being strongly aligned with the schlieric banding, unlike heterogeneous granitic rock, where some rotation of these elements exists. South of Greens Lane, and towards its southern periphery, Carrigeen Granodiorite develops a pervasive schlieric fabric and also undergoes a transition into diatexite, in the same manner as outlined above.

6.4.2 Diatexite and stromatic migmatite

Diatexites, lithologically similar to those of Robson Creek (section 5.3.4), outcrop in subdued fashion for another 250 m northwards along Schofield Creek, with a 1 m wide stromatic migmatite horizon at the northernmost extremity. The latter has M_2 leucosomes (0.5-6 cm thick) traversing a laminated quartzofeldspathic schist mesosome. The thickest leucosomes (e.g. **98-65A**) are slightly discordant to S_2 in the mesosome, and medium, even-grained, with equal proportions of subhedral plagioclase and tabular alkali feldspar (Table 5.4). A small amount of disseminated biotite occurs, along with clots and foliated schlieren of biotite, which represent entrained melanosome fragments. In thin section, plagioclase is complexly zoned, commonly with calcic cores (up to An_{42}; section 7.2.1). Alkali feldspar also has distinct optical zoning and rarely encloses small tufts of fibrolite, largely replaced by spindles of secondary muscovite. Other leucosomes (sample **98-65B**) are coarser grained, concordant with the mesosome foliation, and contain slightly more alkali feldspar. Biotite is rare, but schlieren of melanosome are entrained where thick leucosomes merge.

Both leucosomes types are bordered by melanosomes of coarse biotite, quartz, and minor muscovite, being thickest adjacent to the coarser, felsic leucosomes (up to 12 mm). With decreasing grainsize and appearance of plagioclase, melanosomes grade into mesosomes that are quite feldspathic, with abundant poikiloblastic alkali feldspar and a small amount of primary muscovite in biotite laminae (**98-65C**) (Table 5.4).

6.4.3 Schofield Adamellite

North of the diatexite horizon, an internally heterogeneous granitic body, the Schofield Adamellite, outcrops continuously for ~2 km along the slopes of Schofield Creek and intermittently for ~3 km along the Glenelg River valley. Given the high calibre of exposure in Schofield Creek, most detailed mapping and systematic geochemical sampling has centred along this watercourse. Here, Schofield Adamellite has a sheeted structure and comprises six lithological 'horizons', labelled (a) to (f) below. An S_2-parallel schlieric foliation of variable intensity is pervasive throughout all.

(a) Felsic plagioclase-rich horizon

The abrupt occurrence of prominent granitic exposure 25 m north of the last migmatite outcrop in Schofield Creek and Puppet Creek (~600 m to the east) signals the onset of the Schofield Adamellite. In both watercourses, Schofield Adamellite immediately north of the boundary contains abundant enclaves of quartzofeldspathic schist and partially disaggregated stromatic

migmatite. A strong planar fabric of biotite-rich schlieren and elongate micaceous enclaves is also evident.

Granitic exposures become more homogeneous after about 20 m in Schofield Creek, and are tonalitic to granodioritic in character. Samples (e.g. **T2-CC9D**) are medium to coarse grained and dominated by blocky plagioclase laths (~3 mm, up to 7 mm), which in thin section have strong oscillatory zoning and irregular corroded cores. Buff coloured poikilitic masses or interstitial grains of alkali feldspar (2-10 mm) are minor, and tend to be concentrated in lenticular patches. Coarse biotite flakes (~2 mm, rarely to 5 mm) are conspicuous, and, with interleaved euhedral muscovite, exhibit a weak alignment parallel to diffuse micaceous schlieren. Alkali feldspar megacrysts are numerous and locally clustered, near where the granitic host contains a higher proportion of matrix alkali feldspar.

This plagioclase-rich horizon is apparently discontinuous, as exposures along strike in Puppet Creek (**98-59**) have significant amounts of alkali feldspar. The northern extent of the lithology in Schofield Creek is also poorly defined, as the distribution of matrix alkali feldspar is erratic. Nevertheless, felsic granitic outcrop with alkali feldspar megacrysts, few metasedimentary enclaves and an overall alkali feldspar-poor character persists for ~200 m north along Schofield Creek, and constitutes an important compositional layer within Schofield Adamellite.

(b) Heterogeneous 'diatexitic' horizon (~120 m wide)

Granitic rock in Schofield Creek abruptly becomes heterogeneous north of the above horizon, with a strong layered aspect imparted by numerous schlieren, elongate micaceous enclaves, and a diffuse banding of more biotite-rich material. Large enclaves of quartzofeldspathic schist and migmatite are aligned with the fabric, which anastomoses around abundant alkali feldspar megacrysts (Figure 6.9). The granodioritic to tonalitic host is fine to medium grained and has sparse plagioclase phenocrysts (5-7 mm). Relative to preceding outcrops it is significantly more biotite-rich, small flakes of which (0.5-1 mm) define a regular foliation, parallelled by biotite clots and subordinate muscovite flakes.

(c) 'Mingled' adamellite horizon

Downstream of the diatexitic unit, prominent outcrop of coarser, relatively alkali feldspar-rich granitic rock occurs in both the watercourse and along the flanks of the valley. The boundary between the two granitic horizons is not exposed but appears to be complexly interfingered. Although the coarser grained Schofield Adamellite of this unit is more felsic overall, it is pervasively heterogeneous, with closely-spaced samples exhibiting variability in biotite content and proportion of alkali feldspar to plagioclase. Metasedimentary enclaves and alkali feldspar megacrysts are common, but also have heterogeneous distribution.

The variation is encapsulated within prominent exposures at WD583849. Outcrops exhibit a pronounced layering (5 cm to 1 m thick), where the predominant medium to coarse grained adamellite (e.g. **98-14C**) is interspersed with finer grained, significantly more biotite-rich material (e.g. **98-14A**) and coarse grained leucogranite containing concentrations of anhedral alkali feldspar megacrysts (**98-14D**) (Figure 6.10). The biotite-rich variant is also adamellitic,

Figure 6.9. 'Diatexitic' Schofield Adamellite horizon, with a distinct schlieric layering, parallelled by a large tapering slab of quartzofeldspathic schist. Note that the micaceous selvedge at the top of the schist enclave is partially disaggregated by the host granodiorite. Alkali feldspar megacrysts of varying sizes are dispersed throughout, mostly having very irregular outlines (Schofield Creek, WD579846).

Figure 6.10. Contorted schlieren-defined layering in 'mingled' Schofield Adamellite outcrops, parallel to a distinct banding of alternating coarser and finer grained granitic material (bottom). Textural heterogeneity in the adamellite is conspicuous in the top half of the photograph (Schofield Creek, WD583849).

but contains prominent disseminated flakes and small clots (~1 cm) of biotite, with plagioclase phenocrysts (5-6 mm) and occasional large alkali feldspar grains. Conversely, the leucogranitic material is dominated by poikilitic alkali feldspar (4-6 mm) and blocky plagioclase laths (3-4 mm), with large, euhedral muscovite plates (~2 mm), but minor biotite.

Layers of the biotite-rich and leucogranitic variants may be impersistent and are commonly contorted, such that the disparate granitic material is intimately intermingled. The layered aspect is enhanced in places by micaceous clots and schlieren (mostly biotite-dominated), which are common throughout and define a distinct planar fabric parallel to the granitic banding (Figure 6.10). Migmatitic schist enclaves (30 cm to 3 m long) are also present but are extensively veined by the granitic host and in the advanced stages of disaggregation. Some biotite schlieren and small micaceous enclaves in the vicinity are clearly derived by this process. Large quartzofeldspathic schist slabs (several metres across) have modal variations on a quartz-plagioclase-biotite ± muscovite mineralogy (e.g. **98-14B**), as is typical of schist enclaves in Schofield Creek granitic rocks.

Schofield Adamellite outcrops at this locality are also traversed parallel to the schlieric banding by an unusual pegmatitic layering, where thin lenticular pockets or sinuous strands of pegmatitic material with diffuse margins are observed (several metres long, up to 8 cm thick). Unlike isolated megacrysts, alkali feldspar forms large euhedral tabular or lance-shaped crystals oriented perpendicular to the overall trend of the pegmatitic band. These megacrystic bands periodically widen into pockets of true pegmatite, where quartz-rich cores have books of muscovite, small garnets and rarely, green apatite crystals up to 1 cm.

(d) Heterogeneous 'diatexitic' horizon

An intrusive garnet adamellite sheet separates the above mingled unit from another strikingly heterogeneous biotite- and plagioclase-rich granitic horizon. This lithology is exposed most prominently along Fishhook Gully, incised into the eastern valley of the main watercourse, and is choked with metasedimentary enclaves (Figures 6.5, 6.11). Numerous schlieren and biotite-dominated micaceous enclaves engender a pronounced diatexite-like layering, which is contorted or complexly folded in some exposures. Large tapering enclaves of quartzofeldspathic schist and migmatite are evident, in the upper part of Fishhook Gully forming large areas (up to 25 m) that are either *in situ* or detached rafts. Significantly, migmatitic schist here has thick M_2 leucosomes that are connected to larger, pond-like leucogranitic bodies (Figure 6.12), this relationship resembling that consistently observed in M_2 migmatite horizons of Robson Creek gorge (section 5.3.5).

(e) Homogeneous horizon (Roseate Adamellite)

The diatexitic Schofield Adamellite exposures are supplanted to the north by a coarse grained, leucocratic and muscovite-rich granitic expanse, mapped as Roseate Adamellite by Kemp (1995). This small body, distinguished by its homogeneous character and pinkish tinge, is dominated by subhedral alkali feldspar, phenocrysts of which impart a speckled aspect to weathered surfaces. Contacts with enclosing Schofield Adamellite horizons are complexly intermingled.

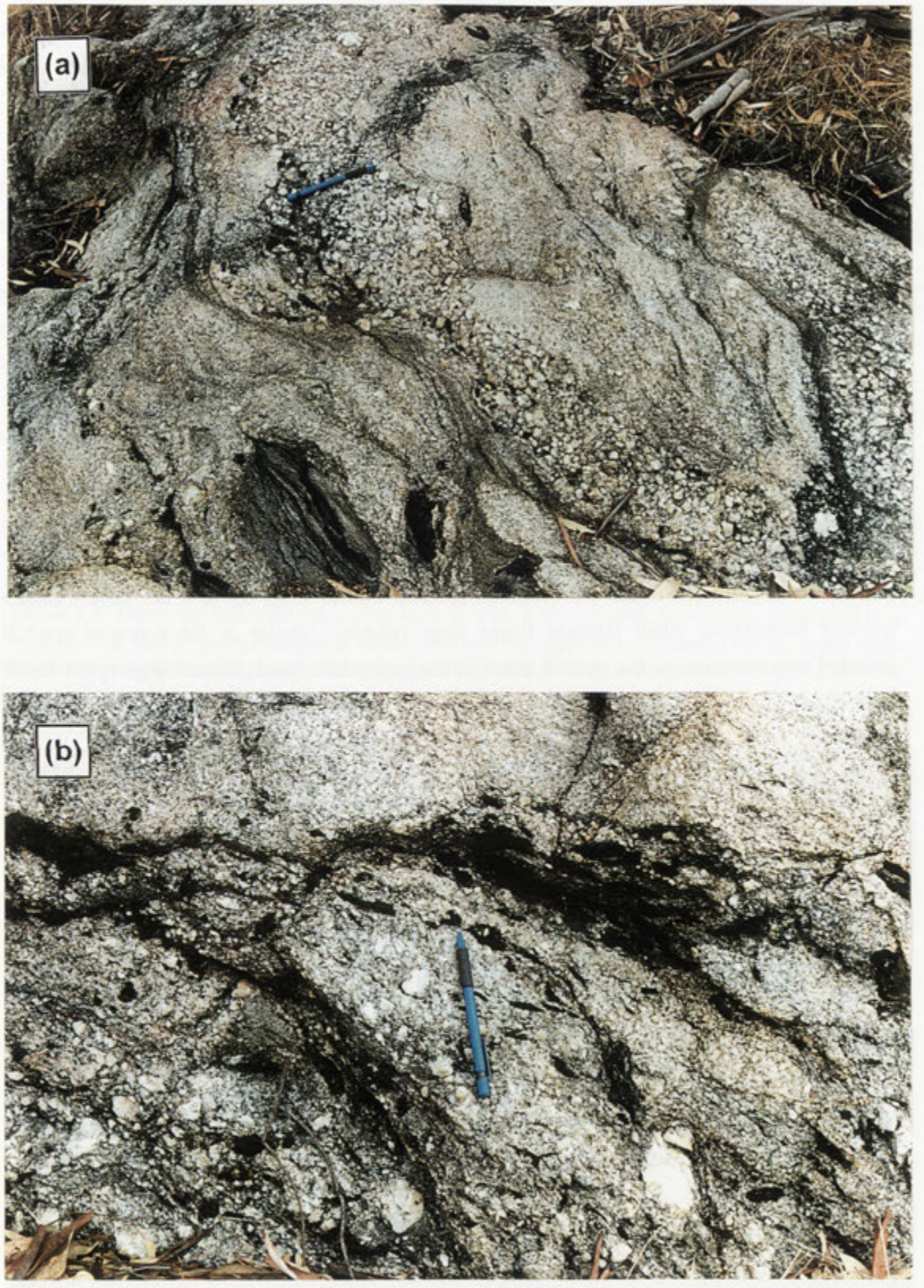

Figure 6.11. Strikingly heterogeneous horizon in Schofield Adamellite. (a) Overview of the outcrop, showing the diatexite-like layering and numerous metasedimentary enclaves. (b) Closer view, illustrating the micaceous enclaves (mostly biotite, some with muscovite or, rarely, sillimanite), anhedral feldspar megacrysts and small scale textural heterogeneity (Schofield Creek, WD585853).

(f) Northern 'mingled' adamellite horizon

Prominent outcrop of 'mingled' Schofield Adamellite commences downstream of Roseate Adamellite, where textural and compositional heterogeneity is pervasive on outcrop and handspecimen scale. The adamellite is typically medium to coarse grained, with coarse plates of non-aligned muscovite, and minor biotite (sample **98-23**, Table 6.1). Blocky plagioclase laths (~3 mm, up to 8 mm) and subhedral, inclusion-free alkali feldspar grains vary in proportions between samples, plagioclase generally being predominant. However, slightly coarser grained and more feldspar-rich leucogranitic material is intimately intermingled. Some samples (e.g. **98-26**) exhibit a subtle banding, such that the coarser leucogranite forms elongate domains of variable thickness (~2-4 cm), that are parallelled by a weak biotite alignment in the rest of the rock. The feldspar-rich material occasionally forms more discrete planar layers (3-4 cm thick), bordered by thin muscovite-biotite schlieren. However, other outcrops exhibit a more haphazard interblending of the coarser felsic rock and 'typical' Schofield Adamellite, with the boundary either marked by diffuse mica schlieren or being intergradational.

Apart from schlieren, Schofield Adamellite samples from this unit also commonly contain graphic alkali feldspar megacrysts (4-12 cm, anhedral-euhedral) and lenticular micaceous enclaves (1-20 cm) (Figure 6.13). The latter are mostly interleaved muscovite and biotite but also contain quartz laminae and pockets of polygonal plagioclase (e.g. **98-SEL**). Larger enclaves of similar rock (up to 50 cm long) also occur (e.g. **98-27B**). Micaceous enclaves and schlieren are rare in the intermixed coarse leucogranitic material.

The northernmost part of the Schofield Adamellite is complexly interlayered with metasedimentary exposures (Figure 6.6). In this vicinity, the adamellite contains abundant enclaves of quartzofeldspathic schist (slabs to 5 m across) and migmatitic gneiss that are aligned with the schlieric fabric of the host. On the eastern flank of Schofield Creek, these enclave-choked granitic exposures are interspersed with larger areas of unmelted schist (up to 75 m long), the S_2 fabric of which is oriented with the regional S_2 trend. As such, it is unclear whether these are large rafts within the granitic host that retain the pre-existing structural orientation or part of an *in situ* schist 'skeleton'.

Schofield Adamellite of the Glenelg River valley

Due to more sporadic, weathered outcrop, a lithological banding similar to that observed in Schofield Creek is difficult to identify in Schofield Adamellite exposures of the Glenelg River valley. One thin biotite-rich granitic horizon, with numerous schlieren and metasedimentary enclaves, can be traced for 800 m, but grades into more felsic adamellite at the extremities. Notably, the distinctive 'diatexitic' horizons recognised along Schofield Creek are not identified northwestwards along strike in the Glenelg River. These observations indicate that the compositional banding evident in the Schofield Adamellite is laterally impersistent.

Although metasedimentary enclaves and micaceous schlieren are common, Schofield Adamellite outcrops of the Glenelg River valley have overall less biotite than those of Schofield Creek. Aplitic to pegmatitic dykes are more numerous, in the vicinity of which the adamellite is

Figure 6.12. Migmatite-enclosed leucogranitic body that has apparently formed by channelling and ponding of *in situ* partial melts from contiguous M_2 leucosomes. The irregular schistose body in the centre of the structure may have originally comprised a metasedimentary 'septa' separating two separate leucogranitic accumulations, subsequently disrupted by magma movement (Schofield Creek, WD588851).

Figure 6.13. Heterogeneous outcrop towards the northern Schofield Adamellite margin, exhibiting variably rotated migmatitic schist enclaves, micaceous enclaves and sinuous muscovite-biotite schlieren. Despite this, the leucocratic nature of the granitic host remains obvious (Schofield Creek, WD589857).

commonly quench textured and contains tiny garnets. Small homogeneous domains of medium to coarse grained muscovite adamellite (100-900 m long) also occur, resembling the Roseate Adamellite (Figure 6.1). These bodies have elongate geometries, concordant with the schlieric fabric of the enclosing Schofield Adamellite, and have complexly interfingering and partly gradational contacts, implying a syn-magmatic relationship with the host.

6.4.4 Northern Metasedimentary Tract

Although quite thin, being ~150 m wide in the Glenelg River valley and ~250 m across in Schofield Creek (Figure 6.1), this wedge of metasedimentary rock is lithologically variable, incorporating massive to laminated quartzofeldspathic schist, muscovite-biotite schist and M_1 stromatic migmatite. Quartzofeldspathic schist has variable quartz-plagioclase-biotite modes, sometimes with alkali feldspar and primary muscovite. M_1 leucosomes (0.5-4 cm thick) are most numerous in laminated and semi-pelitic schist (5-30 cm thick interlayers).

Stromatic migmatite horizons (to 40 cm thick) have medium to coarse grained M_1 leucosomes that are dominated by subhedral plagioclase (to 5 mm) and quartz, though the feldspar/quartz ratio varies dramatically between and within leucosomes. Euhedral muscovite plates occur in more feldspathic portions. Although some leucosomes have sporadically-distributed alkali feldspar, and are connected to decimetre-scale granitic sheets (e.g. leucosome **98-WF2A-2L**, see Table 5.3), most lack alkali feldspar and are tonalitic (e.g. 98-25M1 in Table 5.3). Leucosomes have extensive muscovite-biotite melanosomes (1-12 mm thick), which are thickest and most biotite-rich around quartz-rich leucosome segments, as with migmatites of Robson Creek and the Glenelg River valley. Small pockets or discontinuous laminae of polygonal plagioclase and quartz also occur in some melanosomes, and occasionally grade laterally into leucosomes. Mesosomes are semi-pelitic schist, with abundant S_2-aligned muscovite. Sillimanite, or ragged muscovite that might be replacing sillimanite, is absent.

Undeformed M_2 leucosomes (sample **98-25M2**, Table 5.4) and lenticular, pool-like leucogranitic segregations (10 cm across) also sparsely occur in this metasedimentary tract. A sample of the latter (**98-WF1A**) is surrounded by melanosome (to 1 cm thick) of interleaved S_2-aligned muscovite and biotite. This segregation is contiguous with a 1.5 m wide granitic sheet (sample **98-WF1B**) (Table 5.5), several of which are concordantly interleaved with the metasedimentary sequence. Unlike M_1 leucosomes, M_2 leucosomes, pool-like segregations and granitic sheets contain alkali feldspar (1-2 mm poikilitic grains).

6.4.5 Scrubby Junction Granodiorite

The northernmost granitic body of Schofield Creek (Figure 6.1), the Scrubby Junction Granodiorite is separated from the above metasedimentary tract by a 75 m thick pegmatite sheet. North of this, the granodiorite contains numerous large metasedimentary enclaves, primarily quartzofeldspathic schist (up to 10 x 5 m), though several rafts of distinctive semi-pelitic stromatic migmatite (to 250 m long) also occur. Most enclaves are aligned with the regional S_2 orientation.

Metasedimentary enclaves become less abundant northwards, where typical Scrubby Junction Granodiorite samples are medium grained **(98-38-2)** with a vague schlieric banding. These are distinguished from Schofield Adamellite by a higher quartz content and more biotite-rich character (Table 6.1). In thin section, euhedral biotite flakes are commonly entwined with, and mantled by, sheaves of muscovite, and rounded quartz grains invariably enclose muscovite crystals. Alkali feldspar is interstitial to blocky plagioclase grains or forms larger, subhedral phenocrysts (2-5 mm). As with Schofield Adamellite, more felsic and coarser grained granitic material is intimately intermingled on outcrop scale, and metre-sized garnetiferous leucogranite sheets occur throughout.

6.5 Southern segment of Schofield Creek

This segment of Schofield Creek extends from the southern Carrigeen Granodiorite margin near Greens Lane to the Harrow-Balmoral road ~5 km further south (Figure 6.6).

6.5.1 Interlayered metasedimentary and granitic rocks

Immediately south of the Carrigeen Granodiorite, diatexite marks the onset of an interleaved package of migmatitic metasedimentary rocks and heterogeneous granite that outcrops for another 2 km south along Schofield Creek. The diatexite has the same outcrop and petrographic character as those of Robson Creek (section 5.3.4), and, as with sample **99-R5**, has elongate quartz-plagioclase pockets that contain fibrolite clots (2-12 mm). In places, the schlieric banding is highly contorted, indicating localised mobility of the granitic melt fraction (Figure 6.14a).

Stromatic migmatites also occur and, like those of Robson Creek gorge, are generally dominated by geometrically-complex M_2 leucosomes, such that outcrops have a 'sloppy' appearance. A typical example (Figure 6.14b) has thick, but irregularly-shaped leucosomes bordered by extensive biotite-quartz ± muscovite melanosomes. Leucosomes are mostly medium to coarse grained and feldspathic, though more quartz- and plagioclase-rich segments occur that enclose sillimanite clots (2-8 mm; samples 99-11, 99-12 in Table 5.4). Sillimanite (overgrown by muscovite) also occurs interwoven with biotite in melanosomes, or forms unretrogressed tufts embedded in quartz. In places, the leucosome fraction appears pervasive, such that the outcrop has diatexitic character. Quartzofeldspathic gneiss mesosomes (quartz-plagioclase-biotite, with erratically-distributed alkali feldspar and prograde muscovite) contain routine D_3 folds, whereas leucosomes outline incoherent fold structures that vary non-systematically in orientation. These may result from fluid-like rheology during deformation (McLellan 1984). Notably, entrainment of melanosome into leucosomes is very minor, consistent with an efficient melt segregation mechanism. Further, despite the 'intestinal' aspect, many leucosomes form complexly interconnected networks, and are contiguous with decimetre-sized pool-like granitic bodies, many of which are parallel to S_3 (Figure 6.14b). This behaviour has direct analogy to that documented from M_2 migmatites in Robson Creek (see section 5.3.5) and similarly implies migration of partial melt into larger magmatic structures.

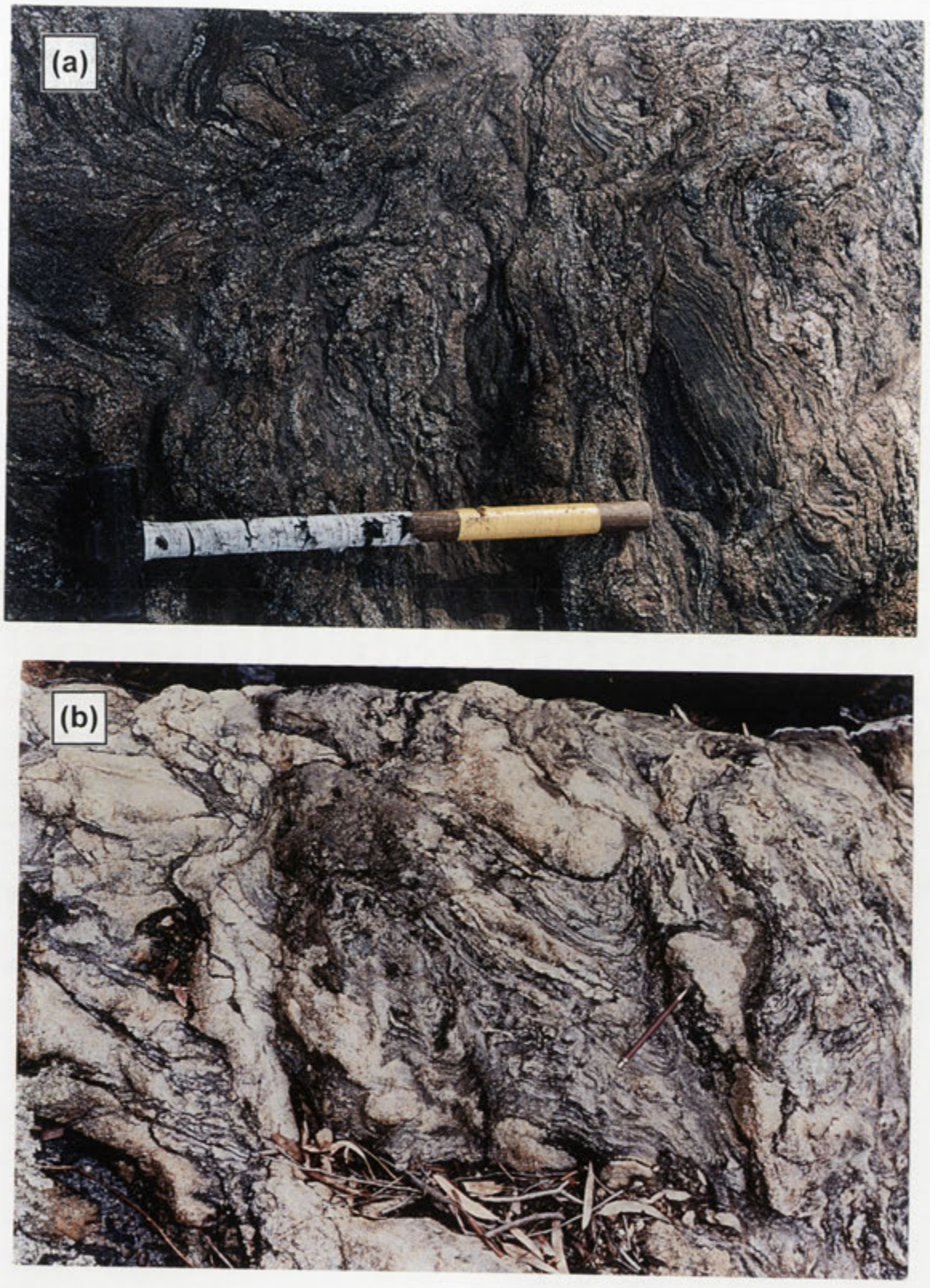

Figure 6.14. Migmatites of southern Schofield Creek. (a) Diatexite with contorted schlieric layering, resulting from mobility of the partially melted (i.e. granitic) fraction. Stromatic migmatite and quartzofeldspathic schist enclaves probably represent fragments of more refractory metasedimentary layers in the diatexite protolith that were disrupted upon anatexis (WD580820). (b) Leucosome-dominated M_2 stromatic migmatite, exhibiting migration of partial melts into pool-like structures that are grossly parallel to S_3 (parallel to the short edge of the photo), consistent with deformation enhanced melt segregation/extraction. Note the efficient melt-residue separation and paucity of entrained melanosome (WD576826).

Diatexite and stromatic migmatite outcrop for a short distance along Schofield Creek before a garnet adamellite pluton is encountered (Figure 6.6). South of this is an interlayered sequence of heterogeneous muscovite granite, quartzofeldspathic schist, stromatic migmatite (some of which is semi-pelitic) and diatexite (5-25 m wide layers); detailed descriptions and outcrop maps are in Kemp (1995). Sheets of pegmatite and relatively homogeneous muscovite leucogranite are also interspersed (5-10 m). This assemblage is traced west along strike to southern tributaries of the Glenelg River (Figure 6.1).

6.5.2 Awaiti Adamellite

About 1 km south of the garnet adamellite, homogeneous, muscovite-bearing granitic rock becomes predominant in the sequence and is here designated Awaiti Adamellite (Figure 6.6). This has conspicuous disseminated biotite and occasional phenocrysts of quartz and alkali feldspar. Some exposures exhibit a northwesterly-trending fabric of diffuse mica schlieren and aligned micaceous enclaves. Other metasedimentary enclaves, primarily migmatitic varieties up to 3 m long, are common at the northern margin and occur sporadically southwards. Some outcrops are also crosscut by thin (1-5 m wide) high strain zones, where biotite is strongly aligned and parallelled by ragged secondary muscovite flakes. These are oblique to S_2 and attributed to D_5 strain partitioning (Kemp & Gray 1999a).

6.5.3 Transition to Tuloona Granodiorite

The transition from the Awaiti Adamellite to the more mafic, magnetite-bearing Tuloona Granodiorite of the central granitic batholith occurs over ~500 m along the southern part of Schofield Creek. This commences at WD577806, where more mafic granitic material (equivalent to Tuloona Granodiorite) is complexly interspersed with the felsic muscovite-rich adamellite, itself more biotite-rich than further north. The felsic adamellite is initially predominant and in places encloses large globules (to 30 cm across) of the mafic granodiorite, accompanied by metasedimentary enclaves. Southwards, the mafic granodiorite, with porphyritic microgranular enclaves, becomes relatively more voluminous, though the muscovite adamellite is still intimately intermingled (Figure 6.15a). The boundary between the two granitic bodies is delineated where the Tuloona Granodiorite becomes predominant and microgranular enclaves are abundant. Large migmatitic rafts with pegmatitic leucosomes occur within the Tuloona Granodiorite along a 300 m stretch of creek south of the boundary, and are extensively disaggregated. This results in a chaotic interblending of alkali feldspar megacrysts, micaceous schlieren, muscovite-rich granitic rock and mafic granodiorite, where globular mafic igneous enclaves are scattered throughout (Figure 6.15b). Further south, granitic outcrop becomes more homogeneous, and is 'typical' Tuloona Granodiorite with swarms of mafic enclaves and occasional migmatitic slabs (section 11.2.1).

6.6 Other Harrow type plutons of the Harrow district

These have been described in detail by Kemp & Gray (1999a) and are briefly reiterated here.

Figure 6.15. (a) Complex syn-magmatic mingling between the relatively mafic Tuloona Granodiorite (top) and megacryst-bearing Awaiti Adamellite (bottom), the former being predominant (Schofield Creek, WD575801). (b) Exposure of Tuloona Granodiorite at its northern margin in Schofield Creek, containing tapering quartzofeldspathic schist rafts, micaceous schlieren and igneous-textured mafic enclaves (near pen) (WD574797). The directional fabric is oblique to the regional trend of S_2 and incoherent on a larger scale, possibly reflecting localised turbulent flow.

6.6.1 Kout Norien Granodiorite

Slabby boulders of Kout Norien Granodiorite are prominent along the Glenelg River valley and Salt Creek immediately east of Harrow (Figure 6.1). The body is crosscut to the south and west by the Tuloona Granodiorite and intruded by the Harrow Granodiorite to the east; the northeastern boundary with the Schofield Adamellite is enigmatic owing to poor outcrop constraints. An apparently concordant contact with interlayered diatexite and muscovite granite is evident in watercourses south of the Glenelg River.

Typical Kout Norien Granodiorite exposures overlooking Harrow (**98-76**) (Table 6.1) are strikingly heterogeneous, but medium grained overall, with tabular plagioclase phenocrysts (~5 mm, up to 15 mm), and abundant randomly disposed flakes (~1 mm) and interleaved aggregates of biotite (2-3 mm). Muscovite forms small inconspicuous grains, and phenocrysts of graphic alkali feldspar (4 mm-3 cm) are also observed, sometimes encircled by biotite-rich selvedges. Sillimanite is common as isolated tufts or as intertwined clots with biotite. In thin section, the rock is an anhedral mosaic of polycrystalline quartz, tabular alkali feldspar and patchy zoned plagioclase. Alkali feldspar is perthitic microcline and encloses quartz, euhedral muscovite, biotite and fibrolite aggregates, the latter also enveloped by ragged secondary muscovite flakes. Primary muscovite is smaller, and invariably interleaved with well shaped biotite.

Distinctively, Kout Norien Granodiorite pavements exhibit an irregular layering, defined by diffuse biotite-rich schlieren. This vague layering is accentuated by lenticular micaceous enclaves (1-15 cm) (Figure 6.16) and trends consistently northwest, concordant with S_2. The fabric intensifies northwards, until outcrops in northern Salt Creek become diatexitic (Figure 6.17). Micaceous enclaves are dominated by coarse biotite, sometimes interwoven with fibrolite, contrasting with those of other Harrow types, which generally contain abundant muscovite without sillimanite. Large enclaves of quartzofeldspathic schist (to 10 m), migmatite (to 50 m) and semi-pelitic to quartzofeldspathic gneiss (to 50 m) are also common in Kout Norien Granodiorite, many of which are sillimanite-bearing; distinctive varieties not recognised in other Harrow type granitic rocks are described in Table 6.2. Commonly, enclaves taper into schlieren, and more micaceous varieties are partially dismantled, releasing biotite-rich clots and selvedges into the adjacent granodiorite. Migmatite and gneissic enclaves also become larger and increasingly abundant northwards, being particularly numerous in Salt Creek. Importantly, F_3 and F_4 structures in metasedimentary enclaves confirm a syn- to post-D_4 emplacement timing for the host granodiorite.

6.6.2 Harrow Granodiorite

Prominent outcrop of homogeneous, muscovite-bearing granitic rock along gullies south of the Glenelg River defines a large oval body, the Harrow Granodiorite. This pluton truncates the schlieric fabric of the Kout Norien Granodiorite to the west (Figure 6.1), and is easily distinguished from this phase by relative paucity of metasedimentary enclaves. Nevertheless, the shared biotite-rich character and content of sillimanite suggests some link between these bodies. The precise location and nature of the eastern boundary with the Schofield Adamellite is poorly defined due to discontinuous outcrop.

Figure 6.16. Typical outcrop surface of biotite-rich Kout Norien Granodiorite near Harrow, with abundant biotite ± muscovite ± sillimanite clots and enclaves. Alkali feldspar megacrysts (anhedral) and smaller tabular phenocrysts are also conspicuous. The pale object at top right with the micaceous selvedge is also a graphic alkali feldspar megacryst (Glenelg River, WD529866).

Figure 6.17. Diatexite outcrop at the northern Kout Norien Granodiorite margin in Salt Creek. Note deflection of the schlieric fabric around the refractory biotite-quartz-plagioclase schist enclave (WD554890).

Lithology	*Occurrence*	*Summary petrographic description*
Semi-pelitic gneiss 98-69	Collected from a 50 m wide raft in the Glenelg River valley	Strongly layered and medium-grained rock. Has discontinuous feldspathic bands (2-5 mm thick) of predominantly quartz and plagioclase (~0.5 mm), which have diffuse contacts with finer grained, biotite-rich layers, or may be bordered by laminae of coarse biotite. Some feldspathic bands are coarser grained (to ~1mm), contain alkali feldspar and have relict igneous textural features (subhedral plagioclase outlines), suggesting that they are recrystallised leucosomes. Small primary muscovite blades are rare in micaceous layers, which commonly contain interwoven aggregates of fibrolite (S_2-aligned). Some samples contain granitic leucosomes, with selvedges of coarse biotite and fibrolite (to 15 mm thick). Elongate fibrolite clots (to 10 mm) are also abundant in the leucosome.
Quartzofelds-pathic gneiss **98-75**	Collected from a 30 m wide raft in the Glenelg River valley	Distinctive, relatively coarse grained layered gneiss not recognised in *in situ* metasedimentary outcrops. Felsic bands (2-6 mm thick) are a mosaic of polygonal quartz (~1 mm), plagioclase and alkali feldspar (which is unusually abundant and has sparse quartz inclusions), with conspicuous disseminated biotite. Quartz and alkali feldspar also form larger amoeboid masses (~2 mm). Felsic bands are separated by discontinuous biotite-rich laminae (0.5-2 mm thick), which contain a small amount of primary muscovite. Small isolated lenticular micaceous clots also occur in feldspathic portions of the rock.
Stromatic (semi-pelitic) **97-286-2**	Forms 1-3 m wide rafts in Salt Creek Glenelg River valley	Equivalent to semi-pelitic migmatitic gneiss horizons in southern migmatite Schofield Creek described by Kemp (1995). Samples contain medium, even-grained leucosomes (2-15 mm thick) with thin biotite-rich melanosomes hosted by layered biotite gneiss mesosomes. Leucosomes are alkali feldspar-rich and variably recrystallised, being isoclinally folded and strongly transposed. In thin section tabular alkali feldspar grains (1-3 mm) are aligned with S_2 and enclose euhedral biotite, muscovite and plagioclase crystals. Plagioclase is mostly anhedral with vague zoning but occasionally lath-shaped outlines and euhedral zone boundaries are preserved. Tufts of fibrolite are embedded within quartz. Melanosomes are discontinuous selvedges of foliated biotite and interwoven sillimanite (1-3 mm wide), most of which is replaced by secondary muscovite.
Diatexite **97-286-1**	Forms 1-2 m wide bands along the east bank of Salt Creek	Has typical interpenetrating leucosome-melanosome structure, but with conspicuous medium grained leucogranitic pockets several centimetres long; these have slightly more alkali feldspar than plagioclase (**97-286-1L**). Schlieren and selvedges of melanosome are interleaved biotite, fibrolite and small amounts of primary muscovite. Fibrolite also forms small lenses (1-5 mm) in more feldspathic areas of the rock.

Table 6.2. Summary petrographic descriptions of metasedimentary enclaves hosted by the Kout Norien Granodiorite. The modes for the first two samples are given by Table 5.6.

Harrow Granodiorite specimens (e.g. **98-86**) are medium grained, and dominated by blocky bluish-white plagioclase grains (2-3 mm) (Table 6.1), occasionally occurring as phenocrysts (5-6 mm). Biotite (1-1.5 mm) is abundant, with euhedral muscovite plates (to 3 mm), and fibrolite tufts (3-10 mm) also occur. Thin sections reveal a pristine magmatic texture, where poikilitic alkali feldspar (to ~3 mm) encloses euhedral plagioclase, muscovite and biotite. Plagioclase phenocrysts have complex twinning and zoning characteristics, with irregularly shaped cores, whereas smaller laths have strong continuous zoning outwards from a euhedral calcic core (see section 9.2.1).

Some Harrow Granodiorite exposures exhibit a weak alignment of biotite flakes and schlieren, most conspicuous at the pluton periphery. However, this foliation has an overall concentric geometry within the pluton and contrasts with the consistent northwesterly-trending fabric of nearby granitic bodies. It therefore reflects magmatic processes rather than a deformational overprint.

6.6.3 Marn Mering Granodiorite

Marn Mering Granodiorite outcrops conspicuously along the Glenelg River and tributaries east of Schofield Creek, intruding the Dunmore Leucotonalite (east) and Scrubby Junction Granodiorite (west) (Figure 6.1). Typical samples from the homogeneous eastern part of the body (**T2-1**) are light bluish-grey, medium to coarse grained, and weakly porphyritic, with tabular alkali feldspar phenocrysts (~1 cm) giving a 'speckled' aspect. Blocky plagioclase laths are predominant (Table 6.1), and in thin section have strong continuous or oscillatory zoning. Muscovite is abundant, mostly occurring as sheaves of euhedral plates, commonly entwined with large biotite grains, concentrated at grain boundaries. Where aligned, these interleaved micaceous aggregates (up to ~8 mm long) impart a weak planar fabric, which is rarely parallelled by schlieren and small lenticular biotite-rich clots (1-4 cm). Apart from the latter, metasedimentary enclaves are absent.

Exposures in the western part of the pluton include more feldspar-rich, biotite-poor domains that are also coarser grained, occasionally with 10 mm plates of muscovite and biotite. Outcrops have a banded aspect, where the felsic material forms layers (~4 cm thick) alternating with typical granodiorite (sample **98-56**). Elsewhere, the coarser variant forms metre-sized areas (sample **98-58**) (Table 6.1). A weak biotite alignment parallel to the banding anastomoses around alkali feldspar megacrysts, suggesting that it may be related to magmatic flow. Notably, the coarse feldspathic granitic portion in these outcrops closely resembles the granitic material intermingled with Schofield Adamellite in Schofield Creek (section 6.4.2). Westernmost Marn Mering Granodiorite outcrops adjacent to Schofield Creek contain tiny euhedral garnets, accompanied by numerous pegmatite lenses and dykes.

6.6.4 Garnet-bearing granitic rocks

a) Northeastern GRC

Dykes and small plutons of garnet-bearing leucoadamellite crosscut other granitic and metasedimentary units of the Harrow district (Figure 6.1). A similar body, the Glengoyne

Lithology	*Sample*	*Co-existing aluminous phase*	*Garnet morphology*
Blair Atholl Adamellite	**97-201** (WR)	mu, bi	Tiny (<0.25 mm) euhedral reddish crystals, most commonly enclosed by feldspars. No inclusions.
Carrigeen Granodiorite	T2-69 (SC)	mu, bi	Small (0.4-0.8 mm), inclusion-free euhedral crystals.
Leucoadamellite	**98-19** (SC)	mu, bi	Anhedral (0.5-2 mm), irregular outlines against plagioclase and quartz. Fractured, with inclusions of muscovite (common) and quartz.
Leucoadamellite	**T2-258** (SC)	mu, bi	Small euhedral crystals (0.3-0.8 mm). No inclusions.
Leucoadamellite	**97-317** (CC)	mu*	Tiny euhedral crystals (0.1-0.3 mm). No inclusions.
Leucoadamellite	**98-60B** (SC)	mu*	Highly irregular grains up to 1 cm across that are complexly intergrown with quartz. Crystal faces against quartz, plagioclase and muscovite are evident in places. Some areas are perforated with tiny elongate quartz blebs. Rare muscovite and biotite inclusions.
Glengoyne Adamellite	**97-98** (CR)	mu*	Euhedral, no fractures or inclusions (0.5-1 mm). Up to 3 mm in other samples, enclosing apatite prisms and muscovite.
Leucoadamellite	**98-30** (SC)	mu	Varies from euhedral and inclusion free (~1 mm) to irregularly shaped, fractured and sometimes angular (to 5 mm). Quartz inclusions are rare. Garnets in pegmatitic lenses are subhedral and reach 1.5 cm across.
Aplite	**97-R2B** (RC)	mu	Tiny euhedral crystals (0.1-0.3 mm). No inclusions.

Table 6.3. Thin section morphology of garnets in Harrow type granitic rocks. Note that samples **98-19** and **T2-258** derive from the same leucoadamellite body in northern Schofield Creek.

*Biotite is very rare in these samples, as ragged spindly flakes, sometimes mantled by muscovite.
(SC = Schofield Creek; SSC = Scabbing Station Creek; CC = Chin Chap Creek; CR = Chetwynd River; RC = Robson Creek)

Adamellite, occupies the Chetwynd River valley (20 km south of Harrow), where it intrudes the Chetwynd Tonalite (see Figure 11.3 and Appendix E). These rocks contain few metasedimentary enclaves but are associated with abundant dykes and pods of undeformed garnetiferous pegmatite and aplite. Dominated by alkali feldspar (see Table 6.1 and Figure 6.2), the grainsize of garnet adamellites varies non-systematically from pegmatitic to microgranitic and commonly has an aplitic, quench-textured aspect. In thin section, alkali feldspar (microcline) is commonly euhedral against quartz, suggesting early appearance on the liquidus, but also forms anhedral pools enclosing tiny plagioclase laths. Sheet-like leucoadamellite bodies commonly exhibit a distinct layering of alternating coarser and finer grained material, parallelled by pegmatitic

lenses (2-5 cm long) and trains of graphic alkali feldspar megacrysts (1-8 cm, euhedral to anhedral). In places, the latter are bordered by garnet-rich laminae (5-10 mm). Garnets vary from tiny pink euhedral crystals, commonly embedded in feldspars or muscovite, to larger, irregularly-shaped grains (0.25-10 mm across) sieved with quartz and muscovite inclusions (Table 6.3). Both morphologies may occur within the same body and even in the same thin section. Small biotite flakes are very minor and commonly ragged and 'spindly'.

Leucogranitic garnet-bearing material also forms diffuse domains within the large Carrigeen Granodiorite, Schofield Adamellite and Marn Mering Granodiorite plutons, apparently representing part of the normal spectrum of magmatic variation within the body.

(b) Blair Atholl Adamellite (early syn-compressional, southwestern metamorphic zonation)

The only large primary muscovite-bearing pluton of the southwestern metamorphic zonation, Blair Atholl Adamellite outcrops along the Wando River valley ~32 km southwest of Harrow (see Figure 10.1). The body intrudes early syn-compressional granitic rocks but is foliated and similarly overprinted by D_2. Fresh samples are mottled tan, medium to coarse grained and leucocratic, with tiny garnets (~0.25 mm) disseminated throughout (**97-201**, Tables 6.1, 6.3). The foliation (S_2) is imparted by aligned, but distorted, muscovite and biotite flakes (~1-3 mm) and elongate recrystallised quartz masses (5-10 mm). Rectangular alkali feldspar phenocrysts (5-20 mm) and, to a lesser extent, palest green plagioclase laths (2-5 mm) are also oriented with the fabric. Large migmatitic gneiss enclaves (many melanosome-rich and partially disaggregated) and micaceous schlieren occur at the margins, becoming rare towards the centre of the body. Mafic microgranular enclaves (5-15 cm across) are also present in some outcrops, having plagioclase and quartz phenocrysts (2-3 mm) in a light grey, biotite-rich matrix.

Chapter 7: Mineral chemistry and geochemistry of migmatites, leucosomes and small granitic bodies

7.1 Introduction

The northeastern migmatite zone encompasses an interplay between various metasedimentary rocks, migmatites, decimetre- to metre-scale granitic pools, sheets and dykes[1] and Harrow type plutons (Chapters 5 and 6). The intimacy of the field relations implies a petrogenetic link between each, which can be further explored and more clearly defined by geochemical investigation. Accordingly, this chapter documents the mineral chemistry and whole-rock geochemistry of metasedimentary rocks, *in situ* leucosomes and small granitic bodies, as a precursor to an evaluation of their petrogenesis. Analytical techniques and uncertainty estimates are outlined in Appendix A.

7.2 Mineral chemistry of migmatites and small granitic bodies

The chemical composition of the major minerals within various unmelted metasedimentary rocks, tonalitic migmatites, M_2 granitic migmatites (including diatexite **97-286-1**), and small granitic bodies are given in Appendix B. All mineral compositions reported in this thesis were determined by microprobe analysis from polished thin sections (see Appendix A for operating parameters). A complete discussion of the compositional characteristics of each mineral phase is beyond the scope of this thesis; instead the main chemical features of each are outlined.

7.2.1 Plagioclase

The compositional characteristics of analysed plagioclase grains are summarised by Tables 7.1 and 7.2 and Figures 7.1, 7.2 and 7.3. Grains exhibiting the strongest optical zoning were sequentially analysed from core to rim to establish the full compositional range of plagioclase within each sample.

Plagioclase within leucosomes, melanosomes and mesosomes of individual tonalitic migmatite samples exhibits a similar compositional range, mostly oligoclase to sodic andesine, (except sample **G2**) but may have different zoning characteristics (Table 7.1). Leucosome grains are either unzoned (G3), continuously zoned (T2-161, T2-162), or exhibit complex oscillatory zoning (**G2**). Leucosome plagioclase of **TL4** has euhedral cores (An_{28}), overgrown by more calcic plagioclase with complexly mottled or patchy zoning (~An_{32}-An_{35}) (Figure 7.4). Schofield Creek migmatite 98-25M1 has slightly more sodic plagioclase than other samples (Figure 7.1).

Mesosome plagioclase in all samples is polygonal, and consists of an anhedral core with one or two discrete to vague overgrowths that may be slightly more or less calcic. Melanosome plagioclase of sample **TL4**, occurring as clumps of small polygonal grains enveloped by micaceous selvedge, has anhedral cores (An_{25}-An_{31}) with more calcic overgrowths (An_{34}-An_{35}) and thin rims of similar composition to the core. Apart from the sodic rims, this is

[1]For convenience, decimetre- to metre-scale granitic pools, sheets and dykes are collectively referred to as 'small granitic bodies' in the ensuing discussion.

compositionally very similar to plagioclase of interlayered unmigmatitic quartzofeldspathic gneiss **T2-2B** (Figure 7.1). Sample **G2** is distinct from other tonalitic migmatites in having markedly more calcic plagioclase (Figure 7.1, Table 7.1). Leucosome laths also exhibit less textural modification than plagioclase of other M_1 samples, with crystal outlines and euhedral zone outlines more common. For example, leucosome grain 1A has complex zoning, such that a euhedral core (An_{41}) has a series of euhedral to irregular overgrowths (with internal oscillatory zoning) which range up to An_{50}. Mesosome and melanosome plagioclase is nearly as calcic, where cores (An_{37}-An_{46}) have sharp, relatively sodic rims (An_{31}-An_{32}).

Despite morphological differences, plagioclase within leucosomes, melanosomes and mesosomes of granitic migmatites 97-244, 98-RG3, **98-R5B** and **98-25M2** exhibits a similar, limited compositional range (mostly oligoclase) with low K content (generally less than 0.1 molar percent; Figure 7.2, Table 7.2). Leucosome plagioclase of **98-25M2** exhibits the same compositional character as that within nearby M_1 tonalitic sample 98-25M1, though a small, relatively calcic core is evident in one grain (An_{33}). However, samples **98-65A**, **98-65B** (Schofield Creek) and **98-102** (Chin Chap Creek) have more calcic and strongly zoned plagioclase (Figure 7.2). Oscillatory zoning is common in **98-102**, where anhedral or euhedral cores range up to ~An_{47} (Figure 7.5) Similarly, plagioclase grains within leucosome **98-65A** have euhedral, anhedral or corroded calcic cores (~An_{40}-An_{42}) with more sodic overgrowths. Other grains have large, complexly mottled cores, parts of which are equally calcic (Figure 7.5). Within the same migmatitic horizon, large patchy-zoned plagioclase cores are more numerous in adjacent leucosome **98-65B**, but extend to less calcic compositions. In contrast, sample **98-65C**, the host mesosome for leucosome **98-65A** and **98-65B**, has simply zoned plagioclase, where anhedral cores (An_{28}-An_{32}) have discrete, more calcic rims (An_{31}-An_{34}). Importantly, plagioclase of mesosome **98-65C** is more calcic than that of other granitic migmatite mesosomes, correlating with the more anorthitic plagioclase of adjacent leucosomes (Table 7.2).

Plagioclase analyses for diatexite **97-286-1** derive from either large subhedral crystals in the granitic 'leucosome' portions or smaller polygonal grains associated with biotite schlieren, designated 'mesosome'. Regardless, grains are weakly zoned and compositionally identical (most ~An_{26}-An_{28}; Figure 7.2, Table 7.2).

The plagioclase of small granitic bodies **98-SC** and **98-WF1B** (from northern Schofield Creek) is similar (oligoclase to sodic andesine, Table 7.2 and Figure 7.3), though rims of the former are slightly more sodic (~An_{18}-An_{20}). Notably, plagioclase of these granitic bodies has the same compositional range and zoning characteristics as that of adjacent migmatite **98-25M2**.

7.2.2 Alkali feldspar

Alkali feldspar in analysed migmatite leucosomes and small granitic bodies is bracketed between Or_{82} and Or_{90}; calcium was not detected (Table 7.3 and Figures 7.2 and 7.3). Many grains exhibit zoning, most pronounced in samples **98-65A** and especially **98-65B**, such that distinct, irregularly shaped cores (Or_{83}-Or_{85}) are enveloped by more potassic rims (Or_{85}-Or_{90}). This sense of zoning is shared by alkali feldspar in samples **98-102** and granitic sheet **98-WF1B**, but the opposite occurs in migmatite **98-R5B** and diatexite **97-286-1**.

Table 7.1. Summary of plagioclase compositional characteristics in M_1 (98-25M1, T2-161, T2-162, **G2**) and M_2 (G3, **TL4**) tonalitic migmatites and migmatite zone quartzofeldspathic gneiss **T2-2B**, as determined by microprobe analysis (full results in Appendix B). The compositions listed represent individual analyses arranged according to their relative location within the plagioclase grain. (An% = molar percent anorthite, An/An+Ab+Or).

Sample	*Grain*	*Plag composition (An%)* CORE ➤ ➤ RIM				*Comment*
98-25M1						
Leucosome	1A	21.6		26.8	17.8	large anhedral core, euhedral overgrowth, rim
	6A	22.7		27.0	17.9	large anhedral core, euhedral overgrowth, rim
	6B	22.5			18.0	euhedral core, thick rim
	7A	22.5		27.2	17.8	large anhedral core, euhedral overgrowth, rim
T2-161						
Leucosome	1A	33.3	31.6	27.8	26.0	diffuse continuous zoning
Mesosome	4A	30.0			30.0	unzoned
	4B	30.6			34.0	rim is diffuse overgrowth on anhedral core
	4D	28.6			32.3	rim is diffuse overgrowth on anhedral core
	4E	33.2			30.5	rim is diffuse overgrowth on anhedral core
	5A	30.5			29.8	rim is diffuse overgrowth on anhedral core
	8A	28.0			27.5	rim is diffuse overgrowth on anhedral core
T2-162						
Leucosome	1A	29.0, 30.1	32.2	33.2	29.0	vague oscillatory zoning; rim is overgrowth
	2A	28.5			28.8	unzoned
	2B	30.5		33.2	29.2	vague continuous zoning; rim is overgrowth
Mesosome	7A	28.9		32.0	28.6	large anhedral core, two diffuse overgrowths
	7B	33.1			29.5	anhedral core, diffuse overgrowth
	7C	30.0			32.6	anhedral core, distinct overgrowth
	7D	30.7			30.1	anhedral core, distinct overgrowth
G2						
Leucosome	1A	41.2	36.2	50.4	40.1, 30.6	euhedral core with discrete overgrowths
	1B	44.8			30.9	anhedral core with overgrowth
	4A	44.1		38.3	34.1	oscillatory zoning; rim is overgrowth
Mesosome	7A	37.3			32.2	anhedral core with overgrowth
	7B	41.0			32.1	anhedral core with overgrowth
Melanosome	8A	45.5		40.1	31.7	anhedral core with overgrowths
	8B	45.8			31.5	anhedral core with overgrowth
G3 (M_2)						
Leucosome	6A			32.4		optically unzoned
	7A	32.1				optically unzoned
	7B	34.6			34.3	optically unzoned
TL4 (M_2)						
Leucosome	1A	28.0	34.8	31.6	27.1	euhedral core, patchy zoned overgrowth, rim
	9A	35.4			29.6	patchy zoned core, thin sodic overgrowth
	11A	34.0			29.0	patchy zoned core, thin sodic overgrowth
Melanosome	3A	30.7		34.1		anhedral core, irregular overgrowth
	3B	28.8		34.2	30.8	anhedral core, irregular overgrowth, rim
	4A	30.3		34.9	31.4	anhedral core, irregular overgrowth, rim
	4B	25.5		35.4	31.2	anhedral core, irregular overgrowth, rim
	9B			34.0	29.0	irregular overgrowth, rim

Table 7.1 contd. next page

Table 7.1 contd.

Sample	*Grain*	*Plag composition (An%)* CORE ➤ ➤ RIM			*Comment*
T2-2B					
gneiss	1A	27.8	34.8	34.2	anhedral core, irregular overgrowth, rim
(unmelted)	1B	28.0		35.3	anhedral core, rim
	2A	26.7	32.8	35.3	anhedral core, irregular overgrowth, rim
	2B	32.3	31.7	35.4	anhedral core, irregular overgrowth, rim
	3A	36.5	29.2	34.8	anhedral core, irregular overgrowth, rim
	5A	28.5	32.0		anhedral core, thick overgrowth

Table 7.2. Summary of plagioclase compositional characteristics in M_2 granitic migmatites, diatexite **97-286-1** and small granitic bodies (**98-SC, 98-WF1B**) as determined by microprobe analysis (see Appendix B for full results). The compositions represent individual analyses arranged according to their relative location within the plagioclase grain (An% = molar percent anorthite). Note that sample **98-65C** represents the complementary mesosome-melanosome pair to granitic leucosome **98-65A** and the mesosome to leucosome **98-65B**. The leucosome portion of sample **98-65C** is equivalent to leucosome **98-65A.**

Sample	*Grain*	*Plag composition (An%)* CORE ➤ ➤ RIM			*Comment*
97-244					
Leucosome	3A	18.9		21.4	small euhedral core, overgrowth
	3B	20.0	19.7	23.9	euhedral core, irregular overgrowth, rim
	4A	18.1		22.3	anhedral core, thick overgrowth
	7A	17.7		24.5	corroded core, patchy zoned overgrowth
Melanosome	4A	24.4	23.6		anhedral core, thick overgrowth
	4B	25.8	23.0		anhedral core, thick overgrowth
	8A	23.0		24.5	anhedral core, thick overgrowth
98-R5B					
Leucosome	1A	27.3		27.4	optically unzoned
	1B	24.6			optically unzoned
	3A	22.0			optically unzoned inclusion in microcline
	4A	22.2		24.6	weak continuous zoning
Melanosome	10A	23.5		24.3	weak continuous zoning
Mesosome	6A	24.0	26.5	21.8	anhedral core, discrete overgrowths
	6B	23.6	25.3		anhedral core, discrete overgrowths
	7A	23.7	24.0	23.7	anhedral core, discrete overgrowths
98-R5B(2)					
Melanosome	3A	25.6		25.8	optically unzoned
	3B	26.0		23.6	weak continuous zoning
Mesosome	4A	26.7		22.2	weak continuous zoning
	6A	27.5		23.2	anhedral core, thin rim
	6B	24.7		25.8	weak continuous zoning
98-RG3					
Leucosome	1A	22.1	23.4	27.4	patchy zoned core, thick overgrowth

Table 7.2 contd. next page

Table 7.2 contd.

Sample	*Grain*	*Plag composition (An%)* CORE ➤ ➤ RIM				*Comment*
98-RG3 contd.						
Melanosome	2A	31.8			22.6	anhedral core, overgrowth
	2B	30.6			24.9	anhedral core, overgrowth
Mesosome	3A	28.2			26.7	anhedral core, overgrowth
	3B	27.6			23.8	anhedral core, overgrowth
	4A	26.9			22.9	anhedral core, overgrowth
98-65A						
Leucosome	1A	40.0		26.9		euhedral core, oscillatory zoned overgrowth
	1B	39.6		30.0		anhedral core, continuous zoned overgrowth
	2A	41.7	24.6	29.6	32.1	corroded core, irregular overgrowths
	5A	23.8	38.9	25.8	31.2	patchy zoned core (first two), overgrowth, rim
	6A	33.1		25.4	31.6	euhedral core, irregular overgrowth, rim
	6B			29.0		inclusion in microcline
98-65B						
Leucosome	1A	30.4	33.3	27.4	33.5, 27.8	patchy zoned core, 2 euhedral overgrowths
	2A	33.3			26.8	large euhedral core, overgrowth
	2B	32.0	27.9		32.0	patchy zoned core (first 2), overgrowth
	3A	25.0	32.5		32.6	patchy zoned core (first 2), overgrowth
	5A	33.2	24.3		32.3	patchy zoned core (first 2), overgrowth
	6A	28.6			32.9	large core, rim
	7A	32.8	24.3		33.0	patchy zoned core (first 2), overgrowth
98-65C						
Leucosome	1A	42.3	34.3		29.9	corroded core, irregular overgrowth, rim
	2A	32.0	37.1		29.9	patchy zoned core, euhedral overgrowth, rim
Mesosome	5A	29.0			33.3	anhedral core, overgrowth
	5B	32.5			29.6	anhedral core, overgrowth
	6A	32.2			33.8	anhedral core, overgrowth
	6B	30.9			31.6	anhedral core, overgrowth
	7A	28.8			33.3	anhedral core, overgrowth
	7B	28.7			33.6	anhedral core, overgrowth
	8A	28.2			30.5	anhedral core, overgrowth
	8B	28.9			32.8	anhedral core, overgrowth
98-25 M2						
Leucosome	1A	21.7		25.9	17.3	large euhedral core, euhedral overgrowth, rim
	1B	17.6	21.3			irregular patch within large euhedral core
	2A	22.0		25.7	17.2	large anhedral core, euhedral overgrowth, rim
	2B	33.5	22.7	25.7	18.6	irregular core with overgrowths
	3A	24.1	25.1	26.5	19.8	small euhedral core with overgrowths
Melanosome	9A	23.7			19.0	anhedral core, thin unzoned rim
	9B	25.0			20.0	anhedral core, thin unzoned rim
Mesosome	12A	22.0			19.1	anhedral core, thin unzoned rim
	12B	23.6			10.6	anhedral core, thin unzoned rim
	12C	22.8			24.6	anhedral core, thin unzoned rim
	13A	23.1		26.7	20.5	anhedral core, discrete overgrowths

Table 7.2 contd. next page

Table 7.2 contd.

Sample	*Grain*	*Plag composition (An%)* CORE ➤ ➤ RIM				*Comment*
98-102						
Leucosome	2A	34.5			26.9	euhedral core, rim
	3A	29.3	37.1	32.2	28.8	oscillatory zoning from euhedral core
	5A	27.4	34.5	31.6	26.2	oscillatory zoning from corroded core
	6A	43.9		28.2	32.2	large corroded core, thin overgrowths
	8A	34.9			30.0	euhedral core, thick overgrowth
	10A	46.9			32.1	small euhedral core, thick outer rim
97-286-1						
Diatexite	1A	26.4			26.2	optically unzoned
	3A	29.7		26.5	26.5	euhedral core, thick unzoned rim
	3B	25.6		27.8		euhedral core, overgrowth
	6A	28.0		24.8		anhedral core, overgrowth
	6B	28.3			28.2	optically unzoned
'mesosome'	7A	26.4			25.1	anhedral core, diffuse rim
	8A	28.1			26.1	anhedral core, diffuse rim
	8B	26.8			25.4	anhedral core, diffuse rim
	9A	25.6			27.8	anhedral core, diffuse rim
	9B	26.7			26.7	optically unzoned
98-SC	3A	34.4			18.0	small irregular core, discrete overgrowth
Granitic pool	3B	27.5		23.5	18.2	core, diffuse overgrowth, rim
	5A	28.5			19.8	large core, discrete rim
	6A	27.2			19.3	large euhedral core, discrete rim
	7A	25.9	23.8		18.6	large mottled zoned core (first two), sharp rim
	7B	25.9			18.4	mottled zoned core, discrete rim
98-WF1B	1A	33.3		23.0	25.1	mottled zoned core, euhedral overgrowth, rim
Granitic	6A	23.5		29.6		large irregular core, euhedral overgrowth
sheet	6B	26.3				irregularly-shaped core
	8A	35.6			23.6	euhedral core, rim
	8B	22.8		25.8		large irregular core, euhedral overgrowth

Table 7.3 (next page). Composition of alkali feldspar from granitic migmatites, diatexite **97-286-1** and small granitic bodies of the northeastern GRC (Or% = molar percent orthoclase component, Or/Or+Ab). Note that core and rim compositions represent single analysed grains, where as quoted ranges cover a number of individual analyses. Full microprobe analyses are presented in Appendix B.

Sample	*Derivation*	*Compositional range (Or%)* CORE	RIM	*Description*
98-25M2	leucosome		84.0 to 89.7	weak diffuse zoning, finely perthitic
98-R5B	leucosome	86.3	82.3	weak diffuse zoning, finely perthitic
	leucosome		80.5 to 84.9	
	mesosome		85.3 to 88.1	unzoned, not perthitic
97-244	leucosome		84.0 to 89.7	weak diffuse zoning, finely perthitic
98-65A	leucosome	86.7	86.0	distinct, irregularly shaped core
		84.7	86.0	distinct, irregularly shaped core
98-65B	leucosome	83.9	85.3	distinct, irregularly shaped core
		84.5	86.5	distinct, irregularly shaped core
		82.5	89.6	distinct, irregularly shaped core
98-102	leucosome		88.5 to 89.7	weakly zoned, finely perthitic
		86.5	89.3	distinct core
97-286-1	diatexite	85.7	82.3	indistinct zoning
		82.7	82.1	indistinct zoning
		84.7	82.8	indistinct zoning
97-WF1B	granitic sheet	86.5	87.9	diffuse core region
		85.6	89.2	diffuse core region
98-SC	granitic pool	90.4	89.5	distinct core
			85.0 to 87.3	weakly zoned, finely perthitic

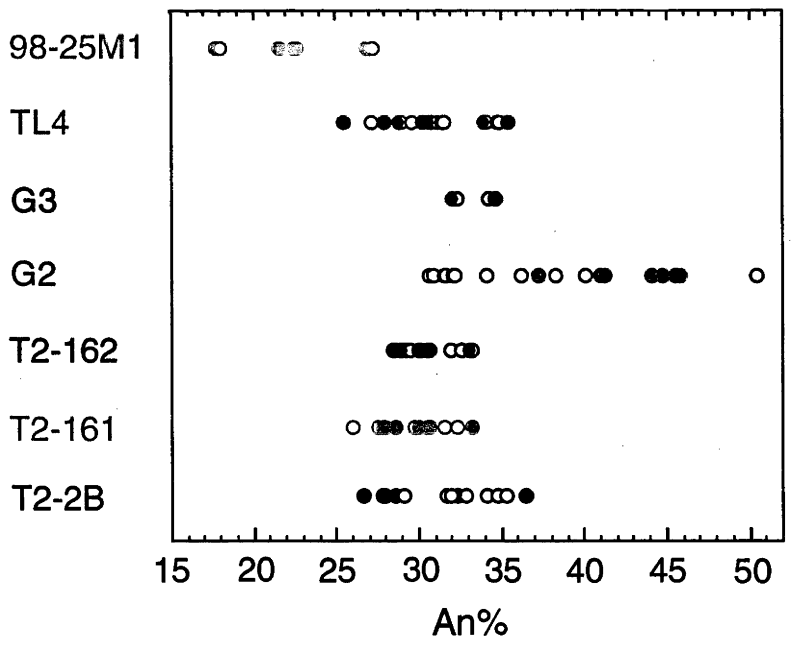

Figure 7.1. Range of plagioclase compositions (as molar percent anorthite) in tonalitic migmatite samples and quartzofeldspathic gneiss **T2-2B** of the northeastern migmatite zone. Filled symbols represent the cores of analysed grains and open symbols represent the rims. Due to compositional similarity (Table 7.1), leucosome, mesosome and melanosome plagioclase is plotted together, though data from samples G3 and 98-25M1 is exclusively of leucosome derivation.

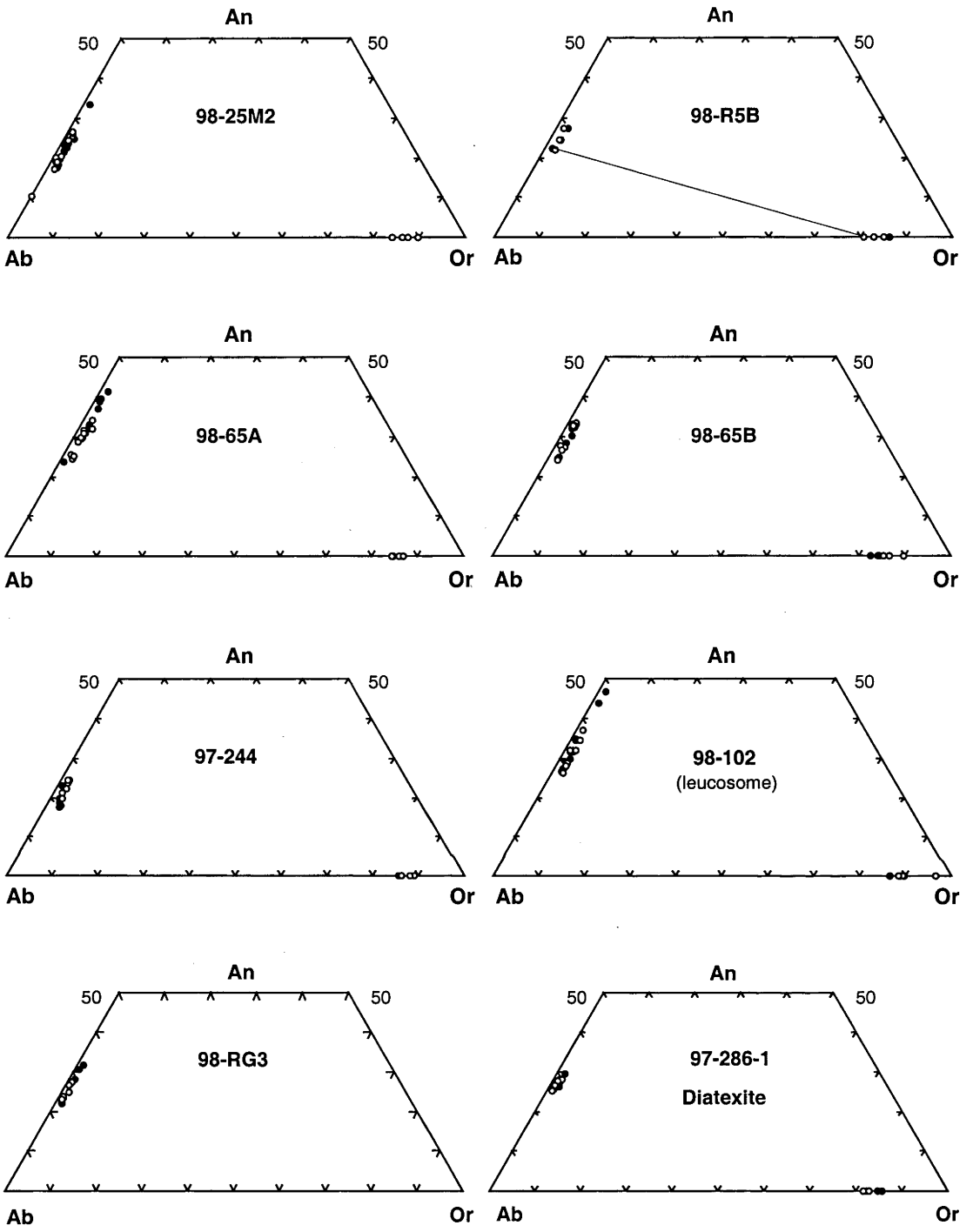

Figure 7.2. Range of plagioclase and alkali feldspar compositions in M_2 granitic migmatite samples of the northeastern migmatite zone (An = atomic Ca/Ca+Na+K; Ab = atomic Na/Ca+Na+K; Or = atomic K/Ca+Na+K). Due to compositional similarity (Table 7.2), leucosome, mesosome and melanosome plagioclase is plotted together. Filled symbols represent the cores of analysed grains, whereas open symbols represent rims. The tie line for sample **98-R5B** connects a plagioclase inclusion with its host alkali feldspar.

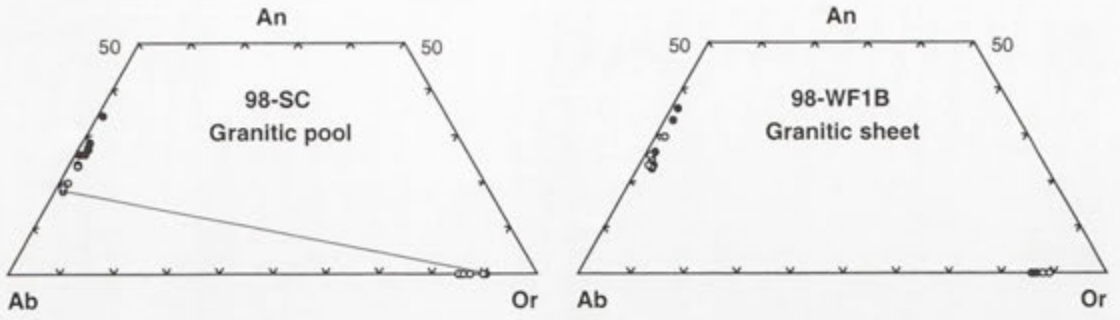

Figure 7.3. Range of plagioclase and alkali feldspar compositions in small granitic bodies of the northeastern migmatite zone (An = atomic Ca/Ca+Na+K; Ab = atomic Na/Ca+Na+K; Or = atomic K/Ca+Na+K). Filled symbols represent the cores of analysed grains, whereas open symbols represent rims. The tie line for **98-SC** connects a plagioclase inclusion with its host alkali feldspar.

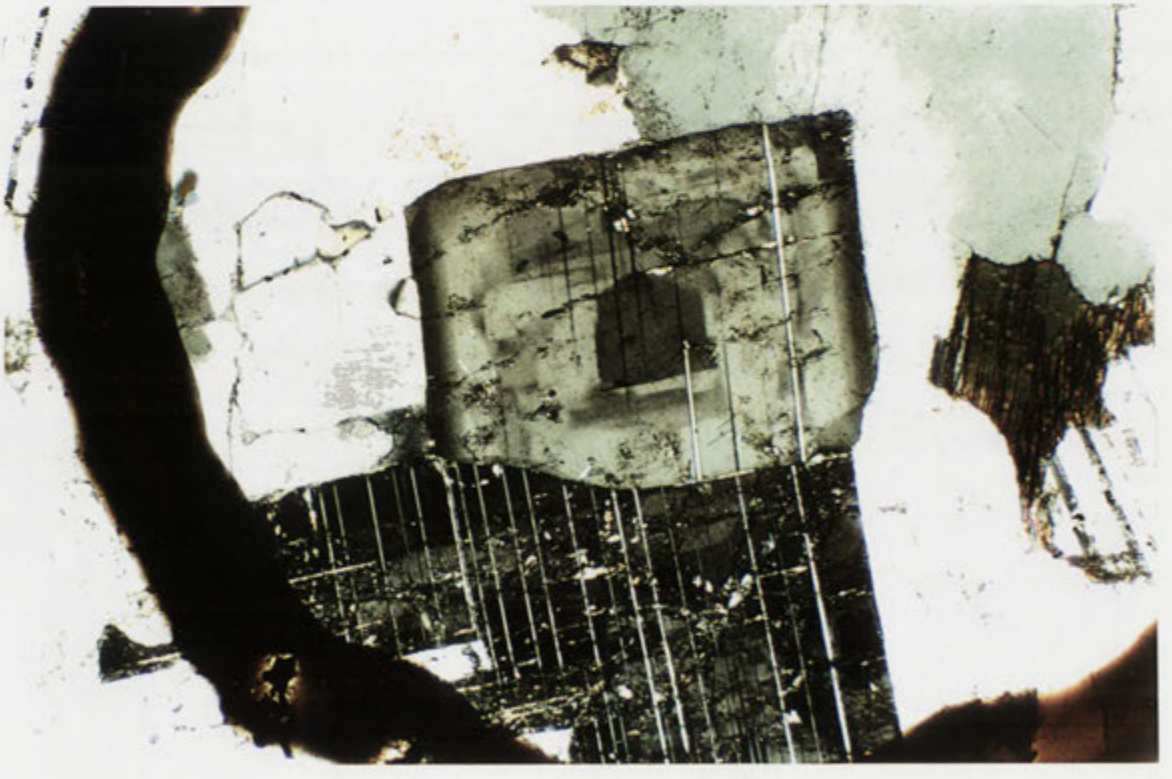

Figure 7.4. Euhedral leucosome plagioclase grain in tonalitic migmatite **TL4**, exhibiting irregular patchy zonation (An_{32}-An_{35}) about a euhedral core of similar composition to the rim (~An_{28}) (field of view ~2.5 mm).

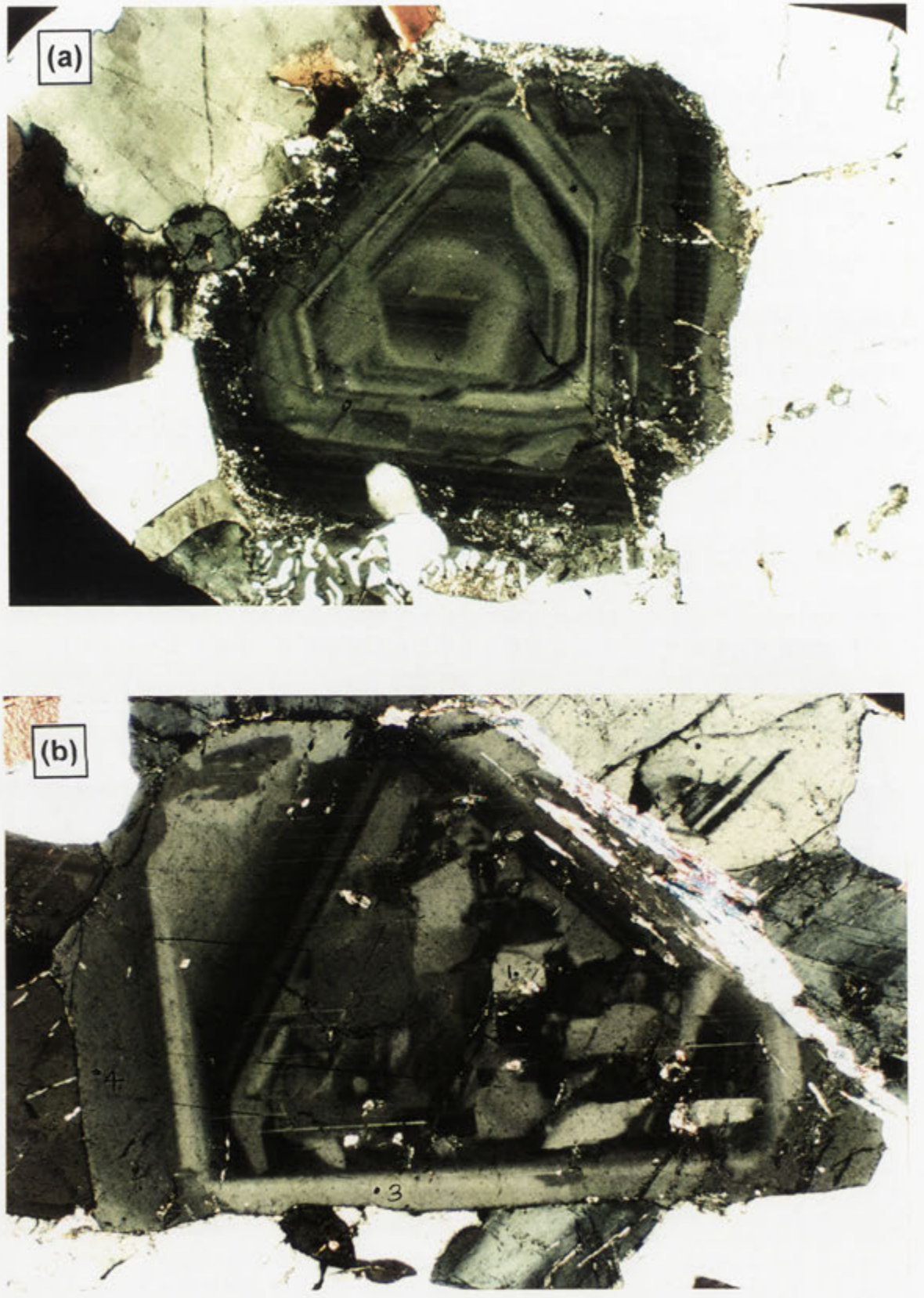

Figure 7.5. Plagioclase in M_2 granitic migmatites; the field of view in both cases is ~2.5 mm. (a) Oscillatory zoning in Chin Chap Creek leucosome **98-102**. Core is An_{47}, rim is An_{32}. (b) Mottled zonation within plagioclase core of leucosome **98-65A** (An_{23}-An_{39}), with overgrowths of more sodic plagioclase (An_{31}-An_{26}). Secondary muscovite (right) replaces sillimanite.

7.2.3 Biotite

The major compositional variables for biotite within both M_1 and M_2 migmatitic rocks are summarised by Tables 7.4 (tonalitic migmatites and gneiss **T2-2B**) and 7.5 (granitic migmatites and granitic sheet **98-WF1B**). In all cases, analysed biotite grains in melanosomes and mesosomes are aligned with S_2. Biotite in leucosomes occurs as disseminated, slightly ragged to euhedral flakes (also in granitic sheet **98-WF1B**), or interleaved groups of several grains with muscovite.

Within a single tonalitic migmatite sample, the compositional range of biotite from melanosomes, mesosomes and leucosomes with respect to Al, Ti and Mg# is very similar (Table 7.4). Most noteworthy is that in all samples melanosome biotite extends to slightly higher Ti contents (up to 0.38 atoms per 22 oxygens in G2), though the range overlaps considerably with leucosome and mesosome biotite. A mild tendency is for melanosome biotite to be slightly less aluminous than mesosome biotite in M_1 tonalitic migmatites; the opposite feature occurs in M_2 sample G3. Leucosome biotite in sample T2-161 has slightly lower Mg# than mesosome or melanosome biotite, though this is not obvious in other samples.

As a group, biotite of analysed M_1 tonalitic migmatites has slightly higher Mg# and Ti content than that of M_2 migmatite samples (Figure 7.6). The melanosome biotite of tonalitic migmatite 98-25M1 has distinctly lower Ti and Mg# than both groups (Figure 7.6). Both M_1 and M_2 tonalitic migmatites have a wide, but similar range of total Al content (~3.3-3.5 atoms per 22 oxygens). Biotite of quartzofeldspathic gneiss **T2-2B** plots with M_1 tonalitic migmatites (Figure 7.6).

The biotite within leucosomes, mesosomes and melanosomes of M_2 granitic migmatite samples is also chemically very similar (Table 7.5). Unlike tonalitic migmatites, systematic differences in Ti content between melanosome and leucosome are not observed, except in diatexite **97-286-1**, where euhedral biotite in granitic portions has slightly lower Ti than schlieren grains. Melanosome biotite of **98-25M2** is similar to that of adjacent tonalitic migmatite 98-25M1. Notably, biotite within Schofield Creek granitic migmatites (**98-25M2**, **98-65A** and **98-65B**) extends to lower Mg# and Ti than other samples, but is more aluminous (Figure 7.7). The low Ti, high Al character is shared by biotite of granitic sheet **98-WF1B**. Biotite from Robson Creek migmatites (**98-R5B**, 98-RG3, 97-244) has higher Mg#, with minor differences between samples, and overlaps with that of tonalitic migmatites. Biotite from sample **98-102** (Chin Chap Creek) has similar Mg# but extends to slightly lower Ti and Al. Diatexite biotite (**97-286-1**) plots towards the higher Ti and Mg# range of analysed biotite.

7.2.4 Muscovite

In natural systems pure end-member muscovite, $K_2Al_4[Al_2Si_6O_{20}](OH)_4$, shows solid solution towards paragonite, $Na_2Al_4[Al_2Si_6O_{20}](OH)_4$, and celadonite, $K_2Al_2(Fe,Mg)_2[Si_8O_{20}](OH)_4$, where octahedrally coordinated Al is displaced by ferromagnesian elements (Fe, Mg, Ti). Accordingly, muscovite compositions from analysed migmatite samples are listed in Tables 7.6 and 7.7 in terms of K/(K+Na), a measure of the amount of paragonite substitution, versus (Fe+Mg+Ti) a measure of the celadonite component. The Ti contents are also indicated.

Sample	*Parameter*	*BIOTITE COMPOSITION*		
		Mesosome	*Melanosome*	*Leucosome*
98-25M1	Ti	-	0.20-0.24	-
	Al	-	3.44-3.49	-
	Mg#	-	39.7-40.7	-
T2-161(M_1)	Ti	0.27-0.33	0.30-0.35	0.31
	Al	3.37-3.48	3.34-3.44	3.38-3.42
	Mg#	43.72-45.60	43.85-45.21	42.99-43.57
T2-162(M_1)	Ti	0.28-0.29	0.29-0.34	0.30
	Al	3.49-3.50	3.43-3.49	3.50
	Mg#	44.9-45.0	44.0-45.5	44.9
G2(M_1)	Ti	0.30-0.32	0.29-0.38	0.32
	Al	3.39-3.43	3.32-3.43	3.44-3.46
	Mg#	43.7-44.5	43.1-44.7	43.5-43.7
G3(M_2)	Ti	-	0.28-0.31	0.29
	Al	-	3.38-3.48	3.36-3.37
	Mg#	-	42.0-43.0	42.9-43.0
TL4(M_2)	Ti	-	0.27-0.31	-
	Al	-	3.39-3.51	-
	Mg#	-	42.2-43.4	-
T2-2B	Ti	0.32-0.34	-	-
Gneiss	Al	3.39-3.44	-	-
	Mg#	43.0-45.1	-	-

Table 7.4. Range of Ti (atoms per formula unit, based on 22 oxygens), Al (atoms per formula unit) and magnesium number (Mg# = $Mg/Mg+Fe^{2+}$) in biotite of tonalitic migmatites and migmatite zone quartzofeldspathic gneiss **T2-2B** (full analyses in Appendix B).

No systematic compositional difference exists between the euhedral, melt-precipitated muscovite plates in tonalitic leucosomes and the elongate, S_2-oriented grains in complementary mesosomes/melanosomes (Table 7.6). Leucosome muscovite in M_2 sample **TL4** has slightly lower Ti than melanosome muscovite, though this tendency is not exhibited by other samples. A ragged, secondary muscovite flake overprinting S_2 in the mesosome of T2-161 is also indistinguishable from adjacent euhedral, foliated (prograde) mesosome grains.

In contrast, coarse leucosome muscovite in granitic migmatite **98-25M2** has clearly lower celadonite content (i.e. Fe+Mg+Ti) than muscovite of adjacent mesosomes/melanosomes (Table 7.7). A similar feature is apparent for diatexite **97-286-1**, where muscovite grains in a granitic portion of the sample have lower (Fe+Mg+Ti) than S_2-oriented grains in biotite schlieren. Unfortunately, muscovite is absent from melanosomes of other analysed granitic migmatite samples, so it is unknown whether this feature is typical of granitic migmatites in general. The retrograde muscovite enclosing sillimanite in leucosome **98-65A** is compositionally very distinctive, with no Ti and the lowest paragonite (5 molar percent) and celadonite components. As such, it approaches the composition of pure end-member muscovite.

Sample	*Parameter*	*BIOTITE COMPOSITION*		
		Mesosome	*Melanosome*	*Leucosome*
98-25M1	Ti	-	0.20 - 0.24	-
	Al	-	3.44 - 3.49	-
	Mg#	-	39.7 - 40.7	-
98-25M2	Ti	0.22 - 0.25	0.20 - 0.23	0.22 - 0.23
	Al	3.41 - 3.47	3.46 - 3.56	3.46 - 3.57
	Mg#	39.2 - 39.8	39.3 - 40.0	39.3 - 39.4
98-R5B	Ti	0.28 - 0.32	0.29 - 0.33	0.30 - 0.34
	Al	3.38 - 3.50	3.41 - 3.46	3.33 - 3.48
	Mg#	43.6 - 44.4	43.7 - 44.8	44.0 - 44.4
98-R5B-2	Ti	0.30 - 0.34	0.29 - 0.32	-
	Al	3.35 - 3.46	3.39 - 3.46	-
	Mg#	43.2 - 43.5	43.2 - 44.1	-
98-RG3	Ti	0.29 - 0.38	0.31 - 0.34	-
	Al	3.32 - 3.48	3.39 - 3.45	-
	Mg#	43.3 - 45.1	43.9 - 44.6	-
97-244	Ti	0.27 - 0.32	0.25 - 0.31	0.27 - 0.28
	Al	3.35 - 3.39	3.30 - 3.44	3.43 - 3.44
	Mg#	42.9 - 43.3	42.1 - 43.6	41.7 - 42.8
98-65A	Ti	-	0.22 - 0.28	0.25 - 0.26
	Al	-	3.55 - 3.59	3.52 - 3.55
	Mg#	-	39.8 - 40.8	39.4 - 39.6
98-65B	Ti	-	0.25 - 0.27	-
	Al	-	3.51 - 3.54	-
	Mg#	-	38.9 - 39.8	-
98-65C	Ti	0.25 - 0.27	0.24 - 0.27	-
	Al	3.51 - 3.58	3.49 - 3.55	-
	Mg#	39.1 - 40.9	39.0 - 39.7	-
98-102	Ti	-	-	0.25 - 0.27
	Al	-	-	3.28 - 3.39
	Mg#	-	-	43.6 - 44.7
97-286-1 Diatexite	Ti	0.32 - 0.35	-	0.29 - 0.31
	Al	3.39 - 3.48	-	3.41 - 3.47
	Mg#	44.2 - 45.7	-	44.9 - 45.5
98-WF1B Granitic sheet	Ti	-	-	0.21 - 0.25
	Al	-	-	3.48 - 3.58
	Mg#	-	-	41.1 - 42.1

Table 7.5. Range of Ti (atoms per formula unit, based on 22 oxygens), Al (atoms per formula unit) and magnesium number (Mg# = Mg/Mg+Fe^{2+}) in biotite of M_2 granitic stromatic migmatites and diatexite **97-286-1**, and granitic sheet **98-WF1A**. Biotite grains of M_1 tonalitic migmatite 98-25M1 are listed for comparative purposes. The melanosome of **98-65A** corresponds to entrained biotite-sillimanite schlieren within the leucosome. The 'mesosome' of diatexite **97-286-1** comprises the schlieric portion of the sample, where constituent biotite flakes are interwoven and foliated, whereas the 'leucosome' represents a leucogranitic domain where biotite flakes are euhedral and enclosed by subhedral alkali feldspar.

To facilitate comparison between samples, the muscovite compositions of tonalitic and granitic migmatites are depicted on a diagram of K/(K+Na) against (Fe+Mg+Ti) and total aluminium versus magnesium number (Figures 7.8, 7.9).

Muscovite of individual tonalitic migmatites is very similar on both diagrams, though that of 98-25M1 extends to slightly lower paragonite and celadonite content (Figure 7.8). However, some discrimination is possible for granitic migmatites (Figure 7.9). Muscovite from Chin Chap Creek leucosome **98-102** has the highest K/(K+Na) and ferromagnesian element content, but the lowest

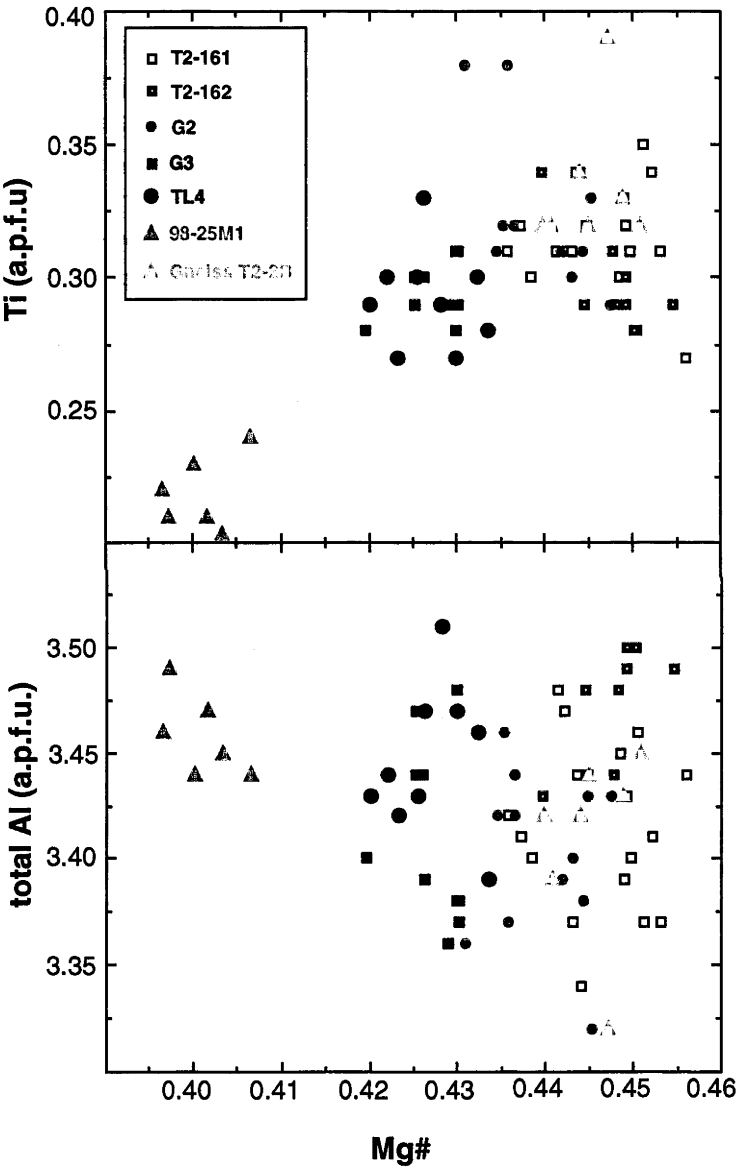

Figure 7.6. Biotite composition from analysed M_1 (T2-161, T2-162, **G2**, 98-25M1) and M_2 (G3, **TL4**) tonalitic migmatites, together with quartzofeldspathic gneiss **T2-2B** (a.p.f.u = atoms per formula unit, based on 22 oxygens). To facilitate comparison, biotite from the leucosome, mesosome or melanosome of individual samples is not separated; note however that biotite of samples 98-25M1 and **TL4** derives entirely from melanosomes.

total Al and Mg#. In comparison to Robson Creek migmatites (97-244, **98-R5B**), muscovite of Schofield Creek samples (**98-25M2**, **98-65A**, **98-65B**) has lower (Mg+Fe+Ti) but is slightly more aluminous. As with biotite, the muscovite of small granitic bodies **98-SC** and **98-WF1B** overlaps with that of Schofield Creek migmatites.

Upon comparison of Figures 7.8 and 7.9 it is clear that the compositional field of muscovite from granitic migmatites as a group overlaps considerably with that of tonalitic migmatites.

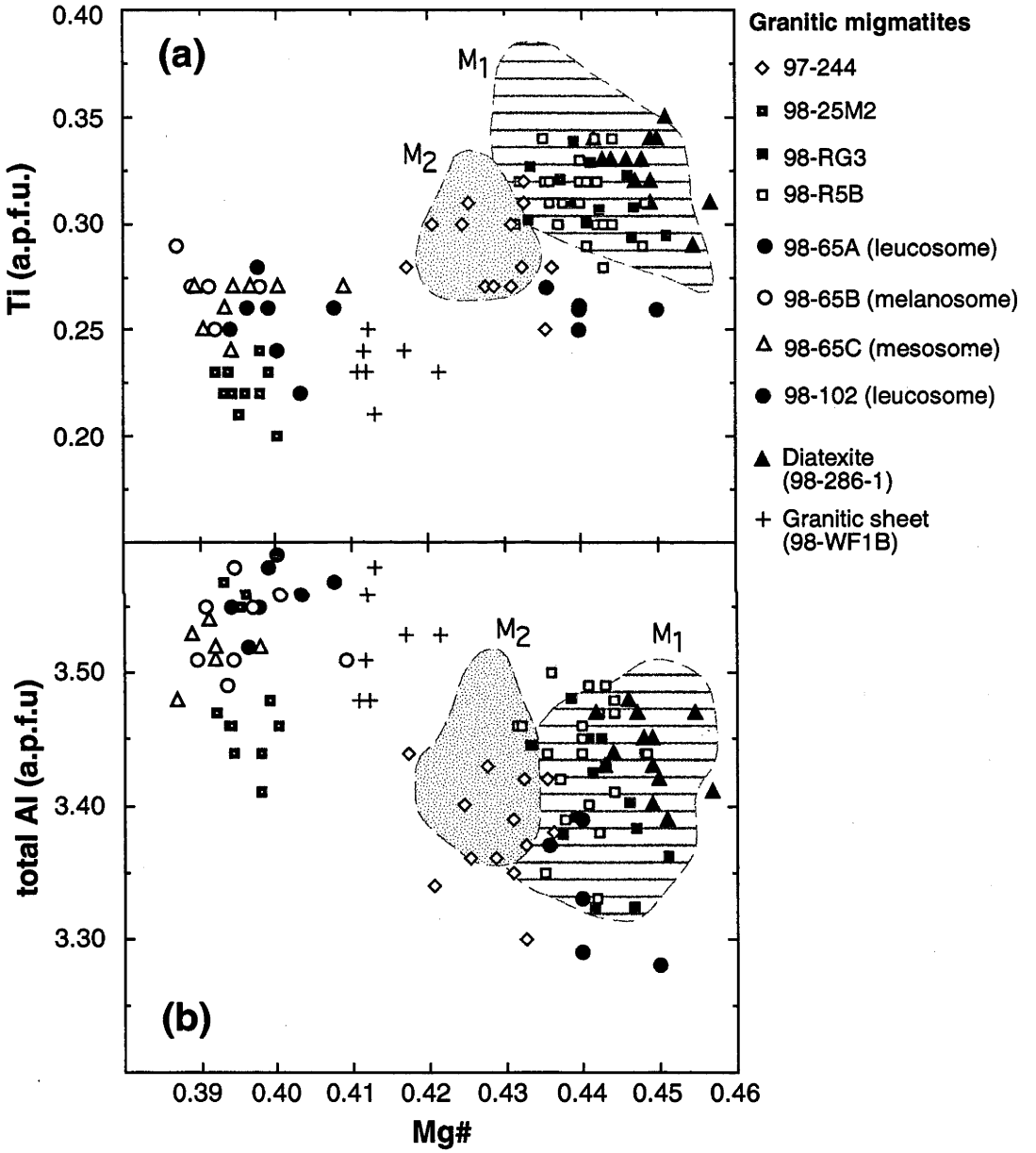

Figure 7.7. Biotite composition from analysed M_2 granitic migmatites, diatexite **97-286-1** and granitic sheet **98-WF1B** (a.p.f.u = atoms per formula unit, based on 22 oxygens). Due to compositional similarity, biotite from the leucosome, mesosome or melanosome of individual migmatites is not plotted separately. Note however that biotite in samples **98-65A** (Schofield Creek) and **98-102** (Chin Chap Creek) derives entirely from leucosomes. Samples **98-65C** represents the complementary mesosome to leucosome **98-65A**, whereas **98-65B** is the melanosome biotite. The field of biotite from M_1 (horizontal lines) and M_2 (dots) tonalitic migmatites in Figure 7.6 is indicated for comparison.

Sample	*Parameter*	*MUSCOVITE COMPOSITION*		
		Mesosome	*Melanosome*	*Leucosome*
98-25M1	K/K+Na	-	0.91	-
	Fe+Mg+Ti	-	0.34 - 0.37	-
	Ti	-	0.04 - 0.05	-
T2-161	K/K+Na	0.92 - 0.93	0.92 - 0.93	-
	Fe+Mg+Ti	0.41 - 0.45	0.37 - 0.43	-
	Ti	0.09 - 0.14	0.09 - 0.14	-
T2-161	K/K+Na	0.92 - 0.93	-	-
(secondary grains)	Fe+Mg+Ti	0.39 - 0.47	-	-
	Ti	0.08 - 0.14	-	-
T2-162	K/K+Na	-	0.92 - 0.93	0.95
	Fe+Mg+Ti	-	0.37 - 0.43	0.41
	Ti	-	0.07 - 0.10	0.10
G2	K/K+Na	-	0.93- 0.94	-
	Fe+Mg+Ti	-	0.39 - 0.47	-
	Ti	-	0.08 - 0.12	-
G3	K/K+Na	-	0.92	0.91 - 0.93
	Fe+Mg+Ti	-	0.38 - 0.44	0.39 - 0.41
	Ti	-	0.07 - 0.11	0.08 - 010
TL4	K/K+Na	-	0.91 - 0.93	0.91 - 0.93
	Fe+Mg+Ti	-	0.37 - 0.43	0.36 - 0.39
	Ti	-	0.07 - 0.09	0.05 - 0.07

Table 7.6. Compositional characteristics of muscovite grains within tonalitic migmatite samples (in atoms per 22 oxygens, see Appendix B for full results).

7.3 Discussion of mineral compositions

7.3.1 Micas

Muscovite and biotite grains in GRC migmatites have several possible modes of formation. Those within the melanosome may either be solid phases residual from anatexis (i.e. refractory minerals or excess reactants), peritectic reaction products, or have formed by retrograde 'back reaction' during cooling (see section 4.3.2). Leucosome micas have either crystallised directly from the melt or been physically entrained from the melanosome during segregation, whereas those aligned with S_2 in mesosomes are likely to have formed during prograde metamorphic crystallisation. Which origin is most appropriate is potentially elucidated by textural and chemical characteristics.

However, muscovite grains within most migmatites are compositionally indistinguishable, regardless of profound morphological differences or textural position within the sample. This is most apparent within tonalitic migmatite samples T2-162, G3 and **TL4** where large, euhedral and apparently melt-precipitated muscovite plates in leucosomes are chemically identical to elongate, S_2-aligned grains entwined with biotite in melanosomes and mesosomes. A ragged

Sample	*Parameter*	*MUSCOVITE COMPOSITION*		
		Mesosome	*Melanosome*	*Leucosome*
98-25M2	K/K+Na	0.91 - 0.92	0.90 - 0.93	0.91 - 0.92
	Fe+Mg+Ti	0.33 - 0.39	0.33 - 0.37	0.31 - 0.33
	Ti	0.05 - 0.06	0.04 - 0.05	0.04 - 0.05
97-244	K/K+Na	0.93	0.91 - 0.93	-
	Fe+Mg+Ti	0.38 - 0.44	0.36 - 0.41	-
	Ti	0.07 - 0.09	0.05 - 0.07	-
98-R5B	K/K+Na	-	0.92 - 0.93	-
	Fe+Mg+Ti	-	0.38 - 0.43	-
	Ti	-	0.08 - 0.11	-
98-65A	K/K+Na	-	-	0.92 - 0.93
	Fe+Mg+Ti	-	-	0.33 - 0.42
	Ti	-	-	0.04 - 0.07
98-65A grain 7A (after sillimanite)	K/K+Na	-	-	0.95
	Fe+Mg+Ti	-	-	0.10
	Ti	-	-	0
98-65B	K/K+Na	-	-	0.91 - 0.93
	Fe+Mg+Ti	-	-	0.34 - 0.42
	Ti	-	-	0.05 - 0.09
98-102	K/K+Na	-	-	0.93 - 0.94
	Fe+Mg+Ti	-	-	0.48 - 0.51
	Ti	-	-	0.06 - 0.07
97-286-1 (diatexite)	K/K+Na	0.92	-	0.92 - 0.93
	Fe+Mg+Ti	0.42	-	0.38 - 0.40
	Ti	0.11	-	0.09
98-SC (granitic pool)	K/K+Na	-	-	0.90 - 0.93
	Fe+Mg+Ti	-	-	0.32 - 0.38
	Ti	-	-	0.05 - 0.08
98-WF1B (granitic sheet)	K/K+Na	-	-	0.92 - 0.93
	Fe+Mg+Ti	-	-	0.29 - 0.36
	Ti	-	-	0.03 - 0.06

Table 7.7. Compositional characteristics of muscovite grains (in atoms per 22 oxygens) within granitic migmatite samples, diatexite **97-286-1** and small granitic bodies (**98-SC, 98-WF1B**). Muscovite grain 7A in leucosome **98-65A** is ragged and encloses fibrolite bundles. Muscovite from diatexite **97-286-1** comprises euhedral grains embedded in alkali feldspar in a leucogranitic domain, and foliated grains entwined with biotite in a schlieric part of the sample. These are respectively designated as 'leucosome' and 'mesosome' for convenience. Full analyses are listed in Appendix B.

muscovite flake in T2-161 that overprints S_2 is chemically identical to euhedral, S_2-aligned grains, despite being clearly of retrograde origin. Similarity of muscovite compositions despite different modes of crystallisation most likely reflects re-equilibration between mineral phases by subsolidus cation exchange during cooling. This effect has been recognised for micas in stromatic migmatites elsewhere (e.g. Ashworth 1985; Solar & Brown 2001).

However, euhedral leucosome muscovite in granitic migmatite **98-25M2** has distinctly less (Fe+Mg+Ti) than S_2-oriented grains in the melanosome/mesosome, consistent with crystallisation from the melt. In this case, re-equilibration between melt-precipitated and metamorphic muscovite has been less effective, though the reason is unknown. A similar feature is evident for diatexite **97-286-1**, where magmatic-looking muscovite crystals have a lower celadonite component than foliated grains in biotite schlieren.

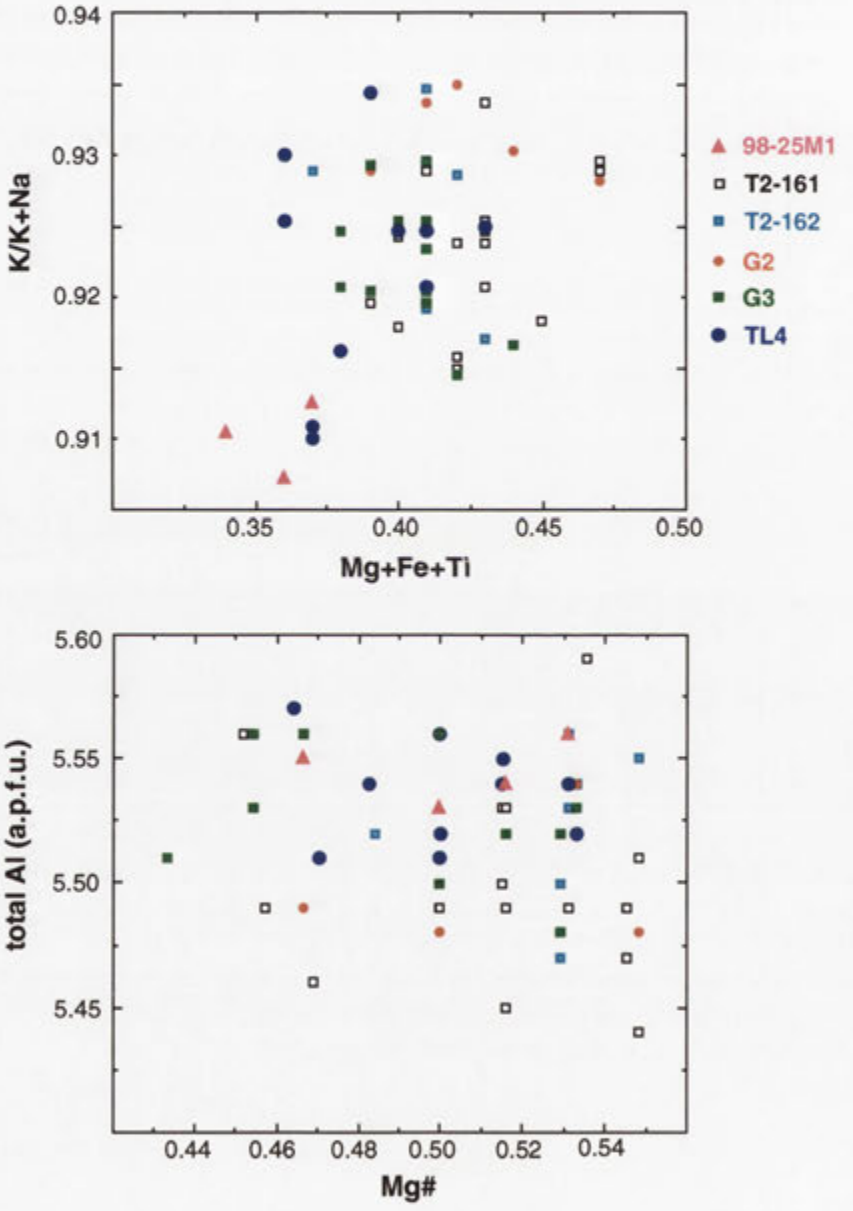

Figure 7.8. Muscovite composition from analysed M_1 (T2-161, T2-162, **G2**, 98-25M1) and M_2 (G3, **TL4**) tonalitic migmatites, together with quartzofeldspathic gneiss **T2-2B** (a.p.f.u = atoms per formula unit, based on 22 oxygens). Due to compositional similarity (see Table 7.5), and to facilitate comparison, muscovite from the leucosome, mesosome or melanosome of individual samples is not plotted separately. However, muscovite from samples 98-25M1 and **G2** is entirely of melanosome derivation.

Re-equilibration might also be responsible for the coincidence of biotite compositions within mesosomes, melanosomes and leucosomes of granitic migmatite samples, despite textural contrasts and hence implied differences in origin. However, biotite was very rare in leucosomes of all analysed samples and it is possible that compositionally distinct melt-precipitated grains were simply not present within the analysed portion of the leucosome. Notwithstanding re-equilibration, biotite plates in leucosomes of all tonalitic migmatite samples have lower Ti contents than some adjacent melanosome grains. Euhedral biotite plates within the granitic

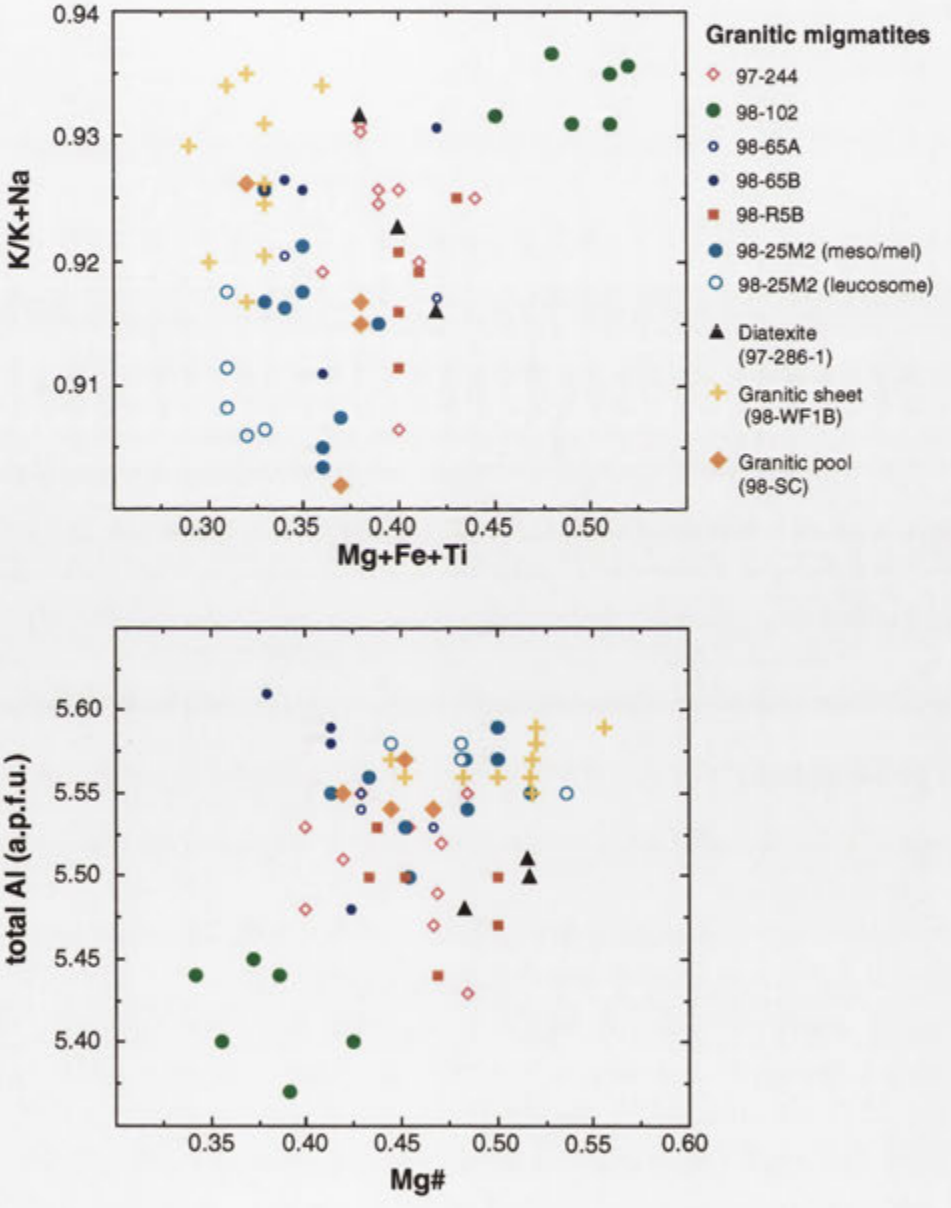

Figure 7.9. Muscovite composition from analysed granitic migmatites, diatexite **97-286-1** and small granitic bodies **98-WF1B** and **98-SC** (in a.p.f.u = atoms per formula unit, based on 22 oxygens). Muscovite from samples **98-65A** and **98-65B** is entirely of leucosome derivation, whereas leucosome muscovite from **98-25M2** is plotted separately from mesosome/melanosome muscovite. Due to compositional similarity (see Table 7.6), muscovite from the leucosome, mesosome or melanosome of individual samples is not distinguished.

portion of diatexite **97-286-1** also have lower Ti than coarser grains in schlieren. This is consistent with low Ti biotite grains having crystallised from the leucosome partial melt, and complementary high Ti grains in melanosomes being residual from anatexis. Sawyer (1998) notes that the biotite population of diatexites from the Opatica subprovince of the Canadian Shield also includes both high and low Ti varieties, the latter similarly inferred to have crystallised from the melt.

Despite re-equilibration, the overall compositions of muscovite and biotite within a particular lithology do show subtle but clear differences from other samples. This is most obvious in the systematically lower Ti, Mg#, and higher total Al contents of biotite within granitic migmatite samples from Schofield Creek (Figure 7.7). Muscovite from these rocks also has lower (Mg+Fe+Ti) and higher total Al (Figure 7.9). Similarly, both biotite and muscovite in leucosome **98-102** from Chin Chap Creek have a distinctive low Al character (Figures 7.7, 7.9). The coupling of biotite and muscovite compositions thus suggests that the systematic difference in mineral chemistry between samples results from differences in bulk rock composition. Unfortunately, as whole rock geochemical data are not available for the pertinent samples, this prospect cannot be further explored. Differences in biotite chemistry between M_1 tonalitic migmatites from Dunmore Creek and Schofield Creek) and M_2 samples of the Glenelg River (Figure 7.7) probably also reflect subtle variations in the respective protoliths.

Importantly, mica compositions in granitic migmatite **98-25M2** from northern Schofield Creek are indistinguishable from melanosome micas of tonalitic sample 98-25M1, collected from a nearby migmatitic horizon of similar (semi-pelitic) bulk rock composition. This indicates that in this case the development of contrasting leucosome types was independent of mica chemistry (and perhaps therefore bulk rock composition), but might reflect different partial melting processes. Also noteworthy is that micas of migmatite **98-25M2** exhibit the same chemical characteristics as those from adjacent small granitic bodies (**98-SC**, **98-WF1B**).

7.3.2 Plagioclase

A host of experimental studies, reviewed by Johannes & Holtz (1996), predict strong Na-Ca fractionation between cotectic melt and residual plagioclase during partial melting, the effect being most pronounced in the granitic (Q-Ab-Or-An) system. In contrast, in many anatectic migmatites leucosome and mesosome plagioclase is almost indistinguishable (Ashworth 1985; Johannes 1985; Whitney & Irving 1994). This has been variously attributed to- (1) homogenisation of plagioclase by subsolidus recrystallisation (Ashworth 1985), (2) 'unstable' or disequilibrium melting of intermediate composition plagioclase (Johannes 1978, 1983, 1985); or (3) re-equilibration of leucosome and mesosome plagioclase compositions during protracted cooling in rocks where segregation of melt and restite minerals was incomplete (Ashworth 1985; Johannes & Holtz 1996).

Plagioclase exhibits a wide range of compositional characteristics in GRC migmatites, but in many cases a calcic melanosome residue was either not preserved or never formed. In some instances this might be accounted for by later homogenisation/equilibration. Plagioclase of M_1

tonalitic migmatites T2-161 and T2-162 is weakly zoned and has the same compositional range in leucosome and mesosome despite morphological differences (Table 7.1). As these samples are strongly deformed, coincidence of plagioclase composition might be attributed to subsequent D_2 recrystallisation. Likewise, plagioclase in leucosomes, melanosomes and mesosomes of M_2 granitic migmatite **98-R5B** is unzoned to weakly zoned and compositionally indistinguishable, the same feature evident in diatexite **97-286-1**. If fractionation of calcic plagioclase between melt and residue occurred in these samples during melting, this could have been erased by re-equilibration during protracted cooling; such a process would be more effective for the diatexite due to limited separation of the hydrous melt from residual phases.

However, in other migmatite samples, mesosome/melanosome plagioclase has sharp zonation, with distinct core and rim relationships, and leucosome plagioclase exhibits oscillatory or intricate mottled zoning (see Figures 7.4, 7.5). Discrete zone boundaries and oscillatory zoning are evident even where rocks have been overprinted and texturally modified by D_2 (tonalitic migmatites **G2** and 98-25M1). Preservation of complex zoning therefore precludes extensive diffusive homogenisation between plagioclase of these samples during cooling, and cannot explain the chemical equivalence between leucosome, mesosome and melanosome plagioclase. Given the extreme lithological and textural heterogeneity of GRC migmatites, it is possible that the calcic plagioclase residue occurs in another part of the sample than the single thin section analysed here; examination of more thin sections from different parts of the migmatite are required to test this. Alternatively, partial melting may not have involved the formation of a more calcic plagioclase residue. While the reasons for this require further investigation, it is consistent with the paucity of plagioclase in melanosomes of GRC migmatites in general (Tables 5.3, 5.4) and has important geochemical ramifications (see section 8.5.2a).

Granitic leucosome **98-65A** represents a different case, in that plagioclase has euhedral to corroded cores that are significantly more calcic (up to An_{42}) than those of the complementary mesosome (**98-65C**, maximum of An_{34}). These cores could represent entrained residual plagioclase grains, but this is unlikely as adjacent melanosomes lack plagioclase. Alternatively, the leucosome may have been generated from a slightly different protolith than represented by the mesosome thin section analysed. Markedly more calcic plagioclase cores are also evident in Chin Chap Creek leucosome **98-102** (to An_{47}).

Similarly, leucosomes of tonalitic migmatite sample **G2** contain plagioclase that is more calcic than the other tonalitic leucosomes analysed. Although corroded calcic cores might be incompletely melted relics entrained from the melanosome, euhedral oscillatory zones ranging up to An_{50} in some plagioclase grains were melt-precipitated. Since equally calcic plagioclase occurs in the complementary mesosome, this might reflect partial melting of a precursor with higher CaO/Na_2O than that of other tonalitic leucosomes. Unfortunately, as geochemical data for the mesosome adjacent to leucosome **G2** was not obtained, the correlation between leucosome plagioclase composition and bulk rock chemistry cannot be checked.

7.4 Geochemistry of GRC metasedimentary rocks

7.4.1 Northeastern migmatite zone

Analysed metasedimentary rocks include unmelted quartzofeldspathic schists, quartzofeldspathic gneisses and semi-pelitic to pelitic schists, together with whole rock stromatic migmatites, diatexites, and migmatite mesosomes (Appendix C). Five micaceous enclaves were also analysed from Harrow type granitic rocks, with samples **98-SEL** and **98-27** collected from the Schofield Adamellite, and samples **98-MEL**, **98-151** and **98-152** obtained from the Dunmore Leucotonalite.

All mesosomes were obtained from large granitic migmatite samples, as the relatively micaceous and quartz-poor mesosomes adjacent to tonalitic leucosomes were unacceptably weathered. Separation involved removal of quartzofeldspathic leucosomes and micaceous melanosomes by splitting, and in some cases by sawing. Samples of each mesosome were examined in thin section and those exhibiting fabric disruption, such as might be imparted by migration of partial melts, were excluded from analysis. The exceptions are samples **99-14** and **99-R5B**, both of which have poor foliations and derive from diffuse, slightly coarser and more biotite-enriched areas surrounding leucosomes; these lithologies may have experienced variable removal of a melt phase and were analysed for comparative purposes. Besides these, mesosome samples are believed to represent primary metasedimentary compositions largely unmodified by partial melting processes, though extraction of small partial melt increments parallel to the foliation, such that mesosomes are slightly residual (i.e., quartz- and biotite-enriched, feldspar-depleted), cannot be discounted from field relations alone.

Diatexite analyses were obtained from whole-rock samples (~10 kg) and include constituent micaceous clots/enclaves, quartz-rich areas and sillimanite clots. However, owing to marked decimetre-scale heterogeneity in the proportion of granitic and residual components, the geochemistry of these samples cannot be considered representative of the diatexite horizon overall.

7.4.2 Comparison with metasedimentary rocks at lower grades

Metasedimentary lithologies from the northeastern migmatite zone (including data from Kemp 1995, Fitzherbert 1998, and C.M. Gray *unpubl. data*) are plotted on selected silica variation diagrams (Figure 7.10), together with data from sub-migmatite zone (i.e. unmelted) metasedimentary rocks. The latter include biotite-grade metagreywackes from the southwestern metamorphic zonation (C.M. Gray *unpubl. data*) and lower - to middle amphibolite facies schists from both the southwestern (Anderson 1990; Ferguson 1993) and northeastern metamorphic zonations (O'Hara 1996; Fitzherbert 1998). Also plotted are migmatite mesosomes and diatexites from this study.

Metasedimentary rocks from the migmatite zone have a larger silica range (from 47.3% to 92.7% SiO_2) than sub-migmatite zone rocks (Figure 7.10). This partly reflects the more complete data set from the migmatite zone, but is also due to the confinement of metaquartzites to the highest metamorphic grades of the GRC. Apart from this, migmatite zone and sub-

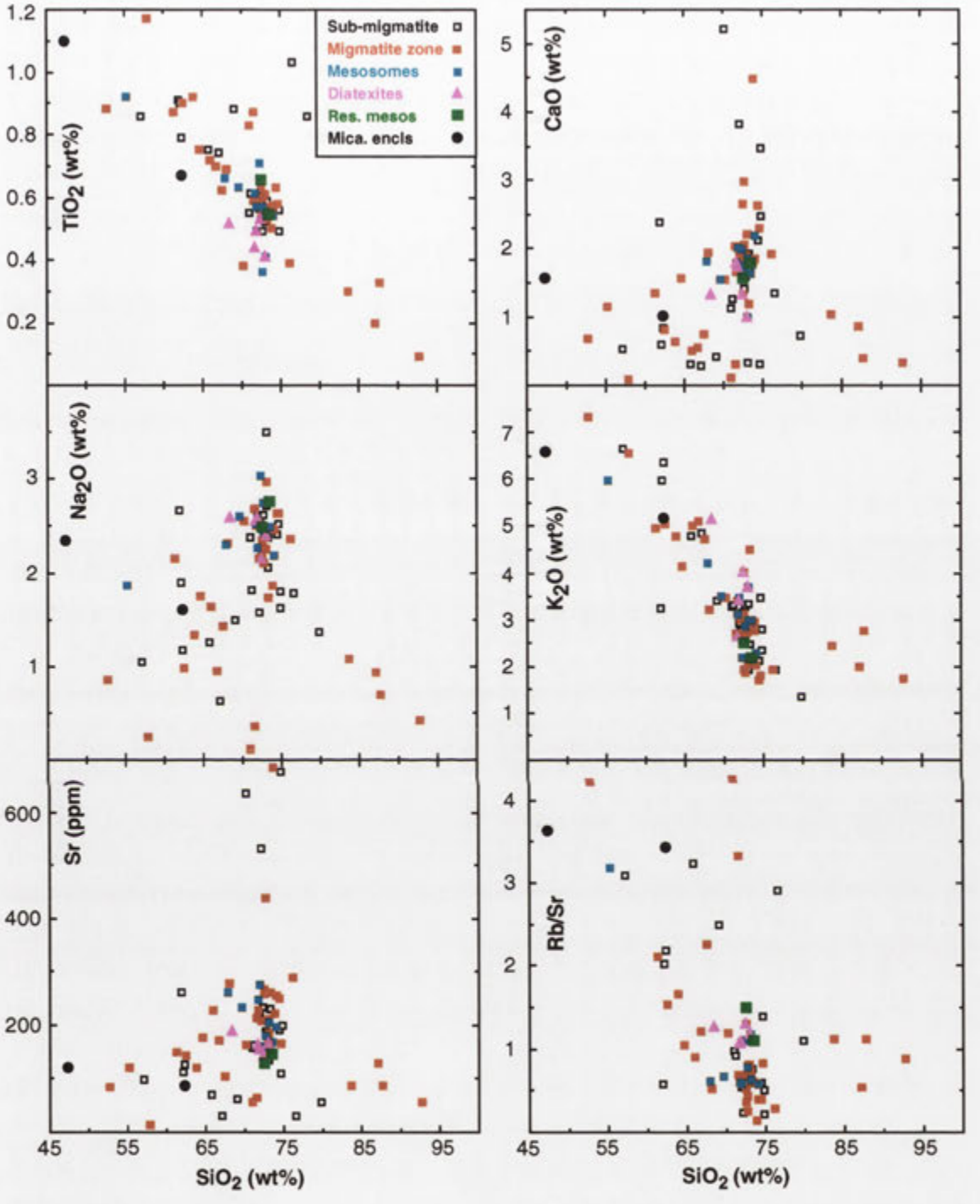

Figure 7.10. Harker variation diagrams for metasedimentary rocks of the GRC. 'Sub-migmatite' encompasses rocks of the amphibolite and greenschist facies which have not experienced partial melting. 'Mica encls.' are micaceous enclaves (samples **98-SEL** and **98-27**) collected from the Schofield Adamellite in northern Schofield Creek, whereas 'res. mesos' are migmatite mesosomes from which a partial melt phase is thought to have been removed. Although a wide compositional range exists overall, most metasedimentary data is clustered between about 70-75% SiO_2. Trends within this cluster are defined by both unmelted (sub-migmatite) and melted (migmatite zone) lithologies, and hence independent of anatectic processes.

migmatite zone metasedimentary rocks are compositionally remarkably similar over a wide silica range for all elements considered. This indicates that there is no systematic chemical difference between metasedimentary rocks of various grades in the GRC, and that sub-migmatite zone and migmatite zone metasedimentary rocks can be treated as a single, coherent system. The geochemical diversity of GRC metasedimentary rocks is therefore controlled by 'primary' mineralogical variations in the sedimentary precursor, and not largely affected by metamorphism or anatexis (but see below). Variations in the protolith are likely to reflect a complex interplay between several different sedimentary components and depositional processes (Anderson & Gray 1994), and are not addressed by this research.

Importantly, most metasedimentary rock data from both the migmatite and sub-migmatite zones is concentrated between about 70-75% SiO_2, forming a distinctive cluster on variation diagrams. This data concentration comprises biotite-grade metagreywackes and unmelted quartzofeldspathic schists of the amphibolite facies, and quartzofeldspathic schists, gneisses and migmatites of the northeastern migmatite zone, and therefore reflects the preponderance of quartzofeldspathic compositions at all metamorphic grades in the GRC metasedimentary sequence. The plagioclase-rich nature of these rocks (and of the precursor) is manifested by moderately high, but variable Na_2O (~1.8-3.0%), CaO (most between ~1.2-3.0%) and Sr (~100-300 ppm). Distinctly elevated CaO (spanning 3.0-5.2%) and Sr (400-700 ppm) and lower Rb/Sr in five quartzofeldspathic samples (Figure 7.10) might also reflect the involvement of a carbonate component in the sedimentary protolith (Anderson & Gray 1994). Calc-silicate horizons in the southwestern GRC manifest a more substantial sedimentary carbonate component, and have up to 11.4% CaO and 2000 ppm Sr (Bushell 1996).

Most migmatite mesosomes also plot within this quartzofeldspathic data cluster on variation diagrams and are therefore chemically indistinguishable from low grade (i.e. unmelted) quartzofeldspathic schists. Mesosomes therefore retain primary metasedimentary compositions and are unmodified by partial melting. For mesosome **98-65C**, this is also corroborated by REE data (see below). In contrast, mesosome samples **99-14** and **98-R5B** have slightly higher Rb/Sr, and are distinctly depleted in Ba and Sr compared to other mesosomes (Figure 7.10; see also Figure 7.14). This supports the petrographic evidence that these samples have been influenced by anatectic processes (see section 8.5.2). Four of the five diatexite samples also fall within the 70-75% silica range and, as with other quartzofeldspathic metasedimentary rocks, exhibit considerable variation in CaO, Na_2O and K_2O. However, diatexites have lower TiO_2 and Sr, but higher Rb/Sr than most rocks of the quartzofeldspathic data cluster. Sillimanite-bearing diatexite **99-5B** is semi-pelitic, with 68.2% SiO_2 and ~15% Al_2O_3, but also has lower TiO_2 than unmelted semi-pelitic rocks. The significance of these features is evaluated in section 8.5.5.

7.4.3 Rare earth elements (REE)

The chondrite-normalised REE patterns for three migmatite zone metasedimentary samples, muscovite-biotite schist **97-317A**, quartzofeldspathic schist **97-R2D** and migmatite mesosome **98-65C**, are presented in Figure 7.11. Besides conspicuous negative Nd anomalies, which are a distinctive aspect, all patterns have similar shape to that of the average post-Archaean

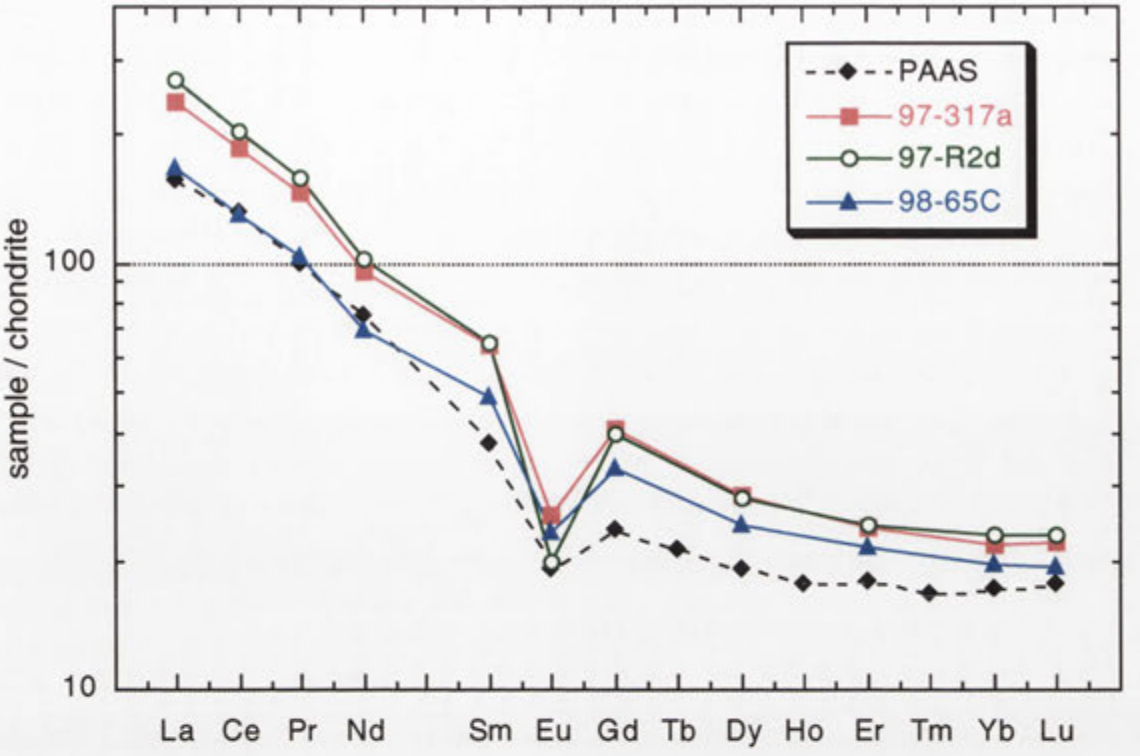

Figure 7.11. Chondrite-normalised REE abundances (normalising values from Anders & Grevesse 1989) for GRC metasedimentary rocks compared to the Post-Archaean average Australian sedimentary rock (PAAS) of McLennan (1989).

Australian sedimentary rock (PAAS), though at higher total REE. This is consistent with derivation of the sedimentary precursor from a REE-enriched provenance (McLennan 1989). Quartzofeldspathic schist **97-R2D** has very similar normalised REE abundances to metapelitic schist **97-317A**, which is unusual, as the clay-rich sedimentary fraction generally contains the highest REE concentration, with detrital quartz having a diluting effect (Rollinson 1993). This may reflect a high proportion of detrital monazite in **97-R2D**, which would account for the slight 'light' REE (LREE) enrichment and greater negative Eu anomaly ($Eu/Eu^* = 0.39$ compared to 0.50 for **97-317A**), as these features are intrinsic to monazite (Bea *et al.* 1994). More importantly, mesosome **98-65C** has distinctly lower total REE, and also has the smallest negative Eu anomaly ($Eu/Eu^* = 0.58$). Both of these argue against removal of partial melt from this sample, as this would result in elevated REE contents and exaggerated negative Eu anomalies (e.g. Solar & Brown 2001).

7.4.4 Protolith composition for granitic migmatites

A significant aspect of quartzofeldspathic metasedimentary rocks is that in the migmatite zone they host the highest concentrations of granitic leucosomes (Chapters 5 and 6). Apart from **99-5B**, melt-rich diatexites are also of broadly quartzofeldspathic composition (Figure 7.10). These observations imply that, relative to other metasedimentary compositions, quartzofeldspathic rocks have the highest 'fertility', or potential to yield the largest melt fraction over the smallest

temperature interval above the solidus (Thompson 1996). The capacity of quartzofeldspathic lithologies to produce copious granitic melt accords with the modal dominance within these rocks of the 'minimum melting' constituents quartz, plagioclase and alkali feldspar, and is also manifest chemically. As outlined above, quartzofeldspathic metasedimentary rocks are characterised by relatively high CaO (~1.0-5.2%) and Na_2O (~1.8-3.0%) contents compared to more psammitic and pelitic compositions, with significant (but strongly variable) K_2O (~1.7-4.0%). As an abundance of these components, together with SiO_2, is essential for the formation of significant quantities of granitic magma, the quartzofeldspathic metasedimentary cluster on variation diagrams approximates the compositional 'window' for optimum fertility to melt production. Notably, lower silica, more aluminous metasedimentary rocks have distinctly lower CaO and Na_2O concentrations, as expected from their more micaceous, feldspar-poor mineralogy. This predicts a diminished melt-producing capacity relative to quartzofeldspathic rocks, consistent with the paucity of anatectic leucosomes in metapelitic schists of the GRC.

7.4.5 Mineralogical controls on fertility to melt production

It is likely that the voluminous partial melts within GRC migmatites were mostly generated from feldspathic metasedimentary protoliths of this optimum fertility composition. This is strongly supported by systematic chemical linkages between *in situ* leucosomes and quartzofeldspathic rocks (section 8.5.2). Yet it is noteworthy that many quartzofeldspathic schists and gneisses in the northeastern migmatite zone that reside within the high fertility window on geochemical variation diagrams have few or no leucosomes. From this study these include low K_2O quartzofeldspathic schists (<2.5% K_2O; samples **T2-2B, T2-CC20, 98-R1, 98-R2, 98-14B**) and higher K_2O schists and gneisses (2.5-4.5% K_2O; samples **T2-146MG, T2-302B, T2-39B, 97-316, 98-75, TKP220**).

A critical aspect of these unmigmatitic rocks is that many lack (or have very small amounts of) prograde muscovite (Table 5.6). For high K_2O schists and gneisses with the assemblage quartz-plagioclase-alkali feldspar, the solidus temperature in the presence of H_2O depends on the anorthite content of the plagioclase (Johannes & Holtz 1996; see section 8.2.1). However, both chemographic relationships (e.g. Thompson & Algor 1977; Thompson & Tracy 1979; Abbott 1985) and experimental considerations (Holtz *et al.* 1992; Joyce & Voight 1994; Johannes & Holtz 1996) predict that the addition of Al_2O_3 (from muscovite) to this assemblage depresses the solidus temperature by around 20-30°C. Consequently, in a layered quartzofeldspathic metasedimentary sequence, muscovite-bearing protoliths will experience anatexis preferentially, and at distinctly lower temperatures, than those that lack muscovite, which remain unmelted.

Hence, despite the geochemical disposition for melt generation, the lack of partial melting in the above schists and gneisses may be attributed to the paucity or absence of muscovite, resulting in a slightly higher relative solidus temperature. Supporting evidence for this is that mesosomes of interlayered stromatic migmatite horizons commonly contain primary muscovite as a significant constituent (Tables 5.3, 5.4). In some migmatites, prograde muscovite also persists in residual melanosomes, implying that it was in excess amounts required for partial melting (section 8.3).

Significantly, most quartzofeldspathic schists of the low K_2O group identified above also lack alkali feldspar (Table 5.6). As K_2O in these rocks is accommodated by biotite, these samples are relatively refractory, and could only yield granitic melt by biotite-melting reactions at much higher temperatures. The markedly less fertile character of these lithologies explains their widespread occurrence as enclaves in Harrow type granitic rocks and diatexites.

7.5 Geochemistry of migmatite leucosomes and small granitic bodies

Seventeen leucosomes, including three of tonalitic composition, were separated from various large (>10 kg) whole-rock stromatic migmatite samples, for which the geochemistry is presented in Appendix C. All analysed leucosomes are bordered by micaceous melanosomes and are thus believed to have formed largely *in situ*. Small foliated tufts of interleaved fibrolite and biotite were dispersed throughout the analysed fraction of leucosome **98-75**, which appear to be entrained melanosome fragments, and could not be effectively removed. This sample was analysed to examine the chemical effect of minor residue incorporation. Note that as the ultimate aim is to compare the composition of *in situ* leucosomes with Harrow type granitic rocks, the sampling strategy was deliberately biased towards more 'granitic' looking and texturally homogeneous leucosomes that are more likely to represent partial melt compositions. Accordingly, the heterogeneous quartz-rich leucosomes of whole-rock migmatite samples were discarded, except for leucosome **98-WF2A-2L**, analysed for comparative purposes.

Two leucogranitic segregations within diatexite horizons were also analysed (samples **97-286-1L** and **98-R3** from diatexites **97-286-1** and **98-R4** respectively, Appendix C). Neither incorporated biotite-sillimanite clots, schlieren or alkali feldspar megacrysts, though **98-R3** has millimetre-sized foliated biotite ± muscovite aggregates of probable restitic origin. Both segregations contained more disseminated biotite than stromatic migmatite leucosomes. This occurs mostly as non-aligned, euhedral flakes that are magmatically precipitated.

In situ granitic leucosomes include both M_1 and M_2 varieties from across the northeastern migmatite zone. These vary from 73.2% SiO_2 (**98-65A**) through to 76.2% SiO_2 (**98-WF1A**), and generally have low TiO_2 (<0.1%) and Fe_2O_3t (<1%). The exception is melanosome-contaminated sample **98-75**, with 0.12% TiO_2 and 1.1% Fe_2O_3t. Quartz-rich leucosome **98-WF2A-2L** has clearly higher SiO_2 (78.7%) and lower Al_2O_3 (12.5%) than other leucosomes, and is also the most K-poor (2.4% K_2O). Despite the narrow silica range, the latter is extremely variable amongst granitic leucosomes, ranging up to 5.5% for Robson Creek sample **98-R5C**. Importantly, samples **98-65A** and **98-65B** (Schofield Creek), together with **98-102** (Chin Chap Creek), have distinctly higher Sr than all other granitic leucosomes, even though CaO contents are not appreciably higher (Figure 7.12a). Nevertheless, these leucosomes have elevated An/Ab ratios (Figure 7.12b) manifested mineralogically by plagioclase that is significantly more calcic (see Figure 7.2).

Diatexite segregations **97-286-1L** and **98-R3** are moderately potassic (4.5% K_2O in **97-286-1L**) and chemically resemble M_2 granitic leucosomes, apart from having higher ferromagnesian element abundances (up to 1.7% Fe_2O_3t in **98-R3**), reflecting the higher biotite content.

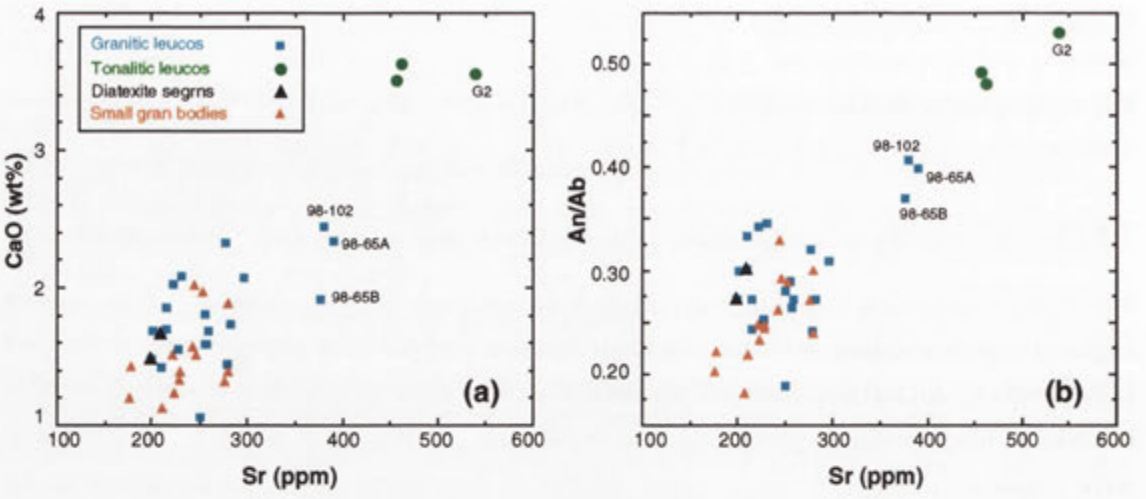

Figure 7.12. Plot of (a) CaO versus Sr and (b) An/Ab (normative anorthite/albite) versus Sr for *in situ* granitic and tonalitic leucosomes, diatexite segregations and small granitic bodies of the northeastern migmatite zone.

The three tonalitic leucosome samples **98-123** (M_1), **G2** (M_1) and **TL4** (M_2) were complementary to semi-pelitic mesosomes and have broadly similar geochemistry, except that **G2** has distinctly higher Sr/Ca (Figure 7.12) and plagioclase that is markedly more calcic (Figure 7.1). Although similarly silica-rich and ferromagnesian element-poor, tonalitic leucosomes are readily distinguished from their granitic counterparts by elevated CaO and Sr (Figure 7.12), reflecting the higher plagioclase proportion. Very low K_2O (<1%) manifests the lack of alkali feldspar.

Appendix C also lists sixteen analyses of post-D_2 small granitic bodies collected from across the migmatite zone, which may be contiguous with M_2 granitic leucosomes but are not bordered by melanosomes. These include thin (5-25 cm thick) discordant sheets, decimetre-sized granitic 'pools', crosscutting bulbous dyke-like bodies and thicker S_2-parallel sills (1-5 m thick). The graphic alkali feldspar megacrysts and small micaceous enclaves present in some samples are considered extraneous to the magma and were therefore removed prior to crushing.

Small granitic bodies are chemically very similar to *in situ* leucosomes, being felsic, with less than 1% total Fe_2O_3 and having a restricted range of SiO_2 content (from 74.0% to 75.5%). In contrast, sample **97-396**, from a heterogeneous biotite-rich sheet in Bryan Creek, has 1.9% Fe_2O_3t. Pronounced K_2O variation is also evident, from 3.0% (**98-WF1B**) to 6.4% (**98-R8**).

7.6 Comparison between *in situ* leucosomes, small granitic bodies and metasedimentary rocks

7.6.1 Normative composition

By way of initial comparison, stromatic migmatite leucosomes, diatexite segregations and small granitic bodies are plotted on a CIPW normative quartz-albite-orthoclase (Q-Ab-Or) ternary diagram (Figure 7.13), together with metasedimentary lithologies from the migmatite zone. Note that granitic leucosomes and small granitic bodies also contain a variable but significant An (anorthite) component (up to 11.6 normative percent, Appendix C), and therefore lie within the 'granite' (Q-Ab-An-Or) tetrahedron. Contained within the tetrahedron are three cotectic surfaces extending from the bounding binary systems, which intersect along a five phase curve (i.e quartz-plagioclase-alkali feldspar-H_2O-melt; Nekvasil & Burnham 1987). Accordingly, the calculated position of this surface, projected into the haplogranite system from anorthite at 500 Mpa (from Nekvasil 1988), is also indicated on Figure 7.13. The anorthite content along this curve varies from zero at the ternary Q-Ab-Or eutectic to a maximum at the Q-Or sideline, which represents the projected Q-An-Or eutectic (see Nekvasil & Burnham 1987; Nekvasil 1988). Initial minimum temperature melts in the Q-Ab-An-Or-H_2O system are therefore located

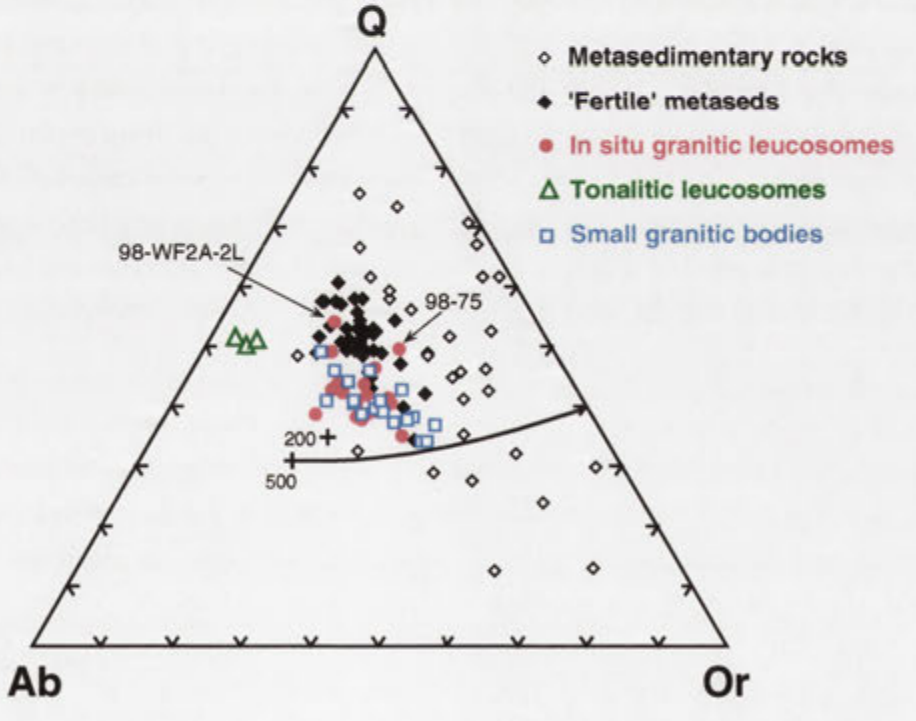

Figure 7.13. CIPW normative composition of metasedimentary rocks of the migmatite zone, *in situ* granitic leucosomes, tonalitic leucosomes and small granitic bodies (Q = quartz, Ab = albite, Or = orthoclase). 'Fertile metaseds' represent quartzofeldspathic metasedimentary rocks of the optimum fertility cluster on variation diagrams. The position of the water-saturated haplogranitic (i.e. Q-Ab-Or) eutectics at 200 Mpa and 500 Mpa (crosses) and the five phase curve (at P_{H_2O} = 500 Mpa) are from Nekvasil (1988).

along this curve (in equilibrium with quartz, alkali feldspar and plagioclase) and progressively displaced towards the Q-Or join with increasing An/Ab ratio (also established experimentally by James & Hamilton 1969). The temperature of the melt (and solidus) also increases with An, though variation is minor (see Figure 9 of Nekvasil 1988).

Immediately evident from Figure 7.13 is that most granitic leucosomes (apart from **98-WF2A-2L** and **98-75**) exhibit a similar range of normative compositions to small granitic bodies. However, the composition of most granitic leucosomes does not coincide with the projected five phase 'minimum melt' surface at 500 Mpa, relevant for the conditions of *in situ* anatexis (section 8.2.2). Instead, granitic leucosomes (and small granitic bodies) define an array that extends from close to the five phase curve towards decreasing orthoclase and increasing quartz at approximately constant albite content, which reflects the marked variation in weight percent K_2O. Importantly, this trend parallels that of fertile metasedimentary rocks and does not extend to the quartz-poor side of the cotectic, even though some metasedimentary rocks plot there. By contrast, tonalitic leucosomes are impoverished in the orthoclase component, as expected from the low K_2O content. The non-minimum composition of both tonalitic and granitic leucosomes is therefore clearly controlled by the large K_2O variation, the reasons for which are explored in the next chapter.

7.6.2 Major and trace element geochemistry

The close chemical resemblance between *in situ* granitic leucosomes and small granitic bodies is obvious on Harker variation diagrams, such that the compositional field of each overlaps for all elements considered (Figure 7.14). Particularly striking is the marked dispersion in K_2O and Ba contents over the small SiO_2 range of both groups, such that sub-vertical arrays are defined which extend to much higher K_2O and Ba than metasedimentary rocks of similar silica. CaO, Sr and Na_2O also exhibit considerable variation. A minor difference is that small granitic bodies are displaced to slightly lower CaO (Figure 7.12a) but higher K_2O contents than granitic leucosomes. Apart from marginally higher ferromagnesian element abundances, leucogranitic diatexite segregations are compositionally indistinguishable from stromatic migmatite leucosomes.

Quartzofeldspathic metasedimentary rocks, conspicuously clustered between ~70-75% SiO_2 on variation diagrams, have the optimum fertility for melt generation and are the probable protoliths to *in situ* partial melts within migmatitic rocks (section 7.4.4). However, relative to this inferred source composition, granitic leucosomes are strongly depleted in TiO_2, (Fe_2O_3t+MgO), Zr and P_2O_5, but enriched in Al_2O_3, Na_2O, K_2O and Ba (Figure 7.14). The range of CaO and Sr variation parallels that of fertile quartzofeldspathic lithologies. Compared directly to complementary mesosomes, *in situ* leucosomes have elevated Pb, Ba and Sr, but depleted concentrations of Rb, P, high field strength elements (HFSE) Zr, Th, Y and Nb and LREE (Figure 7.15a). Considerable diversity between leucosomes with respect to many of these elements is apparent, even though most are envisaged to have formed by anatexis of broadly similar precursors.

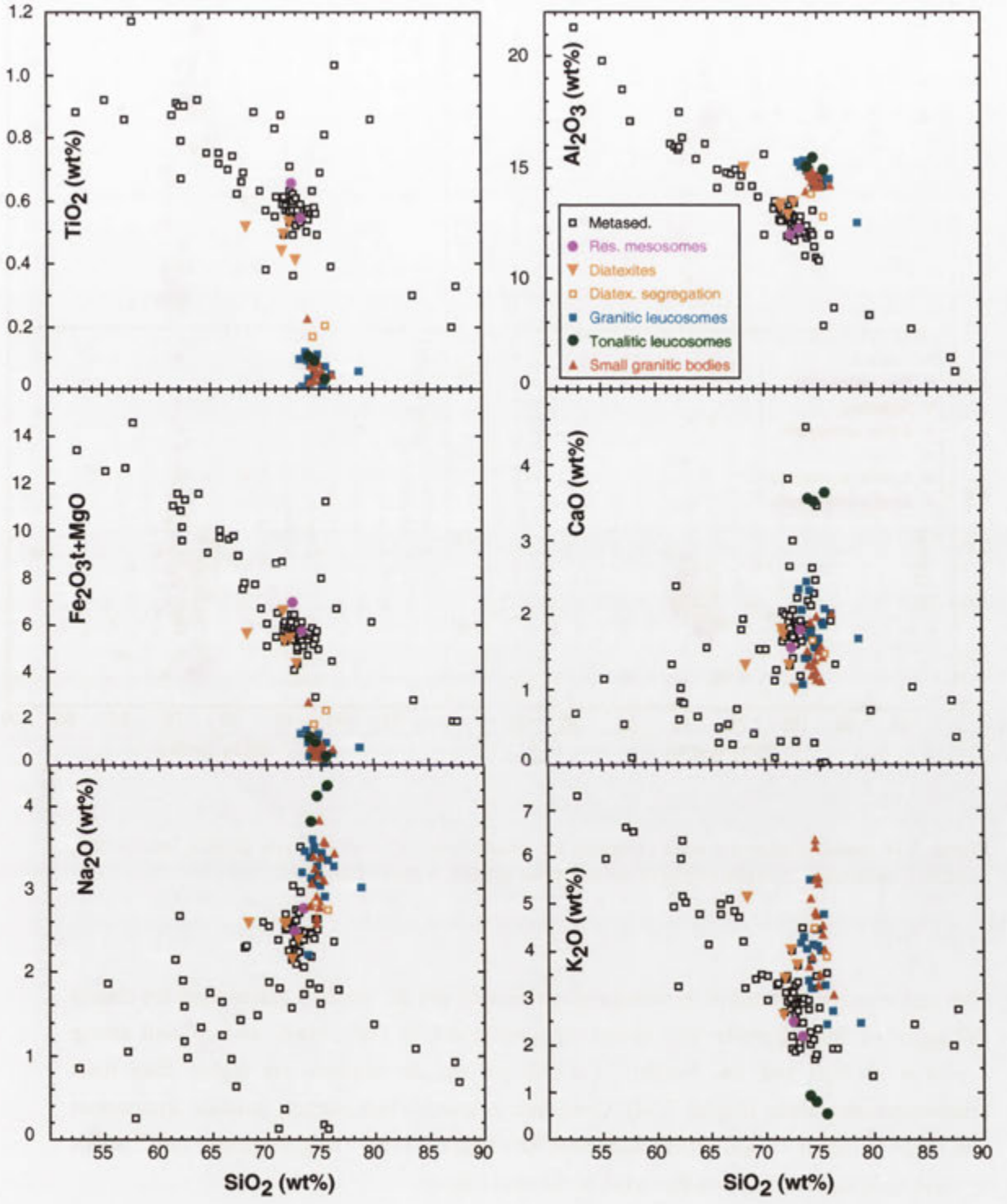

Figure 7.14. Harker variation diagrams for metasedimentary rocks, *in situ* granitic leucosomes, tonalitic leucosomes, diatexite segregations and small granitic bodies of the GRC. Diatexites and 'residual' mesosomes are plotted separately. Due to compositional similarity, metasedimentary rocks from the migmatite zone (including mesosomes) are plotted together with those of the greenschist and amphibolite facies (data sources as for Figure 7.10).

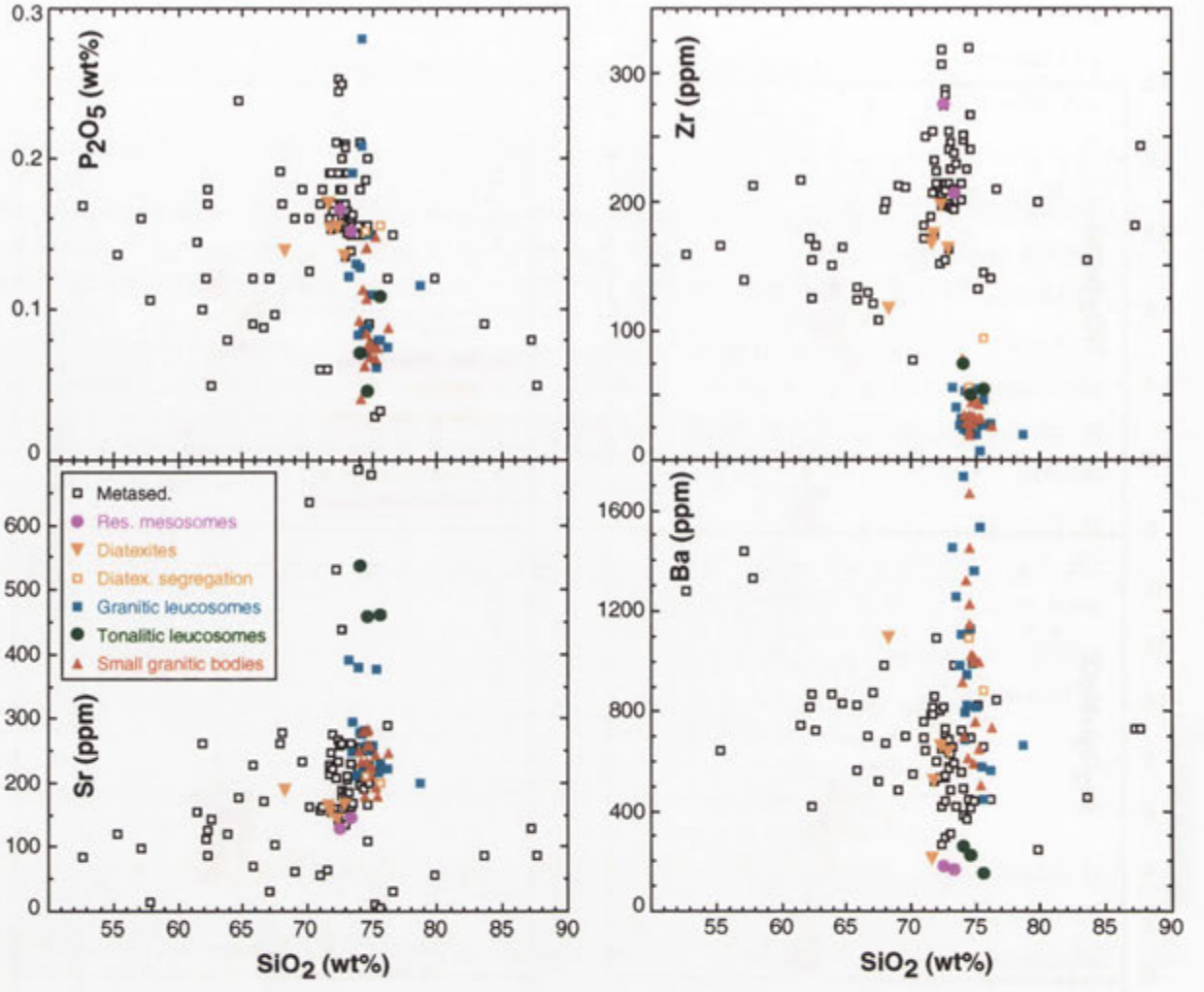

Figure 7.14 contd. Harker variation diagrams for metasedimentary rocks, *in situ* granitic leucosomes, tonalitic leucosomes, diatexite segregations and small granitic bodies of the GRC.

Although equally depleted in ferromagnesian elements and Zr, tonalitic leucosomes are clearly distinguished from granitic leucosomes by enrichment in CaO, Na_2O and Sr and strong depletion in K_2O and Ba. Notably, CaO, Na_2O and Sr contents are higher than most metasedimentary rocks (Figure 7.14). Compared to granitic leucosomes, tonalitic leucosomes also range to higher Th and LREE, and lower Rb (Figure 7.15b). The petrogenetic implications of these chemical features are discussed in the next chapter.

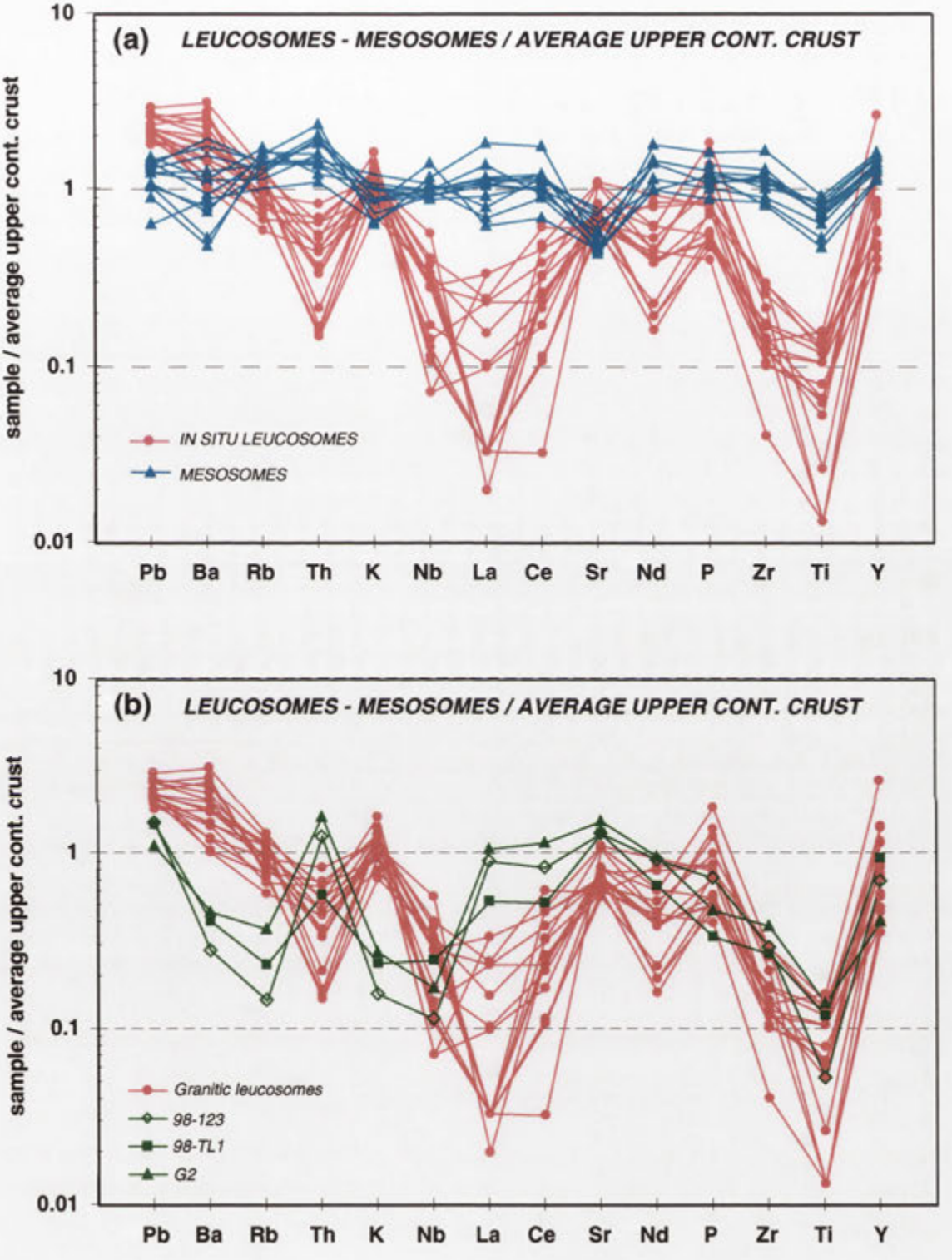

Figure 7.15. Upper continental crust-normalised 'spider diagrams' comparing (a) *in situ* granitic leucosomes and complementary mesosomes and (b) *in situ* granitic leucosomes and tonalitic leucosomes (green). Normalising values are from Taylor & McClennan (1995) except for Ti and Nb (from Plank & Langmuir 1998) and P (taken from Gao *et al.* 1997).

Chapter 8: Petrogenesis of migmatite leucosomes, diatexites and small granitic bodies

8.1 Introduction

This chapter aims to investigate the petrogenesis of migmatite leucosomes and diatexites, and to determine the origin of the small granitic bodies linked to *in situ* leucosome arrays. Specific aspects to be addressed are- (1) the major melting reactions responsible for generation of leucosomes during both M_1 and M_2, (2) the causes of geochemical diversity between leucosomes and diatexites, with implications for 'minimum melt' compositions in complex natural assemblages, and (3) the chemical relationship between small granitic bodies and *in situ* leucosomes.

8.2 Partial melting relations

8.2.1 Insights from mineral assemblages

Partial melting equilibria for muscovite-bearing assemblages are documented by Thompson & Algor (1977), Thompson & Tracy (1979), Thompson (1982) and more recently by Spear *et al.* (1999). Potential melting reactions in fertile muscovite-bearing protoliths, depicted in Figure 8.1, are constrained by a number of factors, including modal mineralogy, the temperature and pressure of anatexis, and the presence or absence of a fluid phase. However the clearest insight into the specific reactions responsible for generating the leucosomes within a migmatite is provided by the mineralogy of adjacent mesosomes and melanosomes, which indicates which phases are consumed, produced, or not significantly involved in anatexis. Upon considering the mineral assemblage of granitic (alkali feldspar-bearing) migmatites from the northeastern migmatite zone (Tables 5.3 and 5.4), several points emerge-

(1) There is no systematic difference between the mineral assemblage of M_1 and M_2 migmatites, suggesting that anatexis in both episodes involved essentially the same reactions;

(2) The predominant melanosome mineral in each sample is biotite, which retains the S_2 orientation and commonly preserves the earlier S_1 fabric. Rather than forming by 'back-reaction' (section 4.3.2), biotite did not significantly participate in partial melting reactions, and was concentrated in the residue as anatexis proceeded. The minor involvement of biotite accords with the absence of ferromagnesian phases such as garnet, cordierite, orthopyroxene or opaque oxides in leucosomes, which are necessary peritectic byproducts of biotite melting (e.g. Vielzeuf & Holloway 1988; Patiño Douce & Johnston 1991; Vielzeuf & Montel 1994). The paucity of well-shaped, melt-precipitated biotite in leucosomes also indicates limited biotite dissolution during partial melting, and partly explains the very low TiO_2 and Fe_2O_3t of *in situ* leucosomes (see below);

(3) Although secondary flakes are common, *prograde* muscovite occurs in many migmatitic rocks and interlayered schists and gneisses, coexisting with quartz and plagioclase. Persistence of primary muscovite indicates that- (a) terminal subsolidus muscovite dehydration reactions

were not encountered during prograde metamorphism in the northeastern GRC, and hence partial melting must have occurred at higher pressures than invariant point I_3 in Figure 8.1, and (b) the upper limit of muscovite stability in quartz-bearing rocks (at $a_{H_2O} = 1$) was not exceeded during anatexis;

(4) Sillimanite is a minor component of many stromatic migmatites (associated with prograde muscovite) but never coexists with alkali feldspar in melanosomes. The assemblage sillimanite + alkali feldspar is only rarely observed in mesosomes of some semi-pelitic migmatites.

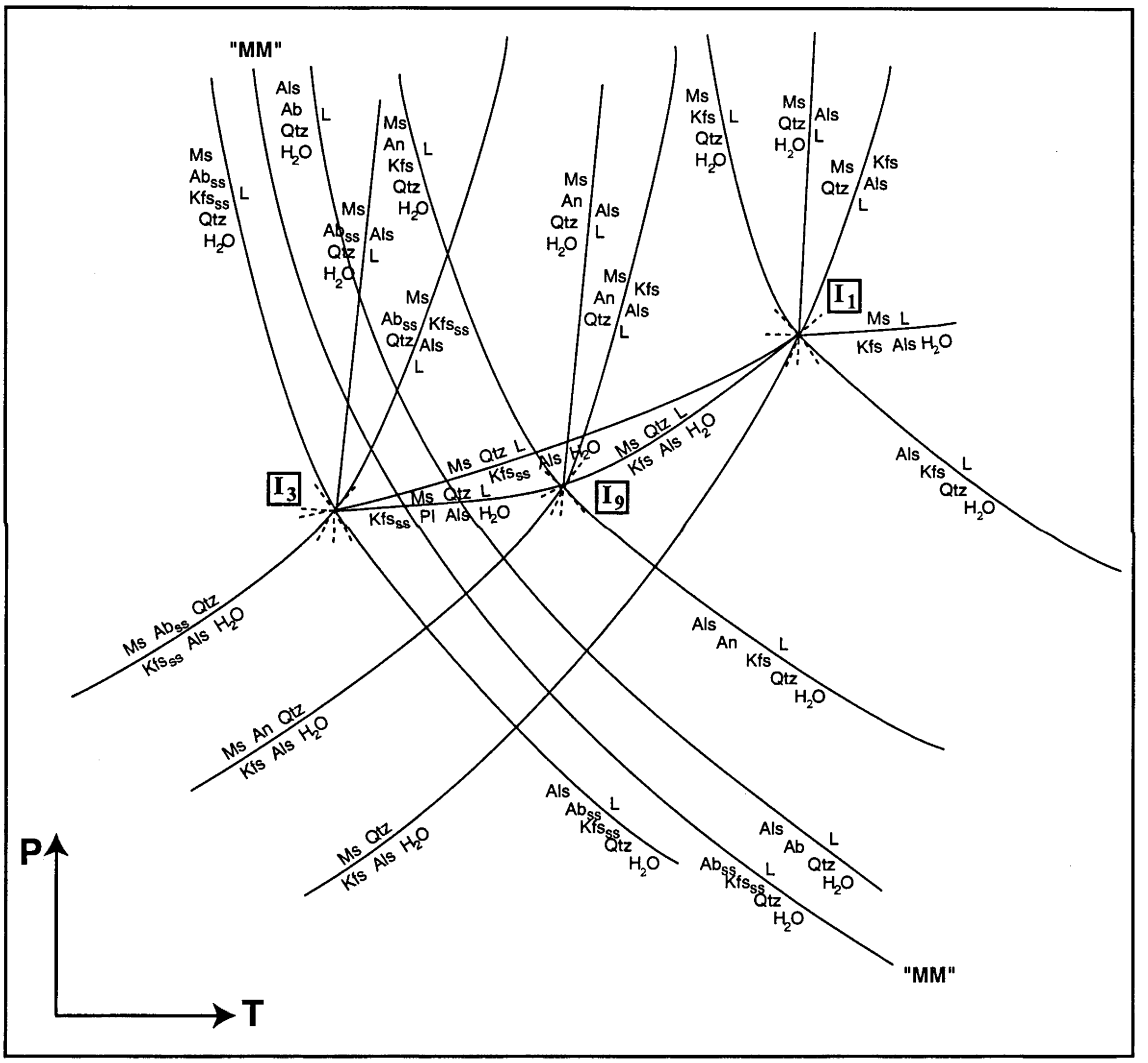

Figure 8.1. Schematic P-T diagram showing univariant equilibria between muscovite (Ms), plagioclase, potassic feldspar, Al_2SiO_5 (Als), quartz, (Qtz), H_2O (at a_{H_2O} ~1) and melt (L). "MM" denotes the haplogranite minimum melting curve. Invariant points are for the K-Na (I_3), K-Ca (I_9) and K (I_1) systems (numbering from Thompson & Tracy 1979). The compositional field is expanded for clarity (modified after Thompson & Tracy 1979). Other mineral abbreviations are: Ab, $NaAlSi_3O_8$; Ab_{ss}, $NaAlSi_3O_8$-$KAlSi_3O_8$ solid solution; An, anorthite; Kfs, $KAlSi_3O_8$; Kfs_{ss}, alkali feldspar (Kfs-Ab solid solution); Pl, plagioclase feldspar (Ab-An solid solution).

Of these, the last observation is particularly significant, as it implies that the peritectic CKNASH melting reaction (e.g. Kerrick 1972) –

muscovite + plagioclase + quartz = sillimanite + alkali feldspar + MELT [8.1]

did not occur. This reaction involves the incongruent breakdown of muscovite without participation of a free fluid phase, and is therefore referred to as a fluid-absent or *dehydration melting* reaction (Thompson 1982). The hydroxyl component liberated from the dissociation of muscovite is dissolved into the melt, leaving newly formed anhydrous minerals in the residue. Melanosomes of migmatites formed by this reaction would contain coexisting peritectic reaction products sillimanite and alkali feldspar, together with biotite and excess reactants. This is observed in dehydration melting experiments on natural muscovite-biotite schists by Patiño Douce & Harris (1998) at 600-1000 Mpa. Here, glass (former melt) is associated with intergrowths of peritectic alkali feldspar, sillimanite and biotite, which are the solid products of the incongruent melting of impure muscovite. Absence of these textures in GRC migmatites therefore argues against a significant role for fluid-absent muscovite dehydration melting (i.e. reaction [8.1]) in the generation of leucosomes.

Melting reactions that proceed at lower temperature than reaction [8.1] require excess aqueous fluid (Figure 8.1), and by inference, anatexis in the northeastern migmatite zone must have proceeded at high a_{H_2O}, such that P_{H_2O} is near P_{total}. The two pertinent CKNASH reactions (from Thompson & Tracy 1979) are -

muscovite + plagioclase + quartz + alkali feldspar + H_2O = MELT [8.2]

muscovite + plagioclase + quartz + H_2O = sillimanite + MELT [8.3]

Reaction [8.2], appropriate for alkali feldspar-bearing protoliths, is near-eutectic[1], and responsible for the formation of most leucosomes of GRC migmatites (see below). Granitic migmatite samples listed in Tables 5.3 and 5.4 formed by this reaction are recognised by lack of residual sillimanite, or retrograde muscovite that might be replacing sillimanite. The amount of granitic melt produced by this reaction is buffered by the supply of fluid. Evidence for this reaction is that the assemblage quartz-plagioclase-alkali feldspar-muscovite is widespread in quartzofeldspathic schists of the northeastern sillimanite zone (the lower grade equivalent of migmatite zone rocks) and is also extant in some migmatite mesosomes. During equilibrium melting in the presence of H_2O, the solidus temperature for this assemblage is determined by the anorthite content of the plagioclase (see Figure 8.1), being 645°C for pure albite at 500 Mpa, and rising to 672°C for plagioclase of An_{40} (Johannes & Holtz 1996).

In contrast, fluid-present incongruent reaction [8.3] proceeds at slightly higher temperatures than [8.2] and may be apposite for migmatites with melanosome sillimanite. The reaction could

[1]Owing to the binary plagioclase loop, where there is always a temperature interval between solidus and complete melting, in the CKNASH or 'haplogranodiorite' system this reaction cannot be strictly eutectic (Johannes & Holtz 1996).

initiate partial melting in originally alkali feldspar-free protoliths (e.g. Thompson & Algor 1977), or occur after exhaustion of alkali feldspar by reaction [8.2]. In either case the amount of *granitic* melt formed by this reaction is buffered by aqueous fluid, as well as the potassic end-member in the muscovite (Harris & Inger 1992). Rocks undergoing melting by reaction [8.3] would progressively evolve towards reaction [8.1] as melting continues and fluid becomes progressively exhausted. This also involves a temperature increase, so a sustained heat source is required for reaction [8.1] to be reached.

8.2.2 P-T regime for anatexis

Anatexis in the northeastern GRC proceeded at higher pressure than invariant point I_3 in Figure 8.1 and is further constrained in P-T space by- (a) near-eutectic reaction [8.2], which demarcates the onset of melting in water-saturated muscovite-feldspar-quartz assemblages, (b) fluid-absent muscovite dehydration reaction [8.1], which was not reached and (c) the stability field of sillimanite. The location of CKNASH melting equilibria in P-T space for a particular protolith is determined by the anorthite content of the plagioclase (section 8.2.1), which for GRC migmatite mesosomes is less calcic than An_{40} (section 7.2.1). Based on this, partial melting in the northeastern GRC is reasonably constrained to between ~620-680°C at 350-700 Mpa (shaded area on Figure 8.2). As most partial melting is inferred to have proceeded between reaction [8.2] and [8.3], this estimate may more appropriately reduce to 630-660°C.

However, melting relations are also affected by additional components in natural systems. For example, the dehydration melting solidi for a muscovite schist (MS) and muscovite-biotite schist (MBS), as experimentally determined by Patiño Douce & Harris (1998), are 50-80°C higher than that obtained for the pure end-member assemblage muscovite-quartz-albite (Figure 8.2). Expansion of the thermal stability of muscovite, quartz and plagioclase assemblages in this case is attributed to the Ca-bearing plagioclase compositions (An_{16} in MS, An_{18} in MBS) and impurities in muscovite (Fe, Ti, Mg and particularly fluorine; Patiño Douce & Harris 1998). Substitution of femic components in muscovite of GRC migmatites (see Figures 7.8 and 7.9) probably also displaces the CKNASH reactions on Figure 8.2 to higher temperatures. Experimental studies on GRC schists are required to establish the magnitude of this shift, and thus the exact P-T location of reactions [8.1], [8.2] and [8.3].

8.2.3 Involvement of biotite in melting

As discussed above, the beginning of melting relations for GRC migmatites can be adequately modelled in the CKNASH system (Figure 8.1). In detail, equilibrium considerations require that some biotite also participates in anatexis, which is predicted to slightly lower the temperature of near-eutectic reaction [8.2] on Figure 8.2 (see Figure 7 in Thompson 1982, Figure 4 in Vielzeuf & Holloway 1988, and Patiño Douce & Johnston 1991). Nevertheless, the scarcity of biotite in leucosomes, together with its enrichment in melanosomes compared to mesosomes, indicates a very small amount of biotite is involved in anatexis. Lowering of the reaction temperatures of melting equilibria on Figure 8.2 is therefore probably of the order of a few degrees only.

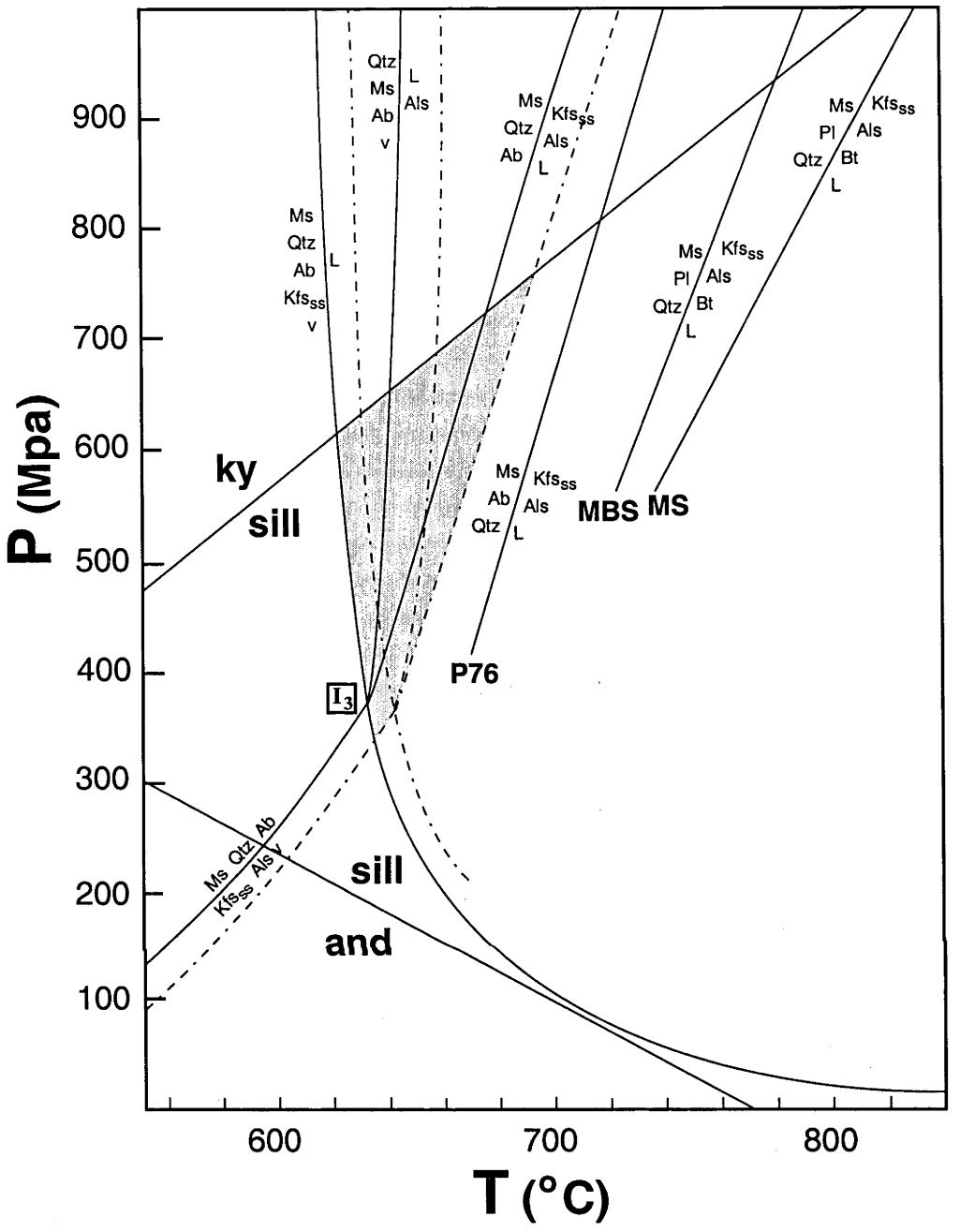

Figure 8.2. Enlargement of I_3 (Figure 8.1) with additional components also shown (mineral abbreviations are as in Figure 8.1; 'v' is aqueous fluid at a_{H_2O} ~1; Bt, biotite). The reactions Ms + Qtz + Ab + Kfs_{ss} + v = L, Ms + Qtz + Ab = Kfs_{ss} + Als + v and Ms + Qtz + Ab = Kfs_{ss} + Als + L are taken from Johannes & Holtz (1996) and appropriate for muscovite of K/K+Na = 0.9 and alkali feldspar of K/K+Na = 0.7. The reaction Ms + Qtz + Ab + v = Als + L is from Thompson & Tracy (1977). Dashed curves represent the above four equilibria for plagioclase of An_{40}, the most calcic plagioclase composition in the protolith to GRC migmatites. Of these, the beginning of melting curve (Ms + Qtz + Pl + Kfs_{ss} + v = L) is from Johannes & Holtz (1996), with the position of the other three estimated assuming a similar temperature displacement. The shaded area represents the possible P-T regime for *in situ* anatexis in the northeastern GRC. The experimentally-determined dehydration melting solidi for end member muscovite-quartz-albite (from Peto 1976, labelled 'P76') and Himalayan muscovite schist ('MS', An_{16}) and muscovite-biotite schist ('MBS', An_{18}) from Patiño Douce & Harris (1998) are also indicated. Al_2SiO_5 polymorph stability relations are from Holdaway (1971).

The role of biotite in *in situ* partial melting is readily appreciated from Figure 8.3, where granitic leucosomes are plotted on a modified AKF ternary diagram, together with muscovite and biotite from the same migmatite sample. As most *in situ* leucosomes fall within the compositional field defined by coexisting feldspar, muscovite and biotite, they have more ($FeO+TiO_2+MgO$) than can be accounted for by melting muscovite-feldspar-quartz assemblages alone, and require some dissolution of biotite. During cooling, these leucosomes must also have crystallised a small amount of biotite. Importantly, diatexite segregations **98-R3** and **97-286-1L** are more ($FeO+TiO_2+MgO$)-rich than the migmatite muscovite field. This reflects the conspicuous melt-precipitated biotite in these samples (which is chemically distinct in **97-286-1L**, Table 7.5) and implies more substantial biotite dissolution during formation of the parental diatexite (section 8.3.3). Elevated ($FeO+TiO_2+MgO$) in **98-R3** is also partly due to minor content of entrained restitic biotite aggregates.

At the opposite extreme, several leucosomes on Figure 8.3b plot close to the feldspar-muscovite join, implying that they are essentially quartz-feldspar-muscovite mixes. For these samples biotite dissolution during melting was negligible.

8.2.4 Origin and significance of muscovite in migmatite melanosomes

Muscovite is common in melanosomes of stromatic migmatites (Tables 5.3, 5.4), and, because of its role in inferred partial melting reactions, potentially provides important information on the nature of *in situ* anatexis (section 4.3.2). Melanosome muscovite occurs either as S_2-parallel euhedral grains interleaved with biotite, or coarse ragged flakes that overprint the foliation. While the latter are obviously secondary, the origin of the well-shaped muscovite requires clarification.

Since M_2 partial melting post-dates development of the regional S_2 foliation, and pervasive mineral alignments are not associated with D_3 or D_4 structures, S_2-aligned muscovite in M_2 migmatites must have crystallised during prograde metamorphism. Foliated melanosome muscovite in these samples is therefore construed as primary and 'residual' from M_2 partial melting, and cannot have formed by retrograde back-reaction during cooling.

Well-shaped muscovite in melanosomes of M_1 migmatites is interwoven with refractory biotite, and morphologically (and chemically) identical to muscovite in adjacent unmelted mesosomes. This suggests it is also residual from partial melting. However, subsequent to solidification M_1 migmatites have been overprinted by D_2, during which retrograde muscovite might also recrystallise parallel to S_2 and therefore be difficult to distinguish from prograde muscovite pre-dating anatexis. Nonetheless, evidence from Robson Creek suggests that retrograde muscovite retains a ragged, spindly appearance even where aligned with S_2 (section 5.3.3). It also tends to 'overgrow' refractory melanosome biotite rather than be intimately interpenetrating, as is the case for euhedral muscovite. Muscovite formed by retrogression of sillimanite is also easily distinguished, having a conspicuous fibrous or 'silky' aspect and invariably enclosing relict fibrolite. This indicates that peritectic sillimanite is incompletely resorbed by back reaction, despite intense deformation.

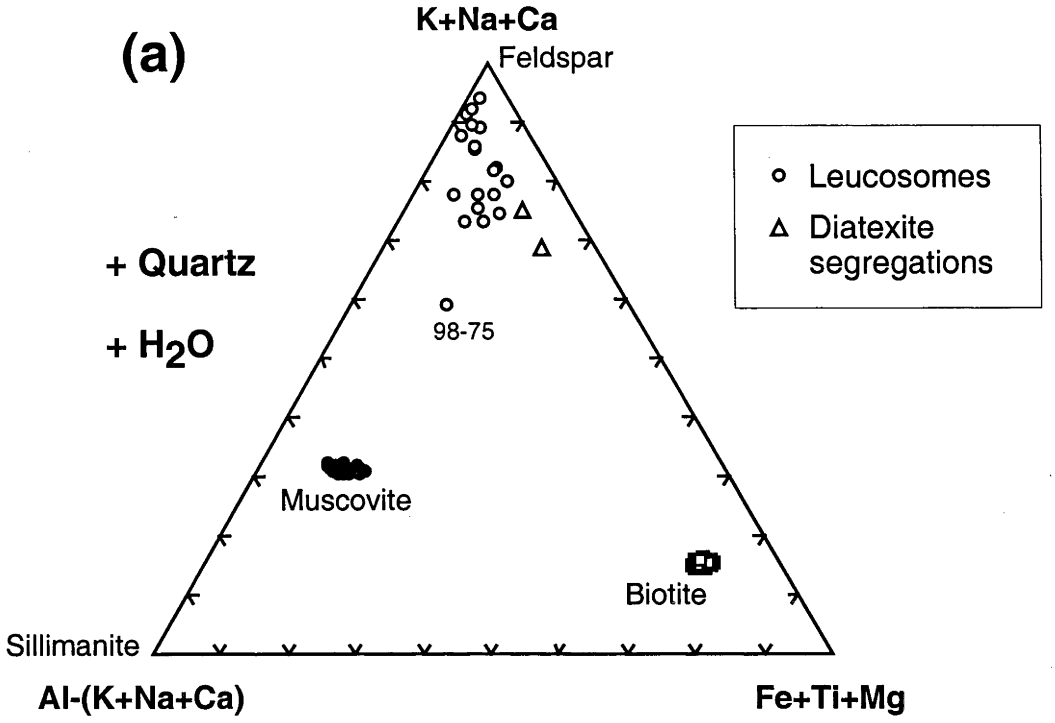

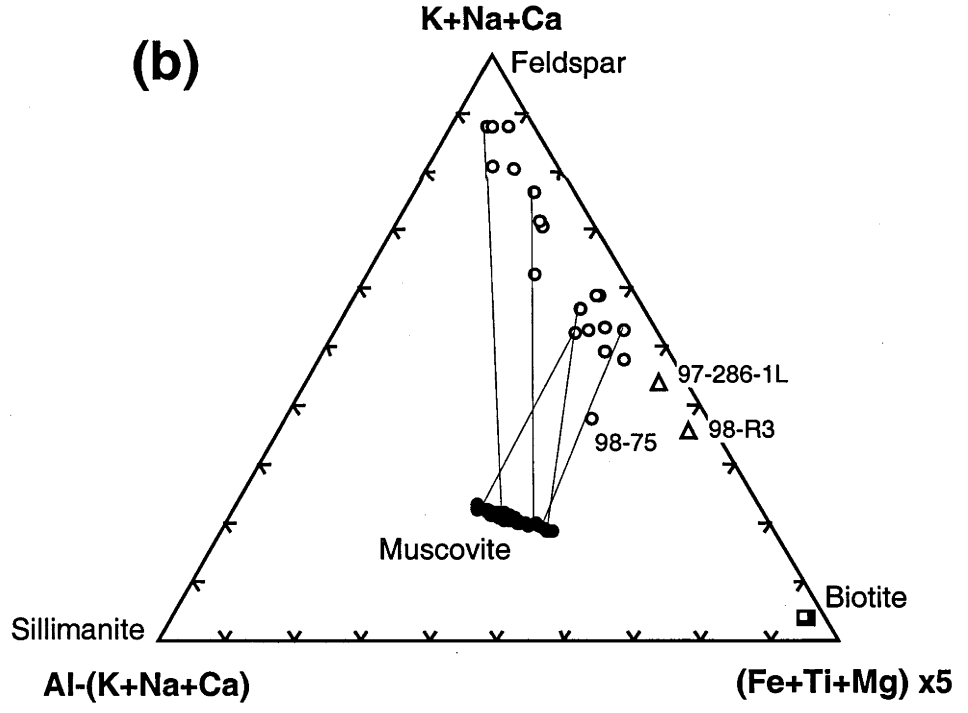

Figure 8.3. (a) Modified AKF diagram (in mole percent) for granitic leucosomes and diatexite segregations, together with coexisting muscovite (n = 51) and biotite (n = 100; from leucosomes, mesosomes and melanosomes). Note the small compositional range of micas despite the large number of analyses from different samples. Sample **98-75**, contaminated by entrained biotite-sillimanite clots, has higher (Fe+Ti+Mg) than other leucosomes (apart from diatexite segregations) and plots closest to the Al-(K+Na+Ca) apex. (b) The same diagram as (a) but with (Fe+Ti+Mg) multiplied by five to expand the compositional range of leucosomes. Tie lines connect leucosomes and muscovite from the same migmatite sample.

Hence, in the ensuing discussion the euhedral S_2-aligned muscovite in melanosomes of M_1 migmatites is also interpreted as a primary mineral in excess amounts required for partial melting.

8.3 Formation of granitic migmatites

Field and petrographic evidence suggests that M_1 and M_2 partial melting in the northeastern migmatite zone was largely controlled by fluid-present, near-eutectic reaction [8.2], though peritectic reaction [8.3] was locally significant, producing residual sillimanite (Table 8.1). Specific examples from various localities are considered below.

8.3.1 Granitic leucosomes formed during M_1 (pre- to syn-D_2)

Lack of sillimanite indicates that the M_1 granitic leucosomes in quartzofeldspathic migmatites of northern Schofield Creek, Chin Chap Creek and Robson Creek valley were generated by reaction [8.2]. Occurrence of residual muscovite in many samples further suggests that anatexis was terminated by the exhaustion of alkali feldspar in the protolith. However, some mesosomes have alkali feldspar and primary muscovite (e.g. **97-R1**), and are still fertile. Most leucosomes of interlayered semi-pelitic schist (e.g. 98-25M1) are alkali feldspar deficient (tonalitic) and are treated in section 8.6. The exception is quartz-rich leucosome **98-WF2A-2L** from northern Schofield Creek, which has minor alkali feldspar (Table 5.3; see below).

More complex partial melting scenarios are manifest in the M_1 stromatic migmatites within unit G of Robson Creek gorge, which contain sillimanite (see section 5.3.3). Enclosure of fibrolite by large ragged muscovite flakes in melanosomes (e.g. 99-5) indicates generation of leucosomes by peritectic reaction [8.3], with retrogression of sillimanite upon back-reaction with cooling, hydrous melt. Subordinate euhedral melanosome muscovite is primary and residual from anatexis. Since mesosomes several centimetres from leucosomes have alkali feldspar, melting was probably initiated by near-eutectic reaction [8.2], but evolved through to peritectic reaction [8.3] as alkali feldspar became locally exhausted.

Occurrence of sillimanite in melanosomes (but not mesosomes) indicates that peritectic reaction [8.3] has also controlled partial melting in other unit G migmatites, where quartz-rich leucosomes contain clots of melt precipitated sillimanite (Table 8.1). The thick biotite-rich melanosomes also imply a high degree of anatexis, such that muscovite was eliminated from the residue. However, since prograde muscovite is extant in melanosomes of more feldspathic leucosomes in the same outcrop, the extent of M_1 partial melting was evidently variable within individual horizons. Nevertheless, the presence of relict, muscovite-enveloped sillimanite strands in melanosomes of feldspathic leucosomes also suggests development by reaction [8.3].

Importantly, leucosomes within unit G outcrops are laterally heterogeneous, such that feldspathic leucosomes commonly grade into quartz-rich leucosomes with minor plagioclase and no alkali feldspar (section 5.3.3). This compositional variability is inconsistent with closed system crystallisation, but implies movement of magma, perhaps during extraction of a melt phase from the partially solidified leucosome. Since textural evidence suggests that the initial liquidus phases of M_1 leucosomes were quartz and plagioclase (section 5.3.3) the residual melt

Sample	*Locality*	*Bulk comp.*	*Melano. (+ qtz)*	*Melt reaction*	*Comment*
M_1					
outcrop	SC (nth), CC	qtzofelds	bi ± mu ± mu*	8.2	Melting terminated by exhaustion of musc and/or afs in protolith
98-WF2A	SC (nth)	semi-pelite	bi, mu	8.2	Leucosomes are quartz-rich, afs-poor, and have experienced melt loss
97-R1	RC valley	qtzofelds	bi, mu* ± mu	8.2	Mesosome still fertile, with musc and afs
99-5	RC gorge (unit G)	semi-pelite	bi, mu*, sill, mu	8.2, 8.3	Melting initiated by reaction 8.2 but evolved through to reaction 8.3 by local exhaustion of afs. Most melanosome muscovite formed by back reaction of sill, but some euhedral flakes are residual.
outcrop	99-5b, 99-7 (RC gorge unit G)	qtzofelds & semi-pelite	bi , sill ± mu*	8.3	Qtz-rich leucos have sill clots and exhibit evidence for melt migration. Higher degree of melting than sample 99-5
M_2					
98-RM1 & 99-1C	RC gorge (unit D)	qtzofelds	bi, mu ± mu*	8.2	Melting ceased with exhaustion of afs
98-R2A & 98-RG3	RC gorge (unit D)	qtzofelds	bi, mu, mu*	8.2	Mesosomes still fertile, with musc + afs
99-7	RC gorge (unit F)	semi-pelite	bi, mu*, mu, sill	8.2, 8.3(?)	Sill is S_2-parallel, suggesting formation prior to M_2. Production of some sill during melting cannot be discounted.
98-R5B	RC gorge (unit H)	qtzofelds	bi, mu*, sill	8.2, 8.3(?)	As above
97-244	RC valley	qtzofelds	bi, mu	8.2	Melting ceased with exhaustion of afs
98-102 & *outcrop*	Chin Chap Ck	qtzofelds	bi ± mu	8.2	Mesos have abundant afs, rarely with primary mu. Sill is absent.
97-349	Bryan Creek	qtzofelds	bi, mu*	8.2	Meso depleted in afs within 3 cm of leuco and lacks mu; suggests reaction 8.2
98-WF1A	SC (nth)	qtzofelds	bi, mu	8.2	Mesosome lacks afs, but has abundant mu
98-25M2	SC (nth)	semi-pelite	bi, mu	8.2	Mesosome lacks afs, but has abundant mu
98-65	SC (nth)	qtzofelds	bi, mu*	8.2	Mesosome has no primary musc
outcrop	SC (sth)	qtzofelds, semi-pelite	bi, mu, ± sill, ±mu	8.3, 8.2?	As some mesosomes have afs, initial melting may have been by reaction 8.2
99-11 & 99-12	SC (sth)	qtzofelds	bi, sill, mu*	8.3	Leuco is rich in qtz and pfs and lost melt. Sill forms unretrogressed clots in leuco.

Table 8.1. Summary of the major inferred melting reactions for granitic migmatites in the eastern GRC (CC = Chin Chap Creek, RC = Robson Creek, SC = Schofield Creek). Mineralogical details for individual migmatites are in Table 5.3 (M_1) and Table 5.4 (M_2). 'Outcrop' in the sample column indicates that the information for the designated locality is summarised from generalised outcrop observations. Abbreviations are as for Table 5.3, with bi = biotite, mu = prograde muscovite, mu* = secondary muscovite.

in equilibrium with these crystals would be enriched in K_2O and H_2O (e.g. Ellis & Obata 1992). Extraction of this could therefore account for the absence of alkali feldspar in quartz-rich leucosomes and the preservation of peritectic sillimanite. In contrast, peritectic sillimanite has undergone extensive back-reaction to muscovite in melanosomes of feldspathic leucosomes, indicating retention of the melt during consolidation. The fugitive melt fraction from quartz-rich leucosomes has either been redistributed within the migmatite or migrated from the outcrop, being now represented by the deformed pegmatitic veins and sheets contained by adjacent metasedimentary rocks.

Hence, rather than representing segregated liquids that crystallised essentially *in situ*, some M_1 leucosomes within Robson Creek migmatites are more likely to be accumulations of early precipitated crystals from which varying amounts of K-rich melt have been extracted. A similar scenario is applicable to Schofield Creek leucosome **98-WF2A-2L**, which exhibits the same outcrop features (section 6.4.4) and is the most siliceous and K_2O-poor of analysed leucosomes (section 7.5). In these cases, leucosome mineral proportions are dictated by the stage of crystallisation at which melt migrates from the rock, and the efficiency of melt extraction.

8.3.2 Granitic leucosomes formed during M_2 (syn-D_3 to post-D_4)

(a) Robson Creek

Significant M_2 anatexis in Robson Creek is confined to lithological units B, D, F and H in the gorge section of the watercourse (Table 5.2). Since stromatic migmatites of unit D have melanosome muscovite without sillimanite they most likely formed by reaction [8.2]. Anatexis may have been terminated by exhaustion of alkali feldspar in the protolith for samples **98-RM1** and 99-1C, whose mesosomes lack alkali feldspar. However mesosomes of adjacent migmatite samples (**98-R2A** and 98-RG3) contain muscovite and alkali feldspar, and could therefore still potentially generate granitic melt.

Migmatites of unit F and H contain a small amount of sillimanite (Table 5.4), though this contains S_2, suggesting crystallisation during an earlier pre- to syn-D_2 reaction unrelated to M_2 anatexis. Development of leucosomes within these rocks therefore occurred primarily by near-eutectic reaction [8.2], with entrainment of foliated sillimanite tufts from the melanosome during segregation of the melt. This is consistent with the occurrence of primary muscovite and alkali feldspar in mesosomes. However, as the latter is erratically distributed, some generation of partial melt within these horizons by peritectic reaction [8.3] cannot be precluded.

M_2 anatexis in the valley section of Robson Creek was more limited (section 5.4) but, as migmatites lack sillimanite, was apparently controlled by reaction [8.2] (Table 8.1).

(b) Schofield Creek

M_2 stromatic migmatites in northern Schofield Creek lack sillimanite and have therefore evolved by reaction [8.2], which ceased with exhaustion of muscovite or alkali feldspar (Table 8.1). In contrast, leucosomes and melanosomes of southern Schofield Creek migmatites contain fibrolite. The absence of sillimanite in mesosomes of these rocks suggests that its crystallisation

was linked to anatexis, and development of leucosomes by melting reaction [8.3] is therefore indicated. As some mesosomes are alkali feldspar-bearing, part of the melt fraction may initially have also been generated by near-eutectic reaction [8.2]. Although melt migration features are obvious in outcrop, most peritectic sillimanite has retrograded to muscovite, except where armoured by quartz.

(c) Chin Chap Creek and Bryan Creek

Sillimanite is rare in M_2 migmatites of Chin Chap Creek, which together with alkali feldspar-bearing mesosomes (e.g. **98-102**, Table 5.4) suggests partial melting by near eutectic reaction [8.2] (Table 8.1). Although not examined in detail, quartzofeldspathic migmatites of Bryan Creek appear to have also undergone anatexis by reaction [8.2] (Table 8.1). Peritectic melting reactions may have been reached in semi-pelitic horizons, which contain sillimanite (section 5.7.2).

8.3.3 Diatexites

Unlike stromatic migmatites, diatexites in Schofield Creek, Bryan Creek and Robson Creek have a large pervasive melt fraction, such that separation of melt from the solid residue is comparatively limited (section 5.3.4); a fundamentally different melt generation and segregation mechanism is implicit. Although S_2-aligned sillimanite bundles in the schlieric portions of these rocks were probably inherited from the protolith, sheaves of unaligned sillimanite indicate that anatexis involved an aluminosilicate-producing reaction. The paucity of prograde muscovite in micaceous enclaves accords with a high degree of partial melting, such that this phase was largely eliminated from the residue. A high degree of anatexis is also suggested by the numerous magmatic biotite grains in leucogranitic domains, consistent with greater biotite dissolution during melting compared to stromatic migmatites (section 8.2.3). The poor melt-residue segregation in diatexites accounts for the abundant secondary muscovite (see Table 5.6), formed by back reaction upon cooling.

As sillimanite coexists with alkali feldspar in diatexites, it is difficult to unequivocally determine whether the melt fraction was generated by fluid-present peritectic reaction [8.3] or muscovite dehydration-melting reaction [8.1]. In the latter case, alkali feldspar in diatexites would have formed as a solid peritectic reaction product, as well as being an early liquidus phase. However, textural evidence indicates that rather than forming early, alkali feldspar in Robson and Schofield Creek diatexites crystallised from the melt simultaneously with quartz in the latter stages of solidification (section 5.3.4). Further, residual sillimanite in diatexites is associated with quartz and plagioclase rather than alkali feldspar, which also argues against reaction [8.1]. Hence, petrographic evidence is most consistent with formation of diatexites by fluid-present melting reaction [8.3], with significant participation of biotite.

8.4 Discussion: synthesis of partial melting in granitic migmatites

8.4.1 Melting reactions

It is noteworthy that in stromatic migmatites thought to have undergone anatexis by peritectic reaction [8.3] the modal proportion of sillimanite (including that replaced by muscovite) is very minor, generally less than 1%. This contrasts with the much higher sillimanite proportions estimated for migmatites formed by muscovite-involved peritectic reactions elsewhere. For example, migmatites in British Columbia formed by muscovite dehydration melting contain an average of 20 vol. % sillimanite (Nyman *et al.* 1995). Similarly, in a metapelitic protolith from the High Himalaya, Harris & Inger (1992) calculate residual sillimanite contents of 22 and 15 wt. % from the incongruent melting of muscovite under fluid present and fluid absent conditions respectively, based on mass balance constraints.

The paucity of sillimanite in GRC stromatic migmatites therefore implies that reaction [8.3] contributed only minimally to the *in situ* melt fraction, with most of the leucosome volume instead generated by near-eutectic reaction [8.2]. Reaction [8.3] may have only proceeded in some migmatitic horizons late in the anatectic evolution as alkali feldspar was exhausted by prior partial melting. Melting in other migmatites (e.g. northern Schofield Creek and Robson Creek) did not reach peritectic reaction [8.3], despite the abundance of muscovite with plagioclase and quartz in mesosomes (Table 8.1).

8.4.2 Source of aqueous fluid

Although petrological evidence suggests that partial melting in the northeastern GRC proceeded in the presence of aqueous fluid, the characterisation of this fluid phase is not addressed by this study. Nevertheless, some general comments are possible. The limited nature of melting during M_1 implies either a waning heat source or restriction in the fluid supply. As M_1 (pre- to syn-D_2) and M_2 (pre-D_3 to post-D_4) are part of the same short-lived orogenic cycle, significant fluctuations in the regionally-perturbed geotherm are unlikely, with exhaustion of the fluid phase being more feasible. In view of this, it is possible that the source of water for M_1 was trapped pore fluid, which would be minor and rapidly consumed by anatexis, leading to low melt fractions (Clemens & Vielzeuf 1987).

To account for the rapid and more voluminous (but selective, see below) partial melting of M_2 it is necessary to appeal to ingress of externally-derived fluid into the metasedimentary pile, which remained at temperatures above the water-saturated solidus following cessation of M_1.

8.4.3 Origin of Robson Creek layering

The confinement of significant partial melting (both M_1 and M_2) to discrete horizons is a striking aspect of the Robson Creek gorge metasedimentary sequence (section 5.3). Further, intensely migmatitic rocks are interspersed with quartzofeldspathic gneisses that exhibit no leucosome development, despite in many cases having the mineralogical reactants necessary to undergo partial melting by near-eutectic reaction [8.2]. This localisation of partial melting

implies variable fluid ingress, such that some parts of the sequence experienced fluid flushing, whereas adjacent horizons received insufficient fluid flux to initiate partial melting. The reasons for variable fluid flow through the metasedimentary sequence are unknown, but as partial melting was syn-deformational, it is possible that fluid infiltration was controlled or channelled into discrete bands by deformation (see below). Nevertheless, many migmatite mesosomes in Robson Creek gorge contain fertile assemblages and are still capable of yielding granitic melt. Anatexis in these rocks was arrested either by temperature and/or pressure decrease, or by exhaustion of aqueous fluid.

8.4.4 Implications for the formation of diatexites

Structures in diatexites are interpreted to reflect bulk magmatic flow, stimulated by the partitioning of D_3 shear strain into the melt-rich diatexite horizon during anatexis (section 5.8.1). Syn-melting shearing might also account for the pervasive melt fraction of diatexites. As discussed above, the localisation of M_2 anatexis in Robson Creek gorge may reflect structural controls on the ingress of aqueous fluid. However, it is likely that fluid flow would be particularly focussed into zones of concentrated shear strain. In this case, more pervasive, grain-scale fluid infiltration through the shearing rock matrix at hypersolidus temperatures would promote generation of a large, more pervasive melt fraction. Dramatic mechanical weakening of the rock matrix would further localise shear strain, and as the melt fraction throughout the rock increased, ultimately bulk magmatic flow would occur. It is during this stage that disruption of interlayered refractory horizons is expected, leading to the formation of the 'enclaves' or rafts of unmelted quartzofeldspathic schist within GRC diatexites.

Note that non-coaxial deformation stimulates migration of partial melt into dilational sites, such as boudin necks and extensional shear zones, facilitating efficient segregation of melt from residue (Brown 1994; Sawyer 1994; Brown *et al.* 1995). Accumulation of melt to high proportions in syn-deformational GRC diatexites without effective segregation therefore requires that the rate of melt generation surpassed the rate at which melt could be extracted (Sawyer 1994, 2000). This accords with the triggering of rapid anatexis by channelled fluid infiltration, a similar scenario envisaged by Sawyer (1998) for diatexites of the Opatica subprovince in the Canadian Shield.

8.5 Origin of the chemical character and diversity of granitic leucosomes

8.5.1 Melt versus cumulate origin for in *situ* leucosomes

Anatectic leucosomes of migmatitic rocks may represent 'frozen' partial melts or alternatively comprise variable combinations of former melt and crystals, the latter being either melt-precipitated or entrained residual phases (peritectic reaction products and/or refractory minerals). At the extreme, leucosomes may even be 'cumulates' of early liquidus or peritectic crystals from which an evolved melt phase has been extracted (Sawyer 1987; Ellis & Obata 1992; Solar & Brown 2001).

In GRC migmatites, several lines of evidence suggest that most analysed leucosomes formed by crystallisation of a locally derived melt phase containing few suspended crystals. Firstly, outcrop

relationships demonstrate efficient segregation of partial melt during leucosome formation, such that biotite-rich residual material was not significantly entrained. This is supported by chemical evidence (section 8.2.3 and 8.5.3). The only exception is leucosome **98-75**, where spalled fragments of sillimanite-biotite melanosome result in clearly higher (Fe+Mg+Ti) and excess Al_2O_3 (Figure 8.3). Secondly, petrographic and chemical evidence precludes leucosomes being largely cumulates of liquidus minerals following migration of a fractionated melt. Plagioclase and quartz were the first minerals to crystallise (section 8.3.1), and hence these would be the cumulus phases. However, plagioclase laths do not form a contiguous framework in leucosomes, as is characteristic of cumulate rocks, but are separated by quartz grains or embedded in poikilitic alkali feldspar. Textural heterogeneities that typify melt extraction (see section 8.3.1) are not present within analysed leucosome portions. The chemical effects of melt loss are exemplified by M_1 leucosome **98-WF2A-2L**, which compared to other leucosomes has anomalously high silica and low K_2O (section 7.5).

Finally, and most compelling, are coherent chemical linkages between leucosomes and complementary mesosomes (see below) and geochemical equivalence with residue-poor granitic pools, dykes and sheets (section 7.6) and larger leucogranitic plutons (section 9.5). While the higher Sr leucosomes (**98-65A**, **98-65B**, **98-102**) do not have granitic dyke/sheet correlatives[2], they have abundant modal alkali feldspar, lack commensurate CaO enrichment (Figure 7.12) and have high Ba contents (>1100 ppm). Such features are inconsistent with accumulation of liquidus plagioclase and extraction of K_2O-rich melts during crystallisation, but imply derivation from a relatively Sr-rich metasedimentary precursor (below).

8.5.2 Interpretation of leucosome geochemistry

To evaluate the geochemistry of formerly melt-dominated leucosomes it is necessary to take several factors into account. Paramount of these are- (1) the bulk source rock composition, which dictates the assemblage and compositions of mineral phases, (2) the degree of partial melting, and (3) the nature of the partial melting reactions, which are in turn controlled by P, T and presence/absence of a fluid phase. Disequilibrium processes may also be influential for elements accommodated by accessory minerals such as zircon or apatite (e.g. Sawyer 1991; Watt & Harley 1993; Bea 1996a, 1996b; Watt *et al.* 1996). Modification of primary leucosome compositions by fractional crystallisation during movement of partial melt from the generative site has also been documented (Sawyer 1987). Of these factors, the melting reaction is particularly important, as it governs which minerals participate in (or are largely inert during) anatexis, and therefore controls the distribution of chemical components between the melt and refractory phases. The extent to which this chemical fractionation signature is recorded by the leucosome geochemistry depends on how effectively the melt fraction segregates from residual material during formation of the leucosome.

[2] Note however that leucosome **98-102** from Chin Chap Creek is compositionally very similar to adjacent muscovite-bearing 'Kassingbrook type' granitic rocks, which are discussed in Part III.

The leucosomes of GRC migmatites were generated by quartz-feldspar-mica partial melting reactions in protoliths of limited chemical variability. Hence, the overall chemical character and marked compositional diversity of granitic leucosomes is investigated in terms of elements controlled by- (1) feldspars (K, Sr, Ba, Pb), (2) micas (Ti, Fe, Mg, Rb), and (3) accessory minerals (P, Y, HFSE, REE).

(1) Elements controlled by feldspars

(a) Potassium

Granitic leucosomes are characterised by striking variation in K_2O content, which is obvious on a Harker variation diagram (Figure 7.14) as well as a normative Q-Ab-Or plot (Figure 7.13). Since most K_2O is accommodated by alkali feldspar, with lesser (almost trivial) amounts in muscovite and biotite, this manifests mineralogically in differing modal proportions of alkali feldspar (see Table 5.4). Importantly, strong normative orthoclase and K_2O variation parallel to that of granitic leucosomes is also apparent within quartzofeldspathic metasedimentary rocks of the 'optimum fertility window' (Figures 7.13, 7.14). As these are envisaged to be the potential protoliths to *in situ* partial melts, this raises the possibility that the K_2O spread of granitic leucosomes is largely a function of source rock composition.

This is confirmed by the systematic geochemical correlation between each leucosome and its adjacent mesosome, such that high K_2O mesosomes are consistently associated with high K_2O leucosomes, and lower K_2O mesosomes are complementary to low K_2O leucosomes (Figure 8.4). In all cases leucosomes are more siliceous and K_2O-rich than coexisting mesosomes. A similar relationship is evident for leucocratic segregations in diatexite horizons (**98-R3** and **97-286-1L**) and their host. The regularity of this geochemical coupling implies that *in situ* leucosomes and mesosomes are fundamentally related, and is consistent with the host mesosome approximating the specific protolith composition for each adjacent leucosome. Note that although being chemically analogous to the source composition, in many instances the mesosomes lack a necessary reactant, either alkali feldspar or muscovite, to be fertile and cannot alone have generated the coexisting leucosome (Table 5.4). However, other mesosome samples in Table 5.4 contain the necessary minerals for melt production and, allowing for subtle modal variations in metasedimentary horizons, may more closely approach the protolith composition.

Hence, the large spread in K_2O contents exhibited by granitic leucosomes directly reflects a similar K_2O dispersion within the inferred source rock, itself a function of sedimentation processes.

(b) Ba and Sr

Coherent chemical linkages between *in situ* leucosome-mesosome pairs are also evident on a Ba versus Sr plot (Figure 8.5). Here, leucosomes have consistently higher Ba and Sr concentrations than their complementary mesosome and inferred source, suggesting preferential partitioning of these elements into the melt upon anatexis. Leucocratic segregations also have markedly higher Ba and Sr than their host diatexite. Most Sr within the protolith is expected to reside within plagioclase, with a smaller amount in alkali feldspar (Bea *et al.* 1994), both of which participate

in the postulated melting reactions (section 8.2.1). Production of Sr-enriched leucosomes therefore requires that these phases (especially plagioclase) be mostly consumed in the source during anatexis, leaving a residue for which Sr is largely incompatible. This is consistent with the mineralogy of migmatite melanosomes, which mostly lack plagioclase and are dominated by biotite and quartz, neither of which accommodates Sr. Thus, upon anatexis Sr partitions into the melt fraction, imparting the distinctive high Sr signature of granitic leucosomes. To some extent, the Sr abundance of leucosomes also images its concentration in the protolith (which is relatively high), though the relationship is less systematic than for K_2O. The source-based influence is best exemplified by the Sr-enriched leucosomes **98-65A** and **98-65B**, which are hosted by the highest Sr mesosome (**98-65C**; Figure 8.5). Notably, the high Sr character of these leucosomes correlates with higher whole rock An/Ab (Figure 8.6), resulting in crystallisation of relatively calcic plagioclase (section 7.2.1). This also reflects the adjacent mesosome **98-65C**, which has higher An/Ab and plagioclase that is more anorthitic than other mesosomes (Figure 8.6; section 7.2.1). Together with the elevated Sr concentration, higher Ca/Na accords with a

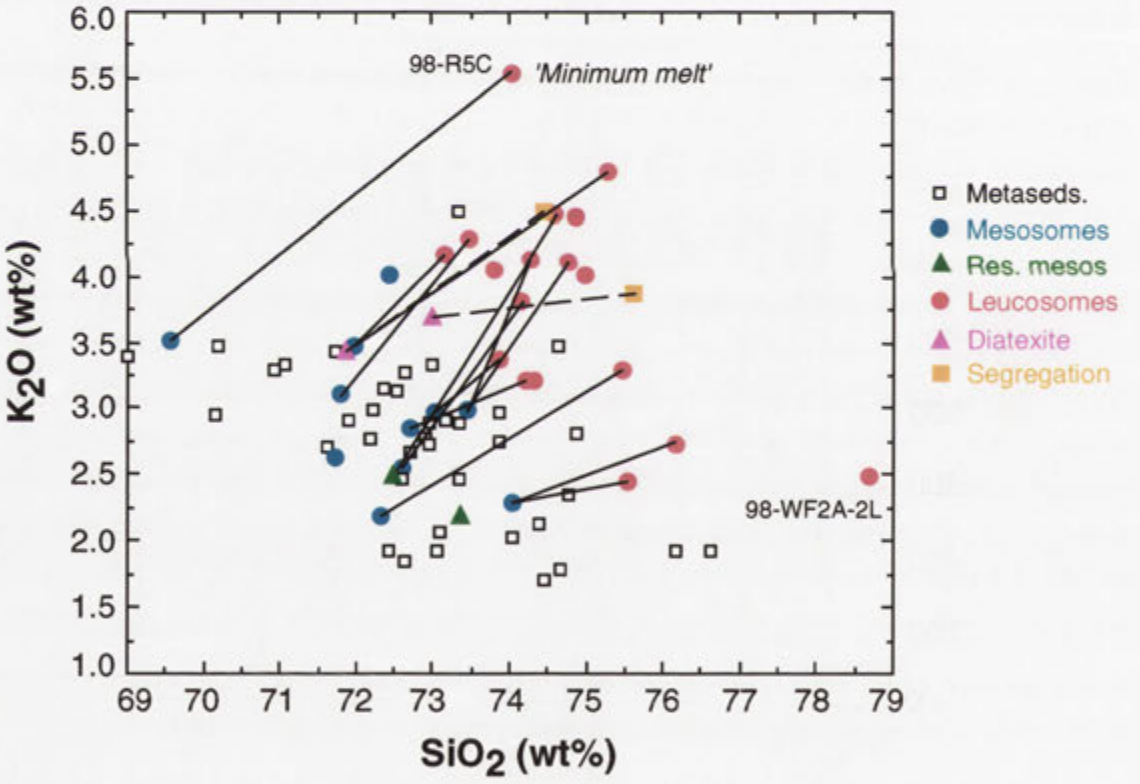

Figure 8.4. K_2O vs SiO_2 (in weight percent) for *in situ* leucosomes of granitic migmatites and complementary mesosomes (connected by tie lines). Whole rock diatexite samples are also joined to their leucogranitic segregations by the lines (dashed). 'Metaseds' are metasedimentary rocks of both migmatite and sub-migmatite grade from across the GRC. 'Res. mesos' are residual mesosomes **99-5RB** and **99-14**, from which a partial melt fraction has been extracted. Note that the most potassic leucosome, **98-R5C**, approaches the 'minimum melt' composition in the haplogranodiorite system at neutral peraluminosity (i.e. A.S.I = 1.0; section 8.5.4). The most siliceous leucosome, **98-WF2A-2L** is enriched in liquidus quartz.

small sedimentary carbonate component in the protolith to mesosome **98-65C** (section 7.4.2). Leucosome **98-102** also has high Sr and calcic plagioclase, which similarly implies derivation from a high Sr, high Ca/Na metasedimentary protolith.

Similarly, strong partitioning of Ba into leucosomes upon partial melting indicates formation of a Ba-depleted residue and elimination of Ba-accommodating mineral phases, chiefly alkali feldspar and muscovite, from the protolith during partial melting. Crystallisation of peritectic alkali feldspar in melanosomes is also precluded, which accords with the fluid-present anatexis proposed for GRC migmatites, where the alkali feldspar component is alternatively dissolved in the melt. Pronounced Ba-enrichment in leucosomes also indicates incompatibility with residual biotite, consistent with the low partition coefficient (D) for Ba between melanosome biotite and leucosome partial melt (~0.59) measured by Bea *et al.* (1994) from natural migmatites; significantly, the melt composition used by these authors is peraluminous and K_2O-rich, therefore resembling leucosomes of this study. As with Sr, the content of Ba within leucosomes to some extent images that in the complementary mesosome and inferred source rock, with the highest Ba leucosomes adjacent to the highest Ba mesosomes (Figure 8.5).

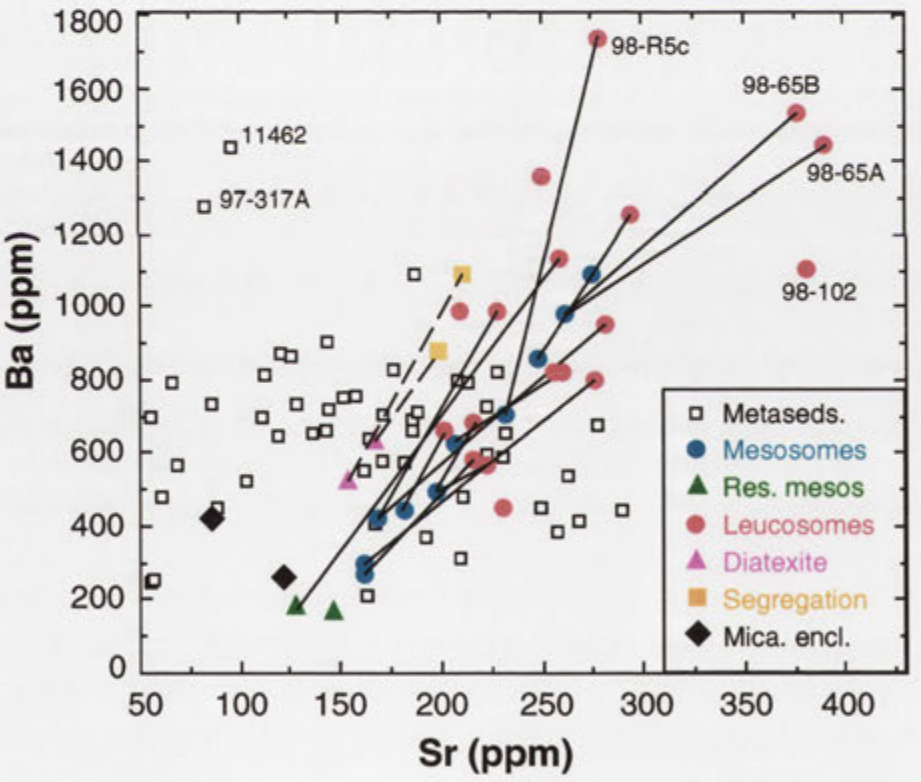

Figure 8.5. Ba vs Sr for *in situ* leucosomes of granitic migmatites and complementary mesosomes (connected by tie lines). Whole rock diatexite samples are also joined to their leucogranitic segregations by dashed tie lines. 'Metaseds' are metasedimentary rocks of both migmatite and sub-migmatite grade from across the GRC, whereas 'Res. mesos' are mesosomes from which a partial melt has been extracted (**99-5B** and **99-14**). Micaceous enclaves (mica. encl.) **98-SEL** and **98-27**, collected from the Schofield Adamellite, are shown for comparison with sillimanite schist 11462 (from Ferguson 1993) and muscovite schist **97-317A** (migmatite zone).

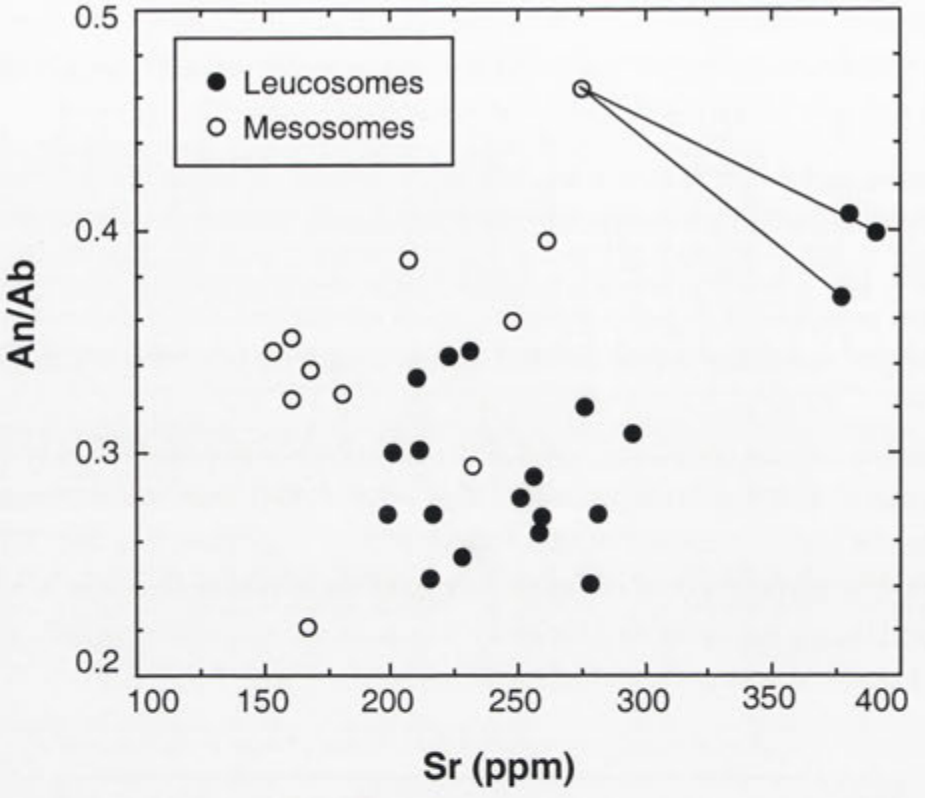

Figure 8.6. CIPW normative An/Ab as a function of Sr for *in situ* leucosomes and adjacent mesosomes. The tie line connects leucosomes **98-65A** and **98-65B** (lower An/Ab) with the host mesosome **98-65C**.

Two further points emerge from Figure 8.5. Firstly, by dual tie lines, leucosomes with slightly different Ba and Sr contents may be complementary to a single mesosome composition, the same feature apparent for K_2O (Figure 8.4). Given the small volume of leucosome material analysed, this could be an artefact of inadequate sample size. However, it could also relate to sequential leucosome formation during progressive partial melting, the most potassic and Ba-rich leucosomes being lower percent melts of the protolith. As anatexis proceeds, greater consumption of plagioclase produces more Sr-rich melts and dilutes K_2O and Ba concentrations. Chemical differences between leucosomes of the same migmatite might also reflect small-scale heterogeneities in the distribution of alkali feldspar and plagioclase in the protolith, consistent with the observed subtle and erratic modal variations of these minerals within metasedimentary rocks. More data on leucosome compositions within individual migmatite horizons is required to evaluate these possibilities.

Secondly, also indicated on Figure 8.5 are the 'residual' mesosome samples, **99-14** and **99-5B**, which are complementary to granitic leucosomes. Textural evidence suggests that these have experienced extraction of partial melt (section 7.4.1), which is compatible with the depletion in Ba and Sr relative to unmodified metasedimentary rocks. Similarly, the low Ba of micaceous enclaves **98-SEL** and **98-27** is distinct from primary metasedimentary metapelite compositions (e.g. muscovite schist **97-317A**, sillimanite schist 11462 of Ferguson 1993) which have elevated

Ba contents by contrast (Figure 8.5). This suggests that the micaceous enclaves represent melanosome fragments, entrained by the host adamellite.

(c) Pb

Marked enrichment of Pb in leucosomes relative to mesosomes (Figure 7.15) suggests strong partitioning into the melt upon anatexis. This is consistent with consumption of alkali feldspar and plagioclase, which accommodate most Pb in the protolith (Bea *et al.* 1994), and incompatibility with residual biotite ($D_{Pb}^{bio/melt} = 0.04$; Bea *et al.* 1994).

(2) Elements controlled by biotite

(a) Ti, Fe, Mg

Leucosomes have strongly depleted TiO_2 and total Fe_2O_3+MgO contents relative to their mesosomes and inferred protolith composition (Figures 7.14, 7.15). As opaque iron oxides are absent, most of these elements in mesosomes and fertile metasedimentary rocks are contained within biotite, with lesser amounts in muscovite. Hence, this confirms that both dissolution and physical incorporation of biotite into leucosomes during stromatic migmatite formation was very minor, reflecting the near-refractory behaviour of biotite during anatexis (section 8.2.3) and the effective segregation of partial melt from melanosome residues (see Chapter 5). The slightly higher TiO_2, Fe_2O_3t and MgO in sample **98-75** compared to other leucosomes (see Figure 8.3), results from small clots of entrained melanosome (section 7.5).

(b) Rb

As with Ba, the Rb budget of metasedimentary rocks is shared between potassic phases biotite, muscovite and alkali feldspar (Harris *et al.* 1995). However, strong decoupling between Rb and Ba occurs during anatexis (Figure 7.15), whereby leucosomes have systematically lower Rb than their complementary mesosome and inferred protolith (Figure 8.7). This is mostly a result of Rb retention within melanosome biotite, in accord with the high partition coefficient for Rb between biotite and K-rich leucosome partial melt (6.98) determined by Bea *et al.* (1994). Elevated Rb concentrations in 'residual' mesosome samples (Figure 8.7) and especially micaceous enclaves are consistent with this (see Figure 8.12). The concentration of Rb in melanosomes, together with partitioning of Sr into the melt, results in leucosomes having lower Rb/Sr ratios relative to source-rock mesosomes (see Figure 8.7b).

Rb is therefore an indicator of the entrainment of residual biotite, and its depletion from leucosomes further highlights the efficient segregation process envisaged during partial melting. Small, erratic variation in Rb content between other leucosomes may also be partly attributed to minor incorporation of Rb-enriched residual biotite (e.g. **98-75**), or variability in the dissolution of biotite during melting. However, as with K_2O, the Rb content of most leucosomes ultimately mirrors that in the source prior to melting (Figure 8.7a). The exception is leucosome **98-R5C**, which, although biotite-deficient (0.04% TiO_2), has an elevated Rb concentration (146 ppm) that is only slightly lower than its complementary mesosome (155 ppm). The reason for this is unclear. One possibility is that the higher Rb concentration results from incomplete equilibration

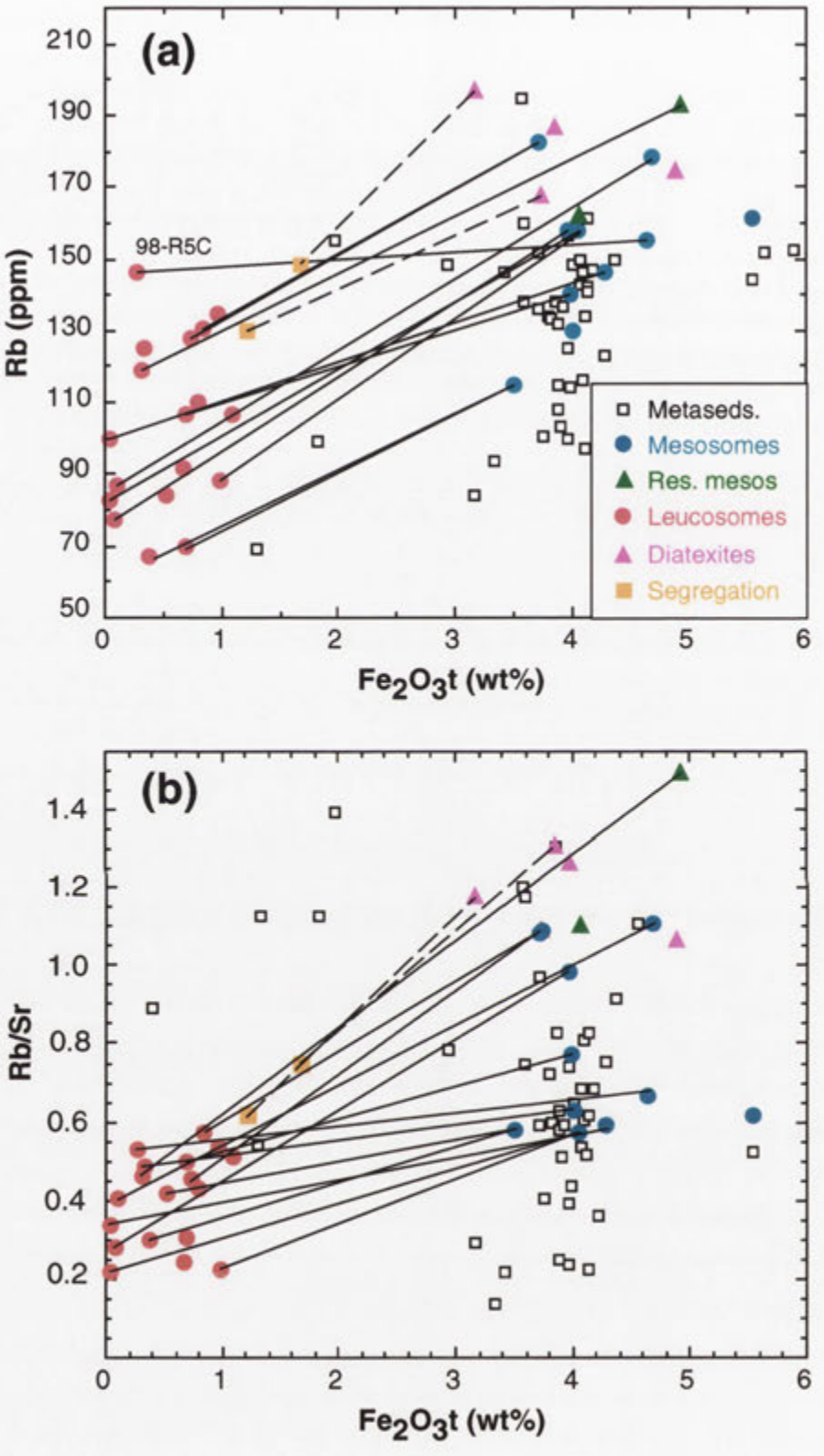

Figure 8.7. Plot of (a) Rb against total Fe_2O_3 and (b) Rb/Sr versus total Fe_2O_3 for *in situ* leucosomes of granitic migmatites and complementary mesosomes (connected by tie lines). Whole rock diatexite samples are similarly joined to their leucogranitic segregations by tie lines (dashed). 'Metaseds' are metasedimentary rocks of both migmatite and sub-migmatite grade from across the GRC.

between the partial melt and biotite-rich residue, such that the Rb content of the leucosome was governed by its concentration in minerals undergoing partial melting, rather than by residue-melt partition coefficients. This has been proposed to account for the Rb enrichment in some Himalayan leucogranites (Harris *et al.* 1995).

(3) Elements controlled by accessory minerals

Apatite and zircon are ubiquitous in GRC metasedimentary rocks and accommodate most P and Zr respectively, as well as being major reservoirs for Y, Th, Nb and the REE. Monazite also occurs and probably incorporates most of the LREE (i.e. La to Gd) and also Th (Bea *et al.* 1994). Similarly, if present, most Y and 'heavy' REE would reside within xenotime. Being essential structural constituents of accessory phases, the concentrations of P, Zr, Th, Y and the REE in migmatite leucosomes is therefore governed by the behaviour and stability of the host mineral during anatexis, rather than by bulk partition coefficients (Watt & Harley 1993). This involves an interplay between- (1) the solubility and dissolution kinetics of the host mineral in the partial melt (e.g. Harris *et al.* 1995; Bea 1996a, 1996b), (2) the ability of the accessory phase to interact with the melt (Bea 1996a, 1996b), and (3) the extent to which residual crystals of the host mineral are entrained into the partial melt.

Leucosomes of GRC migmatites are depleted in Zr, P, Y, Th, Nb and LREE (La, Ce, Nd) relative to the quartzofeldspathic protolith (Figures 7.14, 7.15), this feature being shared by stromatic migmatites elsewhere (e.g. Brouand *et al.* 1990; Sawyer 1991; Watt & Harley 1993; Bea *et al.* 1994; Watt *et al.* 1996). For P and Zr, this is attributed to the meagre solubility of both apatite (Harrison & Watson 1984; Pichavant *et al.* 1992) and zircon (Watson & Harrison 1983) in low temperature partial melts such as those represented by GRC leucosomes (see below). Zircon solubility (equivalent to the dissolved amount of Zr required to stabilise $ZrSiO_4$) is depressed even further in siliceous peraluminous liquids (Watson & Harrison 1983). This predicts that zircon and apatite should be residual phases during anatexis of aluminous crustal rocks, leaving a P- and Zr-impoverished melt, consistent with the enrichment of these minerals in melanosomes of GRC migmatites. The concentration of La, Ce, Nd and Th in leucosomes is likely to be buffered by the dissolution of monazite (Ayers & Harris 1997), which is also limited in low temperature, peraluminous melts (Montel 1986; Rapp & Watson 1986). Retention of refractory monazite in melanosomes is therefore probably responsible for the depletion of LREE and Th in GRC leucosomes. The possible role of accessory xenotime in fractionating Y and 'heavy' REE between melt and residue in GRC migmatites requires further investigation.

Nevertheless, Zr and P concentrations exhibit considerable variability between leucosomes (Figure 7.15), which requires explanation. Figure 8.8 compares the measured Zr abundance in GRC leucosomes with the maximum amount of Zr that can dissolve in a partial melt of the same composition (calculated using the empirical equations of Watson & Harrison 1983; see Appendix D). At 650°C, eight leucosomes contain less Zr than that required to saturate the melt, despite mesosomes having >150 ppm Zr (only 60 ppm Zr is required in the protolith for melt saturation, Watson 1988). The most Zr-poor leucosome (**98-65B**, 8 ppm) corresponds to a Zr melt saturation temperature of ~580°C, which is well below the solidus and therefore meaningless. Conversely,

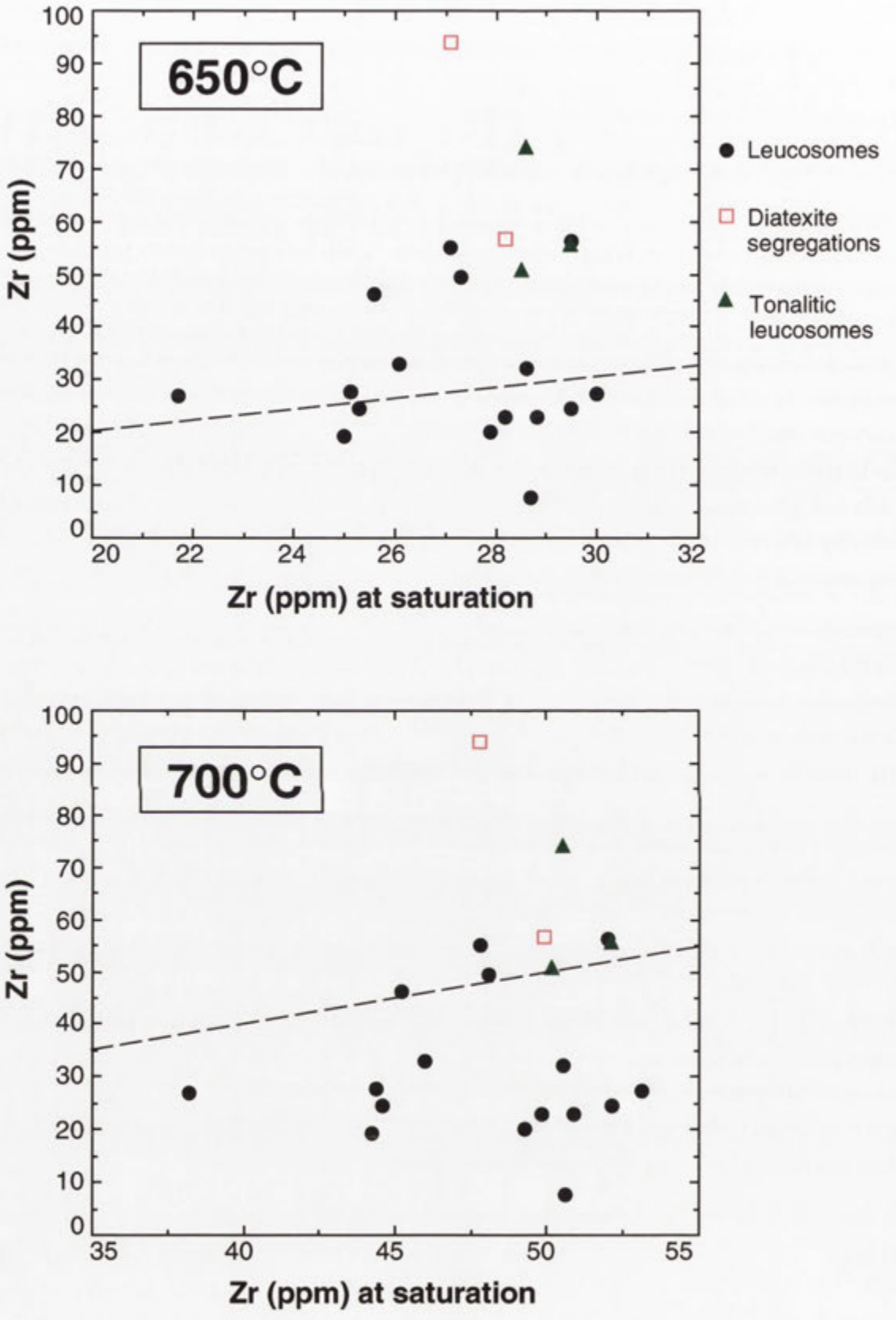

Figure 8.8. Measured Zr abundance of *in situ* leucosomes and diatexite segregations plotted against the Zr concentration required to saturate a partial melt of that composition at 650ºC and 700ºC (estimated from the solubility model of Watson & Harrison 1983, see Appendix D). Dashed lines indicate where Zr (measured) = Zr (at melt saturation).

eight leucosomes have more Zr than can be dissolved under equilibrium conditions. At 700°C, which is the maximum inferred temperature for GRC anatexis (Figure 8.2), all but four leucosomes are undersaturated with respect to Zr.

Importantly, the degree of Zr saturation of leucosomes is correlated with total Fe_2O_3 (Figure 8.9), indicating that the Zr content of the melt is governed by biotite. Although biotite accommodates negligible Zr, it encloses most zircon grains within fertile GRC metasedimentary rocks (section 5.3.2). Hence, as biotite is progressively concentrated in residual melanosomes upon anatexis, zircon is essentially shielded from the melt reservoir. This impedes equilibration between zircon and melt, resulting in Zr undersaturation in leucosomes. A similar explanation is favoured by Bea *et al.* (1994) and Bea (1996b) for the Peña Negra migmatites of Spain. The trend to higher Zr with Fe_2O_3t reflects either the incipient dissolution of biotite during partial melting or minor entrainment of residual biotite flakes during leucosome segregation, such that zircon crystals are also incorporated. The latter is most likely responsible for the excess Zr of some leucosomes over that required for saturation at 700°C; note that only a small degree of biotite contamination is necessary, given the abundance of zircon inclusions in melanosome biotite and the low Zr saturation concentration (~50 ppm at 700°C).

The P_2O_5 depletion in leucosomes relative to the protoliths is less marked than Zr, with leucosomes defining an array that extends from low P_2O_5 to concentrations exceeding those of the source rocks (Figures 7.14 and 7.15). This is partly explained by the experimental results of Pichavant *et al.* (1992) and Wolf & London (1994), which predict enhanced apatite dissolution

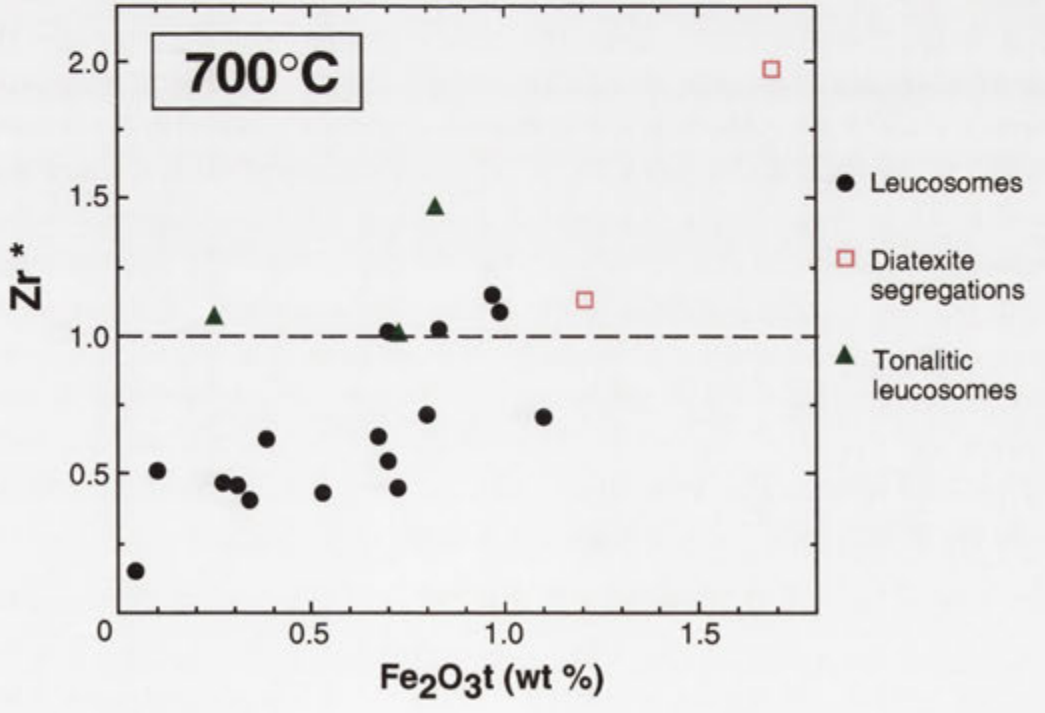

Figure 8.9. Zr* (Zr measured/Zr concentration at melt saturation) versus total Fe_2O_3 for *in situ* leucosomes and diatexite segregations of the GRC.

in evolved peraluminous melts, whereas zircon solubility diminishes in such compositions. However, these studies also suggest that apatite solubility (and therefore P_2O_5 content) in such compositions increases with A.S.I. and SiO_2, which is not observed for leucosomes of GRC migmatites (see Appendix C).

Despite this, as with Zr, the P_2O_5 content of most GRC leucosomes is below that required for apatite saturation (estimated from the equation of Pichavant *et al.* 1992, see Appendix D), even at 650°C (Figure 8.10). Assuming that the formula of Pichavant *et al.* (1992) adequately models apatite solubility in peraluminous liquids, this is most easily reconciled by occlusion of apatite grains by refractory minerals (chiefly biotite) during anatexis, such that the protolith does not constitute an infinite reservoir for apatite. Unlike zircon, however, the degree of P_2O_5 saturation is poorly correlated with total Fe_2O_3 (Figure 8.11), indicating that the P_2O_5 concentration of leucosomes was not exclusively controlled by the behaviour of apatite-bearing biotite. Such scatter could reflect the random entrapment of residual apatite during segregation of the leucosome, this being favoured by the greater proportion of apatite crystals occurring along quartz-feldspar grain boundaries in migmatite protoliths (section 5.3.2). As a result, some apatite grains could be physically entrained by the newly-formed melt, though this was evidently insufficient to engender P_2O_5 saturation. In view of this, some non-systematic P_2O_5 variation in GRC leucosomes (Figure 8.11) may therefore relate to subtle differences in the textural position of apatite crystals between the different leucosome protoliths.

8.5.3 Summary of the geochemistry and petrogenesis of granitic leucosomes

The systematic chemical linkages discussed above indicate that granitic leucosomes of GRC migmatites were generated by water-fluxed partial melting of a muscovite-bearing quartzofeldspathic protolith that is chemically very similar to the coexisting mesosome. The resultant fractionation of elements between the melt and residual phases is summarised by Figure 8.12. Anatexis involved elimination of plagioclase and alkali feldspar in the protolith, such that leucosomes have elevated K_2O, Ba, Sr and Pb compared to their source rock composition. Although the sources for all granitic leucosomes are broadly quartzofeldspathic, differences in the abundances of K_2O, Ba, and Sr between leucosomes mirror variation in these elements between specific protoliths, in turn reflecting mineralogical variations in the sedimentary precursor. As biotite was essentially refractory, the residual material is relatively enriched in TiO_2, (Fe_2O_3t+MgO) and Rb, complementary to strong depletion in these components in leucosomes. Decoupling between Rb and Sr, resulting from different compatibilities with respect to the residual assemblage also results in partial melts having markedly lower Rb/Sr ratios than their inferred source rock.

Also evident on Figure 8.12 is the lower P, Y, HFSE and LREE contents of leucosomes relative to mesosomes, reflecting limited dissolution of accessory apatite, zircon and monazite during low T anatexis. Depletion in Zr, and possibly P_2O_5, in most leucosomes relative to that required for melt saturation is attributed to sequestration of protolith zircon and apatite by refractory biotite.

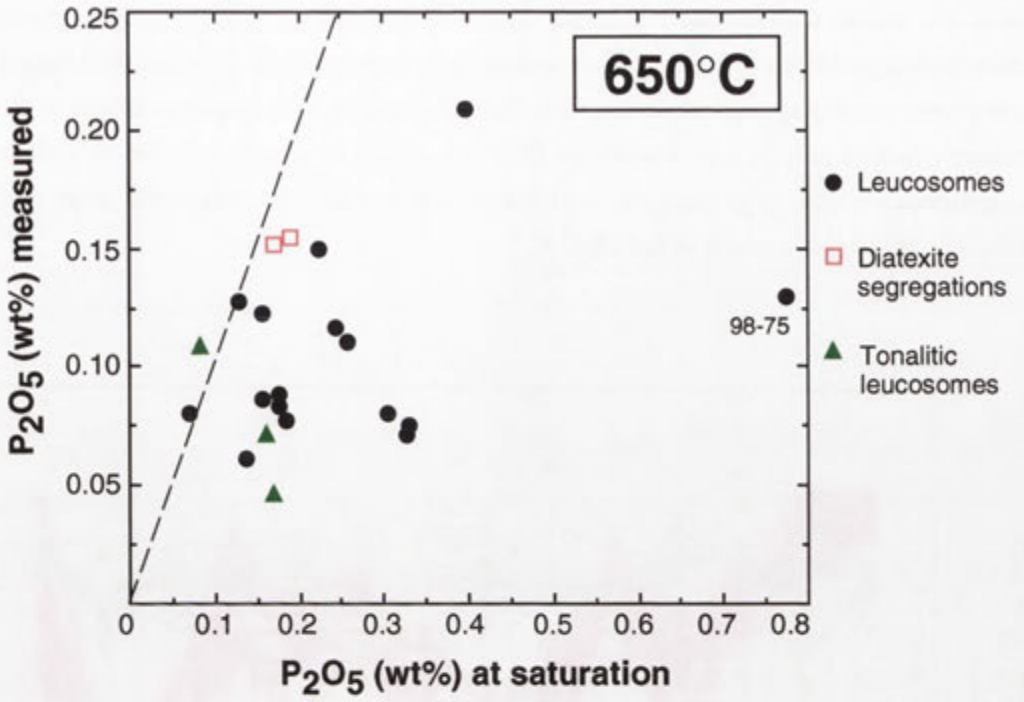

Figure 8.10. Actual P_2O_5 content of *in situ* leucosomes and diatexite segregations versus the amount of P_2O_5 required for apatite saturation at 700ºC (calculated from equations in Pichavant *et al.* (1992). The dashed line corresponds to the P_2O_5 content at apatite saturation. The large estimated P_2O_5 solubility of sample **98-75** reflects entrained residual sillimanite, and is therefore not appropriate for the melt component of the leucosome. Nevertheless, this demonstrates the sensitivity of P_2O_5 solubility calculations to excess Al_2O_3.

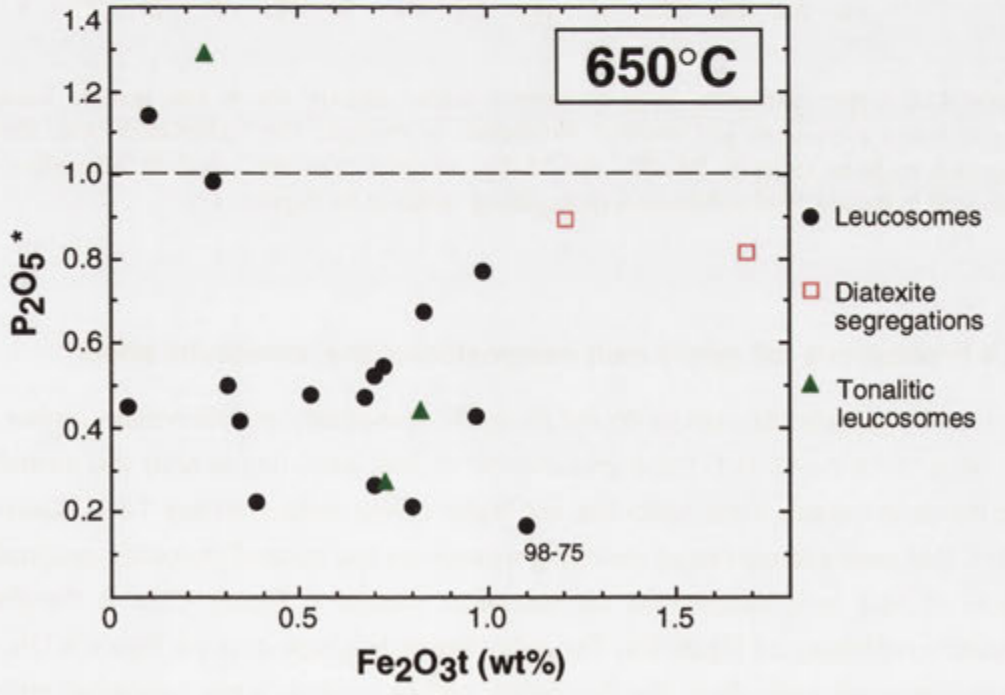

Figure 8.11. Degree of P_2O_5 saturation at 650°C (P_2O_5* = P_2O_5 measured / P_2O_5 at saturation) with respect to total Fe_2O_3 for *in situ* leucosomes and diatexite segregations. The marked P_2O_5 undersaturation of leucosome **98-75** is spurious, resulting from content of residual sillimanite (which enhances theoretical apatite solubility).

Finally, the preservation of the highly fractionated elemental pattern of granitic leucosomes relative to their protoliths in Figure 8.12 is testament to the remarkably efficient melt segregation process operative during migmatisation, such that entrainment of melanosome biotite or residual accessory minerals into the melt was minor. Efficient separation of melt from biotite-rich residue is conspicuous within migmatite outcrops across the northeastern migmatite zone and is a dominant petrogenetic process in the GRC.

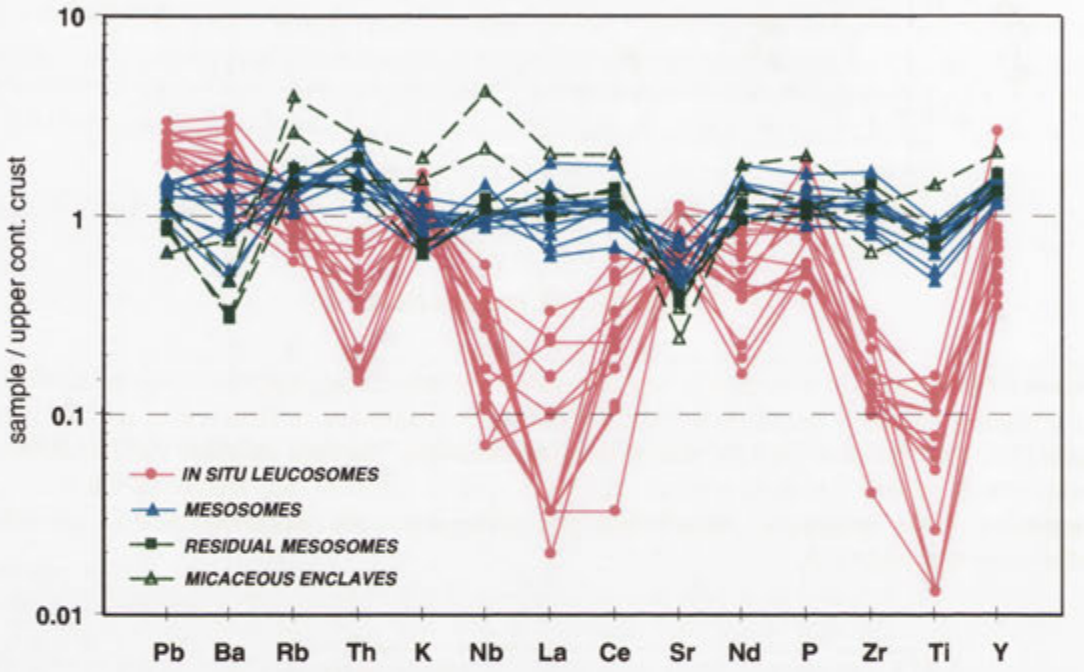

Figure 8.12. Upper continental crust-normalised 'spider diagram' for *in situ* granitic leucosomes, complementary mesosomes and 'residual' mesosomes of stromatic GRC migmatites. Also shown are micaceous enclaves (samples **98-SEL** and **98-27**) collected from the Schofield Adamellite, which correspond to fragments of melanosome (normalising values as for Figure 7.15).

8.5.4 Implications for partial melt compositions: the 'muscovite effect'

Most *in situ* granitic leucosomes do not lie on the five-phase 'minimum melt' surface in the normative Q-Ab-An-Or-H_2O (haplogranodiorite) system, but define an array that extends from near the curve towards lower orthoclase and higher quartz content (section 7.6.1, Figures 7.13, 8.13a). This array mirrors that of coexisting mesosomes and inferred protoliths, confirming the control of bulk rock composition on leucosome chemistry; Figure 8.13a is therefore the normative expression of Figure 8.4. The same feature is conspicuous on Figure 8.13b, where leucosomes trend away from the five phase surface towards lower normative orthoclase; leucosome **98-R5C** again plots closest to the curve.

Since leucosomes approximate crystallised partial melts (section 8.5.1), the apparent discrepancy with the five phase surface must be intrinsic to the melt composition, possibly

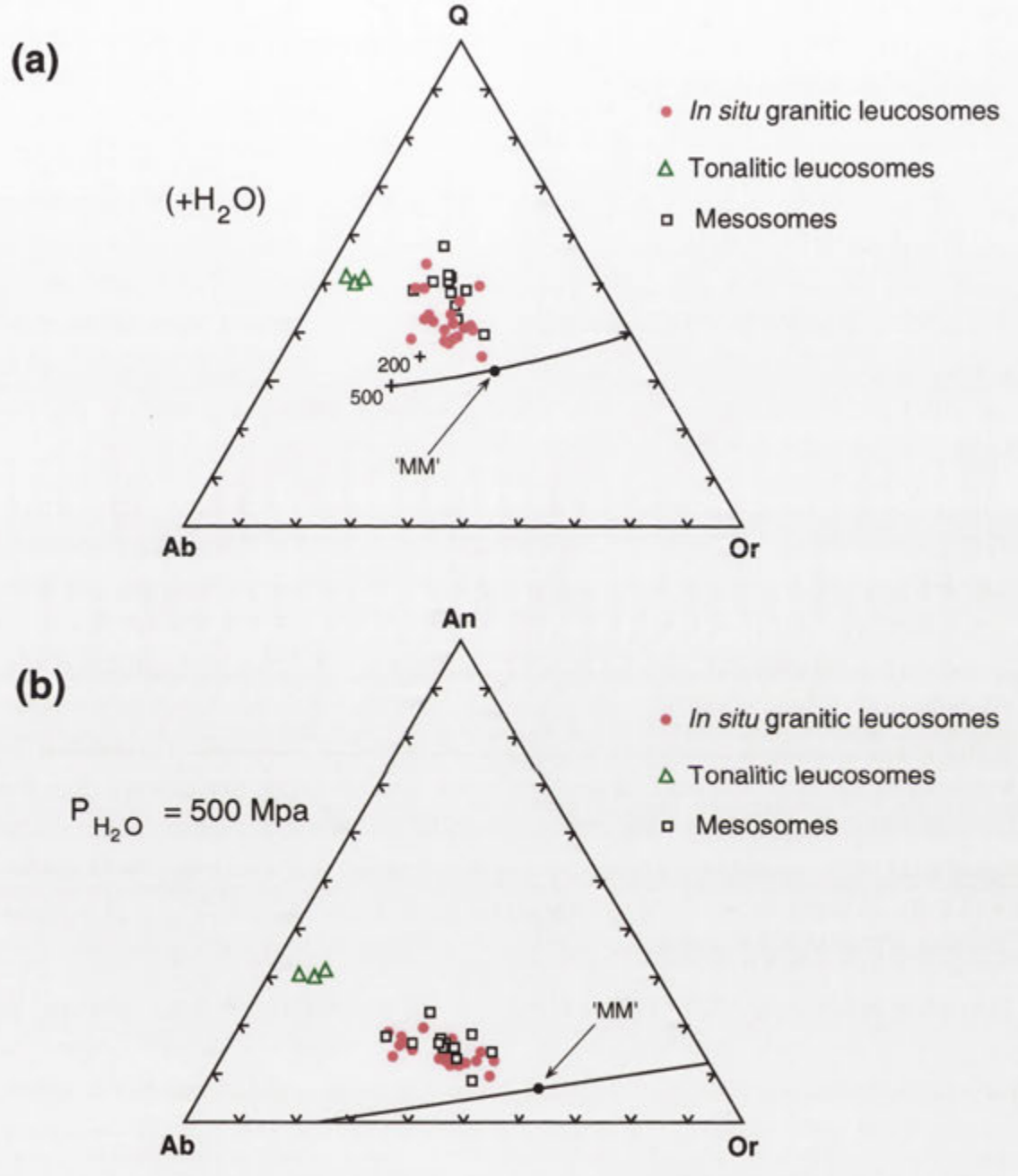

Figure 8.13. CIPW normative composition of *in situ* leucosomes and complementary mesosomes for GRC migmatites. (a) Normative quartz (Q), albite (Ab) and orthoclase (Or). The eutectics at P_{H_2O} = 200 and P_{H_2O} = 500 Mpa (crosses) and the five phase curve (Q-Plag-Or-H_2O-melt) are also indicated (from Nekvasil 1988). (b) Normative anorthite (An), albite and orthoclase at P_{H_2O} = 500 Mpa. The position of the five phase curve is taken from Nekvasil & Burnham (1987). Note that in both diagrams 'MM' corresponds to the 'minimium melt' composition in the haplogranodiorite system without excess Al_2O_3 (i.e. A.S.I. = 1, see Figure 8.14 for details).

reflecting different protoliths and/or the influence of additional components. With respect to the latter, it is significant that all migmatite leucosomes have formed by muscovite-involved melting reactions and crystallised muscovite, implying some dissolution of Al_2O_3 in the melt. Addition of Al_2O_3 to the Q-Ab-Or-H_2O system at 200 Mpa has experimentally been shown to displace the cotectic curve towards slightly more quartz-rich and orthoclase-poor compositions, together with lowering of the liquidus temperature by 25±5°C (Holtz *et al.* 1992; Joyce & Voigt 1994). A more pronounced shift of the eutectic towards the quartz apex is anticipated at higher pressures, as more Al_2O_3 may be incorporated into the melt (Johannes & Holtz 1996). That the composition of GRC leucosomes correlates with excess Al_2O_3 is supported by a linear relationship between A.S.I. and the proportion of normative quartz, such that the latter increases strongly as leucosomes become more peraluminous (Figure 8.14a). The reverse effect is exhibited by normative orthoclase, which decreases linearly with A.S.I. (Figure 8.14b). Note that this trend cannot simply reflect increasing amounts of leucosome muscovite, since, being calculated as normative orthoclase+corundum, this would produce a *positive* correlation between Or/(Q+Ab+Or) and A.S.I.

A line of best fit through leucosomes on Figure 8.14b (ignoring sillimanite-contaminated sample **98-75**) extrapolates to ~40 normative percent orthoclase at A.S.I. = 1.0. This point is plotted onto the five phase surface on Figure 8.13a, and corresponds to the minimum melt composition in the haplogranodiorite system at neutral aluminosity and an average anorthite content. Hence, the leucosome that lies closest to this point, **98-R5C**, is the closest to the predicted haplogranodiorite minimum melt composition at 500 Mpa. This predicts that this leucosome formed by the lowest degree of partial melting, consistent with it exhibiting the largest melt-source fractionation for K_2O and Ba (Figures 8.4, 8.5). Other leucosomes form an array that extends from the haplogranodiorite minimum to lower orthoclase content (and bulk K_2O), which corresponds to higher A.S.I and SiO_2 (see Figure 8.4). Note that excluding non-melt leucosomes **98-75** and **98-WF2A-2L**, the scatter in leucosome compositions in Figure 8.13a parallel to the five phase curve could result from varying anorthite content.

The effect of excess Al_2O_3 (as muscovite or sillimanite) on melting relations in quartzofeldspathic rocks is investigated by Thompson & Algor (1977), who construct a petrogenetic grid (see Figure 8.1) and show possible liquidus configurations in the system $KAlO_2$-$NaAlO_2$-SiO_2-Al_2O_3-H_2O (Figure 8.15a). According to these authors, initial melts in the quartz- and water-saturated Ab-Or-Al_2O_3 projection (at pressures above invariant point I_3 in Figure 8.1) occur at lower temperatures than the 'haplogranite minimum' and are displaced from the Ab-Or sideline towards more Al_2O_3-rich compositions (Figure 8.15a). The same effect is exhibited by GRC leucosomes (Figure 8.15b). Further, most leucosomes define a linear trend that extends towards the projected position of the haplogranodiorite minimum (taken from Figure 8.13a above); as with normative plots, leucosome **98-R5C** is situated closest to the minimum at A.S.I. = 1. That this trend does not reach the Ab-Or sideline is consistent with melting proceeding at lower temperature than the muscovite-absent eutectic reaction Q+Ab+An+Or+H_2O = melt (see Figure 8.1). Instead, the compositional leucosome array broadly corresponds to a cotectic in

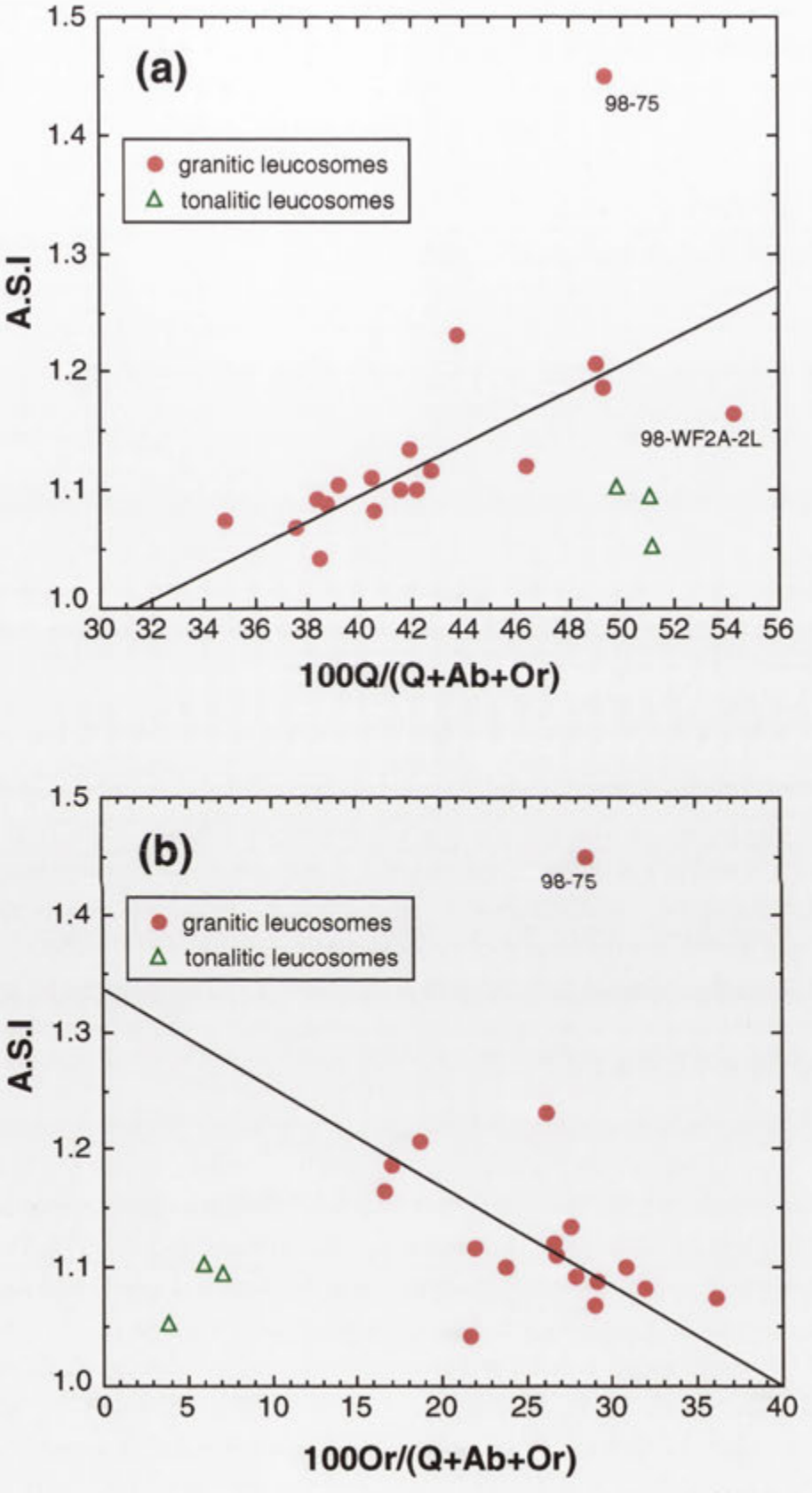

Figure 8.14. Plot of alumina saturation index (A.S.I.) versus (a) proportion of normative quartz and (b) proportion of normative orthoclase for *in situ* granitic and tonalitic leucosomes of the GRC. Approximate lines of best fit for granitic leucosome data are indicated and extrapolated to neutral peraluminosity (A.S.I. = 1.0), excluding sample **98-75**, contaminated with residual sillimanite, and sample **98-WF2A-2L**, enriched in liquidus quartz.

the Ab-Or-Al_2O_3 system (as indicated by Thompson & Algor 1977), parallelling the spread of mesosome compositions (Figure 8.15b). This array can be explained by a model involving progressive anatexis. Initial melts of a given protolith will form by the lowest temperature, near-eutectic reaction [8.2]. As anatexis proceeds and alkali feldspar is eliminated, melt compositions leave the 'eutectic' and move along the cotectic away from the K_2O apex. The distance each melt travels along this path is governed by the source composition, resulting in more K-poor protoliths being complementary to more peraluminous melts; peritectic reaction [8.3] was eventually reached in the most aluminous source rocks. The scatter in leucosome compositions implies that some melts may also have left the cotectic and moved towards the protolith. However, the degree of melting was mostly insufficient for this, as many leucosomes are restricted to the cotectic composition. To explore this further, experimental constraints on the location of the eutectic and cotectics in the quartz- and water-saturated Ab-Or-Al_2O_3 system are required.

Regardless, these observations clearly indicate that the composition of 'minimum-temperature' melts from peraluminous protoliths cannot be adequately modelled in the haplogranite (e.g. Tuttle & Bowen 1958) or haplogranodiorite system (Nekvasil & Burnham 1987). A non-cotectic composition in the Q-Ab-Or-An system therefore does not preclude leucosomes representing frozen accumulations of partial melt (see Ashworth 1985).

8.5.5 Implications for the geochemistry of diatexites

Relative to most metasedimentary rocks of similar silica, diatexites have lower TiO_2, P_2O_5 and Zr and are slightly displaced towards the *in situ* leucosome field (Figure 7.14). There are two aspects to this. For *semi-pelitic* diatexite **99-R5**, this feature could reflect an enrichment in the granitic melt component, as this rock also has high K_2O and Ba (Figure 7.14), and plots crudely along a mixing line between unmelted semi-pelitic metasedimentary rocks (~65% SiO_2), residual biotite and *in situ* leucosomes (Figure 8.16). Such enrichment could be facilitated by separation of biotite-rich residue during bulk magmatic flow or redistribution of partial melt within the diatexite horizon (see section 5.8.1).

However, for *quartzofeldspathic* diatexites (the three samples with >70% silica), enrichment in granitic melt is inconsistent with their low Na_2O, Sr and Ba contents (Figures 7.14 and 8.17a), and especially elevated Rb/Sr compared to unmelted quartzofeldspathic metasedimentary rocks (Figure 8.17b). It is alternatively concluded that these diatexites derive from more Rb-rich but Ti-poor precursors than unmelted metasedimentary rocks. Further, the relatively high Fe_2O_3t and strongly depleted K_2O, Sr and especially Ba of quartzofeldspathic diatexite Y2-312 (labelled on Figure 8.17) actually suggests removal of a partial melt fraction, plausibly during flow-assisted segregation (see section 5.8.1). The fugitive melt may be approximated by the small leucogranitic domains in diatexites, two samples of which have elevated K_2O, Ba and Sr contents relative to their host, with much lower TiO_2, Fe_2O_3t and Rb/Sr (Figures 8.16 and 8.17). Diatexite segregations therefore plot close to the geochemical field of *in situ* granitic leucosomes from stromatic migmatites (Figures 8.16, 8.17, see also Figure 7.14). This indicates that the partial melt composition in GRC migmatites is similar, despite fundamentally contrasting melt generation and segregation mechanisms. It should be noted, however, that diatexite segregations

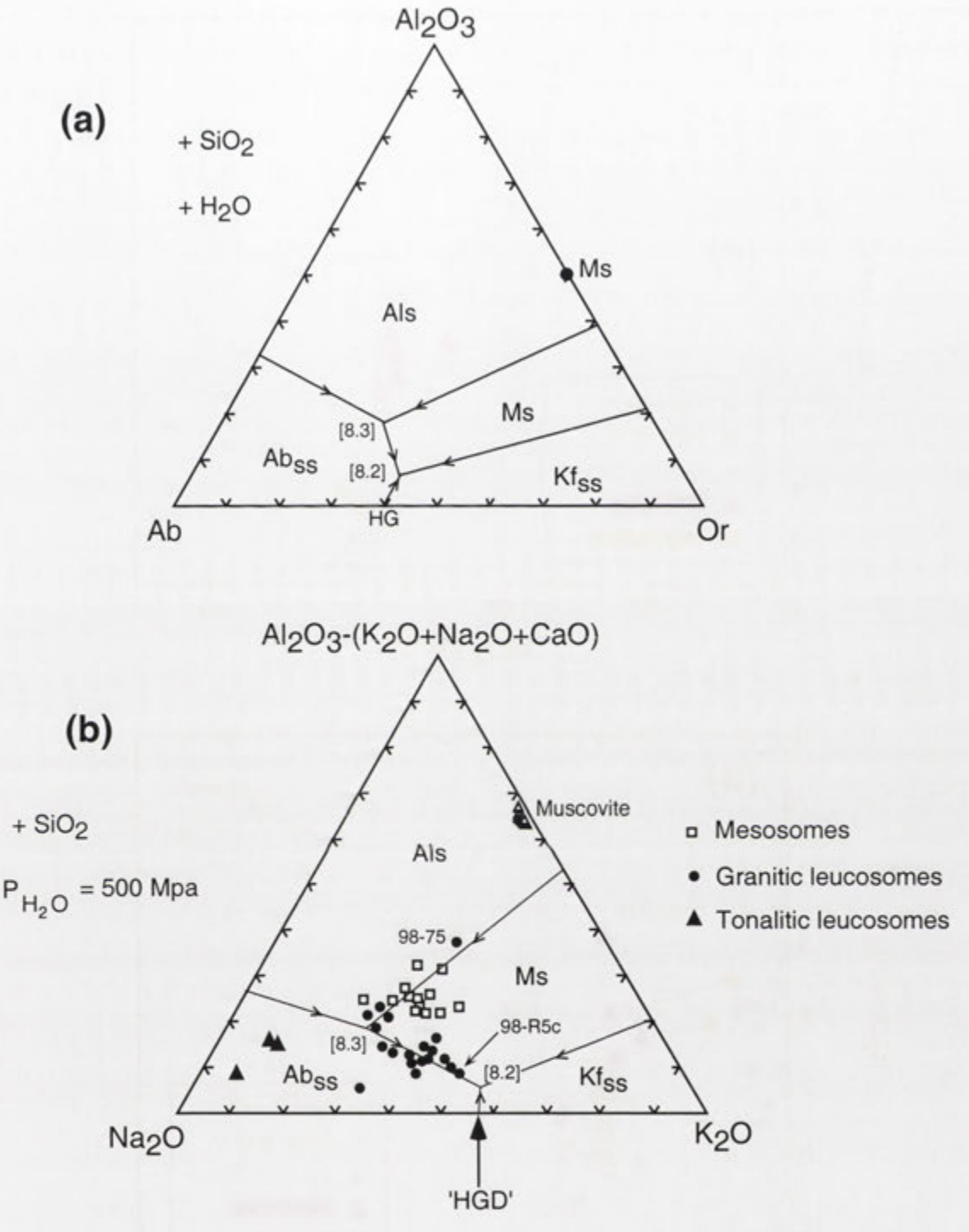

Figure 8.15. (a) Theoretical liquidus configuration for the quartz- and water-saturated part of the KNASH system projected onto the albite (Ab)-orthoclase (Or) and Al_2O_3 plane (after Thompson & Algor 1977) (symbols as in Figure 8.1). Arrows show the direction of decreasing temperature on cotectics. Numbers in brackets correspond to the projected position of the melting reactions discussed in text for plagioclase of An_0. Note that 'HG' is the location of the haplogranite eutectic (Q + Ab + Or + H_2O = melt) at no excess Al_2O_3. (b) Equivalent plot to (a) for leucosomes and mesosomes of GRC migmatites (in mole percent). The field of analysed muscovite from migmatites is also indicated. 'HGD' corresponds to the position of the 'haplogranodiorite minimum' at neutral peraluminosity (i.e. A.S.I = 1), estimated from Figure 8.14. A possible liquidus topology is also indicated.

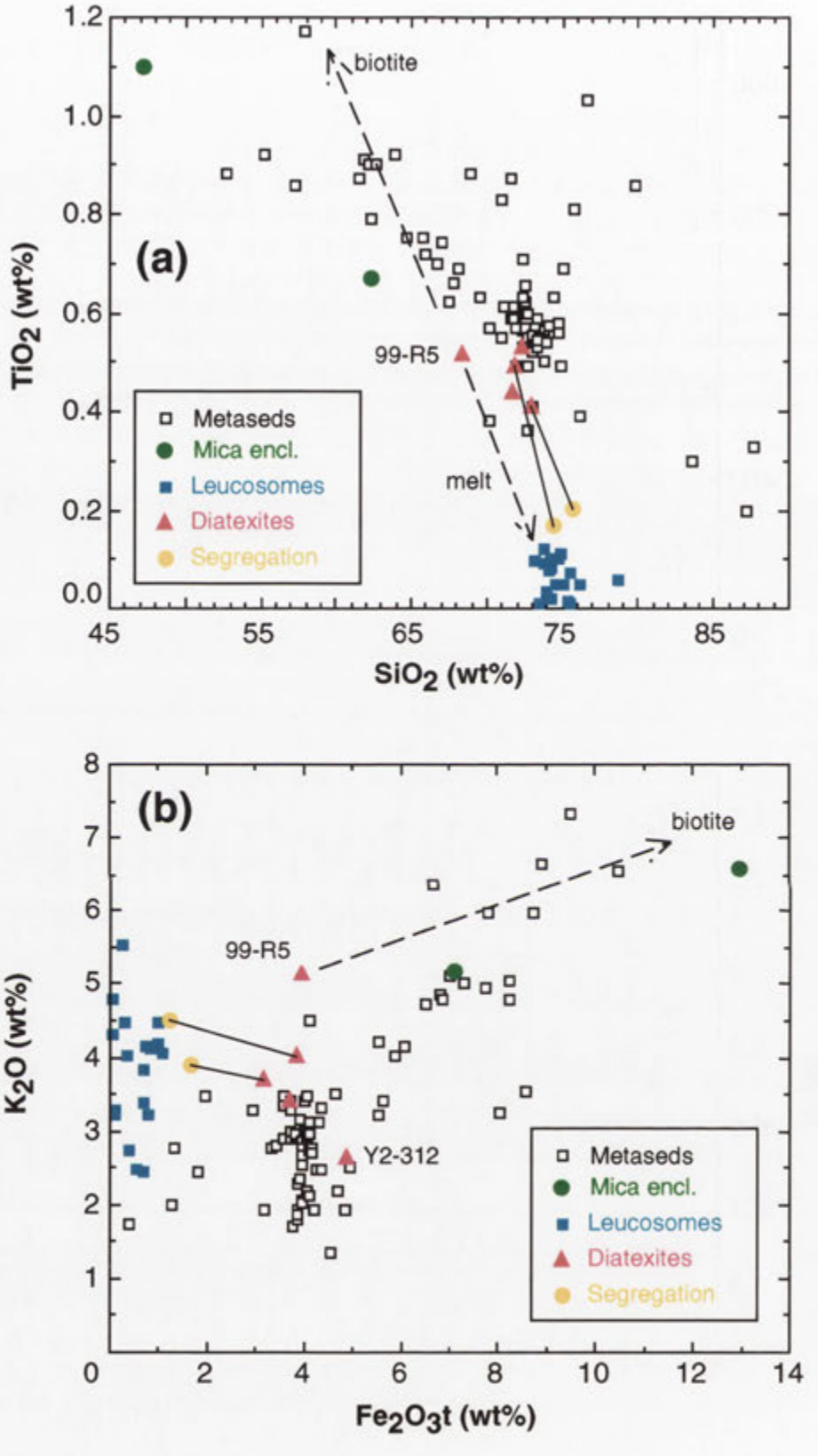

Figure 8.16. Plot of (a) TiO_2 versus SiO_2 and (b) K_2O versus SiO_2 for metasedimentary rocks (migmatite and sub-migmatite grade), micaceous enclaves (mica encl.), *in situ* granitic leucosomes and diatexites of the GRC. Tie lines connect leucogranitic segregations with their host diatexite. Vectors towards the composition of biotite (taken from the average biotite composition in diatexite **97-286-1**, Appendix B) and the partial melt field (*in situ* leucosomes) are also shown (dashed lines).

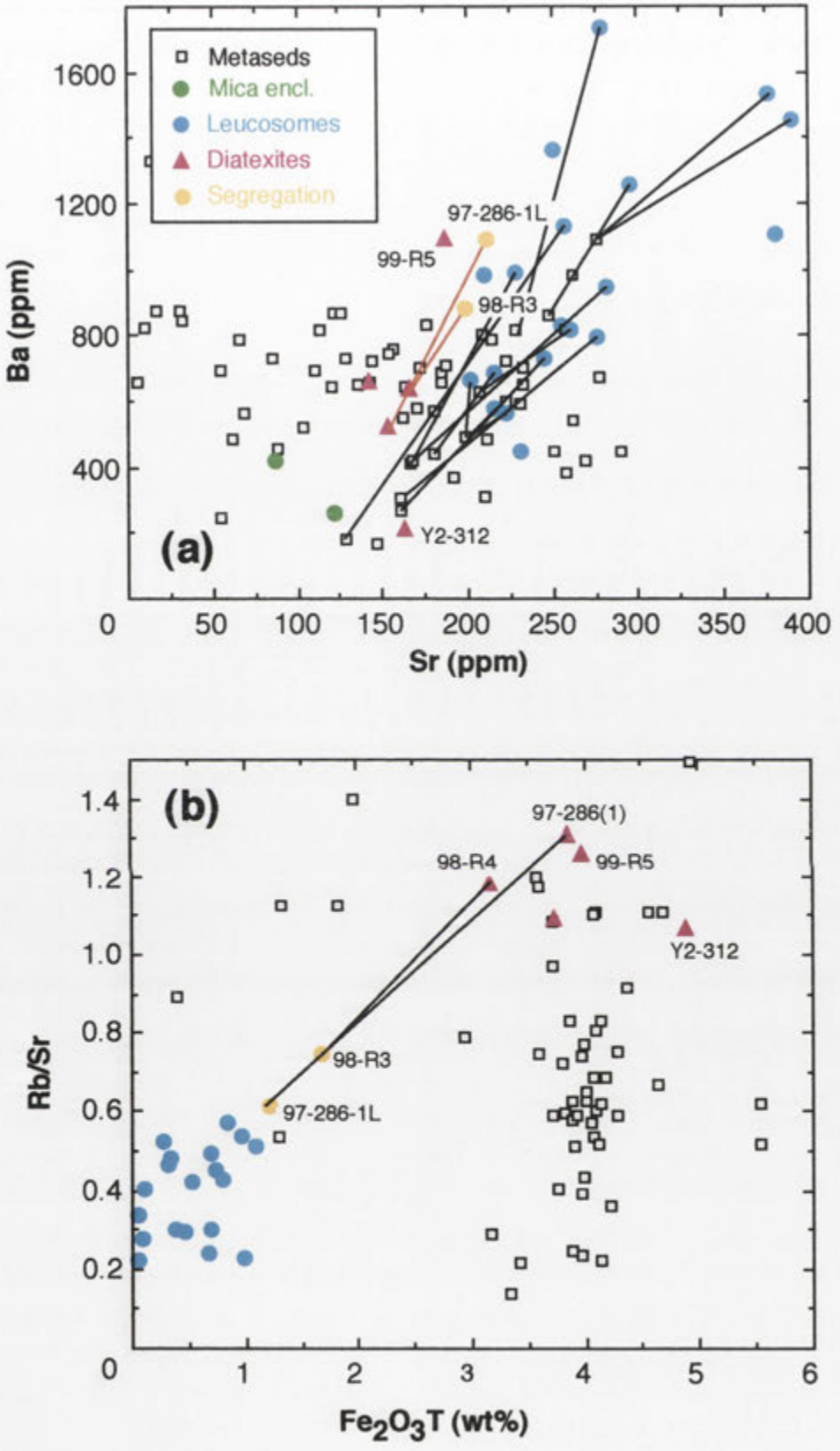

Figure 8.17. Plot of (a) Ba versus Sr and (b) Rb/Sr versus total Fe_2O_3 for metasedimentary rocks (migmatite and sub-migmatite grade), *in situ* granitic leucosomes and diatexites of the GRC. Tie lines connect leucogranitic segregations with their host diatexite (red lines), and *in situ* granitic leucosomes with adjacent mesosomes (black lines).

have slightly higher TiO_2 (Figure 8.16a), Fe_2O_3t and Rb/Sr (Figure 8.17b) than *in situ* stromatic leucosomes, reflecting greater biotite content. As textural and chemical evidence suggests the latter is mostly melt-precipitated (apart from some contamination by restitic biotite in **98-R3**, section 8.2.3), this probably results from a slightly greater degree of partial melting, such that more biotite was consumed (section 8.3.3). Increased biotite dissolution releases tiny included zircon grains, which are unlikely to be efficiently separated from viscous melt during incipient magmatic flow, accounting for the higher Zr contents of diatexite segregations (Figures 8.8, 8.10). The markedly higher Zr of **98-R3** (94 ppm), which corresponds to an unrealistic melt saturation temperature of ~750°C, partly results from the content of restitic debris.

In summary, although imaging the metasedimentary precursor, the geochemistry of analysed diatexites is influenced by changing proportion of melt and residual components, reflecting the outcrop-scale lithological heterogeneity.

8.6 Formation of tonalitic leucosomes

8.6.1 Introduction

Tonalitic (alkali feldspar-poor) leucosomes are numerous in metasedimentary rocks of the Glenelg River valley and tributaries east of Schofield Creek (section 6.2.2), and sparsely occur within M_1 migmatitic horizons of northern Schofield Creek, Chin Chap Creek and Robson Creek (Table 5.3). These are regarded as petrogenetically distinct from quartz-rich leucosomes of adjacent migmatites, which locally have tonalitic character but are contiguous with alkali feldspar-rich granitic leucosomes (section 8.3.1). At all localities, tonalitic leucosomes are hosted by alkali feldspar-absent semi-pelitic schist or gneiss and have melanosomes that are enriched in S_2-aligned muscovite. Splintery muscovite flakes enclosing fibrolite occur in the melanosomes of some M_2 leucosomes. As with granitic leucosomes, lack of alkali feldspar in melanosomes of tonalitic migmatites precludes derivation by dehydration melting reaction [8.1].

8.6.2 Petrogenetic models

Although tonalitic leucosomes are distant from the eutectic composition in the haplogranitic system (Figure 8.13a), they plot at the extrapolation of the granitic leucosome array to lower normative orthoclase (Figures 8.13a and 8.13b). However, tonalitic leucosomes are not markedly peraluminous, and fall off the granitic leucosome trend towards decreasing K_2O with increasing excess Al_2O_3 (Figures 8.14, 8.15b), which corresponds to a projected cotectic in the water-saturated Q-Ab-Or-Al_2O_3 system (section 8.5.4). This suggests that tonalitic leucosomes represent a separate anatectic system, whose K-poor character cannot be accounted for by dissolved Al_2O_3 and KNASH liquidus relationships.

In view of this, three possibilities are envisaged for the origin of tonalitic leucosomes-

(a) they might represent 'cumulates' of early precipitated quartz and plagioclase, from which K_2O-rich melt was extracted during crystallisation. This origin is inferred by Solar & Brown (2001) for trondhjemitic leucosomes in Maine (U.S.A.);

(b) they may result from the extensive 'retrograde' crystallisation of muscovite in the melanosome upon reversal of the melting reaction during cooling. This would deplete K_2O from the residual melt and therefore suppress formation of alkali feldspar. Here, leucosomes may be formed by either reaction [8.2] or [8.3], though in the latter case the 'retrograde' muscovite forms by reaction between peritectic sillimanite and cooling, hydrous melt;

(c) tonalitic leucosomes approximate a 'primary' K_2O-poor melt composition generated by anatexis of a semi-pelitic, alkali feldspar-absent protolith.

Scenario (a) is invoked for the alkali feldspar-depleted, quartz/plagioclase-rich segments of otherwise granitic leucosomes in M_1 migmatite horizons of Robson Creek (section 8.3.1). Following the reasoning used for these samples, some quartz-rich, texturally heterogeneous tonalitic leucosomes in Dunmore Creek may also have experienced migration of residual melt in the latter stages of crystallisation (see section 6.2.2). However, such leucosomes are connected to larger tonalitic sheets and associated with plutonic bodies that are equally alkali feldspar-poor (section 6.2.3). This indicates that a 'fractionated' potassic liquid did not form during crystallisation and melt extraction, and that the K_2O depletion of leucosomes is intrinsic to the original melt. Tonalitic leucosomes in Schofield Creek, Chin Chap Creek and Robson Creek are generally not interconnected, suggesting that melt migration is unlikely, and that leucosomes represent trapped partial melts.

Scenario (b) requires that the abundant muscovite in melanosomes adjacent to tonalitic leucosomes has formed by retrograde crystallisation. However, most melanosome muscovite of M_1 and M_2 tonalitic migmatites is euhedral, S_2-aligned and intimately entwined with refractory biotite, therefore being primary and residual from partial melting (section 8.2.4). Although ragged muscovite in some M_2 samples has formed by retrogression of sillimanite, the mechanism seems intuitively implausible for the production of pluton-scale magmatic bodies that are uniformly tonalitic.

Alternatively, tonalitic leucosomes are considered to be 'primary' partial melt compositions formed by anatexis of a semi-pelitic metasedimentary protolith. This is supported by the normative compositions of analysed samples, which coincide with the experimentally determined 500 Mpa cotectic curve on a water-saturated Q-Ab-An ternary diagram (Figure 8.18). The precursor lithology is possibly represented by semi-pelitic to laminated schists of the northeastern sillimanite zone, with the assemblage quartz-plagioclase-biotite-muscovite. Lack of alkali feldspar in these rocks precludes initial anatexis by near-eutectic reaction [8.2]. Instead, leucosomes were generated by the congruent, fluid-present reaction –

$$\text{muscovite} + \text{plagioclase} + \text{quartz} + H_2O = \text{MELT} \qquad [8.4]$$

As sillimanite occurs in some M_2 tonalitic migmatite melanosomes, the melting reaction may have ultimately progressed to peritectic reaction [8.3] –

$$\text{muscovite} + \text{plagioclase} + \text{quartz} + H_2O = \text{sillimanite} + \text{MELT} \qquad [8.3]$$

as the solubility limit of Al_2O_3 in the melt was reached. A very small amount of biotite was also probably involved in partial melting, slightly lowering the temperature of anatexis (section 8.2.3). The abundant residual muscovite in tonalitic migmatites accords with the semi-pelitic character of the inferred protolith, where this phase is more abundant than in quartzofeldspathic rocks. Since muscovite persists in tonalitic migmatite mesosomes with plagioclase and quartz, these rocks are still able to generate melt. This implies that tonalitic leucosomes have formed by a fairly low fraction of partial melting.

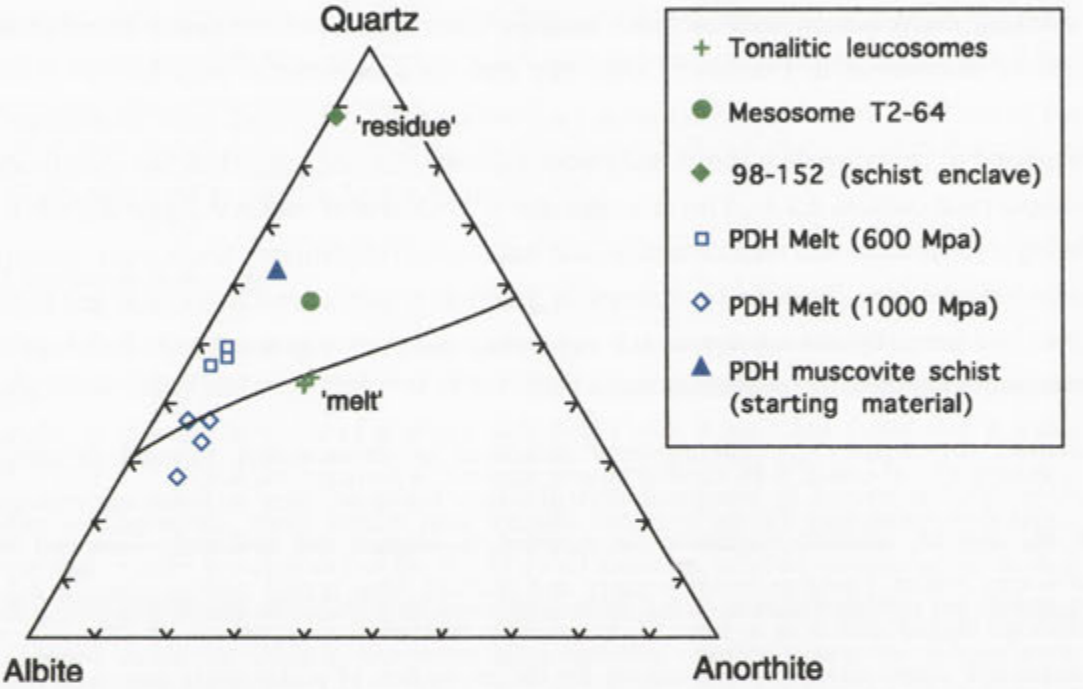

Figure 8.18. Plot of normative quartz, albite and anorthite for tonalitic leucosomes of the GRC, inferred protolith **T2-64**, and inferred residue (micaceous enclave **98-152**) in relation to the Q-Ab-An cotectic at P_{H_2O} = 500 Mpa (from Yoder 1968). Also shown are the experimental partial melts produced by Patiño Douce & Harris (1998) at 600 and 1000 Mpa with variable amounts of added H_2O ('PDH Melt'), together with the starting material, a Himalayan muscovite schist.

8.6.3 Effect of muscovite stability on melt composition

Since biotite is virtually refractory, the K_2O content of the partial melt formed by the above reactions is buffered by muscovite in the protolith rather than by alkali feldspar, unlike in most granitic leucosomes. However, enrichment of prograde muscovite in melanosomes indicates that only a small proportion was consumed by anatexis. Hence, most protolith K_2O remained locked in residual micas, resulting in formation of K-deficient partial melts. The small amount of K_2O contributed to the melt by reactant muscovite was apparently taken up by early precipitation of muscovite in the leucosome, suppressing alkali feldspar crystallisation. Under higher degrees of

anatexis, or reduced water activity, greater consumption of muscovite in the protolith might eventually yield alkali feldspar-bearing 'granitic' leucosomes.

Excellent supporting evidence for this proposition is provided by Patiño Douce & Harris (1998), who report experimental generation of K-poor melts by water-fluxed melting (at 700-775°C) of a natural muscovite schist from the High Himalayan Crystalline Sequence. This is attributed to the stronger depression of the plagioclase-quartz solidus relative to the stability of muscovite with increasing water activity, such that greater proportions of plagioclase were consumed during partial melting, and muscovite was preserved in the residue (Patiño Douce & Harris 1998). Elimination of plagioclase from melanosomes of most GRC tonalitic migmatites is consistent with this. In the example reported by Patiño Douce & Harris (1998), the K-deficient partial melts are trondhjemitic rather than tonalitic (see Figure 8.19b), which may reflect the lower CaO in the starting material (0.94% CaO) compared to the protolith of GRC tonalitic migmatites (1.54% CaO in mesosome **T2-64**). Patiño Douce & Harris (1998) also note congruent dissolution of muscovite during water-present partial melting of quartz-plagioclase-muscovite assemblages, explaining the lack of sillimanite in many GRC tonalitic migmatites.

8.6.4 Geochemical considerations

The partitioning of K_2O between melt and residue leading to the formation of tonalitic leucosomes is easily appreciated from a normative perspective and represented by Figure 8.19. Here, the protolith is approximated by the tonalitic migmatite mesosome sample **T2-64** (semi-pelitic gneiss), whereas the K_2O-rich residue composition is given by mica schist **98-152** (enclave in Dunmore Leucotonalite), which is dominated by the normative orthoclase component. Notably, textural evidence implies that **98-152** has experienced extraction of a melt phase (section 6.2.4), and the plagioclase-depleted character correlates with tonalitic migmatite melanosomes.

This simple relationship is also supported by geochemical variation diagrams, where tonalitic leucosomes, mesosome **T2-64** (64.8% SiO_2) and micaceous enclave **98-152** (57.9% SiO_2) define coherent linear trends (Figure 8.20). In detail, the higher Sr/CaO, An/Ab and more anorthitic plagioclase of leucosome **G2** compared to the other tonalitic leucosome samples (Figure 7.12) requires a slightly more Sr-enriched protolith; this is possibly approximated by its host mesosome, which has equally calcic plagioclase (section 7.2.1). On an upper-crust normalised 'spider-diagram' the pattern produced by all three tonalitic leucosomes is complementary to that of schist **98-152** for most elements, consistent with a melt versus residue relationship (Figure 8.21). The residual nature of **98-152** is corroborated by the extremely low CaO (0.10%), Na_2O (0.25%) and Sr (13 ppm), resulting from almost complete consumption of plagioclase during anatexis; this in turn engenders the elevated concentrations of these components within adjacent leucosomes. This fractionation of Sr between melt and residue is strikingly apparent on Figure 8.20. On the other hand, enrichments in Fe_2O_3t (10.5%), Ba (1333 ppm) and Rb (283 ppm) within **98-152** reflect the preponderance of mica, and are complementary to the depletions of these elements in tonalitic leucosomes (Figure 8.21). Significantly, the concentration of Ba within the residue suggests incompatibility with the coexisting K-poor melt phase, unlike

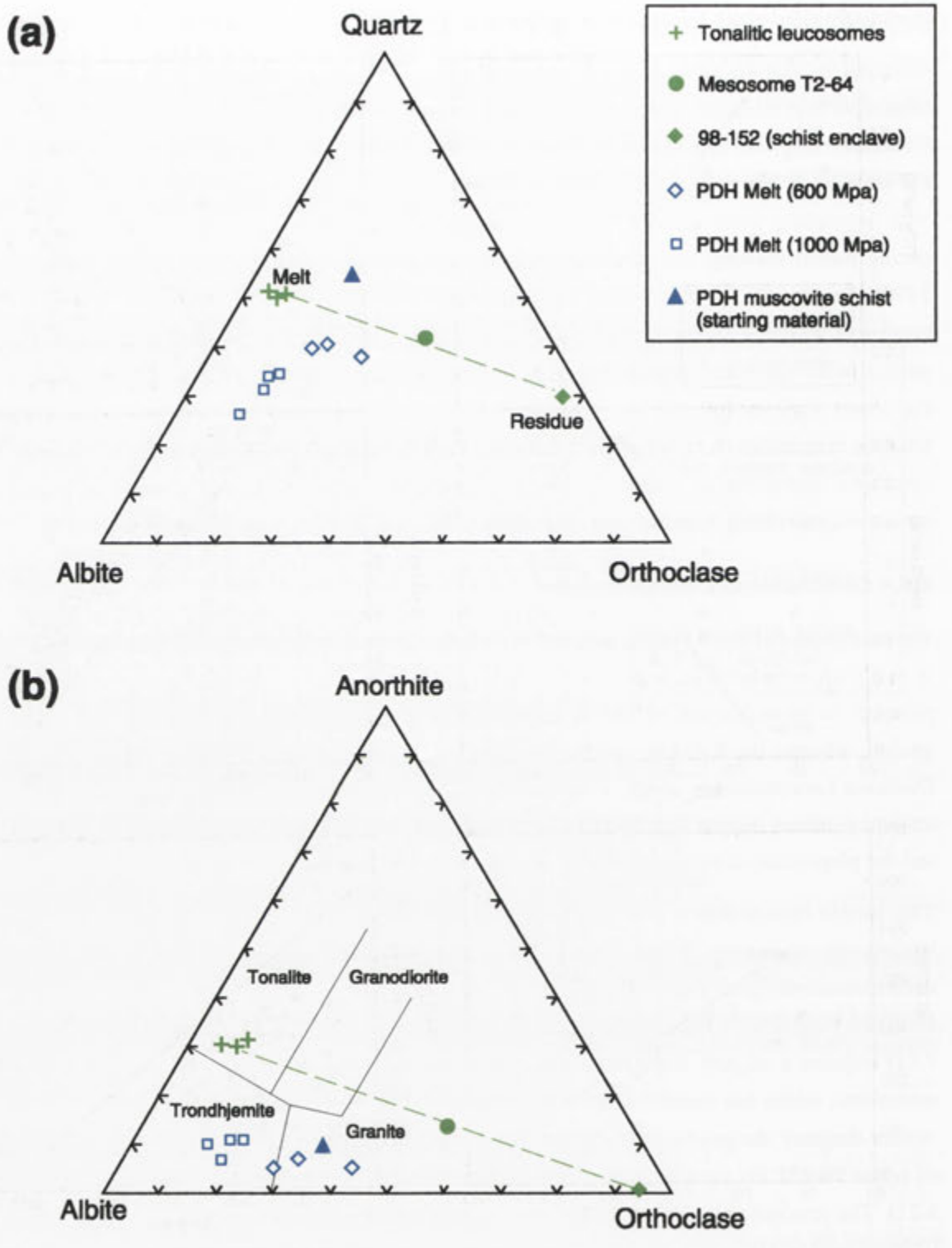

Figure 8.19. Plot of (a) normative quartz, albite and anorthite and (b) normative anorthite, albite and orthoclase for tonalitic leucosomes, inferred protolith **T2-64**, and inferred residue (micaceous enclave **98-152**). The experimental partial melts ('PDH Melt') and starting material of Patiño Douce & Harris (1998) are indicated on both diagrams. Lithological subdivisions on (b) are taken from Barker (1979).

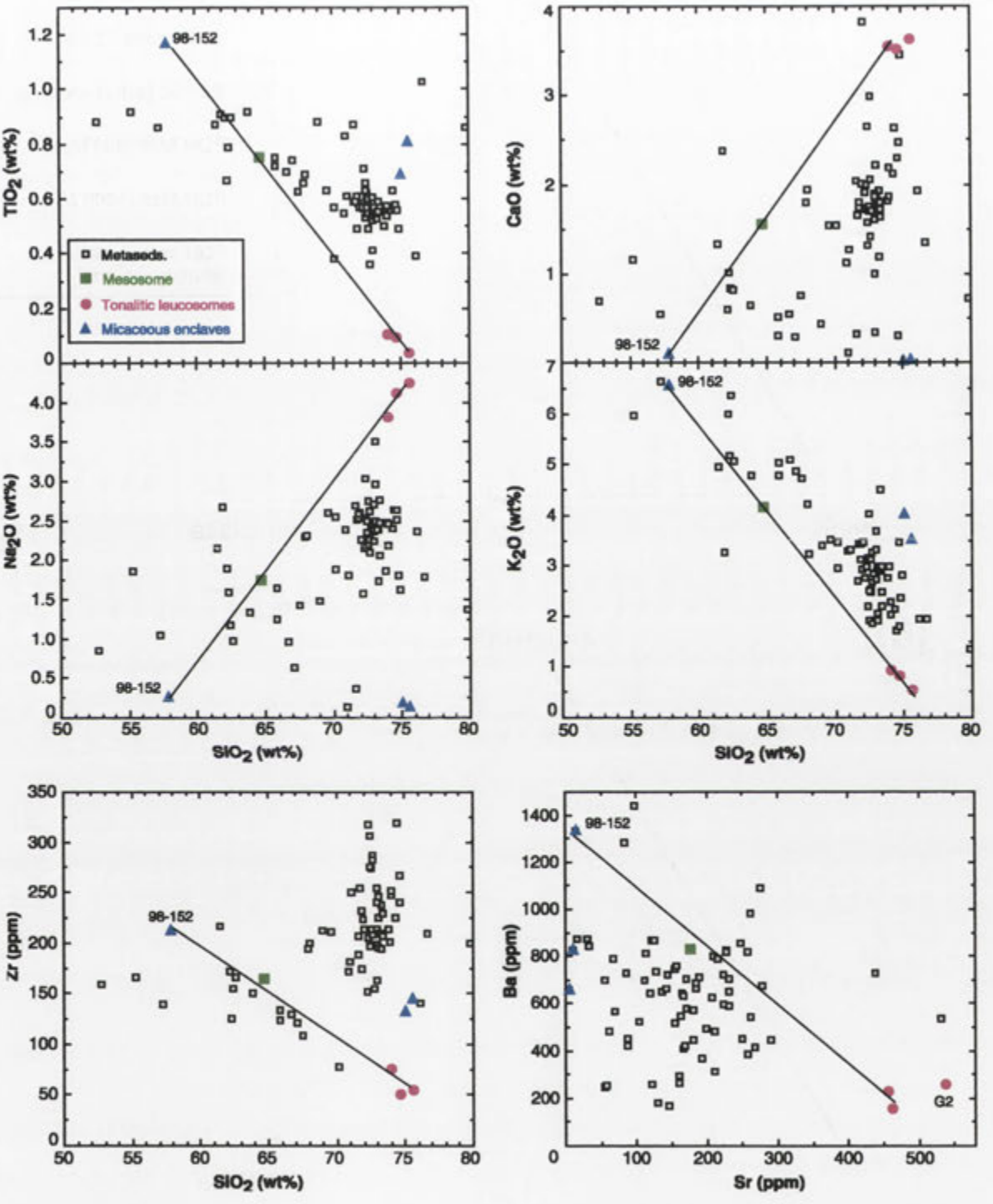

Figure 8.20. Harker variation diagrams for tonalitic leucosomes, semi-pelitic mesosome **T2-64** and micaceous enclaves (**98-MEL**, **98-151**, **98-152**) collected from the Dunmore Leucotonalite. Metasedimentary rocks from both the sub-migmatite and migmatite zone successions are also plotted. Note the linear relationship between leucosomes, mesosome and micaceous enclave **98-152** for all elements.

granitic migmatites where Ba preferentially enters the melt (Figure 8.5). The crystal/liquid partitioning behaviour of Ba is therefore particularly sensitive on the distribution of K_2O between melt and residue.

Note that enrichment of Zr in residual enclave **98-152** results from the low solubility of Zr in tonalitic partial melts, as observed with granitic leucosomes. Nevertheless, all tonalitic leucosomes contain a higher Zr concentration than that required for melt saturation at 700°C, the same feature evident for P_2O_5 in leucosome **98-123** (Figures 8.8, 8.10). Unlike granitic leucosomes, excess Zr is not correlated with biotite content (i.e. Fe_2O_3t), precluding control by residuum entrainment (Figure 8.11). Oversaturation in Zr and P_2O_5 could result from- (1) a higher proportion of apatite and zircon crystals being dispersed in quartz and plagioclase of the semi-pelitic protolith rather than occluded by refractory mica, thereby optimising the amount of these minerals available to react with the melt and facilitating physical entrainment, or (2) accumulation of accessory minerals (either inherited or precipitated) in the analysed portion of the leucosome.

The two other surmicaceous enclaves sampled from the Dunmore Leucotonalite (**98-MEL** and **98-151**) also have depleted chemistries (0.02% and 0.04% CaO) but are more silica-rich (75.6% and 75.1% SiO_2), which reflects the abundant thin quartz laminae of these rocks (section 6.2.4). It is likely that these enclaves are also residual from extraction of partial melt, but derive from a more quartz-enriched portion of the bulk melanosome and are therefore not representative the residue composition overall.

8.6.5 Discussion of tonalitic leucosomes

The chemical features discussed above are consistent with generation of tonalitic leucosomes by partial melting of a semi-pelitic protolith, approximated by migmatite mesosome **T2-64** (or a slightly higher Sr equivalent for **G2**), leaving a micaceous residue similar to schist sample **98-152**. Abundant residual muscovite indicates fluid-rich melting in the muscovite stability field, which, coupled with the low degree of partial melting, resulted in formation of K_2O-depleted leucosomes and K_2O-enriched melanosomes, as most K_2O of the protolith is retained by residual micas. Depression of the plagioclase-quartz solidus facilitated elimination of plagioclase during melting, responsible for the elevated CaO, Na_2O and Sr of tonalitic leucosomes and paucity of plagioclase in residues. Importantly, segregation of partial melts from the micaceous residue was efficient, leading to depletion of TiO_2, (Fe_2O_3t+MgO), Rb and Ba, which are enriched in melanosome biotite.

Tonalitic migmatites exhibit marked and consistent differences in trace element partitioning behaviour to their granitic counterparts, obvious from comparison of the upper continental crust normalised patterns of constituent leucosomes and mesosomes (Figures 7.15b). Firstly, the fractionation of Ba between melt and residue in tonalitic migmatites is opposite to that observed for granitic leucosomes, reflecting incompatibility of Ba with the K-poor melt. Note, however, that Pb is still preferentially partitioned into the tonalitic melt and therefore decoupled from all other LILE. Secondly, the depletion of La, Ce, Nd and especially Th in tonalitic leucosomes relative to

the protolith is much less than in granitic leucosomes, consistent with the greater involvement of monazite in partial melting. This cannot simply reflect greater entrainment of residual, monazite-hosting biotite into tonalitic leucosomes, as these are equally depleted in ferromagnesian elements as granitic leucosomes (section 7.5). Alternatively, it could relate to a higher solubility or dissolution rate of monazite in a tonalitic melt, or, as monazite solubility is strongly influenced by H_2O (Montel 1986), might indicate slightly higher a_{H_2O} during tonalitic leucosome formation. Increased monazite dissolution may also reflect an enhanced ability to interact with the melt during anatexis, such as would be facilitated by localisation along plagioclase-quartz grain boundaries in the protolith, rather than being enclosed by refractory micas. This would also release refractory monazite crystals into the tonalitic melt, contributing towards elevated LREE and Th concentrations. More work is required to evaluate these propositions.

The occurrence of tonalitic leucosomes in the GRC therefore provides a rare natural example of the generation of near-solidus, K-deficient partial melts from micaceous metasedimentary protoliths, as experimentally achieved by Patiño Douce & Harris (1998). Clearly, the compositional character of initial melts in quartz-feldspar-muscovite assemblages is completely different to the Tuttle & Bowen (1958) 'minimum melt', where haplogranitic liquids are in equilibrium with potassic feldspar. Further elucidation of the formation and chemical evolution of these K-poor melts awaits experimental determination of the minimum or eutectic melt composition in the muscovite-quartz-plagioclase-H_2O system.

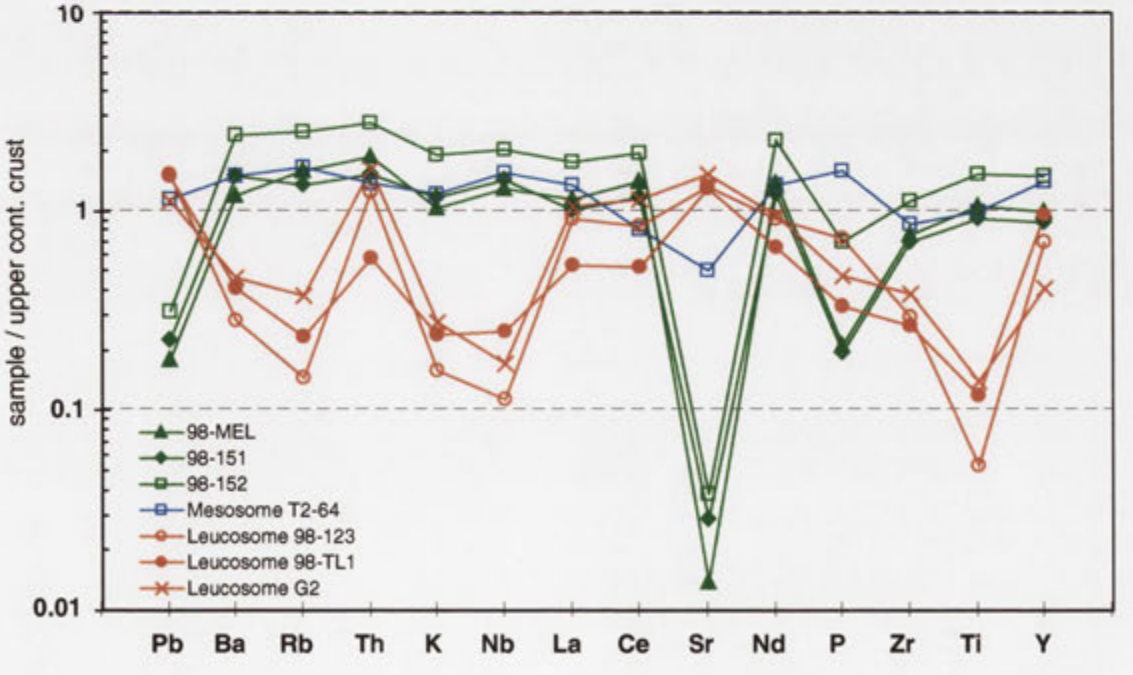

Figure 8.21. Upper continental crust-normalised 'spider diagram' for *in situ* tonalitic leucosomes, mesosome **T2-64** and micaceous enclaves (**98-MEL**, **98-151** and **98-152**) collected from the Dunmore Leucotonalite (normalising values as for Figure 7.15).

8.7 Origin of small granitic bodies

Compelling outcrop relationships, detailed in Chapter 5, combined with the remarkable similarity of both normative composition (Figure 7.13) and whole rock geochemistry (Figure 7.14) indicates formation of small granitic bodies by coalescence of efficiently segregated leucosome partial melts generated within host migmatites. For granitic bodies of northern Schofield Creek (**98-SC** and **98-WF1B**), this origin is substantiated by similarity of feldspar and mica compositions with those of enclosing stromatic migmatites (section 7.3).

Thus, small granitic bodies are properly viewed as magma conduits, through which segregated, metasedimentary-derived partial melt batches are transported from the generative site(s). The small-scale heterogeneities in these bodies reflects the imperfect blending of constituent, chemically-disparate partial melts, which were sourced from different protoliths. The implications of this for the formation of larger scale magmatic bodies, the Harrow type plutons, are explored in the next chapter.

Chapter 9: Mineral chemistry, geochemistry and petrogenesis of Harrow type granitic rocks

9.1 Introduction

Muscovite-bearing 'Harrow type' granitic plutons in the eastern GRC were emplaced synchronous with extensive partial melting within surrounding quartzofeldspathic schists and gneisses, and exhibit intimate, partly transitional field relationships with these migmatitic rocks (Chapters 5 and 6). This demands a fundamental link between the petrogenesis of Harrow type plutons and *in situ* anatexis in the host metasedimentary sequence. The purpose of this chapter is to elaborate this link, documenting mineral and rock chemistry. After chemical subdivision of the Harrow types, the mechanisms controlling the large degree of textural, lithological and chemical variation within and between individual plutons are elucidated. Note that the absence of mafic microgranular enclaves precludes the direct involvement of coeval basic magmas in the formation of Harrow type granitic rocks (apart from the Blair Atholl Adamellite).

9.2 Mineral chemistry

The chemistry of constituent mineral phases from selected Harrow type plutons is presented in Appendix B. Samples were analysed from Kout Norien Granodiorite (**97-302**), Harrow Granodiorite (**98-86**), Carrigeen Granodiorite (garnet-bearing sample T2-69), Marn Mering Granodiorite (**T2-1**), Dunmore Leucotonalite (**T2-20**), Nangkita Adamellite (**97-233**) and a garnet leucoadamellite sheet from Schofield Creek (**98-19**).

9.2.1 Plagioclase

The compositional characteristics of plagioclase within Harrow type granitic bodies is summarised by Table 9.1 and Figure 9.1. The most calcic composition derives from a small anhedral core within a plagioclase grain of Nangkita Adamellite (~An_{47}), though other anhedral plagioclase cores of this sample extend down to ~An_{24}. A similar feature is evident within the Marn Mering Granodiorite, where the composition of plagioclase cores is strongly variable (An_{31}-An_{43}). Apart from the albitic rims of plagioclase grains within the Nangkita Adamellite, which probably result from exsolution of the Na component from the enclosing alkali feldspar, the most sodic plagioclase occurs within the garnet leucoadamellite (An_9-An_{16}). This is clearly more sodic than in the garnet-bearing Carrigeen Granodiorite (plagioclase An_{20}-An_{30}). Due to pervasive alteration, only two plagioclase laths were analysed from the Dunmore Leucotonalite, the composition of which (An_{28}-An_{38}) overlaps that of adjacent tonalitic migmatite leucosomes.

Plagioclase of the Kout Norien Granodiorite is weakly zoned and bracketed in the range An_{20}-An_{30}, similar to that of the enclosed diatexite enclave **97-286-1** (see Figure 7.2). However, plagioclase of the Harrow Granodiorite pluton, which has some petrographic and geochemical affinity with the Kout Norien Granodiorite, is distinctly more calcic, with cores extending up to An_{44}.

Sample	*Grain*	*Plag composition (An%)*				*Comment*
		CORE	➤	➤	*RIM*	
Kout Norien	1A	21.9	27.9	22.3	21.3	Anhedral core with overgrowths
Granodiorite	3A*	26.3			23.1	Anhedral core, rim
97-302	4A		27.1			Unzoned grain
	8A	23.5				Unzoned grain
	10A	24.6		27.2	20.6	Weak patchy zoning, rim
Harrow	1A	43.9	27.5	30.6	27.1	Oscillatory zoned from euhedral core
Granodiorite	2A	42.4		33.0	25.1	Anhedral core with overgrowths
98-86	5A	36.0			32.6	Anhedral core with overgrowth
Marn Mering	2A	39.3			19.2	Anhedral core, rim
Granodiorite	3A	30.8	23.9		29.6	Anhedral core, irregular overgrowth, rim
T2-1	4A	42.8	27.6		24.2	Euhedral core, irregular overgrowth, rim
	5A	34.0			16.5	Diffuse core, rim
	9A	34.5		26.0	20.1	Anhedral core, thick overgrowths
Nangkita	1A	34.4		28.9	21.6	Anhedral core, irregular overgrowth, rim
Adamellite	4A	24.1		28.0	18.3	Anhedral core, irregular overgrowth, rim
97-233	7A	30.3			27.5	Weak continuous zoning
	7B*	26.5			2.6	Unzoned grain, discrete irregular rim
	9A*	46.9		27.7	3.0	Continuous zoning, discrete rim
	9B*	39.7		34.4	2.9	anhedral core, overgrowth, discrete rim
Dunmore	5A	37.2	35.4	37.6	32.0, 28.3	Anhedral core, oscillatory overgrowths
Leucotonalite	6A	33.0			29.3	Corroded core, discrete rim
T2-20						
Carrigeen	5A	23.3			25.3	Weak continuous zoning
Granodiorite	5B	30.1			23.7	Weak continuous zoning
T2-69	9A	28.5			26.5	Corroded core, discrete rim
(garnet-bearing)	10A	29.5		23.7	25.9	Corroded core, irregular overgrowths
Garnet	8A	11.9			9.8	Weak continuous zoning
Adamellite	9A	13.7			11.6	Weak continuous zoning
98-19	11A	13.9	16.1		9.2	Diffuse oscillatory zoning

Table 9.1. Summary of plagioclase compositional characteristics in Harrow type granitic rocks (full microprobe analyses are in Appendix B). The compositions listed represent individual analyses, arranged according to their relative location within the plagioclase grain (An% = mol. percent anorthite). Grains marked with an asterisk are inclusions within alkali feldspar.

9.2.2 Alkali Feldspar

Unlike plagioclase, alkali feldspar has a narrow compositional range within and between analysed Harrow type rocks (Figure 9.1). The exception is the alkali feldspar of the Kout Norien Granodiorite, which exhibits pronounced zonation from relatively sodic cores (~Or_{80}) through to more potassic rims (~Or_{87}). This is a similar compositional range to alkali feldspar of the diatexite raft **97-286-1** (see Table 7.3).

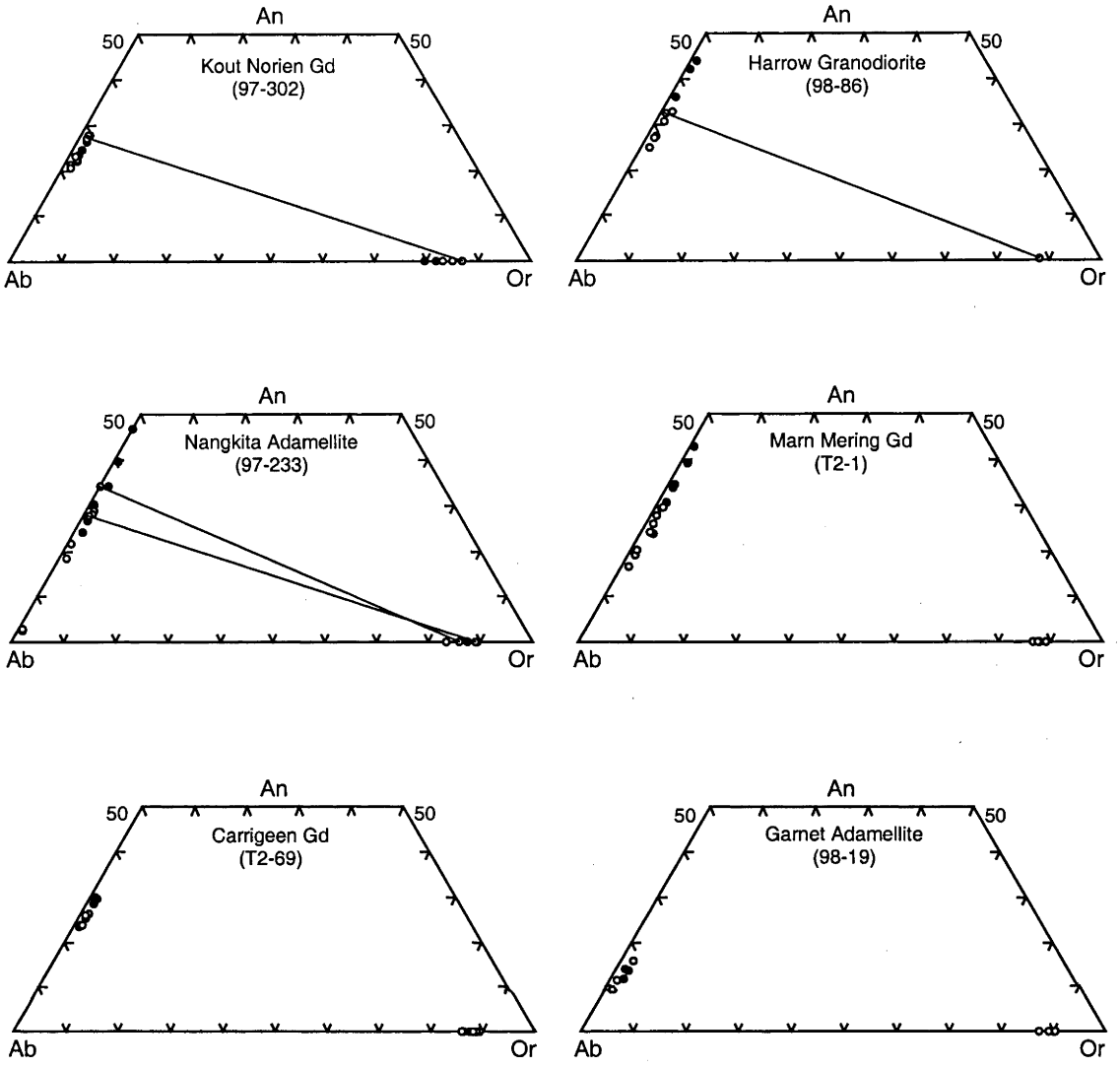

Figure 9.1. Range of plagioclase and alkali feldspar compositions for Harrow type granitic rocks (An = atomic Ca/Ca+Na+K, Ab = atomic Na/Ca+Na+K, Or = atomic K/Ca+Na+K) (full analyses are in Appendix B). The filled symbols represent the cores of analysed grains and open symbols the rims. Tie lines connect plagioclase inclusions with their host alkali feldspar.

9.2.3 Biotite

Biotite from Harrow type granitic rocks is aluminous (>3.35 Al atoms per 22 oxygens) and collectively forms a scattered array tending towards lower total Al but higher Ti contents with increasing Mg# (Figure 9.2). However, biotite from each pluton is compositionally distinct, with clear differences in Mg# and range of total Al and Ti contents, the latter two parameters being quite variable within individual samples. Biotite from the most mafic body, the Kout Norien Granodiorite, has the highest Mg# and extends to the highest Ti content, being similar to diatexite **97-286-1** biotite. Biotite of the nearby Harrow Granodiorite pluton has slightly lower Mg# and Ti, overlapping with that of Schofield Creek migmatites and granitic sheet **98-WF1B**, whereas Carrigeen Granodiorite biotite has marginally lower Mg# and Ti than this. Although only one

grain was analysed, biotite from the Dunmore Leucotonalite overlaps the range of Al and Ti within tonalitic migmatites (similar to the Robson Creek biotite field in Figure 9.2) but has slightly lower Mg#.

In contrast, biotite of the garnet adamellite and Marn Mering Granodiorite has much lower Mg# and extends to more aluminous compositions, plotting remote from the migmatite biotite field. The single biotite analysis from Nangkita Adamellite also has considerably lower Mg# and Ti than that of adjacent migmatites.

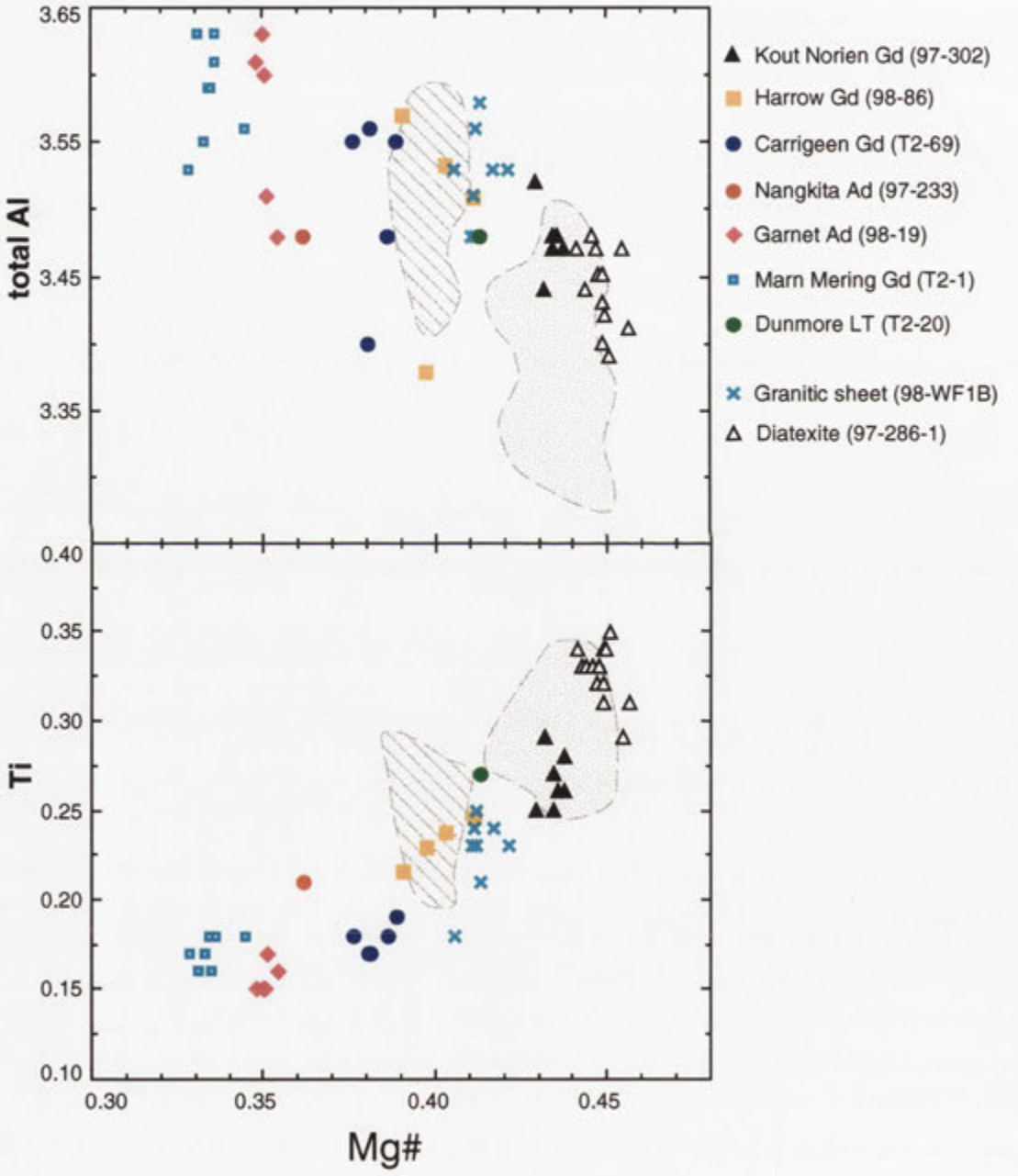

Figure 9.2. Biotite composition (in atoms per 22 oxygens) for Harrow type granitic rocks analysed by this study, compared to that of granitic sheet **98-WF1B** and diatexite **97-286-1** (Ad = adamellite, Gd = granodiorite, LT = leucotonalite). The biotite field for migmatites from Schofield Creek (diagonal stripes) and Robson Creek (dots) is also shown (Mg# = Mg/Mg+Fe).

9.2.4 Muscovite

All muscovite compositions from Harrow type granitic rocks were obtained from euhedral, platy grains of magmatic origin. These overlap the field of muscovite from metasedimentary rocks (Figure 9.3) apart from muscovite of the garnet adamellite and Nangkita Adamellite, which has lower and higher (Fe+Mg+Ti) contents respectively. Nangkita Adamellite muscovite is, however, indistinguishable from that of Chin Chap Creek leucosome **98-102**. Marn Mering Granodiorite muscovite resembles that of the small granitic bodies from Schofield Creek, whereas muscovite within the Kout Norien Granodiorite and Carrigeen Granodiorite overlaps compositionally with that of diatexite **97-286-1**. Dunmore Leucotonalite muscovite is chemically variable, but similar to that of tonalitic migmatites.

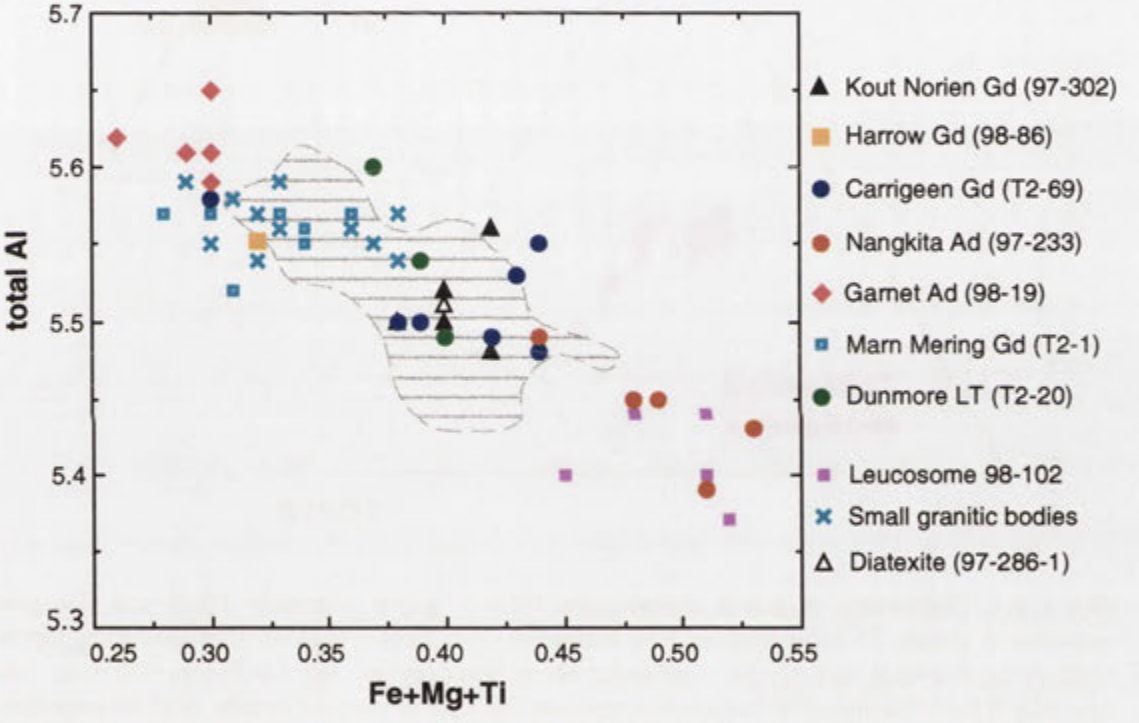

Figure 9.3. Muscovite composition (in atoms per 22 oxygens) for Harrow type granitic rocks compared to that of small granitic bodies (**98-WF1B** and **98-SC**), diatexite **97-286-1** and stromatic migmatites (shaded field, includes both granitic and tonalitic varieties). Muscovite from leucosome **98-102** is plotted separately (Ad = adamellite, Gd = granodiorite, LT = leucotonalite).

9.2.5 Garnet

The texturally contrasting garnets of Carrigeen Granodiorite T2-69 and leucoadamellite **98-19** (Table 6.3) are manganiferous and dominated by the almandine and spessartine components (up to 35% spessartine in **98-19**) (Figure 9.4), as is typical of garnets in peraluminous leucogranitic rocks (Clarke 1981). Garnets of T2-69 also exhibit a weak reverse compositional zonation, such that the spessartine and grossular components increase marginally from core to rim, with

concomitant decrease in the almandine and pyrope components (Figure 9.4). Conversely, garnets of **98-19** are more strongly zoned in the opposite sense, where spessartine content decreases towards the margin of the grain, with increase in the almandine component. Garnets within this sample also contain slightly lower molar proportions of grossular (1.8-2.0%) and pyrope (5.8-6.3%) than those of T2-69 (1.5-3.0% grossular, 6.6-9.0% pyrope). Differences in chemical zonation, as well as morphologies, imply that garnets within these two samples have a different petrogenesis (section 9.9.2).

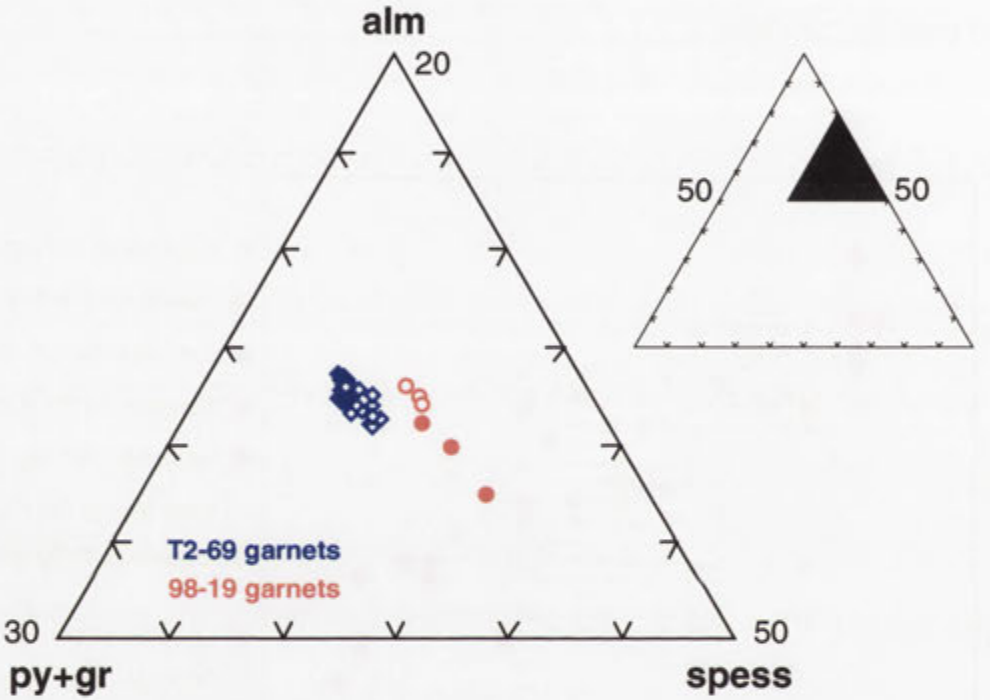

Figure 9.4. Comparison of garnet compositions between garnet adamellite **98-19** and Carrigeen Granodiorite sample T2-69 in terms of their almandine (alm, Fe/(Fe+Mg+Mn+Ca), spessartine (spess, Mn/(Fe+Mg+Mn+Ca)) and pyrope + grossular components (py+gr, Mg+Ca/(Fe+Mg+Mn+Ca); see Appendix B for full analyses). Filled symbols represent the cores of analysed garnets. Note the large core-to-rim 'normal' zonation in garnets of **98-19**, in contrast to weak 'reverse' zonation and higher py+gr of Carrigeen Granodiorite sample T2-69.

9.3 Geochemistry of Harrow type granitic rocks

The geochemistry of forty five Harrow type granitic rocks is tabulated in Appendix C. Analyses were obtained from large samples (10-20 kg) from which extraneous material, such as graphic alkali feldspar megacrysts and micaceous clots or selvedges, was excluded. The exception is Carrigeen Granodiorite sample **98-64A**, the analysed portions of which contain small alkali feldspar megacrysts. Schofield Adamellite samples from the southern 'mingled' horizon (**98-12**, **98-13** and **98-14D**) and Marn Mering Granodiorite sample **98-56** are texturally heterogeneous, containing variable amounts of coarser, more feldspar-rich granitic material (section 6.4.3).

9.3.1 Overview of the major and trace element characteristics

Harrow type granitic rocks have a limited range of SiO_2 (71.7% to 76.7%) and low ferromagnesian element concentrations, with total Fe_2O_3 being mostly less than 1.5%. As distinct from the other magma types of the GRC (Part III), elemental abundances of Harrow types are poorly correlated with silica on geochemical variation diagrams, though scattered linear trends are evident for Al_2O_3 and ferromagnesian elements (Figure 9.5). This is exemplified by the A.S.I, which, although mostly greater than 1.1, exhibits large variation independent of SiO_2 content (Figure 9.5j). Distinctively, Harrow types also exhibit dramatic dispersion in K_2O content, extending continuously from 1.1% to 6.0%, which produces a near-vertical array on variation diagrams. A sympathetic trend is also produced by Ba.

Chemical and physical characteristics enable resolution of Harrow type granitic rocks into four distinct categories, mafic granodiorites, felsic adamellites to granodiorites (which are volumetrically predominant), leucotonalites and garnet-bearing adamellites.

Mafic granodiorites encompass the relatively biotite-rich and sillimanite-bearing Kout Norien Granodiorite, Bryan Creek Granodiorite, Harrow Granodiorite and the Carrigeen Granodiorite. These bodies host numerous metasedimentary enclaves, including sillimanite-rich varieties not recognised in felsic plutons, and extend to lower silica and Al_2O_3, but clearly higher TiO_2, (Fe_2O_3t+MgO) and A.S.I. than other Harrow types (Figure 9.5), the latter manifesting sillimanite content. Moderately high Rb contents (to 170 ppm for the Bryan Creek Granodiorite) result in higher Rb/Sr than other Harrow types, excepting garnet-bearing phases. On Harker variation diagrams, mafic granodiorites define scattered negative trends for TiO_2, (Fe_2O_3t+MgO), MnO, and P_2O_5 with progression to higher silica (Figure 9.5). Flatter trends are defined by CaO, Na_2O and Rb/Sr, whereas K_2O and Ba exhibit more complex variation. Unlike other Harrow types, mafic granodiorites also exhibit a coherent decrease in K/Rb with progression to higher total Fe_2O_3 (Figure 9.6), which reflects an increasing modal proportion of biotite, a major reservoir for Rb (e.g Bea *et al.* 1994). Note that the Carrigeen Granodiorite evolves to more leucocratic compositions that overlap chemically with felsic Harrow types.

Felsic adamellites to granodiorites include the Nangkita Adamellite of the Coleraine district and the leucocratic plutons outcropping around Harrow, of which the well-exposed Schofield Adamellite has been most thoroughly sampled (see below). Collectively, these rocks exhibit similar geochemical trends to mafic Harrow type plutons, but mostly have lower TiO_2, (Fe_2O_3t+MgO) and K/Rb, reflecting the paucity of biotite (Figures 9.5, 9.6). However, strong variation in K_2O (from 2.9% to 5.6%) and Ba (550-2100 ppm) over the narrow silica range is the most striking chemical attribute of this group. Another important aspect of felsic plutons is that Sr contents exceed 200 ppm, ranging up to ~340 ppm (Marn Mering Granodiorite **98-58**), but Rb concentrations are generally less than 120 ppm. As a result, Rb/Sr ratios are below 0.6 (Figure 9.5). Low Rb/Sr ratios, combined with the extreme K_2O variation, is the definitive signature of felsic Harrow types.

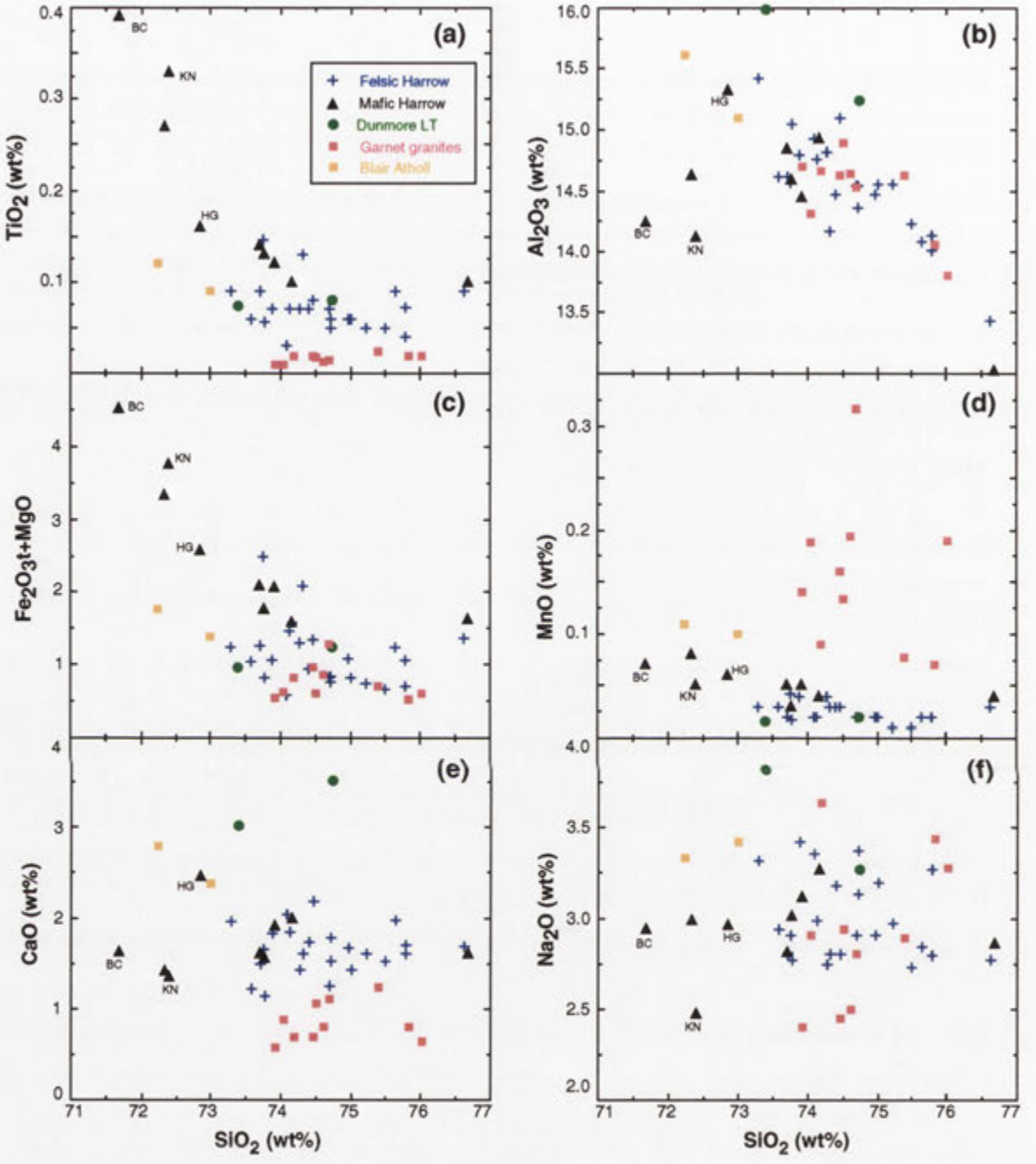

Figure 9.5 (a-f). Harker variation diagram for different Harrow type granitic rocks of the GRC (LT = Leucotonalite). Mafic granodiorites are labelled individually; BC = Bryan Creek Granodiorite, KN = Kout Norien Granodiorite, HG = Harrow Granodiorite. All other mafic Harrow types are samples of the Carrigeen Granodiorite pluton. The lowest silica Blair Atholl Adamellite composition is sample W7-128 of Bushell (1996).

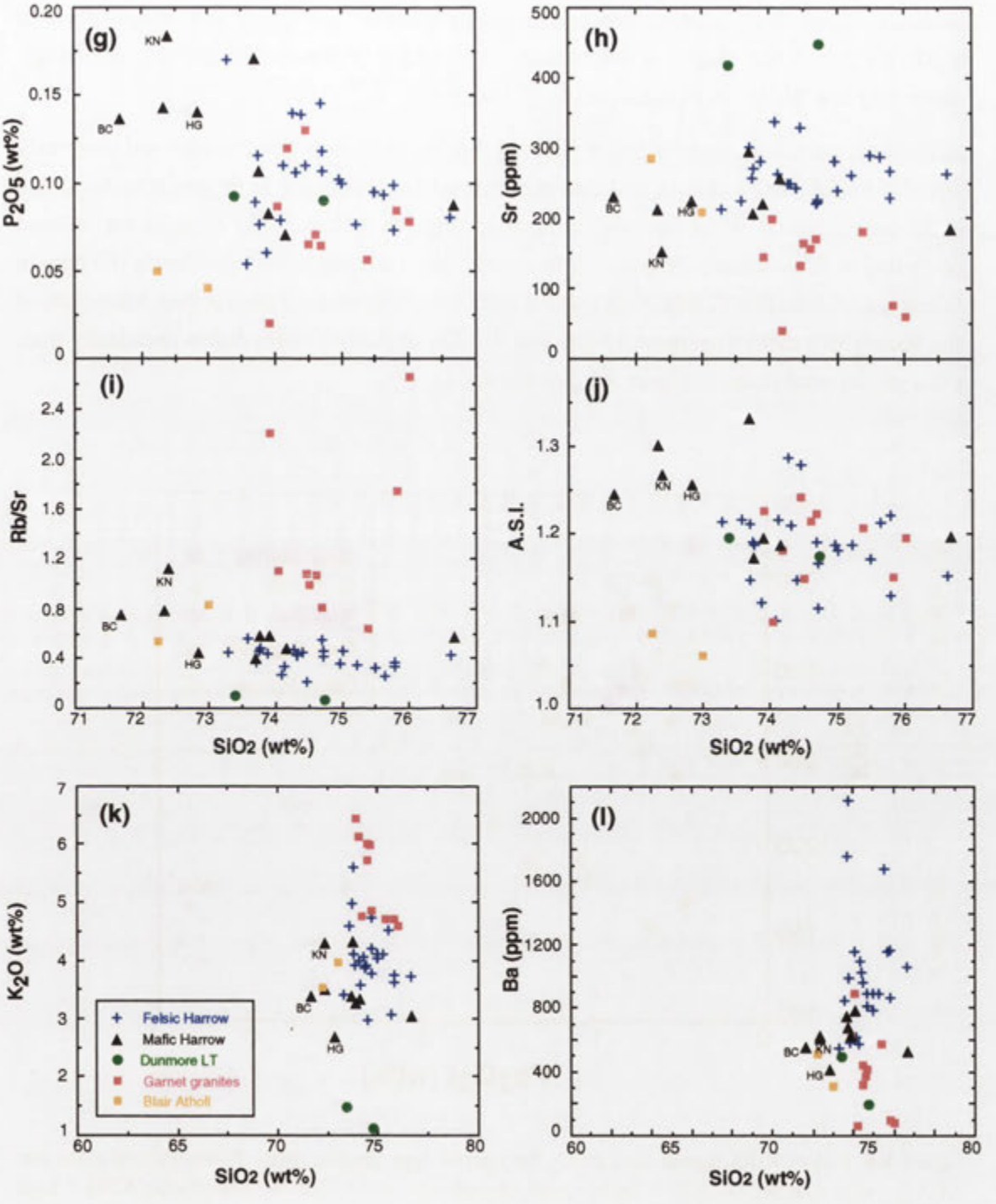

Figure 9.5 (g-l). Harker variation diagram for different Harrow type granitic rocks of the GRC (LT = Leucotonalite). Mafic granodiorites are labelled; BC = Bryan Creek Granodiorite, KN = Kout Norien Granodiorite, HG = Harrow Granodiorite. All other mafic Harrow types are samples of the Carrigeen Granodiorite pluton. Note that the abscissa for Figures (K) and (L) has been expanded to emphasise the marked variation in K_2O and Ba over the small silica range.

Dunmore Leucotonalite samples are also low in ferromagnesian elements, but relative to felsic adamellite-granodiorite plutons have conspicuously elevated CaO and Sr, and strongly depleted K_2O, reflecting the plagioclase-dominated, but alkali feldspar-impoverished mineralogy. Extremely low Rb/Sr (<0.1) is diagnostic (Figure 9.5I).

In contrast, **garnet-bearing rocks** are resolved from other Harrow types by high and complexly variable Rb/Sr, MnO and K_2O, and strongly depleted TiO_2, CaO and Sr (Figure 9.5). Na_2O and K/Rb also exhibit a wider compositional range (Figures 9.5f, 9.6). Ba contents are reduced compared to felsic adamellite-granodiorites (<400 ppm) and fall to very low levels (60 ppm in Glengoyne Adamellite **97-98**). Note that the early syn-compressional Blair Atholl Adamellite of the Wando Vale district (samples **97-201** and W7-128 of Bushell 1996) differs chemically from other garnet adamellites in Figure 9.5 (section 9.9.3).

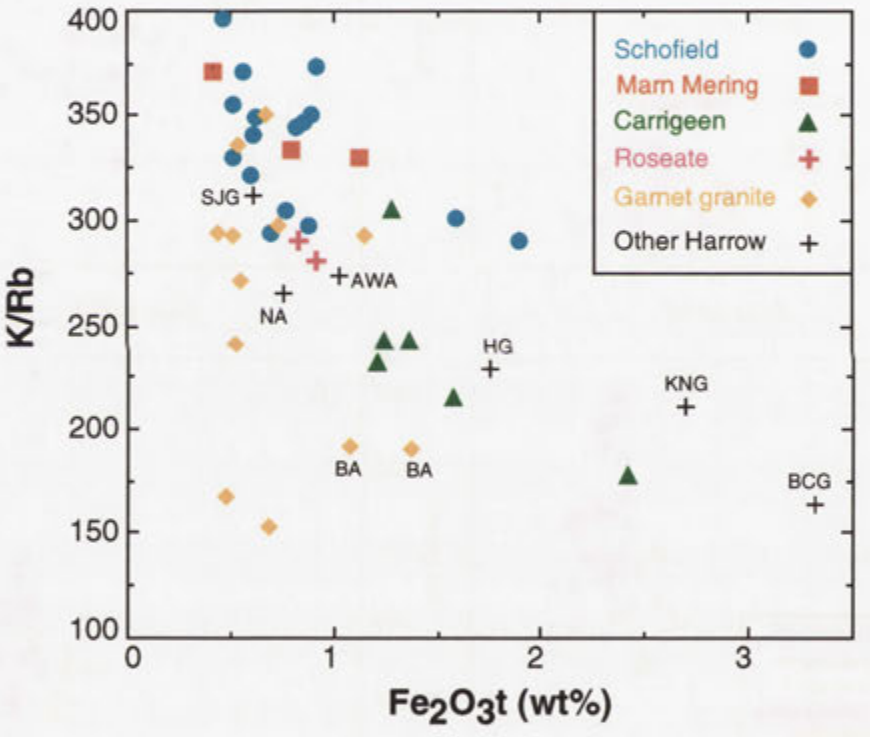

Figure 9.6. Plot of K/Rb against total Fe_2O_3 for Harrow type granitic rocks. Pluton abbreviations are: AWA = Awaiti Adamellite; BCG = Bryan Creek Granodiorite; HG = Harrow Granodiorite; KNG = Kout Norien Granodiorite; NA = Nangkita Adamellite; SJG = Scrubby Junction Granodiorite. The Blair Atholl Adamellite samples are labelled separately (BA) from other garnet-bearing granitic rocks.

Distinction between mafic granodiorites, felsic adamellite-granodiorites and leucotonalites is also obvious when elemental concentrations are normalised to those of the upper continental crust (Figure 9.7). Mafic granodiorites have reasonably flat patterns, with minor relative depletion in Sr, Zr and Ti, and enrichment in Pb and Rb. More complex variation is apparent for

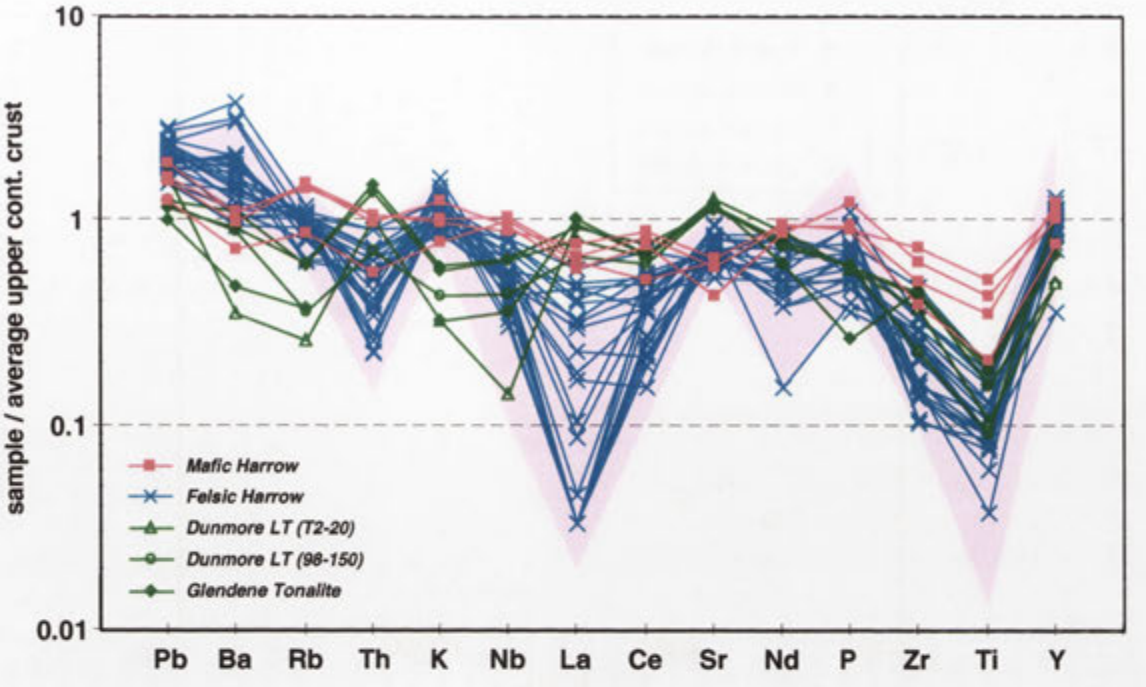

Figure 9.7. Upper continental crustal-normalised abundance diagram comparing mafic Harrow type granodiorites, felsic Harrow type adamellites-granodiorites and leucotonalites; normalising values are as for Figure 7.15 (LT = Leucotonalite). The compositional field for migmatite leucosomes (shaded) is also indicated (from Figure 7.15). Data for the three Glendene Tonalite samples is from Fitzherbert (1998).

felsic Harrow type plutons, which, apart from differences outlined above, compared to mafic granodiorites have variable enrichment in Pb, Ba and Sr, and depletion in Rb, P, HFSE (Y, Zr, Th, Nb) and LREE (La, Ce, Nd). This results in extension to much higher Ba/La and slightly higher K/Th (Figure 9.8). Felsic adamellite-granodiorites therefore have strongly fractionated chemistry relative to the upper continental crust.

Dunmore Leucotonalite samples exhibit very distinctive upper crustal-normalised patterns unlike those of other felsic Harrow types, with marked Pb, Ba, K and Rb depletion but higher Th, La and Ce; the elevated Sr is also very conspicuous (Figure 9.7). Accordingly, the leucotonalite has lower K/Th and Ba/La compared to all other Harrow type granitic rocks (Figure 9.8). The Glendene Tonalite samples of Fitzherbert (1998) have identical features, implying that the petrogenesis of these two plutons is similar (section 9.8). Further, Dunmore Leucotonalite sample **98-150** has a slightly different chondrite-normalised REE pattern than that of a typical felsic Harrow type pluton (Schofield Adamellite **98-13**), with greater LREE (La-Gd) enrichment (Figure 9.9). As HREE concentrations are indistinguishable, this results in higher $(La/Yb)_N$ for **98-150** (~7.2) compared to **98-13** (La_N /Yb_N ~3.3). Nevertheless, the REE patterns of both Harrow type samples have similar shape, with conspicuous positive Eu anomalies. Apart from the latter, these patterns mirror that of their potential metasedimentary protoliths at systematically lower total REE concentrations, particularly regarding the distinctive negative Nd anomaly (which is not exhibited by other GRC granitic types, see Figures 15.7, 15.10).

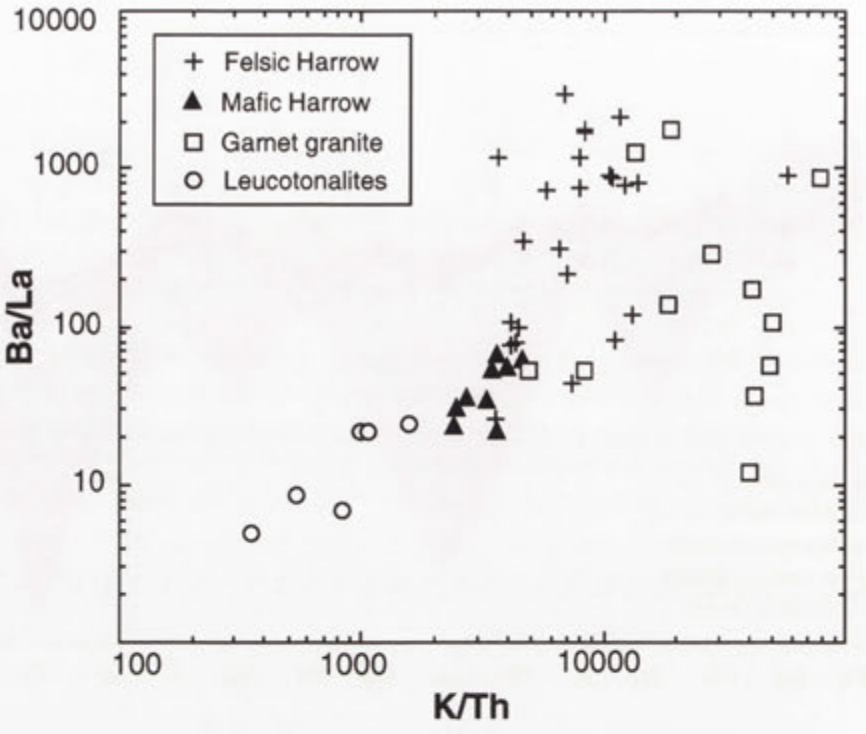

Figure 9.8. Ba/La against K/Th (logarithmic scale) for Harrow type rocks. Leucotonalites include the Dunmore Leucotonalite and the Glendene Tonalite, data for the latter from Fitzherbert (1998). The two garnet granite samples with the highest K/Th are Blair Atholl Adamellite.

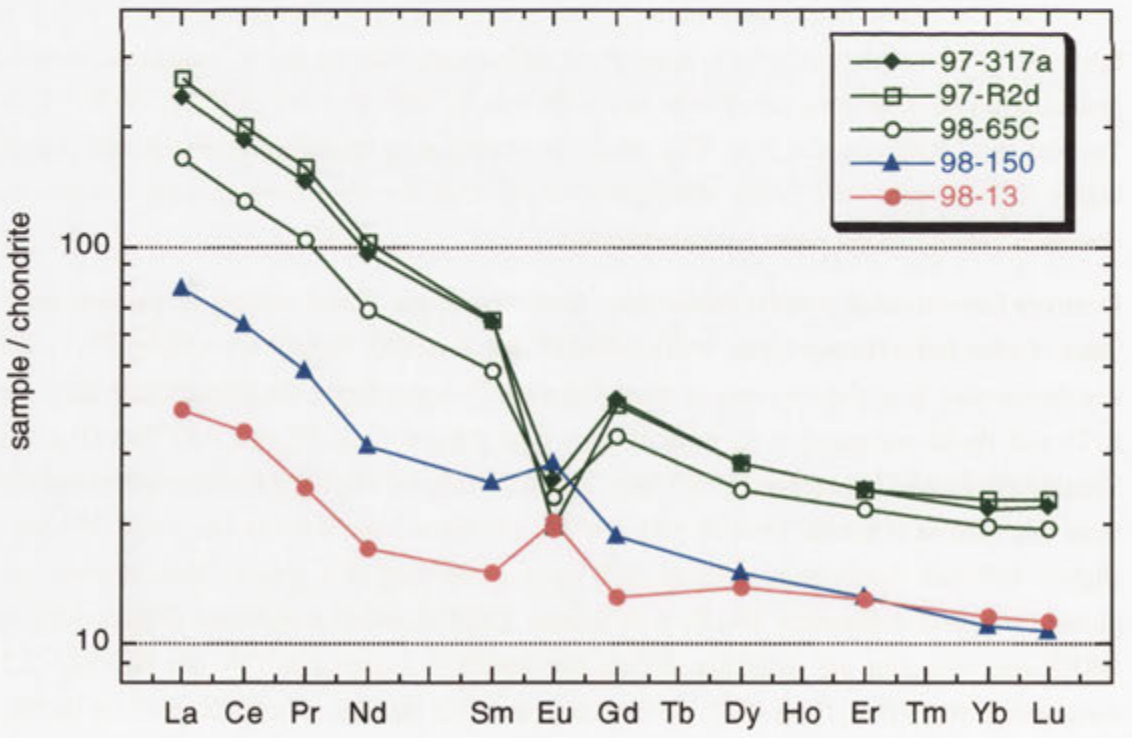

Figure 9.9. Chondrite-normalised REE abundances (normalising values from Anders & Grevesse 1989) for Schofield Adamellite **98-13** and Dunmore Leucotonalite **98-150** compared to GRC metasedimentary rocks (green).

9.3.2 Geochemical resolution of individual leucocratic plutons

Apart from leucotonalites and garnet-bearing phases, individual felsic Harrow type plutons are not easily resolved on geochemical variation diagrams. Plutons for which multiple analyses exist (Schofield Adamellite, Marn Mering Granodiorite, Roseate Adamellite) exhibit large internal variation and consequently have mutually overlapping compositional fields for many elements. Silica-rich variants of the Carrigeen Granodiorite also overlap chemically with leucocratic Harrow types (Figures 9.5, 9.6). Nevertheless, some subtle differences are recognised. Schofield Adamellite extends to the highest K_2O contents and has dramatic variation in K_2O over a small range of Fe_2O_3t (Figure 9.10); clearly the striking K_2O variation of felsic Harrow types is present to a significant degree in this one pluton. The Carrigeen Granodiorite has distinctly higher total Fe_2O_3 than Schofield Adamellite and Marn Mering Granodiorite samples of the same K_2O, and extends towards the mafic Kout Norien Granodiorite (Figure 9.10). Note however that two Schofield Adamellite samples (**98-14A-1** and **98-14A-2**) have higher total Fe_2O_3 contents than other analyses of the pluton, and overlap with the field of mafic granodiorites. These rocks derive from a heterogeneous biotite-rich domain in the southern 'mingled' unit of the body (see section 6.4.3c).

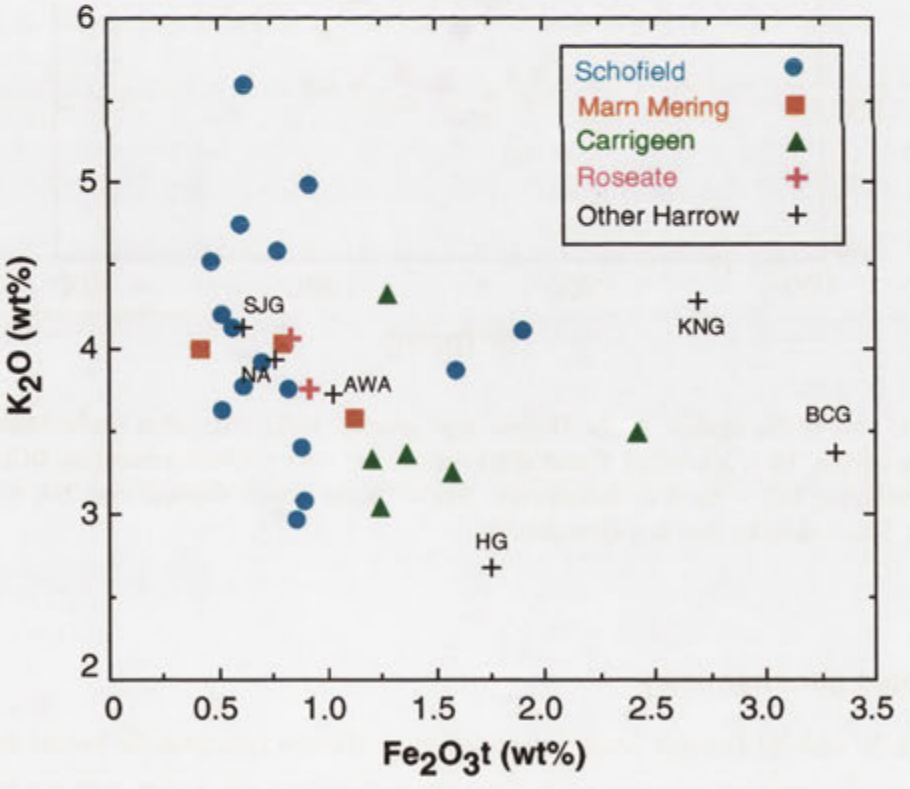

Figure 9.10. Plot of K_2O versus total Fe_2O_3 for Harrow type granitic rocks. Note that two Schofield Adamellite samples (**98-14A-1** and **98-14A-2**) have clearly higher total Fe_2O_3 than other felsic plutons. Pluton abbreviations are: AWA = Awaiti Adamellite; BCG = Bryan Creek Granodiorite; HG = Harrow Granodiorite; KNG = Kout Norien Granodiorite; NA = Nangkita Adamellite; SJG = Scrubby Junction Granodiorite.

Felsic plutons also extend to markedly higher Ba contents than does the Carrigeen Granodiorite (Figure 9.11). For a given Ba content, Marn Mering Granodiorite samples have higher Sr than the Schofield Adamellite. Significantly, the most Ba- and Sr-rich Schofield Adamellite samples (**98-12**, **98-13** and **98-14D**) contain variable amounts of the intermingled more feldspathic granitic material (section 6.4.3c). The Marn Mering Granodiorite also incorporates this ingredient, a higher proportion of which is in the more Sr- and Ba-rich sample **98-58**. This intermingled granitic component may therefore be partly responsible for the elevated Ba and Sr of the Schofield Adamellite and Marn Mering Granodiorite plutons.

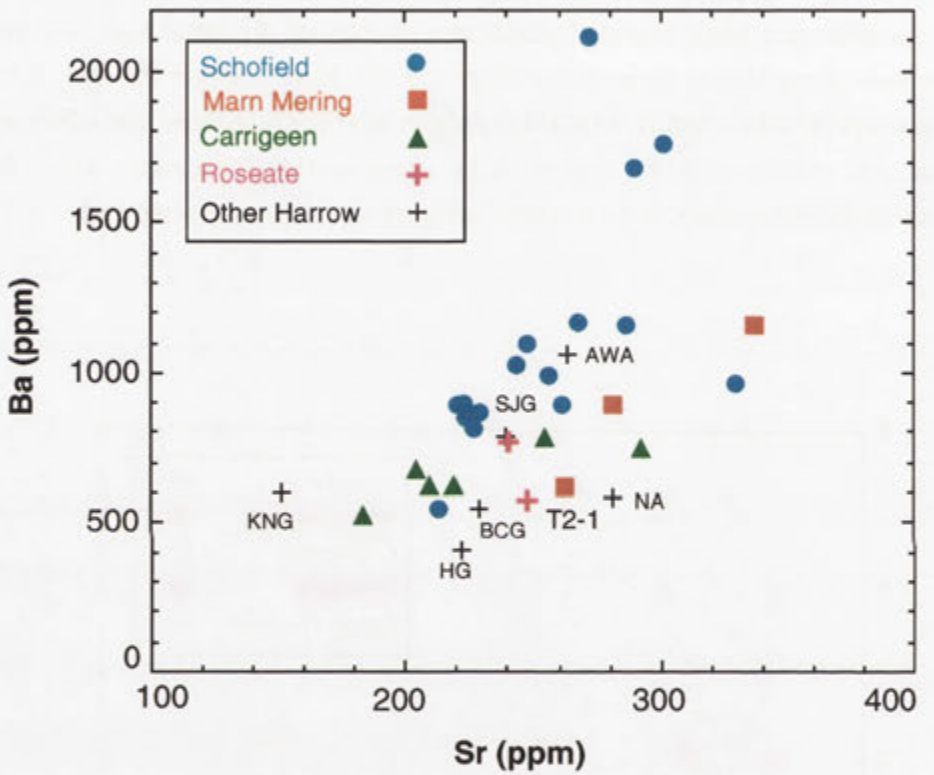

Figure 9.11. Plot of Ba against Sr for Harrow type granitic rocks. The most mafic Marn Mering Granodiorite sample, **T2-1**, is labelled. Pluton abbreviations are: AWA = Awaiti Adamellite; BCG = Bryan Creek Granodiorite; HG = Harrow Granodiorite; KNG = Kout Norien Granodiorite; NA = Nangkita Adamellite; SJG = Scrubby Junction Granodiorite.

9.4 Isotopic geochemistry

Whole-rock Sr and Nd isotopic compositions of three Harrow type granitic bodies and three quartzofeldspathic metasedimentary rocks from the northeastern migmatite zone are presented in Table 9.2 and Figure 9.12; analytical techniques are outlined in Appendix A.

Harrow type rocks have similar Nd isotopic compositions at 500 Ma (within ~0.5 epsilon units) but exhibit distinct variation in Sr isotopic ratios. The least radiogenic sample with respect to Sr at 500 Ma is **98-56** from the Marn Mering Granodiorite ($^{87}Sr/^{86}Sr$ ~0.7129), closely followed by

Sample	*Lithology*	*Rb (ppm)*	*Sr (ppm)*	$^{87}Rb/^{86}Sr$	$^{87}Sr/^{86}Sr$	$^{87}Sr/^{86}Sr$ (t)	*Sm (ppm)*	*Nd (ppm)*	$^{147}Sm/^{144}Nd$	$^{143}Nd/^{144}Nd$	ε_{Nd} (t)
T2-MG	Qf gneiss	114	262	1.261	0.72520±2	0.71621	7.28	39.39	0.1117	0.511852±08	-10.8
T2-301	Qf gneiss	143	208	1.994	0.73197±1	0.71776	6.55	34.17	0.1159	0.511896±10	-10.2
97-316	Qf gneiss	133	222	1.736	0.73051±1	0.71814	6.42	33.26	0.1167	0.511961±10	-9.0
861-120	Schist	237	133	5.161	0.75869±4	0.72192	4.28	22.7	0.1141	0.511796±27	-12.1
T2-302	Awaiti Ad	113	264	1.240	0.72374±1	0.71491	3.34	16.15	0.1250	0.511936±15	-10.0
98-23	Schofield Ad	110	243	1.312	0.72448±1	0.71513	3.16	11.93	0.1599	0.512069±09	-9.7
98-56	Marn Mering Gd	90	338	1.029	0.72026±1	0.71293	2.88	10.24	0.1698	0.512113±13	-9.5
861-12*	?Harrow Gd	238.4	134.8	4.093	0.74587±2	0.71671	3.67	15.76	0.1408	0.512021±37	-9.4
9156#	Carrigeen Gd	122.9	257.8	1.381	0.72316±2	0.71332	-	-	-	-	-

Table 9.2. Strontium and neodymium isotopic composition of migmatite zone metasedimentary rocks and Harrow type plutons of the GRC. Initial ratios and epsilon values are calculated for an inferred crystallisation age (t) of 500 Ma (Qf = Quartzofeldspathic; Ad = Adamellite; Gd = Granodiorite).

(* from *Turner et al.* 1993a, recalculated to 500 Ma; # from Gray 1990)

the Carrigeen Granodiorite sample (~0.7133) of Gray (1990). Slightly higher initial ratios are evident for Awaiti Adamellite (~0.7149) and Schofield Adamellite (~0.7151), whereas sample 861-12 of Turner *et al.* (1993a), referred to as 'Harrow Granodiorite', is the most radiogenic, with $^{87}Sr/^{86}Sr$ ~0.7167. The identity of the latter lithology is unclear, as although the sample locality indicated by Turner e*t al.* (1993a) falls inside the Harrow Granodiorite pluton delineated by Kemp (1995), the quoted whole-rock geochemistry, particularly high K_2O (4.46%), Fe_2O_3t (3.16%) and Rb (238 ppm), suggests a more biotite-rich character and affinity with Kout Norien Granodiorite. Note that the initial Sr isotopic composition of Harrow types has no correlation with total Fe_2O_3t (Figure 9.13), with the most mafic sample (861-12 of Turner *et al.* 1993a) being the most isotopically evolved.

Metasedimentary rocks are isotopically more variable, with considerable spread in both Sr initial ratios and ε_{Nd} (Figure 9.12). Metapelitic schists of Turner *et al.* (1993b) are clearly the most radiogenic for Sr, as expected from the clay-dominated, and therefore Rb-enriched, nature of the sedimentary precursor. In contrast, quartzofeldspathic gneisses derive from immature sedimentary protoliths, where Sr remains locked in detrital feldspars and the clay component is minor, resulting in lower Rb/Sr and therefore $^{87}Sr/^{86}Sr$ at the time of metamorphism. These rocks have a similar Sr isotopic composition to quartzofeldspathic schists of the Kanmantoo Group in South Australia, which have a mean $^{87}Sr/^{86}Sr$ ratio of ~0.7164 at 500 Ma (Gray 1990).

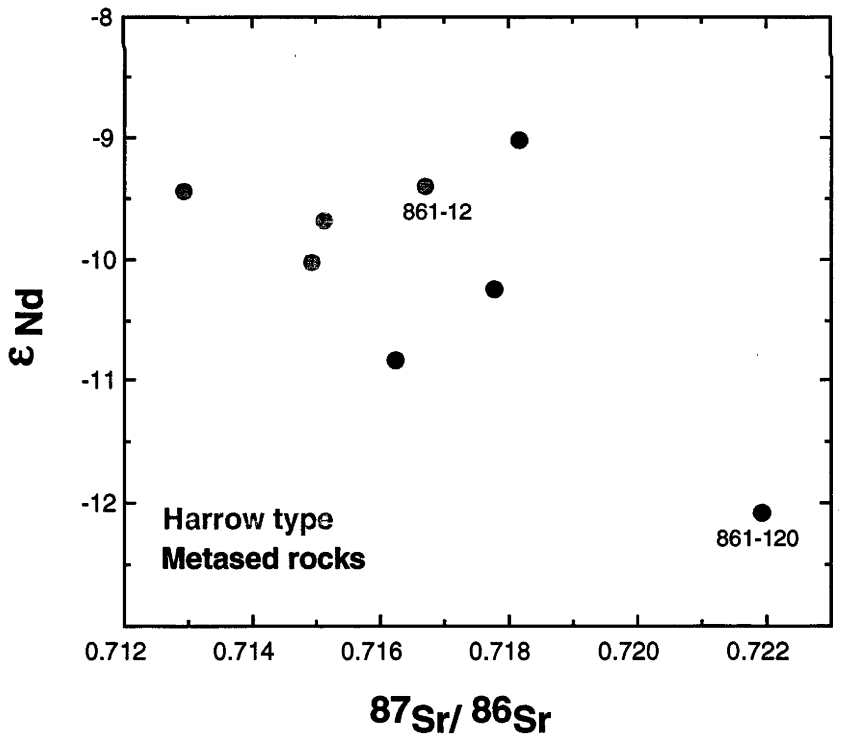

Figure 9.12. Strontium and neodymium isotopic composition of Harrow type granitic rocks and metasedimentary rocks of the migmatite zone, calculated at 500 Ma. Samples 861-12 ('Harrow Granodiorite') and 861-120 (metapelitic schist) of Turner *et al.* (1993a) are also plotted.

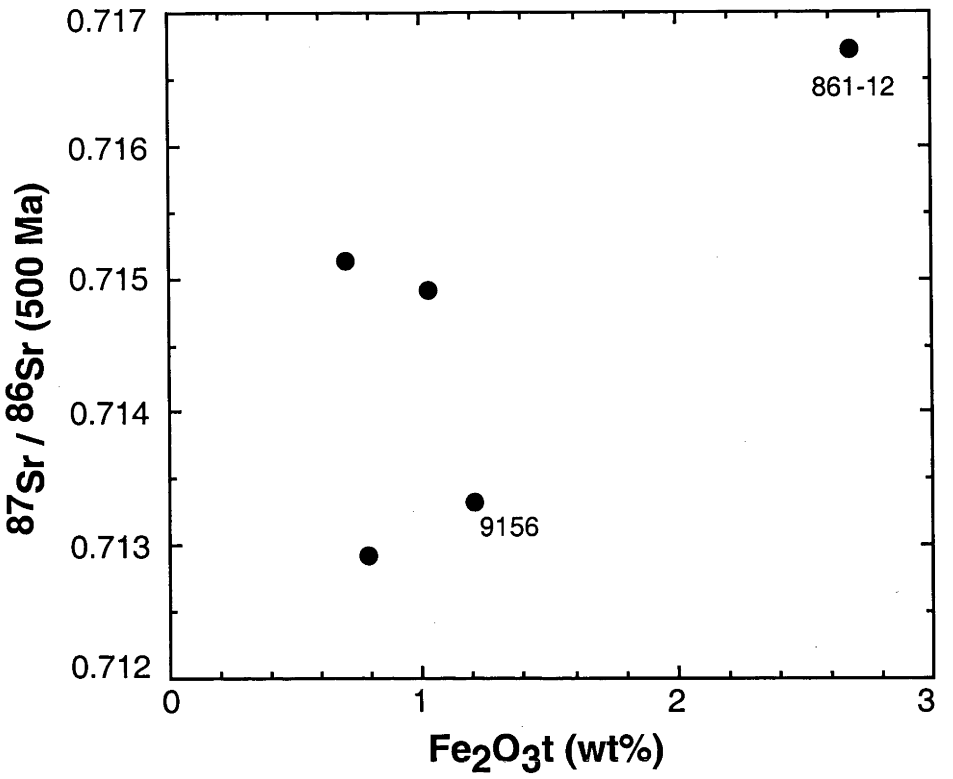

Figure 9.13. $^{87}Sr/^{86}Sr$ (at 500 Ma) versus total Fe_2O_3 for Harrow type granitic rocks. Sample 9156 of Gray (1990) and 861-12 of Turner *et al.* (1993a) are labelled separately.

Comparing isotopic compositions for Harrow types and quartzofeldspathic metasedimentary rocks, it is significant that the two data groups overlap for ε_{Nd} (500 Ma) but Harrow type rocks have consistently lower initial Sr ratios, sample 861-12 of Turner *et al.* (1993a) being a notable exception.

9.5 Chemical relationship between *in situ* anatexis and Harrow type granitic rocks

Compelling petrographic and field evidence indicates a relationship between the formation of Harrow type plutons and *in situ* partial melting within the host metasedimentary sequence (section 9.1). This is supported by the coincidence between the normative composition of Harrow type granitic rocks and that of migmatite leucosomes and linked decimetre- to metre-scale granitic bodies (Figure 9.14). Leucotonalitic plutons also have similar normative composition to tonalitic leucosomes of adjacent migmatites (Figure 9.14). That the distinctive chondrite-normalised REE patterns of Harrow type plutons parallel those of metasedimentary rocks, but at systematically lower REE concentration, also argues for a petrogenetic relationship (Solar & Brown 2001).

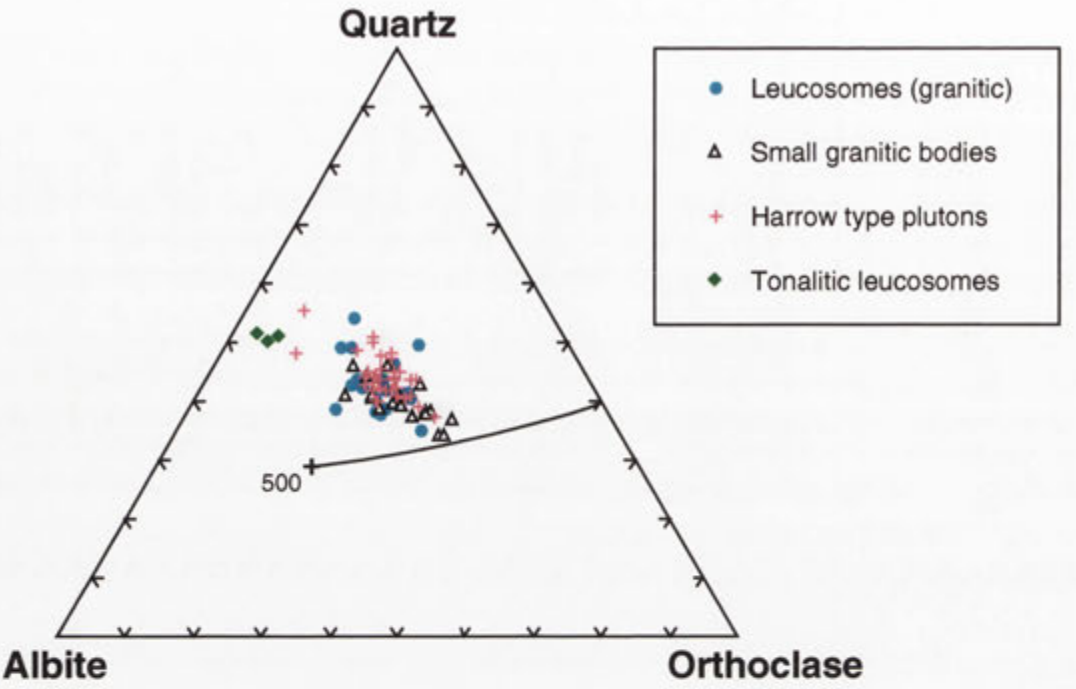

Figure 9.14. Comparison of the normative compositions of Harrow type plutons with those of *in situ* migmatite leucosomes and small granitic bodies. The five phase surface at P_{H_2O} = 500 Mpa is also indicated (from Nekvasil 1988). The two most orthoclase-poor Harrow type compositions are samples of the Dunmore Leucotonalite.

To further investigate this, Harker variation diagrams depicting metasedimentary rocks, diatexites, *in situ* leucosomes, small granitic bodies and all Harrow type plutons are presented in Figure 9.15. Due to compositional similarity and the genetic relationship, *in situ* migmatite leucosomes and small granitic bodies are plotted together, whereas tonalitic leucosomes and Dunmore Leucotonalite samples are distinguished.

The critical aspects of these diagrams are encapsulated by three observations. Firstly, the compositional range exhibited by felsic Harrow type granitic rocks is indistinguishable from that of *in situ* granitic leucosomes and small granitic bodies for all major and trace elements. Particularly instructive is that the distinctive high Sr signature and striking K_2O dispersion over a small SiO_2 range that characterises Harrow type plutons is also shared by leucosomes. As with migmatite leucosomes, felsic Harrow types are strongly depleted in TiO_2, (Fe_2O_3t+MgO), Zr and P_2O_5 relative to the inferred quartzofeldspathic source composition. Felsic granitic plutons are also equally undersaturated in Zr and P_2O_5 as *in situ* leucosomes (see Figures 9.16 and 9.17). The chemical link between felsic Harrow types and migmatite leucosomes is further reinforced by nearly identical upper continental crust normalised patterns (Figure 9.7).

Secondly, for all elements, mafic Harrow type granodiorites overlap with, or plot close to, the compositional field of diatexites, implying related petrogenesis. Notably, for TiO_2, Al_2O_3, (Fe_2O_3t+MgO) and Zr, diatexites and mafic Harrow type granodiorites span the conspicuous gap

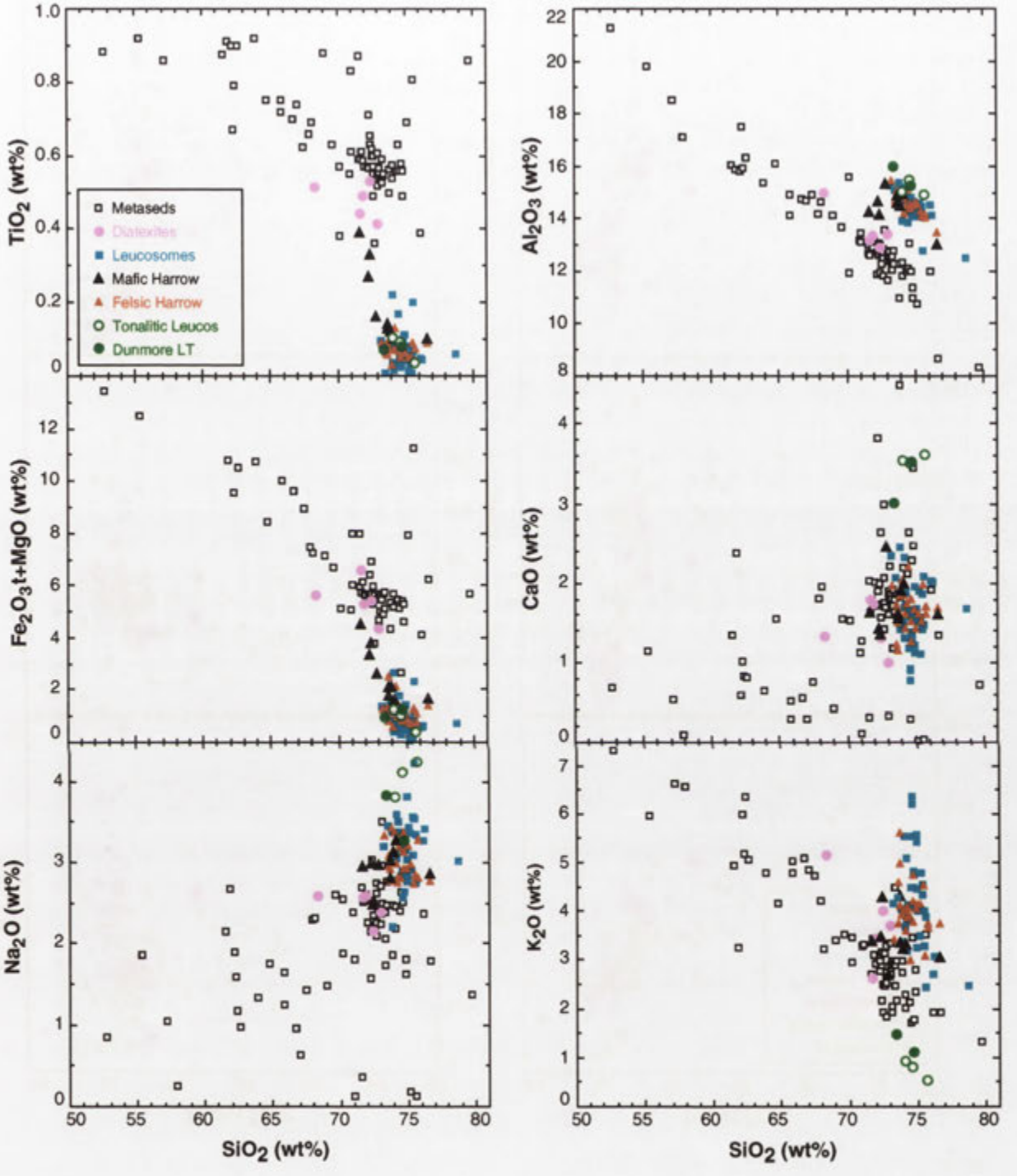

Figure 9.15. Harker variation diagrams for metasedimentary rocks, migmatite leucosomes (also incorporating small granitic bodies) and Harrow type plutons of the GRC. Metasedimentary rock data is from all grades across the GRC (sources as for Figure 7.10). The large silica range for the abscissa was chosen to highlight the clustering of granitic and metasedimentary rocks, and emphasise the large variation in some other elements.

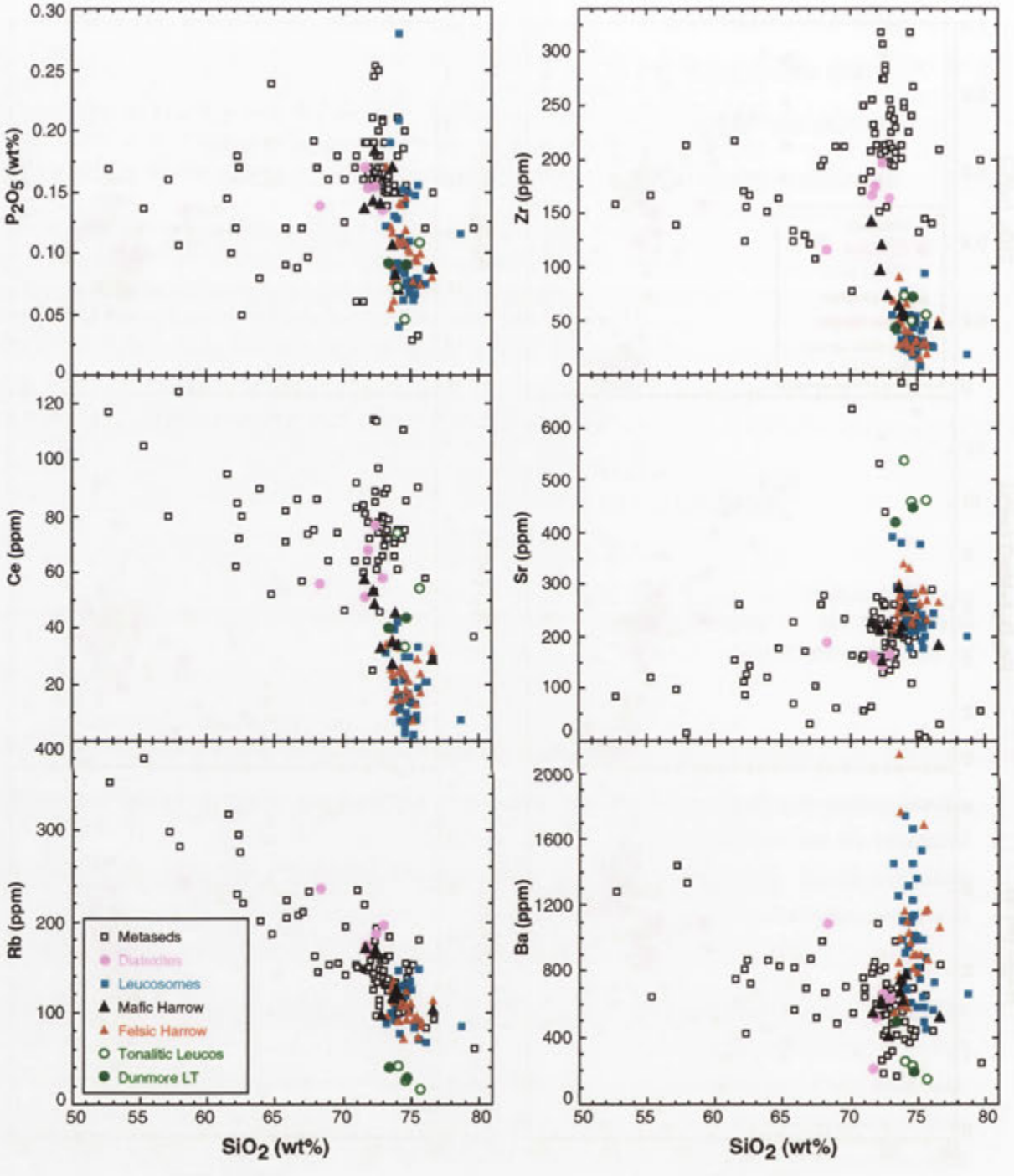

Figure 9.15 contd. Harker variation diagrams for metasedimentary rocks, migmatite leucosomes (also incorporating small granitic bodies) and Harrow type plutons of the GRC. Metasedimentary rock data is from all grades across the GRC (sources as for Figure 7.10).

between leucocratic granitic bodies (felsic Harrow types, leucosomes, granitic dykes/sheets) and clustered quartzofeldspathic metasedimentary rocks.

Thirdly, Dunmore Leucotonalite samples and *in situ* tonalitic leucosomes are chemically very similar, and together exhibit chemical variation independent to that of other Harrow types. This involves a broadly linear decrease in K_2O but increase in CaO and Sr with progression to higher silica. Accordingly, tonalitic leucosomes and the Dunmore Leucotonalite comprise a separate petrogenetic system from other Harrow type granitic rocks.

These observations have fundamental implications for the petrogenesis of felsic adamellite to granodiorite plutons, mafic Harrow type granodiorites and leucotonalites, as elaborated separately below. The formation of garnet-bearing granitic rocks is discussed following this.

9.6 Petrogenesis of felsic adamellite to granodiorite plutons

9.6.1 General model

Although heterogeneity is pervasive, it is emphasised that **felsic Harrow types are compositionally identical to leucosomes of adjacent stromatic migmatites (see Figures 9.7, 9.14 and 9.15). This remarkable and exact link, together with intimate field relations, demonstrates unequivocally that Harrow type plutons are ponded accumulations of leucosome-derived partial melts, generated *in situ* within the host metasedimentary sequence.**

The first order chemical and petrographic features of felsic Harrow type bodies therefore reflect the anatectic processes involved in the formation of migmatite leucosomes.

9.6.2 Insights from the Schofield Adamellite

The essence of the pluton-forming process is manifest along Robson Creek, where efficiently-segregated partial melts generated from various migmatitic horizons are channelled into a network of sheet-like magma conduits, which ultimately coalesce into the Nangkita Adamellite (section 5.5). This is corroborated by the sheeted Schofield Adamellite pluton, a cross-section through which is exposed in Schofield Creek (section 6.4.3). The striking K_2O, Sr, Ba and Rb/Sr variation across this body is wholly contained within the compositional field of *in situ* leucosomes (Figures 9.18, 9.19, 9.20), which confirms that the pluton is an amalgamation of partial melts derived from a range of different migmatitic protoliths (section 8.5.2). The profound compositional heterogeneity within the Schofield Adamellite therefore records chemical variations between metasedimentary horizons in the source region. As with the Nangkita Adamellite, the compositionally layered or sheeted architecture of the Schofield Adamellite indicates pluton construction by sequential coalescence of multiple, sheet-like magma conduits, whereupon leucosome-derived partial melts were emplaced as individual, chemically-distinct 'batches'. Lack of significant intermixing or homogenisation between these magma batches, now represented by the lenticular lithological 'horizons' throughout the body (section 6.4.3), is responsible for the preservation of source-related heterogeneities.

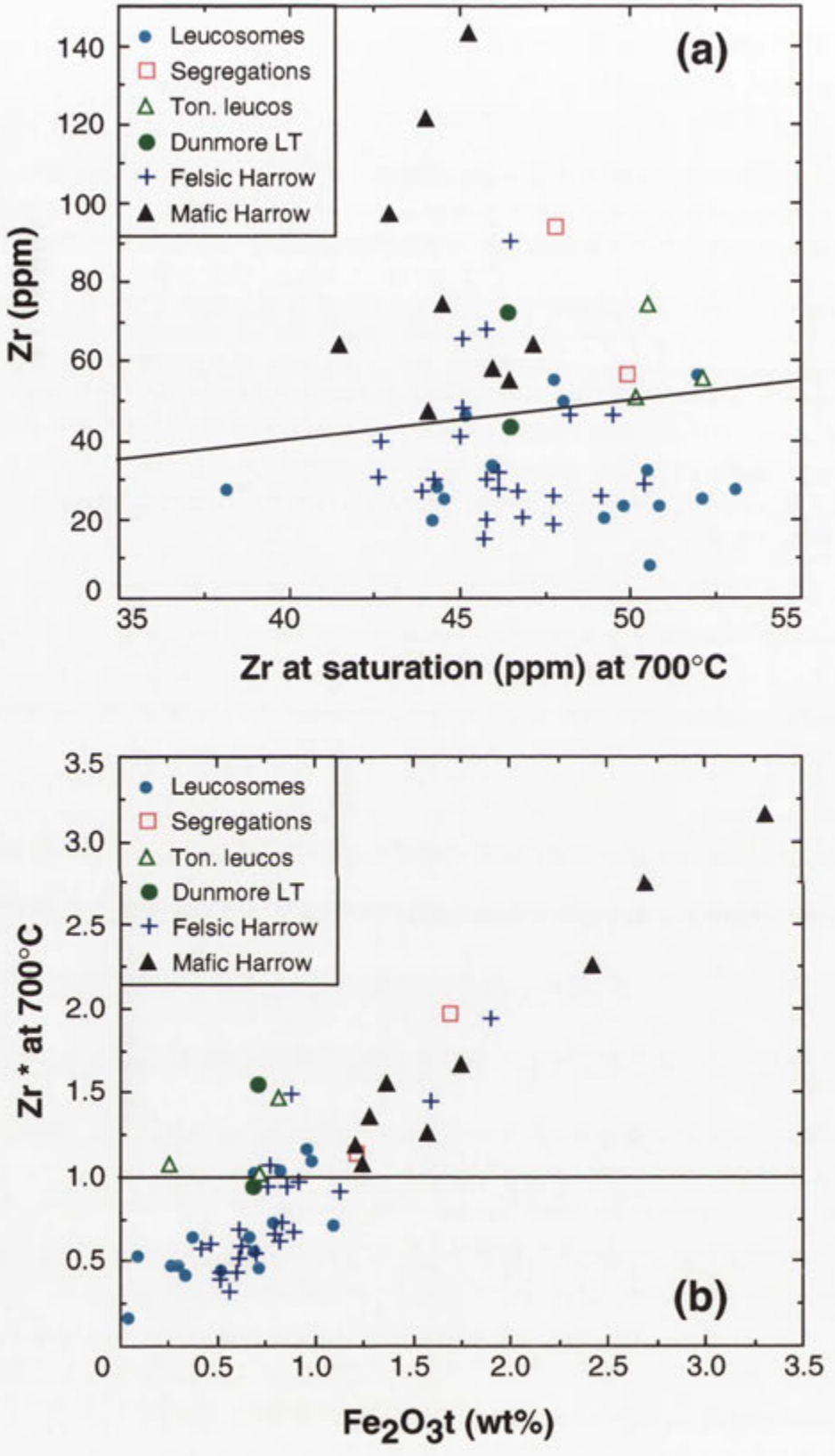

Figure 9.16. (a) Measured Zr concentration of Harrow type granitic rocks (LT = Leucotonalite), diatexite segregations and leucosomes plotted against the amount required to saturate a melt of that composition at 700°C (calculated from equations in Watson & Harrison 1983, see Appendix D). (b) Zr* (Zr measured / Zr concentration at melt saturation) versus total Fe_2O_3 for the same rock types. The two felsic Harrow types plotting along the mafic Harrow type trend are Schofield Adamellite samples **98-14A-1** and **98-14A2**.

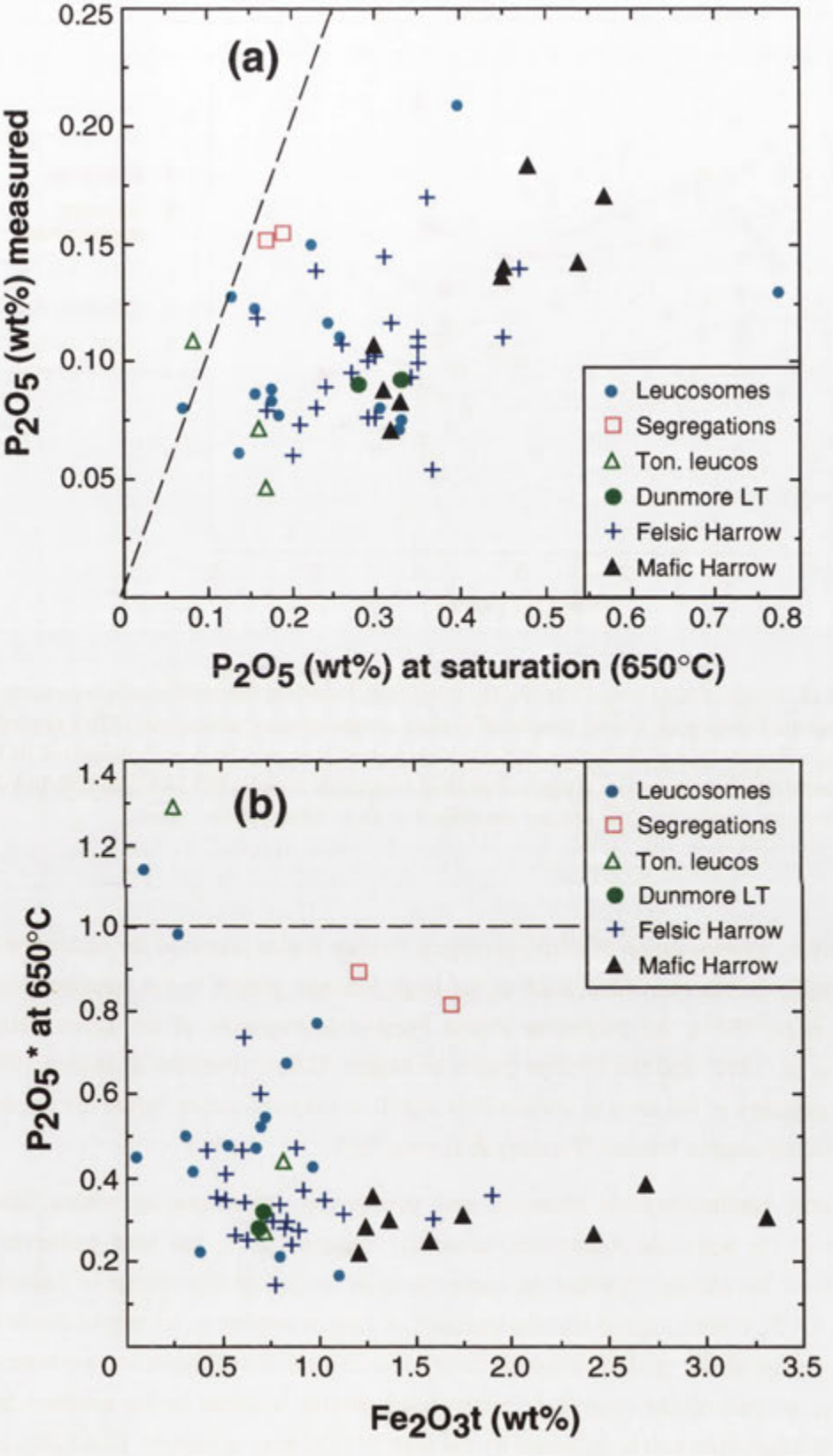

Figure 9.17. (a) Actual P_2O_5 content of Harrow type granitic rocks (LT = Leucotonalite), diatexite segregations and leucosomes plotted against the amount required to saturate a melt of that composition at 650°C (estimated from equations in Pichavant *et al.* 1992, see Appendix D). (b) P_2O_5* (P_2O_5 measured / P_2O_5 at melt saturation) versus total Fe_2O_3 for the same rock types.

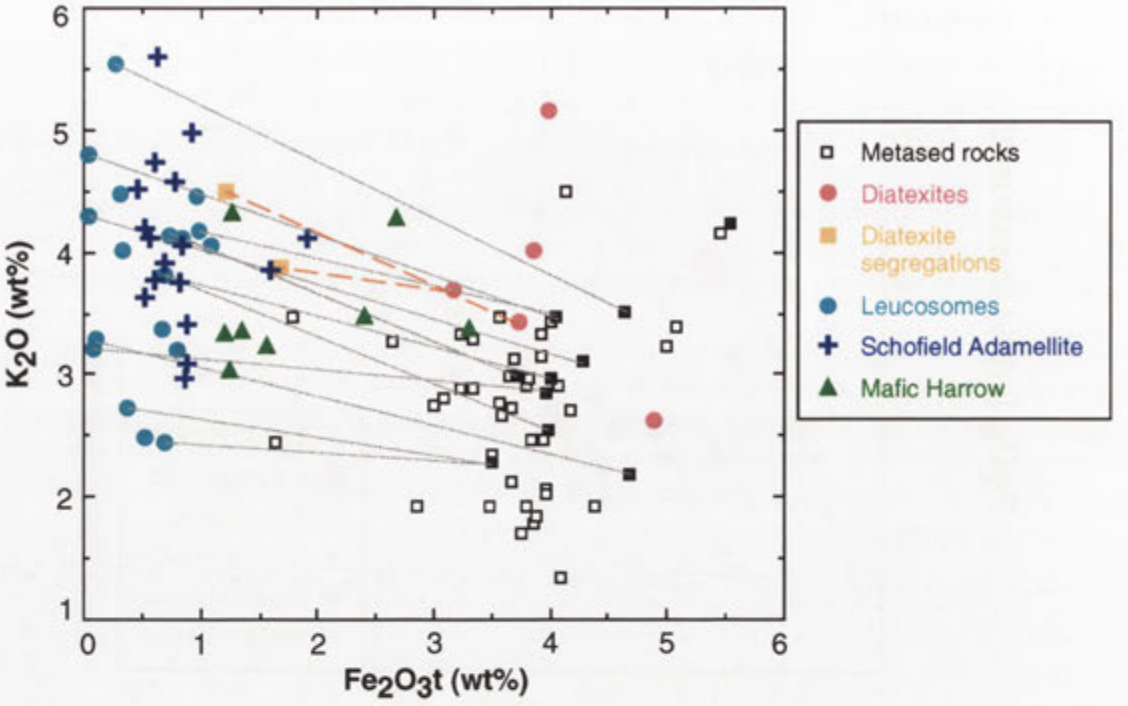

Figure 9.18. Graph of K_2O versus total Fe_2O_3, comparing Schofield Adamellite samples with the field of *in situ* granitic leucosomes, shown connected to their complementary mesosomes (filled symbols) by tie lines. Mafic Harrow type granodiorites and diatexites (joined to segregations with dashed red tie lines) are also plotted. Note that the two most mafic Schofield Adamellite samples (**98-14A-1** and **98-14A-2**) do not overlap with the leucosome field and are considered to be of diatexitic derivation.

Assembly by amalgamation of multiple magma batches is also proposed for muscovite-bearing leucogranitic bodies elsewhere, such as the large Manaslu granite in the Nepalese Himalayas (Deniel *et al.* 1987), the polyphase Shisha Pangma leucogranite of the Tibetan Himalayas (Searle *et al.* 1997) and the Phillips pluton in Maine, U.S.A. (Pressley & Brown 1999). The sheeted structure of the latter is attributed to significant crystallisation before the emplacement of succeeding magma batches (Pressley & Brown 1999).

Importantly, centimetre-scale chemical and petrographic heterogeneity within lithological horizons of the Schofield Adamellite, especially 'mingled' units, has been preserved during formation of the pluton. This feature, conspicuous in 'feeder' granitic sheets of Robson Creek (section 5.4.3), further implies that the transport of magma batches to the emplacement site was rapid, such that blending of the disparate leucosome-derived melt aliquots was prevented. Local derivation of part of the complexly interspersed granitic material in the southern 'mingled' Schofield Adamellite unit is indicated by the high Sr (330 ppm in sample **T2-CC9D**) and high Ba (1759 ppm in sample **98-12**) character, which correlates with that of leucosomes in adjacent stromatic migmatites (376 ppm Sr and 1532 ppm Ba in leucosome **98-65B**). Similarly, the lower Ba and Sr contents of northern Schofield Adamellite samples (**98-24**, **98-26**, **98-27**) may partly reflect contributions from segregated partial melts generated within the northern metasedimentary tract, characterised by the same features (e.g. leucosome **98-WF1A**, 568 ppm

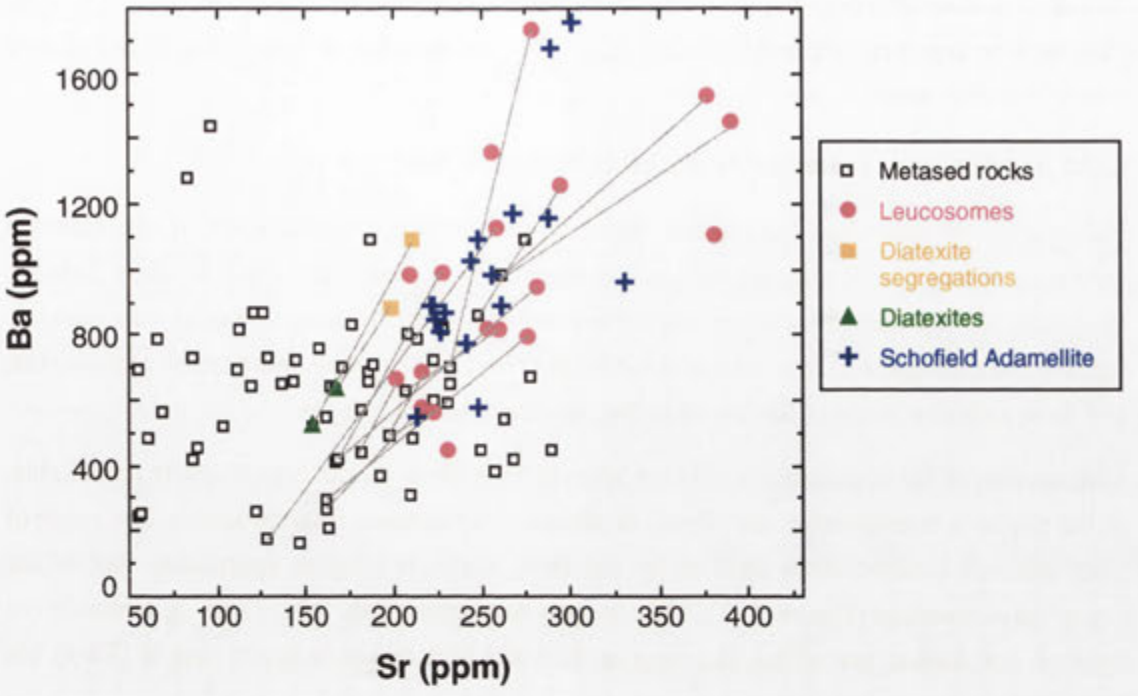

Figure 9.19. Diagram of Ba versus Sr comparing Schofield Adamellite samples with *in situ* leucosomes of granitic migmatites (connected to mesosomes by tie lines) and diatexite segregations. 'Metaseds' are metasedimentary rocks of both migmatite and sub-migmatite grade from across the GRC.

Ba, 223 ppm Sr). Graphic alkali feldspar megacrysts in the Schofield Adamellite require constituent magma batches to also incorporate pegmatitic debris, as is evident within 'feeder' granitic sheets (see section 5.3.5a). However, as the variation within the pluton is entirely contained within the compositional field of *in situ* leucosomes, the geochemical influence of this component is evidently quite minor.

More biotite-rich granitic material containing numerous micaceous schlieren and enclaves is another important ingredient of the Schofield Adamellite. This is complexly interspersed within more felsic adamellite outcrops and also forms lenticular domains throughout the pluton with a distinctive 'diatexitic' character (section 6.4.3). On variation diagrams, samples of this material (**98-14A-1** and **98-14A-2**) plot within the field of mafic Harrow types (e.g. Figures 9.18, 9.20), and have a similar Zr excess, clearly related to entrainment of refractory, zircon-enclosing biotite (Figure 9.16). These features indicate an affinity with residue-contaminated diatexites rather than leucosome-derived partial melts (see section 9.7.1). Hence, it is concluded that the Schofield Adamellite also incorporates diatexite-sourced magma, some of which could have originated from the *in situ* diatexite horizons immediately south of the pluton. This may have been introduced as discrete, sill-fed batches, forming the lenticular domains, or as a minor, intermingled component of more efficiently segregated partial melt aliquots.

Of final note concerning the Schofield Adamellite is the enclosure of small, texturally homogeneous bodies of muscovite-rich leucogranite, represented in Schofield Creek by the

Roseate Adamellite. These bodies do not postdate the Schofield Adamellite (section 6.4.3) but alternatively represent separate batches of more homogeneous granitic magma introduced during pluton assembly.

9.6.3 Implications for other felsic plutons of the GRC

Recognition of individual lithological 'units' or geochemical quantification of the variation within other large felsic plutons, such as the Marn Mering Granodiorite and Scrubby Junction Granodiorite, is hindered by lower calibre exposure. Nevertheless, conspicuous outcrop-scale lithological heterogeneity implies that these bodies also comprise disparate granitic components, and have a similar mode of formation to the Schofield Adamellite.

Maintenance of heterogeneities within the Marn Mering Granodiorite is particularly remarkable, as the pluton is transgressive and clearly displaced some distance from its source. The range of trace element concentrations defined by the three analysed samples approaches that of the Schofield Adamellite (Figure 9.11). This implies derivation of the Marn Mering Granodiorite from several distinct protoliths. The most mafic Marn Mering Granodiorite sample (**T2-1**) has

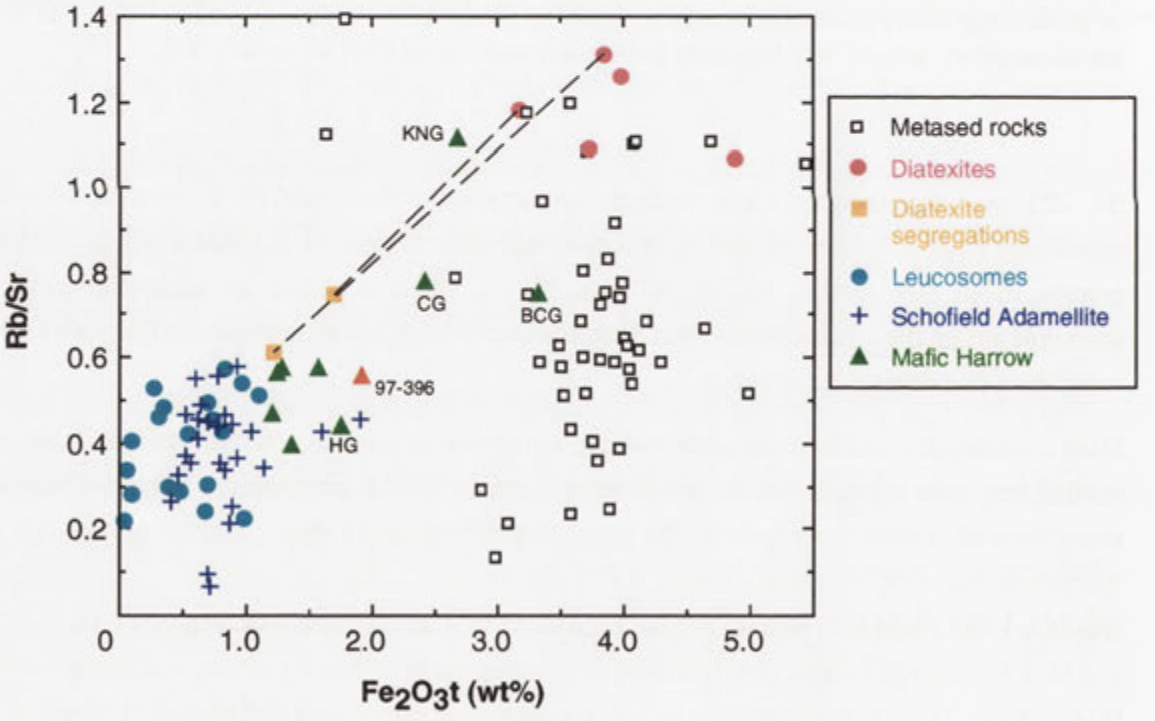

Figure 9.20. Plot of Rb/Sr versus total Fe_2O_3 for Harrow type granitic rocks, diatexites (joined to leucogranitic segregations by a dashed tie line) and metasedimentary rocks of the GRC (both sub-migmatite and migmatite zone lithologies). Granitic sheet **97-396** from Bryan Creek (red triangle) is plotted for comparison to the Bryan Creek Granodiorite. Mafic Harrow type plutons are labelled (BCG = Bryan Creek Granodiorite; CG = Carrigeen Granodiorite; HG = Harrow Granodiorite; KNG = Kout Norien Granodiorite). Unlabelled mafic Harrow type points are Carrigeen Granodiorite samples. Note that two felsic Harrow type samples (**98-14A-1** and **98-14A-2** from the Schofield Adamellite) have elevated Fe_2O_3t and overlap with the field of mafic granodiorites.

clearly higher Sr than Schofield Adamellite samples of similar Ba contents (Figure 9.11). Given the proximity to tonalitic migmatites, this might reflect a contribution from locally-derived leucotonalitic partial melts, which are Sr-enriched (section 7.5). However, the more felsic samples **98-56** and **98-58** trend towards strongly increasing Sr and Ba, consistent with greater incorporation of a Ba- and Sr-rich component similar to that of migmatite leucosomes south of the Schofield Adamellite (e.g. samples **98-65A, 98-65B**).

Finally, it is emphasised that, as with *in situ* leucosomes, the low TiO_2, (Fe_2O_3t+MgO), P_2O_5 and Rb of felsic adamellite-granodiorite plutons reflects the efficient segregation of partial melts in source migmatites, such that constituent magma batches mostly lack biotite-rich residue. Depletions in P_2O_5, HFSE and REE compared to metasedimentary protoliths indicate limited entrainment of insoluble accessory phases, the same feature characteristic of migmatite leucosomes.

9.7 Petrogenesis of mafic Harrow type plutons

9.7.1 The diatexite connection

The systematic petrographic and chemical differences between mafic Harrow type granodiorites and more felsic Harrow type rocks suggest that, although sharing a metasedimentary source, the two groups have a different petrogenesis. In particular, the numerous metasedimentary enclaves indicate that in contrast to felsic plutons, an ineffective segregation mechanism operated during formation of mafic granodiorites, facilitating entrainment of residual source material. Content of sillimanite and paucity of muscovite in micaceous selvedges imply formation by a higher degree of partial melting and/or derivation from a different metasedimentary protolith. The former is also consistent with the greater proportion of magmatically-precipitated biotite in mafic Harrow types, indicating greater dissolution of this phase during anatexis. Together with entrapment of biotite-rich residue, this engenders the markedly higher TiO_2, Fe_2O_3t, Rb and Rb/Sr but lower SiO_2 of mafic granodiorites compared to felsic Harrow types (Figure 9.5). Strongly elevated Zr concentrations over those required to saturate a melt at 700°C (the maximum inferred temperature for GRC anatexis; Figure 9.16a) also accord with significant entrainment of biotite-rich residue in mafic Harrow types, since the Zr excess is well correlated with Fe_2O_3t (Figure 9.16b). As P_2O_5 solubility is enhanced in peraluminous compositions, entrained mica-sillimanite residuum causes overestimation of theoretical apatite solubility in mafic granodiorites, reflected by a similar (but artificial) degree of P_2O_5 undersaturation as felsic Harrow types (Figure 9.17).

Alternatively, chemical evidence supports a close genetic link between mafic Harrow type plutons and diatexites (Figure 9.15). This is emphasised by Figure 9.20, where the relatively high Rb/Sr and Fe_2O_3t of diatexites, imparted by the high proportion of entrained residual biotite, is shared by mafic Harrow types but clearly different from the low Fe_2O_3t and Rb/Sr of most felsic Harrow types. A connection between mafic Harrow type plutons and diatexites is compatible with the intergradational field relationships (Chapters 5 and 6) and petrographic similarities, especially content of sillimanite and abundant biotite. Importantly, the sillimanite-biotite selvedges and schlieren that characterise mafic Harrow type plutons can be directly correlated

with residual melanosomes in flanking diatexite horizons. Links between the Kout Norien Granodiorite and enclosed diatexite rafts are reinforced by the identical biotite, plagioclase and alkali feldspar compositions (section 9.2).

9.7.2 Implications for the formation and evolution of mafic Harrow types

Although plotting close to diatexites on Harker variation diagrams, mafic granodiorites define an array for TiO_2, Al_2O_3, (Fe_2O_3t+MgO), Na_2O, Zr and Rb/Sr that extends from the diatexite compositional field towards felsic Harrow types (Figure 9.15). This reflects lesser proportions of residual biotite and accessory zircon, but a higher granitic melt fraction within mafic Harrow types, and suggests that these plutons comprise variable combinations of residue-rich diatexite magma and felsic magma. This trend may arise by variable mixing between a diatexite magma of fixed composition and an externally-derived leucogranitic magma. However, as no field evidence of such interaction is evident, it is more likely that the trend is generated by variable separation of a biotite- and quartz-rich restitic component from a mobilised parental diatexite. Separation of the residual fraction may have been driven by flow-enhanced melt segregation, conspicuous in melt-dominated diatexite outcrops of Robson and Bryan Creek (section 5.8.1). Under this scenario, mafic Harrow types correspond to the most melt-enriched parts of *in situ* diatexites and represent an intermediate stage in the progression to a residue-free melt component, represented on a small scale by the leucogranitic segregations in diatexites.

This evolutionary sequence is exemplified by the Carrigeen Granodiorite. The pluton is choked with metasedimentary enclaves and diatexite-like at the periphery, but grades through to a homogeneous, relatively felsic and residue-free centre. This variation is largely controlled by the progressive separation of refractory source material from the enveloping diatexite, such that ultimately a 'clean' granitic magma is produced. As the melt phase within diatexites resembles stromatic migmatite leucosomes, this process drives the granitic composition towards that of felsic Harrow type plutons, resulting in geochemical similarity at the high silica end. Such a chemical progression occurs within the Carrigeen Granodiorite, with evolution of samples to lower TiO_2, Fe_2O_3t and Zr compositions by separation of residual biotite and included zircon (Figure 9.5). Nevertheless, despite the compositional convergence, some distinction between the evolved Carrigeen Granodiorite samples and felsic Harrow type plutons is possible (section 9.3.2). This is maintained even after feldspar fractionation, with more calcic plagioclase, Fe-Mg-Ti-rich micas and Mg-Ca-rich garnets in garnet-bearing Carrigeen Granodiorite sample T2-69 compared to garnet adamellite **98-19** (section 9.2). Complex variation in K_2O, Rb/Sr (Figure 9.5) and K/Rb (Figure 9.6) between Carrigeen Granodiorite samples suggests the operation of processes other than residue separation, such as modification of the magma by interaction with enclaves of less fertile metasedimentary rock, or local fragmentation of pegmatitic dykes within the diatexite protolith. The latter may apply to marginal sample **98-64A**, which contains concentrations of graphic alkali feldspar megacrysts and has elevated K_2O and K/Rb, consistent with incorporation of a pegmatitic component (section 9.3.2). Heterogeneities inherited from internal 'primary' compositional variations in the metasedimentary protolith to the diatexite also cannot be discounted.

A similar relationship may exist between the biotite-rich granitic sheet **97-396** from Bryan Creek, which is distinctly more mafic than other granitic sheets of the migmatite zone (section 7.5), and the nearby, petrographically similar Bryan Creek Granodiorite. Relative to the latter, the granitic sheet has lower TiO_2, Fe_2O_3t, P_2O_5, Zr and Rb/Sr, but higher K_2O, Ba and Sr (see Figure 9.20 and Appendix C). This accords with derivation of **97-396** from a magma similar to the Bryan Creek Granodiorite by separation of a biotite-rich residual component (including apatite and zircon), probably represented by the abundant biotite-rich clots and enclaves within the latter body. Granitic sheet **97-396** therefore represents a more advanced stage in the magmatic lineage from a parental diatexite, and may itself be transitional to the leucogranitic bodies of Bryan Creek (e.g. sample **97-396B**).

An origin by separation of residual material from a parental diatexite may also be appropriate for the homogeneous but sillimanite-bearing Harrow Granodiorite, distinguished by its reasonably mafic character but low K_2O, Ba and K/Rb, with intermediate Sr and Rb/Sr (Figure 9.5). Unlike felsic Harrow type adamellite-granodiorites, this composition is outside the range of *in situ* migmatite leucosomes. The Harrow Granodiorite pluton is partially enclosed by the diatexite-like Kout Norien Granodiorite, from which it may have evolved by separation of biotite-rich residuum. However, this simple link is inconsistent with the more calcic plagioclase and lower K_2O and Ba of the Harrow Granodiorite. Alternatively, the body may derive from a slightly different diatexite protolith at depth.

Hence, it is envisaged that mafic Harrow type plutons formed by variable separation of a residual component from a mobilised diatexite progenitor, possibly during shear-driven magmatic flow, and are transitional to more felsic compositions. Diatexite sample **99-R5** is melt-enriched relative to the inferred protolith composition (section 8.5.5) and thus represents an earlier stage in this evolution to an ultimately residue-free magma. Finally, it is emphasised that the abundant entrained residual material characterising mafic Harrow types is a direct reflection of the inefficient segregation mechanism prevailing during formation of the parental diatexite. This enabled fragmentation and incorporation of large enclaves of less fertile source horizons, such as the rafts of quartzofeldspathic schist, gneiss and stromatic migmatite within Kout Norien Granodiorite, upon mobilisation of the enclosing diatexite.

9.8 Petrogenesis of muscovite leucotonalites

9.8.1 Dunmore Leucotonalite

Depleted in K_2O, Ba and Rb, but enriched in CaO, Na_2O and Sr, the Dunmore Leucotonalite is geochemically distinct from other Harrow type plutons, but closely resembles leucosomes of adjacent tonalitic migmatites (Figures 9.21, 9.22), and shares a similar Zr excess and P_2O_5 deficiency compared to that required for melt saturation (Figures 9.16b, 9.17b). Plagioclase and mica chemistries are also very similar (section 9.2). The chemical link between the Dunmore Leucotonalite and tonalitic leucosomes is strengthened by the intimate outcrop relationships between the pluton and tonalitic migmatites (section 6.2.3).

These features suggest that the Dunmore Leucotonalite pluton is coalesced leucosome-derived tonalitic melt, which was generated by small degrees of anatexis from surrounding semi-pelitic gneisses (Figure 9.22; see also section 8.6.2). Outcrop relationships suggest that, as with felsic adamellites-granodiorites, efficiently-segregated partial melts from tonalitic migmatites were emplaced by a network of dykes or sheets, possibly in batches (see section 6.2.3). Small chemical differences between the two leucotonalite samples (see Figure 9.22) may therefore reflect variations between constituent magma batches, relating to slightly different precursor gneisses or degrees of partial melting. To shed light on this, the composition of the 'feeder' dykes and sheets linked to tonalitic leucosomes needs to be investigated, supplemented by more geochemical data on tonalitic leucosome-mesosome pairs. Note however that since both Dunmore Leucotonalite samples have similar TiO_2 and (Fe_2O_3t+MgO) (Figure 9.22), compositional control by variable residual biotite entrainment (within 'feeder' tonalitic sheets) or separation (in the pluton itself) is precluded.

Finally, as with major and other trace elements, the subtle differences in REE patterns between Dunmore Leucotonalite **98-150** and Schofield Adamellite **98-13** (Figure 9.9) probably relate to different anatectic behaviour in the respective metasedimentary sources. The relative LREE enrichment of the leucotonalite directly reflects that of *in situ* tonalitic leucosomes and accords with greater dissolution or entrainment of accessory monazite during partial melting (section

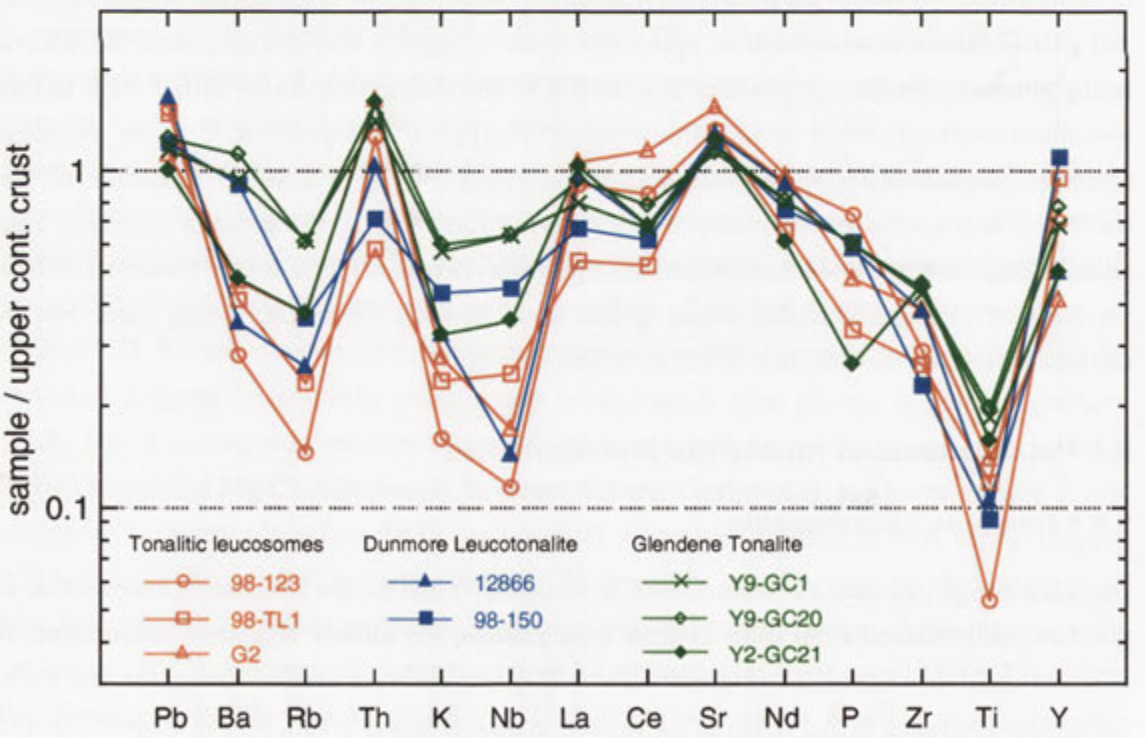

Figure 9.21. Upper crustal normalised abundance diagram comparing the Dunmore Leucotonalite and Glendene Tonalite with *in situ* tonalitic leucosomes (normalising values as for Figure 7.15). Data for the Glendene Tonalite is taken from Fitzherbert (1998).

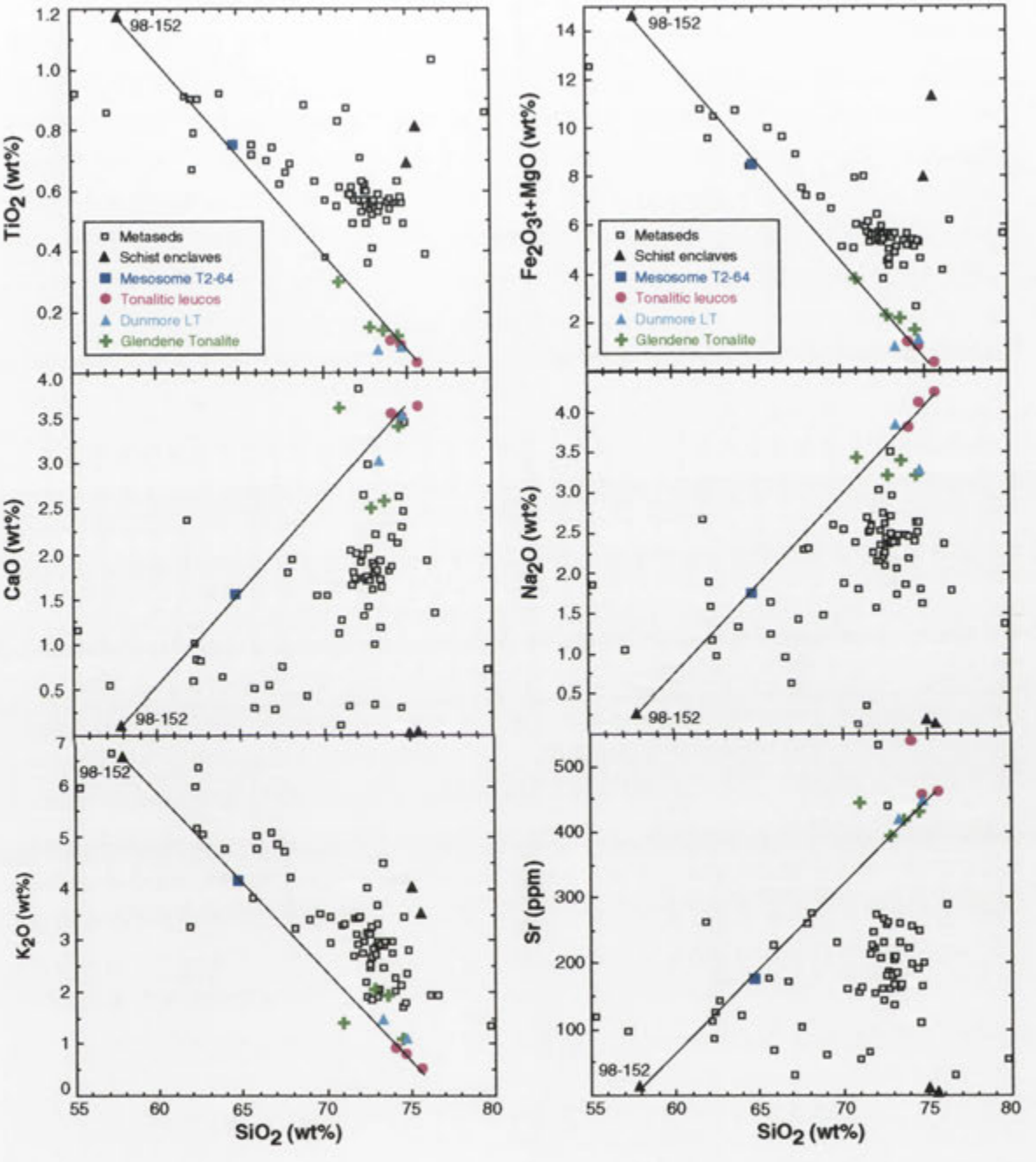

Figure 9.22. Harker variation diagrams for metasedimentary rocks, *in situ* tonalitic leucosomes and Harrow type tonalitic plutons of the GRC (LT = leucotonalite). Data for the Glendene Tonalite is from Fitzherbert (1998). 'Schist enclaves' are from the Dunmore Leucotonalite. Straight lines depict formation of tonalitic leucosomes by partial melting of semi-pelitic mesosome **T2-64** (blue square), leaving a residue similar to that of schist enclave **98-152** (labelled) (see section 8.6.4). Note that samples of both leucotonalite plutons plot close to these lines.

8.6.5). This also accounts for the elevated Th contents of leucotonalite samples compared to more potassic Harrow types. Note that higher LREE and Th contents in the leucotonalite does not result from greater content of entrained monazite-enriched melanosome biotite, as both Harrow type plutons in Figure 9.9 have identical (and very low) total Fe_2O_3 contents (~0.7%, see Appendix C). The positive Eu anomalies of both samples are similarly explicable in terms of source-based processes. Unlike the trivalent REE, Eu^{2+} is strongly compatible in feldspars (Bea *et al.* 1994) and thus is sensitive to fractionation or accumulation of these minerals in a magma, or their retention in the source during partial melting. However, feldspar accumulation is very unlikely in Harrow types, given chemical equivalence to leucosomes, which are demonstrably melt compositions (Chapter 8). Hence, the positive Eu anomaly of the Dunmore Leucotonalite and Schofield Adamellite must simply reflect preferential partitioning of Eu into the partial melt relative to the other REE, which are retained in the residue by refractory accessory minerals (section 8.5.2). This is consistent with the near-elimination of plagioclase from the melanosomes in tonalitic and granitic migmatites, and the low compatibility of Eu with the major residual phase, biotite ($D_{Eu}^{bio/melt}$ ~0.05; Bea *et al.* 1994). More data on other Harrow type granitic rocks and *in situ* leucosomes are required to investigate REE partitioning further.

9.8.2 Glendene Tonalite

Outcropping east of the Dunmore Leucotonalite, the migmatite-enclosed Glendene Tonalite is thought to have formed by anatexis of the surrounding metasedimentary sequence (Fitzherbert 1998). Both plutons have essentially the same chemical features (Figure 9.7), though Glendene Tonalite samples are more mafic (1.2-2.7% Fe_2O_3t), with slightly higher K_2O (1.1-2.1%) and Rb/Sr (0.11-0.17) (data from Fitzherbert 1998). On variation diagrams most Glendene Tonalite samples form an array bracketed between tonalitic leucosomes and their inferred protolith, semi-pelitic mesosome **T2-64**, that projects back to the residual micaceous enclave **98-152** (Figure 9.22). This implies that the Glendene Tonalite comprises variable proportions of tonalitic partial melt and mafic residue, or encompasses a number of disparate magma batches produced by a different degree of anatexis of the protolith. Since the Glendene Tonalite has not been examined by this study these possibilities cannot be satisfactorily resolved. Nevertheless, both scenarios require a semi-pelitic source rock similar to that inferred for the Dunmore Leucotonalite.

9.9 Petrogenesis of garnet-bearing Harrow types

9.9.1 Origin of field, petrographic and chemical features

Apart from the Blair Atholl Adamellite (see below), garnet adamellites have systematic geochemical differences from other Harrow types (Figure 9.5), with much lower CaO, resulting in markedly more sodic plagioclase, and extremely low TiO_2, Fe_2O_3t and MgO, manifesting the paucity of biotite. Th contents below 3 ppm (Appendix C) result in much higher K/Th than other Harrow type rocks (Figure 9.8). Deficiency in ferromagnesian elements allows greater Al substitution into octahedral mica sites and may explain the more aluminous muscovite and biotite compositions of garnet-bearing rocks (Figures 9.2, 9.3). Despite this, MnO is enriched in

garnet adamellites (Figure 9.5d), reflected by the occurrence of spessartine-rich garnets. K_2O contents are also high, according with the modal dominance and early crystallisation of alkali feldspar. Most characteristically, garnet-bearing rocks are enriched in Rb, but variably depleted in Sr and Ba compared to other Harrow types, exhibiting exponential evolution to elevated Rb/Sr and K/Ba ratios (up to 6.29 and ~660 respectively in Glengoyne Adamellite; Figure 9.23). Nevertheless, the broad geochemical continuum between Harrow type rocks and garnet-bearing adamellites on Figure 9.23 suggests an evolutionary link, as does the field progression of some large Harrow type plutons through to garnetiferous compositions. Note that the slight difference in trends between garnet adamellites and other Harrow type rocks on Figure 9.23 (see inset) implies compositional control by different mechanisms.

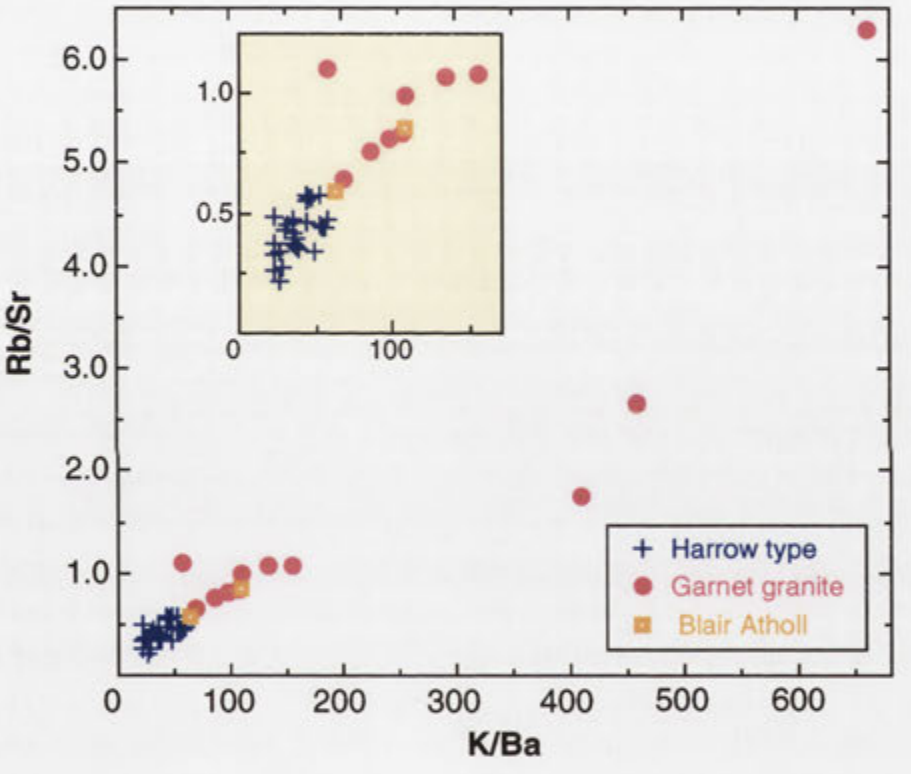

Figure 9.23. Plot of Rb/Sr against K/Ba for garnet-bearing granitic rocks and felsic Harrow type adamellites-granodiorites. The inset represents the bottom left hand corner of the main graph, expanded for clarity.

The chemical compositions of garnet-bearing granitic rocks are consistent with an origin by fractional crystallisation of biotite and (primarily) feldspars from a Harrow type magma, followed by rapid crystallisation at the water-saturated granitic solidus. This accords with the more sodic plagioclase, rarity of metasedimentary enclaves and development of quench textures. As Sr partitions strongly into plagioclase ($D_{Sr}^{plag/melt}$ ~15.6, Nash & Crecraft 1985), becoming even more compatible with decreasing anorthite content (Blundy & Wood 1991), removal of this

phase increases Rb/Sr in the residual magma. Sympathetically increasing K/Ba reflects progressive Ba depletion during magmatic evolution. Since Ba partitions primarily into alkali feldspar during crystallisation of leucogranitic magma ($D_{Ba}^{af/melt}$ ~3.77; Bea *et al.* 1994), with a smaller proportion accommodated by muscovite (e.g. Harris *et al.* 1995), this results from prolonged fractionation of liquidus alkali feldspar. The increasing K/Ba ratio indicates that Ba was enriched in early-precipitated alkali feldspar, such that the K/Ba of the separating phase was lower than that of the bulk residual magma.

9.9.2 Paragenesis of garnet

Numerous competing models have been proposed to account for the presence and compositional character of garnet in granitic rocks (see Clarke 1981), some of which have evoked considerable controversy (e.g. Abbott 1981; Miller & Stoddard 1981a, 1981b, 1982; Clemens & Wall 1982). In the GRC, lack of garnet in migmatites, together with evidence that garnet-bearing granitic rocks are fractionated, precludes garnets being a solid, refractory phase entrained from the metasedimentary source, as advocated by White & Chappell (1977) and Chappell *et al.* (1987). Based on inferred crystallisation pathways in igneous reaction space, Hogan (1996) suggests that the late precipitation of garnet in granitic rocks occurs at the expense of biotite due to increasing melt aluminosity during fractional crystallisation. However, GRC garnet granites are no more peraluminous than other Harrow types (Figure 9.5j), which militates against this specific mechanism, though peritectic reactions may be applicable in some instances (see below).

Alternatively, as the stability field and crystallisation interval of garnet is expanded by Mn (Green 1977), the occurrence of garnet in GRC adamellites may be linked to the distinctive MnO enrichment of these rocks. Reviewing occurrences of granitic-hosted garnets, Miller & Stoddard (1981a) conclude the garnets typically crystallise from magmas with unusually elevated molar Mn/(Mg+Fe) ratios (>0.04). This value exceeds 0.06 in GRC garnet adamellites and ranges to 0.31, much larger than for felsic Harrow types that do not contain garnet (Figure 9.24). Increasing Mn/(Mg+Fe) is a feature of normal magmatic differentiation trends (Goldschmidt 1954) and attributed to fractional crystallisation, since Mn is incompatible with most igneous silicates and a minor constituent of biotite only (Miller & Stoddard 1981a). For example, molar Mn/(Mg+Fe) for the average biotite composition of Marn Mering Granodiorite **T2-1** (~0.014) is less than half that of the bulk rock (~0.03). Prolonged fractionation of feldspars and biotite from a magma of this composition will therefore concentrate MnO and progressively increase the Mn/(Mg+Fe) ratio of the remaining liquid. This effect is enhanced considerably by the abundant crystallisation of muscovite, which contains significant FeO and MgO but no MnO (Appendix C). That fractionation of Harrow type magmas was accompanied by dramatic increase in Mn/(Mg+Fe) is confirmed by Figure 9.24. Ultimately, this process promotes the nucleation of garnet and explains the occurrence of the Mn-rich garnets in many evolved Harrow types and late stage aplitic and pegmatitic dykes. The weak reverse zonation (Fe-rich cores, Mn-rich rims) exhibited by euhedral garnets in T2-69 is typical of early-precipitated garnets of differentiated granitic rocks, such as those of the South Mountain Batholith, Nova Scotia (Allan & Clarke 1981), the southeastern Arabian Shield (du Bray 1988) and the Coastal Maine Magmatic Province (Hogan 1996). This

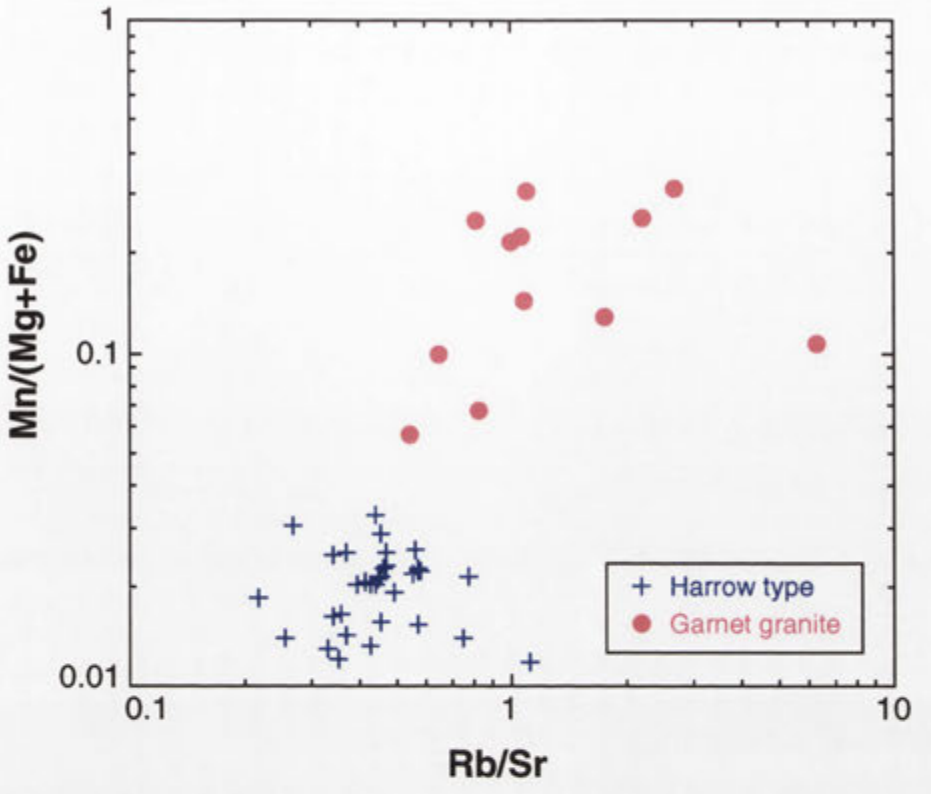

Figure 9.24. Graph of molar (Mn/Mg+Fe) against Rb/Sr (logarithmic scale), showing the relative Mn-enrichment in garnet granites compared to non-garnetiferous Harrow types, and that this initially increases with differentiation. The lower Mn/(Mg+Fe) in the most fractionated sample may reflect extensive garnet precipitation.

has been attributed to decreasing pressure and temperature during garnet crystallisation (e.g. Allan & Clarke 1981), as experimental studies have established that these conditions favour the incorporation of Mn relative to Fe (Green 1977; Clemens & Wall 1981). Alternatively, reverse zonation may reflect increasing magmatic Mn/(Fe+Mg) during garnet growth (Clarke 1981; du Bray 1988), such as could be sustained by co-crystallisation of relatively large volumes of Mn-poor biotite (Bogoch *et al.* 1997) and muscovite. This interpretation is favoured for the garnets of T2-69, as biotite and muscovite are modally much more abundant than garnet, unlike other garnet-bearing samples (see Table 6.1).

In contrast, garnets of the relatively biotite-poor GRC adamellites (e.g. **98-19**) have irregular morphologies that suggest formation later in the crystallisation history (Table 6.3), perhaps at a greater stage of magmatic evolution. The precipitation of these garnets may be related to peritectic reactions between early formed minerals and residual melt such as –

biotite + (Mn, Al, Si)-rich melt = muscovite + garnet (Miller & Stoddard 1981a)

This reaction occurs in response to continued Mn enrichment during magmatic differentiation, and is compatible with the ragged biotite morphology and occurrence of muscovite inclusions

within garnets. The pronounced normal zoning (Mn-rich cores, Fe-rich rims) in garnets of **98-19** is consistent with- (a) the inferred trajectory of the reaction curve in an AFM liquidus projection, which trends towards decreasing Mn at lower temperatures (Miller & Stoddard 1981b), and (b) the rapid depletion of Mn from the melt attending garnet crystallisation (Anderson & Rowley 1981; Bogoch *et al.* 1997), since co-precipitation of biotite was very minor, being probably impeded by very low Fe_2O_3t (~0.4%). More work is required to ascertain whether this compositional trend is representative of the irregularly-shaped, late crystallising garnets in other GRC leucoadamellites.

Both early formed, euhedral garnets and anhedral inclusion-sieved garnets commonly occur within a single leucogranitic body (section 6.6.4), suggesting that garnet crystallisation was a multi-stage process. This may have occurred initially by direct precipitation from the melt, but later by reaction of biotite following more extensive magmatic differentiation/crystallisation. Similarly complex crystallisation histories, involving various stages of garnet growth and resorption, are documented for peraluminous granitic rocks elsewhere (e.g. Allan & Clarke 1981; Hogan 1996).

9.9.3 The Blair Atholl Adamellite

Elevated MnO, K/Ba and Rb/Sr relative to felsic Harrow types (Figures 9.5d, 9.23) suggest that the early syn-compressional Blair Atholl Adamellite experienced similar differentiation processes to the post-D_2 garnet leucogranites of the northeastern GRC. Abundant garnetiferous aplite pegmatite dykes and migmatitic enclaves at the margins, indicating passage through partially melted metasedimentary rocks, are additional unifying features. Yet, compared to other garnet adamellites, the Blair Atholl Adamellite has higher TiO_2, Al_2O_3, (Fe_2O_3t+MgO), and CaO, with lower SiO_2, K_2O and Rb/Sr (Figure 9.5); K/Th is also lower (Figurer 9.8). The CaO and Al_2O_3 contents are particularly high, and outside the range of most Harrow type plutons. Uniquely, despite the peraluminous mineralogy, Blair Atholl Adamellite samples have A.S.I. values below 1.1 (Figure 9.5j).

Importantly, unlike other garnetiferous rocks, Blair Atholl Adamellite contains igneous-textured mafic microgranular enclaves (section 6.6.4). Thus, it is likely that the original composition of the pluton has been modified by interaction with a more mafic, metaluminous magma. This proposition is strengthened by the abundant evidence for magma mingling in the surrounding early syn-compressional hornblende-rich tonalitic rocks (section 10.2.3), confirming that mafic magma was coeval with granitic plutonism in this part of the GRC. To pursue this idea, the relationship between the Blair Atholl Adamellite and adjacent, more mafic granitic lithologies is investigated in Part III.

9.10 Petrogenetic insights from isotopic compositions

The Sr and Nd isotopic character of Harrow type plutons and metasedimentary rocks is outlined in section 9.4 and summarised by Figure 9.12. Field and geochemical evidence indicates derivation of Harrow types exclusively by anatexis of metasedimentary protoliths without

contribution from external (magmatic) components. Involvement of coeval mafic magma in the petrogenesis of Harrow type rocks is further precluded by the lack of correlation between initial $^{87}Sr/^{86}Sr$ and total Fe_2O_3t (Figure 9.13). Hence it can be confidently assumed that the initial isotopic composition of these plutons is largely inherited from the metasedimentary source (e.g. Gray 1990; Wickham 1990). Accordingly, although partial melting scenarios are complex and involve many different metasedimentary precursors, and only a limited amount of data exists, some broad constraints on the geochemical and isotopic character of the source rocks are possible.

From Figure 9.12 it is apparent that sample 861-12 of Turner *et al.* (1993a), which geochemical evidence suggests corresponds to the Kout Norien Granodiorite, has higher $^{87}Sr/^{86}Sr$ at 500 Ma than samples of felsic plutons Awaiti Adamellite, Schofield Adamellite and Marn Mering Granodiorite. This indicates derivation from a slightly more radiogenic protolith (with respect to Sr), which in turn is consistent with the higher Rb/Sr of parental diatexites than inferred sources (mesosomes) for felsic plutons (Figure 9.20). Note however, that sample 861-12 plots within the isotopic field of migmatite zone quartzofeldspathic gneisses, suggesting that the precursor diatexite formed by melting similar lithologies. This precludes significant involvement of metapelitic rocks in magma generation, which are too radiogenic at 500 Ma (see Figure 9.12). Importantly, the Carrigeen Granodiorite, thought also to have formed by separation of entrained residue from a mobilised diatexite, has a much lower initial $^{87}Sr/^{86}Sr$. This suggests either derivation from a much less radiogenic precursor or incorporation of an additional (crustally-derived) magmatic component with low $^{87}Sr/^{86}Sr$ (see below).

Felsic granitic phases of the GRC comprise amalgamations of leucosome-derived partial melts from multiple source rocks, and exemplify a more complex petrogenetic system. The initial isotopic composition of these plutons is likely to average that of each disparate source component to some extent, though as mixing between source-specific magma contributions was apparently minimal the isotopic integrity of individual protoliths may be preserved (e.g. Pressley & Brown 1999). In any case, Figure 9.12 indicates that the initial Sr isotopic composition of felsic plutons requires a metasedimentary source component less radiogenic than the quartzofeldspathic gneisses analysed in this study. A broad correlation between decreasing initial $^{87}Sr/^{86}Sr$ and increasing whole-rock Sr concentration for felsic plutons (Table 9.2) also suggests that this relatively unradiogenic component has elevated Sr contents. In view of this, the most likely candidates are the distinctively calcic quartzofeldspathic schist horizons of the GRC, which are plagioclase-rich and have high Sr and low Rb/Sr (section 7.4.2). Since the calcic, Sr-enriched character is considered to be imparted by a sedimentary carbonate component (Anderson & Gray 1994), a higher proportion of Sr within these rocks is likely to be non-radiogenic, resulting in a lower $^{87}Sr/^{86}Sr$ ratio. Incorporation of partial melts from such horizons, or assimilation of enclaves of this material, may therefore account for the lower $^{87}Sr/^{86}Sr$ ratio of felsic Harrow types. More data from metasedimentary rocks is required to test the proposition.

9.11 Discussion

9.11.1 Controls on geochemical variation

Field, petrographic and geochemical evidence discussed in this chapter unequivocally demonstrates that the voluminous Harrow type granitic rocks of the northeastern GRC (encompassing both leucocratic adamellite-granodiorites and mafic residue-rich granodiorites) were formed exclusively by partial melting of predominantly quartzofeldspathic horizons within the host metasedimentary sequence. This is summarised in Figure 9.25. Significant partial melt contributions from metapelitic rocks are discounted on isotopic grounds and consistent with the lower proportion of leucosome within metapelitic horizons. More micaceous, semi-pelitic gneisses were the precursors to Harrow type leucotonalites.

The spectrum of petrographic and geochemical diversity observed within and between individual plutonic phases is controlled by an interplay between two main factors- (1) the mechanisms of melt segregation and migration in the source region, and (2) subtle differences in the mineralogy and bulk composition of the quartzofeldspathic metasedimentary protolith(s).

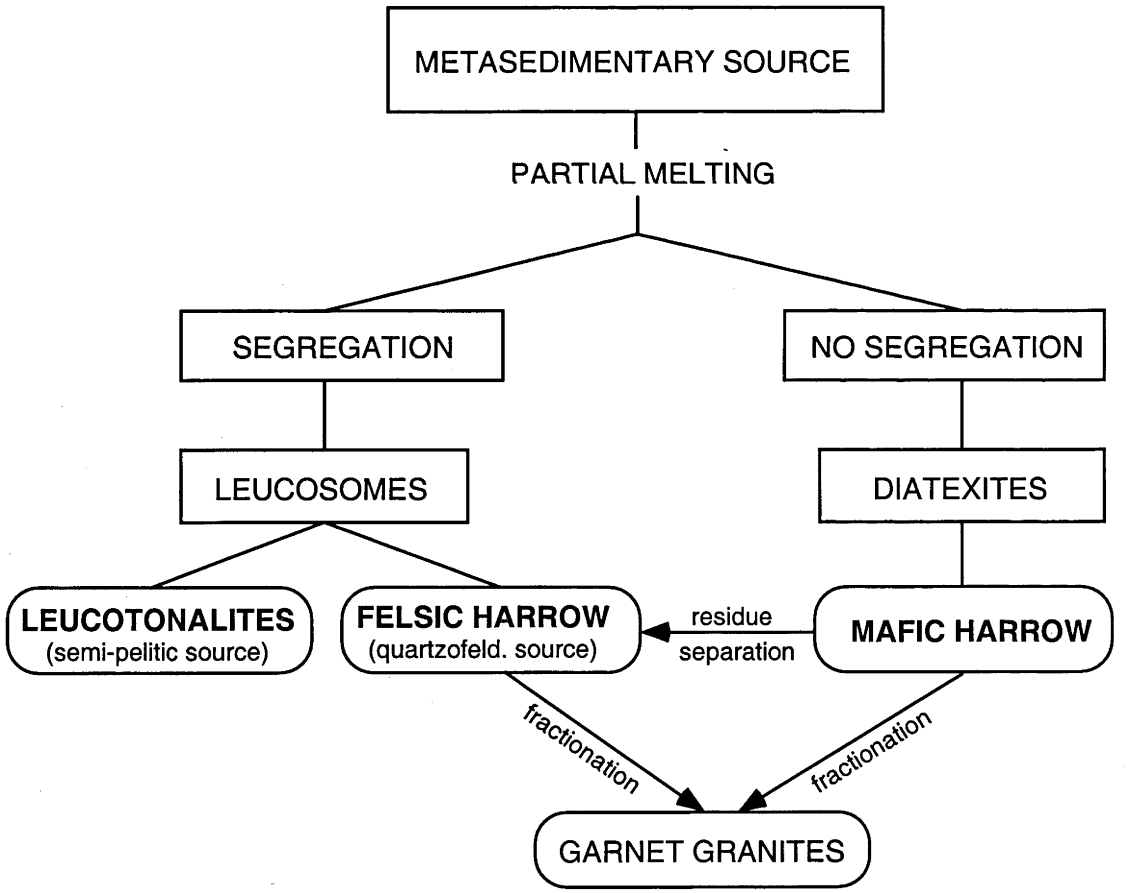

Figure 9.25. Petrogenetic model summarising the formation of the four groups of Harrow type granitic rocks recognised in the GRC.

With respect to the former, compelling outcrop and chemical evidence suggests that leucocratic adamellite-granodiorite bodies comprise accumulations of partial melt aliquots derived from *in situ* leucosomes of nearby migmatitic horizons, and transported from the source region via dyke or sheet-like magma conduits. Due to consumption of alkali feldspar and plagioclase in the protolith, promoted by the extensive water-fluxed and muscovite-involved anatexis, the latter are characteristically enriched in feldspathic components but low in ferromagnesian elements, as biotite remained essentially inert during melting. That these partial melt increments have efficiently disengaged from the refractory biotite-rich melanosome, and migrated into larger-scale magma escape structures, without significant entrainment of residue is therefore directly responsible for the elevated K_2O, Sr and Ba, and strongly depleted TiO_2, (Fe_2O_3t+MgO), Rb, P, HFSE and REE in derivative felsic plutons relative to the inferred protolith. Hence, the remarkably effective segregation of the melt component has strongly fractionated biotite-compatible elements and maximised the geochemical signature of partial melting. Given the preponderance of leucogranitic rocks, this is clearly the dominant petrogenetic process in the GRC. The segregation of the melt phase and migration into larger bodies without residue-contamination may have been motivated and enhanced by compressive stresses, as anatexis was synchronous with regional deformation, this process being exemplified within migmatitic exposures (see Figure 5.11). Note that the subsequent magmatic evolution of these felsic adamellite-granodiorite bodies involves homogenisation within and between constituent magma batches, followed by fractional crystallisation to produce garnet-bearing compositions.

In contrast, the mafic Harrow type plutons, formed by wholesale mobilisation of melt-rich diatexites, are replete with biotite-rich residue, directly inherited from the poorly-segregated precursor. The latter chemically resemble quartzofeldspathic metasedimentary rocks of the optimum fertility 'window', but were generated by pervasive melting during shear-localised fluid infiltration (section 8.4.4). As such, mafic Harrow types more closely approach the bulk composition of their ultimate (sedimentary) source rocks, which is reflected by geochemical similarity to the upper continental crust (Figure 9.7). With progressive separation of the residuum component during migration, these plutons become more melt-rich and evolve towards the field of felsic Harrow types. Despite this, evolved diatexite-sourced granodiorites retain a slightly more biotite-rich character, reflecting the more mafic partial melt of the parental diatexite compared to that of stromatic migmatites (section 8.5.5). Some fractionation of magmatic biotite may be required before complete chemical overlap with leucocratic Harrow types is achieved.

The influence of source composition in imparting the petrochemical diversity of Harrow type granitic rocks is most evident with respect to leucocratic adamellite-granodiorite bodies, and the Schofield Adamellite pluton in particular. Field relationships suggest that this sheeted body comprises an accretion of multiple, chemically-distinct magma batches, formed by the migration and coalescence of leucosome-derived partial melts. The striking geochemical variation across the pluton is ascribed to compositional differences between and within these constituent magma batches, in turn reflecting the poorly-blended melt contributions from different quartzofeldspathic metasedimentary precursors. The compositional diversity of the pluton was therefore essentially inherited from heterogeneous source rocks. An important implication is that

the Schofield Adamellite does not have a single, unique protolith composition, which also applies to other the internally heterogenous leucocratic Harrow type bodies. Notably, this is only evident due to the lack of homogenisation between constituent magma batches during assembly of the pluton, such that the geochemical signature of each separate source component (or mixture of source components) is preserved. In granitic bodies emplaced at higher levels within the crust, these important source-related heterogeneities may be erased by magmatic homogenisation processes, so that the evidence for multiple protoliths is masked or obliterated. The large Marn Mering Granodiorite pluton lacks a sheeted structure and may represent an arrested stage towards this extreme, though marked geochemical heterogeneity is extant.

Apart from bulk composition, the significance of source mineralogy in controlling the geochemistry of metasedimentary-derived granitic rocks of the GRC is clearly exemplified by the formation of leucotonalitic plutons. Although these also comprise locally-derived magma batches, and have the low ferromagnesian element signature indicating efficient melt-residue separation, leucotonalites are distinguished from other felsic Harrow types by depleted K, Ba and Rb. This reflects derivation from an alkali feldspar-absent, semi-pelitic (as opposed to quartzofeldspathic) protolith by water-fluxed melting, whereby these elements are retained in residual muscovite and biotite. Further, the enriched LREE and Th concentrations of leucotonalitic plutons, imparting lower Ba/La and K/Th ratios, are consistent with greater involvement of accessory monazite in generation of tonalitic partial melts. Although the reason for this is speculative, it may well reflect enhanced solubility of monazite in K-poor partial melt, or the greater ability of monazite grains in the protolith to interact with the melt reservoir. In any case, the fundamental geochemical differences between leucotonalites and felsic adamellite-granodiorite plutons can be traced back to the outcrop- or even grain-scale anatectic processes responsible for the formation of migmatite leucosomes.

9.11.2 Broader implications for the petrogenesis of granitic rocks

This interpretation of crustally-derived magmatism in the northeastern GRC indicates that both leucocratic granitic rocks and mafic, residue-rich plutons may be generated from broadly similar protoliths under similar anatectic conditions during the same geodynamic episode. However, a major conclusion of this study is that rather than representing end-members of a single magmatic lineage, this petrological dichotomy reflects the operation of fundamentally different magma segregation and transport processes in the source region, which in turn governs the subsequent geochemical evolution of derivative plutons.

Many aspects concerning the formation of Harrow type granitic rocks challenge the restite model espoused by White & Chappell (1977) and Chappell *et al.* (1987). This asserts that the compositional diversity of granitic suites results from differential separation of felsic melt and residual source material (restite) during pluton ascent (see section 1.3.2). The model, derived from studies of upper crustal plutons, is therefore underpinned by the *assumption* that granitic magmas entrain significant amounts of unmelted residue upon migration from the source. However, outcrop relations in the GRC demonstrate that batches of granitic magma are

efficiently extracted from metasedimentary protoliths at low melt percentages, *without* wholesale entrainment of refractory material. Transfer and emplacement of these segregated magma batches occurred in pulses along sheet-like conduits, resulting in the formation of large, restite-poor adamellite to tonalite plutons *close to the source region*. This scenario therefore undermines the fundamental tenet of the restite model, *viz.* that granitic plutons depart the source region restite-replete. Accordingly, compositional control by restite separation in felsic Harrow type rocks is negligible, chemical variation instead being inherited from heterogeneous source rocks. This process also obviates the necessity for total, buoyancy-driven source mobilisation at high melt fractions as required by the restite model, and represents an efficient mechanism for the rapid construction of pluton-scale magma accumulations at depth (see also Petford 1996 and Brown & Solar 1998). The Schofield Adamellite includes residue-contaminated magma batches derived from diatexites, which are also transported as sheet-like bodies rather than in diapir-like manner, as exemplified by the Bryan Creek Granodiorite. Elsewhere, diatexite-derived magma pulses coalesce into plutons (e.g. the Kout Norien Granodiorite) but, as shown by the internal variation within the Carrigeen Granodiorite, lose their entrained residual component close to the generative region.

The striking efficacy of melt-residue segregation in the GRC is consistently exhibited by anatectic terranes worldwide (e.g. Brown 1994; Brown *et al.* 1995), and therefore questions the extent to which a residual component is incorporated into granitic magmas during formation. This in turn casts serious doubt upon the general applicability of restite separation for engendering geochemical diversity within high level granitic plutons. In this light, the many implications of the restite model for granite petrogenesis and crustal evolution, as outlined by Chappell *et al.* (1987), Chappell (1996b) and Chappell *et al.* (2000), require re-evaluation. Specifically, the restite model holds that granitic rocks form a geochemical 'image' of their protoliths, and therefore provide some insight into the composition of inaccessible parts of the crust. This approach has some utility for the volumetrically minor mafic Harrow type granodiorites, which retain the broad compositional character of their diatexite precursors. However, by virtue of efficient melt segregation, felsic Harrow type plutons are very poor images of their source rocks, and specific protolith compositions cannot be reliably deduced by regression of chemical trends (cf. Chappell *et al.* 1987). On a larger scale, Chappell (1996b) contends that the upward carriage of refractory lower crustal material by granitic plutons ascending in diapiric fashion might partly account for the granodioritic (as opposed to haplogranitic) composition of the upper crust. Yet, if wholesale entrainment of restitic material by granitic magmas is not the general case, as suggested by this study, this 'intracrustal overturn' mechanism is invalidated. Additional evidence against crustal-scale material redistribution during granitic plutonism is the maintenance of structural coherency in many depleted granulite terranes (Brown & Earle 1983; Clemens 1990), confirming extraction of partial melts at low melt fraction without source mobilisation. However, cleanly-segregated leucogranitic magmas of the GRC have strongly fractionated chemistries relative to the upper crust (Figure 9.7), which taken alone implies that this style of magmatism also had minimal effect on crustal differentiation. The operation of other factors is suggested, and explored further in Part III. Regardless of this, the

combination of low temperature anatexis and efficient melt segregation in the GRC results in enrichment of the most important crustal heat-producing elements, Th and U, in the residual fraction after evacuation of leucogranitic magma. The possible effects of this for the long term lithospheric thermal regime of low P-high T orogenic belts requires careful further study.

Of final note is that the occurrence of large leucotonalitic plutons in the northeastern migmatite zone, together with extensive tracts of tonalitic migmatites, indicates that generation of K-deficient partial melts was an integral part of low temperature crustal anatexis in the GRC. Formation of significant quantities of tonalitic magma clearly does not require granulite facies metamorphism (i.e. >800°C) involving basic igneous protoliths (cf. Tait & Harley 1988; Williams *et al.* 1995; Springer & Seck 1997).

To conclude, the geological evidence presented in Part II of this thesis establishes a remarkable and rarely observed physiochemical link between outcrop-scale partial melting and the formation of granitic bodies of plutonic dimensions. Such a granite-migmatite nexus has been previously dismissed (e.g. Clemens & Mawer 1992; Whitney & Irving 1994), encapsulated by the statements of White & Chappell (1990) that 'The geochemistry of anatectic migmatites tells us little about granite formation' (p224) and 'study of migmatite terranes is unlikely to provide much information about the formation of granitic magmas' (p225). To the contrary, studies of deep-seated terranes such as the GRC clearly demonstrate that in some circumstances migmatites are not 'failed granites' or anatectic cul-de sacs, but represent the essential first stage in the evolution of large volumes of crustally-derived granitic magma.

PART III

Petrology and petrogenesis of metaluminous to weakly peraluminous granitic plutons and mafic to intermediate igneous rocks

(includes Chapters 10 to 18)

Chapter 10: Occurrence and petrology of granitic rocks of the GRC

Part (A) Early syn-compressional phases

10.1 Introduction

Metaluminous to weakly peraluminous granitic rocks of the GRC are subdivided into an early syn-compressional (pre- to syn-D_2) and late syn-compressional (post-D_2 but pre-D_5) structural association (Chapter 4). The former group are largely restricted to the southwestern metamorphic zonation, particularly the Wando Vale and Wennicott Creek areas, where they comprise the Wando, Wennicott and Deep Creek magma types (Table 4.1). This chapter documents each pluton of these magma types, with emphasis upon field relations and mafic microgranular enclaves. Detailed petrographic descriptions of important specimens (sample numbers with asterisks), are presented in Appendix E.

10.2 Wando Type

The Wando River valley north of Casterton is occupied by a large expanse of strongly foliated granitic rock, originally mapped as 'granodiorite gneiss' (Wells 1956), but subsequently subdivided into the Wando Tonalite and various granodioritic phases by Anderson (1990). Turner *et al.* (1993a) report considerable geochemical variation within the Wando Tonalite (from 52.7% to 63.1% SiO_2), and thus it is unlikely that the body represents a single plutonic entity.

Investigating this possibility, mapping by this research has further resolved the granitic exposures of the Wando River valley into six plutonic phases (Figure 10.1). Of these, the Wando Tonalite, Snake River Tonalite and several texturally similar dioritic dykes are grouped as the Wando magma type. These rocks are strongly foliated and quite mafic, with abundant blue-green hornblende and prominent allanite, epidote and magnetite (Table 10.1); felsic mineral proportions are shown in Figure 10.2. Despite internal deformation features, plagioclase laths are characterised by sharp twinning and oscillatory zoning outwards from mostly euhedral cores. Mafic microgranular enclaves are numerous throughout all plutons. Wando type rocks define coherent linear geochemical trends, characterised by high Al_2O_3 and markedly increasing K_2O content with evolution to higher SiO_2 (section 15.3.1).

10.2.1 Wando Tonalite

(a) Field relations and lithology

The Wando Tonalite is an elongate, lenticular pluton aligned parallel to the S_2 foliation in adjacent metasedimentary rocks, and is folded by a macroscopic D_5 antiform. The southern boundary is with amphibolite facies schists in the Wando River and Boundary Creek, while further north, the body is intruded by the Snake River Tonalite (below).

Lithology	*Sample number*	*Grid reference* (WD)	*Modal Percentage*						*Accessory Minerals*
			Quartz	**Plagioclase**	**K-Feldspar**	**Biotite**	**Hornblende**	**Epidote**	
Wando Tonalite	**97-161**	404557	25.2	44.1	3.8	17.3	4.2	4.3	a, all, ca, m, t
MME (A)	**97-160-1**	405559	16.3	31.6	0	16.6	34.3	0	a, ca, t
MME (B)	**97-160-2**	405559	16.0	33.5	0	14.0	35.6	0.2	a, t
MME (B)	**97-161E**	404557	11.8	38.6	0.2	23.3	23.4	2.3	a, all, t
Snake River Tonalite	**97-159**	407560	20.8	51.6	<0.1	14.5	10.8	0.5	a, all, c, ca, m, t
	97-192	384571	21.0	50.1	0	15.1	8.9	3.0	a, c, o, t
	97-214	429541	22.9	46.6	4.7	14.4	9.7	1.0	a, c, m, t
MME (A)	**97-214E**	429541	8.6	26.5	0	16.4	48.3	0.1	
MME (B)	**97-154**	411562	14.3	49.7	0	11.3	23.7	0.4	a, t
MME (B)	**97-155**	410563	17.6	35.9	0	12.0	34.5	0	
MME (C)	**97-159E**	407560	1.0	29.1	0	30.5	37.5	0.5	a, m, t (0.8%)
Quartz Diorite	**98-124**	412543	5.7	56.4	0	3.6	32.1	0	a, c, o, t (1%)
	97-206F	411545	9.8	56.8	0.1	10.0	21.8	0	a, c, t
	97-206E	411545	14.5	42.6	0	19.1	22.9	0	a, c, t
	97-208	412543	21.2	49.6	1.3	14.5	11.8	0.1	a, c, (1.1%), o. t
MME	**97-206C**	411545	10.4	33.4	0	13.0	42.9	0	t

Table 10.1. Mineralogy of Wando type granitic rocks of the Glenelg River Complex, determined by thin section point count (2500 points).

Abbreviations are; a = apatite, all = allanite, c = chlorite, ca = carbonate, m = magnetite, o = opaque mineral, t = titanite.

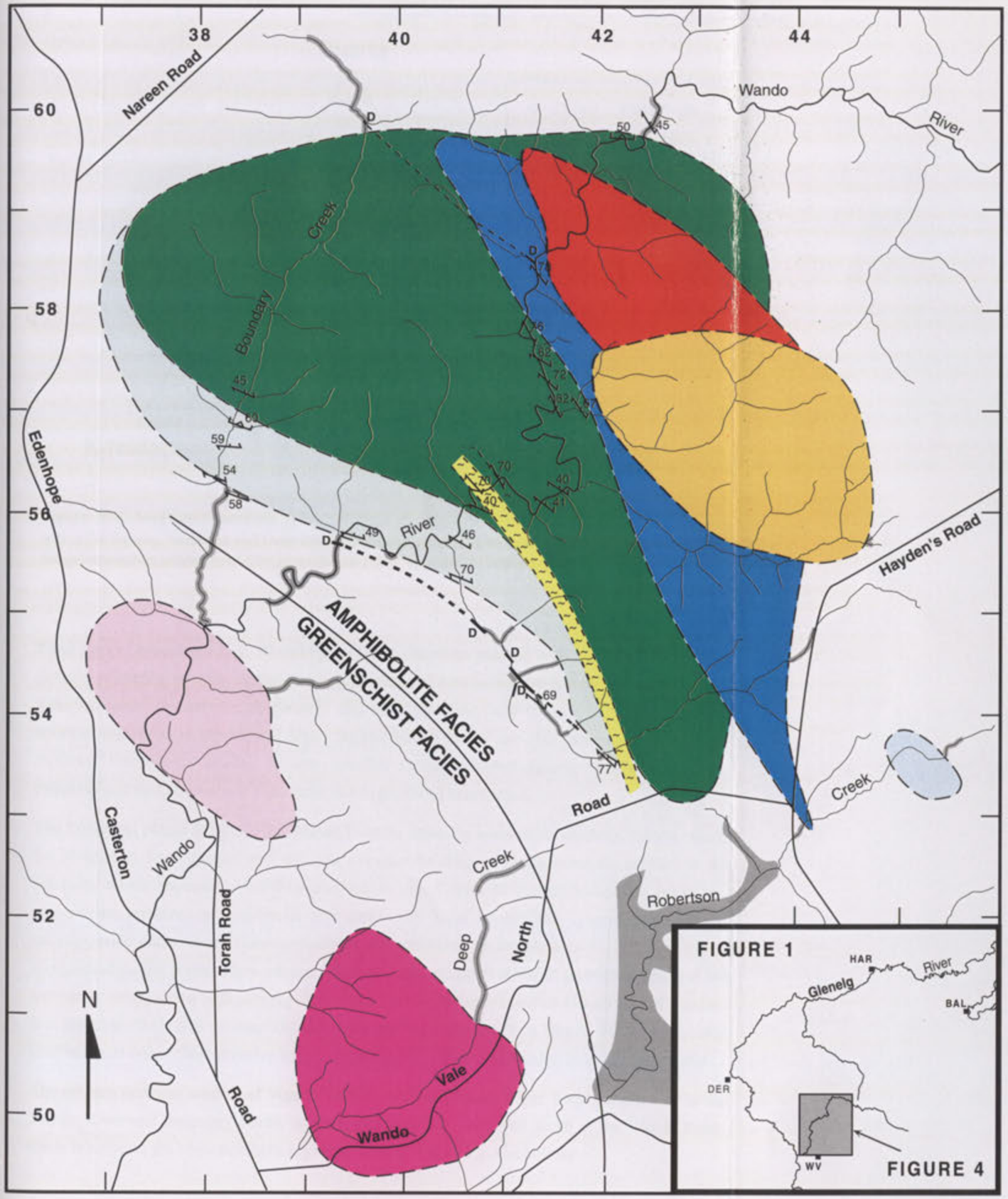

CAMBRO-ORDOVICIAN
- CLOVEN HILLS GRANODIORITE
- DEEP CREEK GRANODIORITE
- TORAH GRANODIORITE
- BLAIR ATHOLL ADAMELLITE
- Unnamed foliated granodiorite
- MEISSEN GRANODIORITE
- SNAKE RIVER TONALITE
- WANDO TONALITE

?MIDDLE CAMBRIAN
- Metasedimentary outcrop

- Road
- Watercourse
- Approx. geological boundary
- Trend of S_2 foliation
- Trend of metasedimentary enclave
- D — Diorite dyke
- Shear zone (boundaries approx.)

0 1 2
KILOMETRES

Figure 10.1. Geological map of the Wando River area, with younger rocks omitted for clarity; inset indicates the location of the area in Figure 4.1. The boundaries of the Torah and Deep Creek Granodiorites are taken from Anderson & Gray (1994) and Kemp *et al.* (2001).

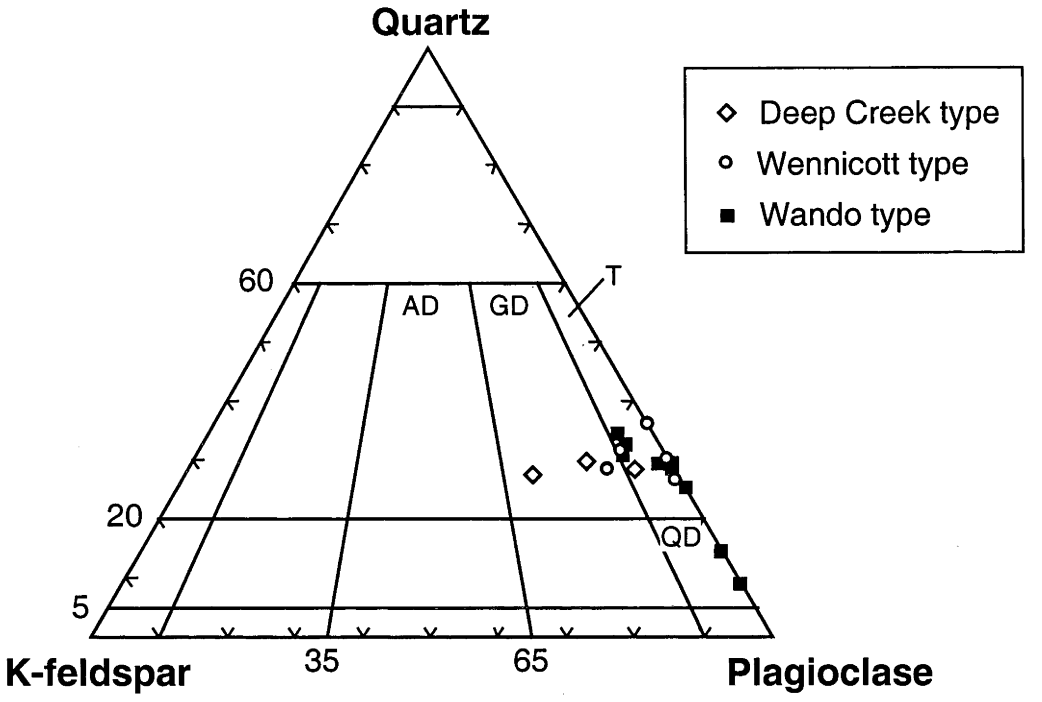

Figure 10.2. Modified Streckeisen (1976) diagram depicting the felsic modal mineralogy of plutons within the Wando, Wennicott and Deep Creek magma types (data from Tables 10.1 and 10.6). Lithological compartments are adamellite (AD), granodiorite (GD), tonalite (T) and quartz diorite (QD).

Fresh typical specimens (e.g. **97-161***) are fine to medium grained with a gneissic fabric (S_2), defined primarily by tiny biotite flakes and smeared biotite-hornblende clots, augmented by flattened quartz masses and moderately aligned plagioclase laths (Figure 10.3). Orthoclase is entirely interstitial to the latter. Larger, ragged biotite scales are also prominent on foliation surfaces. Hornblende prisms, epidote spindles (some euhedral against biotite and simply twinned) and lenticular mafic clots have linear preferred orientation.

The linear and planar fabrics in the Wando Tonalite intensify towards its southern margin, where the tonalite is finer grained and exhibits a vague banding of mafic minerals parallel to the foliation, which approaches a continuous schistosity. Slivers of quartzofeldspathic schist and calc-silicate enclaves are numerous and commonly have asymmetric cross-sections. Mafic microgranular enclaves are likewise flattened and attenuated in the plane of S_2. Adjacent *in situ* quartzofeldspathic schists have intense foliations, rotated alkali feldspar porphyroclasts and are intimately interspersed with sheets (<2 m wide) and asymmetric boudins (10-40 cm) of tonalite. It is therefore likely that the tonalite-schist interleaving at the southern Wando Tonalite boundary is of tectonic rather than intrusive origin, reflecting D_2 strain partitioning towards the contact.

The arcuate northern contact of Wando Tonalite with the Snake River Tonalite, exposed in the Wando River and Boundary Creek, is sharp and intrusive. However, south of the Wando River, these lithologies are separated by a mylonite zone (Figure 10.1, see below).

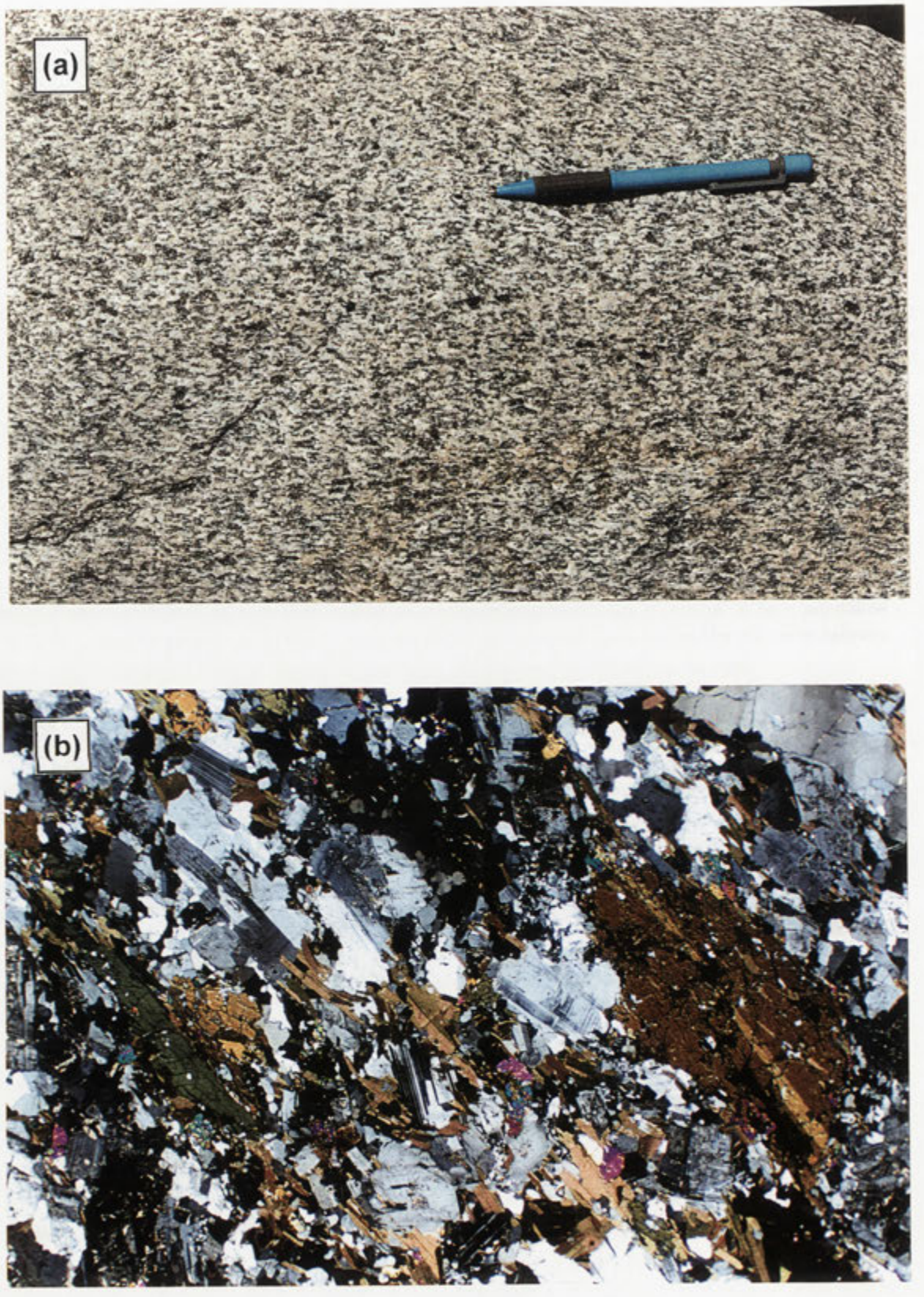

Figure 10.3. Wando Tonalite. (a) Typical outcrop appearance, note the medium, uniform grainsize, small biotite-hornblende clots and strong foliation (top right) (Wando River, WD402557). (b) Thin section view, showing aligned hornblende prisms (simply twinned), plagioclase laths and biotite flakes; the grains with bright interference colours are epidote (crossed polars, field of view ~8.1 mm).

(b) Enclaves

Various metasedimentary enclaves are prominent near the southern Wando Tonalite margin (above), most notable of which are large slabs (up to 5 m long) of migmatitic quartzofeldspathic schist in Boundary Creek. Laminated quartzofeldspathic schist rafts (up to 5 m across) are also encountered adjacent the northern margin with Snake River Tonalite in Boundary Creek and the Wando River, the internal foliation of which (S_2) parallels that of the tonalite. Metasedimentary enclaves have isoclinally folded (F_2) leucosomes and are veined by the host, indicating syn-D_2 emplacement for the Wando Tonalite.

Away from the southern periphery, enclaves in the Wando Tonalite are almost exclusively hornblende-rich mafic microgranular types. These are locally swarmed, but overall less abundant than in the more mafic Snake River Tonalite. Enclaves most commonly have asymmetric lensoidal or teardrop-shaped profiles (1-60 cm long), variably flattened parallel to S_2 in the host and traversed by this fabric; those near the southern margin are highly attenuated, with axial ratios of up to 10:1. Although lithologically diverse, mafic microgranular enclaves are broadly categorised as either 'type A', which are most numerous, or 'type B' (Figure 10.4, Table 10.2). The petrographic attributes of representative enclave samples are summarised in Table 10.3.

Despite the differences between type A and type B microgranular enclaves, several unifying textural features are also apparent. Both types have a strong foliation (S_2), defined by aligned biotite, plagioclase laths, and flattened quartz masses, and a pronounced lineation of matrix hornblende. Plagioclase in thin section also has distorted twin planes and mechanical twinning, whereas groundmass quartz forms a polygonal mosaic. Nevertheless, relict igneous textures are evident in both types. Groundmass plagioclase laths are commonly subhedral and have continuous zoning outwards from euhedral cores. Although plagioclase phenocrysts of type B enclaves are mostly anhedral, they have large, euhedral cores outlined by trains of tiny hornblende inclusions. Significantly, subhedral hornblende prisms in both enclave varieties are enclosed by, or exhibit crystal faces against plagioclase. Apatite invariably has needle-like morphology.

10.2.2 Snake River Tonalite

(a) Field relations and lithology

This large body occurs north of the Wando Tonalite and outcrops for another 4 km northeast along the Wando River valley and Boundary Creek to a contact with metasedimentary rocks (Figure 10.1). The outcrop pattern and a strong aeromagnetic signature imply a curved, elliptical pluton shape, consistent with flexure by the D_5 antiform mentioned above. Magnetic evidence, together with lack of exposure in Vines Creek, suggests that the Snake River Tonalite does not extend northwest of the Edenhope Road (Kemp *et al.* 2001) The southeastern pluton margin is constrained by absence of exposure in Robertson Creek, but complicated by crosscutting granitic bodies (Figure 10.1).

Although similar to the Wando Tonalite, typical Snake River Tonalite specimens of the Wando River (e.g. **97-159***) are slightly darker coloured, coarser grained, and contain more hornblende

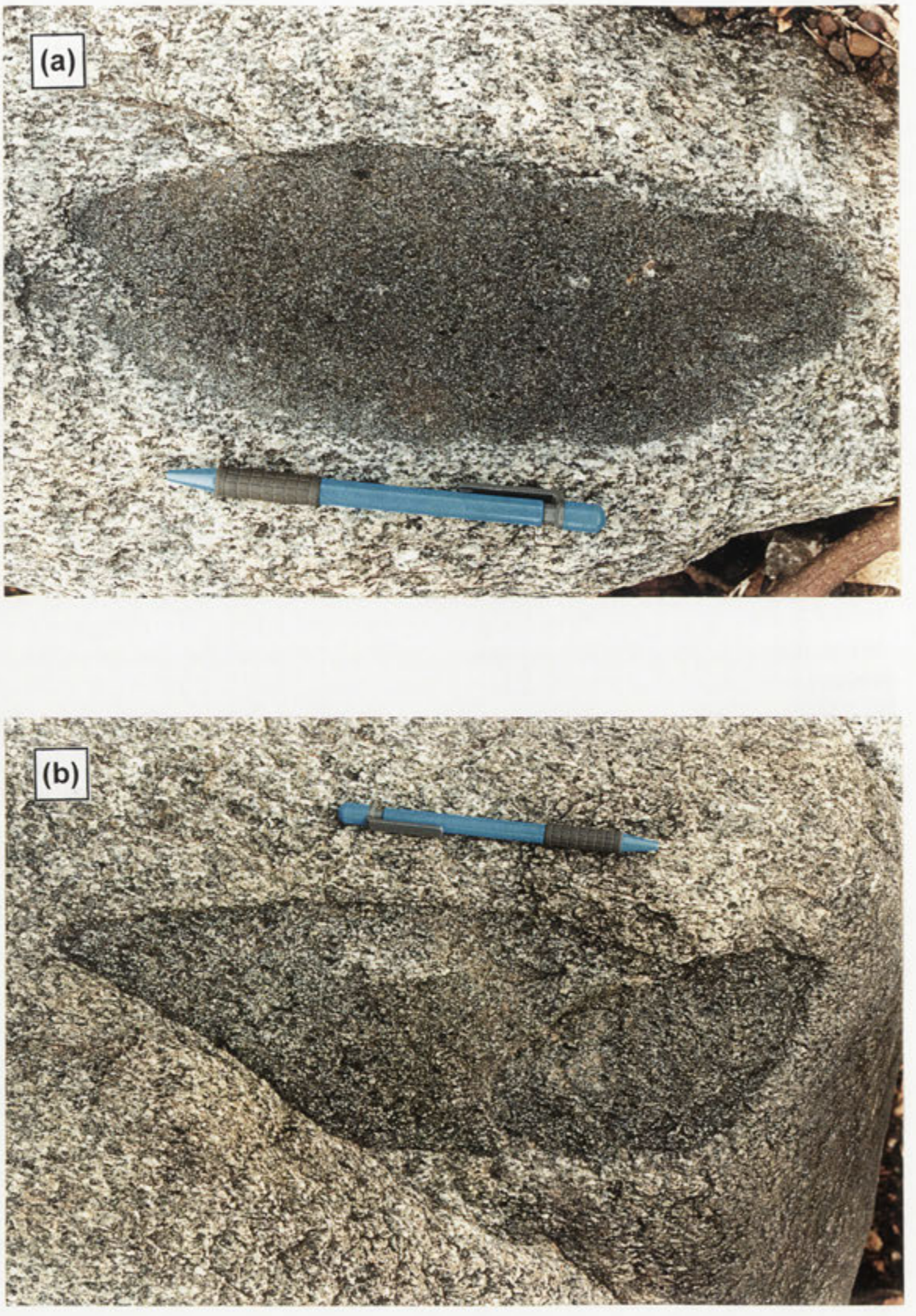

Figure 10.4. Mafic microgranular enclaves in the Wando Tonalite. (a) Fine grained type A enclave; larger biotite plates are visible. (b) Type B enclave, exhibiting coarser grainsize and having a more 'dioritic' appearance (Wando River, WD402557).

prisms (to 7 mm long; Table 10.1). Orthoclase is rare or absent. A gneissic foliation is defined by poikilitic biotite flakes, flattened hornblende-biotite aggregates and large plagioclase laths, though is slightly less intense than that of the Wando Tonalite due to the coarser grainsize. Hornblende prisms, abundant subhedral epidote spindles and attenuated mafic clots are conspicuously aligned, though many hornblende grains are intergrown and oblique to this fabric. Magnetite is concentrated in mafic clots.

Subtle lithological variations are also recognised (see Table 10.1). A relatively mafic variant in Boundary Creek (**97-192**) is finer grained, with more hornblende and lacking poikilitic biotite. Conversely, Snake River Tonalite outcrops in Elbow Creek (e.g. **97-214***) are slightly more felsic than 'typical' samples, with greater amounts of quartz and interstitial orthoclase (Table 10.1).

Partitioning of D_2 strain also occurred towards the margins of the Snake River Tonalite, most notably with the development of a 120 m wide mylonite zone near the southern boundary with the Wando Tonalite (Figure 10.1). A 3 m raft of quartzofeldspathic schist also occurs near here. The northern contacts with metasedimentary rocks are also sheared and the locus of hydrothermal alteration. The presence of large schist enclaves in the tonalite adjacent these boundaries suggests some interleaving with the host metasedimentary rocks.

Enclave type	*Distinctive characteristics*
Type A	Fine grained, dark bluish-grey with large biotite plates. Hornblende-rich groundmass. Plagioclase or quartz phenocrysts very rare.
Type B	Coarser grained, lighter coloured (dark grey), porphyritic 'microdioritic' appearance. Has blades or clots of hornblende and plagioclase phenocrysts which give a 'speckled' aspect. Biotite is more abundant, though of variable proportions.
Type C	Smaller (3-10 cm across), more mafic bodies comprising mainly hornblende prisms and laths or rectangular phenocrysts of plagioclase. Biotite is generally minor (but variable), whereas quartz is rare. May be of similar grainsize to the host, though porphyritic varieties more common.

Table 10.2. Characteristics of mafic microgranular enclaves in Wando Type rocks. Type C enclaves are conspicuous in the Snake River Tonalite only.

(b) Enclaves

Mafic microgranular enclaves (up to 1.5 m long) are abundant throughout the Snake River Tonalite, occasionally forming 'trains' across the outcrop. Enclaves are mostly ellipsoidal, some with asymmetrical profiles, though oval, amoeboid or blocky objects are observed. This contrasts with enclaves of the more highly strained Wando Tonalite, which are smaller, flattened and attenuated.

Although fine grained 'type A' enclaves occur in the Snake River Tonalite, being smaller than those of the Wando Tonalite (5-30 cm long), most have affinity with the 'type B' bodies (Table

10.4). As with the Wando Tonalite, type B enclaves are lithologically variable, ranging from darker versions of the host (Figure 10.5a) through to more mafic, finer grained varieties; contacts vary from sharp to diffuse independently of lithology. Generally, larger type B enclaves are more felsic and commonly composite, hosting numerous, more mafic enclaves, including the type A variety. Some also have irregular, slightly scalloped margins (Figure 10.5b).

Importantly, the Snake River Tonalite also hosts a third variety of mafic microgranular enclave that is poorly represented in the Wando Tonalite, designated as 'type C' (Tables 10.2, 10.4; Figure 10.5c). Relatively mafic character and well-shaped plagioclase phenocrysts are defining attributes (Figure 10.5d).

Sample	*Type*	*Summary petrographic description*
97-160-1	A	Homogeneous, with sparse masses of flattened quartz (~2 mm, up to 4 mm long), elongate ragged biotite flakes (~2 mm, up to 5 mm) and rare chalky plagioclase laths (~3 mm) in a fine grained, hornblende-dominated groundmass. Several lenticular clots (1-3.5 mm) of interleaved, coarser biotite plates and lesser hornblende also occur. In thin section, larger biotite grains enclose tiny hornblende, plagioclase and titanite inclusions. Titanite euhedra and subhedral to anhedral epidote grains are most numerous in biotite-hornblende aggregates.
97-161E	B	Strongly porphyritic, dark grey object with hornblende blades (3-4 mm), many of which are oblique to S_2, and numerous small rectangular plagioclase phenocrysts (most 1-2 mm, greenish-white). No large flakes of biotite, occasional brownish spindles of aligned epidote. Groundmass is fine grained biotite and lesser hornblende, with granules of quartz and plagioclase. In thin section, subhedral hornblende phenocrysts exhibit incipient replacement by biotite; occasionally these minerals form intergrown lenticular clots (1-3.5 mm long) enclosing euhedral epidote grains (0.5-0.8 mm). Plagioclase phenocrysts have serrate boundaries against groundmass minerals but contain large euhedral cores. These have complex mottled zoning in contrast to the continuous or oscillatory zoning of rims.
97-160-2	B	Less porphyritic, medium grey coloured, contains striking clots of hornblende (up to 10x10x1 mm) in a fine to medium grained groundmass of biotite, polygonal quartz granules and bluish-white plagioclase laths. Individual hornblende blades (3-4 mm) are relatively rare. Hornblendic clots are flattened and attenuated in the plane of the foliation, and in thin section form ragged prisms (~0.8 mm) with quartz inclusions. Large anhedral biotite flakes (2-3 mm) are also intergrown with hornblende grains.
97-162	B	Slightly coarser, more felsic variant. Texturally homogenous, even-grained, resembles a more mafic version of the host. Medium grey coloured, and has a thin (1-2 mm) rim of polygonal hornblende grains.

Table 10.3. Summary descriptions of different mafic microgranular enclaves in the Wando Tonalite. Note that hornblende and biotite in each enclave type have the same pleochroic scheme as the host. Modal analyses are presented in Table 10.1.

Sample	*Type*	*Summary petrographic description*
97-214	A	Homogeneous, fine grained, and dark greenish grey. Dominated by needly grains or smeared aggregates of hornblende (1-3 mm long). Plagioclase phenocrysts, quartz masses and larger distorted biotite flakes (~1 mm) are rare. In thin section, mafic clots are interspersed with small biotite flakes (0.5mm) and polygonal plagioclase and quartz grains (0.5-0.8 mm). Plagioclase phenocrysts enclose tiny hornblende and biotite grains at the margins and are anhedral against matrix hornblende. Enclave also hosts small dark olive-green objects (2 cm long) that are mostly microcrystalline hornblende.
97-154	B	Medium bluish-grey, with phenocrysts of greenish plagioclase (~2 mm), hornblende prisms (1-4 mm) and very conspicuous lenticular clots of finer grained hornblende (~2-4 mm) in a finer groundmass of hornblende, plagioclase and sugary quartz. Large ragged biotite plates (up to 4 mm) enclose plagioclase, quartz, hornblende, euhedral epidote and titanite crystals. Groundmass is a mosaic of continuously zoned plagioclase (0.8-1 mm) and quartz (most ~0.8 mm), interspersed with small hornblende and minor biotite grains. Groundmass plagioclase is euhedral against biotite. Apatite occurs as tiny needles or larger euhedral prisms.
97-155	B	Similar to **97-154** but with less plagioclase laths and without individual hornblende blades. Hornblende forms lenticular clumps (2-5 mm across) flattened parallel to S_2, and imparting a spotted character to weathered surfaces; minor fine biotite flakes are intergrown. Also, unlike **97-154**, contains large single quartz grains (~2.5 mm), more groundmass biotite and clots of interleaved biotite flakes (~3 mm).
97-159E	C	Has rectangular plagioclase phenocrysts (~1-3.5 mm) and subhedral hornblende prisms in a groundmass of plagioclase, hornblende and conspicuous biotite (Figure 10.5d). Larger, ragged poikilitic biotite plates are also evident, commonly enclosing tiny epidote euhedra. Groundmass hornblende and plagioclase are anhedral in thin section, though hornblende is occasionally subhedral against plagioclase; both exhibit crystal faces where contacting biotite. Polygonal quartz grains are minor but magnetite is abundant, with apatite needles. Enclave margins are magnetite-enriched and moulded around plagioclase laths in the host tonalite, several of which project into the enclave
97-167	C	Dark greenish-grey, dominated by small grains (~0.8-1 mm) and larger needly prisms (1-4 mm) of hornblende, with lesser blocky plagioclase laths. Strongly altered and contains abundant disseminated pyrite, carbonate and epidote. In thin section plagioclase is replaced by white mica, carbonate and anhedral epidote. Hornblende is overgrown by actinolite and sheaves of chlorite replace biotite. Quartz grains and skeletal titanite blebs also occur. Unaltered areas have interlocking hornblende and plagioclase.

Table 10.4. Summary petrographic descriptions of different mafic microgranular enclaves in the Snake River Tonalite. The modal mineralogy of each sample (except **97-167**) is given by Table 10.1.

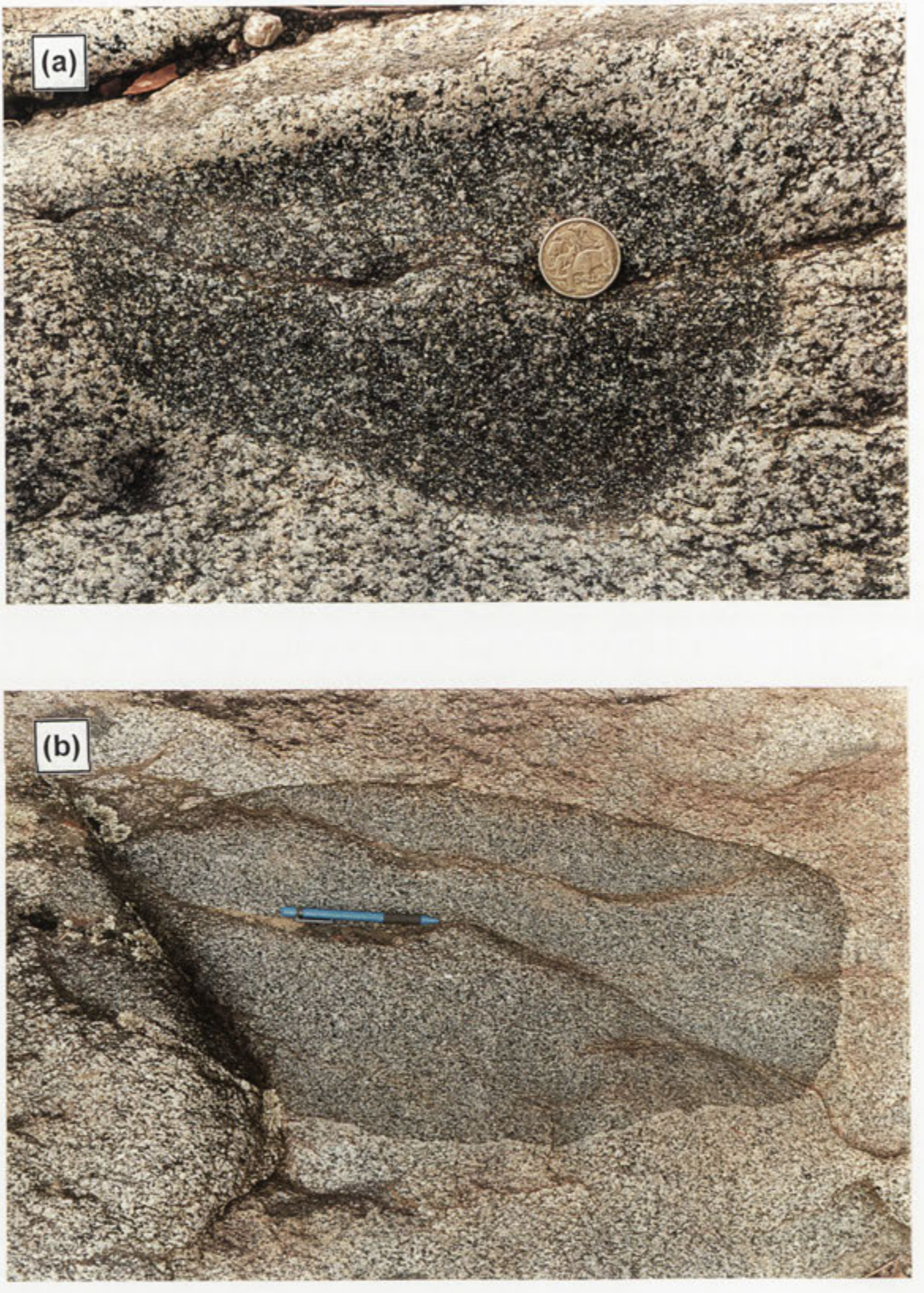

Figure 10.5. Mafic microgranular enclaves in the Snake River Tonalite. (a) Type B enclave; note the more elliptical profile compared to that in Figure 10.4a (Wando River WD414567). (b) Larger type B enclave with sharp, vaguely scalloped margins (Wando River, WD414561).

Figure 10.5 contd. Mafic microgranular enclaves in the Snake River Tonalite. (c) Type C enclave; characteristic doleritic appearance and small plagioclase phenocrysts are conspicuous (Wando River WD415570). (d) Thin section view of type C enclave **97-159E**, showing euhedral, blocky plagioclase phenocrysts dispersed through a hornblende- and biotite-rich groundmass (crossed polars, field of view ~8.1 mm).

10.2.3 Quartz diorite

(a) Field relations and lithology

A mafic dioritic dyke is exposed in the Wando River south of the Wando Tonalite, and traced southeast to Elbow Creek (Figure 10.1), from where a sample was analysed by Turner *et al.* (1993a). The dyke tapers out further south and does not outcrop northwest along strike in Boundary Creek, indicating a curved, lenticular geometry. The thickest portion of the dyke, exposed in Elbow Creek, is crowded with mafic microgranular enclaves.

The dyke is lithologically variable along its length, from quartz diorite in the Wando River to diorite and tonalite in Elbow Creek (Table 10.5). Unlike other Wando type rocks, magnetite is absent and biotite is an unusual orange-brown colour in thin section. The dyke is ~5 m wide in the Wando River but has thinner offshoots (~1 m) that exhibit a complex *lit-par-lit* relationship with diopsidic calc-silicates, blocks of which are engulfed by the dyke material. Two kilometres southeast in Elbow Creek, a 350 m long segment of the dyke (5-10 m thick) intrudes quartzofeldspathic schist, and is disrupted by minor faults. The northernmost 50 m of this outcrop area is very heterogeneous, consisting of quartz diorite (e.g. **97-206E** in Table 10.5) choked with large mafic enclaves that locally comprise up to 80% of the outcrop. Enclaves are concentrated in this section of the dyke, and rapidly diminish in abundance southwards. Surprisingly, lithological variation within the host is minimal at this locality, though slightly more mafic samples containing a higher proportion of biotite occur (see Table 10.1).

Immediately south of the enclave swarm the quartz diorite is complexly interspersed with more felsic tonalitic material (**97-208**), which becomes predominant southwards. The tonalite in turn encloses lenticular domains of distinctive plagioclase-rich diorite (**98-124**), which are sporadically encountered for about 25 m along Elbow Creek. The dyke outcrops for another 100 m south along Elbow Creek and is intersected by a gully a further 500 m southeastwards along strike. Here the dyke intrudes the Snake River Tonalite-quartzofeldspathic schist contact, but is only ~3 m wide and tapers out further south.

(b) Enclaves

On outcrop surfaces, mafic enclaves in the central part of the dioritic dyke have globular, elongate teardrop or irregular amoeboid shaped profiles (to ~60 cm) occasionally forming larger pillow-like bodies (to 1.5 m) (Figure 10.6). These morphologies, together with the sharp cuspate or (more rarely) crenulate margins of many enclaves, suggest that they were incorporated by mingling between the host diorite and a coeval, more mafic magma, with which there was a temperature, compositional or rheological contrast (Barbarin & Didier 1991). Temperature discordance between enclave and host is suggested by the finer grained hornblende-rich rims (1-5 mm) of many enclaves (e.g. Figure 10.6b, c), consistent with rapid crystallisation or chilling (Wiebe 1991). Slivers of these rims are spalled off in places, forming clotty aggregates of polygonal hornblende grains in the diorite. Some enclaves also have angular, shard-like outlines (Figure 10.6b), which are produced during dismemberment of syn-plutonic mafic dykes (Pitcher 1991), or fracturing of closely-packed, chilled mafic pillows

Sample	*Locality*	*Summary Petrographic description*
Quartz Diorite 97-440	Wando River	Dark grey, fine to medium grained with a strong continuous foliation of abundant tiny biotite flakes (also smeared lenticular aggregates) and an intense linear fabric (S_2) of aligned needles (0.5-1 mm) or larger prisms of hornblende (2-4 mm). Plagioclase phenocrysts (to 6 mm) have chalky-white cores and are aligned with the planar fabric. Smaller granules of grey plagioclase occur in the groundmass (0.5-1 mm) with bluish quartz grains. Hosts small dark enclaves (2-3 cm) that are essentially hornblende.
Quartz Diorite 97-206E	Elbow Creek	Grey coloured, homogeneous, medium grained rock with a strong lineation of hornblende prisms (~1.5 mm, up to 6 mm) and yellowish-brown epidote spindles, and a weak foliation of flakes (0.5 mm) or interleaved aggregates of biotite (orange-brown in thin section). Foliation surfaces are also lined by distorted biotite plates (up to 4 mm), that are smeared parallel to the lineation and enclose small plagioclase and quartz grains. Hornblende is ragged in thin section with brownish, finely striated cores overgrown by light blue-green rims; larger prisms enclose irregularly-shaped plagioclase inclusions and are replaced by tiny biotite blades along cracks and cleavages. Greenish, weakly aligned plagioclase laths (1-2mm) are conspicuous, with strong oscillatory and continuous zoning and irregular sodic mantles. Cores (euhedral to anhedral) are extensively replaced by sericite, but, apart from kinked twin planes in some grains, deformation features are minor. Abundant polygonal granules (0.6 mm) or aggregates (~1 mm) of quartz are interstitial to plagioclase and hornblende, whereas titanite blebs (associated with biotite) are a common accessory.
Tonalite 97-208	Southern Elbow Creek	Lighter bluish-grey coloured but texturally similar to **97-206E**, with aligned biotite plates (0.5-1 mm) imparting a distinct foliation, and subordinate prisms (~2 mm, up to 6 mm) and clots of hornblende defining a strong lineation, parallelled by epidote. Plagioclase occurs as small blocky laths and is accompanied by conspicuous cloudy quartz grains (~1 mm). Unlike the quartz diorites, hornblende occurs most commonly as large single prisms rather than disseminated small grains. Replacement by biotite is more advanced. Small hornblende-rich enclaves are rare.
Diorite (plag-rich) **98-124**	Southern Elbow Creek	Medium grained, dominated by blocky, pale olive green plagioclase laths (~1-2 mm) and hornblende prisms (up to 4 mm), the latter also forming clumps of several intergrown grains. In thin section, plagioclase has thick sodic rims about euhedral cores, resulting in irregular boundaries against adjacent minerals, whereas larger laths have vivid oscillatory zoning. Plagioclase sometimes exhibits crystal faces where projecting into hornblende, though the converse relationship is more common. Large subhedral hornblende grains (α=pale yellow, β=brown-green, γ=grassy green) are randomly disposed, with distinct striated and opaque-dusted cores. Smaller euhedral hornblende grains (0.5-0.8 mm) define a lineation, augmented by epidote needles. Biotite is interstitial and less abundant than in diorites, and hence no planar fabric is discernible. Although the rock is considerably lighter coloured than diorites, quartz is rare and the felsic aspect is imparted by more abundant plagioclase. Several large titanite grains (~1 mm) are also encountered.
Mafic enclave 97-206C	Elbow Creek	Fine grained, darkest grey, and dominated by hornblende, either as discrete needly crystals (0.5-1 mm), clots of small grains (2-3 mm, with biotite), or larger, randomly oriented prisms (to ~5 mm). As with the host, hornblende has finely striated brownish cores in thin section, overgrown by lighter rims. Plagioclase laths (~0.6-0.8 mm) are anhedral against hornblende and continuously zoned outwards from euhedral cores. Rare larger phenocrysts (1-1.5 mm) also have euhedral cores overgrown by thick, continuously zoned rims, the interface mantled by tiny hornblende crystals. Aligned hornblende needles impart a strong lineation, whereas a moderate foliation is defined by disseminated biotite flakes (~0.5 mm), and continuous with S_2 in the host. Foliation surfaces are also lined by ragged orange-brown biotite plates (~2-4 mm) that enclose numerous plagioclase, quartz and tiny titanite inclusions. Quartz otherwise forms small polygonal aggregates (~0.5 mm) though larger grains occur in other enclaves.

Table 10.5. Summary description of lithological variants and a mafic microgranular enclave within the composite dioritic dyke of the Wando River-Elbow Creek. Modal analyses are quoted in Table 10.1.

while the granitic host remained partially liquid (Wiebe 1991). Elsewhere, large enclaves are intimately veined and partially fragmented by flame-like intrusions of the host (Figure 10.6d); surrounding clusters of smaller, irregularly shaped enclaves may have been derived by this process. Enclaves towards the margins of the dyke become progressively flattened and attenuated as the S_2 fabric of the host intensifies.

Despite the variation in shape, enclaves are lithologically fairly uniform and resemble 'type A' enclaves of the Wando and Snake River tonalites (Table 10.5, sample **97-206C**). Strikingly poikilitic biotite flakes are conspicuous in some samples, whereas others have a more conspicuous 'clotted' aspect, containing abundant lenticular aggregates of tiny hornblende grains.

10.3 Deep Creek type

Two plutons of this type are recognised, the Deep Creek and Torah Granodiorites of the Wando Vale district. Both are thermally discordant and impose weak contact metamorphism on adjacent metasedimentary rocks (Anderson 1990; Kemp *et al.* 2001), unlike other early syn-compressional granitic bodies. Although petrographically unremarkable, Deep Creek types have distinctive chemical characteristics (high Al_2O_3, Na_2O and Sr, with low TiO_2) that warrant treatment as a separate magma type.

10.3.1 Deep Creek Granodiorite

The Deep Creek Granodiorite corresponds to part of the 'Wando Granodiorite' of Wells (1956), Foden *et al.* (1990) and Turner *et al.* (1993a) and was defined by Anderson (1990). Prominent outcrops in the vicinity of Deep Creek are reconciled as a teardrop-shaped pluton by Anderson & Gray (1990), with an intrusive contact with calcareous metasedimentary rocks recognised in Deep Creek (Figure 10.1). Exposures in the centre of the body are rather felsic, medium grained and exhibit unrecrystallised igneous textures. Large, poikilitic alkali feldspar crystals enclosing plagioclase and biotite are characteristic, while hornblende and small biotite-rich enclaves are rare. Turner *et al.* (1993a) report the composition of plagioclase (An_{30-37}) and biotite (Mg# 0.46).

Deformation features increase towards the pluton peripheries, with development of a weak biotite-defined S_2 foliation. A sample from near the western margin (**97-DC***) is dominated by blocky plagioclase, with a reduced amount of interstitial microcline and quartz. Secondary muscovite flakes are conspicuous.

10.3.2 Torah Granodiorite

The Torah Granodiorite (Anderson 1990) forms a small homogeneous expanse southwest of Boundary Creek, with exposure in the Wando River and Beauty Creek. The northern contact is with greenschist facies metasedimentary rocks, while the southern boundary is not exposed. Specimens are fine to medium grained, with a strong biotite-defined gneissic fabric (S_2) that becomes slightly more intense towards the northern border. Here, foliation planes are lined by ragged secondary muscovite and parallelled by smeared quartz masses and plagioclase augen. The overall fine grainsize is attributed to metamorphic recrystallisation (Anderson & Gray

Figure 10.6. Magma mingling in a quartz diorite dyke of Elbow Creek. (a) Dioritic outcrop (collage of two photos) choked with globules and pillows of mafic material. The irregular, crenulate margins on the latter suggest introduction by syn-magmatic mingling. (b) Mafic enclaves exhibiting both pillow-like and angular morphologies. Note the fine grained rim around the body beneath the lens cap (WD411545).

Figure 10.6 contd. Magma mingling in a quartz diorite dyke of Elbow Creek. (c) Small mafic enclave with a conspicuous fine grained rim; in thin section this is dominated by tiny polygonal hornblende grains. Needle-like hornblende prisms are evident in the host. (d) Large pillow-like mafic enclaves in an arrested state of partial disaggregation. This may be responsible for the abundant, small, angular enclaves in the outcrop (WD411545).

1994). Relative to the Deep Creek Granodiorite, this phase contains less alkali feldspar (Anderson 1990). Titanite and magnetite are prominent accessories, and enclaves are absent.

10.4 Wennicott type

Granitic rocks of Wennicott type comprise two tonalitic plutons exposed along Wennicott Creek west of Coleraine, the Warradale and Wennicott Tonalites, and the more intensely foliated Meissen Granodiorite of the Wando Vale district (see Figure 4.1). Also included are the gneissic tonalite enclaves of the Carrigeen Granodiorite (section 6.4.1b), which have similar geochemistry to the Wennicott Tonalite (Appendix G). Like Wando types, lower silica Wennicott types are hornblende-rich and contain numerous mafic microgranular enclaves. However, Wennicott type plutons lack magnetite, indicating lower magmatic oxygen fugacity or a relatively 'reduced' character, and are not associated with positive aeromagnetic anomalies (Kemp *et al.* 2001). The two magma types are also distinguished geochemically, such that Wennicott type rocks evolve to lower K_2O, contrasting with the steeply increasing K_2O content of Wando types (section 15.3.2). The modes of Wennicott type granitic rocks are given by Table 10.6 and depicted in Figure 10.2.

10.4.1 Wennicott Tonalite

(a) Field relations and lithology

Wennicott Tonalite (Bushell 1996) is poorly exposed for ~3 km along northern Wennicott Creek, where it borders migmatite zone metasedimentary rocks to the west and a garnet adamellite sheet to the south, becoming overlain further north by Jurassic trachyte (see Figure 4.1). Samples are bluish-grey, medium to coarse grained and dominated by interlocking, weakly strained plagioclase laths and quartz (e.g. **97-227B***; Figure 10.7a). Plagioclase is occasionally oriented parallel to aligned interstitial flakes and interleaved aggregates of darkest brown biotite (S_2). Some Wennicott Tonalite outcrops are crosscut by thin (2-50 cm) high strain zones, where the tonalite is gneissic and mafic microgranular enclaves are highly attenuated.

Notably, texturally-similar leucotonalitic sheets are interlayered with the metasedimentary sequence south of the pluton, one of which was analysed by Bushell (1996)

(b) Enclaves

Occasionally, Wennicott Tonalite contains blocky amphibolitic enclaves (e.g. **97-227A**; Table 10.7), though most enclaves are fine to medium grained microgranular types (up to 40 cm long) with plagioclase phenocrysts. These are more abundant throughout the Warradale Tonalite (see below). Rafts of migmatitic gneiss (0.5-5 m wide) also occur near the western boundary of Wennicott Tonalite with metasedimentary rocks, increasing in size and frequency towards the contact. These are partially prised apart by veins of the host tonalite, itself becoming quite heterogeneous, with micaceous clots and diffuse biotite schlieren of metasedimentary derivation.

Lithology	*Sample number*	*Grid reference*	*Modal Percentage*						*Accessory Minerals*
		(WD)	Quartz	Plagioclase	K-Feldspar	Biotite	Hornblende	Epidote	
Wennicott Tonalite	**97-227B**	523466	31.3	54.6	0	13.9	0	0.1	a, o
MME	**97-227A**	523466	19.6	42.0	0.2	21.6	15.9	0	a, o, t
Warradale Tonalite	**97-WA1**	514430	19.3	37.9	3.7	14.8	21.5	0.4	a, c, t (1.0%)
	97-WA2	514420	21.3	48.6	0	18.0	8.0	0.5	a, all, c, ca, o, t
	97-WA3	514420	17.8	48.1	0.4	13.9	17.1	0.1	a, c (1.2%), o, t
MME	**98-WAE1**	514410	6.0	41.6	0	13.8	37.3	0	a, c
	98-WAE3	514420	1.2	35.7	0	10.8	51.7	0	a, all, c, t
	98-WAE-N	514430	2.8	41.2	0	16.1	38.8	0.2	a, c, o, t
Meissen Granodiorite	**97-214**	431541	26	56	9	6	3	<1	a, o, t, z

Table 10.6. Mineralogy of Wennicott type granitic rocks of the Glenelg River Complex, determined by thin section point count (2500 points). Meissen Granodiorite modes are as quoted by Anderson & Gray (1994).

Abbreviations are: a = apatite, all = allanite, c = chlorite, ca = carbonate, o = opaque mineral, t = titanite, z = zircon.

Figure 10.7. Wennicott type rocks in thin section (crossed polars, field of view ~8.1 mm). (a) Wennicott Tonalite **97-227B**. Distorted plagioclase twin planes (centre) reflect D_2 deformation. (b) Warradale Tonalite **97-WA1**, with large hornblende prisms and weakly zoned plagioclase laths.

Sample	*Summary Petrographic description*
97-227A	Tabular amphibolitic enclave (1x3 m) that is weakly porphyritic, with hornblende prisms (2-5 mm) and chalky plagioclase phenocrysts (~3 mm) set in a fine grained, dark grey groundmass. A linear fabric of oriented hornblende needles and elongate biotite flakes is conspicuous, with a weak biotite foliation. Small hornblendic clots (~0.5 mm) are also smeared parallel to the lineation. The groundmass comprises sub-equal biotite (~0.5 mm) and hornblende in a polygonal mosaic of unstrained, weakly zoned plagioclase (~An_{41}) and quartz.
98-WAE3	Darkest grey, dominated by fine-medium grained hornblende with prominent rectangular plagioclase phenocrysts (1.5-4 mm). A 'doleritic' or ophitic texture is evident in thin section, such that interlocking matrix plagioclase laths (0.8-1 mm; An_{37-40}, subhedral-euhedral) project into, and are enclosed by, anhedral masses of hornblende (~1-1.5 mm, rarely to 3 mm). Hornblende also encloses euhedral biotite grains, and forms closely packed ovoid aggregates (4-10 cm across) with interstitial quartz. Within these aggregates, areas of intimately intergrown quartz and hornblende grains occur that possibly represent replaced clinopyroxene. Plagioclase phenocrysts enclose small crystals of biotite and hornblende and exhibit complexly mottled continuous zoning characteristics. They exhibit crystal faces against hornblende but are embayed by groundmass plagioclase laths. Scattered subhedral biotite flakes (~0.5 mm) are intergrown with, and enveloped by hornblende and partially enclose matrix plagioclase. Quartz granules are rare, and interstitial titanite blebs are the most common accessory, with rarer epidote and allanite (collected from a 15 cm long elliptical enclave).
98-WAE1	Most common enclave variety, slightly coarser grained and more felsic than **98-WAE3**. Has abundant rectangular plagioclase crystals (1-3 mm, up to 6 mm) dispersed through a hornblende-dominated matrix (1-3 mm grains). Plagioclase grains are aligned subparallel to the enclave margin, which has a diffuse contact with the host. The thin section texture resembles that of **98-WAE3**, except that granules of quartz (0.6-1 mm) with re-entrants against plagioclase are conspicuous, and biotite is slightly more abundant. Hornblende forms large quartz-sieved masses, also occuring as clumps (3-4 mm across), that enclose or partially enclose plagioclase laths (ophitic to subophitic texture). Titanite grains are an accessory. Also interspersed are felsic domains (up to 8 cm long, 1-2 cm wide) richer in coarse plagioclase and subhedral hornblende prisms (~3-5 mm long). These areas are gradational with the more mafic enclave material and resemble the host tonalite (collected from an 80 cm long elliptical body).
97-WAN	Medium to coarse grained textural variant of **98-WAE1**, where hornblende grains (0.5-3.5 mm) have a greater propensity to form aggregates (~5 mm), and many have lighter coloured, rectangular-shaped cores perforated with tiny quartz grains. Small clinopyroxene blebs occupy these core areas, and rarely relict euhedral clinopyroxene prisms, partly replaced by pale amphibole, occur inside an overgrowth of dark green-brown hornblende. Quartz is rare and interstitial (from a 10 cm long ovoid enclave).
98-WAE2	Uniformly medium grained, dark greenish-grey. Is slightly finer grained relative to **98-WAE1** and lacks plagioclase phenocrysts, being composed predominantly of stubby hornblende prisms. Plagioclase has much lower abundance than in other enclaves and biotite is rare, though quartz granules are more conspicuous. As with other enclaves, plagioclase laths are enclosed by, and euhedral against, hornblende (from a 2 m long tabular enclave).

Table 10.7. Summary petrographic descriptions of mafic microgranular enclaves in Wennicott type granitic rocks (plagioclase compositions are determined optically). All are from the Warradale Tonalite except for **97-227A**, collected from the Wennicott Tonalite. Modal analyses of all samples are in Table 10.6, with the geochemistry presented in Appendix G. Note that hornblende and biotite pleochroic schemes are the same as those of the host.

10.4.2 Warradale Tonalite

(a) Field relations and lithology

Warradale Tonalite outcrops prominently for about 500 m along the slopes of Wennicott Creek 3.4 km south of Wennicott Tonalite (Figure 4.1). Exposures abruptly cease to the north and south, although apparently *in situ* slabs of laminated quartzofeldspathic schist at the margins suggest enclosure by metasedimentary rocks. An S_2-aligned schist enclave near the southern Warradale Tonalite margin contains F_2 structures, which, together with the weak deformation features throughout the pluton, indicates emplacement in the latter stages of D_2.

Typical Warradale Tonalite specimens (e.g. **97-WA1***) are dark blue-grey, medium to coarse grained and equigranular, comprising weakly zoned plagioclase laths, hornblende-biotite aggregates and clots of interleaved biotite (always interstitial to plagioclase), with lesser quartz and interstitial alkali feldspar (Figure 10.7b). Single hornblende prisms (to 7 mm, deep blue-green) are abundant, some having lighter coloured actinolitic cores with vaguely rectangular outlines that are densely perforated with quartz blebs. Allanite spindles are a prominent accessory. The rock has a weak (but pervasive) foliation, defined principally by biotite clots and hornblende-biotite aggregates, whereas oriented hornblende and plagioclase prisms impart a distinct lineation. These fabrics parallel D_2 structures in adjacent metasedimentary rocks and were tectonically imposed. Thin (2-10 cm), strongly foliated D_2 high strain zones also occur.

A moderate degree of petrographic heterogeneity is also evident within the Warradale Tonalite (Table 10.6). Samples from the northern part of the body are slightly more mafic (e.g. **97-WA3**), with a higher proportion of hornblende-biotite clots and less quartz. In contrast, several outcrops towards the centre of the pluton are finer grained and richer in biotite and quartz, imparting a 'sugary' aspect (e.g. **97-WA2***). Large, strikingly poikilitic biotite plates are conspicuous, enclosing numerous plagioclase crystals, but alkali feldspar is absent. These felsic exposures are gradational with the predominant 'typical' Warradale Tonalite.

(b) Enclaves

Mafic enclaves are conspicuous throughout the Warradale Tonalite and range from 2 cm to 2.5 m in length. They are either elliptical or tabular, being typically elongate parallel to S_2 in the host, and medium to coarse grained. The smallest enclaves are mafic clots dominated by hornblende aggregates (up to 80%), with minor interstitial quartz (Figure 10.8a). However most are composed of different proportions of hornblende and plagioclase, with minor, but variable amounts of biotite and quartz (Figure 10.8b). Four enclaves from various parts of the Warradale Tonalite, encompassing the spectrum of textural and compositional variation, were collected for petrographic and geochemical analysis (Table 10.7). All have intact magmatic textures, most apparent with the development of an ophitic or 'doleritic' fabric (Figure 10.9a), and are igneous rocks.

Significant differences are recognised between mafic enclaves of the Warradale Tonalite with the more varied population hosted by Wando type tonalites (Table 10.8). The contrasting grainsize is particularly striking, and might reflect recrystallisation of Wando type enclaves

during intense deformation, according with the more strained character of the host tonalite. Other textural differences are more difficult to evaluate. The 'doleritic' texture of Warradale enclaves suggests that plagioclase was early crystallising, subsequently enveloped by hornblende, which also postdates biotite. However, hornblende in Wando type enclaves is euhedral against plagioclase and enclosed by biotite, suggesting either a fundamentally different crystallisation sequence (i.e. hornblende-plagioclase-biotite) or modification of igneous grain boundary relationships by metamorphic recrystallisation. Nevertheless, it is worth noting that poikilitic biotite characterises dioritic rocks of the Caupaul Igneous Complex, and is conspicuous even in the most deformed variants (section 13.5).

Feature	*Wando type*	*Warradale Tonalite*
Appearance	Fine to medium grained, intensely foliated, strongly porphyritic, conspicuous 'clotted' aspect.	Medium to coarse grained, massive or weakly foliated uniform-textured. Overall distinct 'gabbroic' appearance.
Microfabric	Hornblende is euhedral against plagioclase, occurring as large prisms, or smaller sub-hedral blades interlocking with plagioclase.	Consistently exhibit an igneous ophitic or subophitic ('doleritic') texture, where hornblende encloses, or partially encloses, euhedral plagioclase laths.
	Biotite is poikilitic and encloses, or partially replaces, hornblende prisms.	Biotite is euhedral against, and enveloped by, hornblende.
	Titanite forms euhedral rhombs.	Titanite forms irregular interstitial blebs to plagioclase.
Mineralogy	Interstitial quartz is common.	Quartz is rare, mainly as inclusions in hornblende.
	Magnetite abundant, sulphides rare.	Contain pyrite and chalcopyrite, no magnetite.
	Clinopyroxene absent.	Clinopyroxene relicts common.

Table 10.8. Comparison between mafic microgranular enclaves of the Warradale Tonalite with those of Wando type rocks.

Similarly, it is unclear whether the absence of clinopyroxene in Wando Tonalite magmas is a primary compositional attribute or due to complete recrystallisation to hornblende. In the case of the Warradale enclaves however, persistence of clinopyroxene implies that it was a significant original ingredient of the enclave magmas, subsequently mantled and ultimately replaced by magmatic hornblende (Figure 10.9b). This process releases silica, as hornblende is silica-poor compared to clinopyroxene, accounting for the quartz-perforated central regions of many hornblende prisms. The actinolitic amphibole in the centre of hornblende grains might reflect localised enhancement of silica activity around the original pyroxene, as described in tonalitic rocks of the French Pyrenees (Roberts *et al.* 2000). Since this feature is conspicuous in the

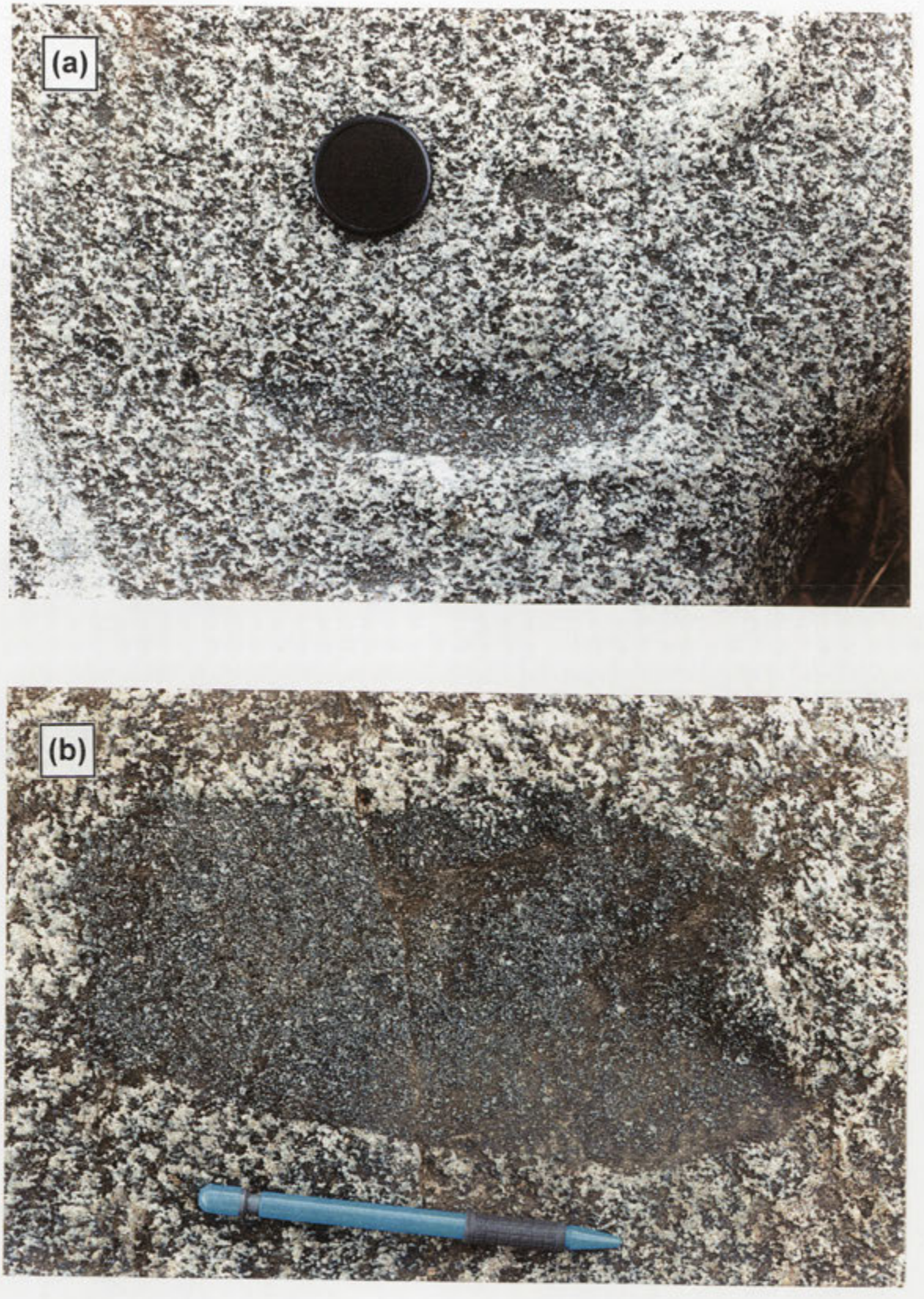

Figure 10.8. Mafic enclaves in the Warradale Tonalite. (a) Elongate, medium grained hornblende-plagioclase enclave that is texturally similar to the host, together with a smaller, hornblende-dominated mafic clot (right of lens cap). Centimetre-sized hornblende aggregates are also visible in the tonalite. (b). Larger, finer-grained enclave, containing plagioclase and hornblende phenocrysts in a hornblende-rich groundmass.

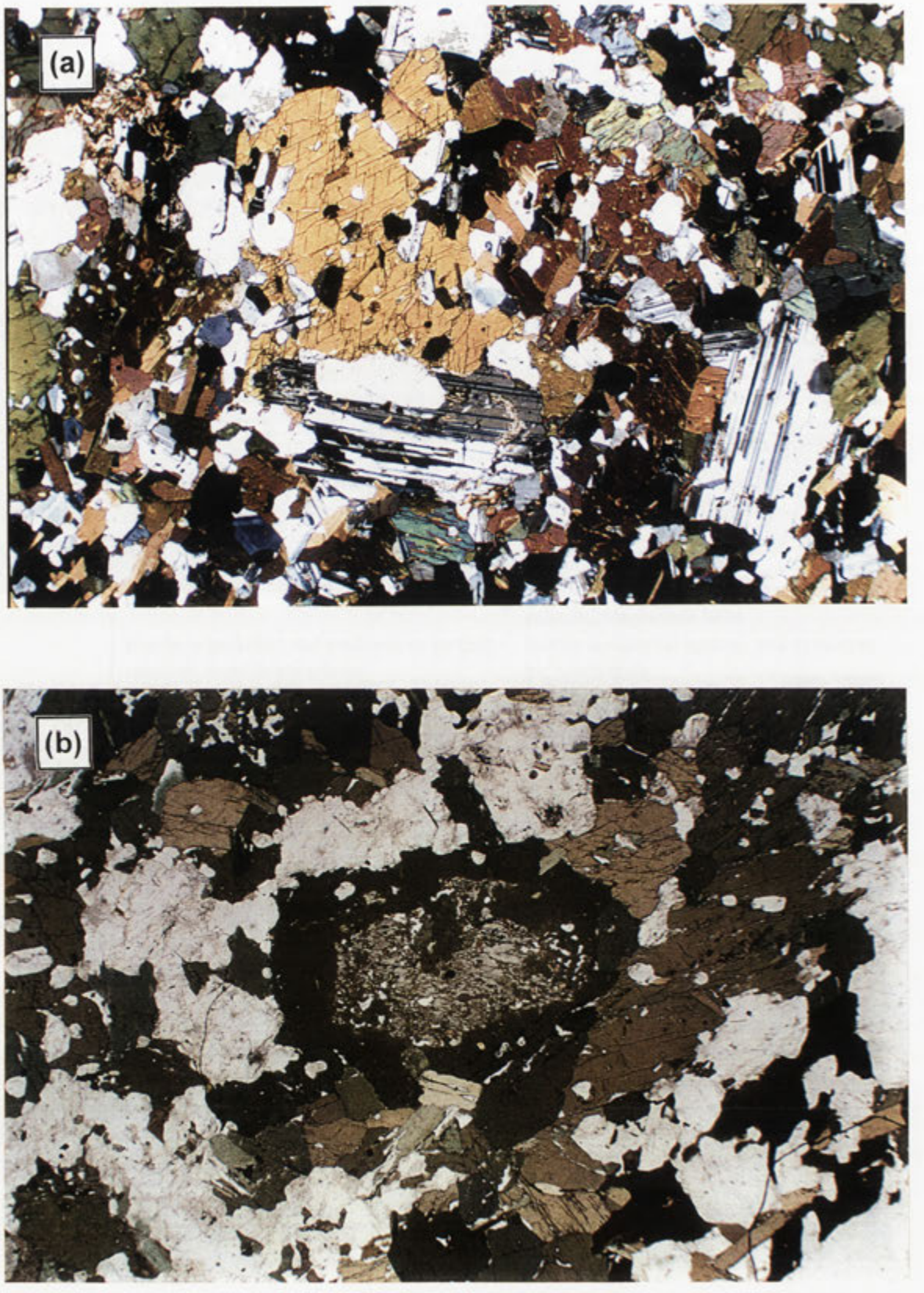

Figure 10.9. Warradale Tonalite enclaves in thin section (field of view ~8.1 mm). (a) Doleritic or subophitic texture in enclave **98-WAE3**, whereby poikilitic hornblende masses partially enclose euhedral plagioclase laths. Note also the plagioclase phenocrysts (crossed polars). (b) Relict blocky clinopyroxene phenocryst in sample **97-WAN**, mantled by hornblende (plane polarised light).

Warradale Tonalite itself, the former presence of clinopyroxene is implicit here also. The occurrence of magnetite in Wando type enclaves, as opposed to its absence in Warradale Tonalite enclaves, could reflect oxidation state differences.

10.4.3 Meissen Granodiorite

(a) Field relations

The lens-shaped Meissen Granodiorite (Anderson 1990) extends northwest from Elbow Creek to tributaries northwest of the Wando River (Figure 10.1). The body intrudes Snake River Tonalite, but is crosscut by the Blair Atholl Adamellite and the Cloven Hills Granodiorite. Towards the former, the Meissen Granodiorite becomes highly strained, with intensification of the foliation, flattening of microgranular enclaves and the occurrence of thin shear zones (2-5 cm wide). These features reflect partitioning of ductile D_2 shear strain towards the boundary with the quartz-rich Blair Atholl Adamellite, where a contrast in mechanical competency is expected. The Meissen Granodiorite pluton tapers south of Elbow Creek, being only 100 m wide in Robertson creek, where it is enclosed by calc-silicate. A 500 m tract of foliated but deeply weathered granitic material further along this watercourse is also tentatively correlated with Meissen Granodiorite.

Despite geographical proximity to Wando type plutons, the low K_2O character of the Meissen Granodiorite clearly indicates affinity with Wennicott type granitic rocks (section 15.3.2).

(b) Lithology

Weathered Meissen Granodiorite surfaces are orange-cream and have conspicuous quartz grains, facilitating distinction from the Snake River Tonalite. Fresh specimens are a distinctive bluish-grey colour, medium to coarse grained and dominated by plagioclase, with a pervasive biotite foliation (S_2). Hornblende prisms and biotite-hornblende clots are conspicuous, but much less abundant than in the Warradale Tonalite (Table 10.6). Light grey microgranular enclaves (to 20 cm long), foliated and flattened parallel to S_2, are uncommon, and hornblende-rich varieties like those of the Warradale Tonalite are occasionally encountered.

Meissen Granodiorite pavements in the Wando River contain numerous sheets of aplite, microgranite and garnetiferous pegmatite (to 1.5 m thick). Pegmatitic dykes are internally deformed, with smeared alkali feldspar megacrysts in a garnet-bearing quartzofeldspathic matrix. Dykes are mostly parallel to the gneissic foliation in the host, but where oblique, manifest the S_2 fabric as an intense fracture cleavage. Undeformed aplite and microgranitic dykes are common near the boundary with Cloven Hills Granodiorite.

Chapter 11: Occurrence and petrology of granitic rocks of the GRC

Part (B) Late syn-compressional phases

11.1 Introduction

Plutons of the late syn-compressional association, which lack pervasive tectonic mineral alignments, are widespread across the GRC and encompass the Tuloona, Loftus Creek, Kassingbrook and Harrow magma types (Table 4.1). Of these, this chapter documents the critical field relations and petrographic character of the extensive Tuloona and Loftus Creek magma types. Complete petrographic descriptions of type specimens and important variants (sample numbers with asterisks) are provided in Appendix E. Felsic mineral proportions are summarised by Figure 11.1.

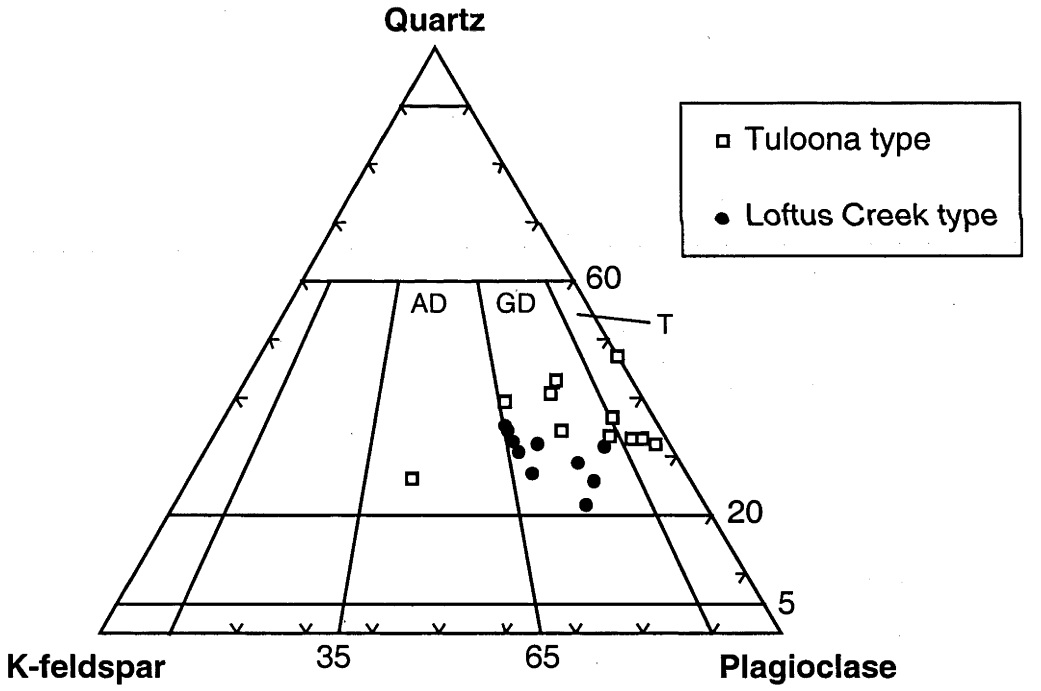

Figure 11.1. Modified Streckeisen (1976) diagram depicting the felsic modal mineralogy of plutons within the Tuloona and Loftus Creek magma types (data from Tables 11.1 and 11.3). Lithological compartments are adamellite (AD), granodiorite (GD), and tonalite (T). Note the extension to more K-feldspar-rich compositions compared to early syn-compressional types (Figure 10.2).

11.2 Tuloona type

Elongate Tuloona type plutons constitute the northwesterly-trending central granitic belt of the GRC, which separates migmatitic rocks of the southwestern metamorphic zonation from those of the northeastern zonation (Figure 4.1). All have pristine igneous textures, with dark greenish-brown biotite and strikingly poikilitic alkali feldspar (Figure 11.2a), which has variable development of microcline twinning. Plagioclase laths form intergrown clumps that exhibit strong oscillatory zoning, though irregular dissolution/resorption features are common at zone boundaries. Cores vary from euhedral to corroded, and many have complex patchy or mottled zoning. Muscovite is an accessory (primary) phase in many plutons (Table 11.1). Magnetite is abundant in more mafic samples, but hornblende occurs only rarely in enclaves. Sheaf-like aggregates of randomly disposed biotite flakes with magnetite ± muscovite (2-5 mm) are a unifying textural feature. Although not particularly abundant, mafic microgranular enclaves occur in each Tuloona type pluton, accompanied by metasedimentary enclaves in more felsic lithologies. Most Tuloona type bodies are associated with positive aeromagnetic anomalies of variable intensity, though these do not underlie all exposed areas of plutons (see Kemp *et al.* 2001).

Tuloona type rocks define reasonably coherent linear trends on geochemical variation diagrams, and compared to Loftus Creek types have slightly higher Al_2O_3 and CaO, lower Na_2O and K_2O, and markedly lower Sr (section 15.4.1).

11.2.1 Tuloona Granodiorite

(a) Field relations

The northernmost unit of the central granitic belt, the Tuloona Granodiorite is an elongate pluton aligned parallel to the regional S_2 foliation, with prominent exposure in southern Schofield Creek and the Glenelg River valley south of Harrow (Kemp 1995; Kemp & Gray 1999a; Figure 11.3). With a decline in mafic igneous enclaves, the granodiorite becomes progressively more leucocratic and muscovite-rich towards its northern periphery in Schofield Creek, ultimately being transitional to muscovite granite and migmatitic rocks of the northeastern zonation (section 6.5.3).

In the Glenelg River valley, the northern Tuloona Granodiorite margin crosscuts the migmatitic Kout Norien Granodiorite, indicating that emplacement postdated the formation of this unit. To the southwest, the Tuloona Granodiorite adjoins the Glendara Adamellite (below), but as the closest outcrops of the two plutons are ~1 km apart, intrusive relationships are unknown.

(b) Lithology

Tuloona Granodiorite exposures in Schofield Creek are medium to coarse grained and dominated by subhedral to anhedral plagioclase laths. Phenocrysts of quartz and tabular poikilitic alkali feldspar (1x3 cm) are also prominent, the latter crowded with plagioclase, quartz, biotite and muscovite crystals (e.g. **T2-135***). Disseminated biotite and subordinate muscovite flakes are non-aligned. Glenelg River valley outcrops contain a higher proportion of

Figure 11.2. Tuloona type granitic rocks. (a) Typical thin section view, showing oscillatory-zoned plagioclase laths enveloped by poikilitic alkali feldspar (crossed polars, ~8.1 mm across). (b) Slabs of mafic Coojar Granodiorite **97-297** (left) and Tuloona Granodiorite **97-299** (right). Note the large quartz grains, and lithological layering in the Tuloona Granodiorite.

Lithology	*Sample number*	*Grid reference* (WD)	*Modal Percentage*						*Accessory Minerals*
			Quartz	Plagioclase	K-Feldspar	Biotite	Muscovite	Opaque	
Tuloona Granodiorite	**T2-135**	570791	37.3	39.6	9.5	11.7	1.6	0.2	a, e
	T2-318	545798	29.4	43.4	12.4	11.8	2.6	0	a, c, z
	97-299	522842	26.1	53.3	1.6	17.1	0	0.8	a, c, e, z
mafic enclaves	**T2-135B**	570792	13.4	44.3	0	39.6	0	2.3	a
	97-294	517836	26.2	38.5	0.6	21.1	11.6	1.6	a
	97-299B	522842	34.3	46.9	0.4	16.2	0	0.8	a, c, e
Glendara Adamellite	**97-145**	478818	24.0	30.2	37.5	4.8	2.9	0.2	a, c
Mooree Granodiorite	**97-36**	478789	36.1	40.5	11.2	8.7	2.3	0.4	a, c, e
Chetwynd Tonalite	**97-53**	451673	27.2	52.0	4.1	14.8	0	1.2	a, all, c
	97-81	393694	31.9	49.9	5.3	11.9	0	0.5	a, c
Coojar Granodiorite	**97-142**	635650	34.9	35.7	18.1	8.3	2.1	0.3	a, c, e
	97-297	635656	28.4	49.7	6.8	12.2	1.0	0.8	a, e
Patawilya Tonalite	**97-382**	680531	29.0	55.5	3.2	9.2	1.2	<1	a, c (1.2%), e
mafic enclave	**97-382A**	680531	38.6	43.3	0	16.3	1.1	<1	a, e

Table 11.1. Mineralogy of Tuloona type granitic rocks of the Glenelg River Complex, determined from thin section point count (2500 pts). The felsic mineralogy for the coarse grained Glendara Adamellite was estimated by point counting a sawn rock slab.

Abbreviations are: a = apatite; all = allanite; c = chlorite; e = epidote; z = zircon.

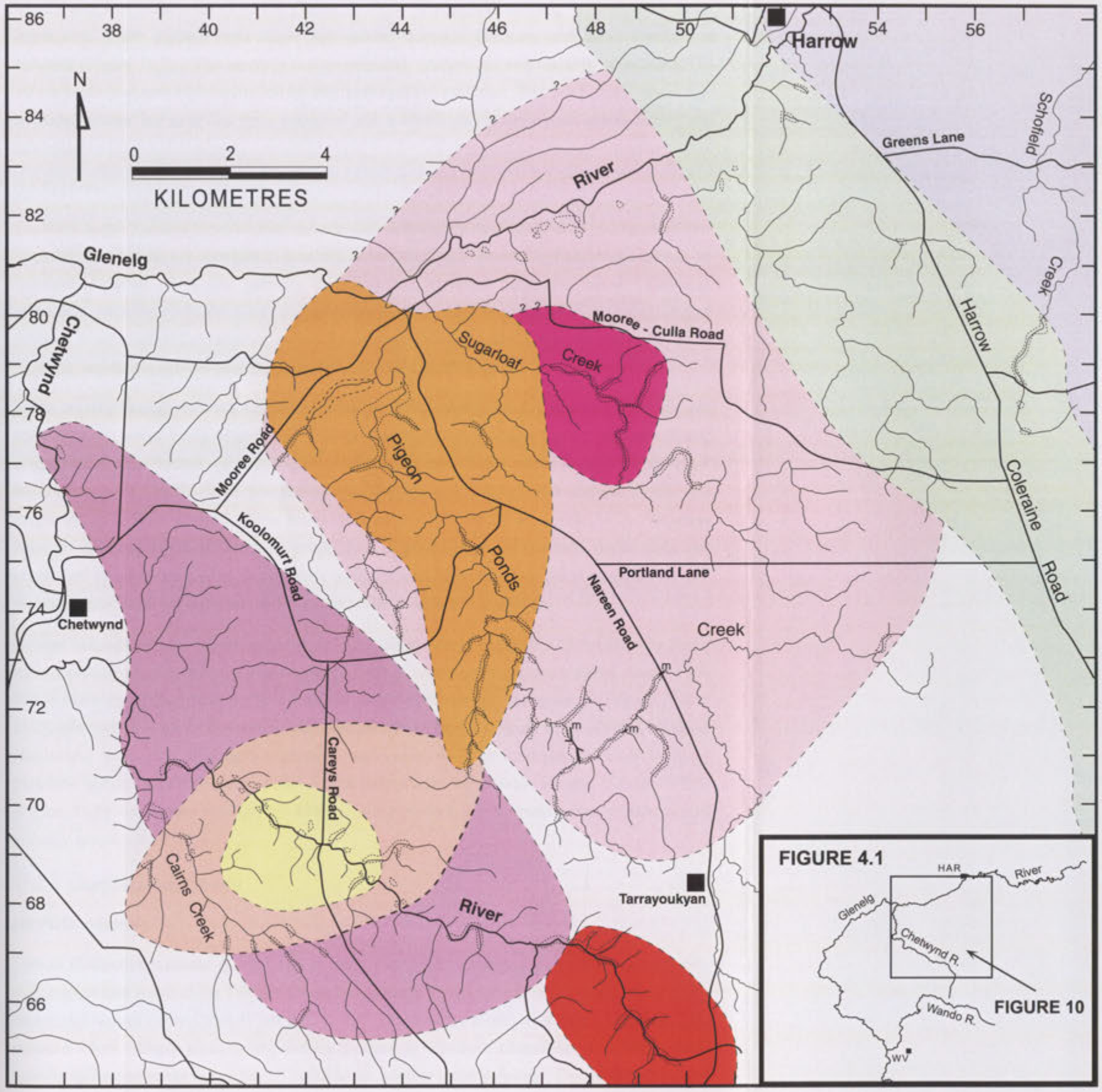

Cambro-Ordovician

- KOOLOMURT GRANODIORITE
- CAIRNS CREEK GRANODIORITE (central phase)
- CAIRNS CREEK GRANODIORITE
- GLENGOYNE ADAMELLITE
- MOOREE GRANODIORITE
- GLENDARA ADAMELLITE
- CHETWYND TONALITE
- TULOONA GRANODIORITE
- Interleaved muscovite granite/ metasedimentary rock

- Road
- Watercourse
- Prominent outcrop
- Approx. geological boundary
- ?—?—? Inferred geological boundary
- m Microgranitic dyke

Figure 11.3. Cambro-Ordovician geology of the central GRC (location indicated in the inset), showing spatial relationships between Tuloona type rocks of the central batholith and Loftus Creek type plutons.

biotite and less muscovite (**97-299**) (Table 11.1). A lithological banding is present in some exposures, where slightly more felsic and coarser domains alternate with more biotite-rich material (Figure 11.2b). The layering is discontinuous, gradational and variable in thickness (1-10 cm bands), commonly parallelled by biotite-magnetite schlieren. Thin high strain zones (<3 m wide), where the rock has finer grainsize and a biotite-secondary muscovite foliation, are attributed to D_5.

(c) Enclaves

Enclaves in the Tuloona Granodiorite include both metasedimentary and mafic igneous-textured varieties. The former are common in southern Schofield Creek, where large tapering enclaves of quartzofeldspathic schist and partially disaggregated stromatic migmatite occur. Lenticular micaceous enclaves (3-12 cm long) and schlieren (1-3 cm thick strands 10-50 cm long), in part stripped from migmatitic enclaves, define a contorted flow structure. Migmatite enclaves have F_4 folds, indicating syn- to post-D_4 emplacement of the granitic host.

Mafic microgranular enclaves are most abundant in Schofield Creek outcrops (up to six per square metre), most being ellipsoidal (5-80 cm long) or, more rarely, equant and subangular (Figure 11.4a); selvedges of non-aligned biotite (1-3 mm thick) occur around some. Most enclaves (e.g. **T2-135B**) have plagioclase phenocrysts and clots of non-aligned biotite and magnetite in a finer grained, more biotite-rich matrix (Figure 11.4a; Table 11.2). Variation between enclaves involves changing proportions of plagioclase phenocrysts, mafic clots and content of groundmass biotite. More felsic samples also have rounded quartz phenocrysts. All microgranular enclaves have interstitial or poikilitic quartz in thin section.

Similar microgranular enclaves occur in Tuloona Granodiorite exposures of the Glenelg River valley, with two important variants recognised, both of which have igneous textures. Sample **97-294** is more mafic than other enclaves and the only one to contain abundant hornblende (Table 11.2). Distinctive features are hornblende-rimmed quartz 'ocelli' (Figure 11.4b, 11.5a), elongate plagioclase laths with 'skeletal' morphology, and enclosure of groundmass minerals by large poikilitic quartz masses (Figure 11.5b), which define a 'poikilomosaic texture' (Shelley 1993) (Figure 11.5). In contrast, enclave **97-299B** is much more felsic, texturally heterogeneous and strongly porphyritic (Table 11.2).

11.2.2 Glendara Adamellite

(a) Field relations

Tors of distinctively coarse grained and strongly porphyritic granitic rock outcrop sporadically over a large area south of the Tuloona Granodiorite, most conspicuously along the Glenelg River valley and Pigeon Ponds Creek (Figure 11.3). All exposures are characterised by large, strikingly euhedral alkali feldspar phenocrysts, and are grouped as Glendara Adamellite. Abundant garnet-bearing aplite-pegmatite dykes (to 0.5 m thick) are another notable feature. Due to discontinuous outcrop and variable aeromagnetic signature, the boundaries of this body are poorly constrained and contact relationships with the surrounding Tuloona type lithologies are unclear.

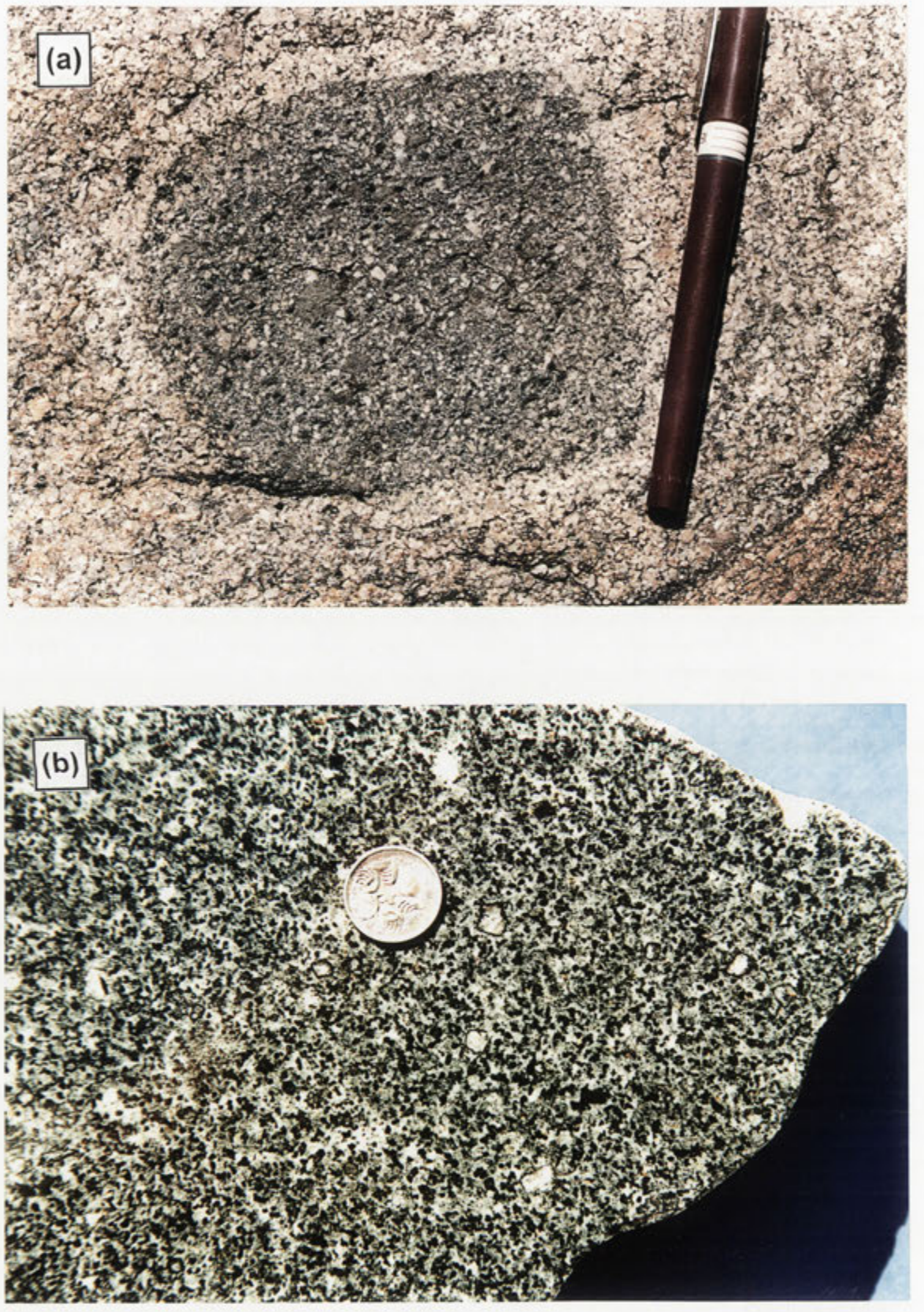

Figure 11.4. Mafic microgranular enclaves in the Tuloona Granodiorite (a) Detail of the enclave pictured in Figure 6.15. Small euhedral plagioclase phenocrysts and biotite clots are prominent features. (b) Slab of microgranular enclave **97-294**, in which hornblende-rimmed quartz ocelli and hornblende-biotite clots are conspicuous. Thin section views are shown in Figure 11.5.

Enclave sample	*Petrographic description*
T2-135B	Dark grey, with plagioclase phenocrysts and clots of non-aligned biotite-magnetite in a finer grained, more biotite-rich matrix. Plagioclase phenocrysts have ragged outlines, and, except for the euhedral cores of larger zoned grains, are densely perforated with tiny biotite and quartz blebs. The remainder of the rock comprises blocky plagioclase grains, also perforated with biotite and quartz inclusions, ragged greenish-brown biotite flakes, abundant magnetite and interstitial quartz.
97-299B	Dioritic in appearance and strongly porphyritic, with numerous rounded quartz grains (most 3-4 mm), plagioclase phenocrysts (to 5 mm) and biotite flakes (1-3 mm) in a finer grained, biotite- and magnetite-rich matrix. Elongate clots of biotite-magnetite (1-3 mm) are rarer. Quartz phenocrysts commonly have thin biotite-rich rims. Sawn slabs exhibit a heterogenous aspect, where diffuse bands of more biotite-rich character (1-2 cm wide) and felsic lenticular pockets are interspersed. In thin section, plagioclase phenocrysts have striking oscillatory zoning (collected from a 60 cm tabular enclave).
97-294	Dark bluish-grey, with prominent phenocrysts of chalky white plagioclase (~3-5 mm) and quartz ocelli (most ~2-8 mm), which are fringed by concentrations of tiny hornblende grains and rarely enclose large biotite plates (2-5 mm across). These are sparsely dispersed through an otherwise fine-medium grained, unfoliated matrix comprising small biotite plates, abundant hornblende prisms, plagioclase laths and bluish-grey quartz. Rounded clots of mafic minerals (to 8 mm) are also common (see Figure 11.4b). In thin section, plagioclase phenocrysts (An_{41}) are generally subhedral but may be sieved by tiny quartz blebs towards the rim. They enclose numerous apatite needles and have mottled continuous zoning outwards from euhedral cores; growth zones are occasionally mantled by bluish-green hornblende granules. Quartz ocelli are polycrystalline and sharply outlined by trains of tiny hornblende crystals, though occasionally they consist of a single grain that merges into groundmass quartz and encloses a rounded 'ring' of contiguous hornblende prisms (Figure 11.5a). Mafic clots comprise hornblende-magnetite concentrations, occasionally accompanied by spindly biotite. Elsewhere, biotite occurs as anhedral orange-brown plates (1-2 mm) or clumps of several grains with magnetite and rare allanite. Plagioclase phenocrysts, quartz ocelli and matrix minerals are set in a mosaic of irregularly shaped poikilitic quartz masses (to 8 mm), described as 'poikilomosaic texture' (Shelley 1993). Groundmass plagioclase laths (~0.4 mm, An_{37}) have a striking radiating arrangement within the enclosing quartz, and have very elongate, skeletal morphologies (Figure 11.5b). Collected from a ~50 cm long enclave.
97-382B	Dark blue-grey, medium grained and texturally identical to the host but with more biotite (darkest brown). Has sparse blocky plagioclase phenocrysts (~4 mm) and polycrystalline quartz (to 3.5 mm) in a slightly finer, even grained matrix. A sugary aspect is imparted by 1-2 mm plagioclase and quartz grains, unlike in other igneous enclaves where most quartz is interstitial and poikilitic. Small flakes of primary muscovite are interwoven with clotty biotite aggregates. Rare larger biotite plates (to 3 mm) also occur (~50 cm across ovoid enclave).

Table 11.2. Summary descriptions of mafic microgranular enclaves from Tuloona type granitic rocks. All are from the Tuloona Granodiorite except for **97-382B**, collected from the Patawilya Tonalite in Bryan Creek. Modal analyses of all samples are in Table 11.1.

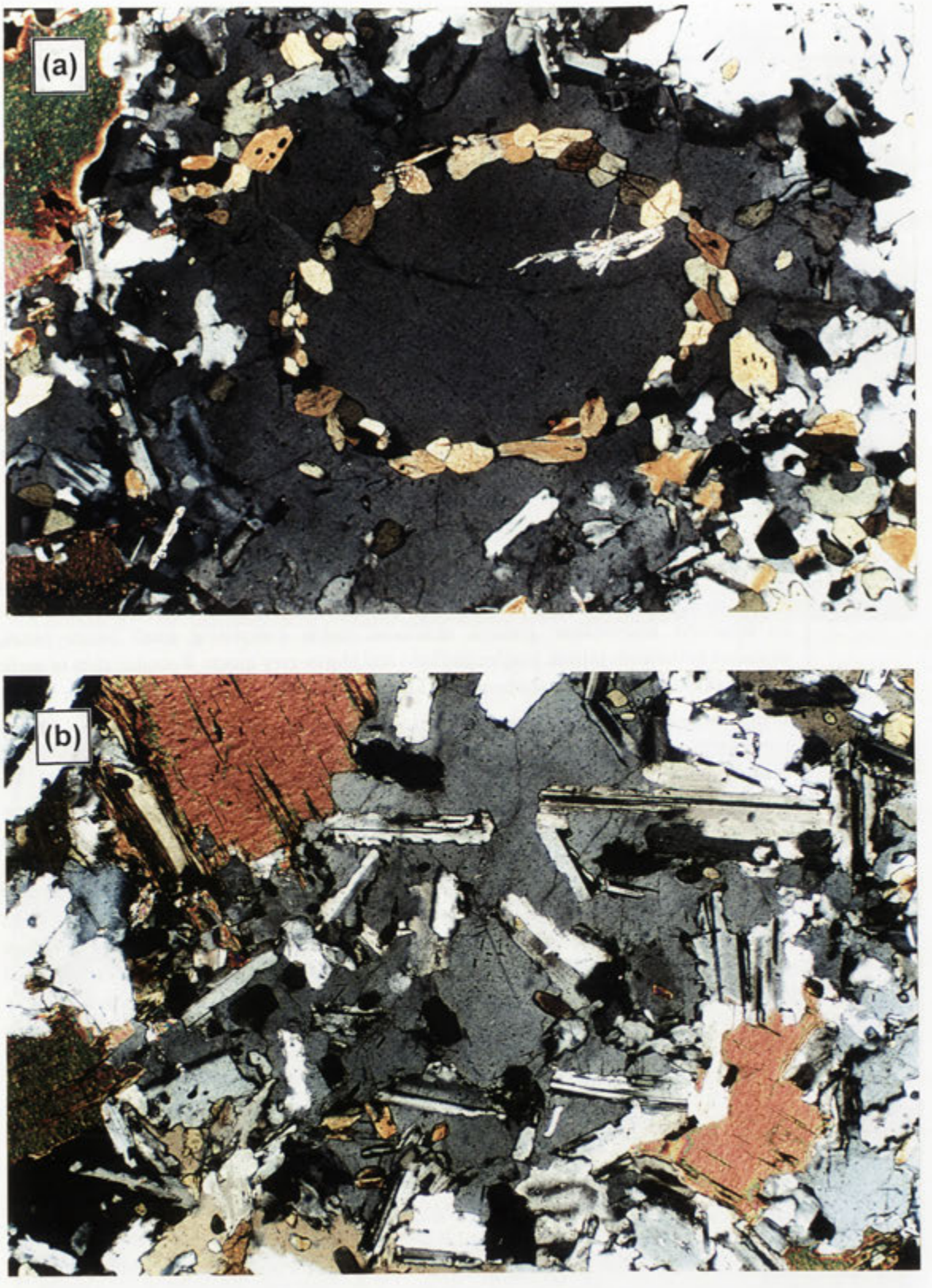

Figure 11.5. Mafic microgranular enclave **97-294** in thin section (crossed polars, field of view ~2.5 mm). (a) Quartz ocelli enclosing a ring of contiguous hornblende prisms. An interpretation of this feature is discussed in section 12.5.2. (b) Poikilitic quartz mass enveloping small hornblende prisms, biotite flakes and elongate plagioclase laths, the latter having irregular skeletal outlines. Note also the apatite needles at the centre of the photo.

However, the southwestern part of the Glendara Adamellite is clearly crosscut by the Loftus Creek type Koolomurt Granodiorite (section 11.3.4), adjacent to which felsic microgranitic dykes (10 cm to 2 m wide) are numerous. Glendara Adamellite exposures cease in Pigeon Ponds Creek near the Mooree road, though isolated outcrops further east indicate that material of this type has wide extent beneath younger cover.

(b) Lithology

At the type locality in the Glenelg River valley, alkali feldspar phenocrysts (2-6 cm long, square to tabular) define a flow foliation and are conspicuously zoned, outlined in part by concentric trails of biotite, plagioclase and quartz inclusions (**97-145***) (see Figure 11.7). Elsewhere plagioclase forms subhedral to anhedral blocky crystals, whereas quartz occurs as very large polycrystalline clumps (up to 1 cm). The rock matrix is felsic, with non-aligned muscovite and biotite, commonly interleaved in small aggregates with magnetite.

(c) Pigeon Ponds Creek exposures

Glendara Adamellite outcrops in eastern Pigeon Ponds Creek resemble those of the type locality, though deep weathering precludes geochemical comparison. However, unlike Glenelg River exposures, mafic microgranular enclaves occur (below) and the adamellite is intimately interspersed with grey microgranitic rock (Barrama Microadamellite; section 11.3.5). In places the microadamellite forms sheets (up to 15 m thick) with sharp contacts against Glendara Adamellite, but elsewhere mutually commingling relationships are observed, which suggest that interactions occurred while both lithologies were partially liquid. Intermingling is most obvious along Pigeon Ponds Creek between WD475718 and WD478710, where boundaries between the two rock types are either scalloped, mutually interfingering, or rarely gradational over about 20 cm. An indication that mixing occurred between the two magmas is provided by the sporadic occurrence of alkali feldspar phenocrysts in the microadamellite, that are clearly seen to be derived by 'digestion' of incorporated globules of Glendara Adamellite (see Figure 11.12).

Mingling also occurs further east at WD489717, where a 10 m thick microadamellite sheet engulfs blocks of partially disaggregated Glendara Adamellite, itself forming irregular protrusions into the margins of the dyke and containing microadamellite enclaves. Note that at this locality (and further west), both microadamellite and Glendara Adamellite are profusely crosscut by numerous composite aplite-pegmatite dykes (5-30 cm thick) and garnetiferous aplites (1-5 cm thick), which imparts further complexity.

Glendara Adamellite outcrops of eastern Pigeon Ponds Creek are also intruded by thin mafic dykes (5 cm-2 m wide) that contain hornblende and resemble tonalitic dykes of Chin Chap Creek (section 12.3.3). These have anastomosing and bifurcating geometries, but in places are parallel to aligned alkali feldspar phenocrysts in the host. A 30 cm thick dyke at WD484713 crosscuts the phenocryst alignment but has crenulate margins, moulded around feldspar phenocrysts, and contains irregular flame-like intrusions of host magma injected into the body of the dyke (Figure 11.6). These features are also consistent with syn-magmatic interaction.

Figure 11.6. (a) Hornblende-bearing mafic dyke crosscutting a typically porphyritic Glendara Adamellite pavement. (b) Closer view, showing injection of the host adamellite into the dyke. Note the crenulate margin of the mafic dyke, which in places appears to be moulded around feldspar phenocrysts in the host (e.g. top left) (WD484713).

(d) Enclaves

Apart from intermingled microgranitic globules, enclaves are rare within the Glendara Adamellite. Mafic microgranular types are rarely encountered in Pigeon Ponds Creek, being typically light grey elliptical objects (3-80 cm long), with small plagioclase phenocrysts set in a finer groundmass of spindly biotite, magnetite and conspicuous muscovite.

However, swarms of microgranular enclaves occur at several localities in Pigeon Ponds Creek in the southeastern part of the pluton. At WD472719, enclaves (up to 1 m long) constitute up to 50-60% of the outcrop extending for ~25 m along the creek bed. They are variously blocky or rounded (commonly elliptical) dark grey bodies, with phenocrysts of plagioclase and quartz, the latter rimmed by biotite, in a fine grained biotite-rich matrix where biotite-magnetite clots are prominent. Many enclaves also have concentric light grey haloes (1-5 cm thick) of slightly more biotite-rich character than the host (Figure 11.7). Alternatively, enclaves may be rimmed by a thick biotite selvedge (1-2 cm), the partial disaggregation of which could be responsible for the numerous biotite clots in the host at this locality. Several of the larger enclaves are also intruded by veins of the host, and therefore in the process of disaggregation. Thick biotite-rich rims and diffuse haloes around enclaves suggest chemical interaction between the enclave magma and the granitic host; notably the latter lacks muscovite in this vicinity, and is more strikingly porphyritic than elsewhere. Unfortunately, intense weathering precludes detailed petrographic or geochemical study on these enclave swarms.

Figure 11.7. Mafic microgranular enclaves with diffuse haloes in a Glendara Adamellite exposure.

11.2.3 Mooree Granodiorite

Prominent exposure of this body occurs in the environs of Sugarloaf Creek, where it abuts Koolomurt Granodiorite to the west and Glendara Adamellite to the east (Figure 11.3); both contacts are concealed beneath Permian cover. A 25 m wide apophyses or dyke of this material also occurs in Pigeon Ponds Creek at the eastern margin of the Glendara Adamellite.

Mooree Granodiorite is a medium grained, pale grey-buff rock that resembles the Tuloona Granodiorite but contains slightly more alkali feldspar and euhedral muscovite (**97-36***). Rectangular alkali feldspar phenocrysts (~5-12 mm long) become more abundant eastwards. In places, a diffuse layering of slightly more biotite-rich bands (2-10 cm across) is visible, parallelled by a weak mica foliation. Alkali feldspar phenocrysts and lenticular micaceous enclaves (~6 cm long) are also aligned with the banding, but a closely spaced fracture trend (spacing 5-15 cm) is oriented perpendicular to this direction. This prominent joint set may reflect D_5 deformation, while the banding and mineral alignment is probably of magmatic origin.

Elliptical microgranular enclaves (to 15 cm) are uncommon and similar to those of Tuloona Granodiorite exposures in Schofield Creek.

11.2.4 Chetwynd Tonalite

(a) Field relations

Occupying the Chetwynd River valley, the poorly outcropping Chetwynd Tonalite occurs as a 1 km tract downstream of Chetwynd, and more extensively along the river, and Cairns Creek, south and east of the township (Figure 11.3). A northwest-trending elliptical shaped pluton is defined and confirmed by aeromagnetics (Kemp *et al.* 2001). The Chetwynd Tonalite pluton is crosscut near its widest dimension by the Cairns Creek Granodiorite (see below), the western and eastern boundaries of which, as exposed in the Chetwynd River, are sharp intrusive contacts. In proximity to these boundaries the Chetwynd Tonalite is invaded by numerous bifurcating and mutually crosscutting aplitic, pegmatitic and microgranitic dykes (~10 cm to 5 m thick). These truncate an earlier generation of muscovite-garnet pegmatitic sheets (2-10 cm thick) in this body. The eastern Chetwynd Tonalite-Cairns Creek Granodiorite boundary in a tributary of Cairns Creek is offset by a minor fault, near where both lithologies are fractured and hydrothermally altered (Figure 11.3). The western boundary in Cairns Creek is also heavily fractured and intruded by Tertiary basalt, suggesting that it might also be faulted.

To the north, in the western tributary of Tom Salt Creek, Chetwynd Tonalite is intruded by sheets of pale grey microadamellite and separated from Glendara Adamellite by a band of this material. The southeastern margin of the Chetwynd Tonalite pluton abuts the garnet-rich Glengoyne Adamellite (section 6.6.4).

(b) Lithology

Chetwynd Tonalite exposures are commonly weathered, but fresh rock is a distinctive bluish-grey colour and moderately coarse grained. With respect to Tuloona Granodiorite, samples are

slightly coarser, more biotite-rich, and characterised by large subhedral quartz grains (up to 10 mm), which facilitate recognition even in deeply weathered profiles (e.g. sample **98-427***). Alkali feldspar is rare and interstitial (Figure 11.2a), whereas muscovite is absent. Unlike other Tuloona types, allanite prisms are conspicuous.

Although the most mafic Tuloona type phase, microgranular enclaves are not abundant within Chetwynd Tonalite, with two or three for every 10 m^2 pavement on average. They resemble the porphyritic biotite-rich types of the Tuloona Granodiorite, being elliptical-lenticular, and not exceeding 30 cm in length.

11.2.5 Coojar Granodiorite

Scattered granitic outcrops occur in the Coojar district southeast of Harrow, most notably along Mather Creek east of the Coleraine road and a 2 km segment of Basin Creek (see Figure 3.1 for locality), and are collectively referred to as Coojar Granodiorite. Two samples collected ~ 1 km apart in Basin Creek (**97-140, 97-142***) are nearly identical, medium to coarse grained, bluish-white rocks that are representative of most granitic exposures in the Coojar district. Relative to Tuloona Granodiorite, they are coarser grained, with more feldspar and magmatic muscovite (Table 11.1). Biotite has a weak preferred orientation in places, whereas enclaves are absent.

Small exposures alongside Mather Creek further north are texturally analogous, but contain more biotite and magnetite with significantly less muscovite and alkali feldspar (e.g. **97-297***) (Figure 11.2b). Enclaves are prominent, primarily biotite-rich microgranular types with plagioclase phenocrysts, though lenticular micaceous enclaves (2-5 cm) also occur.

11.2.6 Patawilya Tonalite

(a) Field relations

The southernmost exposed pluton of the central granitic belt, the Patawilya Tonalite is an elongate body outcropping in Bryan Creek and tributaries ~18 km north of Coleraine (see Figure 5.13). The northern edge of the pluton in Bryan Creek abuts a 2 km expanse of Devonian rhyolite, north of which occurs muscovite-bearing leucogranite of the northeastern migmatite zone. The western extent of the Patawilya Tonalite is unknown, as outcrop ceases west of Bryan Creek, where the pluton is about 1800 m across.

However, towards the south in Bryan Creek the body becomes enveloped by migmatitic rocks in the same manner as the Tuloona Granodiorite, the lobate southern boundary being intersected at several locations in Bryan Creek and tributaries (Figure 5.13). Towards the periphery in northern Bryan Creek the tonalite contains an increasing amount of metasedimentary enclaves, with a concomitant decrease in the amount of mafic igneous enclaves. Migmatitic gneiss rafts (up to 2.5 m long) occur, some of which are disaggregated into clusters of biotite clots and schlieren that locally impart a layered aspect to the host. This schlieric layering intensifies until the tonalite merges into diffusely banded diatexite, the exact contact being difficult to pinpoint. South of this, interleaved stromatic migmatite, laminated quartzofeldspathic schist and heterogeneous biotite-rich granitic rock outcrops (section 5.7).

Where intersected further south along Bryan Creek, the southern Patawilya Tonalite boundary is with stromatic migmatite. Marginal tonalite exposures contain thin micaceous schlieren up to 25 cm long, parallel to the foliation in the adjacent migmatite.

(b) Lithology

Although lithologically variable, typical Patawilya Tonalite, as exposed along Bryan Creek (**97-407B***) is light grey-buff and medium to coarse grained, with equant phenocrysts of cloudy quartz (to 8 mm) and occasional large plagioclase laths (up to 5-7 mm) (Table 11.1). The groundmass is smaller quartz grains and interlocking buff coloured plagioclase, with abundant plates and small clotty aggregates of randomly disposed biotite. Subhedral muscovite plates in these clots may be primary. Alkali feldspar blebs are wholly interstitial to plagioclase laths.

(c) Enclaves

Elliptical-spherical microgranular enclaves (~10-60 cm across) are common in Patawilya Tonalite, with some large pavements in Bryan Creek having one or two per square meter on average. Most are dark grey, fine grained and biotite-rich, with phenocrysts of plagioclase (to ~1 cm) and biotite clots (2-5 mm across). The exception is a large enclave sampled from northern Bryan Creek (**97-382B**), which is medium grained and granitic-textured (Table 11.2).

11.3 Loftus Creek type

Loftus Creek type granodiorites comprise a chain of plutons, outcropping along a broadly north-south axis, which intrude Tuloona type bodies of the central batholith and metasedimentary rocks of the southwestern zonation (Figure 4.1). They are also associated with a series of garnet-bearing felsic dykes. Plutons are either elongate or equant, but are invariably aligned oblique to the regional structural trend, with sharp contacts. Apart from the Koolomurt Granodiorite, all are uniquely characterised by large euhedral biotite books, which are dark chocolate brown in thin section and serve to immediately distinguish this group from other magma types (see Figures 11.8, 11.9). Many biotite books also enclose euhedral plagioclase inclusions. Hornblende is common in more mafic samples, and large euhedral titanite crystals occur throughout (Table 11.3). As with Tuloona types, plagioclase laths exhibit vivid oscillatory zoning and form intergrown clumps with complex zoning characteristics. Magnetite is abundant and responsible for pronounced aeromagnetic anomalies, the perimeters of which sharply coincide with mapped pluton boundaries (Kemp *et al.* 2001). Enclaves are rare and primarily mafic microgranular varieties. Loftus Creek type phases are also geochemically distinctive, with high Na_2O, K_2O and Sr contents (section 15.4.3).

11.3.1 Loftus Creek Granodiorite

A conspicuous D-shaped magnetic anomaly in the eastern Wando Vale district corresponds to the Loftus Creek Granodiorite (see Figure 4.1), first mapped as Sawpit Gully Granodiorite by Anderson (1990). In Corea Creek and tributaries, the pluton intrudes upper amphibolite facies quartzofeldspathic schists and calc-silicates on its western edge (Anderson & Gray 1994). A sharp southern contact with migmatite zone rocks is recognised in Loftus Creek (Bushell 1996).

Lithology	*Sample number*	*Grid reference* (WD)	*Modal Percentage*						*Accessory Minerals*
			Quartz	**Plagioclase**	**K-Feldspar**	**Biotite**	**Hornblende**	**Titanite**	
Loftus Creek Granodiorite	**LTU9572**	454491	22	51	12	10	5	acc.	a, c, e, mt
Cloven Hills Granodiorite	**97-266**	433573	26.4	51.1	13.8	6.6	0	0.1	a, all, c, mt (1.9%)
	97-436	437560	27.6	50.8	8.5	9.8	0.5	0.5	a, all, c, e, mt
Cairns Creek Granodiorite	**97-52**	403706	18.6	52.1	15.2	6.6	3.9	0.9	a, all, mt (1.9%)
	97-65	415697	25.3	46.8	21.3	5.2	0	0.3	a, all, e, mt
	97-71	428692	32.3	38.6	20.6	4.8	acc.	0.4	a, c (1.2%), ca, e, f, mu*, mt
	97-67	424694	29.4	44.2	21.6	3.0	0	0.1	a, c, e, mt, mu*
Koolomurt Granodiorite	**97-295**	456716	27.7	41.5	16.4	12.6	0	0.2	a, all, c, op
microgranular enclave	**98-PP2**	456716	9.4	36.6	19.4	16.2	15.3	1.4	a, all, e, mt (1.2%)
Barrama Microadamellite	**97-126B**	477713	31.8	39.6	10.7	5.5	0	0.1	a, c, mu (1.2%)
	97-296	495727	29.6	40.6	20.5	6.5	0	0.1	a, mt (1.0%), mu (1.6%)

Table 11.3. Mineralogy of Loftus Creek type granitic rocks of the Glenelg River Complex, determined by thin section point count (2500 points) (acc = accessory abundance). Abbreviations are: a = apatite; all = allanite; c = chlorite; ca = carbonate; e = epidote; f = flourite; mt = magnetite; mu = muscovite; mu* = secondary muscovite.

Loftus Creek Granodiorite samples are medium to coarse grained, with euhedral biotite books (5x5x3 mm) and poikilitic alkali feldspar plates (to 1.7 cm long; **98-142**). Hornblende prisms comprise 5% by modal volume in Corea Creek (Anderson 1990), but are less abundant in Loftus Creek, where the rock has slightly higher quartz content. Globular microgranular enclaves (to 10 cm across) are sparsely distributed in Corea Creek and tributaries, but absent from Loftus Creek outcrops. An apophyse of this pluton in Robertson Creek also contains rotated schist enclaves with F_3 structures, indicating syn- or post-D_3 emplacement (Anderson 1990).

11.3.2 Cloven Hills Granodiorite

(a) Field relations and lithology

An oval-shaped body, Cloven Hills Granodiorite is well exposed in watercourses east of the Wando River and north of the Loftus Creek Granodiorite (Figure 10.1). It sharply crosscuts the Meissen Granodiorite and Blair Atholl Adamellite and intrudes sillimanite schist at its eastern periphery.

Cloven Hills Granodiorite outcrops prominently as yellowish tors, though a slabby tendency is imparted by a strong northwesterly trending joint set. At the type locality, samples are light buff coloured and medium to coarse grained, with abundant euhedral plates (3-5 mm) and finer disseminated flakes of biotite (**97-436***; Figure 11.8). Steel grey plagioclase laths and polycrystalline quartz masses (up to 6 mm across) are conspicuous, whereas alkali feldspar occurs as light orange poikilitic grains. Hornblende needles and titanite crystals are minor.

Samples towards the north of the pluton (e.g. **97-266**, **97-430**) are slightly finer grained and more felsic (Table 11.3, Figure 11.8). The bimodal grainsize of biotite is more obvious, with most occurring as small (~0.5 mm) ragged flakes rather than larger euhedral 'phenocrysts'. Plagioclase is palest olive green and enveloped by more common alkali feldspar pools. Titanite euhedra are also slightly more abundant.

Only one enclave was observed in Cloven Hills Granodiorite, a tabular microgranular object (~18 cm long) at WD427566. This is medium grained and unfoliated, with a pseudodoleritic texture, where stubby hornblende prisms interlock with, and partially enclose, plagioclase laths. As such, the enclave resembles mafic dykes occurring in Robertson Creek (see below).

11.3.3 Cairns Creek Granodiorite

(a) Field relations

Intruding the Chetwynd Tonalite, the Cairns Creek Granodiorite forms a large lozenge-shaped pluton aligned NE-SW, and outcrops prominently along the Chetwynd River and Cairns Creek (Figure 11.3). The Chetwynd River obliquely transects the pluton across its shortest axis (~2.4 km), whereby exposing a continuous and concentric zonation within the body, from relatively mafic rock at the perimeters through to quite felsic samples in the pluton core. Enclaves do not occur in any part of the body, and although biotite steadily decreases in abundance from the core to the rim, large euhedral plates are ubiquitous.

(b) Hornblende-bearing phase

Exposure of Cairns Creek Granodiorite, as cream coloured tors, is most prominent at the pluton margins, where the granodiorite contains hornblende. Samples (e.g. **97-62***) are distinctively pale greenish and porphyritic, dominated by coarse phenocrysts of olive green plagioclase (to 6 mm), with abundant hornblende prisms and large euhedral biotite books (up to 4.5 mm across and 3 mm thick) (Figure 11.9) (Table 11.3). Quartz also forms polycrystalline masses to 7 mm. The matrix is a medium grained mosaic of plagioclase, quartz and poikilitic alkali feldspar. Abundant magnetite and titanite crystals are clustered with biotite plates or hornblende.

Rock of this nature occurs at the northwestern and southeastern margins of the Cairns Creek Granodiorite in the Chetwynd River, and also along the southwestern continuation of these boundaries as exposed in Cairns Creek and tributaries. That the hornblendic phase forms a thick 'rind' around the pluton is confirmed by the strong aeromagnetic signature (Kemp *et al.* 2001), further indicating a thickening of this material towards the northeast and southwest extremities.

(c) Central felsic variants

Hornblende rapidly diminishes in abundance towards the centre of the body along the Chetwynd River and disappears about 600 m from the northwest and southeast margins. The granodiorite progressively becomes coarser and more even grained, becoming mottled pink with increasing poikilitic alkali feldspar (Figure 11.9). Samples close to the geographic centre of the pluton are orange-tan, coarse grained and dominated by smoky quartz masses (up to 10 mm) and tabular alkali feldspar phenocrysts (to 2 cm; **97-67***) (Table 11.3). Intense seritisation of feldspars and replacement of plagioclase cores by sheaves of secondary white mica and epidote manifests strong hydrothermal alteration. Sparse biotite flakes are also extensively altered to chlorite, where they occasionally contain purplish fluorite blebs along former cleavage traces.

This lithology (exposed for ~50 m), and the hornblendic rim represent the extremities of variation within the pluton. Aeromagnetic images (Kemp *et al.* 2001) indicate that this felsic core has a low intensity magnetic signature, consistent with the reduced amount of magnetite.

11.3.4 Koolomurt Granodiorite

(a) Boundaries

An irregular teardrop-shaped pluton, the Koolomurt Granodiorite is almost continuously exposed for ~8 km along Pigeon Ponds Creek (Figure 11.3), but is most prominent in the northern stretches, where it forms large tors and extensive boulder fields. The body intrudes the porphyritic Glendara Adamellite, with sharp contacts evident in Pigeon Ponds Creek and Tom Salt Creek. Outcrop patterns and the positive magnetic anomaly (Kemp *et al.* 2001) suggests that the Koolomurt Granodiorite also crosscuts the Chetwynd Tonalite to the south, and Mooree Granodiorite to the north, though boundaries are concealed (Figure 11.3).

(b) Lithology

Typical Koolomurt Granodiorite samples are light greenish-grey, medium to coarse grained and

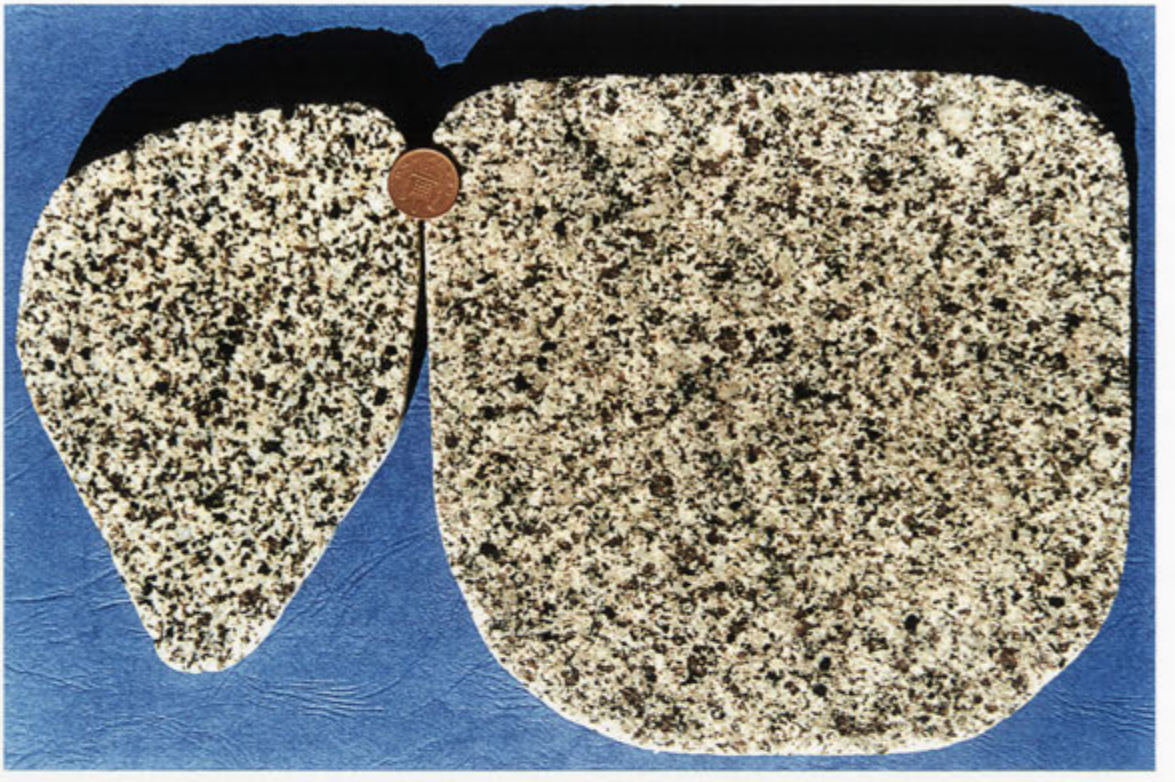

Figure 11.8. Cloven Hills Granodiorite. Type specimen **97-436** (left) and felsic variant **97-430** (right).

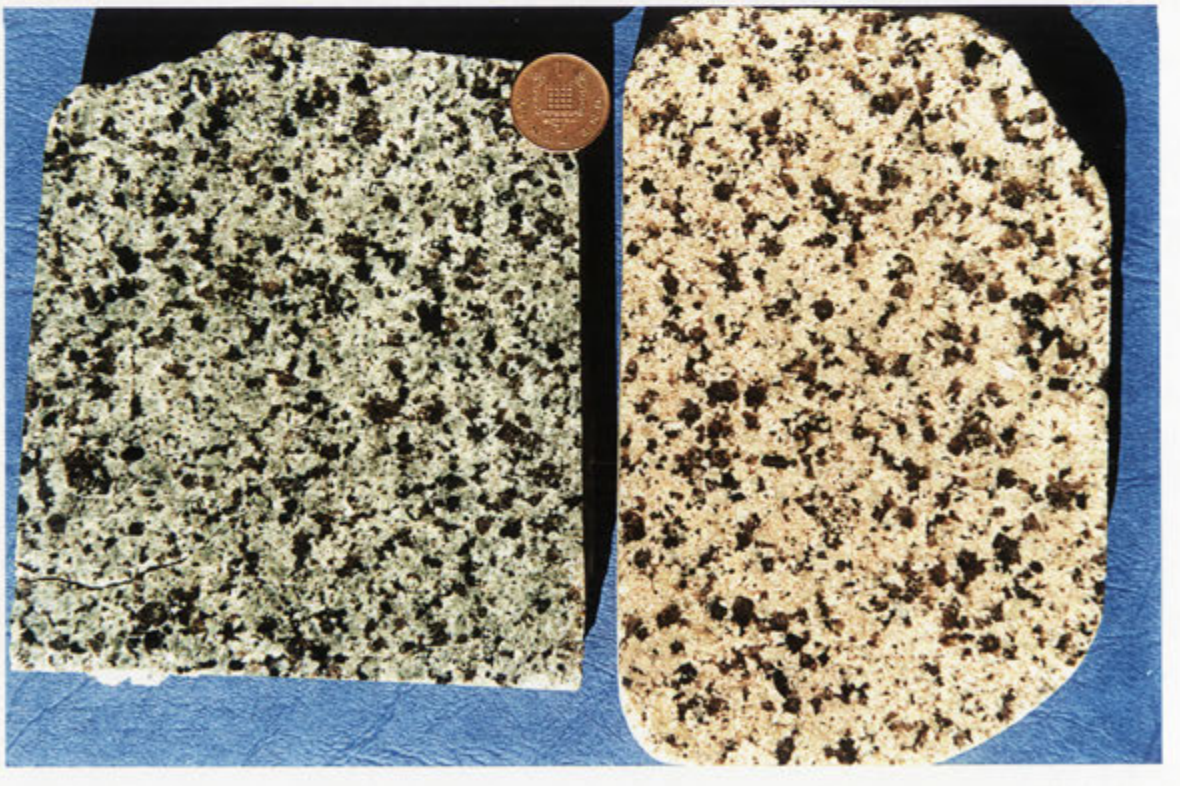

Figure 11.9. Slabs of Cairns Creek Granodiorite, with hornblende-bearing marginal phase **97-62** (left) and felsic central phase **97-67** (right).

approximately equigranular (e.g. **97-293***), though some plagioclase laths reach 7 mm long. Square to rectangular alkali feldspar masses (to 12 mm) are conspicuous, containing minute inclusions of plagioclase, quartz and biotite. In northern Pigeon Ponds Creek, these alkali feldspar crystals occur as striking 'oikocrysts' (up to 4.2 cm across) that are so choked with inclusions as to be not readily distinguishable from the matrix of the rock. Biotite otherwise occurs as ~2-3 mm plates enclosing plagioclase, or smaller grains that may exhibit a weak preferred orientation. Interleaved aggregates of unfoliated biotite (up to 1 cm), with magnetite, titanite and allanite are moderately common, and contorted biotite schlieren are observed in some outcrops. Titanite also forms irregularly-shaped grains (0.5-1 mm) with tiny plagioclase inclusions.

These petrographic features are uniform across the large Koolomurt Granodiorite pluton, which, as demonstrated by three widely spaced geochemical samples, is compositionally homogeneous (Appendix G).

(c) Enclaves

Unlike other Loftus Creek types, mafic microgranular enclaves (up to 1 m long) are ubiquitous throughout Koolomurt Granodiorite and locally clustered (up to six per square metre). They are usually rounded and elliptical to equant, but also exhibit irregular amoeboid or more rarely angular shapes. Contacts with the enclosing granodiorite are generally sharp and without biotite rims, though the margins of the enclaves may be moulded around feldspar crystals in the host. Larger objects sometimes have crenulate or scalloped margins (Figure 11.10a).

Microgranular enclaves are mostly fine to medium grained and have complex igneous textures. They vary from diffuse bodies barely distinguishable from the granitic host through to more mafic hornblende-rich types (Figure 11.10b). The most common variety (~5-20 cm across) is biotite-rich with plagioclase phenocrysts, where matrix biotite, hornblende and plagioclase is set in a framework of rectangular alkali feldspar oikocrysts (to 5 cm across). The proportion of alkali feldspar oikocrysts varies between enclaves, but commonly they encompass 70-80% of the rock and define a poikilomosaic texture. Some of these bodies contain alkali feldspar phenocrysts that are very similar to those in the host granodiorite (Figure 11.10c).

A sample of this enclave type (**98-PP2**) comprises ~50% alkali feldspar oikocrysts (up to 3 cm) occurring through a fine to medium grained matrix, with small plagioclase phenocrysts (2 mm) and hornblende prisms (to 3 mm) (Figure 11.10d) (Table 11.3). The matrix in thin section comprises polygonal quartz, spindly biotite (~0.8-1.5 mm), hornblende (~0.5 mm), titanite crystals (up to 2 mm) and greenish plagioclase (~1 mm); magnetite and apatite needles are abundant accessories. Notably, larger titanite grains enclose tiny groundmass plagioclase laths. Alkali feldspar oikocrysts are densely packed with all of these minerals (except quartz), where they are slightly finer grained and euhedral, apart from plagioclase inclusions which have myrmekitic fringes; phenocrysts and groundmass plagioclase laths that project into oikocrysts also have myrmekitic margins. Where oikocrysts are clumped together a poikilomosaic texture results, boundaries being lined by tiny hornblende grains or myrmekite lobes. Quartz also forms large poikilitic masses (up to ~3 mm), enclosing plagioclase, biotite and hornblende grains, that abut alkali feldspar oikocrysts.

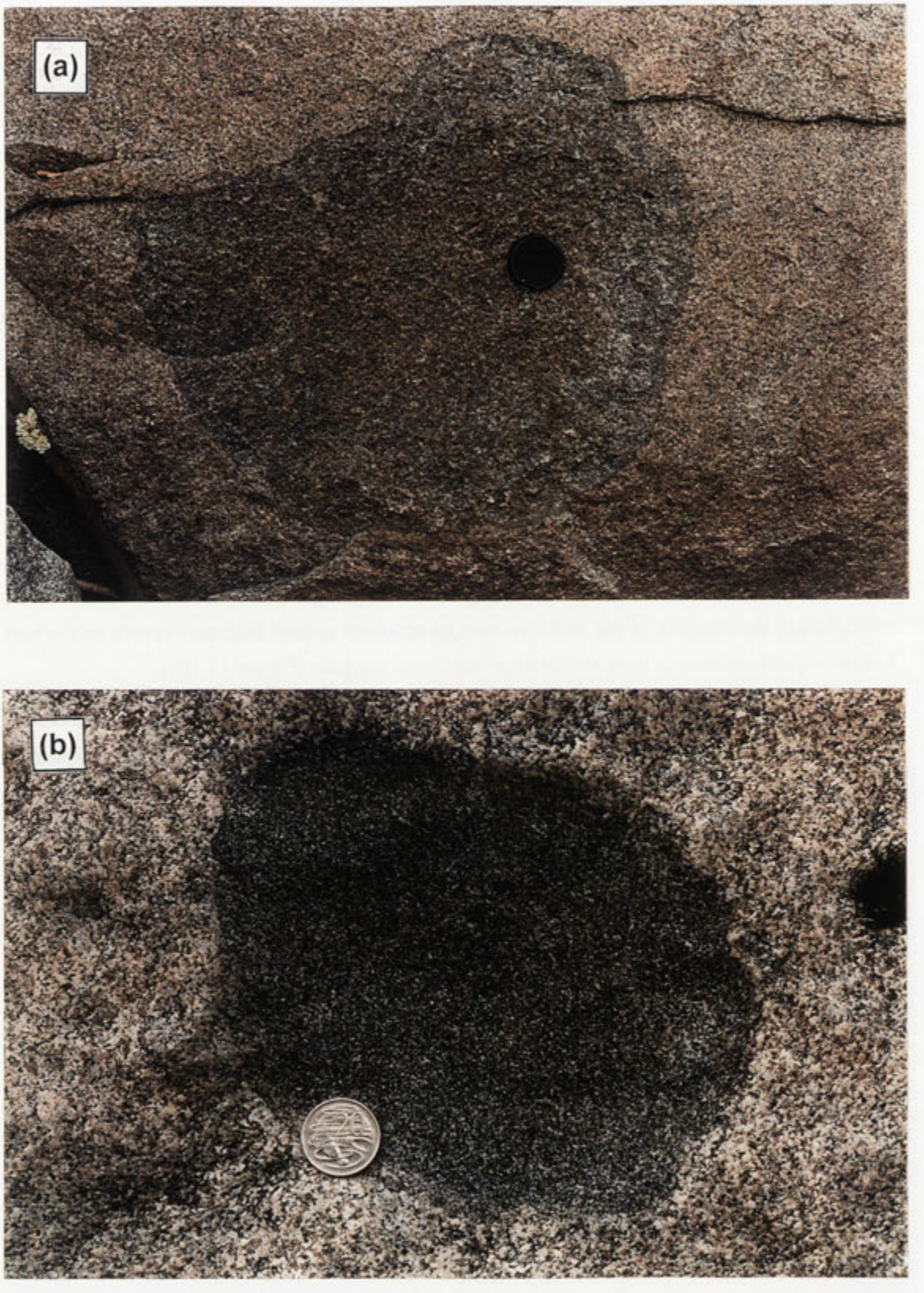

Figure 11.10. Mafic microgranular enclaves in the Koolomurt Granodiorite. (a) Large biotite-rich object exhibiting sharp but irregular contacts against the host. (b) More mafic, hornblende-bearing enclave.

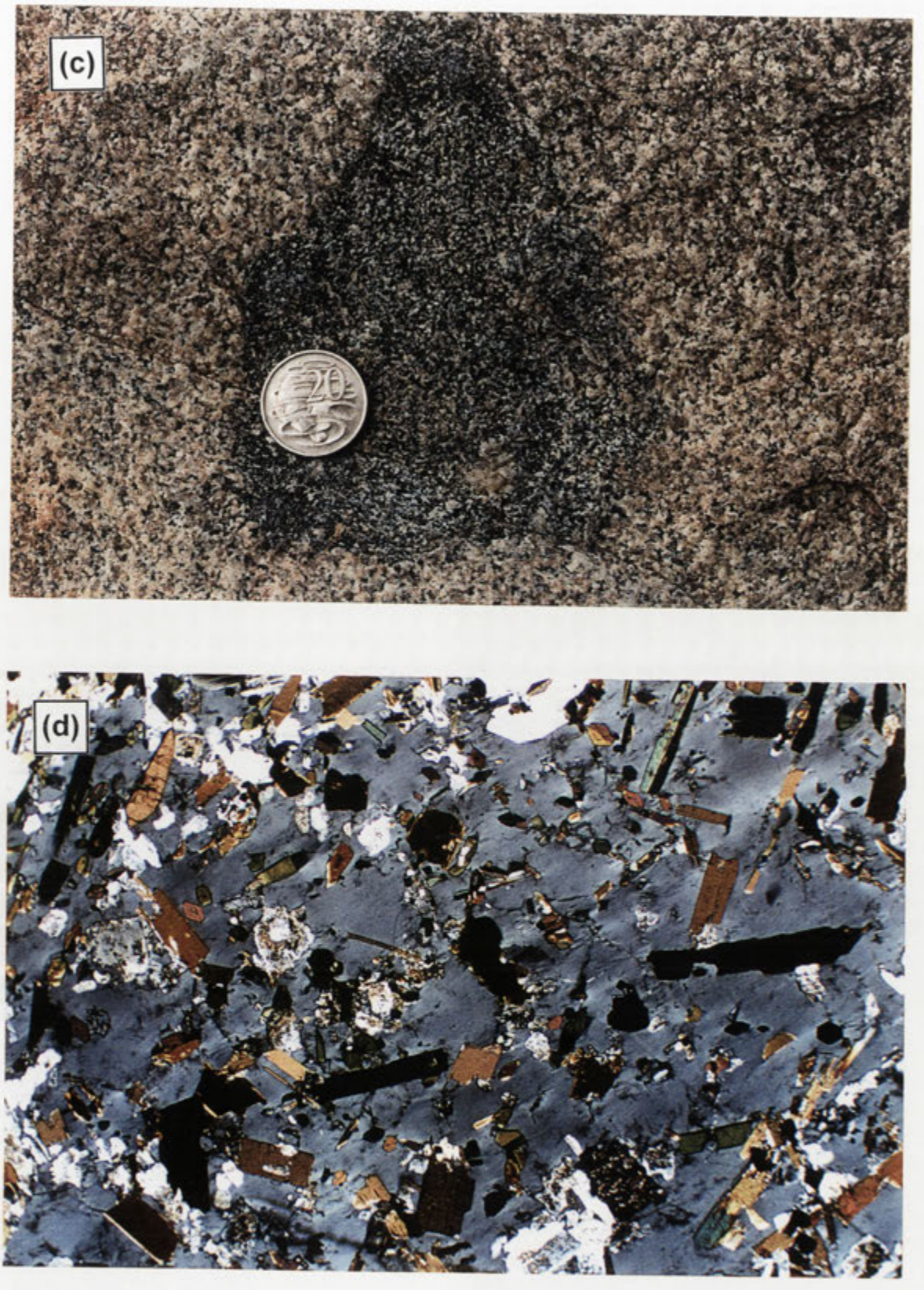

Figure 11.10 contd. Mafic microgranular enclaves in the Koolomurt Granodiorite. (c) Spindly-textured enclave with indistinct margins and containing a poikilitic alkali feldspar phenocryst (bottom centre) similar to that observed in the host. (d) Thin section view of the enclave pictured in (c) (**98-PP2**). Elongate biotite grains with serrated margins, hornblende prisms, plagioclase and titanite (centre left) are set in poikilitic alkali feldspar (crossed polars, ~8.1 mm across) (WD456716).

The largest enclaves are more felsic and have phenocrysts of plagioclase and spindly biotite in a finer, biotite-quartz-alkali feldspar groundmass. One of these, collected from northern Pigeon Ponds Creek (**98-PP1**), has a striking ocellar aspect, where titanite crystals (0.5-2 mm) are contained within a biotite-free felsic halo or ocellus (2-5 mm) that is distinct from a biotite-rich inter-ocellus matrix (Figure 11.11). This feature is referred to as 'sphene (titanite) ocellar texture' and is common in microgranular enclaves of the Sierra Nevada Batholith (Hibbard 1991). In thin section, the felsic ocellus comprises a poikilomosaic of quartz (1.5 mm) and alkali feldspar (up to 5 mm) that enclose numerous needle-like plagioclase laths (~0.5 mm), many of which have skeletal morphology, and acicular apatite grains. Large titanite crystals are euhedral to anhedral and ophitic with respect to tiny plagioclase crystals (Figure 11.11b, c). The inter-ocellus matrix is dominated by interlocking laths (0.5 mm) and larger phenocrysts (1-3 mm) of strongly zoned plagioclase, ragged elongate biotite flakes (0.5-0.8 mm), interstitial pools or sparse poikilitic masses of alkali feldspar (to ~1.5 mm) and larger poikilitic quartz grains (1-2 mm), in places forming a mosaic. Like plagioclase in ocellar regions, matrix plagioclase laths have very elongate habits and are commonly skeletal. Apatite needles and magnetite grains are abundant throughout the matrix, though the latter is more concentrated in the ocellar regions. Large allanite prisms (to 1.5 mm) and small epidote granules are less common accessories.

11.3.5 Barrama Microadamellite

Dykes and sheets of porphyritic Barrama Microadamellite are intermittently exposed for about 4.5 km along Pigeon Ponds Creek and tributaries east of Koolomurt Granodiorite (Figure 11.3). In the western part of Pigeon Ponds Creek the microadamellite forms a series of branching sheets that exhibit complex syn-magmatic intermingling with the Glendara Adamellite, and were clearly injected into this pluton while it was partially liquid (section 11.2.2c). Incorporation and disaggregation of globules of Glendara Adamellite has engendered significant petrographic variation within the microadamellite at outcrop-scale, mostly involving a heterogeneous distribution of large alkali feldspar phenocrysts.

Barrama Microadamellite from here is a light grey-buff coloured, strongly porphyritic rock remarkable for content of tabular alkali feldspar phenocrysts, ranging from 2 cm to 4.5 cm long (e.g. **97-126B***) (Table 11.3). These are conspicuously zoned and poikilitic, with concentrically arranged inclusions of quartz, biotite and euhedral plagioclase (Figure 11.12). Also present, and much more abundant, are smaller flesh-coloured alkali feldspar phenocrysts (0.5-1 cm) that lack inclusions (Figure 11.12). Field evidence suggests that the larger phenocrysts are xenocrysts derived from ingestion of Glendara Adamellite, which is consistent with their generally sparse, but variable abundance and concentration close to the contacts with the porphyritic adamellite. Other phenocrysts include rounded quartz masses (up to 7 mm), euhedral biotite plates (2-5 mm) and plagioclase laths (up to 4 mm). These are dispersed through a fine to medium grained matrix of quartz, alkali feldspar, plagioclase and randomly disposed biotite. Small muscovite plates are also conspicuous.

Barrama Microadamellite also outcrops for ~100 m along Pigeon Ponds Creek near the Mooree Road further east, separated from the Glendara Adamellite by an apophyse of Mooree

Figure 11.11. (a) Microgranular enclave slabs exhibiting a striking titanite-centred ocellar texture (**98-PP1**). Small brown titanite crystals occupy the central parts of biotite-deficient, quartz-feldspar ocelli. (b) Thin section view of a large felsic ocellus containing two ophitic/sub-ophitic titanite prisms, and exhibiting a poikilomosaic texture, defined by alkali feldspar and quartz masses (crossed polars, ~8.1 mm across).

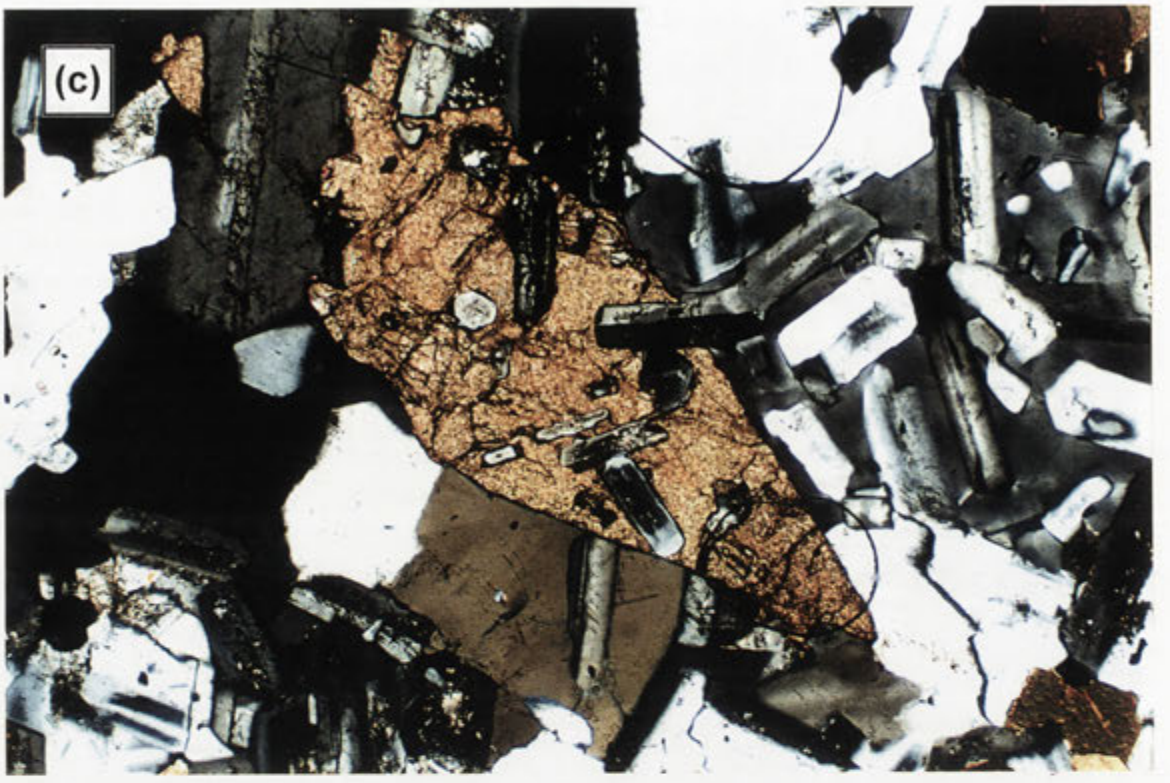

Figure 11.11 contd. (c) Close-up of a titanite crystal enclosing euhedral plagioclase laths. Poikilitic alkali feldspar is conspicuous in the right of the photo (crossed polars, ~2.5 mm across).

Figure 11.12. Alkali feldspar phenocryst (3.6 cm long) within the Barrama Microadamellite near a region of mingling with the Glendara Adamellite. Smaller phenocrysts of quartz and feldspar are also visible.

Granodiorite. Here, the microadamellite is coarser grained and slightly more felsic, with more quartz phenocrysts (e.g **97-296**; Table 11.3). The large alkali feldspar 'xenocrysts' are rarer.

11.3.6 Felsic dykes of Loftus Creek type plutons

Another unifying aspect of Loftus Creek types is the close association with numerous aplitic, pegmatitic and microgranitic dykes, which are commonly garnet-bearing and radiate outwards from pluton peripheries. Although intruding surrounding rocks, in most cases they are truncated by the Loftus Creek type pluton, indicating emplacement prior to that of the main granitic body. This is most apparent for the felsic dykes concentrated at the margins of the Loftus Creek Granodiorite, which are folded by D_3 (Anderson & Gray 1994).

Microgranitic dykes exhibit the most petrographic variability. The metre-sized sheets contained by the Snake River Tonalite near the western edge of the Cloven Hills Granodiorite are pale greenish, with small magnetite phenocrysts (2-3 mm; **97-178B**). Phenocrysts have a felsic halo (1-2 mm wide) and occur in a fine grained quartzofeldspathic matrix with tiny euhedral garnets but without muscovite.

In contrast, microgranitic dykes intruding the Chetwynd Tonalite near contacts with the Cairns Creek Granodiorite (section 11.2.4) are pale tan coloured, with euhedral biotite phenocrysts (to 5 mm), the recessive weathering of which imparts a 'pitted' character to exposed surfaces. Although not established chemically, the petrographic similarity of these dykes to the Cairns Creek Granodiorite implies consanguinity.

Thicker sheets (to 50 m) of pale grey microgranite are abundant in Tom Salt Creek south of the Koolomurt Granodiorite, traversing Glendara Adamellite exposures. These are very silicic, with ovoid clots of muscovite and biotite (1-3 cm), which also preferentially weather out.

11.3.7 Robertson Creek mafic dykes

A series of unusually-textured mafic dykes (0.5-3 m wide) intrude metasedimentary rocks in Robertson Creek between the Cloven Hills and Loftus Creek Granodiorites. One such dyke was included as part of the Wando Tonalite by Turner *et al.* (1993a). Investigation by this study however reveals that the mafic dykes have no affinity with Wando type rocks but share the same distinctive high Sr signature as Loftus Creek type plutons (section 14.3.3).

Most samples are dark greenish-grey, medium grained and dioritic, dominated by needly hornblende prisms (most 1-2 mm), very conspicuous on weathered surfaces, and greenish plagioclase laths (rarely phenocrysts up to 8 mm; e.g. **98-RC1**). Glassy rectangular crystals or irregularly-shaped masses of alkali feldspar (~8-10 mm) are also prominent, enclosing numerous acicular hornblende and plagioclase grains, whereas small quartz grains are interstitial to plagioclase. Titanite crystals, some of which contain tiny plagioclase inclusions, are conspicuous. In thin section, some larger, more blocky hornblende prisms enclose small plagioclase laths and are zoned from light green cores to dark olive rims. No planar fabric is present, though hornblende prisms and plagioclase laths define a distinct lineation.

A paler coloured variant is tonalitic, comprising interlocking plagioclase laths, quartz and lesser hornblende (**98-RC2**). Some poikilitic alkali feldspar masses occur (up to 1 cm long) but are minor. Titanite is an uncommon accessory. In thin section, an ophitic to subophitic texture is apparent, such that elongate pale green hornblende grains enclose or partially enclose plagioclase laths. Clinopyroxene relicts are conspicuous in the centres of many hornblende grains. Quartz is interstitial to plagioclase but also forms larger masses that envelope hornblende.

The absence of deformational features and truncation of the S_2 fabric in host metasedimentary rocks indicates a post-D_2 emplacement timing for these dykes.

Chapter 12: Interspersed granitic and intermediate-mafic-ultramafic rocks

Part (A) Chin Chap Creek

12.1 Introduction

Intimate outcrop relations between granitic and more mafic igneous rocks are most apparent in two areas of the GRC. These are the Caupaul Igneous Complex north of Dergholm (Chapter 13) and Chin Chap Creek in the southeastern corner of the GRC, which also has interspersion between granitic and metasedimentary rocks. Together, these areas encapsulate the full lithological spectrum, from migmatite and felsic plutonic rocks through to lower silica intermediate, mafic and ultramafic lithologies, and therefore link the peraluminous to metaluminous 'granitic' system of the GRC with a 'basaltic' igneous regime. To explore this, the geology of Chin Chap Creek is documented by this chapter, with emphasis upon describing field relationships between granitic and mafic igneous rocks and the formation of microgranular enclaves. The implications for the origin of microgranular enclaves in other GRC granitic plutons are discussed at the end of the chapter.

12.2 Overview of field and lithological relationships

The diverse geology of Chin Chap Creek and tributaries is dominated by heterogeneous granitic material of 'Kassingbrook type', bordered to the north and south by Harrow type rocks (Figure 12.1). Kassingbrook type exposures are resolved into the Kassingbrook Granodiorite and Coolami Granodiorite. The former has extreme variability, ranging from muscovite leucoadamellite to biotite-rich granodiorite and mafic hornblende tonalite (Tables 12.1, 12.2). Many outcrops contain alkali feldspar phenocrysts, whereas mafic microgranular enclaves occur throughout, and are locally clustered. Granitic exposures are complexly interleaved with migmatitic metasedimentary rocks in several places, which form a large raft towards the centre of the outcrop area (Figure 12.1). Kassingbrook Granodiorite also has a sharp contact with diatexite and muscovite leucogranite in an eastern tributary of Chin Chap Creek.

Sample **97-373** is most representative of Kassingbrook Granodiorite overall and is therefore taken as 'typical'. This is medium to coarse grained and leucocratic, with sparse tabular phenocrysts of alkali feldspar (to 1 cm), smaller masses of poikilitic alkali feldspar and abundant bluish-grey plagioclase laths (see Table 12.1). Euhedral muscovite plates are conspicuous, whereas aggregates and ragged flakes of biotite are minor.

Coolami Granodiorite is similar, but with abundant tabular alkali feldspar phenocrysts (to 3 cm) and more flakes and clots of biotite without muscovite (Tables 12.1, 12.2). Although locally intermingled with Kassingbrook Granodiorite (see below), it has most prominent exposure in a western tributary of Chin Chap Creek, bordering interleaved muscovite granite-migmatite to the west and mafic diorite to the east (Figure 12.1). Occasional gneiss and migmatite enclaves

become larger and more common towards the western periphery, and are oriented parallel to strongly aligned feldspar phenocrysts. At the western margin, numerous elongate micaceous enclaves, schlieren and quartzofeldspathic schist slabs impart a layered aspect. Coarse euhedral muscovite is also conspicuous. Boulders of porphyritic rock on the slopes of Chin Chap Creek 1.9 km further south possibly represent the continuation of the body.

Granitic exposures are punctuated by internally heterogeneous bodies of mafic hornblende-rich igneous rock (Figure 12.1), encompassing hornblendite and hornblende gabbro-diorite (which is predominant) through to texturally-distinct dioritic and tonalitic lithologies (Tables 12.3, 12.4 and Figure 12.2). Isolated outcrop of similar rock occurs further south in Robson Creek (below). All lithologies lack deformation features and post-date D_2. Gabbro-diorites are characterised by coarse, blocky hornblende prisms (to ~8 mm), in a finer matrix of clinopyroxene, hornblende and minor interstitial to poikilitic plagioclase (andesine) (Figure 12.3). Hornblende phenocrysts commonly enclose relict clinopyroxene, or very rarely, orthopyroxene (Figure 12.3b, c). Small amounts of alkali feldspar also occur in many samples (<5%). Diorites are also hornblende-rich but the large phenocrysts are less obvious, such that samples are more uniform-textured. Biotite, plagioclase (becoming lath-shaped) and quartz are more abundant, whereas clinopyroxene is absent; clots of intergrown hornblende and biotite are typical. Despite the subdivision, the full textural continuum exists between diorites and gabbro-diorites in the field, with some gabbro-diorite bodies transitional to dioritic margins (see below). Tonalitic samples are more felsic, biotite-rich and 'granitic' textured, and many have plagioclase and quartz phenocrysts.

Due to limited outcrop, the geometry and geological context of these hornblende-rich bodies is unclear. Gabbro-diorites and hornblendites form pod-like exposures and might represent small stocks, whereas diorite and tonalite bodies are sheet-like (2-5 m wide) and may be part of larger dykes (see Figure 12.1). Nevertheless, the most significant field aspect is the extensive outcrop-scale intermingling with enclosing felsic granitic lithologies, with liquid-liquid contacts being conspicuous.

12.3 Description of key localities

To effectively convey the complex igneous-metasedimentary association of Chin Chap Creek, five key localities are separately described, labelled A to E from north to south on Figure 12.1. Emphasis is upon documenting interaction between mafic and felsic igneous rocks.

12.3.1 Key locality A: northern Chin Chap Creek

This locality occurs at the northern margin of the Kassingbrook Granodiorite, where it is separated from interleaved migmatitic metasedimentary rocks and muscovite leucogranite by a pod of coarse hornblende gabbro-diorite (~50 m wide). Granodiorite exposures immediately south of the mafic body are a chaotic mixture of gabbroic enclaves, porphyritic microgranular enclaves and rafts, selvedges, and schlieren of metasedimentary rock. Key locality A extends south from the mafic body to the last occurrence of gabbroic enclaves (~250 m).

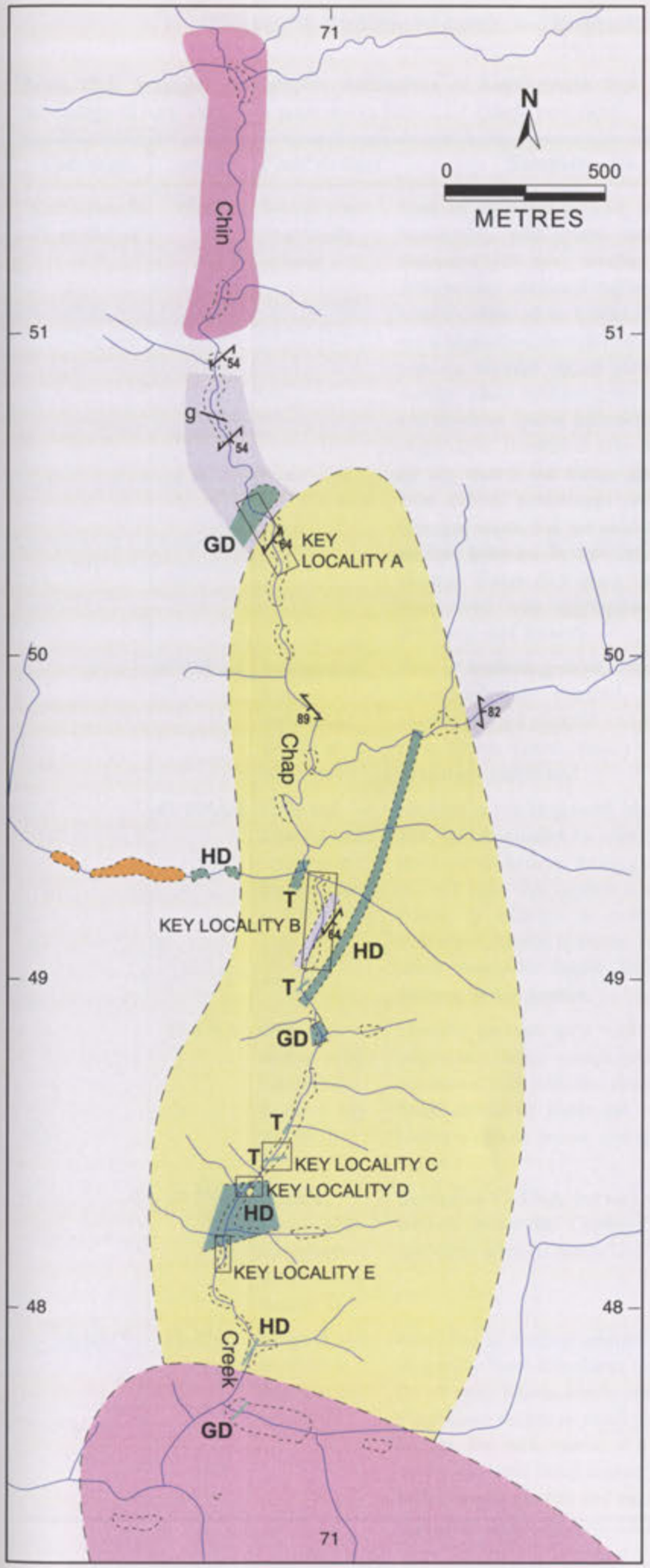

Unnamed muscovite-garnet granite

Hornblende gabbro-diorite (GD), hornblende diorite (HD), hornblende tonalite (T)

Coolami Granodiorite

Kassingbrook Granodiorite

Quartzofeldspathic gneiss, schist, interleaved muscovite granite

Watercourse

Prominent outcrop

Approx. geological boundary

$\overset{24}{\searrow}$ Trend of S_2 foliation

g ⟍ garnet adamellite dyke

Figure 12.1. Simplified geological map of Chin Chap Creek and tributaries. Younger rocks are omitted for clarity. See Figure 5.13 for location.

Table 12.1. Summary petrographic descriptions of Kassingbrook type granitic rocks. The modal mineralogy of most samples is presented in Table 12.2. (contd next page).

Lithology	*sample*	*Field context*	*Summary description*
Kassingbrook Granodiorite	**97-373**	Typical phase from centre of body	Medium to coarse grained, light grey-buff coloured and leucocratic, with sparse tabular phenocrysts of alkali feldspar (3-10 mm), smaller masses of poikilitic alkali feldspar and abundant subhedral bluish-grey plagioclase laths (~2 mm, up to 4 mm). Plates of euhedral muscovite are conspicuous, though less common than in Harrow type plutons, whereas ragged biotite flakes are minor. In thin section, alkali feldspar (microcline) has irregular outlines and contains sparse inclusions of muscovite, biotite and plagioclase, sometimes also with central areas perforated by tiny quartz and biotite grains. Elsewhere, plagioclase laths exhibit pronounced oscillatory zoning, with large euhedral cores, and are moderately seritisised, with small epidote granules in the core regions. Muscovite forms isolated plates (0.5 mm) but more commonly occurs interleaved with aggregates of biotite flakes (α=tan, β=γ=very dark brown).
	97-309A-1	Intermingled with hornblende tonalite at WD709493	Fine to medium grained, white, alkali feldspar-rich rock. Heterogeneously textured, with interspersion between coarser grained material and fine grained, sugary textured rock. Biotite flakes (mostly 0.5-1 mm, up to 3 mm) are irregularly distributed.
	97-309A-2	Collected adjacent to a hornblende tonalite sheet at WD709493	Medium to coarse grained, bluish-white rock similar to **97-373**, but dominated by steel grey plagioclase laths (3-5 mm). Alkali feldspar forms glassy rectangular phenocrysts (to ~15 mm) that contain concentrically-arranged biotite flakes, in addition to quartz and plagioclase grains. Elsewhere, biotite is minor, ragged, and accompanied by small muscovite flakes. Secondary muscovite replaces feldspar in thin section.
	97-376A	Close to contact with hornblende diorite at key locality D	Medium grained, grey rock, with abundant bluish-grey plagioclase laths, conspicuous disseminated biotite and occasional buff, poikilitic alkali feldspar masses, to ~5 mm. Small muscovite plates are conspicuous. In thin section, biotite is darkest brown, and apatite forms stubby prisms to 1 mm.
	97-376B	Close to contact with hornblende diorite at key locality D	Resembles **97-376A**, but with much less alkali feldspar and without muscovite. Contains small clots of interleaved, randomly oriented biotite (2-5 mm).
'Hybrid'	**97-376C**	Mingled with hornblende diorite at key locality D	Grey, fine to medium grained rock, with abundant biotite, as spindly blade-like flakes (1-2 mm) or clotty aggregates (to ~5 mm). Rarely, biotite clots enclose relict hornblende. Plagioclase occurs as small phenocrysts (~3 mm). In thin section, the rock matrix is a mosaic of plagioclase and quartz, the latter being slightly amoeboid. Apatite occurs as both elongate needles and equant granules (0.5 mm).

Table 12.1 contd.

Lithology	*sample*	*Field context*	*Summary description*
Kassingbrook Granodiorite	**97-378-1**	Mingled with hornblende diorite at key locality E	Medium to fine grained, resembles **97-376A**, but with more abundant biotite flakes and less alkali feldspar. Small biotite aggregates (~1-2 mm) appear to be replacing hornblende.
Kassingbrook Granodiorite	**97-378-2**	Adjacent to hornblende diorite at key locality E	Medium grained rock very similar to **97-376A**. Poikilitic masses and interstitial buff alkali feldspar grains are very conspicuous. Biotite flakes are ragged in thin section and extensively replaced by chlorite and epidote.
hornblende-rich phase	**97-274**	Occurs as wispy areas sheathing hornblende diorite globules at key locality E	Fine to medium grained, grey coloured and weakly porphyritic, with blocky phenocrysts of greenish plagioclase (1-2 mm), clots of hornblende grains (1-2 mm), some with minor interleaved biotite, and occasional quartz ocelli mantled by hornblende crystals. Irregularly-shaped poikilitic masses of alkali feldspar are very conspicuous (1-8 mm). The matrix in thin section comprises hornblende granules (0.5 mm; α=pale green, β=khaki, γ=blue green), usually clumped in small aggregates, elongate biotite flakes (0.5 mm; α=pale tan, β=γ= chocolate brown), subhedral plagioclase laths and quartz, with all minerals enveloped by alkali feldspar. Apatite needles are abundant. Plagioclase phenocrysts have large euhedral cores overgrown by sodic rims that are embayed by groundmass quartz.
Coolami Granodiorite	**97-308B**	Intermingled with Kassingbrook Granodiorite	Characterised by abundant tabular phenocrysts of alkali feldspar (up to 3 cm) in a medium to coarse grained, plagioclase dominated matrix with non-aligned biotite and accessory pyrite. In thin section, alkali feldspar phenocrysts (simply twinned microcline) exhibit weak zoning and are crowded with euhedral plagioclase crystals and lesser biotite grains (α=pale tan, β=γ=reddish brown), oriented parallel to growth surfaces in the phenocryst. Microcline phenocrysts have moulded outlines around matrix quartz and plagioclase, with the latter having myrmekitic lobes where projecting into the microcline mass. Larger subhedral plagioclase laths in the rock matrix (up to 4 mm, most ~1.5-2 mm) are intimately intergrown and exhibit strong oscillatory zoning, characterised by complex resorptions and enclosure of small, irregularly-shaped plagioclase grains. Interstices between blocky plagioclase laths are occupied by blebs of alkali feldspar. Biotite occurs as aggregates of 3-6 small flakes (0.5 mm), many of which are replaced by chlorite.

Lithology	*Sample number*	*Grid reference*	*Modal Percentage*						*Accessory Minerals*
		(WD)	Quartz	Plagioclase	K-Feldspar	Biotite	Hornbl.	Musc.	
Kassingbrook Granodiorite									
'typical' phase	**97-373**	709490	29.7	44.7	20.6	2.6	0	1.3	c, e, py
	97-309A-2	707484	44.9	45.4	5.6	2.7	0	0.3	a, c, ca, e
	97-376A	707484	31.2	40.6	22.6	4.4	0	0.2	a, c
	97-376B	707482	30.7	59.2	2.9	6.3	0	0.1*	a, c, e
	97-378-2	707482	28.9	40.3	25.8	3.8	0	0.1*	a, all, c, e
'hybrid'	**97-376C**	707484	28.3	53.9	0.1	16.2	0.1	0	a, e, py, z
'hybrid'	**97-274**	707482	20.4	46.5	6.7	11.8	14.2	0	ca, o, t
Coolami Granodiorite	**97-308**	710493	31.5	53.2	8.1	6.6	0	0	a, c, cp, e

Table 12.2. Mineralogy of Kassingbrook type granitic rocks of the GRC, determined by thin section point count (2500 points) (* indicates subsolidus origin). Note that the mineral proportions of 'hybrid' **97-274** are very similar to those of tonalitic dyke **97-278-2** in Table 12.3.

Abbreviations are: a = apatite; all = allanite; c = chlorite; ca = carbonate; cp = chalcopyrite; e = epidote; py = pyrite; o = opaque mineral; t = titanite; z = zircon.

Lithology	*Sample number*	*Grid reference*	*Modal Percentage*						*Accessory Minerals*
		(WD)	Quartz	Plagioclase	K-Feldspar	Hornblende	Clinopx.	Biotite	
Hbl. gabbro-diorite	**97-319**	708505	4.0	7.0	0.5	81.6	2.6	3.6	a, cp, py, t
	97-320C	708505	3.4	10.6	0	62.4	21.3	1.5	a, cp, py, t
	97-320A	708504	4.3	19.8	2.1	67.7	5.6	0	a, o, t
	97-373A	700489	4.9	9.4	0.1	71.5	0	13.4	a, c, o
	97-377	707483	10.6	24.3	0	52.3	1.0	10.8	a,o
	97-62	707477	11.5	25.8	3.1	55.8	1.9	0	a, c, e, o, t
	97-233B	728435	7.6	29.2	0	60.3	0	0	a, c, e, o, t
	97-244	720431	4.4	21.6	3.0	57.8	12.1	0	a, c, o, t
Hornblende diorite	**97-376**	707485	11.9	33.7	0	45.1	0	8.0	a, c, e
	97-378-3	707481	15.0	43.9	0.2	34.2	0	2.3	a, all, c, e, t
	97-378-4	707482	13.4	28.0	0	58.3	acc	0	a, c, ca
	97-380	709479	14.1	27.6	0	58.0	0	12.4	a, c, o
	97-236B	727435	8.3	34.5	0	44.2	0	12.4	a, c, e
Tonalite dykes	**97-278-2**	708485	18.5	52.3	1.4	15.6	0	11.7	a, c, py
	97-309	709493	21.9	44.1	1.8	13.1	0	18.5	a, all, o
'Spotted' micrgranular enclaves	**97-254B**	727434	19.2	47.0	0.1	0	0	33.4	a, ca

Table 12.3. Modal mineralogy of hornblende-bearing rocks from Chin Chap Creek and Robson Creek, as determined by thin section point count (2500 points) (acc = accessory abundance). Note that 'hornblende' also includes actinolitic amphibole in the sample.

Abbreviations are: a = apatite; all = allanite; c = chlorite; ca = carbonate; cp = chalcopyrite; e = epidote; o = opaque mineral; p = pyrite; t = titanite.

Table 12.4. Summary petrograpic and field aspects of hornblende-rich igneous rocks of Chin Chap Creek. The modal mineralogy of all samples is documented in Table 12.3 (Kbk = Kassingbrook).

Lithology	*sample*	*Field context*	*Summary description*
Hornblende gabbro-diorite	**97-319**	Northern part of pod at key locality A	Weathered surfaces exhibit a coarsely pitted or sponge-like aspect due to preferential dissolution of amphibole phenocrysts. Dark greenish-grey with abundant blocky hornblende prisms (~5-8 mm) set in a matrix of finer, pale blue-green amphibole (actinolite), greenish clinopyroxene granules (0.5 mm), and sparse interstitial patches of plagioclase and quartz (grains up to 3x3 mm). Amphibole phenocrysts are closely packed, in places with triple junctions, imparting a cumulate-like aspect. They also contain obvious ragged-shaped and slightly darker central parts in handspecimen, and in thin section comprise irregular to euhedral-equidimensional, finely striated brownish hornblende cores, thinly enveloped (and partially replaced) by pale green actinolite, providing the euhedral crystal outline; both core and rim are in optical continuity. The brownish hornblende commonly encloses ragged clinopyroxene grains, which themselves have actinolitic 'haloes', and also contains numerous irregular titanite blebs and spindly blades of pale biotite (α=palest tan, β=γ=light orange-brown) where replaced by actinolite. Matrix actinolite is the same colour as the phenocryst rims (α=pale green, β= grass green, γ=blue green) but simply twinned and tends to be more elongate. With small euhedral clinopyroxene crystals, these are commonly embedded in intercumulus masses of weakly zoned plagioclase and quartz. Chalcopyrite and pyrite grains (0.25-0.5 mm) are scattered throughout, with slender apatite prisms. Occasionally, masses of quartz, with minor plagioclase and alkali feldspar, form elongate cm-sized lenses surrounded by selvedges of inwards-projecting clinopyroxene crystals (1-1.5mm).
Hornblende gabbro-diorite	**97-320C**	Central part of pod at key locality A	Similar to **97-319** but matrix clinopyroxene is larger (to ~1.5mm, elongate) and more abundant, forming dense aggregates in the regions between hornblende phenocrysts, and encircling rare and inclusion-free plagioclase masses (1.5 mm). Specimens have a more greenish tinge as a result of the higher clinopyroxene content and lower proportion of amphibole phenocrysts. In thin section, the centres of many clinopyroxene grains are partially repaced by very fine actinolite flakes.
Hornblende gabbro-diorite	**97-320A**	Southern part of pod at key locality A	Olive-green coloured, fine to medium grained, and dominated by amphibole (0.6-1 mm), though felsic minerals are more abundant; quartz grains and irregular poikilitic orthoclase masses (to 4 mm across) are conspicuous. In thin section, the blocky amphibole prisms, with brownish hornblende cores enclosing relict clinopyroxene, are still evident but smaller in size (0.8-1mm), and subordinate to elongate actinolite crystals. Both are enclosed by poikilitic plagioclase plates (to 2 mm long) and project into interstitial granules of quartz and orthoclase. Also evident are larger ovoid or more irregularly-shaped 'pools' of coarser orthoclase (to 4 mm), quartz (1-2 mm) and plagioclase (1-2 mm) that are fringed by clinopyroxene crystals (0.5 mm); quartz and orthoclase commonly exhibit coarse granophryic intergrowths. These felsic 'ocelli' also generally enclose euhedral crystals of hornblende, clinopyroxene and squat apatite granules.

Table 12.4. contd next page

Table 12.4 contd.

Lithology	*sample*	*Field context*	*Summary description*
Hybrid gabbro-diorite	**98-61**	Immediately adjacent to the contact with Kassingbrook Granodiorite at key locality A	More felsic than **97-320C** and contains conspicuous quartz-orthoclase ocelli, rimmed by clinopyroxene and further surrounded by a selvedge of hornblende. A striking texture is apparent in thin section, where aggregates and prisms of hornblende are interspersed with masses of granophyric quartz and alkali feldspar (1-3mm across) and large vermicular intergrowths of plagioclase and quartz (1-3mm across). Elsewhere plagioclase occurs as lath-like grains perforated by tiny quartz blebs. Granophyre is contiguous with poikilitic grains of alkali feldspar, enclosing hornblende and rare clinopyroxene euhedra. Acicular apatite prisms are very numerous (see Figure 12.4).
Hornblende gabbro-diorite	**97-373A**	Sheet near key locality B	Contains less large amphibole crystals relative to **97-319** and lacks clinopyroxene, but has more abundant interstitial masses of plagioclase and grains of quartz. Pale orange biotite is also more prominent, occuring as sheaves of radiating fibrous grains in the rock matrix, as well as spindly flakes in the centre of hornblende prisms. In contrast to **97-319**, hornblende phenocrysts contain no titanite granules, but instead cores have diffuse concentrations of ultra-fine opaque grains. Matrix is dominated by actinolite.
Hornblende gabbro-diorite	**97-377**	Central part of diorite at key locality D	Most felsic gabbro-diorite. Dark greenish-grey, weakly porphyritic, where sparse blocky hornblende phenocrysts occur in a finer groundmass of hornblende, biotite, quartz, and plagioclase. Replacement of hornblende prisms by small plates and clotty sheaves of orange-brown biotite (0.5-0.8 mm) is advanced, masking the brownish hornblende cores. Biotite also occurs as disseminated flakes. The felsic matrix of the rock is more voluminous, and comprises coarser grained, mutually polygonal plagioclase and quartz (0.5-1 mm). Although poikilitic interstitial masses of plagioclase (to 3.5 mm) occur, rare lath-shaped grains are also evident. Apatite needles are abundant, and no clinopyroxene occurs.
Hornblende gabbro-diorite	**98-62**	5m wide sheet within musc -garnet adamellite in southern Chin Chap Ck.	Similar to **97-320C** but with more quartz and plagioclase and no biotite. Plagioclase and alkali feldspar form large, strikingly poikilitic plates (to 6mm across) or interstitial grains enclosing numerous small euhedral hornblende grains. This rock also has irregularly-shaped felsic domains (3-5 mm across) of anhedral quartz, plagioclase and alkali feldspar, generally enclosing or fringed by concentrations of small clinopyroxene grains, imparting a greenish aspect in handspecimen. Irregularly-shaped titanite (0.6 mm) and epidote grains are rare accessories.

Table 12.4. contd next page

Lithology	*sample*	*Field context*	*Summary description*
Hornblende diorite	97-366	200m wide tract in a western tributary of Chin Chap Ck. Sharply borders Kassingbrook Granodiorite (east) & Coolami Granodiorite (west).	Some internal heterogeneity exists, but typical samples are medium to coarse grained, and contain large anhedral hornblende grains (3-6 mm) that are extensively replaced by aggregates of tiny biotite plates, imparting a 'ragged' aspect in handspecimen. Also evident are rounded ocelli of quartz with fine hornblende rims (2-4 mm), and, unlike other dioritic rocks, chalky phenocrysts of plagioclase (laths to 3 mm) and red-brown titanite rhombs (to 1.5mm). In thin section, large blocky hornblende grains contain brownish areas with fine striations and rarely relict clinopyroxene. In addition to numerous biotite flakes, hornblende prisms are also commonly perforated by tiny titanite blebs. Plagioclase phenocrysts are extensively replaced by sericite, and contain euhedral blocky cores overgrown by strongly zoned rims that partially enclose small hornblende grains. As with other dioritic rocks, the matrix of the rock comprises smaller hornblende blades (0.5-1.5 mm, sometimes clumped into aggregates 3-5 mm across), quartz (~0.5-1 mm) and irregular masses of poikilitic plagioclase (1-1.5 mm).
Hornblende diorite	**97-380**	5m wide sheet-intermingled with Kbk Granodiorite in southern Chin Chap Ck.	Fine to medium grained, dark grey, homogeneous and hornblende-rich but contains conspicuous hornblende-rimmed quartz ocelli (2-3 mm) encircled by small hornblende grains. In thin section, quartz comprises single grains with strongly undulose extinction and commonly hosts small rhombs of titanite. Hornblende (α=pale green, β=khaki green, γ=bluish green) occurs as blocky prisms (1.5 mm) or euhedral blades (1-3 mm), set in an anhedral mosaic of poikilitic plagioclase and quartz, both of which enclose small hornblende crystals and apatite needles. Irregular striated brownish patches and cloudy concentrations of fine opaques are evident in the centres of larger hornblende grains.
Hornblende diorite	**97-376**	Northern part of diorite body at key locality D	Fine- to medium grained, medium grey coloured and homogeneous, with sparse chalky phenocrysts of plagioclase (2 mm); more rarely, single rounded quartz grains (~2-3 mm) rimmed by hornblende crystals are observed. Hornblende is predominant, and in thin section tends to occur as clumps of bladed crystals (1-1.5 mm) intergrown with numerous flakes (0.5-1.5 mm) or clots of biotite (1-2mm; α=pale tan, β=γ=reddish-brown). Small subhedral granules of epidote are occasionally present in hornblende-biotite aggregates. Plagioclase occurs either as interlocking subhedral laths (1-1.5mm) that have seritisised cores overgrown by continuously zoned rims, or anhedral masses interstitial to hornblende and enclosing small hornblende crystals. Grains of quartz (0.5 mm) are prominently disseminated.
Hornblende diorite	**97-378-4**	Southern part of diorite body at key locality E	Medium, even grained, dominated by squat hornblende prisms (1-2 mm), which are commonly clumped and form the framework of the rock, with lesser plagioclase grains (~1 mm) and irregularly-shaped felsic domains (3-8 mm). In thin section, many hornblende prisms have lighter central parts perforated with quartz blebs, anhedral titanite grains and (rarely) relict clinopyroxene. Hornblende is partly replaced by dark brown biotite, which also occurs as clusters of coarse ragged flakes intergrown with hornblende clumps. Plagioclase masses are vaguely elongate and interstitial to hornblende and biotite, commonly enclosing the former. They have euhedral cores and thin, continuously zoned rims. In large felsic domains, plagioclase is intimately intergrown with quartz, both minerals enclosing long, branching apatite needles (to ~1.5 mm). Irregularly shaped interstitial quartz grains (0.5 mm) are also scattered throughout the rock.

Table 12.4. contd next page

Table 12.4 contd.

Lithology	*sample*	*Field context*	*Summary description*
Tonalite	97-278	5m thick sheet at key locality C	Fine to medium grained, light grey rock, with prominent blocky phenocrysts of plagioclase (to 6 mm), acicular hornblende prisms (most ~3 mm), abundant spindly biotite flakes (1-1.5 mm) and ovoid mafic clots (2-4 mm) in a finer grained groundmass. Irregularly shaped poikilitic masses of alkali feldspar (to 6 mm) envelope all phases. In thin section, plagioclase phenocrysts have large euhedral cores, enveloped by strongly zoned rims which partially enclose matrix biotite and hornblende. Hornblende prims are anhedral (α=pale yellow-green, β=khaki, γ=blue-green) and partially replaced by dark brown biotite. Mafic clots consist of intergrown aggregates of fine grained hornblende and biotite. The matrix of the rock is a mosaic of quartz (1-1.5 mm) and subhedral to euhedral plagioclase laths, through which are scattered smaller biotite flakes (0.5-1 mm), euhedral hornblende granules (0.5 mm), and apatite needles, all of which are enclosed by interstitial alkali feldspar. Groundmass hornblende and biotite exhibit crystal faces against plagioclase.
microgranular enclave	97-278	Hosted by hbl tonalite sheet (97-278) at key locality C	Contains sparse plagioclase phenocrysts (1-2 mm), elongate hornblende prisms, bladed biotite flakes (~1-1.5 mm) and ovoid hornblende-biotite clots (2-3 mm) encased in a finer, more hornblende-rich matrix. Biotite flakes have irregular outlines, partly moulded around matrix plagioclase grains, whereas plagioclase phenocrysts have euhedral cores and anhedral mantles. All minerals are spectacularly enclosed by a poikilomosaic of alkali feldspar and irregular quartz 'oikocrysts' (to ~1 cm), within which groundmass plagioclase grains have elongate, euhedral to skeletal shapes, and acicular apatite are abundant. Variants are more even-grained but the poikilitic microstructure is ubiquitous.
Tonalite	**97-309-1**	10m wide sheet in Kbk Granodiorite (near key locality B)	Has plagioclase phenocrysts (1.5-2.5 mm) and globular, hornblende-rimmed quartz grains (3-4 mm) occurring in a fine grained, medium grey coloured matrix. The latter comprises dark brown biotite, hornblende, plagioclase laths and abundant interstitial and poikilitic quartz in thin section. Matrix biotite and hornblende grains are included in the anhedral rims of plagioclase phenocrysts, and commonly form small clotty aggregates (1-2 mm). Enclaves of more hornblende-rich dioritic material are densely clustered throughout this lithology. Sample **97-309** from the same body is similar, but has more matrix quartz.
microgranular enclave	97-274a-2	Contained by Kassingbrook type hybrid **97-274**	Has blocky plagioclase phenocrysts (1.5-3 mm) and ovoid to rectangular mafic clots in a fine to very fine grained, dark grey matrix. Small hornblende-ocellar quartz grains are also present. The matrix contains hornblende (some grains very elongate), red-brown biotite (commonly ragged and spindly), subhedral-anhedral plagioclase and equant quartz, all in places enveloped by large alkali feldspar masses (to 1 cm). Poikilitic quartz grains (5-6 mm) also occur. Plagioclase phenocrysts have euhedral, sometimes oscillatory-zoned cores, mantled by unzoned rims that are anhedral against groundmass minerals; some matrix plagioclase laths also have euhedral cores. Mafic clots are dense concentrations of tiny hornblende granules and biotite flakes. Apatite has pronounced acicular morphology.

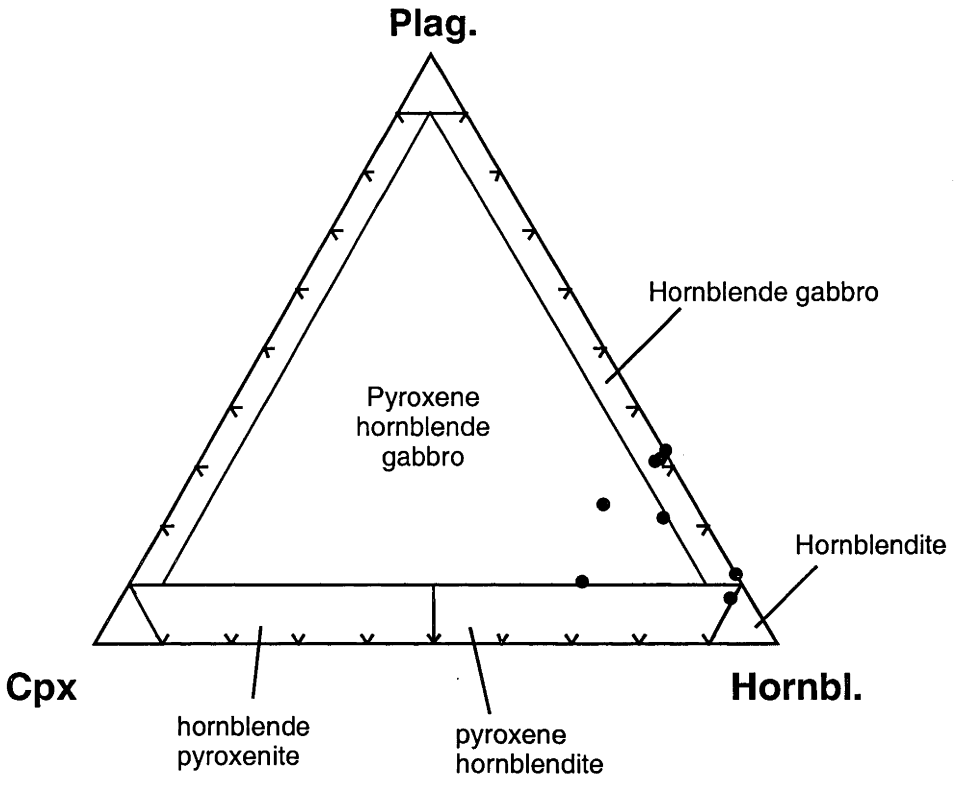

Figure 12.2. Modal mineralogy of Chin Chap Creek gabbro-diorites in terms of plagioclase, clinopyroxene (cpx) and hornblende content. Lithological fields are after Le Maitre (1989).

The gabbro-diorite is the northernmost occurrence of hornblende-bearing rocks in Chin Chap Creek and outcrops prominently as rounded boulders on the east bank of the watercourse. The contact with muscovite leucogranite and migmatite to the north is sharp, however, the boundary with Kassingbrook Granodiorite to the south is more complex, and involves a dramatic change in the nature of the mafic lithology. Samples from the northern part of the mafic body are dark greenish-grey, dominated by coarse, blocky hornblende prisms, and exhibit distinctive, cumulate-like textures (e.g. **97-319**, Table 12.4; see Figure 12.3). Other variants have little or no plagioclase, being essentially hornblendites, or contain higher proportions of matrix clinopyroxene (e.g. **97-320C**). Textural relationships suggest formation of coarse hornblende prisms by high temperature magmatic replacement of early-formed clinopyroxene phenocrysts, accounting for the blocky grainshape. Hornblende was subsequently mantled by actinolite as temperatures waned, though euhedral contacts against (and enclosure by) interstitial plagioclase (Figure 12.3d) suggests that this was also magmatically precipitated. Replacement of the central parts of the hornblende prisms by actinolite and pale biotite may have also occurred at the late magmatic or subsolidus stage. In any case, this process was probably responsible for the formation of titanite blebs, as actinolite is Ti-deficient compared to the brownish hornblende it replaces (see Figure 14.5).

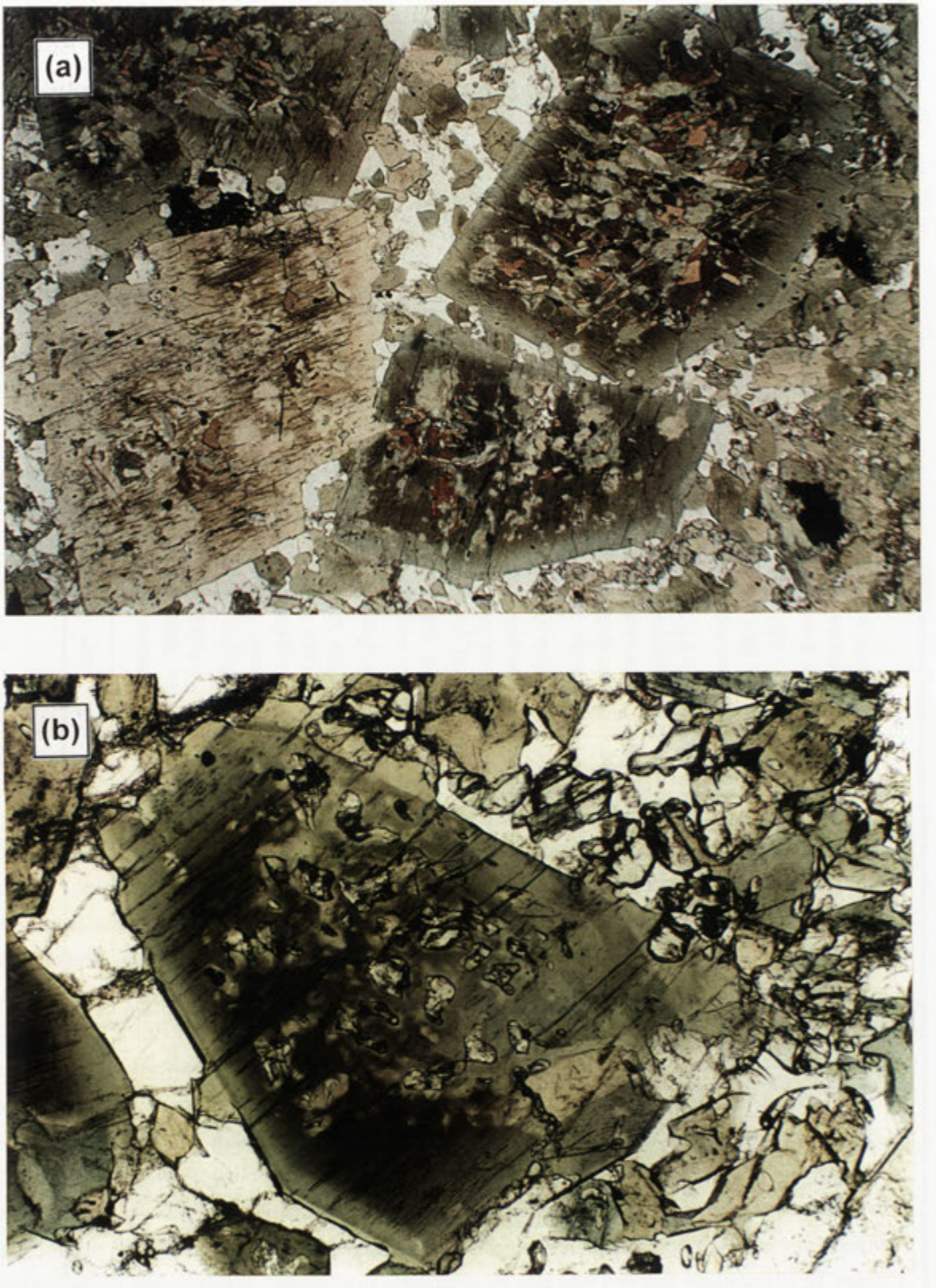

Figure 12.3. Hornblende gabbro-diorites in thin section. (a) Blocky hornblende phenocrysts, partially replaced by pale biotite, in a matrix of plagioclase, clinopyroxene and smaller hornblende grains. Note the lighter margins of hornblende phenocrysts, which are euhedral against plagioclase (plane polarised light, 8.1 mm across). Opaques are pyrite and chalcopyrite. (b) Closer view of a hornblende phenocryst, enclosing small pyroxene and titanite blebs (almost opaque), and matrix clinopyroxene (high relief pale greenish grains) (plane polarised light, 2.5 mm across).

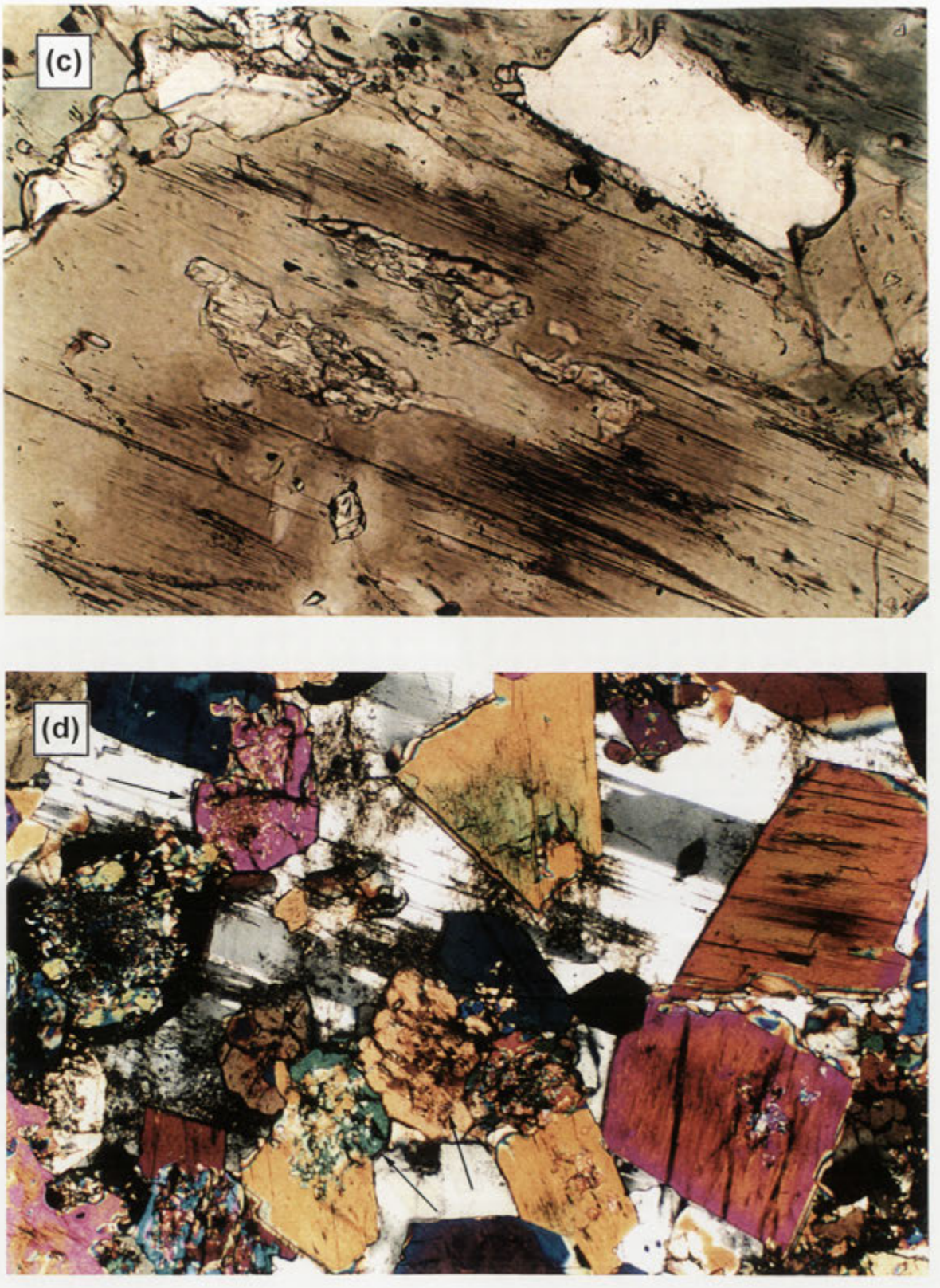

Figure 12.3 contd. Hornblende gabbro-diorites in thin section. (c) Relict clinopyroxene inside hornblende phenocryst (plane polarised light, 1.8 mm across). (d) Hornblende and clinopyroxene (arrowed) prisms enclosed by 'intercumulus' plagioclase (crossed polars, 8.1 mm across).

The gabbro-diorite becomes finer grained towards the southern periphery such that hornblende phenocrysts and the cumulate-like texture are much less apparent (e.g. **97-320A**, Table 12.4). Felsic minerals are also more abundant, including poikilitic orthoclase masses, and form ovoid or more irregularly-shaped 'ocelli', fringed by small clinopyroxene crystals. Quartz-orthoclase ocelli with clinopyroxene-hornblende selvedges are most conspicuous in samples immediately adjacent the contact with Kassingbrook Granodiorite (e.g. **98-61**), which have striking vermicular intergrowths among groundmass felsic minerals (Figure 12.4). This marginal phase of the gabbro-diorite is transected by thin leucogranitic sheets (5-20 cm wide, e.g. **97-320B**) and encloses lenticular pegmatitic domains (2-10 cm long) containing skeletal hornblende crystals (to 8 cm), probably representing fluid-rich pockets within the gabbroic body.

The actual contact with Kassingbrook Granodiorite is sharp, but nevertheless numerous angular to irregularly-shaped enclaves (to 60 cm long) of the distinctive ocellar-textured gabbro-diorite variant are strewn throughout the adjacent granodiorite. These commonly have gradational boundaries and are in various stages of digestion (Figure 12.5a); clots of hornblende (1-5 cm) are spalled from the enclaves and dispersed through the granodiorite host, where they are fringed and partially replaced by biotite. Quartz ocelli, with clinopyroxene rims mantled in turn by hornblende, are also conspicuous in the granodiorite near here. Both hornblende clots and 'gabbroic' enclaves in the granodiorite are concentrated within ~250 m of the gabbro-diorite pod. As most enclaves are angular, they have probably been incorporated as solid or crystal-rich fragments during the emplacement of the granodiorite.

Apart from mafic clots, in this vicinity the Kassingbrook Granodiorite is quite different from 'typical' samples, being strongly porphyritic, with abundant euhedral alkali feldspar phenocrysts (Figure 12.5b). These are erratically distributed, with some outcrops containing up to 30% phenocrysts, and others nearby only having one or two. A coarse grained and muscovite-rich leucogranitic rock is also irregularly interspersed throughout granodiorite exposures, in places forming 5 m wide areas; the relationship between the two granitic phases is not clear, but they are complexly intermingled. Both the porphyritic Kassingbrook Granodiorite and muscovite granite enclose rafts of layered gneiss, quartzofeldspathic schist and M_2 stromatic migmatite (up to 3 m^2 slabs). These are aligned with a conspicuous planar fabric, defined by micaceous clots, schlieren and elongate mica-rich enclaves.

Gabbroic and metasedimentary enclaves at this locality are accompanied by mafic microgranular enclaves, that are wrapped by the schlieric fabric of the host granodiorite (Figure 12.5b). Most of these are fine grained, biotite-rich, globular to elliptical objects (5-60 cm) with plagioclase and occasional quartz phenocrysts. Larger, composite enclaves also occur (up to 2 m long). Elongate clots of interleaved biotite (1-5 mm) are conspicuous and impart a 'spotted' aspect, which typifies most microgranular enclaves of the Kassingbrook Granodiorite pluton (see Table 12.5). Similarly distinctive material is developed at the periphery of hornblende diorite sheets where intermingled with the Kassingbrook Granodiorite (see below).

Metasedimentary and biotite-rich microgranular enclaves remain abundant in the Kassingbrook Granodiorite along Chin Chap Creek south of key locality A. The former are mostly

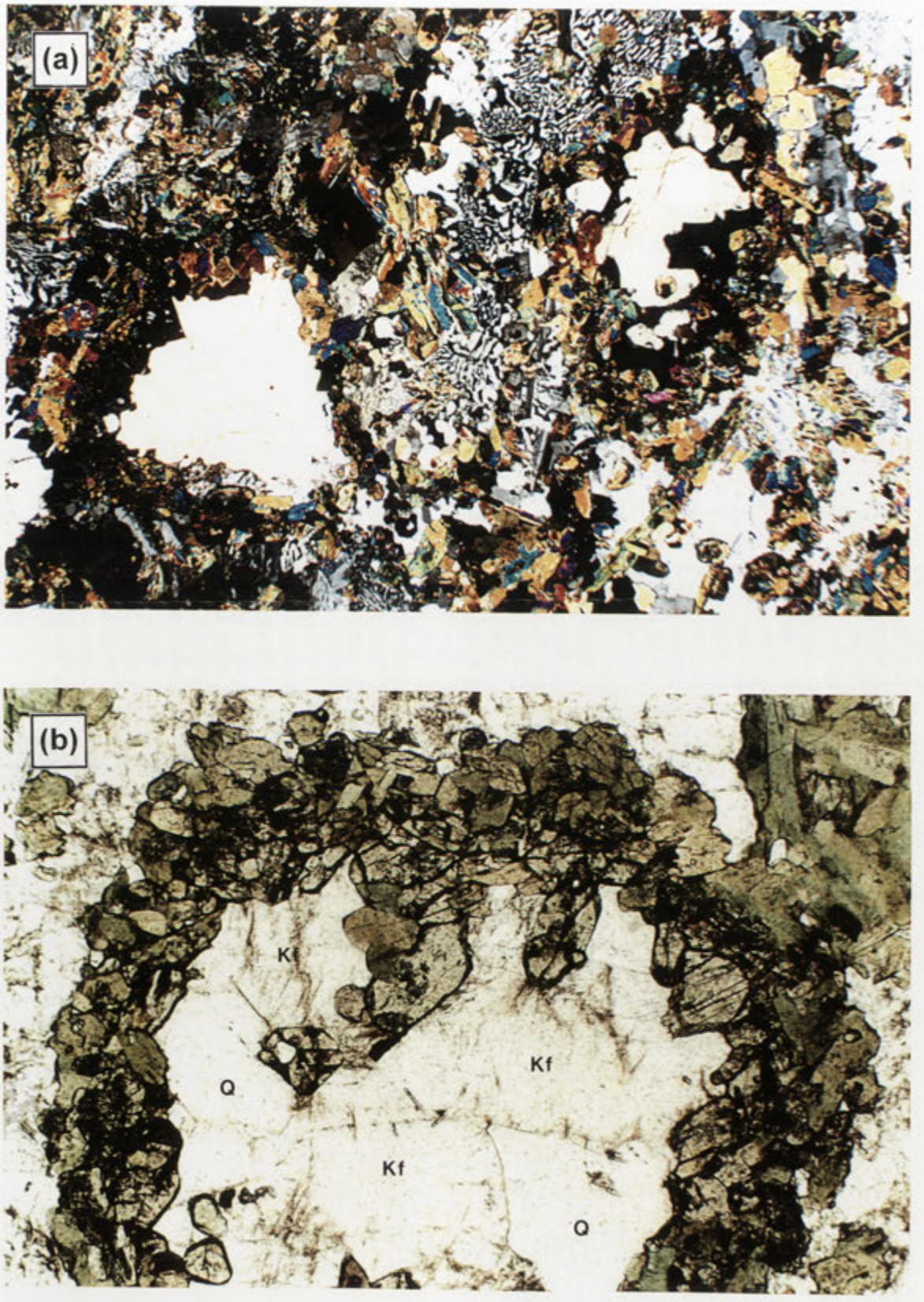

Figure 12.4. Thin section photos of marginal 'hybrid' hornblende gabbro-diorite **98-61** (a) Quartz ocelli, rimmed by mafic minerals, set in a groundmass of hornblende, pyroxene and strikingly intergrown plagioclase, quartz and K-feldspar (crossed polars, 8.1 mm across). (b) Quartz (Q)-alkali feldspar (Kf) ocelli fringed by clinopyroxene (pale green), in turn rimmed by green hornblende (plane polarised light, 2.5 mm across).

Figure 12.5. (a) Partially disaggregated enclaves of the marginal gabbro-diorite in Kassingbrook Granodiorite (Chin Chap Creek, WD708504). (b) Strongly porphyritic Kassingbrook Granodiorite exposure (phenocrysts are alkali feldspar) containing elongate microgranular enclaves (Chin Chap Creek, WD708503).

quartzofeldspathic gneiss and stromatic migmatite slabs (to 6 m long) that are partially disaggregated into micaceous selvedges and schlieren. Kassingbrook Granodiorite outcrops are heterogeneous on a decimetre scale with regard to grainsize, content of muscovite and distribution of alkali feldspar phenocrysts. Some portions are significantly more mafic and retain a clotted aspect, with aggregates of non-aligned biotite (2-7 mm across) abundantly dispersed throughout. These may be recrystallised remnants of the hornblendic clots prominent near the contact with the gabbro-diorite body.

12.3.2 Key locality B: central Chin Chap Creek

Metasedimentary rocks constitute a 15-20 m wide raft within Kassingbrook Granodiorite at this locality, comprising interlayered migmatitic quartzofeldspathic gneiss, quartzofeldspathic schist and sheets (5-50 cm wide) of leucocratic muscovite-rich adamellite (see section 5.6). The raft is aligned with a pronounced and regular schlieric layering in the host granodiorite, where both fabrics parallel the regional trend of S_2. The schlieric layering in Kassingbrook Granodiorite adjacent to the metasedimentary raft is augmented by quartzofeldspathic schist 'screens' and numerous micaceous enclaves (Figure 12.6a). The granodiorite has less biotite and more abundant muscovite (to ~5%) in this vicinity compared with 'typical' samples, resembling Harrow type granitic rocks.

Just north of the large metasedimentary raft, schlieric Kassingbrook Granodiorite exposures are complexly interspersed with Coolami Granodiorite. This forms a 2 m wide sheet, but has irregular off-shoots and forms diffuse isolated domains within the Kassingbrook Granodiorite, suggesting some intermingling.

Mafic microgranular enclaves are also sparsely distributed through Kassingbrook Granodiorite outcrops at key locality B, being enveloped by micaceous schlieren. These are small (3-12 cm), elliptical or irregularly-shaped objects resembling those at key locality A (Figure 12.6b). Larger, elongate microgranular enclaves also form 'trains' across some outcrops, parallel to the pronounced schlieric layering.

12.3.3 Key locality C: southern Chin Chap Creek

The content of muscovite decreases in the Kassingbrook Granodiorite south of key locality B, together with intermixed metasedimentary material, but mafic microgranular enclaves become more prominent, rarely forming clusters of 7 or 8 enclaves. At key locality C, Kassingbrook Granodiorite also encloses a 5 m wide sheet of mafic, 'spindly-textured' tonalite (sample 97-278, Table 12.4, Figure 12.7), which hosts numerous hornblende-rich enclaves (elliptical, 5-12 cm long; Table 12.5). Enclaves have diffuse or gradational margins and exhibit the 'poikilomosaic texture' that characterises microgranular enclaves of the Tuloona Granodiorite (section 11.2.1c). The texture is less evident in other mafic enclaves within the tonalite, though spindly biotite and hornblende grains are ubiquitous.

Adjacent Kassingbrook Granodiorite outcrops contain globules of the mafic tonalite (8-40 cm long), some of which are irregularly shaped and multi-lobate, indicating mingling between the

Figure 12.6. (a) Pronounced schlieric fabric and quartzofeldspathic schist 'screens' in Kassingbrook Granodiorite exposure adjacent to a metasedimentary raft (Chin Chap Creek, WD710492). (b) Microgranular enclave, hosted by Kassingbrook Granodiorite, exhibiting the typical 'spotted' appearance imparted by clots of interleaved biotite ± hornblende. Note the very irregular enclave margin (Chin Chap Creek, WD710491).

two magmas. Hornblende-rich enclaves identical to those in the tonalite sheet are also numerous in the granodiorite (0.5-6 cm), commonly having diffuse margins, from which small fragments have been spalled. Elongate biotite ± hornblende clots (2-8 mm) abundantly dispersed throughout the granodiorite near here reflect this disaggregation process. The Kassingbrook Granodiorite has more biotite at this locality without muscovite.

Similar metre-scale tonalite sheets occur further north in Chin Chap Creek (see Figure 12.1), samples of which exhibit marked textural heterogeneity, involving intimate interspersion of coarser grained 'granitic' material.

12.3.4 Key locality D: southern Chin Chap Creek

This area occurs at the northern margin of a thick hornblende-rich gabbro-diorite to diorite sheet, where it is intermingled with the Kassingbrook Granodiorite (Figure 12.1). Samples from the central parts of the mafic body are dark greenish-grey and have blocky hornblende prisms, resembling the gabbro-diorite at key locality A (sample **97-377**, Table 12.4). However, towards its northern margin, the gabbro-diorite becomes increasingly even grained, involving progressive replacement of hornblende prisms by aggregates of acicular actinolitic hornblende and sheaves of pale biotite (sample **97-376** in Table 12.4). Within 1-2 m of the 'contact', this lithology is transitional to porphyritic 'microgranular' rock, where small plagioclase phenocrysts (1-2 mm) and numerous ovoid to vaguely prismatic clots of interleaved biotite-hornblende (2-5 mm) occur in a finer, biotite-rich groundmass. Apatite needles are also abundant. Intermingling between this 'clotted', microgranular material and the Kassingbrook Granodiorite is extensive, whereby numerous ovoid, elliptical or amoeboid dioritic enclaves (1-60 cm across, lenticular to elliptical in profile) are strewn throughout the granodiorite up to several metres from the contact (Figure 12.8). The main dioritic body also encloses diffuse domains of the granodiorite, elsewhere being complexly 'back-veined' by this material. The scalloped or bulbous margins of the diorite (Figure 12.8b), and the crenulate outline of some enclaves in the Kassingbrook Granodiorite (Figure 12.8c), imply interaction while both lithologies were partially liquid.

Although globules of the peripheral microgranular diorite phase are predominant, enclaves are lithologically variable and range from hornblende-dominated objects through to more felsic, medium grained and 'spindly textured' enclaves resembling the tonalite at key locality C (sample 97-277B, Table 12.5). Some enclaves have sharp, scalloped or cuspate outlines, though irregular 'frayed' margins are more common, where single crystals or aggregates of mafic minerals are detached and entrained by the granodiorite. Enclaves also commonly contain coarser grained pockets of granitic character, indicating small-scale intermingling with the granodioritic host. Significantly, most intermingled enclaves at this locality are texturally identical to the distinctive 'spotted' microgranular enclaves observed elsewhere in the Kassingbrook Granodiorite (compare Figure 12.8d with Figure 12.6b). This suggests that the latter also represent globules of hybridised hornblende diorite, introduced into the Kassingbrook Granodiorite by syn-magmatic mingling.

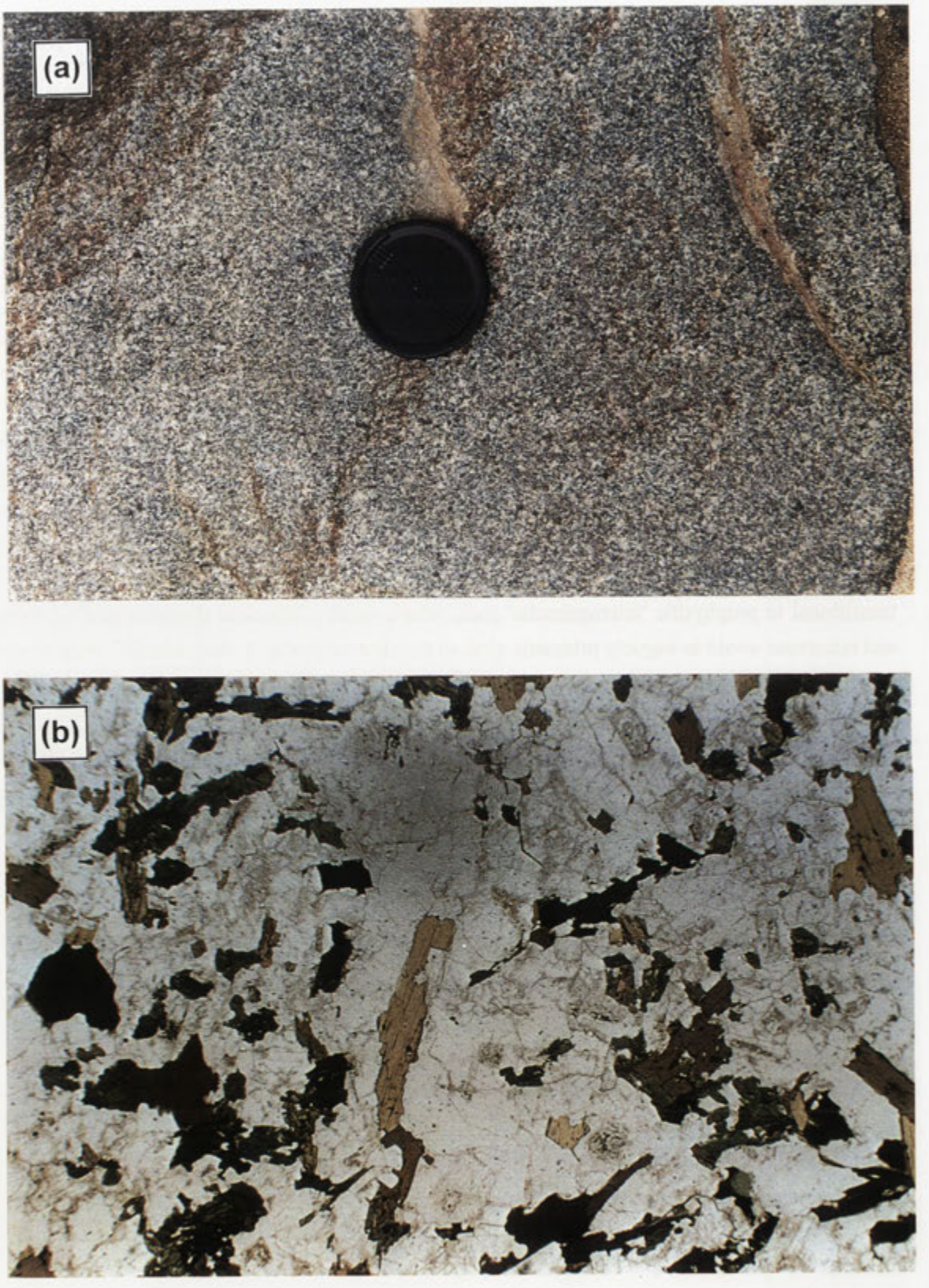

Figure 12.7. Tonalitic sheet at key locality C (WD708485). (a) Outcrop surface. (b) Thin section view, showing elongate, 'spindly' biotite and hornblende grains (top left) (plane polarised light, 8.1 mm across). These morphologies are typically encountered in granitic rocks thought to have formed by magma mixing (e.g. Hibbard 1991).

Table 12.5. Summary petrographic descriptions of mafic enclave samples collected from the Kassingbrook Granodiorite at various localities along Chin Chap Creek. The modal mineralogy of sample **97-378-3** is given by Table 12.3.

Sample	*Locality*	*Type*	*Summary description*	*Remarks*
97-277B	key loc D (felsic)	microgranular	Medium grey coloured, has a distinctive clotted appearance, where interleaved biotite aggregates (1-3.5 mm), together with plagioclase phenocrysts (2-4 mm) and rare quartz masses, occur in a fine grained, biotite-rich matrix. In thin section, the latter comprises subhedral to polygonal plagioclase laths, equant quartz and darkest brown biotite (all ~0.5 mm). Plagioclase phenocrysts are anhedral against groundmass quartz and strongly zoned, with euhedral patchy-zoned cores. Groundmass plagioclase also has small euhedral cores. Pyrite is a rare accessory.	Large globular enclave in the mingling zone. Has diffuse contacts with the host.
97-378-3	key loc E (N)	hbl diorite	Very similar to samples from within the diorite sheet (e.g. **97-378-4**). Medium grained, comprises hornblende prisms (~1 mm) and plagioclase laths (~2 mm, up to 4 mm), with interstitial quartz grains (0.5-2 mm) and rare biotite blades (~2 mm). Anhedral red-brown granules (1-3 mm) are also conspicuous in handspecimen. Hornblende has brownish, striated cores in thin section and is partly replaced by actinolitic hornblende and spindly pale biotite, the latter altered to chlorite. It may form aggregates of several grains, with interstices occupied by irregular titanite masses. Plagioclase laths have oscillatory zoning but are anhedral against hornblende. In places, plagioclase occurs as poikilitic masses interstitial to, and enclosing, hornblende crystals. Many laths have irregular overgrowths that are anhedral against equant quartz. Apatite forms strikingly acicular grains to 1.5 mm.	Large globular enclave near the mingled-granodiorite diorite contact.
97-378-5	key loc E (N)	hbl diorite	Resembles **97-378-3** except that hornblende prisms are more clumped, between which felsic minerals comprise 3-6 mm 'blotchy' domains. Titanite is less conspicuous.	as above
97-274B1	key loc E (S)	microgranular	Light grey, with blocky plagioclase phenocrysts (to ~4 mm) and ovoid biotite clots (2-3 mm) in a microtonalitic matrix (0.5-1 mm) of equant to lath shaped plagioclase, quartz and spindly, pale brown biotite. Some biotite flakes have irregular bladed morphologies up to 3 mm long. Plagioclase phenocrysts have euhedral and oscillatory-zoned cores, some of which are perforated with vermicular quartz blebs, and have irregular contacts against matrix quartz. Matrix plagioclase laths are either subhedral, or also have irregular cuspate margins against quartz. Biotite flakes in mafic clots are densely interwoven, with grain edges lined by concentrations of ultrafine opaques.	From an enclave swarm several metres south of the hornblende diorite at key locality E

Table 12.5 contd next page

Table 12.5 contd

Sample	*Locality*	*Type*	*Summary description*	*Remarks*
97-274B2	key loc E (S)	microgranular	Darker and finer grained enclave, but also has plagioclase phenocrysts (1-2 mm), biotite clots (1-2 mm), some of which have prismatic outlines, and larger biotite flakes (~1 mm) in a biotite dominated matrix. Biotite is an unusual greenish colour in thin section, and clotty aggregates rarely enclose small hornblende granules. The cores of plagioclase phenocrysts contain numerous tiny biotite grains. The matrix has spindly biotite flakes, irregularly shaped plagioclase laths and amoeboid to poikilitic quartz. Apatite needles are common.	From an enclave swarm several metres south of the hornblende diorite at key locality E
97-275E	key loc E (S)	microgranular	Dark grey, approximately even-grained, with small plagioclase laths (0.5 mm), spindly dark-brown biotite flakes, abundant apatite needles and sparse biotite clots (1-2 mm) in a framework of spectacularly poikilitic alkali feldspar (1-8 mm grains). Quartz forms rare polygonal grains between alkali feldspar masses, whereas zoned allanite prisms are conspicuous. Biotite flakes are larger and markedly elongate at periphery, where they are aligned parallel to the enclave margin.	From an enclave swarm several metres south of the hornblende diorite at key locality E

Figure 12.8. Mingling relationships at key locality D (Chin Chap Creek WD707484). (a) Intermingled contact between hornblende diorite dyke and Kassingbrook Granodiorite. (b) Detail of the dyke margin, showing the cuspate nature of the contact and the 'spotted' texture of the peripheral diorite.

Figure 12.8 contd. Mingling relationships at key locality D (Chin Chap Creek WD707484). (c) Globules of the marginal hornblende diorite phase enclosed by Kassingbrook Granodiorite close to the contact. (d) Closer view of a mafic enclave exhibiting the distinctive spotted texture and containing small plagioclase phenocrysts.

Where crowded with mafic enclaves, the Kassingbrook Granodiorite is slightly finer grained than 'typical' samples and lacks muscovite (**97-376A**, **97-376B**, Tables 12.1, 12.2). Biotite is more abundant, generally having an elongate spindly habit with vaguely serrated edges. Clotty aggregates of interleaved biotite, derived by partial disaggregation of microgranular enclaves, are locally numerous and perforated by pyrite grains. In places, granitic rock containing hornblende and abundant blade-like flakes and clotty aggregates of biotite also forms discrete, but irregularly shaped domains (5-30 cm), as represented by **97-376C** (Tables 12.1, 12.2). Alkali feldspar is absent in this rock, whereas apatite occurs as acicular prisms that are similar to those in microgranular enclaves, but unlike the stubby apatite grains of 'typical' Kassingbrook Granodiorite samples. This relatively mafic 'hybrid' tonalite is complexly interspersed with more felsic Kassingbrook Granodiorite, which becomes predominant about two metres from the intermingled diorite contact.

12.3.5 Key locality E: southern Chin Chap Creek

As with the northern margin, the gabbro-diorite sheet described above becomes even-grained towards its southern edge (sample **97-378-4** in Table 12.4), where it is intimately mingled (over ~25 m) with the Kassingbrook Granodiorite (key locality E). The exact nature of the diorite-granodiorite transition is not evident due to limited exposure, but outcrops close to the boundary consist of granodiorite choked with large globules of medium grained hornblende diorite (up to 80 cm across). Thick 'tongues' of dioritic material (1 m across) with irregular protrusions also extend into the granodiorite, some hosting small teardrop-shaped granodiorite bodies (Figure 12.9a). Unlike key locality E, a biotite-rich 'clotted' marginal dioritic phase is not developed at this contact, but does occur further south (below). Hornblende diorite enclaves comprise up to seventy percent of the exposure, and are commonly multi-lobate or amoeboid-shaped (Figure 12.9b,c). They resemble dioritic material from the southern part of the sheet but are coarser grained, with more interstitial quartz and lath-shaped plagioclase (Table 12.5). Sample **97-378-5** also has conspicuous titanite. The margins of these enclaves are diffuse and gradational into Kassingbrook Granodiorite over several centimetres; many also enclose intermingled pockets of granodiorite or are disaggregated into smaller, irregularly shaped objects with frayed, flame-like margins (Figure 12.9d). The adjacent granodiorite is markedly heterogeneous, with vague biotite-rich areas and hornblende-biotite clots that have clearly been entrained from disintegrating dioritic enclaves. Similarly, some dioritic globules have single quartz grains (to 7 mm) that have apparently been introduced from the granodiorite and are now rimmed by selvedges of hornblende; a similar crystal-exchange process may be responsible for the formation of ocelli in other mafic bodies (see below). Clearly, physical and chemical interaction has occurred between Kassingbrook Granodiorite and hornblende diorite at this locality, resulting in distinct petrological changes in each.

Importantly, in places the Kassingbrook Granodiorite is separated from the mafic diorite by hornblende-bearing tonalitic rock (sample **97-274**; Figure 12.10, Tables 12.1, 12.2), which is mineralogically, texturally and geochemically (see section 15.4.2b) very similar to the tonalitic sheets further north in Chin Chap Creek. This 'hybrid' material is largely confined to the

immediate zone of intermingling, where it forms irregular wispy areas (up to 40 cm across) sheathing clustered dioritic globules (see Figure 12.9d), and grades into the heterogeneous Kassingbrook Granodiorite away from the dioritic enclaves. Euhedral cores of plagioclase phenocrysts have overgrowths of up to An_{65}, which is markedly more calcic than plagioclase of other granodiorite samples (section 15.2.1). This lithology also hosts small dark grey enclaves (3-5 cm) with irregular margins that are richer in hornblende and hornblende-biotite clots, but otherwise texturally identical to the host, and contain the same blocky plagioclase phenocrysts (Figure 12.10; Table 12.5). Alkali feldspar 'oikocrysts' (to 1.5 cm) are conspicuous, and in some cases single, optically continuous oikocrysts straddle the interface between enclave and the host. This indicates that crystallisation of alkali feldspar was synchronous in both lithologies, and therefore, that both were partially liquid at the same time.

Several metres south of the intermingled granodiorite-hornblende diorite contact, the Kassingbrook Granodiorite contains swarms of biotite-rich microgranular enclaves like those of key locality E, irregular teardrop morphologies being most common (Figure 12.11a; Table 12.5). In some cases, these are clearly introduced by mingling between the granodiorite and grey dioritic rock, that has the same distinctive clotted texture as the peripheral phase developed at the northern margin of the hornblende diorite sheet. The clotted dioritic material occurs as small areas (1-2 m) irregularly interspersed with granodiorite exposures, against which it has interfingering or strikingly crenulate contacts, consistent with liquid-liquid interaction (Figure 12.11b).

Microgranular enclaves, mafic clots and a slightly biotite-rich character persist in Kassingbrook Granodiorite exposures for ~100 m south of key locality E.

12.3.6 Other areas of mafic-felsic interaction in Chin Chap Creek

Several other less well exposed areas of mafic-felsic interaction are encountered along Chin Chap Creek and tributaries. The most notable occurs towards the centre of the Kassingbrook Granodiorite at WD710489 (Figure 12.1). Here, the granodiorite borders a ~60 m wide tract of heterogeneous hornblende-rich mafic rock which is internally heterogeneous. The northernmost 25 m is hornblende gabbro-diorite with same striking porphyritic-cumulate texture as **97-319**, but minus clinopyroxene (**97-373A**, Table 12.4). The contact between this lithology and Kassingbrook Granodiorite to the north is sharp. However, further south the gabbro-diorite grades into more felsic hornblende diorite with a conspicuous clotted appearance, whereby hornblende phenocrysts are replaced by biotite and actinolitic hornblende. This 'clotted' dioritic lithology becomes progressively lighter coloured and more biotite-rich towards the south and ultimately disintegrates into swarms of enclaves within the Kassingbrook Granodiorite at the southern margin; although variable, enclaves share the distinctive biotite-rich 'spotted' character.

Another area occurs near the southern Kassingbrook Granodiorite margin (WD708479), where granitic exposures contain microgranular enclave clusters and are interspersed with spindly-textured hornblende tonalite (like sample **97-274**) and mafic hornblende diorite (1 m wide band, sample **97-380**, Table 12.4). Importantly, micaceous schlieren and schistose enclaves occur in

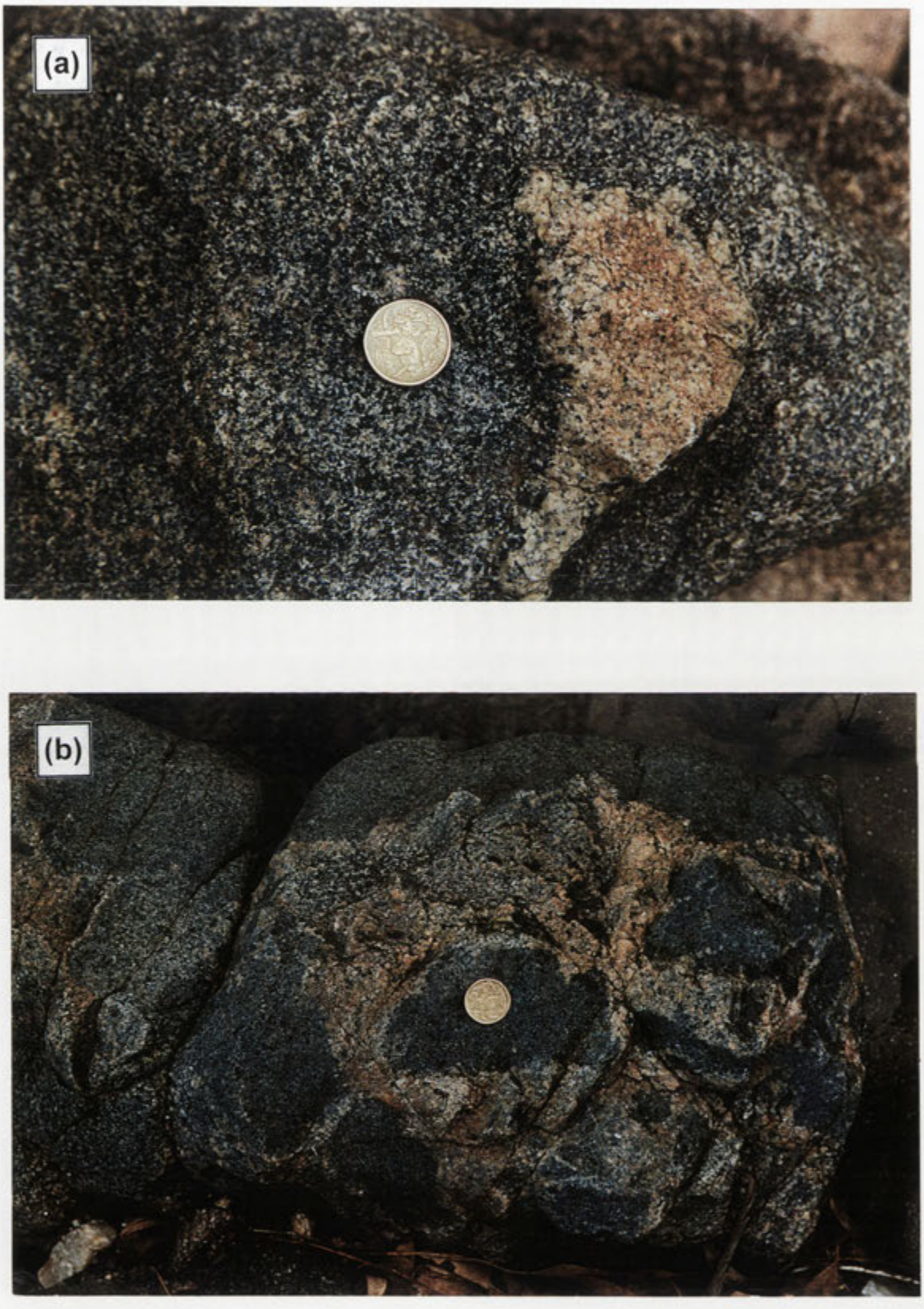

Figure 12.9. Mingling relationships at key locality E (Chin Chap Creek WD707482). (a) Globule of Kassingbrook Granodiorite hosted by hornblende diorite near the intermingled contact between the two lithologies. (b) Cluster of hornblende diorite enclaves within the Kassingbrook Granodiorite. Note the crenulate margins of most enclaves.

Figure 12.9 contd. Mingling relationships at key locality E (Chin Chap Creek WD707482). (c) Tightly packed and irregularly-shaped diorite globules in the granodiorite. (d) Sawn slab, highlighting the diffuse margin of a large hornblende diorite 'pillow', small scale textural heterogeneity in the Kassingbrook Granodiorite, and localised development of an intermediate 'hybrid' tonalitic lithology between dioritic globules (arrowed).

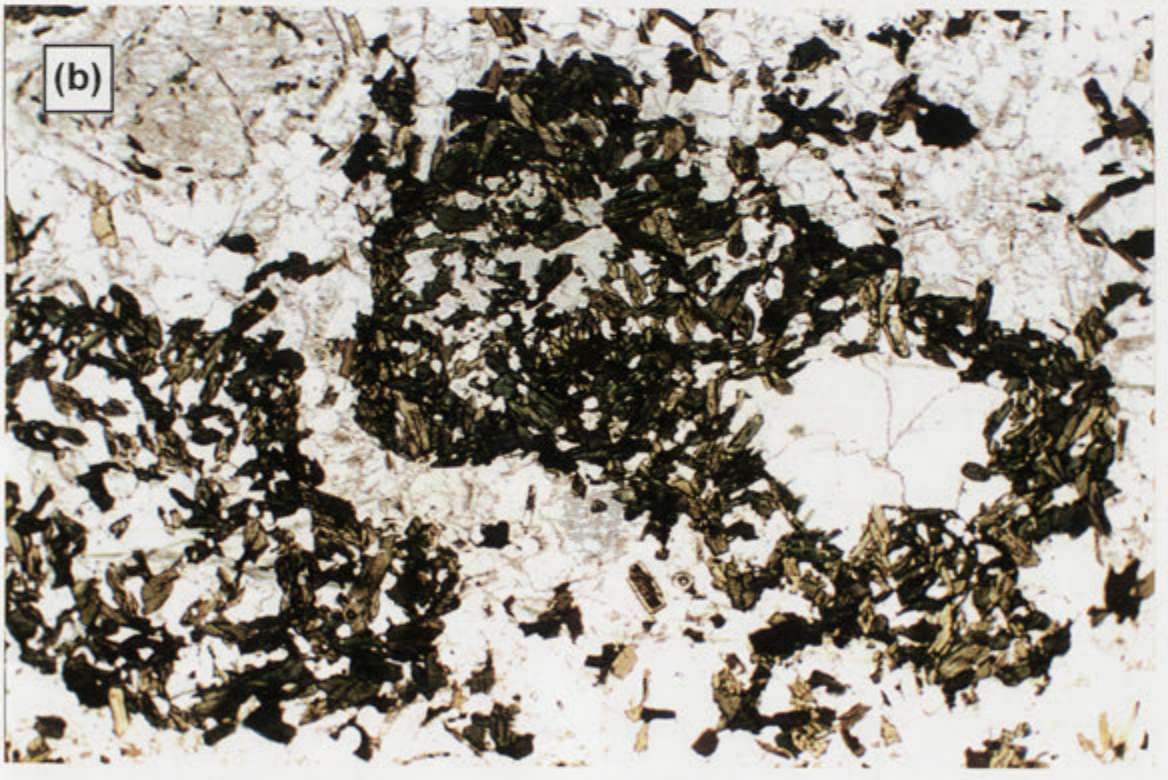

Figure 12.10. Hybrid hornblende tonalite **97-274**. (a) Sawn slab, note the blocky plagioclase phenocrysts and abundant hornblende-rich clots and enclaves, some of the latter also having plagioclase phenocrysts. (b) Thin section photo, showing quartz ocelli rimmed by dense concentrations of small hornblende crystals (plane polarised light, 8.1 mm across).

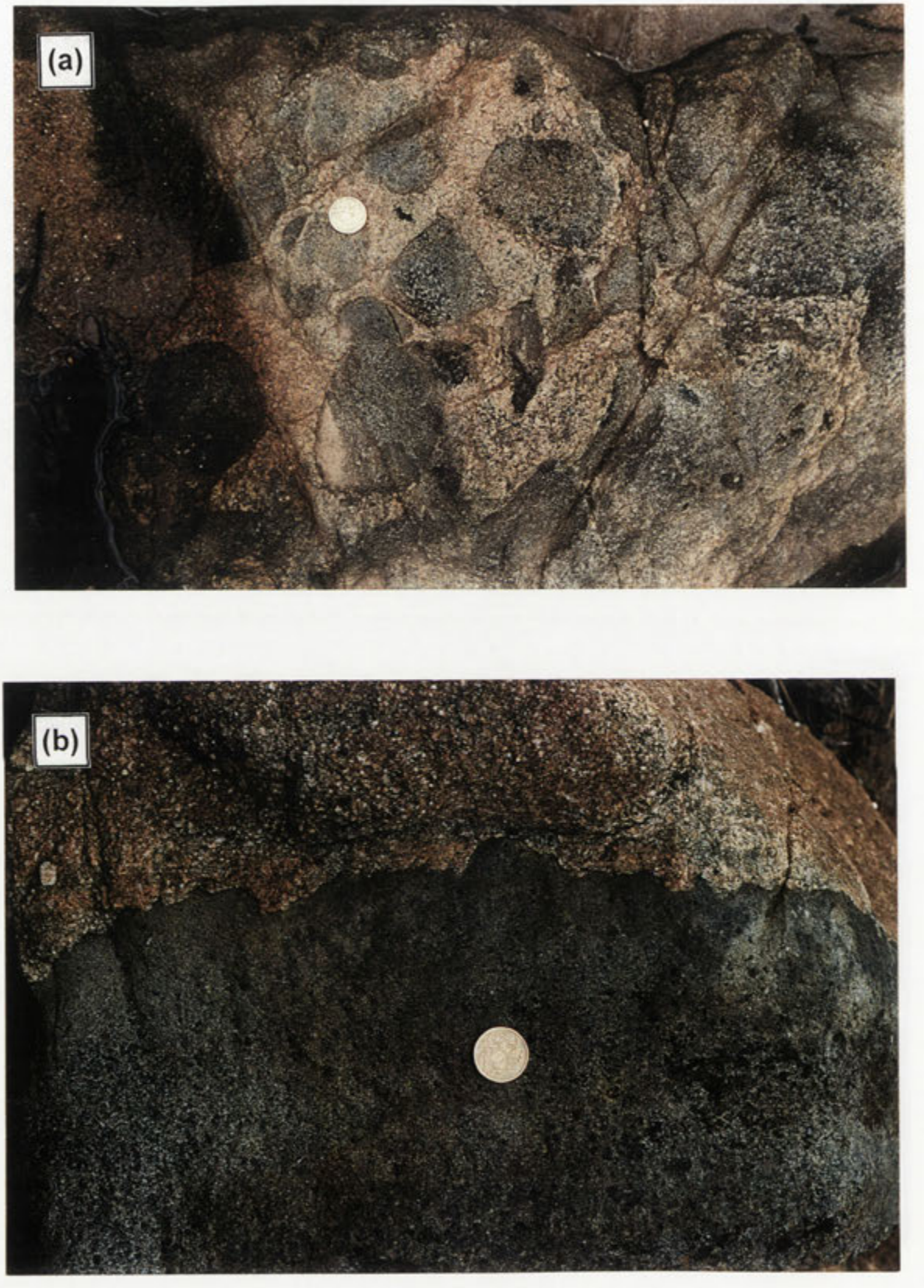

Figure 12.11. (a) Swarm of 'spotted', biotite-rich microgranular enclaves in Kassingbrook Granodiorite south of key locality E. (b) Crenulate margin of a hornblende diorite dyke with the same clotted texture as the microgranular enclaves in (a). The cuspate contacts against the granodiorite are consistent with each lithology being simultaneously liquid (WD707482).

some outcrops, confirming that a metasedimentary ingredient is pervasive throughout the Kassingbrook Granodiorite pluton.

12.4 Mafic rocks of Robson Creek

Small outcrops of hornblende-rich igneous rocks similar to those of Chin Chap Creek also occur in eastern Robson Creek (see Figure 5.10 and Table 12.6). Most of these occur as single, isolated boulders of uncertain context within the Nangkita Adamellite. A 5 m wide expanse of gabbroic saprock, dominated by large amphibole prisms (to 3 cm across), is also enclosed by the Nangkita Adamellite. It is important to emphasise however that, unlike the Kassingbrook Granodiorite, the Nangkita Adamellite is outwardly unchanged in proximity to these mafic exposures.

Nangkita Adamellite adjacent to the dioritic outcrops also encloses two 'spotted' microgranular enclaves, sheathed by a thin pegmatitic rind, that closely resemble microgranular enclaves of the Kassingbrook Granodiorite (Figure 12.12; samples **97-254A** and **97-254B** in Table 12.6). Both have crenulate margins against the host adamellite, consistent with incorporation in a partially liquid state. The largest enclave (~70 cm across, **97-254A**) is also intermingled with its pegmatitic envelope, containing small pegmatitic globules that are encircled by oriented biotite clots and a groundmass biotite foliation. Since emplacement of the Nangkita Adamellite post-dates major deformation, the enclave fabric, which is oblique to the inherited S_2 orientation in the adamellite, must result from magmatic flow. Pegmatitic globules were possibly detached by internal magmatic turbulence during intermingling.

Figure 12.12. Large 'spotted' microgranular enclave in a heterogeneous Nangkita Adamellite exposure. Note the pegmatitic envelope (left). Metasedimentary enclaves (top right and centre right) and alkali feldspar megacrysts (centre) are conspicuous (WD727434).

Table 12.6. Summary description of hornblende-bearing igneous rocks of Robson Creek and mafic microgranular enclaves in Nangkita Adamellite.

Lithology	*Field context*	*Summary description*
Hornblende gabbro-diorite Sample **97-244**	Isolated boulder (2x1.5 m) surrounded by schist. Rubble of similar nature in the creek-bed suggests that the boulder may be part of a small pod or dyke.	Dark greenish-grey, medium grained, and containing abundant blocky hornblende crystals (1-3 mm). Also evident are felsic ocelli (most ~2 mm), sometimes single grains of quartz or alkali feldspar, rimmed by tiny light green clinopyroxene granules; occasionally, larger clinopyroxene prisms (to 1 mm) are enclosed within the felsic minerals. Hornblende in thin section has finely striated brownish cores with blebs of titanite, and (rarely) small grains of seritisised plagioclase. Interstices between hornblende prisms are occupied by poikilitic plagioclase masses, enclosing smaller hornblende grains and numerous euhedral clinopyroxene crystals; consequently, these intercumulus areas, which also contain alkali feldspar and quartz, appear greenish in handspecimen. Apatite needles (to 1.5 mm) and anhedral titanite grains are accessory phases.
Hornblende gabbro-diorite Sample **97-233B**	Thin sheet (0.5 m wide) enclosed by the Nangkita Adamellite	Dominated by squat hornblende prisms (most 3-4 mm) with minor felsic intercumulus and accessory chalcopyrite (to 2 mm). The intercumulus varies in proportion across the sample, with some areas of the rock consisting of adcumulates of hornblende (2-8cm domains), but overall the texture is orthocumulate in character. In thin section, the intercumulus comprises polygonal aggregates of seritisised plagioclase (0.5-3 mm) and quartz, the former enclosing sparse small hornblende crystals. Clinopyroxene is absent. Larger hornblende prisms have brownish striated patches dusted by fine opaques, and contain spindly chlorite blades after biotite.
Hornblende diorite Sample **97-236B**	Isolated 2 m high boulder enclosed by Nangkita Adamellite at WD727435	Dark grey, fine to medium grained, consists of hornblende aggregates (1-5 mm), commonly with biotite, interspersed with blocky plagioclase grains and quartz. Single hornblende prisms (1-3 mm) are also common, enclosed by plagioclase. Hornblende in thin section is green (α=pale green, β=khaki, γ=blue green) but encloses small brownish areas with fine striations, and some grains exhibit incipient replacement by pale orange-brown biotite. However, biotite mostly occurs as vaguely rectangular clots of finely interleaved plates (1-2 mm) towards the centre of hornblende aggregates or in the core of large hornblende grains; this implies that biotite is pseudomorphing a pre-existing mineral, possibly a pyroxene. Square to rectangular plagioclase grains (1-2 mm) are strongly zoned outwards from large euhedral cores, and enclose hornblende crystals, also partially enveloping hornblende-biotite aggregates. Plagioclase has cuspate boundaries against quartz.
Hornblende diorite Sample **97-236A**	Collected from same boulder as **97-236B**	Similar to **97-236B** but with irregularly-shaped felsic domains (5-7 mm across) which impart a 'blotchy' aspect. Blocky hornblende prisms are also less abundant. Felsic domains comprise large subhedral plagioclase laths (to 8mm long), with interstitial quartz. Blotchy patches also contain sparse hornblende prisms, which project into plagioclase. Hornblende ocellar quartz grains (to 1.5 mm) also occur.

Table 12.6 contd. next page

Table 12.6 contd.

Lithology	*Field context*	*Summary description*
Hornblende diorite Sample 97-254C	Isolated outcrop (1x2 m) enclosed by Nangkita Adamellite at near WD727435	Dark grey, has coarse interlocking hornblende prisms (~5 mm, to 8 mm) forming vaguely radiating aggregates, interstitial to which are masses of quartz and chalky plagioclase. Also apparent are large spindly biotite plates (to 5 mm) and orange-red titanite grains between hornblende prisms. In thin section, hornblende has finely striated cores clouded by dense concentrations of fine opaques, mantled by thin olive-green rims. Many are also partially replaced by ragged, blade-like flakes of pale biotite (α=palest tan, β=γ=light orange-brown).
'Clotted' MME Sample **97-254B**	Hosted by Nangkita Adamellite near 97-254C	Dark blue-grey, contains numerous lenticular biotite clots (2-5 mm) which have a preferred orientation, and small greenish plagioclase phenocrysts (1-2 mm) in a fine grained, biotite-rich matrix. Thin sections reveal that biotite clots are dense, non-foliated aggregates of interleaved dark-orange brown flakes (0.5-1.5 mm), and that plagioclase phenocrysts are anhedral against the matrix, but strongly zoned outwards from a large euhedral core. Also evident are elongate quartz grains (1-2 mm), surrounded by dense selvedges of fine grained biotite. The groundmass consists of aligned spindly biotite flakes, which anastomose around biotite clots and plagioclase phenocrysts, plagioclase grains and abundant quartz granules. Groundmass plagioclase varies from lath-like with serrated margins to equant grains perforated with quartz and alkali feldspar blebs. Apatite needles are a significant accessory.
'Clotted' MME Sample **97-254A**	Hosted by Nangkita Adamellite near 97-254C (50 cm long)	Similar to above enclave, but lighter coloured, by virtue of a slightly more felsic groundmass, and has tiny blebs of chalcopyrite within mafic clots. Also evident are small ellipsoidal relatively biotite-rich bodies (2-4cm long), similar objects being also apparent within **97-254B**.

12.5 Discussion

12.5.1 Synthesis of field and lithological relationships in Chin Chap Creek

The geology of Chin Chap Creek has many critical aspects, four of which deserve further discussion.

(a) Relationship between the Kassingbrook Granodiorite and migmatites

The intimate association between the felsic and muscovite-bearing Kassingbrook Granodiorite and migmatitic metasedimentary rocks (key localities A and B) implies a genetic relationship, in a similar manner to that between Harrow type granitic rocks and migmatites (Chapter 9). The link is strengthened by the chemical equivalence of typical Kassingbrook Granodiorite samples to *in situ* leucosomes of associated migmatites (section 15.4.2).

(b) Interaction between coeval mafic and felsic magmas

The emplacement of the Kassingbrook Granodiorite was broadly contemporaneous with intrusion of mafic hornblende-rich igneous bodies, such that syn-magmatic mingling was extensive. Outcrop relationships strongly imply that the array of petrographic variation exhibited by these rock types partly results from this mutual physical and associated chemical interaction. For mafic bodies, this involved hybridisation near the contacts with the Kassingbrook Granodiorite, which has two different manifestations. The gabbro-diorite pod at key locality A exhibits development of a finer grained, alkali feldspar-bearing marginal variant (sample **98-61**), characterised by striking hornblende-clinopyroxene ocellar quartz ovoids. Quartz ocelli of this nature are almost ubiquitous in microgranular enclaves of 'calc-alkaline' granitic rocks (see review by Vernon 1990), and are thought to be 'xenocrysts' introduced into a hotter, basic magma during mixing with a coeval quartz-phyric felsic magma (Vernon 1990; Hibbard 1991, 1995). The rim of fine grained mafic minerals is attributed to partial dissolution of the subsequently unstable quartz grain, which locally undercools the enclosing mafic liquid and promotes rapid crystallisation onto the surface of the xenocryst (Vernon 1990). In the case of **98-61**, precipitation of clinopyroxene onto the ocelli occurred first, which was subsequently mantled and partially replaced by hornblende, perhaps during later cooling of the magma; similar features are observed in basic pillows enclosed by granite in southwestern Finland (Lindberg & Eklund 1988). Other ocelli in **98-61** are composed of quartz, alkali feldspar and plagioclase, suggesting that they were incorporated into the gabbro-diorite as globules of felsic melt. Digestion of such globules by the mafic host could account for the abundant poikilitic alkali feldspar present throughout the hybrid gabbro-diorite matrix. Rheological modelling suggests that such mixing would be effective in this case, as the large proportion of mafic magma compared to the felsic melt droplet permits thermal equilibration and reduces viscosity contrasts (Sparks & Marshall 1986). The occurrence of similar quartz-plagioclase-alkali feldspar domains with clinopyroxene selvedges from the centre of the gabbrodiorite pod indicates that dispersal of felsic melt droplets throughout the mafic body was pervasive. Pyroxene-mantled felsic globules and quartz ocelli in gabbro-diorite **97-244** (Robson Creek) imply incorporation of felsic partial melt from surrounding migmatitic rocks.

In contrast, the gabbro-diorite sheet at key locality D developed a more felsic and biotite-rich 'envelope' near contacts with the enclosing granodiorite, attesting to more extensive material exchange between the disparate magmas. By analogy, identical biotite-rich rock at key locality E, that disintegrates into microgranular enclaves, probably formed by hybridisation at the margin of the hornblende diorite sheet below the current exposure level. The striking 'clotted' texture of biotite-rich hybrid rocks clearly results from the progressive replacement of hornblende phenocrysts by biotite sheaves during hybridisation, which requires movement of K_2O, SiO_2 and H_2O into the mafic body from the adjacent granodiorite. This may have been achieved by chemical diffusion across the mafic-felsic interface, driven by compositional gradients, as described by Wiebe (1973), Debon (1991), Orsini *et al.* (1991) and experimentally established by Watson & Jurewicz (1984) and Johnston & Wyllie (1988), since replacement of hornblende by biotite becomes more pronounced towards the periphery of the mafic body. The efficacy of K_2O migration into basaltic magmas in particular is emphasised by Watson (1982). Note that reciprocal diffusion of certain elements, such as CaO, FeO and MgO, into the felsic granodiorite from the adjacent hornblende diorite is also expected (e.g. Johnston & Wyllie 1988; Debon 1991). This mutual interdiffusion will ultimately establish compositional equilibrium between the originally contrasting juxtaposed magmas (Debon 1991). Another well documented mechanism is the migration of volatiles from the felsic to mafic magmas, with associated transfer of Si, K and LILE (see Orsini *et al.* 1991). Some infiltration of hydrous, K-rich, felsic melt into the partially crystalline gabbro-diorite magma also cannot be precluded. Rare biotite-hornblende rimmed quartz ocelli in the hybridised diorite envelope also suggest limited crystal exchange across the mafic-felsic contact.

Chemical diffusion is most effective if the juxtaposed lithologies are partially melted (Barbarin & Didier 1992) and enhanced by the presence of aqueous fluid (Johnston & Wyllie 1988). Both requirements are met in Chin Chap Creek. Liquid-liquid contacts between the diorite (and enclaves of this material) and the granodiorite indicate that the mafic-felsic interaction was syn-magmatic, whereas the presence of muscovite in the Kassingbrook Granodiorite and primary hornblende in the gabbro-diorite indicate that both were hydrous magmas. In a fluid-fluxed scenario, Johnston & Wyllie (1988) note that precipitation of biotite from a hybridised mafic magma provides a sink for potassium, thereby lowering the K_2O concentration from the mafic melt fraction. This induces further diffusion of K_2O into the hybrid magma, perpetuating biotite crystallisation. Given the large reservoir of felsic melt, the continuation of this process would ultimately result in the K_2O content of the bulk hybrid magma (i.e. melt+crystals) exceeding that of the adjacent felsic granodiorite (Johnston & Wyllie 1988). This accounts for the high biotite content of the marginal 'clotted' hybrid rock enveloping hornblende diorite bodies, and has implications for the geochemistry of microgranular enclaves in granitic rocks (Chapter 16).

The spindly, blade-like morphology of biotite flakes in the microgranular diorite phase (and microgranular enclaves, see Table 12.5) and hornblende tonalitic dykes is also commonly encountered in environments of magma mixing and hybridisation (Hibbard 1991). This is thought to arise from rapid nucleation and growth, as the mineral is stabilised by combination of

an Fe- and Mg-rich magma and a hydrous, potassic magma (Johnston & Wyllie 1988; Hibbard 1991). The elongate, serrated form could also reflect undercooling and co-precipitation with plagioclase (Hibbard 1995).

(c) Formation of mafic enclaves in the Kassingbrook Granodiorite

Outcrop relationships in Chin Chap Creek clearly demonstrate the *in situ* formation of mafic microgranular enclaves in the Kassingbrook Granodiorite by interaction with coeval mafic hornblende diorite magmas. This occurred in two stages, initially involving marginal hybridisation of the mafic body as described above, followed by intermingling of this hybridised material with the felsic granodioritic host to produce the 'clotted' enclave swarms. Disintegration of the diorite into partially liquid globules within the granodiorite would have facilitated further hybridisation, by virtue of increasing the contact surface area between mafic and felsic components (Gamble 1979). This may be responsible for the more felsic and biotite-rich nature of some microgranular enclaves at key locality D, where quartz is more abundant and hornblende is totally replaced by biotite. Similar mingling occurred in the Nangkita Adamellite of Robson Creek further south, as evidenced by the 'spotted' microgranular enclaves with magmatic flow structures and liquid-liquid contacts against the host. Sequential hybridism and intermingling has also been inferred by Hibbard (1981) and Vernon (1983, 1984), though the location of the initial hybridisation of the mafic magma was not specified by either author. At key locality E, mingling also occurred directly between the granodiorite and the mafic hornblende diorite, without development of a hybridised biotite-rich envelope around the latter.

Modification of the felsic, peraluminous granodiorite in these areas was most obviously facilitated by the mechanical disaggregation and ingestion of globules of the intermingled mafic magma, which amounts to magma mixing. This imparts extreme small-scale petrographic heterogeneity, such that the granodiorite becomes more biotite-rich, locally hornblende-bearing and contains either hornblende ocellar quartz, hornblende aggregates or clots of biotite ± hornblende, depending upon the nature of the dismantled mafic enclaves. Many of the disseminated biotite flakes within granodiorite samples at key locality D have a spindly, blade-like habit containing apatite needles, and have therefore clearly derived from the disintegration of microgranular enclaves, where the same distinctive feature is apparent. The absence of muscovite from the granodiorite adjacent to mafic bodies suggests either that its crystallisation was suppressed or that early formed grains were rendered unstable, and resorbed by the modified granodiorite magma. Diffuse granitic pockets within many mafic enclaves also indicate smaller-scale intermingling between the granodiorite host and enclave magmas, which may have assisted enclave disintegration. Diffusion of components such as CaO, FeO and MgO from the hybridised mafic magma into the granodiorite magma during intermingling is also anticipated (see above), and may be responsible for the gradational or 'blurred' margins of hornblende diorite globules at key locality E. However, the quantification of the diffusional exchange between mafic and felsic magmas has not been attempted.

Although the petrographic effects of interaction between mafic and felsic rocks is most dramatic proximal to intermingled contacts, the scale of dispersal of mafic material through the

Kassingbrook Granodiorite is indicated by the widespread 'spotted' microgranular enclaves. These correspond to the distinctive hybridised material developed at the margins of mafic dioritic bodies, and were therefore also most likely introduced into the granodiorite by syn-magmatic mingling.

(d) Formation of intermediate 'hybrid' granitic rocks

Finally, following from above, interaction between mafic hornblende diorite and Kassingbrook Granodiorite at key localities D and E involved localised production of intermediate or 'hybrid' metaluminous tonalitic material (samples **97-376C** and **97-274**). The relatively homogeneous nature of these rocks suggests formation by more extensive diffusional exchange and/or thorough mechanical blending between the juxtaposed mafic and felsic magmas. Both processes are favoured at key locality E, as the tonalitic hybrid (**97-274**) is only developed where hornblende diorite pillows are volumetrically predominant in the granodiorite host. This would allow local thermal equilibration between mafic and felsic magmas, leading to reduction in viscosity contrast, maintenance of partially melted conditions (as opposed to freezing) and therefore more effective hybridisation (Sparks & Marshall 1986; Frost & Mahood 1987; Barbarin & Didier 1992). The irregular, frayed margins of dioritic globules and lack of chilled margins are compatible with this concept.

Importantly, the hornblende-rich hybrid **97-274** closely resembles tonalite dykes contained by the Kassingbrook Granodiorite elsewhere along Chin Chap Creek. This raises the possibility that the more felsic hornblende-bearing igneous rocks of Chin Chap Creek represent the larger-scale products of efficient mixing between the peraluminous Kassingbrook Granodiorite magma and a mafic gabbro-diorite magma. This proposition is investigated in Chapter 16.

To summarise, the granitic rocks of Chin Chap Creek link *in situ* partial melting within metasedimentary rocks on the one hand to mafic to ultramafic magmatism on the other. The coupling between these fundamentally different styles of geology is evaluated chemically in Chapter 16.

12.5.2 Implications for the origin of microgranular enclaves in other GRC granitic rocks

Field evidence indicates that the array of mafic enclaves within the Kassingbrook Granodiorite result from variable hybridisation and intermingling between coexisting mafic and felsic magmas. Such evidence invalidates a restitic origin for the enclaves, as espoused by Chappell *et al.* (1987), Chen *et al.* (1991) and White *et al.* (1999). Spectacular examples of microgranular enclave production by magma mingling are documented from many other granitic terranes worldwide, including the Lachlan Fold Belt, southeastern Australia (e.g. Vernon 1984; Vernon *et al.* 1988; Keay *et al.* 1997), Sierra Nevada Batholith, California (Reid *et al.* 1983) and the Coastal Maine Magmatic Complex, U.S.A. (Wiebe 1991, 1994, 1996).

As 'spotted' microgranular enclaves similar to those of the Kassingbrook Granodiorite are hosted by Tuloona and Loftus Creek type granitic rocks (Chapter 11), it is reasonable to propose that these also originated through interpenetration and hybridisation of felsic and mafic magmas. An igneous affinity for these enclaves is suggested by plagioclase phenocrysts with euhedral oscillatory zoning and well-shaped groundmass minerals, including biotite plates, titanite

crystals, hornblende prisms and plagioclase laths, set in a framework of poikilitic quartz or alkali feldspar. As discussed by Vernon (1983, 1990) and Dorais *et al.* (1990), these features are not compatible with a restitic origin for the enclaves. The elongate, skeletal morphology and radiating arrangement of matrix plagioclase inside poikilitic minerals suggests rapid nucleation and growth during undercooling, such as would be induced by inclusion in a more felsic magma (Vernon 1991). This is also supported by the occurrence of acicular apatite needles, attributed to growth during rapid magma solidification (Reid *et al.* 1983; Vernon 1983; Hibbard 1991). The poikilomosaic texture in **98-PP2** (Koolomurt Granodiorite) is commonly developed during simultaneous crystallisation of two or more phases with different nucleation characteristics in quenched basaltic rocks (Shelley 1993), and resembles the 'snow-flake' texture of some rhyolites and obsidians (e.g. Swanson *et al.* 1989). A similar feature is exhibited by basaltic globules in the Cerro del Hoyazo dacite (Spain) where quenched pyroxene, hornblende and plagioclase crystals are enclosed by pools of glass (Zeck 1992). Alternatively, Vernon (1990) proposes development of poikilitic microstructure following initial quenching of the enclave, where residual, interstitial liquid cools at the same rate as the enclosing granitic magma. This results in formation of relatively few nuclei, and a slow growth rate of late-crystallising quartz and alkali feldspar, leading to the enclosure of quenched minerals. Such an effect may be exemplified by enclaves in the tonalitic hybrid **97-274**, where single alkali feldspar oikocrysts straddle the enclave-host boundary, suggesting simultaneous crystallisation of interstitial melt in both lithologies. For hybrid rocks of Chin Chap Creek (and microgranular enclaves derived therefrom) developed at the hornblende diorite-Kassingbrook Granodiorite interface, poikilitic quartz and feldspar may also reflect the prior diffusion-promoted crystallisation of biotite (see above). This is because this process would continue until the residual melt in the hybrid magma was too depleted in mafic components to form biotite, whereupon equilibration of K_2O between the hybrid and the adjacent felsic granodiorite would rapidly result (Johnston & Wyllie 1988). Hence, the last melt fraction in the hybrid magma would be siliceous and K-rich, favouring alkali feldspar and/or quartz crystallisation. In any case, poikilitic textures accord with igneous crystallisation (Hibbard 1995) and characterise microgranular enclaves considered to have formed by syn-magmatic mingling elsewhere (e.g. Dorais *et al.* 1990; Poli *et al.* 1996).

Hybridisation textures like those in Chin Chap Creek mafic rocks also occur in enclaves of Tuloona and Loftus Creek type granitic plutons. This is most apparent with the hornblende ocellar quartz ovoids in **97-294** (Tuloona Granodiorite), which were plausibly introduced into the parental enclave magma from a partially crystallised felsic magma as xenocrysts. Marginal solution imparts the rounded shape (Hibbard 1995). The epitaxial quartz mantle on the quartz ocelli which 'locks in' the hornblende corona is explained by either a second surge of felsic magma into the system (Hibbard 1991, 1995) or, more simply, by overgrowth during slow cooling of interstitial melt in the hybrid enclave magma (Vernon 1990), which also gives rise to the poikilitic quartz (see above). As with enclaves in the Kassingbrook Granodiorite, blade-like biotite is ubiquitous in microgranular enclaves of Tuloona and Loftus Creek type plutons, and might arise by hybridisation, as previously discussed. The striking biotite-quartz perforation of plagioclase laths and phenocrysts in **T2-135B** (Tuloona Granodiorite) may result from diffusion

of K_2O, SiO_2 and H_2O into the enclave from the host granodiorite. This process may also account for the biotite-rich rim around this and other enclaves in the Tuloona Granodiorite, as has been invoked to explain this feature for microgranular enclaves elsewhere (e.g. Bussy 1991; Orsini *et al.* 1991).

The unusual titanite-ocellar texture of **98-PP1** (Koolomurt Granodiorite) is also attributed to complex hybridisation processes attending several stages of magma mixing (Hibbard 1991, 1995). The process, as envisaged by Hibbard (1991), initially involves rapid crystallisation of titanite, plagioclase and minor hornblende from an undercooled mafic magma, with the lower nucleation rate of titanite resulting in enclosure of quenched plagioclase laths. Intermixing by a more felsic magma pulse induced precipitation of quartz, sodic plagioclase and alkali feldspar around the early-crystallised titanite-plagioclase units, forming dispersed titanite-centred felsic ocelli. These were subsequently engulfed in turn by second stage mafic magma, giving rise to the biotite-rich, inter-ocellar matrix. Early titanite nucleation suggests that the original mafic magma involved in the formation of Koolomurt Granodiorite enclaves was different to the enclave magmas of Tuloona type plutons, which lack titanite. Notably, large subophitic titanite crystals occur in mafic dykes of Robertson Creek, and are a unifying feature of Loftus Creek type granitic rocks (section 11.3).

Microgranular enclaves in Tuloona and Loftus Creek type rocks are therefore interpreted as intermingled globules of variably hybridised, more mafic magma. Hybridisation may have preceded the dispersal of enclaves throughout the granitic pluton, in deeper mafic-felsic mixing zones, occurred simultaneously with incorporation of the enclave into the felsic host, or both. Hybrid features are less obvious in other enclaves of Tuloona types (e.g. **97-299B**, **97-382B**) which are essentially more mafic versions of the host. Heterogeneous textures in **97-299B** do, however, suggest some interaction between host and enclave magmas.

Relict magmatic textures, chilled margins and a pillow-like mode of occurrence strongly suggests that mafic hornblendic enclaves of Wando type granitic rocks were also introduced by mingling with a contemporaneous basic magma (section 10.2). Such an origin is incontrovertible for mafic enclaves of the Warradale Tonalite, which have unmodified gabbroic textures (section 10.4.2). Geochemical aspects of enclave formation in all GRC granitic rocks, with petrogenetic implications for the host pluton, are discussed in Chapter 16.

Chapter 13: Interspersed granitic and intermediate-mafic-ultramafic rocks

Part (B) The Caupaul Igneous Complex

13.1 Introduction

The Caupaul Igneous Complex in the northwestern GRC incorporates an array of intimately enmeshed igneous rocks, from hornblende tonalite and quartz diorite, through diorite, gabbro, gabbronorite and hornblende pyroxenite. To underline their significance, mafic rocks of this assemblage are taken as a template for the lower silica end of the GRC granitic system.

13.2 Geological overview

First mapped by Ferguson (1993), rocks of the Caupaul Igneous Complex outcrop sporadically for ~6 km along the Glenelg River valley and tributaries north of Dergholm, hosted by metasedimentary rocks that prograde from lower greenschist to amphibolite facies from south to north (Figure 4.1). A strong teardrop-shaped magnetic anomaly indicates that the igneous exposure corresponds to the southeast corner of the plutonic body, which continues for some distance north and west under younger cover. The lithological components of the Caupaul Igneous Complex are summarised by Kemp *et al.* (2001) and Figure 13.1. Mafic hornblende tonalite is predominant, occurring primarily along the western Glenelg River valley and supporting a pervasive (locally mylonitic) S_2 foliation, indicating intrusion pre- to syn-D_2. This lithology is named Ferres Creek Tonalite, variants of which have significant alkali feldspar. The eastern flank of the river has a more complex assemblage of Ferres Creek Tonalite and relatively quartz-deficient 'dioritic' rocks. The latter contain both clinopyroxene and orthopyroxene, with a distinct paucity of hydrous minerals, and exhibit comparatively subtle deformation features only. However, diorites were probably also emplaced pre- to syn-D_2, with paucity of quartz and biotite, but abundance of pyroxene imparting greater resistance to penetrative deformation.

Dioritic rocks of the eastern Glenelg River valley also envelope various small mafic to ultramafic bodies, which are collectively termed 'Kooreelah Gabbro' by Ferguson (1993). These encompass coarsegrained, cumulate-textured bodies of basaltic parentage, comprising hornblende gabbronorite to hornblende pyroxenite, some of which exhibit considerable internal variation. Also included in this group are more plagioclase-rich 'gabbroic' exposures, which are texturally and chemically distinct. As with intermediate rocks, both hydrous (hornblende-rich) and anhydrous (pyroxene-rich) gabbroic varieties are recognised.

The modal mineralogy of all samples from the Caupaul Igneous Complex is given by Table 13.1 and summarised by Figures 13.2 (mafic to ultramafic rocks) and Figure 13.3 (intermediate rocks).

13.3 Hornblende pyroxenite to mafic hornblende gabbronorite

Most mafic to ultramafic bodies delineated by Ferguson (1993) are predominantly pyroxenite with very minor proportions of feldspar, though evolution through to hornblende gabbronorite occurs within one (below). All are surrounded by rubbly outcrop of dioritic and metasedimentary rocks, though as no contacts are exposed the nature of the bodies, and their relationship to other igneous lithologies, is somewhat enigmatic. Similarly, the emplacement timing is uncertain, because although they exhibit largely unmodified igneous textures without tectonic foliations, strained plagioclase in some samples indicates that they have experienced deformation.

The largest body, an elliptical expanse (~450 m long) adjacent to McPherson's Creek (Figure 13.1), varies irregularly from hornblende pyroxenite and mafic hornblende gabbronorite at the periphery, through to a pyroxenite horizon and ultimately a small area of pyroxene hornblendite in the core (Ferguson 1993). The whole rock geochemistry and isotopic character (Sr, Nd) of the outer gabbronorite has been determined by Turner *et al.* (1993a), who also report the composition of plagioclase (An_{90}) and orthopyroxene (Mg# 0.73). Ferguson (1993) documents an average plagioclase composition of An_{86} for all lithologies within the body.

Hornblende pyroxenite from the western periphery of the McPherson's Creek mass (CP11726*) is a medium to coarse grained mesocumulate, dominated by mutually polygonal clinopyroxene (up to 6 mm) and orthopyroxene prisms (to 4 mm), in places enclosed by striking masses of intercumulus hornblende (to 10 mm, greenish-brown in thin section; Figure 13.4a). Minor plagioclase is interstitial to pyroxene but has crystal faces against hornblende; internal deformation features are conspicuous.

The plagioclase content gradually increases towards the centre of the body, accompanied by decrease in hornblende. Sample **98-CP2**, collected from slightly above the pyroxenite horizon, is a mafic gabbronorite with approximately equal proportions of plagioclase, orthopyroxene and clinopyroxene (Table 13.1, Figure 13.2). Although irregular poikilitic masses are evident, hornblende mostly forms smaller interstitial grains (1-2 mm). In thin section, the cumulate aspect is much less pronounced, with a broadly gabbroic fabric imparted by moderately aligned plagioclase laths (up to 3.5 mm). Pyroxene grains typically occur as elongate euhedral prisms, with many clinopyroxene crystals thinly mantled by green-brown hornblende. Magnetite is abundant but interstitial to pyroxenes.

The northernmost ultramafic body outcrops north of Fords Creek (Figure 13.1), where scattered pyroxenitic rubble surrounds a raised area of prominent bouldery outcrop towards the top of the Glenelg River valley. Samples from here (**98-CP8**) are very distinctive, consisting of large, vaguely rhombohedral hornblende prisms (5-10 mm) in a finer grained, pale green-brown matrix of equant clinopyroxene and orthopyroxene (0.5-3 mm). In thin section, hornblende is light orange-brown and encloses numerous orthopyroxene crystals, with lesser clinopyroxene and plagioclase (Figure 13.4b); hornblende prisms are mostly overgrown by paler greenish-brown amphibole. Clinopyroxene and orthopyroxene are polygonal where in contact but enveloped

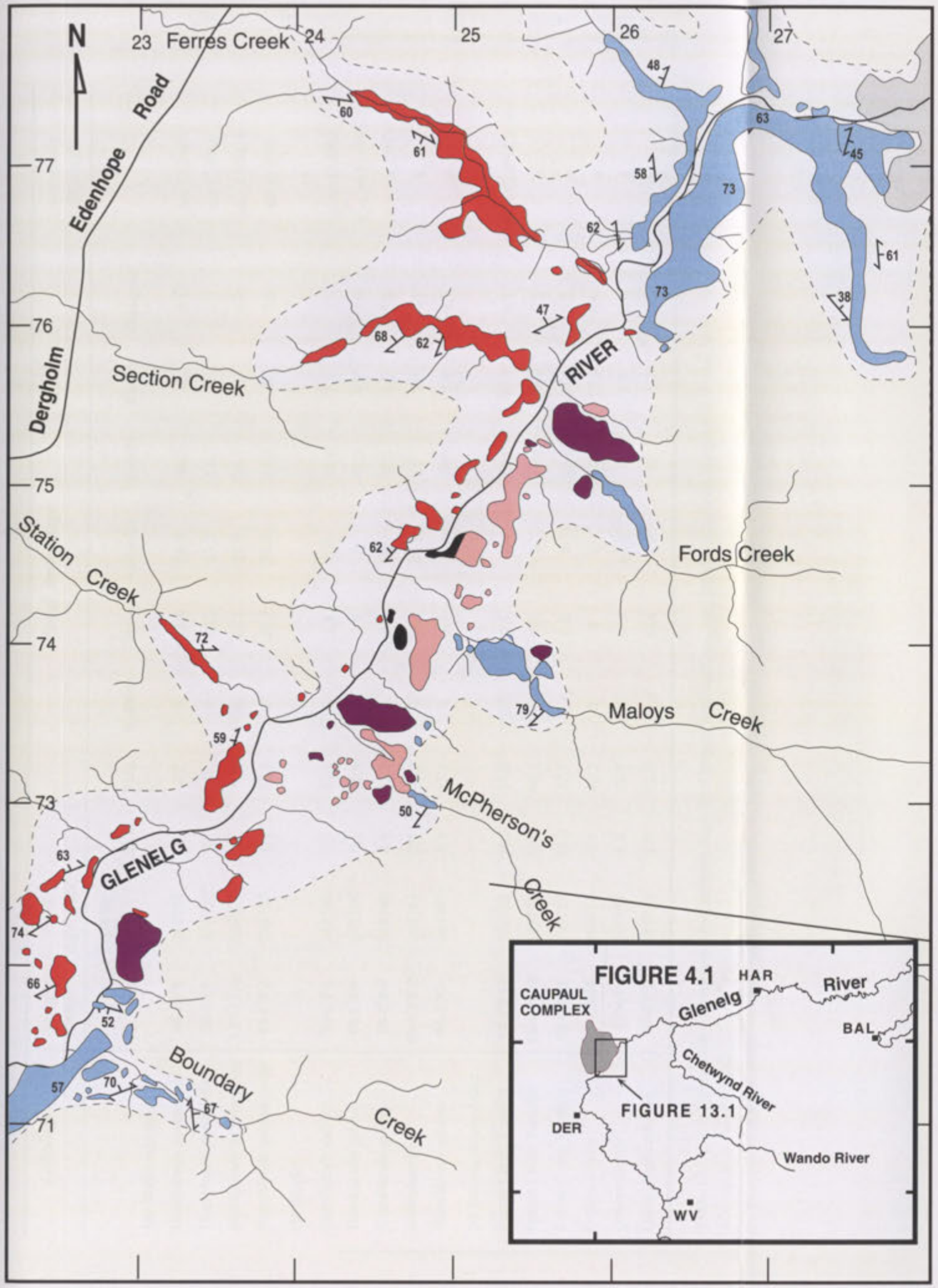

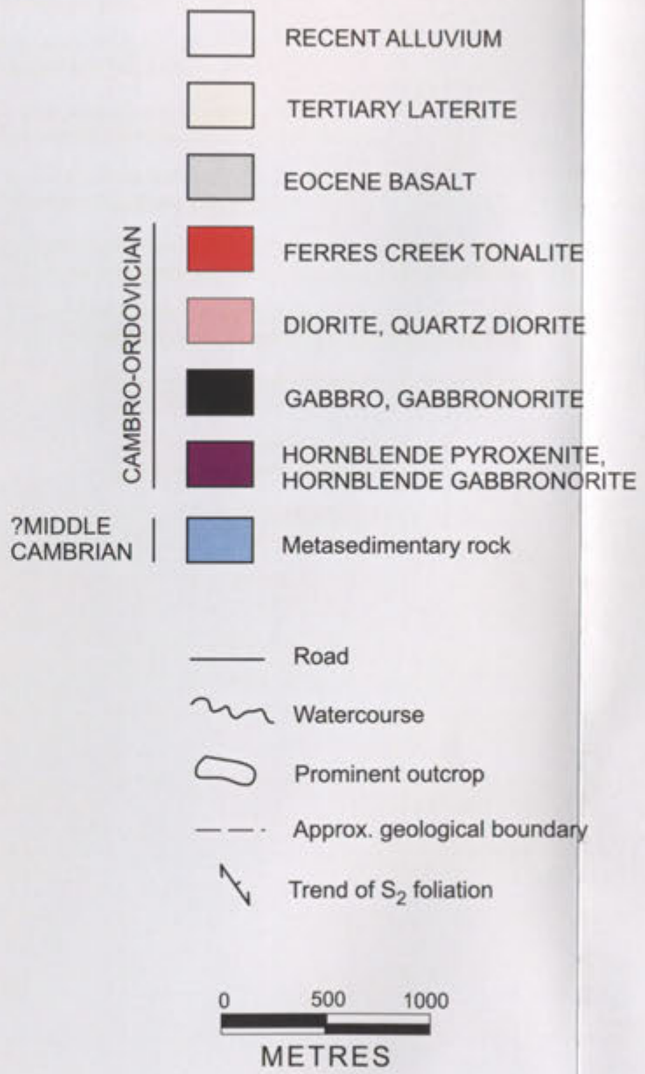

Figure 13.1. Simplified outcrop map depicting the distribution of lithologies in the Caupaul Igneous Complex; the location in Figure 4.1 is shown in the inset (modified from Ferguson 1993).

Lithology	*Sample number*	*Grid reference*	*Modal Percentage*								*Accessory Minerals*
		(WD)	Qtz	Plag.	K-Felds	Clinopx	Orthopx	Hornbl	Biotite	Opaques	
(a) Mafic-ultramafic											
Hornblende pyroxenite	**98-CP8**	260751	0	4.8	0	28.6	16.2	46.7	0	0.1	am (3.2%)
Hornblende pyroxenite	**98-CP9**	258750	0	0	0	68.3	13.3	15.3	0	0.3	am (2.9%)
Hornblende gabbronorite	CP11726	245737	0	8.4	0	41.1	23.9	21.7	0	0.2	am (4.6%), c
Hornblende gabbronorite	**98-CP2**	246737	0.2	30.6	0	25.7	24.9	15.5	0	1.0	am (1.8%)
(b) Mafic											
Hornblende gabbro	**98-CP4**	248746	0.5	47.1	0	1.8	5.8	37.6	2.7	2.7	a, cu (1.6%)
Hornblende gabbro	**98-CP5**	248746	0.6	45.6	0	0.5	0	42.6	4.7	3.6	a, c, cu (1.6%)
Hornblende gabbro	**98-CP6**	248746	0.1	52.7	0	0.1	0	30.1	1.9	5.6	a, c, cu (9%)
Gabbronorite	**98-CP129**	246741	0.2	46.3	0	27.6	23.0	0	2.0	1.1	a
Hornblende gabbro	**98-CP3**	249747	6.3	47.1	0	0.7	0	36.6	8.4	0.9	a
(c) Intermediate-felsic											
Ferres Creek Tonalite	**98-CP12**	223723	20.2	37.0	2.7	0.5	0	16.6	19.1	0.1	a, all, e (3.4%), t, tm
Ferres Creek Tonalite	**98-CP140**	249759	16.6	40.1	5.9	4.3	0	12.4	15.0	0.6	a
Ferres Creek Tonalite	**98-CP11**	236728	16.0	37.1	12.6	0.8	0	19.2	13.6	0.2	a
Quartz diorite	**98-CP10**	260750	4.4	42.3	0	0	0	34.8	17.9	0.5	a
Quartz diorite	**11904**	245733	4.5	48.9	4.9	21.4	10.0	0	9.8	0.1	a
Quartz monzodiorite	**98-CP7**	243733	7.0	52.7	10.4	10.4	13.0	0	4.3	2.2	a

Table 13.1. Modal mineralogy of representative samples from the Caupaul Igneous Complex. Opaque minerals comprise fine magnetite-ilmenite intergrowths. Abbreviations are: a = apatite; all = allanite; am = secondary amphibole; c = chlorite; cu = cummingtonite; e = epidote; t = titanite; tm = tourmaline.

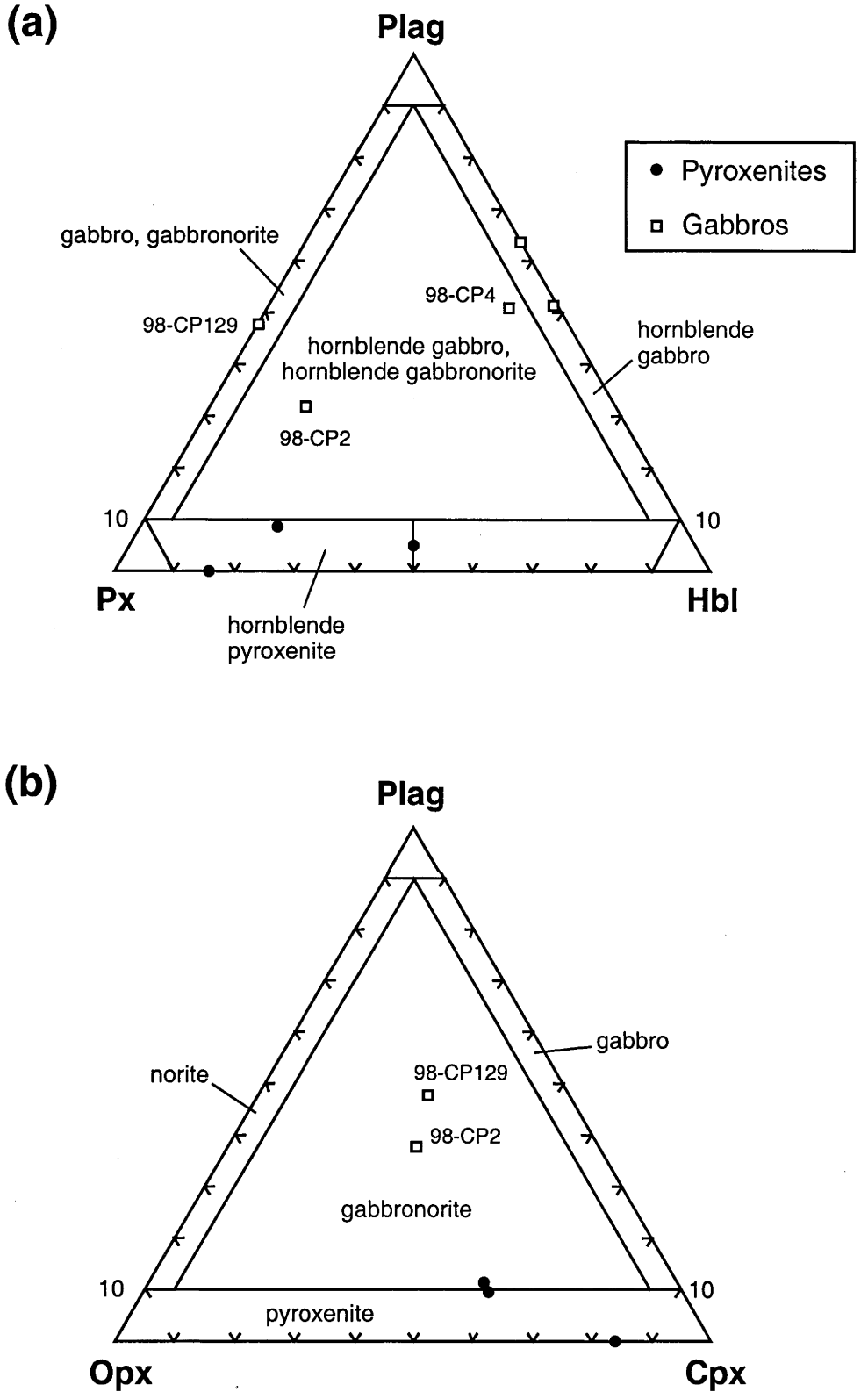

Figure 13.2. Modal mineralogy of ultramafic and mafic rocks of the Caupaul Igneous Complex (data from Table 13.1). (a) Plagioclase, pyroxene and hornblende. (b) Plagioclase, orthopyroxene and clinopyroxene. Hornblende gabbros contain <5% pyroxene and are therefore not plotted in (b). Lithological fields are after Le Maitre (1989).

(and partially replaced) by irregular masses of the pale amphibole. Interstices between pyroxenes are otherwise occupied by small plagioclase grains.

In contrast, another oval-shaped hornblende pyroxenite outcrop on the south side of Fords Creek is a uniformly coarse grained adcumulate of predominantly clinopyroxene, with lesser orthopyroxene (to 6 mm; **98-CP9**, Table 13.1). Intercumulus hornblende is relatively minor and plagioclase is absent.

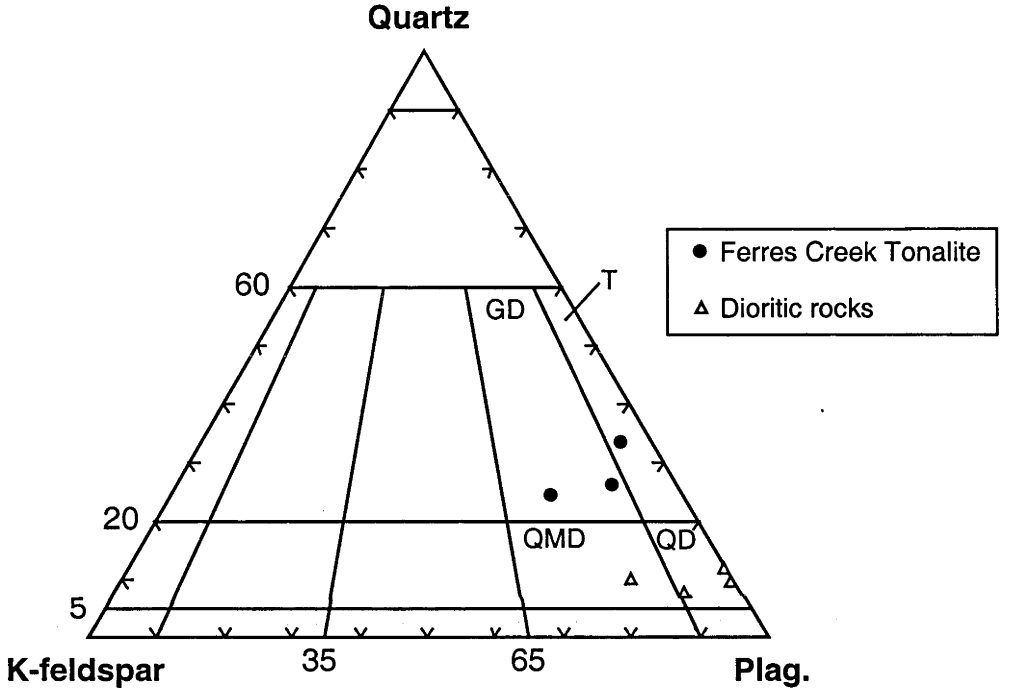

Figure 13.3. Modified Streckeisen (1976) diagram depicting the felsic mineralogy of the Ferres Creek Tonalite and pyroxene-bearing dioritic rocks of the Caupaul Igneous Complex. Lithological compartments are quartz diorite (QD), quartz monzodiorite (QMD), tonalite (T) and granodiorite (GD).

13.4 Gabbroic rocks (gabbronorite and hornblende gabbro)

Relatively plagioclase-rich and gabbroic-textured mafic rock containing the S_2 fabric forms a series of small exposures along the eastern bank of the Glenelg River (Figure 13.1), though relationships to adjacent dioritic outcrops are unclear. Gabbroic samples are either anhydrous and dominated by pyroxenes, being classified as gabbronorites (e.g **98-CP129***) (Figure 13.2) or have significant amounts of hornblende with minor pyroxene (e.g. hornblende gabbros **98-CP4***, **98-CP5** and **98-CP6**; Table 13.1). Although hornblende gabbro samples have lower silica and higher MgO than the gabbronorite, both rock types have distinctively high Al_2O_3 (>18%) and Sr (>330 ppm) (section 14.3.1).

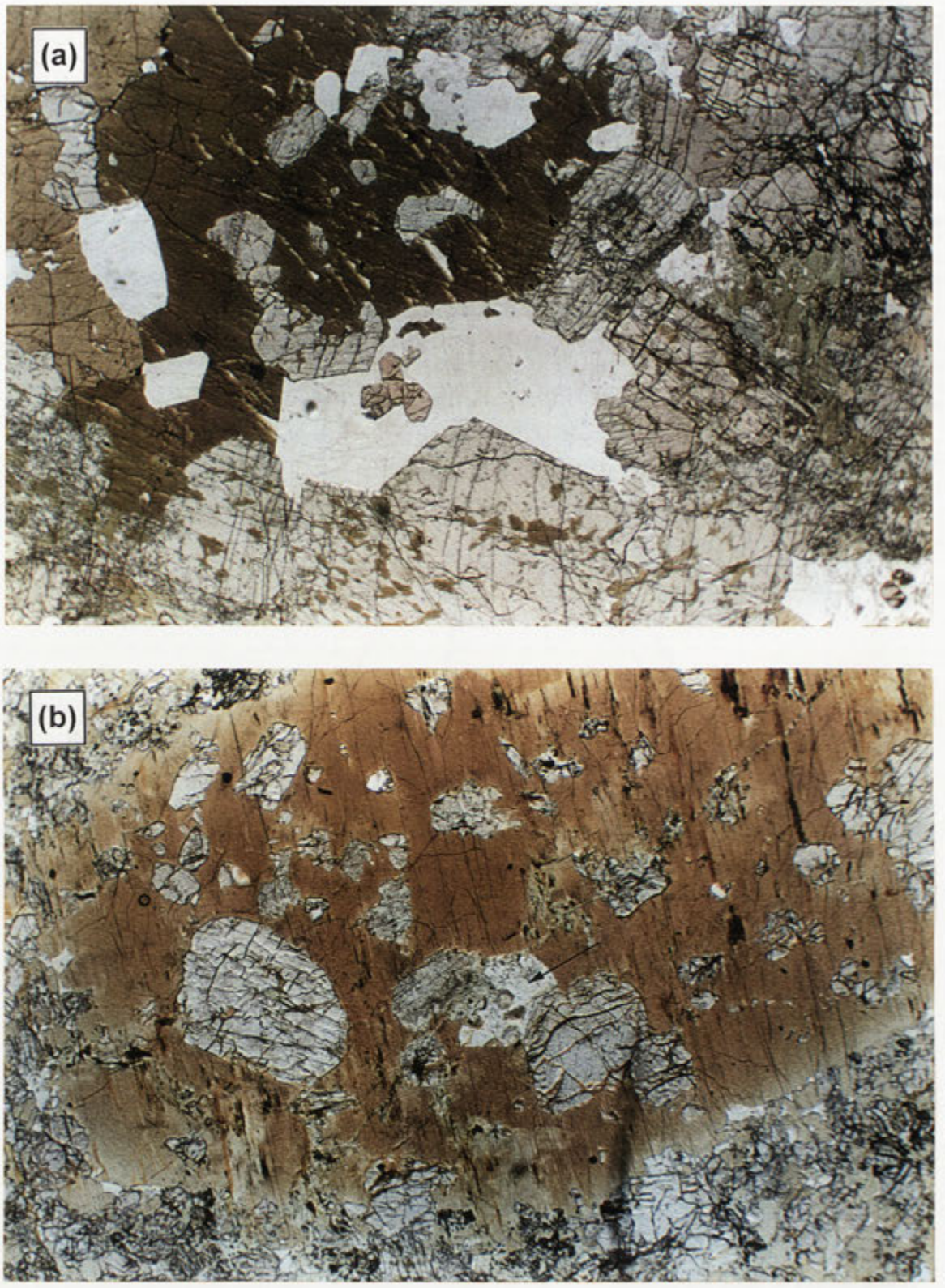

Figure 13.4. Ultramafic and mafic rocks of the Caupaul Complex in thin section (field of view of all photos is 8.1 mm) (a) Hornblende pyroxenite CP11726, with intercumulus hornblende and plagioclase and cumulate orthopyroxene (brownish) and clinopyroxene (pale greenish, incipient replacement by hornblende) Secondary blue-green amphibole is visible at centre left (plane polarised light). (b) Large brown hornblende prism in pyroxenite **98-CP8** enclosing numerous pyroxene crystals and a small plagioclase grain (arrowed).

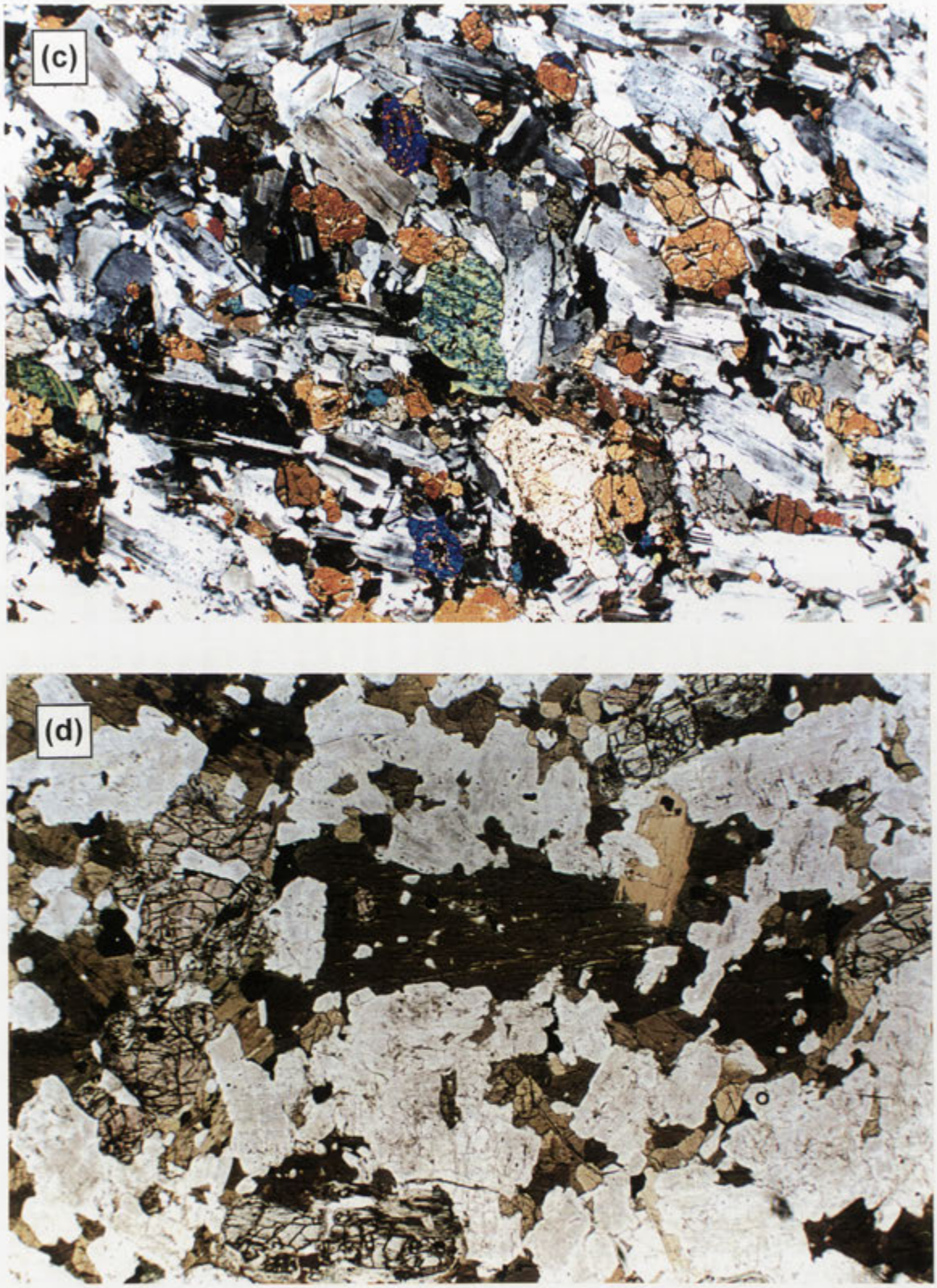

Figure 13.4 contd. Ultramafic and mafic rocks of the Caupaul Complex in thin section (field of view of all photos is 8.1 mm) (c) Moderately aligned plagioclase prisms in gabbronorite **98-CP129**. Orthopyroxene (orange to grey interference colours) and clinopyroxene (mostly bright interference colours) are abundant (crossed polars). (d) Hornblende gabbro **98-CP4**, with orthopyroxene (brownish) and clinopyroxene, the latter enveloped by cummingtonite and hornblende. Biotite flakes and magnetite granules are also visible (plane polarised light).

The gabbronorite, collected from a small outcrop north of McPherson's Creek, is fine to medium grained and dark brownish-grey, reflecting the high orthopyroxene content. Plagioclase laths and subhedral clinopyroxene prisms are also conspicuous, with both pyroxene and feldspar exhibiting a distinct preferred orientation (Figure 13.4c). Interstitial biotite is minor and, unlike the gabbronorites associated with ultramafic bodies, hornblende is absent. Plagioclase is anhedral against pyroxene but subhedral elsewhere, with oscillatory and mottled continuous zoning, and occasionally sieved by tiny pyroxene and opaque grains. Deformation features, such as distorted twin planes and zones of intracrystalline recrystallisation, are conspicuous in many laths. Magnetite is abundant.

Hornblende-rich gabbro outcrops further north along the river exhibit minor textural and mineralogical variability. Sample **98-CP4*** is dark grey-black, medium, even-grained and dominated by aligned hornblende prisms and plagioclase laths, with minor orthopyroxene and rare clinopyroxene (all grains ~1-3 mm). In thin section, the latter is invariably mantled and replaced along cleavages by hornblende, and orthopyroxene is mostly fringed by fibrous cummingtonite, except where enclosed by brownish hornblende (Figure 13.4d). Plagioclase laths exhibit patchy continuous zoning, and some have kinked twin planes. Ragged poikilitic biotite flakes (to 1 mm) are minor.

Samples **98-CP5** and **98-CP6** are very similar but lack pyroxene, this mineral being entirely pseudomorphed by decussate cummingtonite sheaves, sometimes overgrown in turn by blue-green hornblende. Hornblende gabbro 11903 of Ferguson (1993), collected from a nearby outcrop, is texturally identical, but with a slightly higher proportion of plagioclase.

An adjacent, more felsic hornblende gabbro outcrop supports an intense planar fabric of aligned hornblende and plagioclase laths and large distorted biotite flakes (**98-CP3**, Table 13.1). This foliation is mylonitic but parallels the regional trend of S_2, and was thus probably imposed by D_2.

13.5 Ferres Creek Tonalite and 'dioritic' rocks

Despite the striking mineralogical differences, the hornblendic Ferres Creek Tonalite and pyroxene-rich dioritic rocks are geochemically very similar (section 14.3.1c). Together, they have a small range in SiO_2 (56.4% to 60.3%) that overlaps with that of Wando type tonalites, though Caupaul rocks have lower Sr but higher MgO and K_2O at a given silica content (section 15.3.1a). Enclaves are not encountered in either Ferres Creek Tonalite or dioritic outcrops.

13.5.1 Ferres Creek Tonalite

Tors from the southern part of the Ferres Creek Tonalite (e.g. **98-CP12***) are light creamy-grey, medium to coarse grained, and dominated by blocky hornblende prisms (to 5 mm) and greenish plagioclase laths (~1.5 mm). Large distorted biotite flakes (to 5 mm) enclosing plagioclase are very conspicuous and define a pervasive foliation (S_2) of variable intensity. Although felsic mineralogy classifies the rock as tonalite, samples are more akin to quartz diorite given the unusually high mafic mineral content (up to ~40%, see Table 13.1). In thin section (Figure 13.5a), blue-green hornblende encloses plagioclase laths, spindly biotite flakes, and opaque

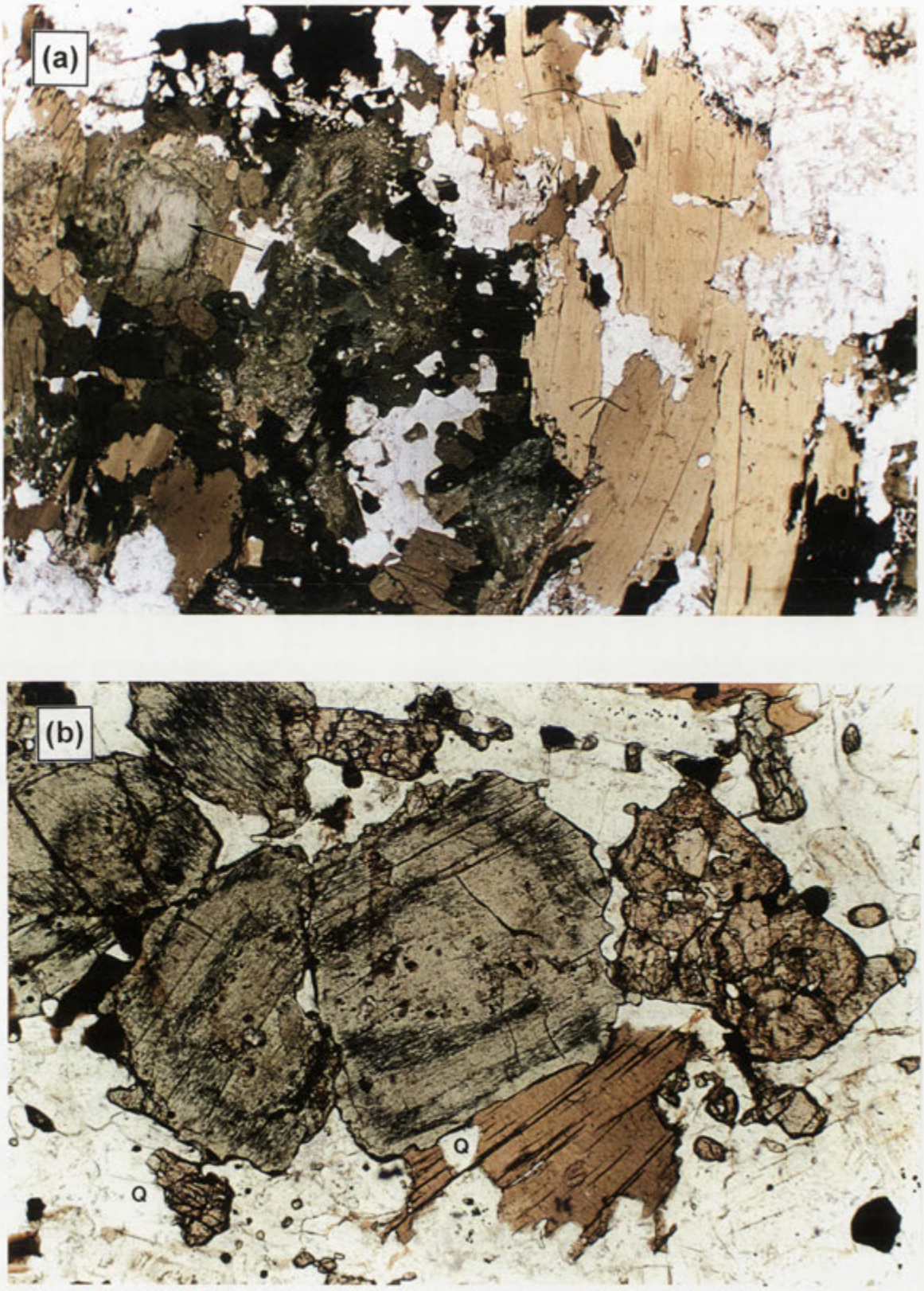

Figure 13.5. Intermediate rocks of the Caupaul Complex in thin section. (a) Ferres Creek Tonalite, exhibiting large, distorted biotite flakes and relict clinopyroxene enclosed by blue-green hornblende (left, arrowed) (plane polarised light, 8.1 mm across). (b) Typical appearance of pyroxenes (clinopyroxene pale green, orthopyroxene pale brown) and interstitial biotite in a quartz diorite. Note the fine exsolution in clinopyroxene prisms and small quartz granules (labelled Q) (plane polarised light, 2.5 mm across).

grains, being occasionally perforated with quartz. Many rectangular hornblende grains also contain relict clinopyroxene, indicating formation by replacement of this mineral. Interstices between plagioclase laths are quartz or microcline (~1 mm), the latter occasionally forming poikilitic masses (3-5 mm) enveloping hornblende and plagioclase. Anhedral to subhedral epidote is conspicuous.

Tonalite outcrops north of here are more intensely foliated and contain high strain zones where banded mylonitic rocks are developed. Exposures in Section Creek are also transected by discrete shear zones (1-1.5 m wide), where the mylonitic fabric is oblique to the S_2 foliation in the tonalite. Tonalite samples from here (98-CP140) are finer grained, with more microcline but less quartz (Table 13.1). Boulders of a similar lithology are prominent on the east side of the Glenelg River valley south of Kinks Creek (see Figure 13.1), though samples are darker coloured, finer grained and relatively alkali feldspar-rich, such that the rock is granodioritic (**98-CP11**). A strong foliation of smeared biotite, hornblende and recrystallised quartz aggregates is evident. Despite the greater degree of metamorphic modification, the poikilitic biotite flakes and hornblende-mantled clinopyroxene prisms that characterise typical Ferres Creek Tonalite samples are conspicuous in these variants.

13.5.2 Dioritic rocks

Finer grained and hornblende-deficient dioritic outcrops are scattered along the eastern Glenelg River valley north of Kinks Creek, and, with enclosed mafic-ultramafic bodies, extend ~2.9 km north to Fords Creek (Figure 13.1). Typical samples (e.g. **98-CP7**) are indistinguishable from gabbronorite **98-CP129**, being dark grey-brown coloured and uniformly fine to medium grained (~1 mm), with slightly larger plagioclase laths and clinopyroxene prisms (up to 2.5 mm). Some samples in this vicinity also have large poikilitic biotite flakes (4-6 mm). A pristine igneous texture is evident in thin section (Figure 13.5b) that is nearly identical to that of **98-CP129** except for the occurrence of interstitial blebs and poikilitic pools of microcline, accompanied by tiny grains of interstitial quartz. Deformation features are limited to curvature of plagioclase twin planes, though strongly foliated variants are noted by Kemp *et al.* (2001).

Dioritic samples north of McPherson's Creek near the hornblende pyroxenite-gabbronorite mass are finer grained and weakly porphyritic, where plagioclase and pyroxene phenocrysts occur in a very fine grained matrix of plagioclase, pyroxene, quartz and poikilitic microcline (**98-CP1**).

The northernmost dioritic sample (**98-CP10**) was collected from a 50 m wide dyke intruding metasedimentary rocks in Fords Creek; contacts with enclosing rocks are sharp, and rotated calc-silicate enclaves occur towards the northern dyke margin. Specimens are dark grey-black and fine to medium grained, with conspicuous biotite flakes (some poikilitic to 3 mm) defining a distinct planar fabric (S_2). Pyroxene is pseudomorphed by pale green amphibole in thin section, in turn mantled by khaki green hornblende; the blocky outline of the original pyroxene is preserved, and some grains also have relict unaltered pyroxene. Distorted plagioclase laths are aligned with the biotite foliation and have cuspate re-entrants against polygonal quartz aggregates. This rock is considered to be a deformed and recrystallised equivalent of the

unmodified pyroxene-rich quartz diorite. Notably, texturally-similar metamorphosed quartz diorite to mafic tonalitic dykes intrude calc-silicate rocks in Corea Creek of the Wando Vale district, ~30 km to the southeast (Anderson 1990). These also have chemical affinity with Caupaul intemediate rocks (section 14.3.1c).

Chapter 14: Mineral chemistry and geochemistry of mafic to ultramafic and intermediate rocks

14.1 Introduction

This chapter documents the mineral chemistry and bulk geochemistry of lithologies within the Caupaul Igneous Complex, the intermediate-mafic-ultramafic rocks of Chin Chap Creek-Robson Creek and the dioritic dykes of Robertson Creek. The implications of this for the petrogenesis of these rock types are discussed at the end of the chapter. In particular, it will be shown that the compositional characteristics of Caupaul gabbros and Robertson Creek diorites strongly suggest formation in a supra-subduction zone environment.

14.2 Mineral chemistry

Microprobe analyses of minerals from nine Caupaul Igneous Complex samples, two hornblende gabbro-diorites and a diorite from Chin Chap Creek, and a hornblende diorite from Robertson Creek are listed in Appendix F. The broad compositional attributes of the major minerals are outlined below.

14.2.1 Pyroxenes

Orthopyroxene and clinopyroxene compositions are plotted in Figures 14.1 and 14.2, according to the projection methods of Lindsley (1983). Most derive from rims (where free of secondary amphibole alteration), though cores of larger grains were also analysed; however, in most cases compositional zonation is minor (see Appendix F). Note that pigeonitic clinopyroxene occurs in several Caupaul samples, coexisting with augite and orthopyroxene. All pyroxenes were analysed in 'area scan' mode by the SEM to compensate for the ultra-fine exsolution features present in some grains (see Figure 13.5b). Nevertheless, this is likely to impart additional uncertainty to the temperature estimates.

The most magnesian pyroxenes are those of the Chin Chap Creek gabbro-diorites (Mg# 0.81-0.84), which, not coexisting with orthopyroxene, are the most Ca-rich and plot in the diopside field (Figure 14.1). Notably, the relict clinopyroxene grains enclosed by the hornblende phenocrysts of these samples are indistinguishable from matrix diopsides (Appendix F).

Of the Caupaul Complex samples, pyroxenes of hornblende pyroxenite **98-CP8** are the most Mg-rich (clinopyroxene Mg# 0.82-0.79, orthopyroxene Mg# 0.74-0.68), those of pyroxenite **98-CP9** and hornblende gabbronorite **98-CP2** having marginally lower Mg#. Pyroxenes of the latter are unusual in having much higher Al_2O_3 contents than other samples, ranging to 3.8% for clinopyroxene and 3.2% for orthopyroxene (compared to a maximum of 2.5% and 1.8% for **98-CP9** respectively). Despite the relatively felsic mineralogy, pyroxenes of quartz diorites are unusually magnesian, having augites that overlap compositionally with those of pyroxenite **98-CP8**. As a result, both clinopyroxene and orthopyroxene of diorite 11904 are clearly more

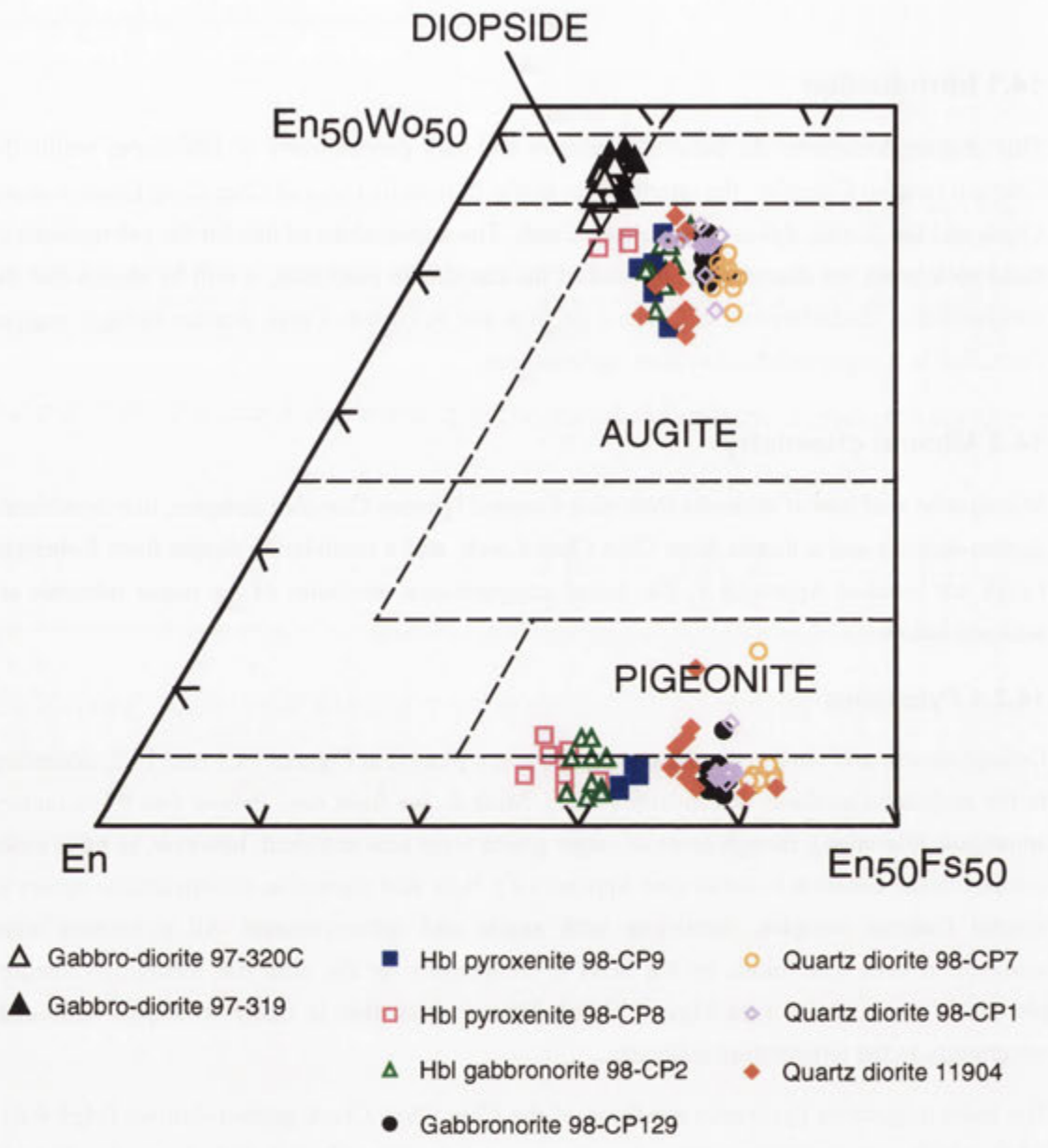

Figure 14.1. Composition of pyroxenes within rocks of the Caupaul Igneous Complex and Chin Chap Creek gabbro-diorites, plotted according to the formulation of Lindsley (1983) (hbl = hornblende). Note that only the bottom left hand corner of the pyroxene quadrilateral is represented. Compositional fields are taken from Deer *et al.* (1966).

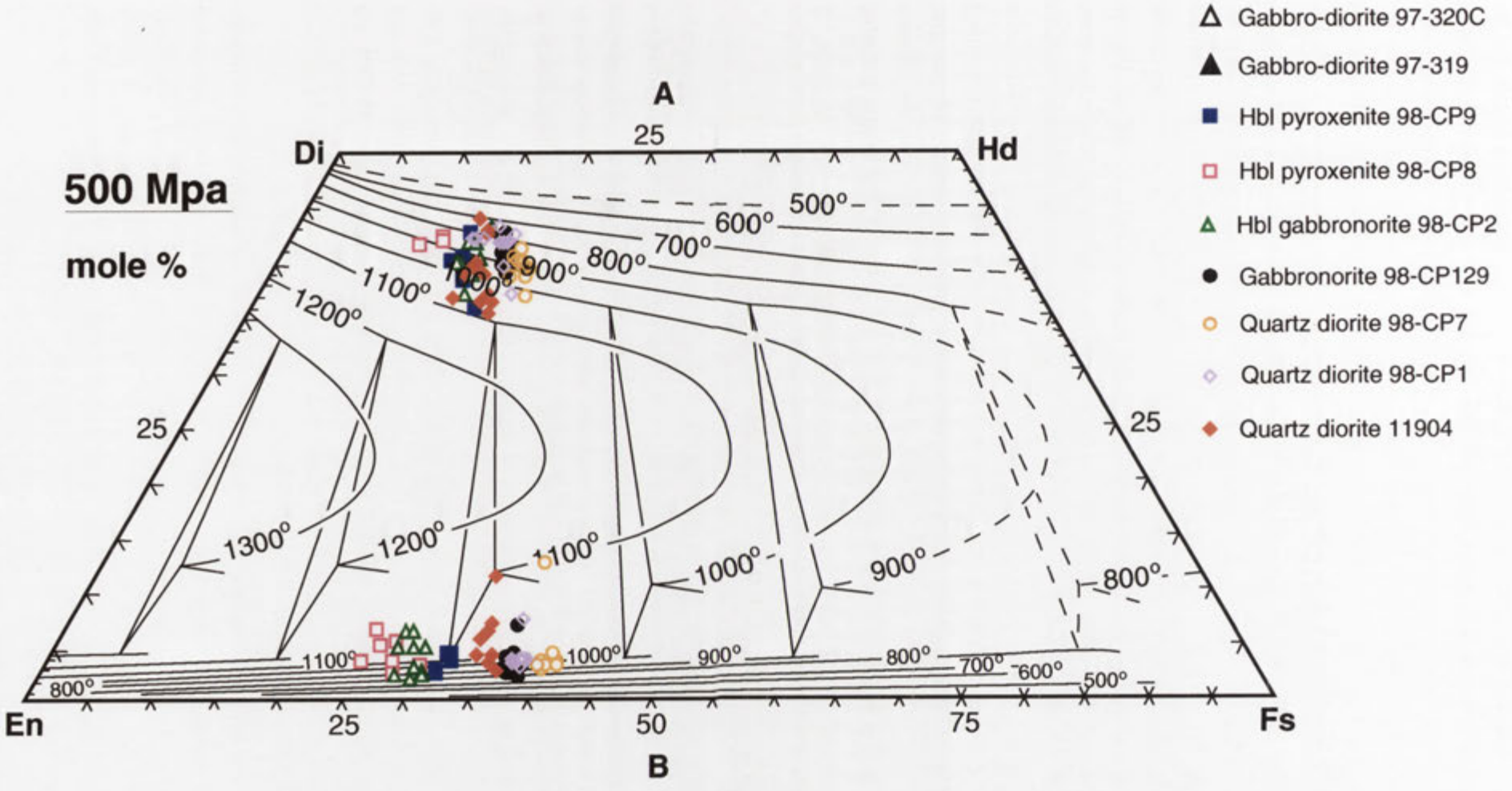

Figure 14.2. Coexisting clinopyroxene and orthopyroxene grains from Caupaul Igneous Complex samples shown in comparison to the orthopyroxene-augite-pigeonite phase relations at 5 Mpa, contoured at 100°C intervals (from Lindsley 1983). Pyroxenes compositions were recalculated and projected according to the scheme of Lindsley (1983).

Mg-rich than those of the gabbronorite **98-CP129**. This has important implications for the relationship between these lithologies, elaborated in section 14.4.2. Some clinopyroxene grains in diorite 11904 also exhibit normal core-to-rim zonation, the most pronounced being from Mg# 0.81 to Mg# 0.73. Clinopyroxenes of quartz diorite **98-CP1** also extend to more magnesian compositions than those of the gabbronorite, whereas pyroxenes of the other quartz diorite sample (**98-CP7**) are slightly more Fe-rich.

Pyroxenes within individual Caupaul Igneous Complex samples exhibit the greatest variation in wollastonite component, resulting in a spread of inferred temperatures, from ~700-1100°C for clinopyroxene and ~700- >1200°C for orthopyroxenes (Figure 14.2). This may partly reflect variable exsolution, which is probably responsible for the scattering of orthopyroxene compositions above the 1200°C isotherm and into the pigeonite field. However, the two clinopyroxene grains of quartz diorites plotting in the pigeonite field near the 1100°C isotherm are regarded as 'primary' compositions. Furthermore, as clinopyroxene and orthopyroxene commonly exhibits slight core-to-rim increase and decrease respectively in wollastonite component (see Appendix F), it is likely that the temperature range mostly reflects continuing re-equilibration of orthopyroxene-clinopyroxene pairs during protracted cooling. Despite this, within the limits of uncertainty (±50°C, Lindsley 1983), pyroxene pairs within the different Caupaul Complex samples yield remarkably similar temperatures, although differing considerably in Mg#. The maximum temperatures are probably ~1100°C, constrained by the orthopyroxene-augite-pigeonite assemblage of dioritic samples 11904 and **98-CP7**.

14.2.2 Amphiboles

These show a range of compositions within individual samples, mostly plotting in the pargasite or edenite fields (Figure 14.3). Exceptions to this are the more aluminous tschermakites of Chin Chap Creek gabbro-diorite **97-320C** and the pale green actinolitic amphiboles of gabbro-diorite **97-319**, which are also the most Mg-rich. Some of the latter are probably secondary, clearly mantling diopsidic clinopyroxene grains, accounting for the magnesian and sub-aluminous character. However, most analyses derive from the rims of brownish hornblende phenocrysts, which are euhedral against interstitial plagioclase, suggestive of magmatic crystallisation. Hornblende diorite **97-376** also has two distinct amphibole compositions (Figure 14.3), with actinolitic hornblende rims mantling markedly more aluminous hornblende cores. Although more alkaline for a given Al^{iv}, hornblende prisms of Robertson Creek diorite **98-RC1** are similarly zoned. Amphiboles of hornblende gabbronorite **98-CP2** have high Al contents, according with the unusually aluminous pyroxenes within the sample.

Amphiboles also exhibit considerable variation in Mg# (Figure 14.4a) which broadly correlates with that of coexisting clinopyroxenes (Figure 14.4b). There is also a marked correlation between Mg# and Ti for most samples (Figure 14.5), though Chin Chap Creek hornblende diorite **97-376** has considerably less Ti than that of Caupaul gabbro **98-CP6**, despite similar Mg#. The relatively Fe-rich amphiboles of the Ferres Creek Tonalite and Robertson Creek diorite (rims) share this low Ti signature.

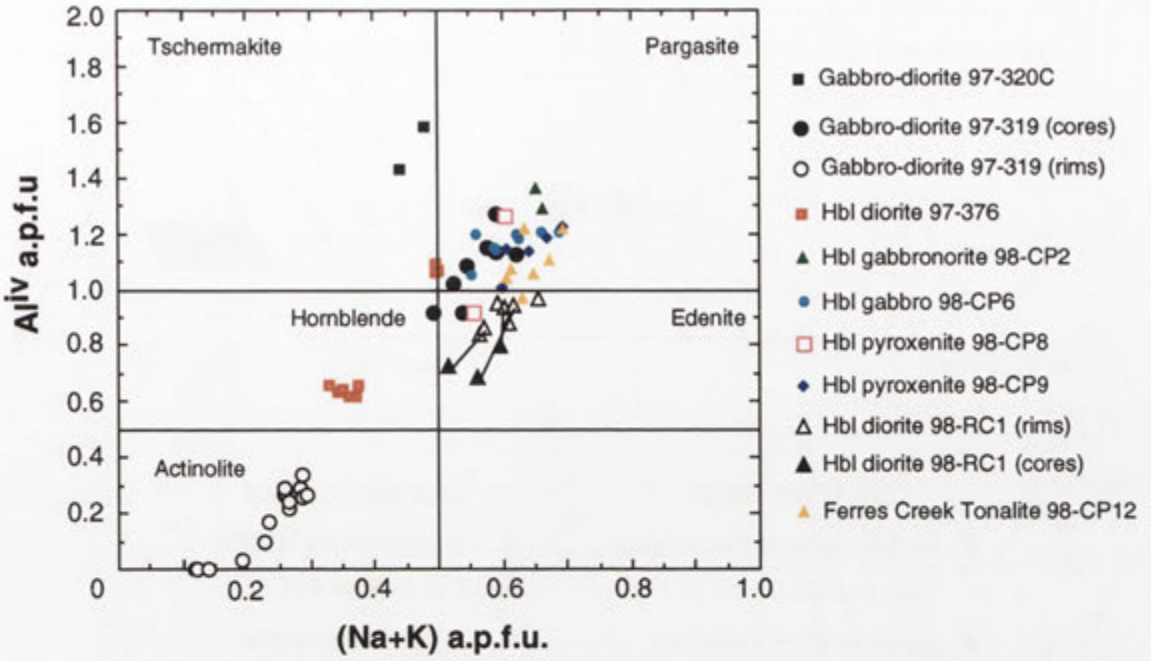

Figure 14.3. Amphibole compositions of Caupaul Igneous Complex and Chin Chap Creek samples, and Robertson Creek diorite 98-RC1 (all in atoms per 24 O). Tie lines connect amphibole cores and rims in **98-RC1**. Compositional fields from Deer *et al.* (1966). The open symbols for sample **97-319** includes both actinolitic rims around hornblende phenocrysts and matrix actinolite crystals. The low Al, low Na+K amphibole population of sample **97-376** corresponds to hornblende rims.

14.2.3 Plagioclase

Plagioclase compositions are summarised by Figure 14.6. Note that K_2O content is very minor in all samples.

(a) Caupaul Complex samples

Intercumulus plagioclase of Caupaul Complex pyroxenite **98-CP8** and hornblende gabbronorite **98-CP2** is bracketed between An_{87} and An_{93}, that of the latter being slightly more calcic (Figure 14.6). Plagioclase of **98-CP8** is unzoned, whereas **98-CP2** plagioclase exhibits small differences between cores and rims, with both normal (grain 1B, An_{93} to An_{90}) and reverse (grains 3A and 3B, An_{90} to An_{91}) zonation observed.

Plagioclase laths in gabbroic and dioritic samples exhibit more irregular patchy zonation. Due to the complexity of this, no attempt has been made to ascertain the complete chemical variation within individual grains; instead, the broad compositional character of these is described.

Cores of plagioclase grains in hornblende gabbro **98-CP6** are mostly labradorite (An_{52} to An_{61}), and overgrown by thick, marginally more calcic rims (An_{56} to An_{65}), many of which have weak oscillatory zoning. The exception is grain 3A, where the mottled-zoned interior encloses a small, corroded core that is substantially more calcic (An_{74}). In contrast, cores of grains 1A and 3A in gabbronorite **98-CP129** (~An_{52}) are overgrown by a thin euhedral 'shell' of markedly more calcic plagioclase (~An_{83}), mantled in turn by a thick, more sodic rim (~An_{48}). Grain 6A is similar,

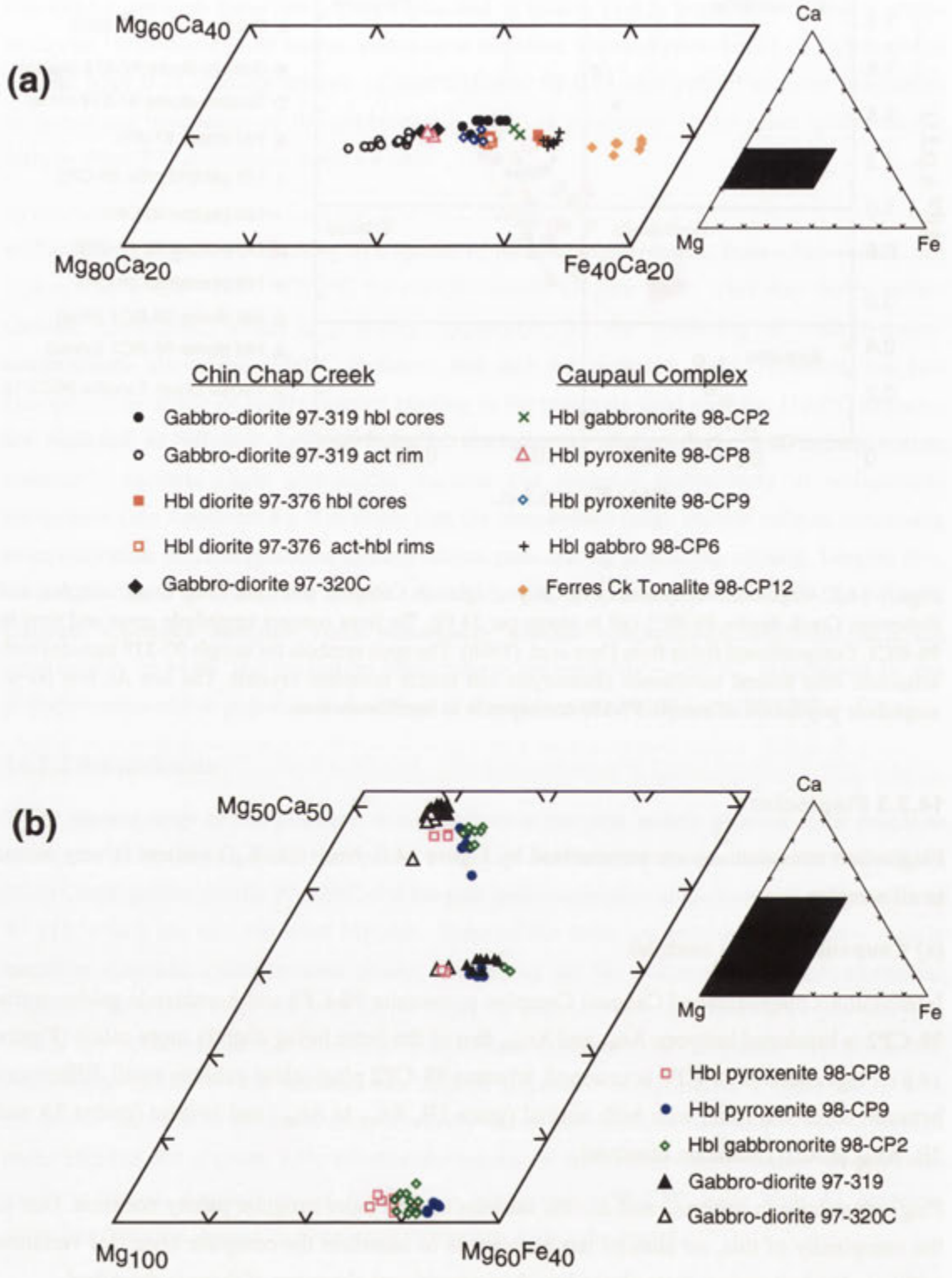

Figure 14.4. (a) Amphiboles in GRC mafic-ultramafic rocks in terms of atomic Ca, Mg and Fe proportions. Note the large variation in Mg-Fe compared to Ca for all samples (act = actinolite; hbl = hornblende). (b) Coexisting clinopyroxene (top), hornblende (centre) and orthopyroxene (bottom) within mafic-ultramafic rocks in terms of atomic Ca, Mg and Fe.

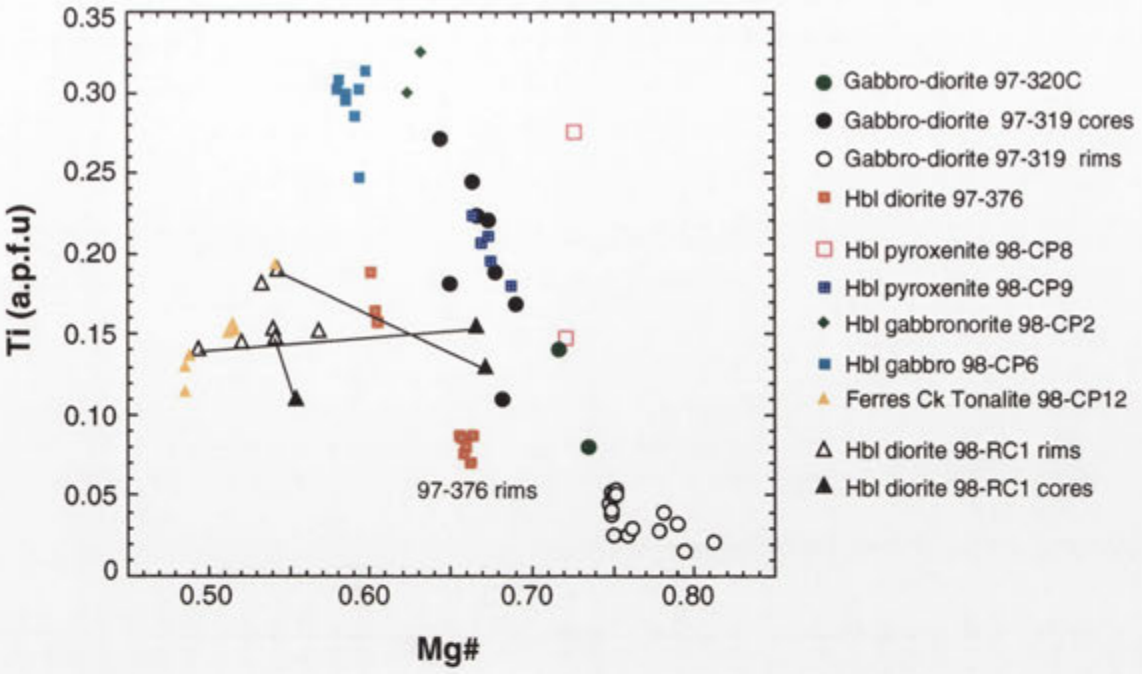

Figure 14.5. Plot of Ti (atoms per 24 O) versus Mg# (atomic Mg/Mg+Fe) for hornblende grains within rocks of the Caupaul igneous Complex, Chin Chap Creek and Robertson Creek diorite **98-RC1**. Tie lines connect hornblende cores with rims in the latter. Analytical uncertainty in Ti is 0.01 a.p.f.u.

though the core is more calcic (to An_{65}). Plagioclase of quartz diorite **98-CP7** has similar compositional character to the gabbronorite, such that large cores (~An_{58} to An_{62}) have thin euhedral overgrowths (An_{73} in 5A) and more sodic rims (~An_{47}-An_{48}).

Plagioclase phenocrysts in quartz diorite **98-CP1** have even more complex zoning characteristics. The cores of these consist of intimately intergrown calcic labradorite (An_{60}-An_{64}) and bytownite (An_{80}-An_{82}), the latter becoming predominant outwards. This is euhedrally overgrown by more regular zones of labradorite (An_{53}-An_{56}) and labradorite-bytownite (An_{65}-An_{72}) respectively, rimmed in turn by sodic labradorite to calcic andesine (An_{53}-An_{47}).

Less calcic plagioclase occurs within other intermediate Caupaul Complex rocks. Quartz diorite 11904 has small, mottled-zoned cores (An_{60} to An_{63}) continuously zoned out to more sodic rims (An_{41}-An_{44}). Two unzoned plagioclase grains enclosed by poikilitic alkali feldspar are An_{57} and An_{45}. A larger plagioclase lath (grain 7A) has a patchy-zoned core, varying from An_{61} to An_{57}, overgrown by a thin rim of An_{44}. The small plagioclase laths of Ferres Creek Tonalite **98-CP12** are mostly unzoned (An_{47} to An_{51}), or have weak continuous zoning (An_{51} to An_{49} in grain3B). Larger grains have mottled cores that are slightly more calcic (An_{57} in grain 4A).

(b) Chin Chap Creek samples

Although having higher bulk rock CaO (>11%; see below), interstitial plagioclase of Chin Chap Creek gabbro-diorites **97-320C** and **97-319** is much less calcic than that of the Caupaul pyroxenite, grains being weakly (normally) zoned andesine (An_{37} to An_{41}). More calcic

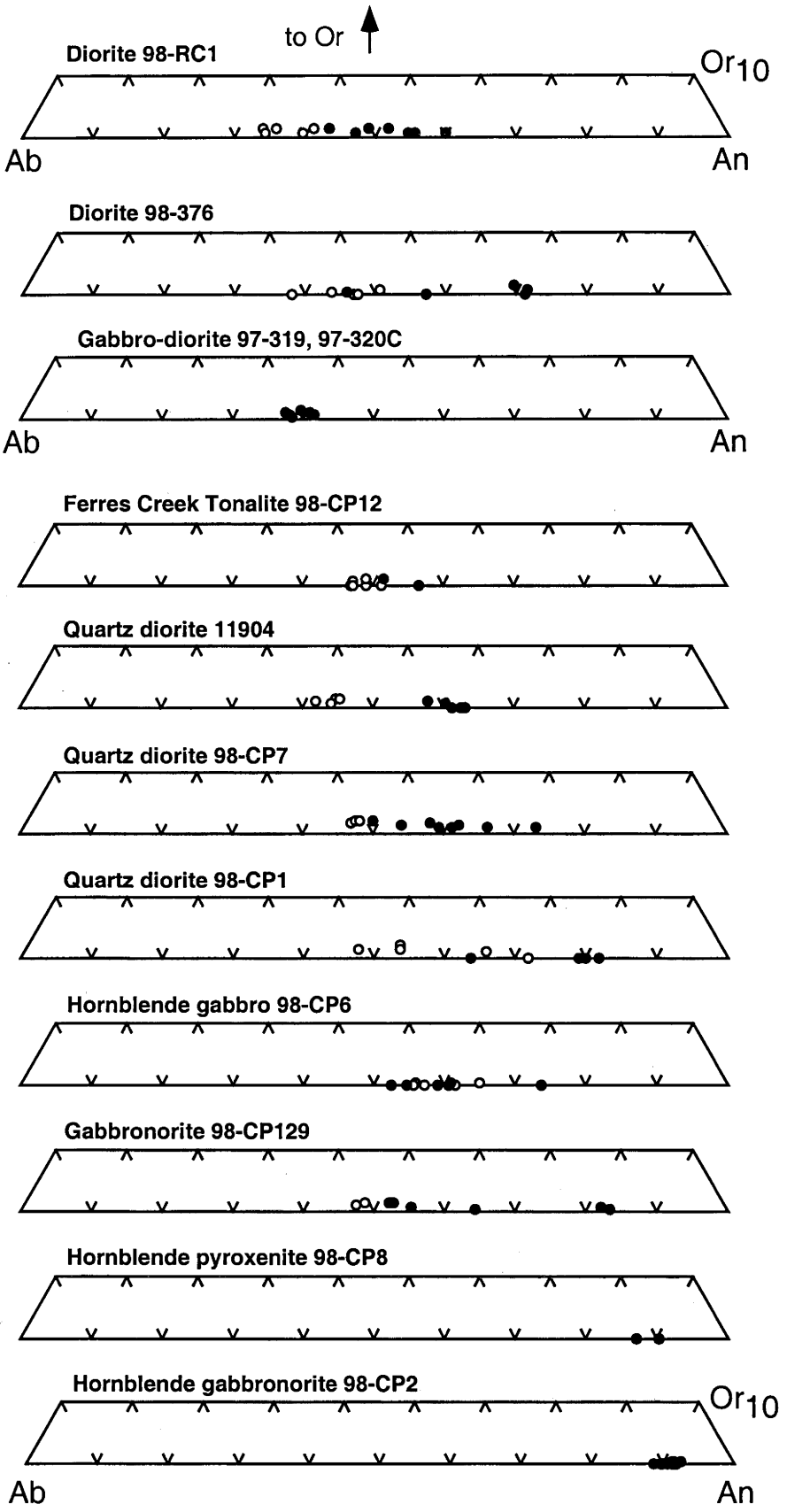

Figure 14.6. Plagioclase composition for rocks of the Caupaul Complex, Chin Chap Creek and Robertson Creek diorite **98-RC1** in terms of albite, anorthite and orthoclase components (atomic Na, Ca and K respectively). Only the bottom part of the compositional triangle is shown (i.e. Or_0 to Or_{10}) Filled symbols represent core compositions and open symbols are rim compositions.

compositions are evident in hornblende diorite **97-376**, where euhedral, unzoned cores extend to An_{71} (grains 4A and 6A). These are overgrown by thick, relatively sodic rims, varying from An_{50} in grain 6A to An_{38} in 4B, which are optically uniform or show weak continuous zoning.

(c) Robertson Creek diorite

Most small plagioclase laths in diorite **98-RC1** have irregularly-shaped or (less commonly) euhedral cores (to An_{60}) that are continuously zoned to relatively sodic rims (An_{35}). Others have more complex zoning, such as grain 9A, where a euhedral core (An_{54}) has discrete overgrowths of An_{42} and An_{55}, with a normally-zoned sodic rim (An_{34}). Despite intricate mottled zoning, the cores of larger blocky plagioclase grains (e.g 7A) are compositionally fairly uniform (~An_{47}-An_{50}) and mantled by thin, normally zoned rims (An_{33}).

14.2.4 Biotite

Biotite grains were analysed from Ferres Creek Tonalite **98-CP12** and Chin Chap Creek diorite **97-376** (Appendix F). The latter are magnesian (Mg# 0.61-0.63) and contain significant amounts of TiO_2 (2.4-2.9%) and Al^{iv} (2.3-2.4 a.p.f.u.). Biotite of **98-CP12** is comparatively Fe-rich (~Mg# 0.50), but has similar TiO_2 (2.5-2.7%) and Al^{iv} content (~2.4 a.p.f.u.).

14.3 Geochemistry

14.3.1 Caupaul Igneous Complex

The geochemistry of 14 rocks from the Caupaul Complex, including hornblende gabbro 11903 of Ferguson (1993), is presented in Appendix G.

(a) Gabbros

Hornblende-rich gabbros **98-CP4**, **98-CP5** and **98-CP6** are compositionally almost indistinguishable, with low silica (46.6%-46.9%) at moderate MgO contents (6.5-7.0%) and Mg# (0.52-0.54)[1], lower than that of N(normal)-MORB (Mg# 0.60-0.70; Sun & McDonough 1989). Samples have 0.75-0.82% K_2O and therefore fall into the medium-K or calc-alkaline field (Figure 14.7). Hornblende gabbro 11903 is chemically very similar, but with slightly higher SiO_2 (48.3%) and Na_2O (2.5%), and less MgO (6.4%) and TiO_2 (0.9%). Gabbroic sample **98-CP3** is more evolved, with 52.6% SiO_2 and 1.3% K_2O. Most distinctively, all hornblende gabbros are characterised by high Al_2O_3 (>18%) and moderately high Sr (~330-370 ppm), reflecting the plagioclase-rich nature, and are therefore high-Al gabbros according to the criteria of Crawford *et al.* (1987). Caupaul gabbros have low Ni (<70 ppm) and Cr (<60 ppm) compared to average N-MORB (130 and 300 ppm Ni and Cr respectively, Sun & McDonough 1989), as is typical of high-Al basaltic rocks (e.g. Brophy 1986; Crawford *et al.* 1987). However, Sc concentrations (45-51 ppm) are distinctly higher than N-MORB (38 ppm Sc). Pyroxene-dominated gabbronorite **98-CP129** is more siliceous (50.7% SiO_2) than primitive hornblende gabbros, with lower MgO (6.0%) and K_2O (0.5%), but also shares the high Al, high Sr signature (18.5% Al_2O_3, 360 ppm Sr).

[1] Calculated as molar MgO/(MgO+total FeO)

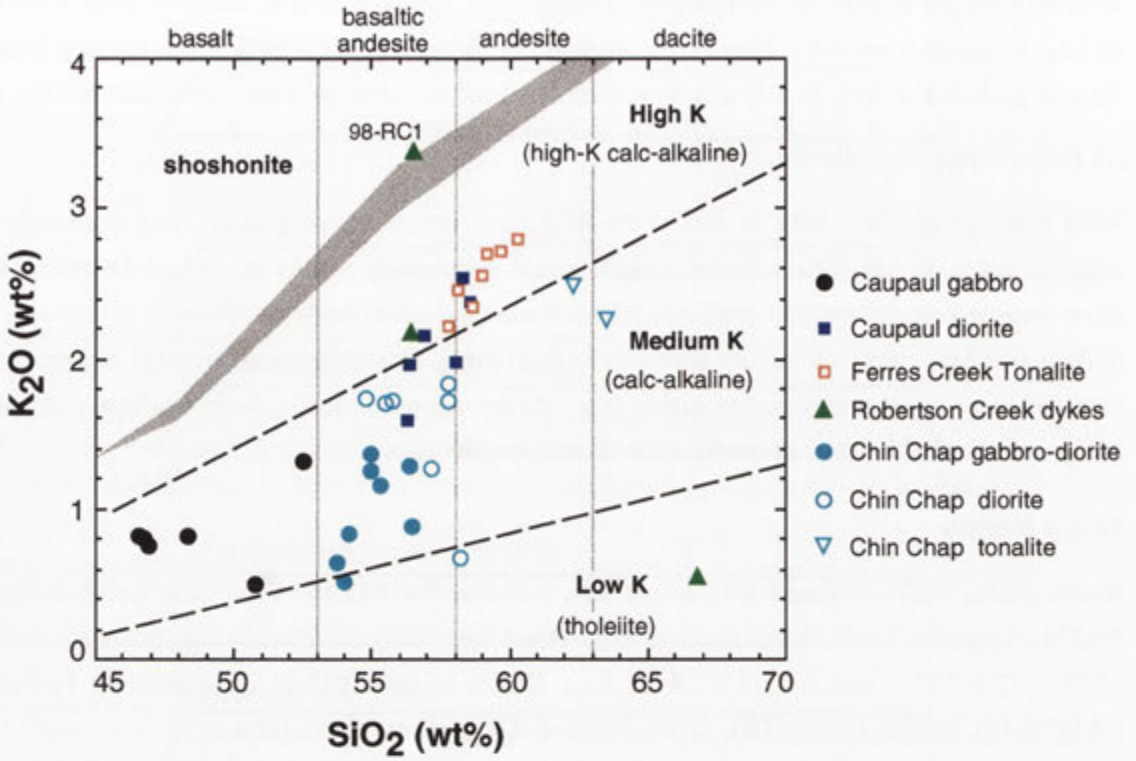

Figure 14.7. K_2O versus SiO_2 plot for rocks of the Caupaul Igneous Complex, Chin Chap Creek and dioritic-tonalitic dykes from Robertson Creek. The dashed subdivisions are from Le Maitre *et al.* (1989), with the nomenclature in parentheses from Rickwood (1989). The shaded band separating the shoshonite and high-K calc-alkaline rock series encapsulates the boundary lines of many different authors, as summarised by Rickwood (1989). Vertical grey lines at 53%, 57% and 63% SiO_2 separate basalt, basaltic andesite, andesite and dacite compositions (from Tatsumi & Eggins 1995).

All gabbroic samples exhibit striking Pb enrichment on a primitive mantle-normalised multi-element diagram (Figure 14.8), with elevated LILE, Th, U compared to the primitive mantle and average N-MORB, and depletion in Nb relative to K (particularly in **98-CP3**). The LILE, Th and U enrichment is weakest for gabbronorite **98-CP129** and most marked for **98-CP3**, which in this respect resembles Caupaul diorites (see below). Hornblende gabbros **98-CP6** and 11903 exhibit pronounced depletion in Zr and Hf relative to Sm and N-MORB, whereas all samples have slightly depleted Ti, Y and Yb compared to N-MORB.

Hornblende gabbros have similar, fractionated chondrite-normalised REE patterns (La_N / Yb_N = 4.38-6.4; Figure 14.9), which results from marked LREE enrichment (~80 times chondrite), combined with depletion in the HREE (Dy to Lu) relative to N-MORB. Sample **98-CP6** has the highest normalised REE abundances, apart from La and Ce, which results in a distinctively convex LREE pattern similar to that of hornblende pyroxenites. REE abundances from Pr to Lu are lower in slightly more felsic gabbro 11903, and the lowest in the most evolved sample (**98-CP3**). Gabbronorite **98-CP129** has clearly lower HREE concentrations than all hornblende gabbros, which together with mineralogical differences, suggests a slightly different petrogenesis. Importantly, all samples have small negative Eu anomalies, which are greater in the most mafic

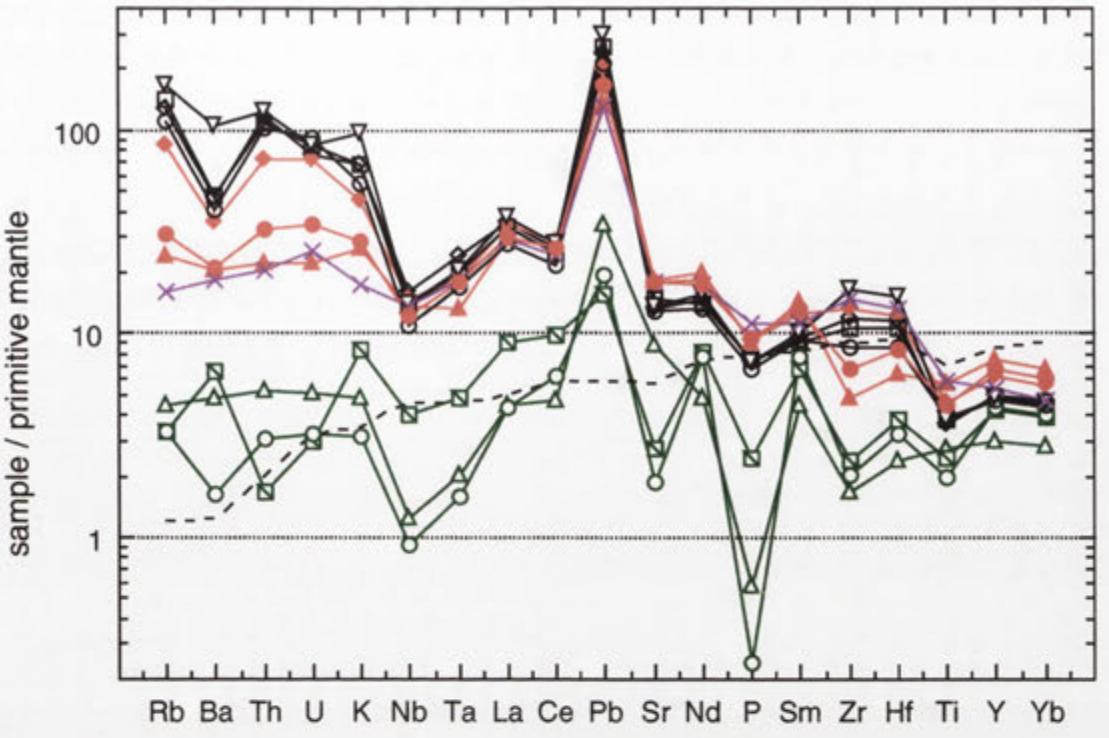

Figure 14.8. Rocks of the Caupaul Igneous Complex normalised to the primitive mantle of McDonough & Sun (1995), except for Pb, taken from Sun & McDonough (1989). Diorites and Ferres Creek Tonalite **98-CP11** are shown in black, whereas hornblende gabbros are majenta and pyroxenites are green (see Figure 14.9 for symbols). Gabbronorite **98-CP129** is plotted in purple. The average N-MORB of Sun & McDonough (1989) is plotted for comparison (dashed line).

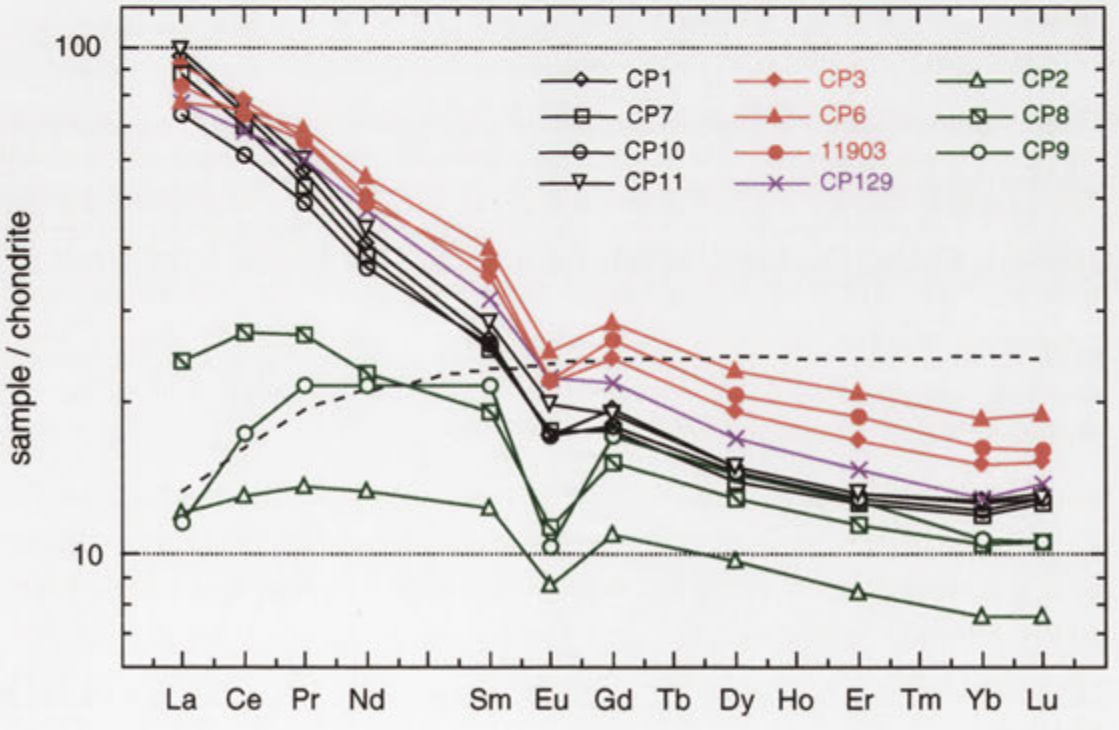

Figure 14.9. Chondrite-normalised (values from Anders & Grevesse 1989) REE plot for rocks of the Caupaul Igneous Complex (colour scheme as for Figure 14.8). N-MORB of Sun & McDonough (1989) is also shown for comparison (dashed line). Note the systematic LREE increase from the most mafic (**98-CP10**) to the most felsic (**98-CP11**) intermediate sample.

hornblende gabbros (Eu/Eu* of 0.70 in 11903) compared to evolved gabbro **98-CP3** (Eu/Eu* = 0.75), and especially gabbronorite **98-CP129** (Eu/Eu* = 0.85). Since Eu behaves almost compatibly with plagioclase in basaltic melts (Figure 14.10), this precludes significant plagioclase accumulation in gabbros, which would alternatively impart a positive Eu anomaly.

Hornblende gabbro **98-CP6** is isotopically evolved for a basaltic rock, with $^{87}Sr/^{86}Sr = 0.7075$ and $\varepsilon_{Nd} = -4.6$ at the inferred time of crystallisation (500 Ma) (see Appendix A). Gabbronorite **98-CP129** has similar, but marginally more evolved initial isotopic ratios ($^{87}Sr/^{86}Sr = 0.7077$, $\varepsilon_{Nd} = -5.9$). These values are well outside the range for MORB and most ocean island basalts, but overlap with the most radiogenic basalts erupted from some mature arcs (Figure 14.11).

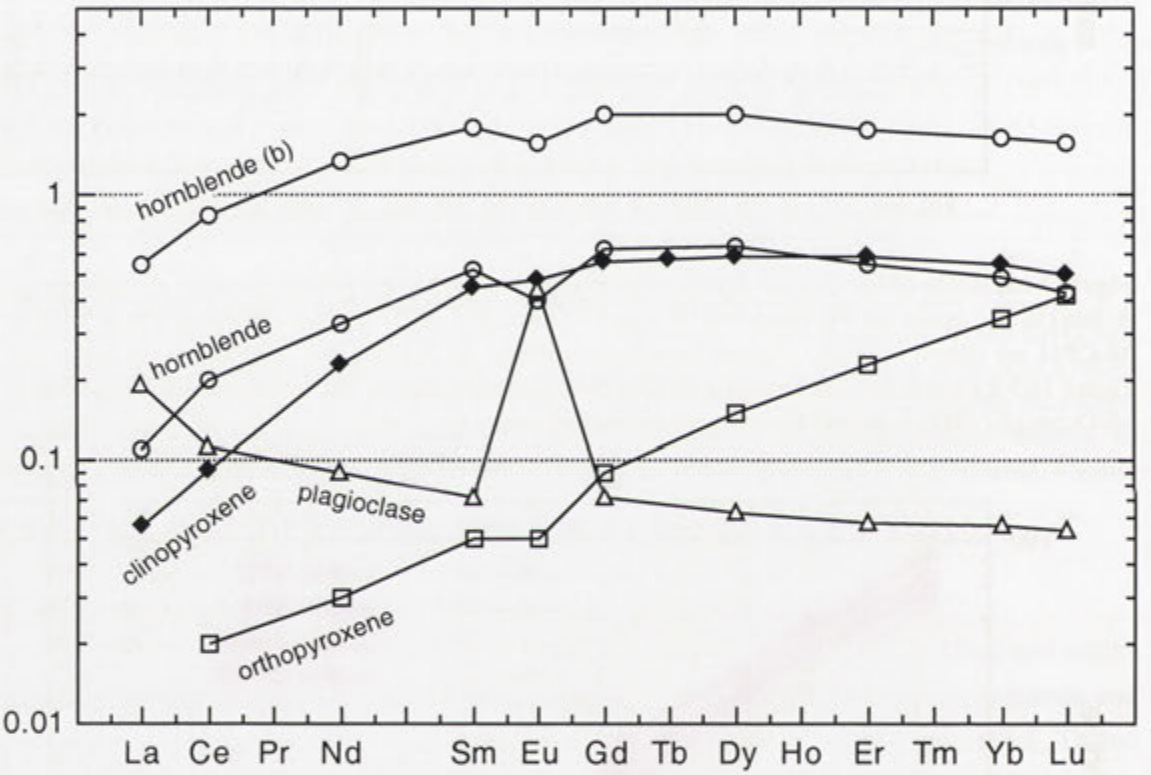

Figure 14.10. Plot of partition coefficients for the REE between orthopyroxene, clinopyroxene, hornblende, and plagioclase and a melt of basaltic composition (data sources in Rollinson 1993). Hornblende (b) is for a basaltic andesite liquid with 56% SiO_2.

(b) Pyroxenites

According with the pyroxene-dominated mineralogy, hornblende pyroxenites **98-CP8** and **98-CP9** have very high MgO (18.6% and 16.5% respectively), Cr (>1300 ppm), Ni (>200 ppm) and Sc (>70 ppm), with low TiO_2 (<0.5%). Reduced Al_2O_3 (2.7% in **98-CP9**), Sr and Na_2O abundances reflect the paucity and extreme anorthite content of plagioclase. These attributes are

shared by pyroxenitic samples from the margin of the McPherson's Creek pyroxenite-gabbronorite mass analysed by Turner *et al.* (1993a) and Ferguson (1993). A gabbronorite from this body has $^{87}Sr/^{86}Sr = 0.7096$ and $\varepsilon_{Nd} = -7.7$ (calculated at 500 Ma from data quoted in Turner *et al.* 1993a). The preponderance of clinopyroxene in **98-CP9** further results in elevated CaO (16.5%) and Sc (93 ppm) compared to other pyroxenitic rocks.

Compared to high-Al gabbros, hornblende pyroxenites are strongly depleted in elements that are not readily incorporated by pyroxenes, such as LILE, HFSE and especially P (Figure 14.8). The effect is less pronounced for the least incompatible elements Hf, Ti, Y and Yb. Nevertheless, normalised Ba, Rb and Pb abundances of pyroxenites are greater than those of N-MORB, especially for **98-CP8**, which is slightly more enriched than **98-CP9** and also has elevated K. REE abundances of pyroxenites are also considerably less than those of gabbros (Figure 14.9), especially the LREE, which are most strongly incompatible with pyroxenes (Figure 14.10). This gives rise to convex-upwards chondrite-normalised LREE patterns, most strikingly for **98-CP9**, in which La concentration falls to ~10 times chondritic. Notwithstanding this, both **98-CP8** and the more depleted **98-CP9** have Ce, Pr and Nd concentrations greater than N-MORB. Both pyroxenites also have significant negative Eu anomalies, the largest being for **98-CP9** (Eu/Eu* = 0.54), but have similar HREE patterns to those of gabbros.

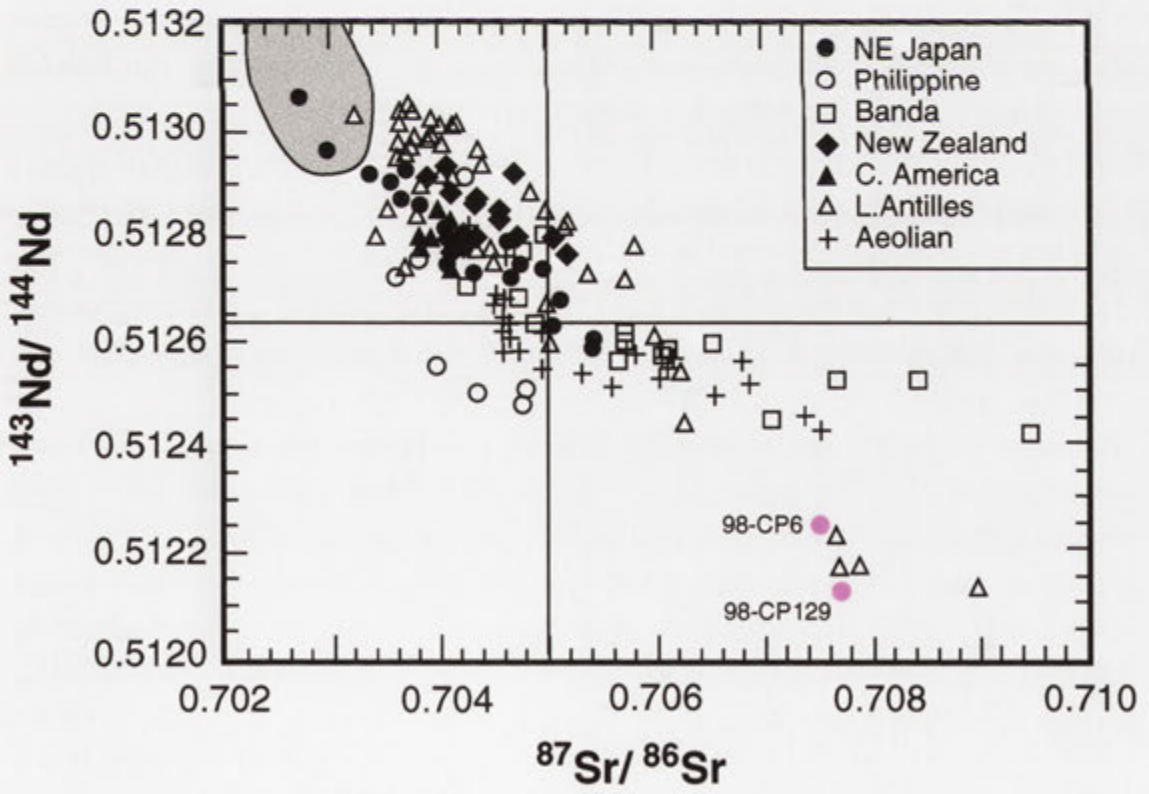

Figure 14.11. Comparison between the initial Sr and Nd isotopic composition of Caupaul gabbros **98-CP6** and **98-CP129** and that of various subduction zone basalts and the MORB field (shaded) (modified from Tatsumi & Eggins 1995).

Relative to the surrounding pyroxenites, hornblende gabbronorite **98-CP2** from the McPherson's Creek mafic body has lower MgO (12.9%) and higher Al_2O_3 (12.5%), TiO_2 (0.6%), and Sr (175 ppm), which manifest the greater plagioclase proportion (section 13.3). However, this rock has similar incompatible element-depleted characteristics to pyroxenites (Figure 14.8), and clearly has affinity with these rocks rather than with the high-Al gabbros, as is suggested by field relations (section 13.3). REE abundances of **98-CP2** are also strongly depleted and actually lower than pyroxenites, though the convex LREE pattern and Eu anomaly are less conspicuous (Figure 14.9).

(c) Intermediate rocks

As recognised by Ferguson (1993), pyroxene-rich dioritic rocks are geochemically very similar to Ferres Creek Tonalite samples, though in detail the tonalite evolves to slightly higher silica (60.3% in **98-CP11**) and K_2O (Figure 14.7), with lower MgO (3.8%), Cr (60 ppm), and Mg# (0.50) (Appendix G). The most mafic sample is quartz diorite 11904 of Ferguson (1993) with 6.9% MgO and Mg# ~0.64, thus the chemical range of intermediate rocks is quite large. Notably, the Mg# of dioritic samples (0.55-0.64) exceeds that of Caupaul hornblende gabbros.

With an average of 57.7% SiO_2, Caupaul dioritic-tonalitic rocks have the unusual combination of being quite magnesian (average of 4.9% MgO), but moderately potassic (2.2% K_2O). Cr contents are also very high (up to 403 ppm) and exceed those of Caupaul gabbros. The average Wando type quartz diorite has much lower MgO (3.8%), K_2O (1.4%) and Cr (~57 ppm) by contrast (Table 15.1). However, the metamorphosed dioritic dykes of Corea Creek (eastern Wando Vale) reported by Anderson (1990) (section 13.5.2) share the magnesian and potassic signature of Caupaul intermediate rocks (see Appendix G). This demonstrates that high-Mg magmatism was widespread across the southeastern GRC.

On variation diagrams (see Figure 16.1), Caupaul dioritic-tonalitic rocks plot as a cluster of points (TiO_2, Al_2O_3, Na_2O, P_2O_5) or define linear arrays that decrease gradually with SiO_2 (Fe_2O_3t, MgO, CaO). The exception is the LILE, which exhibit very steep linear increases with SiO_2. This results in evolution from the medium-K to the high-K field on Figure 14.7. Dioritic and tonalitic rocks also form a coherent group on Figure 14.8 and have similar patterns to high-Al gabbros, apart from elevated LILE, Th and U concentrations, which accentuate the negative Nb spike. The LILE (including Pb) and Th enrichment is strongest for the Ferres Creek Tonalite **98-CP11** and less pronounced for dioritic samples, **98-CP10** being the least enriched, and also containing lower normalised abundances of all other elements. Sr, P, Ti and Y concentrations of all tonalite-diorite samples are also less than for gabbros. **98-CP10** has slightly lower Zr and Hf than Sm, in contrast to other samples which have elevated Zr compared to Sm; the Zr/Sm ratio increases exponentially with decreasing Mg# (see Figure 16.4). Intermediate rocks have steep chondrite-normalised REE patterns, which are at lower normalised abundances than Caupaul gabbros, apart from La, Ce and Lu, which overlap (Figure 14.9). Accordingly, the LREE pattern of Caupaul diorite-tonalites is slightly more fractionated than that of the gabbros, and the HREE trend is more concave or bell-shaped. All intermediate rocks have small negative Eu anomalies ($Eu/Eu^* = 0.76$-0.85), which are comparable to those of gabbros. Although normalised Gd to Lu abundances of Caupaul diorite-

tonalite samples are almost identical, the LREE concentrations are inversely correlated with MgO, such that diorite **98-CP10** (6.2% MgO) has the lowest LREE (La_N/Yb_N = 6.28), and Ferres Creek Tonalite **98-CP11** (3.8% MgO) has the highest LREE (La_N/Yb_N = 8.14). The latter also has smaller Eu/Eu* (0.85) than diorite **98-CP10** (Eu/Eu*= 0.80).

14.3.2 Chin Chap Creek and Robson Creek

(a) Gabbro-diorites and hornblende diorites

Together, hornblende-rich rocks of Chin Chap and Robson Creeks have a small silica range (53.7-58.2% SiO_2) but exhibit striking variation in MgO (7.2-15.8%) and Al_2O_3 (7.2-15.1%), which are inversely correlated (Figure 14.12a) (see Appendix G). The chemical gradation between hornblende gabbro-diorite and hornblende diorite apparent on Figure 14.12 reflects the textural continuum between the two lithologies (Chapter 12). All rocks of the group are further characterised by high Mg# (up to 0.78) but low TiO_2 (mostly <0.7%; Appendix G). Relative to Wando type diorite-tonalite of similar silica, they also have lower Al_2O_3, Sr, Na_2O, manifested by the minor modal plagioclase, but clearly higher MgO (Figure 16.1).

Clinopyroxene-bearing gabbro-diorites have >10% CaO, with very high MgO (to 13.9%), Sc (58-73 ppm) and Cr (up to 1800 ppm) at low Al_2O_3 (<9%), thereby resembling pyroxenitic rocks of the Caupaul Complex. CaO/Al_2O_3 is very high (0.79-1.84) and increases with MgO (Figure 14.12b). However, LILE abundances are much higher than Caupaul pyroxenites (see below), with K_2O ranging from 0.5 to 1.4% (Figure 14.7). Gabbro-diorite **97-373A**, which lacks clinopyroxene, has much lower CaO (<8%), Sc (~46 ppm) and CaO/Al_2O_3 than other mafic gabbro-diorites but retains high Cr character (1680 ppm Cr). Sample **97-373A** also has distinctly higher MgO (15.8%) than pyroxene-bearing gabbro-diorites of the same Mg#.

Quartz diorites without obvious hornblende phenocrysts are less magnesian (7.2-9.2% MgO) and range to higher Al_2O_3 and Sr (to 15.1% Al_2O_3 and ~310 ppm Sr in **97-376**), according with the greater proportion of plagioclase. CaO/Al_2O_3 extends to lower values than gabbro-diorites (0.73-0.50) (Figure 14.12b) and K_2O is relatively high (~1.3-1.7%) apart from **97-380**, which has 0.7% K_2O (see Figure 14.7). Two dioritic 'globules' enveloped by the Kassingbrook Granodiorite at key locality E (**97-378-3** and **97-378-5**) have higher Al_2O_3, Sr, K_2O, Rb and Ba than other hornblende diorites, reflecting higher feldspar content, but the lowest MgO (<6.3%), CaO and CaO/Al_2O_3 (Figure 14.12) (Appendix G).

Normalised to the primitive mantle, mafic rocks of Chin Chap Creek/Robson Creek exhibit enrichment in LILE and Nb-Ta depletion relative to K (Figure 14.13). P and Ti also show distinct negative spikes, with HFSE (from P to Yb) being depleted compared to N-MORB (apart from **97-376**, which has higher Sm). Accordingly, multi-element patterns of Chin Chap Creek/Robson Creek rocks resemble those of Caupaul diorites-tonalites, though at lower elemental abundances. Zr and Hf are depleted relative to Sm in all Chin Chap Creek/Robson Creek samples, though normalised Zr/Sm increases slightly with decreasing Mg# and overlaps with that of Caupaul diorites (see Figure 16.4). Although enrichment in Rb relative to Ba is common to all, LILE

abundances of Chin Chap/Robson Creek diorites are less coherent than those of Caupaul intermediate rocks. Nonetheless, most samples have higher LILE concentrations than primitive Caupaul gabbro **98-CP6** (Figure 14.13)

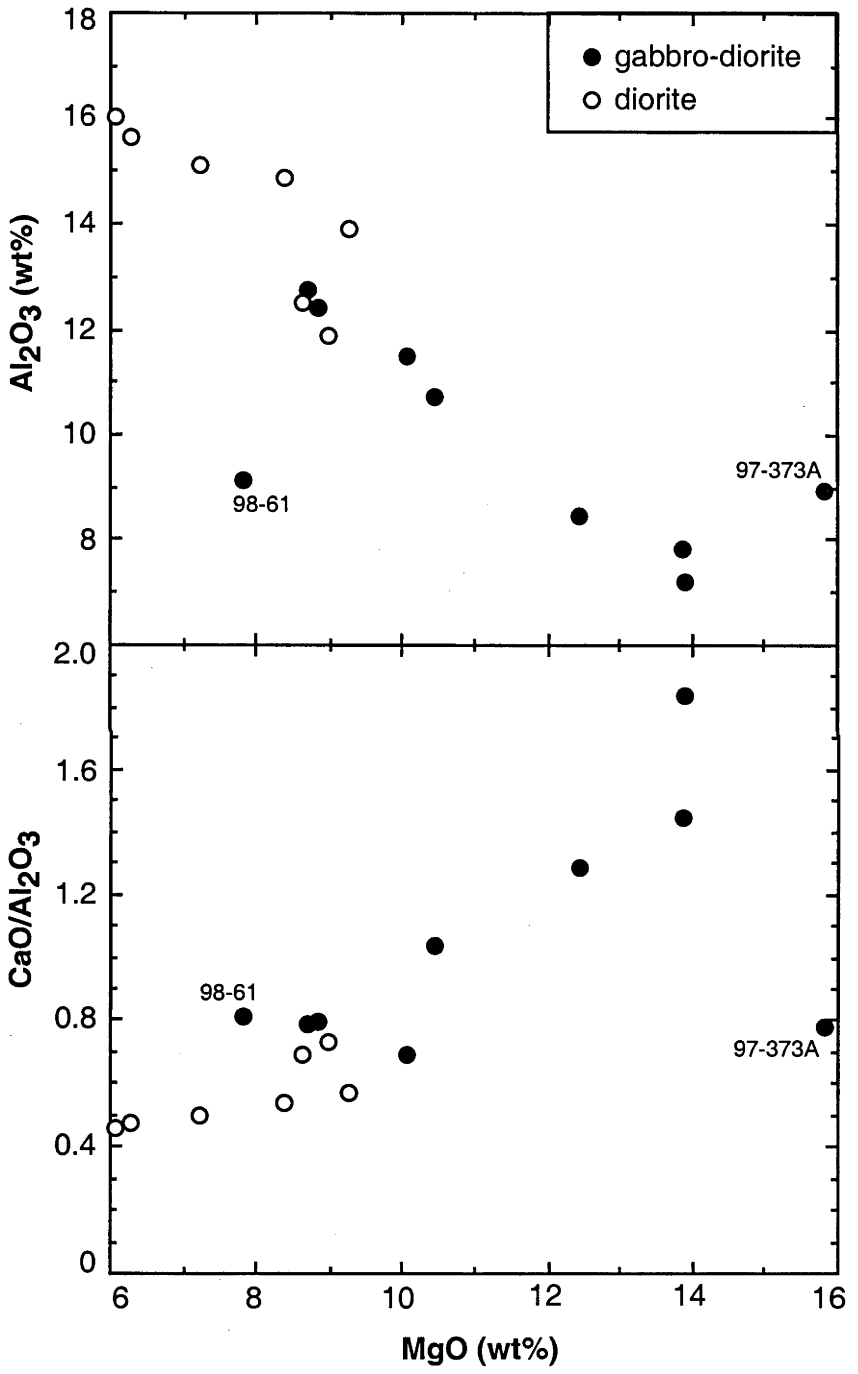

Figure 14.12. Plots of (a) Al_2O_3 versus MgO and (b) CaO/Al_2O_3 versus MgO for gabbro-diorites and diorites of Chin Chap Creek/Robson Creek. Clinopyroxene-absent gabbro-diorite **97-373A** is labelled, together with hybridised gabbro-diorite **98-61**.

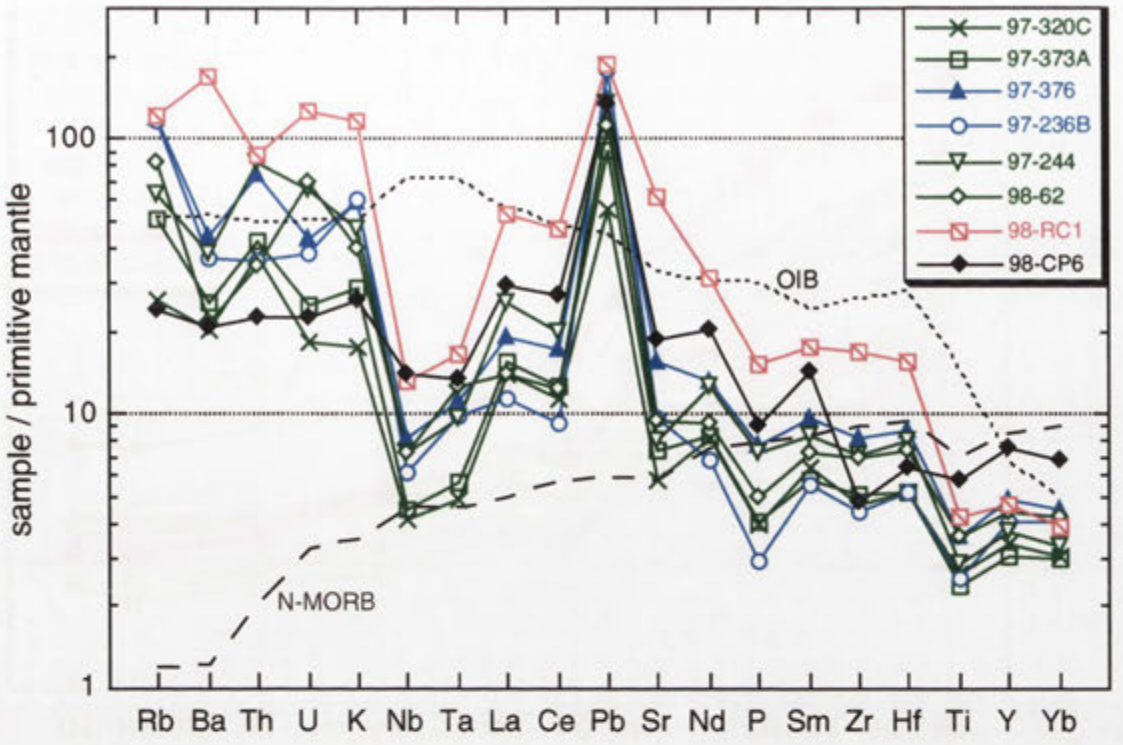

Figure 14.13. Primitive mantle-normalised multi-element diagram for hornblende gabbro-diorites (green) and hornblende diorites (blue) of Chin Chap/Robson Creeks and diorite **98-RC1** from Robertson Creek (normalising values as for Figure 14.8). Caupaul gabbro **98-CP6** and the average N-MORB and ocean island basalt (OIB) of Sun & McDonough (1989) are plotted for comparison (dashed lines).

Hornblende-rich rocks of Chin Chap Creek/Robson Creek have almost identical chondrite-normalised REE patterns to Caupaul diorite-tonalite samples, though at lower normalised concentrations (Figure 14.14). However, Chin Chap Creek/Robson Creek rocks are less coherent, with no systematic relationship between total REE abundances, $(La/Yb)_N$ or Eu/Eu* with MgO. The greatest variation is exhibited by the LREE, with La ranging from ~30 times chondrites for diorite **97-236B** to ~70 times chondritic values for gabbro-diorite **97-244**. Note that hornblende diorite **97-236B** has distinctly lower REE abundances than **97-376**, and also has greater depletion in the REE. Both samples have clearly lower REE abundances than Caupaul gabbro **98-CP6**, which, together with relative depletion in Ti and Y (Figure 14.13), implies derivation from a more compatible element-depleted source.

(b) Other igneous rocks of Chin Chap Creek

These include the ocellar-textured 'hybrid' from the margin of the gabbro-diorite body at key locality A (**98-61**) and two tonalitic dykes (**97-309**, **97-309-1**).

Compared to less modified gabbro-diorite samples, the hybrid sample has much higher silica (65.4%), K_2O (2.6%), Rb (100 ppm) and Ba (~390 ppm) with lower MgO (7.8%) (Appendix G; see Figure 16.1). Nevertheless, **98-61** retains high CaO/Al_2O_3 (0.82), and the Mg# (~0.77) is comparable with that of the most mafic gabbro-diorites.

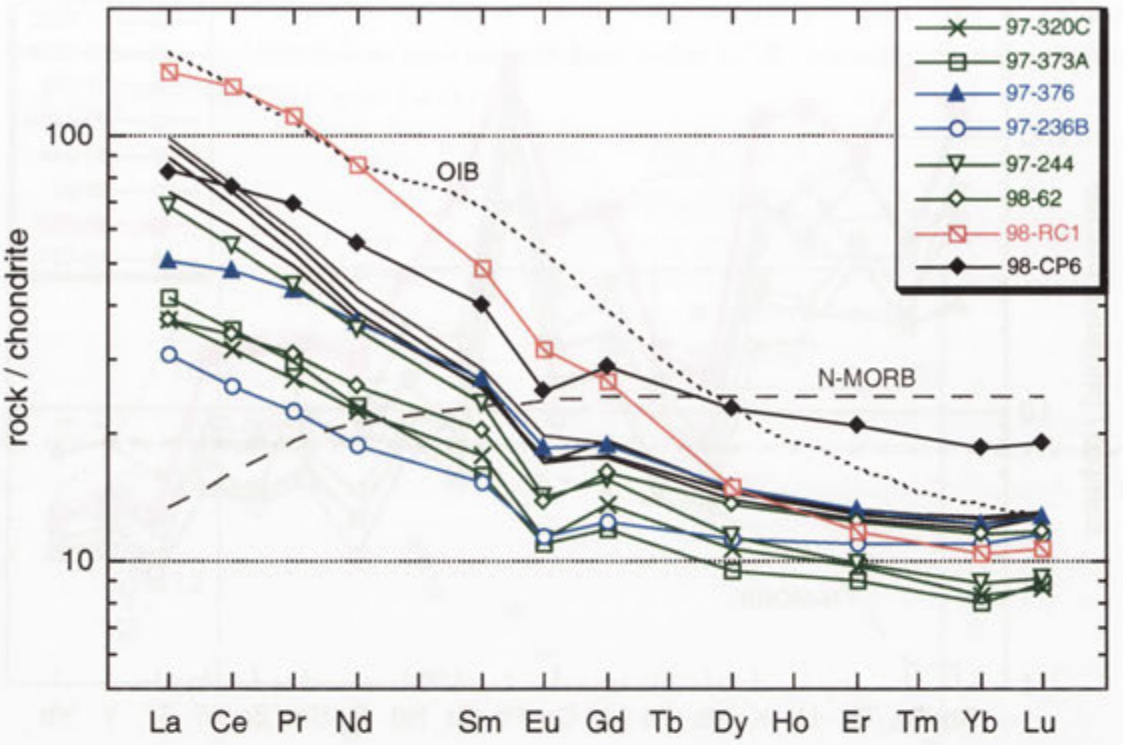

Figure 14.14. Chondrite-normalised REE plot for Chin Chap Creek/Robson Creek hornblende gabbro-diorites (green symbols) and hornblende diorites (blue symbols), and Robertson Creek diorite **98-RC1** (normalising values as for Figure 14.9). Caupaul diorites-tonalites (black lines), high-Al gabbro **98-CP6** and the N-MORB and ocean island basalt (OIB) of Sun & McDonough (1989) are plotted for comparison.

The tonalitic dyke samples contain higher SiO_2 (62.3% and 63.4%) and considerably less MgO (3-3.2%) than hornblende diorites. However, they share the distinctive magnesian signature, with Mg# (0.52-0.53) comparable to that of Caupaul gabbros and much higher than other GRC tonalites of similar silica (e.g. Mg# 0.43 in Wando Tonalite **97-161**, see Appendix G). They have higher Rb (>100 ppm), Ba (to 440 ppm) and K_2O (>2.3%) than hornblende diorites, but do not plot at the continuation of the steep K_2O trend for other Chin Chap Creek/Robson Creek rocks (Figure 14.7).

14.3.3 Robertson Creek diorites

At 56.5% SiO_2, sample **98-RC1** has high Na_2O (3.4%) and very high K_2O (3.4%), classifying it as a shoshonite (Figure 14.7). Strongly elevated Sr (~1200 ppm) and Ba (~1120 ppm) are also typical of the shoshonite magma series (Morrison 1980). Compared to Chin Chap Creek diorites of similar silica, **98-RC1** also has higher Al_2O_3 (17.8%) and TiO_2 (0.86%), though is a low-Ti shoshonite according to the subdivision of Kepezhinskas (1994). A similar dioritic rock analysed by Turner *et al.* (1993a) from Robertson Creek has 1072 ppm Sr, but lower K_2O (2.2%) and Ba (432 ppm) at 56.4% SiO_2, and is a high-K basaltic andesite (Figure 14.7).

Diorite **98-RC1** has a very distinctive primitive mantle-normalised multi-element pattern, with higher Ba, K and U compared to other dioritic rocks, and marked enrichment in LREE, P and Sr

(Figure 14.13). Zr and Hf are also higher than all other intermediate rocks, except the most felsic Caupaul sample (**98-CP11**), and the Nb-Ta trough is very well developed. The latter, combined with the pronounced Pb-Sr spike and LILE enrichment, clearly distinguishes **98-RC1** from the average ocean island basalt (OIB) of Sun & McDonough (1989), despite LREE concentrations being similar. Although **98-RC1** has an overall more enriched chemistry than other GRC diorites, compatible elements Ti, Y and the HREE are equally depleted relative to N-MORB, resulting in a more strongly fractionated REE pattern (La_N /Yb_N=13.9) (Figure 14.14). The rounded LREE pattern is another distinctive attribute of **98-RC1**, whereas a small negative Eu anomaly is also evident (Eu/Eu*=0.88).

The more felsic Robertson Creek dyke sampled by this study (**98-RC2**, 66.9% SiO_2) also has extremely high Sr (1000 ppm) and a strongly sodic character (3.7%) but is markedly depleted in K_2O (0.5%) and Ba (120 ppm) by contrast.

14.4 Discussion: petrogenesis of mafic rocks

The origin of the intermediate-mafic-ultramafic lithologies is best described in a later chapter in-conjunction with that of the other GRC igneous rocks. However, at this stage several fundamental petrogenetic observations are pertinent.

14.4.1 Origin of Caupaul pyroxenites

The chemical characteristics of hornblende pyroxenites, particularly the high MgO, very low Al_2O_3, and depleted incompatible element concentrations, do not accord with formation by crystallisation from a melt, but are consistent with accumulation of liquidus pyroxene from a parental basic magma. Convex LREE patterns are especially characteristic, as La and Ce are most strongly excluded by pyroxenes. A cumulate origin for pyroxenites is further supported by the textures of these rocks (section 13.3) and anorthitic nature of the intercumulus plagioclase. The geochemistry of pyroxenites is therefore controlled by a complex interplay between the composition of the crystallising magma, and the amount of interstitial liquid trapped between cumulate minerals. The negative Eu anomaly of pyroxenites is likely to have been 'inherited' from the crystallising magma, since as pyroxenes do not have an Eu anomaly (Figure 14.10), accumulation of these phases cannot by itself give rise to this feature. Further, although pyroxenites have depleted chemistry relative to other Caupaul rocks, they have elevated LREE compared to N-MORB (except for La in **98-CP9**), indicating derivation from an enriched parental magma. Although matching cumulate rocks and complementary liquids is potentially complicated by fractional crystallisation, magma mixing and crustal assimilation, several features suggest such a relationship between pyroxenites and high-Al hornblende gabbro **98-CP6**. These include the spatial association, shared REE enrichment, distinctive convex LREE pattern, negative Eu anomaly and similar HREE depletion relative to MORB (Figure 14.9). This notion is entirely compatible with the higher Mg# of pyroxenes and hornblende and more calcic plagioclase in pyroxenites compared to gabbro **98-CP6** (above). Note, however, that overlapping HREE patterns virtually preclude a cumulate-melt relationship between pyroxenites and Caupaul

diorites-tonalites (Figure 14.9). This is because the pyroxene/melt partition coefficients for the HREE are <1, and thus these elements must be enriched in derivative liquids relative to cumulate rocks. Pyroxenes of some diorite samples are equally magnesian as those of the pyroxenites, which also argues against a complementary melt-cumulate relationship for these rocks.

Assuming a similar parental magma, the higher LREE abundances in **98-CP8** compared to **98-CP9** are consistent with greater entrapment of the fractionated, incompatible element-rich melt between cumulate minerals. This is manifested by the higher proportion of intercumulus hornblende and plagioclase in pyroxenite **98-CP8** (see Table 13.1). Hornblende gabbronorite **98-CP2** is even more plagioclase-rich and plots between pyroxenites and gabbros on variation diagrams (see Figure 16.1), suggesting that it incorporates a larger melt component. However, the much lower REE abundances of the gabbronorite, together with the more calcic plagioclase and distinctive pyroxene and hornblende compositions, indicates derivation from a different parental liquid than that of the pyroxenites. The very low HREE concentrations of the gabbronorite further suggest that it was sourced from a basaltic melt that was less enriched than Caupaul high-Al gabbros. This accords with the isotopic differences between Caupaul gabbros and a sample of the gabbronorite body, which is considerably more evolved at 500 Ma (see above).

14.4.2 Relationship between mafic and intermediate rocks of the Caupaul Igneous Complex

Although petrographically similar and intimately associated in the field, chemical evidence prohibits a direct genetic link between Caupaul gabbros and diorites-tonalites. Derivation of the latter by fractional crystallisation of plagioclase and pyroxene from a hornblende gabbro magma is precluded by the more magnesian pyroxenes of some diorite samples, together with extension to higher bulk rock Mg# and Cr. This is also ruled out by the lower REE abundances and similar negative Eu anomaly of diorites-tonalites, when fractional crystallisation from a parental gabbroic magma would result in higher REE contents (as $D_{REE}<1$) and lower Eu/Eu*. A relationship by two-component magma mixing is also most unlikely, as the linear trends defined by diorites-tonalites on variation diagrams do not project back to Caupaul gabbros for some elements (e.g. MgO, K_2O and Sr; see Figure 16.1). Finally, formation of Caupaul intermediate rocks from hornblende gabbros by assimilation of metasedimentary rock is not compatible with REE evidence. Metasedimentary samples have higher total REE than the gabbros (compare Figure 14.9 with Figure 7.11), and thus contamination would lead to elevated REE contents, when in fact diorites-tonalites have lower REE abundances than gabbros.

It is concluded that Caupaul gabbros and diorites-tonalites have different parental magma compositions, and belong to separate petrogenetic systems.

14.4.3 Origin of Caupaul gabbros

As a group, Caupaul high-Al gabbros are compositionally quite unlike N-MORB, particularly in elevated LILE abundances and the large positive Pb anomaly (Figure 14.8). The disparity is further highlighted by the moderate Ba/La of Caupaul gabbros (~11 for **98-CP3**), since this ratio rarely exceeds 3 for N-MORB and intra-plate basalts (Arculus & Powell 1986). Pronounced

LREE enrichment is also inconsistent with MORB derived from depleted mantle (Figure 14.9), as are lower Mg#, Cr and Ni. The depleted HFSE and HREE of gabbro **98-CP6** cannot be produced by realistic degrees of melting of a normal MORB-type mantle source (Tatsumi & Eggins 1995), or fractional crystallisation of pyroxenes from MORB, since Ti, Zr, Hf and HREE have pyroxene/melt partition coefficients below unity. More specifically, Caupaul gabbros are also chemically distinct from the 'MORB-like' metabasites of the southwestern GRC (section 3.3), which typically have- (1) CaO >12.5% (Anderson 1990; Turner *et al.* 1993a; C.M. Gray, *unpubl. data*), compared to a maximum of 10.9% CaO in **98-CP6**, (2) higher MgO (8.7-10%) relative to Caupaul gabbros (6-7% MgO), (3) lower Sr (<250 ppm), and (4) much higher Ni (>150 ppm) and Cr (600-800 ppm). The mantle-normalised trace element patterns are also fundamentally different, with a metabasite sample from the amphibolite facies of Wando Vale having more depleted LILE and LREE abundances but higher Ti, Y and Yb (Figure 14.15).

Simple geochemical arguments also indicate that Caupaul gabbros cannot be exclusively derived from MORB-like parental magmas by contamination with GRC metasedimentary rocks. For example, all Caupaul gabbros have higher Sr but lower Y and HREE than both N-MORB and GRC schists (Figure 14.16), and therefore cannot be modelled as MORB-metasedimentary rock mixes. However, some assimilation of metasedimentary materials by Caupaul gabbros cannot be precluded.

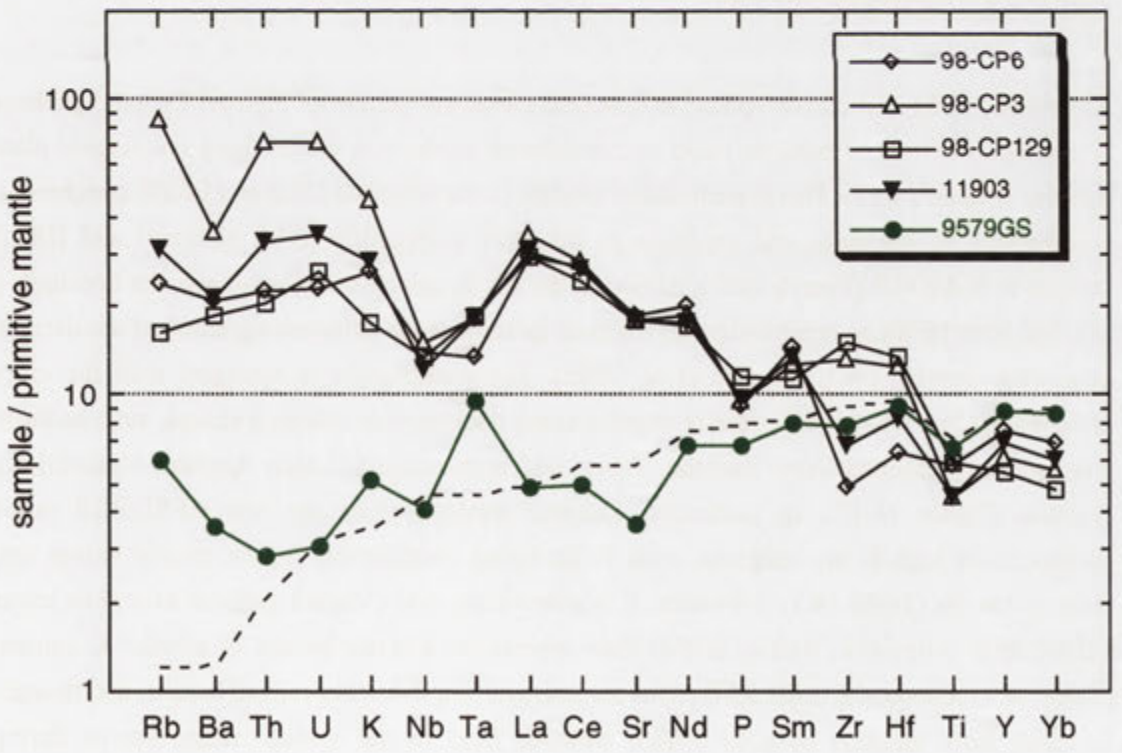

Figure 14.15. Comparison between Caupaul gabbros and metabasite 9579GS from the Wando Vale district (from Kemp & Eggins, *unpubl. data*). Note the similarity of the latter to N-MORB (dashed line) of Sun & McDonough (1989). Normalising values are as for Figure 14.8.

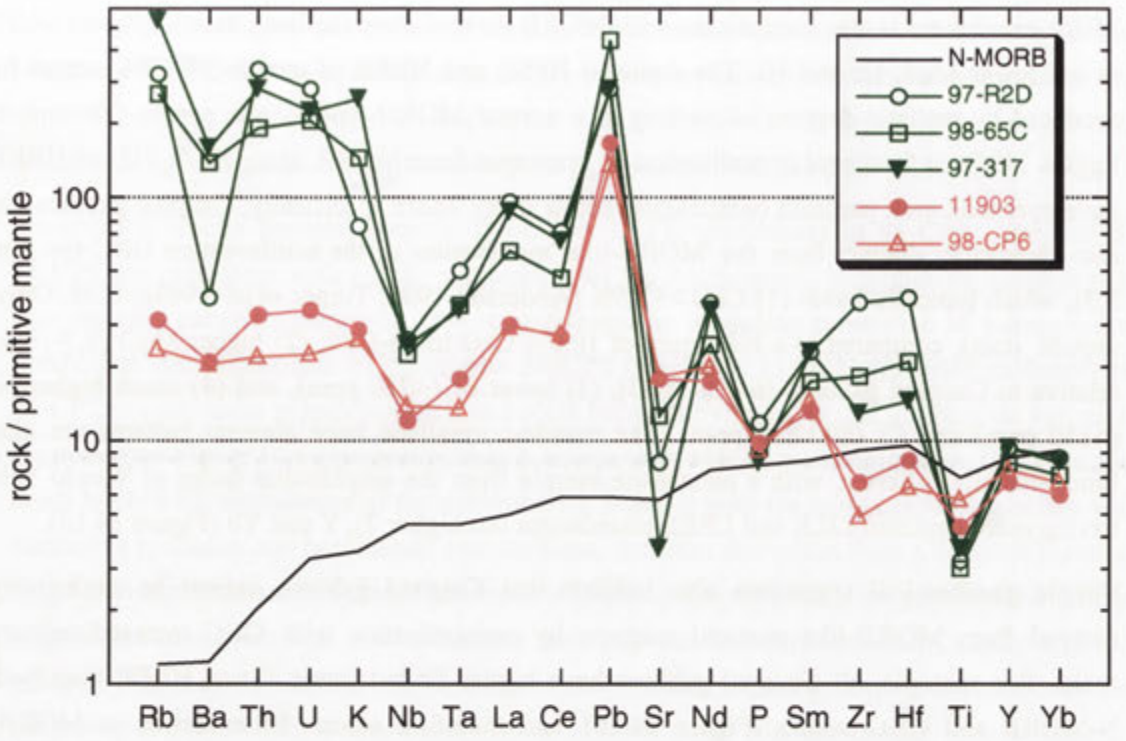

Figure 14.16. Primitive mantle normalised plot of Caupaul gabbros (pink), GRC metasedimentary rocks (green) and the Sun & McDonough (1989) N-MORB (black line) (normalising values are as for Figure 14.8). High Sr but low Zr, Hf, Y and Yb precludes formation of gabbros by simple mixing between N-MORB and metasedimentary rock..

Alternatively, the distinctive 'spiked' normalised elemental pattern of high-Al Caupaul gabbros is analogous to that of basaltic rocks erupted above subduction zones along convergent plate margins (Figure 14.17). This is particularly evident in the selective LILE and LREE enrichment, conspicuous Pb anomaly, and depletion in the more compatible HFSE elements and HREE relative to N-MORB (Pearce 1982). Although the Nb trough is less pronounced, the decoupling of LILE from HFSE as exhibited by all Caupaul gabbros is the hallmark signature of arc-derived lavas (e.g. Pearce 1983; Gamble *et al.* 1993). The resemblance is strongest with the more enriched medium- to high-K basalts erupted along backarc-side volcanic chains, such as those from some continental (New Zealand, Japan) and intra-oceanic (Lesser Antilles, Vanuatu) arc systems (Figure 14.17). In particular, Caupaul gabbros share the low HFSE/REE ratios diagnostic of high-K arc magmas, with Ti/Eu being considerably below mantle values and oceanic basalts (Table 14.1). However, it is noteworthy that Caupaul gabbros extend to lower LILE/LREE ratios (i.e. Ba/La, Sr/Nd) than typical arc-derived basalts of similar K content (Table 14.1). Elevated LILE/LREE ratios are intrinsic to subduction-related basalts, and thought to result from addition of a LILE-rich aqueous fluid to the mantle wedge source during dehydration of the subducted oceanic slab (see Tatsumi & Eggins 1995 for discussion). Lower Sr/Nd in Caupaul gabbros may be partly reconciled by incipient plagioclase fractionation, given the high partition coefficient for Sr between plagioclase and basaltic liquid (~4.5) (Arth & Hanson 1975); this is also compatible with the small negative Eu anomalies of these rocks.

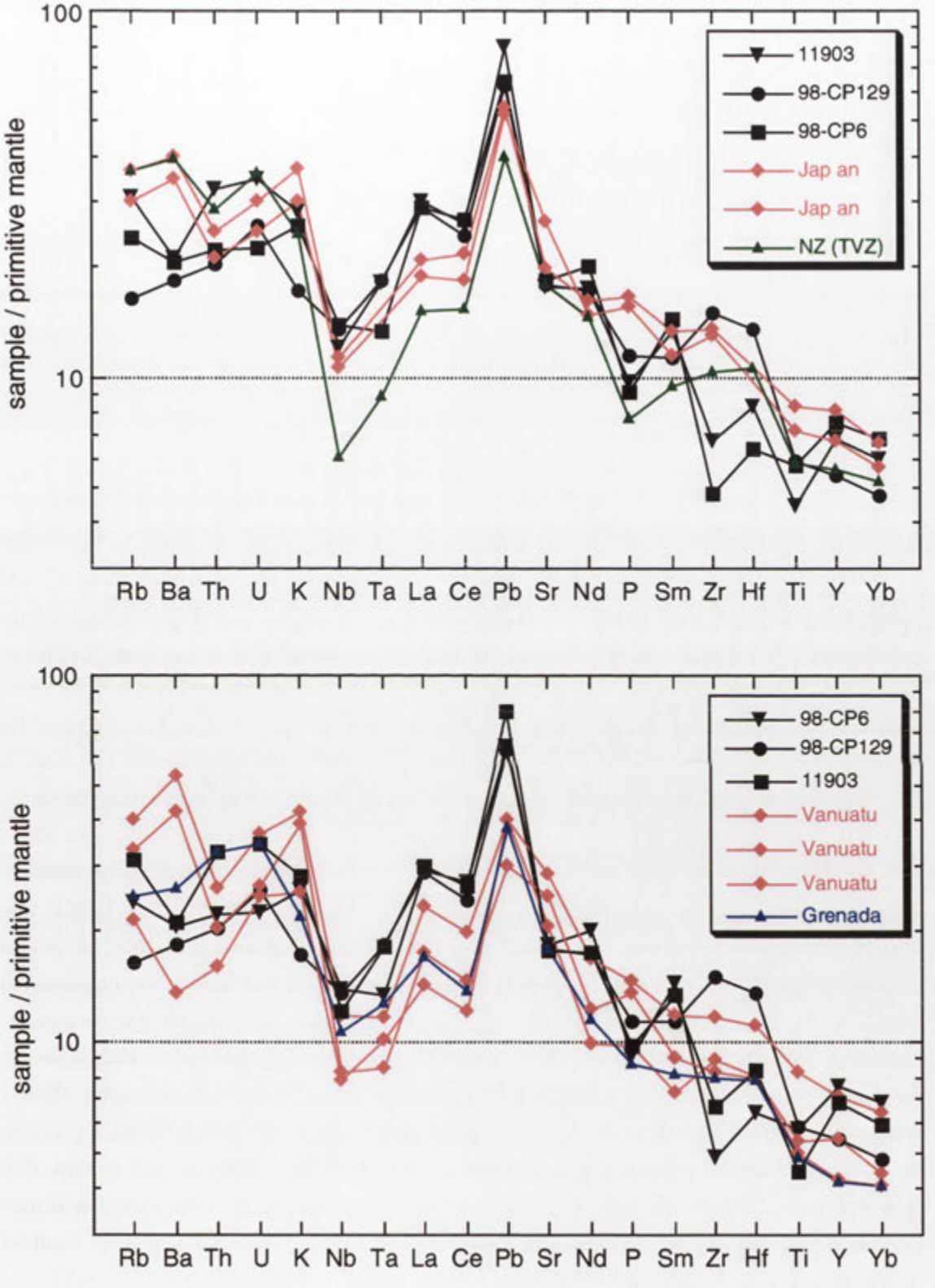

Figure 14.17. Primitive mantle-normalised plot comparing Caupaul gabbros with basalts from continental (top) and intra-oceanic arcs (bottom). Data sources are; Japanese arc, Pouclet *et al.* (1994); New Zealand (Taupo Volcanic Zone), Gamble *et al.* (1993); Vanuatu arc, Peate *et al.* (1997) and Grenada (Lesser Antilles arc), Turner *et al.* (1996).

Rock	*Ti/Eu*	*Ti/Zr*	*La/Yb*	*Ba/La*	*Sr/Nd*
Arc basalt	**3500 - 6500**	**40 - 100**	**4 - 9**	**15 - 50**	**20 - 50**
98-CP3	4480	40	9.2	10.8	16
98-CP6	4950	136	6.3	7.2	15
98-CP129	5700	45	9.0	6.5	17
11903	4360	76	7.5	7.1	17
N-MORB	7450	102	0.8	2.4	12
Prim. mantle	7740	116	1.4	10.1	15

Table 14.1. Comparison between some key elemental ratios of Caupaul high-Al gabbros and the range in those ratios exhibited by unfractionated arc basalts of similar K and La contents (compiled from data in Tatsumi & Eggins 1995). These ratios are considered diagnostic of petrogenetic processes specific to subduction zone environments. The values for N-MORB and the primitive mantle of Sun & McDonough (1989) are also indicated.

The high-Al_2O_3 character of Caupaul gabbros is also typical of magmatism in subduction environments, with high-Al basalts being the dominant basalt type erupted in intra-oceanic island arcs (Brophy 1986). Caupaul gabbros also share the low Mg# (<0.6), Cr and Ni and high Rb and Sr that epitomises high-Al arc basalts (Brophy 1986). For Caupaul gabbros, depleted Cr and Ni contents probably reflect pyroxene fractionation, since these elements are enriched in the inferred complementary cumulates (hornblende pyroxenites **98-CP8**, **98-CP9**). Although the origin of the high-Al signature is controversial (e.g. Crawford *et al.* 1987), the negative Eu anomaly in Caupaul gabbros is inconsistent with acquisition of this by plagioclase accumulation.

14.4.4 Affinity of Robertson Creek diorites

The subduction geochemical signature (i.e. LILE enrichment, depletion in HREE and incompatible elements relative to N-MORB, and marked Nb/Ta depletion relative to La) is also present in Robertson Creek diorite **98-RC1**, which closely resembles the shoshonites erupted from both intra-oceanic and continental arcs (Figure 14.18). As with arc-related shoshonites (e.g. those of Fiji, Gill & Whelan 1989), the marked incompatible element enrichments are superimposed on depleted HFSE and HREE concentrations, suggesting derivation from a compatible element-depleted source. Note that the very high Sr contents of **98-RC1** preclude exclusive derivation of the elevated LILE content by assimilation of metasedimentary rock. The only candidates for this could be calc-silicates (which range to 2000 ppm Sr), though a Wando type dioritic dyke visibly contaminated by calc-silicate in the Wando River lacks such Sr enrichment (section 10.2.3, sample **97-208**).

14.4.5 Concluding statement

Detailed exposition of the compositional features of Caupaul gabbros, such as the high Al_2O_3 and LREE enrichment, in the context of subduction-related processes is outside the scope of this thesis. However, the fundamental point emerging from the above discussion is that the chemistry

of the gabbros argues for formation in a supra-subduction zone setting, corroborated by the occurrence of diorites with arc-shoshonite affinities. This obviously has profound implications for the origin of other GRC igneous rocks and the tectonic evolution of the eastern Delamerian Orogen, both of which are pursued in later chapters.

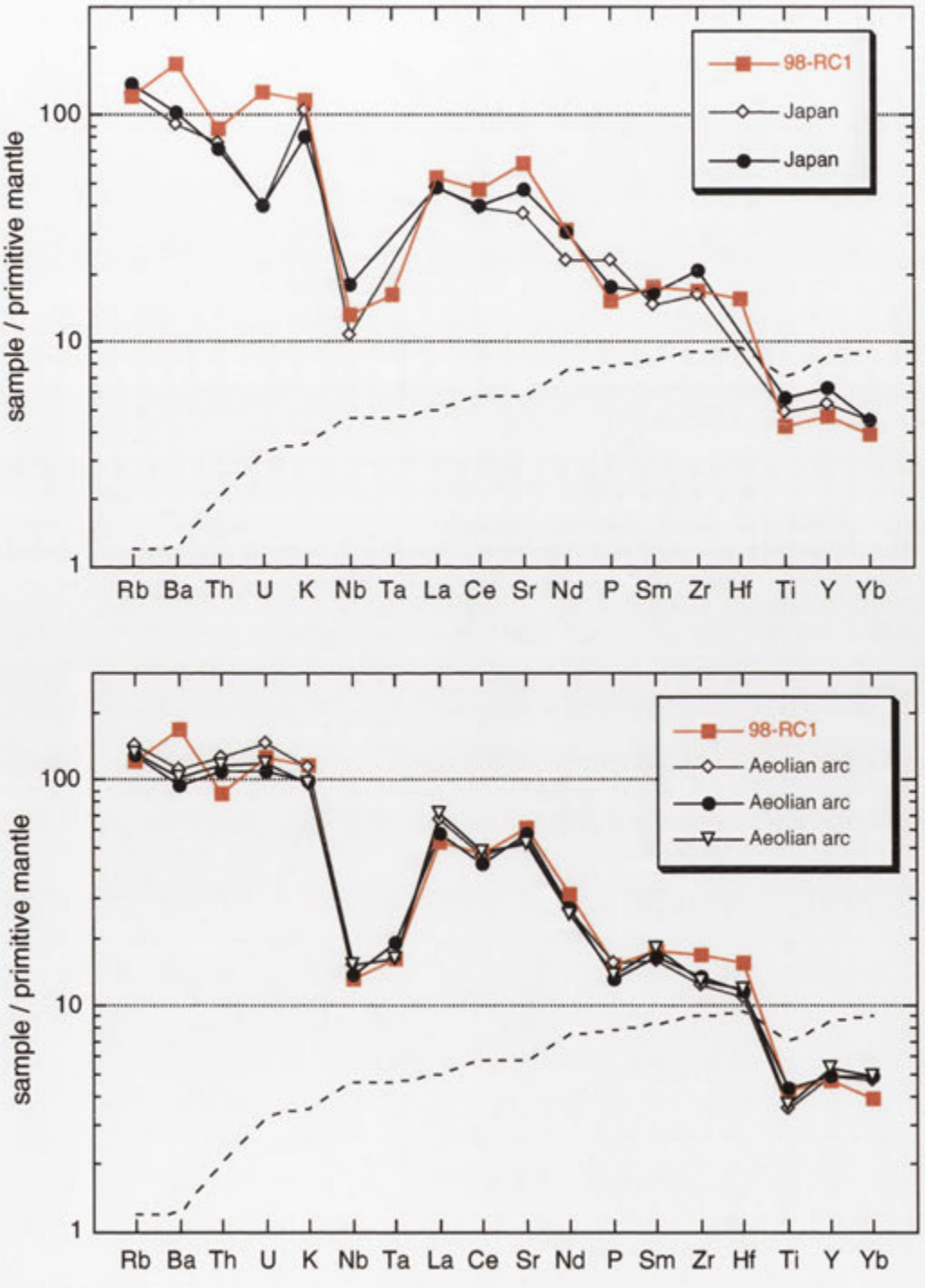

Figure 14.18. Primitive mantle-normalised plots comparing Robertson Creek diorite **98-RC1** with shoshonites from the continental Japanese arc (top) and the island of Vulcano in the Aeolian arc (bottom). The N-MORB of Sun & McDonough (1989) is also plotted (dashed line). Data sources are; Japanese arc, Pouclet *et al.* (1994); Aeolian arc, De Astis *et al.* (2000). Normalising values are as for Figure 14.8.

Chapter 15: Mineral chemistry and geochemistry of metaluminous to weakly peraluminous granitic rocks

15.1 Introduction

This chapter describes the mineral chemistry and geochemistry of metaluminous to weakly peraluminous granitic rocks and enclaves of the GRC.

15.2 Mineral chemistry

The compositions of minerals from the various granitic types are listed in Appendix F. Representative or distinctive samples from within each magma type were chosen with reference to Harker variation diagrams, so as to encompass the full compositional range of the granitic system.

15.2.1 Feldspars

Feldspar compositions are plotted in Figure 15.1.

(a) Early syn-compressional rocks

Plagioclase cores of quartz diorite **97-206F** (Wando type) are the most calcic of all analysed samples, but vary widely in composition, from An_{70} to An_{52}. All exhibit oscillatory zoning to more sodic compositions (rims An_{46}-An_{36}) apart from grain 6B, which is reversely zoned (core An_{53}, rim An_{57}). Less calcic plagioclase is evident within Wando Tonalite **97-161**, with sodic labradorite cores (An_{54}-An_{51}) mantled by andesine rims (An_{47}-An_{42}). Grain 7B has slightly different character, in that the large euhedral core (An_{48}) is euhedrally overgrown by more calcic plagioclase (An_{54}). Although lacking the oscillatory zoning, plagioclase of the Warradale Tonalite **97-WA1** (Wennicott type) has a similar compositional range to the Wando Tonalite, with An_{52}-An_{48} cores zoned to more sodic rims (An_{46}-An_{41}).

(b) Late syn-compressional rocks

Plagioclase laths of Chetwynd Tonalite **97-427** (Tuloona type) have oscillatory zonation, from An_{52} to An_{38}. Many grains also enclose small, corroded or indistinct cores (An_{48}-An_{42}). Alkali feldspar within the sample is very potassic (Or_{93}), despite the low bulk rock K_2O (1.9%). Tuloona Granodiorite **T2-135** plagioclase is also oscillatory-zoned, from An_{49} to An_{35}, though many laths enclose small, irregular cores (An_{43}-An_{40}) like those of the Chetwynd Tonalite. The large poikilitic alkali feldspar grains within the sample vary from Or_{90} (core) to Or_{88} (rim).

Both phenocryst and groundmass plagioclase grains of the Cairns Creek Granodiorite **97-52** (Loftus Creek type) have euhedral cores (An_{49}-An_{46}) that are oscillatory-zoned to markedly more sodic rims (An_{22}-An_{19}). The exceptions are grains 3A and 4A, the cores of which are relatively sodic (An_{34} and An_{36} respectively). Alkali feldspar is slightly less potassic than that of the Tuloona Granodiorite (Or_{88}-Or_{86}).

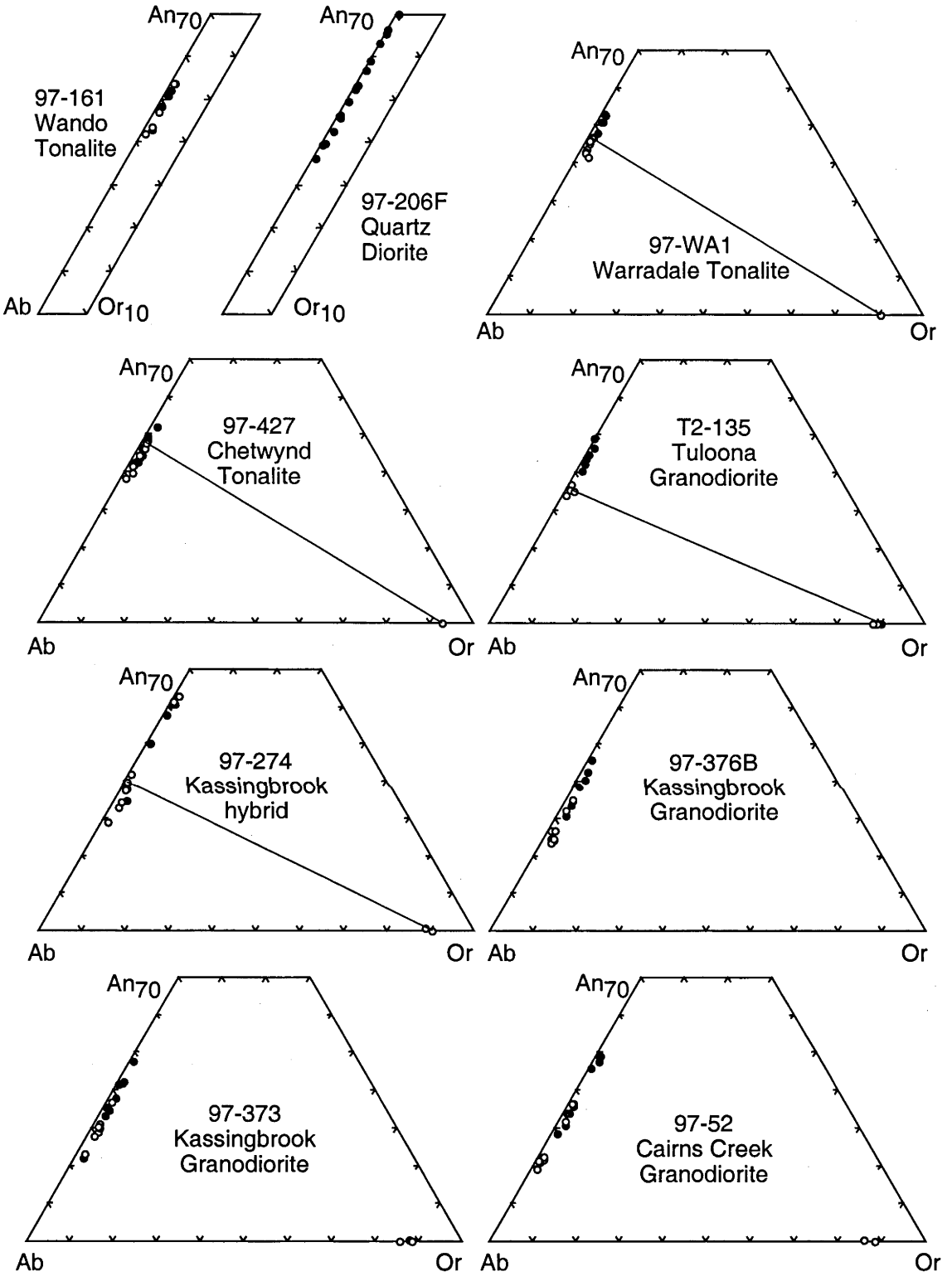

Figure 15.1. Plagioclase composition for GRC granitic rocks (excluding Harrow types) in terms of albite, anorthite and orthoclase components (atomic Na, Ca and K respectively). All plots extend up to An_{70}, whereas those for **97-206B** and **97-161** only range to Or_{10}. Filled symbols represent core compositions and open symbols are rim compositions. Tie lines connect potassic feldspar with their plagioclase inclusions.

Plagioclase laths within 'typical' muscovite-bearing Kassingbrook Granodiorite (**97-373**) (Kassingbrook type) have large euhedral-subhedral andesine cores (An_{48} to An_{34}), zoned to oligoclase rims (An_{30}-An_{24}). The large subhedral core of grain 4A is considerably more sodic (An_{22}) (Figure 15.1). Alkali feldspar grains also have euhedral cores, which in grain 1A is slightly more potassic (Or_{88}) than the rim (Or_{86}). Plagioclase of a more biotite-rich Kassingbrook Granodiorite sample (**97-376B**) has similar compositional and zonation characteristics to **97-373** (cores An_{46} to rims An_{25}) (Figure 15.1), despite proximity to a mafic hornblende diorite sheet (section 12.3.4). Importantly, the plagioclase of both Kassingbrook Granodiorite samples resembles that of an *in situ* leucosome from the surrounding migmatitic rocks (sample **98-102**, see Table 7.2).

However, plagioclase is markedly more calcic within the hornblende-bearing 'hybrid' Kassingbrook type tonalite (**97-274**). The blocky phenocrysts have large, rounded cores (An_{36}-An_{38}), similar to those of felsic Kassingbrook type samples, overgrown by a thin, euhedral 'shell' of calcic labradorite (An_{63}-An_{65}). This is rimmed in turn by plagioclase of similar composition to the core. Such calcic 'spikes' characterise plagioclase of granitic rocks thought to have formed by magma mixing (Wiebe 1968; Hibbard 1991; Hibbard 1995). Groundmass plagioclase laths have euhedral, calcic cores (An_{58}-An_{61}), with more sodic rims (varying from An_{42} to An_{29}).

15.2.2 Hornblende

Analysed hornblende grains from five granitic rocks are represented in Figure 15.2 and plotted with coexisting biotite in Figure 15.3. Two different groups are discerned. The main group forms a broadly linear array, bracketed between actinolite and pargasite end-members, and includes, in order of increasing Al^{iv} substitution, hornblende of the tonalitic hybrid **97-274**, quartz diorite **97-206F**, Warradale Tonalite and Wando Tonalite. This sequence also corresponds to decreasing Mg# (Figure 15.3).

The second group comprises hornblende of the Cairns Creek Granodiorite (**97-52**), the compositional trend of which parallels the main array but is off-set to higher (Na+K) for a given Al^{iv} content (Figure 15.2). As a result, hornblende compositions resemble those of Robertson Creek 'shoshonite' **98-RC1** (shaded field on Figures 15.2, 15.3). Despite the relatively evolved bulk rock chemistry (~69% SiO_2), Cairns Creek Granodiorite hornblendes are also unusually magnesian (Mg# 0.54-0.56), the same character being evident for biotite (see below).

15.2.3 Biotite

Collectively, biotite grains of granitic rocks form a broadly linear array of decreasing Al^{iv} but increasing Ti contents with Mg#, that overlaps the compositional field of biotite from Harrow type plutons (Figure 15.4). Biotite of the Cairns Creek Granodiorite and hybrid tonalite **97-274** (Kassingbrook type) is the most Mg-rich (Mg# 0.55-0.57), followed by Chetwynd Tonalite biotite (Tuloona type), which is only marginally less magnesian, but distinctly more aluminous. The more felsic and muscovite-bearing Tuloona type sample (Tuloona Granodiorite **T2-135**) has biotite of much lower Mg#, similar to that of the Warradale Tonalite (~0.47-0.49); the latter, however, has higher Ti and lower Al^{iv} contents. Despite having clearly

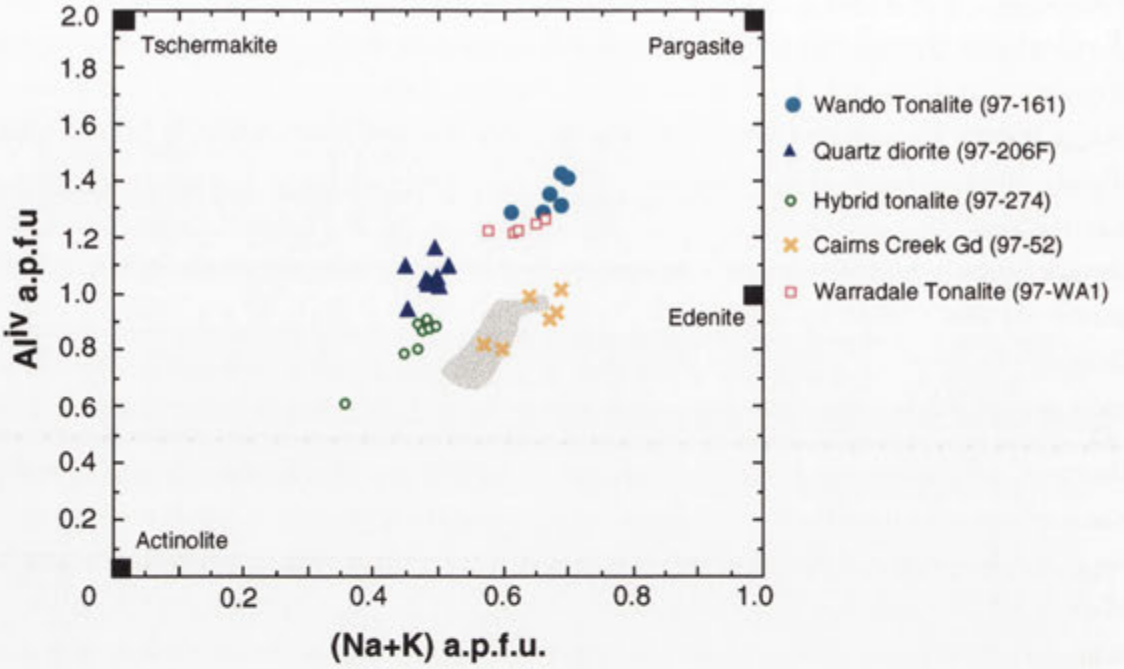

Figure 15.2. Amphibole compositions of GRC granitic rocks (in atoms per formula unit, a.p.f.u.) relative to end-member compositions (from Deer *et al.* 1966). The shaded field represents hornblende of Robertson Creek shoshonite **98-RC1**.

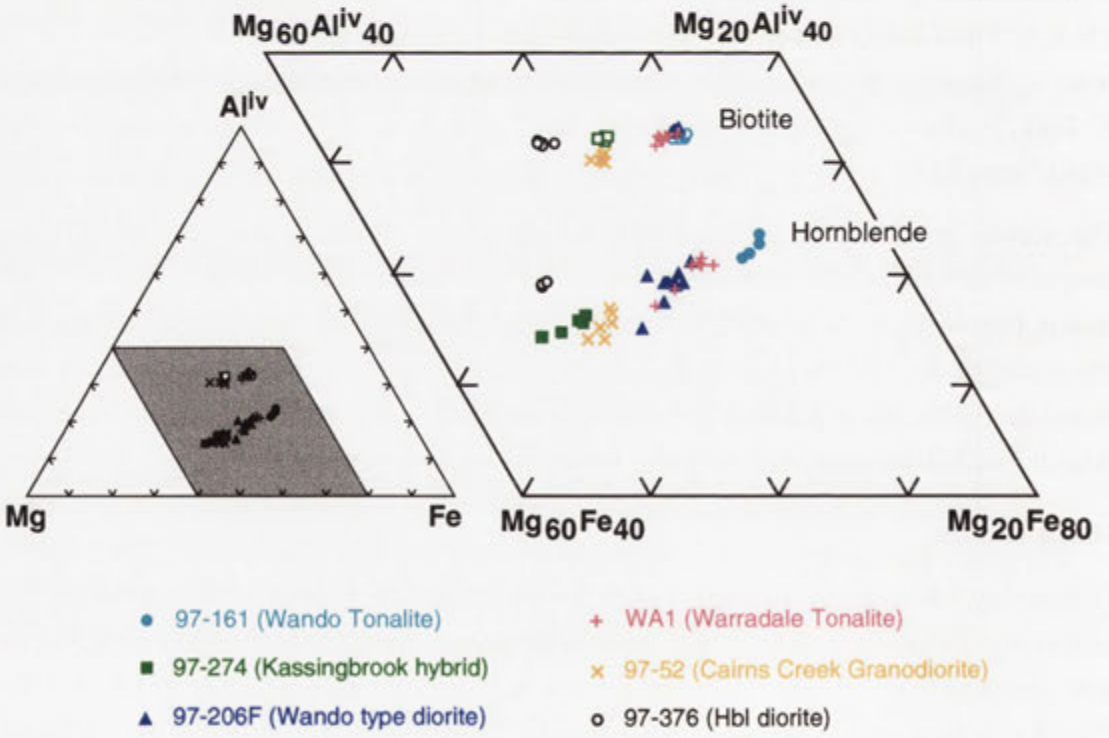

Figure 15.3. Triangular Al^{iv}, Mg and Fe plot (all in atomic proportions) for coexisting biotite (top, open symbols) and hornblende (bottom, closed symbols) for GRC granitic rocks. Biotite and hornblende from Chin Chap Creek hornblende diorite **97-376** is also plotted for comparison.

more magnesian hornblende, biotite of Wando type diorite **97-206F** has the same Mg# as that of the Wando Tonalite (~0.45-0.47). Kassingbrook Granodiorite sample **97-376B** has slightly lower Mg# than this (~0.45-0.46) but is markedly more aluminous. The biotite of 'typical' Kassingbrook Granodiorite **97-373**, which coexists with primary muscovite, is the least magnesian (Mg#0.41-0.42) and the most aluminous (Al^{iv} 2.51-2.59 a.p.f.u), plotting amongst the Harrow type biotite array.

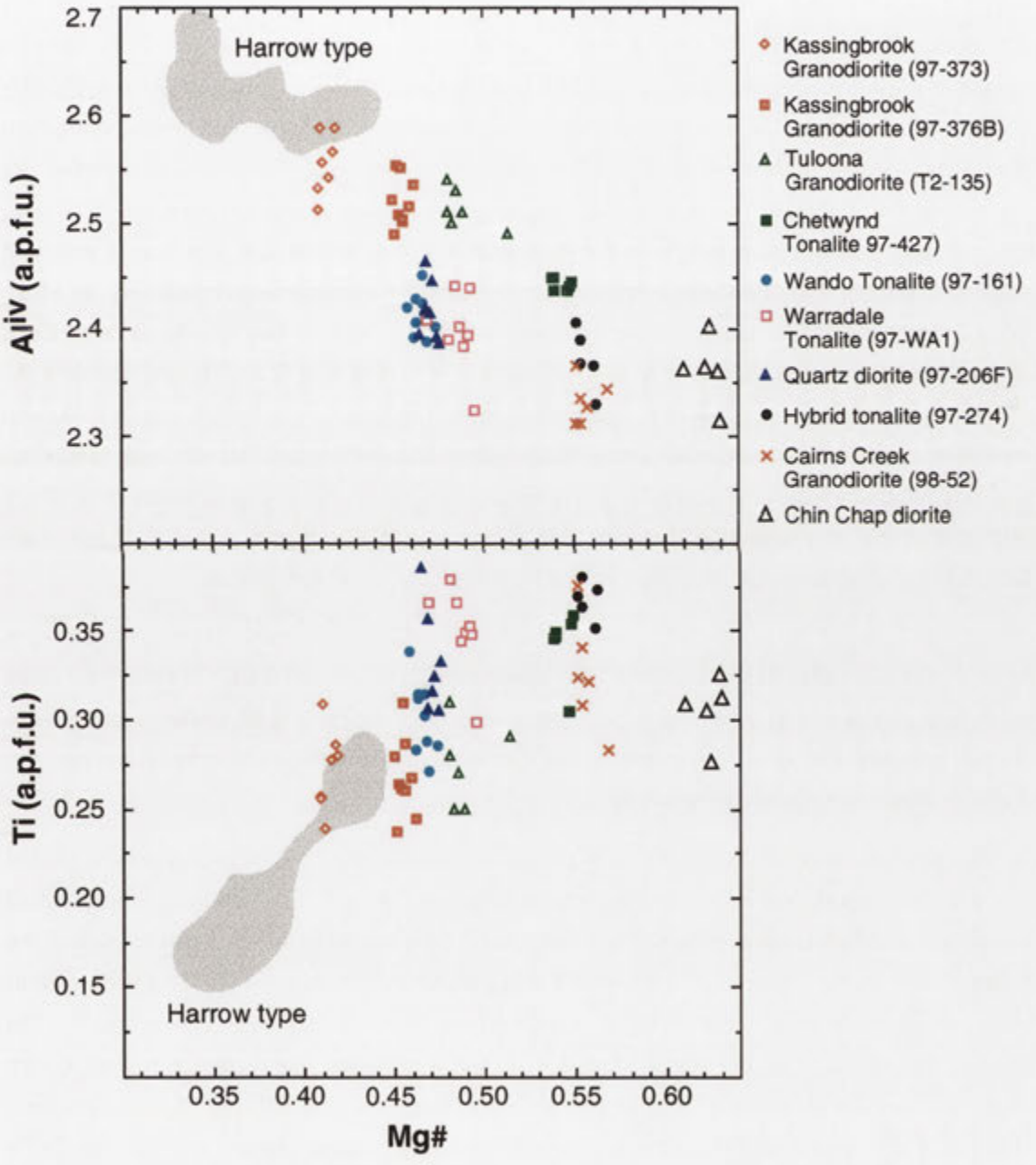

Figure 15.4. Biotite composition (in atoms per 22 oxygens) for GRC granitic rocks. Biotite from Harrow type plutons (shaded field) and mafic Chin Chap Creek hornblende diorite **97-376** ('Chin Chap diorite') is also plotted.

15.3 Geochemistry of early syn-compressional igneous rocks

15.3.1 Wando type

(a) Diorites and tonalites

Collectively, these rocks extend from 53.5% to 63.1% SiO_2 (Appendix G). The Elbow Creek dioritic dyke contains the most mafic samples and has the largest compositional range, evolving from near-gabbroic (53.5% SiO_2 in **98-124**) through to tonalitic (60.3% SiO_2 in **97-208**), with 'typical' quartz diorite samples bracketed between 56% and 58% SiO_2. The Snake River Tonalite varies from 58.4% SiO_2 and 7.1% Fe_2O_3t near the southern periphery in Boundary Creek (**97-192**) to 61.2% SiO_2 and 6.3% Fe_2O_3t near the eastern margin in Elbow Creek (**97-214**). Samples are distinctly more primitive than the Wando Tonalite, which has 63.1% SiO_2 at 5.4% Fe_2O_3t (**97-161**); an even more felsic variety with 65.9% SiO_2 is reported by Anderson (1990). Apart from the latter, which is weakly peraluminous (A.S.I. = 1.06), all Wando type samples are metaluminous (A.S.I. <1.0). Despite this, a high Al_2O_3 signature is characteristic for the Wando magma type, extending up to 20.4% for plagioclase-rich diorite **98-124**. On Harker variation diagrams, Wando type rocks define broadly linear trends for most major elements (Figure 15.5). With increasing SiO_2, these involve decreasing TiO_2, Al_2O_3, Fe_2O_3t, MgO and CaO, approximately constant Na_2O, P_2O_5, and Sr, and steeply increasing K_2O. The exception is the Elbow Creek diorite sample **98-124**, which plots below the linear array for TiO_2 and Fe_2O_3t and well above for Al_2O_3, Sr and particularly Na_2O. These features suggest that this rock comprises an accumulation of plagioclase crystals, consistent with its plagioclase-dominated mineralogy and occurrence as a lenticular domain within the body of the dyke (section 10.2.3a). Such localised accumulation was possibly induced by heterogeneous magma flow.

Importantly, despite the similar SiO_2 contents, only limited overlap occurs between Wando types and the compositional field of Caupaul diorites-tonalites (see Figure 16.1). Wando type rocks have clearly higher Al_2O_3, Na_2O and Sr, but lower Fe_2O_3t, MgO and K_2O. Differences between the two groups are clearest with regard to K_2O, as the Caupaul linear trend is much steeper, and diverges from that of Wando types.

For comparison, representative samples of the early syn-compressional magma types are plotted on a primitive mantle-normalised multi-element diagram (Figure 15.6). Note that on this, and all subsequent multi-element diagrams for granitic rocks, Pb is placed to the far left-hand side of the diagram next to the other LILE with which it is geochemically compatible. This differs from multi-element diagrams in the previous chapter where Pb is situated between Ce and Sr. The reasons for the modified elemental order are- (1) in a granitic system, the consistent Ce-Pb coupling observed for oceanic basalts (Sun & McDonough 1989) is unlikely to be maintained, as the REE are controlled by accessory minerals and Pb by potassic phases, and thus the Ce/Pb ratio is of reduced importance, and (2) to produce a smoother pattern, specifically to more easily contrast the behaviour of Sr relative to the REE for the different magma types. Similar elemental orders are adopted by other workers for granitic rocks (e.g. Champion & Chappell 1992; Wyborn

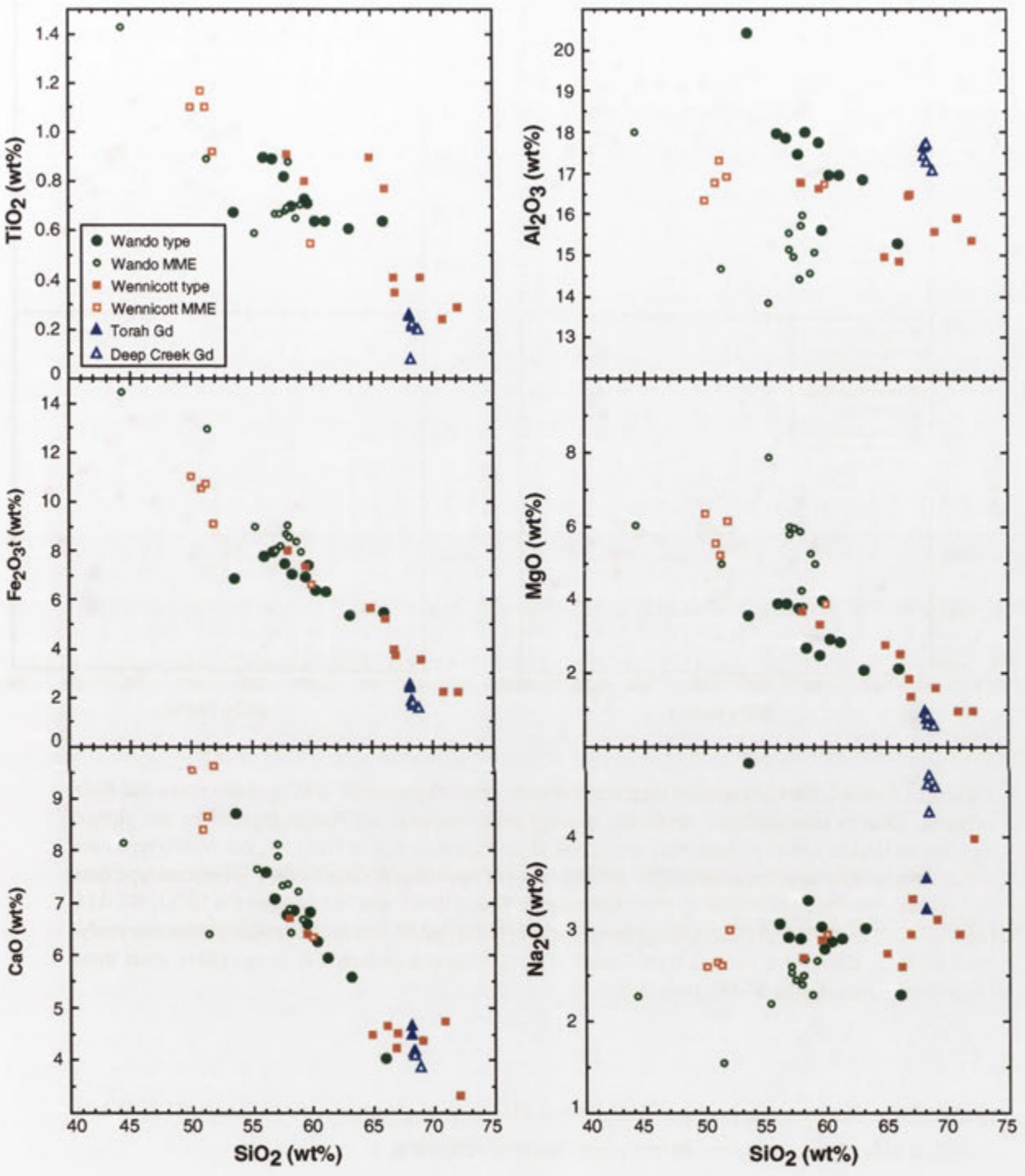

Figure 15.5. Harker variation diagrams for early syn-compressional GRC granitic rocks and their enclaves. Due to compositional similarity, microgranular enclaves of Wando type rocks are plotted together on Harker variation diagrams irrespective of petrographic type or host rock. All Wando type data is from this study except for sample 9581 (65.9% SiO_2) of Anderson & Gray (1994). Wennicott type data includes sample 9567 (70.9% SiO_2) from Anderson & Gray (1994) and W7-130 (64.8% SiO_2), W7-126 (66.8% SiO_2), and W7-125 (72.1% SiO_2) from Bushell (1996). MME data derives entirely from this study. Data for Deep Creek type rocks is from Turner *et al.* (1993a) and Anderson & Gray (1994), apart from Deep Creek Granodiorite **97-DC** (this study).

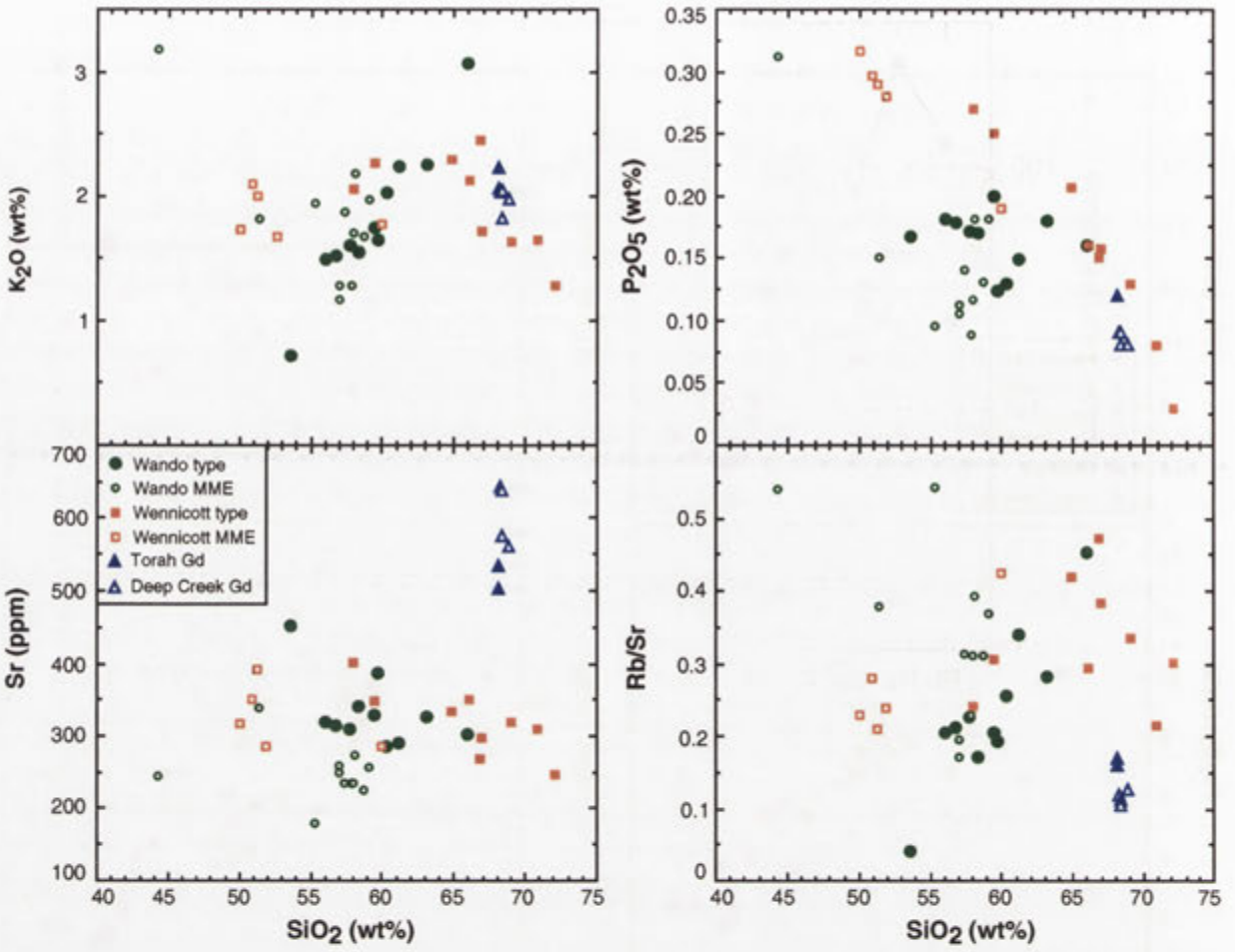

Figure 15.5 contd. Harker variation diagrams for early syn-compressional GRC granitic rocks and their enclaves. Due to compositional similarity, microgranular enclaves of Wando type rocks are plotted together on Harker variation diagrams irrespective of petrographic type or host rock. All Wando type data is from this study except for sample 9581 (65.9% SiO_2) of Anderson & Gray (1994). Wennicott type data includes sample 9567 (70.9% SiO_2) from Anderson & Gray (1994) and W7-130 (64.8% SiO_2), W7-126 (66.8% SiO_2), and W7-125 (72.1% SiO_2) from Bushell (1996). MME data derives entirely from this study. Data for Deep Creek type rocks is from Turner *et al.* (1993a) and Anderson & Gray (1994), apart from Deep Creek Granodiorite **97-DC** (this study).

et al. 1992). The average Lachlan Fold Belt (LFB) 'I-type' granitic rock of Chappell & White (1992) is also plotted as a convenient compositional reference.

Wando type samples have similar primitive mantle normalised patterns, Wando Tonalite **97-161** being slightly more enriched than quartz diorite **97-206F** for most elements, apart from Ti, Y and Yb, which are more depleted (Figure 15.6). Both rocks have distinctly lower Rb, Th, U, K, Nd and Sm but higher Ti, Sr and P than the average LFB I-type granite.

On a chondrite-normalised REE plot, the quartz diorite exhibits moderate light REE enrichment (La ~74 times chondrites), a small negative Eu anomaly (Eu/Eu*= 0.754) and flat heavy REE pattern (Figure 15.7). In contrast, the REE pattern of the Wando Tonalite is much more fractionated, with $(La/Yb)_N$ ~17. The LREE enrichment is also more pronounced, with La~150

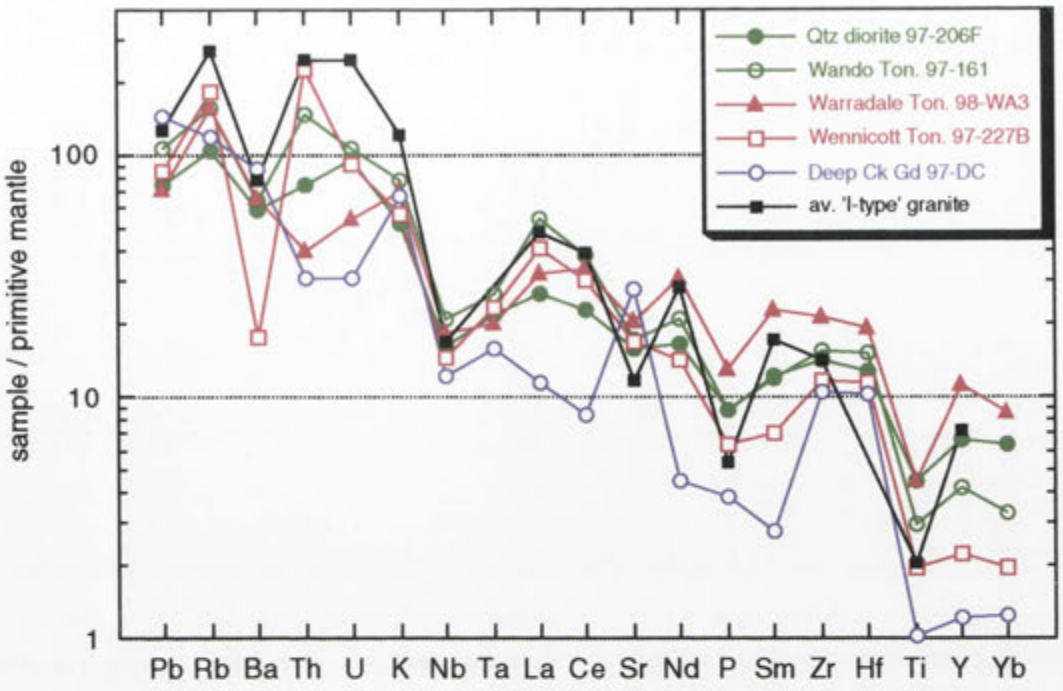

Figure 15.6. Primitive mantle-normalised multi-element diagram (values as for Figure 14.8) for early syn-compressional Wando type (**97-206F**, **97-161**), Wennicott type (**98-WA3**, **97-227B**) and Deep Creek type (**97-DC**) granitic rocks. The average LFB 'I-type' granite of Chappell & White (1992) is shown for comparison.

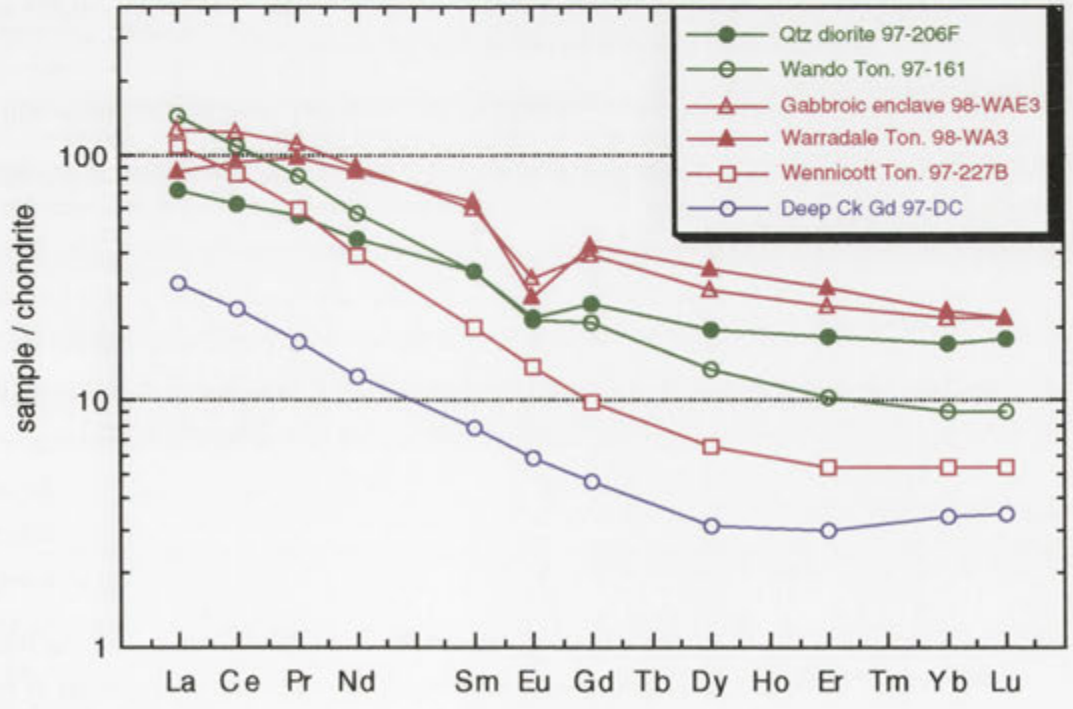

Figure 15.7. Chondrite-normalised REE abundances (normalising values from Anders & Grevesse 1989) for early syn-compressional Wando type (**97-206F**, **97-161**), Wennicott type (**98-WA3**, **97-227B** and enclave **98-WAE3**) and Deep Creek type (**97-DC**) granitic rocks.

times chondritic, however the negative Eu anomaly (Eu/Eu* = 0.80) is slightly smaller than the quartz diorite (Eu/Eu* = 0.75).

The isotopic composition of three Wando type rocks has been ascertained by Turner *et al.* (1993a). Snake River Tonalite 861-86 (58.8% SiO_2) is quite primitive, with initial $^{87}Sr/^{86}Sr$= 0.7061 and ε_{Nd} = -4.2, whereas sample 861-130 (62.9% SiO_2) from the same pluton is much more evolved, having initial $^{87}Sr/^{86}Sr$= 0.7085 and ε_{Nd} = -7.3. Interestingly, a sample from the Elbow Creek dioritic dyke (861-121), which is chemically identical to plagioclase-cumulative sample **98-124** (see above), is markedly more isotopically evolved than the Snake River Tonalite (initial $^{87}Sr/^{86}Sr$= 0.7116 and ε_{Nd} = -8.2) despite substantially lower silica. These large isotopic variations place important constraints on the origin of Wando type rocks (section 16.4.2).

(b) Microgranular enclaves

According with lithological differences, the three microgranular enclave types recognised within Wando type rocks are also resolved chemically, with enclaves of a particular type sharing the same geochemical features irrespective of the host lithology. The two type C enclaves analysed from the Snake River Tonalite are considerably more mafic than other enclaves, **97-159E** having 44.3% SiO_2 and 14.5% Fe_2O_3t, whereas **97-167** has 51.4% SiO_2 at 12.95% Fe_2O_3t. Elevated K_2O (3.2%) in the former reflects the abundant biotite within the sample. Despite the low silica, MgO, Mg# and Cr are moderately low (6.0% MgO at Mg# 0.45 in **97-159E**). The more numerous type A and type B enclaves are bracketed between 55-59% SiO_2. The former have slightly lower SiO_2 (55-57.8%) and higher MgO (5.8-7.9%) and CaO (7.3-8.1%) than type B enclaves (58-59% SiO_2, 3.8-5.3% MgO and 6.4-7.2% CaO), reflecting greater hornblende content. Type A enclaves are also distinctly more magnesian (Mg# 0.57-0.64) than type B enclaves (Mg# 0.47-0.55) and extend to higher Cr contents (780 ppm in **97-214E**) (see Figure 16.3).

On variation diagrams, the two type C microgranular enclaves plot at the lower silica extrapolation of the linear trends defined by the host plutons for TiO_2, Fe_2O_3t, MgO and, apart from **97-159E**, for P_2O_5 and Sr (Figure 15.5). In contrast, type A and type B enclaves form some steep arrays that are at a high angle to the granitic trends, most notably for Al_2O_3, MgO, Na_2O and Sr (Figure 15.5). Importantly, these trends are very similar to those defined by the hornblende-rich gabbro-diorites and diorites of Chin Chap Creek diorites (see Figure 16.1). Type A and type B enclave compositions have greater overlap with the Wando type trends for other elements, though besides Fe_2O_3t and CaO, these are poorly correlated with SiO_2.

15.3.2 Wennicott type

(a) Major elements and Sr

Wennicott type plutons extend to more felsic compositions than Wando types, ranging from ~58% to 71% SiO_2 (Figure 15.5 and Appendix G); this range becomes even greater if the tonalitic dyke W7-025 of Bushell (1996) is included (72.1% SiO_2). The most mafic pluton is the Warradale Tonalite, which varies from 57.9% SiO_2 and 8.0% Fe_2O_3t (**98-WA3**) through to 66.0% SiO_2 and 5.3% Fe_2O_3t (**97-WA2**). This is followed by the tonalite gneiss enclave **98-3**

(66.9% SiO_2) and Wennicott Tonalite **97-227B** (68.9% SiO_2). Notably, a sample of the latter analysed by Bushell (1996) from the northern part of the body (W7-126) has slightly lower silica (66.8%) and is chemically very similar to the tonalite gneiss **98-3**. Apart from tonalitic dyke W7-025, the most felsic pluton is the Meissen Granodiorite, with 70.9% SiO_2 and 2.2% Fe_2O_3t (data from Anderson 1990). Distinctively, K_2O exceeds 2% in the more mafic samples of this magma type, considerably higher than in Wando type rocks of similar SiO_2 content, but becomes lower in more evolved members (1.6% K_2O in Meissen Granodiorite).

Grouping of these rocks as a single magma type is justified by coherent geochemical trends, which, although scattered, are broadly linear for most elements (Figure 15.5). Although there is an apparent compositional 'gap' between ~60-65% SiO_2, this range is in fact spanned by analyses from the Warradale Tonalite pluton, and therefore reflects insufficient data only. Apart from greater scatter and extension to higher SiO_2, Wennicott type trends are indistinguishable from those of Wando types for TiO_2, Fe_2O_3t, MgO, CaO and Na_2O. Trends are also very similar for the two magma types for Al_2O_3 and Sr, though Wennicott types have slightly lower Al_2O_3 and higher Sr at the same SiO_2 content. The primary chemical difference between Wando and Wennicott types occurs for K_2O, which increases steeply with SiO_2 for Wando type rocks but actually decreases slightly for Wennicott types. A similar difference occurs for P_2O_5, which exhibits pronounced decrease with increasing SiO_2 for Wennicott types, but remains approximately constant for Wando types.

Four mafic enclaves collected from the Warradale Tonalite have primitive, essentially basaltic compositions, with low SiO_2 (50-51.9%), and high Fe_2O_3t (9-11%), MgO (5.5-6.4%) and CaO (8.4-9.6%), though the high-K character is still evident (2.0% K_2O in **97-WAE1**). The amphibolitic enclave collected from Wennicott Tonalite (**97-227A**) is more felsic, with 59.9% SiO_2, though a similar enclave with 51.8% SiO_2 is reported by Bushell (1996).

Unlike the case for Wando types, mafic enclaves in Wennicott type granitic rocks plot at the lower silica extension of the geochemical trends defined by their hosts (Figure 15.5). This strongly implies kinship between mafic enclaves and Wennicott type plutons, which are therefore taken as a coupled petrogenetic system.

(b) Other trace elements and the REE

Two Wennicott type samples, **98-WA3** (Warradale Tonalite) and **97-227B** (Wennicott Tonalite) have similarly shaped mantle-normalised trace element patterns, apart from the latter having unusually elevated Th and depleted Ba (Figure 15.6). According with the more mafic character, elements from Ce to Yb are clearly more enriched in the Warradale Tonalite. The latter also has higher trace element (and REE, see Figure 15.7) abundances than Wando type quartz diorite **97-206F** (except Th and U), indicating that Wennicott types are more 'enriched' than Wando types at the lower silica end. The compatible element-enriched nature of the Warradale Tonalite is underlined by the higher Nd, Sm and Y compared to the average LFB I-type granite, which is not evident for any other GRC pluton.

The Warradale Tonalite has a distinctive chondrite-normalised REE pattern, with a convex LREE trend and large negative Eu anomaly (Eu/Eu* = 0.51) (Figure 15.7). The REE pattern of basaltic enclave **98-WAE3** (contained by the Warradale Tonalite) is almost indistinguishable from this, indicating that the enclave-host coupling intrinsic to the Wennicott magma type extends to the REE. However, the REE pattern of Wennicott Tonalite **97-227B** is markedly different, being much more strongly fractionated (La_N /Yb_N~21 compared to ~3 for the Warradale Tonalite), lacking a convex LREE pattern or negative Eu anomaly and, apart from La, having much lower REE contents (Figure 15.7). Besides the absence of a Eu anomaly, the Wennicott Tonalite REE pattern resembles that of the Wando Tonalite **97-161**, though at distinctly lower abundances.

15.3.3 Deep Creek type

The Torah and Deep Creek Granodiorites of this magma type are fairly homogeneous and chemically quite similar, with high Al_2O_3 (>17%) Na_2O (>3.2%) and Sr (>500 ppm), and moderately low TiO_2 (<0.25%) and K_2O (<2.1%) over a very narrow silica range (68.2-68.4% SiO_2) (elemental concentrations from Anderson 1990 and Turner *et al.* 1993a). The major differences between the bodies is that Deep Creek Granodiorite extends to higher Na_2O (4.6%) and Sr (~640 ppm) than the Torah Granodiorite (to 3.6% Na_2O, ~530 ppm Sr), and has distinctly higher Na/Ca (1.0-1.1 compared to 0.7-0.8 for Torah Granodiorite).

Deep Creek type granitic rocks have conspicuously elevated Al_2O_3, Na_2O, Sr and Ba, but lower TiO_2, Fe_2O_3t and P_2O_5 relative to other early syn-compressional phases of similar silica (Figure 15.5), justifying their treatment as a separate magma type. This is reinforced by the markedly different multi-element diagram of Deep Creek Granodiorite **97-DC** compared to other early syn-compressional granitic rocks, particularly with regard to the conspicuous Sr spike and overall more depleted chemistry, especially Ti, Yb and Y (Figure 15.6). The REE abundances of **97-DC** are also clearly lower than Wando and Wennicott types, with the strongly fractionated character (La_N /Yb_N ~ 9), lack of Eu anomaly and pronounced HREE depletion being notable features (Figure 15.7).

The isotopic composition of both Deep Creek type plutons has been determined by Turner *et al.* (1993a), who report initial $^{87}Sr/^{86}Sr$= 0.7077 and ε_{Nd} = -4.9 for the Deep Creek Granodiorite and initial $^{87}Sr/^{86}Sr$ = 0.7098 and ε_{Nd} = -9.6 for the Torah Granodiorite (calculated at 500 Ma). A sample of Deep Creek Granodiorite analysed by Gray (1990) is slightly less radiogenic than that of Turner *et al.* (1993a), with initial $^{87}Sr/^{86}Sr$ = 0.7071 at 500 Ma.

15.4 Geochemistry of late syn-compressional igneous rocks

15.4.1 Tuloona type

(a) Granitic rocks

Tuloona types extend from 66.9% SiO_2 (Chetwynd Tonalite **97-427**) through to 73.5% SiO_2 for the porphyritic Glendara Adamellite (**97-145**) (see Appendix G). All are weakly peraluminous, with A.S.I. bracketed between 1.03 (Chetwynd Tonalite) and 1.10 (Mooree Granodiorite). Broad

chemical similarity between widely-spaced samples suggests that most plutons of this type are internally homogeneous, despite heterogeneous distribution of microgranular and metasedimentary enclaves. The exception is the Coojar Granodiorite, which ranges from 67.8% SiO_2 and 3.6% Fe_2O_3t (**97-297**) to 72.3% SiO_2 and 2.0% Fe_2O_3t (**97-142**).

On Harker variation diagrams, elemental abundances of Tuloona type rocks are well correlated with SiO_2, defining negative linear trends for TiO_2, Al_2O_3, Fe_2O_3t, MgO, CaO and P_2O_5, a flat trend for Na_2O, and a steeply positive trend for K_2O and Rb/Sr (Figure 15.8). Sr exhibits more scatter, but overall decreases slightly against SiO_2. Mantle normalised multi-element patterns of Tuloona Granodiorite samples **97-299** and **T2-135** are very similar (Figure 15.9). As with early-syn-compressional plutons, these rocks have lower Rb, Th, U, K, Nd, Sm and Y, but higher Sr and P than the average LFB I-type. The REE patterns of both Tuloona Granodiorite samples are steep (La_N/Yb_N ~28 for **97-299**) and virtually indistinguishable, apart from a slight Dy to Lu depletion in **97-299** (Figure 15.10). Both rocks have small negative Eu anomalies (Eu/Eu* = 0.74 in **97-299**).

The Tuloona Granodiorite exhibits some isotopic variability, with **97-299** having initial $^{87}Sr/^{86}Sr$= 0.7093 and ε_{Nd} = -9.5, whereas more felsic sample **T2-318** is considerably more evolved, with initial $^{87}Sr/^{86}Sr$= 0.7114 and ε_{Nd} = -12.6 (at 500 Ma; Appendix A).

(b) Microgranular enclaves

These overlap with the lower silica end of the Tuloona type granitic compositional range, varying from 69.5% SiO_2 for an enclave from the Patawilya Tonalite (**97-382B**) to 63.1% SiO_2 for sample **97-294**, collected from Tuloona Granodiorite (Figure 15.8). A microgranular enclave from the Coojar Granodiorite of similar composition to **97-294** is documented by O'Hara (1996). Apart from the most silicic sample, microgranular enclaves define reasonably coherent linear arrays on variation diagrams, which is not generally the case for enclaves of granitic rocks (see Debon 1991). These fall at the low SiO_2 continuation of the Tuloona type granitic trends for some elements (TiO_2, Fe_2O_3t and CaO), but occur at an angle to the trends of their host plutons for Al_2O_3, MgO, Na_2O, K_2O and Sr.

15.4.2 Kassingbrook types

(a) Granitic rocks

The petrographic heterogeneity of the Kassingbrook Granodiorite is reflected chemically, the pluton ranging from 74.7% SiO_2 and 1.2% Fe_2O_3t for 'typical' muscovite-bearing samples (**97-373**) to 70.8% SiO_2 and 1.9% Fe_2O_3t for a sample adjacent to a hornblende diorite sheet (**97-275**) (Appendix G). The porphyritic Coolami Granodiorite (**97-308B**) falls within this range, with 71.9% SiO_2 and 1.6% Fe_2O_3t. Despite the siliceous nature, all Kassingbrook type samples have high Sr contents (340-450 ppm), mirroring that of *in situ* leucosomes of interleaved migmatites, which range from 380 ppm for leucosome **98-102** through to ~410-490 ppm for three samples of Dean (2000). Extreme variation in K_2O (1.6-5.4%) and Ba (~270-1500 ppm) is another distinctive attribute of Kassingbrook type granitic rocks, resulting in a vertical array on variation diagrams (Figure 15.8). It is worth noting that this eccentric variation is contained

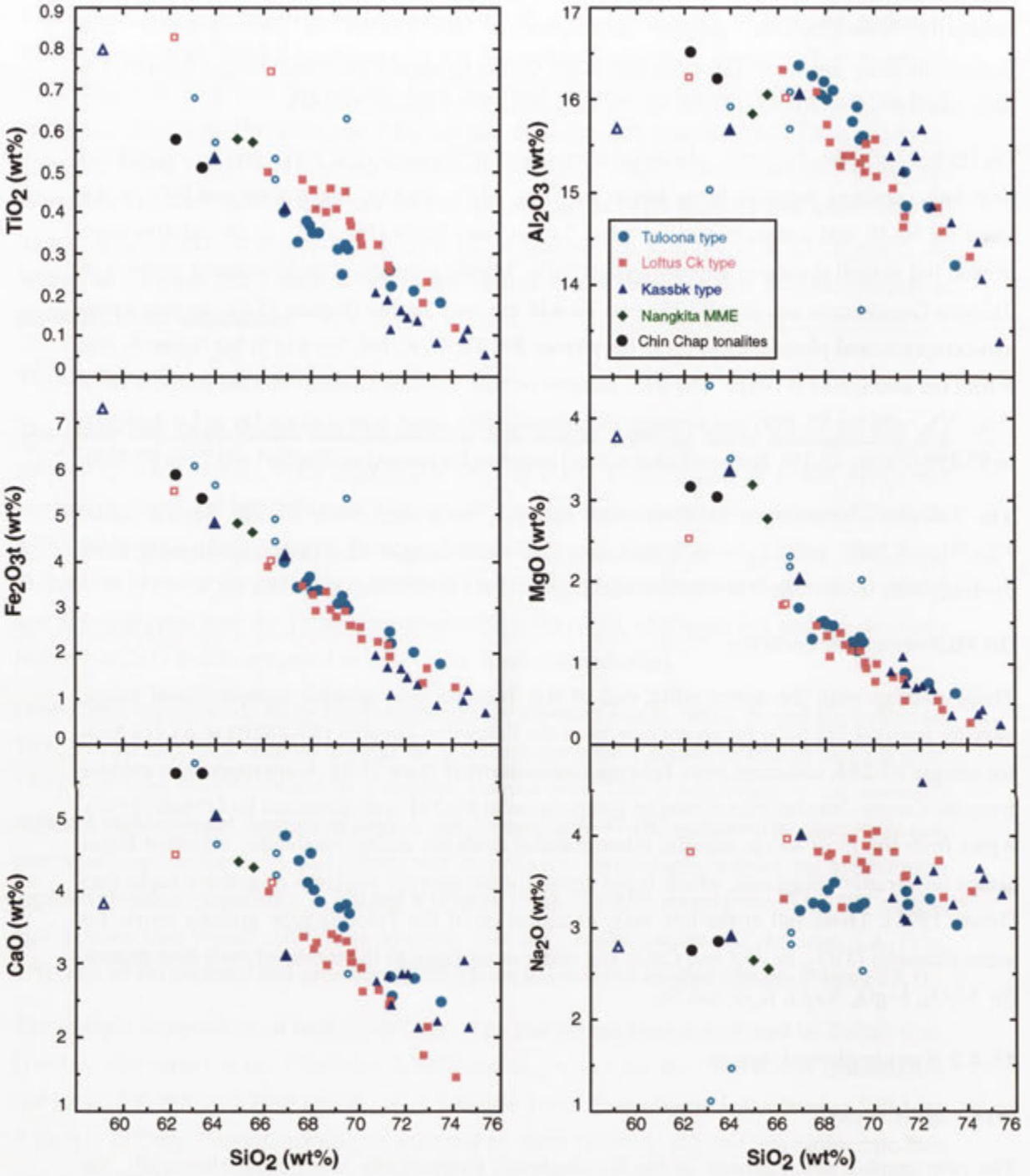

Figure 15.8. Harker variation diagrams for late syn-compressional granitic rocks of the GRC. Open symbols represent MME. Large blue triangles are the hybrid Kassingbrook Granodiorite samples **97-376C** (~66% SiO_2) and **97-274** (~64% SiO_2). Chin Chap Creek tonalites (**97-309** and **97-309-1**) and microgranular enclaves within the Nangkita Adamellite (**97-254A**, **97-254B**) are also plotted. All data is from this study (Appendix G), apart from Loftus Creek Granodiorite samples 9572 (66.2% SiO_2) (Anderson & Gray 1994) and W7-078 (67.6% SiO_2) (Bushell 1996). A Tuloona Granodiorite enclave (S14, 64% SiO_2) is also taken from O'Hara (1996).

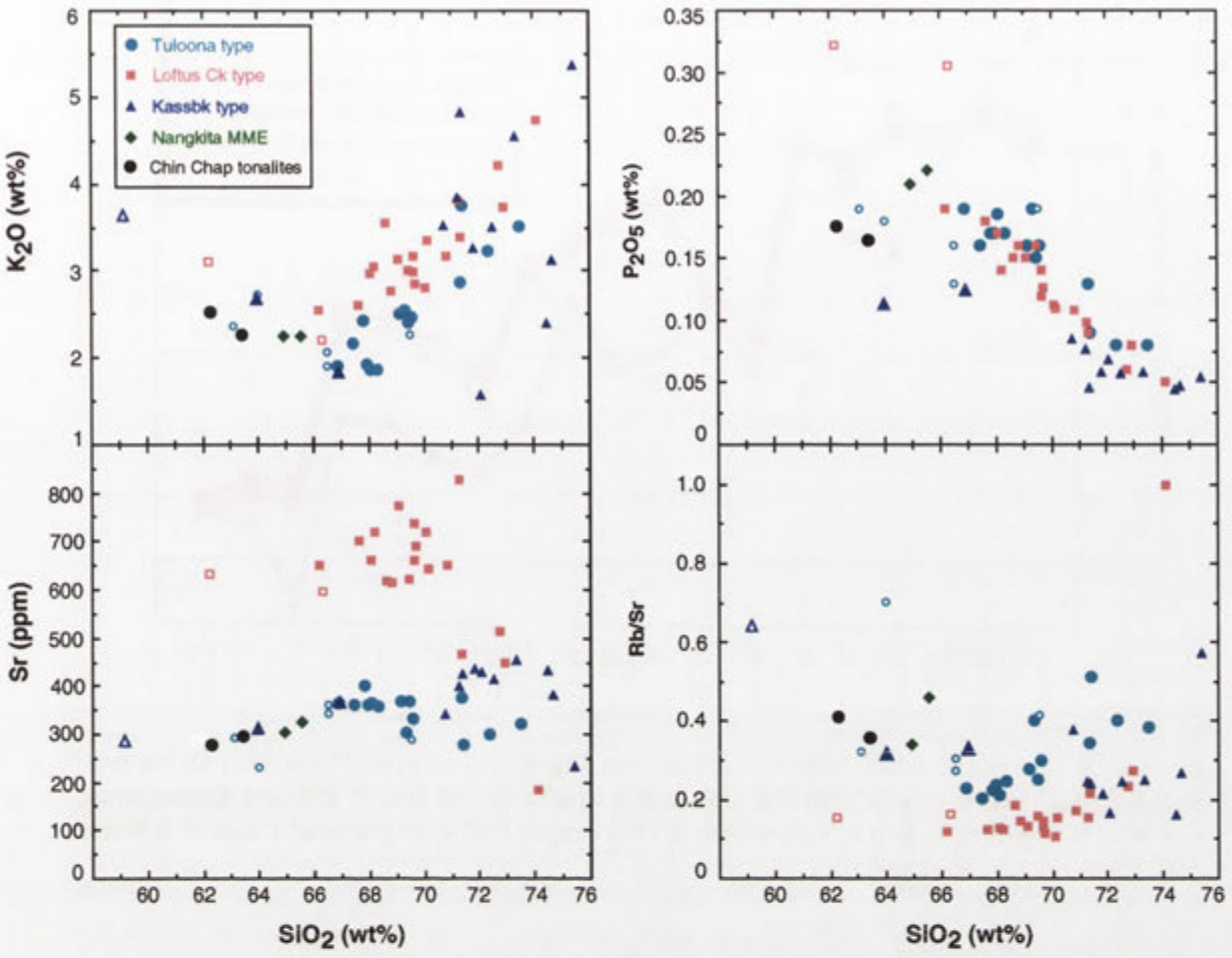

Figure 15.8 contd. Harker variation diagrams for late syn-compressional granitic rocks of the GRC. Open symbols represent MME. Large blue triangles are the hybrid Kassingbrook Granodiorite samples **97-376C** (~66% SiO_2) and **97-274** (~64% SiO_2). Chin Chap Creek tonalites (**97-309** and **97-309-1**) and microgranular enclaves within the Nangkita Adamellite (**97-254A**, **97-254B**) are also plotted. All data is from this study (Appendix G), apart from Loftus Creek Granodiorite samples 9572 (66.2% SiO_2) (Anderson & Gray 1994) and W7-078 (67.6% SiO_2) (Bushell 1996). A Tuloona Granodiorite enclave (S14, 64% SiO_2) is also taken from O'Hara (1996).

largely within the Kassingbrook Granodiorite, which, although heterogeneous, is demonstrably a single body. Similar internal variation is the hallmark characteristic of felsic Harrow type plutons (see Figure 9.15). Apart from K_2O, Kassingbrook type samples define scattered linear trends for most other elements on variation diagrams (Figure 15.8).

The mantle normalised multi-element pattern of Kassingbrook Granodiorite **97-376A** (Figure 15.9) is markedly more depleted than other late syn-compressional granitic rocks, apart from an unusual Pb enrichment. Strong decoupling of Sr from Nd and Sm is another distinctive feature. The LREE depleted character is strikingly evident (Figure 15.10), although the HREE trend is concave-shaped and consequently Yb and Lu concentrations overlap with those of Loftus Creek types. The REE pattern is much flatter than that of Tuloona and Loftus Creek types (La_N /Yb_N ~6.3) and a small positive Eu anomaly is present (Eu/Eu* = 1.19).

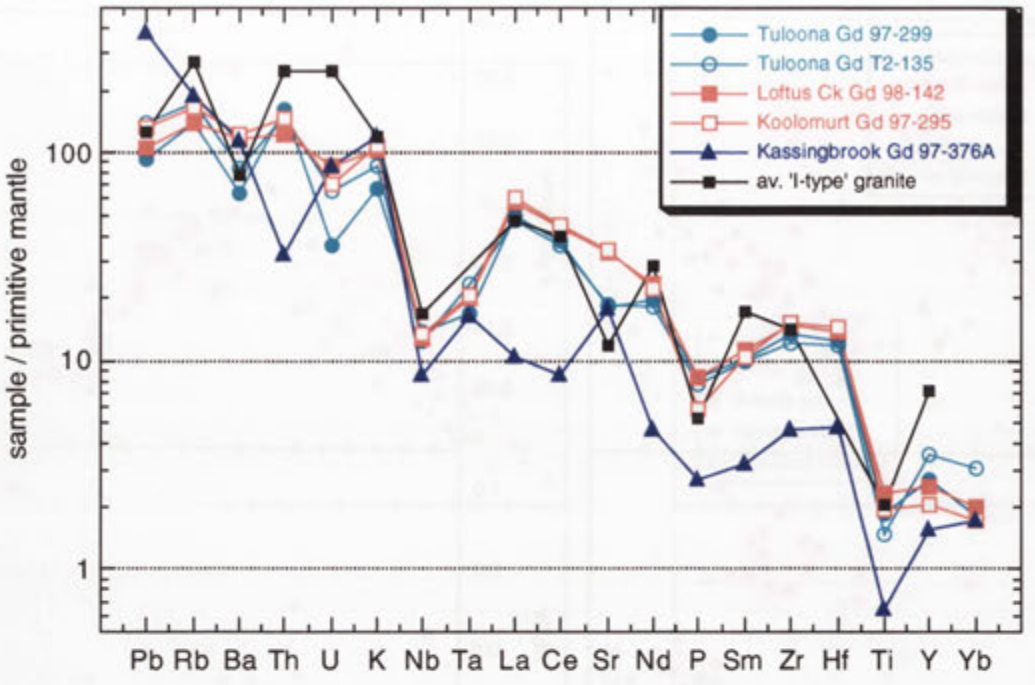

Figure 15.9. Primitive mantle-normalised multi-element diagram (values as for Figure 14.8) for late syn-compressional Tuloona type (**97-299**, **T2-135**), Loftus Creek type (**98-142**, **97-295**) and Kassingbrook type (**97-376A**) granitic rocks (Gd = granodiorite). The average LFB 'I-type' granite of Chappell & White (1992) is shown for comparison.

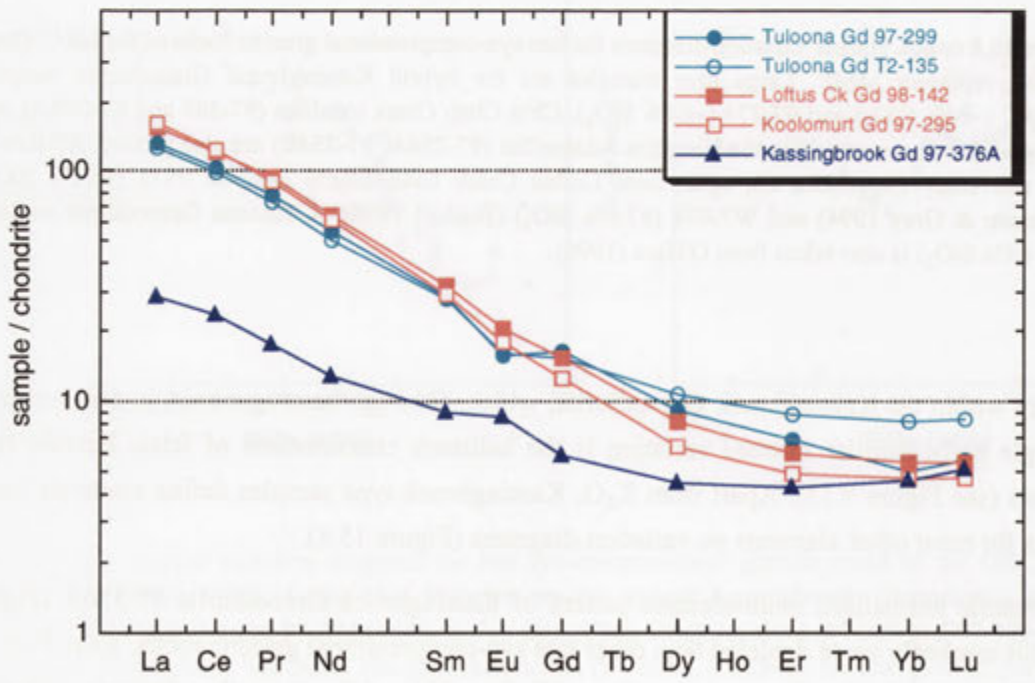

Figure 15.10. Chondrite-normalised REE abundances (normalising values from Anders & Grevesse 1989) for Late syn-compressional Tuloona type (**97-299**, **T2-135**), Loftus Creek type (**98-142**, **97-295**) and Kassingbrook type (**97-376A**) granitic rocks.

The REE pattern of Kassingbrook Granodiorite **97-376A** has similar shape to that of Dunmore Leucotonalite **98-150**, though at significantly lower normalised REE abundances (Figure 15.11). Other differences are the less conspicuous Nd anomaly, smaller positive Eu anomaly and more bell-shaped HREE trend of **97-376A**. The REE pattern of **97-376A** is in fact remarkably similar to that of Deep Creek Granodiorite **97-DC**, apart from the positive Eu anomaly and slightly greater HREE abundances (Figure 15.11). This accords with the similar mantle-normalised multi-element trends, especially the shared Sr spike, Pb enrichment, depleted Th relative to Ba, and strongly depleted Ti, Yb and Y (Figure 15.12).

(b) Hybrid variants

The 'hybrid' Kassingbrook Granodiorite variants **97-376C** and **97-274** are considerably more mafic than other samples of the pluton, the latter having 64.0% SiO_2 at 4.8% Fe_2O_3t and being quite magnesian, with 3.3% MgO. The magnesian signature of **97-274** is emphasised upon comparison with Wando type tonalites of similar silica, which have markedly lower MgO (e.g. 2.1% MgO in **97-161**). Hybrid **97-376C** is less mafic, with 66.9% SiO_2 and 2.0% MgO. On variation diagrams, hybrid rocks plot near the extrapolation of the Kassingbrook type linear trend for TiO_2, Al_2O_3, MgO, CaO, P_2O_5 and Sr, thereby extending this back to 64% SiO_2 (Figure 15.8). As the hybrid variants have lower Sr contents (310 ppm Sr in **97-274**), this results in Kassingbrook types defining a positive gradient for Sr against silica, in contrast to the negative gradient of other magma types. The large, non-systematic K_2O variation in the Kassingbrook Granodiorite is also evident for the hybrids, **97-376C** having 1.9% K_2O as opposed to 2.7% K_2O for the more mafic **97-274**.

Significantly, the tonalitic hybrid **97-274** has geochemical affinity with nearby mafic hornblende-bearing rocks of Chin Chap/Robson Creek, most notably with the shared Mg-rich character. This is reflected by the occurrence of Mg-rich biotite and hornblende in **97-274** that resembles that of the hornblende diorite **97-376** (Figures 15.3, 15.4). In particular, apart from marginally lower CaO, the major element composition of **97-274** closely resembles that of the Chin Chap Creek tonalitic dykes **97-309** and **97-309-1** (section 14.3.2b), which therefore also fall close to the Kassingbrook type geochemical array on variation diagrams (Figure 15.8). Primitive mantle-normalised diagrams are also similar, minor differences being the lower Ce and P abundances of **97-274** (Figure 15.13). The chondrite-normalised REE pattern of **97-274** has similar shape to, and plots within the range of, Chin Chap Creek hornblende diorites (Figure 15.14).

(c) Microgranular enclaves

A 'spotted' microgranular enclave from key locality E in Chin Chap Creek (**97-275E**) has 59.2% SiO_2 at 3.8% MgO and 3.6% K_2O, the latter reflecting abundant biotite and alkali feldspar. The two texturally-analogous microgranular enclaves in the Nangkita Adamellite (**97-254A**, **97-254B**) are more evolved and less potassic, with 65.9% and 63.2% SiO_2 respectively at 2.2% K_2O. All three enclaves conform to the linear Kassingbrook type granitic trend for TiO_2, Al_2O_3, MgO, CaO (apart from **97-275E**) and Sr on silica variation diagrams, though plot above the trend for P_2O_5 (Figure 15.8). Importantly enclaves **97-254A** and **97-254B** plot close to Chin Chap Creek tonalitic dykes (**97-309**, **97-309-1**) for most elements and have virtually indistinguishable

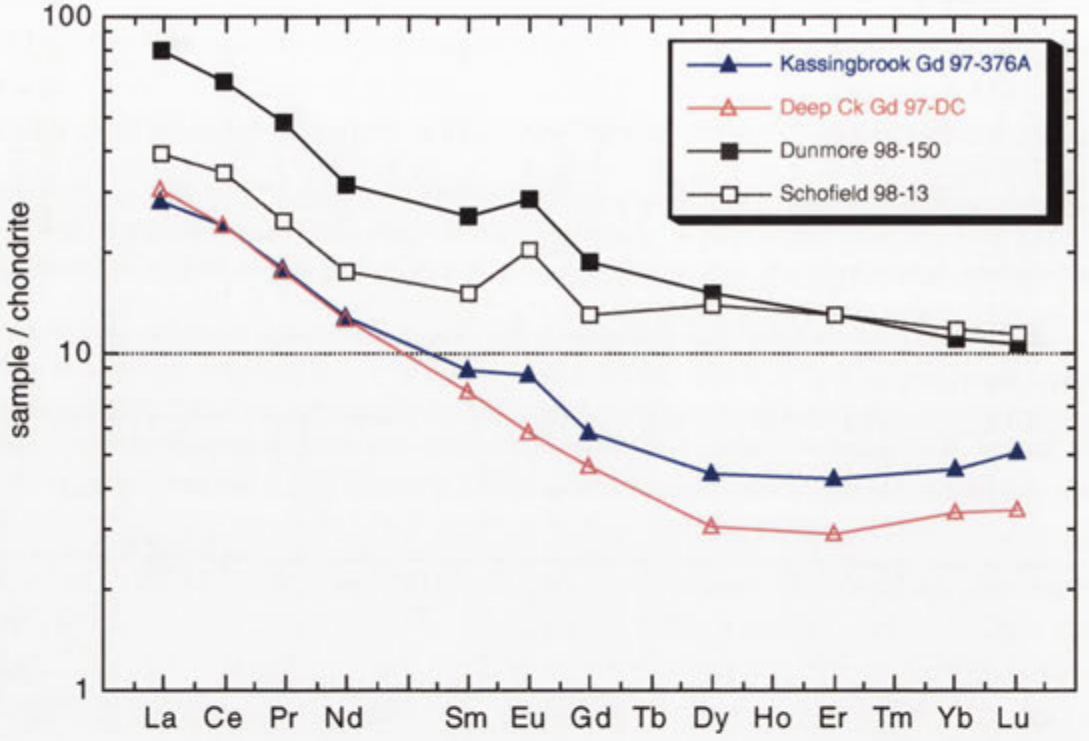

Figure 15.11. Comparison between chondrite-normalised REE abundances of Kassingbrook Granodiorite **97-376A** with those of Deep Creek Granodiorite **97-DC** and the Harrow type Schofield Adamellite **98-13** and Dunmore Leucotonalite **98-150** (normalising values from Anders & Grevesse 1989).

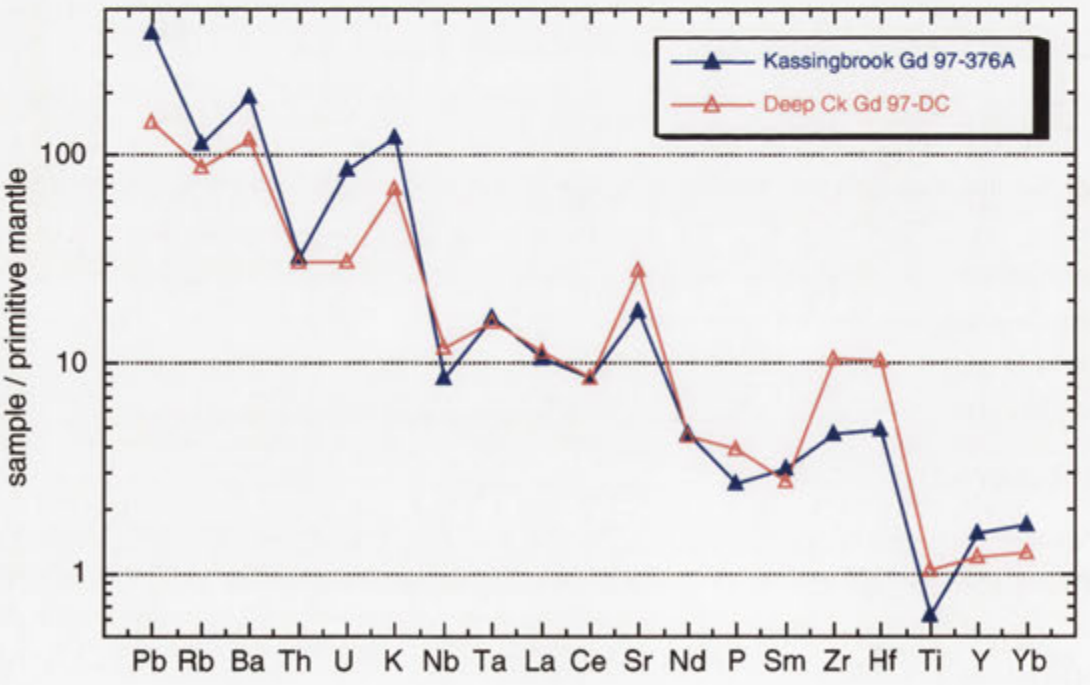

Figure 15.12. Primitive mantle-normalised multi-element diagram (values as for Figure 14.8) comparing Kassingbrook Granodiorite **97-376A** with Deep Creek Granodiorite **97-DC**.

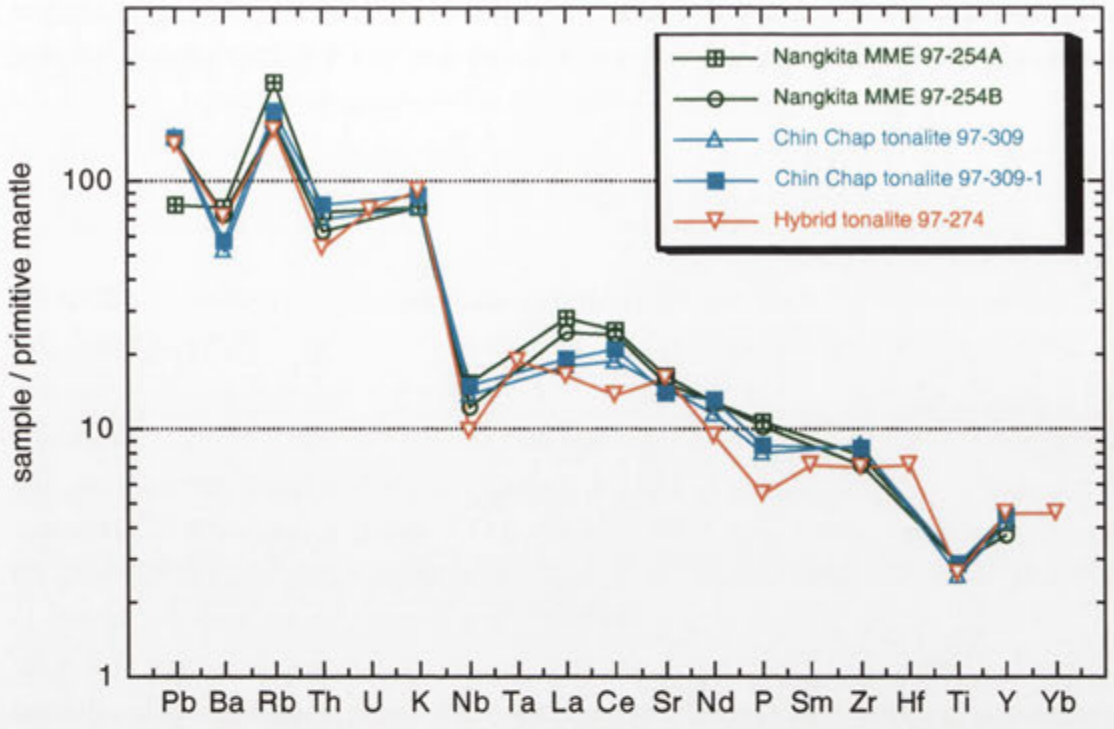

Figure 15.13. Primitive mantle-normalised multi-element diagram (values as for Figure 14.8) comparing Kassingbrook type tonalitic hybrid **97-274** with Chin Chap Creek tonalites (**97-309**, **97-309-1**) and Nangkita Adamellite microgranular enclaves (**97-254A**, **97-254B**).

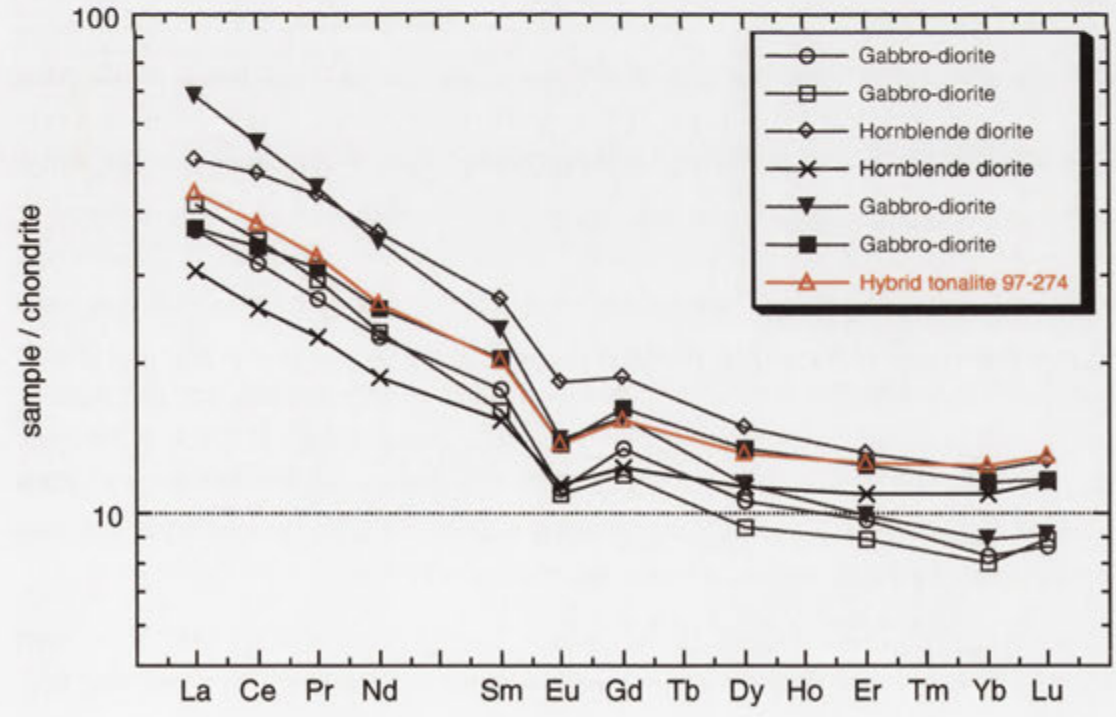

Figure 15.14. Chondrite-normalised REE abundances of Kassingbrook type tonalitic hybrid **97-274** compared to those of Chin Chap Creek hornblende diorites and gabbro-diorites (normalising values from Anders & Grevesse 1989).

mantle-normalised trace element patterns (Figure 15.13). A genetic relationship between these enclaves and the tonalitic dykes is therefore strongly implied. However, microgranular enclave **97-275E** has lower silica and CaO and is K-enriched relative to tonalite dykes.

15.4.3 Loftus Creek types

(a) Granitic rocks

The most mafic pluton of this type is the Loftus Creek Granodiorite, ranging from 66.2% SiO_2 and 3.9% Fe_2O_3t in Corea Creek (Anderson 1990) to 68.0% SiO_2 at 3.3% Fe_2O_3t in Loftus Creek (sample **97-142**). This is followed by the Cloven Hills Granodiorite (three samples spanning 68.2-70.1% SiO_2) and the Koolomurt Granodiorite (68.9-69.6% SiO_2), three widely-spaced samples of which (**97-47**, **97-293**, **295**) are almost chemically indistinguishable. The largest geochemical variation occurs within the zoned Cairns Creek Granodiorite (six samples), which ranges from 69.1% SiO_2 and 2.8% Fe_2O_3t at the hornblendic periphery (**97-62**) to 72.7% SiO_2 and 1.3% Fe_2O_3t at the felsic core (**97-67**). The Barrama Microadamellite extends to slightly higher silica (71.3-72.9% SiO_2), whereas the most felsic Loftus Creek type rock is the garnet microadamellite dyke **97-178B** (74.1% SiO_2, 1.3% Fe_2O_3t) that is probably affiliated with the Cloven Hills Granodiorite. All samples of this magma type are weakly peraluminous (A.S.I. between 1.0 and 1.1), except for the Koolomurt Granodiorite **97-47** (A.S.I. = 0.99) and Cairns Creek Granodiorite **97-62** (A.S.I. = 0.96), which are metaluminous.

Loftus Creek type granitic rocks define linear trends on Harker variation diagrams that are broadly parallel to, and overlap with, the Tuloona type geochemical array for all major elements (Figure 15.8). Nevertheless, at the same silica content, Loftus Creek types have slightly lower CaO and systematically higher TiO_2, K_2O and Na_2O than Tuloona types, trends for the latter converging at ~74% SiO_2. However, Loftus Creek type granitic rocks are most easily discriminated from Tuloona type plutons on the basis of uniquely high Sr concentrations, which are clustered between ~600-830 ppm, and distinctly higher Ba (Figure 15.8). The elevated Sr contents of Loftus creek type plutons also results in markedly lower Rb/Sr than for Tuloona type bodies. However, Sr concentrations are much lower in the most felsic Loftus Creek type rocks such as the central Cairns Creek Granodiorite **97-67** (515 ppm), and fall to only ~180 ppm in microgranitic dyke **97-178B**. This is well below those of Tuloona types, which exhibit slight Sr decrease with silica only. Consequently, there is an exponential increase in Rb/Sr at the felsic end of the Loftus Creek type array (i.e. above ~70% SiO_2), to a maximum of 1.0 for **97-178B** (Figure 15.8). This contrasts with the more moderate linear trend for Tuloona types, the most siliceous sample of which (Glendara Adamellite **97-145**) has Rb/Sr <0.4.

Loftus Creek type rocks **98-142** (Loftus Creek Granodiorite) and **97-295** (Koolomurt Granodiorite) have nearly identical multi-element patterns, that are only clearly resolved from those of Tuloona type samples by the higher Ba and Sr (Figure 15.9). Both of the Loftus Creek type samples also produce very similar, strongly fractionated chondrite-normalised REE trends, with Sm to Lu abundances being slightly less for **97-295** (Figure 15.10). These patterns resemble those of Tuloona type rocks, though the Loftus Creek type plutons have negligible Eu anomalies.

(b) Microgranular enclaves

The two enclaves collected from Koolomurt Granodiorite (**98-PP1, 98-PP2**) have 66.3% and 62.3% SiO_2 respectively, and plot close to the linear extrapolation of the Loftus Creek type trend for major elements (Figure 15.8). The exception is K_2O, where **98-PP2** (3.1% K_2O) plots well above the continuation of the steep granitic trend. Both enclaves share the characteristic high Na_2O, high Sr signature of the host lithology, and are clearly distinguished from Tuloona type microgranular enclaves on this basis.

15.5 Discussion: Comparison between GRC granitic rocks and those of other orogenic belts

The average composition of some plutonic rocks from the GRC and other orogenic belts is compiled in Table 15.1 (analyses labelled A to R), together with those of the various GRC magma types. Consistent with the trace element differences highlighted above, GRC granitic rocks are unlike the Siluro-Devonian plutons of the LFB, having lower K_2O, but higher CaO, Na_2O and Na/K at the same silica content. On a general level, this is manifested by the abundance of mafic tonalitic rocks in the GRC as opposed to the prevalence of K-rich granodiorites across the LFB. However, the differences are most apparent in specific examples. Both the average Wando (analysis B) and Wennicott type (analysis D) tonalites are distinctly more calcic and less potassic than the uncommon mafic hornblende tonalites (with 59-61% SiO_2) from the I-type batholiths of the eastern LFB (analysis A). Differences between the average hornblende granodiorite of the Bega Batholith with between 66-69% SiO_2 (analysis I) and the Chetwynd Tonalite (analysis L) are even greater, especially regarding Na/K and Rb/Sr. Although the average Loftus Creek type pluton and Loftus Creek Granodiorite (analyses M and N) actually have lower CaO than the average LFB I-type and Bega Batholith granitic rock (analyses H and I), Na_2O and Na/K are still distinctly higher in both cases.

Alternatively, GRC granitic rocks are analogous to those of the continental margin 'cordilleran I-type' batholiths of the circum-Pacific, whose formation occurred above a subducted slab of oceanic lithosphere at a convergent plate boundary (Pitcher 1982) (Table 15.1). In general, as with primitive arc-derived lavas, cordilleran-type plutons are characterised by low TiO_2 and K_2O, but high CaO, Na_2O, Sr and Na/K (Chappell & Stephens 1988), features which are intrinsic to GRC granitic rocks. The resemblance is strongest with the tonalite-dominated Peninsula Ranges Batholith (PRB) of Baja California, formed during Cretaceous subduction beneath the North American plate (Silver & Chappell 1988). The average granitic rock from this batholith with >53% SiO_2 (analysis J) is compositionally quite similar to the Tuloona type Chetwynd Tonalite, the latter having slightly higher mean CaO but lower TiO_2 and Na_2O. Equally, mafic PRB tonalites (those with between 59-61% SiO_2, analysis E) resemble the average Wando and Wennicott type tonalite (analyses B and D), apart from slightly higher Na_2O and lower K_2O. These tonalites in turn are comparable to medium-K volcanic rocks from more mature continental arcs of the NE Pacific (analysis G).

Analysis	*A* *LFB* *I-type* (59-61%)	*B* *Wando type*	*C* *Wando QD*	*D* *Wennicott type*	*E* *PRB* (59-61%)	*F* *PRB QD*	*G* *NE Pacific*
Average	n = 35	n = 11	n = 6	n = 14	n = 16	n = 22	n = 695
SiO_2	60.51	59.28	56.76	59.92	60.08	58.63	59.18
TiO_2	0.73	0.72	0.80	0.74	0.86	0.87	0.91
Al_2O_3	15.60	17.37	17.86	16.09	16.43	16.77	17.06
Fe_2O_3t	6.80	6.81	7.49	6.90	6.76	7.30	7.18
MnO	0.12	0.13	0.15	0.14	0.11	0.11	0.12
MgO	3.42	3.12	3.82	3.86	3.19	3.65	3.66
CaO	6.10	6.57	7.39	6.62	6.63	7.07	6.71
Na_2O	2.62	3.08	3.29	2.79	3.43	3.31	3.85
K_2O	2.34	1.80	1.40	1.90	1.35	1.29	1.57
P_2O_5	0.18	0.16	0.16	0.21		0.15	0.22
Na/K	1.12	1.71	2.35	1.47	2.54	2.57	2.45
Rb/Sr	0.228	0.224	0.166	0.301		0.124	0.084

Analysis	*H* *LFB* *I-type*	*I* *Bega bath.* (66-69%)	*J* *PRB* (>53%)	*K* *Tuloona type*	*L* *Chetwynd Tonalite*	*M* *Loftus Ck Type*	*N* *Loftus Ck Gd*
Average	n = 1074	n = 97	n = 297	n = 13	n = 2	n = 19	n= 3
SiO_2	69.50	67.79	67.12	69.46	67.17	69.69	67.29
TiO_2	0.41	0.52	0.63	0.30	0.36	0.37	0.48
Al_2O_3	14.21	14.59	15.98	15.64	16.21	15.32	16.05
Fe_2O_3t	3.47	4.35	4.34	3.01	3.70	2.65	3.54
MnO	0.07	0.08	0.07	0.07	0.06	0.05	0.07
MgO	1.38	1.65	1.75	1.22	1.50	1.02	1.51
CaO	3.07	3.90	4.55	3.65	4.59	2.95	3.52
Na_2O	3.16	2.82	3.84	3.26	3.20	3.71	3.64
K_2O	3.48	3.01	2.13	2.53	2.03	3.17	2.71
P_2O_5	0.11	0.12		0.15	0.17	0.13	0.18
Na/K	0.91	0.94	1.80	1.29	1.58	1.17	1.34
Rb/Sr	0.698	0.56		0.295	0.218	0.151	0.123

Table 15.1. Average chemical analyses of some plutonic rocks from the GRC, LFB and Peninsula Ranges Batholith (PRB) (Gd = granodiorite; QD = quartz diorite). The average volcanic rock from NE Pacific island and continental arcs (Silver & Chappell 1988, calculated from data in Ewart 1979) is also listed.

GRC averages were calculated from the same data sources as for Figures 15.5 and 15.8. Due to chemical coherence, microgranular enclaves were included in the average Wennicott type calculation, but excluded from averages of other magma types. The average LFB I-type with 59-61% SiO_2 (from the exclusively I-type Moruya, Bega and Marulan batholiths) and average Bega Batholith I-type granite with 66-69% SiO_2 are estimated from Chappell (*unpubl. data*), whereas the average LFB I-type is from Chappell & White (1992). PRB data for >53% SiO_2 and 59-61% SiO_2 are from Chappell & Stephens (1988), and the PRB quartz diorite average is from Silver & Chappell (1988).

However, the most striking aspect of Table 15.1 is the remarkable resemblance between the average Wando type quartz diorite (analysis C) and quartz diorites from the western PRB (analysis F). The latter have close chemical affinity with the mafic 'M-type' (mantle-derived) quartz diorites of some primitive intra-oceanic island arcs (Silver & Chappell 1988), which is taken to suggest commonality of process or source (Chappell & Stephens 1988). The viability and implications of this notion for the petrogenesis of GRC granitic magmas are evaluated in the following chapters.

Chapter 16: Petrogenesis of igneous rocks of the GRC

16.1 Introduction

The preceding chapters in Part III have emphasised the field and petrographic continuity of the GRC igneous system, from migmatite-derived Harrow type bodies, through weakly peraluminous to metaluminous granitic plutons and thence to mafic-intermediate rocks. To investigate the genetic linkages between these entities, the geochemical variation of all granitic and mafic igneous rocks is presented in Figure 16.1. Despite the enormous lithological diversity and emplacement at different stages of the deformational history, the igneous rocks define two simple geochemical trends. The dominant, strikingly linear trend (hereafter the **'granitic array'**) extends from Caupaul high-Al gabbros at low silica through to Harrow type plutons at high silica, and encompasses all of the granitic magma types described in Part III (excluding Deep Creek types). This suggests that the various granitic types are related through a common process or source material. Nevertheless, the geochemical trends of individual granitic types differ for some elements, especially K_2O and Sr, reflecting the compositional features intrinsic to each (Chapter 15). In detail, therefore, the petrogenesis of each granitic type is slightly different.

The second, steeper trend is defined by hornblende-rich dioritic rocks of Chin Chap Creek/Robson Creek and, at slightly higher silica, Caupaul intermediate rocks (hereafter the **'dioritic array'**). This branches from the granitic array at 58-60% SiO_2 and extends at lower silica to markedly higher MgO and CaO, and lower TiO_2, Al_2O_3, Na_2O, P_2O_5 and Sr. The trend is vaguely hyperbolic for Al_2O_3, MgO and Sr. Caupaul pyroxenites consistently plot at the lower silica extremity of this array, but trace element evidence suggests that these are the complementary cumulates to high-Al gabbros, and not part of the dioritic petrogenetic system (see section 14.4.1). Nevertheless, the positioning of pyroxenites on variation diagrams provides some insight into the origin of the dioritic array. Although sharing the magnesian signature (section 14.3.2b), Chin Chap Creek tonalites (those points on Figure 16.1 with ~62% and 63% SiO_2) do not plot along the dioritic trend for some elements (e.g. TiO_2, K_2O and P_2O_5) but fall within the granitic array (see also Figure 15.8).

This chapter investigates this remarkable bifurcating data array, to ultimately elucidate the petrogenesis and causes of geochemical variation of the constituent igneous rocks. Deep Creek type plutons plot sufficiently remotely from either the granitic or dioritic trends to warrant separate discussion at the end of the chapter.

16.2 The dioritic array

This trend is produced by fractional crystallisation from a parental **boninitic** magma, approximated by Chin Chap Creek hornblende diorites, resulting in a range of mafic cumulates (Chin Chap Creek/Robson Creek gabbro-diorites) and variably evolved derivative liquids (Caupaul diorites-tonalites). The details of this are now discussed.

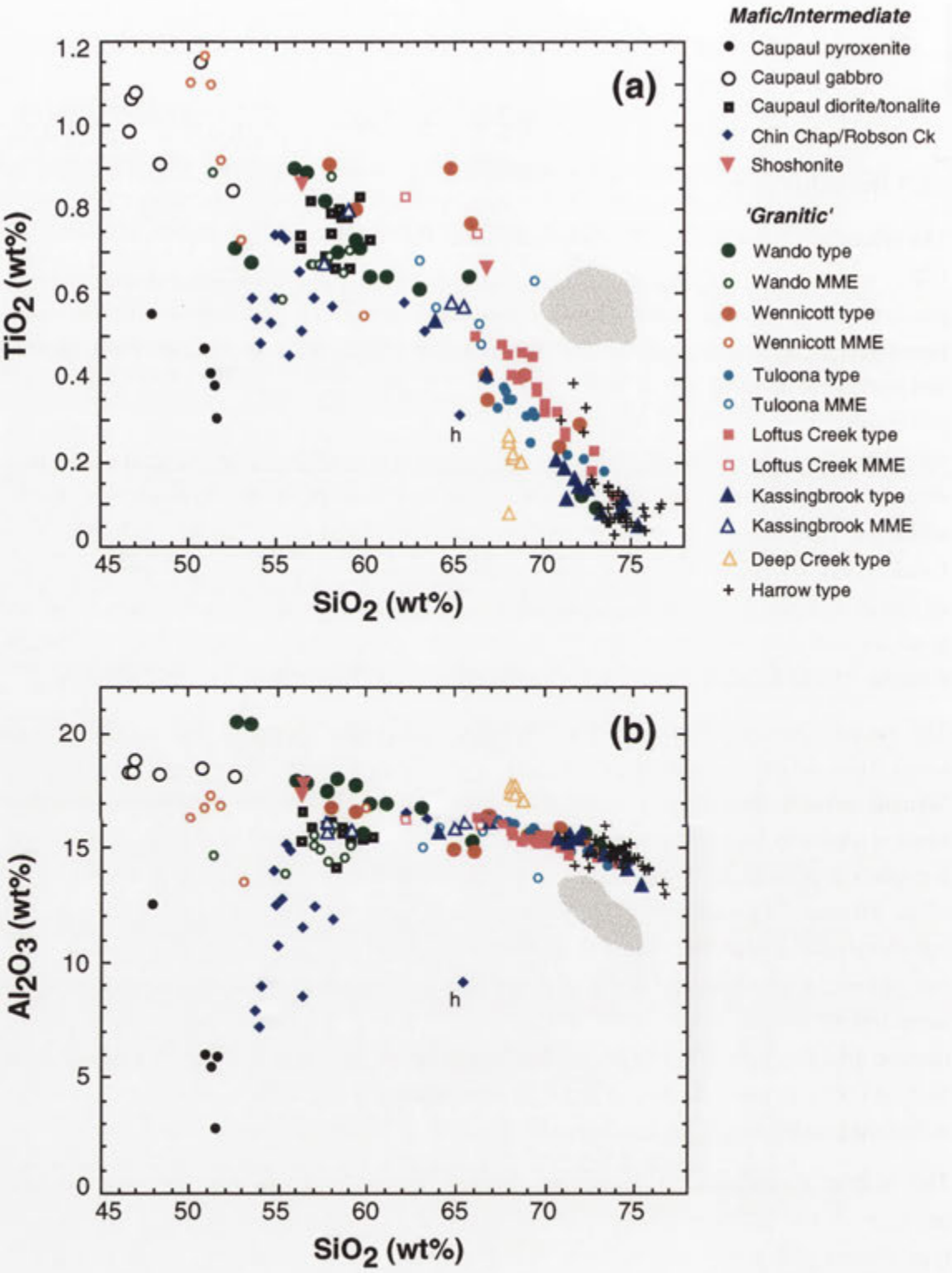

Figure 16.1 (a-b). Variation diagrams depicting ultramafic-mafic-intermediate rocks and all granitic magma types of the GRC (MME = mafic microgranular enclaves); the shaded area represents the field of metasedimentary rocks of the 'optimum fertility cluster'. The Chin Chap Creek sample labelled 'h' is hybrid gabbrodiorite **98-61**. Note that for convenience Nangkita Adamellite enclaves **97-254A** and **97-254B** are plotted as Kassingbrook type MME, and Blair Atholl Adamellite samples (at ~72% and 73% SiO_2) are plotted with the same symbols as Wando types. Harrow types occupy the same compositional field as *in situ* migmatite leucosomes. Data sources are as for Figure 15.5 and Figure 15.8.

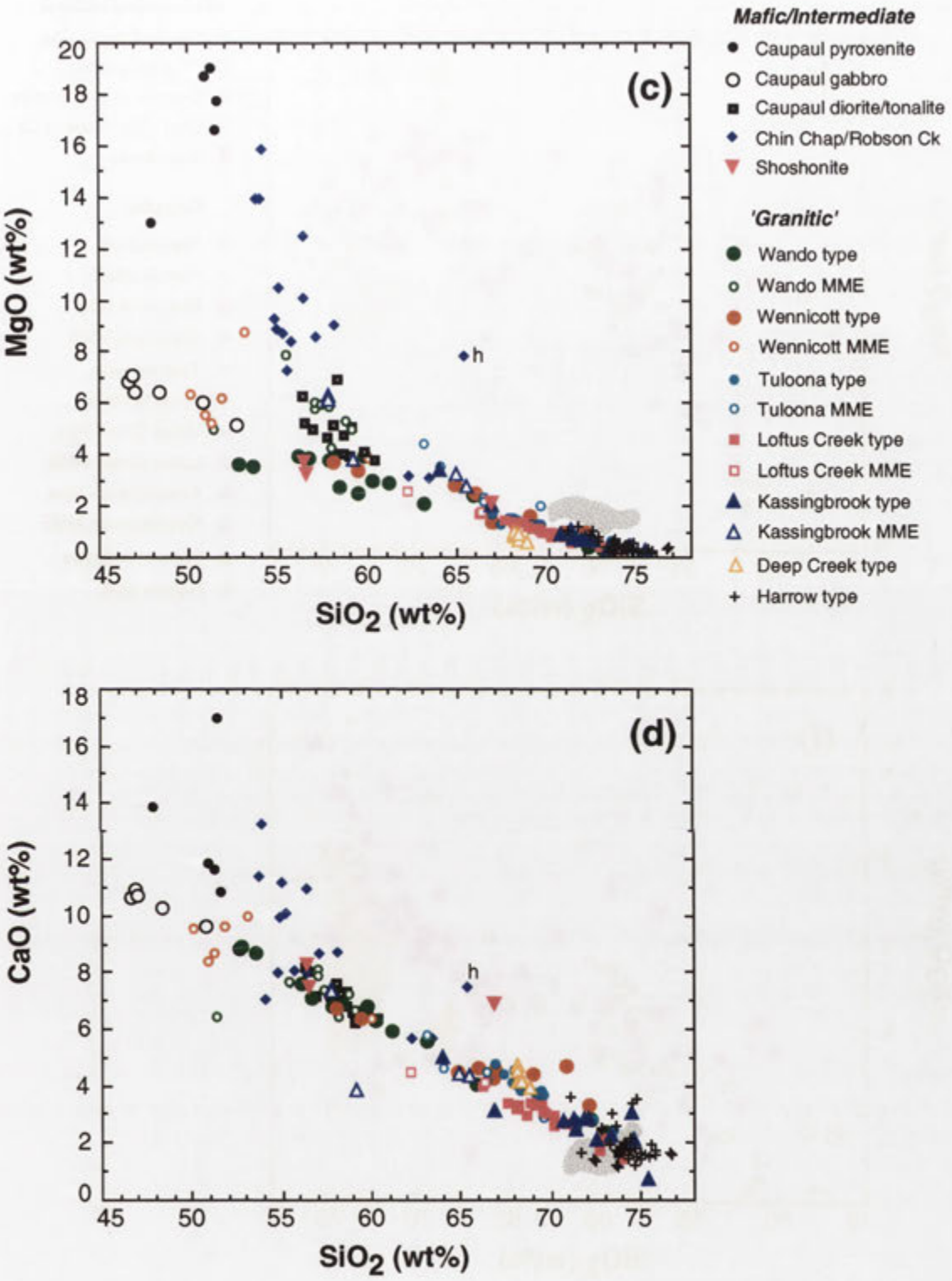

Figure 16.1 (c-d). Variation diagrams depicting ultramafic-mafic-intermediate rocks and all granitic magma types of the GRC (MME = mafic microgranular enclaves); the shaded area represents the field of metasedimentary rocks of the 'optimum fertility cluster'. The Chin Chap Creek sample labelled 'h' is hybrid gabbrodiorite 98-61. Note that for convenience Nangkita Adamellite enclaves **97-254A** and **97-254B** are plotted as Kassingbrook type MME, and Blair Atholl Adamellite samples (at ~72% and 73% SiO_2) are plotted with the same symbols as Wando types. Harrow types occupy the same compositional field as *in situ* migmatite leucosomes. Data sources are as for Figure 15.5 and Figure 15.8.

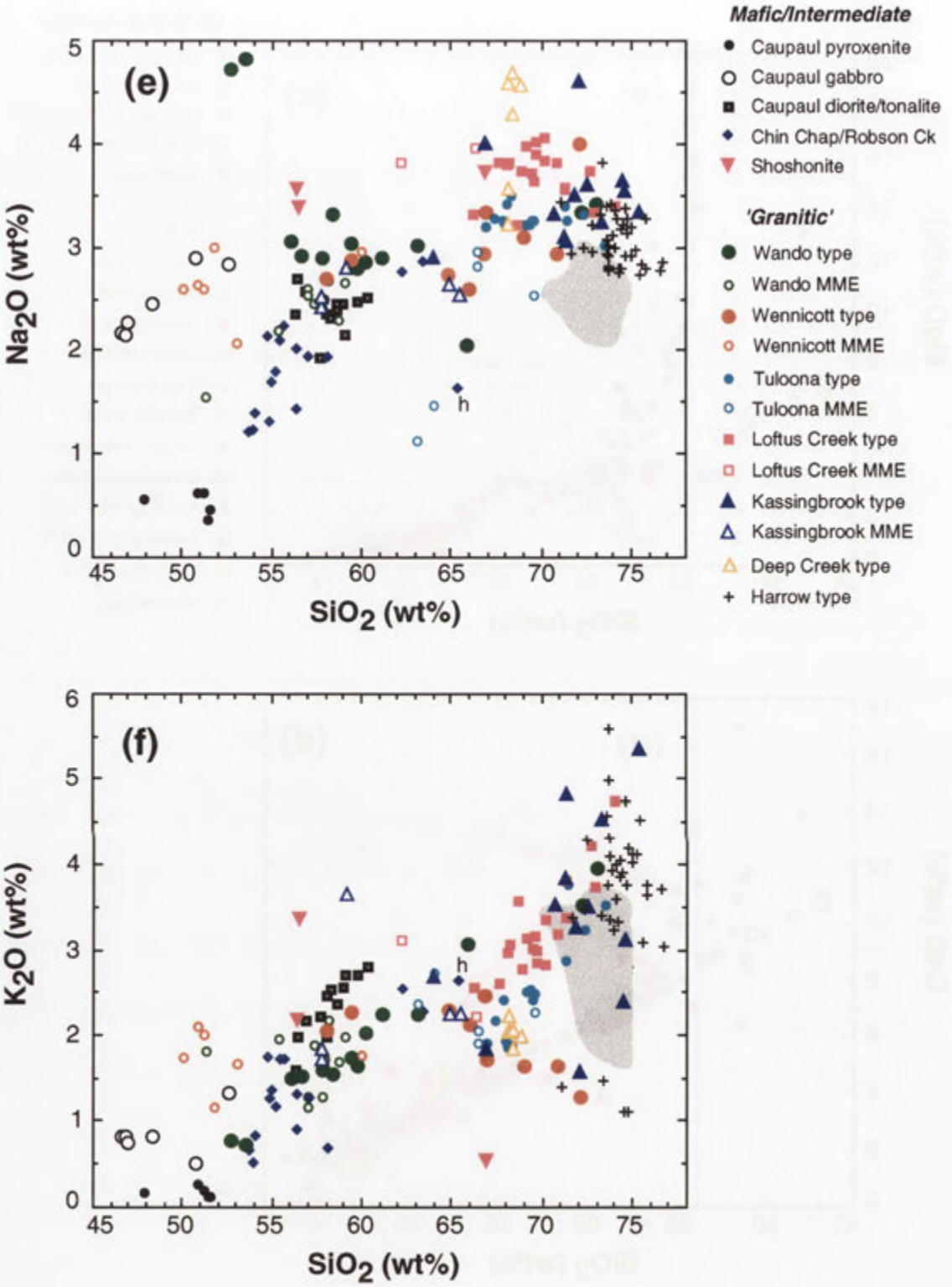

Figure 16.1 (e-f). Variation diagrams depicting ultramafic-mafic-intermediate rocks and all granitic magma types of the GRC (MME = mafic microgranular enclaves); the shaded area represents the field of metasedimentary rocks of the 'optimum fertility cluster'. The Chin Chap Creek sample labelled 'h' is hybrid gabbrodiorite 98-61. Note that for convenience Nangkita Adamellite enclaves **97-254A** and **97-254B** are plotted as Kassingbrook type MME, and Blair Atholl Adamellite samples (at ~72% and 73% SiO_2) are plotted with the same symbols as Wando types. Harrow types occupy the same compositional field as *in situ* migmatite leucosomes. Data sources are as for Figure 15.5 and Figure 15.8.

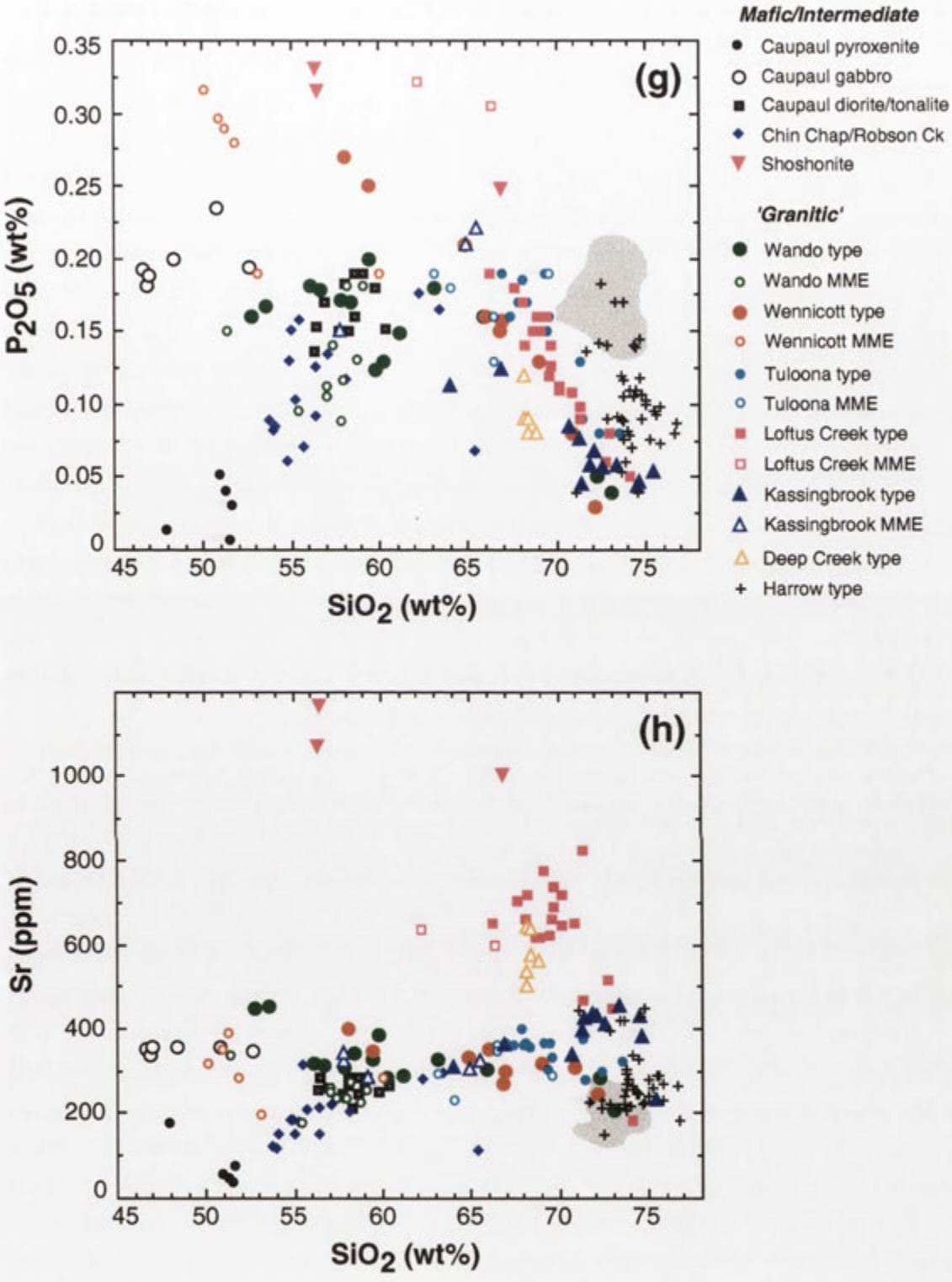

Figure 16.1 (g-h). Variation diagrams depicting ultramafic-mafic-intermediate rocks and all granitic magma types of the GRC (MME = mafic microgranular enclaves); the shaded area represents the field of metasedimentary rocks of the 'optimum fertility cluster'. The Chin Chap Creek sample labelled 'h' is hybrid gabbrodiorite 98-61. Note that for convenience Nangkita Adamellite enclaves **97-254A** and **97-254B** are plotted as Kassingbrook type MME, and Blair Atholl Adamellite samples (at ~72% and 73% SiO_2) are plotted with the same symbols as Wando types. Harrow types occupy the same compositional field as *in situ* migmatite leucosomes. Data sources are as for Figure 15.5 and Figure 15.8.

16.2.1 Petrogenesis of Chin Chap Creek/Robson Creek mafic rocks

At lower silica, the linear trends defined by hornblende gabbro-diorites and diorites of Chin Chap Creek/Robson Creek consistently project towards Caupaul hornblende pyroxenites (Figure 16.1), which are pyroxene cumulates, and ultimately to the composition of clinopyroxene (Figure 16.2). This suggests that hornblende gabbro-diorites and diorites are related through crystal accumulation-fractional crystallisation processes, predominantly controlled by clinopyroxene. Under this scenario, the most primitive samples, Chin Chap Creek hornblende gabbro-diorites with >13% MgO, represent accumulations of early precipitated clinopyroxene crystals with small amounts of trapped melt. This accords with the cumulate-like textures of these rocks and relict Mg-rich clinopyroxene phenocrysts, subsequently enveloped by hornblende at the late magmatic stage. Apart from resulting in distinctively high CaO (>10%), such that gabbro-diorites plot well above the granitic array, clinopyroxene accumulation imparts elevated Sc (to 73 ppm) and CaO/Al_2O_3 (up to 1.8), both of which exceed the range of basaltic andesite melt compositions. High Cr contents are another manifestation of clinopyroxene accumulation (Figure 16.3). Note that the most magnesian gabbro-diorite (**97-373A**) has much lower CaO than other gabbro-diorites and plots towards the orthopyroxene field (Figure 16.2b), suggesting enrichment in cumulate orthopyroxene, as well as clinopyroxene. This also accounts for the unusually low CaO/Al_2O_3 (Figure 16.3b). The existence of cumulate orthopyroxene in other gabbro-diorites (prior to replacement by amphibole) is more difficult to assess.

The steep trend away from the most mafic gabbro-diorites towards those with lower MgO, Mg#, CaO, Cr and CaO/Al_2O_3 (Figures 16.2. 16.3) reflects an increasing proportion of liquid to cumulus pyroxene, consistent with the diminishing content of blocky hornblende prisms (which are replacing pyroxene phenocrysts). Strongly increasing TiO_2, Al_2O_3, Na_2O, K_2O, P_2O_5 and Sr with increasing SiO_2 (and thus decreasing MgO) (Figure 16.1) accords with the incompatibility of these with the crystallising assemblage, and the increase in interstitial feldspar (i.e. trapped melt). Clinopyroxene preferentially accommodates Sm relative to Zr in basaltic andesite liquids (D_{Sm} ~0.16, D_{Zr} ~0.38, Fujimaki *et al.* 1984) resulting in slightly increasing Zr/Sm with decreasing Mg# and reduced crystal/liquid ratios (Figure 16.4). In the simplest scenario, total REE abundances would also increase systematically with decreasing MgO, as clinopyroxene/melt partition coefficients for the REE are less than unity in basaltic andesite liquids (see data compilation in Rollinson 1993). Furthermore, since the LREE are the most strongly excluded, the REE pattern should become progressively more fractionated as the crystal/liquid ratio decreases. That neither of these occurs is most easily reconciled by the involvement of slightly different parental liquids for gabbro-diorite samples (see below).

Rocks of the dioritic array therefore become progressively crystal-poor from gabbro-diorites to relatively felsic hornblende diorites, which approach the composition of the 'parental' liquid(s). This is consistent with the absence of relict clinopyroxene phenocrysts and lack of CaO enrichment in hornblende diorites, both of which preclude content of cumulus pyroxene. The melt-dominated nature of Chin Chap Creek hornblende diorites is confirmed by intimate syn-magmatic mingling and mixing (see below) with the Kassingbrook Granodiorite, against which

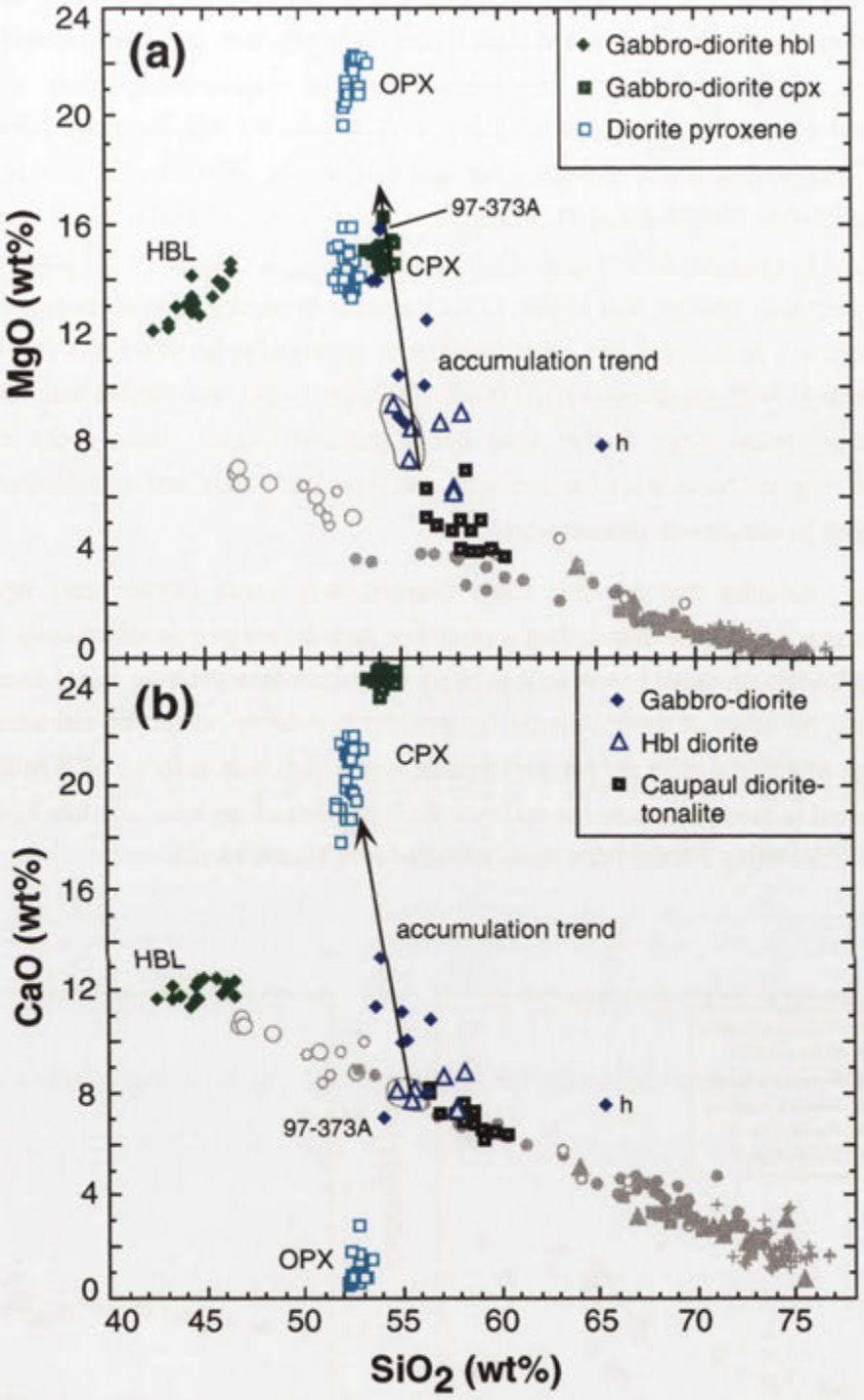

Figure 16.2. Plots of (a) MgO and (b) CaO versus silica comparing the dioritic array with the composition of hornblende, clinopyroxene and orthopyroxene from Chin Chap Creek gabbro-diorites (green symbols) and Caupaul diorites (open blue squares). Note the projection of the dioritic array towards the clinopyroxene field. The most magnesian gabbro-diorite, **97-373A**, has higher MgO than most clinopyroxene grains and plots towards the orthopyroxene field on (b), suggesting compositional control by both cumulate orthopyroxene and clinopyroxene. All gabbro-diorite and hornblende diorite samples lying above the granitic array in (b) contain an accumulation of liquidus clinopyroxene. Note that the scatter to higher silica exhibited by some samples reflects hybridisation with crustal melt (see Figure 16.5). Circled hornblende diorite samples **97-236A**, **97-236B** and **97-376** (in order of silica content) are believed to approximate the parental magma composition.

dioritic sheets and intermingled dioritic globules have liquid-liquid contacts (section 12.3.4); clearly, hornblende diorites behaved as liquids upon injection into the granodiorite due to low crystal contents. In view of this, the specific parental magma composition is probably approximated by hornblende diorites **97-236A**, **97-236B** and **97-376**, bracketed between ~55-56% SiO_2 and ~7-9% MgO, 7.6-8% CaO and CaO/Al_2O_3 ~0.5-0.6 (Figures 16.2, 16.3). Hornblende diorites **97-378-4** and **97-380** are also close to this inferred parental composition, but have slightly elevated CaO (Figure 16.2b) and CaO/Al_2O_3 (Figure 16.3b) implying minor content of cumulate phases, and higher silica contents, reflecting hybridisation with crustal melts (see below). In contrast, two other hornblende diorite samples (**97-378-3** and **97-378-5**) are more evolved, with much lower MgO (<6.3%) (Figure 16.2a), and overlap with the Caupaul diorite compositional field. Rather than being parental liquids, these rocks may have experienced incipient hornblende fractionation, accompanied by localised hybridisation with the adjacent felsic Kassingbrook Granodiorite.

Hence, it is concluded that the Chin Chap Creek/Robson Creek dioritic array represents a clinopyroxene accumulation trend from a primitive parental magma geochemically similar to hornblende diorites. In detail however, it is likely that rather than deriving solely from a single magma batch, the array of gabbro-diorite compositions probably reflects crystal accumulation from a range of slightly different parental liquids, imparting complexity in REE patterns. This is substantiated to some extent by the different REE patterns of 'parental' diorites **97-236B** and **97-376**, the latter being considerably more enriched (see Figure 14.14).

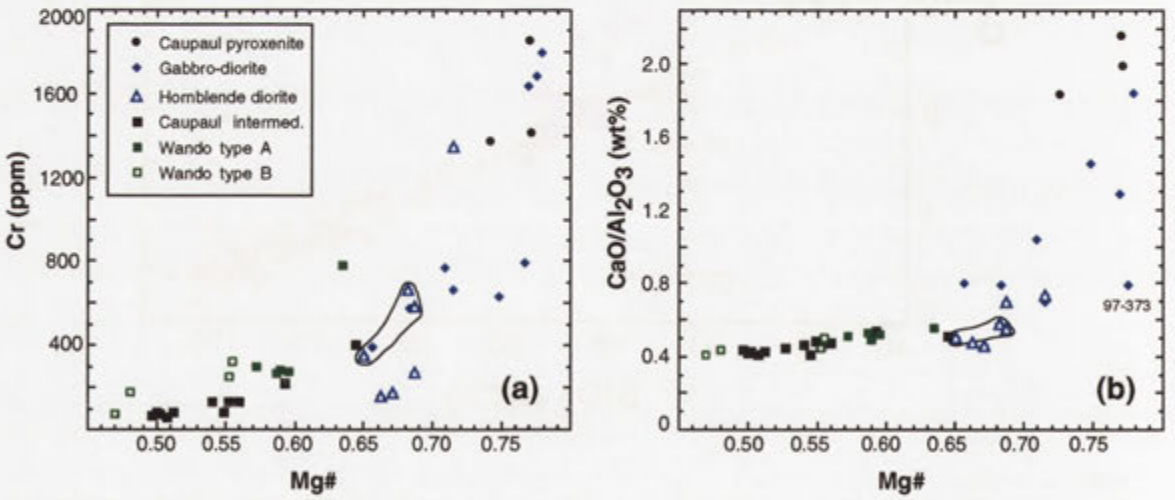

Figure 16.3. Plots of (a) Cr and (b) CaO/Al_2O_3 versus Mg# for rocks of the dioritic array and mafic microgranular enclaves (type A and type B) of Wando type plutons. Gabbro-diorite **97-373A** has very low CaO/Al_2O_3 and is orthopyroxene cumulative. Hornblende diorites **97-376**, **97-236A** and **97-236B** (in order of increasing Mg#) are circled and believed to approximate the parental magma to the dioritic array. Caupaul pyroxenites are plotted to show the Cr contents and CaO/Al_2O_3 of rocks formed by pyroxene accumulation.

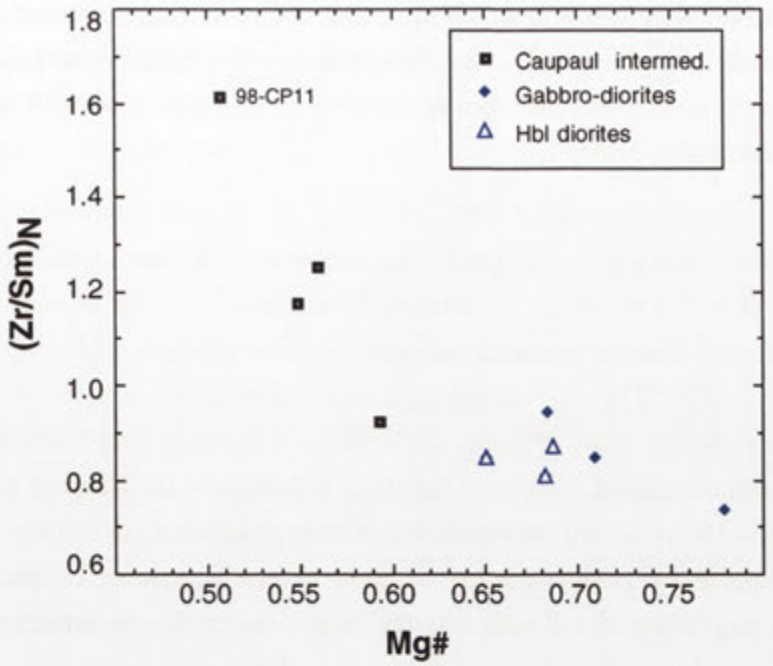

Figure 16.4. Primitive mantle-normalised (Zr/Sm) plotted against Mg# for rocks of the dioritic array (normalising values as for Figure 14.8). Ferres Creek Tonalite sample **98-CP11** is labelled separately.

16.2.2 Hybridisation with crustally-derived melt

A minor aspect of the Chin Chap Creek/Robson Creek dioritic array is that some samples are displaced to slightly higher SiO_2 contents, which imparts a non-systematic scatter parallel to the silica axis. This effect is most dramatic for sample **98-61** (labelled 'h' on Figures 16.1, 16.2), which consistently plots midway between the dioritic array and the field of *in situ* partial melts. As discussed in section 12.5.1b, this sample derives from the margin of a gabbro-diorite pod and exhibits clear field and textural evidence for extensive hybridisation with the adjacent Kassingbrook Granodiorite. Thus, **98-61** actually defines a mixing line between a crystal-rich gabbro-diorite magma and metasedimentary-derived partial melt (see Figure 16.5). Interestingly, despite the substantial chemical modification, **98-61** preserves the very high Mg# (~0.77) of pristine gabbro-diorite samples.

Given the intimate association with the enclosing Kassingbrook Granodiorite, it is likely that other hornblende diorites have also been locally hybridised, giving rise to a series of mixing lines to more silicic compositions (Figure 16.5). This could have occurred by infiltration of felsic partial melts into the mafic body, or by diffusion of silica and other components across the mafic-felsic interface (see below).

16.2.3 Implications for intermediate rocks of the Caupaul Igneous Complex

Despite the different emplacement timing, and location on the opposite side of the GRC, Caupaul diorites-tonalites consistently overlap with the most evolved portion of the Chin Chap Creek/Robson Creek data array on geochemical variation diagrams, in many cases imparting a

hyperbolic aspect to the dioritic array (Figures 16.1, 16.3 and 16.4). Links between these rocks are strengthened by the shared high-Mg, high-Cr character and similar chondrite-normalised REE patterns, Caupaul diorites-tonalites having systematically higher total REE abundances (see Figure 14.14 and section 14.3).

These features are therefore consistent with derivation of Caupaul intermediate rocks by fractional crystallisation from a magmatic progenitor similar to Chin Chap Creek/Robson Creek hornblende diorites (but with lower a_{H_2O} to account for preservation of the primary anhydrous mineralogy), such that the Caupaul sequence becomes progressively more evolved from diorites to the Ferres Creek Tonalite. The most magnesian Caupaul diorites conform to the Chin Chap Creek/Robson Creek dioritic array (Figures 16.1, 16.3), suggesting that fractionation was initially clinopyroxene-dominated. However, the slight inflection in the Caupaul trend below ~6% MgO (see Figure 16.2a) reflects the separation of other phases, such as orthopyroxene and plagioclase, corroborated by the occurrence of these as phenocrysts in Caupaul diorites. Significant liquidus plagioclase crystallisation at this stage is responsible for inflection in Al_2O_3

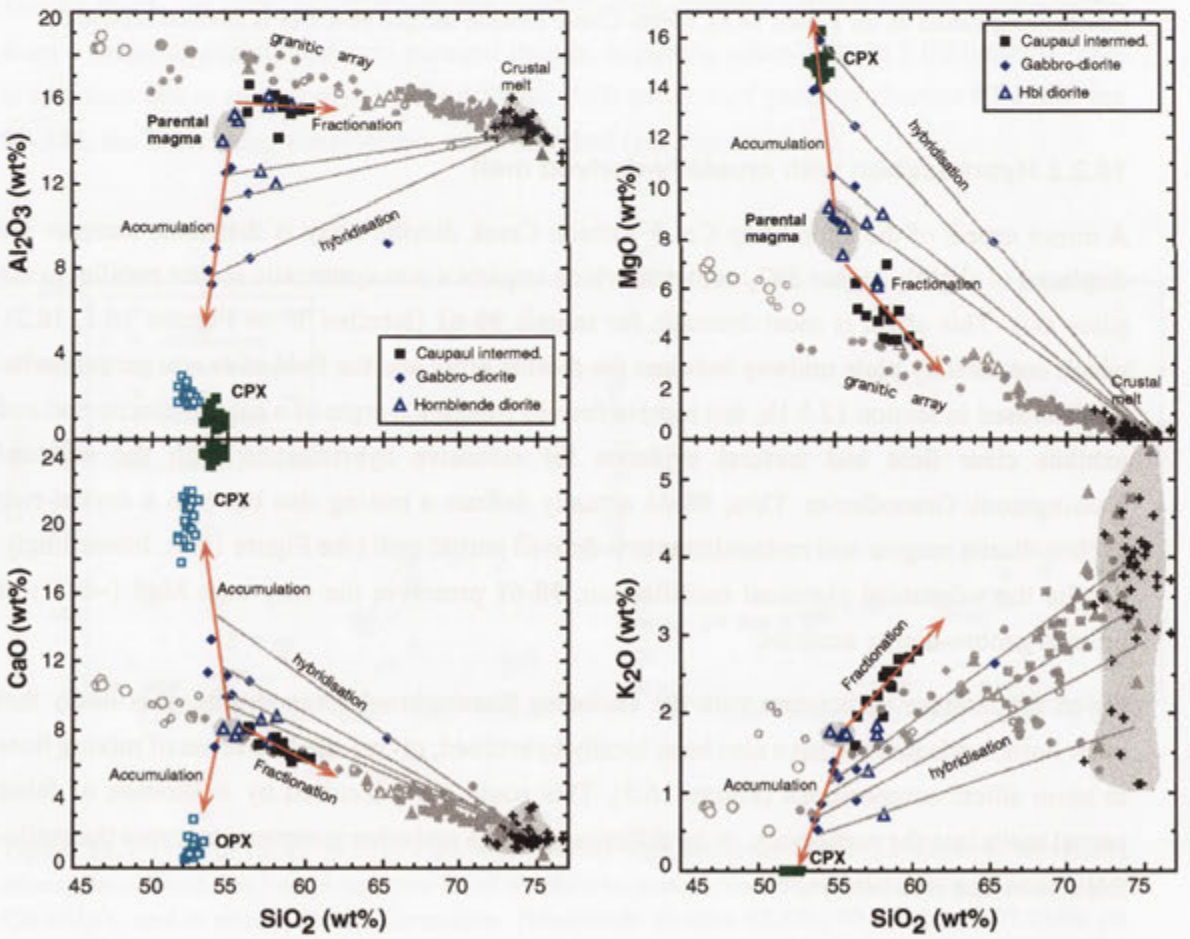

Figure 16.5. Selected variation diagrams summarising the formation of the dioritic array from a parental boninite magma. Annotated vectors indicate the main petrogenetic processes producing the observed compositional spectrum. Crustal hybridisation lines (grey) are approximate and for illustrative purposes only. Pyroxene symbols are as for Figure 16.2.

and Sr trends (Figures 16.1b, 16.1h). Note, however, that Eu/Eu* increases progressively with decreasing MgO (section 14.3.1c), suggesting that the bulk distribution coefficient for Eu with the fractionating assemblage remained <1.

Production of the Caupaul diorite-tonalite trends by fractionation also accords with- (1) decreasing Mg# of pyroxenes from diorites **11904**, **98-CP1** and **98-CP7** (see Figure 14.1), correlating with decrease in bulk rock Mg#, (2) systematic increase in REE abundance and $(La/Yb)_N$ from the most mafic to the most felsic sample (Figure 14.9), the regularity of which indicates derivation of all Caupaul intermediate rocks from a single magmatic parent, and (3) exponential increase in $(Zr/Sm)_N$ with decreasing Mg#, reflecting the incompatibility of Zr relative to Sm during differentiation (Figure 16.4). The latter effect is magnified for Caupaul intermediate rocks, as the compatibility difference between Zr and Sm in clinopyroxene increases with silica (Fujimaki *et al.* 1984). The trend of steeply increasing K_2O and P_2O_5 from diorites to Ferres Creek Tonalite shows that these elements behaved incompatibly throughout the fractionation sequence. Appearance of hornblende in Ferres Creek Tonalite samples possibly manifests increasing magmatic water activity during differentiation, which (with elevated K_2O contents) also promoted crystallisation of biotite. Precipitation of silica-poor hydrous phases therefore favoured crystallisation of abundant quartz and suppressed alkali feldspar (as K_2O was accommodated by biotite), accounting for the profound mineralogical differences from Caupaul diorites, despite similar whole rock geochemistry (Kemp *et al.* 2001). Hornblende fractionates Sm from Zr more strongly than clinopyroxene (Fujimaki *et al.* 1984; Pearce *et al.* 1992; see below), as Zr is more incompatible than Sm by a factor of ~5 between amphibole and tonalitic melts (Klein *et al.* 1997). This may contribute towards the much higher $(Zr/Sm)_N$ of Ferres Creek Tonalite **98-CP11** compared to the pyroxene-bearing Caupaul diorites.

16.2.4 Nature of the primary magma

Hence, Chin Chap Creek/Robson Creek gabbro-diorites and Caupaul diorites-tonalites are considered to have evolved from a broadly similar magmatic progenitor by crystal accumulation and crystal fractionation processes respectively. This parental high-Mg diorite composition (hereafter 'HMD'), approximated by hornblende diorites, lies close to the junction between the accumulation-fractionation trends on variation diagrams (Figure 16.5) and, at ~55-56% SiO_2 and 7-9% MgO, is characterised by elevated Mg# (~0.65-0.70) and Cr (>300 ppm), but low Ti (<0.7%). It is emphasised that this is must be a primary *liquid* (rather than cumulate) composition, given the clearly melt-dominated nature of hornblende diorites (section 16.2.1). The distinctive chemical features of HMD are most unlike Caupaul gabbros, but diagnostic of the boninite magma series[1], an unusual and diverse group of Mg-rich, mantle-derived intermediate lavas erupted in certain intra-oceanic and continental arc systems (Table 16.1, see review by Crawford *et al.* 1989). The late plagioclase crystallisation of hornblende diorites is also typical of boninitic lavas, where plagioclase is confined to the groundmass, at least in relatively unevolved varieties (Crawford *et al.* 1989). This reflects high magmatic water activity.

[1] The boninite magma series encompasses rocks with >53% SiO_2 and Mg# >0.6 following Crawford *et al.* (1989).

Specifically, HMD closely resembles the type 2 low-Ca 'alkaline' boninite series of Crawford *et al.* (1989), which include lavas of the Setouchi Volcanic Belt (SW Japan) and Baja California (Mexico). These have low CaO/Al_2O_3 (<0.6), generally less than 10% MgO, and distinctly higher total alkali contents than other boninite suites ($Na_2O+K_2O>3\%$) (Crawford *et al.* 1989) (Table 16.1 and Figure 16.6). The resemblance is most striking with the Setouchi lavas, which have the same LREE enrichment as HMD and virtually identical normalised multi-element

Location	*GRC*	*GRC*	*Setouchi Belt, Japan*	*Setouchi Belt, Japan*	*Mariana forearc*	*Cape Vogel, PNG*	*Tonga Trench*	*Bonin Islands*
sample	**97-236B**	**97-377**	**SH-7201**	**SD-261**	**50-23**	**52-1A**	**7-18**	**1**
SiO_2	54.76	56.40	55.46	55.52	54.75	54.41	54.72	56.20
TiO_2	0.45	0.65	0.70	0.65	0.26	0.21	0.45	0.23
Al_2O_3	13.92	11.50	15.54	15.55	13.28	10.93	10.90	10.57
Fe_2O_3t	8.49	7.95	6.71	6.92	8.31	9.22	8.65	8.87
MnO	0.16	0.15	0.13	0.17	0.13	0.17	-	0.16
MgO	9.25	10.06	9.33	7.21	10.72	10.65	12.97	11.19
CaO	7.98	7.98	6.94	7.04	8.11	7.98	9.65	7.44
Na_2O	2.13	2.00	2.90	2.84	1.50	1.01	1.52	1.54
K_2O	1.74	1.29	1.63	2.25	0.91	0.41	0.71	0.40
P_2O_5	0.06	0.12	0.16	0.17	0.05	0.03	0.07	0.02
LOI	1.77	1.77		1.96	3.03	5.44	1.69	3.95
TOTAL	99.69	99.83	99.50	100.28	100.47	99.69	101.33	99.85
Mg#	0.68	0.72	0.73	0.67	0.71	0.69	0.75	0.71
Ca/Al	0.57	0.69	0.45	0.45	0.61	0.73	0.91	0.70
Sc	35	47		22	30	37	44	38
V	181	171			164	203	223	164
Cr	660	658		342	548	510	760	695
Ni	164	122	132	148	184	134	189	194
Rb	67	57	61	114		8	12	9
Sr	183	210	245	267	90	83	348	61
Y	15	18	16	15	10	8	7	5
Zr	45	72	107	80	50	25	53	20
Nb	3	4	8	5	4	1	8	1
Ba	245	254	288	195		28	230	30
La	7.4	6.4		9.2		2	16	0.8
Ce	15.4	18		21.6		4	38	1.8
Th	2.9	3.7	4.5	4.8		0.3		0.1

Table 16.1. Comparison between GRC high-Mg diorites and primitive boninites from type localities. GRC sample **97-236B** is an inferred primary liquid composition, whereas sample **97-377** is liquid-rich, but also contains sparse blocky hornblende prisms (~3%) that are interpreted to be replacing early-formed pyroxene phenocrysts. The Setouchi Volcanic Belt samples are from Shimoda *et al.* (1998) (REE in SD-261 are quoted in Tatsumi & Ishizaka 1982), the Marianas sample is from Bloomer & Hawkins (1987), the Cape Vogel (Papua New Guinea, PNG) and Bonin Islands boninites are from Cameron *et al.* (1983) and the Tonga Trench boninite analysis is quoted in Falloon *et al.* (1989).

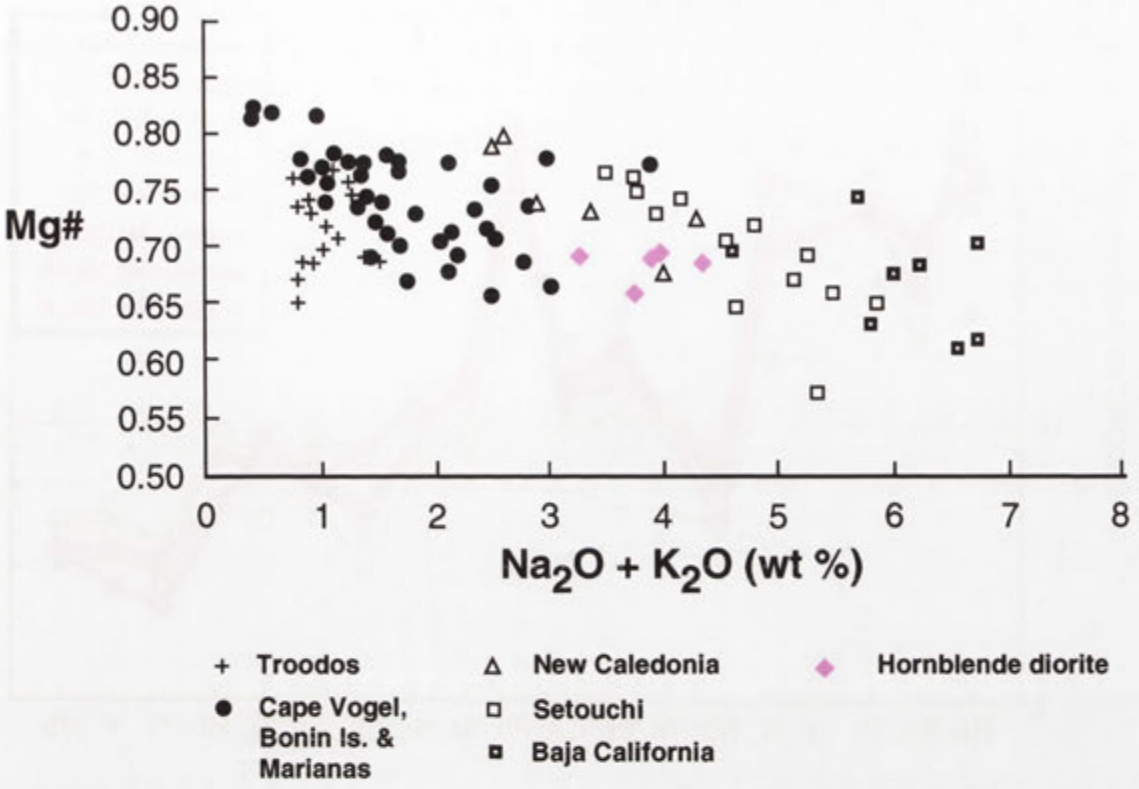

Figure 16.6. Comparison between hornblende diorites of the GRC (pink) and the reference boninite suites of Crawford *et al.* (1989) (modified from Crawford *et al.* 1989).

patterns (Figure 16.7). Furthermore, hydrous melting experiments have shown that Setouchi boninite magmas would be in equilibrium with mantle peridotite at liquidus temperatures of 1100-1150°C (Tatsumi 1981, 1982), which is compatible with the pyroxene equilibration temperatures yielded by Caupaul diorites (~1100°C, section 14.2.1).

Although models for boninite petrogenesis are complex, the consensus is that they are only readily formed in subduction settings, with unusually high temperatures and water-rich fluid being key ingredients (see Crawford *et al.* 1989). This scenario, and its geotectonic implications for the GRC, is elaborated in the next chapter.

16.3 The granitic data array

While there are many petrogenetic mechanisms for the generation of granitic rocks (section 1.3), it will be demonstrated below that the metaluminous to weakly peraluminous GRC granitic types result from mixing between a crustally-derived 'minimum melt' at source and various mafic, arc-derived magmas; this is summarised by Figure 16.8. In some cases the mixing system has been blurred by subsequent fractional crystallisation. Remarkably, both felsic (migmatite leucosomes) and mafic (variably high-Al gabbro, boninite and shoshonite) end-members of the different magma types are identified in outcrop, obviating any requirement for unexposed components. The scenario for each granitic type, and enclaves therein, is investigated separately.

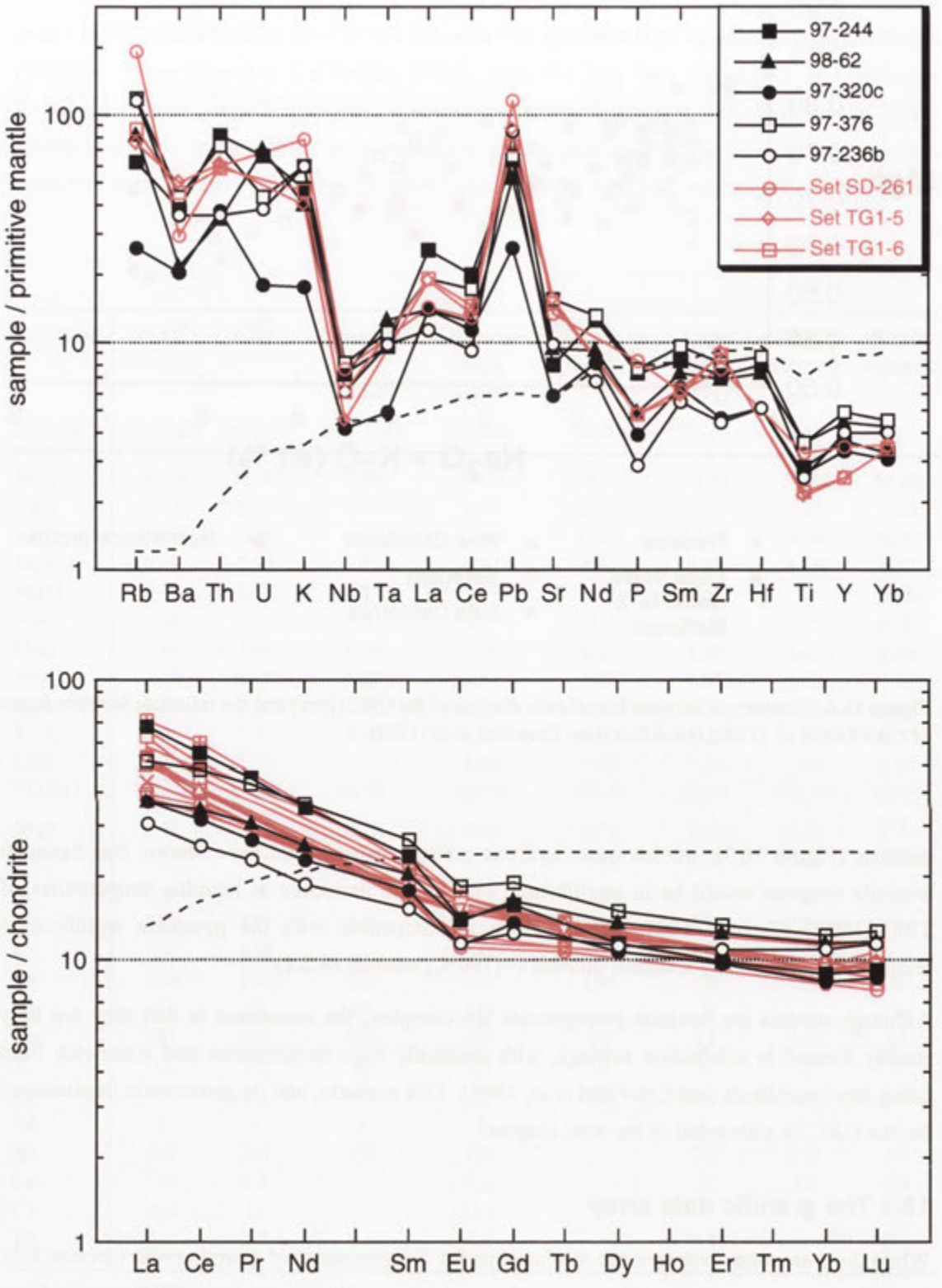

Figure 16.7. Comparison between hornblende gabbro-diorites (filled symbols) and hornblende diorites (open symbols) of Chin Chap Creek/Robson Creek with boninites from the Setouchi Volcanic Belt, SW Japanese arc (data from Tatsumi & Ishizaka 1982 and Shimoda *et al.* 1998). Normalising values are as for Figures 14.8 and 14.9. The average N-MORB of Sun & McDonough (1989) is also plotted (dashed line).

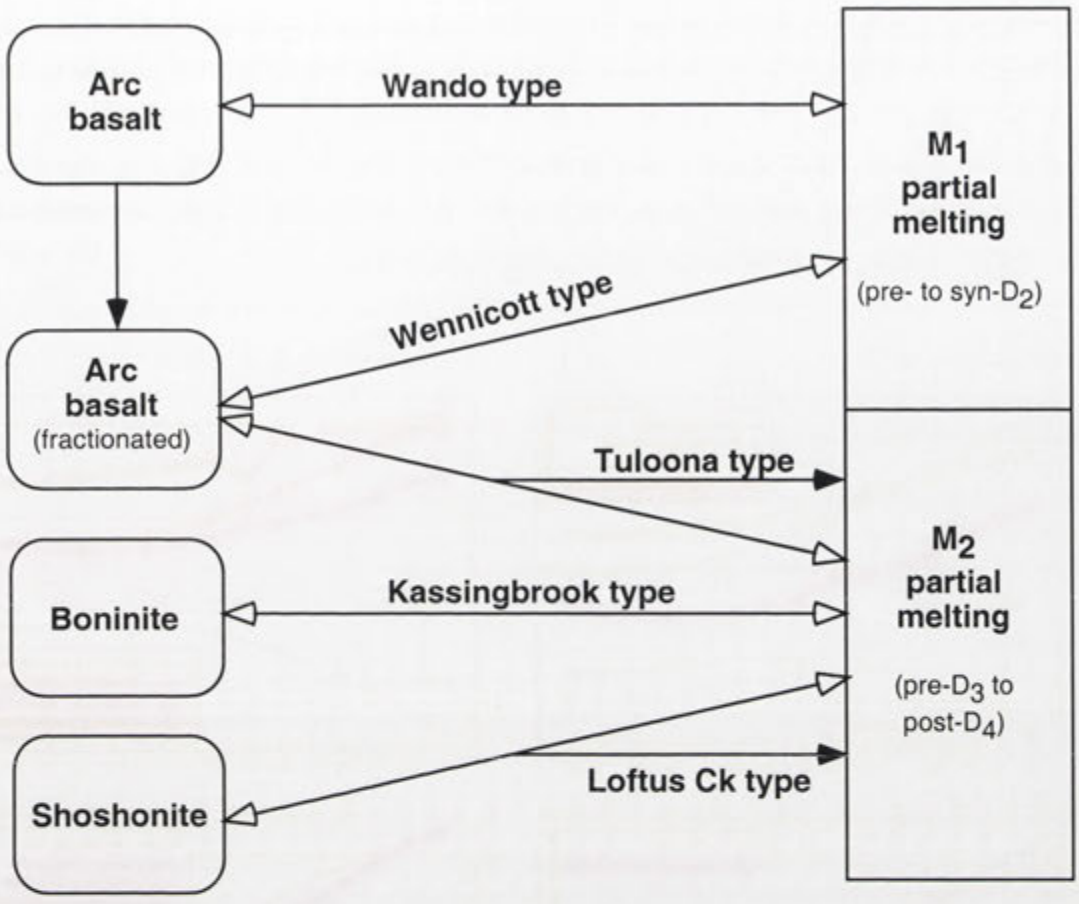

Figure 16.8. Synoptic flow chart summarising the formation of the various granitic types of the GRC. Open arrows denote mixing between arc-related magmas and *in situ* partial melts, whereas filled arrows represent a fractional crystallisation trend.

16.4 Wando types

16.4.1 Petrogenesis of Wando type rocks

Assuming consanguinity, the linear geochemical variation of Wando type rocks may be attributed to either fractional crystallisation, restite unmixing or magma mixing. Elbow Creek diorite **98-124** is probably plagioclase accumulative (section 15.3.1) and therefore not considered further.

(a) Fractional crystallisation

This holds that Wando type rocks derived by sequential fractional crystallisation from a more primitive parent lithology, most plausibly a Caupaul gabbro, as these plot at the lower silica extrapolation of the Wando type trend. Evolution to lower TiO_2, CaO, MgO and Fe_2O_3t requires a mafic fractionating phase, such as clinopyroxene, hornblende or Fe-Ti oxide, whereas decreasing Al_2O_3 with silica is only reconciled by separation of feldspars. However, substantial plagioclase fractionation from Wando type magmas cannot be reconciled with the flat Sr trend against SiO_2 (Figure 16.1h) and is virtually precluded by the smaller negative Eu anomaly in the

more felsic Wando type sample (Figure 15.7). Furthermore, since pyroxenes and hornblende have $D_{REE}<1$ in basaltic liquids, fractionation of these phases from Caupaul gabbros would result in elevated total REE contents, when in fact dioritic dyke **97-206F** actually has systematically lower REE contents than gabbro **98-CP6** (Figure 16.9a). Finally, fractional crystallisation is a closed system process, and therefore this mechanism by itself cannot explain the pronounced isotopic variation of Wando type granitic rocks.

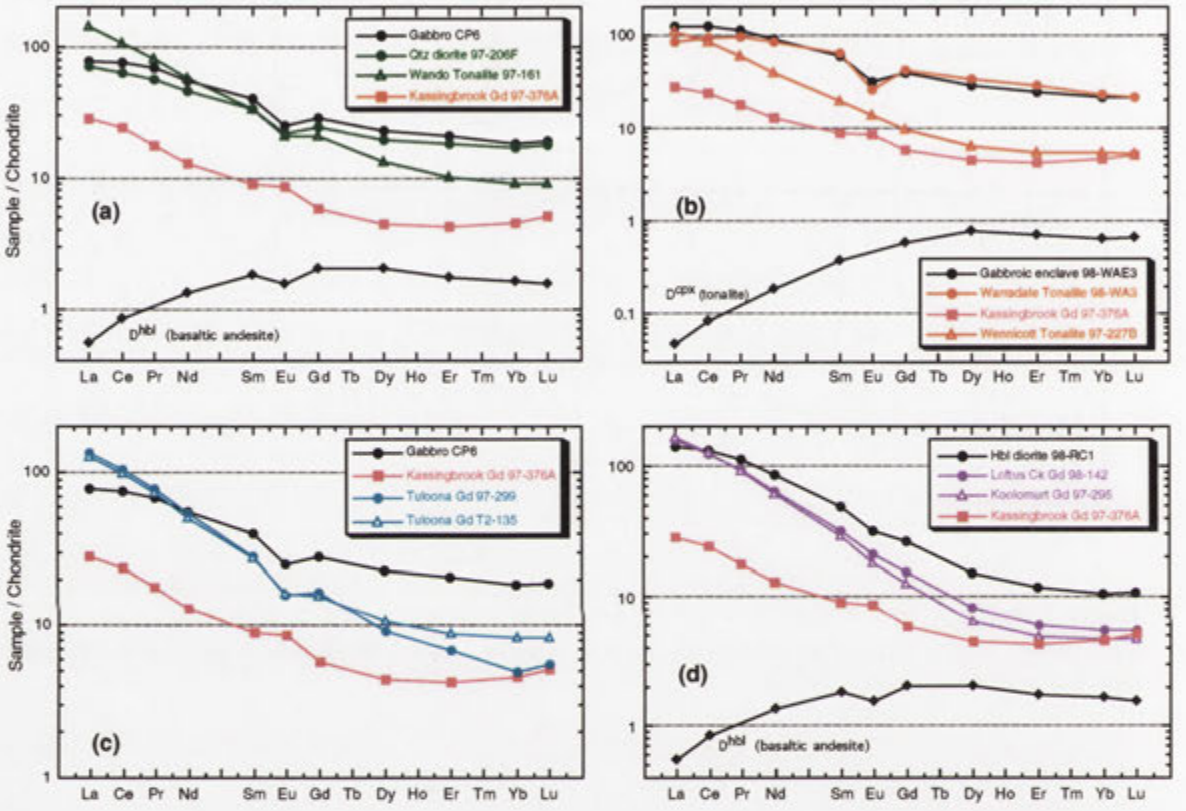

Figure 16.9. Chondrite-normalised REE plots for the different granitic magma types and their inferred end-members (normalising values after Anders & Grevesse 1989). (a) Wando types, (b) Wennicott types (c) Tuloona types and (d) Loftus Creek types. The partition coefficients for the REE between hornblende and basaltic andesite melt (a and d) and clinopyroxene and tonalitic melt (b) are also plotted (all values from Fujimaki *et al.* 1984).

(b) Restite unmixing

Under this scenario, Wando types comprise mixtures of partial melt and restite, the proportion of the latter decreasing from the most mafic to the most felsic rocks, which are therefore relatively melt-rich. However, there are serious deficiencies in the application of this model to Wando types. Firstly, as with fractional crystallisation, restite separation is a closed system process and is thus similarly incapable of producing the isotopic variation of Wando type rocks. Secondly, the relict igneous textures of mafic microgranular enclaves suggest a purely magmatic

origin (section 10.2.1b), and are incompatible with incorporation as solid fragments of unmelted restite. Moreover, field relationships indicate that most enclaves were actually introduced by mingling with a contemporaneous mafic magma (see below). Thirdly, there is scant petrographic evidence for the presence of restite in Wando type magmas. Chappell *et al.* (1987) state that 'the presence of rather uniform calcic plagioclase cores is the best single line of evidence for the presence of a restitic component' (p1128). Restitic plagioclase cores are also supposedly partially resorbed or corroded, and of similar composition in all members of a granitic suite (Chappell *et al.* 1987). However, plagioclase cores of Wando type rocks are invariably euhedral, exhibit a wide range of compositions within a single sample, and become markedly more calcic in more mafic rocks (Figure 15.1), all of which are inconsistent with a restitic affinity. Furthermore, although present, the aggregates of mafic minerals in Wando types that are elsewhere interpreted as restite (Chappell *et al.* 1987) are clearly derived by disaggregation of microgranular enclaves (section 10.2.3b).

(c) Magma mixing

The most critical aspect of the Wando type trend is that it extrapolates to Caupaul high-Al gabbros at lower silica (particularly gabbronorite **98-CP129**) and Harrow type plutons at higher silica, (Figure 16.1). This suggests that the Wando type geochemical spectrum formed by variable mixing between mantle-derived gabbro of similar composition to **98-CP129** and a leucocratic, restite-poor partial melt sourced from the local metasedimentary sequence. Specifically, at higher silica the Wando type trend consistently projects to samples of the Blair Atholl Adamellite, suggesting that, despite the large range of crustal melt compositions (especially for K_2O), this Harrow type pluton approximates the felsic end-member in the mixing system (Figure 16.10). This is compatible with the geographical proximity of this pluton to Wando type bodies, and the shared pre- to syn-D_2 emplacement timing. Note, however, that the Blair Atholl Adamellite has higher TiO_2, (Fe_2O_3t+MgO) and CaO, but lower SiO_2 than other GRC garnet adamellites (section 9.9.3) and is therefore displaced along the mixing line towards Caupaul gabbros. This indicates that the Blair Atholl Adamellite has also been modified by interaction with basic magma, as suggested by contained igneous-textured microgranular enclaves. Hence, the purely metasedimentary-derived felsic end-member for the Wando magma type actually lies at a slightly higher silica projection of the mixing trend.

Finally, although approximated by Caupaul gabbro and Blair Atholl Adamellite, the 'noisy' Na_2O and P_2O_5 mixing trends defined by Wando types probably reflect subtle variations in the end-member compositions. Such scatter is most likely to be imparted by variation in the felsic component, given the large compositional range of crustal melts for these elements compared to gabbros (Figure 16.10).

16.4.2 Isotopic and REE constraints

Although a simple mixing model for Wando type rocks satisfies most major and trace element criteria, isotopic and REE evidence require the operation of additional processes and/or end-members in the mixing system. Firstly, Caupaul gabbros are actually more isotopically evolved

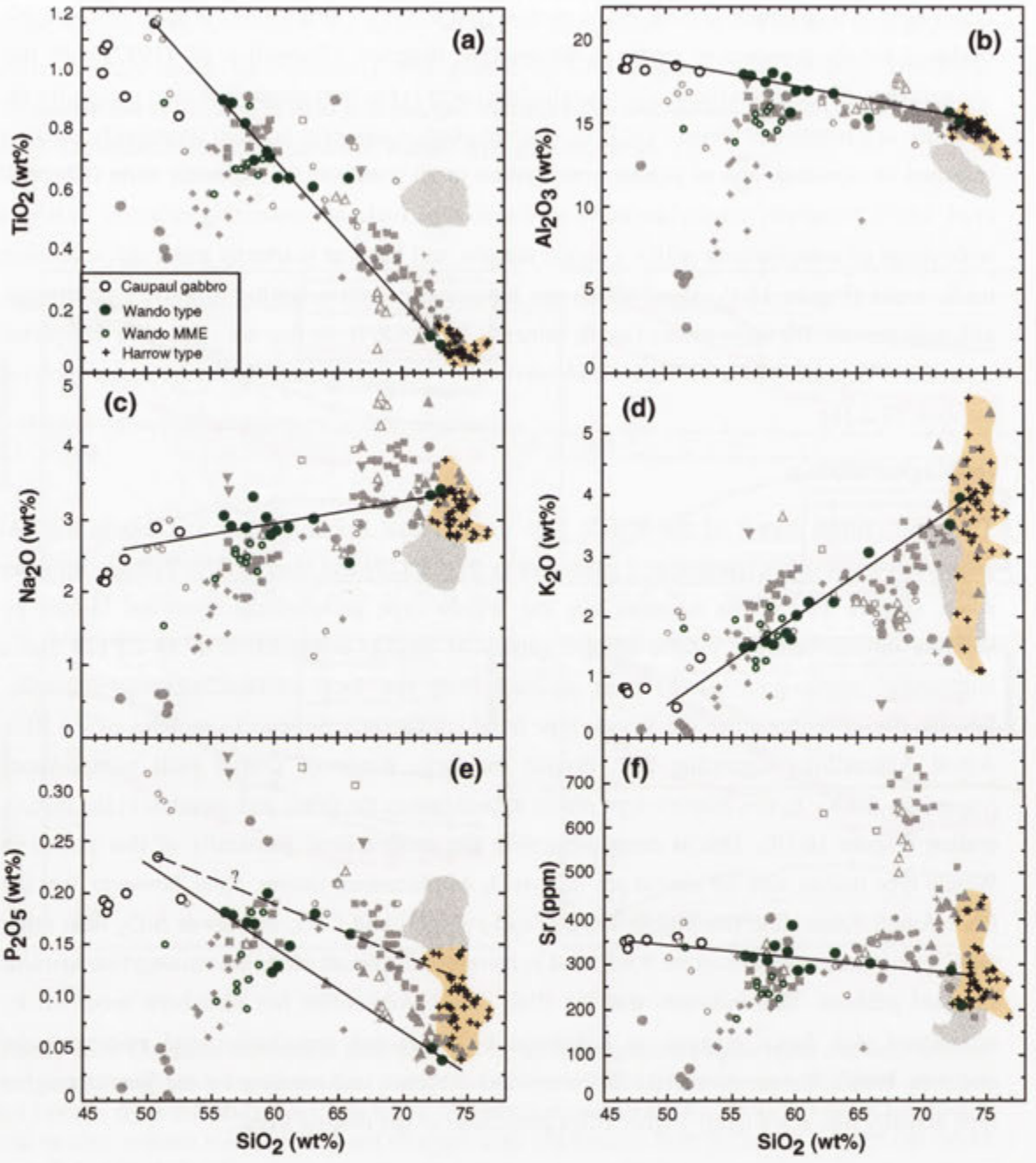

Figure 16.10. Inferred mixing lines between high-Al Caupaul gabbro and metasedimentary-derived partial melt (orange shaded field, defined by felsic Harrow and Kassingbrook types) producing the spectrum of Wando type compositions. The specific felsic end-member, Blair Atholl Adamellite samples at 72% and 73% SiO_2, have the same symbols as Wando types for distinction. The plagioclase-cumulative Elbow Creek diorite sample (**98-124**) is not plotted. The scatter for P_2O_5 could reflect variation in the end-member compositions, with another possible mixing line shown (dashed). The grey shaded area represents that of fertile metasedimentary rocks.

than the most mafic Wando type samples at 500 Ma (Figure 16.11). Thus, Caupaul gabbro samples analysed by this study cannot be the specific end-members in the mixing system. However, these rocks are consistent with the ε_{Nd}-initial $^{87}Sr/^{86}Sr$ isotopic array, and it is therefore possible that Caupaul gabbros have been driven to more radiogenic compositions than their parental magmas by interaction with isotopically-evolved crustal materials. Assimilation of metasedimentary rock and/or contamination by crustally-derived melts are possibilities, the latter supported by geochemical trends (see below). That some gabbros contain orthopyroxene is also consistent with crustal contamination. This is because introduction of Al_2O_3 favours plagioclase crystallisation, which, removing CaO, induces precipitation of Ca-poor orthopyroxene at the expense of clinopyroxene. It is also possible that part of the evolved isotopic signature of Caupaul gabbros reflects subduction-related processes during magma genesis- this aspect is explored in section 17.2.2c.

Secondly, although the REE abundances in quartz diorite **97-206F** are consistent with mixing between a Caupaul gabbro and crustal melt (Figure 16.9a), Wando Tonalite **97-161** cannot be modelled in this fashion. This is because the REE pattern of the tonalite is much more fractionated than that of the quartz diorite, such that the LREE contents exceed those of the inferred mafic end-member (Figure 16.9a). A similar effect is evident for all other granitic magma types (see below), and is most easily reconciled by removal of a phase that accommodates HREE but excludes LREE. The preferred candidates in metaluminous rocks are accessory zircon and apatite, which may contain up to 60% of the HREE budget (Bea 1996a); crystallisation of minute amounts of these minerals can therefore drastically alter REE abundances in coexisting melts. However, apart from difficulties with efficiently separating small crystals from viscous melt (Bea 1996a), Wando Tonalite **97-161** has higher Zr than quartz diorite **97-206F** and identical P_2O_5 content (Appendix G), which excludes zircon or apatite separation. The only other mineral capable of fractionating REE patterns is calcic hornblende, which can host ~30-35% of the total HREE (Bea 1996a), and with which La and Ce are incompatible (i.e. partition coefficients <1 in tonalitic magmas, Klein *et al.* 1997). This implies that the Wando Tonalite has either experienced incipient hornblende fractionation or contains a heterogeneous distribution of hornblende crystals. More work is required to investigate this.

16.4.3 Implications for Caupaul high-Al gabbros

Caupaul gabbros also define linear trends on variation diagrams that are continuous with the granitic data array (Figure 16.1). These trends to more felsic compositions cannot be wholly caused by either fractional crystallisation or assimilation of metasedimentary rocks, as both of these would result in elevated total REE and larger negative Eu anomalies (section 14.4.2), when in fact the higher silica gabbros have lower REE abundances and smaller Eu/Eu* (section 14.3.1a). Alternatively, the data are consistent with evolution from the most mafic (**98-CP6**) to the most felsic (**98-CP3**) hornblende gabbro by incorporation of progressively larger amounts of REE-poor, crustally-derived melt, of similar composition to the felsic end-member in the Wando type mixing system. Such contamination may have occurred during passage of the gabbroic magma through partially melted metasedimentary rocks at depth, and may be partly responsible

for the evolved isotopic composition of the gabbros. This means that Wando type granitic rocks and Caupaul gabbros may be considered as a coupled petrogenetic system.

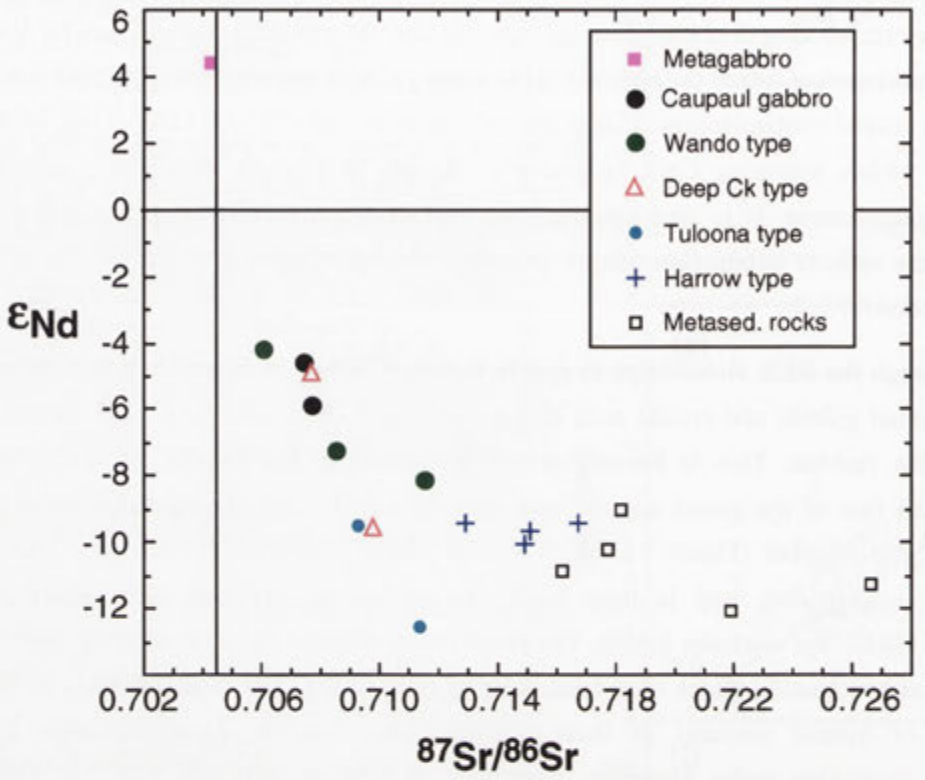

Figure 16.11. Sr and Nd isotopic composition of rocks of the GRC calculated at 500 Ma (the full isotopic analyses are quoted in Appendix A). The metagabbro, a MORB-like sample from Wando Vale, is from Turner *et al.* (1993a), along with data for Wando and Deep Creek type granitic rocks. Harrow type and metasedimentary rock samples are as quoted for Figure 9.12.

16.4.4 Origin of mafic microgranular enclaves

(a) General model and the formation of type C enclaves

The problematic origin of microgranular enclaves in granitic plutons has been reviewed by Barbarin & Didier (1991) and is discussed in Chapter 12. However, the relict igneous textures characterising microgranular enclaves of Wando type rocks, and those of other GRC plutons, are only consistent with formation by crystallisation from a magma (section 12.5.2). Enclaves may therefore represent- (a) cumulates or aggregates of early formed crystals (e.g. Vernon 1984; Dodge & Kistler 1990), (b) fragments of a chilled marginal facies, or (c) globules of hybridised or unmodified mafic magma (Barbarin 1990). The first hypothesis is inconsistent with the fine grainsize and elongate apatite needles in all Wando type microgranular enclaves, suggesting rapid crystallisation during undercooling (section 12.5.2). The second option is negated by the total absence of chilled margins at the contacts of Wando type bodies or any other granitic pluton in the GRC. Furthermore, margins

of type C enclave **97-159E** are moulded around plagioclase phenocrysts in the host tonalite, suggesting that this body was incorporated in a partially liquid state.

Regarding the last possibility, it is significant that type C microgranular enclaves plot along the Caupaul gabbro-Wando type mixing line for some elements on variation diagrams, suggesting that they have affinity with this system (Figure 15.5). However, they plot well below the trend for Al_2O_3, Na_2O and CaO, but above the trend for K_2O, with enclave **97-159E** also having lower SiO_2 than the gabbros. Although some of this scatter may reflect the small (and possibly unrepresentative) sample size, and the significant hydrothermal alteration of enclave **97-167**, it is unlikely that the type C enclaves exemplify simple Caupaul gabbro-crustal melt mixtures. One option is that they represent globules of another mafic magma unrelated to the petrogenesis of Wando type granitic rocks. Another possibility is that enclaves are intermingled globules of hornblende gabbro that have been variously modified by complex hybridisation processes, such that their composition can no longer be modelled by binary mixing (e.g. Debon 1991; Orsini *et al.* 1991). For example, the elevated K_2O content of type C enclaves accords with diffusion of K_2O into the partially melted enclave from the tonalitic host, as stimulated by extensive biotite precipitation from the enclave magma (section 12.5.1b). Diffusion of Al_2O_3, CaO and Sr from the enclave into the adjacent tonalitic magma is also predicted (Johnston & Wyllie 1988; Orsini *et al.* 1991), which may partly account for the lower abundances of these elements in type C enclaves. Apart from diffusion, depletion in Al_2O_3, CaO, Na_2O and (for **97-159E**) SiO_2 may also result from expulsion of a residual melt during solidification and synchronous deformation of the enclave (Bacon 1986; Vernon 1991). The scenario here is that initial quenching of the mafic magma upon injection into the cooler felsic magma results in a structurally-coherent framework of mafic minerals, with residual liquid in interconnected pore spaces (Stephens *et al.* 1991). Variable amounts of the latter, which is enriched in feldspathic components and incompatible elements, become subsequently squeezed from the partially solid enclave during magmatic or tectonic deformation. This mechanism is uniquely applicable to enclaves in Wando type rocks, as emplacement and crystallisation of the host plutons was synchronous with D_2, and microgranular enclaves typically have flattened and sheared profiles. More compositional data on type C enclaves are required to properly evaluate this process.

(b) Type A and B enclaves

In contrast to type C enclaves, the geochemical trends of the more abundant type A and B enclaves are distinct from those of Wando type rocks (see Figure 15.5) but invariably conform to the dioritic array, particularly regarding steeply decreasing MgO but increasing P_2O_5 and Sr with silica (Figure 16.1), and markedly increasing Cr with Mg# (Figure 16.3a). In fact, the broad geochemical features of type A enclave **97-214E** (*viz.*, ~55% SiO_2, 0.6% TiO_2 and 7.8% MgO) are indistinguishable from those of the parental HMD magma of the dioritic array. This strongly suggests that these enclaves are genetically unrelated to the Wando type mixing system, but represent fragments of a high-Mg, low-Ti magma analogous to HMD. In the case of the Elbow Creek quartz diorite, such enclaves were clearly introduced as liquid globules by mingling with a coeval mafic magma (section 10.2.3b), similar to that forming the thick high-Mg dioritic dykes

in Corea Creek. As type A and type B microgranular enclaves in the Wando and Snake River Tonalites are virtually identical to those in the Elbow Creek quartz diorite, they were probably incorporated in a similar fashion. This could have occurred by intermingling in the feeder dykes, whereupon HMD globules were transported into (and dispersed throughout) the tonalitic magma chamber, or by direct injection of high-Mg magma into the pluton itself. Notably, enclave compositions become more evolved from type A to type B (Figure 16.3 and section 15.3.1b), indicating progressive differentiation of the coeval mafic magma during intermingling.

Hence, type A and type B microgranular enclaves confirm the existence of a second mantle-derived component in Wando type rocks, introduced close to the emplacement site. That these enclaves are abundantly distributed throughout Wando type plutons and preserve primary magmatic compositions indicates the lack of hybridisation between the invading HMD magma and tonalitic host. This in turn probably reflects rapid quenching of the more primitive magma upon intermingling with the cooling, partly-crystallised tonalite (especially formation of chilled margins on pillows), prohibiting major chemical exchange. The geochemical influence of the HMD component on the host body is therefore likely to be minimal, but it might at least account for some of the scatter in Wando type geochemical trends on variation diagrams.

16.5 Wennicott types

Wennicott type plutons and their enclaves are distinguished by the unusual progression to *lower* K_2O with increasing SiO_2, in contrast to all other GRC magma types (Figure 16.1) and most granitic suites of other orogenic belts. As with Wando type rocks, Wennicott types also have a flat Sr trend and evolve to higher Na_2O with silica, both of which preclude substantial plagioclase fractionation. The latter is also prohibited by the smaller negative Eu anomaly of the more felsic Wennicott type sample (Figure 15.7). Production of the distinctive Wennicott type geochemical trends by normal igneous fractionation is therefore most unlikely, as it requires separation of a potassic phase, such as K-feldspar or biotite, without removal of plagioclase, which clearly appeared earlier in the crystallisation sequence (section 10.4).

Alternatively, geochemical trends are consistent with generation of Wennicott type rocks by mixing between a mafic magma of similar composition to enclosed gabbroic enclaves, and a low-K felsic melt (Figure 16.12). The gabbroic enclaves therefore approximate unmodified globules of the end-member mafic magma. Regression of the Wennicott type trends indicates that the felsic end-member has <2% K_2O and ~300 ppm Sr, and is therefore close to the composition of muscovite-bearing tonalitic sheets interlayered with migmatites along Wennicott Creek reported by Bushell (1996). These tonalitic bodies have a similar inferred petrogenesis to Harrow type leucotonalites of the northeastern migmatite zone. Hence, as with Wando type rocks, Wennicott type plutons incorporate a significant ingredient of efficiently-segregated, metasedimentary-derived partial melt.

Although plotting close to Caupaul high-Al gabbros, the mafic end-member in the Wennicott type mixing system is compositionally more evolved, with higher SiO_2, K_2O and P_2O_5, as approximated by gabbroic enclave **98-WAE3**. It has a similarly-shaped REE pattern to

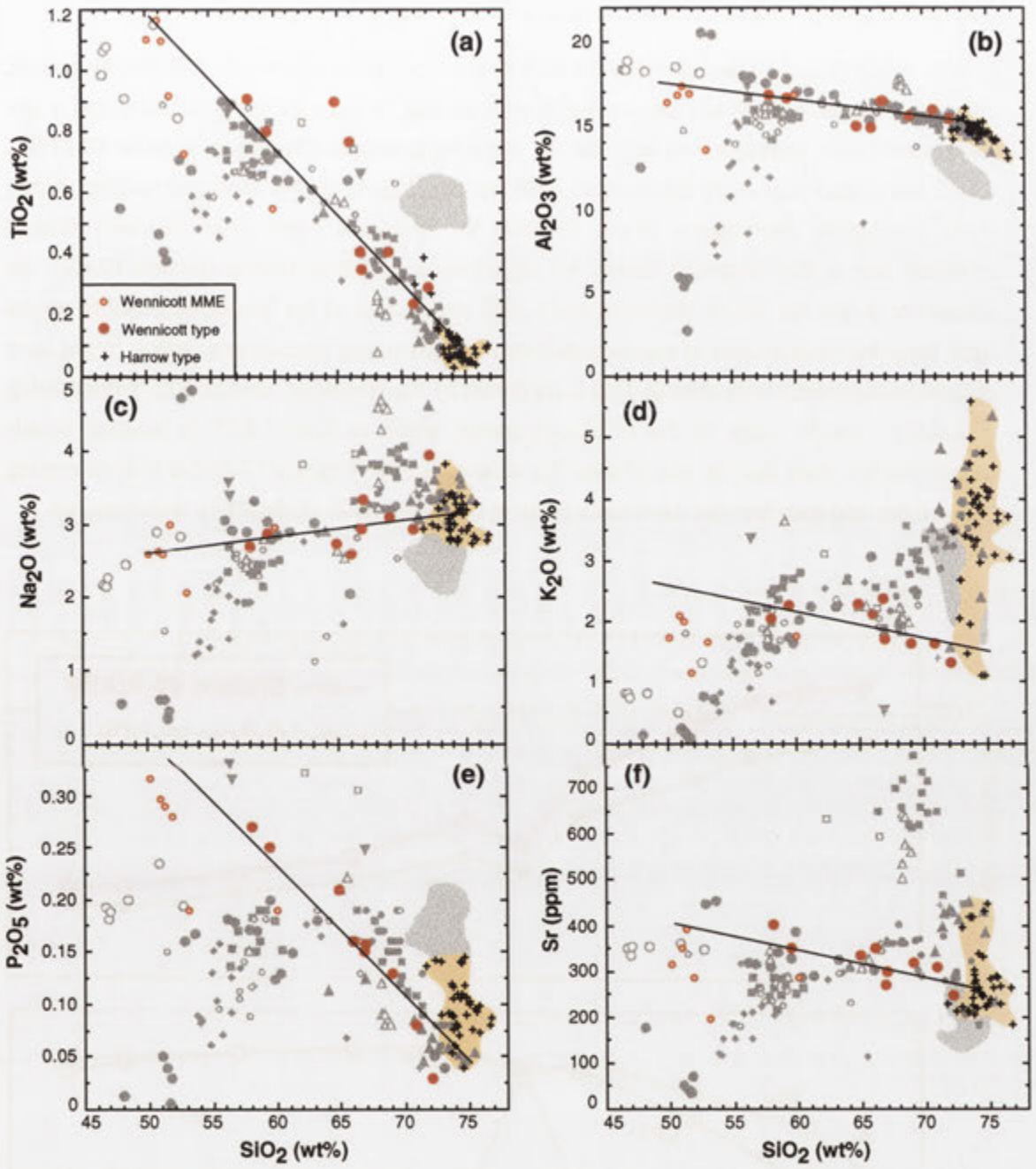

Figure 16.12. Formation of Wennicott type granitic rocks by mixing between a mafic end-member, approximated by contained gabbroic enclaves, and a low-K crustal melt. The field of metasedimentary-derived partial melts (orange shading, outlined by felsic Harrow and Kassingbrook types) and fertile metasedimentary rocks (grey shading) are indicated.

hornblende gabbro **98-CP6**, but at higher total REE abundances, with greater LREE enrichment and a larger negative Eu anomaly (Figure 16.13). These features are entirely consistent with derivation of the gabbroic Wennicott type enclave magma by fractional crystallisation of plagioclase-clinopyroxene-hornblende from a Caupaul hornblende gabbro.

Finally, as with Wando types, although the REE abundances of the most mafic Wennicott type rock (Warradale Tonalite **98-WA3**) are consistent with mixing between gabbroic enclaves and a low REE crustal melt, complications arise for the more felsic sample (Wennicott Tonalite **97-227B**), which has a markedly more fractionated REE pattern (Figure 16.9b). However, unlike Wando types, hornblende fractionation is not favoured for Wennicott types, since this only formed relatively late in the magmatic history by replacement of clinopyroxene (section 10.4.2). An alternative is that the HREE depletion and LREE enrichment of the Wennicott Tonalite results from incipient fractionation of early-crystallising clinopyroxene phenocrysts, which might have occurred concurrently with mixing. This is supported by the Wennicott Tonalite REE pattern being essentially a mirror image of that of clinopyroxene, which excludes LREE in tonalitic liquids (Figure 16.9b). Note that the non-existent Eu anomaly in the Wennicott Tonalite reflects mixing with a felsic end-member that itself has a positive Eu anomaly, as exhibited by leucotonalites.

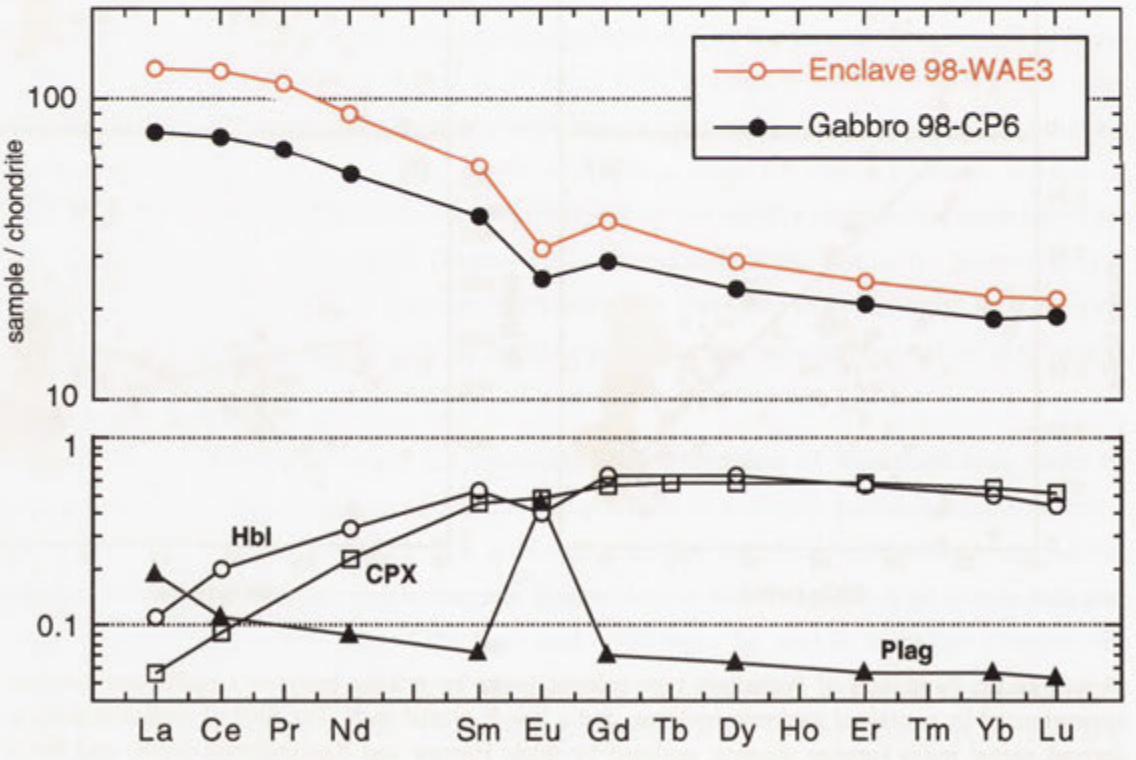

Figure 16.13. Comparison between the chondrite-normalised REE patterns of Caupaul gabbro **98-CP6** and Warradale Tonalite 'gabbroic' enclave **98-WAE3** with partition coefficients of the REE for hornblende, clinopyroxene and plagioclase in a basaltic melt. Higher total REE and larger $(La/Yb)_N$, together with a greater negative Eu anomaly, are consistent with derivation of **98-WAE3** from **98-CP6** by fractionation of a clinopyroxene ± hornblende - plagioclase assemblage.

16.6 Kassingbrook types

16.6.1 Petrogenesis of Kassingbrook type rocks with >70% SiO_2

The unusual combination of high Sr and extreme K_2O variation in felsic Kassingbrook type samples is petrogenetically diagnostic, as this uniquely characterises partial melts generated from GRC metasedimentary rocks and leucosome-derived Harrow type plutons (section 9.6, see Figure 16.1). Another powerful link between crustal anatexis and Kassingbrook types is the compositional similarity of the latter with *in situ* leucosomes of Chin Chap Creek migmatites, particularly regarding the distinctive high-Sr signature and calcic plagioclase cores (section 15.2.1). Biotite of 'typical' Kassingbrook Granodiorite sample **97-373** also overlaps chemically with that of Harrow type plutons (Figure 15.4).

Accordingly, these chemical features, together with intimate association with migmatites and content of magmatic muscovite, indicate derivation of felsic Kassingbrook type granitic rocks by partial melting of the surrounding metasedimentary sequence. As with Harrow types, the large K_2O variation within the Kassingbrook Granodiorite reflects pluton construction by amalgamation of disparate batches of partial melt, sourced from slightly different metasedimentary horizons (section 9.6.2). The low ferromagnesian element contents result from efficient partial melt extraction from the migmatitic protoliths, such that refractory biotite is not significantly entrained. This also accounts for the marked REE depletion (Figure 16.9), since REE-rich accessory minerals are both insoluble and concentrated in residual micas, and thus retained in the source (section 8.5.3).

16.6.2 Production of lower silica Kassingbrook types and microgranular enclaves

Despite the purely metasedimentary derivation of the more felsic samples, as a group, Kassingbrook type rocks extend to distinctly lower silica but higher TiO_2, MgO and CaO than the compositional field of *in situ* leucosomes and felsic Harrow type plutons (Figure 16.14). Further, biotite of Kassingbrook Granodiorite sample **97-376B**, collected from adjacent to a hornblende diorite sheet, is more magnesian than 'typical' sample **97-373** and Harrow type plutons (Figure 15.4). Field evidence, outlined in Chapter 12, clearly indicates that this reflects modification of the 'typical' felsic, muscovite-bearing Kassingbrook Granodiorite by mingling and incipient mixing with contemporaneous high-Mg hornblende diorite (boninite) magma. Hybridisation occurred primarily by physical disaggregation and digestion of mafic magma globules, augmented by diffusional exchange across the mafic-felsic interface (section 12.5.1c). Locally, more effective blending between the mafic boninitic magma and the felsic granodiorite generated the two 'hybrid' tonalitic samples (section 12.5.1d), which have markedly lower silica contents than other Kassingbrook types (~64% and 67% SiO_2, see section 15.4.2b). A chemical link between hornblende-rich hybrid **97-274** and the boninitic hornblende diorite is suggested by the similarity of mineral and whole-rock geochemical compositions, most notably the shared magnesian signature, and an indistinguishable REE pattern (section 15.4.2b). Other obvious hybridisation effects in Chin Chap Creek include the development of biotite-rich envelopes with distinctive clotted textures around the mafic hornblende diorite sheets (section 12.3.4).

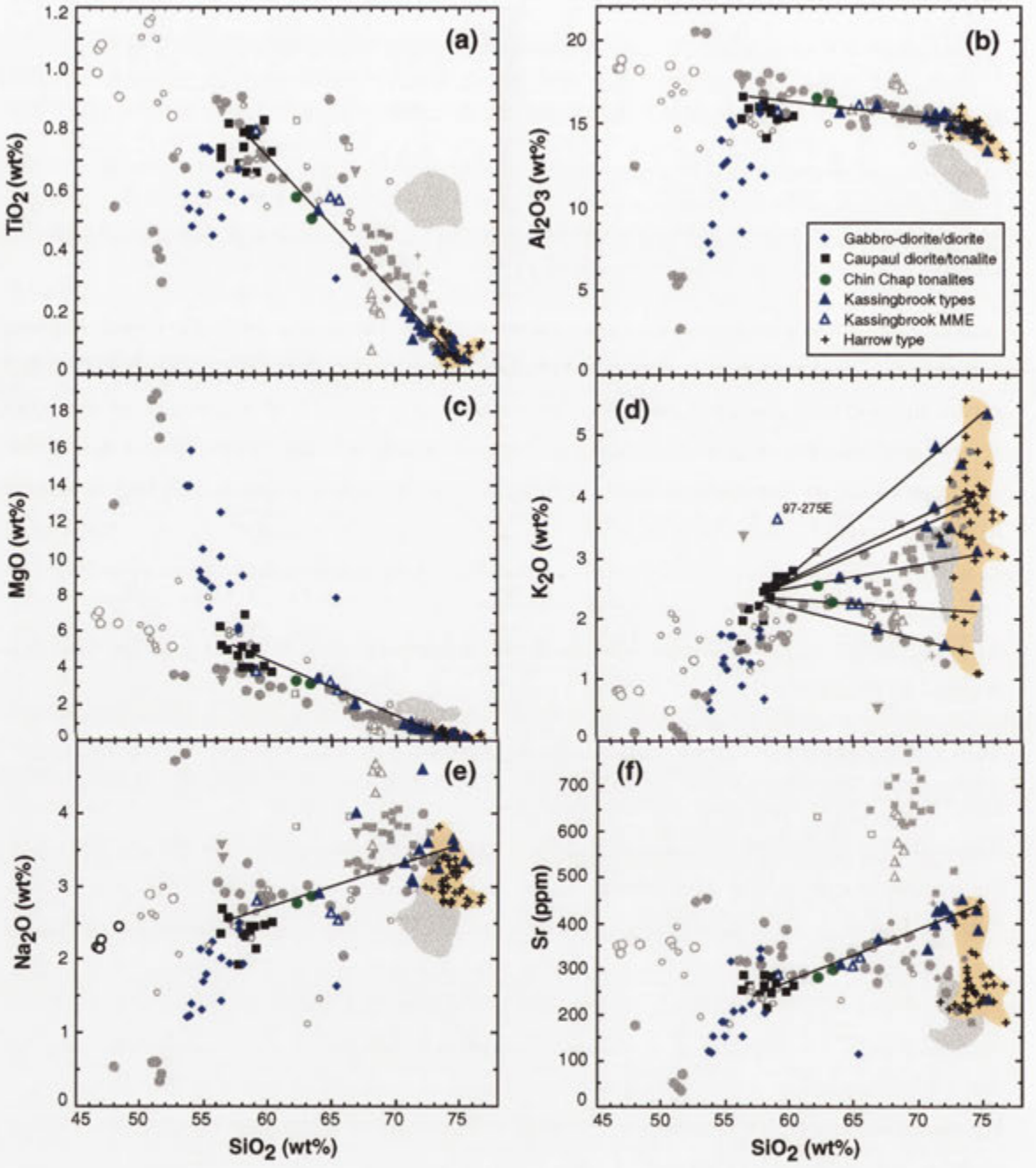

Figure 16.14. Production of Kassingbrook type trends by mixing between an evolved boninitic mafic magma and metasedimentary-derived partial melt. The latter is approximated by the most felsic Kassingbrook Granodiorite samples, which fall within the field of felsic Harrow types (orange shading). Microgranular enclaves are contained within the mixing array and therefore represent intermingled fragments of hybridised magma. Chin Chap Creek tonalites plot close to the inferred mixing lines and have the same petrogenesis. The grey shaded area represents that of fertile metasedimentary rocks.

The extensive intermingling of this material with Kassingbrook Granodiorite resulted in formation of the 'spotted' mafic enclave swarms near hornblende diorite margins, and, by extension, the texturally-similar microgranular enclaves dispersed throughout the pluton, and the Nangkita Adamellite further south (section 12.5.1c).

The compelling field evidence for hybridisation between the felsic, metasedimentary-derived Kassingbrook Granodiorite and boninitic hornblende diorite is corroborated by geochemical variation diagrams. Here, the more mafic Kassingbrook type samples, tonalitic hybrids, and the 'spotted' microgranular enclaves define linear trends on variation diagrams that project back to the high-Mg dioritic array (Figure 16.14), the exception being K_2O (below). Although the mixing trend exhibits some scatter, it is strengthened by the hornblende tonalite dykes of Chin Chap Creek, which are part of the mixing system (see below). The uniqueness of the trend is underlined by Figure 16.15, where all Kassingbrook types (including the hybrid samples) and contained microgranular enclaves exhibit strongly increasing Cr with MgO, which characterises rocks of the dioritic array and is therefore diagnostic of boninite involvement in mixing. Regression lines from the mixing trends intersect the Caupaul diorite-tonalite compositional field (Figures 16.14, 16.15), indicating that hybridisation mostly occurred with slightly fractionated boninitic magmas. Conceivably, this could reflect the initial crystallisation of mafic minerals by

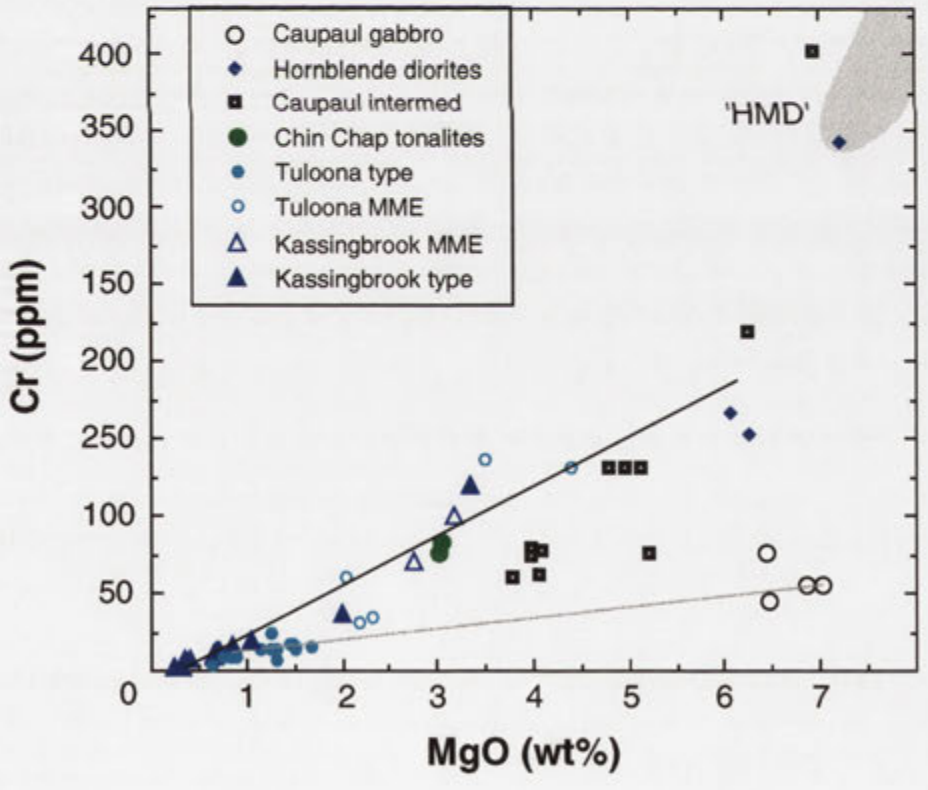

Figure 16.15. Plot of Cr versus MgO, showing formation of the Kassingbrook type trend, microgranular enclaves and Chin Chap Creek tonalites by mixing between felsic magma and an evolved high-Mg mafic magma. The two hybrid Kassingbrook type samples have the highest MgO. Note that microgranular enclaves in Tuloona types also plot close to the inferred mixing line, but host plutons define a linear trend towards the low-Cr Caupaul gabbros (grey line).

the high temperature boninitic magma upon contact with the cooler, felsic granodiorite (see section 1.3.1, p.5-7). Due to the large K_2O range of Kassingbrook type compositions, no unique mixing line occurs on the K_2O-SiO_2 plot (Figure 16.14d). Instead, the two hybrid tonalitic rocks have large K_2O differences, reflecting different crustally-derived end-members. The Kassingbrook Granodiorite samples affected by hybridisation are displaced to lower SiO_2 on Figure 16.14d, imparting greater scatter parallel to the silica axis than occurs for Harrow type plutons. Note that microgranular enclave **97-275E** is unusually K-rich relative to other enclaves and tonalitic hybrids, and plots well above any possible mixing line (Figure 16.14d). This K_2O enrichment is attributed to more extensive diffusion of K_2O into the partially liquid enclave, possibly in response to biotite precipitation, prior to, or synchronous with, intermingling (see section 12.5.1b).

Further insight into the specifics of the magma mixing process evident along Chin Chap Creek is provided by plagioclase grains in hybrid tonalite **97-274** (section 15.2.1). Phenocryst cores have the same composition as plagioclase of 'typical' felsic Kassingbrook Granodiorite samples, indicating that the felsic end-member magma was partly crystalline prior to mixing. Quartz ocelli in **97-274** also probably represent original phenocrysts. Influx of HMD into the felsic magma, followed by mixing, subsequently induced precipitation of the calcic plagioclase 'spike' from the more mafic hybrid magma, which is of similar composition to plagioclase in hornblende diorite **97-376**. Early formed plagioclase crystals apparently acted as a substrate for nucleation of the calcic plagioclase shell, though the rounded outlines are also consistent with some resorption by the hotter hybrid magma (Wiebe 1968). Heat loss to the juxtaposed felsic granodiorite also promoted rapid crystallisation of the equally calcic groundmass plagioclase laths in hybrid **97-274** and nucleation of hornblende around quartz ocelli. Zonation to relatively sodic mantles around phenocrysts and groundmass plagioclase grains subsequently occurred during cooling (Hibbard 1995). That these overlap compositionally with plagioclase rims of typical Kassingbrook Granodiorite samples (Figure 15.1) implies thermal and chemical equilibration between the residual melt in the hybrid magma and that of the adjacent felsic granodiorite at this time (Hibbard 1991, 1995).

16.6.3 Implications for Chin Chap Creek tonalites

Hornblende-bearing tonalitic dykes of Chin Chap Creek are petrographically and geochemically analogous to the Kassingbrook type hybrid **97-274** (sections 12.3.5 and 15.4.2b), unified in particular by the high-Mg signature, and chemically resemble the 'spotted' microgranular enclaves (section 15.4.2c). Accordingly, the hornblende tonalite dykes plot along the Kassingbrook Granodiorite-HMD mixing lines (Figures 16.14, 16.15, see also Figure 15.8) and were similarly produced by mixing between metasedimentary-derived partial melt and mafic boninitic magma. Tonalitic dykes therefore represent the larger-scale manifestation of the effective hybridisation occurring at intermingled granodiorite-hornblende diorite contacts, consistent with the hybrid textural features (e.g. quartz ocelli and 'spindly' texture) and lithological heterogeneity, combined with the occurrence of hornblende-rich enclaves (section 12.3.3). Locally, mingling and partial disaggregation of the hybrid tonalitic magmas within the

Kassingbrook Granodiorite (e.g. at key locality C in Chin Chap Creek) resulted in further modification of the host granodiorite (i.e. second-stage hybridisation).

16.7 Tuloona types

16.7.1 Petrogenetic models

Critical aspects of Tuloona type rocks are- (a) content of microgranular enclaves with hybrid igneous textural features, (b) transitional boundaries with Harrow type rocks, and (c) occurrence of metasedimentary enclaves. The first suggests a role for coeval mafic magmas in the petrogenesis of Tuloona types, whereas the last two points indicate a link with *in situ* partial melting in the metasedimentary sequence. This implies, that as with Wando and Wennicott type plutons, Tuloona type rocks are related by variable degrees of mixing between a mantle-derived mafic magma and a metasedimentary-derived partial melt. However, serious complications for simple mixing models arise for Sr and K_2O, since there is no mafic igneous composition at the lower silica extrapolation of either trend on variation diagrams (Figures 16.1f, 16.1h). This problem is most severe for the steep and well-correlated K_2O trend, and results in this being 'off-set' from the Wando type mixing array. The problem is circumvented if each Tuloona type sample represents a discrete magma batch produced by mixing between the same mafic end-member but felsic end-members of different K_2O, which is not inconceivable given the extreme K_2O variation of the crustally-derived partial melts. However, this also requires that successively higher K mafic-felsic mixes must also be displaced to progressively higher silica and fortuitously lie along the same trend. This seems unrealistic, as each mixed magma batch should either have approximately the same silica, or define trends parallel to the inferred mixing lines and silica axis.

It is therefore concluded that the linear trends of Tuloona type rocks on variation diagrams are not mixing lines between mafic and felsic end-members, but largely reflect evolution from a single parental lithology by restite unmixing or fractional crystallisation. Control by restite unmixing requires that the lowest silica Tuloona type rocks are restite replete, and therefore approach the bulk source composition. However, the most mafic plutons (e.g. Chetwynd Tonalite) are lithologically homogeneous and contain a paucity of material that could be considered restitic. Mafic tonalites of supposedly restite-controlled I-type granitic suites of the LFB are strikingly heterogeneous by contrast, with abundant ragged aggregates of mafic minerals (including pyroxenes), corroded calcic plagioclase cores (to An_{80} in the Jindabyne Tonalite, Hine *et al.* 1978), and are crowded with microgranular enclaves (Chappell *et al.* 1987, 1991). Although the Chetwynd Tonalite has corroded plagioclase cores, these are highly variable in composition, relatively sodic, and are commonly overgrown by more calcic plagioclase (Figure 15.1), suggesting that they cannot be the refractory residue of partial melting. Furthermore, the igneous texture of microgranular enclaves in Tuloona types indicates derivation from a coeval mafic magma and is totally inconsistent with a restitic origin (section 12.5.2).

Hence, it is more likely that the progression to increasingly felsic and potassic compositions reflects fractional crystallisation of plagioclase, biotite and magnetite from a parental magma. This is consistent with the strong linear increase in Rb/Sr, but decrease in Sr with K_2O (Figure 16.16),

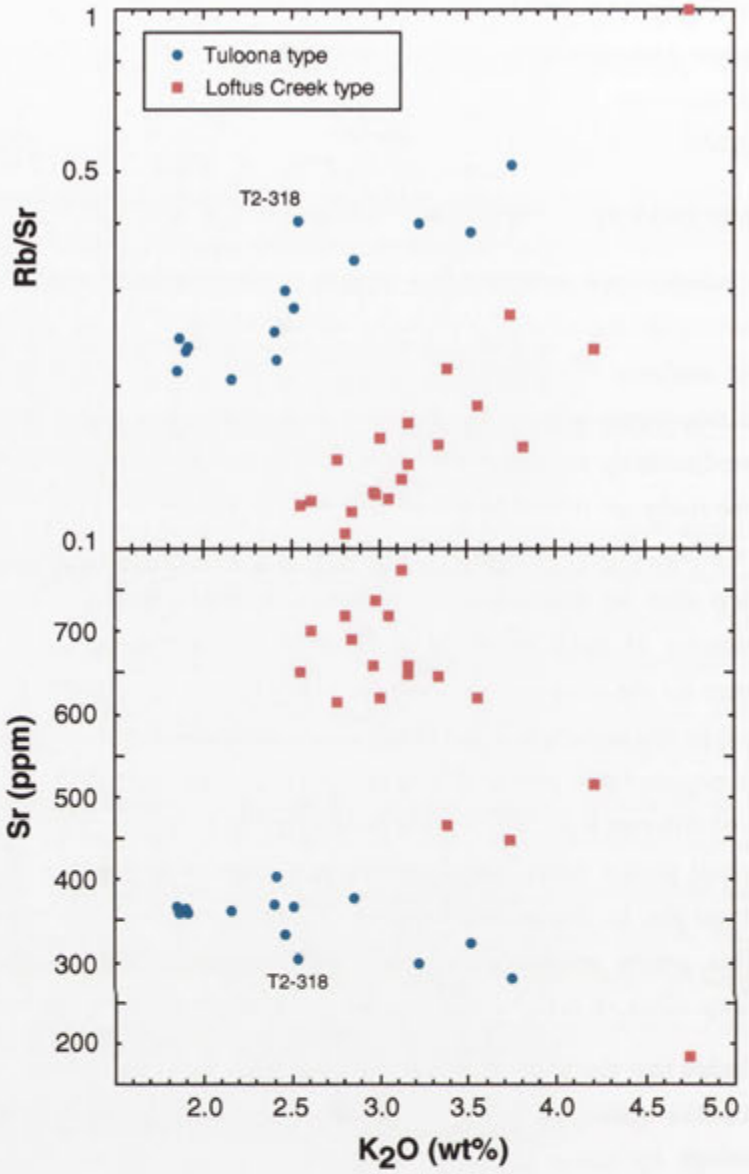

Figure 16.16. Plots of Rb/Sr (top; note the logarithmic scale) and Sr (bottom) against K_2O for Tuloona and Loftus Creek type granitic rocks.

as plagioclase accommodates Sr but excludes Rb, and appearance of alkali feldspar phenocrysts in the more felsic samples, according with a greater degree of magmatic differentiation. As zircon crystals are concentrated within biotite in Tuloona type rocks, their removal may be responsible for the steeper REE pattern relative to the inferred gabbroic end-member composition (Figure 16.9c). Fractional crystallisation also accords with changes in mineral chemistry, such that plagioclase is zoned to slightly more sodic compositions in Tuloona Granodiorite **T2-135** compared to the more mafic Chetwynd Tonalite **97-427** (see Figure 15.1). Biotite in the latter is also considerably more magnesian and Ti-rich (Figure 15.4). Under this scenario, the most fractionated pluton is the Glendara Adamellite, supported by the general absence of enclaves, lithological homogeneity over a large area, striking abundance of large alkali feldspar

phenocrysts and association with numerous garnetiferous aplite-pegmatite dykes. Hence, the convergence of Tuloona type geochemical trends into the Harrow type compositional field on Figure 16.1 does not represent a mixing array, but simply reflects evolution of successively fractionated granitic liquids towards the H_2O-saturated 'minimum melt' composition.

A final point is that Tuloona Granodiorite sample **T2-318** has lower Sr (~300 ppm) and elevated Rb/Sr (0.4) relative to other granodiorite samples with similar silica content (e.g. **T2-78B**, 370 ppm Sr, Rb/Sr =0.25) (Figure 16.16). Since **T2-318** derives from the edge of the pluton, where choked with migmatite enclaves and complexly intermingled with Awaiti Adamellite, this plausibly reflects either contamination by metasedimentary rock or localised hybridisation with lower Sr Harrow type partial melt. Either of these could be responsible for the markedly more evolved isotopic composition of this rock compared to Tuloona Granodiorite sample **97-299**.

16.7.2 Origin of parental Tuloona type magma

As the most mafic Tuloona type samples cluster around 67-68% SiO_2 and ~1.9-2% K_2O, this probably approximates the parental magma composition. Being remote from Harrow type plutons and the field of metasedimentary rocks (Figure 16.1), this is unlikely to be a purely metasedimentary-derived partial melt, especially as the latter are strongly peraluminous and lack magnetite. Furthermore, mafic Tuloona Granodiorite **97-299** has a considerably more primitive Sr isotopic composition than the metasedimentary rocks (Figure 16.11). Derivation of Tuloona type magmas by higher temperature anatexis of an unexposed, more 'primitive' metasedimentary rock, such as a biotite-plagioclase-quartz ± amphibole metagreywacke, is precluded by the consistently siliceous, strongly peraluminous melts produced by such rocks under a range of experimental conditions (e.g. Beard & Lofgren 1991; Patiño Douce & Beard 1996; Stevens *et al.* 1997).

An alternative is that parental Tuloona type magmas were produced by partial melting of a metamorphosed mafic igneous protolith, which, given the outcrop area of Tuloona type rocks, would need to be extensive below the current exposure level. The most likely candidates are quartz amphibolites with bulk compositions corresponding to calc-alkaline basalt and basaltic andesite, as experimental melts from these rocks are moderately siliceous and plot within the medium-K field (Roberts & Clemens 1993; see summary in Johannes & Holtz 1996). However, mafic Tuloona type rocks are systematically more magnesian and potassic than experimental melts of appropriate SiO_2 contents from a range of meta-igneous starting materials under various P-T-a_{H_2O} conditions (Figure 16.17). In fact, an acute discrepancy between experimental melts and 'Cordilleran' hornblende granites worldwide with regard to K_2O is recognised by Patiño Douce (1999). Furthermore, experimental melts produced by hornblende dehydration melting are equilibrated with varying combinations of residual hornblende, clinopyroxene, orthopyroxene and garnet (Patiño Douce & Beard 1995, Johannes & Holtz 1996), none of which (or their relics) are encountered in Tuloona type plutons. This could only be explained by extremely efficient extraction of partial melts from the source, combined with protracted fractional crystallisation of liquidus mafic phases. Partial melts generated from normal meta-basaltic to meta-andesitic precursors are also likely to be isotopically primitive, and thus require massive crustal contamination to approach the relatively evolved isotopic composition of mafic Tuloona types.

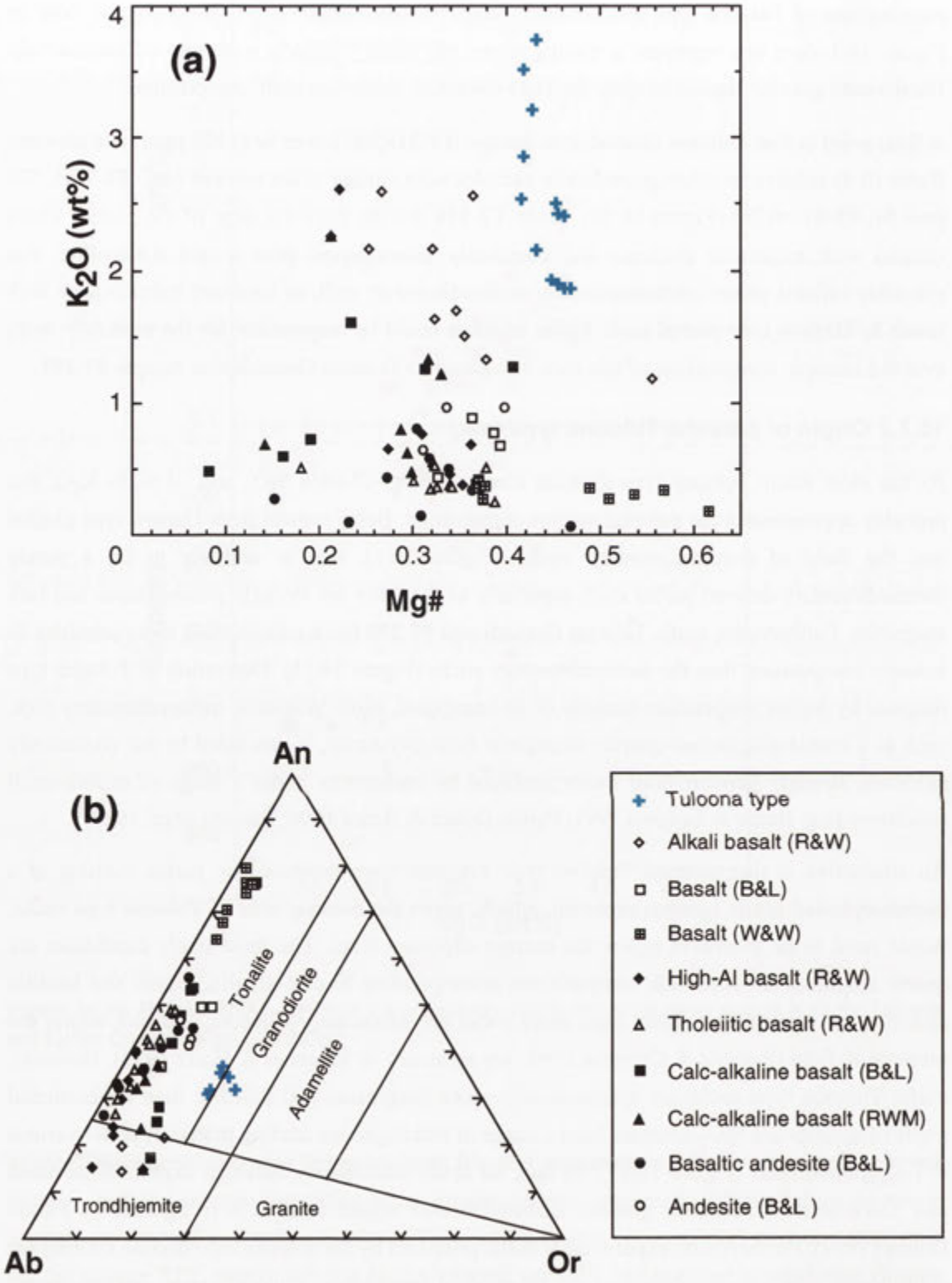

Figure 16.17. Comparison between mafic Tuloona type rocks and experimental partial melts with 55-66% SiO_2 obtained from various bulk rock compositions in terms of (a) K_2O against Mg# and (b) CIPW normative anorthite (An), Albite (Ab) and orthoclase (Or). Note that only quartz-normative compositions are plotted in (b). Data sources are: B&L, Beard & Lofgren (1991); R&W, Rapp & Watson (1995); RWM, Rapp *et al.* (1991); W&W, Wolf & Wyllie (1991). The lithological fields in (b) are after O'Connor (1965).

Given the difficulties with derivation from common crustal rocks, it is instead proposed that parental Tuloona type magmas are actually hybrids, formed by large-scale mixing between a mafic magma and a peraluminous metasedimentary-derived partial melt. The magnesian character therefore reflects the mantle-derivation of the mafic magma. The trend to more siliceous and potassic compositions was subsequently generated by fractional crystallisation. The moderate P_2O_5 contents of mafic Tuloona type rocks require the mafic end-member to have an enriched composition similar to that of Wennicott type rocks (see Figure 16.1g), whereas the felsic end-member is specified as a leucotonalite or Kassingbrook type rock, to account for the low K but moderately high Sr contents of mafic Tuloona types (Figure 16.18). Under this scenario, the negative Eu anomaly of mafic Tuloona Granodiorite **97-299** (which approximates a parental composition) was simply inherited from the mafic magma, but reduced in size by the addition of leucotonalitic partial melt, which has Eu/Eu*>1. Note that in detail, the scattered Sr trend for Tuloona type rocks can be attributed to variations in the crustal ingredient in the mixing system, such that the parental magmas of different plutons were derived from metasedimentary end-members of different Sr content. For example, the distinctly higher Sr and K_2O of mafic Coojar Granodiorite samples indicates a more Sr-rich and potassic end-member for this pluton, such as a Kassingbrook type rock (Figure 16.18). Some subtle variation in precise end-member compositions of different Tuloona type plutons is inevitable, given the compositional diversity of metasedimentary-derived partial melts and the large area of the central granitic batholith. Nonetheless, textural and compositional similarity between mafic samples from different plutons confirms that the end-members were broadly similar in composition for the entire magma type.

16.7.3 Origin of microgranular enclaves in Tuloona type rocks

Field and petrographic evidence indicates that microgranular enclaves of Tuloona type rocks represent intermingled globules of a contemporaneous hybrid mafic magma (section 12.5.2). In the simplest scenario, this would be produced by mixing between the same mafic and felsic end-members that generated the host rocks. However, this is unlikely, as the enclaves have lower Al_2O_3 and Sr but higher MgO than the postulated mixing line (Figure 16.18). Instead, microgranular enclaves of Tuloona types define reasonably coherent trends (apart from **97-382B**) that conform to the mixing line between Kassingbrook type granitic rocks and high-Mg (boninitic) hornblende diorite (Figure 16.18). Affinity with the latter is confirmed by the strongly increasing Cr with MgO of Tuloona type microgranular enclaves (Figure 16.15), since this is the hallmark HMD signature.

Accordingly, it is suggested that microgranular enclaves in Tuloona types are unrelated to the mixing system of the host plutons, but represent intermingled globules of coeval mafic magmas produced by hybridisation between the Kassingbrook Granodiorite and a mafic boninitic magma. This accords with lithological resemblance between Tuloona type microgranular enclaves and hybrid rocks of Chin Chap Creek, particularly regarding the shared biotite-rich nature and distinctive 'clotted' texture. Development of melt-precipitated hornblende in the most mafic enclaves (e.g. **97-294**) is another unifying feature; the absence of this mineral in the host (which is actually peraluminous) is consistent with the enclaves being sourced from a different magmatic

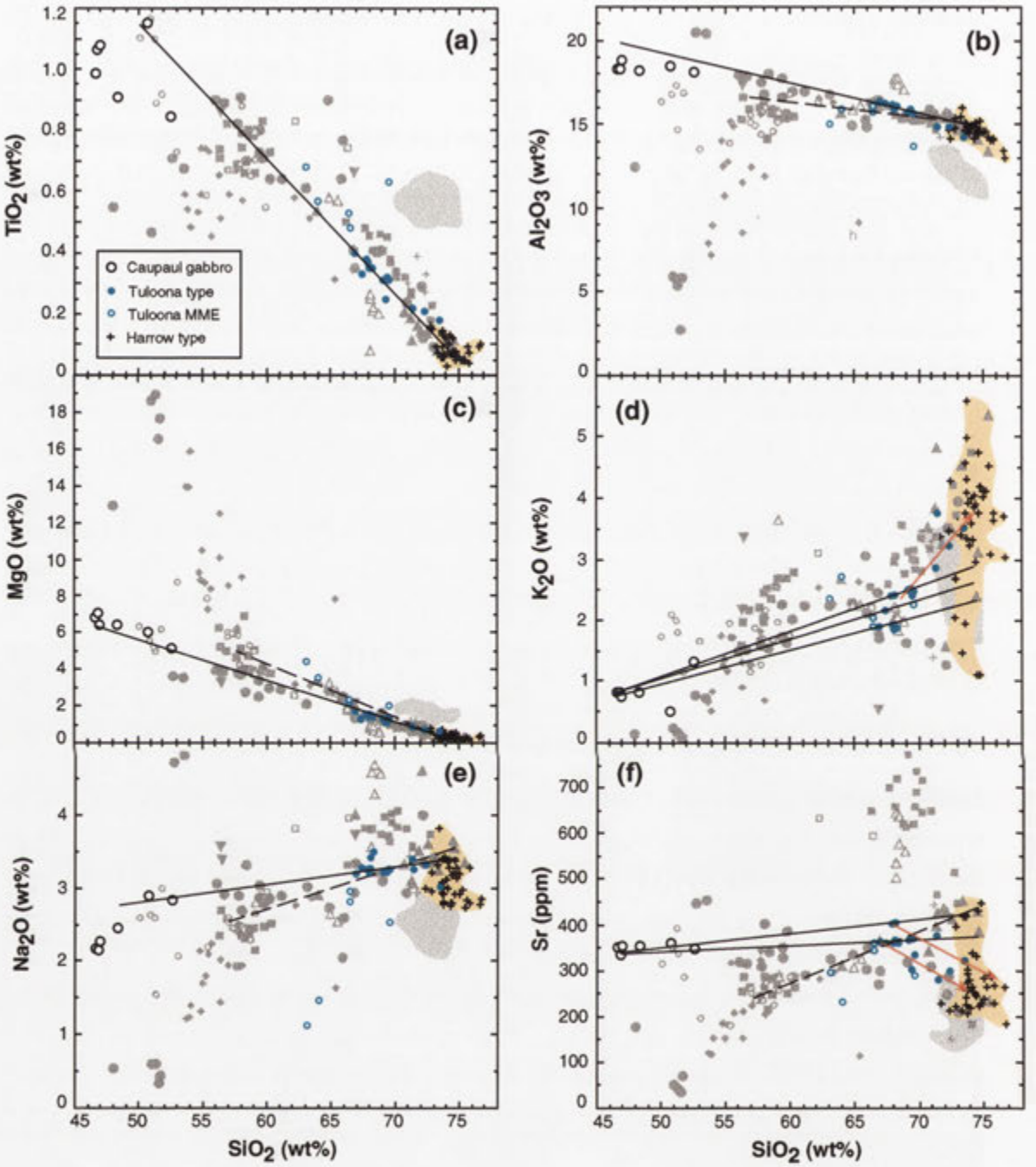

Figure 16.18. Production of parental Tuloona type magma by mixing between a Caupaul gabbro-like magma and metasedimentary-derived partial melt; several possible mixing lines are indicated for K_2O and Sr, according with the large compositional variation of the felsic end-member. The subsequent fractionation trends (where not parallel to the mixing line) are shown with an arrowed red line. Note that microgranular enclaves of Tuloona types plot close to the Kassingbrook type mixing line (dashed line). The field of metasedimentary-derived partial melts (orange shading, outlined by felsic Harrow and Kassingbrook types) and fertile metasedimentary rocks (grey shading) are indicated.

parent than the enclosing granodiorite. An extraneous origin for the microgranular enclaves is further implied by their occurrence in evolved Tuloona types, especially the Tuloona Granodiorite exposures in Schofield Creek (where enclaves are larger and more abundant than in mafic Tuloona types, section 11.2.1c). This is because such enclaves would be removed very early in magmatic differentiation if they were restitic or hybrid magma globules formed during the same mixing event that formed the host plutons. Formation of the 'clotted' microgranular enclave swarms in the strongly fractionated Glendara Adamellite outcrops of Pigeon Ponds Creek was clearly related to syn-mingling with syn-plutonic biotite-rich mafic dykes (section 11.2.2d). These resemble the tonalitic dykes of Chin Chap Creek, confirming that high-Mg mafic magmas were coeval with Tuloona type plutonism.

The extent to which Tuloona type magmas were modified by interaction with hybridised high-Mg diorite is uncertain, though the modest increase of Cr with MgO, and relatively low MgO of Tuloona types in general (Figure 16.15), suggest that this was minor. Such mingling may therefore have occurred close to the emplacement site of Tuloona type plutons at an advanced stage in the crystallisation history, as was the case for the Glendara Adamellite.

16.8 Loftus Creek types

16.8.1 Significance of chemical variation

Combined field, petrographic and geochemical features indicate that the compositional diversity of Loftus Creek type granitic rocks mostly results from fractional crystallisation from a parental liquid. These include- (1) paucity of microgranular or metasedimentary enclaves, (2) petrographic homogeneity on outcrop scale, (3) absence of anhedral plagioclase cores or mafic clots of possible restitic affinity, (4) appearance of alkali feldspar phenocrysts in the most felsic samples, manifesting the steeply increasing K_2O with silica, (5) association with abundant garnetiferous felsic dykes, and (6) strong decrease in Na_2O and Sr, but exponential increase in Rb/Sr with evolution to higher silica (section 15.4.3) and K_2O (Figure 16.16), according with removal of feldspars. Fractionation is most obviously manifest with the striking concentric zonation within the Cairns Creek Granodiorite, consistent with progressive separation of plagioclase and mafic phases (hornblende, biotite, titanite and magnetite) during rim to core crystallisation. Systematic variation of this nature cannot be produced by mixing with metasedimentary-derived partial melt, and there is no evidence for any interaction between Loftus Creek type plutons and Harrow type granitic rocks. Hence, as with Tuloona type plutons, the convergence of Loftus Creek type geochemical trends towards the Harrow type field is not a mixing line (see Figure 16.1), but is due to evolution of granitic liquids towards the H_2O-saturated 'minimum melt' composition with increasing fractionation. The appearance of muscovite in felsic samples testifies to increasing peraluminosity during differentiation, resulting from fractionation of metaluminous minerals. This is also consistent with the experimental observation that minimum temperature granitic liquids have slightly peraluminous compositions (Ellis & Thompson 1986). Transitions from metaluminous to peraluminous chemistry are therefore characteristic of strongly fractionated granitic suites (White & Chappell 1977).

16.8.2 Origin of the parental magma

Robertson Creek shoshonites outcrop in proximity to Loftus Creek type plutons, share the same high Sr, high Ba signature and contain similarly distinctive alkaline amphiboles and ophitic titanite crystals. The REE patterns of shoshonite **98-RC1** and Loftus Creek type samples also have similar shape (Figure 16.9d). These linking features imply a petrogenetic relationship between Robertson Creek shoshonites and Loftus Creek type plutons. However, derivation of the latter by fractionation from a shoshonitic magma is precluded by- (a) the high K_2O contents of shoshonites, which therefore plot remote from the Loftus Creek type trend for K_2O (see Figure 16.1f), and (b) the lower REE contents and larger Eu/Eu* of Loftus Creek type rocks relative to the inferred parental shoshonite (Figure 16.9d).

Alternatively, geochemical trends are consistent with production of the parental magmas for each Loftus Creek type pluton by mixing between a shoshonitic magma similar to **98-RC1** and a metasedimentary-derived leucotonalitic melt (Figure 16.19). Subsequent fractionation generated the full range of granitic compositions. This relationship holds for all elements on variation diagrams except for Na_2O, where a slightly more sodic mafic end-member than **98-RC1** is required (Figure 16.19c). The coherent trends defined by Loftus Creek type rocks as a group indicate that parental magmas for each pluton were compositionally very similar, and approximated by the lowest silica granitic sample, Loftus Creek Granodiorite 9572 of Anderson (1990). In detail, minor, non-systematic differences in Na_2O and Sr between (and within) plutons probably reflect the involvement of slightly different felsic end-members in the mixing system, given the large compositional range of *in situ* partial melts. This is corroborated by similar scatter in Tuloona type trends for these elements, since these plutons share the same crustal end-member.

A hybrid origin for parental Loftus Creek type magmas is also supported by REE evidence, where total REE contents of mafic Loftus Creek Granodiorite and Koolomurt Granodiorite samples plot between shoshonite **98-RC1** and a crustal melt composition approximated by Kassingbrook Granodiorite **97-376A** (see Figure 16.9d). The slight clockwise rotation of the patterns, which is greater for the more evolved Koolamurt Granodiorite, accords with incipient hornblende fractionation, as this will elevate La and Ce ($D^{hbl/melt}<1$) and lower the abundances of all other REE, whose D>1 for a melt of basaltic andesite composition (i.e. **98-RC1**). Lack of significant Eu anomalies despite the inferred small degree of plagioclase fractionation could indicate that Eu/Eu* for the parental magma was greater than unity, since the leucotonalitic end-member in the mixing system is likely to have had a positive Eu anomaly.

The enriched Sr, Ba and K that uniquely characterises Loftus Creek type rocks was therefore imparted by the shoshonitic end-member in the mixing system, facilitating clear distinction from Tuloona types, despite both magma types sharing the same crustal end-member and evolving by fractional crystallisation. The shoshonitic end-member may also account for the distinctive biotite phenocrysts of Loftus Creek types, since blending of the mafic, K-rich magma with hydrous partial melt would have promoted early biotite precipitation.

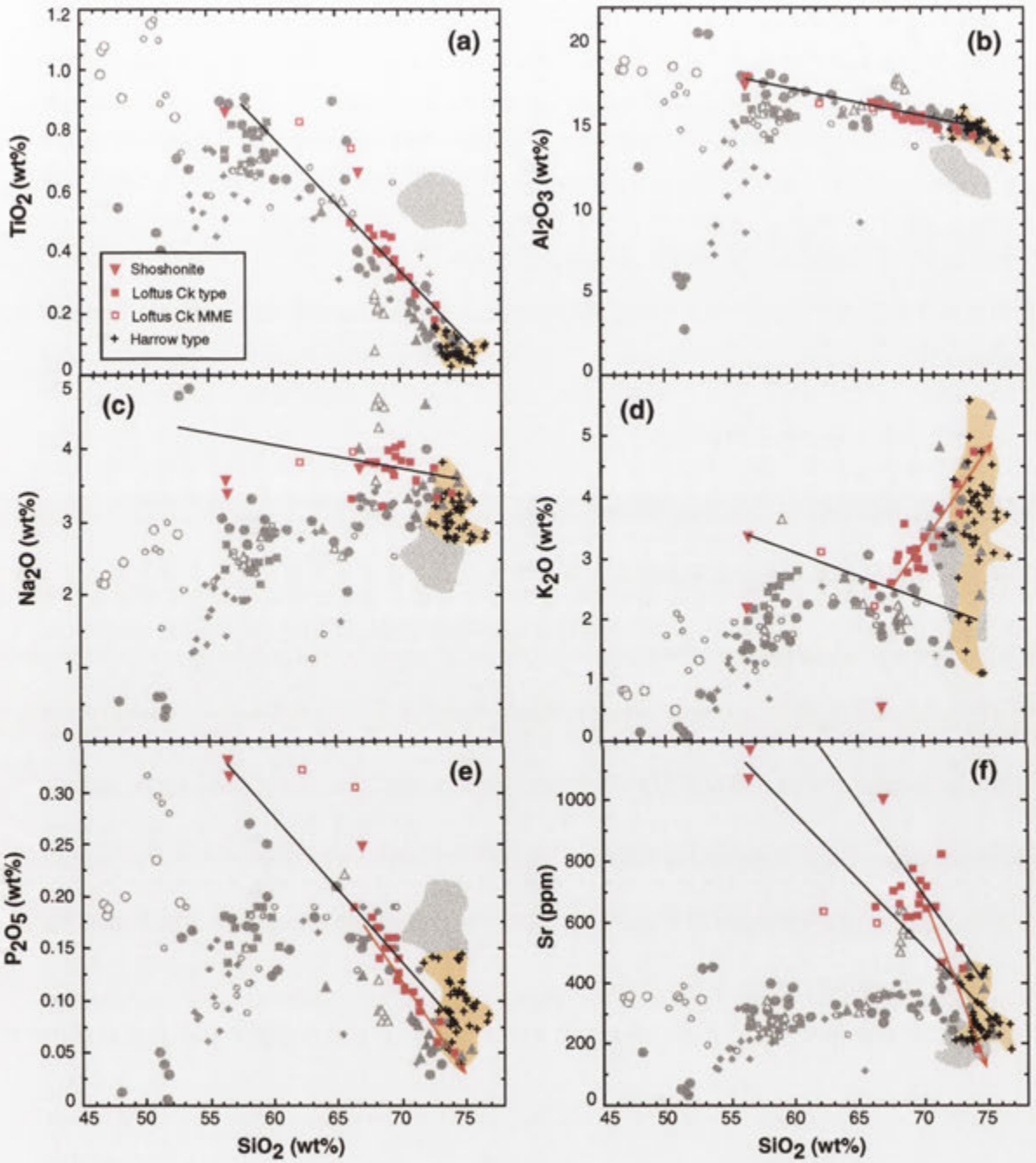

Figure 16.19. Formation of parental Loftus Creek type magma by mixing between a shoshonite and low-K metasedimentary-derived partial melt. Two possible mixing lines are shown to account for the Sr variation of Loftus Creek types. The subsequent fractionation trends (where not parallel to the mixing line) are indicated with an arrowed red line. The field of metasedimentary-derived partial melts (orange shading, outlined by felsic Harrow and Kassingbrook types) and fertile metasedimentary rocks (grey shading) are indicated.

16.8.3 Microgranular enclaves

The clustering of large igneous-textured microgranular enclaves in the Koolomurt Granodiorite, which is inferred to have undergone some fractionation, suggests introduction by mingling with a more mafic magma close to the emplacement site. The petrographic diversity and complex hybrid textures of the enclaves suggests either multiple pulses of different hybrid magmas into the Koolomurt pluton, or that only one mafic magma was involved, globules of which were variously modified by interaction with the host granodiorite; some combination of these is also plausible (section 12.5.2). In any case, the enclaves clearly have affinity with the Loftus Creek type mixing system, as they contain ophitic titanite, have high Sr contents, and plot close to the shoshonite-leucotonalite mixing line for most elements (Figure 16.19).

Unlike other Loftus Creek types, the Koolomurt Granodiorite has therefore experienced a three-stage evolution, namely- (1) formation by shoshonite-leucotonalite mixing, (2) subsequent fractional crystallisation and emplacement, and (3) second stage mingling (and possibly hybridisation) with mafic magma.

16.9 Petrogenesis of Deep Creek type plutons

16.9.1 The adakite connection

A number of unique compositional attributes discriminate Deep Creek type granitic rocks from all others of the GRC (Figure 16.1). These include- (1) unusually high Al_2O_3 and Na_2O and low P_2O_5 compared to other granitic rocks of comparable SiO_2, (2) considerable variation in some elements (e.g TiO_2, Na_2O and Sr) at almost constant silica content, (3) pronounced depletion in HFSE, especially Ti, Y and Yb, (4) a markedly depleted REE pattern (Figure 15.7), and (5) strongly enriched Pb and Sr relative to Ce and Nd, imparting large spikes in these elements on multi-element diagrams (Figure 15.6).

As such, Deep Creek type rocks do not plot within the granitic array and cannot be formed by fractional crystallisation from any other GRC granitic type or simple mixing between any known mafic and felsic GRC magmas. An origin by plagioclase accumulation is precluded by the slightly negative Eu anomaly (Figure 15.7). Although the REE pattern resembles that of Kassingbrook Granodiorite **97-376A** (Figure 15.7), derivation of Deep Creek types by direct melting of metasedimentary rock is very unlikely, given- (1) the content of hornblende, (2) lack of metasedimentary enclaves or field association with migmatites, and (3) considerable displacement from the compositional field of *in situ* partial melts or metasedimentary rocks on variation diagrams (Figure 16.1).

Instead, the geochemistry of Deep Creek type plutons is similar to that of adakites, distinctive Na-rich intermediate to felsic lavas (i.e. hornblende andesites to rhyolites) erupted in some oceanic and continental arcs (Table 16.2). This is most evident in- (1) the high Al_2O_3, Na_2O and Sr contents (2) striking similarity of primitive mantle-normalised multi-element patterns, especially regarding high Zr/Sm and Y depletion (Figure 16.20), and (3) steep chondrite-normalised REE trend, with very low HREE contents and negligible Eu anomaly (Figure 16.20).

Average	*Deep Ck type*	*Average adakite*	*Cenozoic adakite*	*El Valle Dacite (Panama)*	*Dacite (Panama)*	*Adakite (Philippines)*	*Adakite AVZ (S. Chile)*
	n = 6	n = 394	n = 140	n = 10	LY29-2-88	Q90-21	Reclus-2
SiO_2	68.37	67.91	63.89	66.63	67.60	64.80	67.00
TiO_2	0.20	0.42	0.61	0.38	0.34	0.31	0.40
Al_2O_3	17.46	16.58	17.4	16.86	16.50	16.75	16.60
Fe_2O_3t	1.98	3.66	4.67	3.06	2.50	3.19	3.88
MnO	0.08	0.06	0.08	0.09	0.06	0.07	0.09
MgO	0.78	1.53	2.47	0.95	0.88	1.81	1.49
CaO	4.25	3.89	5.23	4.54	3.90	2.57	4.43
Na_2O	4.20	4.77	4.40	4.18	4.40	7.36	4.19
K_2O	2.02	1.67	1.52	1.56	2.22	2.44	1.53
P_2O_5	0.10	0.14	0.19	0.15	0.12	0.16	0.17
Mg#	0.44	0.43	0.48	0.36	0.41	0.53	0.41
Na/K	2.08	2.86	2.89	2.95	1.98	3.0	2.74
Sr/Y	120	104	121	71	86	123	59
$(La/Yb)_N$	9.3	24	13.3	7.7	16.6	5.5	12.1
Zr/Sm	97	65	47	47	28	52	53

Table 16.2. Comparison between Deep Creek type granitic rocks and adakites. Note that the quoted $(La/Yb)_N$ and Zr/Sm values for Deep Creek types are those of Deep Creek Granodiorite **97-DC**. Data sources are: average adakite and Cenozoic adakite, Drummond *et al.* (1996); El Valle Dacite (Central American arc), calculated from data in Drummond & Defant (1990) and Defant *et al.* (1992); Panama dacite LY29-2-88, Defant *et al.* (1992); Philippines adakite Q90-21, Sajona *et al.* (1993); Austral Volcanic Zone (AVZ) adakite from Stern & Kilian (1996).

These features are most unlike those of 'normal' subduction-related dacites-rhyolites (see Drummond *et al.* 1996). Moreover, the combination of impoverished Y (mostly <7 ppm) and moderately high Sr contents in Deep Creek types result in unusually elevated Sr/Y (to ~240). This is much higher than other GRC granitic rocks and classical island or continental arc andesite-dacite-rhyolite (ADR) suites, but diagnostic of the adakite magma type (Drummond & Defant 1990) (Figure 16.21). The strongly depleted Yb of **97-DC** (Yb_N ~3.4) is also typical of adakites, which have Yb_N<7 (Martin 1986).

16.9.2 Origin of adakites

Since adakites are confined to certain convergent margin settings, their formation is implicitly linked to the subduction of oceanic crust. However, unlike other arc magmas, the geochemical character of adakites requires high pressure partial melting of a basaltic source (>15 kbar at >700°C), involving elimination of plagioclase and formation of a garnet amphibolite or eclogite residue (see reviews by Defant & Drummond 1990, Drummond & Defant 1990, Peacock *et al.* 1994, Drummond *et al.* 1996, and Martin 1999). Under these conditions, Sr behaves incompatibly, whereas Y and HREE are retained by residual garnet, imparting the characteristic high Sr/Y and La/Yb but low Y and HREE signature of adakites (references as cited above).

Breakdown of plagioclase and formation of a subaluminous refractory assemblage also accounts for the high Al_2O_3 (Drummond *et al.* 1996). Most uncertainty with adakite genesis concerns the nature of the basaltic source. Many petrogenetic models infer derivation of adakitic magmas by direct fusion of the MORB component in the descending slab of oceanic lithosphere, which requires atypical subduction conditions (see Drummond *et al.* 1996 and section 17.2.2c). However, mafic, garnet-bearing lower crust may also be a viable source candidate in overthickened continental arc terranes (Atherton & Petford 1993), such as the Andean Volcanic Zone (Davidson *et al.* 1990).

Given the remarkable chemical resemblance to modern adakites, formation by melting a metabasaltic protolith at the amphibolite-eclogite transition is also apposite for Deep Creek type plutons. Further, the very high Zr/Sm of Deep Creek types indicates a fundamental role for residual amphibole during magma genesis, as this excludes Zr relative to Sm (Pearce *et al.* 1992), indicating that melting occurred below the amphibole-out curve (Figure 16.22).

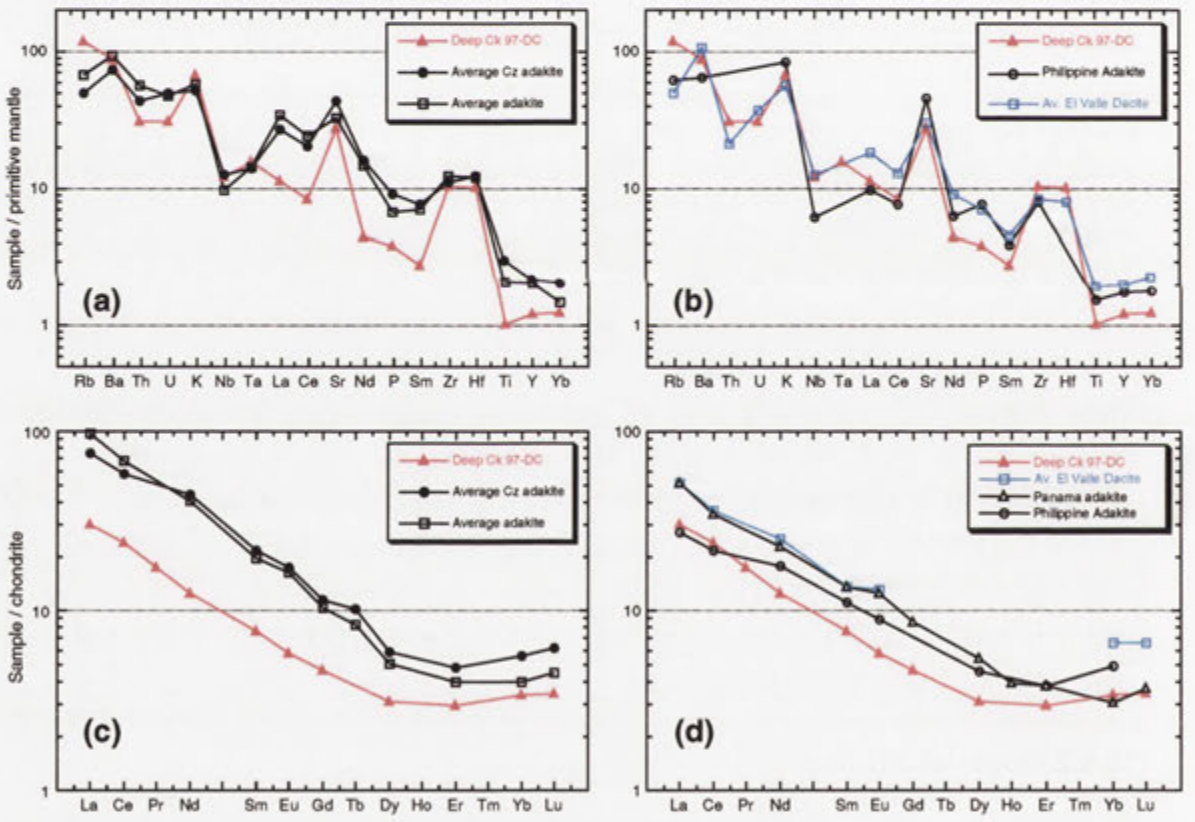

Figure 16.20. Comparison between Deep Creek Granodiorite **97-DC** and adakites in terms of primitive mantle-normalised multi-elements (a and b) and chondrite-normalised REE (c and d) (normalising data as for Figures 14.8 and 14.9). The average adakite and Cenozoic adakite are from Drummond *et al.* (1996) (see also Table 16.1), the Philippine adakite is sample Q90-21 of Sajona *et al.* (1996), and the average El Valle Dacite (from the Central American arc) is calculated from data in Drummond & Defant (1990) and Defant *et al.* (1992). The Panama adakite in (d) is also from Defant *et al.* (1992) (sample LY29-2-88, see Table 16.2), and is plotted because the middle REE data are unavailable for the El Valle Dacite.

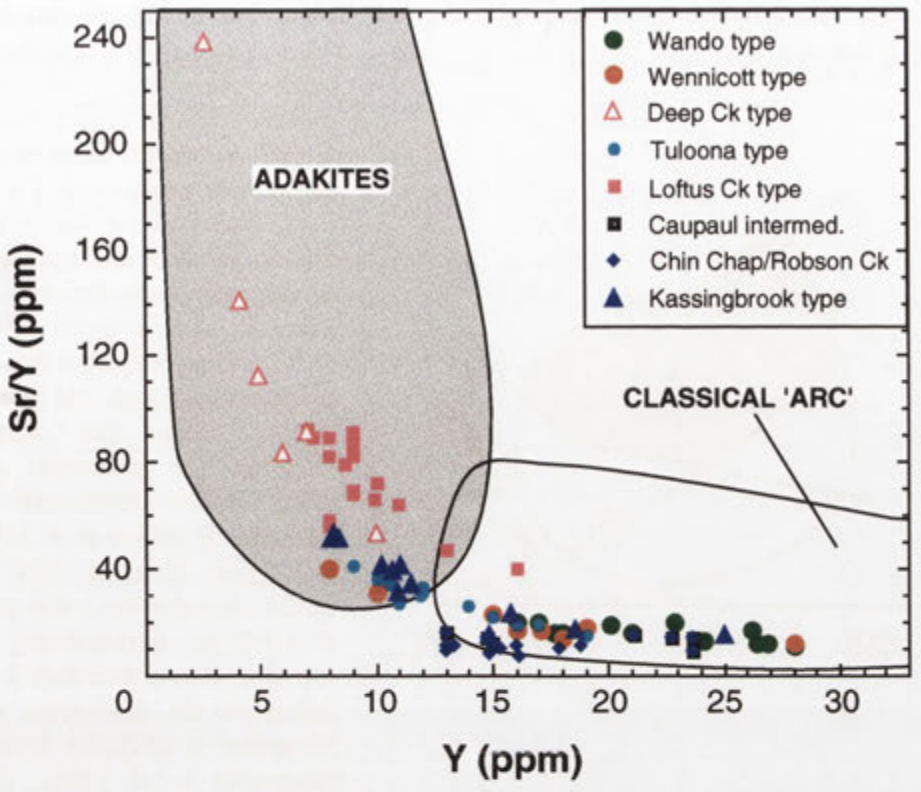

Figure 16.21. Plot of Sr/Y versus Y for GRC igneous rocks, showing discrimination between adakitic (grey field) and classical arc calc-alkaline (white field) compositions (from Drummond & Defant 1990). Owing to high Sr contents, Wennicott, Tuloona, Loftus Creek and Kassingbrook types extend into the adakite field, though these have systematically lower Y contents than Deep Creek type plutons.

Accordingly, **97-DC** almost exactly matches the calculated magma composition produced by 30% partial melting of a MORB source, leaving a 10% garnet amphibolite residue (Drummond *et al.* 1996) (Figure 16.23). The modelled 30% partial melting value is probably not fortuitous, as this represents the optimum melt fraction for segregation from a garnet- and hornblende-bearing metabasaltic protolith (Rapp 1995). Significant residual amphibole could also impart the marked Ti and Nb depletion of **97-DC**, as these are strongly amphibole-compatible. However, HFSE could also be retained in the source region by a refractory titanate phase such as rutile or ilmenite, consistent with the residual occurrence of these minerals in hornblende dehydration melting experiments (e.g. Rapp *et al.* 1991).

A minor discrepancy is that Deep Creek type plutons are isotopically more evolved than most adakites, which, according with derivation from MORB and the common intra-oceanic setting, typically have $^{87}Sr/^{86}Sr$ below 0.7045 (Drummond *et al.* 1996). This requires a radiogenic component in the source region of Deep Creek types, and/or crustal contamination during magma ascent and emplacement. Both possibilities are evaluated in the next chapter.

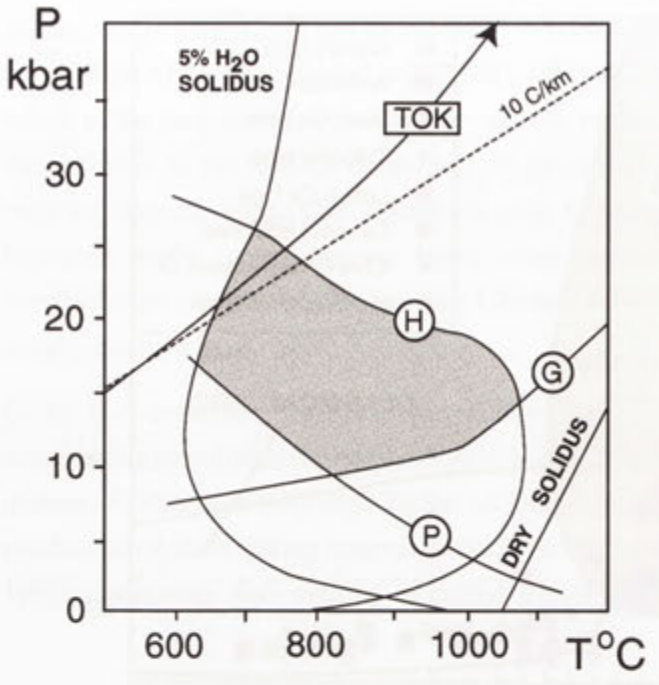

Figure 16.22. P-T diagram depicting the dry (Wyllie 1971) and 5% hydrous basalt solidus (Green 1982), with the stability fields of garnet, plagioclase and hornblende, delimited by the G, P and H lines respectively. The shaded field, bracketed by the wet basalt solidus, garnet-in and hornblende-out curves, represents the P-T regime where an adakitic liquid derived by partial melting of hydrous tholeiite can coexist with a garnet- and hornblende-bearing residue (i.e. hornblende eclogite). The geothermal gradient along modern subduction zones, estimated by Toksov *et al.* (1971), is also shown (labelled 'TOK"). The dashed line represents a slab geotherm of 10°C/km, corresponding to the special conditions necessary to initiate fusion of the descending oceanic lithosphere in subduction zones (from Drummond *et al.* 1996). Diagram modified after Martin (1999).

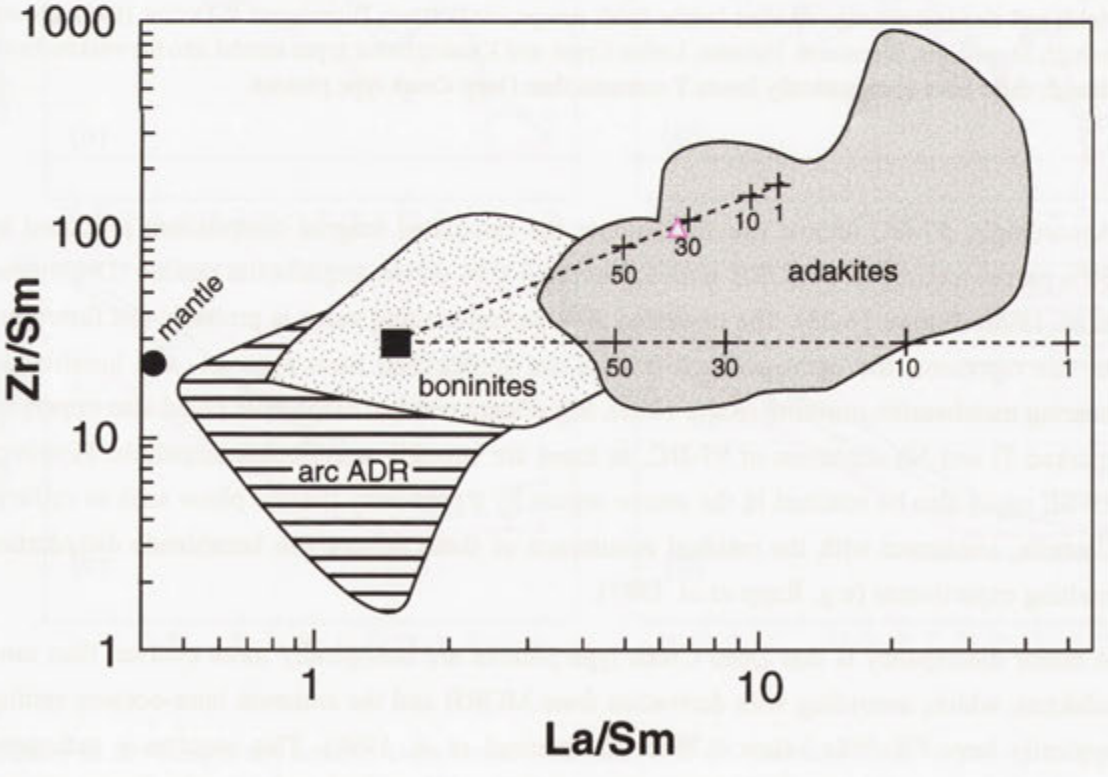

Figure 16.23. La/Sm versus Zr/Sm (all in ppm) showing the fields of 'arc' ADR suites, boninites and adakites relative to partial melting curves of MORB (black square) leaving either a 10% garnet amphibolite (top curve) or eclogite (lower curve) residue. Partial melting percentages along each curve are indicated (modified after Drummond *et al.* 1996). The Deep Creek Granodiorite **97-DC** (pink triangle) plots along the upper curve, very close to the 30% melting value.

16.10 Summary

The striking geochemical dichotomy of GRC igneous compositions, represented by the divergent granitic and dioritic arrays, exemplifies two contrasting petrogenetic systems; these are nonetheless fundamentally interrelated in the overall geotectonic evolution of the GRC (Chapter 17). The **dioritic array** derives from crystal fractionation/accumulation processes from a primitive boninitic magma ('HMD'), which intruded pre- to syn-D_2 in the Caupaul Igneous Complex and post-D_3 in the southeastern GRC. The former area contains fractionated derivatives from this parental magma, whereas the latter exposes a range of mafic cumulate compositions. HMD magmas were also involved in granitic formation, conferring an important role in the magmatic evolution of the GRC, and linking the disparate granitic and dioritic arrays in a petrogenetic sense. Emplacement of Deep Creek type 'adakitic' plutons coincided with the first pulse of HMD magmatism, which is not fortuitous, as adakites and boninites are spatially and genetically related in many modern subduction zone environments (section 17.2.2c). This association places powerful constraints on the physiochemical conditions of magma formation during Delamerian orogenesis.

Rocks of the **granitic array** were generated by combination between mafic magma and segregated partial melt from metasedimentary protoliths, different granitic types having different mafic end-members. Hence, despite the diversity, all granitic rocks are related by commonality of process and inextricably linked to the host metasedimentary sequence through *in situ* anatexis and leucosome formation. This explains the striking coherence of the GRC granitic system, from both a field and geochemical perspective. The changing nature of granitic magmatism throughout the deformational history of the GRC, leading to formation of the various metaluminous/weakly peraluminous granitic types, reflects an interplay between three factors-

(1) the geochemical evolution of the mantle-derived component in the mixing system,

(2) the involvement of different felsic end members,

(3) the growing significance of fractional crystallisation.

The development of the granitic array, depicted schematically in Figure 16.8, can be summarised as follows. Intrusion of Caupaul gabbros synchronous with crustal anatexis pre- to syn-D_2 resulted in generation of Wando type diorites-tonalites. The distinctive high-Al signature of this group therefore images that same feature in the gabbroic end-member. Steep progression through to more K-rich compositions results from increasing proportion of potassic metasedimentary-derived partial melt. Fractional crystallisation of Caupaul gabbros produced the more evolved mafic end-member of Wennicott type granitic rocks. As a result, mafic Wennicott types are more potassic and incompatible element-rich than Wando types of similar silica, though plutons were driven to lower K_2O contents by blending with metasedimentary-derived leucotonalitic partial melt. Continued interaction between evolved basaltic liquid and K-poor partial melt after D_2 yielded the parental Tuloona type tonalites, the fractionation of which yielded more potassic compositions. In contrast, Kassingbrook types record interaction between crustal melt and coeval boninitic magmas, resulting in formation of distinctive hornblende-bearing 'hybrid' tonalites.

Here, the marked K_2O variation and high Sr content characteristic of metasedimentary-derived partial melt is overprinted by the distinctive high Mg, high Cr boninite signature. High-Al basalt and boninite intrusion was supplanted late in the structural history by shoshonitic magmatism, resulting in generation of the relatively K-rich Loftus Creek type granodiorite. The inherent potassic nature of these was amplified by subsequent fractionation. Lastly, even more potassic and fractionated magmas, the Dergholm types, were emplaced after compressional deformation, and are also linked to basalt intrusion (Turner *et al.* 1992; sections 3.5.1). The dominance of fractional crystallisation late in the magmatic evolution of the GRC is a notable feature, and could result from progressive orogenic crustal thickening, providing greater opportunity for differentiation during magma ascent.

Ignoring the effects of fractionation, it is obvious that the definitive geochemical features of the GRC granitic types reflect the different mantle components of their parentage and the processes involved in generating the felsic end-member from metasedimentary rock. That the former ultimately result from subduction partly accounts for the general resemblance to igneous rocks formed at convergent margin settings (section 15.5). However, processes involved in forming the felsic end-member are also pivotal in this regard. For example, the efficient segregation of the crustally-derived partial melts from their mafic residues is instrumental in imparting a low TiO_2 signature to the various GRC granitic types, this being typical of supra-subduction zone lavas. The paucity of metasedimentary 'restite' enclaves in metaluminous to weakly peraluminous GRC granitic types despite the significant supracrustal ingredient is further testament to the effective extraction of the felsic end-member partial melt. This effect also explains the low REE concentrations of each granitic type relative to the metasedimentary protolith and mantle-derived end-member, as REE-accommodating minerals have limited solubility in low-T, fluid-rich melt and are concentrated within refractory biotite, which is not entrained. High Sr contents are another arc-like feature of GRC plutons, which, for mafic samples, were clearly inherited from the subduction-related mafic end-member. However, the high Sr contents of felsic plutons reflects both- (1) the Sr-rich nature of the metasedimentary protolith, and (2) the preferential partitioning of this element into leucosomes during anatexis, as fluid-rich melting facilitated elimination of plagioclase. Involvement of a leucotonalite end-member is responsible for the overall low-K and calcic character of Wennicott types, and of the unfractionated Tuloona type tonalites, both of which characterise granitic rocks of subduction environments (section 15.5).

Chapter 17: A synthesis of the magmatic and tectonic evolution of the GRC and eastern Delamerian Orogen

17.1 Introduction

Unequivocally subduction-related igneous rocks intruded throughout the deformational history of the GRC. These range temporally from medium-K arc basalts (Caupaul gabbros) to shoshonites, a sequence typically associated with arc 'maturation', but also include adakitic plutons and boninitic diorites. This hitherto unrecognised aspect discredits previous tectonic models for the GRC (e.g. Taylor *et al.* 2000; section 2.5) and, by extension, the eastern Delamerian Orogen, and is only reconciled by development of the terrane in a supra-subduction zone setting. The significance of this is amplified by the critical role of these subduction-related mafic magmas in generating GRC granitic rocks, whereby the systematic geochemical evolution of granitic types throughout convergent orogenesis reflects the parallel evolution of the mafic, arc-derived ingredient in the mixing system. The spectrum of igneous rock compositions in the GRC is therefore the direct manifestation of physiochemical processes operating in an actively evolving Cambrian subduction zone, which must also control the structural and metamorphic development of the terrane as well.

The purpose of this final chapter is to - (1) use igneous rock compositions and their changes throughout the deformational history to deconvolve the physiochemical evolution of the subduction regime, and erect a coherent tectonic framework for the GRC. Particularly instructive in this regard is the occurrence of boninites and adakites, whose formation requires specialised conditions only rarely realised in modern arcs, and (2) to elaborate the geological evolution of the GRC from an integrated magmatic, metamorphic and tectonic perspective, thereby presenting the first comprehensive geodynamic synthesis of the eastern Delamerian Orogenic Belt. This will also incorporate physical models for formation of the granitic rocks, to complement the previous geochemical models. The pertinent magma generation models for subduction zone environments are reviewed in Appendix H, to provide the background for the following discussion.

17.2 Magmatic and tectonic evolution of the GRC

The inferred model for the tectonic development of the GRC and eastern Delamerian Orogenic Belt is shown in Figure 17.1, and envisages the Delamerian Orogeny as resulting from arc-arc collision at a west-dipping subduction zone. The model is subdivided into six stages, and discussed below in parallel with Figure 17.2, which tracks the lithological and geochemical evolution of the GRC.

17.2.1 STAGE 1: Passive, pre-orogenic sedimentation

Prior to the Delamerian Orogeny, the eastern Gondwana margin in southeastern Australia is envisaged as a tectonically stable Proterozoic continental margin - back-arc basin - rifted forearc

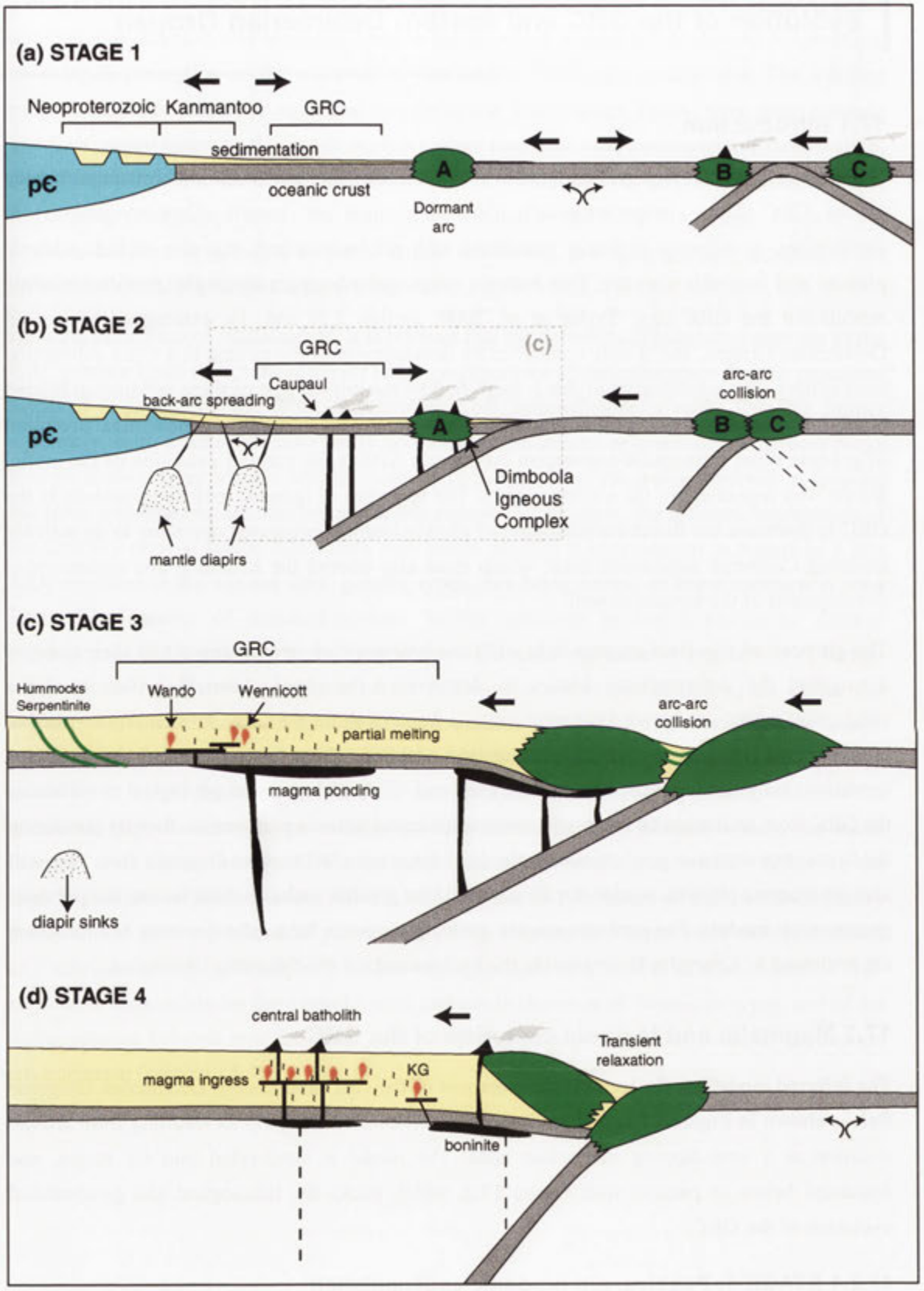
(a) STAGE 1
Neoproterozoic
Kanmantoo
GRC
sedimentation
pC
oceanic crust
A
Dormant arc
B
C
(b) STAGE 2
GRC
(c)
Caupaul
back-arc spreading
arc-arc collision
pC
A
B
C
Dimboola Igneous Complex
mantle diapirs
(c) STAGE 3
GRC
Hummocks Serpentinite
Wando
Wennicott
partial melting
arc-arc collision
magma ponding
diapir sinks
(d) STAGE 4
central batholith
Transient relaxation
magma ingress
KG
boninite

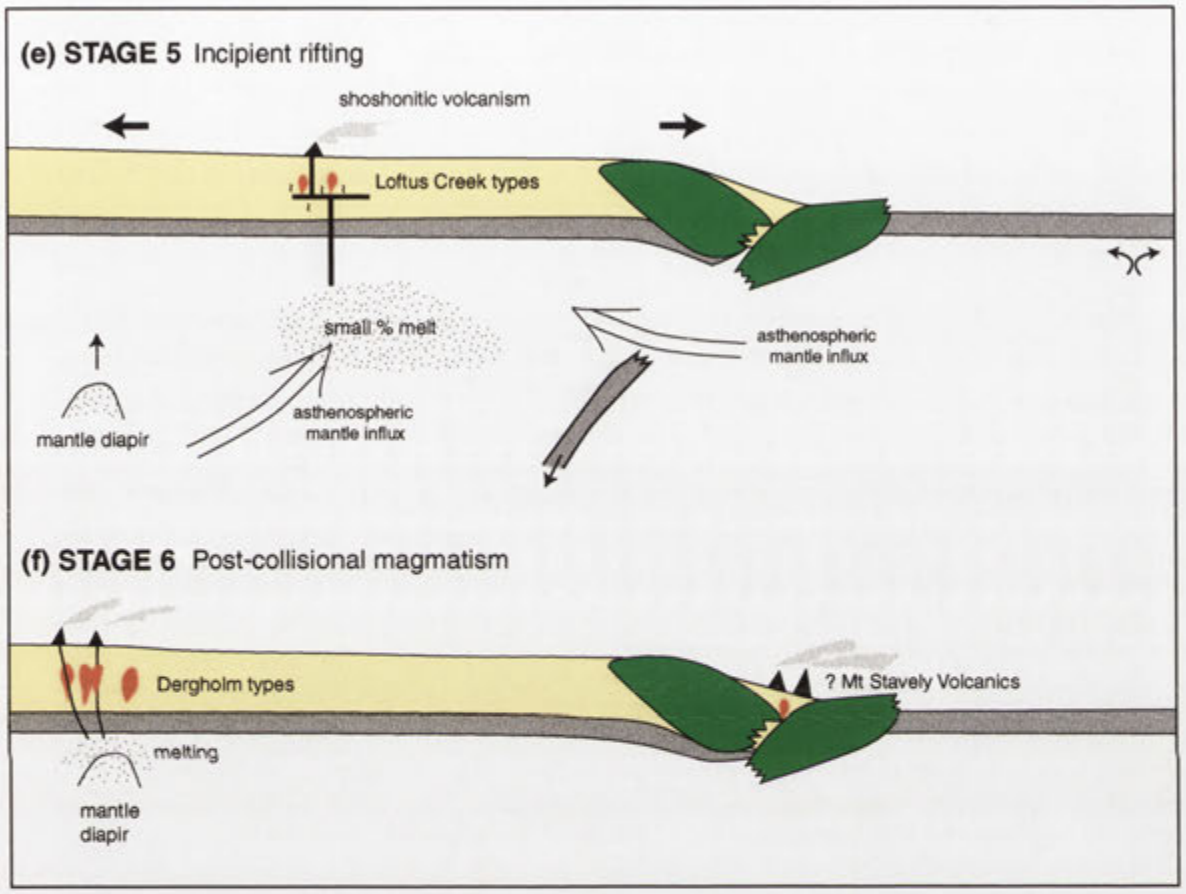

Figure 17.1. Simplified and schematic model of the Delamerian Orogeny in southeastern Australia, as deduced by this study. Arrows indicate the direction of plate motion and tectonic stresses.

(a) Stage 1. Passive, pre-orogenic sedimentation.

(b) Stage 2. Collision between outlying arcs, initiation of subduction and back-arc spreading. Generation of high-Al gabbros and boninites. Rapid closure of the oceanic basin to the east.

(c) Stage 3. Arc-arc collision, isoclinal folding and crustal thickening of the marginal basin turbidite sequence. Formation of early syn-compressional plutons, ponding of arc magmas.

(d) Stage 4. Transient relaxation, ingress of pooled arc magmas, extensive *in situ* anatexis and formation of the central batholith. Boninite intrusion, formation of Kassingbrook types (KG).

(e) Stage 5. Incipient rifting, shoshonite generation and production of Loftus Ck type plutons.

(f) Stage 6. Asthenospheric upwelling, emplacement of post-collisional granitic belt.

scenario, with oceanic crust extending some distance to the east (Figure 17.1a). The open ocean regime in the east is confirmed by the metamorphosed tholeiitic-boninitic volcanic associations of the Heathcote Belt in central Victoria and the Mount Wellington Belt in eastern Victoria (see Figure 2.3), which comprise part of Cambrian intra-oceanic island arc - back-arc basin systems (Crawford *et al.* 1984; Crawford & Keays 1987). The configuration in Figure 17.1a plausibly developed during earlier Chilean-style subduction of the Pacific plate underneath the ancient Gondwana craton; such convergence is postulated further south in eastern Antarctica, commencing ~550 Ma, to explain the formation of the Granite Harbour Intrusives (Ricci *et al.* 1997). West-directed subduction along the Tasmanian portion of the Gondwana margin is also envisioned at this time (Everard 2000), though the situation here is more complex (see below). Although subduction persisted beneath Antarctica until ~500 Ma, its cessation along the southeastern Australian Gondwana segment sometime in the Early to Middle Cambrian stalled active back-arc rifting and marginal sea opening. At this stage (and also during the previous convergence), thick terrigenous sediment piles were accumulating in the marginal basin, introduced by turbidity currents. Detritus was probably locally sourced from the rifted continental margin and volcanic apron of the remnant forearc, though zircon age inheritance patterns (in Kanmantoo Group metasediments) suggest that the subduction-related volcanic-plutonic rocks of Antarctica further south were the major provenance (Ireland *et al.* 1998, see discussion in Veevers 2000). This resulted in formation of the GRC sedimentary protoliths proximal to the arc, whereas the Kanmantoo group further west manifests deposition of similar materials adjacent to the continental margin. The immature, feldspathic nature of the Kanmantoo-GRC metasedimentary sequence therefore reflects the intermediate to felsic igneous provenance and minimal transport and reworking of the arc-derived detritus, as accords with turbiditic deposition. VandenBerg *et al.* (2000) speculate that GRC sediments overly an attenuated Proterozoic crustal substrate. However, at present there is no evidence of Proterozoic crustal fragments in western Victoria, and it is therefore more likely that GRC turbidites blanket purely oceanic crust.

17.2.2 STAGE 2: Initiation of subduction and onset of the Delamerian Orogeny

(a) Back-arc spreading

The first magmatic manifestation of the Delamerian Orogeny was the submarine intrusion of MORB-like dolerites and gabbros in the southwestern GRC (Figure 17.2a) and Mount Lofty Ranges, now converted to metabasites. In South Australia, these rocks are thought to be related to intra-cratonic rifting near the Gondwana continental margin in the Early Cambrian (Belperio *et al.* 1998). A rifting interpretation is also favoured in the GRC by VandenBerg *et al.* (2000), with eruption in an oceanic setting. However, MORB-like emplacement in South Australia and western Victoria persisted during compressional deformation (D_1 and D_2), suggesting that these rocks relate in more direct fashion to the underlying causes of the orogeny. As such, it is proposed that they record the initiation of back-arc extension and upwelling of asthenospheric mantle, resulting from the rejuvenation of active subduction beneath the quiescent forearc at ~510-500 Ma (Figure 17.1b). This is supported by the N-MORB to E-MORB type compositions

of the GRC metabasites, some of which have arc signatures (section 3.3), diagnostic of back-arc basalts whose mantle source is being progressively modified by an enriching slab-derived component (e.g. Pearce *et al.* 1994). For subduction to recommence requires that the dormant marginal basin - remnant forearc system passed abruptly from a passive or extensional regime to a compressional/convergent regime, as could be facilitated by collision between two outboard island arcs (Figure 17.1b). Given the magnitude and trans-Gondwana scale of the Delamerian Orogeny, it is also possible that resumption of subduction was linked to a global plate rearrangement at this time.

(b) Volcanic arc / forearc magmatism

Resumption of westward subduction near the southeastern Australian continental margin at ~510-500 Ma would also result in renewed volcanic activity at (or near) the older rifted arc front. The contemporary location of these eruptive products is uncertain, given intense later deformation, faulting and the cover of younger volcanic and sedimentary rocks. They may now be partly represented by the metabasites of the Black Range Volcanics at the western fringe of the Grampians Ranges (section 2.4.1). An obvious candidate for the forearc portion of the postulated Cambrian volcanic arc is the mafic to ultramafic Dimboola Igneous Complex (section 2.4.1), the predominant boninitic component of which indicates formation in a near-trench setting. Boninite generation requires anomalously high heat flow in the sub-forearc mantle wedge (Appendix H), and typically occurs at the inception of subduction into thermally undisturbed mantle, as proposed here. An enhanced thermal gradient in the forearc region of the rejuvenated Cambrian arc is also consistent with- (1) the likelihood that the consumed oceanic crust was newly born by back-arc spreading processes (Figure 17.1a), as virtually confirmed by the occurrence of adakites (below), and (2) the onset of subduction being coeval with the re-initiation of back-arc spreading, as this allows replacement of 'cold' forearc mantle by hot asthenospheric mantle advected from the back-arc (Shimoda *et al.* 1998).

In summary, thermal conditions at the arc front during the re-initiation of subduction enabled boninite generation. It is therefore probable that part of the Dimboola Igneous Complex formed *in situ* above a west-dipping subduction zone, contrasting with the outboard or allochthonous origin proposed by Taylor *et al.* (2000) and VandenBerg *et al.* (2000) (see section 2.5). Independent support for this is that boninites, low Ti tholeiites and ultramafic cumulates were also forming further south in Tasmania during intra-oceanic subduction prior to the Tynnean Orogeny (Crawford & Berry 1992; Everard 2000). However, the geometry of the Cambrian subduction-accretion system in Tasmania is in dispute, with both east-directed (Crawford & Berry 1992) and west-directed (Everard 2000) subduction proposed.

(c) Rear-arc magmatism

The geochemistry of high-Al metagabbros in the southwestern GRC also suggest the formation of a chain of rear-arc basaltic volcanoes behind the rejuvenated forearc during this active subduction phase, the eroded magma chamber of one being the Caupaul Igneous Complex (Figure 17.2a). Adakitic lavas also formed in the rear arc at this time (i.e. Deep Creek type

plutons), and were most likely derived by fusion of subducted oceanic lithosphere at the amphibolite-eclogite transition. This is because the alternative, melting a mafic lower crustal source, requires exceptionally thick crust (>50 km) (Drummond *et al.* 1996), unrealistic for the proto-GRC in the Cambrian. Importantly, modern adakitic volcanism is restricted to subduction zones with abnormally high geothermal gradients (see Appendix H), mostly where young (<25 Ma), hot oceanic lithosphere is being subducted (Defant & Drummond 1990; Drummond *et al.* 1996), or at the inception of subduction into warm, pristine mantle, before significant depression of geotherms by the foundering oceanic lithosphere (Peacock *et al.* 1994). The generation of slab-derived melts in the GRC therefore supports the notion that the terrane developed above an infant west-dipping subduction zone, consuming young, hot oceanic crust.

Apart from depleted mantle and basaltic crust, the evolved initial Sr and Nd isotopic composition of Caupaul gabbros and Deep Creek type plutons requires substantial involvement of crustal material in their genesis. This has been attributed to contamination by crustal partial melts or metasedimentary rock upon intrusion into the marginal basin turbidite sequence (section 16.4.3). However, part of the evolved isotopic signature of these rocks could also result from the subduction of sedimentary materials. The most convincing demonstration of this effect is provided by the oceanic Tonga-Kermadec (Gamble *et al.* 1993) and Lesser Antilles (White & Dupre 1986) arcs. Lavas from these become systematically more enriched and isotopically evolved from north to south, reflecting greater sediment input with increasing proximity to New Zealand and South America respectively. In this light, introduction of sediment into the mantle melting zone of Caupaul gabbros would be inevitable, given the proximity of the Cambrian subduction zone to a Proterozoic continental landmass, and the imminent collision with an outboard arc, shedding further arc-derived detritus into the trench. Furthermore, melting of the sediment component during subduction is also favoured, given- (1) the high geothermal gradient along the descending slab, and (2) the likelihood that that the subducted sediment is terrigenous rather than pelagic, being dominated by 'minimum melting' constituents quartz and feldspar. For Caupaul gabbros, infiltration of sediment-derived melt into the depleted mantle source would impart evolved Sr and Nd isotopic compositions to derivative magmas. This also has important implications for the trace element geochemistry of Caupaul gabbros, as some elements, such as Zr and Nb, are preferentially transported from the slab into the mantle melting column by silicate melt rather than aqueous fluid (Pearce & Peate 1995). Participation of subducted sediment in the formation of adakitic melts during slab fusion is intrinsically unavoidable; this is proposed to explain the elevated $^{87}Sr/^{86}Sr$ (~0.7055) of adakitic lavas in the Andean Austral Volcanic Zone relative to those erupted in oceanic settings (Stern & Kilian 1996).

Importantly, the Caupaul Igneous Complex also incorporates boninitic rocks (high-Mg diorites/tonalites), suggesting that elevated temperatures were attained in the shallow mantle wedge at some distance from the forearc. Sediment-derived partial melts may also have been instrumental in the production of these. A plausible mechanism is that boninitic magmas were generated upon addition of a water-rich sediment melt to shallow, refractory peridotite, previously depleted by extraction of arc basalt (i.e. Caupaul gabbro). The extra heat input required for second stage mantle melting could result from proximity to hot upwelling

asthenosphere and MORB magmatism in the back-arc region. Strong support for this proposition lies in the striking geochemical similarity of Caupaul high-Mg diorites with boninites of the Setouchi Volcanic Belt (SW Japanese arc) (Figure 16.7), where this petrogenesis is inferred (Shimoda *et al.* 1998). Here also, boninite generation occurred adjacent to a continental landmass and was triggered by commencement of back-arc spreading (section H4.2 in Appendix H). Similar processes must be responsible for formation of the Chin Chap/Robson Creek boninites further east and slightly later in the deformational history, given the resemblance between the inferred parental magmas. An alternative possibility, that the GRC boninites were produced by adakite-peridotite reaction in the shallow mantle wedge (see section H4.1, Appendix H), cannot be precluded, but is less likely as Caupaul diorites lack the distinctive high Na_2O, high Sr signature imparted by an adakitic source component (see Pearce & Peate 1995). The isotopic compositions of the high-Mg GRC diorites are required to further evaluate these possibilities.

(d) Metamorphism and deformation

Basaltic and boninitic magmas generated during the short burst of subduction intruded the thick, water-rich and immature turbidites of the southwestern GRC. Inevitably, this, combined with enhanced heat flux from upwelling mantle in the back-arc, promoted extensive metamorphism and *in situ* partial melting of the sequence (i.e. M_1), and is believed responsible for formation of the low-P high-T regional metamorphic zonation (Figure 17.2a). Note that the symmetrical distribution of high grade metamorphic zones and migmatites around the central granitic belt further east indicates that the major heat source driving metamorphism was actually located in the central GRC. Hence, most arc-derived basaltic magma was initially channelled through this part of the terrane en route to eruption. It is also possible that the first deformational fabric in the GRC metasedimentary sequence (S_1) developed at this time, in response to transient compression behind the arc during vigorous subduction. The D_1 fabric might also signal the incipient stages of the major impending collision.

17.2.3 STAGE 3: Arc-arc collision

The major convergent stage of the Delamerian Orogeny in southeastern Australia (D_2) involved terrane-wide isoclinal folding, crustal thickening and development of the pervasive S_2 foliation. This is attributed to a major collisional event at the arc front, perhaps as an outboard island arc was progressively drawn westwards during subduction to ultimately collide with the trench (Figure 17.1c). Fragments of the colliding arc(s) would be obducted onto the active boninitic forearc (i.e. the Dimboola Igneous Complex) at this time, along with any accretionary wedge materials sandwiched between the converging arcs. Serpentinite diapirs in the forearc basin and accretionary prism would be thrust up and over the active forearc, partly accounting for the ultramafic component of the Dimboola Igneous Complex. Since the leading edge of the encroaching arc would tend to be thrust beneath the active forearc as convergence continued, the latter should be progressively obducted westwards onto its marginal basin (meta)sedimentary sequence. As a result of this arc-craton convergence, the dominantly tensional regime of the rifted continental margin-marginal basin system would revert rapidly to a compressional setting. The effects of this are threefold -

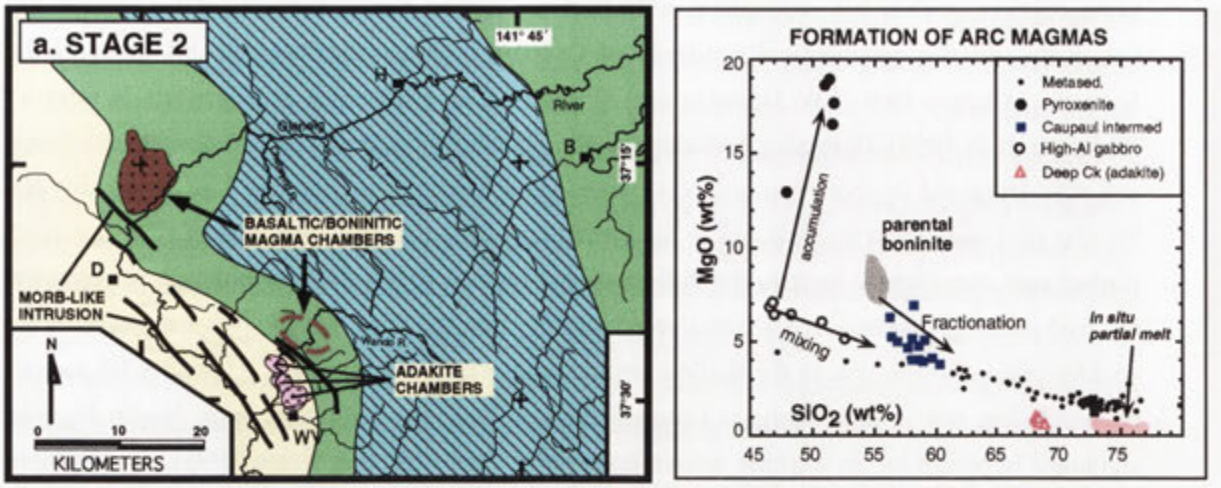

(a) Back-arc MORB intrusion, rear-arc basaltic/boninitic/adakitic volcanism and metamorphism of the turbiditic metasedimentary sequence. Striped pattern indicated extent of *in situ* partial melting. Position of MORB bodies is approximate only.

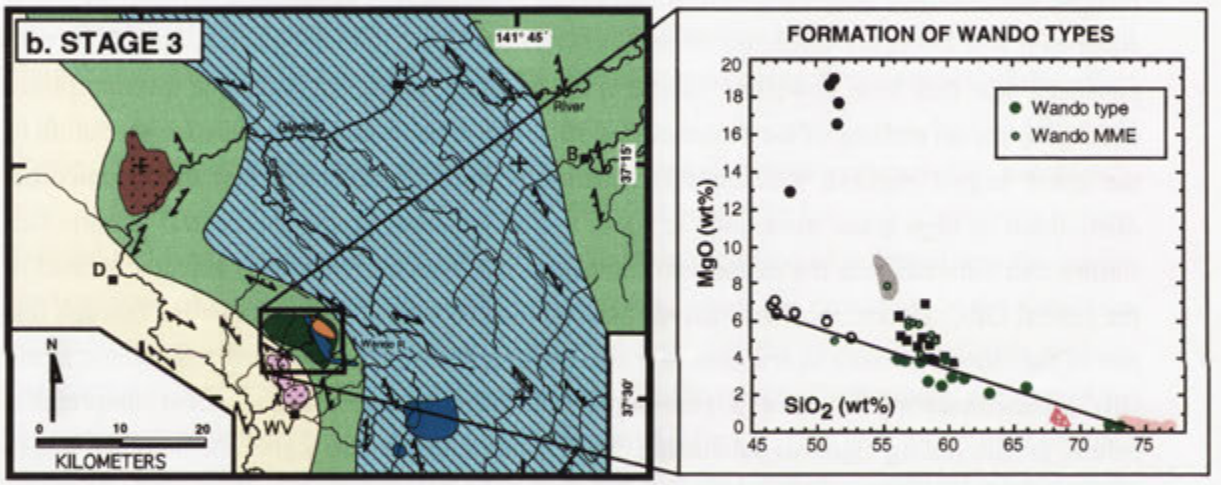

(b) Arc-arc collision, deformation of the sedimentary sequence (D_2), mixing of ponded mafic magmas and crustally-derived partial melts to produce the early syn-compressional Wando and Wennicott granitic types.

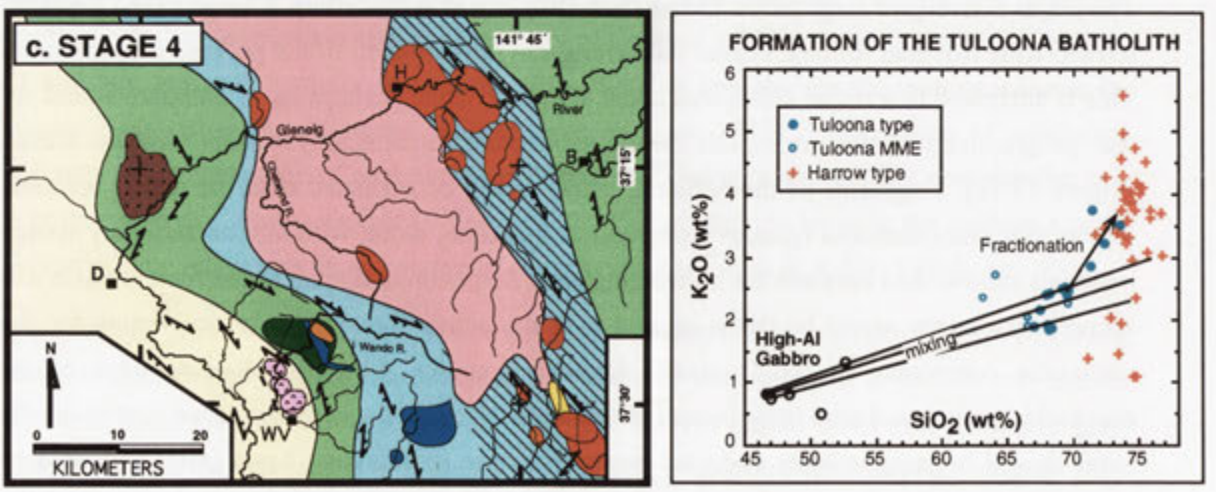

(c) Transient relaxation and concomitant intrusion of basaltic and boninitic magmas, leading to extensive *in situ* anatexis in the northeastern migmatite zone (striped pattern) and formation of Harrow type granitic rocks. Central Tuloona type batholith and Kassingbrook types produced by interaction between these and the various coeval mafic magmas.

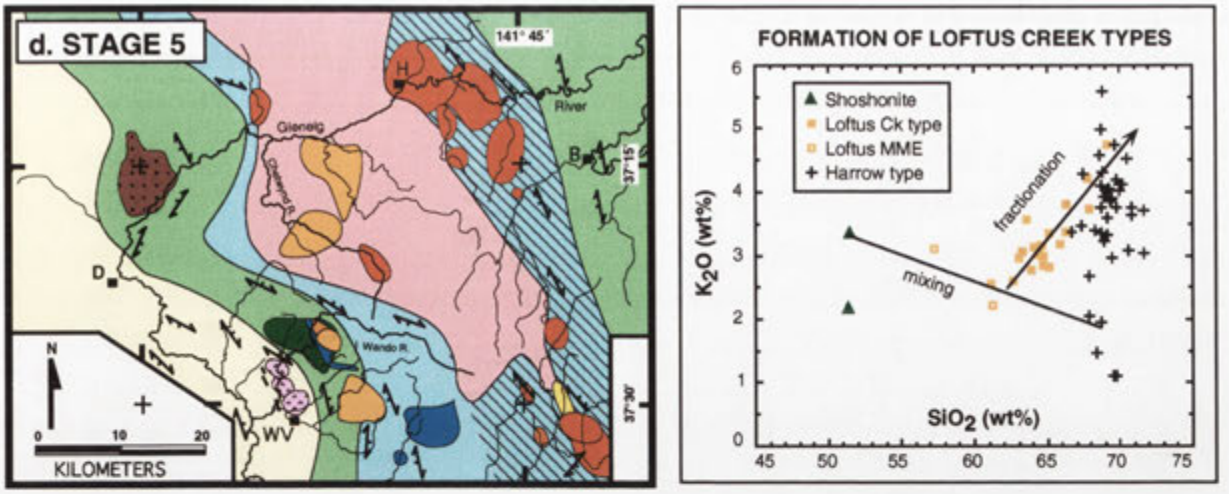

(d) Incipient rifting, intrusion of shoshonite, mixing with metasedimentarily-derived melt to produce Loftus Creek type putons (extent of *in situ* anatexis is shown by the striped patten).

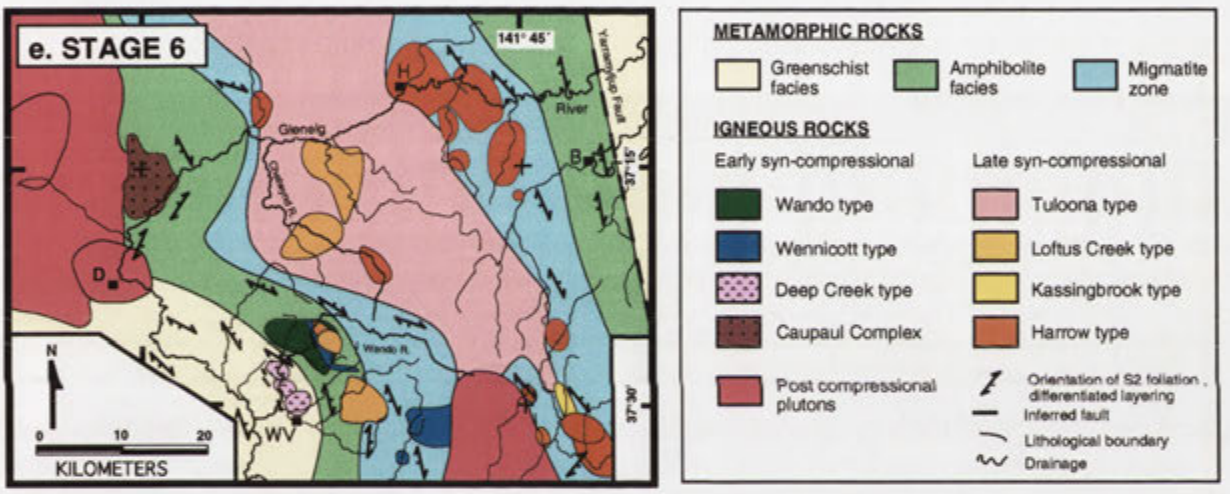

(e) Post-collisional extension, uplift, emplacement of post-compressional granitic rocks. Development of the Yarramyljup Fault.

Figure 17.2. Summary of the geological evolution of the GRC. Geodynamic stages correspond to those of 17.1. Note that the curved metamorphic isograds, imposed by D_5 folding, are retained in all stages to preserve geographical context. The chemical development of important igneous components is shown on the left by selected variation diagrams.

(1) upwelling of asthenospheric mantle diapirs into the back-arc would cease, curtailing MORB emplacement in the southwestern GRC, and explaining the absence of these intrusives after D_2;

(2) the back-arc metasedimentary sequence, partially melted and ductile from passage of arc magmas, would be shortened considerably and thrust westwards towards the craton. Incorporation of rifted oceanic crust fragments and slivers of upper mantle into the telescoped metasedimentary package possibly resulted in formation of the layer parallel metabasalt-serpentinite bodies.

(3) further ingress of high-Al arc basalt and boninite into the deforming supra-crustal sequence would be prohibited. Such magmas would alternatively pond at the crust-mantle interface, some also being trapped in lower crustal magma chambers in the vicinity of the central GRC.

The latter is especially critical in the context of granite formation, as this circumstance promotes extensive interaction between the pooled arc-derived basaltic magma and leucocratic partial melts derived from the surrounding fertile metasedimentary rocks. Ultimately, this produces the early syn-compressional Wando type plutons in deep crustal mixing zones (Figure 17.2b). The mafic nature of Wando type rocks indicates that the crustal ingredient was subordinate in the mixing system, and was probably introduced into a convecting basaltic magma chamber, in a manner similar to that modelled by Huppert & Sparks (1988). Although such interaction was likely to have been complex (see section 1.3.1), blending between the two magmas was possibly favoured by the relatively low T, water-rich nature of the volumetrically predominant basalt (solidifying as hornblende gabbro) and the low viscosity of the felsic magma, which was crystal-poor. Injection of basaltic and boninitic magma pulses into the hybrid, partially crystallised plutons at the emplacement site lead to the distribution and local swarming of type C and type A/B enclaves respectively.

Differentiation of the pooled basalt to more evolved compositions, accompanied by continued mixing with crustally-derived melt, generated the array of Wennicott type plutons (Figure 17.2b). Their wider compositional range suggests that mixing occurred between more variable proportions of the mafic and felsic end-members, implying reduced thermal and viscosity contrasts. This accords with the anticipated lower temperature and higher fluid content of the fractionated end-member mafic magma. Periodic recharge of the hybrid magma chambers by fresh basalt (tapped from underlying magma chambers), yielded the distinctive gabbroic enclaves of Wennicott types.

17.2.4 STAGE 4: Formation of the central granitic batholith

Following the initial collision at the arc front, a transient relaxational/extensional phase is likely, permitting renewed ingress of the ponded arc basalt magmas at the base of the crust into the overlying, thickened supra-crustal sequence (Figure 17.1d). The ascent of these magmas would preferentially occur along previous magmatic conduits, and therefore be localised in the central GRC. The abrupt influx of heat accompanying basaltic intrusion is considered responsible for M_2, whereupon voluminous *in situ* partial melt was generated from the metasedimentary sequence under near water-saturated conditions. The requisite fluid for this anatectic episode was plausibly derived by dehydration of low grade, originally arc-proximal metasedimentary rocks, which would have been underthrust from the east during the arc-trench collision/obduction. The reasons for the confinement of partial melting to the eastern GRC at this time could reflect- (a) waning heat flow in the southwest associated with cessation of back-arc spreading, or (b) that the influx of solidus-lowering aqueous fluid was largely restricted to the east, closer to the collisional zone. Heat flow in the eastern GRC would have also been locally enhanced by the intrusion of boninitic magmas, now represented by the Chin Chap Creek/Robson Creek high-Mg diorites. Continued (but waning) pulses of compressional deformation following the main collisional

event could reflect the spasmodic underthrusting of the leading edge of the colliding arc, as stimulated by ridge-push forces, a readjustment of the arc-trench system to the collisional stresses, and/or rollback or even detachment of the subducted slab from the collided arc (Figure 17.1d). These convergent pulses were registered in the metasedimentary sequence as D_3 and D_4. The latter was essentially localised in the mechanically weakened migmatitic rocks of the northeastern GRC, and (with D_3) was instrumental in stimulating segregation and migration of *in situ* partial melt into the large Harrow type plutons (Figure 17.2c).

Importantly, formation of extensive sheet-like chambers of low-T silicic magma across the central GRC would eventually provide an effective thermal and mechanical barrier to the penetration of basaltic magma into the upper crust. Evolved basaltic liquid, derived from fractionating deep crustal magma chambers, would therefore pool beneath these Harrow type plutons, further accelerating crustal fusion and favouring extensive mingling and mixing between the contrasting mantle-derived and metasedimentary-derived magmas. Ultimately, this would produce a volumetrically important hybrid tonalitic (Tuloona type) magma. The episodic tapping of this during subsequent fractionation produced the different Tuloona type plutons of the central granitic belt (Figure 17.2c). The elongate nature of these plutons, parallel to the former trench, implies structurally controlled, syn-deformational emplacement, perhaps in a transient D_4 dilational site.

Subordinate mixing between boninitic magmas and crustal melts in the southeastern GRC at this time also formed the more mafic Kassingbrook type rocks. Some of these hybrid, high-Mg magmas were subsequently injected into Tuloona type magma chambers, to be dispersed as microgranular enclaves. That such enclaves are widespread throughout Tuloona types suggests that boninite-crustal melt interactions were probably more extensive below the exposure level. It is likely that the boninitic rocks of Chin Chap Creek/Robson Creek were derived by selective tapping of a boninitic magma reservoir ponded beneath the forearc.

17.2.5 STAGE 5: Incipient intra-arc rifting and shoshonitic magmatism

With the termination of subduction by collision at the arc front, the generation of basaltic and boninitic magmas in the underlying mantle wedge ceased, and an extensional tectonic regime became predominant. This circumstance is conducive to incipient rifting of the volcanic arc (Figure 17.1e), as occurred in the Vanuatu arc following collision with an Eocene volcanic edifice (Laporte & Briqueu 1993). Such rifting is commonly accompanied by eruption of high-K to *shoshonitic* lavas. Although shoshonite generation potentially involves multiple sources (see Pearce & Peate 1995), the distinctive arc signature in GRC shoshonites (i.e. pronounced Nb and HREE depletion relative to N-MORB) indicates melting of depleted mantle peridotite that has been overprinted by an enriched subduction component. A similar petrogenesis is inferred for the post-rifting shoshonitic volcanoes of the northern Mariana arc (Lin *et al.* 1989) and the Japanese arc (Pouclet *et al.* 1994), the latter geochemically resembling GRC shoshonites (Figure 14.18). It is therefore proposed that GRC shoshonites formed by small degrees of partial melting of a metasomatised mantle source, potentially stimulated by influx of hotter peridotite into the mantle wedge at the cessation of subduction (Figure 17.1e). This accounts for the marked

enrichment in incompatible elements (LILE, LREE) but similar depletion in Ti, Y and HREE as boninitic diorites of Chin Chap Creek/Robson Creek. An analogous situation is proposed for the Fijian Islands of the southwestern Pacific. Here, a transition from basaltic to shoshonitic volcanism is attributed to progressively lower degrees of fusion of the same source, following Pliocene rifting of the nascent Tonga and Vanuatu arcs (Gill & Whelan 1989).

Intrusion of shoshonites into the central GRC after the main convergent deformation, and the resulting combination with metasedimentary-derived partial melts, was responsible for formation of Loftus Creek type granitic rocks (Figure 17.2d). In contrast to Tuloona types, the markedly cross-cutting and variable geometry of these plutons indicates minimal structural control on their emplacement. However, that they collectively form a north-south aligned chain may reflect such control on ingress of shoshonitic magmas into the metasedimentary sequence.

17.2.6 STAGE 6: Post-collisional plutonism

The final Delamerian magmatic episode in southeastern Australia is the ~490-480 Ma emplacement of the large post-compressional bimodal batholith along the Padthway Ridge, which includes Dergholm type plutons of the western GRC (Figure 17.2e). Ar-Ar cooling ages of detrital micas in surrounding metasedimentary rocks indicate that intrusion coincided with substantial uplift and exhumation of 10-15 km of orogenic crust (Turner *et al.* 1996). As fluid-present melting curves have negative P-T slopes (Figure 8.1), such decompression would effectively terminate *in situ* anatexis in the GRC metasedimentary sequence.

Post-collisional granitic rocks are thought to be formed by prolonged fractional crystallisation (~90%) of contemporaneous tholeiitic basalt (Turner *et al.* 1992), requiring widespread mantle melting at this time. The inferred parental gabbros in South Australia are isotopically primitive, but exhibit LREE and incompatible-element enrichment with low Nb, interpreted as reflecting derivation from an enriched, lithospheric mantle source (Turner 1996). Their generation following compressional orogenesis is linked to convective delamination of thickened lithospheric mantle (Turner *et al.* 1996). This elevates the asthenospheric-lithospheric boundary to higher levels in the mantle column, where increased heat flow from the underlying convecting asthenosphere promotes fusion of hydrous domains in the shallow mantle lithosphere (Turner *et al.* 1996).

In the context of the tectonic model presented here, an alternative explanation is that the parental basaltic magmas for the post-compressional granitic plutons were derived from asthenospheric mantle previously enriched by addition of a slab-derived component and/or delamination of sub-arc lithosphere during subduction (Figure 17.1f). This is consistent with the negative Nb anomaly and high LILE/HFSE reported for these basalts by Turner (1996), which are subduction signatures. Diapiric rise of subduction-fertilised asthenosphere is favoured by the extensional regime and uplift following collision. In general terms, melting of asthenospheric mantle during orogenesis is considered unlikely, as thickened lithosphere impedes upwelling and therefore limits decompression melting (e.g. McKenzie & Bickle 1988). However, it is noteworthy that post-compressional granitic rocks are restricted to the far southwestern GRC where the MORB-like basaltic dykes are most voluminous, and therefore plutons must have intruded close to the

former back-arc spreading centre. Here, the lithospheric mantle would be thinnest, permitting extensive decompression melting of ascending subduction-modified peridotite. Furthermore, this area is also a zone of pre-existing crustal weakness, greatly facilitating and localising ingress of basaltic magmas, to be followed by protracted fractionation at shallow crustal levels. Although conjectural, this model does, however, explain the occurrence of the post-collisional granitic belt between the rifted cratonic margin and former volcanic arc.

17.3 Discussion

17.3.1 GRC plutons as geodynamic tracers

Barbarin (1999) emphasised that in some instances granitic rocks may trace the geodynamic evolution of an orogenic belt. This is elegantly exemplified by the GRC, where the temporal zonation of the various granitic types records major changes in the tectonic environment during their genesis. This is largely because each granitic type has a different mantle-derived end-member, the formation of which is specific to certain geodynamic regimes. Hornblende-rich early syn-compressional granitic rocks (Wando and Wennicott types) correspond to the active **subduction** to incipient collisional phase, incorporate arc-derived high-Al basalt, and therefore resemble the mafic subduction-related tonalites of the Sierra Nevada batholith (Bateman 1992) or Peruvian Coastal batholith (Pitcher *et al.* 1985). These were supplanted by late syn-compressional plutons (Tuloona, Harrow and Kassingbrook types), which are dominated by metasedimentary components and formed during subsequent **collision**, convergent deformation and crustal thickening. Emplacement conceivably occurred during transient relaxation between convergent pulses. Of this ensemble, the purely crustally-derived Harrow types most closely resemble the leucocratic plutons formed by fluid-fluxed crustal anatexis typical of other collisional orogens, such as those of the Hercynian belt of western Europe (Strong & Hanmer 1981; Castro *et al.* 2000) and the High Himalayas (Le Fort 1981; Le Fort *et al.* 1987).

The transition from convergence to **extension** in the GRC manifests with intrusion of the distinctive K-rich Loftus Creek granodiorites, associated with shoshonitic magmatism. These plutons are equivalent to the 'K-rich calc-alkaline granites' of Barbarin (1999), which similarly mark the switch from compression to tension in the Caledonian Fold belt of Scotland (Halliday & Stephens 1984) and the Hercynian belt of western Europe (Pagel & Leterrier 1980; Barbarin 1999). Emplacement of the subvolcanic Padthway suite represents the final pulse of the Delamerian magmatic cycle, as extension and uplift continued along the Gondwana margin. Alkaline, anorogenic (i.e. 'A-type') granitic plutons of this type are consistently emplaced (commonly as ring complexes) at the cessation of orogenesis (Bonin 1990), such as in the Pan-African Orogen (Liégeois *et al.* 1987).

17.3.2 Implications for regional geology and tectonics

Although GRC geology is entirely and uniquely explicable by subduction/collision processes, a wider reconstruction of the tectonic scenario leading to the Delamerian Orogeny in southeastern Australia is hindered by- (1) poor exposure at the inferred collisional site, and (2) the lack of

proper age and petrological constraints on the Dimboola Igneous Complex and the numerous faulted slivers of mafic to ultramafic rock in the sub-surface. Geological deconvolution of the buried Dimboola Igneous Complex in particular is not straightforward, as rather than a single belt of boninitic-tholeiitic lava formed above a subduction system, it more likely comprises a collage of obducted and accreted materials from outlying island arcs of different age and geochemistry. Regional tectonic models are therefore loosely constrained and necessarily speculative at this stage.

The greatest uncertainty surrounds the identification of the outboard island arcs involved in the collisions leading up to, and culminating in, the Delamerian Orogeny. Nevertheless, several plausible scenarios exist. A candidate for the colliding arc (i.e. 'B' in Figure 17.1) is the Mount Stavely Volcanic Complex, which is structurally intercalated with the Dimboola Igneous Complex along its eastern margin. In this scenario- (1) the upper dacitic units of the Mount Stavely assemblage (dated at ~500 Ma, see section 2.4.1) were erupted immediately following the collision (e.g. VandenBerg *et al.* 2000, see Figure 2.5), and (2) the underlying andesitic lavas must manifest a earlier period of east-directed intra-oceanic subduction prior to collision, as proposed by Scheibner & Veevers (2000) and depicted in Figure 17.1a.

Alternatively, the Mount Stavely lavas may be part of the Dimboola Igneous Complex, and manifest the final stages of arc-related magmatism above the west-dipping subduction zone prior to collision. Although the simplest hypothesis, this is impossible to properly assess, as geochemical data for the Mount Stavely or Dimboola Igneous Complex rocks are not currently available. However, should this prove correct, the outboard colliding arc responsible for the Delamerian Orogeny could be the Mount Dryden Belt, immediately east of the Mount Stavely Volcanic Complex (section 2.4.1). This sequence incorporates low-Ti tholeiities and boninites and has a sheet-like geometry (VandenBerg *et al.* 2000), both of which are consistent with it being an obducted slice of oceanic arc crust. Given the pronounced linear magnetic anomaly, it is also tempting to speculate that the accreted oceanic arc is now represented by the Magdala Volcanics, lying to the east of the Moyston Fault (see Figure 2.3). The subduction-related affinity of this assemblage is confirmed by the presence of boninites. Under this scenario, the highly strained Moornambool Metamorphic Complex (sandwiched between the Dimboola and Magdala belts) represents accretionary wedge sediments/metavolcanics of Cambrian age, subsequently thrust over the Dimboola Igneous Complex during collision. A corollary of this is that the Delamerian Orogen-Lachlan Fold Belt boundary in southeastern Australia occurs further east than the Moyston Fault. The resolution of this tectonic conundrum awaits detailed geochemistry and radiometric dating on the various geological components.

Chapter 18: Conclusions and broader implications

18.1 Conclusions

The major conclusions of Part III condense into two fundamental and inter-related points;

(1) **The magmatic, metamorphic and structural aspects of the GRC are uniquely explicable by development of the terrane in a supra-subduction zone setting.**

This is summarised by Figure 18.1 and involved successive (a) extension, (b) subduction, (c) arc-arc collision, and (d) post-collisional extension, which collectively exemplify the tectonic cycle of the Delamerian Orogeny. Each of these phases is 'fingerprinted' by the intrusion of geochemically-distinct, mantle-derived mafic magma. As such, the GRC represents the *exhumed plutonic core of an accreted Cambrian continental-oceanic arc system.* This conclusion invalidates earlier tectonic models and is a major advance towards understanding the eastern Delamerian Orogen and its correlatives in Tasmania and Antarctica.

(2) **Metaluminous to weakly peraluminous granitic plutons of the GRC formed by interaction between mantle-derived mafic magma and efficiently-segregated Harrow type 'minimum melts', generated by low T, fluid-fluxed anatexis of the host metasedimentary sequence.**

The GRC 'granitic' system therefore forges a hitherto unpostulated genetic link between metasedimentary migmatite leucosomes and mafic magmas of sub-crustal origin; the latter also provide the heat input driving *in situ* partial melting. The systematic petrographic and geochemical differences between each successive granitic type mostly reflect variation in the mafic end-member in the mixing system, itself relating to the changing geodynamic environment. Hence, secular variation in granitic geochemistry effectively tracks the tectonic evolution of the orogen.

In summary, the GRC preserves an unusually complete and coherent record of igneous petrogenesis in a dynamic convergent margin setting. In particular, the terrane provides an exceptional insight into *source-based* magma formation processes, illuminating the interplay between compressional deformation, crustal anatexis and mantle-derived magmatism in generating granitic rock. Such an interplay is exemplified by the remarkable field, lithological and geochemical continuity of GRC geology, *such that migmatites and muscovite granites, diverse weakly peraluminous/metaluminous granitic plutons and subduction-related mafic-intermediate rocks all comprise part of the same petrogenetic lineage.* The findings of this study therefore hint at the processes that may be active in granitic source regions of other orogenic belts, and have immense implications for granitic petrogenesis and crustal growth/evolutionary mechanisms in general; the most significant of these are discussed below.

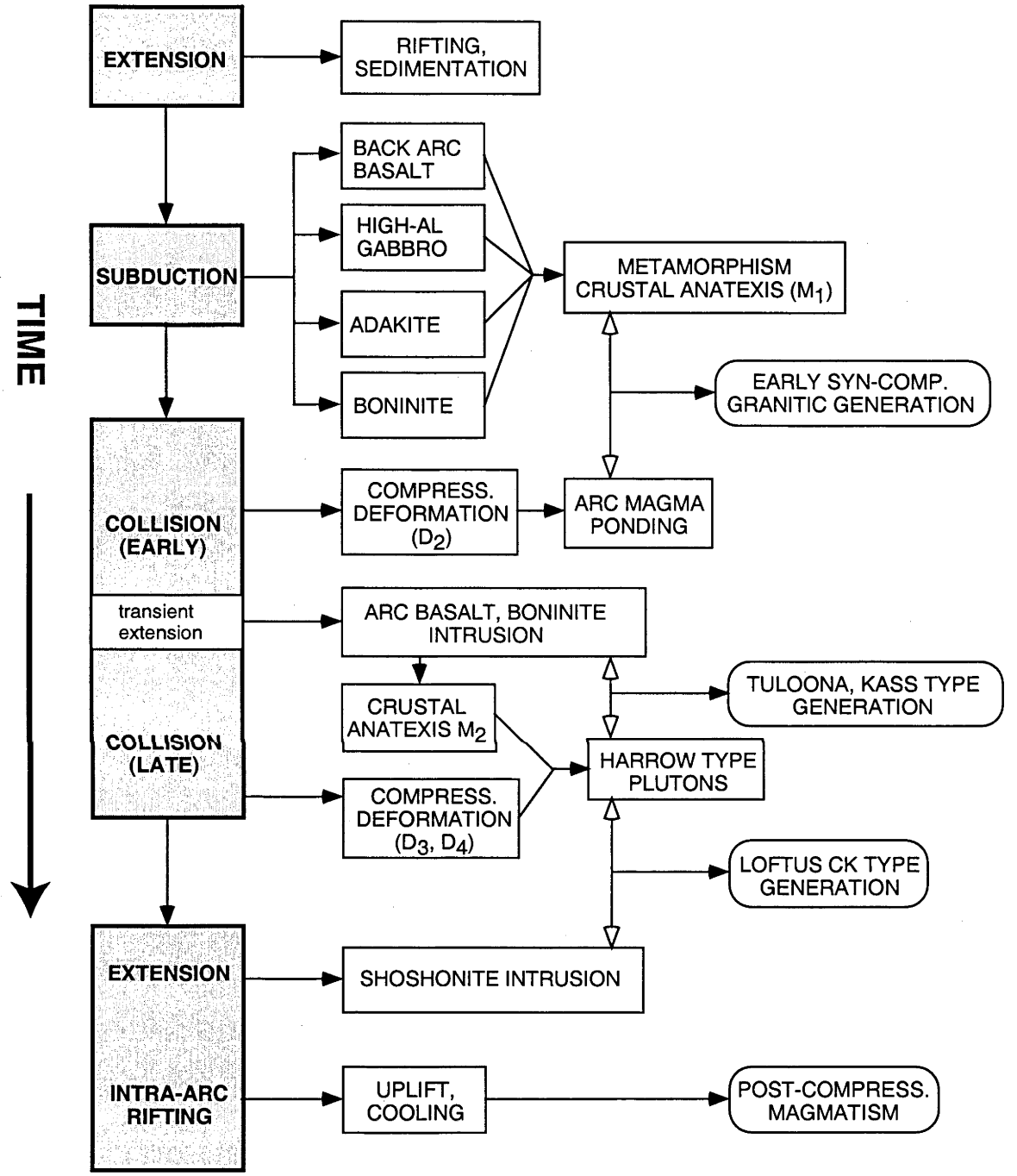

Figure 18.1. Summary of the geological evolution of the GRC as inferred from this study.

18.2 Broader implications

18.2.1 Re-evaluating the leucosome-granite connection

It is commonly assumed that migmatite leucosomes formed by water-saturated partial melting represent 'failed granites' and bear no connection with the upper crustal batholithic I- and S-type granitic plutons of many orogenic belts (section 9.11.2). In contrast, these are thought to form by high temperature biotite- and hornblende dehydration melting (e.g. Chappell *et al.* 1987) or mobilisation of melt-rich diatexites, followed by residue separation during flow (Sawyer 1996, 1998). As a result of effective melt-residue segregation, Sawyer (1996) concludes that leucosome partial melts are too siliceous and too depleted in TiO_2, (FeOt+MgO), P_2O_5, Rb, HFSE, Y and the REE to be the parental melts for crustally-derived granitic magmas. It should be recalled, however, that strongly peraluminous Harrow type GRC granitic rocks are compositionally identical to migmatite leucosomes, and formed by amalgamation of such melts (section 9.6). Furthermore, as demonstrated by Part III, leucosome partial melts may also be instrumental in production of the more mafic, weakly peraluminous to metaluminous granitic plutons, such as those considered by Sawyer (1996), by virtue of *comprising one end-member in a magma mixing system*. The subtle chemical signature of such a component in metaluminous granitic rocks is mostly camouflaged or potentially swamped by the participating mafic magma, though a likely outcome is a felsic hornblende-bearing pluton with an evolved isotopic signature (see section 18.2.3). Although such plutons may have a substantial crustal component, metasedimentary enclaves will be absent, given the efficient melt-residue separation of felsic end-member. This makes the crustal ingredient even harder to resolve, particularly for the general case of where granitic rocks occur in upper crustal settings removed from the generative region. Poorly-segregated diatexite magmas could also be the crustal end-member in mixing systems (e.g. Gray 1984, 1990; Collins 1996), though here the resulting hybrid magma will be distinguished by a high complement of residual material. This situation could pertain to the more mafic, cordierite-bearing granitic rocks of the LFB such as the Cowra Granodiorite, which contain igneous-textured mafic enclaves as well as abundant refractory metasedimentary material (Wyborn *et al.* 1991).

The possibility that efficiently-segregated leucosome partial melts are intimately involved in the formation of **both** peraluminous and metaluminous granitic rocks in other orogenic belts can therefore no longer be ignored. In such a scenario, migmatite development represents the essential first stage in the evolution of granitic plutons, conferring first order petrogenetic significance on the processes responsible for the generation, segregation and migration of leucosome partial melts. This conclusion reinforces the migmatite-granite link and further sullies the view of White & Chappell (1990, p.225) that the 'study of migmatite terranes is unlikely to provide much information about the formation of granitic magmas'.

18.2.2 Upper-crustal granitic plutons should not be used to deduce the composition of the source rocks

Chappell (1979, 1984, 1994) and Chappell *et al.* (1987) advocate that in granitic suites controlled by restite unmixing, the source composition must lie along geochemical variation trends and is

approximated by the most mafic pluton of a particular suite (section 1.3.2). In this way granitic rocks 'image their sources' (Chappell 1979) and provide compositional information on the deep crust (Chappell *et al.* 1988). However, the present study demonstrates that using upper-crustal granitic rocks to infer the chemical character of the protolith or deep crustal composition is fraught with uncertainty, given the possibility of- (a) granite formation by magma mixing and (b) the crustal component representing a partial melt (leucosome) composition. As an example, consider Tuloona type tonalites. These are calcic, weakly peraluminous, have moderately high Sr, and contain magnetite, green-brown biotite and hornblende-bearing microgranular enclaves; they are also more isotopically primitive than metasedimentary-derived Harrow type rocks. These features firmly classify them as 'I'-type according to the criteria of Chappell & White (1992), which indicates a mafic igneous source. However, Tuloona type tonalites cannot be derived exclusively by melting common igneous rocks under a variety of P-T-a_{H_2O} conditions (section 16.7.2), and were instead produced by mixing between high-Al basalt and a crustally-derived magma. Furthermore, as the latter is a leucosome composition, it bears little compositional resemblance to its protolith, given efficient partial melt-residue separation (section 8.5.3). Hence, deducing the nature of the ultimate metasedimentary source ingredient in granitic mixing systems is virtually impossible except in areas like the GRC, where the full range of petrogenetic phenomena is exposed in a near-source environment. Tuloona types therefore do not compositionally image their source rocks, but reflect processes involved in formation of the crustal melt and mantle-derived end-members. Similar circumstances apply for the other GRC granitic types. Regression lines from these project at lower silica to the mafic end-member magma and are therefore meaningless in terms of deducing crustal source materials. Such examples from deep seated terranes expose the futility of assigning specific source materials to upper crustal granitic rocks, where the problem is potentially exacerbated by fractional crystallisation or crustal assimilation. The simplistic I- and S-type classification is invalidated as a result.

18.2.3 Metaluminous granites are unlikely to be derived by melting meta-igneous protoliths

Hornblende-bearing 'I-type' granitic rocks are the most voluminous plutonic constituent of orogenic belts, and are generally considered to have formed by amphibole dehydration melting of mafic lower crustal (or underplated) igneous precursors (Chappell *et al.* 1987; Chappell & Stephens 1988; Silver & Chappell 1988; Clemens 1990; Roberts & Clemens 1993; Roberts *et al.* 2000). This implies that vast tracts of partially melted meta-igneous rocks yielding granitic liquids should be exposed in deeply eroded orogenic terranes. However, while localised examples of this phenomenon exist (e.g. Tait & Harley 1988), migmatitic metabasic lithologies are extremely rare, and generally subordinate to metapelitic migmatites in granulitic terranes. This might largely reflect geological difficulties with attaining the very high (800-1000°C) crustal temperatures imperative for extensive fusion of metabasic rocks. Furthermore, where present, mafic migmatites host Na-rich leucosomes that do not resemble hornblende-bearing granitic plutons, but are more akin to trondhjemite (Sorensen 1988; Sawyer 1991). Experimental liquids generated from various mafic to intermediate starting materials also have K-poor, Fe-rich compositions unlike natural metaluminous/weakly peraluminous granites (Patiño Douce 1999).

These simple observations diminish the viability of producing hornblende-bearing granites by melting mafic to intermediate meta-igneous source rocks alone.

However, these inconsistencies are entirely reconciled by the current model, which proposes that hornblende granites exemplify mixtures of mantle-derived mafic magma and low T, metasedimentary-derived partial melt. The requirement for sustained high temperatures within large areas of the lower crust is therefore eliminated. In addition, where partial melts derive by water-fluxed anatexis of feldspathic metasedimentary rocks in the muscovite stability field, the felsic end-member may be tonalitic (section 8.6.3). This results in formation of K-poor granitic bodies, such as the Wennicott types of the GRC, and may provide a ready explanation for some unusually isotopically evolved tonalitic plutons of the LFB, such as those of the Jindabyne suite (Compston & Chappell 1979; McCulloch & Chappell 1982).

18.2.4 Restite is not an important component of granitic magmas

The restite model (White & Chappell 1977; Chappell *et al.* 1987) *requires* that granitic magmas leave the source region as suspensions of felsic melt and entrained residual material, the progressive separation of which generates the compositional variation of granitic suites (section 1.4.2). That this premise is fundamentally flawed for the GRC is demonstrated by leucosome-derived Harrow type plutons, which, although contiguous with their migmatitic protoliths, mostly lack restitic debris (Chapter 9). Since the extensive weakly peraluminous to metaluminous granitic rocks of the complex formed by mixing between Harrow type partial melts and coeval mafic magma, restite is virtually absent from these also.

Such rare insights from the generative region of granitic magmas raise the possibility that wholesale restite entrainment may not apply for granitic plutons in general. As an example, it is contended above that rather than melting meta-igneous materials, many metaluminous to weakly peraluminous granitic plutons may have actually formed by combination of mafic mantle magmas and migmatite-derived partial melts. Under this scenario, the microgranular enclaves and mafic mineral aggregates observed in hornblendic granitic rocks, supposedly restitic, cannot be refractory relics from an igneous precursor. Instead, these are byproducts of the magma mixing process, which for microgranular enclaves accords with distinctive textural features attributed to igneous crystallisation and hybridisation (Vernon 1990; see section 12.5.2). This is demonstrated by the Kassingbrook Granodiorite of the southeastern GRC. Microgranular enclave swarms in this pluton were irrefutably introduced by syn-magmatic mingling with variably hybridised high-Mg diorite at the current exposure level; disaggregation of these objects dispersed the biotite-hornblende clots throughout the host (section 12.5.1c). Hybridised fragments of the basaltic end-member also occur in Wando type plutons (type C enclaves). Notably, for some elements these do not conform to inferred mixing lines, which reflects the complexity and multifarious nature of the hybridisation processes (section 12.5.1b); in some instances, the latter may result in compositions that are quite unlike that produced by simple mixing between two melts (e.g. Dorais *et al.* 1991; Debon 1990; Orsini *et al.* 1991). A corollary of this is that dismissing a hybrid origin for microgranular enclaves on the basis of not plotting

on granitic trends (Chen *et al.* 1990) or having an apparently 'non-igneous' composition (Wyborn *et al.* 1999; Chappell 1996a; White *et al.* 1998) is naïve.

18.2.5 Granitic rocks cannot be used to estimate temperatures in the source

The temperatures of high level granitic melts, estimated from experimental liquidus studies (e.g. Clemens & Wall 1981) or zircon saturation thermometry (e.g. Miller *et al.* 1988), extrapolated to the inferred crustal source, may bear little relevance to regional metamorphic temperatures at depth. This is because in granitic liquids formed by magma mixing, the crustal component could have been generated by low temperature (<700°C) fluid-present anatexis, not the higher temperature granulite-facies melting reactions required to satisfy many thermometric estimates (e.g. 800-850°C for the peraluminous Strathbogie granite of the Lachlan Fold Belt, Clemens & Wall 1981). Inferences on the thermal regime of granitic source regions drawn from upper crustal plutons, with attendant implications for the conditions and materials involved in magma generation (e.g. Clemens & Wall 1981; Miller *et al.* 1988), may therefore be meaningless.

18.2.6 More than one mafic magma may participate in magma mixing

Although most magma mixing models invoke basalt as the mafic end-member (e.g. Gray 1984; Dorais *et al.* 1990; Keay *et al.* 1997), other mantle-derived magmas may also interact with crustal melts, especially in subduction environments. The GRC is a striking demonstration of this, with both boninitic and shoshonitic end-members identified in granitic mixing systems. Importantly, some igneous-textured enclaves in granitic plutons may result from injection of such diverse mafic magmas into the magma chambers at the emplacement site. This is indicated for Wando type granitic rocks, which contain an abundant mafic enclave population derived from coeval boninitic magmas unrelated to the formation of the host pluton. That enclaves of 'extraneous magmas' plot remote from basalt-crustal melt mixing lines does not preclude a hybrid origin for the granitic host. Indeed, the characteristic scatter of microgranular enclave compositions on variation diagrams relative to the host pluton (Chen *et al.* 1990; Debon 1991; Chappell 1996a) could in part reflect the derivation of such enclaves from a range of coeval mafic magmas, in combination with complex hybridisation effects.

18.2.7 Implications for REE, Zr, Y, Th and U modelling

As a result of residence in accessory minerals, such as zircon, apatite and monazite, and the likelihood that these are selectively included in major minerals, Bea (1996a) concludes that the REE, Zr, Y, Th and U are unsuitable for petrogenetic modelling of granitic rocks through equilibrium trace element fractionation equations. For similar reasons, inferences about source geochemistry from REE contents/patterns of granitic rocks derived from crustal protoliths containing REE-rich phases are also potentially unreliable (e.g. Bea *et al.* 1994; Bea 1996b). A good example of this is provided by felsic Kassingbrook type samples. Compelling field and geochemical relationships indicate that these represent accumulations of leucosome-derived partial melts extracted from surrounding quartzofeldspathic migmatites. As accessory phases have low solubility in low-T, peraluminous melts, and are shielded from the melt by refractory

biotite concentrated in melanosomes, segregated leucosomes are extremely depleted in Zr, Y, Th, U and the REE, imparting this character to the derivative pluton (section 9.6.3). For the Kassingbrook Granodiorite, this results in a REE pattern that is strikingly similar to that of adakites (and the Deep Creek Granodiorite), generated by melting a garnet-bearing basaltic source at depth. Clearly, in some cases REE patterns of granitic rocks are process-specific rather than source-specific. A corollary of this is that *depleted HREE and Y concentrations in granitic rocks do not require garnet fractionation or retention of this mineral in the residue.* Such depletions could equally arise by melt extraction from a garnet-absent metasedimentary protolith, without entrainment of refractory accessory minerals. Granitic genesis models invoking residual source garnet on the basis of HREE/Y depletion, which seem to be particularly favoured for the Australian Proterozoic (Wyborn *et al.* 1992), require re-evaluation. Furthermore, as a substantial leucosome component occurs in other GRC granitic rocks, these also have depleted REE concentrations relative to their ultimate metasedimentary source rocks and mantle-derived end-members. Low and fractionated REE contents in granitic rocks are therefore a powerful link to the efficient segregation of the crustal melt component, and strongly implicate the involvement of a metasedimentary-derived leucosome ingredient in granite petrogenesis.

18.2.8 Growth and differentiation of the continental crust

There is growing appreciation of the fundamental role of destructive plate margin magmatism in generating new continental crust, via mass transfer from the mantle wedge (Ellam & Hawkesworth 1988; Keleman 1995; Arculus 1999; Davidson & Arculus 2001). This is well exemplified by the Delamerian Orogen, where influx of various mantle-derived magmas, and attendant granite generation, resulted in significant juvenile crustal addition to the eastern Gondwana continental margin. Nevertheless, there remains uncertainty as to the specific mechanisms of intra-crustal differentiation (section 9.11.2). As the net mantle-derived flux through the Moho in Phanerozoic subduction zones is basaltic (Arculus 1981; Ellam & Hawkesworth 1988), considerable fractionation of this, combined with delamination of mafic lower crustal residues/cumulates (Kay & Mahlburg-Kay 1991), is required to produce the overall andesitic composition of the continental crust. However, the average crust has higher Mg# and Ni contents than has been produced by experimental fractional crystallisation (or partial melting) of basalt (Keleman 1995). Furthermore, progressive intra-crustal differentiation of basalt should result in the upper crust being haplogranitic in composition, when in fact it is granodioritic. Chappell (1996b, p.168) contends that the latter reflects the high proportion of entrained mafic restite within upper crustal granitic plutons, and that orogenesis therefore involves vertical re-distribution or recycling of crustal materials (section 9.11.2). However, this study suggests that the restitic component of granitic plutons is trivial, since- (1) metasedimentary-derived granitic magmas effectively disengage from refractory residue at source, and (2) hornblende-bearing plutons are probably not exclusively (or even generally) derived from older meta-igneous rocks, and are therefore incapable of transporting such mafic material *en masse* into the upper crust. Yet cleanly-segregated, crustally-derived partial melts also pose a problem for crustal differentiation, due to their extremely fractionated chemistry relative to the upper continental crust (section

9.11.2). A solution to this dilemma is that residue-free crustal melts are only one end-member of a mixing system, and that granitic plutons form in the lower to middle crust by combination of this component and coeval mantle-derived mafic magma. Ascent of these mixed magmas therefore represents an efficient mechanism for transporting more mafic and isotopically-primitive material into the upper crust, reconciling the requirement for a granodioritic upper crust and the observation that granites contain little restite.

18.3 Concluding statement

The ultimate conclusions of this thesis highlight the further need for careful field-based studies in lower crustal anatectic terranes, if the mechanisms of granite generation and crustal differentiation are to be properly understood. The GRC provides an elegant case history that places new constraints on models of these processes.

References

Abbott, R.N. 1981. The role of manganese in the paragenesis of magmatic garnet: an example from the Old Woman-Piute Range, California: a discussion. *Journal of Geology*, **89**, 767-772.

Abbott, R.N. 1985. Muscovite-bearing granites in the AFM liquidus projection. *Canadian Mineralogist*, **23**, 553-561.

Allan, B.D. & Clarke, D.B. 1981. Occurrence and origin of garnets in the South Mountain batholith, Nova Scotia. *Canadian Mineralogist*, **19**, 19-24.

Anders, E. & Grevesse, N. 1989. Abundances of the elements: meteoric and solar, *Geochimica et Cosmochimica Acta,* **53**, 197-214.

Anderson, J.A.C. 1990. The geology of the Glenelg River Complex in the Wando Vale district of western Victoria. B.Sc. (Hons) thesis, La Trobe University, Melbourne, (*unpubl.*).

Anderson, J.A.C. & Gray, C.M. 1994. Geological affinities of the Glenelg River Complex, western Victoria. *Australian Journal of Earth Sciences,* **41**, 141-155.

Anderson, J.A.C., Price, R.C. & Fleming, P.D. 1998. Structural analysis of metasedimentary enclaves: implications for tectonic evolution and granite petrogenesis in the southern Lachlan Fold Belt, Australia. *Geology*, **26**, 119-122.

Anderson, J.L. & Rowley, M.C. 1981. Synkinematic intrusion of peraluminous and associated metaluminous granitic magmas, Whipple Mountains, California. *Canadian Mineralogist*, **19**, 83-101.

Arculus, R.J. 1981. Island arc magmatism in relation to the evolution of the crust and mantle. *Tectonophysics*, **75**, 113-133.

Arculus, R.J. 1999. Origins of the continental crust. *Journal and Proceedings of the Royal Society of New South Wales*, **132**, 83-110.

Arculus, R.J. & Powell, R. 1986. Source component mixing in the regions of arc magma generation. *Journal of Geophysical Research*, **91**, 5913-5926.

Arth, J.G. & Hanson, G.N. 1975. Geochemistry and origin of the early Precambrian crust of northeastern Minnesota. *Geochimica et Cosmochimica Acta*, **39**, 325.

Ashworth, J.R. 1985. Introduction. *In* Ashworth, J.R. (ed) *Migmatites.* Blackie, Glasgow, 1-35.

Ashworth, J.R. & McLellan, E.L. 1985. Textures. *In* Ashworth, J.R. (ed) *Migmatites.* Blackie, Glasgow. 180-203.

Atherton, M.P. & Petford, N. 1993. Generation of sodium-rich magmas from newly underplated basaltic crust. *Nature*, **362**, 144-146.

Ayres, M. & Harris, N. 1997. REE fractionation and Nd-isotope disequilibrium during crustal anatexis: constraints from Himalayan leucogranites. *Chemical Geology*, **139**, 249-269.

Azevado, M.R. & Nolan, J. 1998. Hercynian late-post-tectonic granitic rocks from the Fornos de Algodres area (Northern Central Portugal). *Lithos*, **44**, 1-20.

Bacon, C.R. 1986. Magmatic inclusions in silicic and intermediate volcanic rocks. *Journal of Geophysical Research*, **91**, 6091-6112.

Barbarin, B. 1988. Field evidence for successive mixing and mingling between the Piolard Diorite and the Saint-Julien-la-Vêtre Monzogranite (Nord Forez, Massif Central, France). *Canadian Journal of Earth Sciences*, **25**, 49-59.

Barbarin, B. 1990. Plagioclase xenocrysts and mafic magmatic enclaves in some granitoids of the Sierra Nevada Batholith, California. *Journal of Geophysical Research*, **95**, 17747-177456.

Barbarin, B. 1991. Enclaves of the Mesozoic calc-alkaline granitoids of the Sierra Nevada Batholith, California. *In* Didier, J. & Barbarin, B. (eds) *Enclaves and Granite Petrology*. Elsevier Science, Amsterdam, 135-153.

Barbarin, B. 1996. Genesis of the two main types of peraluminous granitoids. *Geology*, **24**, 295-298.

Barbarin, B. 1999. A review of the relationships between granitoid types, their origins and their geodynamic environments, *Lithos*, **46**, 605-626.

Barbarin, B. & Didier, J. 1991. Review of the main hypotheses proposed for the genesis and evolution of mafic microgranular enclaves. *In* Didier, J. & Barbarin, B. (eds) *Enclaves and Granite Petrology*. Elsevier Science, Amsterdam, 367-371.

Barbarin, B. & Didier, J. 1992. Genesis and evolution of mafic magmatic enclaves through various types of interactions between coeval felsic and mafic magmas, *Transactions of the Royal Society of Edinburgh: Earth Sciences*, **83**, 145-153.

Barbero, L. & Villaseca, C. 1992. The Layos Granite, Hercynian Complex of Toledo (Spain): an example of parautochthonous restite-rich granite in a granulitic area. *Transactions of the Royal Society of Edinburgh: Earth Sciences*, **83**, 127-138.

Barbero, L., Villaseca, C., Rogers, G. & Brown, P.E. 1995. Geochemical and isotopic disequillibrium in crustal melting: an insight from the anatectic granitoids from Toledo, Spain. *Journal of Geophysical Research*, **100**, 15745-15765.

Barker, F. 1979. Trondhjemite: definition, environment, and hypothesis of origin. *In* Barker, F. (ed) *Trondhjemites, Dacites and Related Rocks. Developments in Petrology*, **6**, Elsevier, Amsterdam.

Bateman, R., Martin, M.P. & Castro, A. 1992. Mixing of cordierite granitoid and pyroxene gabbro, and fractionation, in the Santa Olalla tonalite (Andalucia). *Lithos*, **28**, 111-131.

Bea, F. 1996a. Residence of REE, Y, Th and U in granites and crustal protoliths; implications for the chemistry of crustal melts. *Journal of Petrology*, **37**, 521-552.

Bea, F. 1996b. Controls on the trace element composition of crustal melts. *Transactions of the Royal Society of Edinburgh: Earth Sciences*, **87**, 33-41.

Bea, F., Fershtater, G. & Corretgé, L.G. 1992. The geochemistry of phosphorus in granitic rocks and the effect of aluminium. *Lithos*, **29**, 43-56.

Bea, F., Pereira, M.D. & Stroh, A. 1994. Mineral/leucosomes trace-element partitioning in a peraluminous migmatite (a laser ablation–ICP–MS study). *Chemical Geology*, **117**, 291-312.

Beard J.S. & Lofgren G.E. 1991. Dehydration melting and water-saturated melting of basaltic and andesitic greenstones and amphibolites at 1, 3 and 6.9 kb. *Journal of Petrology*, **32**, 365-401.

Belperio, A.P., Preiss, W.V., Fairclough, M.C., Gatehouse, C.G., Gum, J., Hough, J. & Burtt, A. 1998. Tectonic and metallogenic framework of the Cambrian Stansbury Basin - Kanmantoo Trough, South Australia. *AGSO Journal of Australian Geology & Geophysics*, **17**(3), 183-200.

Bennett, V.C., Nutman, A.P. & McCulloch, M.T. 1993. Nd isotopic evidence for transient, highly depleted mantle reservoirs in the early history of the Earth. *Earth & Planetary Science Letters*, **119**, 299-317.

Blake, S. & Campbell, I.H. 1986. The dynamics of magma mixing during flow in volcanic conduits. *Contributions to Mineralogy and Petrology*, **94**, 72-81.

Bloomer, S.H. & Hawkins, J.W. 1987. Petrology and geochemistry of boninite series volcanic rocks from the Mariana trench. *Contributions to Mineralogy and Petrology*, **97**, 361-377.

Blundy, J.D. & Wood, B.J. 1991. Crystal-chemical controls on the partitioning of Sr and Ba between plagioclase feldspar, silicate melts, and hydrothermal solutions. *Geochimica et Cosmochimica Acta*, **55**, 193-209.

Bogoch, R., Bourne, J., Shirav, M. & Harnois, L. 1997. Petrochemistry of a Late Precambrian garnetiferous granite, pegmatite and aplite, southern Israel. *Mineralogical Magazine,* **61**, 111-112.

Bonin, B. 1990. From orogenic to anorogenic settings: evolution of granitoid suites after a major orogenesis. *Journal of Geology*, **25**, 261-270.

Bowen, N.L. 1928. *The Evolution of the Igneous Rocks*. Dover, New York.

Brophy, J.G. 1986. The Cold Bay volcanic center, Aleutian Volcanic Arc. *Contributions to Mineralogy and Petrology*, **93**, 368-380.

Brown, C.M., Tucker, D.H. & Anfiloff, V. 1988. An interpretation of the tectonostratigraphic framework of the Murray Basin region of southeastern Australia, based on an examination of airborne magnetic patterns. *Tectonophysics,* **154**, 309-333.

Brown, M. 1979. The petrogenesis of the St. Malo migmatite belt, Amorican Massif, France, with particular reference to the diatexites. *Neues Jahrbuch fur Mineralogie Abhandlung,* **135,** 48-74.

Brown, M. 1983. The petrogenesis of some migmatites from the Presqu'ile de Rhuys, Southern Brittany, France. *In* Atherton, M.P. & Gribble, C. (eds) *Migmatites, Melting and Metamorphism.* Shiva, Nantwich, 174-200.

Brown, M. 1994. The generation, segregation, ascent and emplacement of granite magma: the migmatite-to-crustally-derived granite connection in thickened orogens. *Earth Science Reviews,* **36**, 83-130.

Brown, M., Averkin Y.A., McLellan E.L. & Sawyer E.W. 1995. Melt segregation in migmatites. *Journal of Geophysical Research*, **100**, 15655-15679.

Brown, M. & D'Lemos, R.S. 1991. The Cadomian granites of Mancellia, north-east Armorican Massif of France: relationship to the St. Malo migmatite belt, petrogenesis and tectonic setting. *Precambrian Research*, **51**, 393-427.

Brown, M. & Earle, M.M. 1983. Cordierite-bearing schists and gneisses from Timor, eastern Indonesia: P-T conditions of metamorphism and tectonic implications. *Journal of Metamorphic Geology*, **1**, 183-203.

Brown, M. & Solar, G.S. 1998. Granite ascent and emplacement during contractional deformation in convergent orogens. *Journal of Structural Geology*, **20**, 1365-1395.

Brouand, M., Banzet, G. & Barbey, P. 1990. Zircon behaviour during crustal anatexis. Evidence from the Tibetan Slab migmatites (Nepal). *Journal of Volcanology and Geothermal Research*, **44**, 143-161.

Buckland, G.L. 1986. Geology and mineral potential of the Mount Stavely Volcanic Complex. *Geological Survey of Victoria, Report* **80**, 1-66.

Bushell, D.J. 1996. The geology of part of the southeastern Glenelg River Complex, western Victoria. B.Sc. (Hons) thesis, La Trobe University, Melbourne, (*unpubl.*).

Bussy, F. 1991. Enclaves of the Late Miocene Monte Caponne granite, Elba Island, Italy. *In* Didier, J. & Barbarin, B. (eds) *Enclaves and Granite Petrology*. Elsevier Science, Amsterdam, 167-178.

Cameron, W.E., McCulloch, M.T. & Walker, D.A. 1983. Boninite petrogenesis: chemical and Nd-Sr isotopic constraints. *Earth and Planetary Science Letters*, **65**, 75-89.

Campbell, I.H. & Turner, J.S. 1985. Turbulent mixing between fluids with different viscosities. *Nature*, **313**, 39-42.

Campbell, I.H. & Turner, J.S. 1986. The influence of viscosity on fountains in magma chambers. *Journal of Petrology*, **27**, 1-30.

Campbell, I.H. & Turner, J.S. 1989. Fountain in magma chambers. *Journal of Petrology*, **30**, 885-923.

Carroll, M.R. & Wyllie, P.J. 1989. Experimental phase relations in the system tonalite-peridotite-H_2O at 15 kb: implications for assimilation and differentiation processes near the crust-mantle boundary. *Journal of Petrology*, **30**, 1351-1382.

Castro, A., Guillermo, C., El-Biad, M., El-Hmidi, H., Fernandez, C. & Patiño Douce, A.E. 2000. Experimental constraints on Hercynian anatexis in the Iberian Massif, Spain. *Journal of Petrology*, **41**, 1471-1488.

Cayley, R.A. & Taylor, D.H. 1997. Grampians special map area geological report. *Geological Survey of Victoria Report*, **107**.

Cayley, R.A. & Taylor, D.H. 1998. The Lachlan margin, Victoria: the Moyston Fault, a newly recognized terrane boundary. *Geological Society of Australia, Abstracts,* **49**, 73.

Cayley, R.A. & Taylor, D.H. 1999. The Grampians and western Lachlan margin excursion, Halls Gap, Victoria – recent mapping supporting an intra-plate tectonic setting for the western Lachlan fold belt. *Specialist Group in Tectonics and Structural Geology Field Guide,* **8**, Geological Society of Australia.

Champion, D.C. & Chappell, B.W. 1992. Petrogenesis of felsic I-type granites: an example from northern Queensland. *Transactions of the Royal Society of Edinburgh: Earth Sciences*, **83**, 115-126.

Chappell, B.W. 1979. Granites as images of their source rocks. *Geological Society of America Program Abstract*, **11**, 400.

Chappell, B.W. 1984. Source rocks of I- and S-type granites in the Lachlan Fold Belt, southeastern Australia. *Philosophical Transactions of the Royal Society of London*, **A310**, 693-707.

Chappell, B.W. 1994. Lachlan and New England: fold belts of contrasting magmatic and tectonic development. *Journal and Proceedings of the Royal Society of New South Wales*, **127**, 47-59.

Chappell, B.W. 1996a. Magma mixing and the production of compositional variation within granite suites: evidence from the granites of southeastern Australia. *Journal of Petrology*, **37**, 449-470.

Chappell, B.W. 1996b. Compositional variation within granite suites of the Lachlan Fold Belt: its causes and implications for the physical state of granitic magma. *Transactions of the Royal Society of Edinburgh: Earth Sciences*, **88**, 159-170.

Chappell, B.W. & Stephens W.E. 1988. Origin of infracrustal (I-type) granite magmas. *Transactions of the Royal Society of Edinburgh: Earth Sciences*, **79**, 71-86.

Chappell, B.W. & White, A.J.R. 1992. I- and S-type granites in the Lachlan Fold Belt. *Transactions of the Royal Society of Edinburgh: Earth Sciences*, **83**, 1-26.

Chappell, B.W., White A.J.R., & Hine, R. 1988. Granite provinces and basement terranes in the Lachlan Fold Belt, southeastern Australia. *Australian Journal of Earth Sciences*, **35**, 505-521.

Chappell, B.W., White, A.J.R. & Williams, I.S. 1991. *A Transverse Section Through Granites of the Lachlan Fold Belt. Second Hutton Symposium Excursion Guide*, Bureau of Mineral Resources, Geology and Geophysics.

Chappell, B.W., White, A.J.R., Williams, I.S., Wyborn, D., Hergt, J.M. & Woodhead, J.D. 1999. Discussion: Evaluation of petrogenetic models for Lachlan Fold Belt granitoids: implications for crustal architecture and tectonic models. *Australian Journal of Earth Sciences*, **46**, 827-831.

Chappell, B.W., White, A.J.R., Williams, I.S., Wyborn, D. & Wyborn, L.A.I. 2000. Lachlan Fold Belt granites revisited: high- and low-temperature granites and their implications. *Australian Journal of Earth Sciences*, **47**, 123-138.

Chappell, B.W., White, A.J.R. & Wyborn, D. 1987. The importance of residual source material (restite) in granite petrogenesis. *Journal of Petrology*, **28**, 1111-1138.

Chen, Y., Chappell, B.W. & White, A.J.R. 1991. Mafic enclaves of some I-type granites of the Palaeozoic Lachlan Fold Belt, southeastern Australia. *In* Didier, J. & Barbarin, B. (eds) *Enclaves and Granite Petrology*. Elsevier Science, Amsterdam.

Chen, Y.D., Price, R.C. & White, A.J.R. 1990. Mafic inclusions from the Glenbog and Blue Gum Granite Suites, southeastern Australia. *Journal of Geophysical Research*, **95**, 17557-17785.

Clarke, D.B. 1981. The mineralogy of peraluminous granite: a review. *Canadian Mineralogist*, **19**, 3-17.

Clemens, J.D. 1990. The granite-granulite connexion. *In* Vielzeuf D. & Vidal P.H. (eds) *Granulites and crustal evolution*. Netherlands, Kluwer Academic Publishers, 25-36.

Clemens, J.D. & Mawer, C.K. 1992. Granite magma transport by fracture propagation. *Tectonophysics*, **204**, 339-360.

Clemens, J.D. & Vielzeuf, D. 1987. Constraints on melting and magma production in the crust. *Earth and Planetary Science Letters*, **86**, 287-306.

Clemens, J.D. & Wall, V.J. 1981. Origin and crystallization of some peraluminous (S-type) granitic magmas. *Canadian Mineralogist*, **19**, 111-131.

Clemens, J.D. & Wall, V.J. 1982. The role of manganese in the paragenesis of magmatic garnet; a discussion. *Journal of Geology*, **90**, 339-341.

Collins W.J. 1996. Lachlan Fold Belt granitoids: products of three component mixing. *Transactions of the Royal Society of Edinburgh: Earth Sciences*, **88**, 171-181.

Collins W.J. 1999. Reply: Evaluation of petrogenetic models for Lachlan Fold Belt granitoids: implications for crustal architecture and tectonic models. *Australian Journal of Earth Sciences*, **46**, 831-836.

Collins, W.J. & Sawyer, E.W. 1996. Pervasive granitoid magma transfer through the lower-middle crust during non-coaxial compressional deformation. *Journal of Metamorphic Geology*, **14**, 565-579.

Compston, W. & Chappell, B.W. 1979. Sr-isotope evolution of granitoid source rocks. *In* McElhinny, M.E. (ed) *The Earth: its Origin, Structure and Evolution*, Academic Press, London, 377-426.

Cooper, J.A., Jenkins, R.J.F., Compston, W. & Williams, I.S. 1992. Ion-probe zircon dating of a mid-Early Cambrian tuff in South Australia. *Journal of the Geological Society of London*, **149**, 185-192.

Crawford, A.J. 1988. Cambrian. *In* Douglas, J.G. & Ferguson, J.A. (eds) *Geology of Victoria.* Victorian Division, Geological Society of Australia, Melbourne, 37-62.

Crawford, A.J. & Berry, R.F. 1992. Tectonic implications of Late Proterozoic-Early Palaeozoic igneous rock associations in western Tasmania. *Tectonophysics*, **214**, 37-56.

Crawford, A.J., Cameron, W.E. & Keays, R.R. 1984. The association boninite-low-Ti andesite-tholeiite in the Heathcote Greenstone Belt, Victoria: ensimatic setting for the early Lachlan Fold Belt. *Australian Journal of Earth Sciences*, **31**, 197-208.

Crawford, A.J., Donaghy, A.G., Black, L.P. & Stuart-Smith, P.G. 1996. Enhancing the prospectivity of Victoria: Identification of Mount Read Volcanics correlatives in western Victoria. *Geological Society of Australia, Abstracts No.* **41**, 100.

Crawford, A.J., Falloon, T.J. & Eggins, S. 1987. The origin of island arc high-alumina basalts. *Contributions to Mineralogy and Petrology*, **97**, 417-430.

Crawford, A.J., Falloon, T.J. & Green, D.H. 1989. Classification, petrogenesis and tectonic setting of boninites. *In* Crawford, A.J. (ed) *Boninites and Related Rocks*, Unwin Hyman, London, 2-44.

Crawford, A.J. & Hilyard, D. 1990. Geochemistry of Late Proterozoic tholeiitic flood basalts, Adelaide Geosycline, South Australia. *In* Jago, J.B. & Moore, P.S. (eds) *The Evolution of a Late Precambrian-Early Palaeozoic Rift Complex: The Adelaide Geosyncline*. Geological Society of Australia, Special Publication **16,** 49-67.

Crawford, A.J. & Keays, R.R. 1987. Petrogenesis of Victorian Cambrian tholeiites and implications for the origin of associated boninites. *Journal of Petrology*, **28**, 1075-1109.

Daily, B., Firman, J.B., Forbes, B.G. & Lindsay, J.M. 1976. Cambrian of the Adelaide Region. *In* Twidale, C.R., Tyler, M.J. & Webb, B.P. (eds) *Natural History of the Adelaide Region.* Royal Society of South Australia.

Daily, B. & Milnes, A.R. 1971. Stratigraphic notes on lower Cambrian fossiliferous metasediments between Campbell Creek and Tunkalilla Beach in the type section of the Kanmantoo Group, Fleurieu Peninsula, South Australia. *In* Daily, B. (ed) *Geological Excursions Handbook*, ANZAAS, **95**, 23-30.

Daily, B. & Milnes, A.R. 1973. Stratigraphy, structure and metamorphism of the Kanmantoo Group (Cambrian) in its type section east of Tunkalilla Beach, South Australia. *Transactions of the Royal Society of South Australia*, **97(3)**, 213-242.

Davidson, J.P. & Arculus, R.J. 2001. The significance of Phanerozoic arc magmatism in generating continental crust. *In* Brown, M. & Rushmer, T. (eds) *Evolution and Differentiation of the Continental Crust*, Cambridge University Press.

Davidson, J.P., McMillan, N.J., Moorbath, S., Worner, G. Harmon, R.S. & Lopez-Escobar, L. 1990. The Nevados de Payachata volcanic region (18°S, 69°W, N Chile) II. Evidence for widespread crustal involvement in Andean magmatism. *Contributions to Mineralogy and Petrology*, **105**, 412-432.

Dean, G.R.B. 2000. Igneous and high grade metamorphic geology of the southeastern Glenelg River Complex, western Victoria. B.Sc. (Hons) thesis, La Trobe University, Melbourne, (*unpubl.*).

Debon, F. 1991. Comparative major element chemistry in various "microgranular enclave-plutonic host" pairs. *In* Didier, J. & Barbarin, B. (eds), *Enclaves and Granite Petrology*. Elsevier Science, Amsterdam, 293-310.

Defant, M.J. & Drummond, M.S. 1990. Derivation of some modern arc magmas by melting of young subducted lithospere. *Nature*, **347**, 662-665.

Defant, M.J., Jackson, T.E., Drummond, M.S., De Boer, J.Z. Bellon, H., Feigenson, M.D., Maury, R.C. & Stewart, R.H. 1992. The geochemistry of young volcanism throughout western Panama and southeastern Costa Rica: an overview. *Journal of Geological Society, London*, **149**, 569-579.

Deniel, C., Vidal, P., Fernandez, A., Le Fort, A. & Peucat, J-J. 1987. Isotopic study of the Manaslu granite (Himalaya, Nepal): inferences on the age and source of Himalayan leucogranites. *Contributions to Mineralogy and Petrology*, **96**, 78-92.

Didier, J. 1973. *Granites and their enclaves: the bearing of enclaves on the origin of granites. Developments in Petrology*, **3**, Elsevier, Amsterdam.

Didier, J. & Barbarin, B. 1991. The different types of enclaves in granites – Nomenclature. *In* Didier, J. & Barbarin, B. (eds) *Enclaves and Granite Petrology*. Elsevier Science, Amsterdam, 19-21.

Di Vincenzo, G., Andriessen, P.A.M. & Ghezzo, C. 1996. Evidence of two different components in a Hercynian peraluminous cordierite-bearing granite: the San Basilio intrusion (central Sardinia, Italy). *Journal of Petrology*, **37**, 1175-1206.

D'Lemos, R.S., Brown, M. & Strachan, R.A. 1992. The relationship between granite and shear zones: magma generation, ascent and emplacement within a transpressional orogen. *Journal of the Geological Society of London*, **149**, 487-490.

Dodge, F.C.W. & Kistler, R.W. 1990. Some additional observations on inclusions in the granitic rocks of the Sierra Nevada. *Journal of Geophysical Research*, **95**, 17841-17848.

Dorais, M.J., Whitney, J.A. & Roden, M.F. 1990. Origin of mafic enclaves in the Dinkey Creek Pluton, Central Sierra Nevada batholith, California. *Journal of Petrology*, **31**, 853-881.

Douglas, J.G. & Ferguson, J.A. 1988. (eds) *Geology of Victoria*. Victorian Division, Geological Society of Australia, Melbourne.

Douglas, J.G. & Spencer-Jones, D. 1971. *Hamilton 1:250 000 Geological Map*. Geological Survey of Victoria, Melbourne.

Drexel, J.F. & Preiss, W.V. 1995. (eds) *The Geology of South Australia, Volume 2: The Phanerozoic*. South Australia Geological Society Bulletin, **54**.

Drummond, M.S. & Defant, M.J. 1990. A model for trondhjemite-tonalite-dacite genesis and crustal growth via slab melting: Archaean to modern comparisons. *Journal of Geophysical Research*, **95**, 21503-21521.

Drummond, M.S., Defant, M.J. & Kepezhinskas, P.K. 1996. Petrogenesis of slab-derived trondhjemite-tonalite-dacite/adakite magmas. *Transactions of the Royal Society of Edinburgh: Earth Sciences*, **87**, 205-215.

du Bray, E.A. 1988. Garnet compositions and their use as indicators of peraluminous granitoid petrogenesis – southeastern Arabian Shield. *Contributions to Mineralogy and Petrology*, **100**, 205-212.

Eggins, S.M., (*in prep*). Laser ablation-ICPMS analysis of geological materials prepared as Lithium-borate glasses.

Eggins, S.M., Kinsley, L.P.J. & Shelley, J.M.G. 1998. Deposition and element fractionation processes during atmospheric pressure laser sampling for analysis by ICP-MS. *Applied Surface Science*, **127-129**, 278-286.

Elburg, M.A. 1996. U-Pb ages and morphologies of zircon in micrograniteoid enclaves and peraluminous host granite: evidence for magma mingling. *Contributions to Mineralogy and Petrology*, **123**, 177-189.

Elburg, M.A. & Nicholls, A. 1995. Origin of micrograniteoid enclaves in the S-type Wilson's Promontory Batholith, Victoria: evidence for magma mingling. *Australian Journal of Earth Sciences*, **42**, 423-435.

Ellam, R.M. & Hawkesworth, C.J. 1988. Is average continental crust generated at subduction zones? *Geology*, **16**, 314-317.

Ellis, D.J. & Obata, M. 1992. Migmatite and melt segregation at Cooma, New South Wales. *Transactions of the Royal Society of Edinburgh: Earth Sciences*, **83**, 95-106.

Ellis, D.J. & Thompson, A.B. 1986. Subsolidus and partial melting reactions in the quartz-excess CaO + MgO + Al_2O_3 + SiO_2 + H_2O system under water-excess and water-deficient conditions to 10 kb: some implications for the origin of peraluminous melts from mafic rocks. *Journal of Petrology*, **27**, 91-121.

Everard, J.L. 2000. Neoproterozoic basalts from northwest Tasmania: multiple mantle sources during continental rifting. *Geological Society of Australia Abstracts*, **59**, 145.

Ewart, A. 1979. A review of the mineralogy and chemistry of Tertiary-Recent dacitic, latitic, rhyolitic, and related salic volcanic rocks. *In* Barker, F. (ed) *Trondhjemites, Dacites and Related Rocks*, Elsevier, Amsterdam, 13-21.

Falloon, T.J., Green, D.H. & McCulloch, M.T. 1989. Petrogenesis of high-Mg and associated lavas from the north Tonga Trench. *In* Crawford, A.J. (ed) *Boninites and Related Rocks*, Unwin Hyman, London, 358-392.

Fanning, C.M., Ludwig, K.R., Forbes, B.G. & Preiss, W.V. 1986. Single and multiple grain U-Pb zircon analyses for the early Adelaidean Rook Tuff, Wilburan Ranges, South Australia. *Geological Society of Australia Abstracts Series*, **15**, 71-72.

Ferguson, D.J. 1993. The geology of the Glenelg River Complex in the Dergholm district of western Victoria. B.Sc. (Hons) thesis, La Trobe University, Melbourne (*unpubl.*).

Fitzherbert, J. 1998. Geology of the Glenelg River Complex in the Balmoral district of western Victoria. B.Sc. (Hons) thesis, La Trobe University, Melbourne (*unpubl.*).

Fleming, P.D. & White, A.J.R. 1984. Relationships between deformation and partial melting in the Palmer migmatites, South Australia. *Australian Journal of Earth Sciences*, **31**, 351-360.

Flood, R.H. & Vernon, R.H. 1978. The Cooma Granodiorite, Australia: an example of *in situ* crustal anatexis? *Geology*, **6**, 81-84.

Flottmann, T., Haines, P., Jago, J., James, P., Belperio, A. & Gum, J. 1998. Formation and reactivation of the Cambrian Kanmantoo Trough, SE Australia: implications for early Palaeozoic tectonics at eastern Gondwana's plate margin. *Journal of the Geological Society of London*, **155**, 525-539.

Foden, J., Sandiford, M., Dougherty-Page, J. & Williams, I. 1999. Geochemistry and geochronology of the Rathjen Gneiss: implications for the early tectonic evolution of the Delamerian Orogen. *Australian Journal of Earth Sciences*, **46**, 377-389.

Foden, J.D., Turner, S.P. & Morrison, R.S. 1990. Tectonic implications of Delamerian magmatism in South Australia and western Victoria. *Geological Society of Australia Special Publication*, **16**, 465-482.

Foster, D.A., Gray, D.R. Kwak, T.A.P. & Bucher, M. 1998. Chronology and tectonic framework of turbidite-hosted gold deposits in the western Lachlan Fold Belt, Victoria: ^{40}Ar-^{39}Ar results. *Ore Geology Reviews*, **13**, 229-250.

Foster, D.A. & Hyndman, D.W. 1990. Magma mixing and mingling between synplutonic mafic dykes and granite in the Idaho-Bitterroot batholith. *Geological Society of America Memoir,* **174**.

Fourcade, S., Martin, H., De Bremond d'Ars, J. 1992. Chemical exchange in migmatites during cooling. *Lithos*, **28,** 45-53.

Frost, T.P. & Mahood, G.A. 1987. Field, chemical and physical constraints on mafic-felsic magma interaction in the Lamarck Granodiorite, Sierra Nevada, California. *Geological Society of America Bulletin*, **99**, 272-291.

Fujimaki, H., Tatsumoto, M. & Aoki. 1984. Partition coefficients of Hf, Sr and REE between phenocrysts and groundmass. Proceedings of the 14th Lunar Planetary Science Conference Part 2, *Journal of Geophysical Research,* **89**, Supplement B662-B672.

Furman, T. & Spera, F.J. 1985. Co-mingling of acid and basic magma with implications for the origin of mafic I-type xenoliths: field and petrochemical relations of an unusual dyke complex at Eagle Lake, Sequoia National Park, California, U.S.A. *Journal of Volcanology and Geothermal Research*, **24**, 151-178.

Gamble, J.A. 1979. Some relationships between coexisting granitic and basaltic magmas and the genesis of hybrid rocks in the Tertiary central complex of Slieve Gullion, northeast Ireland. *Journal of Volcanology and Geothermal Research*, **5**, 297-316.

Gamble, J.A., Smith, I.E.M., McCulloch, M.T., Graham, I.J. & Kokelaar, B.P. 1993. The geochemistry and petrogenesis of basalts from the Taupo Volcanic Zone and Kermadec Island Arc, S.W. Pacific. *Journal of Volcanology and Geothermal Research*, **54**, 265-290.

Gao, S., Luo, T.-C., Zhang, B.-R., Zhang, H.-F., Han, Y.-W., Zhao, Z.-D. & Hu, Y.-K. 1997. Chemical composition of the continental crust as revealed by studies in East China. *Geochimica et Cosmochimica Acta,* **62**, 1959-1975.

Gibson, G.M. & Nihill, D.N. 1992. Glenelg River Complex: Western margin of the Lachlan Fold Belt or extension of the Delamerian Orogen into western Victoria? *Tectonophysics*, **214**, 69-91.

Gill, J. & Whelan, P. 1989. Early rifting of an oceanic island arc (Fiji) produced shoshonitic to tholeiitic basalts, *Journal of Geophysical Research,* **94**, 4561-4578.

Goldschmidt, V.M. 1954. *Geochemistry*. Clarendon Press, Oxford.

Gravestock, D.I. & Gatehouse, C.G. 1995. Stansbury Basin. *In* Drexel, J.F. & Preiss, W.V. (eds*) The Geology of South Australia, Volume 2, The Phanerozoic*. South Australia Geological Society Bulletin, **54**.

Gray, C.M. 1984. An isotopic mixing model for the origin of granitic rocks in southeastern Australia. *Earth and Planetary Science Letters*, **70**, 47-60.

Gray, C.M. 1990. A strontium isotope traverse across the granitic rocks of southeastern Australia: Petrogenetic and tectonic implications. *Australian Journal of Earth Sciences*, **37**, 331-349.

Gray, C.M., Kemp, A.I.S., Anderson, J.A.C., Bushell, D.J., Ferguson, D.J., Stevenson, M.D. & Fitzherbert, J. 2001. The Delamerian Tectonic Zone, western Victoria. Part 1- geology and metamorphism of stratiform rocks. *Australian Journal of Earth Sciences, in press.*

Gray, C.M. & Webb, J.A. 1995. Provenance of Palaeozoic turbidites in the Lachlan Orogenic Belt: strontium isotopic evidence. *Australian Journal of Earth Sciences*, **42**, 95-105.

Gray, D.R., Allen, R.L., Etheridge, M.A., Ferguson, C.L., Morand, V.J. & Wilson, C.J.L. 1988. Structure and tectonics. *In* Douglas, J.G. & Ferguson, J.A. (eds) *Geology of Victoria*. Victorian Division, Geological Society of Australia, Melbourne, 1-36.

Gray, D.R. & Foster, D.A. 1997. Orogenic concepts- application and definition: Lachlan Fold Belt, eastern Australia. *American Journal of Science*, **297**, 859-891.

Green, D.H. 1982. Anatexis of mafic crust and high pressure crystallisation of andesite. *In* Thorpe, R.S. (ed) *Andesites*. Wiley, New York, 465-487.

Green, T.H. 1977. Garnet in silicic liquids and its possible use as a P-T indicator. *Contributions to Mineralogy and Petrology*, **65**, 59-67.

Griffin W.L., Wang X., Jackson S.E., Pearson N.J., O'Reilly S.Y. & Xul X. 2000. Tracking magma mixing: *In situ* Hf-isotope analysis of zircons. *Geological Society of Australia Abstracts*, **59**, 194.

Haines, P.W. & Flottmann, T. 1998. Delamerian Orogeny and potential foreland sedimentation: a review of age and stratigraphic constraints. *Australian Journal of Earth Sciences*, **45**, 559-570.

Haines, P.W., Jago, J.B. & Gum, J. 2001. Turbidite deposition in the Cambrian Kanmantoo Group, South Australia. *Australian Journal of Earth Sciences*, **48**, 465-478.

Halliday, A.N. & Stephens, W.E. 1984. Crustal controls on the genesis of the 400 Ma old Caledonian granites. *Physics of the Earth and Planetary Interiors*, **35**, 89-104.

Harris, N., Ayres, M. & Massey, J. 1995. Geochemistry of granitic melts produced during the incongruent melting of muscovite: implications for the extraction of Himalayan leucogranite magmas. *Journal of Geophysical Research*, **100**, 15767-15777.

Harris, N.B.W. & Inger, S. 1992. Trace element modelling of pelite-derived granites. *Contributions to Mineralogy and Petrology*, **110**, 46-56.

Harrison, T.M. & Watson, E.B. 1984. The behaviour of apatite during crustal anatexis: equilibrium and kinetic considerations. *Geochimica et Cosmochimica Acta*, **48**, 1467-1477.

Hibbard, M.J. 1981. The mixing origins of melted feldspars. *Contributions to Mineralogy and Petrology*, **76**, 158-170.

Hibbard, M.J. 1991. Textural anatomy of twelve magma-mixed granitoid systems. *In* Didier, J. & Barbarin, B. (eds) *Enclaves and Granite Petrology*. Elsevier Science, Amsterdam, 431-443.

Hibbard, M.J. 1995. *Petrography to petrogenesis*. Prentice Hall, Englewood Cliffs, N.J.

Hilyard, D. 1990. Willouran Basic Province of Late Proterozoic tholeiitic flood basalts, Adelaide Geosyncline, South Australia. *In* Jago, J.B. & Moore, P.S. (eds) *The Evolution of a Late Precambrian-Early Palaeozoic Rift Complex: The Adelaide Geosyncline*. Geological Society of Australia, Special Publication **16,** 34-48.

Hine, R., Williams, I.S., Chappell, B.W. & White, A.J.R. 1978. Contrasts between I- and S-type granitoids of the Kosciusko Batholith. *Journal of the Geological Society of Australia*, **25**, 235-247.

Hogan, J.P. 1996. Insights from igneous reaction space: a holistic approach to granite crystallisation. *Transactions of the Royal Society of Edinburgh: Earth Sciences*, **87**, 147-157.

Holdaway, M.J. 1971. Stability of andalusite and the aluminium silicate phase diagram. *American Journal of Science*, **271**, 97-131.

Holtz, F., Johannes, W. & Pichavant, M. 1992. Peraluminous granites: the effect of alumina on melt composition and coexisting minerals. *Transactions of the Royal Society of Edinburgh: Earth Sciences*, **83**, 409-416.

Huppert, H.E. & Sparks, R.S.J. 1988. The generation of granitic magmas by intrusion of basalt into continental crust. *Journal of Petrology*, **29**, 599-624.

Huppert, H.E., Sparks, R.S.J. & Turner, J.S. 1984. Some effects of viscosity on the dynamics of replenished magma chamber. *Journal of Geophysical Research*, **89**, 6857-6877.

Ireland, T.R., Flottmann, T., Fanning, C.M., Gibson, G.M. & Preiss, W.V. 1998. Development of the early Paleozoic Pacific margin of Gondwana from detrital-zircon ages across the Delamerian Orogen. *Geology*, **26**, 243-246.

James, R.S. & Hamilton, D.L. 1969. Phase relations in the system $NaAlSi_3O_8$-$KAlSi_3O_8$-$CaAlSi_3O_8$-SiO_2 at 1 kilobar water vapour pressure. *Contributions to Mineralogy and Petrology*, **21**, 111-141.

Johannes, W. 1978. Melting of plagioclase in the system Ab-An-H_2O and Qz-Ab-An-H_2O at P_{H_2O} = 5 kbars, an equilibrium problem. *Contributions to Mineralogy and Petrology,* **66**, 295-303.

Johannes, W. 1983. On the origin of layered migmatites. *In* Atherton, M.P. & Gribble, C.D. (eds) *Migmatites, Melting and Metamorphism.* Shiva, Nantwich, 234-248.

Johannes, W. 1985. The significance of experimental studies for the formation of migmatites. *In* Ashworth, J.R. (ed) *Migmatites.* Blackie, Glasgow, 36-82.

Johannes, W. & Gupta, L.N. 1982. Origin and evolution of migmatite. *Contributions to Mineralogy and Petrology*, **79**, 114-123.

Johannes, W. & Holtz F. 1996. *Petrogenesis and Experimental Petrology of Granitic Rocks*. Springer-Verlag, Berlin.

Johnston, A.D. & Wyllie, P.J. 1988. Interaction of granitic and basic magmas: experimental observations on contamination processes at 10 kbar with H_2O. *Contributions to Mineralogy and Petrology*, **98**, 352-362.

Joplin, G.A. 1942. Petrologic studies in the Ordovician of New South Wales I: The Cooma Complex. *Proceedings of the Linnean Society of NSW*, **67**, 156-96.

Joyce, D.B. & Voigt, D.E. 1994. A phase equilibrium study in the system $KAlSi_3O_8$-$NaAlSi_3O_8$-SiO_2-Al_2SiO_5-H_2O and petrogenetic implications. *American Mineralogist*, **79**, 304-512.

Kay, R.W. 1978. Aleutian magnesian andesites: melts from subducted Pacific ocean crust. *Journal of Volcanology and Geothermal Research*, **4**, 117-132.

Kay, R.W. & Mahlburg-Kay, S. 1991. Creation and destruction of lower continental crust. *Geol. Rundsch*, **80**, 259-278.

Keay, S., Collins, W.J. & McCulloch, M.T. 1997. A three component Sr-Nd isotopic mixing model for granitoid genesis, Lachlan Fold Belt, eastern Australia. *Geology*, **25**, 307-310.

Keleman, P.B. 1990. Reaction between ultramafic wall rock and fractionating basaltic magma: Part I. Phase relations, the origin of calc-alkaline magma series and the formation of discordant dunite. *Journal of Petrology*, **31**, 51-98.

Keleman, P.B. 1995. Genesis of high Mg# andesites and the continental crust. *Contributions to Mineralogy and Petrology*, **120**, 1-19.

Kemp, A.I.S. 1995. The geology of the Glenelg River Complex in the Harrow district of western Victoria. B.Sc. (Hons) thesis, La Trobe University, Melbourne, (*unpubl.*).

Kemp, A.I.S., Ellis, D.J. & Gray, C.M. 2000. Genesis of peraluminous granitic rocks: a source-based perspective. *Geological Society of Australia Abstracts,* **59**, 274.

Kemp, A.I.S. & Gray, C.M. 1999a. Geological context of crustal anatexis and granitic magmatism in the northeastern Glenelg River Complex, western Victoria. *Australian Journal of Earth Sciences*, **46**, 406-420.

Kemp, A.I.S. & Gray, C.M. 1999b. A synthesis of deformation and partial melting in the Glenelg River Complex: implications for the Delamerian Orogeny. *Geological Society of Australia Abstracts* **53**.

Kemp, A.I.S., Gray, C.M., Ellis, D.J., Anderson, J.A.C & Ferguson, D.J. 2001. The Delamerian Glenelg Tectonic Zone, western Victoria: Part II. Characterisation and synthesis of igneous rocks. *Australian Journal of Earth Sciences, in press*.

Kepezhinskas, P. 1994. Diverse shoshonitic magma series in the Kamchatka Arc: relationships between intra-arc extension and composition of alkaline magmas. *In* Smellie, J.L. (ed) *Volcanism Associated with Extension at Consuming Plate Margins*, Geological Society Special Publication **81**, 249-264.

Kerrick, D.M. 1972. Experimental determination of muscovite + quartz stability with $P_{H_2O} < P_{total}$. *American Journal of Science*, **272**, 946-958.

Klein, M., Stosch, H-G. & Seck, H.A. 1997. Partitioning of high field-strength and rare-earth elements between amphibole and quartz-dioritic to tonalitic melts: an experimental study. *Chemical Geology*, **138**, 257-271.

Koyaguchi, T. 1985. Magma mixing in a conduit. *Journal of Volcanology and Geothermal Research*, **25**, 365-369.

Koyaguchi, T. 1987. Magma mixing in a squeezed conduit. *Earth and Planetary Science Letters,* **84**, 339-344.

Koyaguchi, T. & Blake, S. 1989. The dynamics of magma mixing in a rising magma batch. *Bulletin of Volcanology*, **52**, 127-137.

Kriegsman, L.M. 2001. Partial melting, partial melt extraction and partial back reaction in anatectic migmatites. *Lithos*, **56**, 75-96.

Laporte, C. & Briqueu, L. 1993. Spatial and temporal magmatic evolution of the New Hebrides arc: Pb, Sr and Nd isotopic evidence from the coexistence of two mantle components beneath the arc. *Terra Abstracts*, **5**, 582.

Le Breton, N. & Thompson, A.B. 1988. Fluid-absent (dehydration) melting of biotite in metapelites in the early stages of crustal anatexis. *Contributions to Mineralogy and Petrology*, **99**, 226-237.

Le Fort, P. 1981. Manaslu leucogranite: a collision signature of the Himalaya. A model for its genesis and emplacement. *Journal of Geophysical Research*, **86**, 10545-10568.

Le Fort, P., Cuney, M., Deniel, C., France-Lanord, F., Sheppard, S.M.F., Upreti, B.N. & Vidal, P. 1987. Crustal generation of the Himalayan leucogranites. *Tectonophysics*, **134**, 39-57.

Le Maitre, R.W. 1989 *A Classification of the Igneous Rocks and Glossary of Terms*. Blackwell, Oxford.

Liégeois, J.P., Bertrand, J.M., Black, R. 1987. The subduction- and collision-related Pan-African composite batholith of the Adrar des Iforas (Mali). A review. *Journal of Geology*, **22**, 185-211.

Lin, P-N., Stern, R.J. & Bloomer, S.H. 1989. Shoshonitic volcanism in the northern Mariana Arc 2. Large-ion lithophile and rare earth element abundances: evidence for the source of incompatible element enrichments in intraoceanic arcs. *Journal of Geophysical Research*, **94**, 4497-4514.

Lindberg, B. & Eklund, O. 1988. Interactions between basaltic and granitic magmas in a Svecofennian postorogenic granitoid intrusion, Aland, southwest Finland. *Lithos*, **22**, 13-23.

Lindsley, D.H. 1983. Pyroxene thermometry. *American Mineralogist*, **68**, 477-493.

Liu, S.F. & Fleming, P.D. 1990. Mafic dykes and their tectonic setting in the southern Adelaide Foldbelt, South Australia. *In* Parker A.J., Rickwood P.C. and Tucker D.H. (eds) *Proceedings of the Second International Dyke Conference, Adelaide, Australia*, pp. 401-413, Balkema, Rotterdam.

Longerich, H.P., Jackson, S.J., & Gunther, D. 1996. Laser ablation inductively coupled mass-spectrometric transient signal data acquisition and analyte concentration calculation. *Journal of Analytical and Atomic Spectrometry*, **11**, 899-904.

Maher, S., VandenBerg, A.H.M., McDonald, P.A. & Sapurmas, P. 1997. The geology and prospectivity of the Wangaratta 1:250 000 map sheet area. *Victorian Initiative for Minerals and Petroleum Report,* **46**, Department of Natural Resources and Environment.

Mahood, G.A. and Cornejo, C. 1992. Evidence for ascent of differential liquids in a silicic magma chamber found in a granitic pluton. *Transactions of the Royal Society of Edinburgh: Earth Sciences*, **83**, 63-69.

Mancktelow, N.S. 1990. The structure of the southern Adelaide Fold Belt, South Australia. *In* Jago, J.B. & Moore, P.S. (eds) *The Evolution of a Late Precambrian-Early Palaeozoic Rift Complex: The Adelaide Geosyncline.* Geological Society of Australia, Special Publication **16,** 369-395.

Martin, H. 1986. Effect of steeper Archaean geothermal gradient on geochemistry of subduction-zone magmas. *Geology*, **14**, 753-756.

Martin, H. 1999. Adakitic magmas: modern analogues of Archaean granitoids. *Lithos*, **46**, 411-429.

McCulloch, M.T. & Chappell, B.W. 1982. Nd isotopic characteristics of S- and I-type granites. *Earth and Planetary Science Letters*, **58**, 51-64.

McDonough,W.F. and Sun, S.-S. 1995. Composition of the Earth. *Chemical Geology*, **120**, 223-253.

McKenzie, D.P. & Bickle, M.J. 1988. The volume and composition of melt generated by extension of the lithosphere. *Journal of Petrology*, **29**, 625-679.

McLellan, E.L. 1984. Deformational behaviour of migmatites and problems of structural analysis in migmatite terrains. *Geological Magazine*, **121**, 339-345.

McLennan, S.M. 1989. Rare earth elements in sedimentary rocks: Influence of provenance and sedimentary processes. *In* Lipin, B.R. & McKay, G.A. (eds) *Geochemistry and Mineralogy of Rare Earth Elements*, MSA Reviews in Mineralogy, 21, 169-200.

Mehnert, K.R. 1968. *Migmatites and the origin of granitic rocks*. Elsevier, Amsterdam.

Meijer, A. 1980. Primitive arc volcanism and a boninite series: examples from western Pacific island arcs. *In Initial Reports of the Deep Sea Drilling Project*, vol **60**, US Government Printing Office, Washington DC, 709-730.

Menendez, M. & Ortega, L.A. 1999. Evidence of magmatic hybridization related with feeding zones: the synkinematic Guitiriz granitoid, NW Iberian Massif. *In* Castro, A. Fernandez, C. & Vigneresse, J.L. (eds) *Understanding Granites: Integrating New and Classical Techniques*. Geological Society, London, Special Publications, **168**, 255-272.

Mengel, K., Richter, M. & Johannes, W. 2001. Leucosome-forming small-scale geochemical processes in the metapelitic migmatites of the Turku area, Finland. *Lithos*, **56**, 47-73.

Miller, C.F., Hanchar, J.M., Wooden, J.L., Bennett, V.C., Harrison, T.M., Wark, D.A. & Foster, D.A. 1992. Source region of a granite batholith: evidence from lower crustal xenoliths and inherited accessory minerals. *Transactions of the Royal Society of Edinburgh: Earth Sciences,* **83**, 49-62.

Miller, C.F. & Stoddard, E.F. 1981a. The role of manganese in the paragenesis of magmatic garnet: an example from the Old Woman-Piute Range, California. *Journal of Geology*, **89**, 233-246.

Miller, C.F. & Stoddard, E.F. 1981b. The role of manganese in the paragenesis of magmatic garnet: an example from the Old Woman-Piute Range, California: a reply. *Journal of Geology*, **89**, 767-772.

Miller, C.F. & Stoddard, E.F. 1982. The role of manganese in the paragenesis of magmatic garnet: a reply. *Journal of Geology*, **90**, 341-343.

Miller, C.F., Stoddard, E.F., Bradfish, L.J. & Dollase, W.A. 1981. Composition of plutonic muscovite: genetic implications. *Canadian Mineralogist*, **9**, 25-34.

Miller, C.F., Watson, E.B. & Harrison, T.M. 1988. Perspectives on the source, segregation and transport of granitoid magmas. *Transactions of the Royal Society of Edinburgh: Earth Sciences,* **79**, 135-156.

Milnes, A.R. 1990. The Encounter Bay Granites, Fleurieu Peninsula and Kangaroo Island. *In* Jago, J.B. & Moore, P.S. (eds) *The Evolution of a Late Precambrian-Early Palaeozoic Rift Complex: The Adelaide Geosyncline.* Geological Society of Australia, Special Publication No. **16,** 421-449.

Milnes, A.R., Compston, W. & Daily, B. 1977. Pre- to syn-tectonic emplacement of early Palaeozoic granites in southeastern South Australia. *Journal of the Geological Society of Australia*, **24**, 84-106.

Montel, J.M. 1986. Experimental determination of the solubility of Ce-monazite in SiO_2-Al_2O_3-K_2O-Na_2O melts at 800°C, 2kbar, under H_2O-saturated conditions. *Geology*, **14**, 659-662.

Morand, V.J., Wohlt, K.E., Cayley, R.A., Kemp, A.I.S., Taylor D.H. & Magart, A.P.M. 2001. *Glenelg special map area report.* Geological Survey of Victoria Report, *in press.*

Moreno-Ventas, I., Rogers, G. & Castro, A. 1995. The role of hybridization in the genesis of Hercynian granitoids in the Gredos Massif, Spain: inferences from Sr-Nd isotopes. *Contributions to Mineralogy and Petrology*, **120**, 137-149.

Munskgaard, N.C. 1988. Source of the Cooma Granodiorite, New South Wales – a possible role of fluid-rock interactions. *Australian Journal of Earth Sciences*, **35**, 363-377.

Nash, W.P. and Crecraft, H.R. 1985. Partition coefficients for trace elements in silicic magmas. *Geochimica et Cosmochimica Acta*, **49**, 2309-2322.

Nekvasil, H. 1988. Calculated effect of anorthite component on the crystallization paths of H_2O-undersaturated haplogranitic melts. *American Mineralogist*, **73**, 966-981.

Nekvasil, H. & Burnham, C.W. 1987. The calculated individual effects of pressure and water content on phase equilibria in the granite system. *In* Mysen, B.O. (ed) *Magmatic Processes: Physicochemical Principles.* The Geochemical Society, Special Publication, **1**.

Norrish, K & Chappell, B.W. 1977. X-ray fluorescence spectrometry. *In* Zussman, J. (ed) *Physical Methods in Determinative Mineralogy*. 201-272.

Norrish, K & Hutton, J.T. 1969. An accurate X-ray spectrographic method for the analysis of a wide range of geological samples. *Geochimica et Cosmochimica Acta,* **33**, 431-454.

Nyman, M.W., Pattison, D.R.M. & Ghent, E.D. 1995. Melt extraction during formation of K-Feldspar + sillimanite migmatites, west of Revelstoke, British Colombia. *Journal of Petrology*, **36**, 351-374.

O'Connor, J.T. 1965. A classification of quartz-rich igneous rocks based on feldspar ratios. *US Geological Survey Professional Paper*, **525B**, 79-84.

Offler, R. & Fleming, P.D. 1968. A synthesis of folding and metamorphism in the Mount Lofty Ranges, South Australia. *Journal of the Geological Society of Australia*, **15**, 245-266.

Offler, R., McKnight, S. & Morand, V. 1998. Tectonothermal history of the western Lachlan Fold Belt, Australia – insights from white mica studies. *Journal of Metamorphic Geology*, **16**, 531-540.

O'Hara T. 1996. Geology of the Glenelg River Complex in the Balmoral District of western Victoria. B.Sc. (Hons) thesis, La Trobe University, Melbourne, (*unpubl.*).

Oldenberg, C.M., Spera, F.J., Yuen, D.A. & Sewell, L.G. 1989. Dynamic mixing in magma bodies: theory, simulations and implications. *Journal of Geophysical Research*, **94**, 9215-9236.

Oliver, N.H.S. & Barr, T.D. 1997. The geometry and evolution of magma pathways through migmatites of the Halls Creek Orogen, Western Australia. *Mineralogical Magazine*, **61**, 3-14.

Olsen, S.N. 1985. Mass balance in migmatites. *In* Ashworth, J.R. (ed) *Migmatites*. Blackie, Glasgow.

Orsini, J.B., Cocirta, C. & Zorpi, M.J. 1991. Genesis of mafic microgranular enclaves through differentiation of basic magmas, mingling and chemical exchanges with their host granitoid magmas. *In* Didier, J. & Barbarin, B. (eds), *Enclaves and Granite Petrology*. Elsevier, Amsterdam, 445-463.

Pagel, M. & Leterrier, J. 1980. The subalkaline potassic magmatism of the Ballons Massif (southern Vosges France). Shoshonitic affinity. *Lithos*, **13**, 1-10.

Parker, A.J. 1986. Tectonic development and metallogeny of the Kanmantoo Trough in South Australia. *Ore Geology Reviews*, **1**, 203-212.

Patiño Douce A.E. 1999. What do experiments tell us about the relative contribution of crust and mantle to the origin of granite magmas? *In* Castro A., Fernandez C. & Vigneresse, J.L. (eds) *Understanding Granites: Integrating New and Classical Techniques*. Geological Society, London, Special Publications, **168**, 55-76.

Patiño Douce, A.E. & Beard, J.S. 1995. Dehydration-melting of biotite gneiss and quartz amphibolite from 3 to 15 kbar. *Journal of Petrology*, **36**, 707-746.

Patiño Douce, A.E. & Beard, J.S. 1996. Effects of P, f(O_2) and Mg/Fe ratio on dehydration melting of model metagreywackes. *Journal of Petrology*, **37**, 999-1024.

Patiño Douce, A.E. & Harris, N. 1998. Experimental constraints on Himalayan anatexis. *Journal of Petrology*, **39**, 689-710.

Patiño Douce, A.E. & Johnston, A.D. 1991. Phase equilibria and melt productivity in the pelitic system: implications for the origin of peraluminous granitoids and aluminous granulites. *Contributions to Mineralogy and Petrology*, **107**, 202-218.

Peacock, S.M., Rushmer, T. & Thompson, A.B. 1994. Partial melting of subducting oceanic crust. *Earth and Planetary Science Letters*, **121**, 277-244.

Pearce, J.A. 1982. Trace element characteristics of lavas from destructive plate boundaries. *In* Thorpe, R.S. (ed) *Andesites: Orogenic Andesites and Related Rocks*. Wiley, Chichester, 525-548.

Pearce, J.A. 1983. Role of the sub-continental lithosphere in magma genesis at active continental margins. *In* Hawkesworth, C.J. & Norry, M.J. (eds) *Continental Basalts and Mantle Xenoliths*. Shiva, Nantwich, 230-249.

Pearce, J.A., Ernewein, M., Bloomer, S.H., Parson, L.M., Murton, B.J. & Johnson, L.E. 1995. Geochemistry of Lau Basin volcanic rocks: influence of ridge segmentation and arc proximity. *In* Smellie, J.L. *Volcanism Associated with Extension at Consuming Plate Margins*. Geological Society of London Special Publication, Bath.

Pearce, J.A. & Peate, D.W. 1995. Tectonic implications of the composition of volcanic arc magmas. *Annual Review of Earth and Planetary Sciences*, **23**, 251-285.

Pearce, J.A., van der Laan, S.R., Arculus, R.J., Murton, B.J., Ishii, T., Peate, D.W. & Parkinson, I.J. 1992. Boninite and harzburgite from leg 125 (Bonin-Mariana Forearc): a case study of magma genesis during the initial stages of subduction. *Proceedings of the Ocean Drilling Program, Scientific Results*, **125**, 623-656.

Peate, D.W., Pearce, J.A., Hawkesworth, C.J., Colley, H.C., Edwards, C.M.E. & Hirose, K. 1997. Geochemical variations in Vanuatu arc lavas: the role of subducted material and variable mantle wedge. *Journal of Petrology*, **38**, 1331-1358.

Petford, N. 1996. Dykes or diapirs? *Transactions of the Royal Society of Edinburgh: Earth Sciences*, **87**, 105-114.

Peto, P. 1976. An experimental investigation of melting relations involving muscovite and paragonite in the silica-saturated portion of the system K_2O-Na_2O-Al_2O_3-SiO_2-H_2O to 15 kb total pressure. *Progress in Experimental Petrology*, **3**, 41-45.

Pichavant, M., Montel, J-M. & Richard, L.R. 1992. Apatite solubility in peraluminous liquids: experimental data and an extension of the Harrison-Watson model. *Geochimica et Cosmochimica Acta*, **56**, 3855-3861.

Pidgeon, R.T. & Compston, W. 1965. The age and origin of the Cooma Granite and its associated metamorphic zones, New South Wales. *Journal of Petrology*, **6**, 193-222.

Pitcher, W.S. 1982. Granite type and tectonic environment. In Hsu, K.J. (ed) *Mountain Building Processes*. Academic Press, London.

Pitcher, W.S. 1991. Synplutonic dykes and mafic enclaves. *In* Didier, J. & Barbarin, B. (eds) *Enclaves and Granite Petrology*. Elsevier, Amsterdam, 383-391.

Pitcher, W.S. 1997. *The Nature and Origin of Granite*. Chapman and Hall, London.

Pitcher, W.S., Atherton, M.P., Cobbing, E.J. & Beckinsale, R.D. (eds) 1985. *Magmatism at a Plate Edge: the Peruvian Andes*. Blackie and Son, Glasgow.

Pitcher, W.S. & Bussell, M.A. 1985. Andean dyke swarms: andesite in synplutonic relationship with tonalite. *In* Pitcher, W.S., Atherton, M.P., Cobbing, E.J. & Beckinsale, R.D. (eds) *Magmatism at a Plate Edge: The Peruvian Andes*. Blackie Halstead, Glasgow.

Plank, T. & Langmuir, C.H. 1998. The geochemical composition of subducting sediment and its consequences for the crust and mantle. *Chemical Geology* **145**: 325-394.

Platevoet, B. & Bonin, B. 1991. Enclaves and mafic-felsic associations in the Permian alkaline province of Corsica, France: physical and chemical interactions between coeval magmas. *In* Didier, J. & Barbarin, B. (eds) *Enclaves and Granite Petrology*. Elsevier Science, Amsterdam, 191-204.

Poli, G. & Tommassini, S. 1991. Model for the origin and significance of microgranular enclaves in calc-alkaline granitoids. *Journal of Petrology*, **32**, 657-666.

Poli, G. & Tommassini, S. 1999. Geochemical modeling of acid-basic magma interaction in the Sardinia-Corsica Batholith: the case study of Sarrabus, southeastern Sardinia, Italy. *Lithos*, **46**, 553-571.

Poli, G., Tommasini, S. & Halliday, A.N. 1996. Trace element and isotopic exchange during acid-basic magma interaction processes. *Transactions of the Royal Society of Edinburgh: Earth Sciences* **87**, 225-232.

Preiss, W.V. 1990. A stratigraphic and tectonic overview of the Adelaide Geosyncline, South Australia. *Geological Society of Australia Special Publication*, **16**, 1-33.

Preiss, W.V. 1993. Neoproterozoic. *In* Drexel, J.F., Preiss, W.V. & Parker, A.J. (eds) *The Geology of South Australia*. Geological Survey of South Australia, 171-203.

Pressley, R.A. & Brown, M. 1999. The Phillips pluton, Maine, USA: evidence of heterogeneous crustal sources and implications for granite ascent and emplacement mechanisms in convergent orogens. *Lithos*, **46**, 335-366.

Rapp R.P. 1995. Amphibole-out phase boundary in partially melted metabasalt, its control over liquid fraction and composition, and source permeability. *Journal of Geophysical Research*, **100**, 15601-15610.

Rapp, R.P. & Watson, E.B. 1986. Monazite solubility and dissolution kinetics: implication for the Th and light rare-earth chemistry of felsic magmas. *Contributions to Mineralogy and Petrology*, **94**, 304-316.

Rapp, R.P. & Watson, E.B. 1995. Dehydration melting of metabasalt at 8-32 kbar: implications for continental growth and crust-mantle recycling. *Journal of Petrology*, **36**, 891-931.

Rapp, R.P., Watson, E.B. & Miller, C.F. 1991. Partial melting of amphibolite/eclogite and the origin of Archaean trondhjemites and tonalites. *Precambrian Research*, **51**, 1-25.

Reid, J.B., Evans, O.C. & Fates, D.G. 1983. Magma mixing in granitic rocks of the central Sierra Nevada, California. *Earth and Planetary Science Letters*, **66**, 243-261.

Ricci, C.A, Talarico, F. & Palmieri, R. 1997. Tectonothermal evolution of the Antarctic Paleo-Pacific active margin of Gondwana: A northern Victoria Land perspective. *In* Ricci, C.A. (ed) *The Antarctic Region: Geological Evolution and Processes. Proceedings of the VII International Symposium on Antarctic Earth Sciences*, Tierra Antarctica Publication, 213-218.

Richards J. R. & Singleton O. P. 1981. Palaeozoic Victoria, Australia: igneous rocks, ages and their interpretation. *Journal of the Geological Society of Australia* **28**, 395-421.

Rickwood, P.C. 1989. Boundary lines within petrologic diagrams which use oxides of major and minor elements. *Lithos*, **22**, 247-263.

Roberts M.P. & Clemens J.D. 1993. Origin of high-potassium, calc-alkaline, I-type granitoids. *Geology*, **21**, 825-828.

Roberts, M.P., Pin, C., Clemens, J.D. & Paquette, J-L. 2000. Petrogenesis of mafic to felsic plutonic rock associations: the calc-alkaline Quérigut Complex, French Pyrenees. *Journal of Petrology*, **41**, 809-842.

Rollinson, H. 1993. *Using Geochemical Data: Evaluation, Presentation, Interpretation.* Longman Scientific & Technical, Essex.

Royer, J-Y. & Rollet, N. 1997. Plate-tectonic setting of the Tasmanian region. *Australian Journal of Earth Sciences*, **44**, 543-560.

Sajona, F.G., Maury, R.C., Bellon, H., Cotten, J., Defant, M.J. 1996. High field strength element enrichment of Pliocene-Pleistocene island arc basalts, Zamboanga Peninsula, Western Mindanao (Philippines). *Journal of Petrology*, **37**, 693-726.

Sajona, F.G., Maury, R.C., Bellon, H., Cotten, J., Defant, M.J. & Pubellier, M. 1993. Initiation of subduction and the generation of slab melts in western and eastern Mindanao, Philippines. *Geology*, **21**, 1007-1010.

Sandiford, M. & Flottmann, T. 1999. Overview of the Geology of the southeastern Adelaide Fold Belt. *In* Wilson, C.J.L. (ed) *The Great Southern Transect II: A Geological Section Incorporating the Lachlan Fold Belt, Adelaide Fold Belt and Gawler Craton, Halls Gap (Victoria) to Port Lincoln (S.A.)*. Specialist Group in Tectonics and Structural Geology Field Guide No. **6**, Geological Society of Australia.

Sandiford, M., Foden, J., Zhou, S. & Turner, S. 1992. Granite genesis and the mechanics of convergent orogenic belts with application to the southern Adelaide Fold Belt. *Transactions of the Royal Society of Edinburgh: Earth Sciences*, **83**, 83-93.

Sawyer, E.W. 1987. The role of partial melting and fractional crystallization in determining discordant migmatite leucosome compositions. *Journal of Petrology*, **28**, 445-473.

Sawyer, E.W. 1991. Disequilibrium melting and the rate of melt-residue separation during migmatisation of mafic rocks from the Grenville Front, Quebec. *Journal of Petrology*, **32**, 701-738.

Sawyer, E. W. 1994. Melt segregation in the continental crust. *Geology*, **22**, 1019-1022.

Sawyer, E. W. 1996. Melt segregation and magma flow in migmatites: implications for the generation of granitic magmas. *Transactions of the Royal Society of Edinburgh: Earth Sciences* **87**, 85-94.

Sawyer, E.W. 1998. Formation and evolution of granite magmas during crustal reworking: the significance of diatexites. *Journal of Petrology*, **39**, 1147-1167.

Sawyer, E.W. 1999. Criteria for the recognition of partial melting. *Physics and Chemistry of the Earth*, **24**, 269-279.

Sawyer, E.W. 2000. Diatexite or metatexite? The importance of melt generation rate. *Geological Society of Australia, Abstracts,* **59**, 437.

Scheibner, E. & Veevers, J.J. 1999. Tasman Fold Belt system. *In* Veevers, J.J. (ed) *Billion-year Earth History of Australia and Neighbours in Gondwanaland.* GEMOC Press, Sydney, 154-233.

Searle, M.P., Parrish, R.R., Hodges, K.V., Hurford, A. & Ayres, M.W. 1997. Shisha Pangma leucogranite, south Tibetan Himalya: field relations, geochemistry, age, origin, and emplacement. *Journal of Geology*, **105**, 295-317.

Sederholm, J.J. 1967. *Selected Works: Granites and Migmatites*. Oliver & Boyd, Edinburgh.

Shelley, D. 1993. *Igneous and Metamorphic Rocks Under the Microscope.* Chapman & Hall, London.

Silver, L.T. & Chappell, B.W. 1988. The Peninsular Ranges Batholith: an insight into the evolution of the Cordilleran batholiths of southwestern North America. *Transactions of the Royal Society of Edinburgh: Earth Sciences*, **79**, 105-121.

Shimoda, G., Tatsumi, Y., Nohda, S., Ishizaka, K. & Jahn, B.M. 1998. Setouchi high-Mg andesites revisited: geochemical evidence for melting of subducting sediments. *Earth and Planetary Science Letters*, **160**, 479-492.

Sisson, T.W. & Grove, T.L. 1993. Temperatures and H_2O contents of low-MgO high-alumina basalts. *Contributions to Mineralogy and Petrology,* **113**, 167-184.

Sisson, T.W., Grove, T.L. & Coleman, D.S. 1996. Hornblende gabbro sill complex at Onion Valley, California, and a mixing origin for the Sierra Nevada batholith. *Contributions to Mineralogy and Petrology,* **126**, 81-108.

Slater, K.R. 1995. An appraisal of new airborne geophysical data over the Glenelg region, North West VIMP area, Victoria. *Victorian Initiative for Minerals and Petroleum Report,* **14**. Department of Agriculture, Energy and Minerals, Melbourne.

Solar, G.S. & Brown. M. 2001. Petrogenesis of migmatites in Maine, USA: possible source of peraluminous leucogranite in plutons? *Journal of Petrology, in press.*

Sørensen, S.S. 1988. Petrology of amphibolite-facies mafic and ultramafic rocks from the Catalina Schist, southern California: metasomatism and migmatization in a subduction zone metamorphic setting. *Journal of Metamorphic Geology*, **6**, 405-435.

Sparks, R.S.J. & Marshall, L.A. 1986. Thermal and mechanical constraints on mixing between mafic and silicic magmas. *Journal of Volcanology and Geothermal Research*, **29**, 99-124.

Spear, F.S., Kohn, M.J. & Cheney, J.T. 1999. P-T paths from anatectic pelites. *Contributions to Mineralogy and Petrology*, **134**, 17-32.

Spencer-Jones, D. 1965. The geology and structure of the Grampians area, western Victoria. *Memoirs of the Geological Survey of Victoria,* **25**.

Sprigg, R.C. & Campana, B. 1953. The age and facies of the Kanmantoo Group. *Australian Journal of Science*, **16,** 12-14.

Springer W. & Seck H.A. 1997. Partial fusion of basic granulites at 5 to 15 kbar: implications for the origin of TTG magmas. *Contributions to Mineralogy and Petrology*, **127**, 30-45.

Stephens, W.E., Holden, P. & Henney, P.J. 1991. Microdioritic enclaves within the Scottish Caledonian granitoids and their significance for crustal magmatism. *In* Didier, J. & Barbarin, B. (eds) *Enclaves and Granite Petrology*. Elsevier Science, Amsterdam, 125-133.

Stern, C.R. & Kilian, R. 1996. Role of the subducted slab, mantle wedge and continental crust in the generation of adakites from the Andean Austral Volcanic Zone. *Contributions to Mineralogy and Petrology*, **123**, 263-281.

Stern, R.J., Jackson, M.C., Fryer, P., Ito, E. 1993. O, Sr, Nd and Pb isotopic composition of the Kasuga cross-chain in the Mariana arc: a new perspective of the K-h relationship. *Earth and Planetary Science Letters*, **119**, 459-475.

Stevens, G., Clemens, J.D. & Droop, G.T-R. 1997. Melt production during granulite-facies anatexis: experimental data from "primitive" metasedimentary protoliths. *Contributions to Mineralogy and Petrology*, **128**, 352-270.

Streckeisen, A.L. 1976. To each plutonic rock its proper name. *Earth Science Reviews*, **12**, 1-33.

Strong, B.F. & Hanmer, S.K. 1981. The leucogranites of southern Brittany: Origin by faulting, frictional heating, fluid flux and fractional melting. *Canadian Mineralogist*, **19**, 163-176.

Stuart-Smith, P. & Black, L. 1994. The Mount Stavely Volcanic Complex, western Victoria: mainland equivalents of the Tasmanian Cambrian Mount Read Volcanics. *Australian Geological Survery Organisation Newletter*, Dec 1994.

Sun, S.-s. & McDonough, W.F. 1989. Chemical and isotopic systematics of oceanic basalts: implications for mantle composition and processes. *In* Saunders, A.D. & Norry, M.J. (eds) *Magmatism in the Ocean Basins*, Geological Society Special Publication, **42**, 313-345.

Swanson, S.E., Naney, M.T. & Westrich, A. 1989. Crystallisation history of Obsidian Dome, Inyo Domes, California. *Bulletin of Volcanology*, **51**, 161-176.

Tait, R.E. & Harley, S.L. 1988. Local processes involved in the generation of migmatites within mafic granulites. *Transactions of the Royal Society of Edinburgh: Earth Sciences*, **79**, 209-222.

Tate, M.C., Clarke, D.B. & Heaman, L.M. 1997, Progressive hybridisation between Late Devonian mafic-intermediate and felsic magmas in the Meguma Zone of Nova Scotia, Canada. *Contributions to Mineralogy and Petrology*, **126**, 401-415.

Tatsumi, Y. 1981. Melting experiments on a high-magnesian andesite. *Earth and Planetary Science Letters*, **54**, 357-365.

Tatsumi, Y. 1982. Origin of high-magnesian andesites in the Setouchi volcanic belt, southwest Japan, II. Melting phase relations at high pressures. *Earth and Planetary Science Letters*, **60**, 305-317.

Tatsumi, Y. & Eggins, S. 1995. *Subduction zone magmatism*. Blackwell, Oxford.

Tatsumi, Y. & Ishizaka, K. 1982. Origin of high-magnesian andesites in the Setouchi volcanic belt, southwest Japan, I Petrographical and chemical characteristics. *Earth and Planetary Science Letters*, **60**, 293-304.

Tatsumi, Y. & Maruyama, S. 1989. Boninites and high-Mg andesites: tectonics and petrogenesis. *In* Crawford, A.J. (ed) *Boninites and Related Rocks*, Unwin Hyman, London. 50-71.

Taylor, D.H., Cayley, R.A., Morand, V.J., Wohlt, K.E. & Moore, D.H. 2000. The Delamerian Orogeny in western Victoria: consequence of arc-continent collision. *Geological Society of Australia Abstracts*, **59**, 492.

Taylor, S.R. & McLennan, S.M. 1995. The geochemical evolution of the continental crust. *Reviews of Geophysics*, **33**, 241-265.

Thompson, A.B. 1982. Dehydration melting of pelitic rocks and the generation of H_2O-undersaturated granitic liquids. *American Journal of Science*, **282**, 1567-1595.

Thompson, A.B. 1996. Fertility of crustal rocks during anatexis. *Transactions of the Royal Society of Edinburgh: Earth Sciences*, **87**, 1-10.

Thompson, A.B. & Algor, J.R. 1977. Model systems for anatexis of pelitic rocks. I. Theory of melting reactions in the system $KAlO_2$-$NaAlO_2$-Al_2O_3-SiO_2-H_2O. *Contributions to Mineralogy and Petrology*, **63**, 247-269.

Thompson, A.B. & Tracy, R.J. 1979. Model systems for anatexis of pelitic rocks. II. Facies series melting and reactions in the system CaO-$KAlO_2$-$NaAlO_2$-Al_2O_3-SiO_2-H_2O. *Contributions to Mineralogy and Petrology*, **70**, 429-438.

Thomson, B.P. 1969. Precambrian basement cover, the Adelaide System. *In* Parkin, L.W. (ed) *Handbook of South Australian Geology.* Geological Survey of South Australia, Adelaide, 49-83.

Tindle, A.G. & Pearce, J.A. 1981. Petrogenetic modelling of *in situ* fractional crystallisation in the zoned Loch Doon pluton, Scotland. *Contributions to Mineralogy and Petrology*, **78**, 196-207.

Toksov, M.N., Minearm J.W., Julian, B.R. 1971. Temperature fields and geophysical effects of a downgoing slab. *Journal of Geophysical Research*, **76**, 1113-1138.

Turner, S.P. 1996. Petrogenesis of the late-Delamerian gabbroic complex at Black Hill, South Australia: implications for convective thinning of the lithospheric mantle. *Mineralogy and Petrology*, **56**, 51-89.

Turner, S.P., Adams, C.J., Flottman, T. & Foden, J.D. 1993a. Geochemical and geochronological constraints on the Glenelg River Complex, western Victoria. *Australian Journal of Earth Sciences*, **40**, 275-292.

Turner, S. & Foden, J. 1990. The nature of mafic magmatism through the evolution of the Adelaide Foldbelt and subsequent Delamerian Orogeny. *In* Parker, A.J., Rickwood, P.C. & Tucker, D.H. (eds) *Mafic Dykes and Emplacement Mechanisms*, Balkema, Rotterdam.

Turner, S. & Foden, J. 1996. Magma mingling in late-Delamerian A-type granites at Mannum, South Australia. *Mineralogy and Petrology*, **56**, 147-169.

Turner, S.P., Foden, J.D. & Morrison, R.S. 1992. Derivation of some A-type magmas by fractionation of basaltic magma: an example from the Padthaway Ridge, South Australia. *Lithos* **28**, 151-179.

Turner, S.P., Foden, J., Sandiford, M. & Bruce, D. 1993b. Sm-Nd isotopic evidence for the provenance of sediments from the Adelaide Fold Belt and southeastern Australia with implications for episodic crustal addition. *Geochimica et Cosmochimica Acta,* **57**, 1837-1856.

Turner, S.P., Kelley, S.P., VandenBerg, A.H.M., Foden, J.D., Sandiford, M. & Flottmann, T. 1996. Source of the Lachlan Fold Belt flysch linked to convective removal of the lithospheric mantle and rapid exhumation of the Delamerian-Ross fold belt. *Geology*, **24**, 941-944.

Tuttle, O.F. & Bowen, N.L. 1958. Origin of granite in the light of experimental studies in the system $NaAlSi_3O_8$-$KAlSi_2O_8$-SiO_2-H_2O. *Geological Society of America Memoir,* **74**.

VandenBerg, A.H.M. 1999. Timing of orogenic events in the Lachlan Orogen. *Australian Journal of Earth Sciences*, **46**, 691-701.

VandenBerg, A.H.M. & Wilkinson, H.E. 1982. Victoria. *In* Cooper, R.A. & Grindley, G.W. (eds) *Late Proterozoic to Devonian sequences of southeastern Australia, Antarctica and New Zealand and their correlation. Journal of the Geological Society of Australia Special Publication*, **9**, 36-47.

VandenBerg, A.H.M., Willman, C.E., Maher, S., Simons, B.A., Cayley, R.A., Taylor, D.H., Morand, V.J., Moore, D.H. & Radojkovic, A. 2000. The Tasman Fold Belt system in Victoria. *Geological Survey of Victoria Special Publication.*

Van der Laan, S.R., Flower, M.F.J. & van Groos, A.F.K. 1989. Experimental evidence for the origin of boninites: near liquidus phase relations to 7.5 kbar. *In* Crawford, A.J. (ed) *Boninites and Related Rocks*, Unwin Hyman, London. 112-147.

Veevers, J.J. 2000. Antarctic Beardmore - Ross and Mirny Provenances saturate Paleozoic-Mesozoic east Gondwanaland with 0.6-0.5 Ga zircons. *In* Veevers, J.J. (ed) *Billion-year Earth History of Australia and Neighbours in Gondwanaland.* Gemoc Press, Sydney, 110-130.

Vernon, R.H. 1983. Restite, xenoliths and microgranitoid enclaves in granites. *Journal and Proceedings of the Royal Society of New South Wales,* **116**, 77-103.

Vernon, R.H. 1984. Microgranitoid enclaves: globules of hybrid magma quenched in a plutonic environment. *Nature*, **304**, 438-439.

Vernon, R.H. 1990. Crystallization and hybridism in microgranitoid enclave magmas: microstructural evidence. *Journal of Geophysical Research*, **95**, 17849-17859.

Vernon, R.H. 1991. Interpretation of microstructures of microgranitoid enclaves. *In* Didier, J. & Barbarin, B. (eds) *Enclaves and Granite Petrology*. Elsevier Science, Amsterdam, 277-290.

Vernon, R.H. & Collins, W.J. 1988. Igneous microstructures in migmatites. *Geology*, **16**, 1126-1129.

Vernon, R.H., Etheridge, M.A. & Wall, V.J. 1988. Shape and microstructure of microgranitoid enclaves: indicators of magma mingling and flow. *Lithos*, **22**, 1-11.

Vielzeuf, D. & Holloway, J.R. 1988. Experimental determination of the fluid-absent melting relations in the pelitic system. *Contributions to Mineralogy and Petrology*, **98**, 257-276.

Vielzeuf, D. & Montel, J.M. 1994. Partial melting of metagreywackes. Part 1. Fluid-absent experiments and phase relationships. *Contributions to Mineralogy and Petrology*, **117**, 375-393.

Waight, T.E., Maas, R. & Nicholls, I.A. 2000. Fingerprinting feldspar phenocrysts using crystal isotopic composition stratigraphy: implications for crystal transfer and magma mingling in S-type granites. *Contributions to Mineralogy and Petrology*, **139**, 227-239.

Wall, V.J., Clemens, J.D. & Clarke, D.B. 1987. Models for granitoid evolution and source compositions. *Journal of Geology*, **95**, 731-749.

Watson, E.B. 1982. Basalt contamination by continental crust: some experiments and models. *Contributions to Mineralogy and Petrology*, **56**, 119-134.

Watson, E.B. 1988. The role of accessory minerals in granitoid geochemistry. *Transactions of the Royal Society of Edinburgh: Earth Sciences*, 19-20.

Watson, E.B. & Harrison, M. 1983. Zircon saturation revisited: temperature and composition effects in a variety of crustal magma types. *Earth and Planetary Science Letters*, **64**, 295-304.

Watson, E.B. & Jurewicz, S.R. 1984. Behaviour of alkalis during diffusive interaction of granitic xenoliths with basalt magma. *Journal of Geology*, **92**, 121-131.

Watt, G.R., Burns, I.M. & Graham, G.A. 1996. Chemical characteristics of migmatites: accessory phase distribution and evidence for fast melt segregation rates. *Contributions to Mineralogy and Petrology*, **125**, 100-111.

Watt, G.R. & Harley, S.L. 1993. Accessory phase controls on the geochemistry of crustal melts and restites produced during water-undersaturated partial melting. *Contributions to Mineralogy and Petrology*, **114**, 550-566.

Wedepohl, K.H. 1991. Chemical composition and fractionation of the continental crust. *Geol. Rundsch*, **80**, 207-223.

Wells, B.E. 1956. Geology of the Casterton District. *Proceedings of the Royal Society of Victoria*, **68**, 85-110.

White, A.J.R. & Chappell, B.W. 1977. Ultrametamorphism and granitoid genesis. *Tectonophysics*, **43**, 7-22.

White, A.J.R. & Chappell, B.W. 1990. Per migma ad magma downunder. *Geological Journal*, **25**, 221-225.

White, A.J.R., Chappell, B.W. & Cleary, J.R. 1974. Geologic setting and emplacement of some Australian Paleozoic batholiths and implications for intrusive mechanisms. *Pacific Geology*, **8**, 159-171.

White, A.J.R., Chappell, B.W. & Wyborn, D. 1999. Application of the restite model to the Deddick Granodiorite and its enclaves – a reinterpretation of the observations and data of Maas *et al.* (1997). *Journal of Petrology*, **40**, 413-421.

White, A.J.R., Compston, W. & Kleeman, A.W. 1967. The Palmer Granite – A study of a granite within a regional metamorphic environment. *Journal of Petrology*, **8**, 29-50.

White, W.H. & Dupre, B. 1986. Sediment subduction and magma genesis in the Lesser Antilles: isotopic and trace element constraints. *Journal of Geophysical Research*, **91**, 5927-5941.

Whitney, D.L. & Irving, A.J. 1994. Origin of K-poor leucosomes in a metasedimentary migmatite complex by ultrametamorphism, syn-metamorphic magmatism and subsolidus processes. *Lithos,* **32**, 173-192.

Wickham, S.M. 1987. The segregation and emplacement of granitic magmas. *Journal of the Geological Society of London*, **144**, 281-297.

Wickham, S.M. 1990. Isotopic modification of the continental crust: implications for the use of isotope tracers in granite petrogenesis. *In* Ashworth, J.R. & Brown, M. (eds) *High-temperature Metamorphism and Crustal Anatexis*, Unwin Hyman, London.

Wiebe, R.A. 1968. Plagioclase stratigraphy: a record of magmatic conditions and events in a granite stock. *American Journal of Science*, **266**, 690-703.

Wiebe, R.A. 1973. Relations between coexisting basaltic and granitic magmas in a composite dyke. *American Journal of Science*, **273**, 130-151.

Wiebe, R.A. 1980. Commingling of contrasted magmas in the plutonic environment: examples from the Nain Anorthositic Complex. *Journal of Geology*, **88**, 197-209.

Wiebe, R.A. 1991. Commingling of contrasted magmas and generation of mafic enclaves in granitic rocks. *In* Didier, J. & Barbarin, B. (eds) *Enclaves and Granite Petrology*. Elsevier Science, Amsterdam, 393-401.

Wiebe, R.A. 1994. Silicic magma chambers as traps for basaltic magmas: the Cadillac Mountain Intrusive Complex, Mount Desert Island, Maine. *Journal of Geology*, **102**, 423-437.

Wiebe, R.A. 1996. Mafic-silicic layered intrusions: the role of basaltic injections on magmatic processes and the evolution of silicic magma chambers. *Transactions of the Royal Society of Edinburgh: Earth Sciences*, **87**, 233-242.

Williams, I.S., Chappell, B.W., Chen, Y.D. & Crook, K.A.W. 1992. Inherited and detrital zircons – vital clues to the granite protoliths and early igneous history of southeastern Australia. *Transactions of the Royal Society of Edinburgh: Earth Sciences, Abstract,* **83**, 503.

Williams, M.L., Hanmer, S., Kopf, C. & Darrach, M. 1995. Syntectonic generation and segregation of tonalitic melts from amphibolite dikes in the lower crust, Striding-Athabasca mylonite zone, northern Saskatchewan. *Journal of Geophysical Research*, **100**, 15717-15734.

Wilson, C.J.L., Will, T.M., Cayley, R.A. & Chen, S. 1992. Geologic framework and tectonic evolution in western Victoria, Australia. *Tectonophysics*, **214**, 93-127.

Wilson, M. 1989. *Igneous Petrogenesis*. Chapman and Hall, London.

Woodhead, J., Eggins, S. & Gamble, J. 1993. High field strength and transition element systematics in island arc and back-arc basin basalts: evidence for multi-stage melt extraction and an ultradepleted mantle wedge. *Earth and Planetary Science Letters*, **114**, 491-504.

Wolf, M.B. & London, D. 1994. Apatite dissolution into peraluminous haplogranitic melts: an experimental study of solubilities and mechanisms. *Geochimica et Cosmochimica Acta*, **58**, 4127-4145.

Wolf, M.B. & Wyllie, P.J. 1991. Dehydration-melting of solid amphibolite at 10 kbar: textural development, liquid interconnectivity and applications to the segregation of magmas. *Mineralogy and Petrology*, **44**, 157-179.

Wyborn, D. 1998. From molten granite to solid rock – how does fractional crystallisation work? *Australian Geological Survey Organisation Record,* **33**, 45.

Wyborn, D., Turner, B.S. & Chappell, B.W. 1987. The Boggy Plain Supersuite: a distinctive belt of I-type igneous rocks of potential economic significance in the Lachlan Fold Belt. *Australian Journal of Earth Sciences*, **34**, 21-43.

Wyborn, D., White, A.J.R. & Chappell, B.W. 1991. Enclaves in the S-type Cowra Granodiorite. Second Hutton Symposium on Granites and Related Rocks, Canberra. Excursion guide, 25. *Bureau of Mineral Resources, Geology and Geophysics, Australia, Record* **24**.

Wyborn, L.A.I., Wyborn, D., Warren, R.G. & Drummond, B.J. 1992. Proterozoic granite types in Australia: implications for lower crust composition, structure and evolution. *Transactions of the Royal Society of Edinburgh: Earth Sciences*, **83**, 201-209.

Wyllie, P.J. 1971. The role of water in magma genesis and initiation of diapiric uprise in the mantle. *Journal of Geophysical Research*, **76**, 1328-1338.

Xu, X., Donga, C., Lia, W. & Zhoua, X. 1999. Late Mesozoic intrusive complexes in the coastal area of Fujian, SE China: the significance of the gabbro-diorite-granite association. *Lithos*, **46**, 299-315.

Yoder, H.S. 1968. Albite-anorthite-quartz-water at 5 kbar. *Carnegie Institute of Washington Yearbook*, **66**, 477-478.

Yogodzinski, G.M., Volynets, O.N., Koloskov, A.V., Seliverstov, N.I. & Matvenko, V.V. 1994. Magnesian andesites and the subduction component in a strongly calc-alkaline series at Piip volcano, far western Aleutians. *Journal of Petrology*, **35**, 163-204.

Zeck, H.P. 1992. Restite-melt and mafic-felsic magma mixing and mingling in an S-type dacite, Cerro del Hoyazo, southeastern Spain. *Transactions of the Royal Society of Edinburgh: Earth Sciences*, **83**, 139-144.

Zen, E. 1986. Aluminium enrichment in silicate melts by fractional crystallisation, some mineralogical and petrographic constraints. *Journal of Petrology*, **27**, 1095-1117.

Zen, E. 1988. Phase relations of peraluminous granitic rocks and petrogenetic implications. *Annual Review of Earth and Planetary Sciences*, **16**, 21-51.

Zorpi, M.J., Coulon, C. & Orsini, J.B. 1991. Hybridization between felsic and mafic magmas in calc-alkaline granitoids – case study in northern Sardinia, Italy. *Chemical Geology*, **92**, 45-86.

APPENDIX A

Analytical procedures

A.1. Mineral chemistry

The mineral compositions from forty seven GRC rocks were ascertained by electron probe microanalysis of polished thin sections using a JEOL JSM-6400 SEM, equipped with an Oxford light element EDS detector, housed at the Electron Microscopy Unit, Research School of Biological Sciences, Australian National University. Analyses were conducted with a 1 nA beam current and 15 kV accelerating voltage, using a defocussed beam to yield a 20-30 um spot size. Elements were calibrated against natural mineral and simple oxide standards. Data was reduced by Link ISIS SEMquant software and ZAF corrections were applied. Acceptable analyses from samples referred to in Part II and Part III are listed in Appendices B and F respectively.

A.2. Whole rock geochemistry (X-ray fluorescence spectrometry)

The major and trace element geochemistry has been determined for 227 GRC rocks (Appendices C and G), mostly collected using a petrol-driven drill. Weathered surfaces from representative samples were removed by sledgehammer and hydraulic splitting, after which the sample was reduced to gravel size by a vertical tungsten carbide plate crusher and milled to <10 μm particle size in a tungsten carbide ring mill.

For migmatite samples, separation of leucosomes involved firstly removing as much mesosome and melanosome material as possible from the leucosome body by hydraulic splitting, followed by crushing the remainder of the sample into gravel-sized particles and handpicking the quartzofeldspathic leucosome portion. Leucosome particles with adhering melanosome were discarded. Smaller migmatite samples, and those containing texturally heterogeneous leucosomes, were serially slabbed, after which the most homogeneous portion of the leucosome was selected and removed by sawing. This was then inspected for saw contamination, rinsed with ethanol and distilled water, oven-dried and pulverised as outlined above. A similar approach was adopted for diatexites, which were sawn into ~2 cm thick slabs from which the leucogranitic domains (2-4 cm thick) were easily removed from the micaceous matrix by hydraulic splitting.

All analyses were conducted at the Department of Geology, Australian National University, utilising a Phillips PW2400 spectrometer for major elements, and a Spectro X-lab for trace elements. Major element concentrations were determined by duplicate analysis of fused Li-

borate glass discs, according to the method of Norrish & Hutton (1969), whereas trace elements were measured on duplicate to multiple pressed powder pellets, stabilised with several drops of a PVA binder, following Norrish & Chappell (1977).

Where quoted, FeO was determined by duplicate titration against a potassium dichromate standard, using a barium diphenylamine sulphonate indicator.

Loss on ignition (LOI) for all samples represents the percentage change in weight after heating ~0.8 g of sample powder in an 1100°C furnace for 1 hour.

A.3. Trace element and REE geochemistry: Laser Ablation ICP-MS

The trace element geochemistry of 35 samples was also determined by laser ablation ICP-MS, the instrument being housed at the Research School of Earth Sciences (A.N.U.) and operated by Dr S.M. Eggins. This was done to obtain concentration of the rare earths and other elements, such as Hf and U, that are difficult to analyse precisely by XRF, and enabled cross-checking of the other trace element abundances determined by XRF. Note that as the same sample powders were used as those prepared for the XRF, Ta concentrations are possibly unreliable, due to contamination from the tungsten carbide mill.

Analyses were obtained according to the method described by Eggins (in prep.). Samples were prepared as Li-borate glasses following the standard procedures for fusion discs employed for XRF analysis (Norrish & Hutton 1969). The flux used was a 12:22 mixture of Li-tetraborate and Li-metaborate. A 3:1 mixture of flux (~1.5 g) to powdered sample (~0.5 g) was weighed into Pt crucibles, then stirred, a drop of NH_4I added, and the mixture placed in a muffle furnace for 15 minutes at 1050°C. The molten mixture was then poured onto a graphite mould and pressed to form a thin (~1mm) glass disc (30 mm diameter). The glass discs were glued in stacks of 10-12 then set in epoxy resin blocks, which, upon curing, were cut with a diamond saw to expose the discs as a sandwich in cross-section. This surface was ground flat and then polished.

The ArF (193 nm) EXCIMER laser sampling system and ICP-MS instrumentation (Agilent 7500s) employed for analysis are described in detail by Eggins *et al.* (1998). A broad (25x8mm) UV laser beam is used to illuminate an aperture, the image of which is demagnified by 20 times onto the sample surface using a 150 mm focal length, silica doublet lens. Sample ablation is conducted in a He atmosphere in order to minimise sample recondensation during ablation about the target site, and thereby maximise sample transport to the ICP. The He flow

(300 cc/min) containing the ablation products was subsequently combined with the main Ar carrier flow (~1000 cc/min) prior to delivery via a signal smoothing device that damps the intrinsic laser pulsations in the signal, into the ICP.

The instrument was optimised for maximum sensitivity on ^{43}Ca, ^{165}Ho and ^{238}U by rastering (scanning) a 100 μm circular spot at a laser pulse repetition rate of 10 pulses/second across the NIST612 glass while maintaining ThO^+/Th^+ ratios <0.5%. Sensitivities for other analyte elements vary subject to the ionisation efficiency, isotope abundance and position in the mass spectrum (with sensitivity generally increasing with mass). For the operating conditions outlined above, most analyte isotope sensitivities range between ~3000 and 30000 counts/sec/ppm.

All standards and unknowns were analysed using the rastering procedure. The analysis protocol involved external calibration of the instrument using the NIST 612 glass and subtraction of 'gas' (laser off) background count rates from all measured signal intensities. Between each calibration were measured six Li-borate discs and a secondary reference standard (in this case BCR2g glass). All reference materials, unknowns and background measurements were analysed for a period of 120 seconds, operating the ICP-MS in simultaneous pulse counting/peak hopping mode, and acquiring data on a single point per isotope using 30 millisecond dwell times for all internal standard and analyte isotopes. ^{44}Ca was employed as the internal standard and some 25 analyte element isotopes were analysed (see Appendices C and G). Data reduction was performed following the procedures outlined by Longerich *et al.* (1996). A drift correction was applied to the unknowns between the bracketing NIST612 calibrations, assuming a linear variation in measured signal intensity ratios with the analysis sequence. The internal standard (BCR2g) and the NIST 612 glass element concentrations are given in Eggins (in prep.).

A.4. Rb-Sr and Sm-Nd isotopic analyses

The Sr and Nd isotopic compositions of seven igneous and three metasedimentary rocks of the GRC are tabulated in Table A.1. Analyses were made from whole rock powder splits following the procedures given in Bennett *et al.* (1993) and McCulloch and Chappell (1982). Dissolutions were effected in a teflon capsule under pressure using HF and HNO3. The Nd and Sr isotopic compositions were measured at the Research School of Earth Sciences, the Australian National University, using a Finnigan MAT 261 multicollector mass spectrometer in the static mode. The Nd isotopic ratios have been normalised to $^{146}Nd/^{144}Nd = 0.7219$ and the Sr isotopic ratios normalised to $^{88}Sr/^{86}Sr = 0.1194$.

ε_{Nd} at the inferred crystallisation age (500 Ma) was computed according to -

ε_{Nd} **(500 Ma)** = [{($^{143}Nd/^{144}Nd$) sample (500 Ma) / ($^{143}Nd/^{144}Nd$) CHUR (500 Ma)}-1] x 10^4

where the present day chondritic $^{143}Nd/^{144}Nd = 0.512685$, $^{147}Sm/^{144}Nd = 0.1967$.

The ratio $^{87}Rb/^{86}Sr$ for samples in Table A.1 was derived from XRF Rb and Sr weight concentrations (verified by ICP-MS) using –

^{87}**Rb** = Rb (ppm) / 307.055

^{86}**Sr** = Sr (ppm)/ [826.885+(86.909 x $^{87}Sr/^{86}Sr$)]

APPENDIX B

Table B.1:

Composition of mineral phases of metasedimentary rocks, migmatite leucosomes, small granitic bodies and Harrow type granitic rocks analysed by electron microprobe.

Rock	Qf gneiss T2-2B																					
Mineral	biotite	biotite	biotite	biotite	biotite	biotite	biotite	plag A core	plag A rim	plag A rim	plag B core	plag B rim	plag A core	plag A rim	plag B core	plag B rim	plag B rim	plag core	plag rim	plag rim	plag core	plag rim
Context																						
spot	3.1	3.2	5.1	5.2	5.3	6.2	6.3	1.1	1.2	1.3	1.4	1.5	2.1	2.2	2.4	2.5	2.6	3.3	3.4	3.5	5.4	5.5
Na2O	0.26	0.37	0.29	0.32	0.29	0.27	0.27	8.14	7.39	7.40	8.08	7.35	8.42	7.57	7.63	7.64	7.19	7.11	7.88	7.31	8.01	7.71
MgO	8.74	8.41	8.62	8.46	8.65	8.67	8.56	0.00	0.00	0.00	0.00	0.00	0.00	0.00	0.00	0.00	0.00	0.00	0.00	0.00	0.00	0.00
Al2O3	18.43	18.81	18.88	18.99	19.08	19.26	19.29	24.55	25.83	25.64	24.44	25.87	24.41	25.32	25.38	25.01	25.50	25.84	24.75	25.60	24.51	25.43
SiO2	35.44	35.04	35.47	35.38	35.39	35.46	35.87	61.37	59.79	59.91	61.45	59.33	62.00	60.46	60.20	60.50	59.22	59.32	60.89	59.99	61.74	60.51
K2O	9.52	9.78	9.78	9.76	9.80	9.69	9.94	0.29	0.16	0.12	0.22	0.22	0.25	0.15	0.21	0.13	0.18	0.23	0.20	0.15	0.18	0.14
CaO	0.00	0.00	0.00	0.00	0.00	0.00	0.00	5.76	7.27	7.05	5.79	7.40	5.69	6.75	6.74	6.51	7.24	7.55	6.00	7.13	5.86	6.62
TiO2	3.38	2.97	2.76	2.80	2.85	2.75	2.81	0.00	0.00	0.00	0.00	0.00	0.00	0.00	0.00	0.00	0.00	0.00	0.00	0.00	0.00	0.00
MnO	0.30	0.00	0.00	0.00	0.00	0.34	0.28	0.00	0.00	0.00	0.00	0.00	0.00	0.00	0.00	0.00	0.00	0.00	0.00	0.00	0.00	0.00
FeO	19.23	18.78	19.42	19.22	18.99	18.84	19.03	0.00	0.00	0.00	0.00	0.00	0.00	0.00	0.00	0.00	0.00	0.00	0.00	0.00	0.00	0.00
TOTAL	95.17	94.26	95.51	94.99	95.24	95.32	96.06	100.11	100.44	100.12	99.98	100.17	100.77	100.25	100.16	99.79	99.33	100.05	99.72	100.18	100.30	100.41
Na	0.08	0.11	0.09	0.10	0.09	0.08	0.08	2.80	2.54	2.55	2.78	2.54	2.88	2.61	2.63	2.64	2.50	2.46	2.72	2.52	2.74	2.65
Mg	1.99	1.93	1.96	1.93	1.97	1.97	1.93	0.00	0.00	0.00	0.00	0.00	0.00	0.00	0.00	0.00	0.00	0.00	0.00	0.00	0.00	0.00
Al	3.32	3.42	3.39	3.42	3.43	3.45	3.44	5.13	5.40	5.38	5.11	5.43	5.07	5.30	5.32	5.26	5.39	5.44	5.19	5.36	5.10	5.31
Si	5.41	5.40	5.41	5.41	5.40	5.40	5.42	10.89	10.61	10.66	10.91	10.56	10.93	10.74	10.70	10.78	10.62	10.58	10.83	10.66	10.91	10.71
K	1.85	1.92	1.90	1.90	1.91	1.88	1.92	0.06	0.04	0.03	0.05	0.05	0.06	0.03	0.05	0.03	0.04	0.05	0.05	0.03	0.04	0.03
Ca								1.10	1.38	1.34	1.10	1.41	1.07	1.29	1.28	1.24	1.39	1.44	1.14	1.36	1.11	1.26
Ti	0.39	0.34	0.32	0.32	0.33	0.32	0.32	0.00	0.00	0.00	0.00	0.00	0.00	0.00	0.00	0.00	0.00	0.00	0.00	0.00	0.00	0.00
Mn	0.04	0.00	0.00	0.00	0.00	0.04	0.04	0.00	0.00	0.00	0.00	0.00	0.00	0.00	0.00	0.00	0.00	0.00	0.00	0.00	0.00	0.00
Fe	2.46	2.42	2.48	2.46	2.42	2.40	2.41	0.00	0.00	0.00	0.00	0.00	0.00	0.00	0.00	0.00	0.00	0.00	0.00	0.00	0.00	0.00
cation sum	15.54	15.54	15.55	15.54	15.55	15.54	15.56	19.98	19.97	19.96	19.95	19.99	20.01	19.97	19.98	19.95	19.94	19.97	19.93	19.93	19.90	19.96
An%								27.8	34.8	34.2	28.0	35.3	26.7	32.8	32.3	31.7	35.4	36.5	29.2	34.8	28.5	32.0

Rock	98-25M1 migmatite																					
Mineral	Biotite	Biotite	Biotite	Biotite	Biotite	Biotite	musc	musc	musc	musc	plag core	plag rim	plag rim	plag core	plag rim	plag rim	plag core	plag rim	plag core	plag rim	plag rim	
context	melano	melano	melano	melano	melano	melano	melano	melano	melano	melano	leuco	leuco	leuco	leuco	leuco	leuco	leuco	leuco	leuco	leuco	leuco	
spot	1.2	1.3	1.5	2.1	3.1	3.2	1.1	1.4	5.1	5.2	4.1	4.2	4.3	6.1	6.2	6.3	6.4	6.5	7.1	7.3	7.2	
Na2O	0.34	0.30	0.30	0.29	0.28	0.27	0.81	0.71	0.71	0.72	8.70	8.21	9.51	8.76	8.13	9.23	8.68	9.50	8.69	8.15	9.21	
MgO	8.15	7.87	7.98	7.84	7.80	7.87	0.78	0.84	0.70	0.79	0.00	0.00	0.00	0.00	0.00	0.00	0.00	0.00	0.00	0.00	0.00	
Al2O3	19.12	18.95	18.76	19.13	19.03	19.37	34.97	35.02	35.18	34.99	23.40	24.29	22.73	23.99	24.64	22.76	24.06	23.00	23.87	24.56	22.99	
SiO2	34.97	34.86	34.64	34.99	34.93	35.01	45.70	45.24	45.84	45.53	62.56	61.04	64.32	62.44	61.89	64.10	62.83	63.89	62.29	61.08	64.00	
K2O	9.81	9.90	9.75	10.10	10.10	9.98	10.64	10.92	10.70	10.85	0.52	0.23	0.11	0.43	0.38	0.24	0.51	0.35	0.52	0.34	0.16	
CaO	0.00	0.00	0.00	0.00	0.00	0.00	0.00	0.00	0.00	0.00	4.54	5.55	3.78	4.78	5.61	3.68	4.74	3.87	4.77	5.64	3.64	
TiO2	1.78	1.96	2.06	1.86	1.76	1.82	0.54	0.54	0.40	0.52	0.00	0.00	0.00	0.00	0.00	0.00	0.00	0.00	0.00	0.00	0.00	
MnO	0.57	0.52	0.37	0.47	0.42	0.60	0.00	0.00	0.00	0.00	0.00	0.00	0.00	0.00	0.00	0.00	0.00	0.00	0.00	0.00	0.00	
FeO	21.44	21.03	20.77	21.30	20.72	21.30	1.38	1.37	1.44	1.34	0.00	0.00	0.00	0.00	0.00	0.00	0.00	0.00	0.00	0.00	0.00	
TOTAL	96.18	95.39	94.63	95.98	95.04	96.22	94.82	94.64	94.97	94.74	99.72	99.32	100.45	100.40	100.65	100.01	100.82	100.61	100.14	99.77	100.00	
Na	0.10	0.09	0.09	0.09	0.09	0.08	0.21	0.18	0.18	0.19	3.00	2.84	3.24	3.00	2.78	3.16	2.96	3.24	2.98	2.81	3.15	
Mg	1.86	1.81	1.85	1.80	1.80	1.80	0.16	0.17	0.14	0.16	0.00	0.00	0.00	0.00	0.00	0.00	0.00	0.00	0.00	0.00	0.00	
Al	3.45	3.44	3.44	3.46	3.47	3.49	5.53	5.56	5.55	5.54	4.90	5.12	4.70	5.00	5.12	4.73	4.98	4.77	4.98	5.15	4.77	
Si	5.36	5.38	5.38	5.38	5.41	5.36	6.14	6.09	6.14	6.12	11.12	10.91	11.30	11.04	10.91	11.30	11.04	11.23	11.03	10.86	11.28	
K	1.92	1.95	1.93	1.98	1.98	1.95	1.82	1.88	1.83	1.86	0.12	0.05	0.03	0.10	0.09	0.05	0.11	0.08	0.12	0.08	0.04	
Ca	0.00	0.00	0.00	0.00	0.00	0.00	0.00	0.00	0.00	0.00	0.86	1.06	0.71	0.91	1.06	0.70	0.89	0.73	0.90	1.08	0.69	
Ti	0.20	0.23	0.24	0.22	0.21	0.21	0.05	0.05	0.04	0.05	0.00	0.00	0.00	0.00	0.00	0.00	0.00	0.00	0.00	0.00	0.00	
Mn	0.07	0.07	0.05	0.06	0.05	0.08	0.00	0.00	0.00	0.00	0.00	0.00	0.00	0.00	0.00	0.00	0.00	0.00	0.00	0.00	0.00	
Fe	2.75	2.71	2.70	2.74	2.68	2.73	0.16	0.15	0.16	0.15	0.00	0.00	0.00	0.00	0.00	0.00	0.00	0.00	0.00	0.00	0.00	
cation sum	15.71	15.68	15.68	15.73	15.69	15.70	14.07	14.08	14.04	14.07	20.00	19.98	19.98	20.05	19.96	19.94	19.98	20.05	20.01	19.98	19.93	
An%											21.6	26.8	17.8	22.7	27.0	17.9	22.5	18.0	22.5	27.2	17.8	

Rock	Diatexite 97-286-1																					
Mineral	Biotite	Biotite	Biotite	Biotite	Biotite	Biotite	Biotite	Biotite	Biotite	Biotite	Biotite	Biotite	Biotite	Biotite	musc	musc	musc	plag core	plag rim	plag core	plag rim	plag rim
Context	Melano	Leuco	Melano	Leuco	Melano	Melano	Mesosome	Mesosome	Mesosome	Mesosome	Mesosome	Mesosome	Mesosome	Mesosome	melano	leuco	leuco	leuco	leuco	leuco	leuco	leuco
spot	1.6	1.7	6.1	2.1	2.2	2.3	7.1	7.2	7.3	8.1	8.2	8.3	9.1	9.2	2.4	4.3	4.4	1.4	1.5	3.1	3.2	3.3
Na2O	0.25	0.42	0.28	0.23	0.32	0.3	0.51	0.23	0.31	0.22	0.4	0.33	0.37	0.31	0.65	0.61	0.52	8.29	8.41	7.99	8.36	8.42
MgO	8.56	8.92	8.66	8.81	8.87	8.72	8.7	8.51	8.77	8.62	8.64	8.92	8.79	8.57	0.73	0.77	0.73	0	0	0	0	0
Al2O3	19.35	19.17	18.98	19.22	19.34	19.51	19.12	18.71	18.76	19.14	19.48	19.02	19.09	19.25	34.32	34.76	34.57	24.18	24.16	25.08	24.41	24.26
SiO2	35.07	35.54	34.91	35.11	35.38	35.55	35.24	35.5	34.68	35.08	35.45	35.23	35.13	35.51	45.16	45.52	45.51	61.47	61.2	60.47	61.52	61.32
K2O	9.86	9.91	9.75	9.83	9.84	9.97	9.93	9.5	9.72	9.86	9.82	9.79	9.83	9.86	10.69	11.15	11.09	0.4	0.32	0.29	0.31	0.27
CaO	0.00	0.00	0.00	0.00	0.00	0.00	0.00	0.00	0.00	0.00	0.00	0.00	0.00	0.00	0.00	0.00	0.00	5.58	5.55	6.26	5.56	5.63
TiO2	2.95	2.71	2.85	2.53	2.70	2.85	2.99	2.9	2.93	2.91	2.87	3.08	2.8	2.91	1.12	0.89	0.85	0	0	0	0	0
MnO	0.00	0.40	0.39	0.44	0.29	0.36	0.45	0	0.5	0	0	0.54	0.42	0.42	0	0	0	0	0	0	0	0
FeO	19.27	18.91	19.47	18.84	19.32	19.14	18.96	20.46	19.17	19.03	19.07	19.35	19.22	19.18	1.42	1.29	1.21	0	0	0	0	0
TOTAL	95.31	95.98	95.29	95.01	96.06	96.40	95.90	95.81	94.84	94.86	95.73	96.26	95.65	96.01	94.09	94.99	94.48	99.92	99.64	100.09	100.16	99.90
Na	0.07	0.12	0.08	0.07	0.09	0.09	0.15	0.07	0.09	0.07	0.12	0.1	0.11	0.09	0.17	0.16	0.14	2.86	2.91	2.75	2.87	2.91
Mg	1.94	2.01	1.98	2.01	2.00	1.96	1.97	1.95	2.01	1.97	1.95	2.01	2	1.94	0.15	0.16	0.15	0	0	0	0	0
Al	3.47	3.41	3.43	3.47	3.45	3.47	3.42	3.4	3.4	3.45	3.48	3.39	3.43	3.44	5.48	5.51	5.5	5.07	5.07	5.25	5.1	5.09
Si	5.34	5.36	5.35	5.37	5.36	5.37	5.35	5.32	5.34	5.37	5.37	5.33	5.36	5.38	6.12	6.12	6.14	10.93	10.91	10.75	10.9	10.91
K	1.91	1.91	1.90	1.92	1.90	1.92	1.92	1.87	1.91	1.92	1.9	1.89	1.91	1.91	1.85	1.91	1.91	0.09	0.07	0.07	0.07	0.06
Ca	0.00	0.00	0.00	0.00	0.00	0.00	0.00	0.00	0.00	0.00	0.00	0.00	0.00	0.00	0.00	0.00	0.00	1.06	1.06	1.19	1.06	1.07
Ti	0.34	0.31	0.33	0.29	0.31	0.32	0.34	0.34	0.34	0.33	0.33	0.35	0.32	0.33	0.11	0.09	0.09	0	0	0	0	0
Mn	0.00	0.05	0.05	0.06	0.04	0.05	0.06	0	0.07	0	0	0.07	0.05	0.05	0	0	0	0	0	0	0	0
Fe	2.45	2.39	2.49	2.41	2.45	2.42	2.41	2.64	2.47	2.43	2.42	2.45	2.45	2.43	0.16	0.15	0.14	0	0	0	0	0
cation sum	15.52	15.56	15.61	15.60	15.60	15.60	15.62	15.59	15.63	15.54	15.57	15.59	15.63	15.57	14.04	14.10	14.07	20.01	20.02	20.01	20.00	20.04
An%																		26.4	26.2	29.7	26.5	26.5

Rock	Diatexite 97-286-1																						
Mineral	plag B core	plag b rim	plag A core	plag A core	plag B core	plag B rim	plag core	plag rim	plag A core	plag A rim	plag B core	plag B rim	plag A core	plag A rim	plag B core	plag B rim	Kf rim	Kf core	Kf core	Kf rim	Kf A core	Kf A rim	Kf B rim
context	leuco	leuco	leuco	leuco	leuco	leuco	meso	meso	meso	meso	meso	meso	meso	meso	meso	meso	leuco	leuco	leuco	leuco	leuco	leuco	leuco
spot	3.4	3.5	6.2	6.3	6.4	6.5	7.4	7.5	8.4	8.5	8.6	8.7	9.3	9.4	9.5	9.6	1.1	1.2	4.1	4.2	5.1	5.2	5.3
Na2O	8.64	8.16	8.07	8.38	8.29	8.09	8.31	8.57	8.22	8.39	8.32	8.47	8.43	8.36	8.24	8.26	2.01	1.65	1.96	2.02	1.72	2.1	1.94
MgO	0	0	0	0	0	0	0	0	0	0	0	0	0	0	0	0	0	0	0	0	0	0	0
Al2O3	24.01	24.55	24.75	24.29	24.59	24.86	24.55	24.18	24.6	24.17	24.46	24.19	24.3	24.49	24.62	24.31	18.87	18.76	18.65	18.61	18.78	18.68	18.57
SiO2	61.61	61.06	61.05	61.86	60.82	61.16	61.14	61.27	61.1	61.78	61.24	61.23	61.19	61.34	61.4	61.55	64.95	64.41	64.56	65.08	64.5	64.46	64.49
K2O	0.23	0.31	0.28	0.44	0.21	0.31	0.27	0.2	0.37	0.2	0.24	0.19	0.22	0.17	0.21	0.16	14.17	15.02	14.2	14.15	14.64	13.96	14.35
CaO	5.47	5.84	5.82	5.19	6.05	5.91	5.53	5.3	5.99	5.4	5.61	5.28	5.36	5.9	5.54	5.53	0	0	0	0	0	0	0
TiO2	0	0	0	0	0	0	0	0	0	0	0	0	0	0	0	0	0.3	0.33	0	0	0.25	0	0
MnO	0	0	0	0	0	0	0	0	0	0	0	0	0	0	0	0	0	0	0	0	0	0	0
FeO	0	0	0	0	0	0	0	0	0	0	0	0	0	0	0	0	0	0	0	0	0	0	0
TOTAL	99.96	99.92	99.97	100.16	99.96	100.33	99.80	99.52	100.28	99.94	99.87	99.36	99.50	100.26	100.01	99.81	100.30	100.17	99.37	99.86	99.89	99.20	99.35
Na	2.98	2.82	2.79	2.88	2.86	2.78	2.87	2.96	2.83	2.89	2.87	2.93	2.91	2.87	2.83	2.85	0.71	0.59	0.7	0.72	0.62	0.75	0.7
Mg	0	0	0	0	0	0	0	0	0	0	0	0	0	0	0	0	0	0	0	0	0	0	0
Al	5.03	5.15	5.19	5.07	5.15	5.2	5.15	5.08	5.14	5.06	5.13	5.09	5.1	5.11	5.15	5.09	4.07	4.07	4.06	4.02	4.08	4.07	4.05
Si	10.94	10.87	10.87	10.96	10.81	10.85	10.89	10.92	10.83	10.98	10.9	10.93	10.91	10.86	10.9	10.94	11.89	11.87	11.92	11.94	11.88	11.91	11.92
K	0.05	0.07	0.06	0.1	0.05	0.07	0.06	0.05	0.08	0.04	0.05	0.04	0.05	0.04	0.05	0.04	3.31	3.53	3.34	3.31	3.44	3.29	3.38
Ca	1.04	1.11	1.11	0.98	1.15	1.12	1.05	1.01	1.14	1.03	1.07	1.01	1.02	1.12	1.05	1.05	0	0	0	0	0	0	0
Ti	0	0	0	0	0	0	0	0	0	0	0	0	0	0	0	0	0.04	0.05	0	0	0.03	0	0
Mn	0	0	0	0	0	0	0	0	0	0	0	0	0	0	0	0	0	0	0	0	0	0	0
Fe	0	0	0	0	0	0	0	0	0	0	0	0	0	0	0	0	0	0	0	0	0	0	0
cation sum	20.04	20.02	20.02	19.99	20.02	20.02	20.02	20.02	20.02	20.00	20.02	20.00	19.99	20.00	19.98	19.97	20.02	20.11	20.02	19.99	20.05	20.02	20.05
An%	25.6	27.8	28.0	24.7	28.3	28.2	26.4	25.1	28.1	26.0	26.8	25.4	25.6	27.8	26.7	26.6							

Rock	98-25M2 Granitic migmatite																							
Mineral	Biotite	Biotite	Biotite	Biotite	Biotite	Biotite	Biotite	Biotite	Biotite	Biotite	Biotite	musc	musc	musc	musc	musc	musc	musc	musc	musc	musc	musc	musc	musc
Context	Leuco	Leuco	melano	melano	melano	melano	Mesosome	Mesosome	Mesosome	Mesosome	Mesosome	leuco	leuco	leuco	leuco	leuco	leuco	melano	melano	melano	melano	meso	meso	meso
spot	1.5	7.1	8.1	8.2	9.7	9.8	10.1	10.2	10.3	12.6	12.7	2.3	3.5	4.1	7.2	7.3	8.3	8.4	9.1	9.2	10.4	10.5	10.6	
Na2O	0.26	0.26	0.29	0.28	0.28	0.34	0.23	0.27	0.22	0.34	0.36	0.63	0.74	0.71	0.68	0.70	0.57	0.72	0.60	0.77	0.66	0.65	0.71	
MgO	7.57	7.73	7.85	7.57	7.70	7.64	7.90	7.70	7.77	7.85	7.90	0.63	0.66	0.73	0.59	0.66	0.58	0.80	0.65	0.72	0.74	0.74	0.72	
Al2O3	19.74	18.99	18.90	19.49	19.18	19.46	18.76	18.90	18.98	18.75	18.99	34.91	34.84	34.70	34.97	34.93	34.91	34.97	34.73	34.82	34.36	34.85	34.96	
SiO2	34.97	34.86	34.64	34.60	34.92	34.56	34.36	34.39	34.58	34.97	34.91	45.11	45.17	45.30	45.15	45.16	45.56	45.54	45.09	44.93	45.14	45.05	45.82	
K2O	9.82	9.66	9.93	9.74	10.04	9.88	9.88	9.67	9.86	9.86	9.78	10.91	10.59	10.64	10.71	10.85	10.85	10.84	10.79	10.82	10.56	10.93	10.56	
CaO	0.00	0.00	0.00	0.00	0.00	0.00	0.00	0.00	0.00	0.00	0.00	0.00	0.00	0.00	0.00	0.00	0.00	0.00	0.00	0.00	0.00	0.00	0.00	
TiO2	1.93	1.96	1.69	1.87	2.02	1.77	1.89	1.92	2.12	1.88	2.06	0.41	0.45	0.50	0.42	0.35	0.43	0.43	0.46	0.51	0.61	0.53	0.47	
MnO	0.46	0.32	0.50	0.67	0.64	0.50	0.49	0.52	0.48	0.66	0.47	0.00	0.00	0.00	0.00	0.00	0.00	0.00	0.00	0.00	0.00	0.00	0.00	
FeO	20.76	21.22	21.04	20.62	20.61	20.83	21.59	21.34	21.23	21.19	21.31	1.27	1.19	1.15	1.31	1.23	1.55	1.48	1.50	1.42	1.57	1.33	1.47	
TOTAL	95.51	95.00	94.84	94.84	95.39	94.98	95.10	94.71	95.24	95.50	95.78	93.87	93.64	93.73	93.83	93.88	94.45	94.78	93.82	93.99	93.64	94.08	94.71	
Na	0.08	0.08	0.09	0.09	0.08	0.10	0.07	0.08	0.07	0.10	0.11	0.17	0.19	0.19	0.18	0.19	0.15	0.19	0.16	0.20	0.17	0.17	0.19	
Mg	1.73	1.78	1.82	1.75	1.77	1.76	1.83	1.79	1.79	1.81	1.81	0.13	0.13	0.15	0.12	0.13	0.12	0.16	0.13	0.15	0.15	0.15	0.14	
Al	3.57	3.46	3.46	3.56	3.48	3.55	3.44	3.47	3.46	3.41	3.44	5.58	5.57	5.55	5.58	5.58	5.55	5.54	5.56	5.57	5.50	5.57	5.53	
Si	5.37	5.39	5.38	5.36	5.38	5.35	5.34	5.36	5.35	5.40	5.37	6.12	6.13	6.14	6.12	6.12	6.14	6.13	6.12	6.10	6.14	6.11	6.15	
K	1.92	1.91	1.97	1.92	1.97	1.95	1.96	1.92	1.95	1.94	1.92	1.89	1.83	1.84	1.85	1.88	1.87	1.86	1.87	1.87	1.83	1.89	1.81	
Ca	0.00	0.00	0.00	0.00	0.00	0.00	0.00	0.00	0.00	0.00	0.00	0.00	0.00	0.00	0.00	0.00	0.00	0.00	0.00	0.00	0.00	0.00	0.00	
Ti	0.22	0.23	0.20	0.22	0.23	0.21	0.22	0.23	0.25	0.22	0.24	0.04	0.05	0.05	0.04	0.04	0.04	0.04	0.05	0.05	0.06	0.05	0.05	
Mn	0.06	0.04	0.07	0.09	0.08	0.07	0.06	0.07	0.06	0.09	0.06	0.00	0.00	0.00	0.00	0.00	0.00	0.00	0.00	0.00	0.00	0.00	0.00	
Fe	2.67	2.74	2.73	2.67	2.66	2.70	2.81	2.78	2.75	2.74	2.74	0.14	0.14	0.13	0.15	0.14	0.17	0.17	0.17	0.16	0.18	0.15	0.17	
cation sum	15.62	15.63	15.72	15.66	15.65	15.69	15.73	15.70	15.68	15.71	15.69	14.07	14.04	14.05	14.04	14.08	14.04	14.09	14.06	14.10	14.03	14.09	14.04	
An%																								

Rock	98-25M2 Granitic migmatite																							
Mineral	musc	musc	plag core	plag core	plag rim	plag rim	plag B core	plag B rim	plag core	plag rim	plag core	plag core	plag rim	plag rim	plag core	plag core	plag rim	plag rim	plag A core	plag A rim	plag b core	plag B rim	plag A core	
context	meso	meso	leuco	leuco	leuco	leuco	leuco	leuco	leuco	leuco	leuco	leuco	leuco	leuco	leuco	leuco	leuco	leuco	melano	melano	melano	melano	meso	
spot	12.8	12.9	1.1	1.2	1.3	1.4	1.6	1.7	2.1	2.2	2b.1	2b.2	2b.3	2b.4	3.1	3.2	3.3	3.4	9.3	9.4	9.5	9.6	12.1	
Na2O	0.66	0.64	9.35	9.01	8.60	9.48	9.50	9.04	8.93	8.55	7.63	8.84	8.48	9.39	8.73	8.53	8.36	9.16	8.89	9.49	8.73	9.31	8.90	
MgO	0.72	0.73	0.00	0.00	0.00	0.00	0.00	0.00	0.00	0.00	0.00	0.00	0.00	0.00	0.00	0.00	0.00	0.00	0.00	0.00	0.00	0.00	0.00	
Al2O3	35.20	34.90	22.96	23.54	24.38	23.13	23.07	23.44	23.35	24.02	25.67	23.28	23.98	22.69	23.70	23.98	24.37	23.02	24.10	23.23	24.28	23.25	23.84	
SiO2	45.30	45.44	63.95	62.58	61.37	63.84	64.33	62.64	62.21	60.78	59.17	61.73	61.14	62.89	62.10	60.98	61.01	62.84	62.46	63.63	63.20	62.86	62.14	
K2O	10.86	10.82	0.39	0.33	0.16	0.30	0.43	0.30	0.25	0.16	0.21	0.28	0.27	0.30	0.21	0.40	0.19	0.29	0.26	0.21	0.22	0.15	0.26	
CaO	0.00	0.00	3.86	4.64	5.50	3.68	3.80	4.53	4.69	5.39	7.10	4.77	5.40	3.96	5.07	5.33	5.52	4.20	5.10	4.08	5.35	4.24	4.65	
TiO2	0.53	0.51	0.00	0.00	0.00	0.00	0.00	0.00	0.00	0.00	0.00	0.00	0.00	0.00	0.00	0.00	0.00	0.00	0.00	0.00	0.00	0.00	0.00	
MnO	0.00	0.00	0.00	0.00	0.00	0.00	0.00	0.00	0.00	0.00	0.00	0.00	0.00	0.00	0.00	0.00	0.00	0.00	0.00	0.00	0.00	0.00	0.00	
FeO	1.26	1.20	0.00	0.00	0.00	0.00	0.00	0.00	0.00	0.00	0.00	0.00	0.00	0.00	0.00	0.00	0.00	0.00	0.00	0.00	0.00	0.00	0.00	
TOTAL	94.53	94.24	100.51	100.10	100.01	100.43	101.13	99.95	99.43	98.90	99.78	98.90	99.27	99.23	99.81	99.22	99.45	99.51	100.81	100.64	101.78	99.81	99.79	
Na	0.17	0.17	3.18	3.10	2.96	3.24	3.22	3.11	3.09	2.97	2.65	3.07	2.94	3.25	3.01	2.96	2.90	3.16	3.03	3.23	2.98	3.20	3.06	
Mg	0.14	0.15	0.00	0.00	0.00	0.00	0.00	0.00	0.00	0.00	0.00	0.00	0.00	0.00	0.00	0.00	0.00	0.00	0.00	0.00	0.00	0.00	0.00	
Al	5.59	5.55	4.75	4.92	5.10	4.80	4.76	4.90	4.91	5.08	5.41	4.92	5.06	4.77	4.96	5.06	5.13	4.82	5.00	4.81	5.03	4.86	4.98	
Si	6.10	6.14	11.23	11.10	10.89	11.23	11.25	11.11	11.09	10.90	10.59	11.07	10.95	11.22	11.03	10.93	10.90	11.16	11.00	11.17	10.95	11.15	11.01	
K	1.87	1.86	0.09	0.07	0.04	0.07	0.09	0.07	0.06	0.04	0.05	0.07	0.06	0.07	0.05	0.09	0.04	0.07	0.06	0.05	0.05	0.03	0.06	
Ca	0.00	0.00	0.73	0.88	1.05	0.69	0.71	0.86	0.89	1.04	1.36	0.92	1.04	0.76	0.97	1.02	1.06	0.80	0.96	0.77	1.01	0.81	0.88	
Ti	0.05	0.05	0.00	0.00	0.00	0.00	0.00	0.00	0.00	0.00	0.00	0.00	0.00	0.00	0.00	0.00	0.00	0.00	0.00	0.00	0.00	0.00	0.00	
Mn	0.00	0.00	0.00	0.00	0.00	0.00	0.00	0.00	0.00	0.00	0.00	0.00	0.00	0.00	0.00	0.00	0.00	0.00	0.00	0.00	0.00	0.00	0.00	
Fe	0.14	0.14	0.00	0.00	0.00	0.00	0.00	0.00	0.00	0.00	0.00	0.00	0.00	0.00	0.00	0.00	0.00	0.00	0.00	0.00	0.00	0.00	0.00	
cation sum	14.06	14.06	19.98	20.07	20.04	20.03	20.03	20.05	20.04	20.03	20.06	20.05	20.05	20.07	20.02	20.06	20.03	20.01	20.05	20.03	20.02	20.05	19.99	
An%			18.3	21.7	25.9	17.3	17.7	21.3	22.0	25.7	33.5	22.7	25.7	18.6	24.1	25.1	26.5	19.9	23.7	19.0	25.0	20.0	22.0	

Rock	98-25M2 Granitic migmatite										98-R5B Granitic migmatite										
Mineral	plag A rim	plag B core	plag B rim	plag C core	plag C rim	plag core	plag rim	plag rim	kf (rim)	kf (rim)	kf (rim)	kf (rim)	Biotite	Biotite	Biotite	Biotite	Biotite	Biotite	Biotite	Biotite	Biotite
Context	meso	meso	meso	meso	meso	meso	meso	meso	leuco	leuco	leuco	leuco	Leuco	Leuco	Leuco	Leuco	Melanosome	Melanosome	Melanosome	Melanosome	Melanosome	Melanosome
spot	12.2	12.3	12.4	12.4	12.5	13.1	13.2	13.3	4.2	4.3	5.1	6.1	1.4	2.1	2.2	3.1	5.1	5.2	5.3	8.1	8.2	8.3
Na2O	9.36	8.65	10.40	8.91	8.67	8.83	8.48	9.11	1.41	1.17	1.57	1.79	0.24	0.29	0.20	0.25	0.34	0.29	0.27	0.22	0.34	0.28
MgO	0.00	0.00	0.00	0.00	0.00	0.00	0.00	0.00	0.00	0.00	0.00	0.00	8.64	8.54	8.50	8.36	8.58	8.48	8.58	8.42	8.29	8.61
Al2O3	23.05	23.81	21.39	23.76	24.15	23.61	24.56	23.16	18.85	18.52	18.85	18.81	18.45	19.27	19.00	19.38	19.11	18.66	18.99	19.18	19.06	18.96
SiO2	63.32	62.25	65.95	62.16	62.40	62.13	61.26	62.94	64.87	64.56	64.29	64.50	35.31	35.50	35.33	35.31	35.23	34.97	35.15	35.32	35.68	35.35
K2O	0.28	0.14	0.00	0.26	0.22	0.25	0.19	0.25	14.98	15.42	15.00	14.22	10.02	9.97	9.84	9.85	9.98	9.73	9.81	9.68	10.08	9.83
CaO	4.04	4.91	2.24	4.82	5.17	4.87	5.65	4.34	0.00	0.00	0.00	0.00										
TiO2	0.00	0.00	0.00	0.00	0.00	0.00	0.00	0.00	0.00	0.21	0.00	0.21	2.93	2.83	2.59	3.01	2.74	2.82	2.55	2.88	2.63	2.65
MnO	0.00	0.00	0.00	0.00	0.00	0.00	0.00	0.00	0.00	0.00	0.00	0.00	0.44	0.40	0.50	0.58	0.47	0.28	0.33	0.58	0.34	0.48
FeO	0.00	0.00	0.00	0.00	0.00	0.00	0.00	0.00	0.00	0.00	0.00	0.00	19.51	19.43	19.08	18.66	18.81	21.67	18.91	19.08	19.02	19.21
TOTAL	100.05	99.76	99.98	99.91	100.61	99.69	100.14	99.80	100.11	99.88	99.71	99.53	95.54	96.23	95.04	95.40	95.26	96.90	94.59	95.36	95.44	95.37
Na	3.21	2.98	3.53	3.06	2.96	3.04	2.92	3.13	0.50	0.42	0.56	0.64	0.07	0.09	0.06	0.07	0.10	0.08	0.08	0.07	0.10	0.08
Mg	0.00	0.00	0.00	0.00	0.00	0.00	0.00	0.00	0.00	0.00	0.00	0.00	1.97	1.93	1.94	1.90	1.95	1.84	1.97	1.91	1.88	1.96
Al	4.80	4.98	4.42	4.97	5.01	4.95	5.14	4.84	4.08	4.04	4.10	4.09	3.33	3.44	3.43	3.48	3.44	3.20	3.44	3.45	3.42	3.41
Si	11.20	11.06	11.56	11.02	10.98	11.05	10.87	11.16	11.91	11.94	11.87	11.91	5.40	5.38	5.41	5.38	5.38	5.10	5.40	5.39	5.44	5.40
K	0.06	0.03	0.00	0.06	0.05	0.06	0.04	0.06	3.51	3.64	3.53	3.35	1.95	1.93	1.92	1.91	1.94	1.81	1.92	1.88	1.96	1.91
Ca	0.77	0.93	0.42	0.92	0.98	0.93	1.08	0.82	0.00	0.00	0.00	0.00										
Ti	0.00	0.00	0.00	0.00	0.00	0.00	0.00	0.00	0.00	0.03	0.00	0.03	0.34	0.32	0.30	0.34	0.31	0.31	0.29	0.33	0.30	0.30
Mn	0.00	0.00	0.00	0.00	0.00	0.00	0.00	0.00	0.00	0.00	0.00	0.00	0.06	0.05	0.07	0.07	0.06	0.03	0.04	0.07	0.04	0.06
Fe	0.00	0.00	0.00	0.00	0.00	0.00	0.00	0.00	0.00	0.00	0.00	0.00	2.49	2.46	2.44	2.38	2.40	2.38	2.43	2.43	2.42	2.45
cation sum	20.04	19.98	19.93	20.03	19.98	20.03	20.05	20.01	20.00	20.07	20.06	20.02	15.61	15.60	15.57	15.53	15.58	14.75	15.57	15.53	15.56	15.57
An%	19.1	23.6	10.6	22.8	24.6	23.1	26.7	20.4														

Rock	98-R5B Granitic migmatite																				
Mineral	Biotite	Biotite	Biotite	Biotite	Biotite	Biotite	Biotite	musc	musc	musc	plag core	plag rim	plag (unz)	plag (inc)	plag core	plag rim	plag A core	plag A rim	plag A rim	plag B core	plag B rim	plag core	plag rim
context	Melanosome	Mesosome	Mesosome	Mesosome	Mesosome	Mesosome	Mesosome	melano	melano	melano	leuco	leuco	leuco	leuco	leuco	leuco	meso	meso	meso	meso	meso	meso	meso
spot	10.4	6.6	6.7	6.8	7.4	7.5	7.6	8.4	8.5	8.6	1.1	1.2	1.3	3.2	4.4	4.5	6.1	6.2	6.3	6.4	6.5	7.1	7.2
Na2O	0.29	0.36	0.27	0.20	0.29	0.33	0.32	0.62	0.63	0.61	8.18	8.19	8.63	8.87	8.75	8.55	8.63	8.57	9.04	8.70	8.66	8.43	8.61
MgO	8.65	8.41	8.49	8.77	8.20	8.36	8.48	0.72	0.67	0.83	0.00	0.00	0.00	0.00	0.00	0.00	0.00	0.00	0.00	0.00	0.00	0.00	0.00
Al2O3	19.21	19.50	19.57	18.93	19.31	19.18	19.31	34.68	34.67	34.75	24.74	24.31	23.90	23.62	23.70	24.27	23.79	24.16	23.59	23.93	24.20	23.70	23.89
SiO2	35.00	35.38	35.72	35.41	34.99	35.39	35.18	45.42	45.38	46.05	61.02	60.70	61.30	62.35	62.52	61.32	61.80	61.34	62.22	61.81	61.95	62.15	62.05
K2O	9.73	10.00	9.93	9.92	9.74	9.64	9.81	10.81	10.82	10.68	0.46	0.29	0.43	0.43	0.32	0.34	0.27	0.00	0.23	0.17	0.17	0.33	0.29
CaO								0.00	0.00	0.00	5.79	5.72	5.26	4.70	4.65	5.20	5.05	5.62	4.62	4.92	5.39	4.89	5.02
TiO2	2.70	2.76	2.47	2.80	2.74	2.57	2.61	0.98	0.96	0.86	0.00	0.00	0.00	0.00	0.00	0.00	0.21	0.00	0.00	0.00	0.00	0.00	0.00
MnO	0.39	0.49	0.41	0.48	0.41	0.32	0.56	0.22	0.00	0.00	0.00	0.00	0.00	0.00	0.25	0.00	0.00	0.00	0.00	0.00	0.00	0.00	0.00
FeO	19.63	18.95	18.99	19.71	18.87	18.65	19.14	1.26	1.54	1.43	0.00	0.00	0.00	0.00	0.00	0.00	0.00	0.00	0.00	0.00	0.00	0.00	0.00
TOTAL	95.60	95.85	95.85	96.22	94.55	94.44	95.41	94.71	94.67	95.21	100.19	99.21	99.52	99.97	100.19	99.68	99.75	99.69	99.70	99.53	100.37	99.50	99.86
Na	0.08	0.11	0.08	0.06	0.09	0.10	0.10	0.16	0.16	0.16	2.82	2.84	2.99	3.05	3.01	2.95	2.98	2.96	3.11	3.00	2.97	2.91	2.97
Mg	1.97	1.90	1.92	1.98	1.88	1.91	1.93	0.14	0.13	0.16	0.00	0.00	0.00	0.00	0.00	0.00	0.00	0.00	0.00	0.00	0.00	0.00	0.00
Al	3.46	3.49	3.49	3.38	3.50	3.47	3.47	5.50	5.50	5.47	5.18	5.13	5.03	4.94	4.95	5.09	4.99	5.07	4.93	5.02	5.04	4.97	5.00
Si	5.34	5.37	5.41	5.37	5.38	5.43	5.37	6.12	6.11	6.15	10.85	10.87	10.94	11.07	11.07	10.92	10.99	10.92	11.03	11.00	10.94	11.05	11.02
K	1.90	1.94	1.92	1.92	1.91	1.89	1.91	1.86	1.86	1.82	0.11	0.07	0.10	0.10	0.07	0.08	0.06	0.00	0.05	0.04	0.04	0.08	0.07
Ca								0.00	0.00	0.00	1.10	1.10	1.01	0.89	0.88	0.99	0.96	1.07	0.88	0.94	1.02	0.93	0.96
Ti	0.31	0.32	0.28	0.32	0.32	0.30	0.30	0.10	0.10	0.09	0.00	0.00	0.00	0.00	0.00	0.00	0.03	0.00	0.00	0.00	0.00	0.00	0.00
Mn	0.05	0.06	0.05	0.06	0.05	0.04	0.07	0.02	0.00	0.00	0.00	0.00	0.00	0.00	0.04	0.00	0.00	0.00	0.00	0.00	0.00	0.00	0.00
Fe	2.51	2.41	2.41	2.50	2.43	2.39	2.44	0.14	0.17	0.16	0.00	0.00	0.00	0.00	0.00	0.00	0.00	0.00	0.00	0.00	0.00	0.00	0.00
cation sum	15.62	15.60	15.56	15.59	15.56	15.53	15.59	14.04	14.03	14.01	20.06	20.01	20.07	20.05	20.02	20.03	20.01	20.02	20.00	20.00	20.01	19.94	20.02
An%											27.3	27.4	24.6	22.0	22.2	24.6	24.0	26.6	21.8	23.6	25.3	23.7	24.0

Rock	98-R5B Granitic migmatite																					
Mineral	plag rim	plag core	plag rim	Kf	Kf rim	kf rim	kf core	Kf rim	bio	bio	bio	bio	bio	bio	musc	musc	musc	plag A core	plag A rim	plag B core	plag B rim	plag A core	plag A rim
Context	meso	melano	melano	melano	leuco	leuco	leuco	leuco	melano	melano	melano	melano	meso	meso	melano	melano	melano	melano	melano	melano\	melano	meso	meso
spot	7.3	10.2	10.3	10.1	2.3	4.1	4.2	4.3	1.1	1.2	2.2	2.3	5.1	5.2	1.3	1.4	2.1	3.1	3.2	3.3	3.4	4.2	4.3
Na2O	8.63	8.79	8.72	1.68	1.70	2.21	1.54	1.93	0.32	0.22	0.22	0.28	0.19	0.37	0.58	0.65	0.69	8.39	8.32	8.31	8.42	8.14	8.88
MgO	0.00	0.00	0.00	0.00	0.00	0.00	0.00	0.00	8.47	8.42	8.43	8.44	8.52	8.14	0.77	0.72	0.71	0.00	0.00	0.00	0.00	0.00	0.00
Al2O3	23.52	23.75	24.17	18.71	18.47	18.76	18.45	18.73	19.21	18.76	19.29	18.83	18.57	19.11	34.59	34.88	34.96	24.07	24.37	24.19	23.82	24.21	23.43
SiO2	62.45	62.22	62.01	64.40	64.63	64.72	64.03	64.46	35.47	35.28	35.29	35.52	35.46	35.26	46.13	45.49	45.77	61.69	61.83	61.55	62.06	61.61	62.78
K2O	0.13	0.33	0.32	14.48	14.57	13.94	14.86	14.26	9.98	9.77	9.66	9.81	9.84	9.77	10.87	10.79	10.88	0.31	0.24	0.25	0.31	0.17	0.15
CaO	4.87	4.98	5.16	0.00	0.00	0.00	0.00	0.00	0.00	0.00	0.00	0.00	0.00	0.00	0.00	0.00	0.00	5.35	5.34	5.40	4.83	5.45	4.63
TiO2	0.00	0.00	0.00	0.00	0.00	0.26	0.25	0.26	2.80	2.73	2.76	2.56	2.92	2.60	1.13	0.82	0.93	0.00	0.00	0.00	0.00	0.00	0.00
MnO	0.00	0.00	0.00	0.00	0.00	0.00	0.00	0.00	0.00	0.52	0.33	0.47	0.31	0.39	0.00	0.00	0.00	0.00	0.00	0.00	0.00	0.00	0.00
FeO	0.00	0.00	0.00	0.00	0.00	0.00	0.00	0.00	19.59	19.31	19.74	19.15	19.71	19.07	1.50	1.59	1.54	0.00	0.00	0.00	0.00	0.00	0.00
TOTAL	99.60	100.07	100.38	99.27	99.37	99.89	99.13	99.64	95.84	92.28	95.72	95.06	95.52	94.71	95.57	94.94	95.48	99.81	100.10	99.70	99.44	99.58	99.87
Na	2.97	3.02	2.99	0.60	0.61	0.79	0.56	0.69	0.09	0.06	0.06	0.08	0.06	0.11	0.15	0.17	0.18	2.89	2.86	2.87	2.91	2.81	3.05
Mg	0.00	0.00	0.00	0.00	0.00	0.00	0.00	0.00	1.92	1.93	1.91	1.93	1.94	1.86	0.15	0.14	0.14	0.00	0.00	0.00	0.00	0.00	0.00
Al	4.93	4.96	5.03	4.07	4.03	4.07	4.04	4.07	3.44	3.39	3.46	3.40	3.35	3.46	5.44	5.53	5.50	5.04	5.09	5.07	5.00	5.08	4.89
Si	11.10	11.03	10.95	11.89	11.96	11.90	11.90	11.89	5.38	5.42	5.37	5.44	5.42	5.42	6.15	6.12	6.11	10.96	10.95	10.95	11.05	10.96	11.12
K	0.03	0.07	0.07	3.43	3.44	3.27	3.52	3.35	1.93	1.91	1.87	1.92	1.92	1.91	1.85	1.85	1.85	0.07	0.05	0.06	0.07	0.04	0.03
Ca	0.93	0.95	0.98	0.00	0.00	0.00	0.00	0.00	0.00	0.00	0.00	0.00	0.00	0.00	0.00	0.00	0.00	1.02	1.01	1.03	0.92	1.04	0.88
Ti	0.00	0.00	0.00	0.00	0.00	0.04	0.03	0.04	0.32	0.31	0.32	0.29	0.34	0.30	0.11	0.08	0.09	0.00	0.00	0.00	0.00	0.00	0.00
Mn	0.00	0.00	0.00	0.00	0.00	0.00	0.00	0.00	0.00	0.07	0.04	0.06	0.04	0.05	0.00	0.00	0.00	0.00	0.00	0.00	0.00	0.00	0.00
Fe	0.00	0.00	0.00	0.00	0.00	0.00	0.00	0.00	2.49	2.48	2.51	2.45	2.52	2.45	0.17	0.18	0.17	0.00	0.00	0.00	0.00	0.00	0.00
cation sum	19.96	20.03	20.02	19.99	20.04	20.07	20.05	20.04	15.57	15.57	15.54	15.57	15.59	15.56	14.02	14.07	14.04	19.98	19.96	19.98	19.95	19.93	19.97
An%	23.7	23.5	24.3															25.6	25.8	26.0	23.6	26.7	22.2

Rock	98-R5B Granitic migmatite							97-244 Granitic migmatite															
Mineral	plag A core	plag A rim	plag B core	plag B rim	Kf	Kf A rim	Kf B rim	Biotite	Biotite	Biotite	Biotite	Biotite	Biotite	Biotite	Biotite	Biotite	Biotite	Biotite	Biotite	Biotite	Biotite	musc	musc
context	meso	meso	meso	meso	mesosome	meso	meso	Melanosome	Melanosome	Melanosome	Melanosome	Melanosome	Melanosome	Melanosome	Melanosome	Leucosome	Leucosome	Mesosome	Mesosome	Mesosome	Mesosome	melano	melano
spot	6.1	6.2	6.3	6.4	4.1	5.3	5.4	1.4	1.5	1.6	2.4	2.5	4.6	4.7	3.1	7.1	5.4	5.5	5.6	5.7	1.1	1.2
Na2O	8.15	9.03	8.57	8.34	1.30	1.65	1.37	0.29	0.24	0.23	0.22	0.27	0.21	0.21	0.29	0.00	0.23	0.17	0.24	0.31	0.61	0.56
MgO	0.00	0.00	0.00	0.00	0.00	0.00	0.00	8.54	8.46	8.42	8.41	8.24	8.16	8.51	8.26	8.02	8.40	8.26	8.31	8.25	0.78	0.80
Al2O3	24.34	23.86	24.20	24.71	18.71	18.92	19.10	18.73	18.28	18.97	19.22	18.60	18.34	18.92	18.90	18.90	18.57	18.56	18.36	18.38	34.88	34.25
SiO2	61.65	63.14	62.99	62.99	64.64	65.05	65.37	35.43	35.55	35.38	35.35	35.52	35.16	35.11	35.11	34.96	34.99	35.14	35.06	35.25	45.67	45.93
K2O	0.31	0.20	0.20	0.25	14.81	14.65	14.91	9.72	9.83	9.99	9.99	9.75	9.63	10.12	9.91	9.90	9.76	9.69	9.68	9.79	10.77	10.89
CaO	5.75	4.99	5.17	5.29	0.00	0.00	0.00	0.00	0.00	0.00	0.00	0.00	0.00	0.00	0.00	0.00	0.00	0.00	0.00	0.00	0.00	0.00
TiO2	0.00	0.00	0.00	0.00	0.26	0.00	0.00	2.43	2.66	2.43	2.27	2.67	2.58	2.12	2.35	2.44	2.72	2.54	2.35	2.35	0.69	0.65
MnO	0.00	0.00	0.00	0.00	0.00	0.00	0.00	0.54	0.54	0.51	0.60	0.52	0.58	0.61	0.50	0.62	0.59	0.42	0.40	0.61	0.00	0.00
FeO	0.00	0.00	0.00	0.00	0.00	0.00	0.00	19.68	19.75	19.70	20.34	19.86	20.01	19.72	19.68	19.92	19.64	19.37	19.75	19.37	1.58	1.52
TOTAL	100.20	101.22	101.13	101.58	99.72	100.27	100.75	95.36	95.31	95.63	96.40	95.43	94.67	95.32	95.00	94.76	94.90	94.15	94.15	94.31	94.98	94.60
Na	2.80	3.07	2.91		0.47	0.59	0.48	0.09	0.07	0.07	0.06	0.08	0.06	0.06	0.09	0.00	0.07	0.05	0.07	0.09	0.16	0.15
Mg	0.00	0.00	0.00	2.82	0.00	0.00	0.00	1.95	1.93	1.92	1.91	1.88	1.88	1.95	1.89	1.84	1.93	1.90	1.92	1.90	0.16	0.16
Al	5.08	4.92	4.99	0.00	4.07	4.09	4.11	3.38	3.30	3.42	3.44	3.36	3.34	3.42	3.43	3.44	3.37	3.39	3.36	3.35	5.52	5.43
Si	10.92	11.06	11.03	10.98	11.92	11.93	11.92	5.42	5.45	5.41	5.38	5.44	5.43	5.39	5.41	5.39	5.39	5.44	5.44	5.45	6.13	6.18
K	0.07	0.05	0.04	0.06	3.48	3.43	3.47	1.90	1.92	1.95	1.94	1.90	1.9	1.98	1.95	1.95	1.92	1.91	1.92	1.93	1.84	1.87
Ca	1.09	0.94	0.97	0.99	0.00	0.00	0.00	0.00	0.00	0.00	0.00	0.00	0.00	0.00	0.00	0.00	0.00	0.00	0.00	0.00	0.00	0.00
Ti	0.00	0.00	0.00	0.00	0.04	0.00	0.00	0.28	0.31	0.28	0.26	0.31	0.3	0.25	0.27	0.28	0.32	0.30	0.27	0.27	0.07	0.07
Mn	0.00	0.00	0.00	0.00	0.00	0.00	0.00	0.07	0.07	0.07	0.08	0.07	0.08	0.08	0.06	0.08	0.08	0.06	0.05	0.08	0.00	0.00
Fe	0.00	0.00	0.00	0.00	0.00	0.00	0.00	2.52	2.53	2.52	2.59	2.54	2.59	2.53	2.53	2.57	2.53	2.51	2.56	2.51	0.18	0.17
cation sum	19.96	20.04	19.94	14.85	19.98	20.04	19.98	15.61	15.58	15.64	15.66	15.58	15.58	15.66	15.63	15.55	15.61	15.56	15.59	15.58	14.06	14.03
An%	27.5	23.2	24.7	94.3																		

Rock	97-244 Granitic migmatite																						
Mineral	musc	musc	musc	musc	musc	musc	musc	musc	plag A core	plag A rim	plag b core	plag b rim	plag B rim	plag A core	plag A rim	plag B core	plag b rim	plag core	plag rim	plag core	plag rim	plag core	plag rim
Context	melano	melano	melano	melano	melano	meso	meso	meso	leuco	leuco	leuco	leuco	leuco	?meso	meso	meso	meso	leuco	leuco	leuco	leuco	leuco	leuco
spot	1.3	2.1	2.2	2.3	4.5	5.1	5.2	5.3	3.2	3.3	3.4	3.5	3.6	4.1	4.2	4.3	4.4	7.2	7.3	8.1	8.2	4b.1	4b.2
Na2O	0.60	0.54	0.58	0.57	0.74	0.55	0.58	0.56	9.07	8.97	9.02	8.98	8.63	8.66	8.71	8.37	8.66	9.32	8.52	8.68	8.63	9.09	8.59
MgO	0.59	0.63	0.74	0.80	0.69	0.70	0.73	0.70	0.00	0.00	0.00	0.00	0.00	0.00	0.00	0.00	0.00	0.00	0.00	0.00	0.00	0.00	0.00
Al2O3	35.02	34.75	35.43	35.21	34.86	34.30	34.24	34.40	23.06	23.39	23.22	22.97	23.85	24.00	23.56	24.24	23.55	22.82	24.00	23.66	24.12	22.91	23.40
SiO2	45.54	45.68	46.21	45.89	45.41	45.62	45.08	45.51	64.30	63.41	64.05	63.97	62.64	62.53	62.84	62.36	62.64	63.80	62.12	62.52	62.72	64.32	63.27
K2O	10.63	11.00	11.07	10.79	10.72	10.81	10.77	10.73	0.43	0.33	0.31	0.48	0.29	0.23	0.14	0.24	0.25	0.54	0.33	0.19	0.28	0.52	0.39
CaO	0.00	0.00	0.00	0.00	0.00	0.00	0.00	0.00	3.96	4.49	4.17	4.15	5.04	5.14	4.93	5.34	4.77	3.77	5.13	4.72	5.15	3.77	4.62
TiO2	0.77	0.67	0.68	0.56	0.50	0.75	0.68	0.92	0.00	0.00	0.00	0.00	0.00	0.00	0.00	0.00	0.00	0.00	0.00	0.00	0.00	0.00	0.00
MnO	0.00	0.00	0.00	0.00	0.00	0.00	0.00	0.00	0.00	0.00	0.00	0.00	0.00	0.00	0.00	0.00	0.00	0.00	0.00	0.00	0.00	0.00	0.00
FeO	1.38	1.56	1.59	1.53	1.83	1.39	1.50	1.88	0.00	0.00	0.00	0.00	0.00	0.00	0.00	0.00	0.00	0.00	0.00	0.00	0.00	0.00	0.00
TOTAL	94.53	94.83	96.30	95.35	94.75	94.12	93.58	94.70	100.82	100.59	100.77	100.55	100.45	100.56	100.18	100.55	99.87	100.25	100.10	99.77	100.90	100.61	100.27
Na	0.16	0.14	0.15	0.15	0.19	0.14	0.15	0.15	3.08	3.06	3.06	3.07	2.95	2.96	2.98	2.86	2.98	3.19	2.92	2.98	2.93	3.09	2.94
Mg	0.12	0.13	0.15	0.16	0.14	0.14	0.15	0.14	0.00	0.00	0.00	0.00	0.00	0.00	0.00	0.00	0.00	0.00	0.00	0.00	0.00	0.00	0.00
Al	5.55	5.51	5.53	5.55	5.53	5.47	5.49	5.48	4.76	4.85	4.80	4.77	4.96	4.99	4.91	5.03	4.92	4.75	5.01	4.94	4.99	4.74	4.87
Si	6.12	6.15	6.12	6.13	6.12	6.17	6.14	6.13	11.27	11.15	11.22	11.27	11.05	11.03	11.10	10.99	11.10	11.26	11.00	11.08	11.00	11.28	11.17
K	1.82	1.89	1.87	1.84	1.84	1.87	1.87	1.85	0.10	0.07	0.07	0.11	0.07	0.05	0.03	0.05	0.06	0.12	0.07	0.04	0.06	0.12	0.09
Ca	0.00	0.00	0.00	0.00	0.00	0.00	0.00	0.00	0.74	0.85	0.78	0.78	0.95	0.97	0.93	1.01	0.91	0.71	0.97	0.90	0.97	0.71	0.87
Ti	0.08	0.07	0.07	0.06	0.05	0.08	0.07	0.09	0.00	0.00	0.00	0.00	0.00	0.00	0.00	0.00	0.00	0.00	0.00	0.00	0.00	0.00	0.00
Mn	0.00	0.00	0.00	0.00	0.00	0.00	0.00	0.00	0.00	0.00	0.00	0.00	0.00	0.00	0.00	0.00	0.00	0.00	0.00	0.00	0.00	0.00	0.00
Fe	0.16	0.18	0.18	0.17	0.21	0.16	0.17	0.21	0.00	0.00	0.00	0.00	0.00	0.00	0.00	0.00	0.00	0.00	0.00	0.00	0.00	0.00	0.00
cation sum	14.01	14.07	14.07	14.06	14.08	14.03	14.04	14.05	19.95	19.98	19.93	20.00	19.98	20.00	19.95	19.94	19.97	20.03	19.97	19.94	19.95	19.94	19.94
An%									18.9	21.4	19.9	19.7	23.9	24.4	23.6	25.8	23.0	17.7	24.5	23.0	24.5	18.1	22.3

Rock	97-244 Granitic migmatite				98-65B Granitic migmatite																		
Mineral	Kf rim	Kf core	Kf rim	kf rim	Biotite	Biotite	Biotite	Biotite	Biotite	Biotite	musc	musc	musc	musc	plag core	plag core	plag core	plag rim	plag rim	plag A core	plag A rim	plag b core	
context	leuco	leuco	leuco	leuco	Melanosome	Melanosome	Melanosome	Melanosome	Melanosome	Melanosome	melano	melano	melano	melano	leuco	leuco	leuco	leuco	leuco	leuco	leuco	leuco	
spot	4.8	9.1	9.2	6.1	11.1	11.2	11.3	13.1	13.2	13.3	11.4	11.5	13.4	13.5	1.1	1.2	1.3	1.4	1.5	2.1	2.2	2.3	
Na2O	1.20	1.55	1.31	1.55	0.16	0.36	0.24	0.23	0.25	0.19	0.57	0.52	0.57	0.67	7.77	7.44	8.05	7.51	8.15	7.59	8.19	8.04	
MgO	0.00	0.00	0.00	0.00	7.44	7.66	7.61	7.65	7.64	7.40	0.54	0.69	0.59	0.60	0.00	0.00	0.00	0.00	0.00	0.00	0.00	0.00	
Al2O3	18.63	18.88	18.61	18.57	19.47	19.56	19.41	19.52	19.26	19.45	35.26	34.41	35.16	34.84	25.20	25.49	24.54	25.47	24.50	25.44	24.19	24.63	
SiO2	64.72	64.52	64.87	65.64	34.86	35.18	35.14	35.29	34.95	35.00	45.14	45.36	45.41	44.72	60.56	59.86	61.91	60.22	61.46	60.32	61.52	61.57	
K2O	15.03	14.29	14.68	14.80	9.78	9.79	9.67	9.85	9.63	9.72	10.99	10.90	10.92	10.59	0.41	0.29	0.39	0.29	0.23	0.24	0.37	0.28	
CaO	0.00	0.00	0.00	0.00	0.00	0.00	0.00	0.00	0.00	0.00	0.00	0.00	0.00	0.00	6.38	6.90	5.65	7.06	5.76	6.94	5.57	5.77	
TiO2	0.00	0.00	0.00	0.00	2.34	2.17	2.38	2.17	2.52	2.34	0.46	0.86	0.63	0.72	0.00	0.00	0.00	0.00	0.00	0.00	0.00	0.00	
MnO	0.00	0.00	0.00	0.00	0.29	0.00	0.00	0.38	0.00	0.29	0.00	0.00	0.00	0.00	0.00	0.00	0.00	0.00	0.00	0.00	0.00	0.00	
FeO	0.00	0.00	0.00	0.00	20.61	21.13	20.47	21.17	21.52	20.79	1.58	1.67	1.49	1.54	0.00	0.00	0.00	0.00	0.00	0.00	0.00	0.00	
TOTAL	99.58	99.24	99.47	100.56	94.95	95.85	94.92	96.26	95.77	95.18	94.54	94.41	94.77	93.68	100.32	99.98	100.54	100.55	100.10	100.53	99.84	100.29	
Na	0.43	0.56	0.47	0.55	0.05	0.11	0.07	0.07	0.07	0.06	0.15	0.14	0.15	0.18	2.68	2.57	2.75	2.58	2.81	2.61	2.82	2.76	
Mg	0.00	0.00	0.00	0.00	1.71	1.74	1.74	1.74	1.74	1.70	0.11	0.14	0.12	0.12	0.00	0.00	0.00	0.00	0.00	0.00	0.00	0.00	
Al	4.05	4.11	4.04	4.00	3.54	3.52	3.52	3.51	3.48	3.53	5.61	5.48	5.58	5.59	5.27	5.35	5.10	5.33	5.13	5.32	5.07	5.13	
Si	11.93	11.92	11.96	11.99	5.38	5.37	5.40	5.38	5.35	5.38	6.10	6.13	6.11	6.08	10.75	10.67	10.92	10.68	10.91	10.71	10.94	10.88	
K	3.53	3.37	3.45	3.45	1.93	1.91	1.90	1.91	1.88	1.91	1.89	1.88	1.87	1.84	0.09	0.07	0.09	0.07	0.05	0.05	0.08	0.06	
Ca	0.00	0.00	0.00	0.00	0.00	0.00	0.00	0.00	0.00	0.00	0.00	0.00	0.00	0.00	1.21	1.32	1.07	1.34	1.10	1.32	1.06	1.09	
Ti	0.00	0.00	0.00	0.00	0.27	0.25	0.27	0.25	0.29	0.27	0.05	0.09	0.06	0.07	0.00	0.00	0.00	0.00	0.00	0.00	0.00	0.00	
Mn	0.00	0.00	0.00	0.00	0.04	0.00	0.00	0.05	0.00	0.04	0.00	0.00	0.00	0.00	0.00	0.00	0.00	0.00	0.00	0.00	0.00	0.00	
Fe	0.00	0.00	0.00	0.00	2.66	2.70	2.63	2.70	2.76	2.67	0.18	0.19	0.17	0.17	0.00	0.00	0.00	0.00	0.00	0.00	0.00	0.00	
cation sum	19.94	19.96	19.92	19.99	15.58	15.60	15.53	15.61	15.57	15.56	14.09	14.05	14.06	14.05	20.00	19.98	19.93	20.00	20.00	20.01	19.97	19.92	
An%															30.4	33.3	27.4	33.6	27.8	33.2	26.8	27.9	

Rock	98-65B Granitic migmatite																			
Mineral	plag b core	plag b rim	plag core	plag core	plag rim	plag	plag core	plag rim	plag rim	plag core	plag rim	plag core	plag rim	plag rim	Kf core	Kf rim	Kf rim	Kf core	Kf core	Kf rim
Context	leuco	leuco	leuco	leuco	leuco	melano	leuco	leuco	leuco	leuco	leuco	leuco	leuco	leuco	leuco	leuco	leuco	leuco	leuco	leuco
spot	2.4	2.5	3.1	3.2	3.3	12.1	5.1	5.2	5.3	6.1	6.2	7.1	7.2	7.3	8.1	8.2	9.1	9.2	10.1	10.2
Na2O	7.69	7.65	8.35	7.39	7.49	8.14	7.59	8.43	7.62	7.99	7.43	7.61	8.52	7.53	1.81	1.67	1.50	1.75	2.00	.1.15
MgO	0.00	0.00	0.00	0.00	0.00	0.00	0.00	0.00	0.00	0.00	0.00	0.00	0.00	0.00	0.00	0.00	0.00	0.00	0.00	0.00
Al2O3	25.47	25.15	24.02	25.45	25.74	24.77	25.97	24.09	25.14	24.24	25.24	25.43	23.55	25.69	18.88	18.82	18.69	18.80	18.95	18.64
SiO2	59.98	60.22	61.83	60.05	60.71	61.81	60.42	62.32	59.80	60.92	60.13	59.44	62.24	60.87	65.49	65.00	64.67	65.22	65.80	65.09
K2O	0.26	0.28	0.39	0.30	0.29	0.21	0.17	0.34	0.26	0.36	0.26	0.32	0.41	0.24	14.39	14.59	14.66	14.43	14.18	15.12
CaO	6.71	6.81	5.19	6.59	6.74	5.87	6.97	5.08	6.76	5.93	6.73	6.88	5.09	6.86	0.00	0.00	0.00	0.00	0.00	0.00
TiO2	0.00	0.00	0.00	0.00	0.00	0.00	0.00	0.00	0.00	0.00	0.00	0.00	0.00	0.00	0.22	0.25	0.25	0.24	0.00	0.30
MnO	0.00	0.00	0.00	0.00	0.00	0.00	0.00	0.00	0.00	0.00	0.00	0.00	0.00	0.00	0.00	0.00	0.00	0.00	0.00	0.00
FeO	0.00	0.00	0.00	0.00	0.00	0.00	0.00	0.00	0.00	0.00	0.00	0.00	0.00	0.00	0.00	0.00	0.00	0.00	0.00	0.00
TOTAL	100.11	100.11	99.78	99.78	100.97	100.80	101.12	100.26	99.58	99.44	99.79	99.68	99.81	101.19	100.79	100.33	99.77	100.44	100.93	99.15
Na	2.66	2.64	2.88	2.55	2.56	2.78	2.59	2.89	2.64	2.77	2.57	2.64	2.94	2.57	0.64	0.59	0.54	0.62	0.70	0.41
Mg	0.00	0.00	0.00	0.00	0.00	0.00	0.00	0.00	0.00	0.00	0.00	0.00	0.00	0.00	0.00	0.00	0.00	0.00	0.00	0.00
Al	5.35	5.27	5.03	5.35	5.35	5.14	5.39	5.02	5.30	5.11	5.31	5.36	4.94	5.32	4.05	4.06	4.06	4.05	4.06	4.03
Si	10.70	10.72	10.98	10.71	10.71	10.88	10.64	11.01	10.70	10.89	10.73	10.64	11.07	10.69	11.93	11.91	11.92	11.92	11.95	11.95
K	0.06	0.06	0.09	0.07	0.06	0.05	0.04	0.08	0.06	0.08	0.06	0.07	0.09	0.05	3.34	3.41	3.45	3.37	3.29	3.54
Ca	1.28	1.30	0.99	1.26	1.27	1.11	1.31	0.96	1.29	1.14	1.29	1.32	0.97	1.29	0.00	0.00	0.00	0.00	0.00	0.00
Ti	0.00	0.00	0.00	0.00	0.00	0.00	0.00	0.00	0.00	0.00	0.00	0.00	0.00	0.00	0.03	0.04	0.03	0.03	0.00	0.04
Mn	0.00	0.00	0.00	0.00	0.00	0.00	0.00	0.00	0.00	0.00	0.00	0.00	0.00	0.00	0.00	0.00	0.00	0.00	0.00	0.00
Fe	0.00	0.00	0.00	0.00	0.00	0.00	0.00	0.00	0.00	0.00	0.00	0.00	0.00	0.00	0.00	0.00	0.00	0.00	0.00	0.00
cation sum	20.05	19.99	19.97	19.94	19.95	19.96	19.97	19.96	19.99	19.99	19.96	20.03	20.01	19.92	19.99	20.01	20.00	19.99	20.00	19.97
An%	32.0	32.5	25.0	32.5	32.6	28.2	33.2	24.4	32.3	28.6	32.9	32.8	24.3	33.0						

Rock	98-65C migmatite mesosome/melanosome																						
Mineral	plag core	plag rim	plag rim	plag core	plag core	plag rim	plag A core	plag A rim	plag B core	plag B rim	plag A core	plag A rim	plag B core	plag b rim	plag A core	plag A rim	plag b core	plag b core	plag A core	plag A rim	plag B core	plag B rim	bio
context	leuco	leuco	leuco	leuco	leuco	leuco	meso	meso	meso	meso	meso	meso	meso	meso	meso	meso	meso	meso	meso	meso	meso	meso	melano
spot	1.1	1.2	1.3	2.1	2.2	2.3	5.2	5.3	5.4	5.5	6.1	6.2	6.3	6.4	7.1	7.2	7.3	7.4	8.1	8.2	8.3	8.4	3.1
Na2O	6.30	7.31	7.79	7.53	6.97	7.65	8.00	7.39	7.58	7.80	7.71	7.42	7.84	7.67	8.00	7.56	7.58	7.91	7.96	7.74	7.92	7.40	0.20
MgO	0.00	0.00	0.00	0.00	0.00	0.00	0.00	0.00	0.00	0.00	0.00	0.00	0.00	0.00	0.00	0.00	0.00	0.00	0.00	0.00	0.00	0.00	7.77
Al2O3	26.71	25.53	24.99	25.40	26.13	25.26	24.32	25.33	25.29	24.87	25.30	25.44	24.85	25.02	24.50	25.44	25.22	24.31	24.60	25.34	24.96	25.36	19.45
SiO2	57.26	59.34	60.91	60.14	59.06	60.70	60.97	59.25	60.39	61.55	60.56	60.19	60.53	60.38	61.13	60.21	60.46	61.61	61.76	61.21	61.40	60.33	35.00
K2O	0.21	0.35	0.32	0.33	0.31	0.31	0.37	0.19	0.30	0.18	0.16	0.17	0.23	0.11	0.34	0.20	0.12	0.17	0.26	0.18	0.32	0.30	9.81
CaO	8.56	7.09	6.18	6.62	7.65	6.37	6.02	6.83	6.80	6.03	6.77	6.94	6.47	6.51	6.05	6.92	6.98	5.86	5.80	6.22	5.96	6.72	0.00
TiO2	0.00	0.00	0.00	0.00	0.00	0.00	0.00	0.00	0.00	0.00	0.00	0.20	0.00	0.00	0.00	0.00	0.00	0.00	0.00	0.00	0.00	0.00	2.12
MnO	0.00	0.00	0.00	0.00	0.00	0.00	0.00	0.00	0.00	0.00	0.00	0.00	0.00	0.00	0.00	0.00	0.00	0.00	0.00	0.00	0.00	0.00	0.37
FeO	0.00	0.00	0.00	0.00	0.00	0.00	0.00	0.00	0.00	0.00	0.00	0.00	0.00	0.00	0.00	0.00	0.00	0.00	0.00	0.00	0.00	0.00	21.29
TOTAL	99.04	99.62	100.19	100.02	100.12	100.29	99.68	98.99	100.36	100.43	100.50	100.36	99.92	99.69	100.02	100.33	100.36	99.86	100.38	100.69	100.56	100.11	96.01
Na	2.20	2.53	2.68	2.60	2.41	2.63	2.76	2.58	2.61	2.67	2.65	2.55	2.70	2.66	2.76	2.60	2.60	2.72	2.73	2.65	2.71	2.55	0.06
Mg	0.00	0.00	0.00	0.00	0.00	0.00	0.00	0.00	0.00	0.00	0.00	0.00	0.00	0.00	0.00	0.00	0.00	0.00	0.00	0.00	0.00	0.00	1.77
Al	5.67	5.38	5.22	5.32	5.49	5.28	5.10	5.36	5.29	5.17	5.28	5.32	5.21	5.27	5.13	5.32	5.27	5.09	5.13	5.27	5.20	5.31	3.51
Si	10.32	10.61	10.80	10.70	10.53	10.76	10.86	10.65	10.71	10.86	10.73	10.67	10.77	10.78	10.86	10.69	10.72	10.94	10.92	10.81	10.85	10.73	5.36
K	0.05	0.08	0.07	0.08	0.07	0.07	0.08	0.04	0.07	0.04	0.04	0.04	0.05	0.02	0.08	0.04	0.03	0.04	0.06	0.04	0.07	0.07	1.91
Ca	1.65	1.36	1.17	1.26	1.46	1.21	1.15	1.31	1.29	1.14	1.28	1.32	1.23	1.24	1.15	1.32	1.33	1.11	1.10	1.18	1.13	1.28	0.00
Ti	0.00	0.00	0.00	0.00	0.00	0.00	0.00	0.00	0.00	0.00	0.00	0.03	0.00	0.00	0.00	0.00	0.00	0.00	0.00	0.00	0.00	0.00	0.24
Mn	0.00	0.00	0.00	0.00	0.00	0.00	0.00	0.00	0.00	0.00	0.00	0.00	0.00	0.00	0.00	0.00	0.00	0.00	0.00	0.00	0.00	0.00	0.05
Fe	0.00	0.00	0.00	0.00	0.00	0.00	0.00	0.00	0.00	0.00	0.00	0.00	0.00	0.00	0.00	0.00	0.00	0.00	0.00	0.00	0.00	0.00	2.72
cation sum	19.89	19.96	19.94	19.96	19.96	19.95	19.95	19.94	19.97	19.88	19.98	19.93	19.96	19.97	19.98	19.97	19.95	19.90	19.94	19.95	19.96	19.94	15.62
An%	42.3	34.3	29.8	32.0	37.1	30.9	28.8	33.3	32.5	29.6	32.2	33.8	30.9	31.6	28.8	33.3	33.6	28.7	28.3	30.5	28.9	32.8	

Rock	98-65C migmatite mesosome/melanosome							98-RG3 GRANITIC MIGMATITE															
Mineral	bio	bio	bio	bio	bio	bio	bio	Plag	Plag core	Plag rim	Plag core (a)	Plag rim (a)	Plag core (b)	Plag rim (b)	Plag core (a)	Plag rim (a)	Plag core (b)	Plag rim (b)	Plag core (a)	Plag rim (a)	Biotite	Biotite
Context	melano	melano	melano	?meso	meso	meso	meso	leuco	leuco	leuco	leuco	leuco	leuco	leuco	leuco	leuco	leuco	leuco	leuco	leuco	mel	mel
spot	3.2	4.1	4.2	5.1	7.5	7.6	8.5	1.1	1.2	1.3	2.4	2.5	2.6	2.7	3.5	3.6	3.7	3.8	4.4	4.5	1.4	1.5
Na2O	0.26	0.20	0.37	0.00	0.28	0.23	0.34	8.73	8.57	8.1	7.63	8.95	7.71	8.47	7.98	8.22	8.17	8.7	8.24	8.77	0.32	0.34
MgO	7.60	7.53	7.52	7.85	7.55	7.65	7.58	0	0.04	0.02	0.03	0.09	0	0	0.04	0	0.01	0.01	0.01	0.02	8.63	8.59
Al2O3	19.18	19.60	19.24	19.35	19.65	19.59	19.56	23.48	23.65	24.23	25.03	23.56	24.73	23.85	24.45	24.24	24.13	23.78	24.24	23.85	18.87	18.84
SiO2	34.88	34.99	34.65	35.06	34.57	34.88	34.68	62.99	62.56	61.6	60.16	62.48	60.49	62.05	61.37	61.7	61.72	62.44	61.48	63	35.33	35.13
K2O	9.81	9.67	9.77	9.58	9.39	9.49	9.83	0.23	0.21	0.18	0.2	0.2	0.18	0.26	0.19	0.15	0.13	0.15	0.15	0.16	9.72	9.66
CaO	0.00	0.00	0.00	0.00	0.00	0.00	0.00	4.57	4.82	5.61	6.56	4.81	6.24	5.19	5.76	5.47	5.68	4.97	5.56	4.78	0	0
TiO2	2.25	2.37	2.31	2.34	2.38	2.17	2.32	0	0.01	0.01	0.06	0.05	0.06	0.19	0.02	0.07	0.13	0	0.07	0.18	2.81	2.95
MnO	0.27	0.00	0.00	0.35	0.00	0.00	0.00	0.02	0	0	0.02	0.15	0	0.04	0	0.05	0.12	0.09	0	0.01	0.25	0.48
FeO	20.90	20.48	20.99	20.18	20.64	21.30	20.27	0.12	0	0	0	0.2	0.16	0	0	0	0	0.18	0.21	0.07	19.1	19.57
TOTAL	95.15	94.84	94.85	94.71	94.46	95.31	94.58	100.14	99.86	99.75	99.69	100.49	99.57	100.05	99.81	99.9	100.09	100.32	99.96	100.84	95.03	95.56
Na	0.08	0.06	0.11	0.00	0.08	0.07	0.10	2.991	2.945	2.791	2.641	3.067	2.669	2.911	2.749	2.828	2.808	2.982	2.838	2.985	0.095	0.101
Mg	1.75	1.73	1.73	1.80	1.74	1.75	1.75	0	0	0.005	0.008	0.024	0	0	0.011	0	0.003	0.003	0.003	0.005	1.967	1.955
Al	3.49	3.55	3.51	3.51	3.58	3.55	3.56	4.891	4.941	5.076	5.267	4.908	5.206	4.984	5.122	5.071	5.043	4.956	5.076	4.936	3.403	3.391
Si	5.38	5.38	5.36	5.39	5.34	5.35	5.36	11.129	11.087	10.947	10.738	11.041	10.801	10.998	10.904	10.948	10.941	11.037	10.92	11.061	5.405	5.364
K	1.93	1.90	1.93	1.88	1.85	1.86	1.94	0.052	0.047	0.041	0.046	0.045	0.041	0.059	0.043	0.034	0.029	0.034	0.034	0.036	1.897	1.882
Ca	0.00	0.00	0.00	0.00	0.00	0.00	0.00	0.865	0.915	1.068	1.255	0.911	1.194	0.986	1.097	1.04	1.079	0.941	1.058	0.899	0	0
Ti	0.26	0.27	0.27	0.27	0.27	0.25	0.27	0	0.001	0.001	0.008	0.007	0.008	0.025	0.003	0.009	0.017	0	0.009	0.024	0.323	0.339
Mn	0.04	0.00	0.00	0.05	0.00	0.00	0.00	0.003	0	0	0.003	0.022	0	0.006	0	0.008	0.018	0.013	0	0.001	0.032	0.062
Fe	2.70	2.63	2.71	2.60	2.67	2.73	2.62	0.018	0	0	0	0.03	0.024	0	0	0	0	0.027	0.031	0.01	2.444	2.499
cation sum	15.63	15.52	15.62	15.50	15.53	15.56	15.60	19.947	19.937	19.93	19.964	20.054	19.943	19.969	19.928	19.938	19.939	19.993	19.969	19.958	15.566	15.593
An%								22.1	23.4	27.4	31.8	22.6	30.6	24.9	28.2	26.7	27.6	23.8	26.9	22.9		

Rock	98-RG3 GRANITIC MIGMATITE										98-65A Granitic leucosome											
Mineral	Biotite	Biotite	Biotite	Biotite	Biotite	Biotite	Biotite	Biotite	Biotite	Biotite	Biotite	biotite	biotite	biotite	biotite	biotite	biotite	biotite	musc	musc	musc	musc (sill)
context	mel	meso	meso	meso	meso	meso	meso	meso	meso	meso	leuco	leuco	leuco	leuco	leuco	leuco	leuco	leuco	leuco	leuco	leuco	leuco
spot	1.6	2.1	2.2	2.3	3.1	3.2	3.3	3.4	4.1	4.2	4.3	1.1	1.2	3.1	3.2	3.3	4.1	4.2	1.7	3.4	3.5	7
Na2O	0.41	0.23	0.27	0.43	0.31	0.38	0.23	0.29	0.3	0.28	0.29	0.34	0.35	0.24	0.19	0.32	0.30	0.28	0.60	0.67	0.57	0.39
MgO	8.45	8.66	8.39	8.39	8.35	8.44	8.17	8.33	8.76	8.35	8.73	7.54	7.45	7.71	7.67	7.69	7.47	7.82	0.72	0.73	0.60	0.20
Al2O3	19.05	18.54	18.89	18.74	19.07	18.5	18.97	19.45	18.16	19.21	18.41	19.58	19.55	19.86	19.53	19.73	19.71	19.89	35.16	34.97	34.78	36.98
SiO2	35	35.4	34.97	35.4	35.19	35	35.11	36	34.82	34.88	34.98	35.54	34.90	34.98	34.94	35.16	34.94	35.25	46.08	45.41	45.24	45.40
K2O	9.84	9.86	9.98	9.73	9.96	9.66	9.93	9.97	9.89	9.98	9.83	9.58	9.66	9.62	9.62	9.66	9.76	9.75	10.88	10.98	10.83	10.91
CaO	0.06	0	0	0.02	0.02	0.01	0.02	0.01	0.03	0.1	0	0.00	0.00	0.00	0.00	0.00	0.00	0.00	0.00	0.00	0.00	0.00
TiO2	2.66	3.31	2.84	2.79	2.61	2.64	2.61	2.89	2.52	2.68	2.53	2.25	2.19	2.05	1.93	2.42	2.26	2.28	0.41	0.66	0.49	0.00
MnO	0.37	0.4	0.52	0.57	0.48	0.55	0.52	0.47	0.33	0.26	0.36	0.00	0.32	0.00	0.26	0.00	0.38	0.39	0.00	0.00	0.10	0.00
FeO	18.99	19.53	18.94	19.23	18.89	18.63	19.05	19.41	19.34	19.06	18.93	20.54	20.42	20.52	20.30	20.75	20.12	20.22	1.41	1.79	1.43	0.50
TOTAL	94.83	95.93	94.8	95.3	94.88	93.81	94.61	96.82	94.15	94.8	94.06	95.37	94.84	94.98	94.44	95.73	94.94	95.88	95.26	95.21	94.04	94.38
Na	0.122	0.068	0.081	0.128	0.092	0.114	0.069	0.084	0.09	0.083	0.087	0.10	0.11	0.07	0.06	0.09	0.09	0.08	0.16	0.17	0.15	0.10
Mg	1.935	1.963	1.923	1.912	1.91	1.951	1.876	1.865	2.027	1.913	2.015	1.72	1.71	1.76	1.77	1.75	1.72	1.77	0.14	0.15	0.12	0.04
Al	3.45	3.324	3.425	3.379	3.45	3.383	3.445	3.445	3.324	3.481	3.362	3.52	3.55	3.59	3.56	3.55	3.58	3.57	5.53	5.54	5.55	5.83
Si	5.376	5.384	5.379	5.414	5.4	5.428	5.408	5.408	5.407	5.362	5.419	5.42	5.38	5.37	5.40	5.37	5.38	5.36	6.15	6.10	6.13	6.07
K	1.928	1.913	1.958	1.898	1.95	1.911	1.951	1.911	1.959	1.957	1.943	1.86	1.90	1.88	1.90	1.88	1.92	1.89	1.85	1.88	1.87	1.86
Ca	0.01	0	0	0.003	0.003	0.002	0.003	0.002	0.005	0.016	0	0.00	0.00	0.00	0.00	0.00	0.00	0.00	0.00	0.00	0.00	0.00
Ti	0.307	0.379	0.329	0.321	0.301	0.308	0.302	0.327	0.294	0.31	0.295	0.26	0.25	0.24	0.22	0.28	0.26	0.26	0.04	0.07	0.05	0.00
Mn	0.048	0.052	0.068	0.074	0.062	0.072	0.068	0.06	0.043	0.034	0.047	0.00	0.04	0.00	0.03	0.00	0.05	0.05	0.00	0.00	0.00	0.00
Fe	2.44	2.484	2.436	2.46	2.424	2.416	2.454	2.439	2.511	2.45	2.452	2.62	2.63	2.64	2.62	2.65	2.59	2.57	0.16	0.20	0.16	0.06
cation sum	15.617	15.566	15.599	15.589	15.594	15.585	15.577	15.54	15.662	15.608	15.62	15.50	15.57	15.55	15.56	15.57	15.59	15.55	14.03	14.11	14.03	13.96
An%																						

Rock	98-65A Granitic leucosome																					
Mineral	plag A core	plag A rim	plag B core	plag b rim	plag core	plag rim	plag rim	plag rim	plag core	plag core	plag rim	plag rim	plag core	plag rim	plag rim	plag incl.	Kf rim	kf core	Kf rim	kf core	Kf rim	Kf rim
Context	leuco	leuco	leuco	leuco	leuco	leuco	leuco	leuco	leuco	leuco	leuco	leuco	leuco	leuco	leuco	leuco	leuco	leuco	leuco	leuco	leuco	leuco
spot	1.3	1.4	1.5	1.6	2.2	2.3	2.4	2.5	5.1	5.2	5.3	5.4	6.3	6.4	6.5	6.6	2.1	6.1	6.2	7.1	7.2	8.1
Na2O	6.76	8.20	6.65	7.78	6.42	8.28	7.87	7.20	8.68	6.85	8.28	7.54	7.37	8.28	7.79	7.89	1.78	1.48	1.55	1.70	1.58	1.46
MgO	0.00	0.00	0.00	0.00	0.00	0.00	0.00	0.00	0.00	0.00	0.00	0.00	0.00	0.00	0.00	0.00	0.00	0.00	0.00	0.00	0.00	0.00
Al2O3	26.83	24.61	26.84	24.88	26.66	23.96	24.60	25.71	23.98	26.36	24.08	25.36	25.44	24.08	25.33	24.56	18.66	18.55	18.78	18.73	18.56	18.95
SiO2	58.81	61.38	58.12	60.88	57.26	61.80	60.86	58.96	62.17	58.61	61.84	60.44	59.84	61.86	60.14	60.30	64.90	64.83	64.86	64.71	65.00	64.32
K2O	0.18	0.28	0.19	0.32	0.25	0.41	0.30	0.53	0.15	0.21	0.27	0.30	0.34	0.38	0.24	0.24	14.46	14.77	14.35	14.37	14.65	14.78
CaO	8.26	5.59	8.06	6.21	8.52	5.03	6.13	6.48	4.95	8.02	5.30	6.36	6.78	5.28	6.59	6.01	0.00	0.00	0.00	0.00	0.00	0.00
TiO2	0.00	0.00	0.00	0.00	0.00	0.00	0.00	0.00	0.00	0.00	0.00	0.00	0.00	0.00	0.00	0.00	0.00	0.00	0.00	0.00	0.42	0.21
MnO	0.00	0.00	0.00	0.00	0.00	0.00	0.00	0.00	0.00	0.00	0.00	0.00	0.00	0.00	0.00	0.00	0.00	0.00	0.00	0.00	0.00	0.00
FeO	0.00	0.00	0.00	0.00	0.00	0.00	0.00	0.00	0.00	0.00	0.00	0.00	0.00	0.00	0.00	0.00	0.00	0.00	0.00	0.00	0.00	0.00
TOTAL	100.84	100.06	99.86	100.07	99.11	99.48	99.76	98.88	99.93	100.05	99.77	100.00	99.77	99.88	100.09	99.00	99.80	99.63	99.54	99.51	100.21	99.72
Na	2.33	2.82	2.31	2.68	2.25	2.86	2.72	2.52	2.98	2.37	2.85	2.60	2.55	2.85	2.68	2.75	0.63	0.53	0.55	0.61	0.56	0.52
Mg	0.00	0.00	0.00	0.00	0.00	0.00	0.00	0.00	0.00	0.00	0.00	0.00	0.00	0.00	0.00	0.00	0.00	0.00	0.00	0.00	0.00	0.00
Al	5.63	5.14	5.66	5.21	5.68	5.03	5.16	5.46	5.02	5.55	5.04	5.32	5.35	5.03	5.31	5.19	4.04	4.03	4.07	4.06	4.01	4.12
Si	10.38	10.88	10.40	10.81	10.34	11.01	10.83	10.63	11.03	10.47	10.99	10.75	10.68	10.96	10.70	10.82	11.93	11.95	11.94	11.92	11.92	11.87
K	0.04	0.06	0.04	0.07	0.06	0.09	0.07	0.12	0.03	0.05	0.06	0.07	0.08	0.09	0.05	0.06	3.39	3.47	3.37	3.38	3.43	3.48
Ca	1.58	1.06	1.54	1.18	1.65	0.96	1.17	1.25	0.94	1.54	1.01	1.21	1.30	1.00	1.26	1.15	0.00	0.00	0.00	0.00	0.00	0.00
Ti	0.00	0.00	0.00	0.00	0.00	0.00	0.00	0.00	0.00	0.00	0.00	0.00	0.00	0.00	0.00	0.00	0.00	0.00	0.00	0.00	0.06	0.03
Mn	0.00	0.00	0.00	0.00	0.00	0.00	0.00	0.00	0.00	0.00	0.00	0.00	0.00	0.00	0.00	0.00	0.00	0.00	0.00	0.00	0.00	0.00
Fe	0.00	0.00	0.00	0.00	0.00	0.00	0.00	0.00	0.00	0.00	0.00	0.00	0.00	0.00	0.00	0.00	0.00	0.00	0.00	0.00	0.00	0.00
cation sum	19.96	19.96	19.95	19.95	19.98	19.95	19.95	19.98	20.00	19.98	19.95	19.95	19.96	19.93	20.00	19.97	19.99	19.98	19.93	19.97	19.98	20.02
An%	40.0	26.9	39.6	30.0	41.7	24.6	29.5	32.1	23.8	38.9	25.8	31.2	33.1	25.4	31.6	29.0						

Rock	98-102 Granitic leucosome																					
Mineral	biotite	biotite	biotite	biotite	biotite	musc	musc	musc	musc	musc	musc	plag A rim	plag b core	plag B rim	plag core	plag core	plag rim	plag rim	plag rim	plag core	plag rim	plag rim	plag rim
context																							
spot	2.3	4.1	4.2	4.3	7.1	1.1	4.4	4.5	5.1	5.2	7.4	2.1	2.2	2.4	3.1	3.2	3.3	3.4	3.5	5.3	5.5	5.6	5.7
Na2O	0.20	0.16	0.21	0.36	0.16	0.49	0.52	0.51	0.53	0.54	0.50	7.96	7.36	8.19	8.05	6.94	7.62	7.61	8.00	8.08	7.25	7.64	8.44
MgO	8.62	9.03	8.68	8.90	8.96	0.69	0.82	0.88	0.85	0.81	0.84	0.00	0.00	0.00	0.00	0.00	0.00	0.00	0.00	0.00	0.00	0.00	0.00
Al2O3	18.71	18.14	18.86	18.45	18.39	34.30	34.10	33.98	33.90	34.65	34.39	24.70	26.04	24.54	24.77	26.13	25.31	25.38	24.69	24.51	25.95	25.30	24.33
SiO2	35.50	35.50	35.64	35.39	35.90	45.56	45.85	45.93	45.62	45.87	45.76	61.43	59.91	62.24	60.94	59.15	60.35	60.22	61.67	61.63	60.07	60.72	61.91
K2O	9.89	10.03	10.17	9.91	10.04	11.19	11.00	11.03	11.07	11.09	10.91	0.34	0.19	0.31	0.29	0.22	0.24	0.33	0.34	0.31	0.36	0.37	0.43
CaO	0.00	0.00	0.00	0.00	0.00	0.00	0.00	0.00	0.00	0.00	0.00	5.74	7.12	5.57	6.19	7.59	6.54	6.74	6.02	5.66	7.11	6.58	5.62
TiO2	2.32	2.28	2.17	2.22	2.25	0.70	0.58	0.62	0.53	0.60	0.73	0.00	0.00	0.00	0.00	0.00	0.00	0.00	0.00	0.00	0.00	0.00	0.00
MnO	0.55	0.55	0.32	0.29	0.65	0.00	0.00	0.00	0.00	0.00	0.00	0.00	0.00	0.00	0.00	0.00	0.00	0.00	0.00	0.00	0.00	0.00	0.00
FeO	19.88	19.92	19.81	19.97	19.97	2.36	2.54	2.47	2.03	2.41	2.36	0.00	0.00	0.00	0.00	0.00	0.00	0.00	0.00	0.00	0.00	0.00	0.00
TOTAL	95.67	95.61	95.86	95.49	96.32	95.29	95.41	95.42	94.53	95.97	95.49	100.17	100.62	100.85	100.24	100.03	100.06	100.28	100.72	100.19	100.74	100.61	100.73
Na	0.06	0.05	0.06	0.11	0.05	0.13	0.14	0.13	0.14	0.14	0.13	2.74	2.52	2.79	2.76	2.39	2.63	2.62	2.74	2.77	2.48	2.62	2.89
Mg	1.96	2.06	1.97	2.03	2.03	0.14	0.16	0.18	0.17	0.16	0.17	0.00	0.00	0.00	0.00	0.00	0.00	0.00	0.00	0.00	0.00	0.00	0.00
Al	3.37	3.28	3.39	3.33	3.29	5.44	5.40	5.37	5.40	5.45	5.44	5.16	5.43	5.08	5.16	5.47	5.31	5.32	5.14	5.11	5.41	5.27	5.07
Si	5.42	5.43	5.43	5.42	5.45	6.14	6.16	6.16	6.17	6.12	6.14	10.89	10.60	10.94	10.77	10.50	10.74	10.70	10.89	10.90	10.62	10.73	10.94
K	1.93	1.96	1.98	1.94	1.94	1.92	1.89	1.89	1.91	1.89	1.87	0.08	0.04	0.07	0.06	0.05	0.05	0.07	0.08	0.07	0.08	0.08	0.10
Ca	0.00	0.00	0.00	0.00	0.00	0.00	0.00	0.00	0.00	0.00	0.00	1.09	1.35	1.05	1.17	1.44	1.25	1.28	1.14	1.07	1.35	1.25	1.06
Ti	0.27	0.26	0.25	0.26	0.26	0.07	0.06	0.06	0.05	0.06	0.07	0.00	0.00	0.00	0.00	0.00	0.00	0.00	0.00	0.00	0.00	0.00	0.00
Mn	0.07	0.07	0.04	0.04	0.08	0.00	0.00	0.00	0.00	0.00	0.00	0.00	0.00	0.00	0.00	0.00	0.00	0.00	0.00	0.00	0.00	0.00	0.00
Fe	2.54	2.55	2.53	2.56	2.54	0.27	0.29	0.28	0.23	0.27	0.27	0.00	0.00	0.00	0.00	0.00	0.00	0.00	0.00	0.00	0.00	0.00	0.00
cation sum	15.62	15.66	15.65	15.69	15.64	14.11	14.10	14.07	14.07	14.09	14.09	19.96	19.94	19.93	19.92	19.85	19.98	19.99	19.99	19.92	19.94	19.95	20.06
An%												27.9	34.5	26.9	29.3	37.1	31.8	32.2	28.8	27.4	34.5	31.6	26.2

Rock	98-102 Granitic leucosome													
Mineral	plag core	plag rim	plag rim	plag core	plag core	plag core	plag rim	Kf	kf rim	kf rim	Kf rim	kf core	Kf rim	Kf rim
Context														
spot	6.1	6.2	6.3	8.1	8.2	10.1	10.2	5.4	7.2	7.3	8.3	9.1	9.2	11.1
Na2O	6.21	8.00	7.71	7.31	7.72	5.82	7.62	0.40	1.29	1.21	1.17	1.50	1.21	1.29
MgO	0.00	0.00	0.00	0.00	0.00	0.00	0.00	0.00	0.00	0.00	0.00	0.00	0.00	0.00
Al2O3	27.60	24.67	25.45	26.21	25.05	27.98	25.33	18.39	19.07	18.87	18.83	18.99	18.58	18.86
SiO2	57.66	61.44	60.47	59.44	60.94	56.87	60.30	65.40	64.78	64.99	65.04	64.25	64.87	65.01
K2O	0.27	0.37	0.20	0.17	0.36	0.24	0.40	16.82	15.10	15.17	15.32	14.49	15.35	15.23
CaO	9.02	5.88	6.71	7.22	6.18	9.60	6.72	0.00	0.00	0.00	0.00	0.00	0.00	0.00
TiO2	0.00	0.00	0.00	0.00	0.00	0.00	0.00	0.00	0.31	0.00	0.00	0.79	0.00	0.00
MnO	0.00	0.00	0.00	0.00	0.00	0.00	0.00	0.00	0.00	0.00	0.00	0.00	0.00	0.00
FeO	0.00	0.00	0.00	0.00	0.00	0.00	0.00	0.00	0.00	0.00	0.00	0.00	0.00	0.00
TOTAL	100.76	100.36	100.54	100.35	100.25	100.51	100.37	101.01	100.55	100.24	100.36	100.02	100.01	100.39
Na	2.14	2.74	2.64	2.52	2.65	2.01	2.62	0.14	0.46	0.43	0.41	0.53	0.43	0.46
Mg	0.00	0.00	0.00	0.00	0.00	0.00	0.00	0.00	0.00	0.00	0.00	0.00	0.00	0.00
Al	5.78	5.14	5.31	5.49	5.23	5.88	5.30	3.98	4.12	4.08	4.07	4.11	4.03	4.08
Si	10.24	10.86	10.70	10.56	10.80	10.14	10.70	12.00	11.87	11.92	11.92	11.80	11.93	11.93
K	0.06	0.08	0.04	0.04	0.08	0.06	0.09	3.94	3.53	3.55	3.58	3.39	3.60	3.57
Ca	1.72	1.11	1.27	1.37	1.17	1.83	1.28	0.00	0.00	0.00	0.00	0.00	0.00	0.00
Ti	0.00	0.00	0.00	0.00	0.00	0.00	0.00	0.00	0.04	0.00	0.00	0.11	0.00	0.00
Mn	0.00	0.00	0.00	0.00	0.00	0.00	0.00	0.00	0.00	0.00	0.00	0.00	0.00	0.00
Fe	0.00	0.00	0.00	0.00	0.00	0.00	0.00	0.00	0.00	0.00	0.00	0.00	0.00	0.00
cation sum	19.94	19.93	19.96	19.98	19.93	19.92	19.99	20.06	20.02	19.98	19.98	19.94	19.99	20.04
An%	43.9	28.2	32.2	34.9	30.0	46.9	32.1							

Rock	T2-161 Tonalitic migmatite																							
Mineral	Biotite	Biotite	Biotite	Biotite	Bio	Bio	Bio	Bio	Bio (b)	Biotite	Biotite	Biotite	Biotite	Bio	Bio	Bio	Biotite	Biotite	Biotite	Musc	Musc	Musc	Musc
context	Melanosome	Melanosome	Melanosome	Melanosome	Melanosome	Melanosome	Melanosome	Leucosome	Leucosome	mesosome	mesosome	mesosome	mesosome	mesosome	mesosome	mesosome	mesosome	mesosome	mesosome	melanosome	melanosome	melanosome	melanosome
spot	161.6.7	161.6.8	161.6.9	161.6.10	161.7.4	161.7.5	161.7.6	161.2.1	161.2.2	161.4.1	161.4.2	161.4.3	161.4.4	161.5.2	161.5.3	161.5.4	161.8.3	161.8.4	161.8.8	161.1.7	161.1.8	161.1.9	161.1.10
Na2O	0.27	0.27	0.33	0.35	0.29	0.29	0.34	0.29	0.31	0.18	0.27	0.27	0.29	0.26	0.26	0.22	0.33	0.25	0.28	0.62	0.52	0.60	0.59
MgO	8.68	8.90	8.62	8.89	8.64	8.71	8.82	8.49	8.30	8.53	8.84	8.77	8.78	8.78	8.49	8.67	8.94	8.70	9.00	0.77	0.84	0.87	0.80
Al2O3	18.74	19.03	18.89	18.64	18.88	19.24	18.37	19.07	18.72	18.92	19.27	19.12	18.93	19.33	19.43	19.55	18.83	18.98	18.96	35.40	35.19	34.73	34.82
SiO2	35.49	35.49	35.43	34.99	35.08	35.30	34.85	35.52	35.37	35.23	35.41	35.31	34.97	35.50	35.49	35.66	35.42	34.90	35.27	46.12	46.29	46.38	46.41
K2O	9.80	9.54	9.66	9.49	9.77	9.63	9.52	9.59	9.60	9.51	9.61	9.65	9.72	9.82	9.49	9.69	9.62	9.56	9.67	10.55	10.81	10.58	10.73
CaO	0.00	0.00	0.00	0.00	0.00	0.00	0.00	0.00	0.00	0.00	0.00	0.00	0.00	0.00	0.00	0.00	0.00	0.00	0.00	0.00	0.00	0.00	0.00
TiO2	2.67	2.75	2.58	3.00	2.91	3.02	2.92	2.68	2.66	2.75	2.61	2.75	2.34	2.81	2.72	2.72	2.71	2.45	2.92	na	1.06	0.95	1.07
MnO	0.25	0.52	0.26	0.29	0.50	0.33	0.32	0.00	0.46	0.28	0.30	0.38	0.43	0.39	0.28	0.37	0.61	0.00	0.00	0.00	0.00	0.00	0.00
FeO	19.53	19.40	19.69	19.27	18.69	19.47	19.71	19.67	19.65	19.64	19.40	19.15	18.69	19.54	19.13	19.52	19.30	18.85	19.67	1.18	1.37	1.30	1.38
TOTAL	95.43	95.90	95.46	94.92	94.76	95.99	94.85	95.31	95.07	95.04	95.71	95.40	94.15	96.43	95.29	96.40	95.76	93.69	95.77	94.64	96.08	95.41	95.80
Na	0.08	0.08	0.10	0.10	0.09	0.08	0.10	0.09	0.09	0.05	0.08	0.08	0.09	0.08	0.08	0.06	0.10	0.07	0.08	0.16	0.13	0.16	0.15
Mg	1.98	2.01	1.96	2.03	1.98	1.97	2.03	1.93	1.90	1.95	2.00	1.99	2.02	1.98	1.92	1.95	2.03	2.00	2.03	0.15	0.17	0.17	0.16
Al	3.37	3.40	3.40	3.37	3.41	3.44	3.34	3.42	3.38	3.41	3.45	3.43	3.44	3.44	3.48	3.47	3.37	3.46	3.39	5.59	5.49	5.44	5.45
Si	5.42	5.38	5.40	5.37	5.38	5.35	5.37	5.41	5.42	5.39	5.37	5.38	5.40	5.36	5.40	5.37	5.39	5.40	5.35	6.17	6.13	6.17	6.16
K	1.91	1.84	1.88	1.86	1.91	1.86	1.87	1.86	1.88	1.86	1.86	1.87	1.91	1.89	1.84	1.86	1.87	1.89	1.87	1.80	1.83	1.79	1.82
Ca	0.00	0.00	0.00	0.00	0.00	0.00	0.00	0.00	0.00	0.00	0.00	0.00	0.00	0.00	0.00	0.00	0.00	0.00	0.00	0.00	0.00	0.00	0.00
Ti	0.31	0.31	0.30	0.35	0.34	0.34	0.34	0.31	0.31	0.32	0.30	0.32	0.27	0.32	0.31	0.31	0.31	0.28	0.33	0.09	0.11	0.09	0.11
Mn	0.03	0.07	0.03	0.04	0.07	0.04	0.04	0.00	0.06	0.04	0.04	0.05	0.06	0.05	0.04	0.05	0.08	0.00	0.00	0.00	0.00	0.00	0.00
Fe	2.49	2.46	2.51	2.47	2.40	2.47	2.54	2.50	2.52	2.51	2.46	2.44	2.41	2.47	2.43	2.46	2.45	2.44	2.49	0.13	0.15	0.14	0.15
cation sum	15.59	15.55	15.58	15.59	15.58	15.55	15.63	15.52	15.56	15.53	15.56	15.56	15.60	15.59	15.50	15.53	15.60	15.54	15.54	14.09	14.01	13.96	14.00
An%																							

Rock	T2-161 Tonalitic migmatite																					
Mineral	Musc	Musc	Musc	Musc	Musc	Musc	Musc	Musc	Musc	Musc	Musc	Musc	Musc	Musc (2°)	Musc (2°)	plag core	plag core	plag rim	plag rim	plag rim	plag rim	plag core	plag core
Context	Melanosome	Melanosome	Melanosome	Melanosome	Melanosome	Melanosome	Melanosome	Melanosome	Melanosome	mesosome	mesosome	mesosome	mesosome	Mesosome	Mesosome	leuco	leuco	leuco	leuco	leuco	leuco	leuco	leuco
spot	161.6.1	161.6.2	161.6.3	161.6.4	161.6.5	161.6.6	161.7.1	161.7.2	161.7.3	161.4.5	161.4.6	161.5.1	161.8.5	161.8.1	161.8.2	1.1	1.2	1.3	1.4	1.5	1.6	3.1	3.2
Na2O	0.59	0.53	0.57	0.53	0.58	0.61	0.57	0.56	0.64	0.53	0.61	0.64	0.57	0.53	0.60	7.58	7.61	7.33	7.27	7.30	7.30	7.46	7.60
MgO	0.71	0.89	0.78	0.81	0.82	0.86	0.88	0.82	0.91	0.73	0.77	0.85	0.84	0.87	0.78	0.00	0.00	0.00	0.00	0.00	0.00	0.00	0.00
Al2O3	34.82	33.77	34.36	34.50	34.51	34.52	34.71	34.64	34.61	34.13	34.48	34.70	34.38	34.24	34.65	24.74	24.89	25.29	25.19	25.10	25.47	25.42	25.03
SiO2	44.89	45.40	45.13	45.31	44.75	45.19	45.53	45.41	45.34	45.39	45.38	45.19	45.36	45.06	45.05	61.49	61.23	60.47	60.35	60.57	60.73	61.07	61.94
K2O	10.60	10.70	10.51	10.72	10.71	10.77	10.60	10.73	10.63	10.56	10.43	10.79	10.66	10.60	10.61	0.48	0.41	0.34	0.28	0.21	0.30	0.29	0.41
CaO	0.00	0.00	0.00	0.00	0.00	0.00	0.00	0.00	0.00	0.00	0.00	0.00	0.00	0.00	0.00	6.22	6.50	7.10	6.75	7.05	7.13	6.98	6.68
TiO2	0.91	1.34	1.01	1.00	0.97	1.09	1.03	1.00	0.77	0.87	0.99	1.07	0.87	1.33	0.83	0.00	0.00	0.00	0.00	0.00	0.00	0.00	0.00
MnO	0.00	0.00	0.00	0.00	0.00	0.00	0.00	0.00	0.00	0.00	0.00	0.00	0.00	0.00	0.00	0.00	0.00	0.00	0.00	0.00	0.00	0.00	0.00
FeO	1.49	1.34	1.38	1.36	1.37	1.33	1.35	1.44	1.45	1.46	1.68	1.23	1.29	1.30	1.34	0.00	0.00	0.00	0.00	0.00	0.00	0.00	0.00
TOTAL	94.01	93.97	93.74	94.23	93.71	94.37	94.67	94.60	94.35	93.67	94.34	94.47	93.97	93.93	93.86	100.51	100.64	100.53	99.84	100.23	100.93	101.22	101.66
Na	0.15	0.14	0.15	0.14	0.15	0.16	0.15	0.15	0.17	0.14	0.16	0.17	0.15	0.14	0.16	2.60	2.60	2.52	2.51	2.51	2.50	0.64	0.65
Mg	0.14	0.18	0.16	0.16	0.17	0.17	0.18	0.17	0.18	0.15	0.16	0.17	0.17	0.18	0.16	0.00	0.00	0.00	0.00	0.00	0.00	0.00	0.00
Al	5.56	5.39	5.49	5.49	5.53	5.49	5.49	5.50	5.50	5.46	5.49	5.51	5.49	5.47	5.53	5.15	5.18	5.28	5.29	5.25	5.30	1.32	1.29
Si	6.08	6.15	6.12	6.12	6.08	6.10	6.11	6.12	6.12	6.16	6.13	6.09	6.14	6.11	6.10	10.86	10.81	10.71	10.75	10.75	10.71	2.68	2.71
K	1.83	1.85	1.82	1.85	1.86	1.86	1.82	1.84	1.83	1.83	1.80	1.85	1.84	1.83	1.83	0.11	0.09	0.08	0.06	0.05	0.07	0.02	0.02
Ca	0.00	0.00	0.00	0.00	0.00	0.00	0.00	0.00	0.00	0.00	0.00	0.00	0.00	0.00	0.00	1.18	1.23	1.35	1.29	1.34	1.35	0.33	0.31
Ti	0.09	0.14	0.10	0.10	0.10	0.11	0.10	0.10	0.08	0.09	0.10	0.11	0.09	0.14	0.08	0.00	0.00	0.00	0.00	0.00	0.00	0.00	0.00
Mn	0.00	0.00	0.00	0.00	0.00	0.00	0.00	0.00	0.00	0.00	0.00	0.00	0.00	0.00	0.00	0.00	0.00	0.00	0.00	0.00	0.00	0.00	0.00
Fe	0.17	0.15	0.16	0.15	0.16	0.15	0.15	0.16	0.16	0.17	0.19	0.14	0.15	0.15	0.15	0.00	0.00	0.00	0.00	0.00	0.00	0.00	0.00
cation sum	14.02	14.00	14.00	14.01	14.05	14.04	14.00	14.04	14.04	14.00	14.03	14.04	14.03	14.02	14.01	19.90	19.91	19.94	19.90	19.90	19.93	4.99	4.98
An%																30.3	31.4	34.2	33.4	34.4	34.4	33.3	31.6

Rock	T2-161 Tonalitic migmatite																	
Mineral	plag core	plag rim	plag rim	plag rim	plag A core	plag A rim	plag B core	plag b rim	plag B rim	plag C rim	plag D core	plag D rim	plag E core	plag E rim	plag core	plag rim	plag core	plag rim
context	leuco	leuco	leuco	leuco	meso	meso	meso	meso	meso	meso	meso	meso	meso	meso	meso	meso	meso	meso
spot	3.3	3.4	3.5	3.6	4.1	4.2	4.3	4.4	4.5	4.6	4.7	4.8	4.9	4.10	5.5	5.6	8.6	8.7
Na2O	8.08	8.04	8.25	8.24	7.67	7.68	7.75	7.31	7.38	7.54	8.00	7.60	7.61	7.91	7.89	7.85	8.18	7.71
MgO	0.00	0.00	0.00	0.00	0.00	0.00	0.00	0.00	0.00	0.00	0.00	0.00	0.00	0.00	0.00	0.00	0.00	0.00
Al2O3	24.58	24.51	24.52	23.85	24.44	24.85	24.82	25.41	25.32	25.31	24.80	25.38	25.58	25.02	25.24	25.06	24.78	25.21
SiO2	63.27	63.02	63.55	62.89	62.06	61.72	61.53	60.82	60.90	60.82	61.65	60.31	60.09	60.65	61.48	60.95	61.19	60.13
K2O	0.36	0.31	0.31	0.24	0.37	0.20	0.29	0.32	0.00	0.17	0.28	0.22	0.19	0.25	0.11	0.16	0.22	0.61
CaO	5.80	5.70	5.29	5.41	6.13	6.17	6.35	7.02	6.93	6.75	5.91	6.71	6.94	6.41	6.33	6.11	5.87	5.57
TiO2	0.00	0.00	0.00	0.00	0.00	0.00	0.00	0.00	0.00	0.00	0.00	0.00	0.00	0.00	0.00	0.00	0.00	0.00
MnO	0.00	0.00	0.00	0.00	0.00	0.00	0.00	0.00	0.00	0.00	0.00	0.00	0.00	0.00	0.00	0.00	0.00	0.00
FeO	0.00	0.00	0.00	0.00	0.00	0.00	0.00	0.00	0.00	0.00	0.00	0.00	0.00	0.00	0.00	0.00	0.00	0.00
TOTAL	102.09	101.58	101.92	100.63	100.67	100.62	100.74	100.88	100.53	100.59	100.64	100.22	100.41	100.24	101.05	100.13	100.24	99.23
Na	0.68	0.68	0.69	0.70	2.62	2.62	2.65	2.50	2.53	2.58	2.74	2.61	2.62	2.72	2.69	2.69	2.81	2.68
Mg	0.00	0.00	0.00	0.00	0.00	0.00	0.00	0.00	0.00	0.00	0.00	0.00	0.00	0.00	0.00	0.00	0.00	0.00
Al	1.26	1.26	1.25	1.24	5.07	5.16	5.16	5.29	5.27	5.27	5.15	5.31	5.35	5.23	5.23	5.23	5.18	5.32
Si	2.75	2.75	2.76	2.77	10.93	10.88	10.85	10.74	10.76	10.74	10.87	10.70	10.66	10.76	10.81	10.78	10.84	10.77
K	0.02	0.02	0.02	0.01	0.08	0.05	0.07	0.07	0.00	0.04	0.06	0.05	0.04	0.06	0.02	0.04	0.05	0.14
Ca	0.27	0.27	0.25	0.26	1.16	1.16	1.20	1.33	1.31	1.28	1.12	1.27	1.32	1.22	1.19	1.16	1.11	1.07
Ti	0.00	0.00	0.00	0.00	0.00	0.00	0.00	0.00	0.00	0.00	0.00	0.00	0.00	0.00	0.00	0.00	0.00	0.00
Mn	0.00	0.00	0.00	0.00	0.00	0.00	0.00	0.00	0.00	0.00	0.00	0.00	0.00	0.00	0.00	0.00	0.00	0.00
Fe	0.00	0.00	0.00	0.00	0.00	0.00	0.00	0.00	0.00	0.00	0.00	0.00	0.00	0.00	0.00	0.00	0.00	0.00
cation sum	4.98	4.98	4.97	4.98	19.86	19.87	19.93	19.93	19.87	19.91	19.94	19.94	19.99	19.99	19.94	19.90	19.99	19.98
An%	27.8	27.8	26.0	26.8	30.1	30.3	30.6	34.1	34.1	32.8	28.6	32.3	33.2	30.5	30.5	29.8	28.0	27.5

Rock	T2-162 Tonalitic migmatite																						
Mineral	Biotite	Biotite	Biotite	Biotite	Biotite	Biotite	Biotite	Biotite	Musc	Musc	Musc	Musc	Musc	Musc	Musc	plag core	plag core	plag rim	plag rim	plag rim	plag core	plag rim	plag core
Context	Melano	Melano	Melano	Melano	melano	Leucosome	Mesosome	Mesosome	Leuco	Melano	Melano	Melano	Melano	Melano	Melano	leuco	leuco	leuco	leuco	leuco	leuco	leuco	leuco
spot	162.3.5	162.3.6	162.3.7	162.8.1	162.8.3	162.5.2	162.7.1	162.7.2	162.5.1	162.3.1	162.3.2	162.3.3	162.3.4	162.8.2	162.8.4	1.2	1.3	1.4	1.5	1.6	2.1	2.2	2.3
Na2O	0.37	0.31	0.37	0.27	0.34	0.29	0.32	0.29	0.39	0.53	0.64	0.54	0.55	0.62	0.49	8.01	7.71	7.62	7.48	8.12	8.10	8.15	7.80
MgO	8.72	9.11	8.92	8.91	8.93	8.81	8.85	8.75	0.86	0.81	0.88	0.92	0.86	0.88	0.77	0.00	0.00	0	0.00	0.00	0.00	0.00	0.00
Al2O3	19.54	19.62	19.31	19.68	19.30	19.65	19.61	19.53	35.27	35.35	34.74	34.90	35.24	35.28	35.10	24.95	25.46	25.37	25.55	24.89	25.01	24.76	24.95
SiO2	35.46	35.31	35.14	35.67	35.40	35.22	35.50	35.28	45.57	46.14	45.81	45.87	45.43	45.75	45.70	61.51	60.56	60.07	59.74	61.04	60.71	61.29	61.12
K2O	9.69	9.63	9.72	9.90	9.92	9.72	9.70	9.84	10.80	10.82	11.03	10.85	10.65	10.75	10.89	0.29	0.34	0.34	0.35	0.13	0.28	0.24	0.28
CaO	0.00	0.00	0.00	0.00	0.00	0.00	0.00	0.00	0.00	0.00	0.00	0.00	0.00	0.00	0.00	6.08	6.42	6.75	6.90	6.07	5.99	6.05	6.34
TiO2	2.57	2.56	2.95	2.58	2.74	2.62	2.54	2.46	0.97	0.66	0.91	0.73	1.00	0.94	0.97	0.00	0.00	0	0.00	0.00	0.00	0.00	0.00
MnO	0.40	0.27	0.29	0.39	0.00	0.48	0.34	0.27	0.00	0.00	0.00	0.00	0.00	0.00	0.00	0.00	0.00	0	0.00	0.00	0.00	0.00	0.00
FeO	19.44	19.46	20.20	19.54	19.62	19.24	19.33	19.05	1.21	1.27	1.41	1.39	1.36	1.36	1.44	0.00	0.00	0	0.00	0.00	0.00	0.00	0.00
TOTAL	96.19	96.27	96.90	96.94	96.25	96.03	96.19	95.47	95.07	95.58	95.42	95.20	95.09	95.58	95.36	100.84	100.49	100.15	100.02	100.25	100.09	100.49	100.49
Na	0.11	0.09	0.11	0.08	0.10	0.08	0.09	0.08	0.10	0.14	0.17	0.14	0.14	0.16	0.13	2.74	2.65	2.63	2.58	2.79	2.79	2.79	2.68
Mg	1.97	2.05	2.00	1.99	2.01	1.99	1.99	1.99	0.17	0.16	0.18	0.18	0.17	0.17	0.15	0.00	0.00	0	0.00	0.00	0.00	0.00	0.00
Al	3.48	3.49	3.43	3.48	3.44	3.50	3.49	3.50	5.55	5.54	5.47	5.50	5.56	5.53	5.52	5.18	5.31	5.32	5.37	5.20	5.24	5.16	5.20
Si	5.36	5.33	5.30	5.35	5.35	5.33	5.36	5.37	6.09	6.13	6.12	6.13	6.08	6.09	6.10	10.84	10.72	10.69	10.65	10.82	10.79	10.84	10.81
K	1.87	1.85	1.87	1.90	1.91	1.88	1.87	1.91	1.84	1.83	1.88	1.85	1.82	1.82	1.86	0.07	0.08	0.08	0.08	0.03	0.06	0.05	0.06
Ca	0.00	0.00	0.00	0.00	0.00	0.00	0.00	0.00	0.00	0.00	0.00	0.00	0.00	0.00	0.00	1.15	1.22	1.29	1.32	1.15	1.14	1.15	1.20
Ti	0.29	0.29	0.34	0.29	0.31	0.30	0.29	0.28	0.10	0.07	0.09	0.07	0.10	0.09	0.10	0.00	0.00	0	0.00	0.00	0.00	0.00	0.00
Mn	0.05	0.03	0.04	0.05	0.00	0.06	0.04	0.04	0.00	0.00	0.00	0.00	0.00	0.00	0.00	0.00	0.00	0	0.00	0.00	0.00	0.00	0.00
Fe	2.46	2.46	2.55	2.45	2.48	2.44	2.44	2.43	0.14	0.14	0.16	0.16	0.15	0.15	0.16	0.00	0.00	0	0.00	0.00	0.00	0.00	0.00
cation sum	15.59	15.59	15.64	15.59	15.60	15.58	15.57	15.60	13.99	14.01	14.07	14.03	14.02	14.01	14.02	19.98	19.98	20.01	20.00	19.99	20.02	19.99	19.95
An%																29.0	30.9	32.3	33.2	29.0	28.6	28.8	30.5

Rock	T2-162 Tonalitic migmatite										G2 Tonalitic migmatite												
Mineral	plag rim	plag core	plag rim	plag rim	plag core	plag rim	plag core	plag rim	plag rim	plag core	Biotite	Biotite	Biotite	Biotite	Biotite	Biotite	Biotite	Biotite	Biotite	Biotite	Biotite	Biotite	Biotite
context	leuco	meso	meso	meso	meso	meso	meso	meso	meso	meso	Melano	Melano	melano	Melano	Melano	Melano	Meso	Meso	Meso	Meso	Leuco	Leuco	
spot	2.4	7.3	7.4	7.5	7.6	7.7	7.8	7.9	7.11	7.12	G2.2.1	G2.2.2	G2.5.1	G2.5.4	G2.6.2	G2.6.3	G2.7.1	G2.7.2	G2.7.3	G2.8.1	G2.3.1	G2.4.1	
Na2O	7.60	8.11	7.70	8.20	7.72	8.09	7.95	7.73	7.83	7.81	0.25	0.38	0.25	0.27	0.30	0.40	0.33	0.29	0.29	0.27	0.39	0.31	
MgO	0.00	0.00	0.00	0.00	0.00	0.00	0.00	0.00	0.00	0.00	8.80	8.86	8.61	8.72	8.54	8.77	8.76	8.65	8.74	8.7	8.65	8.49	
Al2O3	25.40	24.83	25.83	24.84	25.81	24.71	25.10	25.67	25.21	25.51	19.09	18.92	19.02	18.87	18.84	18.48	18.93	19.02	18.86	19.05	19.16	19.36	
SiO2	59.97	61.34	60.60	61.44	60.00	61.52	61.32	60.57	60.98	61.61	35.29	35.46	35.23	35.2	35.45	35.52	35.39	35.19	35.46	35.07	34.95	35.29	
K2O	0.22	0.33	0.24	0.15	0.36	0.22	0.40	0.21	0.24	0.27	9.83	9.74	9.58	9.73	9.72	9.61	9.81	9.71	9.7	9.84	9.86	9.96	
CaO	6.96	6.06	6.67	6.06	7.10	6.22	6.34	6.87	6.38	6.21	0.00	0.00	0.00	0.00	0.00	0.00	0.00	0.00	0.00	0.00	0.00	0.00	
TiO2	0.00	0.00	0.00	0.00	0.00	0.00	0.00	0.00	0.00	0.00	2.53	2.71	2.68	3.33	3.35	2.87	2.60	2.80	2.72	2.8	2.83	2.77	
MnO	0.00	0.00	0.00	0.00	0.00	0.00	0.00	0.00	0.00	0.00	0.37	0.32	0	0	0	0.28	0.38	0	0	0.29	0.00	0.00	
FeO	0.00	0.00	0.00	0.00	0.00	0.00	0.00	0.00	0.00	0.00	19.42	19.73	19.95	20.12	20.16	19.44	19.65	19.89	19.6	19.33	19.83	19.63	
TOTAL	100.15	100.67	101.04	100.69	100.99	100.76	101.11	101.05	100.64	101.41	95.58	96.12	95.32	96.24	96.36	95.37	95.85	95.55	95.37	95.35	95.67	95.81	
Na	2.62	2.78	2.63	2.81	2.65	2.77	2.71	2.64	2.68	2.65	0.07	0.11	0.07	0.08	0.09	0.12	0.10	0.08	0.09	0.08	0.11	0.09	
Mg	0.00	0.00	0.00	0.00	0.00	0.00	0.00	0.00	0.00	0.00	2.00	2.00	1.96	1.97	1.93	1.99	1.99	1.96	1.98	1.98	1.96	1.92	
Al	5.33	5.17	5.36	5.17	5.38	5.14	5.21	5.33	5.25	5.27	3.43	3.38	3.42	3.37	3.36	3.32	3.40	3.42	3.39	3.43	3.44	3.46	
Si	10.67	10.84	10.68	10.84	10.61	10.85	10.80	10.68	10.77	10.79	5.38	5.38	5.38	5.33	5.36	5.42	5.39	5.36	5.40	5.36	5.32	5.36	
K	0.05	0.07	0.05	0.03	0.08	0.05	0.09	0.05	0.05	0.06	1.91	1.89	1.87	1.88	1.88	1.87	1.90	1.89	1.89	1.92	1.91	1.93	
Ca	1.33	1.15	1.26	1.14	1.35	1.18	1.20	1.30	1.21	1.17	0.00	0.00	0.00	0.00	0.00	0.00	0.00	0.00	0.00	0.00	0.00	0.00	
Ti	0.00	0.00	0.00	0.00	0.00	0.00	0.00	0.00	0.00	0.00	0.29	0.31	0.31	0.38	0.38	0.33	0.30	0.32	0.31	0.32	0.32	0.32	
Mn	0.00	0.00	0.00	0.00	0.00	0.00	0.00	0.00	0.00	0.00	0.05	0.04	0.00	0.00	0.00	0.04	0.05	0.00	0.00	0.04	0.00	0.00	
Fe	0.00	0.00	0.00	0.00	0.00	0.00	0.00	0.00	0.00	0.00	2.47	2.50	2.55	2.55	2.55	2.48	2.50	2.53	2.50	2.47	2.53	2.49	
cation sum	20.00	20.01	19.98	19.99	20.07	19.99	20.01	20.00	19.96	19.94	15.60	15.61	15.56	15.56	15.55	15.57	15.63	15.56	15.56	15.60	15.59	15.57	
An%	33.3	28.8	32.0	28.6	33.1	29.5	30.0	32.6	30.7	30.2													

Rock	G2 Tonalitic migmatite																						
Mineral	musc	musc	musc	musc	plag core	plag core	plag core	plag core	plag rim	plag rim	plag rim	plag B core	plag b rim	plag core	plag core	plag rim	plag rim	plag rim	plag core	plag rim	plag core	plag core	plag rim
Context	melano	melano	melano	melano	leuco	leuco	leuco	leuco	leuco	leuco	leuco	leuco	leuco	leuco	leuco	leuco	leuco	leuco	meso	meso	meso	meso	meso
spot	2.3	5.2	5.3	6.1	1.1	1.2	1.3	1.4	1.5	1.6	1.7	1.8	1.9	4.2	4.3	4.4	4.5	4.6	7.4	7.5	7.6	8.2	8.3
Na2O	0.55	0.50	0.53	0.52	6.52	6.79	6.50	7.03	5.57	6.85	7.65	6.29	7.71	8.19	6.27	7.15	6.93	7.51	7.03	7.81	6.69	6.17	6.91
MgO	0.81	0.87	0.72	0.87	0.00	0.00	0.00	0.00	0.00	0.00	0.00	0.00	0.00	0.00	0.00	0.00	0.00	0.00	0.00	0.00	0.00	0.00	0.00
Al2O3	35.27	34.80	34.91	34.71	26.89	26.52	26.92	25.82	28.68	27.15	25.55	27.86	25.01	24.76	27.78	26.37	26.62	25.91	26.62	25.29	26.52	27.44	26.65
SiO2	45.76	45.77	45.71	45.48	57.61	58.84	57.66	58.86	56.09	58.67	61.47	57.38	60.24	61.44	57.57	59.45	59.04	60.51	58.60	60.60	57.87	57.40	58.00
K2O	10.78	10.97	10.96	10.61	0.16	0.30	0.30	0.21	0.11	0.24	0.71	0.15	0.11	0.26	0.24	0.21	0.32	0.14	0.29	0.13	0.00	0.00	0.11
CaO	0.00	0.00	0.00	0.00	8.42	8.22	8.34	7.39	10.38	8.50	6.47	9.39	6.34	5.91	9.20	7.42	8.03	7.08	7.83	6.78	8.41	9.33	8.49
TiO2	0.91	1.08	1.19	1.28	0.00	0.00	0.00	0.00	0.00	0.00	0.00	0.00	0.00	0.00	0.00	0.00	0.00	0.00	0.00	0.00	0.00	0.00	0.00
MnO	0.00	0.00	0.00	0.00	0.00	0.00	0.00	0.00	0.00	0.00	0.00	0.00	0.00	0.00	0.00	0.00	0.00	0.00	0.00	0.00	0.00	0.00	0.00
FeO	1.24	1.26	1.40	1.50	0.00	0.00	0.00	0.00	0.00	0.00	0.00	0.00	0.00	0.00	0.00	0.00	0.00	0.00	0.00	0.00	0.00	0.00	0.00
TOTAL	95.32	95.25	95.42	94.97	99.60	100.67	99.72	99.31	100.83	101.41	95.38	101.07	99.41	100.56	101.06	100.60	100.94	101.15	100.37	100.61	99.49	100.34	100.16
Na	0.14	0.13	0.14	0.14	2.27	2.34	2.26	2.45	1.92	2.35	2.59	2.16	2.67	2.80	2.16	2.46	2.38	2.56	2.43	2.68	2.33	2.13	2.40
Mg	0.16	0.17	0.14	0.17	0.00	0.00	0.00	0.00	0.00	0.00	0.00	0.00	0.00	0.00	0.00	0.00	0.00	0.00	0.00	0.00	0.00	0.00	0.00
Al	5.54	5.48	5.49	5.48	5.69	5.56	5.68	5.47	6.02	5.66	5.26	5.82	5.27	5.16	5.81	5.51	5.56	5.38	5.59	5.27	5.61	5.77	5.62
Si	6.10	6.12	6.10	6.09	10.33	10.46	10.33	10.58	9.99	10.38	10.74	10.18	10.77	10.86	10.22	10.55	10.46	10.66	10.43	10.72	10.39	10.24	10.37
K	1.83	1.87	1.87	1.81	0.04	0.07	0.07	0.05	0.03	0.05	0.16	0.03	0.03	0.06	0.06	0.05	0.07	0.03	0.07	0.03	0.00	0.00	0.03
Ca	0.00	0.00	0.00	0.00	1.62	1.57	1.60	1.42	1.98	1.61	1.21	1.78	1.21	1.12	1.75	1.41	1.52	1.34	1.49	1.29	1.62	1.78	1.63
Ti	0.09	0.11	0.12	0.13	0.00	0.00	0.00	0.00	0.00	0.00	0.00	0.00	0.00	0.00	0.00	0.00	0.00	0.00	0.00	0.00	0.00	0.00	0.00
Mn	0.00	0.00	0.00	0.00	0.00	0.00	0.00	0.00	0.00	0.00	0.00	0.00	0.00	0.00	0.00	0.00	0.00	0.00	0.00	0.00	0.00	0.00	0.00
Fe	0.14	0.14	0.16	0.17	0.00	0.00	0.00	0.00	0.00	0.00	0.00	0.00	0.00	0.00	0.00	0.00	0.00	0.00	0.00	0.00	0.00	0.00	0.00
cation sum	14.00	14.02	14.02	13.99	19.95	20.00	19.94	19.97	19.94	20.05	19.96	19.97	19.95	20.00	20.00	19.98	19.99	19.97	20.01	19.99	19.95	19.92	20.05
An%					41.2	39.4	40.7	36.2	50.4	40.1	30.6	44.8	30.9	28.1	44.1	36.0	38.3	34.1	37.3	32.3	41.0	45.5	40.1

Rock	G2 Tonalitic migmatite				G3 Tonalitic migmatite																		
Mineral	plag rim	plag core	plag rim		Biot	Biot	Biotite	Biotite	Biotte	Biotite	Biotite	Biotite	Biotite	Musc	Musc	Musc	Musc	Musc	Musc	Musc	Musc	Musc	Musc
context	meso	meso	meso		leuco	leuco	Melano	Melano	Melano	Melano	Melano	Melano	Melano	Leuco	Leuco	Leuco	Leuco	Leuco	Leuco	Leuco	Melano	Melano	Melano
spot	8.4	8.5	8.6		G3.2.5	G3.2.6	G3.3.1	G3.3.2	G3.3.3	G3.4.1	G3.4.2	G3.5.4	G3.5.5	G3.1.1	G3.1.2	G3.1.3	G3.2.1	G3.2.2	G3.2.3	G3.2.4	G3.3.4	G3.3.5	G3.3.6
Na2O	7.70	6.26	7.74		0.38	0.25	0.33	0.39	0.28	0.30	0.26	0.29	0.22	0.62	0.60	0.52	0.64	0.56	0.54	0.55	0.59	0.66	0.58
MgO	0.00	0.00	0.00		8.68	8.57	8.36	8.21	8.46	8.26	8.31	8.42	8.57	0.81	0.82	0.78	0.90	0.71	0.81	0.75	0.77	0.90	0.77
Al2O3	25.54	27.63	25.43		18.81	18.56	18.78	19.07	18.88	18.94	19.32	19.46	18.87	35.11	34.85	34.91	34.93	35.01	34.86	34.63	34.91	34.60	35.15
SiO2	59.80	56.90	60.83		35.29	35.27	35.19	35.25	35.15	34.94	35.40	35.59	35.55	45.28	45.56	45.09	45.46	45.06	45.41	45.42	45.38	45.50	45.32
K2O	0.19	0.00	0.11		9.65	9.64	9.76	9.60	9.72	9.63	9.56	9.68	9.66	10.66	10.78	10.71	10.65	10.81	10.71	10.71	10.85	10.88	10.60
CaO	6.53	9.58	6.47		0.00	0.00	0.00	0.00	0.00	0.00	0.00	0.00	0.00	0.00	0.00	0.00	0.00	0.00	0.00	0.00	0.00	0.00	0.00
TiO2	0.00	0.00	0.00		2.53	2.47	2.62	2.60	2.46	2.58	2.55	2.45	2.73	0.86	0.82	0.88	0.81	0.95	0.90	0.92	0.80	0.95	1.07
MnO	0.00	0.00	0.00		0.28	0.00	0.38	0.00	0.00	0.00	0.38	0.33	0.30	0.00	0.00	0.00	0.00	0.00	0.00	0.00	0.00	0.00	0.00
FeO	0.00	0.00	0.00		20.51	20.35	20.02	19.78	20.93	19.88	19.96	19.86	20.21	1.45	1.38	1.42	1.42	1.41	1.26	1.36	1.63	1.46	1.36
TOTAL	99.76	100.37	100.58		96.13	95.11	95.44	94.90	95.88	94.53	95.74	96.08	96.11	94.79	94.81	94.31	94.81	94.51	94.49	94.34	94.93	94.95	94.85
Na	2.66	2.17	2.66		0.11	0.08	0.10	0.12	0.08	0.09	0.08	0.08	0.07	0.16	0.16	0.14	0.17	0.15	0.14	0.14	0.15	0.17	0.15
Mg	0.00	0.00	0.00		1.97	1.96	1.91	1.88	1.93	1.90	1.88	1.90	1.94	0.16	0.16	0.16	0.18	0.14	0.16	0.15	0.15	0.18	0.15
Al	5.37	5.81	5.31		3.37	3.36	3.39	3.44	3.40	3.44	3.47	3.48	3.38	5.56	5.52	5.56	5.52	5.56	5.53	5.50	5.53	5.48	5.56
Si	10.67	10.15	10.77		5.37	5.41	5.39	5.40	5.37	5.39	5.39	5.39	5.40	6.08	6.12	6.09	6.10	6.08	6.11	6.12	6.10	6.12	6.08
K	0.04	0.00	0.02		1.88	1.89	1.91	1.88	1.89	1.89	1.86	1.87	1.87	1.83	1.85	1.85	1.82	1.86	1.84	1.84	1.86	1.87	1.81
Ca	1.25	1.83	1.23		0.00	0.00	0.00	0.00	0.00	0.00	0.00	0.00	0.00	0.00	0.00	0.00	0.00	0.00	0.00	0.00	0.00	0.00	0.00
Ti	0.00	0.00	0.00		0.29	0.29	0.30	0.30	0.28	0.30	0.29	0.28	0.31	0.09	0.08	0.09	0.08	0.10	0.09	0.09	0.08	0.10	0.11
Mn	0.00	0.00	0.00		0.04	0.00	0.05	0.00	0.00	0.00	0.05	0.04	0.04	0.00	0.00	0.00	0.00	0.00	0.00	0.00	0.00	0.00	0.00
Fe	0.00	0.00	0.00		2.61	2.61	2.57	2.54	2.67	2.56	2.54	2.52	2.57	0.16	0.15	0.16	0.16	0.16	0.14	0.15	0.18	0.16	0.15
cation sum	19.99	19.96	19.99		15.64	15.60	15.62	15.56	15.62	15.57	15.56	15.56	15.58	14.04	14.04	14.05	14.03	14.05	14.01	13.99	14.05	14.08	14.01
An%	31.6	45.8	31.5																				

Rock	G3 Tonalitic migmatite							TL4 Tonalitic migmatite														
Mineral	Musc	Musc	Musc	plag	plag	plag core	plag rim	Biotite	Biotite	Biotite	Biotite	Biotite	Biotite	Biotite	Biotite	Biotite	musc core	musc rim	musc	musc	musc	musc
Context	Melano	Melano	Melano	leuco	leuco	leuco	leuco	Melano	Melano	Melano	Melano	Melano	Melano	Melano	Melano	Melano	leuco	leuco	melano	melano	melano	melano
spot	G3.5.1	G3.5.2	G3.5.3	6.1	7.2	7.1	7.3	TL4.3.3	TL4.4.8	TL4.7.2	TL4.7.3	TL4.8.1	TL4.8.2	TL4.8.3	TL4.9.2	TL4.9.3	2.1	2.2	3.4	4.9	7.3	7.1
Na2O	0.61	0.58	0.60	7.65	7.66	7.38	7.44	0.29	0.31	0.31	0.34	0.33	0.34	0.33	0.42	0.30	0.64	0.49	0.60	0.62	0.70	0.59
MgO	0.81	0.64	0.76	0.00	0.00	0.00	0.00	8.32	8.59	8.19	8.30	8.27	8.31	8.57	8.43	8.77	0.85	0.86	0.81	0.85	0.80	0.79
Al2O3	34.54	34.80	34.73	25.24	25.70	26.08	25.96	19.45	19.30	19.03	19.03	19.05	19.63	19.24	19.12	18.93	34.70	35.27	35.22	34.84	34.77	35.12
SiO2	45.22	45.71	44.77	60.00	60.49	59.38	60.05	35.18	35.13	35.08	35.10	35.51	35.31	34.87	35.28	35.30	45.12	45.88	45.44	45.11	45.63	45.84
K2O	10.77	10.75	10.70	0.20	0.21	0.17	0.23	9.84	9.60	9.68	9.57	9.9	9.89	9.71	9.85	9.79	10.74	10.88	10.77	10.79	10.63	10.87
CaO	0.00	0.00	0.00	6.75	6.68	7.17	7.20	0.00	0.00	0.00	0.00	0.00	0.00	0.00	0.00	0.00	0.00	0.00	0.00	0.00	0.00	0.00
TiO2	0.65	0.80	0.79	0.00	0.00	0.00	0.00	2.87	2.58	2.61	2.48	2.35	2.58	2.37	2.62	2.45	0.51	0.74	0.91	0.75	0.71	0.91
MnO	0.00	0.00	0.00	0.00	0.00	0.00	0.00	0.47	0.33	0	0.34	0.25	0.34	0.00	0.00	0.37	0.00	0.00	0.00	0.00	0.00	0.00
FeO	1.31	1.49	1.57	0.00	0.00	0.00	0.00	19.98	20.1	19.95	20.43	20.09	19.76	20.33	20.28	20.46	1.41	1.31	1.46	1.41	1.24	1.66
TOTAL	93.91	94.77	93.92	99.84	100.74	100.18	100.88	96.40	95.94	94.85	95.59	95.75	96.16	95.42	96.00	96.37	93.97	95.43	95.21	94.37	94.48	95.78
Na	0.16	0.15	0.16	2.64	2.62	2.55	2.55	0.08	0.09	0.09	0.10	0.10	0.10	0.10	0.12	0.09	0.17	0.13	0.15	0.16	0.18	0.15
Mg	0.16	0.13	0.15	0.00	0.00	0.00	0.00	1.88	1.95	1.87	1.89	1.88	1.88	1.96	1.91	1.99	0.17	0.17	0.16	0.17	0.16	0.16
Al	5.52	5.51	5.56	5.30	5.35	5.47	5.41	3.47	3.46	3.44	3.43	3.42	3.51	3.47	3.43	3.39	5.54	5.54	5.56	5.55	5.52	5.51
Si	6.14	6.14	6.08	10.69	10.69	10.57	10.61	5.33	5.35	5.39	5.37	5.42	5.35	5.34	5.37	5.36	6.11	6.12	6.09	6.09	6.14	6.10
K	1.86	1.84	1.85	0.05	0.05	0.04	0.05	1.90	1.86	1.90	1.87	1.93	1.91	1.90	1.91	1.90	1.86	1.85	1.84	1.86	1.82	1.85
Ca	0.00	0.00	0.00	1.29	1.26	1.37	1.36	0.00	0.00	0.00	0.00	0.00	0.00	0.00	0.00	0.00	0.00	0.00	0.00	0.00	0.00	0.00
Ti	0.07	0.08	0.08	0.00	0.00	0.00	0.00	0.33	0.30	0.30	0.29	0.27	0.29	0.27	0.30	0.28	0.05	0.07	0.09	0.08	0.07	0.09
Mn	0.00	0.00	0.00	0.00	0.00	0.00	0.00	0.06	0.04	0.00	0.04	0.03	0.04	0.00	0.00	0.05	0.00	0.00	0.00	0.00	0.00	0.00
Fe	0.15	0.17	0.18	0.00	0.00	0.00	0.00	2.53	2.56	2.56	2.61	2.56	2.51	2.60	2.58	2.60	0.16	0.15	0.16	0.16	0.14	0.18
cation sum	14.06	14.02	14.06	19.97	19.97	20.00	19.98	15.58	15.61	15.55	15.60	15.61	15.59	15.64	15.62	15.66	14.06	14.03	14.05	14.07	14.03	14.04
An%				32.4	32.1	34.6	34.3															

Rock	TL4 Tonalitic migmatite																					
Mineral	musc	musc	musc	musc	plag core	plag core	plag core	plag rim	plag rim	plag rim	plag core	plag rim	plag core	plag rim	plag core	plag rim	plag rim	plag core	plag core	plag rim	plag rim	plag core	plag rim
context	melano	mel	leuco	leuco	leuco	leuco	leuco	leuco	leuco	leuco	melano	melano	melano	melano	melano	melano	melano	melano	melano	melano	melano	melano	melano
spot	7.2	9.1	10.1	10.2	1.1	1.2	1.3	1.4	1.5	1.6	3.1	3.2	3.5	3.6	4.1	4.2	4.3	4.4	4.5	4.6	4.7	9.6	9.7
Na2O	0.55	0.57	0.69	0.59	8.18	8.08	7.35	7.63	8.22	8.17	7.91	7.45	7.95	7.77	7.81	7.36	7.75	8.37	7.22	8.19	7.48	7.32	7.91
MgO	0.66	0.78	0.75	0.73	0.00	0.00	0	0	0	0	0.00	0	0	0	0	0	0	0.00	0	0	0	0	0
Al2O3	35.51	34.80	34.81	35.38	25.01	24.5	25.84	25.37	24.71	24.38	25.55	26.01	24.99	24.99	25.13	26.11	25.09	24.23	25.95	25.05	25.42	25.93	25.79
SiO2	45.85	45.62	45.65	46.07	61.84	61.83	59.38	61	62.12	61.66	61.03	60.07	61.04	60.45	61.19	59.45	60.6	62.37	59.82	61.56	60.71	59.49	60.69
K2O	10.97	10.71	10.70	10.97	0.3	0.38	0.26	0.22	0.21	0.16	0.31	0.25	0.28	0.18	0.2	0.17	0	0.28	0.28	0.2	0.49	0.2	0.16
CaO	0.00	0.00	0.00	0.00	1.13	5.84	7.29	6.49	5.75	5.58	6.49	7.14	5.95	6.36	6.25	7.27	6.44	5.29	7.3	5.87	6.38	7.28	6.76
TiO2	0.77	0.74	0.74	0.70	0	0	0	0	0	0	0.00	0	0	0	0	0	0	0.00	0	0	0	0	0
MnO	0.00	0.00	0.00	0.00	0	0	0	0	0	0	0.00	0	0	0	0	0	0	0.00	0	0	0	0	0
FeO	1.31	1.41	1.35	1.33	0	0	0	0	0	0	0.00	0	0	0.26	0	0	0	0.00	0	0	0	0	0
TOTAL	95.62	94.63	94.69	95.77	96.46	100.63	100.12	100.71	101.01	99.95	101.29	100.92	100.21	100.01	100.58	100.36	99.88	100.54	100.57	100.87	100.48	100.22	101.31
Na	0.14	0.15	0.18	0.15	2.78	2.77	2.54	2.61	2.8	2.81	2.69	2.55	2.73	2.68	2.67	2.53	2.67	2.86	2.48	2.79	2.56	2.52	2.7
Mg	0.13	0.16	0.15	0.14	0	0	0	0	0	0	0	0	0	0	0	0	0	0	0	0	0	0	0
Al	5.57	5.52	5.51	5.54	5.17	5.1	5.42	5.29	5.12	5.1	5.28	5.41	5.22	5.24	5.23	5.46	5.25	5.03	5.43	5.19	5.3	5.43	5.34
Si	6.10	6.14	6.14	6.12	10.85	10.92	10.57	10.78	10.91	10.93	10.7	10.6	10.81	10.76	10.8	10.55	10.75	10.99	10.61	10.82	10.73	10.58	10.67
K	0.00	1.84	1.84	1.86	0.07	0.09	0.06	0.05	0.05	0.04	0.07	0.06	0.06	0.04	0.05	0.04	0	0.06	0.06	0.04	0.11	0.05	0.04
Ca	1.86	0.00	0.00	0.00	1.13	1.11	1.39	1.23	1.08	1.06	1.22	1.35	1.13	1.21	1.18	1.38	1.22	1	1.39	1.11	1.21	1.39	1.27
Ti	0.00	0.08	0.07	0.07	0	0	0	0	0	0	0.00	0	0	0	0	0	0	0.00	0	0	0	0	0
Mn	0.08	0.00	0.00	0.00	0	0	0	0	0	0	0.00	0	0	0	0	0	0	0.00	0	0	0	0	0
Fe	0.15	0.16	0.15	0.15	0	0	0	0	0	0	0.00	0	0	0.04	0	0	0	0.00	0	0	0	0	0
cation sum	14.03	14.05	14.04	14.03	20.00	19.99	19.98	19.96	19.96	19.94	19.96	19.97	19.95	19.97	19.93	19.96	19.89	19.94	19.97	19.95	19.91	19.97	20.02
An%					28.4	28.0	34.8	31.6	27.5	27.1	30.7	34.1	28.8	30.8	30.3	34.9	31.4	25.5	35.4	28.2	31.2	35.1	31.7

Rock	TL4 Tonalitic migmatite				98-WF1A Granitic sheet																	
Mineral	plag core	plag rim	plag core	plag rim	plag core	plag rim	plag rim	plag A core	plag A rim	plag b core	plag A core	plag A rim	plag B core	plag b rim	Kf rim	kf A rim	Kf A core	kf B core	Kf B rim	biotite (mel)	biotite (mel)	biot (mel)
Context	leuco	leuco	leuco	leuco																		
spot	9.4	9.5	11.1	11.2	1.1	1.2	1.3	6.1	6.2	6.3	8.2	8.3	9.4	9.5	2.4	9.1	9.2	9.4	9.5	3.1	3.2	4.1
Na2O	7.19	8.02	7.43	8.03	7.60	8.56	8.31	8.39	8.01	8.29	7.18	8.56	8.57	8.49	1.36	1.37	1.49	1.63	1.20	0.26	0.30	0.26
MgO	0	0.00	0.00	0.00	0.00	0.00	0.00	0.00	0.00	0.00	0.00	0.00	0.00	0.00	0.00	0.00	0.00	0.00	0.00	7.88	8.03	8.12
Al2O3	25.73	24.82	25.59	25.13	25.20	23.53	24.07	23.53	25.07	24.50	26.04	23.79	23.80	24.10	18.69	18.86	18.80	18.79	18.73	19.01	19.56	19.57
SiO2	60.03	61.43	59.42	61.42	60.23	62.69	61.82	62.36	61.60	62.65	59.98	63.01	62.54	62.45	65.02	64.50	65.56	65.38	65.22	34.82	35.14	35.39
K2O	0.24	0.14	0.30	0.30	0.28	0.44	0.27	0.42	0.31	0.28	0.21	0.29	0.43	0.18	15.16	15.07	14.55	14.85	15.16	9.70	9.93	9.61
CaO	7.26	6.16	7.10	6.10	7.07	4.77	5.14	4.81	6.28	5.50	7.33	4.88	4.76	5.39	0.00	0.00	0.00	0.00	0.00	0.00	0.00	0.00
TiO2	0	0.00	0.00	0.00	0.00	0.00	0.00	0.00	0.00	0.00	0.00	0.00	0.00	0.00	0.00	0.00	0.25	0.00	0.25	1.99	2.10	2.07
MnO	0	0.00	0.00	0.00	0.00	0.00	0.00	0.00	0.00	0.00	0.00	0.00	0.00	0.00	0.00	0.00	0.00	0.00	0.00	0.49	0.54	0.56
FeO	0	0.00	0.00	0.00	0.00	0.00	0.00	0.00	0.00	0.00	0.00	0.00	0.00	0.00	0.00	0.00	0.00	0.00	0.00	20.08	19.96	20.67
TOTAL	100.45	100.57	99.84	100.98	100.38	99.99	99.61	99.51	101.27	101.22	100.74	100.53	100.10	100.61	100.23	99.80	100.65	100.65	100.56	94.23	95.56	96.25
Na	2.47	2.75	2.57	2.74	2.62	2.94	2.87	2.89	2.73	2.82	2.46	2.92	2.94	2.90	0.49	0.49	0.53	0.58	0.43	0.08	0.09	0.08
Mg	0	0	0	0	0.00	0.00	0.00	0.00	0.00	0.00	0.00	0.00	0.00	0.00	0.00	0.00	0.00	0.00	0.00	1.82	1.83	1.84
Al	5.37	5.17	5.38	5.21	5.27	4.91	5.05	4.94	5.19	5.06	5.43	4.94	4.97	5.01	4.04	4.10	4.04	4.04	4.04	3.48	3.53	3.51
Si	10.64	10.85	10.6	10.8	10.69	11.10	11.00	11.10	10.81	10.98	10.61	11.09	11.07	11.01	11.93	11.90	11.96	11.92	11.94	5.41	5.38	5.38
K	0.05	0.03	0.07	0.07	0.06	0.10	0.06	0.10	0.07	0.06	0.05	0.06	0.10	0.04	3.55	3.55	3.39	3.45	3.54	1.92	1.94	1.87
Ca	1.38	1.17	1.36	1.15	1.34	0.91	0.98	0.92	1.18	1.03	1.39	0.92	0.90	1.02	0.00	0.00	0.00	0.00	0.00	0.00	0.00	0.00
Ti	0	0.00	0.00	0.00	0.00	0.00	0.00	0.00	0.00	0.00	0.00	0.00	0.00	0.00	0.00	0.00	0.03	0.00	0.03	0.23	0.24	0.24
Mn	0	0.00	0.00	0.00	0.00	0.00	0.00	0.00	0.00	0.00	0.00	0.00	0.00	0.00	0.00	0.00	0.00	0.00	0.00	0.06	0.07	0.07
Fe	0	0.00	0.00	0.00	0.00	0.00	0.00	0.00	0.00	0.00	0.00	0.00	0.00	0.00	0.00	0.00	0.00	0.00	0.00	2.61	2.56	2.63
cation sum	19.91	19.97	19.98	19.97	19.98	19.96	19.96	19.95	19.98	19.95	19.94	19.93	19.98	19.98	20.01	20.04	19.95	19.99	19.98	15.61	15.64	15.62
An%	35.4	29.6	34.0	29.0	33.3	23.0	25.1	23.5	29.6	26.3	35.6	23.6	22.8	25.8								

Rock	98-WF1A Granitic sheet															98-SC Granitic pool						
Mineral	biot (mel)	biot (mel)	biot (mel)	biot (mel)	biotite	musc	musc	musc	musc (mel)	musc (mel)	musc (mel)	musc (mel)	musc (mel)	musc (mel)	musc		Kf rim	Kf A core	Kf A rim	Kf B rim	Kf rim	plag A core	plag A rim
context																							
spot	4.2	4.3	5.1	5.2	8.1	2.1	2.2	2.3	3.3	3.4	4.4	4.5	5.3	5.4	9.3		1.1	3.1	3.2	3.3	5.2	3.4	3.5
Na2O	0.28	0.29	0.23	0.29	0.34	0.48	0.51	0.59	0.61	0.45	0.52	0.64	0.53	0.60	0.54		1.69	1.09	1.20	1.42	1.56	7.41	9.61
MgO	8.17	8.15	8.04	7.90	7.82	0.69	0.63	0.73	0.77	0.68	0.70	0.61	0.65	0.72	0.72		0.00	0.00	0.00	0.00	0.00	0.00	0.00
Al2O3	19.39	19.81	19.29	19.55	19.92	35.04	35.11	35.10	35.31	35.24	35.23	35.31	35.56	35.17	35.19		18.74	18.44	18.42	18.86	18.77	25.49	23.18
SiO2	34.71	35.01	35.26	35.26	35.57	45.50	45.46	45.60	46.06	45.88	45.81	45.72	46.05	46.04	45.38		64.97	64.65	64.19	63.89	64.96	59.19	64.12
K2O	9.76	9.98	9.80	9.92	9.79	10.86	10.70	10.97	10.83	10.76	10.81	10.97	10.82	10.78	10.97		14.50	15.56	15.52	14.81	14.53	0.17	0.25
CaO	0.00	0.00	0.00	0.00	0.00	0.00	0.00	0.00	0.00	0.00	0.00	0.00	0.00	0.00	0.00		0.00	0.00	0.00	0.00	0.00	7.11	3.87
TiO2	2.00	1.97	2.20	1.57	1.80	0.48	0.57	0.36	0.28	0.38	0.47	0.55	0.44	0.32	0.54		0.00	0.23	0.00	0.23	0.00	0.00	0.00
MnO	0.40	0.30	0.45	0.48	0.33	0.00	0.00	0.00	0.00	0.00	0.00	0.00	0.00	0.00	0.00		0.00	0.00	0.00	0.00	0.00	0.00	0.00
FeO	19.99	20.72	20.39	20.68	19.87	1.15	1.08	1.27	1.30	1.32	1.49	1.38	1.10	1.20	1.09		0.00	0.00	0.00	0.00	0.00	0.00	0.00
TOTAL	94.70	96.23	95.66	95.65	95.44	94.20	94.06	94.62	95.16	94.71	95.03	95.18	95.15	94.83	94.43		99.90	99.97	99.33	99.21	99.82	99.37	101.03
Na	0.08	0.09	0.07	0.09	0.10	0.13	0.13	0.15	0.16	0.15	0.13	0.17	0.14	0.16	0.14		0.60	0.39	0.43	0.51	0.56	2.57	3.26
Mg	1.88	1.85	1.83	1.81	1.78	0.14	0.13	0.15	0.15	0.14	0.14	0.12	0.13	0.14	0.15		0.00	0.00	0.00	0.00	0.00	0.00	0.00
Al	3.53	3.56	3.48	3.53	3.58	5.57	5.58	5.56	5.56	5.56	5.56	5.57	5.59	5.55	5.59		4.06	4.01	4.03	4.13	4.07	5.38	4.78
Si	5.36	5.33	5.39	5.40	5.42	6.13	6.13	6.13	6.16	6.15	6.13	6.12	6.14	6.16	6.12		11.93	11.94	11.93	11.86	11.95	10.61	11.22
K	1.92	1.94	1.91	1.94	1.90	1.87	1.84	1.88	1.85	1.84	1.84	1.87	1.84	1.84	1.89		3.40	3.67	3.68	3.51	3.41	0.04	0.06
Ca	0.00	0.00	0.00	0.00	0.00	0.00	0.00	0.00	0.00	0.00	0.00	0.00	0.00	0.00	0.00		0.00	0.00	0.00	0.00	0.00	1.37	0.73
Ti	0.23	0.23	0.25	0.18	0.21	0.05	0.06	0.04	0.03	0.04	0.05	0.05	0.04	0.03	0.06		0.00	0.03	0.00	0.03	0.00	0.00	0.00
Mn	0.05	0.04	0.06	0.06	0.04	0.00	0.00	0.00	0.00	0.00	0.00	0.00	0.00	0.00	0.00		0.00	0.00	0.00	0.00	0.00	0.00	0.00
Fe	2.58	2.64	2.61	2.65	2.53	0.13	0.12	0.14	0.15	0.15	0.17	0.15	0.12	0.13	0.12		0.00	0.00	0.00	0.00	0.00	0.00	0.00
cation sum	15.63	15.68	15.60	15.66	15.56	14.02	13.99	14.05	14.06	14.03	14.02	14.05	14.00	14.01	14.07		19.99	20.04	20.07	20.04	19.99	19.97	20.05
An%																						34.4	18.0

Rock	98-SC Granitic pool														
Mineral	plag B core	plag B rim	plag core	plag rim	plag core	plag rim	plag A core	plag A rim	plag b core	plag C core	musc	musc	musc	musc	musc
Context															
spot	3.6	3.7	5.3	5.4	6.1	6.2	7.1	7.2	7.3	7.4	1.2	2.1	4.1	5.1	9.1
Na2O	8.39	8.78	8.35	9.34	8.04	9.02	8.55	9.43	8.45	8.31	0.64	0.79	0.66	0.66	0.59
MgO	0.00	0.00	0.00	0.00	0.00	0.00	0.00	0.00	0.00	0.00	0.70	0.67	0.72	0.70	0.59
Al2O3	24.74	24.17	25.05	22.97	24.50	23.30	23.58	22.89	24.12	24.29	34.27	35.12	35.24	34.85	34.87
SiO2	60.96	62.57	61.30	63.12	61.50	63.60	62.18	63.62	61.27	61.62	45.76	45.68	45.48	45.19	45.60
K2O	0.28	0.33	0.25	0.31	0.33	0.16	0.29	0.23	0.15	0.30	10.87	10.76	10.70	10.83	10.93
CaO	5.90	4.97	6.17	4.27	5.59	3.95	4.93	3.96	5.41	5.39	0.00	0.00	0.00	0.00	0.00
TiO2	0.00	0.00	0.00	0.00	0.00	0.00	0.00	0.00	0.00	0.00	0.89	0.56	0.74	0.76	0.53
MnO	0.00	0.00	0.00	0.00	0.00	0.00	0.00	0.00	0.00	0.00	0.25	0.00	0.00	0.00	0.00
FeO	0.00	0.00	0.00	0.00	0.00	0.00	0.00	0.00	0.00	0.00	1.30	1.57	1.52	1.45	1.35
TOTAL	100.27	100.82	101.12	100.01	99.96	100.03	99.53	100.13	99.40	99.91	94.68	95.15	95.06	94.44	94.46
Na	2.89	2.99	2.85	3.21	2.77	3.09	2.95	3.23	2.92	2.86	0.17	0.20	0.17	0.17	0.15
Mg	0.00	0.00	0.00	0.00	0.00	0.00	0.00	0.00	0.00	0.00	0.14	0.13	0.14	0.14	0.12
Al	5.17	5.01	5.19	4.80	5.12	4.85	4.94	4.76	5.07	5.08	5.44	5.55	5.57	5.54	5.54
Si	10.81	11.00	10.79	11.18	10.92	11.22	11.06	11.23	10.92	10.93	6.16	6.12	6.10	6.10	6.15
K	0.06	0.07	0.06	0.07	0.07	0.04	0.06	0.05	0.03	0.07	1.87	1.84	1.83	1.87	1.88
Ca	1.12	0.94	1.16	0.81	1.06	0.75	0.94	0.75	1.03	1.02	0.00	0.00	0.00	0.00	0.00
Ti	0.00	0.00	0.00	0.00	0.00	0.00	0.00	0.00	0.00	0.00	0.09	0.06	0.07	0.08	0.05
Mn	0.00	0.00	0.00	0.00	0.00	0.00	0.00	0.00	0.00	0.00	0.03	0.00	0.00	0.00	0.00
Fe	0.00	0.00	0.00	0.00	0.00	0.00	0.00	0.00	0.00	0.00	0.15	0.18	0.17	0.16	0.15
cation sum	20.05	20.01	20.05	20.07	19.94	19.95	19.95	20.02	19.97	19.96	14.05	14.08	14.05	14.06	14.04
An%	27.5	23.5	28.5	19.8	27.2	19.3	23.8	18.6	25.9	25.8					

Rock	Harrow Granodiorite 98-86															Glenelg Leucotonalite T2-20						
Mineral	Plag core	Plag core	Plag rim	Plag rim	Plag core	Plag rim	Plag rim	Plag core	Plag rim	K-felds	Biotite	Biotite	Biotite	Biotite	Musc	Musc rim	Musc	Musc	Biotite	Plag core	Plag core	Plag core
context																						
spot	1.1	1.2	1.3	1.4	2.1	2.2	2.3	5.4	5.5	5.3	5.1	5.2	6.1	6.2	3.1	1.2	2.1	3.1	T2-20.4	5.1	5.2	5.3
Na2O	6.18	8	7.83	8.24	6.41	7.44	8.41	7.14	7.72	1.33	0.23	0.24	0.27	0.38	0.53	0.36	0.70	0.65	0.28	6.82	7.09	6.90
MgO	0.1	0	0.01	0.01	0	0	0	0.1	0.01	0.02	7.68	7.45	7.73	7.76	0.62	0.80	0.85	0.79	7.99	0.00	0.00	0.00
Al2O3	27.33	24.4	24.87	24.49	26.55	25.29	23.75	26.31	25.16	18.56	19.55	19.73	18.46	19.41	34.45	35.29	34.97	34.74	19.31	25.95	25.80	26.13
SiO2	56.99	61.22	60.94	61.96	57.63	60.18	62.28	59.85	60.8	64.46	35.16	35.1	34.96	35.12	45.02	45.22	45.32	45.57	35.18	58.43	59.15	58.65
K2O	0.18	0.27	0.27	0.24	0.12	0.33	0.27	0.19	0.16	14.96	10.06	10.01	9.75	9.85	10.75	10.99	10.68	10.56	9.86	0.30	0.34	0.36
CaO	8.93	5.61	6.38	5.65	8.63	6.82	5.2	7.39	6.86	0.05	0	0	0.01	0.11	0	0.00	0.00	0.00		7.50	7.26	7.80
TiO2	0.03	0	0.03	0	0	0.01	0.06	0	0.01	0.27	2.06	1.87	1.96	2.13	0.31	0.65	0.80	0.71	2.33	0.00	0.00	0.00
MnO	0	0	0.08	0.06	0.04	0.05	0.08	0.03	0	0	0.65	0.5	0.81	0.99	0.01	0.00	0.00	0.00	0.37	0.00	0.00	0.00
FeO	0	0.05	0.02	0	0	0	0.08	0.04	0.22	0	20.23	20.71	20.9	19.78	1.43	1.28	1.21	1.72	20.12	0.00	0.00	0.00
TOTAL	99.74	99.55	100.43	100.65	99.38	100.12	100.13	101.05	100.94	99.65	95.62	95.61	94.85	95.53	93.12	94.43	94.53	94.74	95.59	99.00	99.64	99.84
Na	2.152	2.764	2.69	2.817	2.237	2.567	2.888	2.442	2.643	0.477	0.068	0.071	0.081	0.113	0.14	0.09	0.18	0.17	0.08	2.38	2.46	2.39
Mg	0.027	0	0.003	0.003	0	0	0	0.026	0.003	0.006	1.754	1.704	1.789	1.773	0.126	0.16	0.17	0.16	1.82	0	0	0
Al	5.787	5.126	5.195	5.091	5.634	5.304	4.959	5.472	5.237	4.046	3.532	3.569	3.379	3.509	5.552	5.6	5.54	5.49	3.48	5.5	5.45	5.5
Si	10.235	10.91	10.798	10.925	10.373	10.706	11.03	10.558	10.735	11.919	5.389	5.386	5.428	5.385	6.155	6.09	6.1	6.11	5.38	10.52	10.59	10.49
K	0.041	0.061	0.061	0.054	0.028	0.075	0.061	0.043	0.036	3.529	1.967	1.96	1.931	1.927	1.875	1.89	1.83	1.81	1.92	0.07	0.08	0.08
Ca	1.718	1.071	1.211	1.067	1.664	1.3	0.987	1.397	1.298	0.01	0	0	0.002	0.018	0	0	0	0	0	1.45	1.39	1.49
Ti	0.004	0	0.004	0	0	0.001	0.008	0	0.001	0.038	0.237	0.216	0.229	0.246	0.032	0.07	0.08	0.07	0.27	0	0	0
Mn	0	0	0.012	0.009	0.006	0.008	0.012	0.004	0	0	0.084	0.065	0.107	0.129	0.001	0	0	0	0.05	0	0	0
Fe	0	0.007	0.003	0	0	0	0.012	0.006	0.032	0	2.593	2.658	2.714	2.536	0.163	0.14	0.14	0.17	2.58	0	0	0
cation sum	19.964	19.94	19.977	19.966	19.942	19.961	19.957	19.949	19.985	20.024	15.625	15.629	15.66	15.635	14.045	14.04	14.04	13.98	15.58	19.92	19.97	19.95
An%	43.9	27.5	30.6	27.1	42.4	33.0	25.1	36.0	32.6											37.2	35.4	37.6

Rock	Glenelg Leucotonalite T2-20						Kout Norten Granodiorite 97-302																
Mineral	Plag rim	Plag rim	Plag rim	Plag core	Plag rim		plag core	plag core	plag core	plag rim	plag rim	plag core	plag rim	plag incl.	plag	plag	plag core	plag rim	Kf rim	Kf core	Kf rim	Kf core	Kf rim
Context																							
spot	5.4	5.5	5.6	6.1	6.2		1.1	1.2	1.3	1.4	1.5	3.3	3.4	4.2	8.3	10.2	10.3	10.4	3.1	4.1	4.3	5.1	5.2
Na2O	7.61	7.96	7.68	7.36	8.00		8.74	8.04	8.71	7.96	8.91	8.24	8.70	8.23	8.48	8.47	8.19	9.12	1.68	2.26	1.48	2.04	1.71
MgO	0.00	0.00	0.00	0.00	0.00		0.00	0.00	0.00	0.00	0.00	0.00	0.00	0.00	0.00	0.00	0.00	0.00	0.00	0.00	0.00	0.00	0.00
Al2O3	25.27	24.35	24.88	25.44	24.98		23.37	24.49	23.74	24.51	23.24	24.30	23.56	24.34	23.82	24.22	24.83	23.60	18.45	18.66	18.73	18.81	18.76
SiO2	59.96	60.59	60.78	60.04	61.03		63.29	61.14	62.74	60.87	63.14	61.17	61.94	61.42	62.92	62.66	62.19	63.72	64.39	64.61	65.09	64.81	64.53
K2O	0.39	0.30	0.37	0.35	0.35		0.42	0.30	0.38	0.22	0.24	0.29	0.20	0.26	0.32	0.30	0.23	0.30	14.53	13.57	14.81	13.93	14.61
CaO	6.69	5.82	6.31	6.78	6.16		4.56	5.75	4.65	5.71	4.40	5.43	4.80	5.66	4.84	5.09	5.65	4.37	0.00	0.00	0.00	0.00	0.00
TiO2	0.00	0.00	0.00	0.00	0.00		0.00	0.00	0.00	0.00	0.00	0.00	0.00	0.00	0.00	0.00	0.00	0.00	0.00	0.00	0.00	0.22	0.00
MnO	0.00	0.00	0.00	0.00	0.00		0.00	0.00	0.00	0.00	0.00	0.00	0.00	0.00	0.00	0.00	0.00	0.00	0.00	0.00	0.00	0.00	0.00
FeO	0.00	0.00	0.00	0.00	0.00		0.00	0.00	0.00	0.00	0.00	0.00	0.00	0.00	0.00	0.00	0.00	0.00	0.00	0.00	0.00	0.00	0.00
TOTAL	99.92	99.02	100.02	99.97	100.52		100.38	99.72	100.22	99.27	99.93	99.43	99.20	99.91	100.38	100.74	101.09	101.11	99.05	99.10	100.11	99.81	99.61
Na	2.63	2.77	2.65	2.54	2.75		2.98	2.77	2.98	2.76	3.06	2.85	3.01	2.84	2.90	2.88	2.79	3.10	0.60	0.81	0.53	0.73	0.61
Mg	0	0	0	0	0		0.00	0.00	0.00	0.00	0.00	0.00	0.00	0.00	0.00	0.00	0.00	0.00	0.00	0.00	0.00	0.00	0.00
Al	5.31	5.14	5.21	5.34	5.22		4.85	5.14	4.94	5.16	4.85	5.11	4.95	5.10	4.95	5.01	5.14	4.87	4.03	4.06	4.05	4.08	4.08
Si	10.69	10.86	10.8	10.69	10.82		11.15	10.88	11.09	10.88	11.18	10.92	11.05	10.91	11.10	11.00	10.93	11.16	11.94	11.93	11.94	11.92	11.91
K	0.09	0.07	0.08	0.08	0.08		0.09	0.07	0.08	0.05	0.05	0.07	0.05	0.06	0.07	0.07	0.05	0.07	3.44	3.19	3.47	3.27	3.44
Ca	1.28	1.12	1.2	1.29	1.17		0.86	1.10	0.88	1.09	0.84	1.04	0.92	1.08	0.91	0.96	1.06	0.82	0.00	0.00	0.00	0.00	0.00
Ti	0	0	0	0	0		0.00	0.00	0.00	0.00	0.00	0.00	0.00	0.00	0.00	0.00	0.00	0.00	0.00	0.00	0.00	0.03	0.00
Mn	0	0	0	0	0		0.00	0.00	0.00	0.00	0.00	0.00	0.00	0.00	0.00	0.00	0.00	0.00	0.00	0.00	0.00	0.00	0.00
Fe	0	0	0	0	0		0.00	0.00	0.00	0.00	0.00	0.00	0.00	0.00	0.00	0.00	0.00	0.00	0.00	0.00	0.00	0.00	0.00
cation sum	20.00	19.96	19.94	19.94	20.04		19.93	19.96	19.97	19.94	19.98	19.99	19.98	19.99	19.93	19.92	19.97	20.02	20.01	19.99	19.99	20.03	20.04
An%	32.0	28.3	30.5	33.0	29.3		21.9	27.9	22.3	27.9	21.3	26.3	23.1	27.1	23.5	24.6	27.2	20.6					

Rock	Kout Norten Granodiorite 97-302												Nangkita Adamellite 97-233									
Mineral	Kf rim	Musc	Musc	Musc	Musc	biotite	biotite	biotite	biotite	bio core	bio rim	biotite	biotite	plag core	plag rim	plag rim	plag core	plag rim	plag rim	plag core	plag rim	plag core
context																						
spot	9.1	6.1	7.1	7.2	11.1	2.1	2.2	2.3	2.4	8.1	8.2	10.1	1.1	1.2	1.3	1.4	4.1	4.2	4.3	7.2	7.3	7.4
Na2O	1.89	0.70	0.57	0.58	0.62	0.21	0.43	0.33	0.28	0.33	0.29	0.30	0.26	7.33	7.80	8.71	8.49	8.07	9.21	7.89	8.18	8.23
MgO	0.00	0.73	0.72	0.72	0.73	8.28	8.20	8.46	8.32	8.37	8.35	8.56	6.97	0.00	0.00	0.00	0.00	0.00	0.00	0.00	0.00	0.00
Al2O3	18.73	33.84	34.54	34.42	34.94	18.90	18.90	19.14	19.12	19.39	19.66	19.36	18.99	25.58	24.75	23.25	23.66	24.68	22.87	24.71	24.54	24.30
SiO2	64.48	44.67	45.21	45.30	45.00	35.00	34.73	35.00	34.98	35.50	35.43	35.48	34.75	59.33	61.03	63.39	61.92	61.27	63.69	60.69	61.42	61.83
K2O	14.21	10.65	10.89	10.89	10.87	9.58	9.64	9.61	9.73	9.78	9.83	9.75	9.43	0.24	0.26	0.14	0.30	0.25	0.25	0.14	0.17	0.22
CaO	0.00	0.00	0.00	0.00	0.00	0.00	0.00	0.00	0.00	0.00	0.00	0.00	0.00	7.15	5.89	4.39	4.99	5.80	3.81	6.28	5.69	5.45
TiO2	0.00	0.48	0.46	0.53	0.48	2.47	2.17	2.41	2.26	2.39	2.18	2.24	1.80	0.00	0.00	0.00	0.00	0.00	0.00	0.00	0.00	0.00
MnO	0.00	0.00	0.00	0.00	0.00	0.57	0.52	0.42	0.50	0.45	0.38	0.39	0.96	0.00	0.00	0.00	0.00	0.00	0.00	0.00	0.00	0.00
FeO	0.00	1.92	1.78	1.86	1.96	19.47	19.00	19.36	19.14	19.45	19.74	19.61	21.88	0.00	0.00	0.00	0.00	0.00	0.00	0.00	0.00	0.00
TOTAL	99.43	92.99	94.17	94.30	94.60	94.49	93.61	94.78	94.43	95.70	95.81	95.79	95.11	99.63	99.73	99.88	99.36	100.07	99.83	99.71	100.00	100.03
Na	0.68	0.19	0.15	0.15	0.16	0.06	0.13	0.10	0.08	0.10	0.09	0.09	0.08	2.55	2.69	2.98	2.93	2.77	3.16	2.73	2.81	2.83
Mg	0.00	0.15	0.15	0.14	0.15	1.91	1.90	1.94	1.91	1.90	1.89	1.94	1.61	0	0	0	0	0	0	0	0	0
Al	4.08	5.48	5.52	5.50	5.56	3.44	3.47	3.47	3.48	3.48	3.52	3.47	3.48	5.4	5.19	4.84	4.97	5.15	4.76	5.2	5.13	5.08
Si	11.92	6.14	6.13	6.14	6.08	5.40	5.41	5.38	5.39	5.40	5.39	5.40	5.4	10.63	10.86	11.19	11.04	10.85	11.25	10.83	10.9	10.96
K	3.35	1.87	1.88	1.88	1.87	1.89	1.92	1.88	1.91	1.90	1.91	1.89	1.87	0.06	0.06	0.03	0.07	0.06	0.06	0.03	0.04	0.05
Ca	0.00	0.00	0.00	0.00	0.00	0.00	0.00	0.00	0.00	0.00	0.00	0.00		1.37	1.12	0.83	0.95	1.1	0.72	1.2	1.08	1.04
Ti	0.00	0.05	0.05	0.05	0.05	0.29	0.25	0.28	0.26	0.27	0.25	0.26	0.21	0	0	0	0	0	0	0	0	0
Mn	0.00	0.00	0.00	0.00	0.00	0.07	0.07	0.05	0.06	0.06	0.05	0.05	0.13	0	0	0	0	0	0	0	0	0
Fe	0.00	0.22	0.20	0.21	0.22	2.51	2.47	2.49	2.47	2.47	2.51	2.49	2.84	0	0	0	0	0	0	0	0	0
cation sum	20.03	14.1	14.08	14.07	14.09	15.57	15.62	15.59	15.56	15.58	15.61	15.59	15.62	20.01	19.92	19.87	19.96	19.93	19.95	19.99	19.96	19.96
An%														34.4	28.9	21.6	24.1	28.0	18.3	30.3	27.5	26.5

Rock	Nangkita Adamellite 97-233										Mam Mering Granodiorite T2-1											
Mineral	plag rim	plag core	plag rim	plag rim	plag core	plag rim	musc	musc	musc core	musc rim	musc	KF	Kf	Kf rim	Kf core	Kf		biotite	biotite	biotite	biotite	biotite	biotite
Context																							
spot	7.5	9.2	9.3	9.4	9.5	9.6	2.1	2.1 (b)	3.1	3.2	6.1	7.1	7.6	8.1	8.2	9.1		1.1	1.2	1.3	2.1	2.2	7.1
Na2O	11.13	5.95	8.18	11.22	6.74	7.49	0.55	0.54	0.42	0.58	0.48	1.91	1.21	1.25	1.40	1.59		0.26	0.18	0.31	0.22	0.00	0.30
MgO	0.00	0.00	0.00	0.00	0.00	0.00	0.68	0.83	0.76	0.68	0.74	0.00	0.00	0.00	0.00	0.00		6.48	6.46	6.41	6.71	6.42	6.66
Al2O3	20.06	27.67	24.72	19.87	27.34	25.81	33.85	34.06	34.11	34.67	33.91	18.66	18.71	18.79	18.80	18.79		19.48	19.46	19.75	19.42	19.73	19.77
SiO2	68.11	56.78	61.28	68.11	58.48	59.87	44.94	45.33	45.85	45.55	44.90	64.74	65.19	65.32	65.09	65.48		34.16	34.78	34.52	34.32	34.28	34.49
K2O	0.16	0.00	0.18	0.14	0.13	0.00	10.69	11.00	11.16	11.12	11.17	14.40	15.40	15.29	14.93	14.73		9.61	9.77	9.86	9.67	9.90	9.92
CaO	0.51	9.54	5.75	0.63	8.14	7.10	0.00	0.00	0.00	0.00	0.00	0.00	0.00	0.00	0.00	0.00		0.00	0.00	0.00	0.00	0.00	0.00
TiO2	0.00	0.00	0.00	0.00	0.00	0.00	0.77	0.36	0.63	0.30	0.42	0.00	0.00	0.00	0.00	0.00		1.53	1.47	1.57	1.50	1.55	1.37
MnO	0.00	0.00	0.00	0.00	0.00	0.00	0.00	0.00	0.00	0.00	0.00	0.00	0.00	0.00	0.00	0.00		0.56	0.50	0.66	0.58	0.54	0.58
FeO	0.00	0.00	0.00	0.00	0.00	0.00	2.68	2.39	2.68	2.43	2.63	0.00	0.00	0.00	0.00	0.00		23.05	23.13	22.65	22.84	22.61	23.59
TOTAL	99.97	99.94	100.11	99.97	100.83	100.27	94.16	94.51	95.61	95.33	94.25	99.71	100.51	100.65	100.22	100.59		95.14	95.84	95.75	95.37	95.10	96.77
Na	3.77	2.07	2.81	3.8	2.32	2.58	0.15	0.14	0.11	0.15	0.13	0.68	0.43	0.44	0.50	0.56		0.08	0.05	0.09	0.07	0.00	0.09
Mg	0	0	0	0	0	0	0.14	0.17	0.15	0.14	0.15	0	0.00	0.00	0.00	0.00		1.51	1.49	1.48	1.56	1.49	1.53
Al	4.13	5.85	5.16	4.1	5.71	5.39	5.43	5.45	5.39	5.49	5.45	4.06	4.04	4.05	4.06	4.04		3.59	3.55	3.61	3.56	3.63	3.59
Si	11.91	10.19	10.86	11.91	10.36	10.61	6.12	6.15	6.15	6.12	6.12	11.94	11.95	11.95	11.93	11.95		5.33	5.39	5.35	5.34	5.35	5.31
K	0.04	0	0.04	0.03	0.03	0	1.86	1.9	1.91	1.91	1.94	3.39	3.60	3.57	3.49	3.43		1.92	1.93	1.95	1.92	1.97	1.95
Ca	0.1	1.83	1.09	0.12	1.55	1.35	0	0	0	0	0	0	0.00	0.00	0.00	0.00		0.00	0.00	0.00	0.00	0.00	0.00
Ti	0	0	0	0	0	0	0.08	0.04	0.06	0.03	0.04	0	0.00	0.00	0.00	0.00		0.18	0.17	0.18	0.18	0.18	0.16
Mn	0	0	0	0	0	0	0	0	0	0	0	0	0.00	0.00	0.00	0.00		0.07	0.07	0.09	0.08	0.07	0.08
Fe	0	0	0	0	0	0	0.31	0.27	0.3	0.27	0.3	0	0.00	0.00	0.00	0.00		3.01	2.99	2.93	2.97	2.95	3.04
cation sum	19.95	19.94	19.96	19.96	19.97	19.93	14.09	14.12	14.07	14.11	14.13	20.07	20.02	20.01	19.98	19.98		15.69	15.64	15.68	15.68	15.64	15.75
An%	2.6	46.9	27.7	3.0	39.7	34.4																	

Rock	Mam Mering Granodiorite T2-1																						
Mineral	biotite	musc	musc	musc	musc	musc	musc	plag core	plag rim	plag core	plag core	plag rim	plag core	plag rim	plag rim	plag core	plag rim	plag core	plag rim	plag rim	Kf	Kf	Kf
context																							
spot	9.3	1.4	2.3	2.4	4.4	5.4	7.2	2.5	2.6	3.1	3.2	3.3	4.1	4.2	4.3	5.1	5.2	9.4	9.5	9.6	3.4	6.1	9.1
Na2O	0.26	0.54	0.60	0.59	0.68	0.63	0.64	6.75	9.16	7.57	8.60	7.84	6.40	8.06	8.52	7.42	9.45	7.24	8.33	8.91	1.24	1.39	1.52
MgO	6.41	0.52	0.58	0.64	0.74	0.60	0.58	0.00	0.00	0.00	0.00	0.00	0.00	0.00	0.00	0.00	0.00	0.00	0.15	0.00	0.00	0.00	0.00
Al2O3	19.22	35.12	34.88	35.34	35.12	35.03	35.43	26.79	23.00	24.83	23.86	24.75	27.16	24.49	24.00	25.82	22.65	25.81	24.20	23.35	18.68	18.84	18.73
SiO2	34.38	45.72	45.17	46.03	46.29	45.63	46.14	58.01	63.44	60.68	62.83	60.40	57.00	61.32	62.66	59.77	64.43	59.78	62.10	63.33	64.90	64.66	65.15
K2O	9.66	10.97	10.86	10.90	10.92	10.97	11.04	0.21	0.24	0.27	0.46	0.25	0.13	0.24	0.25	0.24	0.29	0.17	0.29	0.20	15.44	15.17	14.71
CaO	0.00	0.00	0.00	0.00	0.00	0.00	0.00	8.06	4.04	6.20	5.04	6.10	8.77	5.66	5.03	7.04	3.48	6.99	5.41	4.11	0.00	0.00	0.00
TiO2	1.46	0.32	0.37	0.25	0.00	0.35	0.00	0.00	0.00	0.00	0.00	0.00	0.00	0.00	0.00	0.00	0.00	0.00	0.00	0.00	0.00	0.21	0.25
MnO	0.62	0.00	0.00	0.00	0.00	0.00	0.00	0.00	0.00	0.00	0.00	0.00	0.00	0.00	0.00	0.00	0.00	0.00	0.00	0.00	0.00	0.00	0.00
FeO	23.39	1.53	1.51	1.57	1.47	1.60	1.51	0.00	0.00	0.00	0.00	0.00	0.00	0.00	0.00	0.00	0.00	0.00	0.00	0.00	0.00	0.00	0.00
TOTAL	95.44	94.72	93.97	95.32	95.22	94.81	95.34	99.82	99.88	99.55	100.79	99.34	99.46	99.77	100.46	100.29	100.30	99.99	100.48	99.90	100.26	100.27	100.36
Na	0.08	0.14	0.16	0.15	0.18	0.16	0.17	2.34	3.14	2.62	2.93	2.72	2.23	2.78	2.91	2.55	3.22	2.50	2.85	3.05	0.44	0.49	0.54
Mg	1.49	0.10	0.12	0.13	0.15	0.12	0.11	0.00	0.00	0.00	0.00	0.00	0.00	0.00	0.00	0.00	0.00	0.00	0.04	0.00	0.00	0.00	0.00
Al	3.53	5.57	5.57	5.56	5.52	5.55	5.57	5.65	4.79	5.23	4.95	5.22	5.76	5.13	4.98	5.41	4.69	5.42	5.03	4.86	4.05	4.08	4.04
Si	5.36	6.15	6.12	6.14	6.17	6.14	6.15	10.38	11.20	10.84	11.06	10.82	10.26	10.90	11.04	10.62	11.31	10.65	10.96	11.19	11.95	11.88	11.93
K	1.92	1.88	1.88	1.86	1.86	1.88	1.88	0.05	0.05	0.06	0.10	0.06	0.03	0.05	0.06	0.05	0.06	0.04	0.06	0.05	3.63	3.56	3.44
Ca	0.00	0.00	0.00	0.00	0.00	0.00	0.00	1.55	0.76	1.19	0.95	1.17	1.69	1.08	0.95	1.34	0.65	1.34	1.02	0.78	0.00	0.00	0.00
Ti	0.17	0.03	0.04	0.03	0.00	0.04	0.00	0.00	0.00	0.00	0.00	0.00	0.00	0.00	0.00	0.00	0.00	0.00	0.00	0.00	0.00	0.03	0.03
Mn	0.08	0.00	0.00	0.00	0.00	0.00	0.00	0.00	0.00	0.00	0.00	0.00	0.00	0.00	0.00	0.00	0.00	0.00	0.00	0.00	0.00	0.00	0.00
Fe	3.05	0.17	0.17	0.18	0.16	0.18	0.17	0.00	0.00	0.00	0.00	0.00	0.00	0.00	0.00	0.00	0.00	0.00	0.00	0.00	0.00	0.00	0.00
cation sum	15.68	14.04	14.06	14.05	14.04	14.07	14.05	19.97	19.94	19.94	19.99	19.99	19.97	19.94	19.94	19.97	19.93	19.95	19.96	19.93	20.07	20.04	19.98
An%								39.3	19.2	30.7	23.9	29.6	42.8	27.6	24.2	34.0	16.5	34.5	26.0	20.1			

Rock	Carrigeen T2-69																						
Mineral	Biotite	Biotite	Biotite	Biotite	Biotite	musc	musc	musc	musc	musc	musc	musc	ga core	ga core	ga rim	ga rim	ga rim	ga core	ga rim	ga core	ga rim	ga core	ga rim
Context																							
spot	2.2	5.3	7.1	7.2	8.1	1.1	2.1	2.3	4.3	6.1	6.2	6.3	3.1	3.2	3.3	3.4	3.5	4.1	4.2	5.1	5.2	5.8	5.9
Na2O	0.36	0.35	0.30	0.25	0.23	0.61	0.47	0.67	0.58	0.60	0.50	0.57	0.00	0.13	0.00	0.00	0.00	0.16	0.00	0.00	0.00	0.23	0.00
MgO	7.71	7.72	7.29	7.46	7.29	0.69	0.42	0.70	0.75	0.70	0.68	0.71	2.28	2.11	2.16	1.90	2.06	2.19	1.91	2.21	2.01	2.14	2.04
Al2O3	18.62	19.04	19.29	19.58	19.36	34.86	34.94	34.90	34.32	34.61	34.33	34.39	21.17	20.84	21.19	21.33	20.87	20.62	20.61	20.87	20.95	20.85	21.05
SiO2	34.87	34.54	34.41	35.17	34.47	45.08	45.40	45.41	45.35	45.73	45.45	45.31	36.53	36.99	37.01	37.30	36.87	36.46	36.47	36.82	36.53	36.77	37.35
K2O	9.57	9.74	9.70	9.76	9.69	10.76	10.76	10.97	10.53	10.78	10.69	10.79	0.00	0.00	0.00	0.00	0.00	0.00	0.00	0.00	0.00	0.00	0.00
CaO	0.00	0.00	0.00	0.00	0.00	0.00	0.00	0.00	0.00	0.00	0.00	0.00	0.72	0.74	0.72	0.84	0.82	0.79	1.02	0.70	1.01	0.81	0.82
TiO2	1.43	1.53	1.46	1.67	1.54	0.26	0.30	0.48	0.36	0.20	0.35	0.00	0.00	0.00	0.00	0.00	0.00	0.00	0.00	0.00	0.00	0.00	0.00
MnO	0.56	0.49	0.50	0.38	0.51	0.00	0.00	0.00	0.00	0.00	0.00	0.00	12.15	11.70	11.69	12.34	12.15	11.76	12.39	11.64	11.93	11.81	11.86
FeO	22.34	21.81	21.04	20.88	21.47	2.42	1.60	2.17	2.23	1.99	2.09	2.19	27.83	28.11	28.07	27.70	27.44	28.32	27.00	28.66	27.32	27.97	27.30
TOTAL	95.49	95.28	93.99	95.22	94.62	94.68	93.89	95.30	94.12	94.61	94.09	93.96	100.68	100.62	100.84	101.41	100.21	100.30	99.40	100.90	99.75	100.58	100.42
Na	0.11	0.10	0.09	0.08	0.07	0.16	0.12	0.17	0.15	0.16	0.13	0.15	0.00	0.04	0.00	0.00	0.00	0.05	0.00	0.00	0.00	0.07	0.00
Mg	1.78	1.78	1.70	1.71	1.69	0.14	0.09	0.14	0.15	0.14	0.14	0.14	0.55	0.51	0.52	0.45	0.50	0.53	0.46	0.53	0.49	0.52	0.49
Al	3.40	3.48	3.56	3.55	3.55	5.55	5.58	5.53	5.48	5.50	5.49	5.50	4.03	3.97	4.02	4.03	3.99	3.96	3.97	3.97	4.03	3.99	4.00
Si	5.40	5.36	5.39	5.41	5.37	6.09	6.15	6.10	6.14	6.17	6.16	6.15	5.91	5.98	5.96	5.98	5.99	5.94	5.96	5.95	5.95	5.97	6.03
K	1.89	1.93	1.94	1.92	1.93	1.85	1.86	1.88	1.82	1.85	1.85	1.87	0.00	0.00	0.00	0.00	0.00	0.00	0.00	0.00	0.00	0.00	0.00
Ca	0.00	0.00	0.00	0.00	0.00	0.00	0.00	0.00	0.00	0.00	0.00	0.00	0.12	0.13	0.12	0.14	0.14	0.14	0.18	0.12	0.18	0.14	0.14
Ti	0.17	0.18	0.17	0.19	0.18	0.03	0.03	0.05	0.04	0.02	0.04	0.00	0.00	0.00	0.00	0.00	0.00	0.00	0.00	0.00	0.00	0.00	0.00
Mn	0.07	0.06	0.07	0.05	0.07	0.01	0.00	0.00	0.00	0.00	0.00	0.00	1.66	1.60	1.59	1.68	1.67	1.62	1.72	1.59	1.65	1.62	1.62
Fe	2.90	2.83	2.76	2.69	2.80	0.27	0.18	0.24	0.25	0.22	0.24	0.25	3.76	3.80	3.78	3.71	3.73	3.86	3.69	3.87	3.73	3.79	3.68
cation sum	15.72	15.72	15.68	15.60	15.66	14.10	14.01	14.11	14.03	14.06	14.05	14.06	16.03	16.03	15.99	15.99	16.02	16.10	15.98	16.03	16.03	16.10	15.96
An%																							

Rock	Carrigeen T2-69																				
Mineral	ga core	ga rim	ga core	ga rim	plag core	plag rim	plag core	plag rim	plag core	plag rim	plag core	plag rim	plag rim	Kf	Kf core	Kf rim	Kf	Kf	Kf	Kf	Kf
context																					
spot	8.3	8.4	8.5	8.6	5.4	5.5	5.6	5.7	9.2	9.3	10.1	10.2	10.3	1.2	4.4	4.5	4.6	5.10	8.2	11.1	11.2
Na2O	0.00	0.00	0.00	0.21	8.74	8.48	7.92	8.57	7.98	8.23	7.92	8.49	8.50	1.53	1.30	1.59	1.21	1.34	1.41	1.28	1.35
MgO	2.18	1.94	2.12	1.83	0.00	0.00	0.00	0.00	0.00	0.00	0.00	0.00	0.00	0.00	0.00	0.00	0.17	0.00	0.00	0.00	0.00
Al2O3	20.58	20.75	20.90	20.62	24.04	24.33	25.05	23.81	24.61	24.08	24.75	23.65	24.27	19.00	19.02	18.73	18.62	19.12	18.88	18.75	18.65
SiO2	36.47	36.38	36.21	36.98	62.90	62.20	60.96	62.56	60.85	61.21	60.26	61.97	60.99	65.02	64.63	64.99	64.68	65.65	64.87	64.64	64.45
K2O	0.00	0.13	0.00	0.11	0.21	0.28	0.19	0.23	0.20	0.24	0.25	0.28	0.19	14.71	14.91	14.84	15.14	15.04	14.85	15.28	15.01
CaO	0.65	0.82	0.93	1.03	4.89	5.30	6.27	4.90	5.86	5.46	6.09	4.86	5.43	0.00	0.00	0.00	0.00	0.00	0.00	0.00	0.00
TiO2	0.00	0.00	0.00	0.00	0.00	0.00	0.00	0.00	0.00	0.00	0.00	0.00	0.00	0.00	0.00	0.00	0.00	0.00	0.00	0.00	0.00
MnO	11.52	11.78	11.69	12.33	0.00	0.00	0.00	0.00	0.00	0.00	0.00	0.00	0.00	0.00	0.00	0.00	0.00	0.00	0.00	0.00	0.00
FeO	27.90	27.69	27.94	26.58	0.00	0.00	0.00	0.00	0.00	0.00	0.00	0.00	0.00	0.00	0.00	0.00	0.00	0.00	0.00	0.00	0.00
TOTAL	99.30	99.49	99.79	99.69	100.78	100.59	100.39	100.07	99.50	99.22	99.27	99.25	99.38	100.26	99.86	100.15	99.82	101.15	100.01	99.95	99.46
Na	0.00	0.00	0.00	0.07	2.98	2.90	2.72	2.94	2.76	2.85	2.74	2.94	2.94	0.54	0.46	0.57	0.43	0.47	0.50	0.46	0.48
Mg	0.53	0.47	0.52	0.44	0.00	0.00	0.00	0.00	0.00	0.00	0.00	0.00	0.00	0.00	0.00	0.00	0.05	0.00	0.00	0.00	0.00
Al	3.97	4.01	4.02	3.96	4.98	5.06	5.23	4.96	5.18	5.08	5.21	4.97	5.11	4.10	4.12	4.05	4.05	4.09	4.09	4.07	4.06
Si	5.97	5.96	5.91	6.03	11.06	10.98	10.80	11.07	10.86	10.95	10.76	11.05	10.89	11.90	11.89	11.93	11.93	11.92	11.92	11.91	11.92
K	0.00	0.03	0.00	0.02	0.05	0.06	0.04	0.05	0.05	0.06	0.06	0.06	0.04	3.43	3.50	3.47	3.56	3.48	3.48	3.59	3.54
Ca	0.11	0.14	0.16	0.18	0.92	1.00	1.19	0.93	1.12	1.05	1.17	0.93	1.04	0.00	0.00	0.00	0.00	0.00	0.00	0.00	0.00
Ti	0.00	0.00	0.00	0.00	0.00	0.00	0.00	0.00	0.00	0.00	0.00	0.00	0.00	0.00	0.00	0.00	0.00	0.00	0.00	0.00	0.00
Mn	1.60	1.63	1.62	1.70	0.00	0.00	0.00	0.00	0.00	0.00	0.00	0.00	0.00	0.00	0.00	0.00	0.00	0.00	0.00	0.00	0.00
Fe	3.82	3.79	3.81	3.62	0.00	0.00	0.00	0.00	0.00	0.00	0.00	0.00	0.00	0.00	0.00	0.00	0.00	0.00	0.00	0.00	0.00
cation sum	16.00	16.03	16.04	16.02	19.99	20.00	19.98	19.95	19.97	19.99	19.94	19.95	20.02	19.97	19.97	20.02	20.02	19.96	19.99	20.03	20.00
An%					23.3	25.3	30.1	23.7	28.5	26.5	29.5	23.7	25.9								

Rock	Garnet Adamellite 98-19																						
Mineral	biotite	biotite	biotite	biotite	biotite	biotite	ga rim	ga core	ga core	ga rim	ga core	ga rim	musc	musc	musc	musc	musc	plag core	plag rim	plag core	plag rim	plag core	plag rim
Context																							
spot	5.1	6.1	10.1	10.2	12.1	11.1	1.1	1.2	2.1	2.2	3.1	3.2	4.1	4.2	5.1	5.2	6.3	8.1	8.2	9.1	9.2	11.3	11.4
Na2O	0.00	0.00	0.24	0.19	0.00	0.26	0.19	0.16	0.00	0.00	0.00	0.00	0.67	0.72	0.62	0.60	0.67	10.17	10.80	9.95	10.41	10.03	9.73
MgO	6.86	6.93	7.09	6.90	6.93	6.92	1.52	1.35	1.55	1.44	1.46	1.44	0.63	0.59	0.57	0.65	0.65	0.00	0.00	0.00	0.00	0.00	0.00
Al2O3	19.69	19.37	18.97	19.38	19.48	19.83	20.84	21.13	20.80	20.80	21.05	20.83	35.51	35.41	35.38	35.82	35.76	21.93	21.41	22.04	21.73	22.31	22.67
SiO2	34.17	33.82	34.48	35.27	33.65	34.71	37.11	36.47	36.77	36.69	36.91	36.89	45.80	45.62	45.48	45.57	46.20	65.24	65.93	65.34	66.22	65.26	64.40
K2O	9.64	8.98	9.63	9.73	8.45	9.53	0.00	0.00	0.00	0.00	0.00	0.00	10.72	10.91	10.92	11.11	10.97	0.45	0.13	0.44	0.25	0.31	0.39
CaO							0.61	0.64	0.64	0.65	0.65	0.68	0.00	0.00	0.00	0.00	0.00	2.55	2.11	2.94	2.51	2.99	3.45
TiO2	1.30	1.26	1.38	1.50	1.28	1.27	0.00	0.00	0.00	0.00	0.00	0.00	0.00	0.00	0.26	0.00	0.22	0.00	0.00	0.00	0.00	0.00	0.00
MnO	0.65	0.63	0.53	0.53	0.53	0.71	12.79	15.82	13.36	13.00	14.43	13.32	0.00	0.00	0.00	0.00	0.00	0.00	0.00	0.00	0.00	0.00	0.00
FeO	22.94	22.92	23.12	22.73	22.95	22.91	28.16	26.16	26.96	27.51	26.98	27.94	1.54	1.27	1.36	1.51	1.38	0.00	0.00	0.00	0.00	0.00	0.00
TOTAL	95.51	93.99	95.42	96.28	93.44	96.11	101.22	101.73	100.08	100.09	101.48	101.10	94.87	94.52	94.59	95.26	95.85	100.34	100.38	100.71	101.12	100.90	100.64
Na	0.00	0.00	0.07	0.06	0.00	0.08	0.06	0.05	0.00	0.00	0.00	0.00	0.18	0.19	0.16	0.16	0.17	3.46	3.67	3.38	3.51	3.40	3.31
Mg	1.59	1.63	1.65	1.58	1.63	1.59	0.37	0.33	0.38	0.35	0.35	0.35	0.13	0.12	0.11	0.13	0.13	0.00	0.00	0.00	0.00	0.00	0.00
Al	3.61	3.60	3.48	3.51	3.63	3.60	3.97	4.02	4.00	4.00	4.01	3.97	5.61	5.62	5.61	5.65	5.59	4.54	4.43	4.55	4.46	4.59	4.69
Si	5.31	5.33	5.37	5.42	5.32	5.35	6.00	5.90	5.99	5.98	5.96	5.97	6.14	6.14	6.12	6.10	6.13	11.46	11.56	11.44	11.53	11.39	11.30
K	1.91	1.80	1.91	1.91	1.70	1.87	0.00	0.00	0.00	0.00	0.00	0.00	1.83	1.87	1.87	1.90	1.86	0.10	0.03	0.10	0.06	0.07	0.09
Ca							0.11	0.11	0.11	0.11	0.11	0.12	0.00	0.00	0.00	0.00	0.00	0.48	0.40	0.55	0.47	0.56	0.65
Ti	0.15	0.15	0.16	0.17	0.15	0.15	0.00	0.00	0.00	0.00	0.00	0.00	0.00	0.00	0.03	0.00	0.02	0.00	0.00	0.00	0.00	0.00	0.00
Mn	0.09	0.08	0.07	0.07	0.07	0.09	1.75	2.17	1.84	1.79	1.97	1.83	0.00	0.00	0.00	0.00	0.00	0.00	0.00	0.00	0.00	0.00	0.00
Fe	2.98	3.02	3.01	2.92	3.03	2.95	3.81	3.54	3.68	3.75	3.64	3.78	0.17	0.14	0.15	0.17	0.15	0.00	0.00	0.00	0.00	0.00	0.00
cation sum	15.64	15.61	15.72	15.64	15.53	15.68	16.07	16.12	16.00	15.98	16.04	16.02	14.06	14.08	14.05	14.11	14.05	20.04	20.09	20.02	20.03	20.01	20.04
An%																		11.9	9.8	13.6	11.6	13.9	16.0

Rock	Garnet Adamellite 98-19					
Mineral	plag rim	Kf rim	Kf rim	Kf rim	Kf	Kf
context						
spot	11.5	2.3	3.3	5.3	6.2	11.2
Na2O	10.60	1.12	1.13	1.11	1.27	1.43
MgO	0.00	0.00	0.00	0.00	0.00	0.00
Al2O3	21.55	18.82	18.56	18.80	19.07	18.91
SiO2	66.32	65.11	64.84	64.90	65.48	65.52
K2O	0.26	15.36	15.51	15.66	15.69	15.05
CaO	1.97	0.00	0.00	0.00	0.00	0.00
TiO2	0.00	0.00	0.00	0.00	0.00	0.00
MnO	0.00	0.00	0.00	0.00	0.00	0.00
FeO	0.00	0.00	0.00	0.00	0.00	0.00
TOTAL	100.70	100.41	100.04	100.47	101.51	100.91
Na	3.59	0.40	0.40	0.39	0.45	0.51
Mg	0.00	0.00	0.00	0.00	0.00	0.00
Al	4.44	4.07	4.03	4.06	4.08	4.07
Si	11.59	11.94	11.94	11.90	11.90	11.96
K	0.06	3.59	3.64	3.66	3.64	3.50
Ca	0.37	0.00	0.00	0.00	0.00	0.00
Ti	0.00	0.00	0.00	0.00	0.00	0.00
Mn	0.00	0.00	0.00	0.00	0.00	0.00
Fe	0.00	0.00	0.00	0.00	0.00	0.00
cation sum	20.05	20.00	20.01	20.01	20.07	20.04
An%	9.2					

APPENDIX C

Table C.1:

Whole-rock geochemical composition of metasedimentary rocks, migmatite leucosomes, small granitic bodies, Harrow type granitic rocks and garnet granites, as analysed by XRF (major elements are in weight percent oxide, trace elements are quoted in parts per million). The trace element concentrations of samples marked with an asterisk were determined by ICP-MS. All samples are stored in the museum collection at the Department of Geology, The Australian National University.

	Metasedimentary rocks																					
ANU No.	TKP7	TKP8	TKP94	TKP95	TKP100	TKP101	TKP102	TKP103	TKP106	TKP108	TKP117	TKP118	TKP119	TKP121	TKP124	TKP126	TKP129	TKP133	TKP134	TKP161	TKP163	TKP165
Field No.	97-30A	97-30B	97-R1	97-R2	97-316	97-317A*	97-429	98-MEL	98-R2B	98-R4	98-WF2C	98-13B	98-14B	98-27	98-65C*	98-75B	98-SEL	98-WF2A-2M	98-WF2A2	97-286-1	97-286-2	97-R2D*
Lithology	Tonalitic migmatite	Tonalitic migmatite	Qf schist	Qf schist	Qf gneiss	Mica schist	Mica schist	Bi schist	Qf gneiss	Diatexite	Migmatite	Qf schist	Qf schist	Mica schist	Qf schist	Qf gneiss	Micaceous enclave	Mesosome	Migmatite	Diatexite	Migmatite	QFS
Grid ref.	640833	640833	708434	709434	707508	707507	652835	623840	708433	709433	519863	580848	581849	557858	558843	533868	557858	519863	591863	546879	54547878	720431
SiO2	76.17	68.09	74.67	73.09	73.87	52.73	66.71	75.63	73.44	73.00	67.47	73.04	74.46	62.29	67.89	73.33	47.26	55.26	70.19	72.43	71.87	72.33
TiO2	0.39	0.69	0.58	0.57	0.56	0.88	0.70	0.81	0.55	0.41	0.62	0.55	0.63	0.67	0.66	0.53	1.10	0.92	0.38	0.53	0.49	0.71
Al2O3	11.97	14.66	11.98	12.71	12.30	21.29	14.77	7.87	12.76	13.38	14.89	12.79	12.12	17.52	14.18	12.04	21.08	19.80	15.59	12.87	13.33	12.60
Fe2O3T	2.86	4.99	3.86	3.96	3.81	9.50	6.98	8.56	3.72	3.18	6.51	4.02	3.75	7.10	5.54	4.12	12.97	8.73	3.57	3.85	3.74	4.69
Fe2O3																						
FeO																						
MnO	0.05	0.08	0.06	0.07	0.05	0.09	0.13	0.09	0.08	0.08	0.11	0.06	0.07	0.12	0.06	0.06	0.29	0.15	0.06	0.07	0.07	0.10
MgO	1.27	2.26	1.52	1.62	1.53	3.93	2.65	2.70	1.38	1.16	2.42	1.47	1.36	2.48	1.96	1.56	4.45	3.78	1.53	1.57	1.55	1.74
CaO	1.93	1.95	2.29	2.22	1.82	0.69	0.55	0.04	1.64	1.00	0.75	1.86	2.64	1.02	1.80	1.18	1.56	1.15	1.54	1.32	1.73	2.00
Na2O	2.36	2.32	2.63	2.96	2.48	0.85	0.95	0.13	2.48	2.39	1.43	2.49	2.63	1.60	2.30	1.74	2.35	1.86	2.55	2.15	2.59	3.04
K2O	1.93	3.22	1.79	2.06	2.97	7.32	5.10	3.52	2.98	3.69	4.72	2.97	1.70	5.17	4.22	4.50	6.60	5.96	3.47	4.02	3.42	2.18
P2O5	0.12	0.17	0.16	0.15	0.16	0.17	0.09	0.03	0.16	0.14	0.10	0.17	0.19	0.18	0.19	0.14	0.30	0.14	0.13	0.15	0.15	0.24
S	0.010	0.010	0.005	0.004	0.003	0.008	0.005	0.006	0.005	0.005	0.004	0.004	0.005	0.004	0.005	0.005	0.006	0.006	0.006	0.004	0.003	0.001
LOI	0.97	1.32	0.74	0.71	0.64	2.41	1.54	0.96	1.03	1.37	1.42	0.79	0.63	1.92	0.89	0.88	1.98	1.88	1.33	1.00	0.85	0.64
Total	100.12	99.86	100.46	100.11	100.39	100.18	100.38	100.53	100.41	99.98	100.63	100.40	100.39	100.25	99.95	100.32	99.93	99.62	100.35	99.97	99.8	100.27
Sc	9	19	14	15	14	30.6	22	26	13	11	20	14	15	25	18.9	16	32	28	14	14	14	15.6
V	41	81	54	63	47	158.5	91	98	57	48	83	47	60	99	61.7	63	94	146	61	62	61	75.4
Cr	40	77	50	52	46	131.9	78	99	47	37	71	45	52	87	53.3	53	137	123	46	49	50	59.4
Ni	18	31	17	20	17	56.2	38	34	17	14	32	16	10	34	23.8	21	51	51	20	20	20	16.2
Cu	21	11	25	4	6	27.9	3	3	1	2	1	3	56	1	0.7	23	2	11	34	6	23	1.0
Zn	55	97	63	69	66	174.2	107	149	70	69	122	84	59	164	120.3	78	290	168	71	66	63	97.9
Ga	14	21	15	16	16	30.1	20	17	16	18	21	16	15	33	18.6	16	41	29	20	16	17	15.3
Rb	84	144	138	157	133	354.1	208	180	183	197	233	130	101	296	161.6	173	442	380	195	187	168	193.0
Sr	289	277	166	211	222	83.8	171	5	169	167	103	207	250	86	261.2	178	122	120	162	143	154	162.8
Y	26	29	30	27	28	39.9	24	22	30	26	23	30	35	31	35.3	24	46	35	20	28	30	40.1
Zr	140	199	267	195	201	137.5	130	144	229	164	109	225	319	125	193.2	185	214	167	78	197	174	389.3
Nb	9	15	12	12	12	16.3	14	18	14	14	16	13	14	30	14.9	13	59	27	16	13	12	17.0
Cs			5	6	7	17.3	5	5	3	7	4	4	7	11	5.91	6	23	14	7	10	8	10.7
Ba	445	675	409	482	725	1281	702	657	419	633	522	628	450	420	980.1	973	261	646	549	661	520	257.0
La	26	38	39	29	26	56.3	31	34	36	21	30	32	52	37	39.1	21	61	45	19	31	28	62.7
Ce	58	86	86	69	70	111.8	86	90	79	58	74	79	111	85	78.1	69	130	105	47	77	68	122.0
Pr			6	2	6	12.94	7	6	7	4	2	5	7	4	9.25	7	2	7	1	6	4	14.00
Nd			38	27	33	43.4	37	36	37	26	28	37	45	35	31.38	36	47	47	21	34	30	47.10
Sm						9.42									7.16							9.57
Eu						1.44									1.31							1.11
Gd						8.06									6.50							7.83
Dy						6.94									5.94							6.88
Er						3.84									3.44							3.88
Yb						3.55									3.19							3.75
Lu						0.54									0.47							0.56
Hf						4.04									5.95							10.82
Ta						1.27									1.32							1.85
Pb	19	20	18	22	33	18.6	23	4	22	31	19	25	18	13	31.2	33	23	22	30	30	29	20.0
Th	13	19	19	14	15	22.3	17	20	17	13	16	17	25	16	15.4	14	27	23	10	17	15	27.1
U	3	3	3	3	3	4.54	2	1	3	6	3	3	4	5	4.08	3	7	6	3	5	4	5.63

ANU No.	TKP206	TKP207	TKP217	TKP218	TKP220	TKP225	TKP226	TKP227	Kemp 95	Kemp 95	Kemp 95	Kemp 95	Kemp 95	Kemp 95
Field No.	98-151	98-152	99-7M	G2-MEL	CCGG	99-R5B	99-R5	99-14	T2-64	T2-146MG	T2-302B	T2-39B	T2-CC20	T2-2B
Lithology	Micaceous	Micaceous	Schist	Schist	Gneiss	Mesosome	Diatexite	Mesosome	Gneiss	Gneiss	Gneiss	QFS	QFS	QFS
	enclave	enclave												
Grid ref.	623840	623840	709431	646835	710492	710432	710432	583849	643839	646840	577809	570867	591863	641839
SiO2	75.11	57.87	61.45	65.57	72.94	73.37	68.37	72.49	64.77	72.70	72.20	72.96	74.02	72.42
TiO2	0.69	1.17	0.87	1.28	0.61	0.55	0.51	0.66	0.75	0.60	0.57	0.54	0.54	0.63
Al2O3	10.77	17.09	16.00	12.47	12.38	12.26	14.99	11.96	16.09	12.73	12.75	12.68	12.35	13.01
Fe2O3T	5.89	10.46	7.75	9.19	4.14	4.08	3.98	4.92	6.05	3.58	3.66	3.68	3.50	3.80
Fe2O3														
FeO														
MnO	0.06	0.11	0.12	0.09	0.05	0.08	0.08	0.09	0.11	0.06	0.07	0.07	0.08	0.06
MgO	2.06	4.12	3.29	3.62	1.80	1.67	1.62	2.01	3.01	1.85	1.93	1.98	1.67	1.91
CaO	0.02	0.10	1.34	1.61	1.86	1.80	1.33	1.57	1.56	2.06	1.91	1.90	2.19	2.65
Na2O	0.18	0.25	2.15	1.04	2.24	2.77	2.58	2.49	1.75	2.26	2.15	2.37	2.19	2.35
K2O	4.02	6.56	4.95	3.83	2.77	2.18	5.15	2.49	4.16	2.66	2.98	2.72	2.28	1.92
P2O5	0.03	0.11	0.15	0.37	0.16	0.15	0.14	0.17	0.24	0.25	0.21	0.21	0.21	0.25
S	0.001	0.001	0.004	0.003	0.002	0.004	0.004	0.005	0.001					
LOI	0.78	2.05	2.01	0.94	0.78	1.54	1.6	1.23	1.38	0.98	0.73	1.53	1.13	0.57
Total	99.61	99.89	100.08	100.01	99.74	100.45	100.35	100.08	99.87	99.8	99.21	100.71	100.24	99.64
Sc	29	33	24	28	14	12	14	18	13	10	11.5	10	10	12
V	86	126	140	152	77	58	66	72	100	57	7	67	64	54
Cr	69	118	113	112	71	50	56	60	94	62	68	60	63	61
Ni	26	67	40	35	19	18	22	22	46	25	3	26	23	25
Cu	<1	<1	62	1	9	11	4	<1	22	27	20	26	27	32
Zn	104	222	150	165	69	85	78	104	106	66	21	69	64	70
Ga	20	32	26	27	18	17	18	18	20	14	16	14	14	14
Rb	152	283	318	194	142	162	236	193	186	114	143	146	115	97
Sr	10	14	154	137	171	147	187	129	176	262	208	181	198	268
Y	19	33	41	37	34	29	23	36	31	33	31	27	28	32
Zr	132	213	217	858	240	206	116	275	164	282	152	214	248	307
Nb	20	28	28	22	13	15	17	17	22	17	8	16	14	17
Cs	4	20	8	<1	2	4	7	5						
Ba	825	1333	748	902	581	169	1088	182	831	540	800	571	493	416
La	30	54	40	94	34	30	22	36	41	51	40	38	42	59
Ce	74	124	95	225	80	72	56	89	52	78	25	58	61	85
Pr	8	16	<1	14	0	4	6	6						
Nd	32	58	30	70	25	25	15	30						
Sm														
Eu														
Gd														
Dy														
Er														
Yb														
Lu														
Hf														
Ta														
Pb	5	6	30	11	25	18	42	17	23	25	28	24	13	17
Th	16	30	23	50	17	15	12	21	12	13	12	12	12	15
U	1	3	6	5	3	4	4	6	3	3	3	4	4	3

	Leucosomes																			
ANU No.	TKP162	TKP107	TKP160	TKP98	TKP104	TKP105	TKP110	TKP115	TKP132	TKP120	TKP122	TKP123	TKP125	TKP158	TKP215	TKP216	TKP222	TKP187	TKP204	TKP215
Field No.	97-286-1L	98-R3	97-R2C	97-RG	98-RM1	98-R2A	98-R5C	98-WF1A	98-WF2A-2L	98-25	98-65A	98-65B	98-102	98-75	99-14	99-7	98-R5L	98-123	98-TL1	G2
Lithology	segregn	segregn	Leucosome	Leucosome	Leucosome	Leucosome	Leucosome	Leucosome	Leucosome	Leucosome	Leucosome	Leucosome	Leucosome	Leucosome	Leucosome	Leucosome	Leucosome	tonalitic leucosome	tonalitic leucosome	tonalitic leucosome
Grid ref.	546879	708433	720431	708433	708434	708433	710432	591863	591863	587858	558843	558843	710491	533868	583849	709431	710432	642838	642838	646835
SiO2	74.47	75.61	75.48	74.77	74.99	74.29	74.03	76.17	78.68	74.15	73.15	75.31	73.85	73.80	74.58	74.88	74.33	75.64	74.66	74.02
TiO2	0.17	0.20	0.01	0.10	0.05	0.08	0.04	0.05	0.06	0.08	0.09	0.01	0.09	0.12	0.05	0.11	0.10	0.04	0.09	0.11
Al2O3	13.82	12.79	14.46	14.13	14.49	14.64	14.80	14.50	12.48	15.12	15.27	14.54	15.04	15.34	14.49	14.64	14.87	14.90	15.45	15.04
Fe2O3T	1.21	1.68	0.10	0.83	0.34	0.72	0.27	0.38	0.53	0.70	0.99	0.05	0.67	1.10	0.31	0.97	0.80	0.25	0.73	0.82
Fe2O3																				
FeO																				
MnO	0.03	0.04	0.02	0.02	0.01	0.02	0.01	0.01	0.02	0.02	0.01	0.00	0.01	0.02	0.01	0.02	0.02	0.01	0.01	0.01
MgO	0.51	0.61	0.05	0.27	0.13	0.24	0.10	0.15	0.22	0.27	0.34	0.04	0.27	0.39	0.13	0.41	0.34	0.13	0.30	0.39
CaO	1.66	1.48	1.86	1.56	1.69	1.74	1.45	2.02	1.69	1.70	2.34	1.91	2.45	1.42	1.59	1.59	1.81	3.63	3.51	3.55
Na2O	2.84	2.75	4.22	3.16	3.43	3.51	3.12	3.28	3.01	3.07	3.20	2.90	3.37	2.20	3.27	3.03	3.47	4.25	4.11	3.82
K2O	4.50	3.87	3.28	4.10	4.01	4.13	5.54	2.72	2.48	3.81	4.16	4.80	3.38	4.05	4.48	4.46	3.20	0.54	0.81	0.94
P2O5	0.15	0.16	0.08	0.15	0.08	0.09	0.13	0.08	0.12	0.21	0.12	0.06	0.08	0.13	0.09	0.11	0.07	0.11	0.05	0.07
S	0.004	0.004	0.004	0.006	0.004	0.004	0.003	0.004	0.004	0.003	0.004	0.004	0.004	0.003	0.003	0.001	0.001	0.01	0.01	0.002
LOI	0.71	0.920	0.54	0.930	0.630	0.730	0.530	0.870	0.79	1.02	0.590	0.490	0.760	1.32				0.74	0.54	1.21
Total	100.07	100.30	100.10	100.20	99.99	100.36	100.27	100.35	100.08	100.30	100.53	100.35	100.18	99.90	99.00	100.22	99.01	100.25	100.27	99.99
Sc	5	5	1	3	2	2	1	5	3	9	3	2	3	7	0	2	2	2	3	2
V	21	23	2	12	5	9	4	7	11	10	12	3	12	9	4	14	14	5	11	15
Cr	14	19	1	9	3	4	3	3	4	8	9	<1	3	3	<1	18	12	3	8	10
Ni	6	8	<1	3	2	4	2	1	2	2	4	1	2	2	<1	5	4	1	3	3
Cu	4	2	<1	1	2	1	2	3	27	<1	1	1	1	8	<1	9	1	1	1	2
Zn	22	37	5	17	6	14	5	7	13	15	22	1	12	22	<1	19	18	5	13	14
Ga	12	13	12	13	12	12	11	15	12	18	14	12	14	18	11	13	15	13	13	15
Rb	130	148	87	131	125	128	147	67	84	107	88	83	91	107	119	135	110	16	26	42
Sr	211	199	216	228	260	282	278	223	201	216	391	376	380	210	258	251	256	462	457	538
Y	15	17	8	13	11	10	26	19	9	19	32	17	13	59	31	17	26	15	21	9
Zr	57	94	27	49	20	23	25	28	19	24	56	8	32	27	23	55	33	56	51	74
Nb	5	9	2	4	2	4	2	5	5	8	5	2	4	6	1	4	4	2	4	2
Cs	8	7	3	8	8	6	11	1	2	4	7	9	8	9	6	2	1	0	1	1
Ba	1092	881	580	988	818	949	1738	568	664	685	1450	1532	1105	987	1131	1361	827	155	227	257
La	<1	5	<1	<1	3	<1	<1	5	<1	1	<1	<1	<1	7	10	10	7	27	16	32
Ce	21	34	7	17	14	7	16	21	7	16	32	2	21	40	30	30	25	54	34	74
Pr	3	3	<1	4	6	1	2	<1	1	1	4	2	6	4	13	1	0	6	6	3
Nd	18	19	4	14	11	5	21	11	6	12	25	12	17	22	10	10	5	24	17	25
Sm																				
Eu																				
Gd																				
Dy																				
Er																				
Yb																				
Lu																				
Hf																				
Ta																				
Pb	46	40	41	44	44	46	60	45	44	38	47	52	45	36	52	54	42	31	30	22
Th	5	8	2	4	2	2	6	5	2	4	8	2	5	9	5	7	6	13	6	18
U	2	4	4	3	2	1	3	2	2	1	2	1	1	3	4	2	3	1	1	1

	Small granitic bodies																		
ANU No.	TKP97	TKP48	TKP49	TKP50	TKP51	TKP52	TKP53	TKP87	TKP88	TKP96	TKP99	TKP109	TKP111	TKP112	TKP113	TKP114	TKP116	Kemp 95	
Field No.	97-R2F	97-R2B	97-R2E	97-R3	97-R3-2A	97-R3-2B	97-11	97-396	97-396B	97-R2D	97-XCL	98-R5A	98-R6	98-R7	98-R8	98-SC	98-WF1B		
Lithology	Granitic	Granitic	Granitic	Granitic	Granitic	Granitic	Granitic	Granitic	Granitic	Granitic	Granitic	Granitic	Granitic	Granitic pod	Granitic pod	Granitic pod	Granitic	Felsic dyke	
	dyke	dyke	dyke	dyke	dyke	dyke	dyke	dyke	dyke	dyke	dyke	dyke	dyke				sheet		
Grid ref.	721431	719431	720431	721431	721431	721431	635835	684506	684506	720431	721431	710432	710431	709431	710431	588851	591863	635835	
SiO2	74.88	74.04	75.33	74.49	74.96	74.96	74.14	74.05	74.71	75.50	75.10	74.56	74.33	74.62	74.62	75.38	76.28	74.66	
TiO2	0.08	0.01	0.06	0.09	0.04	0.06	0.02	0.22	0.06	0.05	0.08	0.03	0.07	0.06	0.02	0.03	0.04	0.03	
Al2O3	14.09	14.31	14.06	14.55	14.29	14.42	14.82	13.89	14.57	14.22	14.56	14.61	14.59	14.49	14.31	14.57	14.4	14.82	
Fe2O3T	0.67	0.55	0.60	0.91	0.32	0.56	0.57	1.89	0.47	0.41	0.61	0.21	0.58	0.49	0.33	0.20	0.46	0.32	
Fe2O3																			
FeO																			
MnO	0.02	0.19	0.04	0.03	0.01	0.02	0.12	0.05	0.02	0.02	0.01	0.01	0.02	0.01	0.01	0.01	0.01	0.02	
MgO	0.26	0.07	0.24	0.34	0.14	0.24	0.11	0.73	0.18	0.16	0.25	0.08	0.23	0.18	0.06	0.08	0.16	0.32	
CaO	1.22	0.88	1.10	1.19	1.12	1.96	1.32	1.51	1.38	1.43	1.51	0.93	1.88	0.90	0.78	1.57	2.02	1.31	
Na2O	2.83	2.91	3.56	3.23	2.77	3.81	3.06	2.79	3.14	3.54	3.36	2.56	3.39	2.89	2.86	3.09	3.41	2.63	
K2O	5.42	6.13	4.33	4.48	5.56	3.26	5.10	3.67	4.75	4.01	3.48	6.19	3.84	5.53	6.36	4.54	3.06	4.81	
P2O5	0.08	0.09	0.07	0.06	0.07	0.07	0.04	0.09	0.08	0.07	0.08	0.11	0.11	0.14	0.08	0.15	0.087	0.07	
S	0.003	0.000	0.010	0.010	0.000	0.000	0.004	0.000	0.005	0.003	0.005	0.004	0.005	0.007	0.004	0.003	0.003	0.01	
LOI	0.70	0.56	0.82	0.91	0.86	0.81	0.88	0.98	0.84	0.80	1.17	1.02	1.04	0.870	0.610	0.660	0.61	1.180	
Total	100.43	99.89	100.32	100.42	100.33	100.30	100.31	100.07	100.38	100.31	100.35	100.54	100.30	100.43	100.27	100.45	100.43	100.13	
Sc	2	2	4	5	3	2	3	7	2	3	5	1	2	2	1	5	3	2	
V	8	3	5	9	5	5	1	20	3	7	12	4	7	6	3	9	3	<1	
Cr	6	<1	<1	<1	<1	<1	<1	20	<1	4	2	1	1	3	1	4	2	2	
Ni	3	<1	1	<1	<1	2	<1	5	1	1	2	1	3	2	1	1	1	<1	
Cu	1	<1	<1	<1	<1	<1	<1	<1	<1	2	1	6	2	5	2	1	2	18	
Zn	17	8	16	<1	9	17	5	38	10	12	12	6	12	9	4	4	8	4	
Ga	12	12	14	17	14	13	14	15	13	14	15	11	12	12	11	13	13	11	
Rb	159	188	149	166	181	110	106	137	134	134	119	172	116	165	185	114	72	95	
Sr	225	198	190	176	212	255	230	246	280	178	222	208	280	256	229	243	245	277	
Y	13	7	15	18	8	13	19	25	16	13	14	9	10	12	9	12	18	17	
Zr	47	28	42	53	28	33	34	78	44	31	32	34	28	23	27	31	25	18	
Nb	5	4	7	13	6	5	2	9	3	6	7	3	3	3	2	3	4	<1	
Cs	7	7	4	4	6	3	4	10	8	3	4	10	10	14	8	5	3		
Ba	1010	891	642	610	990	583	694	909	1019	499	754	1448	1319	1662	1225	989	730	1142	
La	<1	<1	<1	5	<1	2	<1	11	<1	<1	<1	<1	<1	<1	<1	<1	2	1	
Ce	15	2	13	22	8	14	11	42	10	9	13	4	13	5	3	13	21	7	
Pr	6	<1	<1	1	2	<1	1	5	1	1	1	6	6	1	4	3	3		
Nd	13	4	7	12	11	7	8	22	10	8	10	14	16	16	8	10	13		
Sm																			
Eu																			
Gd																			
Dy																			
Er																			
Yb																			
Lu																			
Hf																			
Ta																			
Pb	58	55	47	45	56	45	67	39	49	44	45	59	50	57	58	48	51	60	
Th	4	3	4	6	3	4	3	9	4	2	3	1	3	3	1	3	4	2	
U	2	5	3	3	3	3	3	4	4	2	2	4	1	2	3	1	2	1	

	Harrow type granitic rocks																				
ANU No.	TKP159	12870	12861	TKP30	TKP47	Kemp 95	TKP150	TKP151	TKP157	Kemp 95	TKP136	TKP137	TKP139	TKP1	Kemp 95	TKP140	TKP141	TKP142	TKP143	TKP180	TKP181
Field No.	98-76	556860	587855	97-233A	97-349	T2-1	98-56	98-58	98-64A	T2-CC2	98-1	98-2	98-5	T2-3	CC9D	98-11	98-12	98-13*	98-14A	98-14A	98-14C
Lithology	Kout Norien	Harrow Gd	Roseate	Nangkita	Bryan Ck	Marn Mering	Marn Mering	Marn Mering	Carrigeen	Carrigeen	Carrigeen	Carrigeen	Carrigeen	Carrigeen	Schofield	Schofield	Schofield	Schofield	Schofield	Schofield	Schofield
															Adamellite	Adamellite	Adamellite	Adamellite	Adamellite	Adamellite	Adamellite
Grid ref.	529866	556861	587855	728435	693491	620850	604863	604863	577842	577837	578837	576835	575834	578833	579846	580847	583848	583848	583849	583849	583849
SiO2	72.41	72.84	74.28	73.87	71.70	74.12	74.97	74.09	73.76	73.70	72.35	76.69	73.91	74.16	74.47	75.63	73.71	75.50	74.31	73.76	75.79
TiO2	0.33	0.16	0.07	0.07	0.39	0.07	0.06	0.03	0.13	0.14	0.27	0.10	0.12	0.10	0.08	0.09	0.09	0.05	0.13	0.15	0.07
Al2O3	14.12	15.33	14.82	14.80	14.24	14.76	14.47	14.93	14.59	14.84	14.63	13.03	14.45	14.93	15.10	14.08	14.61	14.23	14.17	14.57	14.13
Fe2O3T	2.69	1.75	0.83	0.76	3.32	1.13	0.79	0.41	1.29	1.37	2.42	1.25	1.58	1.21	0.86	0.89	0.92	0.47	1.59	1.90	0.82
Fe2O3	0.25	0.27	0.11	0.28	0.96	0.26				0.17				0.36	0.11						
FeO	2.20	1.33	0.65	0.43	2.13	0.78				1.08				0.77	0.68						
MnO	0.05	0.06	0.04	0.04	0.07	0.02	0.02	0.02	0.03	0.05	0.08	0.04	0.05	0.04	0.03	0.02	0.02	0.01	0.03	0.04	0.02
MgO	1.06	0.82	0.48	0.31	1.19	0.34	0.29	0.17	0.47	0.71	0.92	0.38	0.48	0.37	0.49	0.36	0.34	0.20	0.50	0.58	0.25
CaO	1.35	2.45	1.43	1.83	1.63	1.83	1.67	2.04	1.56	1.60	1.42	1.60	1.91	1.99	2.19	1.98	1.50	1.52	1.61	1.65	1.60
Na2O	2.47	2.96	2.75	3.42	2.94	2.99	2.91	3.36	3.01	2.81	2.99	2.86	3.12	3.27	2.80	2.84	2.80	2.73	2.80	2.90	2.79
K2O	4.28	2.67	4.06	3.92	3.37	3.58	4.03	4.00	4.31	3.35	3.47	3.03	3.23	3.32	2.97	3.08	4.98	4.52	3.86	4.10	3.75
P2O5	0.18	0.14	0.14	0.06	0.14	0.11	0.10	0.08	0.11	0.17	0.14	0.09	0.08	0.07	0.11	0.09	0.09	0.10	0.11	0.12	0.10
S	0.004	0.01	0.01	0.01	0.010	0.01	0.003	0.003	0.003	0.01	0.006	0.004	0.003	0.01	0.01	0.004	0.003	0.004	0.005	0.003	0.006
LOI	1.12	1.04	1.05	1.11	1.06	0.85	0.93	0.87	0.81	1.12	1.28	0.93	1.12	0.97	0.99	0.92	0.79	0.83	0.85	0.89	0.86
Total	102.53	100.08	99.87	100.15	99.960	99.61	100.24	99.98	100.07	99.74	99.97	100.01	100.06	100.25	100.03	99.97	99.84	100.16	99.96	100.659	100.185
Sc	15	6	4	4	11	4	6	3	5	4	11	5	7	6	5	6	3	5	8	7	9
V	40	11	1	3	45	1	3	2	15	10	29	8	10	5	<1	5	7	4	11	13	<1
Cr	31	11	3	1	44	2	1	<1	8	13	24	5	6	4	5	2	4	1	10	12	1
Ni	12	5	2	<1	11	3	<1	<1	4	6	9	1	2	<1	3	1	2	1	3	4	1
Cu	11	25	22	2	6	20	<1	<1	<1	23	1	3	<1	2	23	2	<1	<1	<1	<1	1
Zn	50	45	21	18	61	30	23	12	28	33	59	32	43	33	22	20	23	13	34	42	17
Ga	17	14	13	14	17	14	16	13	15	13	18	14	17	16	13	15	13	14	16	15	16
Rb	169	97	116	123	171	90	100	90	118	115	163	104	125	119	71	73	111	123.6	106	117	90
Sr	151	222	248	281	229	263	282	337	205	293	210	183	219	255	330	287	302	284	248	256	268
Y	23	17	21	8	25	22	22	20	19	21	27	16	21	19	29	27	25	22.8	24	26	20
Zr	121	74	31	49	143	41	30	29	64	64	97	47	58	55	40	30	47	24.5	66	90	27
Nb	13	14	9	7	12	11	8	4	8	10	15	9	11	8	7	7	6	4.93	10	11	7
Cs	8			1	7		6	8	4		8	3	9	4		6	11	1.95	8	5	6
Ba	596	405	578	580	546	618	893	1155	671	741	616	525	622	780	961	1155	1759	1560	1095	986	1169
La	18	19	7	5	23	14	<1	<1	10	12	20	10	18	15	9	<1	<1	9.13	3	13	5
Ce	49	33	14	10	58	24	21	18	35	27	53	29	46	34	24	29	14	20.61	33	36	24
Pr	2				3		1	3	2	<1	4	2	5	4	<1	4	<1	2.18	5	6	3
Nd	23			4	25		15	12	17		25	13	22	10		21	22	7.88	22	19	13
Sm																		2.21			
Eu																		1.14			
Gd																		2.57			
Dy																		3.38			
Er																		2.05			
Yb																		1.91			
Lu																		0.28			
Hf																		2.67			
Ta																		0.52			
Pb	39	25	39	39	32	37	41	49	43	37	33	31	31	31	36	38	55	64.2	40	41	38
Th	11	6	3	3	12	4	5	4	10	6	12	6	10	8	6	7	5	3.51	7	8	4
U	4	1	1	2	4	1	1	1	3	3	6	2	2	2	2	2	2	1.66	4	5	2

														Garnet granites								
ANU No.	TKP182	TKP145	TKP146	TKP147	TKP148	TKP152	12874	TKP153	TKP154	TKP149	12866	TKP205		Kemp 95	TKP15	TKP26	TKP144	TKP72	TKP183	TKP184	TKP185	TKP186
Field No.	98-14D	98-23	98-24	98-26	98-27	98-59	T2-39	98-60A	98-60C	98-38	638842	98-150*		T2-258	97-98	97-201	98-19	97-317A	98-36-1	98-36-2	98-60B	98-100
Lithology	Schofield	Schofield	Schofield	Schofield	Schofield	Schofield	Schofield	Schofield	Schofield	Scrubby	Dunmore	Dunmore		Garnet Ad	Glengoyne	Blair Atholl	Garnet Ad	Garnet Ad	Garnet Ad	Garnet Ad	Garnet Ad	Garnet Ad
	Adamellite	Adamellite	Adamellite	Adamellite	Adamellite	Adamellite	Adamellite	Adamellite	Adamellite	Junction	LT	LT										
Grid ref.	583849	587855	587856	588858	588858	583843	582868	591864	591864	592865	639842	623840		583849	488657	418580	585852	707507	591870	591870	591864	580820
SiO2	73.77	74.39	73.58	74.70	74.72	75.22	73.29	75.78	74.71	75.00	74.73	73.39		74.47	74.18	72.99	75.82	76.01	74.61	74.69	75.38	74.50
TiO2	0.06	0.07	0.06	0.07	0.06	0.05	0.09	0.04	0.05	0.06	0.08	0.07		0.02	0.02	0.09	0.02	0.02	0.01	0.01	0.02	0.02
Al2O3	15.05	14.47	14.62	14.54	14.54	14.55	15.42	14.01	14.36	14.56	15.24	15.99		14.63	14.66	15.10	14.06	13.81	14.64	14.53	14.63	14.89
Fe2O3T	0.63	0.70	0.77	0.60	0.52	0.56	0.88	0.52	0.61	0.61	0.71	0.68		0.67	0.69	1.08	0.44	0.53	0.74	1.14	0.53	0.51
Fe2O3							0.08				0.00											
FeO							0.72				0.64											
MnO	0.02	0.03	0.03	0.02	0.02	0.01	0.03	0.02	0.02	0.02	0.02	0.01		0.16	0.09	0.10	0.07	0.19	0.19	0.32	0.08	0.13
MgO	0.18	0.24	0.28	0.22	0.24	0.19	0.37	0.19	0.24	0.22	0.53	0.27		0.29	0.13	0.30	0.09	0.08	0.12	0.14	0.17	0.09
CaO	1.14	1.73	1.22	1.26	1.52	1.60	1.96	1.70	1.79	1.43	3.52	3.02		0.69	0.69	2.38	0.80	0.65	0.81	1.10	1.24	1.06
Na2O	2.77	3.18	2.94	2.91	3.13	2.97	3.32	3.27	3.37	3.20	3.27	3.83		2.45	3.64	3.42	3.44	3.28	2.50	2.80	2.89	2.94
K2O	5.59	3.91	4.58	4.74	4.20	4.12	3.40	3.63	3.77	4.12	1.11	1.47		6.00	4.77	3.96	4.71	4.60	5.98	4.87	4.71	5.73
P2O5	0.08	0.14	0.05	0.15	0.11	0.08	0.17	0.07	0.12	0.10	0.09	0.09		0.13	0.12	0.04	0.08	0.08	0.07	0.06	0.06	0.07
S	0.005	0.003	0.004	0.003	0.004	0.004	0.01	0.003	0.003	0.003	0.01	0.003		0.01	0.01	0.01	0.004	0.01	0.004	0.002	0.004	0.003
LOI	0.77	0.98	0.95	0.93	0.95	0.66	1.02	0.74	0.75	0.86	0.88	1.03		0.56	0.85	0.92	0.70	0.83	0.75	0.72	0.79	0.60
Total	100.061	99.85	99.10	100.15	100.01	100.00	100.42	99.96	99.79	100.18	100.12	99.86		100.02	99.83	100.33	100.23	100.13	100.43	100.39	100.50	100.54
Sc	7	7	5	8	5	6	7	4	5	5	5	11		2	2	3	3	2	4	4	6	2
V	6	3	3	5	5	4	6	2	2	3	5	6		<1	2	6	1	2	1	1	1	2
Cr	<1	1	2	1	3	<1	9	2	2	1	5	3		3	1	<1	<1	<1	<1	<1	<1	<1
Ni	1	1	<1	1	1	1	5	1	<1	1	<1	1		2	<1	<1	<1	<1	<1	<1	<1	<1
Cu	1	<1	<1	<1	<1	<1	22	<1	<1	0	19	1		20	4	1	72	<1	1	1	1	1
Zn	17	21	22	16	13	14	20	13	15	16	12	13		4	16	36	9	7	5	5	6	5
Ga	14	15	16	15	14	15	15	13	14	15	13	17		11	17	18	13	14	15	14	15	13
Rb	133	110	125	122	106	92	95	85	92	109	29	47.1		142	258	172	133	158	167	138	116	163
Sr	272	244	224	221	227	262	213	230	223	239	447	421.0		132	41	208	76	60	157	171	180	164
Y	25	24	23	21	16	12	28	14	16	21	11	22.9		19	13	24	8	11	14	20	13	10
Zr	27	26	48	20	21	15	68	19	26	32	72	45.1		25	17	52	18	23	44	53	29	29
Nb	7	7	8	7	6	6	11	5	6	7	2	6.2		3	16	18	6	8	8	7	8	3
Cs	14	8	6	6	6	5		6	5	4		2.1			6	2	4	2	3	3	3	6
Ba	2109	1029	847	889	809	890	547	869	890	785	195	465.0		321	60	310	96	83	371	412	571	438
La	<1	1	3	<1	<1	<1	21	<1	1	<1	29	18.50		3	5	6	2	2	2	3	2	<1
Ce	23	26	25	18	15	7	34	17	23	16	44	38.10		6	12	16	5	6	8	11	9	<1
Pr	11	5	3	2	1	2		3	4	1		4.30			1	<1	<1	<1	3	1	1	<1
Nd	13	17	15	15	11	9		12	17	12		14.20			6	6	4	1	6	5	5	<1
Sm												3.72										
Eu												1.59										
Gd												3.64										
Dy												3.65										
Er												2.07										
Yb												1.79										
Lu												0.26										
Hf												2.54										
Ta												0.44										
Pb	57	43	47	48	45	42	40	49	49	44	33	31.3		58	28	47	44	43	52	46	47	50
Th	4	6	6	4	2	1	8	3	4	3	11	7.23		1	1	4	1	1	1	2	1	1
U	2	2	2	2	2	1	2	2	1	2	1	1.54		1	1	3	2	3	2	2	1	2

APPENDIX D

Calculation of Zr and P_2O_5 saturation concentrations

The theoretical maximum solubility of Zr and P_2O_5 in a partial melt having the composition of *in situ* migmatite leucosomes and Harrow type granitic rocks is listed in Tables D.1 and D.2 respectively. Confidence is placed in these calculations, as geological evidence, discussed in Part II, supports leucosomes and Harrow type rocks (excepting mafic granodiorites) approximating melt compositions.

The concentration of dissolved Zr required to saturate a partial melt, and therefore stabilise the mineral zircon, depends systematically on the melt composition and temperature, according to the experimentally-determined equation (Watson & Harrison 1983) -

$$\textbf{Zr (ppm) at saturation} = 5 \times 10^5 \exp [3.80 + 0.85 (M - 1) - (12900 / T)]$$

Where T is the temperature (in Kelvin) and M is the cation ratio (Na + K + 2Ca) / (Al x Si). The cation fractions of Na, K, Ca, Al and Si for all samples were calculated by normalising the elemental oxides to 6 oxygen atoms. Note that pressure and H_2O content (above 2 wt%) are considered to have negligible effect on zircon solubility (Watson & Harrison 1983).

The P_2O_5 content required to saturate a partial melt in apatite is dependent upon on temperature (positively) and silica content (negatively), described by the relationship (Harrison & Watson 1984) -

$$\textbf{P}_2\textbf{O}_5\ \textbf{(sat)} = 0.475 / \exp [\{(8400 + ((SiO_2 - 0.5) \times 26400)) / T\} - \{(12.4 \times (SiO_2 - 0.51) + 3.1)\}] \times 100$$

However, apatite solubility also increases dramatically with peraluminosity (Bea *et al.* 1992; Pichavant *et al.* 1992), potentially through the formation of alumino-phosphate complexes (Pichavant *et al.* 1992). The effects of excess Al_2O_3 were therefore corrected in Tables D.1 and D.2 using the experimentally-derived expression of Pichavant *et al.* (1992) -

$$\textbf{P}_2\textbf{O}_5\ \textbf{(wt\%) at saturation} = P_2O_5^{HW} + [(A.S.I. - 1) \times \exp (-5900 / T - (3.22 \times SiO_2) + 9.31)]$$

Where T is the absolute temperature and $P_2O_5^{HW}$ is the Harrison & Watson (1984) apatite solubility model at neutral peraluminosity. Note that this formulation is preferred to that of Bea *et al.* (1992), since the latter predicts that all leucosomes and Harrow type plutons contain a large excess P_2O_5 over that required for melt saturation. This is unlikely, given the marked Zr undersaturation of these samples and minimal entrainment of residual minerals.

Table D.1. Whole rock XRF geochemical data for *in situ* leucosomes and diatexite segregations of the GRC, with calculated values of Zr and P_2O_5 saturation for a melt of that composition at the indicated temperatures. Zr* = Zr (measured)/ Zr concentration at melt saturation; P_2O_5* = P_2O_5 (measured)/ P_2O_5 concentration at melt saturation

Oxide (wt%)	Granitic leucosome 97-R2C	Granitic leucosome 97-RG	Granitic leucosome 98-R1	Granitic leucosome 98-R2A	Granitic leucosome 98-R5C	Granitic leucosome 98-WF1A	Granitic leucosome 98-25
SiO_2	75.48	74.77	74.99	74.29	74.03	76.17	74.15
TiO_2	0.01	0.10	0.05	0.08	0.04	0.05	0.08
Al_2O_3	14.46	14.13	14.49	14.64	14.80	14.50	15.12
Fe_2O_3t	0.10	0.83	0.34	0.72	0.27	0.38	0.70
MnO	0.02	0.02	0.01	0.02	0.01	0.01	0.02
MgO	0.05	0.27	0.13	0.24	0.10	0.16	0.27
CaO	1.86	1.56	1.69	1.74	1.45	2.02	1.70
Na_2O	4.22	3.16	3.44	3.51	3.12	3.28	3.07
K_2O	3.28	4.10	4.01	4.13	5.54	2.72	3.82
P_2O_5	0.08	0.150	0.077	0.086	0.128	0.075	0.209
Zr (ppm)	27.4	49.3	20.1	22.8	24.5	27.9	24.4
M	1.36	1.25	1.28	1.31	1.34	1.15	1.16
Conc. of Zr (ppm) saturating melt at-							
650°C	30.0	27.3	27.9	28.8	29.5	25.1	25.3
700°C	40.2	36.4	37.3	38.5	39.4	33.6	33.8
Zr* (700°C)	0.68	1.35	0.54	0.59	0.62	0.83	0.72
Conc. of P_2O_5 (wt%) saturating melt at-							
650°C	0.07	0.22	0.18	0.16	0.13	0.33	0.39
P_2O_5* (650°C)	1.14	0.68	0.43	0.54	0.98	0.23	0.53

Oxide (wt%)	Granitic leucosome 98-65A	Granitic leucosome 98-65B	Granitic leucosome 98-102	Granitic leucosome 98-WF2A-2L	Granitic leucosome 98-75	Granitic leucosome Y2-7b	Granitic leucosome 99-R5l
SiO_2	73.15	75.31	73.85	78.68	73.80	75.53	74.33
TiO_2	0.10	0.01	0.09	0.06	0.12	0.07	0.10
Al_2O_3	15.27	14.54	15.04	12.48	15.34	14.15	14.87
Fe_2O_3t	0.99	0.05	0.67	0.53	1.10	0.70	0.80
MnO	0.01	0.00	0.01	0.02	0.02	0.02	0.02
MgO	0.35	0.04	0.28	0.22	0.39	0.28	0.34
CaO	2.34	1.91	2.45	1.69	1.42	2.08	1.81
Na_2O	3.20	2.90	3.37	3.01	2.20	3.35	3.47
K_2O	4.16	4.80	3.38	2.48	4.05	2.44	3.20
P_2O_5	0.122	0.061	0.083	0.116	0.13	0.08	0.071
Zr (ppm)	56.3	7.7	32.2	19.2	26.9	46	33
M	1.34	1.31	1.30	1.15	0.98	1.17	1.19
Conc. of Zr (ppm) saturating melt at-							
650°C	29.5	28.7	28.6	25.0	21.7	25.6	26.1
700°C	39.4	38.3	38.3	33.4	29.0	34.2	34.9
Zr* (700°C)	1.43	0.20	0.84	0.57	0.93	1.34	0.95
Conc. of P_2O_5 (wt%) saturating melt at-							
650°C	0.15	0.13	0.17	0.24	0.77	0.30	0.33
P_2O_5* (650°C)	0.81	0.47	0.49	0.48	0.17	0.27	0.22

Table D.1 cont. Whole rock XRF geochemical data for *in situ* leucosomes and diatexite segregations of the GRC, with calculated values of Zr and P_2O_5 saturation for a melt of that composition at the indicated temperatures.

Oxide (wt%)	Granitic leucosome 99-14B	Granitic leucosome 99-7	Diatexite segregation 98-R3	Diatexite segregation 97-286-1L	Tonalitic leucosome 98-123	Tonalitic leucosome 98-TL4	Tonalitic leucosome 98-G2
SiO_2	74.58	74.88	75.61	74.47	75.64	74.66	74.02
TiO_2	0.05	0.11	0.20	0.17	0.04	0.09	0.11
Al_2O_3	14.49	14.64	12.79	13.82	14.90	15.45	15.04
Fe_2O_3t	0.31	0.97	1.69	1.21	0.25	0.73	0.82
MnO	0.01	0.02	0.04	0.03	0.01	0.01	0.01
MgO	0.13	0.41	0.61	0.51	0.13	0.30	0.39
CaO	1.59	1.59	1.49	1.66	3.63	3.51	3.55
Na_2O	3.27	3.03	2.75	2.84	4.25	4.11	3.82
K_2O	4.48	4.46	3.87	4.50	0.54	0.81	0.94
P_2O_5	0.088	0.11	0.155	0.152	0.110	0.050	0.071
Zr (ppm)	23	55	94.2	56.6	55.5	50.7	74.0
M	1.29	1.24	1.24	1.29	1.34	1.30	1.30
Conc. of Zr (ppm) saturating melt at-							
650°C	28.2	27.1	27.1	28.2	29.5	28.5	28.6
700°C	37.7	36.2	36.2	37.7	52.1	50.2	50.5
Zr* (700°C)	0.61	1.52	2.60	1.50	1.07	1.01	1.46
Conc. of P_2O_5 (wt%) saturating melt at-							
650°C	0.17	0.25	0.19	0.17	0.084	0.17	0.16
P_2O_5* (650°C)	0.52	0.44	0.82	0.89	1.31	0.29	0.44

Table D.2. Whole rock XRF geochemical data for Harrow type granitic rocks, with calculated values of Zr and P_2O_5 saturation for a melt of that composition at the indicated temperatures. Zr* = Zr (measured)/ Zr concentration at melt saturation; P_2O_5* = P_2O_5 (measured)/ P_2O_5 concentration at melt saturation

Sample Lithology	98-76 Kout Norien	12870 Harrow GD	97-349 Bryan Ck	98-64A Carrigeen	T2-CC2 Carrigeen	98-1 Carrigeen	98-2 Carrigeen	98-5 Carrigeen
SiO_2	72.41	72.84	71.70	73.76	73.70	72.35	76.69	73.91
TiO_2	0.33	0.16	0.39	0.13	0.14	0.27	0.10	0.12
Al_2O_3	14.12	15.33	14.24	14.59	14.84	14.63	13.03	14.45
Fe_2O_3t	2.69	1.75	3.32	1.29	1.37	2.42	1.25	1.58
MnO	0.05	0.06	0.07	0.03	0.05	0.08	0.04	0.05
MgO	1.06	0.82	1.19	0.47	0.71	0.92	0.38	0.48
CaO	1.35	2.45	1.63	1.56	1.60	1.42	1.60	1.91
Na_2O	2.47	2.96	2.94	3.01	2.81	2.99	2.86	3.12
K_2O	4.28	2.67	3.37	4.31	3.35	3.47	3.03	3.23
P_2O_5	0.183	0.14	0.136	0.106	0.17	0.142	0.087	0.082
Zr (ppm)	120.8	74	142.6	63.8	64	97.1	46.9	57.7
ASI	1.27	1.26	1.24	1.17	1.33	1.30	1.20	1.19
M	1.14	1.15	1.18	1.22	1.07	1.12	1.14	1.19
Zr (ppm) saturating melt at-								
650°C	24.9	25.2	25.7	26.7	23.5	24.4	25.0	26.0
700°C	44.0	44.5	45.3	47.2	41.5	43.0	44.1	46.0
Zr* (700°)	2.74	1.66	3.15	1.35	1.54	2.25	1.06	1.26
P_2O_5 (wt%) saturating melt at-								
650°C	0.48	0.45	0.45	0.298	0.57	0.54	0.31	0.33
P* (650°C)	0.38	0.30	0.30	0.36	0.29	0.26	0.28	0.25

Sample Lithology	T2-3 Carrigeen	T2-13 Roseate	97-233a Nangkita	T2-1 Marn Mering	98-56 Marn Mering	98-58 Marn Mering	CC9D Schofield Ad	98-11 Schofield Ad
SiO_2	74.16	74.28	73.87	74.12	74.97	74.09	74.47	75.63
TiO_2	0.1	0.07	0.07	0.07	0.06	0.03	0.08	0.09
Al_2O_3	14.93	14.82	14.8	14.76	14.47	14.93	15.10	14.08
Fe_2O_3t	1.22	0.83	0.76	1.13	0.79	0.41	0.87	0.89
MnO	0.04	0.04	0.04	0.02	0.02	0.02	0.03	0.02
MgO	0.37	0.48	0.31	0.34	0.29	0.17	0.49	0.36
CaO	1.99	1.43	1.83	1.83	1.67	2.04	2.19	1.98
Na_2O	3.27	2.75	3.42	2.99	2.91	3.36	2.80	2.84
K_2O	3.32	4.06	3.92	3.58	4.03	4.00	2.97	3.08
P_2O_5	0.07	0.14	0.06	0.11	0.102	0.079	0.11	0.093
Zr	55	31	46.5	41	30.2	29.2	40	29.9
ASI	1.19	1.29	1.12	1.22	1.19	1.10	1.28	1.21
M	1.21	1.10	1.28	1.17	1.19	1.30	1.11	1.15
Zr (ppm) saturating melt at-								
650°C	26.3	24.1	28.1	25.5	25.9	28.6	24.2	25.0
700°C	46.5	42.6	49.5	45.0	45.8	50.4	42.7	44.2
Zr* (700°)	1.18	0.73	0.94	0.91	0.66	0.58	0.94	0.68
P_2O_5 (wt%) saturating melt at-								
650°C	0.32	0.47	0.2	0.35	0.3	0.17	0.456	0.34
P* (650°C)	0.22	0.30	0.30	0.31	0.34	0.46	0.25	0.27

Table D.2 cont. Whole rock XRF geochemical data for Harrow type granitic rocks, with calculated values of Zr and P_2O_5 saturation for a melt of that composition at the indicated temperatures.

Sample Lithology	98-12 Schofield Ad	98-13 Schofield Ad	98-14A Schofield Ad	98-14C Schofield Ad	98-14D Schofield Ad	98-23 Schofield Ad	98-24 Schofield Ad	98-26 Schofield Ad
SiO_2	73.71	75.50	74.31	75.79	73.77	74.39	73.58	74.70
TiO_2	0.09	0.05	0.13	0.07	0.06	0.07	0.06	0.07
Al_2O_3	14.61	14.23	14.17	14.13	15.05	14.47	14.62	14.54
Fe_2O_3t	0.92	0.47	1.59	0.82	0.63	0.70	0.77	0.60
MnO	0.02	0.01	0.03	0.02	0.02	0.03	0.03	0.02
MgO	0.34	0.20	0.50	0.25	0.18	0.24	0.28	0.22
CaO	1.50	1.52	1.61	1.60	1.14	1.73	1.22	1.26
Na_2O	2.80	2.73	2.80	2.79	2.77	3.18	2.94	2.91
K_2O	4.98	4.52	3.86	3.75	5.59	3.91	4.58	4.74
P_2O_5	0.089	0.095	0.106	0.099	0.076	0.139	0.054	0.145
Zr	46.6	27.6	65.6	27.4	27.3	25.9	47.9	19.8
ASI	1.15	1.17	1.21	1.22	1.19	1.15	1.22	1.19
M	1.25	1.20	1.17	1.14	1.21	1.24	1.17	1.19
Zr (ppm) saturating melt at-								
650°C	27.3	26.1	25.5	24.9	9.4	9.4	9.4	9.4
700°C	48.2	46.1	45.1	43.9	16.7	16.7	16.7	16.7
Zr* (700°)	0.97	0.60	1.45	0.62	1.64	1.55	2.87	1.19
P_2O_5 (wt%) saturating melt at-								
650°C	0.24	0.27	0.36	0.35	0.31	0.23	0.36	0.31
P* (650°C)	0.37	0.35	0.29	0.28	0.25	0.60	0.15	0.47

Sample Lithology	98-27 Schofield Ad	98-59 Schofield Ad	T2-39 Schofield Ad	98-60A Schofield Ad	98-60C Schofield Ad	98-38 Scrubby Junction	T2-20 Dunmore LT	98-150 Dunmore LT
SiO_2	74.72	75.22	73.29	75.78	74.71	75.00	74.73	73.39
TiO_2	0.06	0.05	0.09	0.04	0.05	0.06	0.08	0.07
Al_2O_3	14.54	14.55	15.42	14.01	14.36	14.56	15.24	15.99
Fe_2O_3t	0.52	0.56	0.88	0.52	0.61	0.61	0.71	0.68
MnO	0.02	0.01	0.03	0.02	0.02	0.02	0.02	0.01
MgO	0.24	0.19	0.37	0.19	0.24	0.22	0.53	0.27
CaO	1.52	1.60	1.96	1.70	1.79	1.43	3.52	3.02
Na_2O	3.13	2.97	3.32	3.27	3.37	3.20	3.27	3.83
K_2O	4.20	4.12	3.40	3.63	3.77	4.12	1.11	1.47
P_2O_5	0.107	0.076	0.17	0.073	0.118	0.1	0.09	0.092
Zr	20.6	15.1	68	18.9	25.8	31.8	72	43.6
ASI	1.17	1.19	1.21	1.13	1.12	1.18	1.17	1.19
M	1.21	1.19	1.19	1.24	1.27	1.20	1.20	1.21
Zr (ppm) saturating melt at-								
650°C	9.4	9.4	9.4	27.0	27.8	26.1	26.3	26.4
700°C	16.7	16.7	16.7	47.7	49.1	46.1	46.4	46.5
Zr* (700°)	1.23	0.91	4.08	0.40	0.53	0.69	1.55	0.94
P_2O_5 (wt%) saturating melt at-								
650°C	0.26	0.29	0.36	0.21	0.16	0.29	0.28	0.33
P* (650°C)	0.41	0.26	0.47	0.35	0.74	0.34	0.31	0.28

APPENDIX E

Definition of GRC granitic plutons

Formal definitions of the metaluminous to weakly peraluminous granitic plutons comprising the various GRC magma types (except Harrow types) are listed below in alphabetical order, in some cases accompanied by petrographic descriptions of type specimens and important variants. All pluton names have been assigned by this study, except where indicated. Grid references pertain to the quoted 1:100 000 map sheets.

BARRAMA MICROADAMELLITE

Derivation of name: Property of 'Barrama'

Classification: Late syn-compressional, Loftus Creek type

Type exposures: Pigeon Ponds Creek, WD477713 (Balmoral 7223)

Geological context: Occurs as a series of branching dykes that crosscut Glendara Adamellite in Pigeon Ponds Creek and tributaries. Outcrops between WD475718 and immediately east of the Harrow-Coleraine road.

Description of type sample, 97-126B:

Light grey-buff coloured, strongly porphyritic rock containing large tabular alkali feldspar phenocrysts, ranging from 2 cm to 4.5 cm long. These are conspicuously zoned and poikilitic, with concentrically arranged inclusions of quartz, biotite and euhedral plagioclase. Also present, and much more abundant, are smaller flesh-coloured alkali feldspar phenocrysts (0.5-1 cm) that lack inclusions, rounded quartz masses (~2-3 mm, up to 7mm), coarse plates of generally euhedral biotite (2-5mm) and laths of pale olive green plagioclase (1.5-2 mm, up to 4 mm). These are dispersed through a fine- to medium grained sugary matrix of quartz, alkali feldspar, grey plagioclase and tiny randomly disposed biotite flakes. Small plates of muscovite are also conspicuous.

In thin section alkali feldspar phenocrysts are microcline and have conspicuous euhedral core regions (also internally zoned) that have a much lower density of inclusions than the rims, which are sieved with small quartz droplets and contain numerous euhedral plagioclase inclusions (1-1.5 mm). The interface between core and rim is lined by quartz blebs and several small discrete grains of microcline with different optical orientation. Smaller alkali feldspar phenocrysts commonly exhibit regular oscillatory zoning outwards from a corroded core. Quartz phenocrysts are commonly single grains with cuspate margins against groundmass minerals, whereas plagioclase laths are oscillatory zoned with irregular sodic overgrowths; many are intergrown or clumped together. The groundmass is an equigranular mosaic of quartz, microcline and plagioclase, the latter commonly having myrmekitic lobes and fringes where adjacent to microcline. Ragged small grains of biotite (0.4 mm; α=pale tan β=γ=dark brown) are scattered throughout and commonly interleaved with muscovite. Accessory opaque grains are prominent and euhedral (cubic to rectangular) where enclosed by larger biotite flakes.

CAIRNS CREEK GRANODIORITE

Derivation of name: Cairns Creek

Classification: Late syn-compressional, Loftus Creek type

Type exposures: Chetwynd River, WD403706 (Balmoral 7223)

Geological context: Lozenge-shaped pluton that crosscuts the Chetwynd Tonalite. Compositionally zoned, from hornblende granodiorite at the periphery to a core of felsic adamellite.

Description of typical samples:

Marginal phase, sample 97-62

Distinctively pale greenish and porphyritic, dominated by coarse phenocrysts of olive green plagioclase (laths to 6 mm, most ~3 mm), with abundant hornblende blades (to 5 mm long, most 2-3 mm) and large euhedral biotite books (up to 4.5 mm across and 3mm thick). Quartz also forms polycrystalline masses to 7 mm (most ~3 mm). The matrix is medium grained plagioclase, rounded single quartz grains (1-2 mm) and scattered buff-coloured alkali feldspar, the latter rarely forming larger poikilitic masses; biotite also occurs as sparse tiny flakes. Red-orange crystals of titanite are abundant, with lesser spindles of chalky yellow allanite.

Thin sections reveal a pristine igneous texture, with striking oscillatory zoning in plagioclase, where many laths have patchy zoned cores. Large biotite plates (α=tan β=γ=dark chocolate brown) are commonly accompanied by clusters of magnetite cubes (up to 0.8 mm), stubby apatite prisms (up to 2 mm, most ~0.8 mm) and slender titanite crystals. Well-shaped hornblende prisms (α=pale yellow green, β=khaki green γ=deep blue green) are likewise associated with opaques and titanite rhombs, the latter also occurring as larger (1-1.5 mm) pleochroic, deep red-brown crystals. The groundmass, comprising a mosaic of fine grained quartz, plagioclase and predominantly microcline, is minor and occupies interstices between coarse biotite plates, hornblende, polycrystalline quartz masses and clumped plagioclase laths. Rarely, microcline also forms larger poikilitic grains (1-3 mm) enclosing numerous quartz, hornblende and plagioclase crystals.

Central phase, 97-65

Approximately 1.8 km from the western edge of the pluton, samples are medium to coarse grained and light buff coloured, consisting of polycrystalline quartz (to 6 mm, also single 2-3 mm grains), whitish-grey plagioclase laths (~3 mm, to 6 mm) and large, irregularly-shaped pools or rare tabular phenocrysts of pale orange-tan alkali feldspar (up to 10x6 mm, most 3-4 mm), invariably packed with tiny plagioclase, quartz and biotite inclusions. Occasional biotite books (4-5 mm across) are noted, some of which have tiny plagioclase inclusions. Alkali feldspar and biotite also occur as smaller disseminated grains, and orange-red titanite (crystals to 1 mm) is a rare accessory phase.

The significant textural difference in thin section between this sample and the hornblende-bearing phase described above is the lack of a fine grained matrix and the appearance of large, spectacularly poikilitic masses of perthitic microcline. Magnetite is also less abundant and primarily confined to clusters of small grains enclosed by microcline. As with hornblendic samples, plagioclase exhibits vivid oscillatory zoning and occasionally forms large intergrown masses of subhedral crystals with complex twinning and zoning characteristics. Many large laths also enclose smaller, euhedral plagioclase crystals.

Felsic core, sample 97-67

Samples from the geographic centre of the pluton (~500m west of the Carey's Road bridge) are orange-tan, coarse grained and felsic. Masses of smoky quartz (~5 mm, up to 10 mm) and tabular orange alkali feldspar phenocrysts (to 2 cm, most ~5 mm) are very abundant, the latter being perthitic and commonly enclosing small quartz and plagioclase grains. Greenish blocky plagioclase laths (3-4 mm, up to 6 mm) are relatively reduced in abundance, and most biotite occurs as sparse euhedral books (~2-3 mm with tiny plagioclase inclusions), with disseminated finer flakes uncommon. In thin section feldspars are strongly seritisised and dusted with tiny opaques. Alkali feldspar is coarsely perthitic and exhibits crystal faces against quartz, whereas plagioclase has irregular sodic rims and cores that are replaced by epidote and sheaves of secondary white mica. Ragged flakes of white mica are also associated with large biotite flakes, extensively altered to chlorite.

Eastern phase, sample 97-71

East of Carey's Road another important variant of Cairns Creek Granodiorite is recognised. Representative samples are coarse grained, with a distinctive mottled orange-green colour imparted by large tabular phenocrysts and poikilitic masses of orange-tan alkali feldspar (perthitic, to 15 mm) and interlocking laths of olive green plagioclase (~3 mm, to 7mm). Polycrystalline quartz masses (to 7 mm) are abundant, with euhedral biotite books (to 5 mm, enclosing tiny plagioclase crystals) and scattered smaller grains. Red-brown titanite grains to 1 mm are conspicuous. As such, the rock is a coarser grained equivalent of the intermediate samples (i.e. **97-65**) described above, but with prominent alkali feldspar phenocrysts. In thin section the effects of hydrothermal alteration are conspicuous. Plagioclase laths are strongly altered to white mica and carbonate, but still exhibit strong oscillatory zoning; many grains have irregular sodic overgrowths, especially where enclosed by turbid microcline masses. Large biotite plates are extensively replaced by chlorite and epidote, and where this occurs contains irregular blebs of pale purple fluorite along former cleavage traces. This feature indicates a high fluorine content for biotite in the sample. Ragged plates and sheaves of secondary muscovite are also very common. Titanite crystals are still prominent, usually occurring in groups with magnetite cubes and large yellowish allanite spindles. Tiny hornblende crystals are rarely encountered inside polycrystalline quartz masses.

CAUPAUL IGNEOUS COMPLEX

Derivation of name: Property of 'Caupaul'

Classification: Early syn-compressional

Geological context: Composite plutonic body outcropping for ~6 km along the Glenelg River valley and tributaries north of Dergholm, surrounded to the south, east and north by metasedimentary rocks. A strong teardrop-shaped magnetic anomaly indicates that the igneous exposure corresponds to the southeast corner of body, which continues north and west under younger cover.

Description of geological elements:

Hornblende pyroxenite CP11726

Medium to coarse grained, consisting primarily of abundant greenish clinopyroxene (2-3 mm, to 6 mm), brownish orthopyroxene (~2-4 mm) and striking, irregularly shaped masses of hornblende (to 10 mm, most ~5 mm). Interstitial plagioclase (1-2 mm) is a minor component and encloses smaller euhedral

orthopyroxene crystals. Modal mineralogy classifies the rock as a borderline gabbronorite (Figure 13.2), but hornblende pyroxenite is more appropriate given the preponderance of pyroxene.

In thin section, the texture is purely igneous and that of a pyroxene mesocumulate, with intercumulus hornblende and plagioclase. Hornblende is brownish-green (α=tan, β=olive green, γ=light green-brown) and sparsely poikilitic, enveloping euhedral clinopyroxene, orthopyroxene, plagioclase and opaques, elsewhere being interstitial to these phases. In places it is partially replaced by a pale green actinolitic amphibole. Clinopyroxene occurs as equidimensional twinned prisms that are mutually polygonal or as elongate grains with crystal faces against hornblende and plagioclase. Many are variably replaced by blebs of brownish hornblende parallel to fine exsolution lamellae, and sometimes moderately altered to fine needly actinolite. Orthopyroxene mostly exhibits anhedral grain boundaries against clinopyroxene, which have developed by mutual growth interference. This suggests a largely shared crystallisation interval, though occasional enclosure of small orthopyroxene crystals by clinopyroxene implies that the former was first to precipitate from the magma. Orthopyroxene also tends to be concentrated around interstitial plagioclase, where it forms euhedral prisms or aggregates of grains with triple junctions. Intercumulus plagioclase masses are single grains with crystal faces against hornblende, but also exhibit undulatory extinction, mechanical twinning and domains of intra-crystalline recrystallisation, features that manifest significant internal strain.

Gabbronorite 98-CP129

Fine to medium grained and dark brownish grey coloured due to high content of stubby orthopyroxene crystals. Also evident are black prisms of clinopyroxene and plagioclase laths, with both pyroxene and feldspar exhibiting a strong preferred orientation. Small flakes of biotite (0.5-1 mm) are very minor in abundance. Pyroxenes are pristine euhedral to subhedral elongate prisms in thin section (most ~1-1.5 mm), also occurring in aggregates where grains are more equidimensional and have triple junctions. Occasionally tiny plagioclase euhedra are embedded within pyroxenes. Plagioclase laths (1-1.5 mm, to 2 mm) are largely anhedral against pyroxene but subhedral elsewhere, with oscillatory and mottled continuous zoning, and occasionally sieved by tiny pyroxene and opaque grains. Laths are moderately well aligned, but distorted twin planes suggests that this is most likely a result of tectonic rather than magmatic processes. Magnetite is abundant, mostly as irregular grains interstitial to pyroxene and plagioclase, but sometimes enclosed by these phases. Red-brown biotite flakes are ragged and interstitial.

Hornblende gabbro 98-CP4

Dark grey-black, medium, even-grained and dominated by hornblende prisms (1-3 mm) and plagioclase laths, with minor orthopyroxene (~1 mm) and rare squat prisms of clinopyroxene (1-3 mm). Hornblende is brownish in thin section (α=light green, β=khaki, γ=brown green), being anhedral against plagioclase and containing tiny inclusions of this mineral, with numerous magnetite grains and occasional orthopyroxene prisms. The latter is mostly fringed and partially replaced by fibrous cummingtonite, but disseminated subhedral grains are present also. In contrast, clinopyroxene is invariably mantled by hornblende and has blebs of this mineral parallel to cleavage traces; a rare large grain (4 mm) encloses several smaller grains of orthopyroxene. Interlocking laths of plagioclase project into hornblende but are cuspate against orthopyroxene. Most grains exhibit patchy continuous zoning, and some have mechanical

twins and kinked twin planes. Ragged poikilitic biotite flakes (0.5-1 mm; α=pale tan, β=γ=dark red-brown) are minor, but conspicuous.

Ferres Creek Tonalite 98-CP12

Light creamy-grey coloured and medium to coarse grained, with blocky hornblende prisms (~2 mm, to 5 mm), greenish plagioclase laths (~1.5 mm) and abundant quartz grains (~1 mm); large ragged and distorted biotite flakes (to 5 mm) are very conspicuous and define a pervasive foliation (S_2) of variable intensity. In thin section hornblende (α=pale yellow green, β=khaki, γ=deep blue-green) is anhedral and poikilitically encloses spindly biotite flakes, euhedral plagioclase laths and opaques, being occasionally perforated with quartz. Many rectangular grains are also envelope relict clinopyroxene prisms. Biotite (α=tan, β=γ=dark brown) has frayed edges, kinked cleavage traces and very non-uniform extinction, also partially enclosing plagioclase laths. Both biotite and hornblende are associated with anhedral (rarely subhedral) masses of dirty yellow epidote (0.5-1.5 mm). Interstices between subhedral plagioclase laths, some of which exhibit mechanical twinning, are occupied by polycrystalline quartz or small pools of microcline with vivid tartan twinning. The latter also rarely forms poikilitic masses (3-5 mm) enveloping hornblende and plagioclase. Irregularly-shaped tourmaline grains sieved with inclusions of quartz, plagioclase, hornblende and biotite are an accessory.

CHETWYND TONALITE

Derivation of name: Township of Chetwynd

Classification: Late syn-compressional, Tuloona type

Type exposures: Chetwynd River WD451673 (Balmoral 7223)

Geological context: Northwest-trending elliptical pluton intruded by the Cairns Creek Granodiorite and Glengoyne Adamellite.

Description of type sample, 97-427:

Distinctive medium bluish-grey colour, moderately coarse grained and relatively biotite-rich, being characterised by large subhedral quartz grains (up to 10 mm across, modal size 2 mm). Plagioclase forms steel grey laths to 6mm, whereas biotite (ragged plates to 3 mm with most 1-1.5 mm) is randomly oriented and commonly forms aggregates of small flakes. Occasional corroded allanite prisms are conspicuous, with orange-red iron oxide haloes. No muscovite occurs.

In thin section, euhedral to subhedral plagioclase laths may be clumped together, with interstitial microcline, and may be weakly aligned, though no preferred orientation exists overall. Laths are Carlsbad twinned and exhibit frequent strong oscillatory zoning, with zone boundaries commonly embayed and resorbed; rectangular cross-sections (to 3.5 mm across) have very complex twinning characteristics, patchy zoning and sometimes contain tiny discrete plagioclase crystals. Twin planes are occasionally weakly distorted, perhaps manifesting D_5 strain. Microcline occurs as amoeboid masses (to 5-7 mm across) densely packed with plagioclase and lesser biotite or small interstitial pockets between plagioclase laths or equant to rectangular consertal quartz grains. Biotite (α=pale tan, β=γ=dark chocolate brown, basal sections with a greenish tint) most frequently occurs as elongate intertwined sheaves or aggregates up to ~4 mm long of 3 to 20 grains accompanied by numerous magnetite cubes (to ~1 mm,

modal ~0.5 mm). Larger biotite plates commonly enclose or partially mantle small plagioclase crystals, and are clearly interstitial to this mineral; other inclusions are apatite, magnetite and metamict allanite.

Other features:

At WD422665 the Chetwynd Tonalite also encloses a 10 m wide dioritic body. This material is intensely weathered but bluish grey, fine to medium grained and biotite-rich, with phenocrysts of plagioclase (1 cm) and clots of coarse biotite. In thin section, greenish biotite and plagioclase laths are enclosed by large (1 cm) quartz grains. As such, the rock texturally resembles the microgranular enclaves of Tuloona types. Due to poor outcrop and the occurrence of numerous aplitic and microgranitic dykes, it is not clear whether the diorite is an enclave or a dyke.

CLOVEN HILLS GRANODIORITE

Derivation of name: Property of 'Cloven Hills'

Classification: Late syn-compressional, Loftus Creek type

Type exposures: Sickle Creek, WD437560 (Edenhope 7123)

Geological context: Crosscuts the Meissen Granodiorite and Blair Atholl Adamellite; intrudes sillimanite schist at its eastern margin.

Description of type sample, 97-436:

Light buff coloured and medium to coarse grained, with abundant large euhedral biotite plates (~3 mm, to 5 mm) sometimes enclosing tiny plagioclase grains; biotite also occurs as finer disseminated flakes (0.5-1 mm). Steel grey laths of plagioclase (2-3 mm) and smoky polycrystalline masses of quartz (up to 6 mm across, most ~2 mm) are conspicuous, whereas alkali feldspar occurs as light orange small grains (0.5 mm) or poikilitic masses (~2-3 mm). Small hornblende needles and orange red titanite crystals are also noted. In thin section, large biotite plates (α=pale tan β=γ=dark chocolate brown) commonly enclose magnetite grains (up to 0.8 mm, most ~0.5 mm), which also are abundantly disseminated through the rock, or occur as clusters of several grains with titanite, zoned allanite prisms and irregular epidote grains. Plagioclase laths are euhedral to subhedral and exhibit sharp oscillatory zoning with complexly mottled or patchy zoned cores. They have a tendency to form interlocking clumps, with interstitial pools of microcline, and many enclose tiny euhedral crystals of hornblende. The latter is otherwise sparsely distributed as isolated small prisms (0.8 mm).

Important lithological variants

Cloven Hills Granodiorite has a chilled western contact against Blair Atholl Adamellite in Sickle Creek. Here, samples (97-222) are strongly porphyritic, with abundant phenocrysts of biotite (euhedral books to 7 mm, most ~3 mm), rounded grains (~2 mm) or masses of quartz (to 6 mm) and palest green plagioclase (~4 mm) in a light orange sugary matrix of fine grained quartz, alkali feldspar and plagioclase. Quartz in thin section occurs as mostly as single grains, sometimes with crystal faces, that are embayed or traversed by thin seams of groundmass minerals, that probably represents injection of former melt along cracks. Similarly, where quartz phenocrysts are clumped, they are 'glued' by thin seams of groundmass alkali feldspar and quartz, probably former films of melt. Aggregates of plagioclase laths lack this feature but have sodic rims that are lined and perforated by tiny quartz blebs; vivid oscillatory zoning is common. The groundmass comprises small amoeboid grains of microcline and plagioclase densely perforated by tiny droplets of quartz; this texture is commonly exhibited by aplites and results from quenching.

Microcline also forms small pools (~1 mm) enclosing tiny plagioclase crystals. Tiny biotite flakes are scattered throughout, with rare large allanite prisms (0.5-1 mm) and numerous magnetite grains (0.5-0.8 mm, also occurring as smaller irregular groundmass grains).

COOJAR GRANODIORITE

Derivation of name: Township of Coojar

Classification: Late syn-compressional, Tuloona type

Type exposures: Basin Creek, WD635650 (Balmoral 7223)

Geological context: Part of central granitic belt. Comprises scattered outcrop along upper Mather Creek east of the Edenhope-Coleraine road to Gilberts Lane, and a 2 km segment of lower Basin Creek. Relationships to surrounding lithologies unclear.

Description of typical samples:

Felsic phase, 97-142

Medium to coarse grained, bluish-white rock, with phenocrysts of poikilitic microcline, rounded grains of slightly polycrystalline quartz and prominent primary muscovite flakes. Biotite commonly forms small but conspicuous clots, and a weak preferred orientation of disseminated biotite grains is visible in some samples.

Like other Tuloona type phases, thin sections reveal that plagioclase laths (up to 3.5 mm, modal size 1.5 mm) form interlocking clumps and exhibit oscillatory and complex patchy zoning, with irregular sodic overgrowths. Cores of zoned grains vary from euhedral to corroded; larger zoned laths exhibit evidence for extensive solution/resorption prior to overgrowth by the sodic rim. Some consertal quartz aggregates (to 5 mm) have markedly undulose extinction. Alkali feldspar is microcline and forms zoned masses (up to 4.5 mm) or irregular interstitial pockets to plagioclase. Grains are commonly 1.5 mm, may be elongate and tending towards tabular. They are poikilitic, though inclusions (quartz droplets and small plagioclase crystals) are typically sparse. Biotite flakes (α=pale tan, β=γ=dark brown) are generally ragged and reach about 1.5 mm, most being ~0.8 mm long; alteration to chlorite and epidote is observed but not common. Biotite occurs as single grains but more commonly is the dominant mineral in clotty unfoliated aggregates with primary muscovite flakes (0.6 mm), magnetite and apatite; there may be 4-10 interleaved grains per clot, which can be equant (~2 mm across) or elongate (~3.5 mm long). These appear to be concentrated at plagioclase grain boundaries. Muscovite also forms large euhedral flakes to 1.5 mm.

Mafic phase, 97-297

This rock is texturally very similar to the above described lithology, but contains more biotite with significantly less muscovite and microcline. In thin section, biotite also forms sheave-like aggregates (3-20 interleaved grains) of randomly disposed flakes with magnetite and apatite. The largest biotite flakes in these clots often envelope euhedral plagioclase grains. Rarely, 1 mm euhedral muscovite flakes occur with biotite clots and may be primary; secondary muscovite spindles occur with these as well. Magnetite is more abundant than in **97-142**, as clusters of 3 to 6 grains. Irregular masses of dirty yellow-brown epidote (0.5 mm) occur where biotite is chloritised, but one larger isolated subhedral (?primary magmatic) grain is also noted.

DEEP CREEK GRANODIORITE

Derivation of name: Deep Creek, Wando Vale (Anderson (1990)

Classification: early syn-compressional, Deep Creek type

Type exposures: St Elmo's quarry, WD403503 (described in Anderson & Gray 1994)

Geological context: Intrudes metasedimentary rocks in Deep Creek; other contacts not exposed

Description of marginal deformed phase, sample 97-DC (western pluton margin):

Fine to medium grained rock, which outwardly appears to be unstrained, though deformation features are conspicuous in thin section. Here, plagioclase (60.0%) is predominant as subhedral blocky prisms (to ~2.5 mm) and, more commonly, smaller subhedral to euhedral laths (modal size ~1 mm). Most grains exhibit strong continuous zoning, from calcic, generally euhedral cores to more sodic rims; sharply defined oscillatory zoning also occurs. Laths have no preferred orientation overall, though kinked twin planes in some grains evidences deformation. Alteration to dusty sericite and secondary muscovite flakes is moderately pronounced. Quartz (25.8%) occurs as clumps (0.5-2 mm across) that are recrystallised into subgrains or as single grains (most ~0.5 mm) with markedly undulose extinction. It also forms trains of tiny subgrains around blocky plagioclase crystals, with cuspate re-entrants giving the latter serrated boundaries. Alkali feldspar (5.2%) forms rare interstitial pools (up to 2.5 mm, most 0.25-0.5 mm) between plagioclase laths and has vivid and regular tartan twinning. Commonly, plagioclase has myrmekitic fringes and lobes where projecting into microcline. Minor biotite (6.7%; α=pale tan, β=γ=very dark brown) occurs mostly as smeared aggregates of tiny feathery grains (2-4 mm long), with anhedral granules of epidote (0.5%) and minute titanite blebs (0.1%); this defines a weak foliation that anastomoses around, and occasionally envelopes plagioclase prisms. Larger flakes of biotite (0.5 mm) are distorted and recrystallised at the edges into 'tails' of numerous tiny grains aligned with the foliation. Very small biotite spindles also line some plagioclase grain boundaries and are particularly clustered inside larger microcline masses. Small flakes of secondary muscovite (0.5%) are scattered throughout the rock.

GLENDARA ADAMELLITE

Derivation of name: Property of 'Glendara'

Classification: Late syn-compressional, Tuloona type

Type exposures: Glenelg River valley, WD478818 (Balmoral 7223)

Geological context: Outcrops sporadically over a large area between the towns of Harrow, Mooree, Tarrayoukyan and Pigeon Ponds. Intruded by Koolomurt Granodiorite in Pigeon Ponds Creek.

Description of type sample, 97-145:

Coarse grained and strikingly porphyritic rock, with large tabular to square phenocrysts of alkali feldspar (up to 6 cm long). These define a platy flow foliation in places, and are conspicuously zoned in handspecimen, outlined in part by concentric trails of biotite and quartz inclusions. In thin section, phenocrysts have finely perthitic domains, are weakly zoned and exhibit variable development of tartan twinning; the latter is more conspicuous in smaller elongate groundmass grains (1-3 mm). They are strongly poikilitic and enclose quartz droplets, euhedral biotite plates and plagioclase crystals (inclusions ~0.4-0.6 mm). Both microcline phenocrysts and smaller grains have irregular, serrated boundaries against quartz and plagioclase. Included plagioclase grains are generally altered to sericite and oriented parallel to former growth surfaces. Elsewhere plagioclase forms subhedral to anhedral blocky crystals to 3mm (modal size 1-1.5 mm) with oscillatory zoning and irregular sodic overgrowths, present even in grains

enclosed by microcline. Quartz occurs as very large polycrystalline clumps, some of which also contain small plagioclase laths. The rock matrix is quite felsic, with euhedral plates of muscovite conspicuous (modal size 0.5-0.8 mm). Ragged biotite flakes (~0.8 mm, up to 2.5 mm) are non-aligned and generally interleaved with muscovite forming small unfoliated clotty aggregates (2-3 mm across). Small magnetite grains are present in some clots and epidote occurs where biotite is partially replaced by chlorite.

KASSINGBROOK GRANODIORITE

Derivation of name: Property of 'Kassingbrook'

Classification: Late syn-compressional, Kassingbrook type

Type exposures: Chin Chap Creek, sample **97-373**, WD709490 (Balmoral 7223)

Geological context: Contacts migmatitic metasedimentary rocks to the north and east, and a garnet-bearing adamellite to the south.

KOOLOMURT GRANODIORITE

Derivation of name: Property of 'Koolomurt'

Classification: Late syn-compressional, Loftus Creek type

Type exposures: Pigeon Ponds Creek, WD433776 (Edenhope 7123)

Geological context: Teardrop-shaped pluton that intrudes Glendara Adamellite, with a sharp eastern contact in Pigeon Ponds Creek.

Description of type sample, 97-293:

Homogeneous, light greenish-grey coloured rock that is medium to coarse grained and approximately equigranular. Plagioclase occurs as greenish-white laths (rarely up to 7 mm long) whereas quartz forms large polycrystalline clumps (2-5 mm) or smaller discrete grains (1-2 mm). Square to rectangular glassy alkali feldspar grains (most 1-3 mm, rarely to 12 mm) are conspicuous, containing minute inclusions of plagioclase, quartz and biotite. In northern Pigeon Ponds Creek these alkali feldspar crystals occur as striking 'oikocrysts' (up to 4.2 cm across) that are choked with small plagioclase, quartz and biotite inclusions. Biotite otherwise occurs as large ragged flakes (~2-3 mm) or smaller disseminated grains that may exhibit a weak preferred orientation. Small clots of unfoliated biotite (5-10 mm) are also moderately common. Tiny red-brown titanite crystals and black allanite needles with rusty halos are present to the exclusion of primary muscovite.

In thin section, plagioclase laths are subhedral (~1.5-2 mm long) and exhibit pronounced oscillatory zoning, with distinct euhedral cores. Laths commonly form clumps of 2-8 grains with myrmekitic fringes where projecting into interstitial pools of microcline. Biotite (α=pale tan β=γ=dark chocolate brown) is mostly present as ragged flakes (~1 mm) as part of interleaved aggregates with magnetite, apatite, allanite and titanite crystals. However, occasionally it also forms larger single flakes (~2-2.5 mm) that are subhedral, especially where enclosed by poikilitic microcline masses. Like the larger biotite books in other Loftus Creek types, tiny euhedral plagioclase inclusions also occur. Titanite is conspicuous as euhedral crystals associated with magnetite, but occasionally occurs as larger irregularly shaped grains (0.8-1 mm) with plagioclase inclusions.

Other features

An unusual feature of some outcrops is the presence of diffuse, irregularly shaped biotite-rich heterogeneities (5-8 cm across), sometimes forming bands (30 cm to 1 m long, 1-3 cm wide) that taper into thin schlieren. Bands have concentrated biotite at the margins and may be contorted or complexly folded, perhaps a result of magmatic turbulence. Outcrops are also crosscut by zoned pegmatite dykes (5 cm thick) with feldspar-rich rims and quartzose cores, and composite aplite-pegmatite sheets (to 5 cm to 60 cm thick). Pegmatite also forms irregular patches and thin lenticular bodies. It lacks peraluminous minerals, rather dominated by orange-pink alkali feldspar, with greenish-white albite and rare large spindly plates of biotite (2.5 cm across).

LOFTUS CREEK GRANODIORITE

Derivation of name: Loftus Creek (Morand *et al.* 2001)

Classification: Late syn-compressional, Loftus Creek type

Type exposures: minor tributary of Corea Creek, WD454492 (Balmoral 7223)

Geological context: Intrudes amphibolite facies schists and calc-silicates in Corea Creek and tributaries, and migmatitic rocks in Loftus Creek.

Remarks: Formerly mapped as Sawpit Gully Granodiorite (Anderson & Gray 1994)

MEISSEN GRANODIORITE

Derivation of name: Anderson (1990)

Classification: Early syn-compressional, Wennicott type

Type exposures: Elbow Creek, WD431541 (Edenhope 7123)

Geological context: Lenticular pluton traced northwest from Elbow Creek to tributaries north of the Wando River. Intrudes Snake River Tonalite, crosscut by Blair Atholl Adamellite and the Cloven Hills Granodiorite.

MOOREE GRANODIORITE

Derivation of name: Township of Mooree

Classification: Late syn-compressional, Tuloona type

Type exposures: Sugarloaf Creek, WD478789 (Balmoral 7223)

Geological context: Exposed in the environs of Sugarloaf Creek, adjoining Koolomurt Granodiorite (west) and Glendara adamellite (east); both boundaries are concealed beneath Permian cover. Forms a thin dyke at the Glendara Adamellite-Barrama Microadamellite contact in eastern Pigeon Ponds Creek.

Other features

Commonly contains aplitic and pegmatitic dykes (to 1 m thick), which become numerous adjacent the western boundary with Koolomurt Granodiorite.

PATAWILYA TONALITE

Derivation of name: Property of 'Patawilya'

Classification: Late syn-compressional, Tuloona type

Type exposures: Bryan Creek, WD680531 (Balmoral 7223)

Geological context: Southernmost unit of the central granitic belt. Southern margin transitional to migmatitic rocks in Bryan Creek, separated from leucogranitic rocks to the north by a ~1 km tract of Devonian Rocklands Rhyolite. Northwestern extent of the pluton unknown.

Description of type sample, 97-407B:

Light grey-buff and medium to coarse grained, with phenocrysts of quartz (equant, to 8 mm, modal size ~4 mm), some of which are cloudy, and infrequent large euhedral plagioclase laths (up to 5-7 mm). The groundmass is smaller quartz grains and interlocking buff coloured plagioclase (~1.5 mm), with abundant plates and small clotty aggregates (1-2.5 mm) of randomly disposed biotite. Rare larger biotite flakes occur (3-4 mm) with ragged outlines and enclose tiny plagioclase crystals. Tiny blebs of chalcopyrite are occasionally noted on fresh broken surfaces.

In thin section, blocky prisms and laths of plagioclase (~1.5 mm, to 4 mm) are mostly heavily altered and/or replaced by secondary muscovite blades in the cores. Larger grains show irregular sodic mantles and strong oscillatory zoning, often with complex resorptions and twinning characteristics; rarely, perfectly euhedral cores occur. Mottled zoning is also evident, and tiny plagioclase crystals are found embedded in larger laths. Grains are usually subhedral, and show crystal faces against biotite, quartz and alkali feldspar; the latter is very minor, and small pools are wholly interstitial to plagioclase laths. Quartz typically forms large equant polycrystalline clumps (to ~4.5 mm) within which many grains have very undulose extinction and are recrystallised into subgrains at the edges; mutual contacts are either with subgrains or are strongly interdigitating. These features are probably the result of D_5 deformation, though plagioclase twins are unmodified. Similarly, coarse dark brown biotite plates (to 3 mm, mostly ragged flakes ~0.6-1 mm) exhibit internal kinking, suggestive of some strain. Most biotite is evenly disseminated throughout the rock as individual flakes, sometimes concentrated at plagioclase grain boundaries but occasionally it also forms aggregates of up to 10 small grains (3 mm across). Chlorite alteration and slender epidote prisms (3 mm) also occur in biotite clots, the latter also present as dirty green-yellow anhedral masses. Muscovite also is mostly anhedral secondary spindles or symplectic grains altering plagioclase cores. However, larger subhedral grains (most ~0.5 mm) also occur entwined with biotite; some are euhedral against K-feldspar and have small apatite needles parallel to cleavage traces, which suggest that they may be primary. A mild tendency is for interleaved muscovite and biotite to form short "trains" (2-3 mm) where flakes look to be aligned, although no preferred orientation exists overall.

SNAKE RIVER TONALITE

Derivation of name: Numerous Tiger Snakes at the type locality

Classification: Early syn-compressional, Wando type

Type exposure: Wando River, WD407560 (Edenhope 7123)

Geological context: Intrudes Wando Tonalite to the south and amphibolite facies schists to the north in the Wando River and Boundary Creek; shearing and hydrothermal alteration occur along both contacts. Does not extend west of the Casterton-Edenhope Road. The southeastern margin is complicated by the crosscutting Meissen Granodiorite and Blair Atholl Adamellite plutons.

Description of type sample, 97-159:

Medium to coarse grained, dark blue-grey in colour, and contains abundant bladed hornblende prisms (up to 7 mm long). A foliation is strongly developed, defined by flattened aggregates of biotite and

parallelled by large bluish-grey plagioclase laths (up to 5 mm). Foliation surfaces are lined by ragged poikilitic scales of biotite (3-10 mm across). A lineation of aligned hornblende blades, epidote spindles and elongate biotite clots (5-6 mm long) is also evident, though many hornblende blades are intergrown and oblique to this fabric.

Plagioclase in thin section occurs as subhedral to anhedral laths and blocky prisms (~1-1.5 mm), commonly with sharp oscillatory zoning outwards from complexly mottled calcic cores. Laths form complexly intergrown clumps that exhibit crystal faces where projecting into biotite and (more rarely) hornblende, but have serrate boundaries against quartz. A weak preferred orientation exists, and internal deformation features are minor. Quartz forms elongate consertal masses (~1.5 mm, to 3 mm) between plagioclase, with constituent grains having markedly undulose extinction, sometimes with subgrain development. Ragged elongate grains or subhedral blades of hornblende (most ~1.5-2 mm; α=pale yellow green β=dark brown green γ=deep blue green) are moderately aligned and form interlocking elongate aggregates with biotite flakes, or occur as part of diffuse mafic concentrations (3-10 mm long) with interleaved biotite (~1 mm), subhedral epidote prisms (0.5mm), small titanite crystals. Apart from being a prominent constituent of mafic clots, biotite (α=tan β=γ=dark brown) also occurs as large distorted plates (2-4 mm) that host inclusions of plagioclase, quartz and skeletal titanite grains, and occur as part of discrete trains of smaller foliated biotite flakes. These large biotite plates have markedly undulose extinction and exhibit incipient recrystallisation into smaller grains. Clusters of magnetite crystals (~0.5 mm) are also associated with mafic mineral concentrations. Metamict allanite grains (0.5 mm) fringed by epidote and interstitial carbonate masses are also observed.

Important lithological variants

Samples from eastern Elbow Creek (e.g. **97-214**) are slightly more felsic. Although the intrinsic mafic and plagioclase-rich nature of the tonalite is retained, samples have conspicuous masses of quartz and interstitial pools of recrystallised alkali feldspar (up to 1 mm across), with an overall lower proportion of hornblende prisms. Outcrops are also more strained, such that mafic aggregates are flattened into elongate foliation strands, which anastomose around lenticular domains of smeared quartz and strongly aligned plagioclase laths.

Other features

A 120 m wide zone of intense shearing occurs towards the Snake River Tonalite-Wando Tonalite contact in the Wando River, where a fine grained and pale coloured ultramylonitic rock with retrogressive mineralogy is developed. This intensely foliated lithology is chalky with abundant ragged muscovite flakes in a matrix of fine grained white mica, chlorite and quartz, but encloses coarser grained, less sheared domains where the original tonalitic character is recognisable. Here, plagioclase and hornblende porphyroclasts indicate a northeast over southwest shear sense, though as the mylonitic fabric is very steeply dipping, a more vertical transport direction is implied. Since the mylonitic foliation parallels S_2, the shear zone was probably initiated as metamorphic temperatures waned in the latter stages of D_2, where localisation of shearing was accompanied by channellised fluid flow.

Partitioning of D_2 shear strain also occurred towards the northern boundary of the Snake River Tonalite with metasedimentary rocks. In upper Boundary Creek, marginal tonalite exposures are recrystallised to a finer grainsize, where hornblende and biotite are 'smeared' into elongate microcrystalline masses, and net-veined by alkali feldspar-quartz laminae. Quartzofeldspathic schist at the contact contains intensely boudinaged and asymmetrically-sheared pegmatite and quartz veins, suggesting a northeast over southwest sense of shear. Further east, in the Wando River, Snake River Tonalite is deeply weathered with a 'chalky' clay-rich aspect, reflecting hydrothermal alteration. Weathered tonalite is separated from *in situ* migmatitic quartzofeldspathic schist by ~100m, that has abundant secondary muscovite porphyroblasts, and appears to have experienced retrograde shearing.

TULOONA GRANODIORITE

Derivation of name: Property of 'Tuloona' (Kemp & Gray 1999)

Classification: Late syn-compressional, Tuloona type

Type exposure: Schofield Creek, WD570791 (Balmoral 7223)

Geological context: Elongate pluton that extends southeast from the Glenelg River valley south of Harrow, where it crosscuts the Kout Norien Granodiorite, to Schofield Creek, where it is transitional to muscovite leucogranite and migmatite.

Description of type sample, T2-135:

Medium to coarse grained grey coloured rock with a pristine igneous texture. Phenocrysts of quartz (to 8 mm) and tabular poikilitic microcline (3x1 cm) are striking features, the latter containing sparse euhedral plagioclase, quartz, biotite and muscovite crystals. In thin section, well-shaped plagioclase laths are complexly twinned and strongly zoned, with euhedral calcic cores. Interstices between laths are occupied by alkali feldspar, against which quartz phenocrysts have crystal faces. Disseminated dark greenish-brown biotite (to 2.5 mm, interstitial to plagioclase laths) and subordinate muscovite (up to 2 mm plates) are non-aligned, commonly forming small clots (3-5 mm) with magnetite (to 0.5 mm) and apatite granules. Ragged secondary muscovite flakes also occur and irregular epidote masses are common where biotite is replaced by chlorite.

WANDO TONALITE

Derivation of name: Wando River (Anderson 1990)

Classification: Early syn-compressional, Wando type

Type exposure: Wando River WD404557 (Edenhope 7123)

Geological context: Curved lenticular pluton aligned parallel to the S_2 foliation in adjacent metasedimentary rocks. Borders (and partly interleaved with) amphibolite facies schists to the south in the Wando River and Boundary Creek, and abuts the Snake River Tonalite to the north.

Description of type sample, 97-161:

Brownish-grey and fine- to -medium grained. Has a strong gneissic foliation, defined primarily by tiny flakes of biotite and smeared biotite+hornblende clots (1-3 cm), but also parallelled by flattened quartz masses. Larger ragged biotite scales (2-3 mm) are prominent on foliation surfaces. Hornblende prisms (rarely to 5 mm), yellow-brown epidote spindles and lenticular biotite clots are also strongly aligned, especially conspicuous in marginal exposures.

In thin section, the foliation occurs as semi-continuous strands (0.5-1 mm wide) of concentrated mafic minerals that anastomose around lenticular domains of predominantly quartz and plagioclase (1-20 mm). Within the latter, plagioclase (0.8-1 mm, up to 2 mm) is most common as elongate lath-like grains that are anhedral, with numerous re-entrants of quartz subgrains and alkali feldspar blebs. Albite and Carlsbad twinning is generally sharp, and fine oscillatory zoning outwards from euhedral cores is evident in many grains. Laths exhibit moderate alignment with the foliation but strong internal strain features, such as kinked twin planes and shear bands, suggest that the alignment is tectonic rather than magmatic. Deformation features are especially conspicuous in some larger grains lying oblique to the fabric; these are wrapped by biotite folia and have pressure shadows of recrystallised quartz and smaller plagioclase grains. Quartz occurs as flattened masses (1-8 mm long) of small interdigitating grains (0.25-0.5 mm), with occasional larger grains that have strongly undulose extinction or deformation lamellae parallel to their length. Boundaries between larger grains are commonly lined by tiny subgrains. Highly irregular grains of alkali feldspar occur with quartz (~0.3 mm) and exhibit internal polygonisation. They also form serrate embayments into plagioclase laths.

Foliation domains consist primarily of aligned sheaves of biotite, with lesser hornblende, epidote, and trails of small plagioclase laths; they periodically widen into smeared biotite-hornblende clots and may envelope discrete larger plagioclase grains. Biotite (α=pale tan β=greenish brown γ=dark brown) occurs as small flakes (~0.5mm) or larger ragged masses (to 2 mm) with irregularly-shaped plagioclase inclusions. The larger grains occur mostly in clotty aggregates with hornblende and commonly exhibit distorted cleavage traces. Blades or anhedral grains of hornblende (0.5-2 mm; α=yellow green β=olive green γ=pale bluish green) are cracked and sieved by tiny quartz grains and strongly aligned with foliated biotite. The largest grains (anhedral masses to 3 mm) are found in biotite clots, where they appear to be replaced by biotite along cracks. Subhedral granules of epidote embedded in biotite (~0.5 mm; sometimes euhedral and simply twinned) are most prominent in mafic clots, elsewhere forming conspicuous anhedral quartz-sieved masses (to 1 mm) in biotite folia. Orange-brown titanite (up to 1.5 mm) and metamict allanite prisms are less common accessories, and also concentrated in foliation strands.

WARRADALE TONALITE

Derivation of name: Property of 'Warradale' (Bushell 1996).

Classification: Early syn-compressional, Wennicott type

Type exposures: Wennicott Creek, WD514430 (Coleraine 7222)

Geological context: Outcrops conspicuously for ~500m along Wennicott Creek. Contacts are unexposed, though quartzofeldspathic schist enclaves at the margins suggest enclosure by metasedimentary rocks.

Description of type sample, 97-WA1:

Dark blue-grey, medium to coarse grained and equigranular, comprising essentially coarse hornblende blades (up to 7 mm) and greenish aggregates of plagioclase laths, with lesser cloudy grey quartz, biotite and K-feldspar. Large black allanite prisms (up to 5 mm) are conspicuous and small blebs of deep reddish-brown titanite are apparent. The rock has a prominent foliation (S_2) defined by biotite and hornblende, with the latter also strongly lineated.

In thin section, subhedral hornblende prisms (α=pale olive green β=dark brown green γ=deep blue green) enclose small plagioclase laths, biotite plates and small drop-like quartz grains. Some larger hornblende blades also have noticeably lighter coloured central parts that are densely perforated with tiny quartz inclusions; as evident from mafic igneous enclaves, these areas represent pseudomorphed clinopyroxene grains, and thus many of the large hornblende crystals may have formed by magmatic replacement or overgrowth of original clinopyroxene. Hornblende commonly occurs as groups of several grains or with large plates of biotite. Several clots of hornblende and lesser biotite (~5 mm) are also evident and, significantly, at the centre of these aggregates are rectangular areas (~1.5 mm) of honeycomb-like intergrowths of quartz and hornblende, that also probably represent former clinopyroxene crystals. Biotite (α=pale tan β=γ=dark reddish brown) predominantly occurs as coarse subhedral plates in mafic clots (1.5-2 mm) or interleaved aggregates associated with hornblende. Disseminated flakes are more ragged and enclose plagioclase, quartz and numerous stubby apatite prisms. Alteration to chlorite and dirty yellow-green epidote is prominent. Large subhedral laths and blocky grains of plagioclase (1-1.5 mm, up to 3 mm long) also form clumps that project into biotite and interstitial pools of microcline. Plagioclase laths may be intergrown, but most commonly grain boundaries are polygonal due to mutual interference during crystallisation. Albite twinning is sharp but only weak continuous and mottled zoning is apparent. Laths exhibit a conspicuous preferred orientation parallel to hornblende blades and are sometimes cracked, with distorted twin planes and mechanical twinning. Irregularly shaped consertal quartz masses (~2 mm across) or single grains (0.5-1 mm) occur between hornblende and plagioclase and have weak undulose extinction. Some large crystals of pleochroic orange-brown titanite (1-1.5 mm) are prominent in hornblendic clots, with irregular blebs of secondary titanite concentrated in chloritised biotite. Unusual clusters of skeletal titanite occur in some thin sections. Rare pyrite grains are also encountered.

Important lithological variants:

Finer grained, more felsic tonalitic material outcrops towards the centre of the pluton. Samples (**97-WA2**) are bluish grey, but richer in biotite, such that hornblende is modally subordinate, and quartz is significantly more abundant, imparting a 'sugary' aspect. A distinct foliation of disseminated flakes and small interleaved clots of biotite is apparent and large allanite grains occur. The foliation in thin section is augmented by flattened masses of quartz (up to 3.5 mm) and semi-aligned plagioclase laths, many of which have warped albite twin planes. Hornblende occurs as more ragged single prisms surrounded by, and enclosing, ragged flakes of biotite. Some large strikingly poikilitic plates of the latter are also evident, enclosing numerous small plagioclase crystals. No alkali feldspar occurs, but ilmenite grains are common (~0.5 mm) and concentrated in biotite aggregates.

Other features:

Also conspicuous in the Warradale Tonalite is a band within which concentrated schlieren and elongate hornblende selvedges define a layering, parallelled by elongate enclaves. This band is traced for about 150 m and varies from a diffuse, ~80 cm thick zone in southern outcrops to discrete domains (0.5 m wide) where mafic enclaves are strongly attenuated. In the southern part of the body the layering within the banded zone has a wavy, almost meandering geometry that anastomoses around large metaquartzite enclaves (15-30 cm long), of similar nature to *in situ* metaquartzite horizons outcropping further north in Wennicott Creek. Smaller metaquartzite enclaves form lenticular slivers elongated parallel to the

layering, and enveloped by hornblende-biotite schlieren. Significantly, tonalite from within layered domains is very heterogeneous, but generally coarser grained and more felsic than typical exposures. These features suggest that the banding represents a domain of concentrated magmatic flow, with magmatic shearing responsible for rotation, fragmentation and attenuation of metaquartzite and microgranular enclaves.

WENNICOTT TONALITE

Derivation of name: Wennicott Creek (Bushell 1996)

Classification: Early syn-compressional, Wennicott type

Type exposures: Wennicott Creek, WD523466 (Coleraine 7222)

Geological context: Intrudes migmatitic metasedimentary rocks to the west and truncated by garnet adamellite to the south; borders Jurassic trachyte to the north

Description of type sample, 97-227B:

Bluish-grey, medium equigranular, and dominated by coarse interlocking plagioclase laths (up to 4 mm, most 1.5-2 mm) occasionally oriented subparallel to a distinct biotite foliation. Biotite forms individual ragged flakes up to 4 mm, but is mostly present as smaller grains, rarely in clotted aggregates. Grey quartz grains (~1 mm) and larger slightly smoky coloured masses (3-4 mm) are conspicuous. Plagioclase in thin section is anhedral to subhedral, with cuspate boundaries and embayments against quartz, and forms intergrown clumps. Diffuse oscillatory zoning is present in many laths, and occasional bent twin planes in smaller grains is the only manifestation of deformation. Similarly, most quartz is unstrained, and forms a mosaic of irregularly shaped consertal grains (~1.5 mm) around clumped plagioclase, or lenticular polycrystalline aggregates (2-4 mm). Biotite (α=tan β=γ=darkest chocolate brown) occurs as small trains (2-5 mm long) of aligned plates (0.5-1 mm), interleaved grains concentrated at plagioclase grain boundaries, or individual plates with a moderate preferred orientation. Subhedral epidote granules are sometimes enclosed by larger biotite plates.

Lithological variants and other features

Intimately associated with Wennicott Tonalite are patches of coarse grained leucocratic material containing large orange-tan coloured alkali feldspar plates (5-12 mm across) and greenish-white plagioclase laths (~5 mm) with lesser quartz and disseminated biotite grains; the latter also forms large frayed flakes (~4-10 mm). The Wennicott Tonalite is coarser grained and alkali-feldspar-bearing in the vicinity of this pegmatite-like rock, and appears to grade into it with increasing grainsize and diminishing biotite content. The coarser leucocratic phase itself encloses elongate lenses of true pegmatite (5-20 cm long), with graphic alkali feldspar megacrysts and tiny reddish-coloured garnets.

Wennicott Tonalite outcrops are also crosscut by thin (2-50 cm) high strain zones, where the tonalite has a strong gneissic aspect and mafic enclaves are highly attenuated. In proximity to these zones are several branching sheets of coarse grained hornblende-rich rock that change dramatically in thickness along their length, from swelled areas (~10 cm wide) to thinner parts (~2 cm). Although most are sub-parallel to high strain zones they are offset and sheared where they intersect the zones. Fresh material has stubby hornblende prisms (to 4 mm) and coarse plagioclase laths (most ~3-4 mm) enveloped by irregularly shaped alkali feldspar (1-4 mm across). Rounded quartz clumps (1-3 mm) are conspicuous but biotite is absent.

APPENDIX F

Table F.1:

Mineral composition of rocks from the Caupaul Igneous Complex, hornblende-bearing lithologies of Chin Chap Creek and the various metaluminous to weakly peraluminous granitic types referred to in Part III.

Mineral compositions are given in weight percent oxide. Cation fractions were calculated on the basis of-

feldspars- 32 oxygen atoms
pyroxenes-24 oxygen atoms
amphiboles-24 oxygen atoms
micas-22 oxygen atoms

Rock	98-CP129 Gabbronorite																												
Mineral	opx A rim	opx A core	opx B rim	opx B core	opx core	opx rim	opxA core	opx A rim	opx B core	opx B rim	opx rim	opx core	opx rim	cpx A rim	cpx B rim	cpx C rim	cpx core	cpx rim	cpx core	cpx rim	cpx A rim	cpx B rim	cpx C rim	plag A core	plag A core	plag rim	plag core	plag core	plag rim
Spot	1.1	1.2	1.3	1.4	2.1	2.2	3.1	3.2	3.5	3.6	4.4	5.1	5.2	1.5	1.6	1.7	2.3	2.4	3.3	3.4	4.1	4.2	4.3	1.8	1.9	1.10	3.7	3.8	3.9
Na2O	0.08	0.12	0.17	0.22	0.19	0.23	0.26	0.19	0.15	0.06	0.15	0.19	0.15	0.50	0.40	0.37	0.59	0.38	0.56	0.42	0.38	0.46	0.44	5.37	1.82	5.68	5.26	1.92	5.85
MgO	20.56	20.39	20.40	20.81	20.63	20.65	20.67	20.93	20.38	20.35	20.69	21.13	20.74	13.01	12.62	12.90	12.93	12.69	12.86	12.90	13.06	12.63	13.05	0.00	0.05	0.03	0.01	0.04	0.06
Al2O3	1.04	1.07	0.91	0.98	0.93	0.83	0.72	0.89	0.82	1.04	1.08	0.93	0.86	1.65	1.83	1.77	1.71	1.73	1.70	1.85	1.75	1.71	1.81	28.04	33.67	27.83	27.97	33.18	27.49
SiO2	53.06	52.78	53.21	53.35	53.04	53.03	52.96	53.25	53.29	53.11	53.80	53.40	53.32	52.84	52.72	52.70	52.46	53.12	52.42	52.51	52.91	52.85	53.12	56.10	47.52	57.05	54.96	47.70	56.73
K2O	0.02	0.03	0.05	0.01	0.00	0.04	0.00	0.00	0.00	0.00	0.00	0.00	0.00	0.00	0.00	0.00	0.05	0.04	0.00	0.00	0.00	0.00	0.00	0.22	0.05	0.25	0.25	0.11	0.17
CaO	0.94	0.82	1.07	0.60	0.77	0.93	0.53	0.76	0.78	0.84	1.69	0.71	0.60	22.01	21.86	21.52	21.85	21.79	20.69	21.73	21.22	21.87	21.33	10.60	16.86	9.78	10.67	16.47	9.62
TiO2	0.08	0.21	0.05	0.02	0.00	0.06	0.05	0.06	0.07	0.10	0.18	0.23	0.11	0.17	0.29	0.30	0.35	0.31	0.23	0.30	0.32	0.21	0.42	0.08	0.03	0.00	0.00	0.00	0.02
MnO	0.87	0.73	0.71	0.50	0.80	0.76	0.55	0.84	0.93	0.68	0.82	0.75	0.61	0.52	0.33	0.36	0.42	0.37	0.50	0.44	0.37	0.25	0.33	0.00	0.00	0.00	0.02	0.00	0.00
FeO	23.00	23.14	22.75	23.34	23.26	22.67	23.76	22.75	23.26	23.43	23.04	23.03	22.87	9.63	9.52	10.00	9.74	9.99	10.27	10.21	10.56	10.12	10.18	0.33	0.32	0.29	0.28	0.35	0.31
TOTAL	99.65	99.29	99.32	99.83	99.62	99.20	99.50	99.67	99.68	99.61	101.45	100.37	99.26	100.33	99.57	99.92	100.10	100.42	99.23	100.36	100.57	100.10	100.68	100.74	100.32	100.91	99.42	99.77	100.25
Na	0.023	0.035	0.05	0.064	0.055	0.067	0.076	0.055	0.044	0.017	0.043	0.055	0.044	0.145	0.116	0.107	0.171	0.110	0.164	0.122	0.11	0.133	0.127	1.863	0.646	1.961	1.851	0.685	2.033
Mg	4.602	4.583	4.575	4.644	4.623	4.638	4.643	4.676	4.564	4.559	4.553	4.691	4.646	2.894	2.822	2.879	2.886	2.818	2.891	2.874	2.899	2.816	2.888	0	0.014	0.008	0.003	0.011	0.016
Al	0.184	0.19	0.161	0.173	0.165	0.147	0.128	0.157	0.145	0.184	0.188	0.163	0.152	0.290	0.324	0.312	0.302	0.304	0.302	0.326	0.307	0.302	0.317	5.913	7.265	5.841	5.984	7.194	5.809
Si	7.969	7.96	8.008	7.988	7.975	7.992	7.982	7.983	8.007	7.983	7.944	7.954	8.015	7.886	7.909	7.891	7.856	7.914	7.908	7.849	7.882	7.907	7.889	10.035	8.698	10.156	9.973	8.772	10.168
K	0.004	0.006	0.01	0.002	0	0.008	0	0	0	0	0	0	0	0	0	0	0.010	0.008	0	0	0	0	0	0.05	0.012	0.057	0.058	0.026	0.039
Ca	0.151	0.133	0.173	0.096	0.124	0.150	0.086	0.122	0.126	0.135	0.267	0.113	0.097	3.520	3.514	3.453	3.506	3.479	3.345	3.48	3.387	3.506	3.394	2.032	3.307	1.866	2.075	3.245	1.847
Ti	0.009	0.024	0.006	0.002	0	0.007	0.006	0.007	0.008	0.011	0.02	0.026	0.012	0.019	0.033	0.034	0.039	0.035	0.026	0.034	0.036	0.024	0.047	0.011	0.004	0	0	0	0.003
Mn	0.111	0.093	0.091	0.063	0.102	0.097	0.07	0.107	0.118	0.087	0.103	0.095	0.078	0.066	0.042	0.046	0.053	0.047	0.064	0.056	0.047	0.032	0.042	0	0	0	0.003	0	0
Fe	2.889	2.919	2.863	2.923	2.925	2.857	2.995	2.852	2.923	2.945	2.845	2.869	2.875	1.202	1.194	1.252	1.22	1.245	1.296	1.276	1.316	1.266	1.264	0.049	0.049	0.043	0.042	0.054	0.046
Cat sum	15.943	15.942	15.936	15.956	15.97	15.965	15.986	15.959	15.934	15.922	15.963	15.966	15.919	16.022	15.954	15.973	16.044	15.958	15.996	16.016	15.984	15.985	15.969	19.954	19.994	19.932	19.989	19.986	19.961
Mg#	0.6143	0.6109	0.6151	0.6137	0.6125	0.6188	0.6079	0.6211	0.6096	0.6075	0.6154	0.6205	0.6177	0.7065	0.7027	0.6969	0.7029	0.6936	0.6905	0.6925	0.6878	0.6899	0.6956						
An%																								52.17	83.66	48.76	52.85	82.57	47.60

Rock				98-CP7 Quartz diorite																									
Mineral	plag core	plag core	plag rim		opx A core	opx A rim	opx B rim	opx A rim	opx B core	opx B rim	opx rim	opx	opx	cpx rim	cpx core	cpx rim	cpx core	cpx rim	cpx A core	cpx A rim	cpx B rim	cpx rim	cpx A rim	cpx B rim	cpx rim	plag core	plag core	plag rim	plag core
Spot	6.1	6.2	6.3		1.1	1.2	1.3	3.3	3.4	3.5	4.1	5.4	6.3	1.4	2.1	2.2	3.1	3.2	4.2	4.3	4.4	5.3	6.1	6.2	6.4	2.3	2.4	2.5	5.1
Na2O	4.03	5.07	5.28		0.11	0.15	0.1	0.15	0.15	0.26	0.18	0.19	0.17	0.52	0.43	0.5	0.43	0.49	0.52	0.35	0.4	0.42	0.47	0.41	0.47	4.54	3.77	5.93	2.97
MgO	0.12	0.05	0.02		19.35	19.45	19.71	19.84	19.43	18.96	19.57	19.26	19.81	12.48	12.7	12.49	12.73	12.95	12.59	12.55	12.58	12.58	12.96	12.67	12.6	0.08	0.09	0.03	0.02
Al2O3	30.50	29.00	28.38		1.42	1.05	0.85	0.92	0.97	0.93	1.1	0.91	0.73	1.6	2.73	1.83	1.7	1.66	2.81	1.83	1.78	1.77	1.46	1.56	1.84	29.2	30.23	26.87	31.41
SiO2	52.20	55.09	55.49		52.7	53.17	52.8	52.51	52.7	52.96	53.07	52.96	52.63	52.89	51.59	52.09	51.92	52.86	52.13	52.63	52.85	52.69	53.16	53.02	52.74	53.27	51.52	57.56	50.37
K2O	0.07	0.15	0.22		0.01	0.05	0.02	0.02	0.03	0	0.09	0.01	0	0	0	0	0	0	0.03	0.36	0	0	0.01	0	0.01	0	0.2	0.19	0.31	0.19
CaO	13.26	11.40	10.62		0.91	0.8	0.88	0.72	1.04	3.09	0.78	0.8	0.83	21.42	19.86	21.45	20.72	20.46	21.11	21.23	21.04	21.55	21.21	20.97	21.43	12.1	13.42	9.48	14.8
TiO2	0.03	0.00	0.00		0.13	0.11	0.11	0.04	0.21	0.16	0.19	0.15	0.09	0.25	0.23	0.3	0.46	0.11	0.77	0.34	0.47	0.28	0.16	0.39	0.42	0.08	0.06	0.08	0
MnO	0.00	0.00	0.13		0.59	0.59	0.53	0.74	0.8	0.64	0.61	0.47	0.63	0.35	0.32	0.34	0.41	0.35	0.25	0.19	0.26	0.27	0.2	0.21	0.3	0.15	0	0.06	0
FeO	0.30	0.27	0.31		25.1	24.52	24.39	24.56	24.93	22.99	24.62	25.01	24.23	10.74	11.82	10.59	11.14	11.69	10.38	10.89	11.28	10.32	10.75	11.74	10.68	0.26	0.45	0.08	0.37
TOTAL	100.51	101.03	100.45		100.32	99.89	99.39	99.5	100.26	99.99	100.21	99.76	99.12	100.25	99.68	99.59	99.51	100.6	100.92	100.01	100.66	99.89	100.37	100.98	100.48	99.88	99.73	100.4	100.13
Na	1.413	1.758	1.838		0.032	0.044	0.029	0.044	0.044	0.076	0.052	0.056	0.05	0.151	0.126	0.146	0.126	0.142	0.15	0.102	0.116	0.122	0.136	0.118	0.136	1.598	1.335	2.055	1.05
Mg	0.032	0.013	0.005		4.339	4.365	4.447	4.481	4.366	4.255	4.383	4.338	4.483	2.784	2.855	2.808	2.867	2.884	2.79	2.804	2.797	2.811	2.883	2.812	2.804	0.022	0.024	0.008	0.005
Al	6.502	6.112	6.008		0.252	0.186	0.152	0.164	0.172	0.165	0.195	0.162	0.131	0.282	0.485	0.325	0.303	0.292	0.493	0.323	0.313	0.313	0.257	0.274	0.324	6.25	6.507	5.662	6.753
Si	9.439	9.849	9.964		7.929	8.006	7.993	7.957	7.945	7.974	7.975	8.003	7.991	7.918	7.781	7.858	7.847	7.899	7.752	7.891	7.884	7.901	7.934	7.897	7.874	9.671	9.407	10.289	9.185
K	0.016	0.034	0.05		0.002	0.01	0.004	0.004	0.006	0	0.017	0.002	0	0	0	0	0	0.006	0.068	0	0	0.002	0	0.002	0	0.046	0.044	0.071	0.044
Ca	2.569	2.184	2.043		0.147	0.129	0.143	0.117	0.168	0.499	0.126	0.13	0.135	3.436	3.209	3.467	3.356	3.276	3.364	3.411	3.363	3.463	3.392	3.347	3.428	2.354	2.626	1.816	2.892
Ti	0.004	0	0		0.015	0.012	0.013	0.005	0.024	0.018	0.021	0.017	0.01	0.028	0.026	0.034	0.052	0.012	0.086	0.038	0.053	0.032	0.018	0.044	0.047	0.011	0.008	0.011	0
Mn	0	0	0.02		0.075	0.075	0.068	0.095	0.102	0.082	0.078	0.06	0.081	0.044	0.041	0.043	0.052	0.044	0.031	0.024	0.033	0.034	0.025	0.026	0.038	0.023	0	0.009	0
Fe	0.045	0.04	0.047		3.158	3.088	3.088	3.113	3.143	2.895	3.094	3.161	3.077	1.345	1.491	1.336	1.408	1.461	1.291	1.366	1.407	1.294	1.342	1.462	1.334	0.039	0.069	0.012	0.056
Cat sum	20.021	19.991	19.976		15.948	15.915	15.935	15.98	15.97	15.963	15.941	15.928	15.958	15.988	16.013	16.018	16.012	16.016	16.025	15.96	15.965	15.973	15.987	15.983	15.985	20.015	20.02	19.932	19.986
Mg#					0.5788	0.5857	0.5902	0.5901	0.5814	0.5951	0.5862	0.5785	0.5930	0.6743	0.6569	0.6776	0.6706	0.6638	0.6837	0.6724	0.6653	0.6848	0.6824	0.6579	0.6776				
An%	64.52	55.40	52.64																							59.56	66.30	46.91	73.36

Rock	98-CP7 Quartz diorite									98-CP1 quartz diorite																		
Mineral	plag core	plag A cor	plag A cor	plag A rim	plag B cor	plag B cor	plag B rim	bio		opx A core	opx A rim	opx B (rim	opx A core	opx B	opx C	opx	cpx A core	cpx A rim	cpx B core	cpx B rim	cpx A rim	cpx B rim	cpx C core	cpx C rim	cpx A core	cpx A rim	plag core	plag rim	plag rim
Spot	5.2	7.1	7.2	7.3	7.4	7.5	7.6	6.5		1.1	1.2	1.5	2.1	2.3	2.4	3.5	1.3	1.4	1.6	1.7	3.1	3.2	3.3	3.4	4.1	4.2	2.5	2.6	2.7
Na2O	4.26	4.66	5.02	5.86	4.2	5.53	5.74	0.02		0.00	0.00	0.00	0.00	0.00	0.00	0.00	0.45	0.35	0.46	0.46	0.40	0.46	0.50	0.45	0.38	0.53	2.37	5.20	3.85
MgO	0	0	0.08	0.11	0.05	0.02	0.03	11.38		21.06	21.03	20.83	20.78	20.51	21.12	20.89	13.99	13.97	14.06	14.36	13.32	13.39	13.59	13.52	14.92	13.64	0.00	0.00	0.00
Al2O3	29.69	28.99	28.46	27.04	30.22	27.64	27.28	13.6		0.90	1.05	1.00	1.46	1.09	0.88	0.84	2.05	2.48	2.07	2.08	1.59	1.72	1.75	1.71	2.10	2.15	33.13	28.52	31.02
SiO2	53.3	54.67	55.09	57.18	53.84	56.55	56.86	37.08		52.93	52.37	53.07	52.52	52.38	52.98	52.93	52.29	51.75	52.21	52.32	52.66	52.60	52.77	52.43	52.47	52.27	49.01	54.89	51.84
K2O	0.19	0.33	0.25	0.4	0.22	0.38	0.35	9.02		0.00	0.00	0.00	0.00	0.00	0.00	0.00	0.00	0.00	0.00	0.00	0.00	0.00	0.00	0.00	0.00	0.00	0.00	0.33	0.19
CaO	12.25	11.72	10.66	9.56	12.55	9.95	9.61	0.18		0.81	0.88	0.86	0.85	1.79	0.84	0.93	21.22	19.11	20.26	21.36	21.42	22.00	20.59	21.23	21.03	21.32	16.03	11.04	13.62
TiO2	0	0	0.11	0	0.06	0.04	0.01	5.01		0.00	0.00	0.00	0.35	0.00	0.00	0.00	0.28	0.50	0.00	0.31	0.30	0.35	0.25	0.33	0.45	0.42	0.00	0.00	0.00
MnO	0.06	0	0.02	0.02	0	0	0	0.08		0.66	0.71	0.49	0.49	0.50	0.61	0.63	0.00	0.00	0.00	0.00	0.33	0.36	0.29	0.34	0.00	0.30	0.00	0.00	0.00
FeO	0.11	0.36	0.25	0.16	0.39	0.24	0.22	17.75		23.88	23.72	24.59	24.28	23.45	24.25	23.99	9.42	12.00	10.94	9.01	10.97	9.80	10.83	10.42	9.23	10.09	0.00	0.00	0.00
TOTAL	99.86	100.73	99.94	100.33	101.53	100.35	100.1	94.12		100.53	100.11	100.90	100.87	100.00	100.82	100.48	100.39	100.44	100.87	100.05	101.14	100.64	100.55	100.45	101.00	100.62	100.54	99.98	100.52
Na	1.497	1.623	1.755	2.035	1.454	1.922	1.998	0.006		0.00	0.00	0.00	0.00	0.00	0.00	0.00	0.13	0.10	0.13	0.13	0.12	0.13	0.14	0.13	0.11	0.15	0.83	1.82	1.35
Mg	0	0	0.021	0.029	0.013	0.005	0.008	2.599		4.69	4.71	4.63	4.62	4.60	4.70	4.66	3.10	3.11	3.12	3.19	2.95	2.97	3.02	3.01	3.28	3.02	0.00	0.00	0.00
Al	6.342	6.138	6.05	5.709	6.359	5.841	5.772	2.457		0.16	0.19	0.18	0.26	0.19	0.15	0.15	0.36	0.44	0.36	0.37	0.28	0.30	0.31	0.30	0.36	0.38	7.10	6.07	6.61
Si	9.657	9.818	9.934	10.241	9.61	10.136	10.205	5.681		7.91	7.87	7.92	7.83	7.88	7.90	7.92	7.78	7.73	7.76	7.79	7.83	7.83	7.86	7.83	7.74	7.78	8.91	9.91	9.37
K	0.044	0.076	0.058	0.091	0.05	0.087	0.08	1.763		0.00	0.00	0.00	0.00	0.00	0.00	0.00	0.00	0.00	0.00	0.00	0.00	0.00	0.00	0.00	0.00	0.00	0.00	0.08	0.04
Ca	2.378	2.255	2.06	1.835	2.4	1.911	1.848	0.03		0.13	0.14	0.14	0.14	0.29	0.13	0.15	3.38	3.06	3.23	3.41	3.41	3.51	3.29	3.40	3.32	3.40	3.12	2.13	2.64
Ti	0	0	0.015	0	0.008	0.005	0.001	0.577		0.00	0.00	0.00	0.04	0.00	0.00	0.00	0.03	0.06	0.00	0.03	0.03	0.04	0.03	0.04	0.05	0.05	0.00	0.00	0.00
Mn	0.009	0	0.003	0.003	0	0	0	0.01		0.08	0.09	0.06	0.06	0.06	0.08	0.08	0.00	0.00	0.00	0.00	0.04	0.05	0.04	0.04	0.00	0.04	0.00	0.00	0.00
Fe	0.017	0.054	0.038	0.024	0.058	0.036	0.033	2.275		2.98	2.98	3.07	3.03	2.95	3.02	3.00	1.17	1.50	1.36	1.12	1.36	1.22	1.35	1.30	1.14	1.26	0.00	0.00	0.00
Cat sum	19.943	19.963	19.933	19.968	19.954	19.943	19.946	15.398		16.01	16.04	16.00	16.01	16.03	16.01	16.02	16.04	16.04	16.07	16.05	16.04	16.04	16.02	16.04	16.06	16.08	19.96	20.01	20.01
Mg#								0.5332		0.6115	0.6125	0.6013	0.6039	0.6093	0.6088	0.6084	0.7260	0.6746	0.6964	0.7401	0.6845	0.7088	0.6911	0.6984	0.7421	0.7056			
An%	61.37	58.15	54.00	47.42	62.27	49.86	48.05																				78.99	52.85	65.51

Rock	98-CP1 quartz diorite									Quartz diorite 11904																			
Mineral	plag rim	plag core	plag rim	plag rim	plag rim	plag core	plag core	plag rim		cpx A core	cpx A rim	cpx B core	cpx B rim	cpx C rim	cpx rim	cpx core	cpx rim	cpx rim	cpx core	cpx rim	cpx B core	cpx B rim	cpx	opx core	opx rim	px (cpx)	opx (cpx cor	opx core	
Spot	2.8	5.1	5.2	5.3	5.4	6.1	6.3	6.4		1.1	1.2	1.3	1.4	1.5	2.2	3.1	3.2	4.2	5.1	5.2	5.3	5.4	6.3	1.6	1.7	2.1	2.6	2.3	
Na2O	5.86	2.02	5.11	3.17	5.15	4.10	2.25	4.76		0.51	0.51	0.51	0.57	0.53	0.52	0.55	0.49	0.50	0.38	0.44	0.50	0.47	0.50	0.22	0.26	0.00	0.23	0.18	
MgO	0.00	0.00	0.00	0.00	0.00	0.00	0.00	0.00		14.76	14.63	15.19	14.54	14.11	14.13	15.95	15.10	13.72	15.88	14.20	14.60	15.02	14.07	21.93	22.17	19.71	20.34	21.92	
Al2O3	27.55	33.66	28.67	32.00	28.47	30.69	33.50	29.30		2.77	2.04	2.97	2.24	1.73	2.52	2.00	1.77	2.00	2.56	2.24	2.27	2.27	1.63	1.27	1.00	1.39	1.34	1.38	
SiO2	56.63	47.45	55.24	50.14	55.01	52.48	48.11	54.41		52.28	52.81	51.97	52.61	53.04	52.02	52.64	51.66	52.00	52.27	52.32	52.47	52.46	52.42	53.40	53.15	52.22	52.21	52.64	
K2O	0.28	0.00	0.37	0.00	0.27	0.00	0.00	0.25		0.00	0.00	0.00	0.00	0.00	0.00	0.00	0.00	0.00	0.00	0.00	0.00	0.00	0.00	0.00	0.00	0.00	0.00	0.00	
CaO	9.74	16.49	10.74	14.68	10.89	12.93	16.18	11.32		19.98	19.39	17.84	19.78	21.49	19.18	21.39	19.38	21.64	18.73	20.93	19.86	18.77	21.92	1.53	0.85	0.59	0.55	0.99	
TiO2	0.00	0.00	0.00	0.00	0.00	0.00	0.00	0.00		0.27	0.42	0.52	0.30	0.29	0.83	0.37	0.75	0.54	0.43	0.30	0.49	0.37	0.30	0.27	0.25	0.00	0.00	0.00	
MnO	0.00	0.00	0.00	0.00	0.00	0.00	0.00	0.00		0.00	0.00	0.24	0.27	0.43	0.28	0.34	0.27	0.32	0.40	0.00	0.43	0.28	0.36	0.42	0.48	0.74	0.55	0.47	
FeO	0.00	0.40	0.30	0.00	0.00	0.00	0.32	0.00		9.34	10.96	11.77	10.43	9.69	11.06	6.69	9.94	9.15	9.59	9.20	10.10	10.96	8.79	22.49	23.09	26.08	24.94	22.92	
TOTAL	100.06	100.02	100.43	99.99	99.79	100.20	100.36	100.04		100.60	100.76	101.49	101.05	101.31	100.54	100.47	99.36	99.87	100.65	99.63	101.14	100.60	99.99	101.53	101.25	100.73	100.16	100.50	
Na	2.04	0.72	1.78	1.12	1.80	1.43	0.79	1.66		0.146	0.146	0.146	0.163	0.152	0.150	0.157	0.143	0.145	0.109	0.127	0.143	0.135	0.145	0.063	0.075	0.000	0.067	0.052	
Mg	0.00	0.00	0.00	0.00	0.00	0.00	0.00	0.00		3.251	3.228	3.337	3.203	3.104	3.132	3.497	3.378	3.060	3.492	3.159	3.213	3.319	3.130	4.808	4.884	4.424	4.569	4.864	
Al	5.83	7.28	6.07	6.86	6.05	6.53	7.21	6.22		0.483	0.356	0.516	0.390	0.301	0.442	0.347	0.313	0.353	0.445	0.394	0.395	0.397	0.287	0.220	0.174	0.247	0.238	0.242	
Si	10.17	8.71	9.92	9.12	9.93	9.47	8.79	9.80		7.726	7.819	7.660	7.776	7.828	7.738	7.745	7.756	7.781	7.712	7.811	7.748	7.779	7.825	7.855	7.856	7.865	7.869	7.838	
K	0.06	0.00	0.09	0.00	0.06	0.00	0.00	0.60		0.000	0.000	0.000	0.000	0.000	0.000	0.000	0.000	0.000	0.000	0.000	0.000	0.000	0.000	0.000	0.000	0.000	0.000	0.000	
Ca	1.87	3.24	2.07	2.86	2.11	2.50	3.17	2.18		3.164	3.076	2.817	3.133	3.398	3.057	3.372	3.118	3.470	2.961	3.348	3.142	2.982	3.506	0.241	0.135	0.095	0.089	0.158	
Ti	0.00	0.00	0.00	0.00	0.00	0.00	0.00	0.00		0.030	0.047	0.058	0.033	0.032	0.093	0.041	0.085	0.061	0.048	0.034	0.054	0.041	0.034	0.030	0.028	0.000	0.000	0.000	
Mn	0.00	0.00	0.00	0.00	0.00	0.00	0.00	0.00		0.000	0.000	0.030	0.034	0.054	0.035	0.042	0.034	0.041	0.050	0.000	0.054	0.035	0.046	0.052	0.060	0.094	0.070	0.059	
Fe	0.00	0.06	0.05	0.00	0.00	0.00	0.05	0.00		1.154	1.357	1.451	1.289	1.196	1.376	0.823	1.248	1.145	1.183	1.149	1.247	1.359	1.097	2.767	2.854	3.285	3.144	2.854	
Cat sum	19.97	20.01	19.98	19.96	19.95	19.93	20.01	20.46		16.035	16.030	16.070	16.059	16.065	16.023	16.088	16.074	16.054	16.048	16.022	16.047	16.049	16.070	16.036	16.066	16.011	16.046	16.067	
Mg#										0.7380	0.7040	0.6970	0.7130	0.7219	0.6948	0.8095	0.7302	0.7277	0.7470	0.7333	0.7204	0.7095	0.7405	0.6347	0.6312	0.5739	0.5924	0.6302	
An%	47.10	81.82	52.54	71.86	53.15	63.61	80.05	49.10																					

Rock	Quartz diorite 11904																			Ferres Ck Tonalite 98-CP12								
Mineral	opx rim	opx C	opx core	opx	opx A	opx B	plag core	plag rim	plag core	plag rim	plag A	plag B	plag core	plag rim	plag core	plag core	plag rim	K-felds		rel cpx	rel cpx	hbl A	hbl B	hbl A	hbl B	hbl C	hbl core	hbl rim	plag A rim
Spot	2.4	2.5	4.1	5.5	6.1	6.2	3.3	3.4	4.3	4.4	5.7	5.8	5.9	5.10	7.1	7.2	7.3	5.6		1.1	1.2	1.3	1.4	2.1	2.2	2.3	3.1	3.2	1.5
Na2O	0.00	0.00	0.33	0.20	0.00	0.00	4.19	6.35	4.41	6.58	4.67	6.22	4.15	6.58	4.78	4.34	6.29	1.27		0.45	0.55	1.19	1.20	1.22	1.29	1.39	1.38	1.31	5.53
MgO	22.16	22.03	21.90	22.27	21.27	21.69	0.00	0.00	0.00	0.00	0.00	0.00	0.00	0.00	0.00	0.00	0.00	0.00		13.25	13.02	9.75	9.97	10.56	9.88	10.50	11.13	10.42	0.00
Al2O3	1.14	0.96	1.29	1.02	1.30	1.10	30.33	27.38	30.09	26.89	29.66	27.45	30.41	26.89	29.45	29.98	27.50	19.14		2.98	1.84	10.91	9.72	9.54	10.82	9.32	9.68	9.63	28.70
SiO2	52.89	52.63	52.74	52.71	52.77	52.76	52.03	57.28	52.79	57.66	53.68	56.90	52.70	58.12	52.94	52.63	56.96	64.46		51.67	52.74	42.75	43.76	44.42	43.02	44.63	44.16	44.17	55.46
K2O	0.00	0.00	0.00	0.00	0.00	0.00	0.00	0.26	0.13	0.23	0.23	0.24	0.00	0.16	0.13	0.00	0.12	14.44		0.00	0.00	1.34	1.21	1.18	1.49	1.03	1.29	1.24	0.00
CaO	0.97	0.72	0.60	1.35	2.82	1.76	12.99	9.25	12.19	8.63	11.74	9.33	12.58	8.51	11.92	12.46	9.01	0.40		19.27	21.78	11.70	11.44	11.73	11.68	11.09	11.60	11.65	10.44
TiO2	0.00	0.21	0.00	0.41	0.00	0.40	0.00	0.00	0.00	0.00	0.00	0.00	0.00	0.00	0.00	0.00	0.00	0.00		0.47	0.31	1.08	1.14	1.32	0.96	1.28	1.64	1.28	0.00
MnO	0.50	0.73	0.49	0.36	0.49	0.51	0.00	0.00	0.00	0.00	0.00	0.00	0.00	0.00	0.00	0.00	0.00	0.00		0.45	0.64	0.38	0.53	0.47	0.58	0.50	0.64	0.53	0.00
FeO	21.85	23.18	23.43	22.16	21.66	22.23	0.00	0.31	0.00	0.00	0.00	0.00	0.00	0.00	0.00	0.29	0.00	0.00		10.76	9.71	18.31	18.58	17.64	18.58	17.47	16.76	17.66	0.27
TOTAL	99.51	100.46	100.78	100.48	100.31	100.70	99.54	100.83	99.61	99.99	99.98	100.14	99.84	100.26	99.22	99.70	99.88	99.71		99.30	100.59	97.41	97.55	98.08	98.30	97.21	98.28	97.89	100.40
Na	0.000	0.000	0.095	0.058	0.000	0.000	1.48	2.19	1.55	2.28	1.64	2.16	1.46	2.28	1.69	1.53	2.19	0.45		0.131	0.159	0.366	0.369	0.371	0.395	0.425	0.418	0.400	1.923
Mg	4.937	4.898	4.854	4.932	4.723	4.801	0.00	0.00	0.00	0.00	0.00	0.00	0.00	0.00	0.00	0.00	0.00	0.00		2.971	2.890	2.308	2.354	2.467	2.324	2.467	2.591	2.443	0.000
Al	0.201	0.169	0.226	0.179	0.228	0.193	6.51	5.75	6.44	5.68	6.32	5.80	6.49	5.65	6.32	6.42	5.81	4.15		0.529	0.323	2.043	1.816	1.763	2.013	1.732	1.783	1.786	6.068
Si	7.906	7.851	7.844	7.833	7.862	7.836	9.47	10.21	9.59	10.33	9.70	10.20	9.54	10.36	9.65	9.56	10.21	11.87		7.773	7.855	6.789	6.934	6.964	6.789	7.036	6.898	6.947	9.945
K	0.000	0.000	0.000	0.000	0.000	0.000	0.00	0.06	0.03	0.05	0.05	0.06	0.00	0.04	0.03	0.00	0.03	3.39		0.000	0.000	0.271	0.245	0.236	0.300	0.207	0.257	0.249	0.000
Ca	0.155	0.115	0.096	0.215	0.450	0.280	2.53	1.77	2.37	1.66	2.27	1.79	2.44	1.63	2.33	2.43	1.73	0.08		3.106	3.476	1.991	1.942	1.970	1.975	1.873	1.942	1.963	2.006
Ti	0.000	0.024	0.000	0.046	0.000	0.045	0.00	0.00	0.00	0.00	0.00	0.00	0.00	0.00	0.00	0.00	0.00	0.00		0.053	0.035	0.129	0.136	0.156	0.114	0.152	0.193	0.151	0.000
Mn	0.063	0.092	0.062	0.045	0.062	0.064	0.00	0.00	0.00	0.00	0.00	0.00	0.00	0.00	0.00	0.04	0.00	0.00		0.057	0.081	0.051	0.071	0.062	0.078	0.067	0.085	0.071	0.000
Fe	2.732	2.892	2.914	2.754	2.699	2.761	0.00	0.05	0.00	0.00	0.00	0.00	0.00	0.00	0.00	0.00	0.00	0.00		1.354	1.210	2.432	2.462	2.313	2.452	2.303	2.190	2.323	0.040
Cat sum	15.994	16.041	16.091	16.061	16.024	16.009	19.99	20.03	19.98	20.00	19.98	20.01	19.93	19.96	20.02	19.98	19.97	19.94		15.975	16.028	16.380	16.329	16.302	16.438	16.262	16.355	16.333	19.982
Mg#	0.6438	0.6288	0.6249	0.6417	0.6364	0.6349														0.6869	0.7049	0.4869	0.4888	0.5161	0.4866	0.5172	0.5419	0.5126	
An%							63.09	44.03	60.00	41.60	57.32	44.64	62.56	41.27	57.53	61.36	43.80												51.06

Rock	Ferres Ck Tonalite 98-CP12											98-CP2 Hbl Gabbronorite																
Mineral	plag B rim	plag A	plag B core	plag B rim	plag C rim	plag core	plag rim	bio	bio A core	bio A rim	bio B rim	cpx A core	cpx A rim	cpx B rim	cpx C rim	cpx A rim	cpx A rim	cpx B rim	cpx C rim	cpx D rim	opx A rim	opx B rim	opx A rim	opx B core	opx B rim	opx C core	opx C rim	opx D core
Spot	1.6	3.3	3.4	3.5	3.6	4.1	4.2	1.7	5.1	5.2	5.3	2.1	2.2	2.5	2.6	3.1	5.3	5.4	5.5	5.6	2.4	2.7	3.2	3.3	3.4	3.7	3.8	3.11
Na2O	5.82	6.03	5.52	5.70	6.03	4.94	5.95	0.24	0.00	0.18	0.00	0.28	0.29	0.38	0.33	0.37	0.37	0.31	0.38	0.30	0.14	0.04	0.02	0.05	0.12	0.18	0.15	0.12
MgO	0.00	0.00	0.00	0.00	0.00	0.00	0.00	11.57	11.19	11.51	11.33	13.36	13.53	13.35	13.56	13.12	12.90	12.97	13.24	13.40	23.13	23.85	23.40	23.50	24.14	24.03	23.17	23.63
Al2O3	28.13	28.08	28.86	28.28	28.33	29.73	28.05	15.19	15.76	15.19	15.53	3.28	3.81	2.98	3.16	3.38	3.38	3.09	2.98	2.98	3.07	1.41	2.47	2.96	3.01	3.09	3.19	3.00
SiO2	56.30	56.71	55.26	55.92	56.80	54.41	56.38	36.66	36.68	36.81	36.71	51.91	51.60	51.76	51.85	51.91	51.16	51.78	51.66	51.84	53.11	54.57	53.60	53.16	53.34	53.39	53.30	53.07
K2O	0.00	0.00	0.16	0.20	0.14	0.00	0.00	9.57	9.81	9.87	9.77	0.00	0.00	0.00	0.06	0.00	0.00	0.01	0.05	0.03	0.00	0.03	0.00	0.00	0.01	0.06	0.00	0.00
CaO	10.18	9.69	10.65	9.97	9.72	11.67	9.67	0.00	0.00	0.00	0.00	21.96	20.92	22.36	21.84	22.00	22.49	21.98	22.16	21.10	1.20	0.62	0.51	1.60	0.56	1.21	1.54	1.21
TiO2	0.00	0.00	0.00	0.00	0.00	0.00	0.00	2.58	2.70	2.52	2.73	0.54	0.50	0.68	0.51	0.55	0.52	0.63	0.41	0.51	0.01	0.12	0.00	0.32	0.14	0.22	0.26	0.33
MnO	0.00	0.00	0.00	0.00	0.00	0.00	0.00	0.34	0.26	0.36	0.36	0.16	0.25	0.28	0.19	0.15	0.27	0.23	0.19	0.36	0.39	0.45	0.44	0.31	0.44	0.46	0.37	0.27
FeO	0.00	0.00	0.00	0.45	0.00	0.26	0.00	20.09	20.23	20.12	20.07	7.95	8.69	8.05	7.79	8.45	8.88	8.83	8.45	8.93	18.86	19.45	19.05	17.36	17.83	17.36	17.68	18.40
TOTAL	100.43	100.51	100.45	100.52	101.02	101.01	100.05	96.24	96.63	96.56	96.50	99.49	99.77	99.86	99.48	99.97	100.07	99.83	99.68	99.67	99.99	100.60	99.49	99.28	99.59	100.00	99.66	100.26
Na	2.019	2.087	1.920	1.981	2.078	1.713	2.068	0.071	0.000	0.053	0.000	0.081	0.084	0.110	0.095	0.107	0.107	0.090	0.110	0.087	0.040	0.011	0.006	0.014	0.034	0.051	0.043	0.034
Mg	0.000	0.000	0.000	0.000	0.000	0.000	0.000	2.621	2.524	2.602	2.558	2.968	3.001	2.965	3.014	2.908	2.874	2.886	2.951	2.984	5.052	5.176	5.125	5.137	5.259	5.215	5.052	5.139
Al	5.932	5.908	6.102	5.975	5.936	6.269	5.929	2.722	2.812	2.717	2.774	0.576	0.669	0.524	0.556	0.593	0.596	0.544	0.525	0.525	0.530	0.242	0.428	0.512	0.519	0.531	0.550	0.516
Si	10.071	10.121	9.911	10.021	10.095	9.732	10.108	5.572	5.551	5.584	5.562	7.739	7.680	7.714	7.733	7.721	7.648	7.731	7.725	7.745	7.784	7.947	7.877	7.797	7.796	7.775	7.797	7.745
K	0.000	0.000	0.037	0.046	0.032	0.000	0.000	1.856	1.894	1.910	1.889	0.000	0.000	0.000	0.011	0.000	0.000	0.002	0.010	0.006	0.000	0.006	0.000	0.000	0.002	0.011	0.000	0.000
Ca	1.951	1.853	2.047	1.914	1.851	2.237	1.858	0.000	0.000	0.000	0.000	3.508	3.336	3.571	3.490	3.506	3.603	3.516	3.551	3.378	0.188	0.097	0.080	0.251	0.088	0.189	0.241	0.189
Ti	0.000	0.000	0.000	0.000	0.000	0.000	0.000	0.295	0.307	0.287	0.311	0.061	0.056	0.076	0.057	0.062	0.058	0.071	0.046	0.057	0.001	0.013	0.000	0.035	0.015	0.024	0.029	0.036
Mn	0.000	0.000	0.000	0.000	0.000	0.000	0.000	0.044	0.033	0.046	0.046	0.020	0.032	0.035	0.024	0.019	0.034	0.029	0.024	0.046	0.048	0.056	0.055	0.039	0.054	0.057	0.046	0.033
Fe	0.000	0.000	0.000	0.067	0.000	0.039	0.000	2.554	2.561	2.553	2.543	0.991	1.082	1.003	0.972	1.051	1.110	1.103	1.057	1.116	2.312	2.369	2.341	2.130	2.180	2.114	2.163	2.246
Cat sum	19.973	19.969	20.016	20.004	19.992	19.990	19.962	15.735	15.683	15.752	15.684	15.950	15.961	16.001	15.974	15.972	16.043	15.972	16.017	15.969	15.965	15.924	15.912	15.917	15.947	15.967	15.920	15.965
Mg#								0.5065	0.4964	0.5048	0.5015	0.7497	0.7350	0.7472	0.7561	0.7345	0.7214	0.7235	0.7363	0.7278	0.6860	0.6860	0.6864	0.7069	0.7069	0.7116	0.7002	0.6959
An%	49.14	47.03	51.12	48.57	46.73	56.63	47.33																					

Rock	98-CP2 Hbl Gabbronorite															98-CP8 Hbl pyroxenite												
Mineral	opx core	opx rim	hbl	hbl	plag A cor	plag A rim	plag B cor	plag B rim	plag core	plag	plag core	plag rim	plag core	plag rim		opx A rim	opx B rim	opx A	opx B	opx C	opx	opx rim	cpx rim	cpx A	cpx B	hbl	hbl	plag A	plag B
Spot	4.1	4.2	1.1	6.1	1.2	1.3	1.4	1.5	2.3	2.8	3.9	3.10	5.1	5.2		3.1	3.3	2.1	2.3	2.4	4.1	6.1	2.5	1.1	1.2	3.2	2.2	4.2	4.3
Na2O	0.11	0.07	1.40	1.45	0.90	1.25	0.80	1.15	0.95	0.95	1.11	0.96	1.06	0.95		0.04	0.15	0.12	0.11	0.16	0.12	0.04	0.20	0.10	0.24	1.48	1.55	1.46	1.06
MgO	23.88	23.80	12.08	12.15	0.08	0.04	0.00	0.09	0.00	0.02	0.10	0.12	0.06	0.03		24.38	25.80	24.92	25.28	24.45	24.43	23.70	14.52	14.78	15.21	14.25	14.09	0.07	0.05
Al2O3	2.90	1.86	11.89	11.57	34.91	34.30	34.21	34.33	34.64	35.16	34.62	35.15	34.62	34.61		1.71	0.94	0.96	1.35	1.43	1.33	1.25	0.99	1.11	1.21	10.37	12.48	34.36	34.92
SiO2	53.52	54.21	42.50	43.28	45.03	45.70	45.03	45.42	45.52	45.95	46.17	45.91	45.60	45.59		54.32	55.21	54.82	54.81	54.67	54.74	54.69	54.29	54.14	54.44	46.45	44.54	46.24	46.18
K2O	0.03	0.00	1.15	1.16	0.00	0.02	0.07	0.01	0.07	0.05	0.00	0.03	0.00	0.01		0.03	0.00	0.02	0.00	0.00	0.00	0.00	0.00	0.00	0.00	0.61	0.79	0.00	0.00
CaO	0.72	0.45	11.67	11.64	18.33	17.90	18.65	18.05	18.41	18.58	18.19	18.52	18.38	18.26		0.94	0.89	1.28	1.67	1.42	0.62	0.82	22.46	22.56	22.57	11.73	11.69	17.88	18.17
TiO2	0.27	0.14	2.76	2.57	0.03	0.00	0.00	0.00	0.00	0.00	0.09	0.06	0.00	0.12		0.10	0.09	0.00	0.00	0.12	0.08	0.00	0.12	0.11	0.15	1.28	2.43	0.14	0.00
MnO	0.30	0.56	0.22	0.09	0.00	0.00	0.15	0.09	0.00	0.12	0.15	0.00	0.00	0.00		0.37	0.47	0.23	0.27	0.42	0.40	0.51	0.22	0.26	0.01	0.23	0.14	0.03	0.00
FeO	18.76	18.73	12.43	12.97	0.15	0.35	0.42	0.50	0.38	0.27	0.03	0.36	0.22	0.28		17.50	16.27	16.70	16.38	17.36	17.70	18.97	6.94	7.11	6.11	9.83	9.40	0.03	0.00
TOTAL	100.49	99.82	96.20	96.96	99.43	99.62	99.35	99.85	100.00	101.10	100.46	101.22	100.05	99.97		99.60	100.22	99.39	100.39	100.28	99.65	99.98	99.84	100.22	100.08	96.41	97.45	100.27	100.39
Na	0.031	0.020	0.425	0.436	0.324	0.449	0.289	0.413	0.340	0.336	0.395	0.339	0.379	0.340		0.011	0.042	0.034	0.031	0.045	0.034	0.011	0.057	0.029	0.068	0.438	0.454	0.520	0.376
Mg	5.176	5.188	2.815	2.810	0.022	0.011	0.000	0.025	0.000	0.005	0.027	0.033	0.016	0.008		5.304	5.551	5.417	5.443	5.289	5.310	5.165	3.196	3.245	3.325	3.238	3.175	0.019	0.014
Al	0.497	0.321	2.192	2.117	7.630	7.485	7.509	7.491	7.539	7.567	7.482	7.557	7.526	7.526		0.294	0.160	0.165	0.230	0.245	0.229	0.215	0.172	0.193	0.209	1.864	2.225	7.439	7.541
Si	7.785	7.929	6.646	6.717	8.349	8.459	8.384	8.407	8.403	8.388	8.464	8.372	8.408	8.410		7.929	7.970	7.996	7.918	7.936	7.984	7.997	8.017	7.975	7.986	7.082	6.735	8.492	8.459
K	0.006	0.000	0.229	0.230	0.000	0.005	0.017	0.002	0.016	0.012	0.000	0.007	0.000	0.002		0.006	0.000	0.004	0.000	0.000	0.000	0.000	0.000	0.000	0.000	0.119	0.152	0.000	0.000
Ca	0.112	0.071	1.955	1.936	3.641	3.550	3.721	3.580	3.642	3.634	3.573	3.619	3.631	3.609		0.147	0.138	0.200	0.259	0.221	0.097	0.128	3.554	3.561	3.547	1.916	1.894	3.518	3.566
Ti	0.030	0.015	0.325	0.300	0.004	0.000	0.000	0.000	0.000	0.000	0.012	0.008	0.000	0.017		0.011	0.010	0.000	0.000	0.013	0.009	0.000	0.013	0.012	0.017	0.147	0.276	0.019	0.000
Mn	0.037	0.069	0.029	0.012	0.000	0.000	0.024	0.014	0.000	0.019	0.023	0.000	0.000	0.000		0.046	0.057	0.028	0.033	0.052	0.049	0.063	0.028	0.032	0.001	0.030	0.018	0.005	0.000
Fe	2.282	2.291	1.626	1.684	0.023	0.054	0.065	0.077	0.059	0.041	0.005	0.055	0.034	0.043		2.136	1.964	2.037	1.979	2.108	2.159	2.320	0.857	0.876	0.750	1.253	1.189	0.005	0.000
Cat sum	15.956	15.905	16.254	16.252	19.994	20.021	20.012	20.040	20.003	20.002	19.980	20.006	20.011	19.973		15.909	15.938	15.921	15.952	15.937	15.897	15.901	15.906	15.928	15.919	16.107	16.159	20.025	19.958
Mg#	0.6940	0.6937	0.6339	0.6253												0.7129	0.7387	0.7267	0.7334	0.7150	0.7109	0.6900	0.7886	0.7874	0.8160	0.7210	0.7275		
An%					91.83	88.77	92.79	89.66	91.46	91.54	90.05	91.44	90.55	91.39														87.12	90.46

Rock	98-CP9 Hbl pyroxenite																			98-CP6 Hornblende gabbro							
Mineral	cpx A	cpx A	cpx B	cpx C	cpx A	cpx B	cpx C	cpx	opx	opx A	opx B	opx A	opx A	opx B	hbl	hbl	hbl	hbl A	hbl B	Hbl core	Hbl	Hbl	Hbl core	Hbl rim	Hbl rim	Cumm	Hbl core	Hbl rim
Spot	1.1	4.4	4.5	4.6	3.1	3.3	3.4	2.2	2.3	1.3	1.4	4.2	4.3	4.7	1.2	2.1	3.2	4.1	4.8		1.3	1.4	2.2	2.3	3.1	3.4	5.1	5.2
Na2O	0.44	0.24	0.29	0.33	0.17	0.17	0.37	0.16	0.02	0.17	0.13	0.14	0.08	0.03	1.50	1.69	1.59	1.62	1.70	1.16	1.26	1.11	1.45	1.27	1.09	0.20	1.38	1.03
MgO	13.79	14.05	13.63	14.31	16.06	14.05	14.19	13.75	23.12	22.67	23.25	22.60	22.60	22.63	13.31	12.97	13.86	13.34	12.89	11.43	11.79	11.69	11.63	11.30	11.94	18.16	11.81	11.17
Al2O3	2.36	1.92	2.39	2.24	1.70	2.54	1.92	2.64	1.23	1.50	1.32	1.82	1.48	1.56	10.98	11.47	10.10	10.88	11.74	10.89	10.50	10.46	10.44	10.63	9.87	0.76	10.38	10.42
SiO2	52.17	52.89	52.90	52.94	53.15	52.75	52.68	52.93	53.91	53.31	53.83	53.58	53.46	53.66	44.46	44.20	45.80	44.46	43.76	43.28	43.70	44.30	43.48	43.69	44.83	54.49	43.90	43.97
K2O	0.00	0.00	0.00	0.00	0.07	0.00	0.00	0.00	0.03	0.04	0.00	0.00	0.03	0.00	0.82	0.85	0.67	0.81	0.93	1.02	1.23	1.29	1.26	1.21	1.14	0.08	1.25	1.40
CaO	22.20	21.28	22.12	19.68	16.21	21.72	21.46	21.35	0.74	1.09	0.60	1.13	0.90	1.05	11.51	11.32	11.88	11.53	11.72	11.34	11.53	11.47	11.44	11.35	11.47	0.89	11.51	11.66
TiO2	0.53	0.46	0.23	0.23	0.21	0.36	0.29	0.48	0.02	0.23	0.07	0.11	0.24	0.12	1.82	1.93	1.57	1.69	1.77	2.41	2.68	2.60	2.51	2.62	2.13	0.04	2.57	2.57
MnO	0.19	0.17	0.23	0.29	0.43	0.18	0.25	0.25	0.32	0.51	0.45	0.34	0.51	0.43	0.25	0.30	0.14	0.05	0.12	0.15	0.19	0.38	0.22	0.12	0.24	0.81	0.22	0.33
FeO	8.02	8.31	7.28	9.88	12.02	8.84	8.22	8.31	19.67	19.94	19.80	19.74	20.36	20.10	11.48	11.69	11.24	11.47	11.34	14.12	14.13	14.27	14.62	14.52	14.57	21.56	14.86	14.37
TOTAL	100.02	99.45	99.46	100.34	100.06	100.78	99.64	100.01	99.36	99.49	99.58	99.46	99.89	99.73	96.59	96.63	97.27	96.39	96.21	96.00	97.20	97.78	97.19	96.89	97.48	97.03	98.09	97.08
Na	0.127	0.069	0.084	0.095	0.049	0.049	0.107	0.046	0.006	0.049	0.037	0.040	0.023	0.009	0.449	0.506	0.471	0.485	0.511	0.354	0.380	0.333	0.439	0.385	0.327	0.059	0.414	0.312
Mg	3.057	3.120	3.020	3.160	3.555	3.090	3.151	3.034	5.092	5.008	5.114	4.978	4.978	4.981	3.060	2.983	3.154	3.072	2.978	2.678	2.734	2.694	2.707	2.630	2.757	4.126	2.724	2.597
Al	0.414	0.337	0.419	0.391	0.298	0.442	0.337	0.461	0.214	0.262	0.230	0.317	0.258	0.272	1.997	2.087	1.818	1.982	2.146	2.018	1.926	1.907	1.923	1.957	1.803	0.137	1.894	1.917
Si	7.761	7.880	7.865	7.845	7.894	7.783	7.849	7.837	7.967	7.902	7.945	7.920	7.902	7.926	6.858	6.822	6.993	6.871	6.783	6.803	6.800	6.849	6.792	6.823	6.945	8.307	6.795	6.860
K	0.000	0.000	0.000	0.000	0.013	0.000	0.000	0.000	0.006	0.008	0.000	0.000	0.006	0.000	0.161	0.167	0.131	0.160	0.184	0.205	0.244	0.254	0.251	0.241	0.225	0.016	0.247	0.279
Ca	3.539	3.397	3.524	3.125	2.580	3.434	3.426	3.387	0.117	0.173	0.095	0.179	0.143	0.166	1.903	1.872	1.944	1.909	1.947	1.910	1.922	1.900	1.915	1.899	1.904	0.145	1.909	1.949
Ti	0.059	0.052	0.026	0.026	0.023	0.040	0.032	0.053	0.002	0.026	0.008	0.012	0.027	0.013	0.211	0.224	0.180	0.196	0.206	0.285	0.314	0.302	0.295	0.308	0.248	0.005	0.299	0.302
Mn	0.024	0.021	0.029	0.036	0.054	0.022	0.032	0.031	0.040	0.064	0.056	0.043	0.064	0.054	0.033	0.039	0.018	0.007	0.016	0.020	0.025	0.050	0.029	0.016	0.031	0.105	0.029	0.044
Fe	0.998	1.035	0.905	1.225	1.493	1.091	1.024	1.029	2.431	2.472	2.444	2.440	2.517	2.483	1.481	1.509	1.435	1.482	1.470	1.856	1.839	1.845	1.910	1.896	1.888	2.749	1.924	1.875
Cat sum	16.017	15.927	15.918	15.955	15.963	15.970	15.988	15.894	15.911	15.967	15.944	15.930	15.943	15.921	16.209	16.235	16.193	16.231	16.270	16.182	16.235	16.189	16.297	16.203	16.182	15.658	16.289	16.175
Mg#	0.7539	0.7509	0.7694	0.7206	0.7042	0.7391	0.7547	0.7467	0.6769	0.6695	0.6766	0.6711	0.6642	0.6673	0.6739	0.6641	0.6873	0.6746	0.6695	59.058	59.789	59.346	58.636	58.103	59.355	60.016	58.613	58.074
An%																												

Rock	98-CP6 Hornblende gabbro													Hbl diorite 97-376														
Mineral	Biotite	Plag core	Plag rim	Plag core	Plag rim	Plag core	Plag rim	Plag rim	Plag core	Plag rim	Plag core	Plag rim		Hbl	Hbl (b) cor	Hbl (b) cor	Hbl core	Hbl rim	Hbl core	Hbl rim	Hbl rim	Hbl	plag B rim	plag A cor	plag A rim	plag B core	plag B rim	plag core	plag rim
Spot	1.2	3.2	3.3	5.3	5.4	5.5	5.6	5.7	6.1	6.2	7.1	7.2		1.1	1.2	1.3	2.1	2.2	4.1	4.2	4.2(2)	6.1	1.3	4.3	4.4	4.5	4.6	5.2	5.3
Na2O	0.42	2.94	4.78	5.41	4.44	5.14	4.93	4.36	4.32	4.93	4.61	3.92		0.99	1.35	0.92	1.27	0.94	1.34	0.88	0.92	0.97	0.92	3.20	6.35	6.22	6.97	4.84	5.96
MgO	14.67	0.06	0.04	0.08	0.04	0.12	0.06	0.00	0.00	0.06	0.11	0.01		13.76	12.02	13.71	11.95	13.81	11.96	13.37	13.45	13.57	13.71	0.06	0.00	0.03	0.05	0.08	0.00
Al2O3	15.23	32.36	29.34	28.70	30.15	29.20	29.51	30.28	29.89	28.66	29.66	30.58		8.05	10.83	8.09	11.08	8.00	10.90	8.43	8.17	8.20	8.09	31.95	26.93	27.50	26.12	29.46	27.40
SiO2	37.23	50.13	53.51	55.50	52.97	54.70	54.91	52.82	52.76	53.76	53.11	51.85		48.31	44.78	47.90	44.99	48.72	44.55	47.75	47.98	47.97	47.90	50.40	57.37	56.57	58.77	53.89	56.57
K2O	8.77	0.00	0.02	0.03	0.01	0.00	0.05	0.00	0.09	0.00	0.03	0.05		0.35	0.48	0.38	0.60	0.49	0.47	0.34	0.36	0.44	0.38	0.12	0.07	0.07	0.01	0.02	0.02
CaO	0.08	15.02	11.53	10.88	12.32	11.18	11.38	12.71	12.23	11.20	12.07	13.18		12.02	11.79	11.98	11.86	12.30	11.66	12.01	11.91	12.11	11.98	14.61	8.95	9.52	7.81	11.63	9.54
TiO2	2.56	0.10	0.00	0.02	0.17	0.00	0.00	0.04	0.21	0.00	0.00	0.06		0.61	1.41	0.73	1.36	0.76	1.61	0.66	0.75	0.75	0.73	0.08	0.01	0.07	0.19	0.20	0.00
MnO	0.06	0.00	0.00	0.00	0.10	0.03	0.03	0.00	0.10	0.00	0.00	0.00		0.44	0.30	0.00	0.28	0.33	0.29	0.56	0.47	0.43	0.13	0.09	0.07	0.00	0.06	0.00	0.11
FeO	15.58	0.10	0.22	0.00	0.07	0.10	0.02	0.29	0.29	1.19	0.00	0.18		12.48	14.01	12.59	13.93	12.46	14.18	12.36	12.62	12.61	12.59	0.08	0.14	0.00	0.07	0.02	0.05
TOTAL	94.75	100.71	99.45	100.62	100.27	100.47	100.91	100.54	99.89	99.80	99.59	99.84		97.01	96.97	96.42	97.32	97.81	96.96	96.36	96.63	97.05	96.43	100.59	99.89	99.98	100.05	100.14	99.65
Na	0.122	1.032	1.684	1.877	1.554	1.789	1.707	1.525	1.520	1.737	1.623	1.382		0.293	0.405	0.270	0.38	0.276	0.403	0.262	0.274	0.288	0.365	1.125	2.209	2.166	2.412	1.692	2.081
Mg	3.283	0.016	0.011	0.021	0.011	0.032	0.016	0.000	0.000	0.016	0.030	0.003		3.132	2.774	3.140	2.746	3.118	2.763	3.064	3.076	3.093	4.185	0.016	0	0.008	0.013	0.021	0
Al	2.696	6.907	6.283	6.055	6.418	6.179	6.213	6.439	6.393	6.141	6.348	6.555		1.449	1.977	1.470	2.014	1.429	1.992	1.528	1.478	1.479	1.953	6.83	5.697	5.822	5.495	6.262	5.816
Si	5.590	9.076	9.720	9.932	9.564	9.818	9.807	9.528	9.573	9.771	9.642	9.427		7.378	6.935	7.360	6.938	7.381	6.906	7.343	7.362	7.338	9.81	9.138	10.294	10.159	10.487	9.716	10.185
K	1.680	0.000	0.005	0.007	0.002	0.000	0.011	0.000	0.021	0.000	0.007	0.012		0.068	0.095	0.080	0.118	0.095	0.093	0.067	0.07	0.086	0.099	0.028	0.016	0.016	0.002	0.005	0.005
Ca	0.013	2.914	2.244	2.086	2.384	2.150	2.178	2.457	2.378	2.181	2.348	2.568		1.967	1.957	1.970	1.96	1.997	1.937	1.979	1.958	1.985	2.629	2.838	1.721	1.832	1.493	2.247	1.84
Ti	0.289	0.014	0.000	0.003	0.023	0.000	0.000	0.005	0.029	0.000	0.000	0.008		0.07	0.164	0.080	0.158	0.087	0.188	0.076	0.087	0.086	0.112	0.011	0.001	0.009	0.025	0.027	0
Mn	0.008	0.000	0.000	0.000	0.015	0.005	0.005	0.000	0.015	0.000	0.000	0.000		0.057	0.039	0.000	0.037	0.042	0.038	0.073	0.061	0.056	0.023	0.014	0.011	0	0.009	0	0.017
Fe	1.956	0.015	0.033	0.000	0.011	0.015	0.003	0.044	0.044	0.181	0.000	0.027		1.594	1.815	1.620	1.796	1.579	1.838	1.59	1.619	1.613	2.156	0.012	0.021	0	0.01	0.003	0.008
Cat sum	15.674	19.973	19.983	19.980	19.982	19.987	19.946	20.010	19.972	20.027	19.998	19.984		16.008	16.162	16.000	16.146	16.003	16.158	15.982	15.985	16.023	21.332	20.012	19.969	20.012	19.947	19.974	19.95
Mg#	62.657													0.6627	0.6045	0.6597	0.6046	0.6638	0.6005	0.6584	0.6552	0.6572							
An%		73.84	57.07	52.55	60.49	54.59	55.89	61.70	60.68	55.66	59.03	64.82											85.00	71.11	43.61	45.64	38.21	56.97	46.87

Rock	Hbl diorite 97-376				Hornblende gabbro-diorite 97-319																								
Mineral	Plag core	Plag rim	Plag core	Plag rim	Biotite	Biotite	Biotite	Biotite	Biotite		hbl core	hbl rim	hbl core	hbl rim	hbl	hbl	hbl core	hbl rim	hbl core	hbl rim	hbl	hbl	hbl	hbl core	hbl rim	hbl	hbl core	hbl rim	hbl core
Spot	6.2	6.3	6.4	6.5	3.1	3.2	3.3	3.4	5.1		1.1	1.2	2.1	2.2	2.6	2.6 (b)	3.1	3.2	3.5	3.6	3.7	3.8	3.9	3.10	3.11	4.2	4.3	4.4	5.1
											HBL	ACT	HBL	ACT	ACT	ACT	HBL	ACT	HBL	ACT	ACT	ACT	ACT	HBL	ACT	ACT	HBL	ACT	HBL
Na2O	3.26	5.57	3.32	6.01	0.24	0.29	0.28	0.25	0.27		1.71	0.63	1.56	0.84	0.65	0.64	1.39	0.88	1.47	0.71	0.86	0.76	0.51	1.44	0.85	0.72	1.58	0.77	1.08
MgO	0.00	0.02	0.08	0.00	14.23	14.41	14.15	13.81	13.95		13.03	16.94	12.73	15.83	16.00	16.01	13.67	16.16	12.65	16.48	16.12	16.17	17.33	13.27	15.98	16.27	13.14	16.50	13.75
Al2O3	31.84	28.27	31.81	27.82	15.36	15.46	15.24	15.41	15.20		11.21	4.30	11.06	6.00	5.45	5.45	9.91	5.52	10.89	5.01	5.71	5.29	3.63	10.45	5.68	5.30	11.12	5.05	10.04
SiO2	50.59	55.98	51.23	56.79	37.83	37.13	37.55	37.73	37.81		44.65	52.95	44.55	50.86	51.41	51.41	46.12	51.90	44.86	52.50	51.65	51.93	53.82	45.52	51.34	51.68	44.59	52.17	46.11
K2O	0.00	0.10	0.22	0.02	9.78	9.09	9.57	9.66	9.70		0.57	0.23	0.64	0.21	0.37	0.37	0.41	0.20	0.55	0.16	0.20	0.24	0.24	0.49	0.18	0.26	0.54	0.22	1.11
CaO	14.61	10.36	13.89	9.79	0.00	0.00	0.08	0.15	0.00		11.63	12.63	12.19	12.65	12.87	12.87	12.21	12.44	12.41	12.49	12.31	12.58	12.76	12.48	12.58	12.77	12.39	12.70	12.09
TiO2	0.01	0.04	0.07	0.09	2.72	2.43	2.88	2.75	2.76		1.93	0.35	2.11	0.40	0.48	0.48	1.46	0.46	1.57	0.27	0.23	0.44	0.25	1.64	0.36	0.34	1.90	0.23	0.94
MnO	0.16	0.00	0.00	0.04	0.26	0.22	0.19	0.14	0.27		0.21	0.23	0.29	0.29	0.20	0.00	0.16	0.38	0.32	0.23	0.24	0.35	0.27	0.31	0.35	0.19	0.21	0.40	0.10
FeO	0.03	0.12	0.10	0.09	15.39	15.45	14.84	15.68	14.58		11.63	8.47	11.48	9.52	9.42	9.42	10.88	9.61	12.11	9.20	9.56	9.60	8.79	11.25	9.53	9.73	11.35	9.36	11.44
TOTAL	100.50	100.46	100.72	100.65	95.81	94.48	94.78	95.58	94.54		96.57	96.73	96.61	96.60	96.85	97.06	96.21	97.55	96.83	97.05	96.88	97.65	97.60	96.85	97.08	97.26	96.82	97.40	96.66
Na	1.146	1.934	1.162	2.079	0.069	0.085	0.082	0.072	0.079		0.511	0.182	0.466	0.245	0.189	0.190	0.414	0.254	0.439	0.205	0.250	0.220	0.146	0.428	0.248	0.209	0.471	0.223	0.322
Mg	0	0.005	0.022	0	3.159	3.238	3.167	3.075	3.126		2.991	3.767	2.926	3.556	3.583	3.580	3.129	3.590	2.907	3.664	3.601	3.600	3.822	3.033	3.578	3.630	3.011	3.669	3.148
Al	6.806	5.968	6.77	5.852	2.698	2.748	2.698	2.715	2.694		2.035	0.756	2.011	1.066	0.965	0.960	1.794	0.970	1.979	0.881	1.009	0.932	0.633	1.889	1.006	0.935	2.015	0.888	1.818
Si	9.173	10.024	9.248	10.133	5.635	5.598	5.639	5.638	5.685		6.877	7.901	6.870	7.666	7.725	7.710	7.084	7.736	6.916	7.831	7.742	7.757	7.965	6.980	7.712	7.736	6.855	7.783	7.083
K	0	0.023	0.051	0.005	1.859	1.748	1.833	1.842	1.861		0.112	0.044	0.126	0.040	0.071	0.070	0.080	0.038	0.108	0.030	0.038	0.046	0.045	0.096	0.034	0.050	0.106	0.042	0.218
Ca	2.839	1.988	2.687	1.872	0	0	0.013	0.024	0		1.919	2.019	2.014	2.043	2.072	2.070	2.009	1.987	2.050	1.996	1.977	2.014	2.024	2.051	2.025	2.048	2.041	2.030	1.990
Ti	0.001	0.005	0.01	0.012	0.305	0.276	0.325	0.309	0.312		0.224	0.039	0.245	0.045	0.054	0.050	0.169	0.052	0.182	0.030	0.026	0.049	0.028	0.189	0.041	0.038	0.220	0.026	0.109
Mn	0.025	0	0	0.006	0.033	0.028	0.024	0.018	0.034		0.027	0.029	0.038	0.037	0.025	0.000	0.021	0.048	0.042	0.029	0.030	0.044	0.034	0.040	0.045	0.024	0.027	0.051	0.013
Fe	0.005	0.018	0.015	0.013	1.917	1.948	1.864	1.96	1.833		1.498	1.057	1.481	1.200	1.184	1.180	1.398	1.198	1.561	1.148	1.198	1.199	1.088	1.443	1.197	1.218	1.459	1.168	1.470
Cat sum	19.995	19.965	19.964	19.971	15.675	15.669	15.644	15.653	15.625		16.194	15.795	16.176	15.899	15.869	15.870	16.098	15.873	16.186	15.816	15.872	15.911	15.786	16.148	15.915	15.888	16.206	15.879	16.169
Mg#					0.6223	0.6244	0.6295	0.6107	0.6304		0.6663	0.7809	0.6639	0.7477	0.7516	0.7521	0.6912	0.7498	0.6506	0.7614	0.7504	0.7502	0.7784	0.6776	0.7493	0.7488	0.6736	0.7585	0.6817
An%	71.24	50.39	68.90	47.32																									

Rock	Hornblende gabbro-diorite 97-319																			97-320c Hornblende gabbro-diorite									
Mineral	hbl core	hbl	hbl	hbl rim	cpx	cpx	cpx	cpx	rel cpx 3A	rel cpx	rel cpx	rel cpx	rel cpx	rel cpx	bio	plag	plag	plag		cpx A	cpx B	cpx C	cpx core	cpx rim	cpx A	cpx B	rel cpx	rel cpx	rel cpx
Spot	5.2	5.4	5.5	5.6	2.3	2.4	3.3	3.4	3A	3.1	3.2	6.1	8.1	8.2	5.3	2.5	2.6	4.1		3.3	3.4	3.5	6.2	6.3	7.3	7.4	8.2	6.1	1.1
	HBL	ACT	ACT	ACT																									
Na2O	1.59	0.34	0.39	0.40	0.34	0.36	0.42	0.36	0.44	0.31	0.39	0.51	0.38	0.30	0.23	6.66	6.89	6.55		0.45	0.32	0.42	0.41	0.44	0.37	0.29	0.49	0.33	0.45
MgO	12.38	17.65	18.36	17.82	14.37	14.46	14.42	14.60	14.98	14.99	14.84	15.06	14.62	14.81	15.96	0.01	0.00	0.00		15.28	15.23	14.87	15.18	15.41	15.07	15.05	14.96	15.05	15.18
Al2O3	11.60	2.77	2.12	2.89	0.51	0.55	0.95	0.61	1.20	1.12	1.17	1.20	0.92	0.82	15.55	26.01	25.84	26.17		1.06	0.51	0.91	0.95	0.67	0.96	0.82	1.42	1.06	1.66
SiO2	43.29	54.79	54.96	54.08	54.14	54.33	54.45	54.71	53.96	54.33	53.89	53.79	53.98	54.24	37.99	58.24	58.64	58.34		54.72	54.12	54.32	54.07	54.64	54.15	53.34	53.66	53.60	53.89
K2O	0.56	0.11	0.06	0.13	0.00	0.01	0.01	0.00	0.00	0.00	0.00	0.00	0.00	0.00	9.55	0.22	0.09	0.15		0.00	0.00	0	0	0	0	0	0.00	0.00	0.00
CaO	12.18	12.75	12.77	12.73	24.62	24.40	24.10	24.50	24.15	24.31	24.63	24.50	23.98	24.34	0.11	7.91	7.79	8.20		24.02	24.26	24.23	24.35	24.44	23.8	24.23	24.07	24.18	23.49
TiO2	2.32	0.29	0.19	0.13	0.00	0.00	0.03	0.14	0.00	0.00	0.00	0.33	0.00	0.00	2.24	0.08	0.03	0.02		0.00	0.00	0	0	0	0	0	0.00	0.00	0.24
MnO	0.28	0.19	0.30	0.18	0.20	0.25	0.20	0.31	0.46	0.42	0.37	0.36	0.00	0.34	0.02	0.00	0.00	0.00		0.33	0.00	0	0	0	0	0.27	0.00	0.00	0.00
FeO	12.18	8.40	7.53	8.21	6.09	5.63	6.31	5.51	5.65	5.64	5.73	5.20	5.63	5.51	12.57	0.09	0.14	0.00		5.68	5.12	5.54	5.58	5.25	5.78	5.47	5.05	5.46	5.35
TOTAL	96.38	97.29	96.68	96.57	100.27	99.99	100.89	100.74	100.84	101.08	100.98	100.89	99.83	100.47	94.22	99.22	99.42	99.43		101.54	99.56	100.29	100.54	100.85	100.13	99.47	99.65	99.68	100.26
Na	0.479	0.097	0.112	0.116	0.024	0.026	0.030	0.026	0.060	0.023	0.028	0.035	0.028	0.023	0.066	2.325	2.399	2.280		0.13	0.09	0.12	0.12	0.12	0.11	0.08	0.14	0.09	0.13
Mg	2.868	3.886	4.054	3.955	0.790	0.795	0.787	0.796	1.630	0.815	0.810	0.820	0.805	0.810	3.545	0.003	0.000	0.000		3.30	3.34	3.25	3.31	3.34	3.3	3.32	3.28	3.31	3.31
Al	2.126	0.482	0.370	0.507	0.022	0.024	0.041	0.026	0.100	0.048	0.050	0.053	0.040	0.035	2.733	5.520	5.470	5.540		0.18	0.09	0.16	0.16	0.11	0.17	0.14	0.25	0.18	0.29
Si	6.729	8.094	8.144	8.054	1.998	2.005	1.995	2.002	3.950	1.983	1.973	1.968	1.993	1.990	5.663	10.484	10.529	10.475		7.93	7.97	7.97	7.91	7.95	7.95	7.9	7.89	7.91	7.89
K	0.111	0.021	0.011	0.025	0.000	0.000	0.000	0.000	0.000	0.000	0.000	0.000	0.000	0.000	1.816	0.051	0.021	0.034		0.00	0.00	0	0	0	0	0	0.00	0.00	0.00
Ca	2.029	2.018	2.028	2.031	0.974	0.965	0.946	0.961	1.890	0.950	0.968	0.960	0.950	0.958	0.018	1.526	1.499	1.578		3.73	3.83	3.81	3.82	3.81	3.75	3.84	3.79	3.82	3.68
Ti	0.271	0.032	0.021	0.015	0.000	0.000	0.001	0.004	0.000	0.000	0.000	0.010	0.000	0.000	0.251	0.011	0.004	0.003		0.00	0.00	0	0	0	0	0	0.00	0.00	0.03
Mn	0.037	0.024	0.038	0.023	0.006	0.008	0.006	0.010	0.030	0.013	0.013	0.010	0.000	0.010	0.003	0.000	0.000	0.000		0.04	0.00	0	0	0	0	0.03	0.00	0.00	0.00
Fe	1.583	1.038	0.933	1.023	0.188	0.174	0.193	0.169	0.350	0.173	0.175	0.160	0.175	0.170	1.567	0.014	0.021	0.000		0.69	0.63	0.68	0.68	0.64	0.71	0.68	0.62	0.67	0.66
Cat sum	16.232	15.692	15.712	15.748	4.003	3.996	3.999	3.993	8.010	4.003	4.016	4.015	3.991	3.996	15.661	19.932	19.942	19.910		16.00	15.95	15.99	16.00	15.97	15.99	15.99	15.97	15.98	15.99
Mg#	0.6443	0.7892	0.8129	0.7945	80.78	82.04	80.31	82.49		82.53	82.23	83.67	82.14	82.65	69.35					0.8271	0.8413	0.8270	0.8296	0.8392	0.8229	0.8300	0.8410	0.8317	0.8338
An%																39.11	38.25	40.54											
Rock	97-320c Hornblende gabbro-diorite				Wando Tonalite 97-161																								
Mineral	rel cpx	hbl core	hbl core		hbl rim	hbl	hbl	hbl rim	hbl rim	hbl	biotite	biotite	biotite	biotite	biotite	biotite	biotite	biotite	biotite	plag core	plag rim	Plag core	plag rim	plag core	plag core	plag rim	plag core	plag rim	plag rim
Spot	2.1	1.2	2.2		1.1	2.1	2.2	6.1	6.2	5.1	2.3	2.4	4.1	4.2	5.2	5.3	5.4	6.3	6.4	5.6	5.7	5.8	5.9	6.5	7.1	7.2	7.3	7.4	7.5
		HBL	HBL																										
Na2O	0.41	1.33	1.51		1.20	1.28	1.09	1.21	1.08	1.30	0.23	0.11	0.19	0.23	0.18	0.20	0.19	0.21	0.25	5.32	6.36	5.38	5.77	5.28	5.09	6.24	5.72	5.19	6.20
MgO	16.27	15.14	14.55		7.52	8.03	7.49	7.42	7.62	8.02	10.23	10.15	9.79	9.90	9.95	10.17	10.18	10.36	10.05	0.04	0.00	0.00	0.05	0.04	0.03	0.00	0.00	0.06	0.00
Al2O3	1.91	9.3	10.53		12.33	11.70	12.22	12.42	11.86	11.70	14.85	15.07	15.01	15.02	15.25	15.12	15.40	15.01	15.10	28.12	26.22	27.91	27.34	28.27	28.89	26.49	27.76	28.65	27.01
SiO2	54.18	47.36	46.52		40.72	41.64	41.07	40.48	41.39	41.70	35.41	35.90	35.72	35.77	35.66	36.01	36.33	36.15	36.15	55.54	57.71	55.66	56.43	54.87	55.11	57.98	56.31	55.05	57.88
K2O	0.00	0.43	0.44		1.56	1.40	1.60	1.49	1.31	1.24	9.51	9.79	9.71	9.62	9.85	9.72	9.67	9.78	9.60	0.09	0.10	0.16	0.16	0.15	0.15	0.30	0.16	0.12	0.22
CaO	20.95	12.43	12.32		11.57	11.59	11.52	11.73	11.65	11.61	0.00	0.00	0.00	0.00	0.00	0.00	0.00	0.00	0.00	10.26	8.46	10.34	9.43	10.67	10.95	8.72	9.87	11.08	8.88
TiO2	0.00	0.81	1.3		0.86	0.65	0.69	0.84	0.59	0.48	2.67	2.46	2.88	2.65	2.57	2.71	2.33	2.45	2.43	0.00	0.03	0.00	0.00	0.00	0.00	0.01	0.00	0.00	0.00
MnO	0.00	0	0		0.62	0.59	0.62	0.46	0.81	0.62	0.34	0.58	0.33	0.42	0.33	0.18	0.38	0.59	0.31	0.00	0.10	0.00	0.00	0.01	0.09	0.01	0.10	0.00	0.00
FeO	5.71	9.7	10.27		20.80	20.72	20.73	20.66	20.14	20.56	20.85	20.63	20.66	20.51	20.27	20.98	20.54	20.49	20.93	0.21	0.31	0.20	0.23	0.17	0.24	0.14	0.24	0.06	0.16
TOTAL	99.43	96.50	97.44		97.18	97.60	97.03	96.71	96.45	97.23	94.12	94.74	94.31	94.12	94.08	95.17	95.05	95.07	94.88	99.58	99.29	99.65	99.41	99.46	100.55	99.89	100.16	100.21	100.35
Na	0.12	0.36	0.4		0.377	0.400	0.342	0.381	0.34	0.406	0.07	0.033	0.058	0.07	0.055	0.06	0.057	0.063	0.075	1.862	2.224	1.883	2.02	1.855	1.77	2.169	1.991	1.81	2.145
Mg	3.54	3.13	2.99		1.815	1.920	1.807	1.798	1.843	1.926	2.389	2.353	2.279	2.307	2.319	2.345	2.343	2.391	2.323	0.011	0	0	0.013	0.011	0.008	0	0	0.016	0
Al	0.33	1.52	1.71		2.354	2.220	2.333	2.381	2.269	2.222	2.743	2.764	2.764	2.769	2.811	2.758	2.804	2.74	2.761	5.985	5.574	5.941	5.818	6.039	6.109	5.598	5.876	6.076	5.682
Si	7.90	6.57	6.42		6.593	6.690	6.65	6.582	6.717	6.718	5.549	5.585	5.579	5.593	5.576	5.572	5.611	5.598	5.607	10.027	10.406	10.049	10.186	9.943	9.886	10.392	10.111	9.903	10.329
K	0.00	0.08	0.08		0.322	0.290	0.33	0.309	0.271	0.255	1.901	1.943	1.935	1.919	1.965	1.919	1.905	1.932	1.9	0.021	0.023	0.037	0.037	0.035	0.034	0.069	0.037	0.028	0.05
Ca	3.27	1.85	1.82		2.007	2.000	1.999	2.044	2.026	2.004	0	0	0	0	0	0	0	0	0	1.985	1.635	2	1.824	2.072	2.105	1.675	1.899	2.136	1.698
Ti	0.00	0.08	0.14		0.105	0.080	0.084	0.103	0.072	0.058	0.315	0.288	0.338	0.312	0.302	0.315	0.271	0.285	0.283	0	0.004	0	0	0	0	0.001	0	0	0
Mn	0.00	0	0		0.085	0.080	0.085	0.063	0.111	0.085	0.045	0.076	0.044	0.056	0.044	0.024	0.05	0.077	0.041	0	0.015	0	0	0.002	0.014	0.002	0.015	0	0
Fe	0.70	1.13	1.18		2.817	2.790	2.807	2.809	2.733	2.77	2.733	2.684	2.699	2.682	2.651	2.715	2.653	2.653	2.715	0.032	0.047	0.03	0.035	0.026	0.036	0.021	0.036	0.009	0.024
Cat sum	15.86	14.72	14.74		16.475	16.460	16.437	16.47	16.382	16.443	15.75	15.734	15.697	15.706	15.726	15.723	15.698	15.745	15.716	19.922	19.927	19.941	19.933	19.982	19.962	19.926	19.965	19.978	19.928
Mg#	0.8349	0.7347	0.7170		0.3918	0.4076	0.3916	0.3903	0.4028	0.4101	0.4664	0.4671	0.4578	0.4624	0.4666	0.4634	0.4690	0.4740	0.4611										
An%																				51.32	42.12	51.02	47.00	52.30	53.85	42.81	48.36	53.75	43.62

Rock	Wando Tonalite 97-161			Dioritic dyke 97-206B																									
Mineral	epidote	titanite		hbl	hbl	hbl	hbl	hbl	hbl	hbl	hbl	hbl rim	hbl core	hbl rim	biotite	biotite	biotite	biotite	biotite	biotite	biotite	plag A cor	plag A cor	plag A rim	Plag B core	plag B rim	plag A rim	plag core	plag rim
Spot	5.5	3		1.1	1.2	1.6	1.7	2.1	2.2	3.1	4.1	4.2	7.3	2.8	2.3	2.4	2.5	3.2	3.3	5.1	5.2	1.3	1.4	1.5	1.8	1.9	1.1	3.4	3.5
Na2O	0.10	0.00		1.08	1.16	1.10	1.10	1.12	0.92	1.19	1.03	1.19	1.19	1.06	0.32	0.24	0.15	0.24	0.22	0.25	0.19	6.29	3.40	5.63	4.18	6.80	6.05	3.87	5.98
MgO	0.05	0.13		9.33	9.22	9.06	8.95	8.74	9.83	8.82	8.89	9.56	9.09	8.62	10.44	10.14	10.18	10.28	10.29	10.16	9.82	0.00	0.00	0.08	0.10	0.00	0.00	0.03	0.06
Al2O3	22.96	1.96		10.96	11.24	11.26	11.32	11.50	9.84	11.46	11.88	11.74	11.50	12.47	15.63	15.36	15.77	15.35	15.67	15.64	15.29	26.57	31.68	28.08	30.56	26.56	27.03	30.60	27.56
SiO2	37.75	29.96		45.14	44.13	44.21	44.35	44.13	46.36	44.16	44.20	44.08	44.51	43.75	36.42	36.46	35.75	36.36	36.89	36.37	36.41	57.93	50.92	56.29	52.87	58.97	56.68	51.36	56.60
K2O	0.00	0.00		0.63	0.72	0.74	0.76	0.73	0.56	0.69	0.70	0.78	0.61	0.87	9.53	9.64	9.09	9.80	9.88	9.52	9.77	0.19	0.01	0.11	0.01	0.07	0.14	0.07	0.08
CaO	23.37	27.30		11.72	11.88	11.91	11.76	11.40	11.83	11.54	11.78	11.64	11.89	11.56	0.00	0.04	0.08	0.05	0.00	0.00	0.00	8.62	14.63	10.14	13.04	8.09	9.38	13.51	9.51
TiO2	0.12	36.29		0.68	0.84	1.00	0.90	0.91	0.78	0.80	1.09	1.04	0.85	1.00	2.82	2.88	2.63	2.63	3.14	2.74	3.33	0.01	0.02	0.00	0.09	0.00	0.11	0.00	0.00
MnO	0.20	0.00		0.22	0.42	0.45	0.55	0.43	0.22	0.41	0.46	0.30	0.48	0.49	0.23	0.33	0.39	0.09	0.00	0.34	0.19	0.00	0.00	0.10	0.12	0.00	0.00	0.00	0.05
FeO	13.89	1.59		17.59	17.60	17.10	17.56	17.74	17.02	17.45	17.70	16.82	17.52	18.12	20.74	19.94	20.53	20.23	20.72	20.34	20.13	0.22	0.11	0.17	0.03	0.16	0.19	0.21	0.06
TOTAL	98.44	97.23		97.35	97.21	96.83	97.25	96.70	97.36	96.52	97.73	97.15	97.64	97.94	96.13	95.03	94.57	95.03	96.81	95.36	95.13	99.83	100.77	100.60	101.00	100.65	99.58	99.65	99.90
Na	0.017	0		0.327	0.354	0.336	0.335	0.343	0.277	0.365	0.312	0.362	0.361	0.321	0.095	0.072	0.045	0.072	0.065	0.074	0.057	2.186	1.192	1.952	1.455	2.34	2.115	1.37	2.083
Mg	0.007	0.003		2.174	2.162	2.127	2.096	2.057	2.279	2.078	2.071	2.232	2.118	2.009	2.374	2.326	2.35	2.362	2.32	2.325	2.253	0	0	0.021	0.027	0	0	0.008	0.016
Al	2.396	0.031		2.02	2.085	2.092	2.097	2.141	1.804	2.136	2.189	2.169	2.119	2.299	2.811	2.788	2.879	2.79	2.795	2.831	2.775	5.615	6.754	5.919	6.469	5.556	5.745	6.584	5.836
Si	3.341	0.403		7.058	6.944	6.966	6.97	6.97	7.211	6.98	6.908	6.906	6.958	6.843	5.556	5.613	5.537	5.607	5.582	5.585	5.605	10.385	9.208	10.064	9.493	10.463	10.219	9.374	10.166
K	0	0		0.126	0.145	0.149	0.152	0.147	0.111	0.139	0.14	0.156	0.122	0.174	1.855	1.893	1.796	1.928	1.907	1.865	1.919	0.043	0.002	0.025	0.002	0.016	0.032	0.016	0.018
Ca	2.216	0.393		1.964	2.003	2.011	1.98	1.929	1.972	1.955	1.973	1.954	1.992	1.937	0	0.007	0.013	0.008	0	0	0	1.656	2.835	1.943	2.509	1.538	1.812	2.642	1.83
Ti	0.008	0.367		0.08	0.099	0.118	0.106	0.108	0.091	0.095	0.128	0.123	0.1	0.118	0.324	0.333	0.306	0.305	0.357	0.316	0.386	0.001	0.003	0	0.012	0	0.015	0	0
Mn	0.015	0		0.029	0.056	0.06	0.073	0.058	0.029	0.055	0.061	0.04	0.064	0.065	0.03	0.043	0.051	0.012	0	0.044	0.025	0	0	0.015	0.018	0	0	0	0.008
Fe	0.308	0.018		2.3	2.316	2.253	2.308	2.343	2.214	2.307	2.314	2.204	2.291	2.37	2.646	2.567	2.659	2.609	2.622	2.612	2.592	0.033	0.017	0.025	0.005	0.024	0.029	0.032	0.009
Cat sum	8.308	1.215		16.078	16.164	16.112	16.119	16.096	15.989	16.109	16.095	16.145	16.123	16.137	15.69	15.642	15.638	15.693	15.649	15.653	15.61	19.921	20.01	19.965	19.989	19.936	19.967	20.027	19.966
Mg#				0.4859	0.4828	0.4856	0.4759	0.4675	0.5072	0.4739	0.4723	0.5032	0.4804	0.4588	0.4729	0.4754	0.4692	0.4752	0.4694	0.4709	0.4650								
An%																							42.63	70.36	49.57	63.26	39.50	45.77	65.59

Rock	Dioritic dyke 97-206B										Warradale Tonalite 97-WA1																	
Mineral	plag core	plag rim	plag rim	plag core	plag rim	plag core	plag rim	plag core	plag rim		hbl core	Hbl rim	Hbl rim	Hbl	Hbl	Hbl rim	hbl core	biotite	biotite	biotite	biotite	biotite	biotite	biotite	plag A core	plag A rim	Plag B core	plag B rim
Spot	6.1	6.2	6.3	6.4	6.5	7.1	7.2	2.6	2.7		1.1	1.2	2.1	2.2	2.3	7.1	7.2	1.3	1.4	1.5	3.1	3.2	3.3	7.3	7.4	3.4	3.5	3.6	3.7
Na2O	4.60	5.21	7.19	5.28	4.85	3.71	6.75	5.33	6.02		1.14	1.16	1.03	1.09	1.00	1.16	1.09	0.23	0.22	0.29	0.29	0.25	0.29	0.20	0.18	5.30	6.29	5.41	6.32
MgO	0.03	0.00	0.00	0.00	0.04	0.02	0.00	0.09	0.00		9.30	8.88	8.94	9.83	8.58	8.76	8.65	10.68	10.22	10.80	10.98	10.75	10.45	10.75	10.83	0.02	0.00	0.00	0.07
Al2O3	29.80	28.65	25.73	28.75	29.25	31.05	26.18	28.58	27.32		9.81	11.12	11.04	9.29	11.37	11.08	11.11	14.73	14.90	14.66	15.07	14.59	14.76	14.95	14.88	28.28	26.78	28.13	26.81
SiO2	53.26	55.02	59.85	55.11	53.92	51.74	59.07	55.53	57.44		43.75	42.39	42.34	44.56	42.37	42.09	42.32	36.54	36.45	36.33	36.40	36.52	36.56	36.69	36.42	55.14	57.53	55.17	57.77
K2O	0.01	0.13	0.11	0.06	0.06	0.04	0.13	0.11	0.06		1.28	1.44	1.48	1.12	1.31	1.50	1.36	9.99	9.96	9.69	9.84	9.51	10.00	10.04	9.80	0.15	0.21	0.23	0.24
CaO	12.16	10.95	7.52	10.90	11.68	13.36	8.19	10.77	9.41		11.82	11.84	11.71	11.84	11.75	11.91	11.89	0.04	0.06	0.00	0.01	0.05	0.00	0.00	0.05	10.99	8.98	10.46	8.85
TiO2	0.03	0.03	0.00	0.00	0.00	0.00	0.00	0.01	0.00		1.46	1.19	1.23	1.39	0.81	1.17	1.07	3.02	3.17	2.98	3.03	2.56	3.28	3.07	3.19	0.00	0.04	0.02	0.14
MnO	0.03	0.00	0.00	0.00	0.00	0.01	0.00	0.00	0.05		0.52	0.45	0.34	0.42	0.40	0.58	0.49	0.35	0.34	0.26	0.16	0.14	0.20	0.45	0.39	0.13	0.00	0.00	0.00
FeO	0.16	0.17	0.04	0.00	0.18	0.05	0.01	0.20	0.14		18.18	19.17	18.74	17.80	19.56	19.12	18.91	19.91	20.63	20.28	20.20	19.58	20.11	19.78	20.58	0.28	0.26	0.16	0.00
TOTAL	100.08	100.16	100.44	100.10	99.98	99.98	100.33	100.62	100.44		97.42	97.64	96.85	97.49	97.25	97.37	96.89	95.61	95.95	95.29	95.98	93.95	95.65	95.93	96.32	100.29	100.09	99.58	100.20
Na	1.613	1.819	2.474	1.842	1.7	1.305	2.329	1.851	2.083		0.351	0.358	0.320	0.334	0.310	0.360	0.339	0.069	0.065	0.087	0.086	0.075	0.086	0.059	0.053	1.851	2.186	1.898	2.190
Mg	0.008	0	0	0	0.011	0.005	0	0.024	0		2.201	2.109	2.134	2.313	2.047	2.090	2.067	2.446	2.336	2.480	2.501	2.490	2.390	2.448	2.464	0.005	0.000	0.000	0.019
Al	6.353	6.08	5.383	6.097	6.233	6.64	5.492	6.034	5.748		1.837	2.089	2.085	1.729	2.145	2.091	2.100	2.668	2.695	2.663	2.715	2.673	2.670	2.693	2.678	6.005	5.658	6.001	5.650
Si	9.631	9.905	10.62	9.913	9.747	9.386	10.51	9.944	10.251		6.947	6.755	6.782	7.036	6.782	6.738	6.786	5.615	5.591	5.597	5.562	5.675	5.610	5.606	5.560	9.931	10.311	9.983	10.326
K	0.002	0.03	0.025	0.014	0.014	0.009	0.03	0.025	0.014		0.259	0.293	0.302	0.226	0.268	0.306	0.278	1.958	1.949	1.905	1.918	1.885	1.958	1.957	1.909	0.034	0.048	0.053	0.055
Ca	2.356	2.112	1.43	2.101	2.262	2.597	1.561	2.067	1.799		2.011	2.022	2.010	2.003	2.015	2.043	2.043	0.007	0.010	0.000	0.002	0.008	0.000	0.000	0.008	2.121	1.724	2.028	1.695
Ti	0.004	0.004	0	0	0	0	0	0.001	0		0.174	0.143	0.148	0.165	0.098	0.141	0.129	0.349	0.366	0.345	0.348	0.299	0.379	0.353	0.366	0.000	0.005	0.003	0.019
Mn	0.005	0	0	0	0	0.002	0	0	0.008		0.070	0.061	0.046	0.056	0.054	0.079	0.067	0.046	0.044	0.034	0.021	0.018	0.026	0.058	0.050	0.020	0.000	0.000	0.000
Fe	0.024	0.026	0.006	0	0.027	0.008	0.001	0.03	0.021		2.414	2.555	2.511	2.351	2.618	2.560	2.536	2.559	2.647	2.613	2.582	2.545	2.581	2.528	2.627	0.042	0.039	0.024	0.000
Cat sum	19.996	19.975	19.938	19.966	19.994	19.951	19.923	19.976	19.924		16.665	16.384	16.338	16.254	16.367	16.408	16.344	15.746	15.703	15.722	15.734	15.669	15.699	15.703	15.716	20.009	19.972	19.990	19.953
Mg#											0.47692	0.45219	0.45942	0.49593	0.43880	0.44946	0.44905	0.488711	0.468794	0.486943	0.492032	0.494538	0.480789	0.4919614	0.4839914				
An%	46.55	59.33	An%	36.40	53.10	56.89	66.40	39.82	52.42																	52.95	43.56	50.97	43.02

Rock	Warradale Tonalite 97-WA1												97-427 Chetwynd Tonalite															
Mineral	plag core	plag rim	plag rim	plag core	plag rim	plag core	plag rim	plag core	plag rim	K-felds	titanite		Biottite	Biottite	Biottite	Biottite	Biottite	Biottite	Plag core	Plag rim	plag rim	plag core	plag core	plag rim	plag Acore	plag core	plag A rim	plag B core	plag B rim
Spot	4.2	4.3	5.1	5.2	5.3	6.1	6.2	7.5	7.6	4.1	7.7		1.2	1.3	3.1	3.2	6.7	6.8	4.1	4.2	4.3	4.4	4.5	4.6	5.1	5.2	5.3	5.4	5.5
Na2O	5.45	5.81	6.19	5.82	6.51	5.85	6.03	5.26	6.33	1.09	0.00		0.16	0.21	0.3	0.24	0.19	0.18	6.46	5.92	6.73	5.8	5.32	6.96	6.38	6.18	6.45	5.66	5.98
MgO	0.03	0.00	0.00	0.00	0.03	0.04	0.00	0.00	0.05	0.01	0.06		11.54	11.74	11.86	11.67	11.47	11.34	0.05	0	0.05	0.13	0.07	0	0.03	0.07	0.01	0	0.02
Al2O3	28.03	27.27	27.45	27.49	26.88	27.95	27.35	28.61	26.64	18.68	1.49		15.83	16.07	15.82	15.81	15.71	15.62	27.11	27.61	26.56	27.91	28.35	25.95	26.87	27.48	27.06	28.15	27.65
SiO2	55.72	57.12	57.79	57.15	57.61	56.44	57.59	55.40	58.20	64.91	30.27		36.54	36.81	36.67	36.49	36.12	35.99	57.63	56.82	58.78	56.07	55.04	58.61	58.47	57.6	58.23	56	56.78
K2O	0.20	0.17	0.23	0.22	0.25	0.28	0.18	0.22	0.46	15.38	0.00		9.99	10.05	9.99	9.98	9.92	9.83	0.2	0.19	0.34	0.16	0.25	0.23	0.21	0.3	0.22	0.11	0.26
CaO	10.53	9.36	9.38	9.51	8.93	10.14	9.35	10.82	8.47	0.00	27.67		0	0	0.1	0	0	0.1	8.73	9.46	8.26	10.06	10.69	7.94	8.76	9.21	8.61	10.21	9.55
TiO2	0.01	0.09	0.18	0.00	0.00	0.09	0.16	0.02	0.10	0.17	38.10		3.03	3.16	2.67	3.09	3.02	2.98	0.04	0.03	0.03	0	0.02	0	0.02	0.06	0	0.19	0.09
MnO	0.00	0.00	0.00	0.23	0.00	0.00	0.00	0.00	0.10	0.00	0.14		0.52	0.53	0.64	0.47	0.45	0.63	0	0	0	0	0.01	0	0	0.16	0	0	0
FeO	0.04	0.12	0.09	0.08	0.11	0.18	0.02	0.25	0.15	0.11	0.72		17.57	17.22	17.53	17.22	17.5	17.38	0.09	0.02	0.12	0.1	0.15	0	0.09	0	0	0.17	0
TOTAL	100.01	99.94	101.31	100.50	100.32	100.97	100.68	100.58	100.50	100.35	98.45		95.18	95.79	95.58	94.97	94.38	94.05	100.31	100.05	100.87	100.23	99.9	99.69	100.83	101.06	100.58	100.49	100.33
Na	1.902	2.020	2.126	2.016	2.257	2.024	2.081	1.829	2.189	0.389	0.000		0.047	0.061	0.088	0.071	0.057	0.054	2.237	2.058	2.316	2.019	1.862	2.419	2.195	2.128	2.224	1.965	2.075
Mg	0.008	0.000	0.000	0.000	0.008	0.011	0.000	0.000	0.013	0.003	0.001		2.619	2.641	2.682	2.65	2.626	2.607	0.013	0	0.013	0.035	0.019	0	0.008	0.019	0.003	0	0.005
Al	5.948	5.764	5.732	5.789	5.667	5.879	5.739	6.048	5.600	4.048	0.023		2.841	2.86	2.83	2.84	2.846	2.841	5.709	5.835	5.556	5.906	6.034	5.484	5.622	5.754	5.673	5.943	5.833
Si	10.029	10.242	10.236	10.208	10.303	10.069	10.251	9.934	10.378	11.932	0.401		5.563	5.556	5.564	5.56	5.55	5.552	10.294	10.185	10.43	10.064	9.936	10.506	10.377	10.23	10.355	10.028	10.161
K	0.046	0.039	0.052	0.050	0.057	0.064	0.041	0.050	0.105	3.607	0.000		1.941	1.935	1.934	1.94	1.945	1.935	0.046	0.043	0.077	0.037	0.058	0.053	0.048	0.068	0.05	0.025	0.059
Ca	2.031	1.798	1.780	1.820	1.711	1.938	1.783	2.079	1.618	0.000	0.393		0	0	0.016	0	0	0.017	1.671	1.817	1.57	1.935	2.068	1.525	1.666	1.753	1.641	1.959	1.831
Ti	0.001	0.012	0.024	0.000	0.000	0.012	0.021	0.003	0.013	0.024	0.380		0.347	0.359	0.305	0.354	0.349	0.346	0.005	0.004	0.004	0	0.003	0	0.003	0.008	0	0.026	0.012
Mn	0.000	0.000	0.000	0.035	0.000	0.000	0.000	0.000	0.015	0.000	0.002		0.067	0.068	0.082	0.061	0.059	0.082	0	0	0	0	0.002	0	0	0.024	0	0	0
Fe	0.006	0.018	0.013	0.012	0.016	0.027	0.003	0.037	0.022	0.017	0.008		2.237	2.174	2.225	2.194	2.249	2.242	0.013	0.003	0.018	0.015	0.023	0	0.013	0	0	0.025	0
Cat sum	19.970	19.893	19.963	19.930	20.021	20.023	19.919	19.979	19.955	20.018	1.208		15.663	15.654	15.727	15.671	15.679	15.676	19.988	19.944	19.984	20.01	20.004	19.987	19.931	19.983	19.945	19.971	19.977
Mg#													0.5393	0.5485	0.5466	0.5471	0.5387	0.5376											
An%	51.04	46.62	44.97	46.83	42.51	48.14	45.66	52.53	41.36										42.26	46.38	39.62	48.48	51.86	38.15	42.62	44.39	41.92	49.61	46.18

Rock	97-427 Chetwynd Tonalite							T2-135 Tuloona Granodiorite																				
Mineral	pl B rim	pl A core	pl A rim	pl B core	pl B core	plag B rim	Kf	bio	bio	bio	bio core	bio rim	bio	musc	musc	musc	musc	plag core	plag rim	plag core	plag rim	plag core	plag rim	plag core	plag core	plag rim	plag core	Kf A rim
Spot	5.6	6.2	6.3	6.4	6.5	6.6	6.1	3.2	5.1	6.2	10.1	10.2	11.2	6.1	7.1	10.3	11.1	9.1	9.2	9.3	9.4	12.1	12.2	13.1	13.2	13.3	14.1	8.1
Na2O	6.56	6	5.78	6.21	6.31	6.18	0.8	0.24	0.30	0.28	0.25	0.24	0.26	0.45	0.37	0.40	0.28	6.16	7.40	5.76	7.05	6.55	7.40	6.30	5.93	7.15	6.64	1.22
MgO	0.04	0	0	0.07	0.1	0.04	0.04	9.65	9.73	10.23	9.50	9.76	10.98	0.89	1.04	0.90	1.46	0.00	0.00	0.00	0.00	0.00	0.00	0.00	0.00	0.00	0.00	0.00
Al2O3	26.95	27.33	27.93	27.25	26.98	27.29	18.51	17.59	17.67	17.05	17.84	17.57	16.62	31.93	31.26	31.74	29.51	27.17	25.17	28.14	25.98	27.06	25.72	27.29	27.41	26.04	26.35	18.51
SiO2	57.77	56.59	56.51	57.36	57.44	57.23	64.94	35.54	35.87	35.67	35.70	35.39	36.24	45.27	45.23	44.93	45.54	57.00	59.88	56.45	59.41	58.19	59.10	57.37	57.08	59.68	57.96	64.63
K2O	0.23	0.17	0.22	0.27	0.28	0.21	15.53	9.99	9.76	9.88	9.84	10.04	10.03	10.94	10.96	10.77	11.11	0.13	0.15	0.00	0.13	0.24	0.16	0.14	0.18	0.34	0.20	15.28
CaO	8.55	9.48	9.78	8.95	8.78	9.06	0	0	0.00	0.00	0.00	0.00	0.00	0.00	0.00	0.00	0	9.14	6.98	9.97	7.46	8.84	7.49	8.97	9.54	7.23	8.32	0.00
TiO2	0.07	0.16	0.13	0.07	0	0.14	0.28	2.71	2.20	2.15	2.41	2.33	2.52	0.76	0.62	0.85	0.81	0.00	0.00	0.00	0.00	0.00	0.00	0.00	0.00	0.00	0.00	0.24
MnO	0	0.1	0	0	0	0	0.01	0.45	0.66	0.58	0.50	0.44	0.58	0.00	0.00	0.00	0	0.00	0.00	0.00	0.00	0.00	0.00	0.00	0.00	0.00	0.00	0.00
FeO	0.2	0.15	0.16	0.29	0.14	0.06	0.09	18.56	18.56	19.02	18.31	18.40	18.58	4.80	5.24	4.17	5.76	0.00	0.00	0.00	0.00	0.00	0.00	0.00	0.00	0.00	0.00	0.00
TOTAL	100.37	99.98	100.51	100.47	100.03	100.21	100.2	94.78	94.83	94.81	94.40	94.16	95.78	94.95	94.76	93.87	94.47	99.76	99.62	100.61	99.95	100.89	100.06	99.83	100.16	100.49	99.64	100.00
Na	2.271	2.091	2.004	2.151	2.193	2.144	0.286	0.07	0.09	0.08	0.07	0.07	0.08	0.12	0.10	0.11	0.07	2.15	2.57	1.99	2.44	2.26	2.56	2.19	2.06	2.46	2.31	0.44
Mg	0.011	0	0	0.019	0.027	0.011	0.011	2.21	2.22	2.35	2.18	2.25	2.49	0.18	0.21	0.18	0.3	0.00	0.00	0.00	0.00	0.00	0.00	0.00	0.00	0.00	0.00	0.00
Al	5.674	5.791	5.888	5.739	5.7	5.756	4.016	3.18	3.19	3.09	3.23	3.20	2.98	5.15	5.07	5.16	4.82	5.76	5.30	5.92	5.46	5.66	5.41	5.77	5.78	5.45	5.58	4.03
Si	10.316	10.171	10.104	10.246	10.294	10.238	11.953	5.46	5.50	5.49	5.49	5.47	5.51	6.19	6.22	6.20	6.31	10.25	10.71	10.09	10.59	10.33	10.56	10.28	10.22	10.59	10.41	11.93
K	0.052	0.039	0.05	0.062	0.064	0.048	3.647	1.96	1.91	1.94	1.93	1.98	1.95	1.91	1.92	1.90	1.96	0.03	0.03	0.00	0.03	0.05	0.04	0.03	0.04	0.08	0.05	3.60
Ca	1.636	1.826	1.874	1.713	1.686	1.737	0	0	0.00	0.00	0.00	0.00	0.00	0.00	0.00	0.00	0	1.76	1.34	1.91	1.43	1.68	1.43	1.72	1.83	1.37	1.60	0.00
Ti	0.009	0.022	0.017	0.009	0	0.019	0.039	0.31	0.25	0.25	0.28	0.27	0.29	0.08	0.06	0.09	0.08	0.00	0.00	0.00	0.00	0.00	0.00	0.00	0.00	0.00	0.00	0.03
Mn	0	0.015	0	0	0	0	0.002	0.06	0.09	0.08	0.06	0.06	0.07	0.00	0.00	0.00	0	0.00	0.00	0.00	0.00	0.00	0.00	0.00	0.00	0.00	0.00	0.00
Fe	0.03	0.023	0.024	0.043	0.021	0.009	0.014	2.39	2.38	2.45	2.36	2.38	2.36	0.55	0.60	0.48	0.67	0.00	0.00	0.00	0.00	0.00	0.00	0.00	0.00	0.00	0.00	0.00
Cat sum	20	19.977	19.961	19.981	19.984	19.961	19.966	15.65	15.65	15.72	15.61	15.68	15.72	14.17	14.19	14.13	14.22	19.96	19.95	19.97	19.92	19.99	20.04	19.95	19.93	19.96	19.97	20.04
Mg#								0.4804	0.4826	0.4896	0.4802	0.4860	0.5134	0.2466	0.2593	0.2727	0.3093											
An%	41.32	46.16	47.71	43.63	42.76	44.21												44.67	34.01	48.97	36.67	42.11	35.48	43.65	46.56	35.04	40.40	

Rock	T2-135 Tuloona Granodiorite			98-RC1 Diorite dyke																								
Mineral	Kf A core	Kf B core	Kf B rim	hbl rim	hbl rim	hbl core	hbl rim	hbl A core	hbl A rim	hbl b core	hbl B rim	hbl rim	hbl rim	plag core	plag rim	plag core	plag rim	plag core	plag rim	plag core	plag rim	plag core	plag core	plag core	plag rim	KF	titanite	ttanite
Spot	8.2	8.3	8.4	1.1	1.2	2.1	2.2	3.1	3.2	3.3	3.4	5.2	6.1	2.3	2.4	2.5	2.6	7.1	7.2	7.3	7.4	9.1	9.2	9.3	9.4	4.1	1.3	1.4
Na2O	1.32	1.12	1.31	1.33	1.35	1.15	1.21	1.71	1.23	1.62	1.35	1.38	1.40	5.67	6.80	4.40	6.60	5.92	7.41	5.34	7.19	5.09	6.33	4.94	7.30	1.08	0.00	0.00
MgO	0.00	0.00	0.00	11.81	9.93	11.49	11.15	14.27	10.59	14.42	11.01	10.89	10.89	0.00	0.04	0.00	0.00	0.02	0.04	0.00	0.06	0.00	0.00	0.05	0.00	0.03	0.03	0.05
Al2O3	18.38	18.70	18.85	8.33	8.99	7.78	8.21	8.42	8.92	7.71	8.83	8.69	8.74	27.81	26.41	29.79	26.44	27.41	25.54	28.10	25.46	28.78	26.63	28.93	25.66	18.65	1.36	1.24
SiO2	64.76	65.07	64.29	45.94	44.37	46.82	45.35	47.12	44.79	47.77	44.91	45.44	44.86	56.25	58.61	53.47	58.08	56.72	60.33	55.63	60.21	54.90	57.38	54.71	60.21	65.10	29.87	30.49
K2O	15.13	15.31	14.89	0.83	1.19	0.85	1.02	0.46	1.14	0.42	0.92	0.96	0.96	0.23	0.14	0.11	0.26	0.12	0.20	0.27	0.25	0.12	0.23	0.11	0.14	15.27	0.00	0.00
CaO	0.00	0.00	0.00	11.68	11.80	12.08	11.67	10.92	11.63	10.97	11.77	11.69	11.57	9.93	8.02	12.05	8.34	9.55	6.84	10.49	7.20	11.15	8.71	11.15	6.92	0.00	27.45	27.10
TiO2	0.00	0.00	0.00	1.30	1.18	0.93	1.24	1.34	1.22	1.12	1.61	1.30	1.54	0.12	0.00	0.20	0.07	0.03	0.00	0.10	0.09	0.17	0.06	0.17	0.00	0.03	36.18	37.99
MnO	0.00	0.00	0.00	0.14	0.41	0.19	0.35	0.33	0.23	0.38	0.35	0.32	0.35	0.00	0.00	0.00	0.09	0.01	0.07	0.00	0.00	0.00	0.00	0.08	0.00	0.00	0.00	0.00
FeO	0.00	0.00	0.00	15.97	18.06	16.46	16.77	12.74	17.35	12.50	16.50	16.52	16.92	0.13	0.04	0.07	0.05	0.13	0.12	0.33	0.23	0.09	0.29	0.08	0.15	0.05	1.62	1.10
TOTAL	99.63	100.41	99.76	97.33	97.28	97.75	96.97	97.31	97.10	96.91	97.25	97.19	97.23	100.14	100.06	100.09	99.93	99.91	100.55	100.26	100.69	100.30	99.63	100.22	100.38	100.21	96.51	97.97
Na	0.47	0.40	0.47	0.402	0.415	0.347	0.370	0.507	0.376	0.481	0.411	0.420	0.427	1.974	2.353	1.540	2.292	2.062	2.545	1.862	2.469	1.774	2.209	1.723	2.509	0.385	0.000	0.000
Mg	0.00	0.00	0.00	2.743	2.346	2.661	2.618	3.251	2.491	3.291	2.576	2.546	2.554	0.000	0.011	0.000	0.000	0.005	0.011	0.000	0.016	0.000	0.000	0.013	0.000	0.008	0.001	0.001
Al	4.00	4.05	4.10	1.531	1.680	1.425	1.525	1.517	1.660	1.392	1.634	1.607	1.621	5.886	5.557	6.341	5.584	5.804	5.333	5.957	5.315	6.100	5.650	6.137	5.363	4.041	0.022	0.019
Si	11.97	11.94	11.88	7.161	7.035	7.275	7.144	7.203	7.069	7.316	7.051	7.128	7.058	10.098	10.461	9.654	10.404	10.188	10.685	10.003	10.662	9.871	10.327	9.844	10.674	11.966	0.405	0.406
K	3.57	3.58	3.51	0.165	0.241	0.169	0.205	0.090	0.230	0.082	0.184	0.192	0.193	0.053	0.032	0.025	0.059	0.027	0.045	0.062	0.056	0.028	0.053	0.025	0.032	3.581	0.000	0.000
Ca	0.00	0.00	0.00	1.951	2.005	2.011	1.970	1.789	1.967	1.800	1.980	1.965	1.951	1.910	1.534	2.331	1.601	1.838	1.298	2.021	1.366	2.148	1.680	2.150	1.315	0.000	0.399	0.386
Ti	0.00	0.00	0.00	0.152	0.141	0.109	0.147	0.154	0.145	0.129	0.190	0.153	0.182	0.016	0.000	0.027	0.009	0.004	0.000	0.014	0.012	0.023	0.008	0.023	0.000	0.004	0.369	0.380
Mn	0.00	0.00	0.00	0.018	0.055	0.025	0.047	0.043	0.031	0.049	0.047	0.043	0.047	0.000	0.000	0.000	0.014	0.002	0.011	0.000	0.000	0.000	0.000	0.012	0.000	0.000	0.000	0.000
Fe	0.00	0.00	0.00	2.082	2.395	2.139	2.209	1.629	2.290	1.601	2.166	2.167	2.226	0.020	0.006	0.011	0.007	0.020	0.018	0.050	0.034	0.014	0.044	0.012	0.022	0.008	0.018	0.012
Cat sum	20.02	20.00	20.03	16.205	16.312	16.161	16.234	16.182	16.259	16.141	16.240	16.221	16.259	19.956	19.953	19.931	19.971	19.950	19.944	19.967	19.931	19.957	19.971	19.939	19.915	19.992	1.215	1.205
Mg#				0.56850	0.49483	0.55438	0.54237	0.66619	0.52102	0.67273	0.54323	0.54021	0.53431															
An%														48.51	39.14	59.83	40.51	46.80	33.38	51.23	35.11	54.38	42.62	55.16	34.10			

Rock	98-RC1 Diorite dyke			97-52 Cairns Creek Granodiorite																								
Mineral	titanite	titanite	titanite	hbl	hbl rim	hbl	hbl	hbl	hbl	bio	bio	bio	bio	bi core	bio rim	bio	KF	KF	plag core	plag rim	plag rim	plag core	plag core	plag rim	plag core	plag core	plag rim	plag A core
Spot	5.1	5.3	6.2	1.1	1.2	2.1	3.1	3.2	4.4	4.5	4.6	5.1	5.2	6.1	6.2	6.3	2.3	3.3	3.6	3.7	3.8	4.1	4.2	4.3	4.7	4.8	4.9	7.1
Na2O	0.00	0.02	0.00	1.60	1.63	1.65	1.48	1.32	1.42	0.30	0.20	0.20	0.14	0.17	0.24	0.16	1.32	1.54	7.40	7.45	8.93	7.21	7.57	9.15	8.00	6.06	8.67	5.66
MgO	0.03	0.00	0.00	11.57	11.63	12.05	11.64	11.86	11.53	13.66	13.25	12.93	13.04	13.26	14.35	13.27	0.04	0.06	0.00	0.05	0.00	0.00	0.04	0.04	0.07	0.00	0.00	0.14
Al2O3	1.42	1.42	1.40	8.62	8.29	7.82	8.44	7.54	7.73	14.00	13.59	13.77	13.89	13.62	14.26	13.77	18.37	18.77	25.08	25.01	22.89	25.55	24.83	23.12	24.31	27.36	23.36	28.04
SiO2	30.01	29.66	30.36	44.62	45.65	46.03	45.11	46.19	46.27	37.74	38.10	37.41	37.89	37.75	38.49	38.10	64.96	64.42	60.30	60.51	64.10	59.80	60.63	64.22	61.80	56.92	63.53	56.44
K2O	0.00	0.00	0.01	1.01	0.97	0.90	0.98	0.86	0.85	9.66	9.94	9.63	10.05	9.98	9.93	10.03	15.31	14.57	0.14	0.26	0.21	0.26	0.37	0.24	0.21	0.07	0.19	0.16
CaO	27.53	26.89	27.69	11.55	11.48	11.45	11.55	11.86	11.67	0.04	0.00	0.08	0.04	0.00	0.05	0.09	0.00	0.08	6.97	6.41	4.34	7.38	6.21	3.94	5.89	9.41	4.54	10.07
TiO2	37.78	37.66	38.15	1.15	1.05	1.22	1.21	1.11	0.98	2.51	2.89	3.32	3.03	2.85	2.27	2.75	0.14	0.46	0.00	0.15	0.00	0.01	0.08	0.10	0.08	0.00	0.00	0.08
MnO	0.00	0.00	0.11	0.63	0.71	0.74	0.63	0.69	0.65	0.47	0.45	0.61	0.65	0.57	0.54	0.41	0.05	0.02	0.00	0.00	0.00	0.00	0.02	0.00	0.07	0.15	0.07	0.10
FeO	1.52	1.52	1.19	17.60	18.00	17.89	17.99	16.89	17.34	18.57	19.29	18.80	18.78	18.85	16.85	19.06	0.19	0.31	0.27	0.13	0.10	0.04	0.27	0.23	0.10	0.00	0.24	0.17
TOTAL	98.29	97.17	98.91	98.35	99.41	99.75	99.03	98.32	98.44	96.95	97.71	96.75	97.51	97.05	96.98	97.64	100.38	100.23	100.16	99.97	100.57	100.25	100.02	101.04	100.53	99.97	100.60	100.86
Na	0.000	0.001	0.000	0.486	0.489	0.493	0.446	0.398	0.428	0.087	0.058	0.058	0.041	0.050	0.069	0.046	0.471	0.549	2.552	2.569	3.041	2.487	2.612	3.103	2.740	2.108	2.955	1.958
Mg	0.001	0.000	0.000	2.700	2.683	2.768	2.698	2.749	2.672	3.051	2.948	2.902	2.905	2.969	3.175	2.952	0.011	0.016	0.000	0.013	0.000	0.000	0.011	0.010	0.018	0.000	0.000	0.037
Al	0.022	0.023	0.022	1.591	1.513	1.421	1.547	1.383	1.417	2.474	2.392	2.445	2.448	2.413	2.496	2.423	3.985	4.070	5.259	5.244	4.739	5.358	5.209	4.767	5.062	5.787	4.842	5.896
Si	0.400	0.399	0.401	6.986	7.067	7.095	7.015	7.184	7.195	5.656	5.688	5.633	5.664	5.672	5.715	5.687	11.952	11.850	10.725	10.763	11.258	10.637	10.789	11.231	10.916	10.213	11.169	10.067
K	0.000	0.000	0.000	0.202	0.192	0.177	0.194	0.171	0.169	1.847	1.893	1.850	1.917	1.913	1.881	1.910	3.594	3.419	0.032	0.059	0.047	0.059	0.084	0.054	0.047	0.016	0.043	0.036
Ca	0.393	0.388	0.392	1.938	1.904	1.891	1.925	1.977	1.944	0.006	0.000	0.013	0.006	0.000	0.008	0.014	0.000	0.016	1.328	1.222	0.817	1.407	1.184	0.738	1.115	1.809	0.855	1.925
Ti	0.378	0.381	0.379	0.135	0.122	0.141	0.142	0.130	0.115	0.283	0.324	0.376	0.341	0.322	0.253	0.309	0.019	0.064	0.000	0.020	0.000	0.001	0.011	0.013	0.011	0.000	0.000	0.011
Mn	0.000	0.000	0.001	0.084	0.093	0.097	0.083	0.091	0.086	0.060	0.057	0.078	0.082	0.073	0.068	0.052	0.008	0.003	0.000	0.000	0.000	0.000	0.003	0.000	0.010	0.023	0.010	0.015
Fe	0.017	0.017	0.013	2.305	2.331	2.306	2.340	2.197	2.255	2.328	2.408	2.368	2.348	2.369	2.092	2.379	0.029	0.048	0.040	0.019	0.015	0.006	0.040	0.034	0.015	0.000	0.035	0.025
Cat sum	1.211	1.209	1.209	16.426	16.395	16.389	16.390	16.279	16.280	15.791	15.768	15.723	15.750	15.781	15.758	15.771	20.069	20.036	19.937	19.909	19.917	19.955	19.943	19.950	19.935	19.956	19.909	19.971
Mg#				0.53946	0.53510	0.54553	0.53553	0.55580	0.54232	0.567206	0.550411	0.550664	0.553017	0.556201	0.60281	0.553742												
An%																			33.95	31.74	20.92	35.59	30.52	18.95	28.58	46.00	22.19	49.12

Rock	97-52 Cairns Creek Granodiorite											97-373 Kassingbrook Granodiorite																
Mineral	plag rim	plag rim	plag core	plag rim	plag core	plag core	plag core	plag rim	titanite	titanite		bio	bio	bio	bio	bio	bio	bio	plag core	plag rim	plag core	plag core	plag core	plag rim	plag core	plag rim	plag rim	plag core	plag rim
Spot	7.2	7.3	7.4	7.5	7.6	8.1	8.2	8.3	9.1	3.5		1.1	2.1	2.2	2.3	6.1	7.1	8.2	3.1	3.2	3.3	3.4	3.5	3.6	4.1	4.2	4.3	4.4	4.5
Na2O	7.18	8.76	5.59	8.95	7.02	5.77	7.27	8.77	0.00	0.04		0.18	0.34	0.25	0.15	0.30	0.23	0.17	7.16	7.81	6.30	7.26	6.84	8.07	8.65	7.71	8.47	7.40	7.70
MgO	0.00	0.00	0.00	0.06	0.00	0.00	0.00	0.08	0.03	0.03		8.31	8.09	8.43	8.03	8.08	8.43	8.17	0.00	0.00	0.07	0.03	0.03	0.04	0.00	0.01	0.00	0.07	0.00
Al2O3	26.03	23.24	28.08	23.02	25.77	27.71	25.41	23.25	1.28	1.30		17.84	17.94	17.89	17.90	18.04	17.45	18.08	25.56	24.44	26.69	25.70	26.19	24.42	23.56	24.93	23.30	25.67	24.65
SiO2	59.87	62.74	56.01	63.01	59.33	56.26	59.67	62.88	29.69	29.70		35.39	35.01	35.08	35.51	35.54	35.15	35.17	59.44	60.70	57.62	59.80	58.99	61.87	63.57	60.63	62.67	59.68	60.85
K2O	0.18	0.28	0.13	0.13	0.20	0.27	0.27	0.25	0.01	0.00		9.77	10.00	9.93	10.01	9.92	10.20	9.78	0.12	0.34	0.24	0.29	0.28	0.28	0.37	0.25	0.30	0.24	0.30
CaO	7.53	4.44	9.94	4.43	7.41	9.78	6.88	4.67	26.92	26.60		0.00	0.00	0.01	0.00	0.02	0.02	0.09	7.22	5.94	8.52	7.15	7.76	5.73	4.55	6.43	4.74	6.82	6.15
TiO2	0.00	0.12	0.00	0.01	0.00	0.14	0.08	0.00	37.61	36.95		2.39	2.65	2.41	2.21	2.20	2.46	2.04	0.00	0.00	0.00	0.00	0.10	0.00	0.06	0.00	0.09	0.07	0.00
MnO	0.00	0.00	0.00	0.00	0.00	0.00	0.00	0.00	0.00	0.00		0.63	0.57	0.67	0.65	0.69	0.71	0.73	0.10	0.03	0.00	0.00	0.00	0.00	0.04	0.00	0.08	0.07	0.10
FeO	0.29	0.24	0.05	0.12	0.00	0.36	0.09	0.16	1.63	1.96		20.80	20.71	20.86	20.68	20.81	20.95	20.84	0.11	0.00	0.02	0.00	0.13	0.00	0.03	0.08	0.09	0.02	0.00
TOTAL	101.08	99.82	99.80	99.73	99.73	100.29	99.67	100.06	97.17	96.58		95.31	95.31	95.53	95.14	95.60	95.60	95.07	99.71	99.26	99.46	100.23	100.32	100.41	100.83	100.04	99.74	100.04	99.75
Na	2.459	3.013	1.950	3.078	2.432	2.008	2.519	3.010	0.000	0.001		0.054	0.102	0.075	0.045	0.090	0.069	0.051	2.482	2.710	2.197	2.503	2.361	2.765	2.942	2.658	2.915	2.555	2.660
Mg	0.000	0.000	0.000	0.016	0.000	0.000	0.000	0.021	0.001	0.001		1.910	1.864	1.938	1.850	1.853	1.942	1.885	0.000	0.000	0.019	0.008	0.008	0.011	0.000	0.003	0.000	0.019	0.000
Al	5.421	4.860	5.956	4.813	5.428	5.864	5.353	4.852	0.020	0.021		3.244	3.270	3.254	3.262	3.273	3.181	3.300	5.387	5.157	5.658	5.387	5.498	5.086	4.872	5.226	4.875	5.390	5.177
Si	10.576	11.130	10.076	11.174	10.600	10.098	10.664	11.130	0.400	0.403		5.458	5.413	5.413	5.488	5.469	5.434	5.445	10.625	10.864	10.362	10.632	10.503	10.931	11.150	10.782	11.123	10.629	10.841
K	0.041	0.063	0.030	0.029	0.046	0.062	0.062	0.056	0.000	0.000		1.922	1.972	1.955	1.974	1.948	2.012	1.932	0.027	0.078	0.055	0.066	0.064	0.063	0.083	0.057	0.068	0.055	0.068
Ca	1.425	0.844	1.916	0.842	1.419	1.881	1.317	0.886	0.389	0.386		0.000	0.000	0.002	0.000	0.003	0.003	0.015	1.383	1.139	1.642	1.362	1.480	1.085	0.855	1.225	0.901	1.301	1.174
Ti	0.000	0.016	0.000	0.001	0.000	0.019	0.011	0.000	0.381	0.377		0.277	0.308	0.280	0.257	0.255	0.286	0.238	0.000	0.000	0.000	0.000	0.013	0.000	0.008	0.000	0.012	0.009	0.000
Mn	0.000	0.000	0.000	0.000	0.000	0.000	0.000	0.000	0.000	0.000		0.082	0.075	0.088	0.085	0.090	0.093	0.096	0.015	0.005	0.000	0.000	0.000	0.000	0.006	0.000	0.012	0.011	0.015
Fe	0.043	0.036	0.008	0.018	0.000	0.054	0.013	0.024	0.018	0.022		2.683	2.678	2.692	2.673	2.678	2.709	2.698	0.016	0.000	0.003	0.000	0.019	0.000	0.004	0.012	0.013	0.003	0.000
Cat sum	19.964	19.962	19.936	19.971	19.924	19.986	19.939	19.978	1.209	1.211		15.631	15.681	15.695	15.633	15.658	15.730	15.659	19.936	19.952	19.935	19.958	19.947	19.940	19.919	19.963	19.919	19.972	19.935
Mg#												0.4159	0.4104	0.4186	0.4090	0.4090	0.4175	0.4113											
An%	36.31	21.53	49.18	21.32	36.41	47.61	33.79	22.42											35.78	29.59	42.77	35.24	38.53	28.18	22.52	31.55	23.61	33.74	30.62

Rock	97-373 Kassingbrook Granodiorite								97-376B Kassingbrook Granodiorite																			
Mineral	plag core	plag rim	plag core	plag rim	plag core	kf core	KF rim	KF	bio	bio	bio	bio	bio	bio	bio	bio	plag core	plag core	plag rim	plag rim	plag rim	plag core	plag rim	plag core	plag rim	plag core	plag rim
Spot	6.2	6.3	7.2	7.3	8.1	1.2	1.3	5.1	1.1	1.2	2.1	2.2	3.1	3.2	6.1	6.2	7.1	1.3	1.4	1.5	1.6	1.7	2.3	2.4	4.1	4.2	5.1	5.2
Na2O	5.79	7.81	6.54	7.06	6.47	1.35	1.57	1.31	0.29	0.20	0.22	0.24	0.24	0.27	0.32	0.34	0.27	6.51	7.23	7.08	8.45	8.42	7.52	8.17	6.78	7.23	6.27	8.53
MgO	0.00	0.00	0.02	0.00	0.00	0.00	0.00	0.00	9.14	9.14	9.05	9.09	9.16	9.28	9.32	9.27	9.11	0.00	0.04	0.04	0.00	0.08	0.08	0.02	0.02	0.00	0.00	0.00
Al2O3	27.94	24.64	27.31	25.84	26.45	18.68	18.77	19.09	17.45	17.50	17.74	17.49	17.77	17.61	17.71	17.64	17.74	26.55	25.16	25.33	23.51	23.53	24.87	24.01	26.23	25.27	26.35	23.35
SiO2	56.84	61.17	58.14	59.33	58.34	65.35	64.17	64.80	35.63	35.58	35.40	35.69	36.04	35.51	35.53	35.86	35.86	58.09	59.87	59.83	62.36	62.49	60.40	61.86	59.19	59.84	57.91	62.46
K2O	0.16	0.21	0.22	0.24	0.08	14.88	14.38	15.01	10.09	9.88	9.81	9.73	9.88	10.05	9.96	9.99	9.81	0.37	0.34	0.29	0.45	0.31	0.35	0.13	0.25	0.28	0.24	0.40
CaO	9.70	6.30	8.66	7.57	8.37	0.04	0.00	0.00	0.05	0.00	0.04	0.00	0.00	0.00	0.10	0.12	0.12	8.27	6.84	6.97	5.00	5.11	6.20	5.44	7.85	7.22	8.60	4.84
TiO2	0.00	0.02	0.06	0.04	0.00	0.10	0.48	0.23	2.24	2.42	2.68	2.04	2.50	2.29	2.12	2.32	2.27	0.00	0.05	0.00	0.11	0.00	0.03	0.04	0.00	0.00	0.05	0.03
MnO	0.00	0.03	0.07	0.00	0.08	0.05	0.00	0.10	0.58	0.41	0.67	0.71	0.52	0.65	0.76	0.64	0.64	0.05	0.02	0.01	0.01	0.00	0.00	0.00	0.00	0.00	0.04	0.13
FeO	0.04	0.00	0.00	0.07	0.06	0.14	0.19	0.00	19.41	19.93	19.32	19.73	19.47	20.07	19.34	19.43	19.57	0.00	0.16	0.01	0.00	0.12	0.01	0.11	0.34	0.08	0.16	0.12
TOTAL	100.47	100.18	101.02	100.15	99.85	100.59	99.56	100.54	94.88	95.06	94.93	94.72	95.58	95.73	95.16	95.61	95.39	99.84	99.71	99.56	99.89	100.06	99.46	99.78	100.66	99.92	99.62	99.86
Na	2.004	2.686	2.248	2.439	2.244	0.479	0.563	0.465	0.087	0.060	0.066	0.072	0.071	0.080	0.095	0.101	0.080	2.262	2.505	2.454	2.908	2.892	2.605	2.813	2.334	2.501	2.184	2.937
Mg	0.000	0.000	0.005	0.000	0.000	0.000	0.000	0.000	2.101	2.097	2.076	2.092	2.083	2.121	2.136	2.113	2.079	0.000	0.011	0.011	0.000	0.021	0.021	0.005	0.005	0.000	0.000	0.000
Al	5.881	5.152	5.708	5.428	5.579	4.030	4.091	4.124	3.174	3.177	3.219	3.184	3.197	3.184	3.211	3.181	3.203	5.609	5.300	5.337	4.919	4.914	5.238	5.027	5.491	5.315	5.581	4.889
Si	10.148	10.849	10.307	10.572	10.437	11.957	11.862	11.874	5.497	5.478	5.449	5.511	5.499	5.446	5.464	5.485	5.492	10.409	10.699	10.693	11.067	11.070	10.791	10.986	10.510	10.676	10.405	11.093
K	0.036	0.048	0.050	0.055	0.018	3.474	3.391	3.509	1.986	1.941	1.926	1.917	1.923	1.966	1.954	1.949	1.917	0.085	0.078	0.066	0.102	0.070	0.080	0.029	0.057	0.064	0.055	0.091
Ca	1.856	1.197	1.645	1.445	1.605	0.008	0.000	0.000	0.008	0.000	0.007	0.000	0.000	0.000	0.016	0.020	0.020	1.588	1.310	1.335	0.951	0.970	1.187	1.035	1.493	1.380	1.656	0.921
Ti	0.000	0.003	0.008	0.005	0.000	0.014	0.067	0.032	0.260	0.280	0.310	0.237	0.287	0.264	0.245	0.267	0.261	0.000	0.007	0.000	0.015	0.000	0.004	0.005	0.000	0.000	0.007	0.004
Mn	0.000	0.005	0.011	0.000	0.012	0.008	0.000	0.016	0.076	0.053	0.087	0.093	0.067	0.084	0.099	0.083	0.083	0.008	0.003	0.002	0.002	0.000	0.000	0.000	0.000	0.000	0.006	0.020
Fe	0.006	0.000	0.000	0.010	0.009	0.021	0.029	0.000	2.504	2.566	2.487	2.548	2.485	2.574	2.488	2.485	2.507	0.000	0.024	0.001	0.000	0.018	0.001	0.016	0.050	0.012	0.024	0.018
Cat sum	19.932	19.939	19.981	19.955	19.905	19.990	20.003	20.020	15.693	15.653	15.627	15.654	15.613	15.721	15.710	15.683	15.643	19.960	19.936	19.898	19.963	19.955	19.928	19.917	19.940	19.949	19.918	19.973
Mg#									0.4562	0.4497	0.4550	0.4509	0.4560	0.4518	0.4619	0.4595	0.4533											
An%	48.08	30.83	42.26	37.20	41.70													41.25	34.34	35.23	24.64	25.12	31.30	26.90	39.01	35.56	43.13	23.87

Rock	97-3768 Kassingbrook Granodiorite					97-274 Kassingbrook type hybrid tonalite																								
Mineral	plag core	plag rim	plag rim	plag rim		hbl A	hbl B	hbl C rim	hbl A core	hbl A rim	hbl rim	hbl B	hbl	hbl	bio	bio	bio	bio	bio	plag core	plag rim	plag core	plag rim	plag rim	plag core	plag rim	plag rim	plag A cor	plag A rim
Spot	7.2	7.3	7.4	7.5		1.4	1.5	1.6	2.1	2.2	2.3	2.3	2.4	2.5	1.1	1.2	1.3	3.2	3.3	6.1	6.2	5.1	5.2	5.3	7.1	7.2	7.3	8.1	8.2	
Na2O	5.98	8.13	7.45	8.24		0.97	0.98	1.00	1.03	0.95	1.00	1.02	0.78	0.97	0.08	0.12	0.27	0.17	0.19	7.12	7.14	6.83	4.06	7.00	6.92	4.31	5.89	4.72	7.25	
MgO	0.06	0.00	0.00	0.00		11.32	11.72	11.39	11.58	12.19	11.45	11.44	12.44	11.54	12.15	12.42	12.20	12.20	12.10	0.03	0.04	0.00	0.09	0.00	0.00	0.01	0.00	0.02	0.00	
Al2O3	27.38	24.14	25.28	23.50		9.42	8.84	9.38	9.06	8.50	9.06	9.06	7.55	9.33	15.02	15.16	14.75	14.95	15.06	25.34	24.84	25.86	30.07	25.87	25.67	30.02	23.88	29.48	25.12	
SiO2	56.57	61.53	60.54	62.46		45.41	46.44	45.94	45.87	46.29	45.59	45.60	47.97	46.10	36.88	37.36	36.98	37.53	36.58	59.71	59.84	59.10	52.72	59.89	59.05	52.86	61.52	54.21	60.52	
K2O	0.12	0.29	0.24	0.40		0.95	0.88	0.93	0.95	0.80	0.83	0.83	0.62	0.99	9.68	9.85	9.94	9.97	9.49	0.50	0.32	0.14	0.20	0.20	0.21	0.10	3.57	0.16	0.31	
CaO	9.34	5.48	6.55	5.00		12.11	12.17	12.06	12.05	12.24	12.08	12.09	12.21	12.07	0.04	0.00	0.01	0.03	0.08	7.19	6.94	7.73	12.82	7.77	7.84	12.47	5.55	11.95	6.64	
TiO2	0.02	0.00	0.00	0.00		0.73	0.88	1.00	1.10	0.78	0.74	0.74	0.61	0.89	3.33	3.10	3.18	3.29	3.22	0.08	0.03	0.00	0.00	0.00	0.00	0.08	0.00	0.00	0.06	
MnO	0.07	0.01	0.09	0.00		0.49	0.51	0.39	0.34	0.42	0.45	0.49	0.60	0.42	0.37	0.31	0.16	0.28	0.19	0.00	0.00	0.00	0.00	0.00	0.00	0.00	0.00	0.00	0.03	
FeO	0.00	0.14	0.07	0.13		15.81	15.08	15.57	15.77	14.58	15.83	15.84	14.72	15.75	17.44	17.35	17.59	17.01	17.58	0.09	0.16	0.16	0.17	0.04	0.07	0.09	0.20	0.20	0.03	
TOTAL	99.54	99.72	100.22	99.73		97.21	97.50	97.66	97.75	96.75	97.44	97.11	97.50	98.06	94.99	95.67	95.08	95.43	94.49	100.06	99.31	99.82	100.13	100.77	99.76	99.94	100.61	100.74	99.96	
Na	2.089	2.805	2.564	2.837		0.294	0.294	0.301	0.310	0.287	0.300	0.309	0.233	0.291	0.024	0.035	0.080	0.050	0.056	2.463	2.483	2.367	1.426	2.402	2.401	1.514	2.037	1.643	2.500	
Mg	0.016	0.000	0.000	0.000		2.636	2.706	2.632	2.678	2.830	2.660	2.665	2.856	2.658	2.754	2.792	2.769	2.746	2.758	0.008	0.011	0.000	0.024	0.000	0.000	0.003	0.000	0.005	0.000	
Al	5.815	5.065	5.289	4.920		1.735	1.615	1.715	1.657	1.561	1.670	1.670	1.371	1.700	2.693	2.695	2.648	2.662	2.715	5.329	5.253	5.448	6.420	5.398	5.416	6.412	5.022	6.240	5.266	
Si	10.192	10.950	10.744	11.092		7.095	7.195	7.123	7.118	7.212	7.110	7.129	7.389	7.126	5.610	5.634	5.631	5.669	5.594	10.651	10.733	10.562	9.548	10.600	10.568	9.577	10.975	9.733	10.762	
K	0.028	0.066	0.054	0.091		0.189	0.174	0.184	0.188	0.159	0.170	0.166	0.122	0.195	1.879	1.895	1.931	1.921	1.852	0.114	0.073	0.032	0.046	0.045	0.048	0.023	0.813	0.037	0.070	
Ca	1.803	1.045	1.246	0.951		2.027	2.020	2.004	2.004	2.043	2.020	2.025	2.015	1.999	0.007	0.000	0.002	0.005	0.013	1.374	1.334	1.480	2.488	1.474	1.503	2.421	1.061	2.299	1.265	
Ti	0.003	0.000	0.000	0.000		0.086	0.103	0.117	0.128	0.091	0.090	0.087	0.071	0.103	0.381	0.352	0.364	0.374	0.370	0.011	0.004	0.000	0.000	0.000	0.000	0.011	0.000	0.000	0.008	
Mn	0.011	0.002	0.014	0.000		0.065	0.067	0.051	0.045	0.055	0.060	0.065	0.078	0.055	0.048	0.040	0.021	0.036	0.025	0.000	0.000	0.000	0.000	0.000	0.000	0.000	0.000	0.000	0.005	
Fe	0.000	0.021	0.010	0.019		2.066	1.954	2.019	2.047	1.900	2.060	2.071	1.896	2.036	2.219	2.188	2.240	2.149	2.248	0.013	0.024	0.024	0.026	0.006	0.010	0.014	0.030	0.030	0.004	
Cat sum	19.956	19.953	19.920	19.912		16.193	16.129	16.145	16.174	16.139	16.180	16.187	16.032	16.164	15.614	15.631	15.686	15.612	15.632	19.962	19.915	19.913	19.978	19.925	19.948	19.975	19.939	19.987	19.881	
Mg#						0.56061	0.58069	0.56590	0.56677	0.59831	0.56356	0.56271	0.60101	0.56625	0.5538	0.5606	0.5528	0.5610	0.5509											
An%	46.33	27.14	32.70	25.11																35.81	34.95	38.47	63.57	38.03	38.50	61.52	34.25	58.32	33.60	

Rock	97-274 Kassingbrook type hybrid tonalite																													
Mineral	plag core	plag rim	plag core	plag rim	plag core	plag rim	plag core	plag rim	KF	KF	titanite																			
Spot	8.3	8.4	4.2	4.3	8.4	8.5	8.6	8.7	3.1	4.1	1.7																			
Na2O	4.40	6.59	5.51	6.70	4.39	7.14	4.31	8.01	1.22	1.06	0.00																			
MgO	0.01	0.02	0.00	0.02	0.01	0.02	0.05	0.00	0.07	0.07	0.00																			
Al2O3	30.07	26.53	28.22	26.15	30.05	25.12	29.82	24.36	18.80	18.37	1.53																			
SiO2	53.12	58.37	55.77	58.95	52.61	59.54	53.17	60.88	64.60	64.59	30.49																			
K2O	0.09	0.12	0.15	0.16	0.20	0.32	0.15	0.25	14.86	15.13	0.00																			
CaO	12.44	8.66	10.24	8.11	12.58	6.98	12.36	6.03	0.14	0.00	27.43																			
TiO2	0.05	0.02	0.02	0.00	0.13	0.05	0.03	0.03	0.40	0.26	36.90																			
MnO	0.00	0.02	0.00	0.00	0.04	0.15	0.00	0.06	0.13	0.00	0.18																			
FeO	0.00	0.19	0.10	0.17	0.08	0.16	0.15	0.10	0.05	0.07	1.14																			
TOTAL	100.18	100.52	100.01	100.26	100.09	99.48	100.04	99.72	100.27	99.55	97.67																			
Na	1.541	2.276	1.921	2.315	1.543	2.482	1.512	2.770	0.435	0.380	0.000																			
Mg	0.003	0.005	0.000	0.005	0.003	0.005	0.013	0.000	0.019	0.019	0.000																			
Al	6.403	5.572	5.982	5.493	6.422	5.310	6.362	5.123	4.073	4.008	0.024																			
Si	9.595	10.398	10.028	10.503	9.536	10.675	9.622	10.859	11.873	11.954	0.407																			
K	0.021	0.027	0.034	0.036	0.046	0.073	0.035	0.057	3.484	3.573	0.000																			
Ca	2.408	1.653	1.973	1.548	2.443	1.341	2.397	1.152	0.028	0.000	0.393																			
Ti	0.007	0.003	0.003	0.000	0.018	0.007	0.004	0.004	0.055	0.036	0.371																			
Mn	0.000	0.003	0.000	0.000	0.006	0.023	0.000	0.009	0.020	0.000	0.002																			
Fe	0.000	0.028	0.015	0.025	0.012	0.024	0.023	0.015	0.008	0.011	0.013																			
Cat sum	19.977	19.965	19.956	19.926	20.030	19.941	19.967	19.989	19.995	19.982	1.210																			
Mg#																														
An%	60.98	42.07	50.67	40.07	61.29	35.08	61.32	29.37																						

APPENDIX G

Table G.1:

Whole-rock geochemistry of the Caupaul Igneous Complex, hornblende-bearing lithologies of Chin Chap Creek, and metaluminous to weakly peraluminous granitic rocks, as analysed by XRF (major elements in weight percent oxide, trace elements in parts per million). The trace element concentrations of samples marked with an asterisk were determined by ICP-MS. All samples are stored in the museum collection at the Department of Geology, The Australian National University.

Type	Caupaul Igneous Complex																	
ANU No.	TKP189	TKP190	TKP191	TKP192	TKP193	TKP194	TKP195	TKP196	TKP197	TKP198	TKP199	TKP200	TKP209	Ferguson 93				
Field No.	98-CP1*	98-CP2*	98-CP3*	98-CP4	98-CP5	98-CP6*	98-CP7*	98-CP8*	98-CP9*	98-CP10*	98-CP11*	98-CP12	CP129*	11903*				
Lithology	Diorite	Hbl Gabbronorite	Hbl Gabbro	Hbl Gabbro	Hbl Gabbro	Hbl Gabbro	Diorite	Hbl Pyroxenite	Hbl Pyroxenite	Qtz diorite	Ferres Ck	Ferres Ck	abbronorite	Hbl Gabbro				
Grid (WD)	244733	246737	249747	248746	248746	248746	243733	260751	258750	260750	236728	223733	246741	248746				
SiO2	58.05	47.98	52.56	46.79	46.59	46.91	56.37	50.99	51.58	56.31	60.31	58.07	50.73	48.33				
TiO2	0.74	0.55	0.85	1.06	0.99	1.08	0.71	0.46	0.38	0.74	0.73	0.79	1.15	0.91				
Al2O3	16.18	12.48	18.12	18.30	18.29	18.84	16.60	5.95	2.75	15.32	15.50	16.03	18.45	18.20				
Fe2O3T	8.02	11.54	9.54	11.87	11.74	12.01	8.47	10.91	11.39	8.48	7.24	8.12	10.87	11.31				
Fe2O3	2.01	2.31	3.82	4.75	4.70	4.81	2.12	2.18	2.29	2.55	2.32	2.90	2.72	4.77				
FeO	5.41	8.31	5.15	6.41	6.34	6.49	5.72	7.86	8.20	5.34	4.43	4.70	7.34	5.89				
MnO	0.13	0.19	0.15	0.17	0.17	0.16	0.14	0.21	0.24	0.14	0.12	0.14	0.18	0.17				
MgO	5.13	12.90	5.18	7.03	6.85	6.46	5.21	18.64	16.54	6.24	3.78	4.05	6.01	6.42				
CaO	7.58	13.81	8.81	10.90	10.61	10.67	7.99	11.81	16.89	8.17	6.34	6.92	9.60	10.29				
Na2O	2.69	0.54	2.84	2.14	2.17	2.28	2.69	0.60	0.34	2.35	2.51	2.35	2.90	2.45				
K2O	1.97	0.14	1.32	0.81	0.82	0.75	1.96	0.24	0.09	1.59	2.80	2.46	0.50	0.82				
P2O5	0.15	0.01	0.19	0.18	0.19	0.19	0.15	0.05	0.01	0.14	0.15	0.18	0.24	0.20				
S	0.008	0.022	0.011	0.115	0.026	0.079	0.007	0.01	0.006	0.005	0.01	0.015	0.006	0.12				
LOI																		
TOTAL	100.05	99.24	99.01	98.66	97.75	98.72	99.67	99.00	99.31	98.89	99.00	98.61	99.82	98.57				
Sc	26	76	36	51	45	45	28	73	93	37	28	31	33	38				
V	173	340	221	285	279	253	189	235	358	206	169	189	223	279				
Cr	131	311	58	55	54	45	77	1406	1365	219	60	62	97	76				
Ni	46	156	45	68	68	61	40	251	205	59	23	23	47	63				
Cu	50	35	84	132	127	141	29	42	2	5	56	40	11	91				
Zn	79	68	93	108	104	101	73	80	71	81	73	87	103	101				
Ga	16	12	18	19	19	19	16	8	6	16	15	17	20	25				
Rb	76.4	2.7	51.2	17	20	14.3	86	2	2	66.8	101.5	107	9.8	18.69				
Sr	265	178	357	336	351	369	299	55	37	261	273	285	359	347.6				
Y	21.3	12.7	26.4	33	29	32.5	20	18.4	18.8	20.2	21	25	23.3	29.3				
Zr	124.9	17.7	138.4	49	51	50.7	111.8	25.3	21.6	90.1	172.1	105	157.6	70.3				
Nb	10.49	0.83	9.89	10	8	9.13	9.13	2.67	0.6	7.35	9.31	11	8.9	8.2				
Cs	2.48	0.26	3.93			1.37	4.07	0.11	0.2	5.76	6.21		0.77	1.824				
Ba	308.7	31.9	234	132	141	135.9	313.1	43	10.8	268.1	699.2	411	121	138.6				
La	23.19	2.93	22.63	18	17	18.98	21.6	5.83	2.81	17.93	24.1	29	18.92	19.6				
Ce	44.54	7.87	47.59	46	41	45.38	41.8	16.38	10.44	36.81	46.06	63	40.89	44.3				
Pr	5.03	1.21	5.87			6.12	4.73	2.41	1.9	4.38	5.32		5.32	5.82				
Nd	18.46	6.01	23.06	27	16	25.17	17.46	10.31	9.76	16.58	19.81	24	21.58	22.3				
Sm	3.9	1.82	5.17			5.9	3.71	2.79	3.16	3.8	4.17		4.66	5.45				
Eu	0.96	0.49	1.22			1.4	0.98	0.63	0.58	0.96	1.1		1.24	1.229				
Gd	3.77	2.14	4.75			5.6	3.45	2.97	3.36	3.49	3.7		4.25	5.2				
Dy	3.59	2.36	4.61			5.57	3.36	3.11	3.48	3.53	3.59		4.09	5.00				
Er	2.09	1.33	2.67			3.3	2	1.81	2.02	2.04	2.09		2.33	2.96				
Yb	2.07	1.23	2.45			3	1.94	1.7	1.75	1.98	2.05		2.1	2.62				
Lu	0.32	0.18	0.37			0.46	0.31	0.26	0.26	0.31	0.31		0.33	0.391				
Hf	3.23	0.67	3.44			1.79	2.96	1.05	0.91	2.42	4.28		3.77	2.34				
Ta	0.89	0.08	0.67			0.5	0.75	0.18	0.06	0.63	0.76		0.68	0.667				
Pb	16.8	2.5	14.5	9	10	9.6	18.3	1.1	1.4	15.3	21	21	9.4	12.0				
Th	9.31	0.43	5.73	2	2	1.78	8.77	0.14	0.24	8.2	10.05	21	1.63	2.62				
U	1.51	0.1	1.43	1	1	0.45	1.68	0.06	0.06	1.86	1.7	3	0.52	0.694				

Type	Chin Chap Creek																	
ANU No.	TKP73	TKP74	TKP76	TKP78	TKP83	TKP79	TKP84	TKP156	TKP155	TKP174	TKP173	TKP175	TKP68	TKP69	TKP31	TKP32	TKP33	TKP34
Field No.	97-319	97-320A	97-320C*	97-373A*	97-377	97-376*	97-380*	98-62*	98-61	97-378-4	97-378-3	97-378-5	97-309	97-309-1	97-233B	97-236A	97-236B*	97-244*
Lithology	Hbl Gabbro-	Hbl Gabbro-	Hbl Gabbro-	Hbl Gabbro-	Hbl Gabbro-	Hbl diorite	Hbl diorite	Hbl Gabbro-	Hbl Gabbro-	Hbl diorite	Hbl diorite	Hbl diorite	tonalite	tonalite	Hbl Gabbro-	Hbl diorite	Hbl diorite	Hbl Gabbro-
	diorite	diorite	diorite	diorite	diorite			diorite	diorite		(enclave)	(enclave)			diorite			diorite
Grid (WD)	707505	708504	708505	710489	707483	707484	708479	707477	708505	707482	707482	707482	709493	709493	728435	727435	727435	720431
SiO2	53.73	56.44	53.97	54.15	56.40	55.51	58.16	55.31	65.39	57.15	57.79	57.77	63.42	62.26	54.98	55.74	54.76	55.00
TiO2	0.59	0.51	0.54	0.48	0.65	0.73	0.57	0.74	0.31	0.60	0.67	0.67	0.51	0.58	0.74	0.45	0.53	0.59
Al2O3	7.84	8.45	7.19	8.94	11.50	15.10	11.87	12.73	9.13	12.50	16.04	15.62	16.23	16.52	12.42	14.85	13.92	10.73
Fe2O3T	9.21	7.37	7.82	9.09	7.95	7.68	7.09	7.97	4.71	7.78	5.90	6.31	5.38	5.89	9.15	7.51	8.49	8.50
Fe2O3	2.41	1.85	1.98	2.22	2.24	2.24	2.31	2.20	1.18				1.49	1.75	2.66	1.96	2.12	1.89
FeO	6.18	5.02	5.31	6.25	5.19	4.95	4.35	5.20	3.18				3.54	3.76	5.39	4.45	5.27	5.51
MnO	0.18	0.15	0.16	0.17	0.15	0.15	0.16	0.14	0.12	0.20	0.13	0.14	0.12	0.12	0.16	0.14	0.16	0.16
MgO	13.88	12.43	13.90	15.84	10.06	7.22	8.97	8.70	7.82	8.63	6.07	6.28	3.04	3.16	8.84	8.37	9.25	10.45
CaO	11.36	10.88	13.24	7.00	7.98	7.58	8.66	10.04	7.44	8.65	7.31	7.37	5.61	5.62	9.92	8.04	7.98	11.13
Na2O	1.21	1.43	1.22	1.38	2.00	2.09	1.93	1.78	1.62	1.94	2.51	2.42	2.85	2.75	1.30	2.23	2.13	1.69
K2O	0.65	0.89	0.51	0.83	1.29	1.71	0.68	1.16	2.63	1.27	1.84	1.72	2.27	2.53	1.26	1.72	1.74	1.36
P2O5	0.09	0.09	0.08	0.08	0.13	0.16	0.12	0.10	0.07	0.14	0.15	0.15	0.16	0.18	0.13	0.07	0.06	0.15
S	0.220	0.020	0.110	0.110	0.120	0.014	0.020	0.047	0.015	0.03	0.017	0.018	0.010	0.010	0.21	0.01	0.01	0.03
LOI	1.56	1.49	1.55	2.02	1.77	2.02	1.75	1.54	0.91	1.71	2.04	2.17	0.73	0.80	2.03	1.82	1.77	1.16
TOTAL	99.95	99.91	100.03	99.69	99.59	99.57	99.80	107.65	104.54	100.57	100.46	100.62	100.09	100.16	100.03	99.83	99.69	99.85
Sc	73	56	69	46	47	39	56	67	44	51	35	37	22	23	62	33	35	58
V	218	174	193	160	171	190	214	261	106	188	136	148	137	151	281	158	181	220
Cr	626	1631	1795	1683	658	342	1345	571	791	266	166	152	84	40	383	580	660	760
Ni	134	131	181	420	122	100	117	74	103	84	46	50	12	6	72	153	164	136
Cu	176	26	289	65	74	18	88	40	125	14	8	11	6	13	124	15	15	54
Zn	66	57	56	72	68	74	55	56	43	88	64	69	59	62	71	60	68	66
Ga	10	11	9	10	14	16	13	14	10	14	15	15	18	18	14	14	14	13
Rb	27	30	15.4	30.6	57	70.7	28	49.3	100	62	93	88	106	115	69	70	70.1	37.4
Sr	119	150	116	147	210	311	203	188	112	224	342	325	295	279	184	207	194	159
Y	16	15	14.4	13.1	19	21	15	19	13	24	24	23	18	19	16	13	17.4	15.9
Zr	51	58	49.1	53.5	72	85.4	67	72.1	48	58	63	83	90	88	63	46	46.5	74.7
Nb	4	4	2.74	2.95	5	5.41	5	4.73	6	6	9	8	9	10	5	3	4.01	4.79
Cs	1	<1	1.03	1.3	2	2.35	1	1.83	0	2	1	2	1	1	4	3	3.72	1.26
Ba	145	171	132.5	167	254	290.7	108	142	386	167	271	267	345	445	148	245	240.7	251.9
La	9	10	9	10.09	6	12.44	10	9	8	12	11	11	12	12	8	8	7.42	16.66
Ce	19	19	18.95	21.1	18	28.93	21	20.63	22	31	30	32	32	35	22	16	15.44	33.16
Pr	<1	<1	2.4	2.61	1	3.84	<1	2.74	<1	<1	4	1	1	1	<1	<1	2.01	3.97
Nd	5	3	10.21	10.41	13	16.39	5	11.61	11	13	18	17	14	16	12	8	8.46	15.8
Sm			2.61	2.35		3.93		2.99									2.25	3.44
Eu			0.63	0.62		1.03		0.77									0.64	0.79
Gd			2.65	2.35		3.69		3.17									2.44	3.07
Dy			2.58	2.3		3.6		3.28									2.75	2.77
Er			1.54	1.42		2.1		1.97									1.74	1.57
Yb			1.34	1.3		1.99		1.87									1.78	1.45
Lu			0.21	0.22		0.31		0.28									0.28	0.22
Hf			1.45	1.46		2.41		2.05									1.44	2.23
Ta			0.18	0.21		0.41		0.47									0.37	0.36
Pb	5	9	3.9	6.5	10	10	12	8	19	10	13	12	22	23	8	15	12.8	9.5
Th	2	3	3	3.41	4	5.92	5	2.78	5	4	5	5	6	6	4	4	2.88	6.52
U	0	0	0.36	0.5	1	0.87	1	1.4	1	1	2	2	3	2	2	1	0.77	1.31

Type				Wando type														
ANU No.	TKP35	TKP36		TKP21	TKP22	TKP168	TKP169	TKP20	TKP25	TKP62	TKP63	TKP166	TKP167	TKP23	TKP213	TKP188	TKP57	TKP60
Field No.	97-254A	97-254B		97-161*	97-160-1	97-160-2	97-161E	97-159	97-192	97-214	97-214E	97-154	97-155	97-167	97-159E	98-124	97-206B	97-206E
Lithology	MME	MME		Wando Ton	MME	MME	MME	Snake R.	Snake R.	Snake R.	MME	MME	MME	MME	MME	Dioritic dyke	Dioritic dyke	Dioritic dyke
					(type A)	(type B)	(type B)				(type A)	(type B)	(type B)	(type C)	(type C)			
Grid (WD)	727434	727434		404557	405559	405559	404557	407560	384571	429541	429541	411562	410563	423593	407560	412543	411545	411545
SiO2	65.58	64.92		63.10	57.38	59.09	58.13	59.42	58.39	61.20	55.33	57.95	58.73	51.40	44.27	53.53	56.71	57.78
TiO2	0.57	0.58		0.61	0.67	0.71	0.88	0.73	0.70	0.64	0.59	0.69	0.65	0.89	1.43	0.68	0.89	0.82
Al2O3	16.05	15.85		16.83	14.95	15.07	15.98	17.73	18.01	16.94	13.86	15.71	14.56	14.68	17.99	20.41	17.87	17.45
Fe2O3T	4.62	4.81		5.37	8.21	7.96	8.58	6.95	7.07	6.30	8.95	9.06	8.36	12.95	14.45	6.84	7.95	7.49
Fe2O3	0.82	1.19		2.04	2.34			2.34	2.83					6.36			1.59	1.54
FeO	3.42	3.26		3.00	5.29			4.15	3.82					5.94			5.78	5.41
MnO	0.10	0.10		0.10	0.22	0.20	0.18	0.15	0.14	0.11	0.24	0.23	0.24	0.28	0.34	0.22	0.14	0.12
MgO	2.77	3.18		2.08	5.94	4.98	3.83	2.51	2.70	2.86	7.87	4.24	5.27	4.96	6.00	3.57	3.88	3.77
CaO	4.31	4.40		5.59	7.34	6.68	6.43	6.61	6.86	5.94	7.65	6.87	7.22	6.40	8.15	8.70	7.09	6.77
Na2O	2.54	2.64		3.01	2.44	2.66	2.67	3.03	3.31	2.89	2.19	2.49	2.29	1.54	2.27	4.83	2.91	2.89
K2O	2.24	2.24		2.25	1.87	1.97	2.18	1.74	1.54	2.24	1.94	1.71	1.67	1.81	3.18	0.72	1.52	1.60
P2O5	0.22	0.21		0.18	0.14	0.18	0.18	0.20	0.17	0.15	0.09	0.12	0.13	0.15	0.31	0.17	0.18	0.17
S	0.03	0.01		0.01	0.01	0.01	0.01	0.02	0.02	0	0.01	0.01	0.01	3.10	0.023	0.01	0.03	0.02
LOI	1.03	1.34		1.32	0.92	1.31	1.44	0.93	1.44	1.09	1.37	1.41	1.31	5.33		0.89	1.54	1.56
TOTAL	99.68	99.92		100.12	99.50	100.81	100.50	99.55	99.93	100.12	99.76	100.47	100.45	102.84	98.42	100.56	100.22	100.02
Sc	17	18		12	30	28	31	16	15	21	34	41	33	37	50	27	33	30
V	100	107		85	178	165	157	116	120	125	171	166	164	200	284	178	188	167
Cr	68	99		24	279	246	69	9	8	51	781	178	320	46	36	39	50	59
Ni	17	24		6	61	56	17	3	4	11	129	21	45	42	11	16	13	15
Cu	94	11		8	63	52	39	7	4	6	97	21	33	720	35	2	4	5
Zn	66	69		83	113	123	129	82	78	73	121	113	111	151	180	86	84	78
Ga	17	17		19	16	18	19	19	19	18	18	18	17	20	27	20	20	20
Rb	149	103		94.6	74	94	107	67	58	98	98	73	70	128	132	19	67	70
Sr	325	304		343	236	256	273	329	341	291	180	235	226	338	245	452	315	310
Y	18	16		17.9	19	28	25	21	17	18	29	41	39	22	58	23	26	24
Zr	82	76		163.7	78	73	110	132	133	109	48	83	67	65	166	125	131	136
Nb	10	8		13.7	10	13	14	10	11	12	10	10	10	5	17	9	9	8
Cs				3.37		1	<1			2	4	1	<1		1	<1	<1	<1
Ba	520	485		430.6	280	281	398	365	335	383	194	300	259	205	637	132	379	430
La	18	16		35.13	15	2	9	36	22	14	5	4	2	25	28	22	14	11
Ce	42	40		64.66	34	10	24	74	48	36	16	13	13	50	65	46	40	35
Pr				7.25		<1	<1					4	1		0	0		
Nd	16	16		26.31	14	11	13	24	16	14	10	17	17	22	30	16	20	17
Sm				4.91														
Eu				1.18														
Gd				4.07														
Dy				3.25														
Er				1.62														
Yb				1.46														
Lu				0.22														
Hf				4.27														
Ta				0.98														
Pb	12	22		16	8	11	12	12	10	20	10	12	10	6	12	20	13	12
Th	6	5		11.85	5	1	5	12	8	9	0	0	1	4	1	12	6	5
U	3	2		2.12	1	3	3	1	2	2	0	1	1	2	1	2	1	1

Type								Wennicott type									
ANU No.	TKP61	TKP27	TKP93	TKP56	TKP58	TKP59		TKP28	TKP29	TKP43	TKP44	TKP178	TKP45	TKP46	TKP179	TKP219	TKP138
Field No.	97-206F*	97-208	97-440	97-206A	97-206C	97-206D		97-227A	97-227B*	97-WA1	97-WA2	98-WA3*	97-WAE1	97-WAE2	98-WAE3*	98-WAEN	98-3
Lithology	Dioritic dyke	Mafic dyke	Dioritic dyke	MME	MME	MME		amphibolite	Wennicott	Warradale	Warradale	Warradale	MME	MME	MME	MME	Tonalite gneiss
Grid (WD)	411545	412543	555390	411545	411545	411545		523466	523466	414430	514420	514420	514410	514420	514420	514430	576835
SiO2	56.03	60.28	59.75	56.96	56.99	57.85		59.95	68.99	59.46	66.01	57.99	51.23	53.03	50.07	50.87	66.94
TiO2	0.90	0.64	0.71	0.67	0.67	0.68		0.55	0.41	0.80	0.77	0.91	1.10	0.73	1.11	1.17	0.35
Al2O3	17.96	16.94	15.61	15.53	15.14	14.42		16.75	15.57	16.61	14.87	16.79	17.33	13.50	16.33	16.78	16.47
Fe2O3T	7.76	6.36	7.41	8.07	8.03	8.68		6.63	3.56	7.36	5.25	8.03	10.72	9.15	11.05	10.54	3.72
Fe2O3	1.72	1.52	1.60	1.82	1.75	1.83		2.10	1.21	2.08	1.58		3.18	2.80			
FeO	5.49	4.36	5.28	5.68	5.71	6.23		4.08	2.12	4.76	3.31		6.79	5.72			
MnO	0.13	0.13	0.12	0.14	0.15	0.17		0.12	0.06	0.13	0.07	0.13	0.20	0.16	0.25	0.21	0.10
MgO	3.90	2.95	3.97	5.79	5.99	5.85		3.89	1.60	3.35	2.53	3.71	5.24	8.73	6.35	5.53	1.38
CaO	7.57	6.27	6.83	8.11	7.88	7.37		6.35	4.39	6.39	4.66	6.71	8.66	9.97	9.55	8.40	4.52
Na2O	3.05	2.86	2.79	2.59	2.53	2.40		2.95	3.10	2.88	2.59	2.69	2.60	2.07	2.59	2.64	3.33
K2O	1.49	2.02	1.65	1.16	1.28	1.28		1.77	1.63	2.27	2.12	2.05	2.00	1.67	1.74	2.10	1.72
P2O5	0.18	0.13	0.12	0.11	0.10	0.09		0.19	0.13	0.25	0.16	0.27	0.29	0.19	0.32	0.30	0.16
S	0.02	0.01	0.01	0.04	0.05	0.03		0.01	0.01	0.04	0.01	0.05	0.09	0.01	0.07	0.074	0.04
LOI	1.54	1.84	1.26	1.33	1.45	1.39		1.23	0.89	0.93	1.05	1.26	0.96	1.24	0.99		1.44
TOTAL	100.10	99.94	99.86	100.05	99.79	99.68		100.06	100.10	99.93	99.72	100.57	99.66	99.81	100.37	98.61	100.17
Sc	34	21	31	40	40	36		22	4	25	13	29	36	56	43	44	11
V	180	133	205	197	196	195		112	59	160	106	195	272	243	312	262	62
Cr	47	34	93	264	272	299		113	22	45	45	52	44	419	93	68	8
Ni	12	14	20	46	47	49		48	9	16	11	17	21	99	29	35	3
Cu	5	3	5	38	36	24		74	4	39	12	40	88	32	194	83	35
Zn	82	75	96	73	78	90		64	49	85	66	87	112	70	115	112	58
Ga	20	18	18	17	17	17		16	16	19	17	20	21	13	19	22	16
Rb	62.3	73	74	44	48	54		121	109.9	107	103	95.4	82	43	71.1	98	115
Sr	318	285	386	260	249	236		286	337	349	351	408	392	197	320	351	299
Y	28.2	18	20	22	21	22		17	9.6	28	15	48.1	25	14	39.9	32	17
Zr	147.4	112	107	95	92	41		112	123.4	197	207	223	138	58	153.1	176	104
Nb	10.74	7	7	5	5	6		6	9.53	11	10	12.04	10	2	14.91	15	7
Cs	1.91		<1	<1	<1	<1			5.18			2.99			2.85	<1	9
Ba	393.2	385	518	229	242	290		260	116.4	370	515	438	420	126	225.4	376	400
La	17.43	21	12	11	8	4		21	26.65	26	23	20.91	27	10	30.68	28	22
Ce	38.21	46	36	31	23	14		46	50.38	64	50	56.31	70	24	74.3	90	53
Pr	5.01								5.33			8.58			9.97	5	<1
Nd	20.73	18	17	13	12	10		16	17.75	30	16	38.33	28	12	40.47	35	21
Sm	4.95								2.88			9.45			8.79		
Eu	1.22								0.77			1.48			1.75		
Gd	4.87								1.92			8.31			7.68		
Dy	4.71								1.57			8.24			6.88		
Er	2.87								0.85			4.56			3.86		
Yb	2.78								0.87			3.75			3.52		
Lu	0.43								0.13			0.52			0.52		
Hf	3.58								3.16			5.37			3.66		
Ta	0.81								0.86			0.74			0.75		
Pb	11.2	14	14	9	9	9		10	12.9	17	12	10.9	11	11	11	14	20
Th	6.01	10	7	4	2	1		9	18.39	6	8	3.19	3	8	1.7	2	14
U	1.91	2	1	0	0	0		1	1.83	2	1	1.09	1	3	0.73	1	3

Type	Deep Ck type	Tuloona type																
ANU No.	TKP223	TKP2	TKP3	TKP4	TKP38	TKP6	TKP65	TKP66	TKP9	TKP14	TKP89	TKP41	TKP17	TKP18	TKP19	TKP86	TKP85	TKP212
Field No.	97-DC*	T2-78B	T2-135A	T2-135B*	97-294	T2-318	97-299*	97-299B	97-36	97-80	97-427	97-297	97-140	97-142	97-145	97-382B	97-382A	97-407
Lithology	Deep Ck Gd	Tuloona	Tuloona	MME	MME	Tuloona	Tuloona	MME	Wirreanda	Chetwynd	Chetwynd	Coojar	Coojar	Coojar	Glendara	Patawilya	MME	Patawilya
Grid (WD)	395494	508828	570791	570791	517836	545798	522842	522842	478789	393643	451673	635656	635639	635650	478818	680531	680531	68947
SiO2	68.85	69.47	69.14	66.47	63.07	69.34	67.93	66.48	71.33	67.43	66.90	67.81	71.42	72.34	73.48	68.30	69.52	68.08
TiO2	0.20	0.32	0.31	0.53	0.68	0.25	0.37	0.48	0.26	0.33	0.40	0.38	0.22	0.21	0.18	0.35	0.63	0.35
Al2O3	17.06	15.57	15.77	15.69	15.02	15.93	16.20	16.08	15.22	16.26	16.37	16.05	14.85	14.83	14.21	16.10	13.73	16.00
Fe2O3T	1.56	3.05	3.06	4.90	6.06	3.21	3.67	4.44	2.46	3.42	3.98	3.56	2.21	2.02	1.75	3.37	5.35	3.34
Fe2O3		1.41	1.22	1.94	2.71	0.99	1.56	1.78	0.95	1.40	1.73	1.67	1.10	0.79	0.83	1.06	1.46	
FeO		1.49	1.67	2.67	3.02	2.02	1.92	2.42	1.37	1.84	2.05	1.72	1.01	1.12	0.84	2.10	3.54	
MnO	0.09	0.07	0.07	0.09	0.18	0.06	0.08	0.09	0.08	0.05	0.07	0.07	0.06	0.06	0.05	0.08	0.09	0.07
MgO	0.56	1.32	1.27	2.32	4.40	1.16	1.51	2.18	0.89	1.31	1.68	1.50	0.85	0.76	0.64	1.46	2.03	1.49
CaO	3.88	3.82	3.78	4.22	5.75	3.52	4.52	4.51	2.82	4.42	4.75	4.12	2.56	2.81	2.48	3.86	2.87	4.02
Na2O	4.55	3.25	3.21	2.81	1.12	3.21	3.21	2.95	3.40	3.20	3.19	3.25	3.25	3.31	3.02	3.49	2.43	3.41
K2O	1.97	2.41	2.51	2.06	2.36	2.54	1.92	1.91	2.86	2.16	1.90	2.42	3.75	3.22	3.52	1.87	2.27	1.86
P2O5	0.08	0.15	0.16	0.13	0.19	0.19	0.17	0.16	0.13	0.16	0.19	0.17	0.09	0.08	0.08	0.17	0.19	0.19
S		0.01	0.01	0.01	0.01	0.01	0.005	0.005	0	0.01	0.005	0.01	0	0.01	0.01	0.02	0.03	0.004
LOI		0.81	0.85	0.98	1.49	0.99	0.85	0.95	0.88	0.69	0.82	0.83	0.87	0.60	0.89	1.21	0.98	
TOTAL	98.80	100.08	99.95	99.91	99.98	100.21	100.38	100.14	100.19	99.33	100.18	100.00	100.03	100.14	100.23	100.17	100.03	98.81
Sc	2	9	8	19	26	7	10	13	8	8	10	10	8	7	6	10	17	10
V	16	38	36	98	139	34	44	86	23	36	60	47	28	23	16	50	77	48
Cr	2	13	13	35	131	13	15	31	8	7	15	15	8	8	4	18	60	18
Ni	<1	5	4	12	28	4	2	5	3	3	2	6	3	2	2	3	16	6
Cu	<1	4	3	7	8	2	3	6	2	3	2	4	2	3	2	18	81	1
Zn	39	59	56	73	87	58	62	76	72	55	64	66	40	39	41	63	88	59
Ga	19	18	18	17	18	19	18	18	20	18	19	19	16	16	15	19	18	18
Rb	71.3	93	102	104.2	95	122	84.1	94	129	74	84	90	144	120	124	89	119	78
Sr	560	368	367	369	294	303	363	345	376	361	364	402	280	300	322	359	288	366
Y	5.2	14	14	15.1	21	11	11.6	11	12	10	11	12	19	16	17	11	13	9
Zr	110	125	128	127.9	114	15	139.9	126	98	135	136	132	80	86	86	119	184	120
Nb	7.96	8	8	8.31	9	10	9.06	9	12	8	9	8	10	9	8	8	12	8
Cs	2.15	3	4	5.1		5	2.35	<1	1	<1	<1	<1	4	1	4	1	1	1
Ba	581.1	645	580	550.9	465	525	423.8	442	535	495	409	670	585	580	720	441	609	423
La	7.37	28	26	30.61	26	23	32.32	23	27	24	19	31	23	18	26	14	36	18
Ce	14.27	64	58	59.77	62	50	62.76	54	56	52	45	70	52	44	58	36	86	34
Pr	1.55			6.55			6.93											
Nd	5.65	20	18	22.69	26	16	24.74	21	18	16	17	20	18	12	18	14	34	15
Sm	1.13			4.11			4.2											
Eu	0.33			0.9			0.89											
Gd	0.92			3.06			3.22											
Dy	0.75			2.58			2.21											
Er	0.47			1.4			1.08											
Yb	0.55			1.34			0.8											
Lu	0.08			0.2			0.13											
Hf	2.89			3.32			3.52											
Ta	0.58			0.87			0.62											
Pb	21.5	20	21	20.7	8	25	14.1	12	22	14	14	20	29	27	26	19	15	15
Th	2.47	16	14	11.9	9	11	13.06	10	12	12	8	15	14	11	15	5	17	5
U	0.62	2	2	1.29	2	2	0.72	1	2	1	1	1	2	2	2	2	2	<1

Type	Kassingbrook type																		
ANU No.	TKP67	TKP70	TKP71	TKP77	TKP80	TKP81	TKP82	TKP75	TKP171	TKP172	TKP221	TKP170	TKP214						
Field No.	97-308b	97-309a-1	97-309a-2	97-373	97-376A*	97-376B	97-376C	97-320B	97-378-1	97-378-2	97-275	97-274*	97-275E						
Lithology	Coolami	Kbrook	Kbrook	Kbrook	Kbrook	Kbrook	Kbrook	Kbrook	Kbrook	Kbrook	Kbrook	Kbrook	MME						
Grid (WD)	710493	709493	709493	709490	707484	707484	707484	708505	707482	707482	708490	707482	708490						
SiO2	71.86	73.34	74.52	74.67	72.53	72.11	66.93	75.45	71.29	71.41	70.78	64.00	59.18						
TiO2	0.16	0.08	0.09	0.11	0.13	0.14	0.41	0.05	0.18	0.11	0.20	0.53	0.80						
Al2O3	15.37	14.65	14.45	14.04	14.83	15.66	16.05	13.37	15.22	15.54	15.37	15.67	15.68						
Fe2O3T	1.63	0.84	0.93	1.17	1.29	1.44	4.10	0.69	1.67	1.05	1.94	4.83	7.30						
Fe2O3																			
FeO																			
MnO	0.03	0.02	0.03	0.03	0.04	0.04	0.09	0.01	0.04	0.02	0.07	0.10	0.15						
MgO	0.68	0.34	0.37	0.42	0.66	0.71	2.02	0.24	1.06	0.74	0.88	3.34	3.76						
CaO	2.84	2.21	3.03	2.12	2.13	2.85	3.11	0.70	2.83	2.43	2.74	5.02	3.80						
Na2O	3.50	3.23	3.63	3.53	3.60	4.59	4.00	3.34	3.09	3.06	3.32	2.90	2.79						
K2O	3.25	4.54	2.38	3.11	3.50	1.56	1.83	5.35	3.84	4.81	3.51	2.67	3.64						
P2O5	0.06	0.06	0.04	0.05	0.06	0.07	0.12	0.05	0.08	0.05	0.08	0.11	0.97						
S	0.10	0.01	0.01	0.01	0.07	0.01	0.43	0.14	0.063	0.048	0.002	0.016	0.013						
LOI	0.79	0.67	0.78	0.71	1.16	1.04	1.46	0.92	1.21	1.07		1.22							
TOTAL	100.41	100.25	100.43	100.20	100.16	100.33	100.23	100.42	100.53	100.31	98.89	100.40	98.06						
Sc	5	3	3	4	5	6	16	4	7	5	8	22	30						
V	24	9	10	13	19	18	64	5	28	18	36	116	142						
Cr	10	2	7	7	8	13	36	<1	16	12	13	120	62						
Ni	<1	1	2	2	2	4	<1	<1	4	2	3	30	26						
Cu	121	<1	<1	<1	49	<1	530	92	37	28	2	15	2						
Zn	26	19	21	28	21	34	58	11	25	14	33	53	141						
Ga	15	13	14	13	14	16	18	11	14	12	17	15	25						
Rb	92	112	68	101	113.9	70	120	132	97	102	128	95.3	183						
Sr	434	451	428	381	355	427	363	232	396	424	339	321	285						
Y	8	11	8	25	6.7	10	16	15	12	11	11	19.5	60						
Zr	68	42	63	49	48.9	69	63	21	52	43	57	73.4	267						
Nb	7	4	5	6	5.65	7	13	5	6	4	8	6.49	22						
Cs	4	9	4	8	2.2	1	1	5	6	4	3	3.04	2						
Ba	845	1523	787	1173	744.7	266	256	866	790	869	648	470.6	291						
La	<1	<1	5	0	6.85	9	13	<1	13	11	4	10.67	54						
Ce	7	34	28	26	14.44	23	32	10	30	32	10	22.88	135						
Pr	2	7	2	4	1.58	1	<1	<1	6	2	<1	2.91	5						
Nd	6	26	16	18	5.82	12	13	9	14	16	3	11.83	55						
Sm					1.31							2.97							
Eu					0.48							0.78							
Gd					1.14							3.03							
Dy					1.07							3.21							
Er					0.68							2.01							
Yb					0.75							2.03							
Lu					0.12							0.32							
Hf					1.35							2.03							
Ta					0.61							0.7							
Pb	47	52	36	42	57.5	32	27	51	37	44	33	21.2	24						
Th	2	11	7	7	2.57	5	5	4	6	7	3	4.32	25						
U	2	1	1	3	1.71	2	1	4	1	1	2	1.54	2						

Type	Loftus Creek type																			
ANU No.	TKP11	TKP12	TKP13	TKP54	TKP55	TKP90	TKP64	TKP91	TKP92	TKP24	TKP39	TKP10	TKP37	TKP176	TKP177	TKP40	TKP16	TKP203	TKP130	TKP131
Field No.	97-62	97-67	97-71	97-65	97-69	97-428	97-266	97-430	97-436	97-178b	97-295*	97-47	97-293	98-PP1	98-PP2	97-296	97-126b	98-142*	98-RC1*	98-RC2
Lithology	Hbl Cairns	Cairns Ck	Cairns Ck	Cairns Ck	Cairns Ck	Cairns Ck	Cloven Hills	Cloven Hills	Cloven Hills	Felsic dyke	Koolomurt	Koolomurt	Koolomurt	MME	MME	Microgranite	Microgranite	Sawpit Gully	Mafic dyke	Mafic dyke
Grid (WD)	403706	424694	428692	415697	419701	428694	433573	439570	437560	415570	456716	433776	433776	456717	456716	495727	477713	500410	510423	512425
SiO2	69.08	72.74	70.16	69.67	71.30	70.87	70.11	69.71	68.22	74.10	69.63	69.43	68.85	66.30	62.23	72.89	71.34	68.04	56.52	66.88
TiO2	0.41	0.18	0.32	0.38	0.27	0.32	0.34	0.37	0.41	0.12	0.38	0.45	0.46	0.74	0.83	0.23	0.26	0.46	0.86	0.66
Al2O3	15.39	14.83	15.17	15.36	14.63	15.04	15.57	15.53	15.54	14.30	15.21	15.32	15.40	16.03	16.24	14.57	14.73	15.73	17.80	16.14
Fe2O3T	2.80	1.33	2.32	2.60	2.19	2.26	2.57	2.59	2.93	1.26	2.59	2.92	2.97	4.01	5.54	1.67	1.94	3.27	5.96	2.02
Fe2O3	1.35	0.69	1.17							0.62	1.18	1.30	1.27			0.63	0.94			
FeO	1.31	0.58	1.04							0.58	1.27	1.46	1.53			0.94	0.90			
MnO	0.05	0.03	0.05	0.05	0.05	0.04	0.03	0.05	0.06	0.04	0.05	0.06	0.06	0.08	0.13	0.04	0.04	0.06	0.10	0.05
MgO	1.15	0.55	1.00	0.99	0.81	0.84	0.77	0.94	1.09	0.27	1.02	1.15	1.23	1.74	2.54	0.44	0.54	1.34	3.22	2.05
CaO	3.34	1.77	2.63	3.03	2.45	2.64	2.95	3.03	3.29	1.46	3.14	3.31	3.41	4.10	4.50	2.14	2.50	3.21	7.42	6.89
Na2O	3.97	3.73	3.83	3.89	3.55	3.82	4.05	4.02	3.81	3.39	3.63	3.71	3.74	3.96	3.82	3.33	3.57	3.79	3.37	3.71
K2O	3.13	4.22	3.34	2.98	3.81	3.17	2.81	2.85	3.05	4.74	3.16	3.01	2.76	2.21	3.12	3.74	3.38	2.97	3.36	0.54
P2O5	0.15	0.06	0.11	0.14	0.10	0.11	0.11	0.13	0.14	0.05	0.12	0.16	0.16	0.31	0.32	0.08	0.09	0.17	0.31	0.25
S	0.01	0.01	0.01	0.01	0.01	0	0.01	0	0.01	0.03	0.01	0.01	0.01	0.01	0.01	0.01	0.01	0.01	0.13	0.01
LOI	0.84	0.98	1.44	1.03	1.14	0.90	1.07	1.05	1.26	0.78	0.74	0.85	1.19	0.77	1.03	0.82	0.98		1.14	0.89
TOTAL	100.17	100.37	100.26	100.36	100.56	100.24	100.63	100.51	100.05	100.47	99.54	100.21	100.07	100.26	100.29	99.85	99.28	99.05	100.18	100.08
Sc	6	3	5	5	4	4	4	5	6	3	5	6	6	9	37	3	3	7	19	12
V	39	12	26	31	26	32	28	36	39	3	34	40	42	70	110	10	16	46	122	69
Cr	8	2	5	6	6	6	7	7	7	1	5	7	7	17	14	1	1	7	24	15
Ni	5	1	2	<1	1	<1	<1	<1	1	<1	2	4	3	9	6	<1	1	4	15	6
Cu	2	3	4	<1	1	<1	3	<1	1	4	2	6	4	7	39	1	7	3	28	1
Zn	40	23	45	46	47	40	40	46	44	36	51	64	64	88	104	49	47	50	71	32
Ga	20	19	19	20	20	20	21	20	20	17	19	20	20	21	21	18	19	18	20	17
Rb	104	121	101	93	127	111	77	81	89	183	100.4	99	90	97	99	122	101	83.9	72.9	18
Sr	775	515	645	737	826	649	718	692	718	183	681	620	615	596	634	448	467	671	1231	1001
Y	9	5	7	9	9	7	8	9	10	15	8.7	9	9	14	24	8	8	10.7	20.2	29
Zr	157	92	135	151	132	143	165	161	150	91	158.5	151	161	199	114	149	148	154.9	177.4	132
Nb	8	6	7	10	10	10	11	10	10	17	8.93	9	9	15	21	7	8	8.46	8.75	18
Cs				2	3	2	<1	1	3		2.06			1	2			2.27	1.55	<1
Ba	805	735	730	801	795	786	722	732	895	560	817	785	550	622	928	905	720	776.1	1106	122
La	43	21	35	33	321	28	32	29	28	28	39.49	43	46	50	29	37	36	37.98	34.29	65
Ce	84	42	72	81	80	71	74	72	74	62	74.95	88	98	104	84	74	74	73.45	78.37	179
Pr				5	6	5	7	5	5		8.07			11	11			8.29	9.95	19
Nd	26	14	20	31	33	28	25	28	31	18	27.63	28	30	44	51	20	18	29.05	38.8	92
Sm											4.24							4.67	7.18	
Eu											1							1.17	1.76	
Gd											2.48							3.02	5.18	
Dy											1.54							2.01	3.63	
Er											0.77							0.94	1.86	
Yb											0.76							0.88	1.7	
Lu											0.11							0.13	0.26	
Hf											4.06							3.86	4.3	
Ta											0.75							0.75	0.6	
Pb	15	21	16	18	21	19	13	14	15	31	19.9	21	21	22	23	25	21	15.9	13.3	9
Th	14	14	14	13	17	13	10	10	11	21	11.63	13	15	14	15	17	14	9.78	6.98	12
U	3	2	2	1	4	1	1	1	1	5	1.42	1	2	1	2	2	1	1.73	2.52	2

APPENDIX H

Geotectonic constraints on magma generation in subduction zones

H.1. A general physical model

Although petrogenetic models are many and varied (see Tatsumi & Eggins 1995 for summary), the consensus view is that 'typical' arc magmas (i.e. basaltic-andesite) are generated by melting of the underlying mantle wedge, as induced by influx of aqueous fluid and/or hydrous melt (the 'subduction component') derived from the subducting oceanic lithosphere (Pearce & Peate 1995; Tatsumi & Eggins 1995). This is a multi-stage process, the key aspects of which are highlighted in Figure H.1. Dehydration of the descending slab (including any sediment veneer) by a series of progressive devolatilisation reactions occurs beneath the forearc at shallow depths (generally <60 km), releasing LILE- and LREE-enriched fluids, which subsequently infiltrate and metasomatise the overlying mantle wedge. In rare cases of enhanced heat flow in the sub-forearc mantle, or subduction of young, hot crust, the sediment and/or metabasaltic component of the subducted lithosphere may actually melt rather than evolve aqueous fluid (see below). However, although the derivative silicate liquid may interact with the overlying mantle wedge, generally low temperatures in the shallow mantle wedge prohibit direct peridotite fusion. Instead, the newly formed hydrous, enriched peridotite layer becomes mechanically coupled to the slab (now effectively anhydrous), and is dragged deeper into the mantle with continued subduction, ultimately encountering several important pressure-sensitive dehydration reactions. The first of these occurs at ~60 km and 600°C, corresponding to the breakdown of serpentine. The re-release of aqueous fluids by this reaction is not expected to trigger melting in the overlying forearc wedge, except where anomalously elevated isotherms occur in the sub forearc mantle. In this case boninitic magmas may form, to be erupted in unusually near-trench settings (see below). However, liberation of fluids by amphibole ± chlorite decomposition at ~100-110 km depth instigates hydrous partial melting at the base of the mantle wedge, as these fluids percolate upwards into hotter mantle and encounter the 1000°C isotherm (Figure H.1). The partially-melted mantle diapirs formed by this process subsequently rise from the melting zone upwards through the mantle wedge ('melting column'), undergoing further decompression melting, until their ascent is arrested near the asthenosphere/lithosphere transition. Here, partial melt segregates from residual depleted mantle, some of which ultimately erupts, forming the predominant trench-side volcanic chain of island/continental arcs.

The peridotite solidus is also exceeded above the subducting oceanic lithosphere at ~200 km depth by the dehydration of phlogopite in the hydrous peridotite layer, resulting in the formation of another, considerably deeper partial melting zone in the mantle wedge (Tatsumi & Eggins 1995) (not shown in Figure H.1). Diapirs initiated from here may become stalled at a greater depth in the melting column, as the rheological asthenosphere/lithosphere boundary is thought to coincide with a particular geotherm, and be deeper on the back-arc side of the volcanic arc.

As a consequence, melt segregation occurs at deeper levels and at lower melt fraction. Partial melts tapped from these arrested diapirs migrate into the overlying lithosphere and engender a second, back-arc side volcanic chain in the arc. The magmatic products erupted from these edifices are generally volumetrically subordinate to those of the trench-side chain (Tatsumi & Eggins 1995).

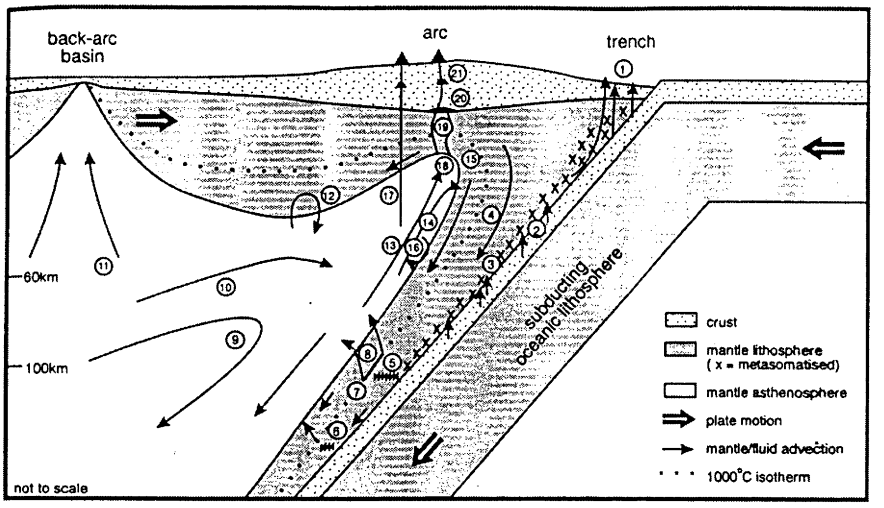

Figure H.1. Diagrammatic summary of the main processes (numbered) involved in generating arc magmas, as discussed in the text (taken from Pearce & Peate 1995). These are:

Slab dehydration and melting 1. Fluid loss via accretionary prisms and serpentinite seamounts. 2. Dehydration and/or partial melting of the subducted oceanic slab and sediment.

Transport of subduction component 3. Hybridisation of subduction component and down-dragged mantle wedge. 4. Slab-induced downward drag of hybridised mantle. 5. Release and lateral migration of aqueous fluids by amphibole breakdown. 6. Release of aqueous fluids by breakdown of other hydrous phases at greater depth. 7. Initiation of hydrous mantle melting at ~1000°. 8. Migration of small volume partial melts into the base of the melting column.

Mantle source processes 9. Slab-driven 'corner flow' of mantle into the mantle wedge. 10. Replenishment of the melting column by mantle advection. 11. Mantle source depletion by melt loss in the back-arc region. 12 Mantle source enrichment by delamination of sub-continental lithosphere.

Melting column processes 13. Buoyancy-driven mantle counter-flow. 14. Decompression mantle melting. 15. Separation of residual mantle from the melting column. 16. Column depletion by re-incorporation of residual mantle. 17. Selective tapping of the mantle column.

Lithosphere-melt interactions 18. Melt segregation at the base of the lithosphere. 19. Interaction within mantle lithosphere. 20. Magma assimilation-storage-homogenisation at the base of the crust. 21. Assimilation-fractional crystallisation at shallower crustal levels (modified after Pearce & Peate 1995).

H.2. Chemical consequences for arc-derived magmas

Many of the diagnostic chemical features of arc magmas, especially the signature LILE enrichment and HFSE depletion, reflect the preferential transfer of relatively 'mobile' (i.e. fluid- or melt-soluble) elements, such as the LILE and, to a lesser extent, the LREE, into the

mantle wedge source region by the slab-derived subduction component. Although the less mobile HFSE and HREE are retained in the oceanic lithosphere, this alone cannot explain the pronounced depletion of these elements, and especially the low HFSE/HREE, compared to N-MORB. Instead, this is reconciled by removal of compatible elements from the source peridotite by prior extraction of basaltic magma (Woodhead *et al.* 1993; Pearce & Peate 1995). Given that the melting column is thought to be replenished during subduction by asthenospheric mantle advection from the back-arc region (see Figure H.1), this prior melting event has conceivably occurred during contemporary back-arc MORB-like magmatism (Woodhead *et al.* 1993). This is compatible with the fact that the most strongly HFSE-depleted magmas are erupted from oceanic arcs with actively spreading back-arc basins (Woodhead *et al.* 1993). The distinctive Ti depletion in high-K arc magmas relative to the REE, manifested by low Ti/Eu values, has been attributed to – (1) presence of a residual titanate phase such as rutile in the melting zone, (2) the diminished capacity of aqueous fluids to transfer TiO_2 at higher pressures, implying involvement of a second, higher-pressure fluid component, or (3) that the subduction component was actually a silicate melt derived from the oceanic slab, which transports Ti less effectively than the REE (Tatsumi & Eggins 1995). These models have some relevance, as low Ti/Eu values typify Caupaul high-Al gabbros, and potentially provide important constraints on the magma-genesis process.

Another important characteristic of subduction zone magmatism is the across-arc geochemical variation of erupted magmas. This is particularly with regard to the systematic increase of incompatible elements, especially K and the LILE, with increasing distance from the trench, and, therefore depth to the subducted slab. Several studies, summarised by Pearce & Peate (1995) and Tatsumi & Eggins (1995), conclude that this most likely reflects decreasing degrees of partial melting in the mantle wedge source from the trench-side to the back-arc side of volcanic arcs. Under this scenario, clinopyroxene, and possibly garnet, are not eliminated from the residue during low degrees of melting, resulting in the greater fractionation of incompatible and compatible elements observed in back-arc side arc magmas (Tatsumi & Eggins 1995). Lower melting degrees beneath the back-arc side volcanic chain plausibly results from – (a) lesser fluid flux into the mantle source by phlogopite breakdown compared to amphibole ± chlorite decomposition (Stern *et al.* 1993), and (b) deeper melt segregation in the melting column, such that decompression-induced melting of the upwelling diapir is minimised (see above).

H.3. Slab melting and the formation of adakites

Unlike most subduction-related magmas, which are derived from metasomatised peridotite, the distinctive geochemical character of adakites requires high pressure melting of a *basaltic* source, involving elimination of plagioclase in the garnet stability field (Chapter 16). Although in some circumstances possibly represented by the lower crust, the preferred source material is

the descending slab of oceanic lithosphere. This is consistent with the restriction of present day adakitic volcanism to subduction zones with abnormally high geothermal gradients, mostly where young (<25 Ma), hot oceanic lithosphere (Defant & Drummond 1990; Drummond *et al.* 1996) or spreading ridge segments (Stern & Kilian 1996) are being subducted, or where oblique convergence and/or rapid subduction rates result in high frictional stresses, as in the western Aleutians (Yogodzinski *et al.* 1994). Such conditions are conducive to fusion of the downgoing slab at the hydrous tholeiite solidus *before* dehydration and loss of fluids to the overriding mantle wedge (see above). Slab melting is also favoured at the inception of subduction into warm, pristine mantle, before significant depression of geotherms by the foundering oceanic lithosphere (Peacock *et al.* 1994), as has been invoked for adakites in western Mindanao (Philippines) (Sajona *et al.* 1993). The optimum P-T regime for significant adakite generation lies between ~70-100 km depth at 700-800°C, consistent with the location of the subducted oceanic plate ~70 to 90 km beneath most modern adakitic volcanoes (Martin 1999). Adakite magmas may form at even shallower depths (~60 km), though this requires even greater geothermal gradients along the subducted slab, such as were more likely achieved in the Archaean (Martin 1999).

It is emphasised that the conditions necessary for adakite genesis are only rarely realised in modern subduction zones, accounting for the comparative paucity of adakitic volcanoes in contemporary arcs. Hence, the occurrence of adakitic plutons in the GRC provides important thermodynamic constraints on the palaeo-subduction zone in this area.

H.4. Formation of boninites

H.4.1. General models

The localisation of contemporary boninitic magmatism to near-trench regions of oceanic arcs suggests that the requisite physiochemical conditions for boninite formation are only attainable in the shallow mantle wedge above a subducted slab of oceanic lithosphere. However, boninites are by no means ubiquitous in ancient or modern arc settings, indicating that these conditions are peculiar even in subduction zone environments. The geochemistry of boninites is also paradoxical, in that although enriched incompatible element concentrations suggest small degrees of melting of a relatively fertile mantle source (i.e. similar to that of MORB), Cr-rich spinel, high Ni content and low CaO/Al_2O_3 imply high degrees of melting from a refractory source (Keleman 1995). To accommodate these aspects, two models for boninite petrogenesis have developed.

MODEL 1: Melting of refractory peridotite (Crawford *et al.* 1989)

Underpinned by experimental (e.g. Van der Laan *et al.* 1989) and geochemical constraints, this model suggests derivation of boninitic magmas by low pressure partial melting (< 50 km depth)

of a refractory mantle peridotite source, more depleted than the residue from MORB generation, that has been selectively enriched in LILE, LREE, Na and Zr (Crawford *et al.* 1989). Imperative to this petrogenetic scenario are – (1) substantial ingress of aqueous fluid, supplied by decomposition of hydrous minerals in the subducted slab, into the shallow mantle source, to depress the refractory peridotite solidus, transfer the enriching components and initiate melting, and (2) unusually high temperatures (1100-1350°C) in the uppermost mantle column to permit melting of the metasomatised upper mantle peridotite. The source peridotite has either been depleted by prior melting events in the back-arc or extraction of basaltic or first stage boninitic magma in the forearc wedge. Rather than an aqueous fluid, for some boninitic magmas the enriching agent is thought to be a partial melt of subducted sediment, as is proposed for the Setouchi lavas (see below), or of the downgoing basaltic crust itself (Pearce *et al.* 1992). The spectrum of primary boninite compositions is attributed to a complex interplay between the degree of depletion of the source peridotite, the nature and amount of the fluxing fluid and the temperature at the melting site (Crawford *et al.* 1989).

Most problematic with this model is the attainment of the anomalously high temperatures necessary to melt refractory peridotite at unusually shallow levels, since geophysical modelling predicts ambient temperatures well below 700°C in the forearc wedge region of 'normal' subduction zones (see Tatsumi & Eggins 1995). The necessary extra heat flux has been variously attributed to – (1) consumption of newly borne, hot oceanic lithosphere into thermally-undisturbed mantle at the earliest stages of subduction (Meijer 1980; Tatsumi 1982). This leads to abnormally shallow slab dehydration, followed by generation of arc tholeiites and ultimately boninites, (2) heat conduction by an ascending MORB-source mantle diapir at the inception of backarc spreading, resulting in contact-melting of hydrated depleted sub-arc peridotite (Crawford *et al.* 1989), or (3) subduction of an active spreading ridge trending parallel to the trench of an intra-oceanic island arc, promoting extensive fusion of the shallow sub-arc mantle to yield the spectrum of boninite compositions (Crawford *et al.* 1989).

MODEL 2: Melt-peridotite reaction (Kay 1978, Keleman 1990, 1995)

Instead of melting previously depleted, and then metasomatised, peridotite, boninitic magmas may also form by hybridisation between ascending liquids and upper mantle peridotite (Kay 1978; Keleman 1995). The liquid end-member could be hydrous slab-derived magma (i.e. adakite) or basaltic melt derived by small degrees of peridotite melting at greater depth. Under the former scenario, felsic, incompatible element-rich slab melts migrating through the mantle wedge by porous flow acquire high MgO and Ni due to olivine dissolution and/or reaction to orthopyroxene, eventually arriving at boninite-like compositions; these are hydrous but olivine saturated and in equilibrium with depleted peridotite. Production of boninitic magmas by this mechanism has been verified experimentally (e.g. Carroll & Wyllie 1989), and obviates the

necessity for a shallow mantle heat source, though thermal conditions during subduction must still be favourable for slab fusion.

Phase relations suggest that high pressure basaltic melts must also react with peridotite during ascent, since these liquids become increasingly pyroxene-undersaturated during decompression (Keleman 1990). This induces assimilation of orthopyroxene from the shallow mantle wedge, increasing the silica content of the melt and driving it towards orthopyroxene-saturated (i.e. andesitic) compositions. Decreasing liquid mass with temperature decrease is invoked to explain the incompatible element abundance and greater H_2O enrichment contents of the hybridised high-Mg melt (Keleman 1995).

A combined slab melt/basalt-wallrock interaction model for boninite formation is envisioned for high-Mg andesites of the western Aleutian arc (Yogodzinski *et al.* 1994), involving three stages. Initially, silicic adakitic slab melts, formed at ~100 km depth, infiltrate previously hydrated peridotite to produce an enriched mantle source. The subsequent upwelling of this material into hotter parts of the asthenospheric mantle column instigates partial melting and the formation of primitive arc basalt magma at high temperatures (~1200°C). This in turn becomes ponded at the base of the crust, as a result of compressional stresses within the overlying arc, where it reacts with shallow, depleted peridotite to generate small volumes of relatively siliceous, high-Mg magma. Ultimately, this gains ingress to the crust and erupts as boninitic andesite. Note however, that the adakitic ingredient in the western Aleutians boninites results in markedly higher Na_2O and Sr than the GRC hornblende diorites, casting doubt on the operation of slab melt-mantle hybridisation processes for formation of the parental HMD magma.

H4.2. Formation of the Setouchi boninites

Boninitic lavas of the Setouchi Volcanic Belt were erupted along a narrow, 600 km-long belt during a shortlived magmatic event at ~13 Ma (Tatsumi & Maruyama 1989). This was related to incipient subduction of the Shikoku basin (of the Philippine sea plate), formed by sea-floor spreading processes slightly earlier (25-17 Ma), beneath the Eurasian plate, to form the SW Japan arc. Significantly, volcanism was broadly contemporaneous with the opening of the Japan Sea by back-arc spreading, which, involving upwelling of hot MORB-source depleted mantle, would have imparted elevated upper-mantle geotherms in the vicinity of the arc. Subduction of the young, hot oceanic lithosphere, combined with injection of MORB-source asthenosphere into the back-arc, therefore contributed towards an enhanced thermal gradient in the sub-fore-arc mantle wedge. As a result, the solidus for hydrous, depleted peridotite was exceeded (~1000°C) at abnormally shallow depths and the boninitic Setouchi magmas were formed. Note that Setouchi lavas require a lower degree of partial melting than other boninites to account for the marginally higher Ti, K_2O and LILE. Enriched Pb-Sr-Nd isotopic compositions require the involvement of an evolved crustal component in Setouchi magma-genesis, which is best

modelled as a direct partial melt from subducted pelagic sediment (Shimoda *et al.* 1998). This tectonic scenario may have relevance for the GRC, given the remarkable similarity between Setouchi boninitic magmas and the HMD composition.